Biophysical studies of metal chelate binding by HSA: Towards an understanding of metallodrug transport



By Sheldon Sookai

MSc (*cum laude)* University of KwaZulu-Natal

A thesis submitted to the Faculty of Science, University of the Witwatersrand, Johannesburg, in fulfilment of the requirements for the degree of Doctor of Philosophy

July 2023

Declaration

I declare that the work presented in this thesis was carried out exclusively by me, unless stated otherwise, under the supervision of Professor Orde Q. Munro. It is being submitted for the Degree of Doctor of Philosophy in the University of the Witwatersrand, Johannesburg. It has not been submitted before for any degree or examination in any other University.



Sheldon Sookai
July 2023

Work contribution of each Chapter:

Chapter 2 **Gold(III) chelates: Dual mode inhibitors of human Topoisomerase II and their complexities of binding to human serum albumin.**

Sheldon Sookai[a], Matthew. P Akerman[b], Olga Færch[c], Yasien Sayed,[d] and Orde Q. Munro*,[a]

O. Q. M. and S. S. co-designed the study. S. S. synthesised and characterised the ligands, carried out the spectroscopy, X-ray crystallography collated the thermodynamic data, and performed the molecular simulations. O. F under the supervision of Y. S performed the ITC experiment and analysis. NCI-60 and topoisomerase data and analysis was obtained from M. P. A. The final data analysis was performed by S. S. The manuscript, final data interpretation and figures were written and produced by S. S under the supervision of O. Q. M.

Chapter 3 **Human serum albumin binds chiral cytotoxic Au(III) chelates as fully intact complexes with unique thermodynamics**

Sheldon Sookai,[a] Matthew P. Akerman[b] and Orde Q. Munro*,[a]

O. Q. M. and S. S. co-designed the study. S. S. synthesised and characterised the ligands, carried out the spectroscopy, initial X-ray crystallography and collated the thermodynamic data. NCI-60 data and analysis was obtained from M. P. A. The final data analysis was performed by S. S. and O. Q. M, who also completed the final X-ray

crystallography section The manuscript and figures were written and produced by S. S and O. Q. M.

Chapter 4 **Spectroscopic and computational study of the interaction of Pt(II) pyrrole-imine chelates with human serum albumin.**
Sheldon Sookai [a] and Orde Q. Munro*[a]

Chapter 5 **Bioimaging Pt(II) Schiff base chelates**
Sheldon Sookai,[a] Shanen Perumal [b] Mandeep Kaur [b] and Orde Munro *[a]

O. Q. M. and S. S. co-designed the study. S. S. synthesised and characterised the ligands, carried out the spectroscopy, X-ray crystallography, calculated the apparent quantum yields, ligand to HSA binding and performed the TD-DFT simulations. S. S. did the final data analysis. These sections of the manuscript and figures were written and produced by S. S under the supervision of O. Q. M. The MTT assay, fluorescence imaging as well as interpreting and writing up the section under the supervision of S.P and M. K

Chapter 6 **Complexities of the interaction of Ni(II), Pd(II) and Pt(II) pyrrole-imine chelates with human serum albumin**
Sheldon Sookai[a] and Orde Q. Munro*,[a]

O. Q. M. and S. S. co-designed the study. S. S. synthesised and characterised the ligands, carried out the spectroscopy, collated the thermodynamic data, and performed the initial molecular simulations. O. Q. M. did the final data analysis, X-ray crystallography, and final molecular simulations. The initial manuscript was written by S. S.; the final manuscript and figures were written and produced by O. Q. M.

Abstract

Human serum albumin (HSA) is the most abundant blood protein, transporting many exogenous compounds including clinically deployed and investigational drugs that are generally organic in nature. HSA may largely influence the pharmacokinetics and pharmacodynamics of these drugs. Therefore, studying their interactions with HSA is vital in progressing drug development. In this thesis we present work on the synthesis and characterisation of five Schiff base bis(pyrrolide-imine) ligands that were metalated with either Au(III) (Chapters 2 and 3) or Pt(II) (Chapters 4 and 5). One of the ligands H_2L1 was further metalated with Ni(II) and Pd(II) (Chapter 6).

In *Chapters 2 and 3* focus on a patented class of anti-cancer bis(pyrrolide-imine) Au(III) Schiff base chelates. Three Au(III) chelates were synthesized in Chapter 2 and underwent National Cancer Institute (NCI)-60 cytotoxic screening. Among them, **AuL1** and **AuL3** underwent full-five dose testing and recorded GI_{50} values of 7.3 μM and 11.5 μM, and IC_{50} values of 15.7 μM and 30.9 μM, respectively. **AuL1** was tested further and found to be an interfacial poison of topoisomerase II at 0.5–5 μM and a catalytic inhibitor at 50 μM. In *Chapter 3*, two chiral tetradentate cyclohexane-1,2-diamine-bridged bis(pyrrole-imine) Au(III) complexes were reported, both of which were found to be cytotoxic in the NCI-60 screen. The chiral Au(III) chelates had a different mode of action compared to **AuL1**. Hierarchical cluster analysis suggest that their mode of action is similar to that of taxol. All five Au(III) chelates bound to HSA with moderate affinity (10^4–10^5 M^{-1}) and minimally perturbed the structure of the protein. This highlights the potential for the Au(III) complexes to be transported by the HSA-mediated pathway.

Chapters 4 and 5 focused on the synthesis of novel and previously reported Pt(II) Schiff base chelates to spectroscopically and computationally study their interaction with HSA and elucidate if the chelates could act as theranostic agents. It was found that switching the linking bis(imine) carbon linkage altered the binding affinity of the complex. However, the Pt(II) ion ensured that all three Pt(II) chelates preferred binding to Sudlow's site II of HSA. The data was corroborated by molecular docking simulations and ONIOM calculations. Only **2** was found to be cytotoxic when irradiated with UV light but was found to act as a photosensitizer rather than a theranostic agent.

Chapter 6 investigated the influence of d^8 metal ions (Ni(II), Pd(II) and Pt(II) within the same ligand scaffold (H_2PrPyrr) binding to HAS, which was investigated by steady state fluorescence quenching. The affinity constants, K_a, ranged from ~3.5×10^3 M^{-1} to ~1×10^6 M^{-1} at 37 °C, following the order Pd(PrPyrr) > Pt(PrPyrr) > Ni(PrPyrr) >

H_2PrPyrr. The Pd(II) chelate was prone to hydrolysis and had a unique binding mode which we attribute to the unusually high binding affinity. The complexes uptake is enthalpically driven, hinging mainly on London dispersion forces.

In summation, twelve metal complexes were successfully synthesized, of which 11 bound to HSA with a moderate binding affinity. The Au(III) chelates preferred Sudlow's site I, while the Pt(II) chelates preferred Sudlow's site II. Overall, the metal complexes bound fully intact to HSA.

Preface

The thesis submitted differs from the ‘classical’ format or a ‘publication’ format but is rather a hybrid of both formats. The thesis begins with a detailed overarching introduction that highlights and summarises literature in the fields covered, within each of the thesis chapters. The introduction is written in the typical thesis format.

Due to the large volume of reported work in the thesis, the document is made up of two volumes, the main thesis, and the supplementary data to the main thesis.

Chapters 2–5 are written in the Royal Society of Chemistry (RSC) journal template. This is done because the chapters are close to being ready for submission to its respective journals. However, we are still waiting for approval from the corresponding authors. Chapter 6 has been submitted to the journal *ChemistryEurope*, which uses the European Journal of Chemistry (EJC) template and is currently under review.

Each chapter has an abstract, introduction, results and discussion, conclusion, and appropriate referencing for the journal we intend to submit the final manuscript to. For the multi-authored papers/chapters, each authors contribution has been acknowledged. The corresponding supplementary material for each chapter is in the second volume of the thesis and is labelled appropriately. The supplementary data contains the materials and methods along with supporting data for each chapter.

Finally, the thesis ends with an overall conclusion of each body of work along with experiments that could advance the studies in the future (i.e., future work).

Acknowledgements

I would like to express my sincere gratitude to everyone who made this thesis possible.

First and foremost, Professor Orde Munro.

Prof, your unwavering support in the supervision of this thesis and the monumental influence you exerted in getting the manuscripts journal ready has been greatly appreciated. There are not enough words to express the impact you've had on my scientific growth. Also, your creative capabilities are some of the most enviable I've seen to date, so thank you for inspiring me to aim higher.

I would also like to acknowledge the most incredible lab mates I've ever known; Rufaro, Mark, Matthew and Monica.

Frankly, I empathise with scientists who have not experienced the sheer privilege of working through countless nights and making merry memories with you talented folk. I am utterly grateful for all the help and all the laughs.

My heartfelt appreciation also goes out to Mia and Prof Sayed.

Mia and Prof Sayed, thank you both for all the effort and heart you poured into the ITC experiments, and casting your expert eyes over the research. I could not have asked for a better or more proficient team to have in my corner.

I would also like to convey gratitude to my family.

To my mom, dad and my dearest brother; I am still in awe of the encouragement you all have shown me over the years.

And many, many, many thanks to my best friend and darling Uraisha.

My sweet Rai, you know first-hand the blood, sweat, tears, and heart palpitations that went into this thesis. Thank you for your understanding, for your love and unwavering confidence in me. Those "late night lab calls" really kept me going.

I would be remiss if I did not acknowledge the ultimate research assistants, my dogs. Bolt, Cassie and Mr. Bunni Bonanza himself, our wrestling matches and your occasional demand for belly rubs kept me sane.

And lastly, I would like to express my appreciation to the NRF.

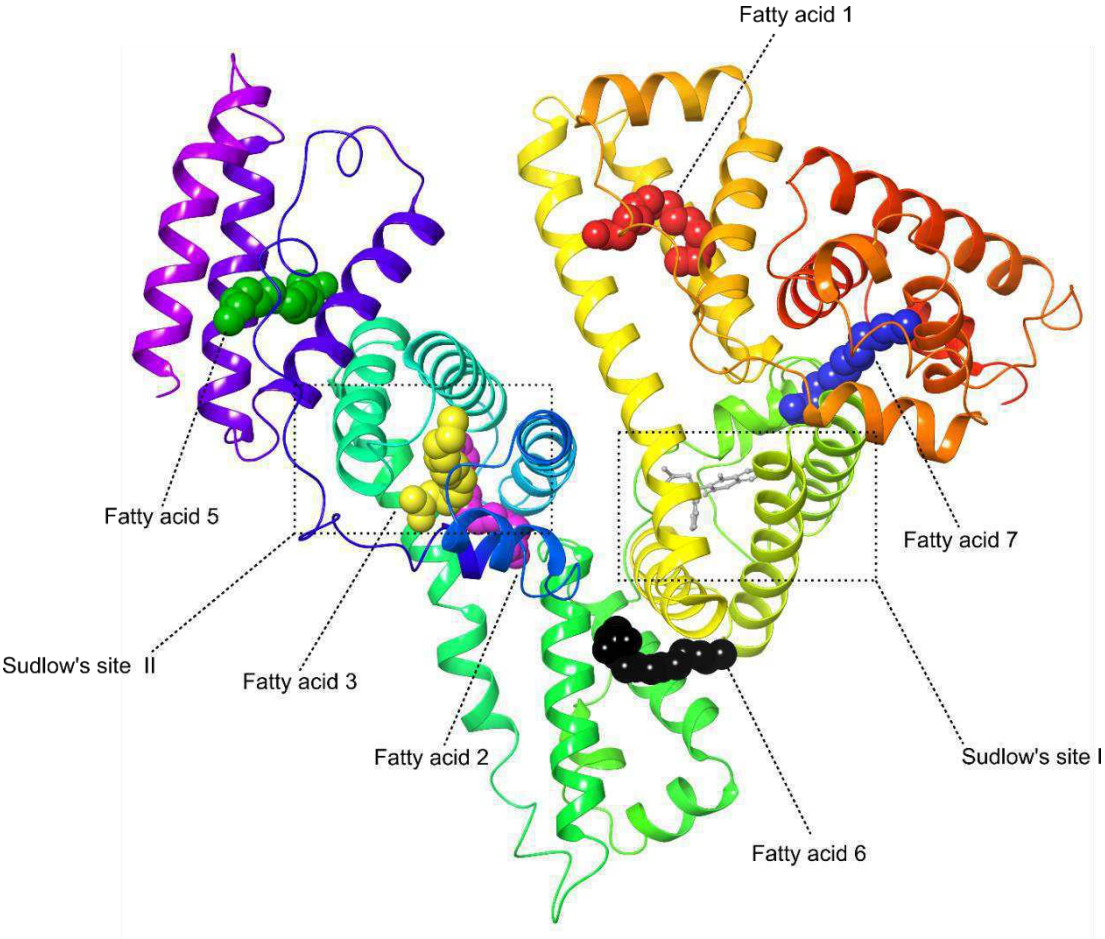
For all the financial support, without which, none of this would have come to fruition

Table of Contents

Declaration i
Abstract iii
Preface v
Acknowledgements vi
Chapter 1 Introduction 1
1.1 Preface 2
General background 2
Organisation of material 3
1.2 An introduction to cancer biology 4
Cyclin-dependent kinases (CDKs) 6
The origin of cancer 6
Role of oncogenes 6
Tumour suppressor genes 6
Triggering of apoptosis 7
Alternative triggers of apoptosis 9
Cancer cell survival mechanisms 9
1.3 DNA 10
DNA structure 10
DNA intercalation 10
DNA topoisomerase I 12
Mechanism of Top1 DNA relaxation 14
Top1 poisons 15
Mechanism of Top2-mediated DNA decatenation 17
Inhibition of Top2 activity 19
Catalytic inhibitors 19
Top2 poisons 21
1.4 Brief survey of selected anticancer metallodrugs 21
FDA-approved metal-based chemotherapeutics 21
Mechanism of action: classical anti-cancer drugs 23
Non-classical anticancer platinum(II) drugs 24
Theranostic platinum-based compounds 24
Cytotoxic theranostic platinum-based complexes 25
Why are Pt(II) chelates effective theranostic agents? 26
Gold chemistry — a brief introduction 26
Gold(I) complexes as potential anticancer drugs 27
Anticancer activity of Au(III) complexes 28

1.5 Human serum albumin 37
Fatty acid binding to HSA 38
Sudlow's site I 38
Sudlow's site II 40
Additional drug-binding sites 42
The binding of anticancer drugs by HSA 42
Platinum complexes 42
Copper in medicine 50
Uptake of Cu-containing prodrugs by HSA 51
Dipeptide (glycylglycine) sulfasalazine 54
Ruthenium complexes binding to HSA 57
Palladium complexes binding to HSA 64
Pd(II)-8-Amininoquinoline 69
Summary of palladium complexes 72
Aims and objectives 76
List of specific objectives 76
Project 1 76
Project 2 77
Project 3 77
References 78
Chapter 2 Gold(III) chelates: Dual mode inhibitors of human Topoisomerase II and their complexities of binding to human serum albumin 88
Chapter 3 Human serum albumin binds chiral cytotoxic Au(III) chelates as fully intact complexes with unique thermodynamics 112
Chapter 4 Spectroscopic and computational study of the interaction of Pt(II) pyrrole-imine chelates with human serum albumin 126
Chapter 5 Bioimaging Pt(II) Schiff base chelates 141
Chapter 6 Complexities of the interaction of Ni(II), Pd(II) and Pt(II) pyrrole-imine chelates with human serum albumin 148
Chapter 7 Conclusion 165
7.1. Conclusion of the Au(III) work 165
7.2. Conclusion of the platinum(II) work 166
7.3. Conclusion of the d^8 metal chelate study 167
7.4. Future work 168

Chapter 1 Introduction



1.1 Preface

General background

According to the World Health Organization (WHO), cancer is the leading cause of death globally, accounting for 10 million cancer-related deaths in 2020.[1] However, data on cancer deaths has been affected by the emergence of the COVID-19 pandemic, making it less reliable.[1] The most prevalent types of cancer are breast cancer in females, lung cancer, colon and rectal cancer, and prostate cancer in males. Developing countries are disproportionately impacted by cancer due to an aging population and population growth.[2]

Alarmingly, in 2018 it was estimated that there were 18.1 million new cases of cancer, with projections indicating that this burden will rise to 29 million new cases by 2040.[2] This is more than five decades after the discovery of cis-diamminedichloroplatinum(II) (cisplatin),[3] one of the leading cancer drugs and at a time when there are many available chemotherapeutic agents.[4] However, a significant limitation of most currently available chemotherapeutic agents is their inability to only target cancer cells, leading to severe toxic side effects and drug resistance in cancer cell lines.[5–7] Therefore, the search for new and improved chemotherapeutic agents is of utmost importance. Given that platinum(II) is the only FDA-approved metal ion complex for cancer treatment, and that Au(III) complexes are isoelectronic (d^8) with platinum(II) and form similar square planar tetradentate structures as cisplatin,[8] it is a logical choice to investigate novel metal complexes incorporating both Pt(II) and Au(III) metal ion centres.

The first recorded use of gold in medicine dates back to 2500 BC in China, where it was used in the pursuit of longevity.[9] However, the first reported use of gold in modern medicine occurred in the 1890s with the gold complex $K[Au(CN)_2]$.[10] This complex was initially reported to have anti-tubercular activity but was later found to be toxic.[10] Currently, two gold complexes, auranofin, and myocrisin are used in medicine as antiarthritic drugs and are undergoing investigation as anticancer therapeutics in clinical trials.[11] There are several reported Au(I) and Au(III) complexes that have the potential to be promising chemotherapeutic agents, but most are in the early stages of investigation.[12] It is worth noting that the high oxidation number of Au(III) has limited literature compared to isoelectronic (d^8) Pt(II) based complexes. This is because Au(III) is readily reduced to Au(I) or Au(0) and often forms $[AuCl_2]^-$ or $[AuCl_4]^-$ highly insoluble salts. Within the cell medium under physiological conditions, Au(III) may be reduced by cellular reductants such as glutathione.[13] These limitations of Au(III)

instability can be overcome by using the appropriate organic ligand framework, such as strong σ-donors, like tetradentate N-donor ligands, which can stabilise the Au(III) ion.

Platinum(II) is a logical choice for the rational design of anticancer drugs due to the success of cisplatin, carboplatin, and oxaliplatin, which are widely administered and successful anticancer clinical drugs.[14] These compounds have the ability to bind to biomolecules and hydrolyse quickly, making them active by targeting DNA. Novel research is being conducted on Pt(II) complexes and their potential as theranostic agents, which requires the metal centre to be chelated with strong σ-donor ligands to prevent non-specific interactions with biomolecules, and therefore, to increase specific cytotoxicity. The imaging aspect of the Pt(II) chelates requires (i) large Stokes shifts, (ii) high quantum yields, (iii) photosensitivity, and (iv) a two-photon absorption cross-section.

It is well-established that serum proteins can impact the efficacy of drugs. One class of these proteins is the serum albumins, which belong to the same family as α-fetoprotein and vitamin D binding protein. These proteins are relatively large and highly soluble, and, unlike α-fetoprotein and vitamin D binding protein, are non-glycosylated.[15] In humans, the serum albumin is known as human serum albumin (HSA), which is synthesised in the liver and is the most abundant protein in the circulatory system, with concentrations around 600 μM.[16] HSA serves various functions in the human body, including maintaining a balanced physiological pH, regulating the osmotic pressure of plasma, and transporting endogenous and exogenous compounds to target organelles.[15,16] One of its most intriguing functions is its ability to reversibly bind to a wide variety of exogenous and endogenous molecules, making it of interest to the pharmaceutical industry for drug development.[17] Understanding how HSA binds to therapeutic small molecules is crucial for the design of new drugs, as small molecules can be designed to either not bind to HSA or bind to it and utilise its transporting ability.[18]

Organisation of material

The structure of this thesis deviates from the traditional thesis format and is divided into five chapters, each of which corresponds to a separate paper that is currently under review or in the process of being submitted to a journal. The first two chapters, Chapters 2 and 3, focus on the synthesis of our previously patented bis(pyrrolide-imine) Au(III) Schiff base chelates as potential anti-cancer agents.[19] The chapters detail the synthesis of five novel Au(III) bis(pyrrolide-imine) chelates, three of which

were found to be stable and cytotoxic against the NCI-60 screen. Chapter 2 demonstrates that the most cytotoxic Au(III) chelate is a specific topoisomerase II poison and inhibitor. The Au(III) bis(pyrrolide-imine) chelates are cationic salts that target DNA by intercalating with TA nucleic acids. We also provide insight into their binding mode to HSA using various spectroscopic techniques. Chapter 3 extends the work of Chapter 2 by investigating chiral Au(III) chelates within the same family of compounds. Specifically, we demonstrate that the two chiral cyclohexyl-bridged bis(pyrrolide-imine) chelates are cytotoxic, but do not interact with DNA. We also determine their binding mode to HSA using various spectroscopic techniques. In Chapters 4 and 5, five bis(pyrrolide-imine) chelates of the isoelectronic ion Pt(II) are synthesised and characterised (two of the compounds are novel), and their theranostic properties and potential against MCF-7 tumour cells delineated. We also present photophysical data for the complexes and determine their binding mode to HSA using various spectroscopic techniques. Finally, Chapter 6 presents an in-depth study of the complexities surrounding the uptake and binding of a series of d^8 metal Schiff base chelates (Ni^{2+}, Pd^{2+}, Pt^{2+}) by HSA, uncovering the role of the metal ion in the process.

The present chapter has been organised into five primary sections. The first section provides an overview of cancer as a disease, including the various drugs that are currently available and their mechanisms of action. The second section gives an overview of gold chemistry, including its various applications. The third section provides an overview of platinum chemistry, including its applications. The fourth section presents an overview of human serum albumin (HSA) and its role in drug efficacy. And finally, the last section outlines the aims and objectives of this study.

1.2 An introduction to cancer biology

1.2.1. Introduction

The progression of the cell cycle is contingent upon two crucial occurrences: replication of the genomic DNA and segregation between daughter cells, which transpires during separate phases of the cell cycle. If a cell deviates from its normal behaviour and continues to divide without undergoing controlled cell division, it may become cancerous (Fig. 1).[20] In eukaryotic organisms, cell division is regulated by a complex network of mechanisms that ensure accuracy during the cell cycle and replication processes.

Eukaryotic organisms experience the mitotic cell cycle, which consists of two primary phases: interphase and metaphase. The entire cell cycle, including all its phases, is

depicted in Fig. 1. During the S phase of interphase, replication of the DNA is initiated, but not completed. The gap phases (G_1 and G_2) are critical periods for cell growth and regulation of the cell cycle. They represent key junctures at which the cell decides to either enter the cell cycle (G_1) and initiate the processes leading to chromosome segregation (G_2), or to enter a non-dividing state (G_0) due to intra- or extracellular signals that instruct the cell to temporarily halt proliferation (in this state the cell is considered quiescent) to differentiate, mature, or initiate apoptosis.[20]

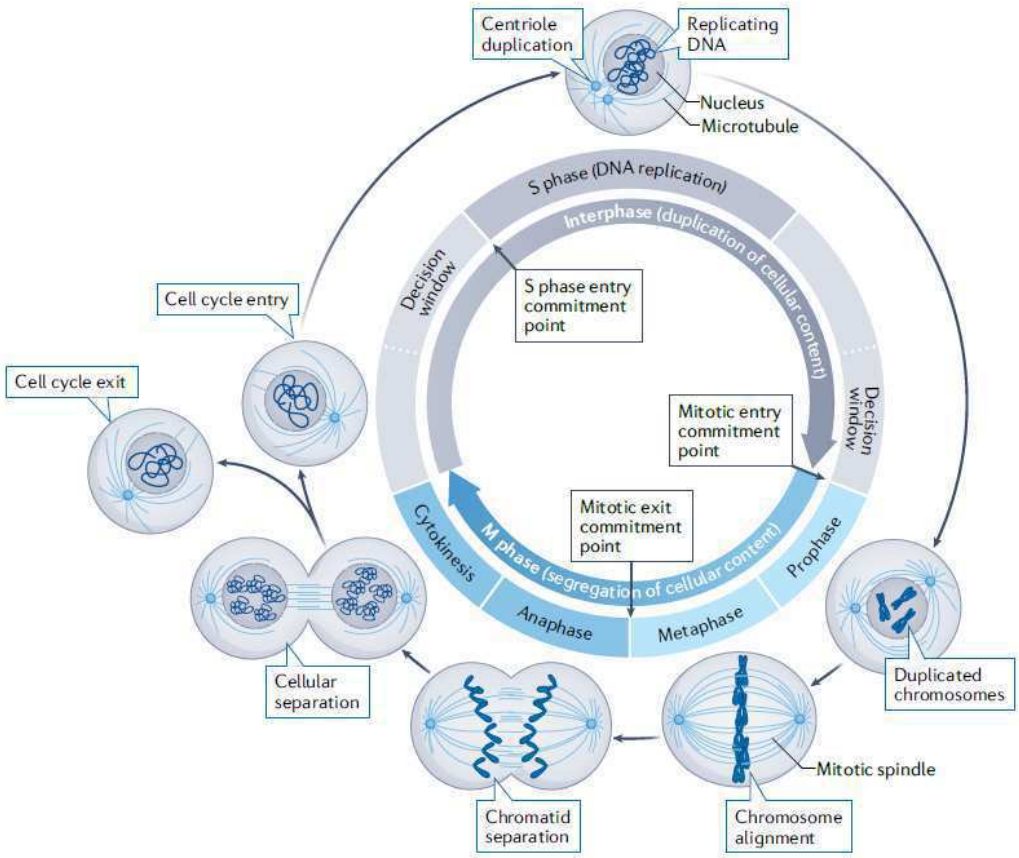


Fig. 1 Cell division cycle of the eukaryotic cell taken from Matthews *et al*.[20] Each step of the cell cycle describes the life of a cell from (i) being initially formed, (ii) dividing of the parent cell, (iii) forming of two daughter cells. The entire cell content is duplicated at the interphase and division occurs at the metaphase. DNA replication occurs at the S-phase and DNA separation happens during the metaphase (mitosis). The completion of the cell cycle occurs when there is segregation of the cellular content at the end of the metaphase (called cytokinesis). At this point, a decision is made for the cell to enter a new cycle of cell division or exit the cell cycle. The cell cycle progression is controlled throughout. A second decision window exists for the cell after the S-phase to enter or exit mitosis, and mitosis exit occurs during the metaphase-anaphase transition.

It is worth noting that the majority of cells in the adult human body exist in a non-proliferative state and must transition to G_1 to initiate DNA replication and enter the cell cycle. Following the G_2 phase, cells can enter metaphase by inducing chromatin

condensation. It is important to emphasise that metaphase serves dual functions: (i) performing mitosis, and (ii) generating two new daughter cells.[20]

1.2.2. Cyclin-dependent kinases (CDKs)

Each stage of the cell cycle is rigorously regulated by a sequence of proteins referred to as cyclin-dependent kinases (CDKs). These proteins are activated through phosphorylation by another group of proteins called cyclins, which exhibit varying concentrations during different stages of the cell cycle. The coordination of events during the cell cycle is based on the type, activity, and concentration of the CDK-cyclin complex within the cell.[20–22]

1.2.3. The origin of cancer

The origin of cancer cells arises from alterations in the cell's genome, primarily multiple mutations in genes responsible for maintaining genomic stability in healthy cells.[23] Two main gene categories have been implicated in the pathogenesis of cancer: tumour suppressor genes and oncogenes.

1.2.4. Role of oncogenes

Healthy cells possess proto-oncogenes, which serve as crucial regulatory factors and perform functions such as acting as growth factors, transmitting cellular signals, and serving as nuclear transcription factors. Mutations of proto-oncogenes alter the behaviour of the genes and modify their protein-encoding mechanisms. The altered protein structures can manifest in cancer cells as activated oncogenes, which drive cell replication and play a pivotal role in the pathogenesis of cancer. The mutations responsible for these structural changes include point mutations, RAS proto-oncogenes, and chromosomal translocations that create hybrid genes such as the Philadelphia translocation (BRC-ABL).[23,24]

1.2.5. Tumour suppressor genes

Tumour suppressor genes play a crucial role in signalling pathways that regulate cell division. A well-known example of this is the mutation in the TP53 gene, which codes for the p53 protein. When the gene is mutated, the protein loses its function, leading to increased cell proliferation and genome instability.[23,24]

In approximately 40% of patients with melanoma and 25% of patients with tumours, the regulation of the mitogen-activated protein kinase (MAPK) signalling pathway becomes impaired due to mutated proteins unable to properly regulate the pathway (Fig. 2). The MAPK pathway stimulates cellular proliferation and is composed of a cascade of proteins encoded by proto-oncogenes, including the Ras protein, which

initiates the cascade by transmitting signals received from extra-cellular growth factors. This may impact downstream transcription factors that are responsible for maintaining cellular functions such as proliferation, differentiation, and apoptosis.[25,26]

1.2.6. Triggering of apoptosis

The formation of tumours is not solely a result of uncontrolled cell proliferation, but also the reduction of apoptosis. Apoptosis is a controlled mechanism of cell death that is regulated by two signalling pathways, namely the intrinsic (also known as the mitochondrial) and extrinsic pathways.[27] The intrinsic pathway is initiated intracellularly in response to DNA damage, depleted growth factors, and oxidative stress. On the other hand, the extrinsic pathway is triggered by extracellular death receptors and has a crucial role in the function of the immune system.[28] The converging signals from both pathways result in the permeabilization of the mitochondrial outer membrane (MOMP),[29] which in turn initiates apoptosis by disrupting vital mitochondrial functions or by releasing pro-apoptotic proteins such as cytochrome c.[30]

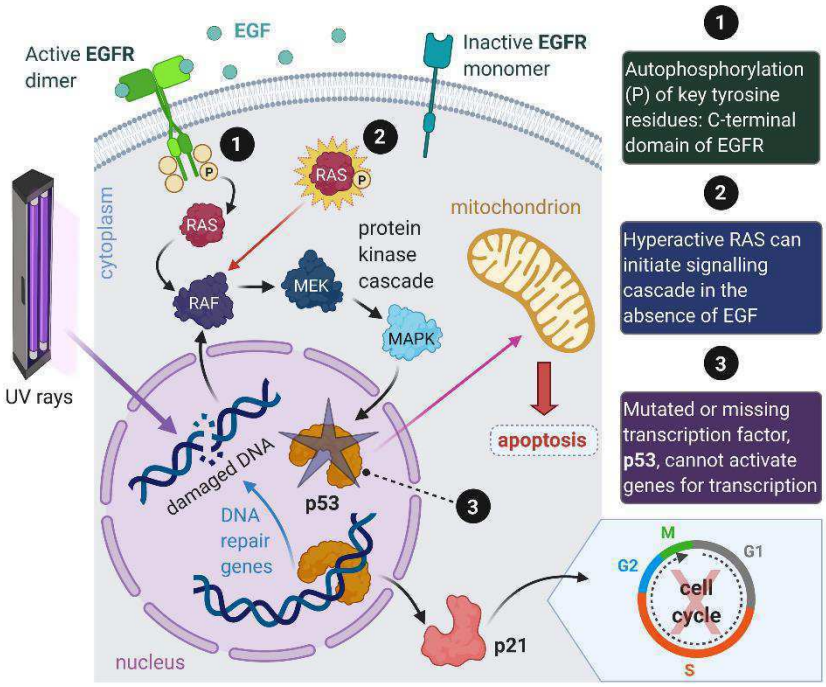


Fig. 2 A simplified representation of the MAPK cell signalling pathway reproduced from van der Westhuizen *et al*.[12] "This pathway is triggered by the binding of external growth factor (e.g., epidermal growth factor, EGF) to the EGF receptor (EGFR) on the membrane of the cell. Ras proteins (small GTPase signalling proteins) are activated by the receptor and initiate the signalling cascade involving a series of protein kinases. The last kinase (MAPK) activates a transcription factor (p53) that allows the synthesis of a protein (p21) that stimulates the cell cycle. (Note: *p21* transcription can be initiated independently of p53.) Excessive cell replication can occur because of a mutated Ras protein, as the pathway can be initiated without the binding of EGF. In the case of UV radiation-induced DNA damage, p53 is activated and promotes either the transcription of genes directly involved in DNA repair, the transcription of p21 that can halt the cell cycle to prevent damaged DNA from being copied, or induce

apoptosis if the DNA is damaged beyond repair. If p53 is missing or defective due to a mutation in TP53, the response system fails to prevent the cell cycle from copying faulty genetic material and fails to induce apoptosis. Acronyms: RAF, proto-oncogene serine/threonine protein kinase; MEK; tyrosine/threonine protein kinase; MAPK, mitogen-activated protein kinase; P, inorganic phosphate."

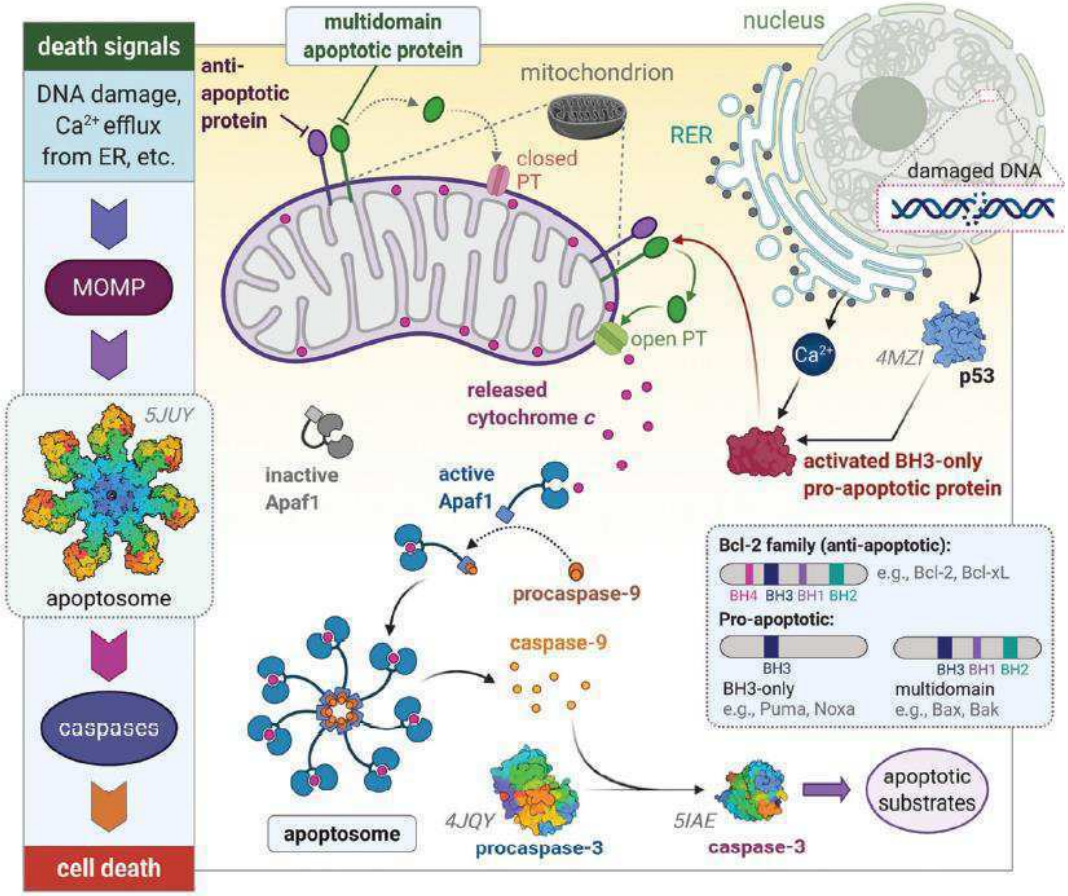


Fig. 3 A simplified representation of the apoptopic signalling pathway reproduced from van der Westhuizen *et al*.[12] "A basic representation of the intrinsic or mitochondrial apoptotic signalling pathway. Internal signals from the cell converge on the mitochondria, resulting in MOMP mediated by pro-apoptotic proteins of the Bcl-2 family. MOMP results in the release of cytochrome c, which binds to Apaf-1 to form an apoptosome with procaspase-9, which is subsequently activated to caspase 9. The effector caspase, procaspase-3, is activated by caspase-9 and activates proteins that execute apoptosis. The insert illustrates how the members of the Bcl-2 family are grouped based on their functions (i.e., anti- and pro-apoptotic) and a number of BH domains. Acronyms: Apaf-1, apoptosis protease-activating factor-1; MOMP, mitochondrial outer membrane permeabilization; PT, permeability transition pore. Protein structures are rendered from their protein data bank (PDB) codes: apoptosome (5JUY), p53 (4MZI), procaspase-3 (4JQY), and caspase-3 (5IAE; the monomeric V266F mutant has been shown for simplicity)."

The mechanism of MOMP entails the opening of permeability transition (PT) pores positioned on the inner mitochondrial membrane (IMM). The IMM quickly becomes more permeable so that it allows ions and water to enter the matrix causing it to swell.

The process is accompanied by a loss in mitochondrial transmembrane potential[31] and causes the outer membrane to rupture (Fig. 3).[32]

This leads to pro-apoptotic proteins like cytochrome c being released into the cytoplasm.[33] Release of cytochrome c initiates a signaling cascade of caspases. Cytochrome c binds to apoptosis protease activating factor 1 enabling the binding of procaspase.[34] Procaspase 9 is activated by cleavage and forms the active caspase 9, which in turn activates procaspase 3 that yields caspase 3.

Apoptosis is initiated by effector caspases, which activate proteins that are vital for the cellular changes linked with apoptosis. Characteristics of these are cell shrinkage, cell membrane blebbing, DNA fragmentation, and chromatin condensation. The cellular debris is packaged into apoptotic bodies that are ingested through the process of phagocytosis by either immune cells or neighboring cells.[27,28,35]

1.2.7. Alternative triggers of apoptosis

The Bcl-2 protein family that controls the events leading to MOMP,[29] BH-3 only proteins that receive a death signal when DNA is damaged,[36]and stress to the endoplasmic reticulum can also initiate apoptosis.[37]

1.2.8. Cancer cell survival mechanisms

It should be noted that B-cell lymphoma has a unique mechanism for survival. Individuals with B-cell lymphoma overexpress the protein Bcl-2, which allows for the regulation of the mitochondrial outer membrane permeabilization (MOMP) pathway, leading to cell survival. Another well-known example of cellular avoidance of apoptosis is the loss of the p53 protein. P53 plays a crucial role in initiating the apoptotic caspase cascade in response to DNA damage or overexpression of oncogenes and other abnormal cell conditions.[38–40]

In contrast to apoptosis, necrosis is a type of cell death that occurs as a result of extensive damage to the cell, leading to changes in the protoplasm and an increase in cell volume, ultimately resulting in cell death.[41]

In order to induce apoptosis in cancer cells, it is necessary to employ chemotherapy. However, it is important to avoid drugs that are not selective, as they can have negative effects on healthy tissue, and drugs with low efficacy, as they can contribute to drug resistance. Multi-drug therapies are favoured in order to have a multi-faceted approach to induce apoptosis in cancer cells.[42,43]

1.3 DNA

1.3.1. DNA structure

Identifying DNA as a target for cancer therapy was a result of chemical warfare during the preceding world wars. When mustard gas bombs were mixed with oil and came into contact with soldiers, the soldiers showed lymphotoxic symptoms.[44] Later in 1946, Alfred Gilman and Fredrick Phillips found that the lymphotoxic symptoms were due to DNA alkylation.[45] It should be noted that in chemical weapons, sulphur mustards were used, while more stable nitrogen mustards were favoured in chemotherapeutics to treat lymphoma. This marked the beginning of modern-day DNA-targeted cancer chemotherapy.[46] The impact of DNA's role as a key target for anticancer drugs can be highlighted by its function in cellular division, controlling cellular processes, and transmission of genetic material. If these processes incur chemically-induced errors, they can lead to the development of cancer.[47]

The structure of DNA was first reported by Watson and Crick in 1953.[48] The structure is a polynucleotide, consisting of four aromatic nitrogenous bases adenine and guanine are the two purines, and cytosine and thymine which are the two pyridines. Above a base, each nucleotide conations a deoxyribose sugar and a phosphate group. Each nucleotide residue is joined by a phosphodiester linkage between the deoxyribose sugar (of either a purine or pyridine) to a phosphate of the complimentary purine or pyridine forming a single DNA strand.[47] The direction of the phosphodiester bond dictates the directions of the DNA strand i.e., a 5′– 3 phosphodiester bond is between the deoxyribose sugar carbon-5 of one nucleotide and the sugar carbon-3 of the linking nucleotide. DNA is a double helix macromolecule with each strand being aligned antiparallel, with hydrogen bonding being responsible for holding the double helix together Fig. 3.[47]

1.3.2. DNA intercalation

Small molecules can bind to DNA in one of six ways: (i) covalent binding, which is exhibited by alkylating agents such as cisplatin and mustard gas,[45] (ii) molecules that bind to the deoxyribose sugar phosphate, groove binders that can either be (iii) major- or (iv) minor-groove binders, (v) binding of a drug into the central triangular-shaped hydrophobic cavity of DNA 3-way junctions, and (vi) intercalators. Due to the scope of work reported in this thesis, DNA intercalators will form the main focus of this introductory review.[49,50]

There is a drive to produce drugs that intercalate with DNA rather than covalently bind to groups on DNA itself.[51] This drive reflects the effectiveness of intercalators to target both DNA and the essential topoisomerase enzymes which regulate DNA topology. DNA intercalators have distinct features and are typically flat (planar) molecules made up of three or four fused rings.[51] This characteristic gives a small molecule intercalator the ability to π stack between nucleic acid base pairs or aromatic DNA.[52] Since DNA is negatively charged (due to the phosphate groups within the backbone strands), intercalators are typically positively charged so they can bind to DNA by harnessing favourable electrostatic interactions. Furthermore, it is not uncommon for an intercalator to have side chains that can hydrogen bond to the DNA helix.

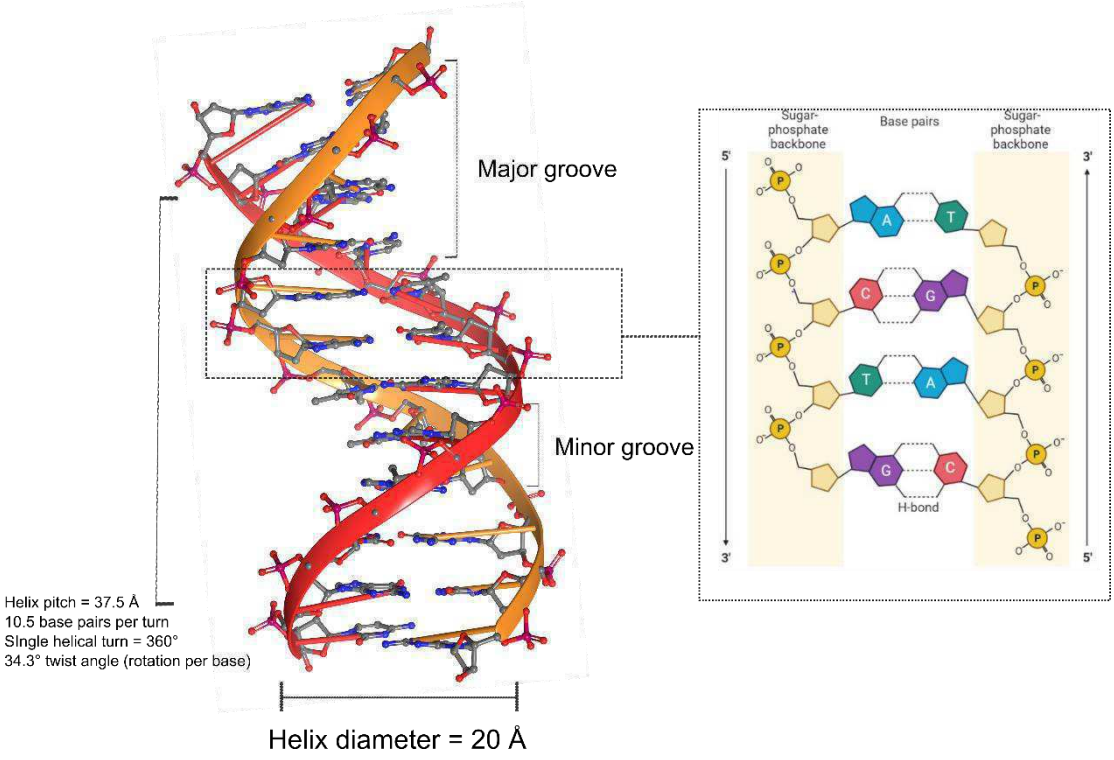


Fig. 4 Double-helical structure of B-form DNA (PDB 9BDNA)[53] prepared using Glide XP (Schrödinger Release 2022-3) with the major and minor grooves highlighted. The structural parameters (helical pitch of 35.7 Å, 10.5 residues per turn, 34.3° twist angle between residues, and a diameter of 20 Å linked to B-DNA are shown. The insert (on the right) shows the chemical structures of the four nucleic acid base pairs (adenine, thymine, guanine, and cytosine).

DNA intercalators work by binding in a sandwich fashion between two nucleic acids and distorting the structure by marked elongation of the double helix with partial unwinding. This structural change can result in the inhibition of DNA replication and gene transcription. Intercalating molecules can also affect the topoisomerase enzymes responsible for maintaining DNA topology (e.g., supercoiling).

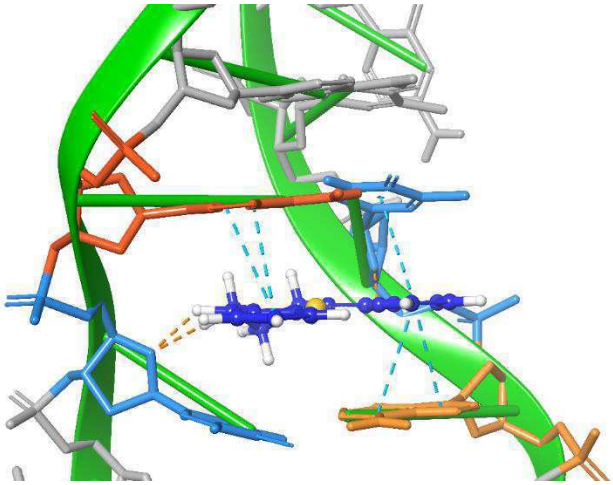


Fig. 5 Au(III) Schiff base chelate **AuL1** (Chapter 2) is shown to intercalate with B-DNA (201I).[54] The **AuL1** chelate inserts itself between AT residues and intercalates DNA. The structure was prepared using Glide XP (Schrödinger Release 2022-3) and the DNA structure was subjected to energy minimization using Macromodel[55] and the S-OPLS force field.[56,57]

1.3.3. DNA topoisomerase I

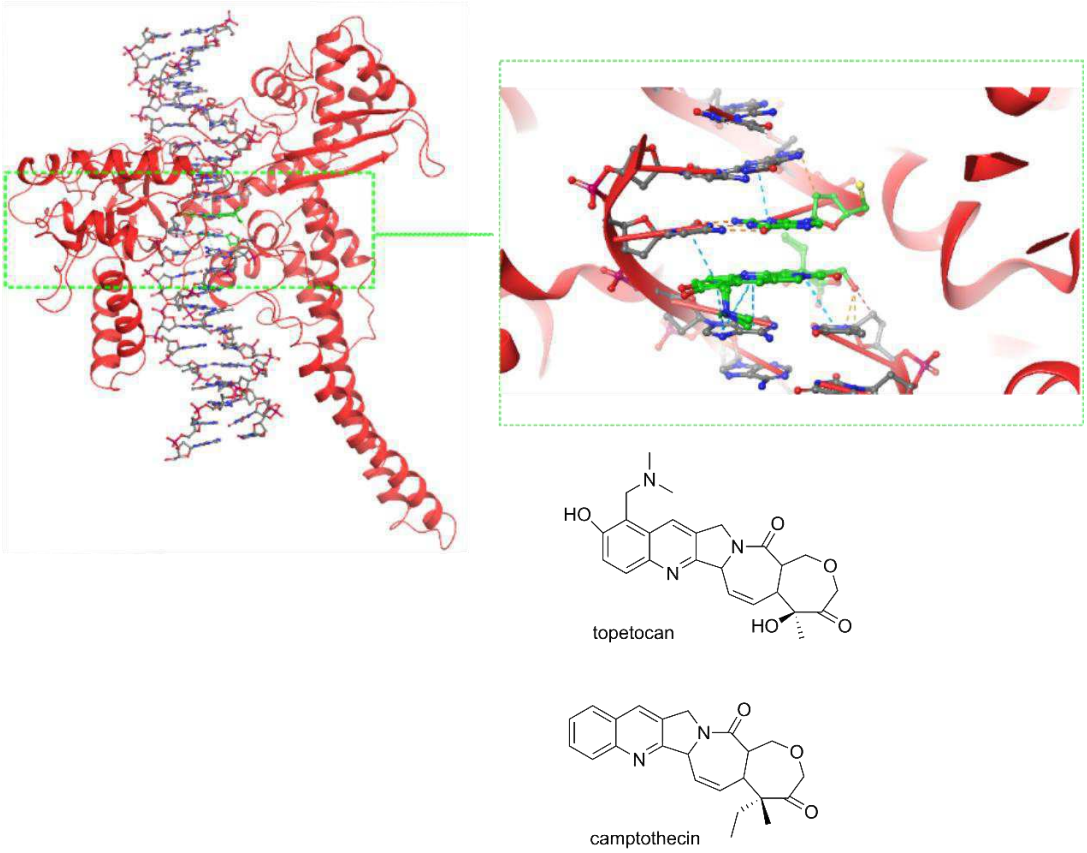


Fig. 6 X-ray structure of human topoisomerase IB (Top1) bound to DNA. Note the nick created within the double helix (1K4T[64]). The structure of Top1 poisons is included.

The DNA strand is intercalated with the natural product drug camptothecin, which is a known Top1 interfacial poison. Human topoisomerase IB (Top1) is a monomeric 91 kDa protein composed of 765 amino acid residues, which are divided into four domains: the N-terminal domain (1-214), the core domain (215-634), the linking region domain (636-712), and the C-terminal domain (713-765) (Fig. 6).[59–61] *In vitro* studies have shown that the N-terminal and linking domains are not required for Top1's catalytic activity and are highly susceptible to proteolytic activity.[60,61] Additionally, these domains are poorly conserved across species. It should be noted that the N-terminal domain contains five nuclear localization signals, which are likely responsible for the enzyme's subcellular localization.[62,63] The C-terminal domain contains the active Tyr-743 residue and, along with the core domain, is essential for Top1 activity. The core domain, the largest of the domains, is further divided into three subdomains: the upper lobe (subdomains I and II) and the lower lobe (subdomain III). The lower lobe also includes the C-terminal domain and is attached to subdomain III by a long alpha-helix. As depicted in Fig. 6, the positioning of the C-terminal domain allows Tyr-743 to face the surface of the central cavity and interact with bound DNA.[60]

Several crystal structures of Top1 bound to DNA, either covalently or non-covalently, have been reported. The common consensus is that the enzyme fully encompasses a double helical strand of DNA (PDB 1K4T).[64] The binding of DNA by Top1 is due to several DNA-protein interactions, with most contacts occurring within 5 base pairs of the cleavage site. The Top1 nucleotide preference is 5′-(A/T)(G/C)(A/T)(T)-3′.[65,66] Above the Tyr-723 residue, there are four other conserved catalytic residues: Arg-488 and Arg-590, Lys-532, and His-632. These four residues position the scissile DNA sugar-phosphate backbone for nucleophilic attack by the Tyr-723 residue. To stabilise the transition state, these four residues interact with the non-bridging 3′-phosphate oxygen. The roles of each amino acid are summarised in Table 1.

Table 1: Amino acid residues within the active site of Top1 and their roles.

Amino acid residue	Role
Arg-458	Clamping DNA
Arg-590	Enhance the nucleophilicity of Tyr-723 by stabilizing the phenolate anion.
Lys-532	Mediate's base specific (–1T or –1C) interaction between Top1 and DNA by contacting the O_2 atom on the base. Donates a 5′–O leaving group to allow for religation after DNA has been relaxed.
His-632	Clamping DNA

1.3.4. Mechanism of Top1 DNA relaxation

Top1-mediated DNA relaxation occurs through controlled rotation, which is distinct from the mechanism of type IA or II enzymes and does not require an energy cofactor (e.g., ATP) or divalent metal ion catalyst. Top1 binds to DNA crossovers (supercoils) and creates a nick in the DNA through transesterification (as illustrated in Fig. 7). The enzyme then allows the DNA to rotate through controlled rotation (as described in Koster *et al*.[67]; Stivers *et al*.[68]). Upon realignment of the DNA through base pairing and stacking across the nick, the DNA 5′-hydroxyl end (OH in lower panels) removes the tyrosyl linkage through reverse transesterification (as illustrated in Fig. 7).

As previously mentioned, Top1 relaxes DNA by inducing a single break in one of the strands through a reversible transesterification reaction. The enzyme does not require external energy cofactors and the energy for the reaction is generated from the torsional strain of the supercoiled double helix DNA. Top1 is able to clamp DNA within its active site (as highlighted in Table 1) and the active Tyr-723 residue acts as a nucleophile and cleaves a single DNA strand. Since eukaryotic topoisomerases are the focus of this review, we will specifically focus on Top1B, which forms a DNA-(3′-phosphotyrosyl)-enzyme covalent complex between the Tyr-723 and the sugar-phosphate backbone and a free 5′-OH DNA end. Once the DNA-(3′-phosphotyrosyl)-enzyme covalent complex is formed, the DNA supercoiled torsional energy is released, resulting in a cleavage complex with a single helix strand break and relaxed DNA. This process continues until DNA is completely relaxed by the removal of random supercoils, and the 5′-OH end is religated to the sugar-phosphate backbone of DNA. Once no more torque is available, the reaction is halted. The rate of religation

is much more rapid than cleavage, therefore, the concentration of the Top1 cleavage complex remains low.[67–69]

1.3.5. Top1 poisons

Topotecan exerts its cytotoxic effect by intercalating into the nick site of DNA generated by Top1, leading to the formation of a ternary Topo 1B-DNA-drug complex that traps the DNA within the Top1 active site.[64] This complex binding is irreversible and results in the formation of cytotoxic DNA lesions, ultimately leading to cell death.[70]

The binding mechanism of topotecan, a derivative of CPT, has been studied using X-ray crystallography (XRD) and a 70 kDa isoform of human Top1 that was covalently bound to a double helix DNA in the presence and absence of topotecan. The resulting ternary Top1-DNA-topotecan adduct indicates that topotecan intercalates at the site of DNA cleavage and is stabilised by base stacking interactions with both the -1 and +1 base pairs. As topotecan is a planar ring system, it mimics a DNA nucleotide and binds to the +1 upstream base pair in the structure in the absence of the drug. The interaction within the binding site is created by conformational changes of the phosphodiester bond between the +1 and -1 base pair from the uncleaved strand of the Top1-DNA-topotecan adduct. This results in the stabilisation of the phosphodiester bond and further stabilization through hydrogen bonds between the Arg-362 and Gly-363 nitrogen atoms. The intercalation binding site was further stabilised by several DNA-Top1 interactions.[64]

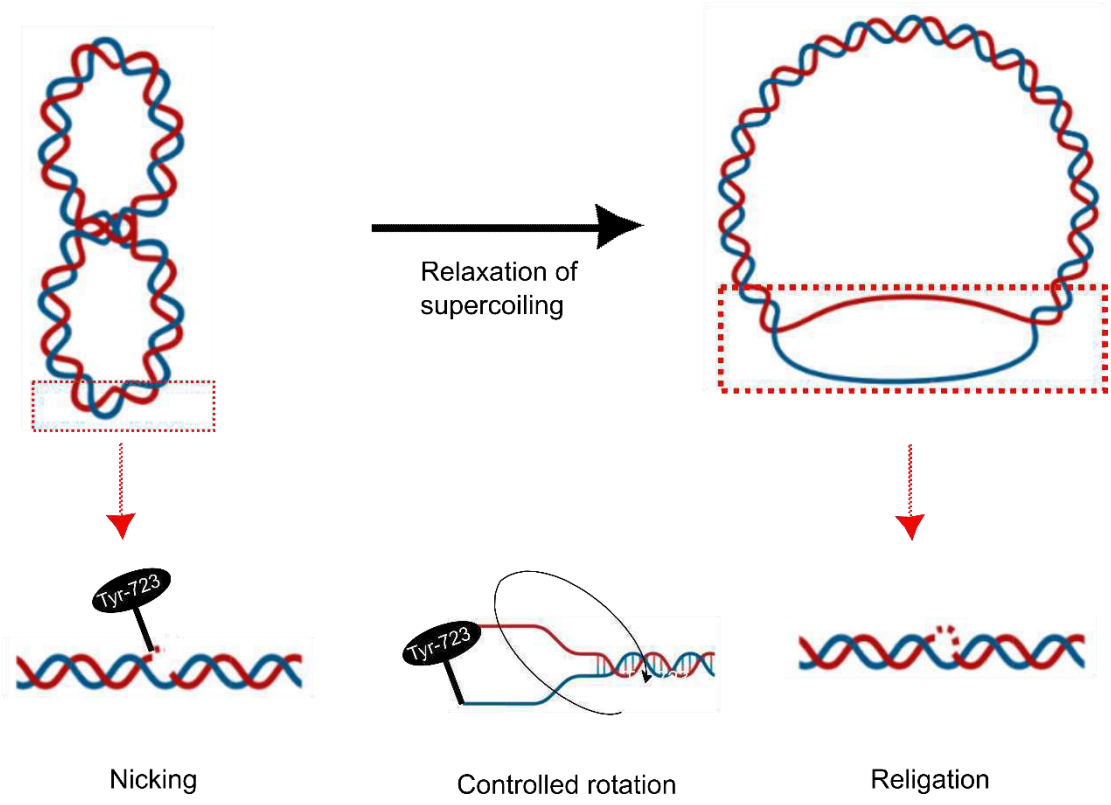


Fig. 7 Illustration of supercoiled DNA relaxation by Top1. Top1 mediates the DNA relaxation by binding to the supercoiled DNA forming a topoisomerase cleavage complex (Top1cc). Within the active site of Top1, the Tyr-723 residue (Y) inserts a nick into the supercoiled DNA (transesterification). Top1 then allows the supercoiled DNA to unwind by controlled rotation. Finally, DNA religation may occur by base pairing and stacking across the nick site. The 5′-hydroxy terminal removes the tyrosyl linkage by a process called reverse transesterification. The lower image is a representation of the 3-phosphotyrosine covalent bond within the Top1cc.

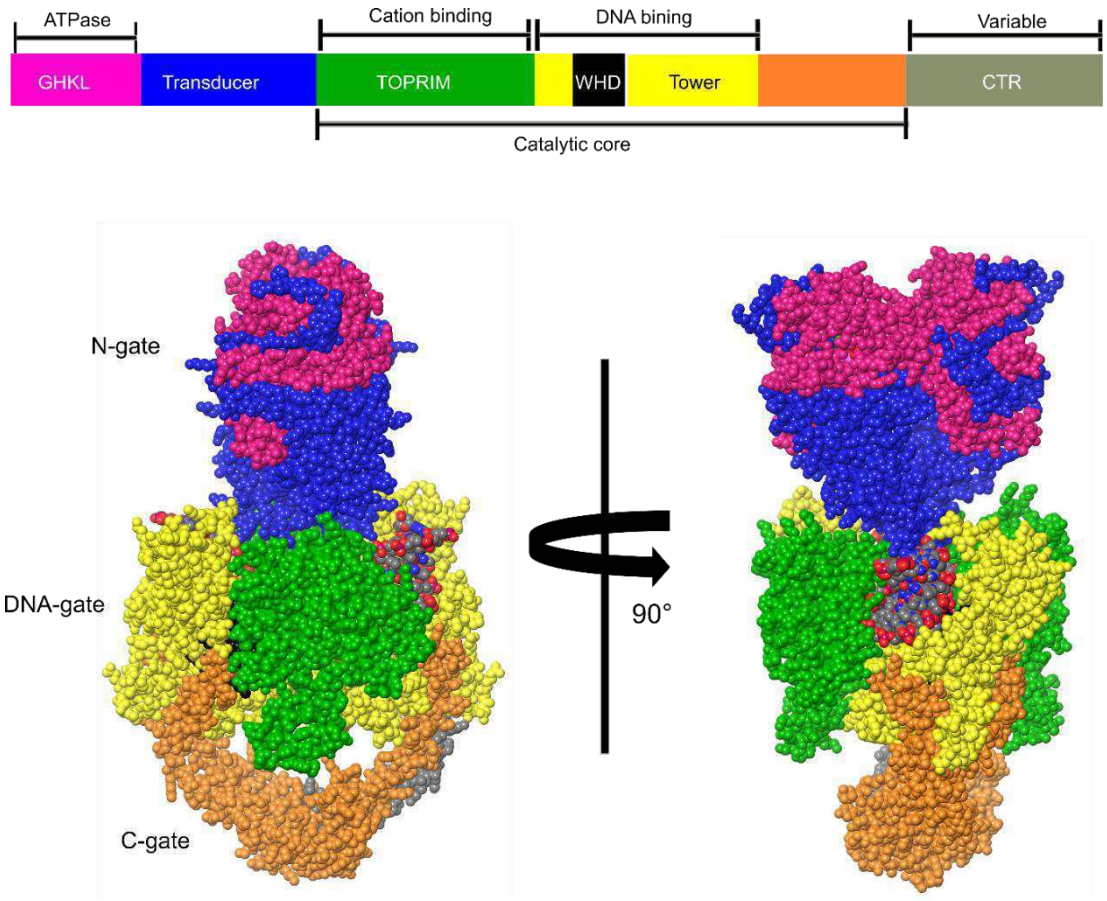


Fig. 8 Top panel: illustration of the organisation of eukaryotic Top2 structural domains. The schematic of the eukaryotic Top2 enzyme was prepared using Maestro (13.3) and is presented in a space-fill model (PDB 4GFH),[71] with the functional regions coloured in accordance with the structural domains. Top2 is covalently bound to a double helix DNA.

1.3.6. Mechanism of Top2-mediated DNA decatenation

Topoisomerase II (Top2) are energy-dependent nucleic acid remodeling enzymes that use divalent metal ions (notably Mg^{2+}) and ATP as cofactors to relax and untangle supercoiled DNA, forming or unlinking DNA knots and tangles. Eukaryotic Top2 isomerases comprise of three interface domains: the N-terminal, DNA gate, and C-terminal (as illustrated in Fig. 8).[72] The N-terminal contains the N-gate, which is the region through which the DNA enters the enzyme, the GHKL domain (Gyrase, Hsp90, Histidine Kinase, MutL), also known as the ATPase domain, which binds to and hydrolyzes ATP, and the transducer domain, which is responsible for transmitting hydrolysis signals to the catalytic core within the DNA-gate (Fig. 8).[69,71,73] The catalytic core is composed of the topoisomerase domain (also known as the primase or TOPRIM domain) which coordinates the binding of Mg^{2+} (or other divalent metal cations) to the active site, the winged helix domain (WHD) which contains the active Tyr residues, and the tower domain which interacts with DNA through polar or

electrostatic interactions.[69,71,73]The last interface of Top2 is the C-terminal region (CTR), which contains nuclear localization signals and post-transcriptional modification sites.[74] The CTR domain is poorly conserved amongst type II topoisomerases and is disordered when not bound to DNA. Furthermore, it is the area that allows Top2α to remove positive supercoils 10-fold faster than negative supercoils.[75,76]

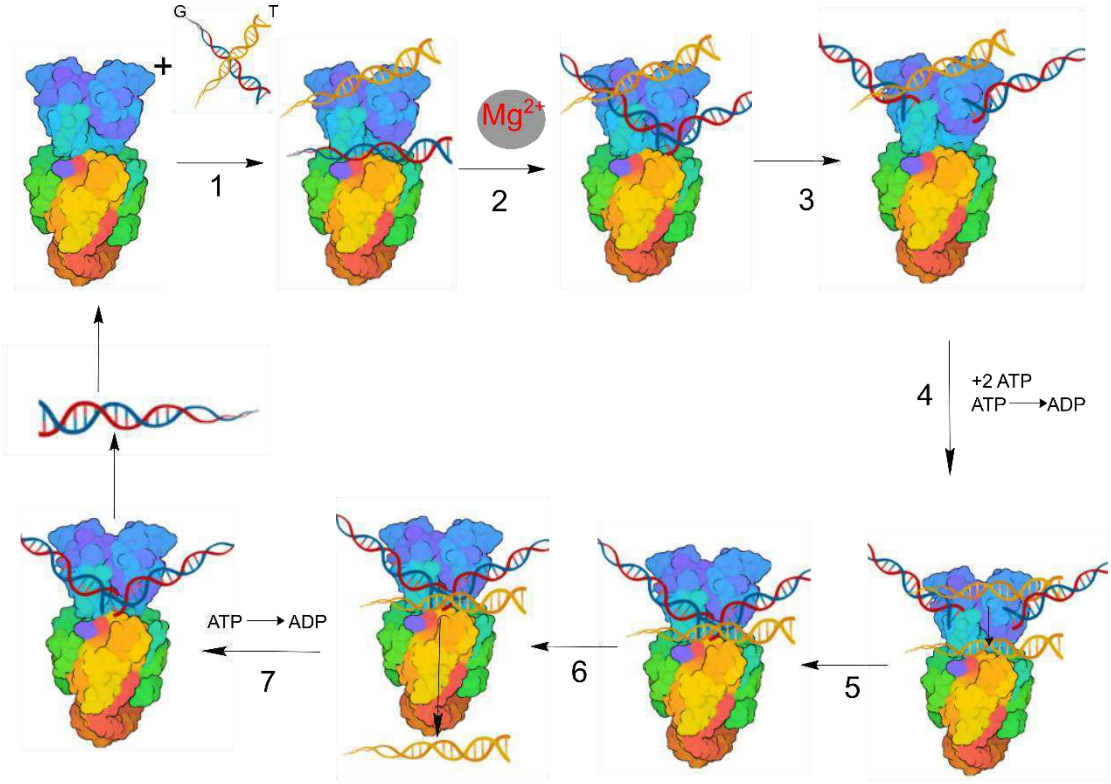


Fig. 9 The catalytic cycle of DNA relaxation by topoisomerase II.

Top2α modifies DNA topology through a double-stranded DNA passage reaction, the steps of which are highlighted in Fig. 9. The reaction begins with Top2α binding to two double-stranded DNA strands at a crossover (i.e., catenanes, supercoils, and knots).[78] The DNA segments are referred to as the gate segment (G-segment) and this is the first segment bound and cleaved by Top2. The second segment is the transport segment (T-segment) (Step 1).[78,79] When Mg^{2+} (or an alternative divalent metal ion) is bound to the TOPRIM domain, the enzyme assesses the flexibility of the G-segment (Step 2)[80,81]. If the G-segment is sufficiently flexible and can bend to approximately 150° it is used as a substrate for Top2 activity (Step 3).[82] Thereafter, cleavage of the G-segment can begin through a nucleophilic attack from the active Tyr residues (Tyr-804 and Tyr-821). Each Tyr cleaves a phosphodiester bond four nucleotides apart on opposite strands of the G-duplex, becoming covalently linked to the 5′-ends of the

broken DNA, forming a phosphotyrosine linkage between each single strand and a tyrosine in each subunit (Step 4). The cleavage of each helix occurs in a coordinated manner, once the first strand is cleaved, cleavage of a second strand occurs at a rate 10-fold faster.[83] The next step is the binding of two ATP molecules, which closes the N-gate, forcing the T-segment through the broken G-segment (Step 5).[84] Once the T-segment passes through the G-segment, the T-segment is released from the clamp of Top2 via the C-terminal (Step 6). The hydrolysis of ATP occurs in two steps (i) assisting with strand passage and (ii) hydrolysis + ADP + an inorganic phosphate allows the clamp to reopen and release the G-segment (Step 7).[85]

1.3.7. Inhibition of Top2 activity

There are two main groups of compounds that alter Top2 activity, namely catalytic inhibitors and interfacial poisons (IFPs).

1.3.8. *Catalytic inhibitors*

Catalytic inhibitor compounds (CICs) inhibit the turnover activity of Top2 without increasing the overall concentration of the enzyme.[73,86,87] These inhibitors may target several steps of the Top2 catalytic cycle, such as DNA binding, DNA cleavage, ATP hydrolysis, and ATP binding.[86–89] If the topoisomerase catalytic inhibitor blocks ATP binding, the cell will be unable to perform the catalytic function of the enzyme. If ATP hydrolysis is blocked, the N-terminal gate of Top2 (as shown in Fig. 10) will fail to open, trapping DNA on the enzyme. If the binding of DNA to Top2 is blocked, the cell will be unable to perform the catalytic role of the enzyme.[86–89]

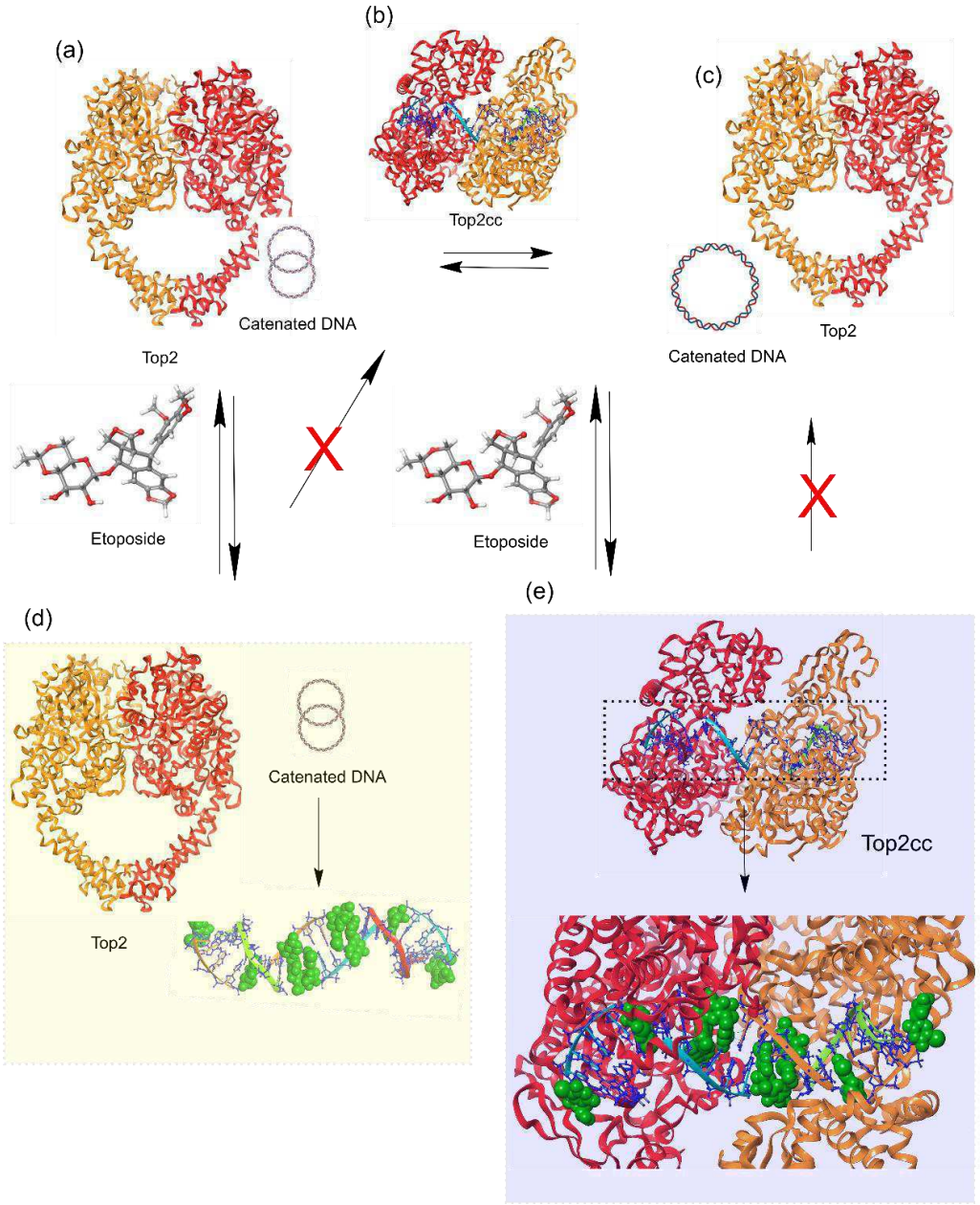


Fig. 10. Illustration of key events in the catalytic cycle of human Top2. Under normal conditions (i.e., absence of chemotherapeutics) (a) catenated DNA is bound by Top2 (dsDNA; 5′-TA-3′). (b) Top2 introduces a double break, one in the G segment where it will later pass the T segment through. When a divalent cation (Mg^{2+}) is present it can activate the tyrosine residues for a nucleophilic attack on the sugar-phosphate backbone of DNA forming a phosphotyrosine linkage between each single strand and a tyrosine in each subunit. The Top2 clamp is closed when two ATP molecules are bound, allowing a T-segment strand to pass. The clamped G-segment is the Top2-DNA cleavage complex (Top2cc). (c) Finally, hydrolysis of ATP-1 may aid in the T-segment passing, while hydrolysis of ATP-2 allows the clamp to open. Top2 returns to its native state with decatenated DNA. (d) If a CIC is present, it may alter the state of the DNA or have an inhibitory effect on Top2, therefore, a Top2cc is not formed. (e) If an IFP is present the Top2 cannot decatenate the DNA and a Top2cc is formed with linear DNA. The enzyme is poisoned and persists as a covalent cleavage complex. Accumulation of Top2cc results in cell apoptosis. The complex AuL1 acts as both a catalytic inhibitor compound (CIC) and interfacial poison (IFP) by targeting two points in the enzyme catalytic cycle.

1.3.9. *Top2 poisons*

Top2 interfacial poisons increase the concentration of Top2cc by intercalating with the DNA G-segment specifically at the DNA strand nick sites (interfacial region), resulting in breaks within its double helix.[69,73,84,90] All relevant Top2 poisons act by preventing the enzyme from religating cleaved DNA.[69,73,84,90] Top2 poisons can act via two mechanisms: interfacial or covalent. Interfacial poisons (IFPs) bind to Top2 close to the Tyr residues at the Top2-DNA interface.[69] IFPs are bifunctional and bind to both Top2 and DNA, resulting in an increase in the levels of DNA scissions. During DNA cleavage, IFPs bind between the ends of the G-segment DNA's cut scissile bonds (i.e., one on each DNA strand) in order to stabilise the double-stranded breaks.[69,73,84,91] IFPs distort the active site of Top2cc and displace Mg^{2+} from the phosphotyrosyl moiety.[92] It is important to note that IFPs are diverse in structure, however, a typical IFP typically consists of a multi-core ring, a pendant ring, and aromatic elements. One of the most common examples of an IFP is the natural product etoposide.[93,94]

1.4 Brief survey of selected anticancer metallodrugs

1.4.1. FDA-approved metal-based chemotherapeutics

Cisplatin is a widely administered chemotherapeutic agent that has been approved for use by the Food and Drug Administration (FDA, USA) since 1978 for the treatment of advanced ovarian, bladder, and testicular cancer.[95] Studies have been conducted to investigate the mechanism of action of cisplatin and other FDA-approved second-generation platinum(II) drugs, such as oxaliplatin and carboplatin (Fig. 11). Additionally, research has been conducted to develop novel drugs that improve the efficacy of metallodrug chemotherapeutics while minimizing the severe side effects associated with platinum(II) based drugs.[7]

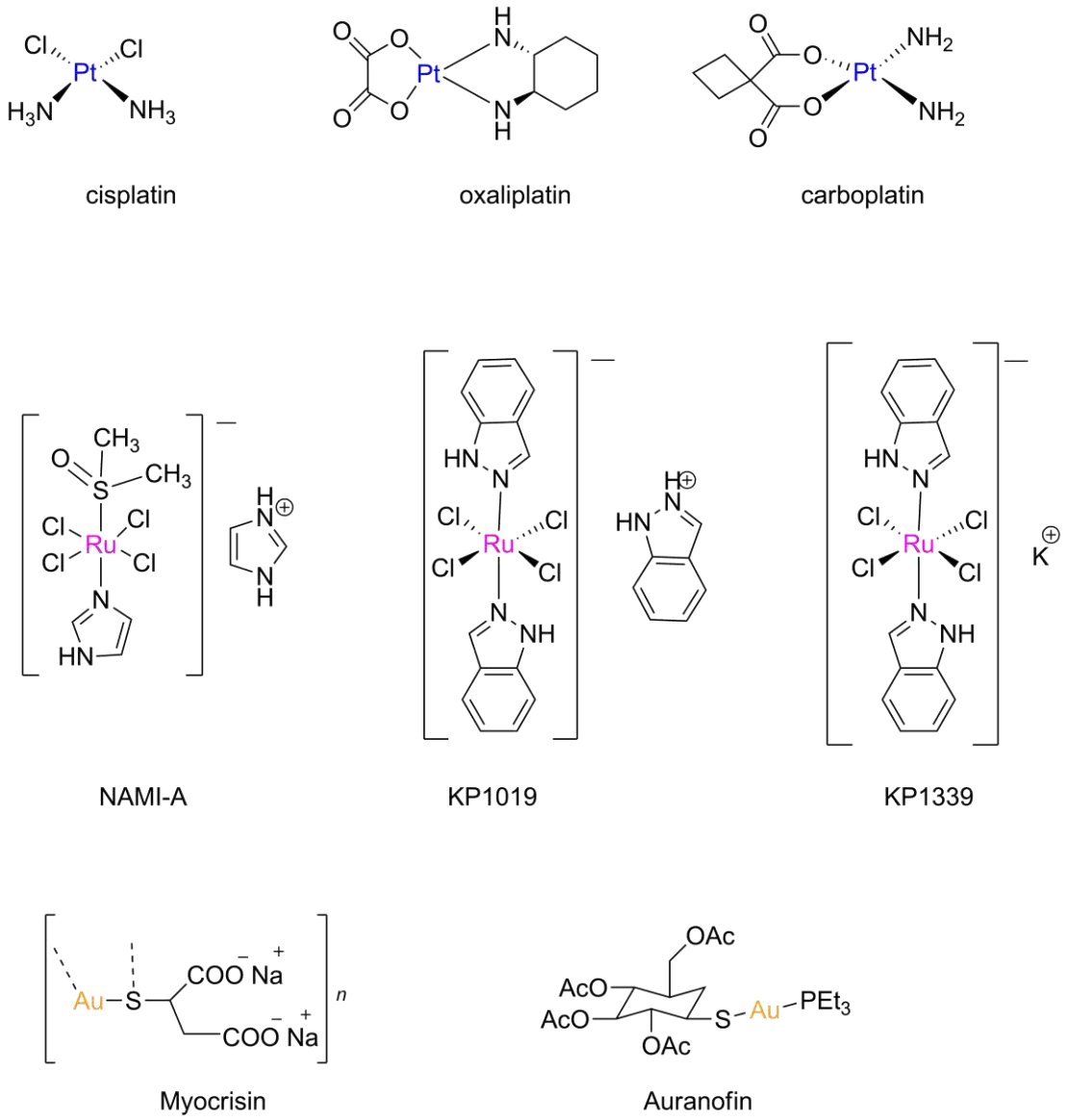


Fig. 11 Structures of selected metal-based chemotherapeutic agents that are in clinical use or are undergoing clinical trials.

The side effects associated with platinum(II) based therapies are a result of their lack of specificity for cancerous tissue. However, the limited specificity of these therapies is attributed to the high nutrient requirements of cancerous tissue, which results in platinum therapeutics being transported to the malignant cells and poisoning the cancerous tissue.[96,97] Cisplatin is known to cause nephrotoxicity, while oxaliplatin and carboplatin are associated with neurotoxicity and myelosuppression, respectively.[7] Due to the toxicity of platinum(II) based compounds, they can only be administered at sub-lethal concentrations, which results in the emergence of drug-resistant cancer as a major drawback.[3,4]

NAMI-A does not enter the cell membrane but rather interacts with it or the extracellular matrix. A study has shown that NAMI-A binds to and interacts with HSA and may be transported to the cancer site via an HSA-mediated pathway.[99] These findings may explain the low cytotoxicity of NAMI-A and its high anti-metastatic effects.[100,101] In contrast, KP-1019 is able to penetrate the cell membrane and induces cytotoxicity through the formation of reactive oxygen species (ROS), leading to the endoplasmic reticulum (ER) stress. Compared to platinum(II) drugs, ruthenium drugs are more selective but less cytotoxic.[101,102]

1.4.2. Mechanism of action: classical anti-cancer drugs

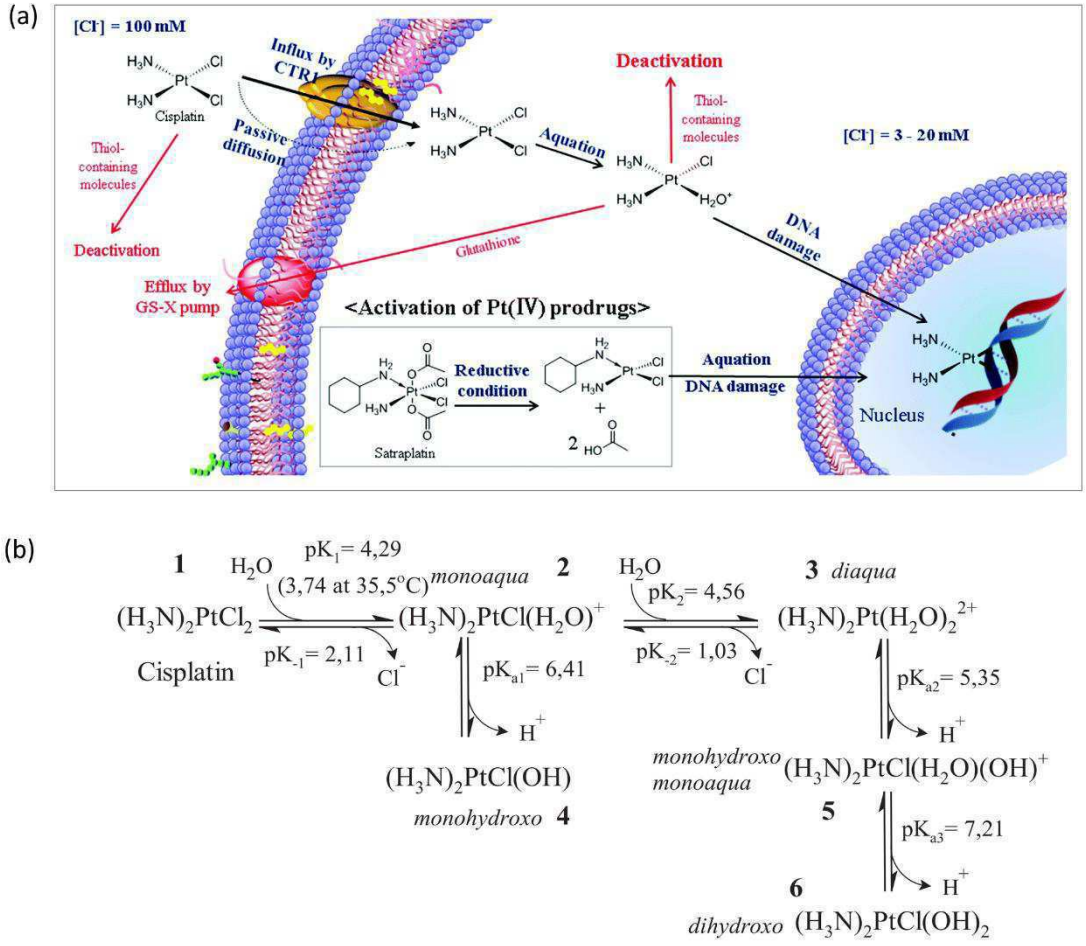


Fig. 12 (a) Cytotoxic pathway of platinum-based drugs. The pathway highlights (i) the aquation of cisplatin before its binding to DNA and (ii) the aquation of satraplatin (a Pt^{4+} prodrug). Figure reproduced from Kim *et al.*[103] (b) A detailed mechanism of the aquation of cisplatin reproduced from Makovec's review.[98]

Despite the severity of the side effects associated with cisplatin, it is widely acknowledged that the FDA approval of cisplatin served as a catalyst for research on metallodrugs as potential new chemotherapeutic agents.[104] Platinum(II), gold(I), and

ruthenium(II/III) are some of the primary metal ions that are the focus of research in next-generation metallodrug chemotherapeutics.[105,106] Currently, Au(I) complexes, such as auranofin and myocrisin,[11] and ruthenium(III) complexes including KP1399,[100,107] NAMI-A,[102] and KP1019[102] are undergoing clinical trials (Fig. 11).

The typical mechanism of action of the three classical anticancer drugs cisplatin, carboplatin, and oxaliplatin is summarised in Fig. 12 and involves the following steps: (i) uptake by the cell, (ii) aquation of the drugs to activate them, (iii) binding to DNA and (iv) cellular processing of Pt(II)–DNA adducts (lesions) leading to apoptosis. Using cisplatin as an example, once it enters the cell, the Cl^- ions are substituted by H_2O.[108,109] The platinum(II) drugs target DNA and react with the N7 donor of adenosine and/or guanosine by nucleophilic attack. This reaction yields an intra-strand crosslink, which causes the DNA double helix to distort.[110] The cellular machinery either bypasses the distorted DNA, attempts to repair the lesion or initiates apoptosis.[95]

1.4.3. Non-classical anticancer platinum(II) drugs

Within the scope of this review, any platinum drug that is not cisplatin, carboplatin, or oxaliplatin will be considered as a non-classical platinum drug. Due to the increasing cases of platinum-resistant cancer cell lines and the severe side effects associated with these drugs, there is a significant effort to find novel platinum drugs.[3,4] The novel drugs differ in their ligand scaffold, with the theory being that changing the ligand will alter the mode of action of the platinum drug. Common ligand scaffolds currently under investigation include poly(platinum) compounds,[111] intercalator-linked species,[112] trans-diamine complexes,[113] photoactivable azide complexes,[114] and platinum (IV) molecules that behave as prodrugs (illustrated in Fig. 12).[115] However, this section of the review will mainly focus on theranostic platinum agents. Theranostic platinum drugs have emerged as a promising area of research within medicinal chemistry in recent times.[101]

1.4.4. Theranostic platinum-based compounds

Theranosis involves a single system that can perform both diagnostic and therapeutic functions.[101] Diagnosis may be achieved through several non-invasive imaging tools such as positron emission tomography (PET), computed tomography (CT), magnetic resonance imaging (MRI), and fluorescence microscopy.[101] Among these techniques, fluorescence microscopy is considered to be the best bioimaging technique for cell work, as it is powerful, produces high-resolution images, and can be performed on live cells.[116,117] The advantages of fluorescence microscopy include the ability to use low

concentrations of fluorophores and the potential to collect multiple wavelength luminescent data, which can be organelle-specific, allowing for the identification of the organelle targeted by a theranostic probe. Platinum-based metallocycles have produced promising metallodrug theranostic agents.[118–120] They serve as ideal candidates due to their unique set of characteristics that make them suitable bioimaging agents. Key characteristics of phosphorescent heavy metal complexes used as diagnostic tools in bioimaging include (i) large Stokes shifts, (ii) high quantum yields, (iii) photosensitivity, (iv) two-photon absorption cross-section, and (v) based on the organic ligand framework, targeting of specific cellular organelles.[121,122]

1.4.5. Cytotoxic theranostic platinum-based complexes

A promising platinum(II) cyclometalated complex is Pt(DMSO)(2,4,6-triphenylpyridine) (Fig. 13a). It has been shown to interact with the nuclear factor (NF) kappa protein and is able to "hitchhike" the protein's machinery, upregulating nuclear translocation in cancer-affected cells but not healthy cells. Fig. 13b illustrates the selectivity of Pt(DMSO)(2,4,6-triphenylpyridine) for cancer cells compared to normal cells. The results of the MTT assay showed that the IC_{50} of Pt(DMSO)(2,4,6-triphenylpyridine) for the HEPG2 cell line (cancer cell line) was 0.28 µM, while for the normal cell line HELF, the IC_{50} was greater than 50 µM. In comparison, cisplatin has an IC_{50} of 3.36 µM.[123]

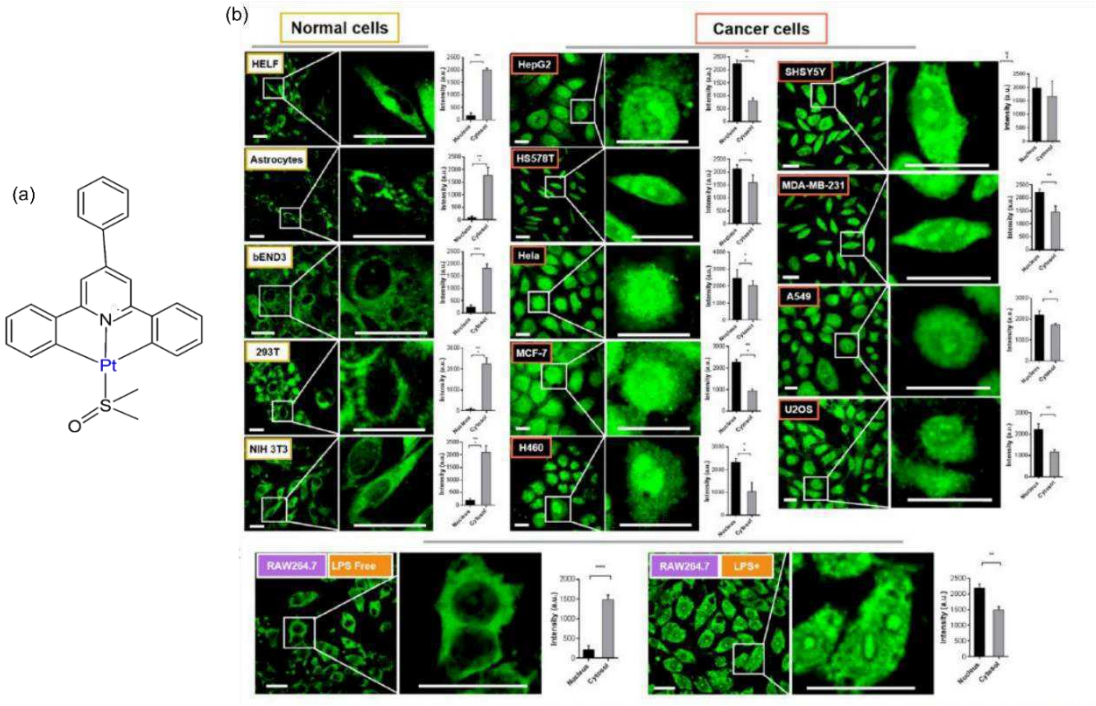


Fig. 13 (a) Chemical structure of Pt(DMSO)(2,4,6-triphenylpyridine). (b) Confocal microscopy images of Pt(DMSO)(2,4,6-triphenylpyridine) targeting the nucleus of cancer cells specifically. The figure has been adapted from Zhu *et al.*[123]

1.4.6. Why are Pt(II) chelates effective theranostic agents?

Platinum(II) chelates exhibit their fluorescence due to the Pt(II) ion inducing strong spin-orbit coupling (SOC). Platinum(II) complexes typically have square planar geometries, unlike the d^6 metal ions Ru(II) and Ir(III) that adopt an octahedral coordination geometry. Square planar Pt(II) complexes have a more flexible excited state due to the vacant axial coordination site(s). Furthermore, the d^6 metal ions emitting triplet excited states are typically metal-to-ligand charge transfer (^{3}MLCT) (MLCT ¼ metal-to-ligand charge transfer). Whereas the emission involving the d^8 configuration of Pt(II) complexes is ^{3}MLCT in character mixed with significant ligand character, from intra-ligand charge transfer (^{3}ILCT) and ligand-centered $^3\pi$–π^* transitions.

Platinum(II) complexes have the second-largest spin-orbit coupling (SOC) constant and the variation of the organic ligand bound to the Pt(II) ion alters the ground and excited state of the complex.[124] The importance of the organic ligand in Pt(II) complexes is critical, as it modulates the stability of the metal complexes. The most common reason for the decomposition of Pt(II) complexes is the breaking of the metal-ligand bond.[125] Two methods for solving the decomposition are using organic ligands that are strong σ-donors and using multidentate ligands (i.e., chelating ligands).[126]

Theranostic agents should not be confused with photodynamic therapeutic agents (PDTs) or photosensitizers. These molecules exert their cytotoxicity by (i) the generation of reactive oxygen species (ROS) such as $O_2^{\bullet-}$ and $OH^{\bullet}$ [127] or (ii) direct energy transfer from the photosensitizer to $^3O_2$ reducing it to $^1O_2$. They have cytotoxic ability but lack diagnostic capabilities or functionality as bioimaging agents.

1.4.7. Gold chemistry — a brief introduction

Gold has been used in medicine since 2500 BC, initially by the Chinese in their pursuit of longevity. Later, the use of gold powder was reportedly used to treat wounds and remove toxins associated with smallpox and skin ulcers.[9] A few centuries later, during the medieval period, potable gold was used as elixirs to restore youth.[9] However, due to the lack of efficacy of gold in medicine at that time, its use in medicine had drastically decreased. Until the 19th century, when a French physician formulated and used a less corrosive mixture of sodium chloride and gold, which was known as the "muriate of gold and soda" and intended to treat syphilis. Unfortunately, the results of the treatment efficacy were ambiguous. However, by the mid-1990s "muriate of gold and soda" was prescribed as a secondary treatment for several illnesses, including lupus, alcohol and morphine addiction, nephritis, and anaemia.[128]

It was not until the 1890s that the first rational use of gold in medicine was adopted when Koch created $K[Au(CN)_2]$.[10] The gold cyanide complex was found to be bacteriostatic against *Mycobacterium tuberculosis* (at the time known as tubercle bacillus). However, during clinical trials of $K[Au(CN)_2]$, it was found that the complex lacked efficacy in treating tuberculosis and caused serious side effects. After the introduction of $K[Au(CN)_2]$, during the gold decade (1925-1935), sodium aurothiosulfate (Au(I) thiol) was administered as a treatment for tuberculosis. However, this was not substantial, as there was limited evidence of its efficacy and the complexes were toxic, even though the Au(I) complexes were less toxic than $K[Au(CN)_2]$.[129,130]

Currently, gold complexes are used in medicine to treat rheumatoid arthritis.[131] Intravenously administered Au(I)-thiolates are now FDA-approved antirheumatic drugs.[132–134] The Au(I)-thiolates have a higher efficacy than potentially the most famous Au(I) drug, auranofin which is also intended to treat rheumatoid arthritis. However, auranofin is still an optional treatment for juvenile rheumatoid arthritis and psoriatic arthritis.[132–134]

1.4.8. Gold(I) complexes as potential anticancer drugs

Fries *et al*.,[135] reported that patients treated with gold-based drugs (auranofin) exhibited a lower malignancy rate, suggesting that gold-based therapeutics may possess chemotherapeutic activity. Later auranofin and its analogues were shown to be cytotoxic to the leukaemia P388 mouse model (*in vitro* and *in vivo*)[136,137] and melanoma *in vitro*.[138] The significance of the study led to the development of novel di-Au phosphine complexes (Au(I) 1,2-bis(diphenylphosphine ethane)).[139] These complexes were shown to be cytotoxic *in vitro*, *in vivo,* and more impressively, were also cytotoxic to cisplatin-resistant cancer cell lines. Unfortunately, further development of the complexes was halted due to their cardiotoxicity in animal testing.[139]

The proposed mechanism of action of Au(I) drugs is that they behave as prodrugs. Using auranofin as an example, it is postulated that the drug, once administered, undergoes rapid ligand exchange, and forms an Au–S cleavage by coordinating with the Cys-34 residue on HSA.[140] The now more active form of auranofin can be transported by the HSA-mediated pathway[141] to a tumour and potentially enter the tumour via the enhanced permeability and retention (EPR) effect.[99] Auranofin may be cytotoxic to leukaemia by one of three pathways: (i) inhibition of DNA and RNA

synthesis, which ultimately results in protein synthesis inhibition,[142] (ii) the ability to generate reactive oxygen species (ROS formation), that causes cellular damage,[143] and (iii) inhibition of mitochondrial thioredoxin reductase (TrxR).[144] All three proposed mechanisms will result in apoptosis.

Trxr catalyses the reduction of thioredoxins (trx). Both groups of proteins along with the energy co-enzyme NADP(H) make up the Trx system. The trx system is responsible for maintaining intracellular redox conditions (Fig. 14). The function of reduced Trx is to reduce cellular proteins that are essential for cell division.[145]

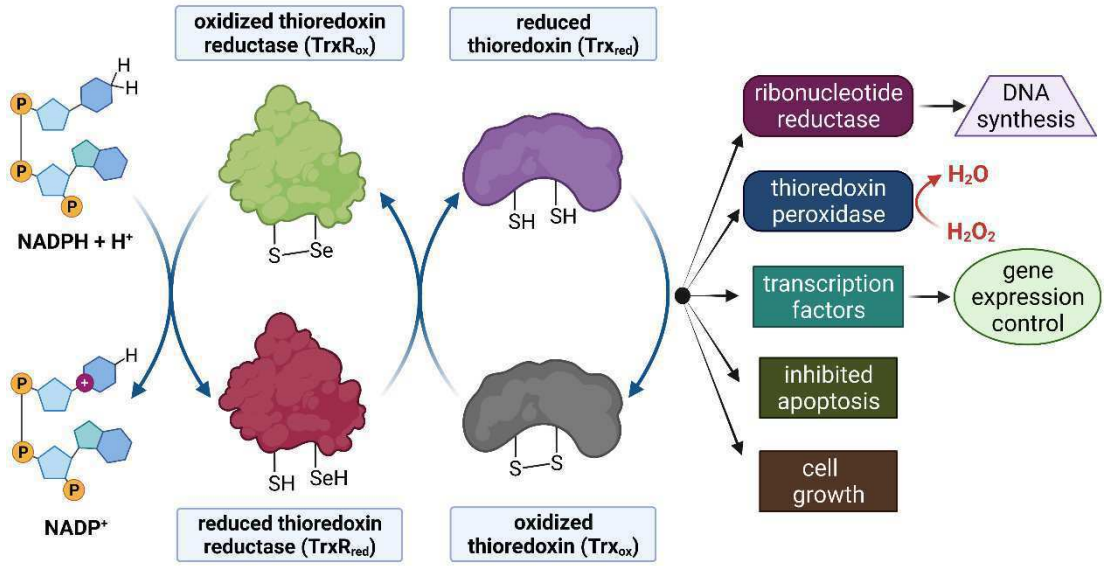


Fig. 14 TrxR mechanism reproduced from van der Westhuizen *et al*.[12] "Schematic illustration of thiol-disulphide exchange in the Trx system. Left: the co-enzyme NADPH is oxidised to NADP$^+$ to reduce TrxR$_{ox}$ (–S–Se–) to TrxR$_{red}$ (–SH, –SeH), which subsequently reduces Trx$_{ox}$ (–S–S–) to Trx$_{red}$ (–SH, –SH), as depicted in the centre two cycles. Trx$_{red}$ is then available to reduce substrate proteins or to carry out required cellular functions (right side). Thus, Trx reduces ribonucleotide reductase, an enzyme that reduces ribose to deoxyribose (the sugar of DNA nucleotides required for DNA synthesis). Trx also reduces other proteins such as thioredoxin peroxidase, which is responsible for converting toxic H_2O_2 to water as well as transcription factors that regulate gene expression. In addition, Trx functions as a cell growth factor and can inhibit apoptosis."

1.4.9. Anticancer activity of Au(III) complexes

Due to the emergence of platinum drug-resistant cancer and the toxicity of platinum(II) drugs,[96,97] Au(III) has been studied as an alternative medicinal metal ion for its potential use as a chemotherapeutic metallodrug, as it is isostructural and isoelectronic to Pt(II) and predominantly exhibits a square-planar coordination geometry.[146,147] Gold has three typical oxidation states (+3), (+1), and 0; however, the (+2) state has been reported.[126] Since Au(III) is electrophilic, it can be reduced to Au(I) or Au(0) under

physiological conditions by reductants such as thiols. A reaction scheme summarizing a potential reduction outcome of Au(III) is summarised in Fig. 15.

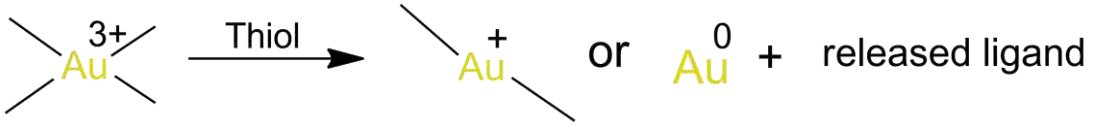


Fig. 15 Reduction of Au(III) by a thiol resulting in the formation of either Au(I) or colloidal gold (Au^0) and the release of a ligand.

The reduction of Au(III) can be minimised by the choice of the organic ligand framework surrounding the Au(III) ion.[148] Typical ligands that stabilise the Au(III) oxidation state are N-donor multidentate ligands, cyclo-metalating ligands containing C-deprotonated donor atoms (C^-), alternate ligands containing C^N bidentate, C^N^C tridentate and C^N^N, N^C^N, N^N^N, dithiocarbamate, and porphyrin-based ligands. Numerous compounds belonging to this group have been reported to stabilise Au(III) under physiological conditions.[149]

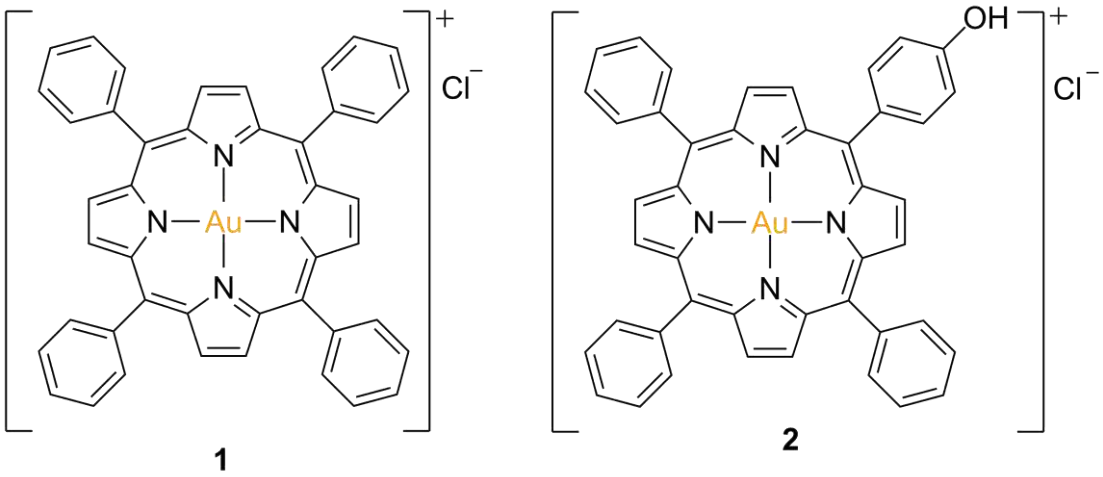


Fig. 16 Gold(III) porphyrins with anticancer activity.[150]

A study by Sun *et al*.[150] revealed that compound **1** induces apoptosis via mitochondrial dysfunction and suppression of Bcl-2. Additionally, compound **1** has been shown to inhibit the cell cycle at the G_0-G_1 phase by inhibiting TrxR and activating P38. Notably, compound **1** has been found to possess anti-tumour activity in vivo, against a variety of cancer types, including NPC metastasis,[151] neuroblastoma, [152] nasopharyngeal carcinoma (NPC),[153] colon cancer,[154] hepatocellular carcinoma (HCC),[155] U-87 MG cancer stem-like cells (CSCs),[156] and melanoma. Within a murine model, compound **1**

was found to be active against human ovarian A2780 tumours, regardless of cisplatin sensitivity.[157]

An analogue of compound **1**, referenced as compound **2** in Fig, 16, was synthesised. Compound **2** contains a meso-hydroxy phenyl group. It has been found to possess promising cytotoxic properties, specifically against breast carcinoma in a murine model. Notably, the mechanism of action of compound **2** differs from that of compound **1** and involves the inhibition of class **1** histone deacetylase activity. This unique mechanism of action of compound **2** is further evidence of the potential utility of Au(III) porphyrins as anticancer agents.[158]

The mechanism of action of Au(III) compounds coordinated by C-deprotonated tridentate (C^N^C) ligands was investigated by Li *et al*.[159] as shown in Fig. 17. The complexes were found to be physiologically stable, and their bioactivity was dependent on the substitution of the ligand at position R. One of the most cytotoxic C^N^C ligands was found to be Di-Au^{3+} (C^N^C) bis(di phenylphosphino)propane $(OTf)_2$, which was active against several cancer cell lines, as listed in Table 3. The IC_{50} values ranged from 0.043 – 2.1 μM.[159,160]

In a murine model, compound **6** inhibited hepatocellular carcinoma tumours by 77% when administered by intraperitoneal injection. When **6** was administered via intravenous injection to mice with hepatocarcinoma and sarcoma tumours, the inhibition was 38.6% and 48.9%, respectively.[160] Furthermore, Sun *et al*.[160] reported that **6** causes stress on the endoplasmic reticulum and inhibits TrxR. Alternative $[Au(III)(C^N^C)L]^{n+}$ complexes are reported in Fig. 17 and their cytotoxicity data are presented in Table 3.

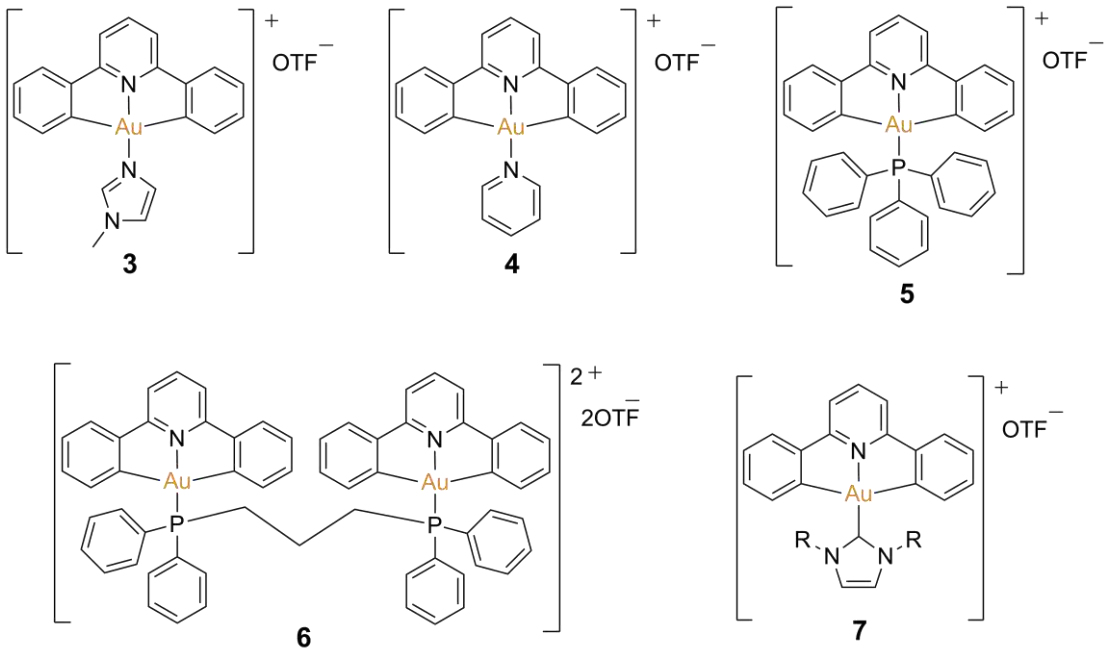


Fig. 17 Gold(III) C-deprotonated tridentate (C^N^C) complexes.[159]

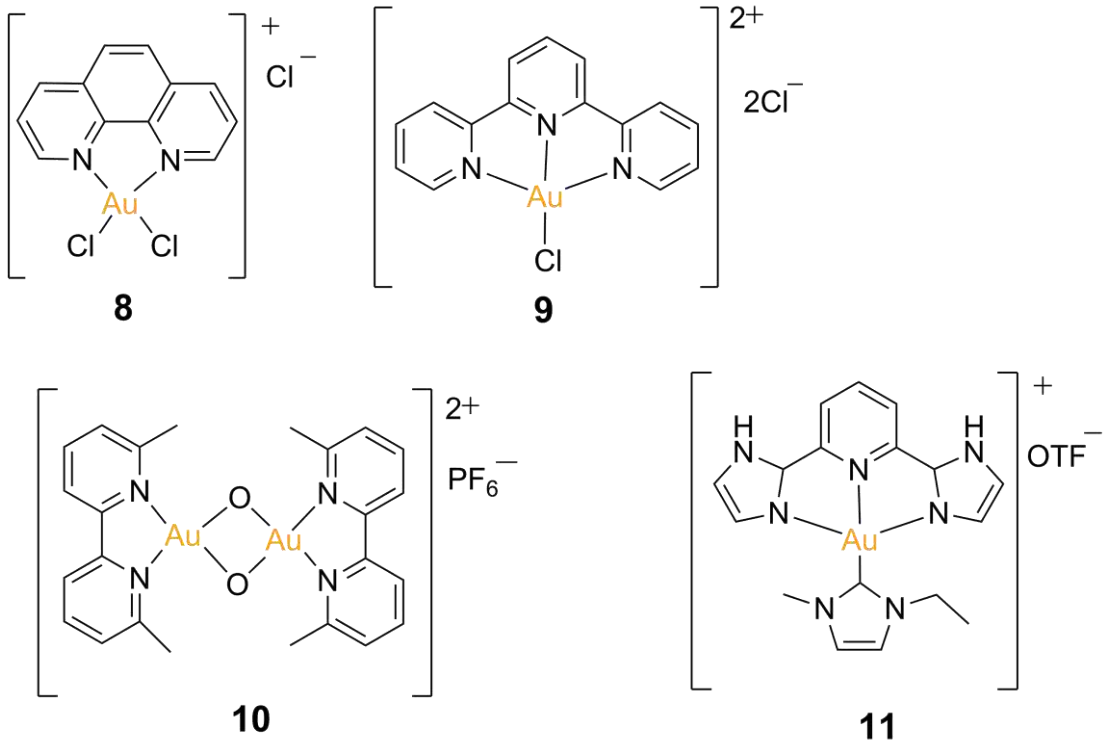


Fig. 18 Cytotoxic Au(III) complexes with N-donor chelating ligands.[161,162]

Complex **11** was determined to be the most stable Au(III) N-donor chelate under physiological conditions (Fig. 18). However, its cytotoxicity against A2780 cells, as

reported in Table 2, was low.[161] Interestingly, complexes **8** and **9** exhibited the highest cytotoxicity against A2780 cells, yet were the least stable. This suggests that the mechanism of action for complexes **8** and **9** follows Fig. 15 where they function as prodrugs. The Au(III) ion is reduced to Au(I) in the presence of phenyl and terpy ligands.[161] Complex **10**, a dimeric oxo-bridged complex, displayed micromolar IC_{50} values against A2780 and A2780R (cisplatin-resistant) cancer cell lines. Complex **10** is largely stable, but aquation may occur, leading to the formation of a monomeric bis-hydroxo complex. Additionally, it is susceptible to physiological reduction.[162] Proteomic studies on A2780 cells treated with complex **10** have been conducted, and it was found that the majority of the proteins involved were in redox homeostasis. This indicates that the formation of reactive oxygen species is the primary mechanism for the cytotoxicity of complex **10**, and the complex may act as a prodrug by being reduced from Au(III) to Au(I).[163]

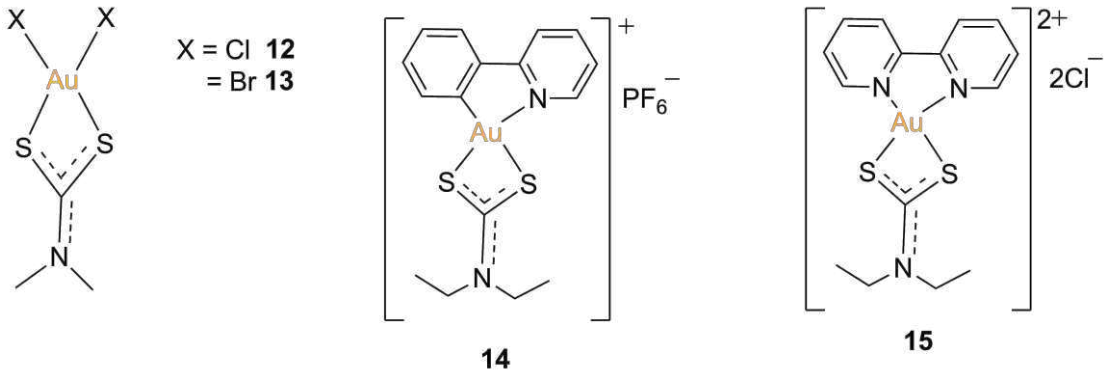


Fig. 19 Cytotoxic Au(III) dithiocarbamate compounds.[164]

Dithiocarbamate (DTC) compounds contain two Au–S bonds that aid in stabilizing the Au(III) oxidation state. Complexes **12** and **13** (Fig. 19) have been analysed in vitro against several cancer cell lines. Both complexes exhibited nanomolar concentration inhibition against leukaemia (HL60), melanoma (MeWo) cells, lymphoma, and were even cytotoxic toward cisplatin-resistant cancer, indicating an alternative target other than DNA.[165] The mechanism of action for complex **12** against PC3 prostate cancer has been shown to involve the overexpression of reactive oxygen species, which inhibit trxR and depolarize the mitochondrial membranes, activating caspase-9 and causing apoptosis. Complex **13** has been shown to target the proteasome.[164]

Alternative complexes to be considered are **14** and **15**, as shown in Fig. 20, which are stable cyclometalated 2-phenylpyridine and 2,2'-bipyridine complexes.[166,167] Complex **14** exhibits its cytotoxicity by inhibiting the ubiquitin pathway through deubiquitination

inhibition activity. Additionally, complex **14** causes apoptosis and possesses antiangiogenic activity in MCF-7 breast cancer cells.[167] Complex **15** is an analogue of **14**, with a 2,2'-bipyridine ligand replacing the cyclometalated ligand. It demonstrates its cytotoxicity by affecting the mitochondrial pathway, resulting in apoptosis.[166]

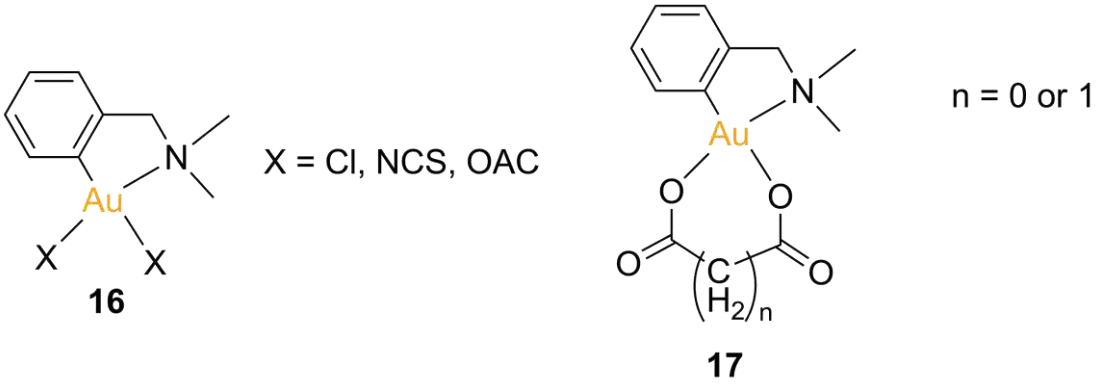
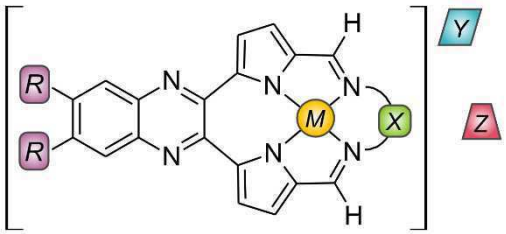


Fig. 20 Cytotoxic cyclometalated Au(III) complexes.[168]

Complexes **16** and **17** are cyclometalated Au(III) complexes with a 2-(*N*,*N*-dimethylamino)methylphenyl ligand. Both complexes have been shown to possess higher cytotoxicity than cisplatin *in vitro* and are cytotoxic to cisplatin-resistant cells (A2780-R). In a murine model, they exhibit cytotoxicity comparable to that of cisplatin. Their mode of action is that they inhibit cysteine protease cathepsin B.[168] Complexes **18** and **19** are analogues of complexes **16** and **17** but contain a pyridyl rather than an $RNMe_2$ moiety. Complex **19** has been shown to inhibit cysteine proteases cathepsin B and K with micromolar concentration cytotoxicity against cancer cells *in vitro*.[169]



	M	X	R	Y	Z
18	Au	$-CH_2CH_2CH_2-$	H	+	PF_6^-
19	Au	$-CH_2C(CH_3)_2CH_2-$	H	+	PF_6^-
20	Au	$-CH_2C(CH_3)_2CH_2-$	H	+	$CF_3SO_3^-$
21	Au	$-CH_2(CH_2)_2CH_2-$	H	+	PF_6^-
22	Au	$-CH_2CHClCH_2-$	H	+	PF_6^-
23	Au	$-CH_2CH_2CH_2-$	CH_3	+	PF_6^-

Fig. 21 Redox-stable gold(III) macrocycles that were designed to specifically target DNA. The illustration is adapted from Akerman *et al*.[170]

Akerman *et al*.[170] reported a series of redox-stable Au(III) macrocycles that were designed to specifically target DNA (Fig. 21). The planar structure of the Au(III) macrocycles enabled them to bind via intercalation to DNA. Additionally, the complexes were found to inhibit human topoisomerase IB by an unconventional catalytic inhibition mechanism (blocking Top1 from binding its DNA substrate). The most cytotoxic compound (**21**, incorporating a butyl chain as the linker) was found to be especially active against leukemia, colon, and CNS cancer in the NCI-60 cell line screen. Unfortunately, negligible cytotoxicity was determined in the murine model.[170]

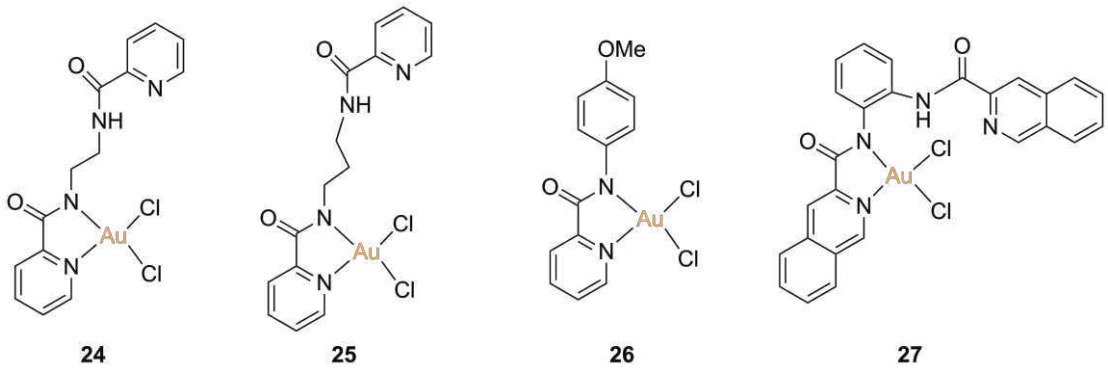


Fig. 22 Gold(III) pyridyl- and isoquinolylamido complexes.[171]

Wilson *et al*.[171] reported a series of Au(III) pyridyl- and isoquinolylamido complexes that were able to bind to and intercalate with DNA (Fig. 22). Complex **27** was selected to undergo the NCI-60 screen and was found to be most cytotoxic against colon, ovarian, and prostate cancer. Further mechanistic characterization of complex **27** revealed that it was able to inhibit both topoisomerase I and topoisomerase II. Complex **27** acts as an interfacial poison of Top1 and Top2, but at concentrations greater than 5 µM, it acts as a catalytic inhibitor of Top2.[171]

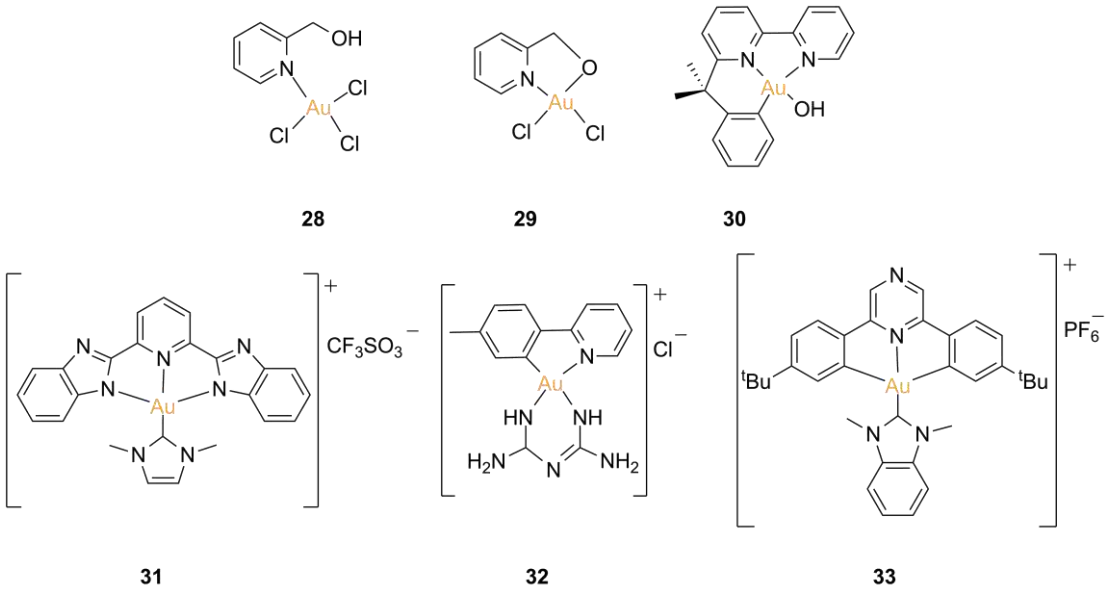


Fig. 23 Gold(III) chelates that have shown activity against A2780R cells.

Table 2. Cytotoxicity of selected Au(III) complexes with the A2780 cancer cell line (human ovarian carcinoma and the equivalent cisplatin-resistant cell line A2780-R.

Entry	Complex	IC_{50} (μM)[a,b] against A2780	IC_{50} (μM)[a,b] against A2780R
1	**8**[161]	3.8 ± 1.1, 72 h (1.2 ± 0.43)	3.5 ± 0.9, 72 h (14.2 ± 2.72)
2	**9**[161]	0.1, 72 h (1.2 ± 0.43)	0.4, 72 h (14.2 ± 2.72)
3	**10**[162]	1.8 ± 0.2, 72 h (2.1 ± 0.1)	4.8 ± 0.5, 72 h (24.4 ± 0.1)
4	**28**[172]	100 (5.3)	21.0 (57.0)
5	**29**[172]	8.4 (5.3)	13.8 (57)
6	**30**[173,174]	3.3 ± 1.4, 72 h	8.2 ± 1.5, 72 h

[a] Cell viability data are reported as the concentration (μM) needed to inhibit 50% of the cultured cell growth (IC_{50}). [b] Where known, the incubation time of the Au(III) chelates with the cells is reported. The IC_{50} values were determined by the sulforhodamine assay.

Table 3. Cytotoxicity data for selected Au(III) complexes against different cancer cell lines and non-cancer cell lines.

Entry	Complex	IC_{50}[a] (μM); cancer cells (cell line, time [b])	IC_{50}[a] (μM); healthy cells (cell line, time [b])
1	**1**[175]	0.3 ± 0.02 (HeLa, 48 h)[c], (11.2 ± 0.96)	0.9 (CCD-19Lu, 48 h)[c]
2	**3**[176]	3.4 ± 0.6 (HeLa, 72 h)[c], (11.0 ± 1)	
3	**4**[176]	8.2 ± 0.5 (HeLa, 72 h)[c], (11.0 ± 1)	
4	**5**[176]	7.2 ± 0.6 (HeLa, 72)[c]	18 ± 0.6
5	**6**[177]	0.04 ± 0.006 (HeLa, 72 h)[c], (11.0 ± 1)	1.6 ± 0.1 (CCD-19Lu, 72 h)[c]
6	**7a**[176]	8.0 ± 0.5 (HeLa, 72 h)[c], (11.0 ± 1)	
7	**7b**[177]	0.08 ± 0.007 (HeLa, 72 h)[c], (11 ± 1)	1.9 ± 0.1 (CCD-19Lu, 72 h)[c]
8	**7c**[178]	0.2 ± 0.05 (NCI-H-460, 72 h)[c] (3.5 ± 1)	25 ± 3.8 (CCD-19Lu, 72 h)[c]
9	**11**[179]	1.4 ± 0.2 (HeLa, 72 h)[c], (1.8 ± 0.1)[e]	
10	**21**[180]	0.280 (non-small lung cancer)[c]	
11	**27**[171]	13 ± 4 (leukaemia)	
12	**31**[179]	14.4 ± 2.2 (HeLa, 72 h)[c], (1.8 ± 0.1)[e]	
13	**33**[181]	0.3 ± 0.15 (HL60, 72 h)[d], (3.70 ± 0.25)	1.4 ± 0.4 (MRC-5, 72 h)[d], (10.7 ± 3.0)
14	**34**[176]	7.7 ± 0.1 (HeLa, 72 h)[c], (5.2 ± 0.1)	32.8 ± 2.6 (CCD-19Lu, 72 h)[c], (36.2 ± 0.4)

[a] Cell viability data are reported as the concentration (μM) needed to inhibit 50% of the cultured cell growth (IC_{50}). [b] Where known, the incubation time of the Au(III) chelates with the cells is reported. Cell viability was measured by either the MTT assay [c] or the MTS assay [d]. [e] IC_{50} of auranofin measured under the same conditions.

1.5 Human serum albumin

HSA is a single polypeptide protein that is heart-shaped and composed of 585 amino acids, with a molecular weight of 66,500 Da. The protein is primarily made up of alpha-helices, which are connected by 17 disulphide bonds, resulting in the formation of 9 loops.[15,182] There are three domains that make up the single polypeptide: domains I, II, and III. Domain I is composed of amino acids 1-195, domain II is composed of amino acids 196-383, and domain III is composed of amino acids 384-585.[15,183] Each domain is further divided into two subdomains, A and B, and each domain consists of 10 α-helices, 6 of which are within subdomain A and 4 of which are within subdomain B. All three domains have a similar 3D conformational structure, and their assembly is highly asymmetric.[15,183] The heart shape of HSA is a result of the asymmetric makeup of HSA. Domains I and II are perpendicular, which forms a T-shape. The tail of subdomain IIA is attached to subdomains IA and IB by hydrophobic interactions and protrudes from IIB, forming a Y-shape. All of this is held together by the 17 disulphide bonds, resulting in the conformationally stable heart-shaped HSA.[183]

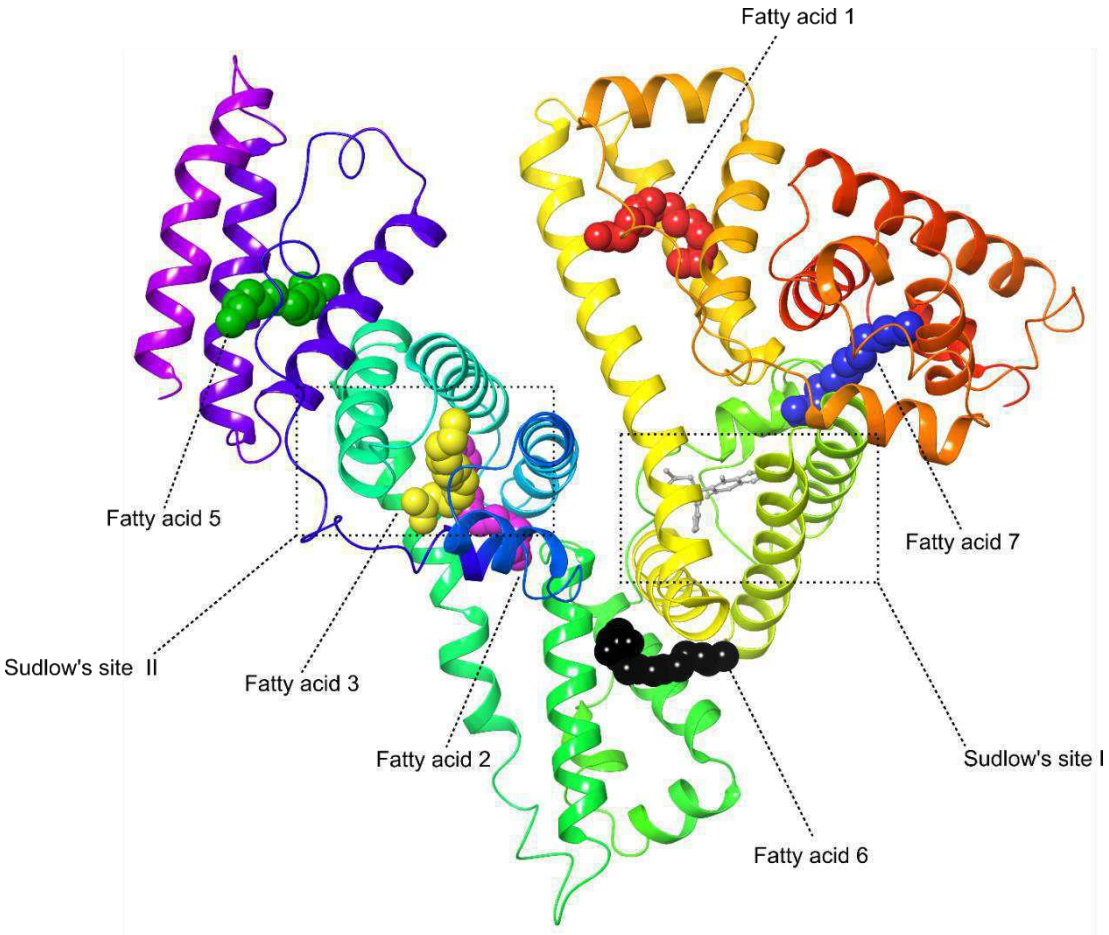


Fig. 24 X-ray structure of HSA with six fatty acids occupying six of the seven fatty acid binding sites; fatty acid 2 was not bound due to warfarin being present in Sudlow's site I (PDB 1HA2).[184]

1.5.1. Fatty acid binding to HSA

HSA is able to bind to seven non-esterified long-chain fatty acids at various sites that populate the protein, as depicted in Fig. 24. Fatty acids are the main binding ligand to HSA, and each fatty acid binding site has a different affinity.[185–187] As shown in Fig. 24, fatty acid sites 1-5 bind the fatty acids by either polar or electrostatic interactions, therefore, they are noncovalently anchored to the protein. Fatty acid-1 forms a salt bridge with Arg-117 within the IB-IIA polypeptide linker. Fatty acid-2 hydrogen bonds with Tyr-150 in subdomain IB, as well as with Arg-257 and Ser-287 in subdomain IIA. Fatty acids-3 and 4 are located within a large cavity in subdomain IIIA that comprises of Sudlow's site II. Fatty acid-3 forms a salt bridge with Arg-348 and Arg-485 and hydrogen bonds with Ser-342. Meanwhile, fatty acid-4 forms a salt bridge with Arg-410 and hydrogen bonds with Tyr-411 and Ser-489. Fatty acid-5 is positioned within subdomain IIIB, with its polar head leaning towards subdomain IIIA. It forms a salt bridge and hydrogen bonds with Tyr-401 and Lys-525. Fatty acid-6 and 7 are postulated to have low affinity for binding to their respective sites, due to the lack of evidence suggesting that they form polar interactions with HSA to anchor the fatty acids.[186–188]

1.5.2. Sudlow's site I

Sudlow's site I is located in the core of subdomain IIA and is composed of six α-helices as well as a loop-helix feature. The interior of Sudlow's site I is mainly apolar but does consist of two groups of polar residues. The first group is located within the cavity towards the bottom of the pocket (Tyr-150, His-242, and Arg-257), while the second group is located in close proximity to the entrance of Sudlow's site I (Lys-195, Lys-199, Arg-218, and Arg-222). The site is divided into three sub-chambers, where Ile-264 separates two hydrophobic subdomains, and the third is formed by Phe-211, Trp-214, Ala-215, Arg-218, and Leu-219. Trp-214 is an important residue in the active site, as it can play a role in π-π stacking with complexes and can be used to determine if a complex binds to Sudlow's site I using tryptophan fluorescence. Tryptophan fluorescence is quenched when there are conformational changes in the active site. Therefore, if a complex were to bind to Sudlow's site I, it would cause a conformational change, resulting in the quenching of Trp-214 fluorescence (Fig. 25). Typically, complexes that bind to Sudlow's site I are bulky, negatively charged heterocyclic compounds with the centre of the complex having a negative charge.[188–191]

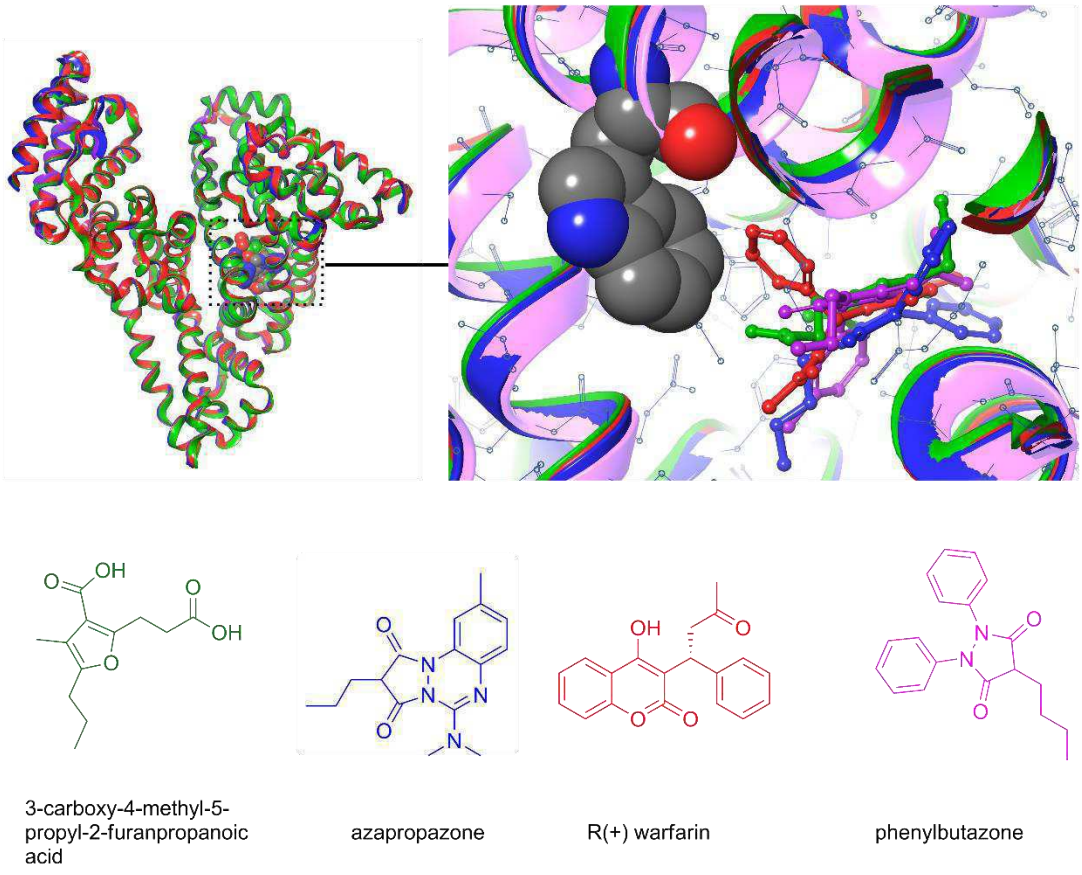


Fig. 25 Overlayed structures of HSA with ligands that target Sudlow's site I (PDB's 2BXD (red) warfarin, 2BXC (purple) phenylbutazone, 2BX8 (blue) azapropazone and 2BXA (green) 3-carboxy-4-methyl-5-propyl-2-furanpropanoic acid).[189] All four ligands are non-covalently bound within Sudlow's site I and bind in close proximity to the Trp-214 residue (highlighted in the space fill model).

Examples of drugs that bind to Sudlow's site I include phenylbutazone,[189] warfarin,[188] 3-carboxy-4-methyl-5-propyl-2-furanpropanoic acid,[189] and azapropazone,[189] which all bind to the centre of the pocket. All these drugs occupy the apolar portion of Sudlow's site I to different degrees. However, only drugs with hydrophobic moieties bind to the left-hand sub-chamber, but all drugs can access the right-hand sub-chamber. Compounds also interact with the inner and outer polar groups, in particular, the hydroxy moiety of Tyr-150.[190] Therefore, Tyr-150 is deemed essential for drug interactions. The stereoselectivity of Sudlow's site I was studied by Petitpas *et al.*,[188] who analysed the R-(+) and S-(-) enantiomers of warfarin bound to HSA by X-ray crystallography.[188] Both enantiomers effectively occupied the same position, with the S-(-) enantiomer having a marginally higher binding constant of 3.8 µM as compared to the R-(+) enantiomers K_a of 2.6 µM.[192] Overall, warfarin forms three hydrogen bonds with either Lys-199 or Arg-222.[188]

The amino acid composition of Sudlow's site I enables HSA to be more selective for the drugs that bind to the protein. There is an abundance of basic amino acids and polar patches, with flanking apolar regions; therefore drugs with electronegative features are generally more specific to this site.[185,193,194] Ghuman *et al*.[189] superimposed HSA-drug complexes for Sudlow's site I and found that there was a minimal distortion of the chains upon binding of small molecules.

1.5.3. Sudlow's site II

Sudlow's site II, which is topologically similar to Sudlow's site I, is composed of six α-helices and a pre-formed hydrophobic cavity with a polar patch. However, there are distinct differences that enable the differentiation of molecules that bind to the site. Firstly, Sudlow's site II is smaller in size and possesses only one sub-chamber, the rear right-hand hydrophobic sub-chamber, which can only be accessed by ligands that induce a conformational change, allowing the side chains to move. The absence of a left-hand sub-chamber is due to the presence of Tyr-411 at the position corresponding to Leu-219 (in subdomain IIA; Fig. 26). Additionally, Sudlow's site II lacks a polar patch at the entrance to the cavity, and, due to the rotation of subdomain IIIB perpendicular to subdomain IIIA, the pocket entrance is more exposed to the solvent. The main polar patch of Sudlow's site II is cantered on Tyr-411 and includes Arg-410, Lys-414, and Ser-489. In comparison to the polar patch located towards the entrance of Sudlow's site I, only Arg-410 and Lys-414 are present at equivalent positions to Arg-218 and Arg-222.[189,191]

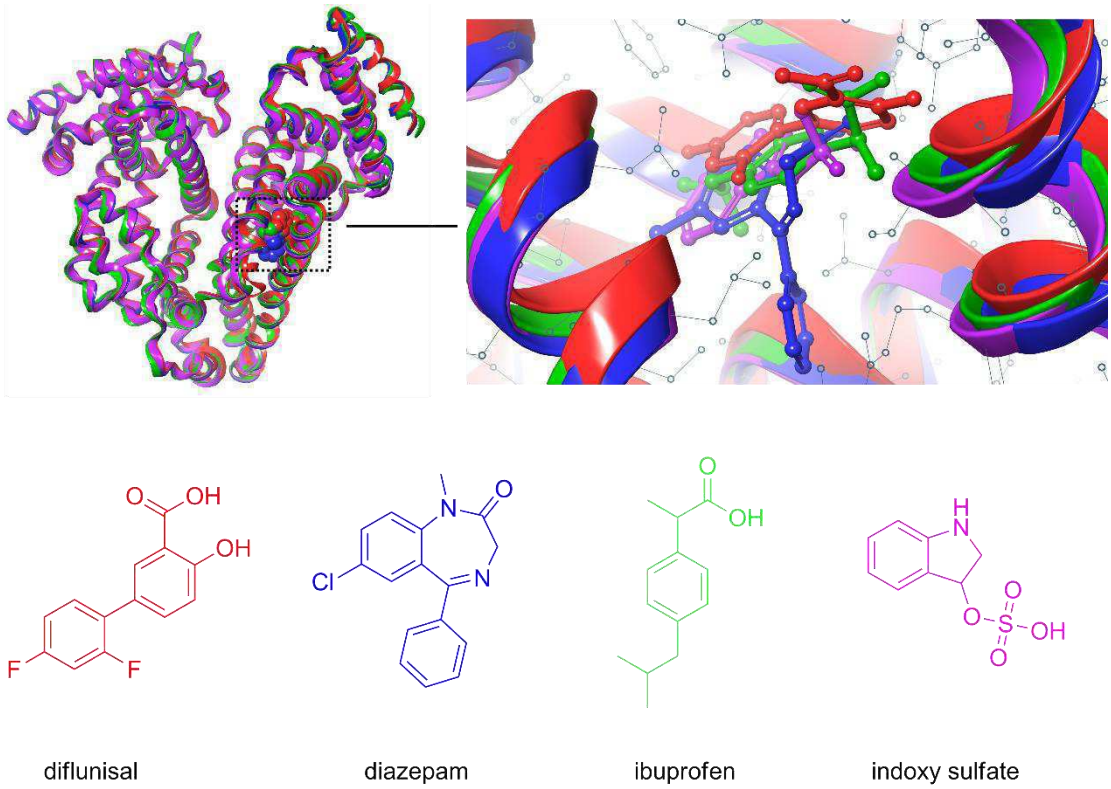


Fig. 26 Overlayed structures of HSA with ligands that target Sudlow's site I (PDB's 2BXE (red) diflunisal, 2BXF (blue) diazepam, 2BXG (green) ibuprofen and 2BXH (purple) indoxy sulfate).[189] All four ligands are non-covalently bound within Sudlow's site II.

In summary, the polarity and size of both Sudlow's sites I and II are distinguishable, which accounts for the difference in binding specificity for each binding site. Common drugs that have been shown to bind to Sudlow's site II include diazepam, diflunisal, indoxyl sulphate, and ibuprofen. All four drugs bind to the centre of Sudlow's site II and orient in a manner that results in at least one oxygen atom overlapping the polar patch. Additionally, in all four cases, the hydroxy group of Tyr-410 hydrogen bonds with the four-drug molecules. This provides further evidence that Sudlow's site II is typically selective for drugs with a peripherally located electronegative group.[189]

Sudlow's site II has an impressive ability to accommodate the binding of various ligands. Small molecules, such as ibuprofen, result in minimal side chain rotation and movement. However, diazepam (molecular weight: 284.7 g/mol), a comparatively larger drug, results in greater side chain movement, as demonstrated by an increase in the distance separation between Lys-387 and Lys-453 from 5.4 Å to 7.7 Å. Furthermore, additional evidence supporting the adaptability of Sudlow's site II is its ability to accommodate two long-chain non-esterified fatty acids (fatty acids 3 and 4) or one thyroxine molecule.[189,190,196]

1.5.4. Additional drug-binding sites

In addition to Sudlow's sites I and II, there are secondary binding sites on HSA that sometimes serve as sites for excess ligands when Sudlow's sites I and II are occupied.[189] These sites are not as well characterised as Sudlow's sites I and II. One such site, considered the third binding site, is located in subdomain IIIB and is responsible for binding hemin.[197] Other binding sites have been identified in a shallow cavity between subdomains IIA and IIB, in subdomain IIIB, and within a cleft between domains I and III.[189,198] Additionally, there are known metal ion binding sites and a site for binding thyroxine.[18]

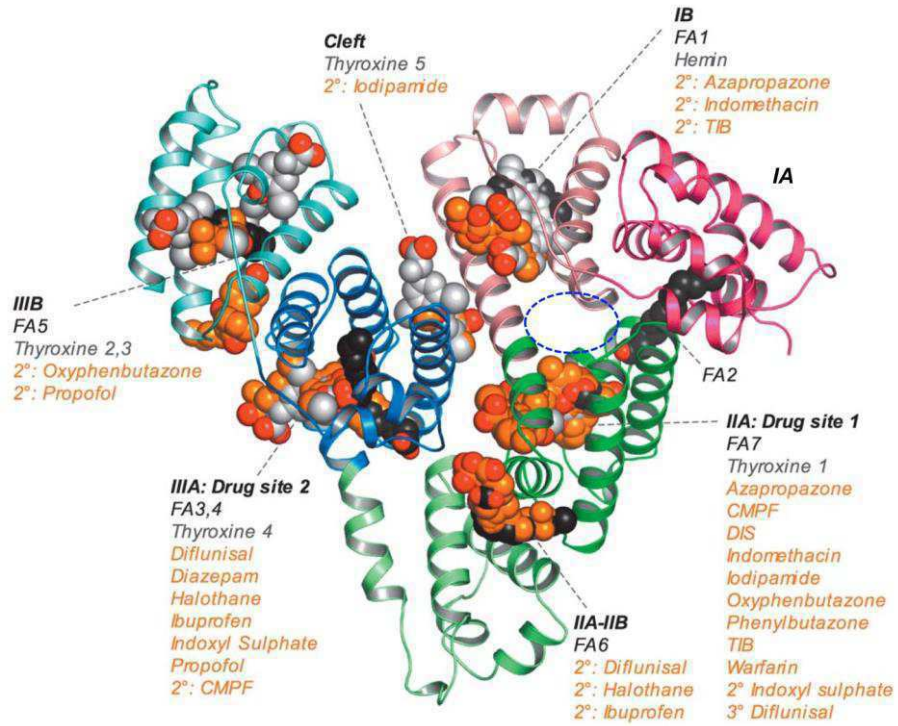


Fig. 27 HSA drug binding sites. Modified from Figure 7 of Ghuman *et al*:[189] "Summary of the ligand binding capacity of HSA as defined by crystallographic studies to date. Ligands are depicted in space-filling representation; oxygen atoms are coloured red; all other atoms in fatty acids (myristic acid), other endogenous ligands (hemin, thyroxin), and drugs are coloured dark-grey, light grey, and orange, respectively." The dashed ellipse indicates where ligands bind adjacent to and in contact with warfarin in the docking studies presented in this thesis (vide infra).

1.6. The binding of anticancer drugs by HSA

1.6.1. *Platinum complexes*

Cisplatin is a widely used anti-tumour drug that interacts with DNA and causes inhibition of DNA replication and transcription. The mechanism of action is not fully understood, but it is believed to involve alkylation and distortion of the double helix of DNA.[199] The chloride ligands of cisplatin can be easily exchanged with H_2O, resulting

in the formation of the *cis*-[PtCl(OH_2)(NH_3)$_2$]$^+$ structure under physiological conditions (Fig. 12b).[103] About 68-98% of cisplatin is bound to HSA within 24 hours of administration, according to literature studies.[200,201]

There is ongoing debate as to whether HSA acts as a reservoir for storing cisplatin or if it binds cisplatin, preventing it from effectively distributing to tissues and rendering the bound drug to have a lower efficacy. This question has been difficult to answer as there has been evidence for both arguments. Holding *et al*.[202] showed that an HSA-cisplatin adduct was still cytotoxic to carcinoma cells. However, studies by Møller *et al*.[203] showed that the HSA-cisplatin adduct was not taken up by Ehrlich Ascites Tumour Cells (EATC) and adherent Ehrlich Lettré Ascites Cells (Lettré) and did not cause cytotoxicity. Similar results were found with NHIK 3025 cells.[204]

Understanding the binding of cisplatin is crucial in developing alternative administration methods to enhance the drug's effectiveness. Early studies suggested that Cys-34 was the major binding site for cisplatin[205,206] because platinum is a soft Lewis acid and therefore prefers soft donors like sulphur. However, several studies have disputed Cys-34's involvement in the binding of cisplatin.[207–209] A study by Ferraro *et al*.[207] used X-ray crystallography to identify all specific binding sites of cisplatin on HSA, with a resolution of 3.16 Å, and found cisplatin bound to His-105, His-288, Met-298, Met-329, and Met-548. Three additional binding sites were found to be His-535, His-64, and His-247 when the HSA crystal was used in a wet soak experiment with cisplatin over 48 hours. These findings are consistent with previous studies suggesting that between 5-10 moles of cisplatin bind to 1 mole of HSA (Fig. 28).[201,210]

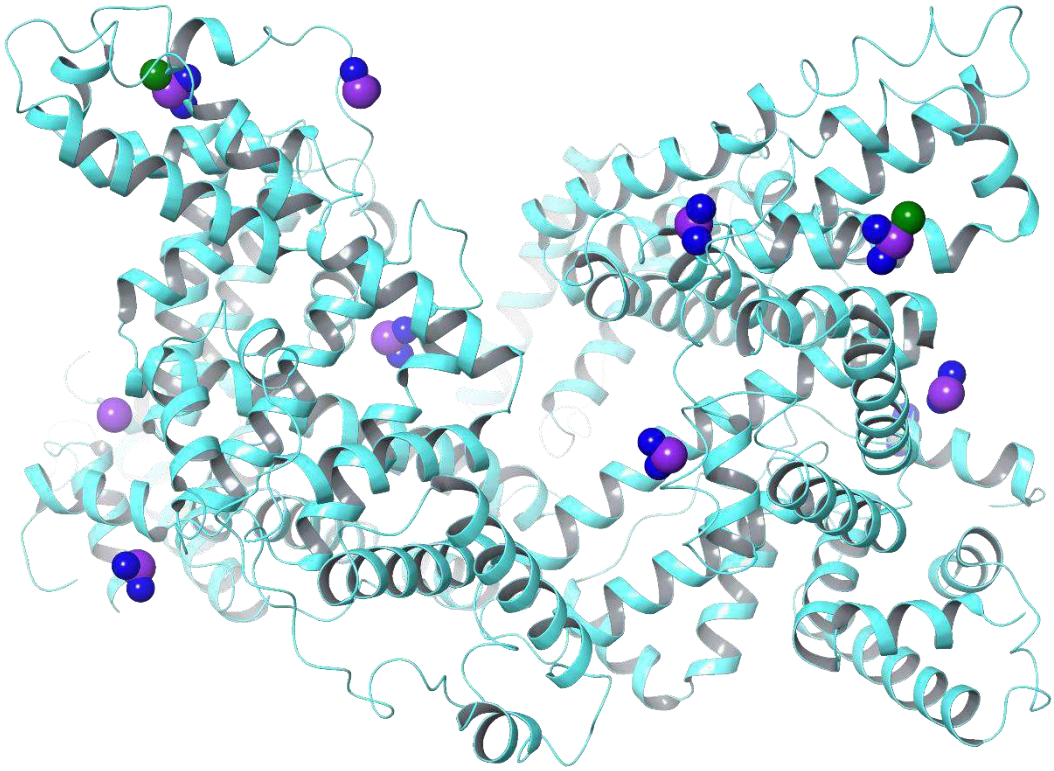
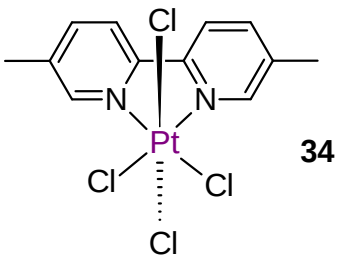


Fig. 28 X-ray crystal structure at 2.90 Å resolution of an HSA crystal soaked with cisplatin for 1 week (PDB code 7WOK)[207] highlighting all bound Pt(II) ions (purple). Nitrogen and chlorine atoms are rendered in blue and green, respectively. One Pt(II) ion exhibits complete ligand exchange, two Pt(II) ions exhibit the exchange of one chloride ligand, and the remaining Pt(II) ions have exchanged both chloride ions.

According to Wiglusz,[211] an investigation revealed that the administration of non-steroidal anti-inflammatory drugs (NSAIDs) in conjunction with cisplatin resulted in a reduction of the number of moles of cisplatin that bound to human serum albumin (HSA). The efficacy of the NSAIDs was found to be in the following order: warfarin > ibuprofen > aspirin > meloxicam. This finding suggests that the co-administration of NSAIDs with cisplatin may lead to an increased concentration of unbound cisplatin in a patient. Additionally, it is noteworthy that transplatin was found to have a high binding affinity for HSA, with 7 moles of transplatin binding per mole of HSA, although its effectiveness as a chemotherapeutic agent has not been established.[211]

Cis-[(1*R*,2*R*)-1,2-cyclohexanediamine-*N*,*N*']oxalato(2-)-*O*,*O*'] platinum (oxaliplatin), is a third-generation platinum-based drug used in the treatment of metastatic colorectal carcinoma, typically in combination with fluoropyrimidines.[212] The molecule contains both a diaminocyclohexane group and an oxalate group, which acts as a leaving group. Studies on the interaction of oxaliplatin with HSA are less common compared to cisplatin. However, a study by Yue *et al*.[213] demonstrated that oxaliplatin

binds to subdomain IIA of HSA near Trp-214 and forms intramolecular hydrogen bonds with Arg-222 and Ala-291. The dissociation constant (K_d) for this binding was found to be 346 µM, and the binding is entropically driven. Additionally, the binding affinity of oxaliplatin to HSA was found to decrease in the presence of other common amino acids or metal ions, likely due to conformational changes in HSA.



34

Fig. 29 Structure of Pt^{IV}(5,5′-dimethyl-2,2′-bipyridine)Cl_4.[214]

The synthesis of Pt(IV) drugs such as **34** represents a promising area of research for the development of next-generation platinum-based chemotherapy agents (Fig. 29).[215,216] These compounds are widely accepted to function as prodrugs[115] and typically have a general formula of *cis*-[$PtA_2X_2Y_2$], where A represents the axial ligands that impart chemical and physical characteristics to the complex, such as increased lipophilicity or enhanced binding to serum proteins, X represents the characteristic ligand, and Y is the monodentate anionic leaving ligand.[217] Pt(IV) drugs are typically prepared by oxidising a square planar Pt(II) complex, which adds two axial ligands, resulting in a 6-coordinate d^6 low-spin octahedral Pt(IV) complex. The benefits of this approach include increased chemical stability and reduced biological reactivity of the complex.[215] The Pt(IV) drug is designed to enter a tumour before being reduced by reductants, such as ascorbate and glutathione, resulting in a more active Pt(II) drug.[215,216] Serum proteins such as HSA are particularly important in this process as they can serve as carriers of the Pt(IV) drugs to the tumour (Fig. 12). The interaction of Pt(IV) drugs with HSA will be discussed in further detail below.

Shahraki *et al*.[214] investigated the binding of **34**, a bidentate N-donor complex, to HSA. The complex, in which the axial and Y ligands are chlorides, has been shown to possess cytotoxic activity against Caco-2, HT-29, and T47D cancer cell lines.[218] The results of the study demonstrated that **34** binds to HSA with moderate affinity, with a K_d of 102 µM, primarily due to electrostatic and Van der Waals forces. The binding site was identified as subdomain IIA. This was further supported by docking studies, which revealed that Ser-480 interacts with the chloride ions, Phe-206 interacts with

the chloride ions, and bipy N, Lys-351, and Trp-214. This interaction resulted in the quenching of the Trp-214 fluorescence.

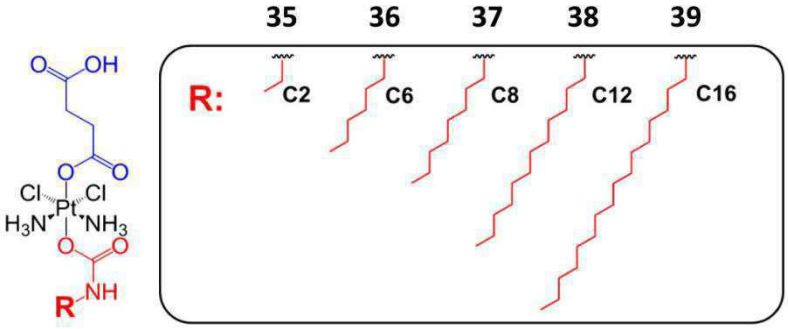


Fig. 30 Structures of platinum(IV) complexes bearing aliphatic tails. The illustration was adapted from the paper by Zheng *et al*.[216]

In a study by Zheng *et al*.[216], five novel Pt(IV) drugs were synthesised by the oxidation of cisplatin and the addition of an axial succinate group. Different length (up to hexadecyl) aliphatic tails were added to represent the structure of a fatty acid (Fig. 30). Complex **39** bearing a C16 aliphatic tail was found to be the most potent of the complexes, exhibiting cytotoxicity superior to cisplatin against A549, A2780, and A2780CP70 cell lines. Additionally, the cellular uptake of **39** was found to be better than cisplatin and it interacted with HSA in a 1:1 mole ratio. The study found that longer aliphatic tails improved the binding of the complex to HSA, with K_d values as follows: **39** (0.962 µM) > **38** (27.0 µM) > **35** (384.6 µM). HSA was also shown to be able to protect the reduction of **39** and the HSA-**39** adduct has similar cytotoxicity to the protein-free complex.

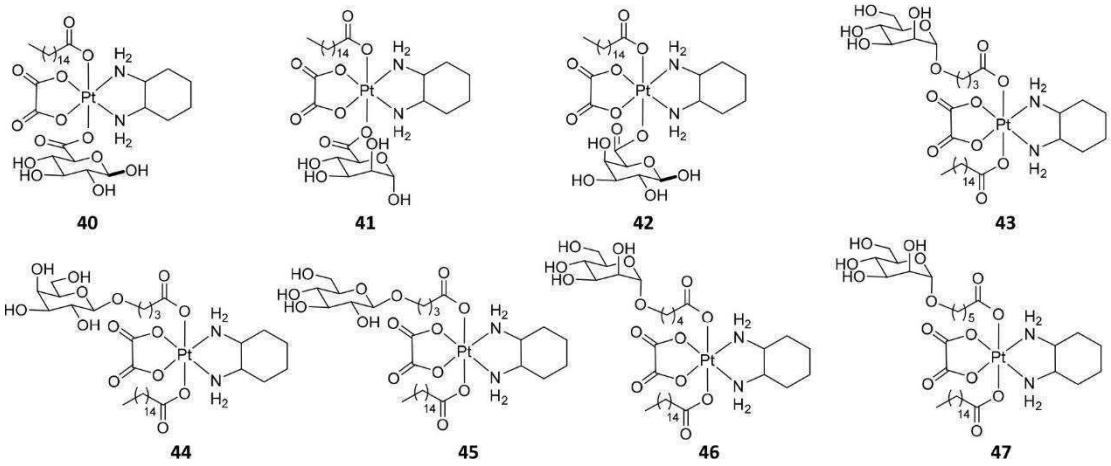
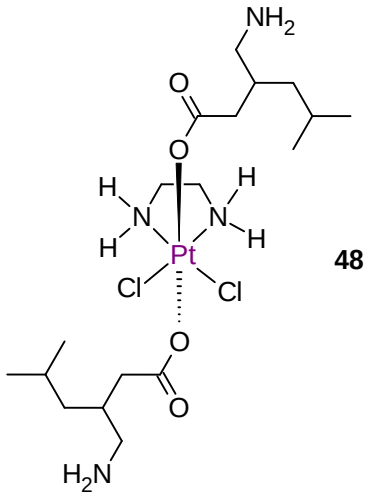


Fig. 31 Structures of a series of glycosylated Pt(IV) complexes adapted from Ma *et al*.[215]

A series of eight glycosylated Pt(IV) oxaliplatin derivatives were synthesised, featuring hexadecenoic acid ligands (aliphatic tails; Fig. 31). The drugs were designed to possess good lipophilicity, thereby allowing them to interact with HSA and function via the EPR effect. Among the compounds synthesised, **45** exhibited the most significant activity against HeLa, MCF-7, LNCaP, and PC3 tumour cell lines, and demonstrated high cytotoxicity against HepG-2, A549, and A549R cell lines. Additionally, results showed that **45** was able to rapidly accumulate in tumours through the utilisation of glucose transporters, organic cation transporters, and HSA. Docking studies revealed that the Pt(IV) ion was non-covalently bound to Arg-222 and Lys-199, the glycosylated moiety interacted with Pro-447, Asp-451, Glu-292, and Asn-295, and the aliphatic tail bound noncovalently to the hydrophobic region containing Tyr-150, Leu-238, Leu-219, Leu-234, Phe-223, Ile-264, Ala-261, and Ile-290.[215]



48

Fig. 32 Structure of the Pt(IV) complex $PtCl_2(en)(pregabalin)_2$.[217]

Satraplatin is a third-generation Pt(IV) prodrug. A derivative of satraplatin, **48**, was developed to possess similar cytotoxic capabilities (Fig. 32).[217] The incorporation of pregabalin, (*S*)-3-isobutyl-γ-aminobutyric acid, which is an amino acid analogue, improves the bioavailability of the drug. Notably, pregabalin does not interact with serum proteins, however, it was observed that HSA can bind to complex **48**. This binding was confirmed to occur in subdomain IIA using a warfarin displacement assay. The interaction between HSA and the complex is relatively weak, with a K_d of 686 µM, and primarily mediated through hydrogen bonding.

In summary, Pt(IV) complexes are designed as prodrugs to exploit the ability of HSA to transport them to tumours. The studies reviewed suggest that aliphatic tails improve the binding of Pt(IV) complexes to HSA[216] with HSA favouring the binding of molecules

with longer aliphatic tails that coil into the hydrophobic region in subdomain IIA.[215] All Pt(IV) complexes investigated exhibited a preference for binding to subdomain IIA, which is noteworthy as the complex with the closest similarity to a fatty acid bound to subdomain IIA, rather than IIIA, despite subdomain IIIA having two fatty acid binding sites.

Table 4: A summary of the biophysical characteristics of platinum(IV) complexes binding to HSA and the cancer cell lines they target.

Name	K_d (μM)	Temperature	Method used to determine K_d	Number of binding sites	Binding site	Electrostatic forces to measure the type of biding	Cancer cell lines targeted
34[218]	ND	ND	ND	1	IIA	ND	Caco-2, HT-29 and T47D
35[216]	384.6	ND	Trp-214 fluorescence	1	IIA	ND	A549, A2780, and A2780CP70 cell lines
38[216]	27.03	ND	Trp-214 fluorescence	1	IIA	ND	A549, A2780, and A2780CP70 cell lines
39[216]	0.9615	ND	Trp-214 fluorescence	1	IIA	ND	A549, A2780, and A2780CP70 cell lines
45[215]	ND	ND	ND	1	IIA	ND	HeLa, MCF-7, LNCaP, PC3, HepG-2, A549, and A549R
48[217]	686	37	Trp-214 fluorescence	1	IIA	ΔH and $\Delta S < 0$ Suggesting electrostatic interactions, H-bonding, and Van Der Waals interactions	N/A

1.6.2. Copper in medicine

Copper has been utilised as a sterilizing agent for centuries, with evidence dating as far back as 2200 B.C.[219] More recently, copper has been incorporated into metallic surfaces for use in the healthcare sector.[220] The mechanism of action involves the dissociation of both wet and dry Cu(II) ions from the metallic surface, which then attack the microbe cell membrane or generate reactive oxygen species (ROS) that result in DNA and genomic damage.[221] Currently, copper-based therapies (CBTs) are being studied as a potential treatment for various medical conditions and diseases, including cancer.[222] To date, hundreds of Cu(I) and Cu(II) complexes have been designed to fight cancer[223] for three main reasons:

(i) Cu(II) ions alone have shown anti-tumour activity on carcinomas,[224,225] although it should be noted that these studies did not measure the actual copper concentration in serum and there are studies that have opposing results.

(ii) Unlike platinum, copper is present in humans as either Cu(I) or Cu(II) and is essential for optimal biological functioning. Copper is tightly regulated due to its redox potential in the formation of ROS that may result in oxidative damage to macromolecules.[226] Copper is also an important cofactor for at least 10 metalloenzymes, including superoxide dismutase, cytochrome-c-oxidase, and tyrosinase.[226]

(iii) Copper-based drugs have at least three mechanisms of action to induce apoptosis in cells: proteasome inhibition,[227] generation of ROS,[228], and DNA damage.[229] All of the foregoing mechanisms make copper complexes suitable candidates for further exploration.

However, one of the major drawbacks of copper complexes is their poor solubility in aqueous solutions. Furthermore, the maximum concentration of dimethyl sulfoxide (DMSO) that can be safely administered to humans is 5000 ppm (since it is a class 3 solvent), making this a poor vehicle for drug delivery. HSA on the other hand has the potential to be used for the delivery of insoluble copper complexes/drugs. HSA is endogenous to humans, non-toxic, and non-antigenic. Moreover, some studies have used HSA to target carcinomas, suggesting enhanced specificity might be feasible with HSA-drug conjugates or co-formulations.

1.6.3. Uptake of Cu-containing prodrugs by HSA

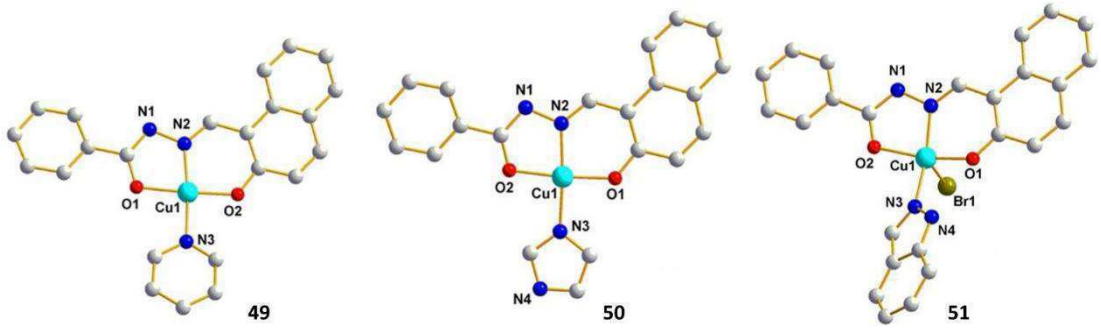


Fig. 33 X-ray structures of the Cu(II) complexes of 2-hydroxy-1-naphthaldehyde benzoyl hydrazone Schiff-bases with pyridine (**49**), imidazole (**50**), and indazole (**51**) co-ligands. Illustration adapted from Gou *et al*.[230]

Typically, pharmaceutical drugs binding to HSA are investigated to determine their pharmacokinetic and pharmacodynamic data. However, Gou *et al*.[230] proposed using copper complexes as prodrugs and utilizing HSA as a carrier protein for the drugs (Figs. 33 and 34). The ligands used in their study were 2-hydroxy-1-naphthaldehyde benzoyl hydrazone Schiff-bases with either a pyridine (**50**), imidazole (**49**), or indazole (**51**) co-ligand group. The goal of the study was to use the 2-hydroxy-1-naphthaldehyde benzoyl hydrazone Schiff-bases (which already possesses anti-cancer activity) and enhance its cytotoxicity by metalating the ligands with a Cu(II) ion. The copper complexes were then reacted with HSA to form HSA-Cu(II)-complex adducts, which were found to be 3 – 5-fold more cytotoxic to MCF-7 breast cancer cells than the free copper chelates. All three copper chelates were found to bind to Sudlow's site I (determined via X-ray crystallography). Unfortunately, neither binding constants nor thermodynamic data for the copper complexes binding to HSA were measured. However, X-ray crystallography did indicate that for **49** and **50**, the Cu^{2+} metal ion centre coordinated to Lys-199 and His-245, whereas the co-ligand of **51** is replaced by Lys-199 and His-242. Atomic absorption spectroscopy revealed that the Cu-complex added to MCF-7 cancer cells was present in higher concentrations when bound to HSA. The mechanism of action was evaluated by measuring the impact of the copper chelates on cyclin activity and reactive oxygen species (ROS) levels. Results showed that when the copper chelates were administrated in the absence of HSA, cyclin activity dropped by 31%, whereas when the copper chelates were added pre-bound to HSA, cyclin activity dropped by 79%. Additionally, ROS levels were found to be higher when the Cu(II) chelates were added pre-bound to HSA, which is a marker for apoptosis.

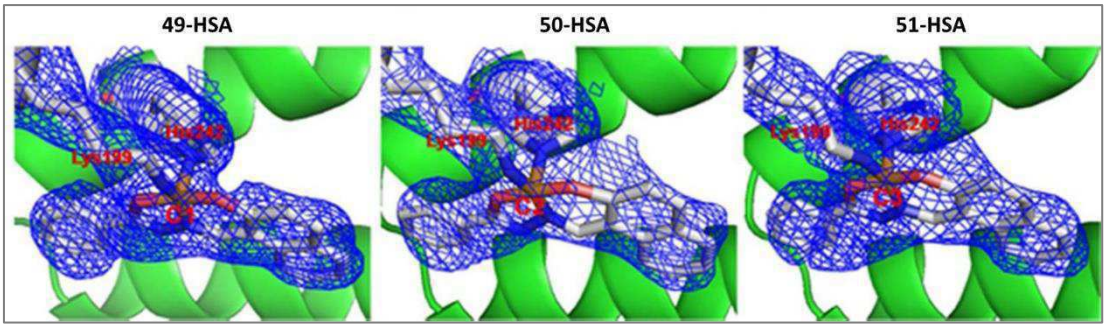


Fig. 34 X-ray structures of the binding site locations of Cu(II) complexes **49**–**51** covalently bound to HSA. Experimental σA weighted 2Fo −Fc electron density maps are shown as blue grids and reveal the substitution of the co-ligands by Lys and His residues of the protein to yield near-identical complex geometries. The illustration was adapted from Gou *et al*.[230]

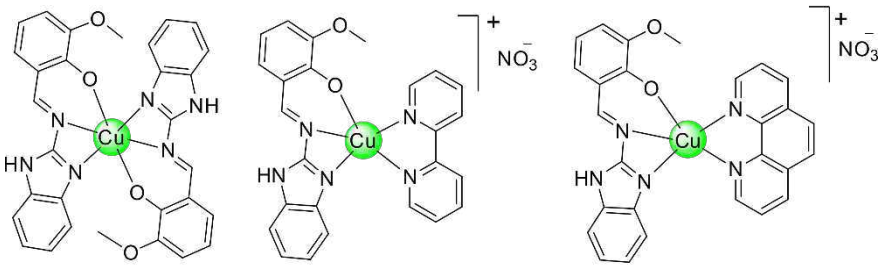


Fig. 35 Structures of Cu(II)-benzimidazole chelates synthesised from 1,10-phenanthroline and/or 2,2′-bipyridine.[231]

Hussain *et al*.[231] conducted a study to investigate the binding of copper(II)-benzimidazole scaffolds synthesised from 1,10-phenanthroline and/or 2,2′-bipyridyl (Fig. 35). The resulting Cu(II) complexes were non-steroid anti-inflammatory drugs (NSAIDs). The study found that all three drugs bound in a 1:1 molar ratio with HSA. However, the complex with the least aromaticity, **53**, had the highest affinity for HSA with a dissociation constant (K_d) of 0.67 µM. *In silico* molecular docking and Trp-214 fluorescence studies suggested that all three complexes bound in Sudlow's site I of HSA, in close proximity to Trp-214.

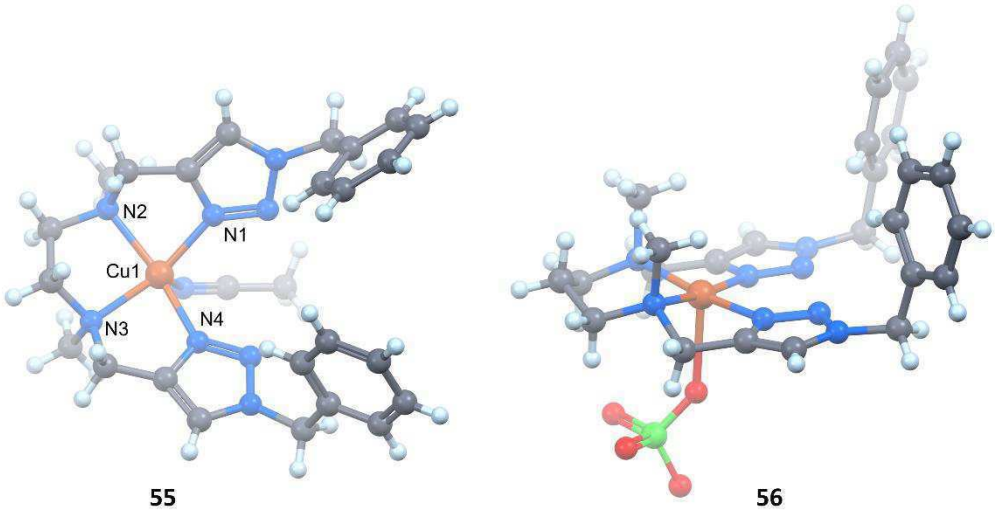
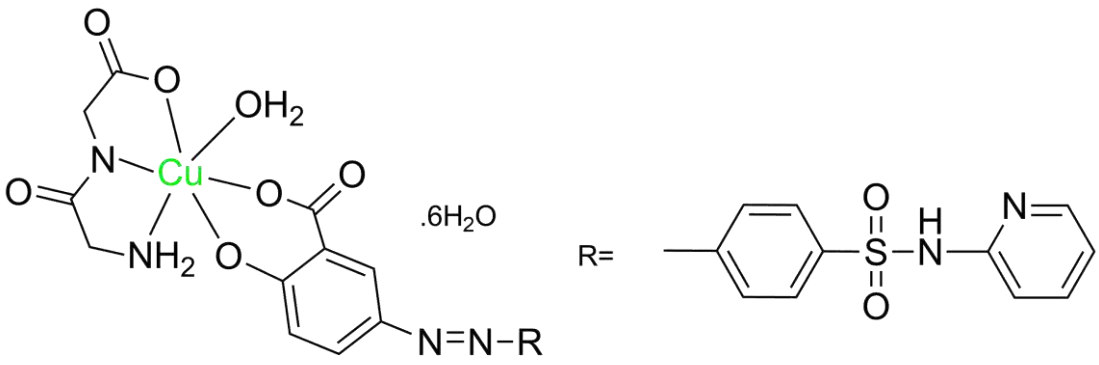


Fig. 36 X-ray structures of **55**, [Cu{*N*,*N'*-*bis*(1-benzyl-1*H*-[1,2,3]triazol-4-ylmethyl)-*N*,*N'*-dimethyl-1,2-diaminoethane}(MeCN)]$(ClO_4)_2$ or [CuL(MeCN)]$(ClO_4)_2$, and **56**, [Cu-{*N*,*N'*-*bis*(1-benzyl-1*H*-[1,2,3]triazol-4-ylmethyl)-*N*,*N'*-dimethyl-1,2-diaminopropane}$(OClO_3)$](ClO_4). Figure redrawn from the CSD coordinates (CCDC 851241 and 851242) deposited by Benkhellat *et al*.[232]

Triazoles and their derivatives are compounds that have been found to exhibit remarkable activity against a variety of microbes and, more recently, cancer.[232] However, triazoles are sometimes unstable and therefore, their stability, pharmacokinetics, and interaction with HSA must be investigated before they can be considered suitable for *in vivo* testing. De Paua *et al*.[233] investigated two complexes synthesised by Benkhellat *et al*.,[232] namely **55** and **56** (Fig. 36). They found that both complexes bound to HSA in a 3:1 molar ratio, as determined by transitions observed by UV-CD spectroscopy. The suggested binding sites were the N-terminal end of HSA composed of Asp-Ala-His, the second site close to Trp-214 in Sudlow's site I, and the third site was to Cys-34 in subdomain IB. The more planar geometry of the Cu(II)(MeCN)$(ClO_4)_2$ complex allowed it to have a marginally higher affinity for HSA.

1.6.4. Dipeptide (glycylglycine) sulfasalazine



57

Fig. 37 Structure of a dipeptide (glycylglycine) sulfasalazine Cu(II) complex, $[Cu(glygly)(ssz)(H_2O)]\cdot 6H_2O$ investigated for HSA binding. Adapted from Tabassum *et al*.[234]

One major limitation of copper complexes is their poor solubility in aqueous media. However, Tabassum *et al*.[234] synthesised a water-soluble copper(II) complex derived from dipeptide (glycylglycine) and sulfasalazine **57**, which exhibits an octahedral geometry and demonstrated anti-cancer activity. The investigation of the binding of **57** to HSA suggests that it binds in a 1:1 molar ratio at subdomain IIA through hydrophobic interactions, with a K_d of 5.14 µM. Docking studies supported these findings and further suggested that **57** binds to Arg-257 through hydrogen bonding, while the carbonyl and sulfone groups interact with Ala-291, Arg-222, and Lys-195.

Kazemi *et al*.[235] and Peng *et al*.[236] investigated the influence of metal cations on the binding of metal complexes to HSA. Kazemi *et al*. utilised the 2-hydroxy-1-allyliminomethyl-naphthalen ligand in combination with Pd(II), Cu(II), V(II)O, and Ni(II), while Peng *et al*. employed N-(2-hydroxyethyl)-N′-benzoylthiourea with Pd(II), Cu(II), Co(II), and Ni(II). The results of both studies indicated that the Pd(II)-complex derivatives exhibited the highest affinity for HSA; similar results have been observed in our work (Chapter 6).

In a review of all copper(II) complexes, only the Cu-triazoles were found to bind to multiple binding sites.[233] Gou *et al*.[230] produced the most definitive study indicating the preferred binding site of their Cu(II)- 2-hydroxy-1-naphthaldehyde benzoyl hydrazine complex bound to Sudlow's site I, as they had the most definitive X-ray crystallography data. The other studies reviewed deduced the preferred binding sites of their copper(II) chelates to HSA by spectroscopic methods such as FRET, Trp-214 fluorescence

quenching, and docking studies. A common observation was all copper complexes were predicated to bind within subdomain IIA of HSA. A summary of all the copper chelate binding data is given in Table. 5

Table 5. A summary of the biophysical characteristics of copper(II) complexes binding to HSA and the cancer cell lines they target.

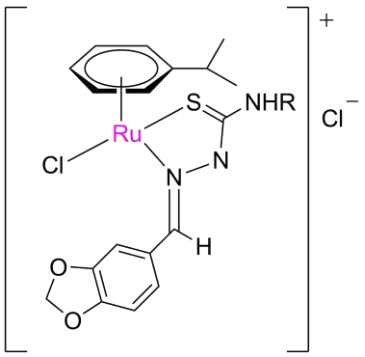
Name	K_d (μM)	Temperature	Method used to determine K_d	No of binding sites	The binding site	Perturbation used to measure the type of biding	Cancer cell lines targeted
49[230]	ND*	ND	ND	1	IIA	Coordination	MCF-7 cells
50[230]	ND	ND	ND	1	IIA	Coordination	MCF-7 cells
51[230]	ND	ND	ND	1	IIA	Coordination	MCF-7 cells
52[231]	1.67	ND	ND	1	IIA	ND	MCF-7 cells
53[231]	0.6589	ND	ND	1	IIA	ND	MCF-7 cells
54[231]	0.9	ND	ND	1	IIA	ND	MCF-7 cells
55[233]	60,98	ND	ND	3	N-terminal end of HSA composed of Asp-Ala-His, close to Trp-214 in IIA, was to Cys-34 in subdomain IB.	ND	N/A
56[233]	58,48	ND	ND	3	N-terminal end of HSA composed of Asp-Ala-His, close to Trp-214 in IIA, was to Cys-34 in subdomain IB.	ND	N/A
57[234]	5.14	35	Trp-214 fluorescence	1	IIA	ΔH and ΔS > 0 Suggesting hydrophobic and ionic interactions	N/A

*ND = no data.

1.6.5. Ruthenium complexes binding to HSA

Ruthenium (Ru)-based organometallic compounds have emerged as a potential new line of anticancer treatments, with two drugs, NAMI-A and KP1339, reaching phase 1 clinical trials. NAMI-A has also progressed to phase 2 trials.[100,107,237] However, there is a prevalent misconception regarding the toxicity and cytotoxicity of Ru complexes, as highlighted in a review by Alessio.[238] For example*, in vitro*, NAMI-A is less toxic compared to KP1019, while *in vivo*, KP1019 is less toxic.[239] Additionally, there is a belief that ruthenium complexes' molecular biology interactions are similar to that of iron. Ruthenium complexes have similar chemistry to iron complexes, due to both elements belonging to group 8 of the transition metals. Both metals share the same oxidation states $Fe^{2+/3+}$/$Ru^{2+/3+}$ and typically prefer an octahedral geometry. However, their molecular biology differs, ruthenium complexes have a higher binding affinity for HSA as compared to apotransferrin (hsTf), while iron complexes prefer hsTf.[238] This is demonstrated by the low affinity of NAMI-A for apo-hsTf and the limited binding of KP1019 to apo-hsTf. In the studies proposed in this review, we highlight that ruthenium complexes have a high affinity for binding to HSA.

η^6-Arene complexes are potentially one of the most studied and reported classes of metallodrugs. Various Ru(II)-arene fragments have been combined with different ligands to yield Ru(II) anticancer complexes.



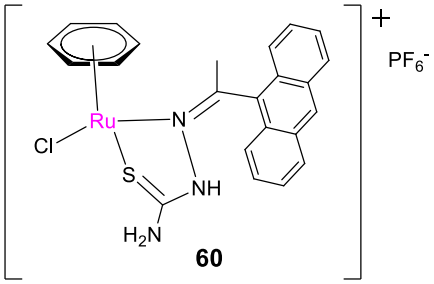
R = C_2H_5 (pEtTSC) **58**
= C_6H_5 (pPhTSC) **59**

Fig. 38 Structures of **58**, ([(η6-*p*-cymene)Ru(pEtTSC)Cl]Cl, and **59**, [(η6-*p*-cymene)Ru(II)(pPhTSC)Cl]Cl.[240]

In the search for new anticancer ruthenium metallodrugs, thiosemicarbazones (TSC) are seen as relevant ligands to combine with Ru(II)-arene fragments to be used as potential chemotherapeutics.[240–242] Mainly because TSC already possesses antitumor,[243] antibacterial, and antiviral properties (Fig. 38).[244]

Some of these complexes reported were **58** and **59**.[240] Both Ru(II) complexes were able to inhibit colon cancer cell lines HCT-116 and Caco-2, inhibit Top2 activity at 20 µM, and bind to HSA. **59** bound more tightly to HSA with a K_d of 7.52 µM while **58** had a K_d of 20.83 µM. It

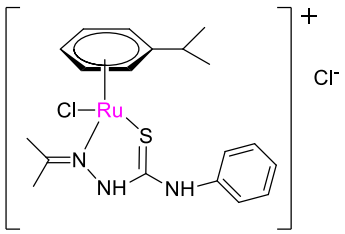
appears as though the aromaticity created by the phenylene ring on the thioamide bond of **59** allowed for greater interaction with HSA compared to the ethyl group on the thioamide bond of **58**.



60

Fig. 39 Structure of [(*η*6-*p*-cymene)Ru(ATSC)Cl]PF_6 **60**.[241]

Complex **60** (Fig. 39) has demonstrated anticancer activity against breast cancer cell lines (MCF-7 and MDA-MB-231) and colon cancer cell lines (HCT-116 and HT 29).[241] The binding of **60** to HSA was found to result in a dual quenching mechanism of HSA. The estimated K_d of the binding was determined by several methods, including (i) double log plots, (ii) Scatchard plots, and (iii) Lineweaver-Burk plots, all yielding similar results with an estimated K_d of 7.63 µM.



61

Fig. 40 Structure of [(η6-*p*-cymene) Ru(II) (acetone-N4-phenylthiosemicarbazone)Cl]Cl (**61**).[245]

Huang *et al*.[245] investigated the binding of **61** to HSA using intrinsic Trp-214 fluorescence quenching (Fig. 40), in the presence of common metal ions on the binding. **61** was found to be a dynamic quencher of HSA and among all the TSC complexes, **61** had the lowest K_d of 0.47 µM. The presence of different metal ions resulted in a higher overall binding affinity, which is likely due to the alteration of HSA conformation and thus reduction of **61** binding affinity. The presence of common metal ions already bound to HSA may reflect a more accurate picture of the nature of HSA in serum.

In summary, all TSC-Ru(II) complexes were found to bind to HSA in a 1:1 ratio, with the binding being driven by entropic forces. The interactions between all Ru(II)-TSC complexes and HSA were primarily through hydrophobic interactions and electrostatic forces, and the complexes were thought to bind to HSA at subdomain IIA, in close proximity to Trp-214. All η6-arene complexes investigated exhibited strong interactions with HSA, and this was evident by their low micromolar K_d binding to HSA. A summary of the thermodynamic data and cytotoxicity is reported in Table 6.

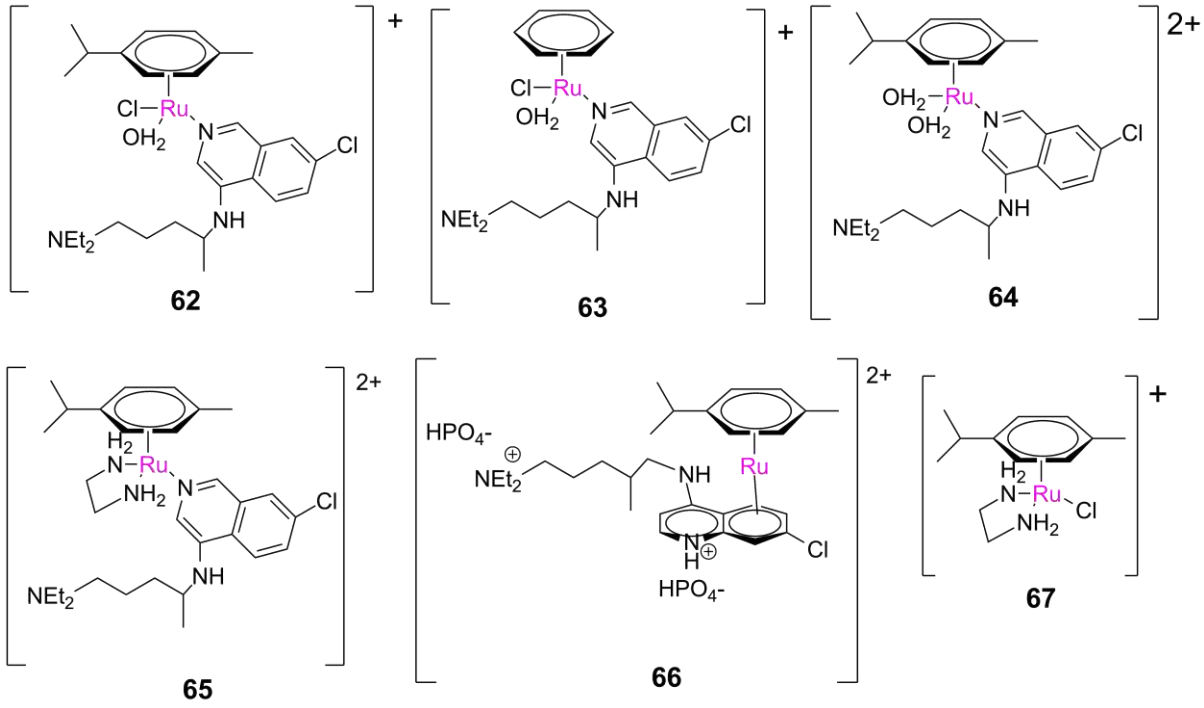


Fig. 41 π-Arene–Ru(II)–chloroquine complexes.[246]

π-Arene–Ru(II)–chloroquine possesses activity against *P. falciparum* drug-resistant malaria and various cancer cell lines including LS141 dedifferentiated liposarcoma, HCT-116 colon cancer, and Jurkat human T lymphocyte leukaemia (Fig. 41).[246–248] One proposed mechanism of action of these molecules is that the chloroquine (CQ) motifs interact with DNA forming Ru(II) complex-DNA adducts, however, their toxicity may be influenced by their ability to bind to HSA. Martinez *et al.*[246] tested the binding of [Ru(η6-*p*-cymene)(CQ)(H_2O)Cl][PF_6] (**62**), [Ru(η6-benzene)(CQ)(H_2O)Cl][PF_6] (**62**), [Ru(η6-*p*-cymene)(CQ)(H_2O)$_2$][PF_6] (**64**), [Ru(η6-*p*-cymene)(CQ)(en)][PF_6]$_2$ (**65**), [Ru(η6-*p*-cymene)(η6-CQDP)][BF_4]$_2$ (**66**) (CQ: chloroquine; DP: diphosphate; en: ethylenediamine), and [Ru(η6-*p*-cymene)(en)Cl][PF_6] (**67**) with HSA. All six π-arene–Ru(II)–chloroquine complexes bound to multiple binding sites on HSA and their affinities ranged from 34.84 μM (**61**) to 325.73 μM (**66**). The study suggested that **62**, **63**, **64**, and **66** are bound by covalent bonds in the hydrophobic sites/cavities of Sudlow's sites I and II. Compounds **65** and **67** are saturated around the Ru(II) cation metal centre, therefore, had

lower binding affinities. Even though the Ru^{2+} ion on **63** was saturated, it did take 20 hours to bind to HSA, the longer binding time required was to allow for the H_2O molecule to be displaced by motifs within the protein's hydrophobic cavities. Overall, the binding affinities of the six ruthenium complexes fall within the typical binding range to HSA, suggesting that HSA may serve as a suitable drug transporting protein for π-arene–Ru(II)–chloroquine complexes. A summary of the binding interactions is reported in Table 6.

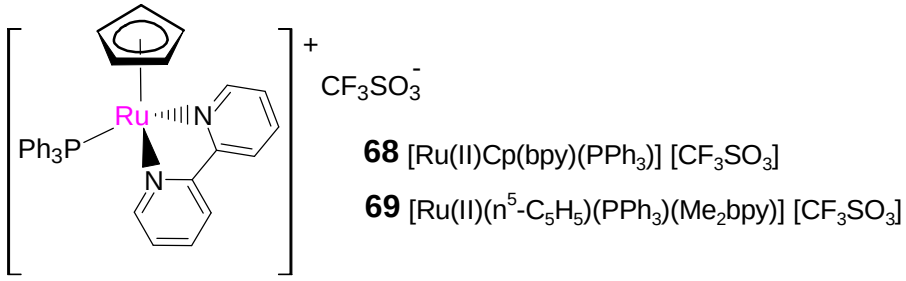


Fig. 42 [Ru(II)Cp(bpy)(PPh$_3$)][CF$_3$SO$_3$] (**68**) and [Ru(η5-C$_5$H$_5$)(PPh$_3$)Cp(Me$_2$bpy)][CF$_3$SO$_3$] (**69**).

Complex **68**, also referred to as TM34, has been shown to possess five times greater activity against HL-60 cells compared to cisplatin.[249] Additionally, TM34 has demonstrated activity against ovarian (A2780/A2780cisR, cisplatin sensitive and resistant cancer cell lines, respectively), breast (MCF-7), and prostate (PC3) adenocarcinomas. Given TM34 activity against cisplatin-resistant cells, it is suggested that its mode of action may differ from cisplatin and may involve the HSA-mediated pathway and EPR.[99] Studies have shown that TM34 binds rapidly to HSA in a 1:1 ratio, with a binding constant, $logK$, of 4. Furthermore, when bound to HSA, TM34 still retained its anticancer activity against the cell lines. Subsequently, a more active Ru(II) complex, **69**, was developed by the same group. The study found that compound **68** exhibited anticancer activity against a range of cell lines, including A2780, A2780CisR, HT29, MCF7, MDAMB231, and PC3. Further investigation revealed that the complex bound more tightly to fatty acid-free human serum albumin (HSA) in Sudlow's site I, as determined by a warfarin displacement assay. Notably, the binding of the complex to HSA did not affect its cytotoxicity, suggesting the potential utility of HSA as a drug carrier for the molecule.[250] A summary of the binding interactions is reported in Table 6.

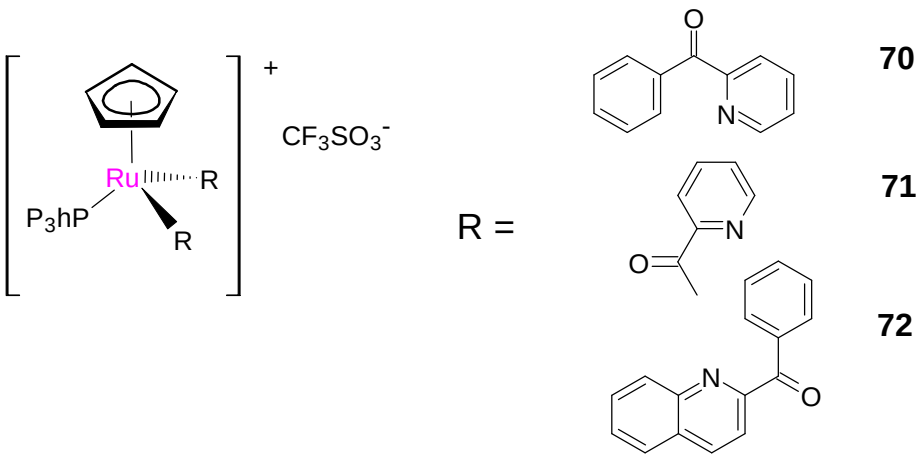


Fig. 43 [Ru(η5-CH_5)(PPh_3)(bopy)][CF_3SO_3] (**70**) , [Ru(η5-C_5H_5)(PPh_3)(2-ap)][CF_3SO_3] (**71**), and [Ru(η5-C_5H_5)(PPh_3)(isoquinpk)][CF_3SO_3] (**72**) [251]

A series of potential η5-arene ruthenium(II) complexes, **70**, **71**, and **72**, (Fig. 43) were found to exhibit *in vitro* anticancer activity against MCF-7 and MDAMB231 cell lines.[251] These molecules consist of heteroaromatic bidentate ligands bound to Ru^{2+} ion through N and O groups. Further analysis revealed that all three complexes bound to both fatty acid-free HSA and HSA-containing fatty acids in Sudlow's site I close to Trp-214, which was confirmed by a warfarin site displacement assay. The presence of fatty acids only inhibited the quenching of Trp-214 fluorescence for **72**, with 83% quenching observed for HSA-containing fatty acids compared to 95% quenching for fatty acid-free HSA, indicating competition with a fatty acid residue. Binding constants were only slightly affected by the presence of fatty acids, primarily for **70** and **71**, which showed increased and decreased binding, respectively. **69** had the highest binding affinity with a K_d of 1.14 μM and had an intermediate level of aromaticity as well as added functional side groups. A summary of the binding interactions is reported in Table 6.

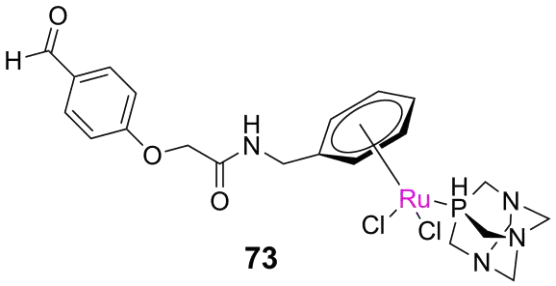


Fig. 44 Structure of a 1,3,5-triaza-7-phosphatricyclo[3.3.1.1]-decane (RAPTA) Ru(II)$(Cl)_2$ derivative.[252]

Ru(II)-arene complex **73**, bearing the 1,3,5-triaza-7-phosphatricyclo[3.3.1.1]-decane (RAPTA) ligand have been synthesised by Ang *et al.* (Fig. 44).[252] These organometallic compounds have been conjugated to recombinant human serum albumin (rHSA) via a hydrazine linker under mild conditions to prevent redox chemistry on the Ru(II) cation centre. The rHSA-RAPTA conjugate exhibited significantly higher activity on A2780 ovarian carcinoma cells compared to the free RAPTA molecules. This highlights the ability of HSA to act as a carrier protein and suggests that the change in pH within the tumour microenvironment would allow for the breaking of the hydrazine bond and for the RAPTA molecule to exert its cytotoxic effects.

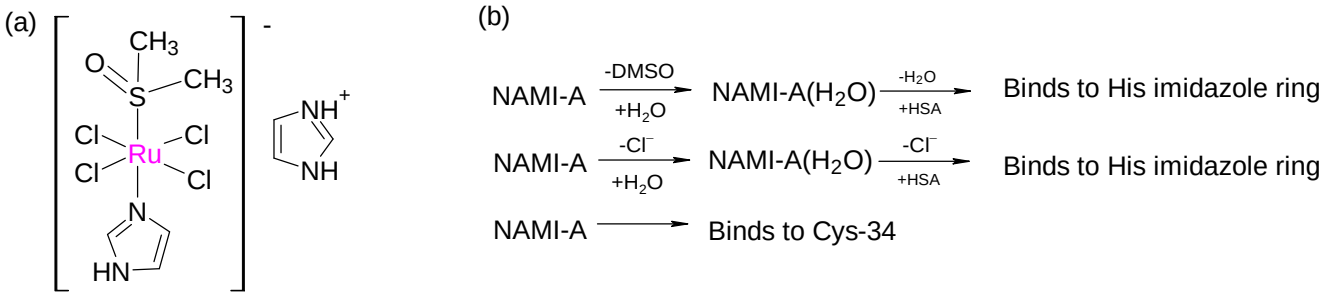


Fig. 45 (a) Structure of NAMI-A. (b) Binding of NAMI-A to predicted amino acid residues on HSA.

A limitation of the literature surrounding NAMI-A is its pharmacokinetic data. Studies have shown that serum proteins like HSA bind up to 97% of NAMI-A (Fig. 45).[253] This is significant as most of the remaining NAMI-A binds to transferrin resulting in a low concentration of unbound drug remaining. NAMI-A has poor binding to DNA suggesting its mechanism of action is different from cisplatin. However, it has been shown to inhibit metastasis by blocking the replication at the G_2M pre-miotic phase.[254] At physiological pH NAMI-A is unstable and is suspectable to hydrolysis mainly of the chloride ligands and the axial DMSO. Furthermore, there has been a suggestion that the Ru^{3+} ion may be further reduced to Ru^{2+} by ascorbate and the hydrolysed NAMI-A fragment may have a higher affinity for HSA.[255] Using electron paramagnetic resonance (EPR) Webb *et al.*[256] showed that three species of NAMI-A could bind to HSA. Results by Webb *et al.*[256] were similar to those of Brindell *et al*.,[255] but Brindell *et al*. predicted that 3.2 moles or 4 moles of NAMI-A can bind to HSA. Webb *et al*. also demonstrated, using electron paramagnetic resonance (EPR), that Ru(II)-NAMI-A is oxidised to Ru(III)-NAMI-A when it is bound to HSA. Both histidine residues are surface residues, while cysteine-34 is located within subdomain IB. An in vivo study by Novohradský *et al*.[253] suggested that NAMI-A is quickly bound by serum proteins and is unlikely to be reduced by ascorbate or glutathione.

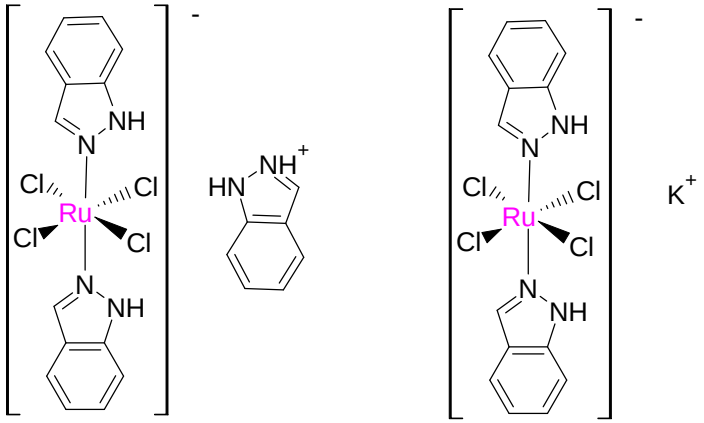


Fig. 46 Chemical structures of KP1019 and KP1339.

An analogue of *trans*-[tetrachlorobis(1H-indazole) ruthenate(III)], known as sodium trans-[tetrachlorobis(1H-indazole) ruthenate(III)] (KP1339), was synthesised as a more soluble alternative to trans-[tetrachlorobis(1H-indazole)ruthenate(III)] (KP1019) due to the poor solubility of the latter compound (Fig. 46). Both compounds are structurally identical, except for their counterions. The poor solubility of KP1019 limited its maximal clinical dose during phase 1 trials, as reported by Lentz *et al*.[257] The mechanism by which KP1019 inhibits metastasis of tumours remains unknown. However, Pongratz *et al*.[258] suggested it may occur through NAMI-A binding to transferrin, while others speculate that NAMI-A may act through the HSA-mediated pathway by entering tumours through EPR.[99,259] Bijelic *et al*.[259] further investigated the binding of KP1019 and KP1339 using X-ray crystallography (PDB ID: 5IFO; Fig. 47).

The results of this study revealed that two Ru^{3+} ions were bound to HSA with the indazoles displaced at sites IB and IIA. Site IB is located near His-146, while IIA is a hydrophobic cavity that is bound to His-242 and coordinated by Lys-199, Trp-214, Arg-218, and H_2O molecules. HSA has a total of ten surface histidine residues; however, the Ru(III) ions were found to be bound to histidine residues within cavities. This suggests that the indazoles acted as a vehicle for the transport of the complex and dissociated once bound to HSA, or that the indazole may have been outcompeted by imidazole on the histidine residues. It is worth noting that previous studies utilizing non-crystallographic methods have found that up to four KP1019 molecules can bind to HSA.

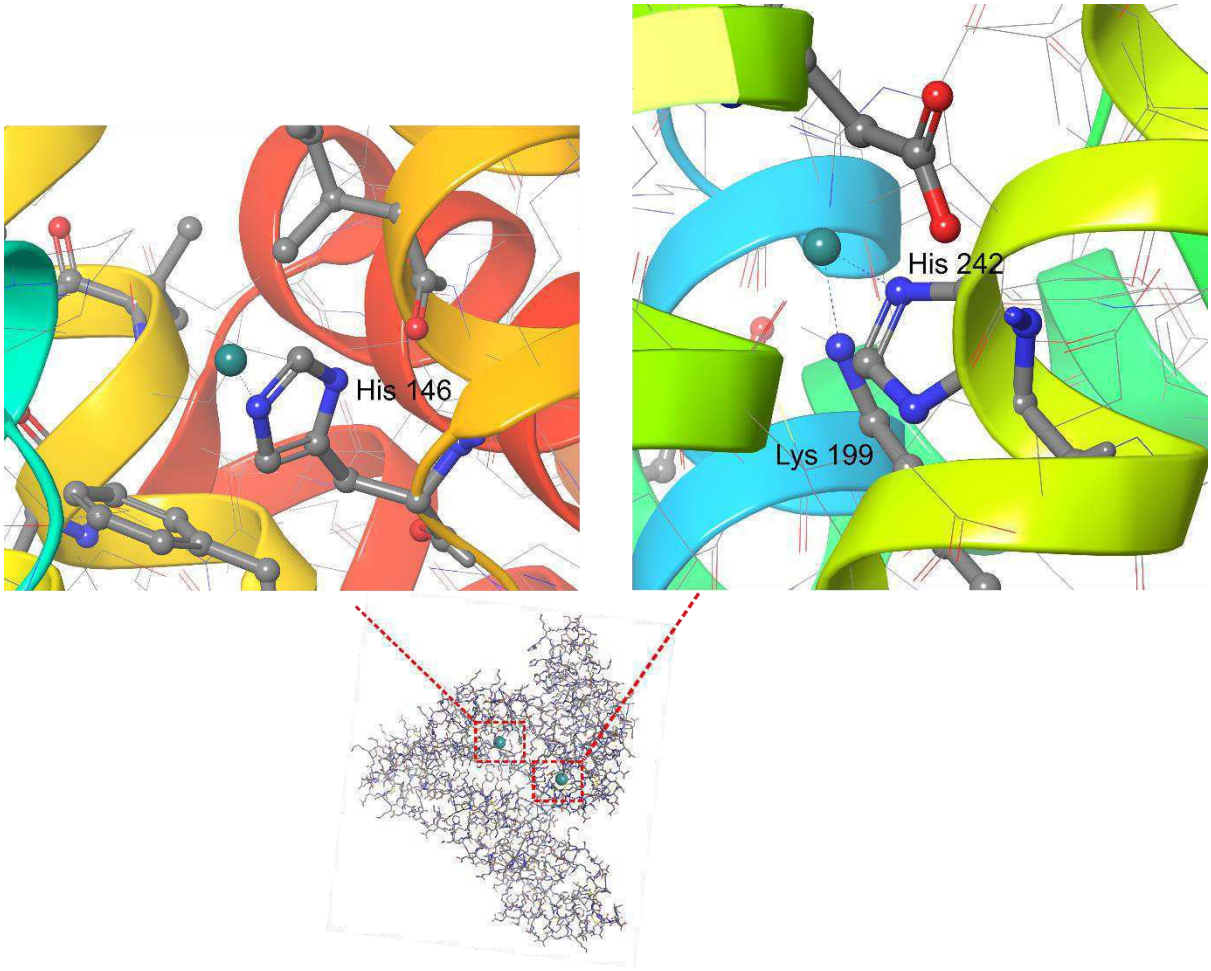


Fig. 47 Crystal structure of KP1019 bound HSA.[259] KP1019 demetalated and the Ru ion is bound to HSA.

1.6.6. Palladium complexes binding to HSA

Pd metal has been clinically deployed (in the form of ^{103}Pd radioisotope seed implants) with good success in prostate carcinoma brachytherapy for over 25 years.[260,261] Although no FDA-approved non-radioactive palladium(II) complexes for cancer chemotherapy currently exist, many interesting palladium(II) derivatives have been described as potential chemotherapeutic agents over the last few decades. The popularity of palladium-based complexes stems from palladium(II) having similar physical and coordination chemistry to platinum(II),[262,263] with the notable benefit of palladium(II) complexes being generally less toxic. Palladium(II) complexes are potentially more beneficial than cisplatin, *cis*-$[PtCl_2(NH_3)_2]$, since slow ligand dissociation from platinum(II) allows it to reach the kidneys as the aquated *cis* isomer, *cis*-$[Pt(OH_2)_2(NH_3)_2]^{2+}$, which underpins its marked nephrotoxicity[264,265] by facilitating platinum-mediated inhibition of cysteine-dependent enzymes in the kidney tubules. A similar mechanism is unlikely to occur with palladium complexes as palladium(II) has a 10^5 times

faster ligand exchange rate than platinum(II),[266,267,268] meaning it is likely to dissociate from simple monodentate ligands long before reaching the kidneys. To thwart ligand dissociation in palladium(II) metallodrug candidates, well-designed macrocyclic or polydentate chelating ligands[269] are mandatory to ensure the intact palladium(II)complex (with function-enhancing ligands) reaches the intended biochemical target (typically DNA or a specific protein earmarked for inhibition). Furthermore, if palladium(II) complexes are to be used as chemo-therapeutic agents, it is of utmost importance to assess the uptake/binding of suitably active complexes by HSA to obtain the appropriate pharmacodynamic and pharmacokinetic data.[270,271]

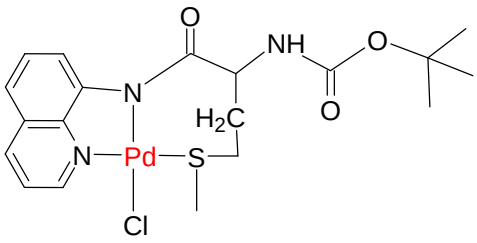
Table 6. A summary of the biophysical characteristics of Ru(II) complexes binding to HSA and the cancer cell lines they target.

Name	K_d (μM)	Temp. (°C)	Method used to determine K_d	Number of binding sites	Binding site	Electrostatic forces characterising the type of biding	Cancer cell lines targeted
58[241]	7.52	35	Trp-214 Fluorescence	1	IIA	ΔH and ΔS > 0 Suggesting electrostatic interactions, H-bonding, and Van Der Waals interactions	colon cancer cell lines HCT-116 and Caco-2
59[241]	20.83	35	Trp-214 Fluorescence	1	IIA	ΔH and ΔS > 0 Suggesting electrostatic interactions, H-bonding, and Van Der Waals interactions	colon cancer cell lines HCT-116 and Caco-2
60[241]	7.63	35	Trp-214 Fluorescence	1	IIA	ΔH and ΔS > 0 Suggesting electrostatic interactions, H-bonding, and Van Der Waals interactions	breast cancer cell lines (MCF-7 and MDA-MB-231 and colon cancer cell lines HCT-116 and HT 29
61[242]	0.465	37	Trp-214 Fluorescence	1	IIA	ΔH and ΔS > 0 Suggesting electrostatic interactions, H-bonding, and Van Der Waals interactions	N/A
62[246]	34.84	25	ITC[a]	6	Several sites. Mainly His residues	Suggestion of covalent binding	Colon cancer HCT-116 LS141 dedifferentiated liposarcoma, Jurkat human T lymphocyte leukemia, and SUP-T1 lymphoma
63[246]	75.19	25	ITC	5	Several sites. Mainly His residues	Suggestion of covalent binding	Colon cancer HCT-116 LS141 dedifferentiated liposarcoma, Jurkat human T lymphocyte leukemia, and SUP-T1 lymphoma

64[246]	55.25	25	ITC	8	Several sites. Mainly His residues	Suggestion of covalent binding	Colon cancer HCT-116 LS141 dedifferentiated liposarcoma, Jurkat human T lymphocyte leukemia, and SUP-T1 lymphoma
65[246]	150.15	25	ITC	3	Several sites. Mainly His residues	Ionic interactions	Colon cancer HCT-116 LS141 dedifferentiated liposarcoma, Jurkat human T lymphocyte leukemia, and SUP-T1 lymphoma
66[246]	80	25	ITC	9	Several sites. Mainly His residues	Suggestion of covalent binding	Colon cancer HCT-116 LS141 dedifferentiated liposarcoma, Jurkat human T lymphocyte leukemia, and SUP-T1 lymphoma
67[246]	325.73	25	ITC	2	Several sites. Mainly His residues	Ionic interactions	Colon cancer HCT-116 LS141 dedifferentiated liposarcoma, Jurkat human T lymphocyte leukemia, and SUP-T1 lymphoma
68[249]	ND[b]	ND	ND	1	ND	ND	A2780/A2780cisR, MCF-7, PC3
69[249]	ND	ND	ND	1	IIA	ND	A2780, A2780CisR, HT29, MCF7, MDAMB231 and PC3.
70[251] - fatty acid HSA	1.684	37	Trp-214	1	IIA	ΔH and $\Delta S > 0$ Suggesting hydrophobic and ionic interactions	N/A
71[251] - fatty acid HSA	83.33	37	Trp-214	1	IIA	ΔH and $\Delta S > 0$ Suggesting hydrophobic and ionic interactions	N/A

72[251] - fatty acid HSA	1.979	37	Trp-214	1	IIA	ΔH and ΔS > 0 Suggesting hydrophobic and ionic interactions	N/A
70[251] - fatty acid-free HSA	1.144	37	Trp-214	1	IIA	ΔH and ΔS > 0 Suggesting hydrophobic and ionic interactions	N/A
71[251] - fatty acid-free HSA	49.50	37	Trp-214	1	IIA	ΔH and ΔS > 0 Suggesting hydrophobic and ionic interactions	N/A
72[251] - fatty acid-free HSA	2.017	37	Trp-214	1	IIA	ΔH and ΔS > 0 Suggesting hydrophobic and ionic interactions	N/A
73[252]	ND	ND	ND	ND	ND	A2780 ovarian carcinoma	N/A

[a]ITC, isothermal titration calorimetry; [b]ND, no data available.



74

Fig. 48 N-(tert-butoxycarbonyl)-L-methionine-N′-8-quinolylamide (**74**).

Pd(II)-8-Amininoquinoline

The Pd(II)-8-aminoquinoline derivative, **74**, (Fig. 48) was found to interact with HSA with high affinity, as determined by a K_d value of 1.66 µM. The binding was determined to be thermodynamically driven. The specific binding site on HSA was not identified, however, it was suggested to be Sudlow's site I close in proximity to Trp-214, based on the observation that the polarity of the hydrophobic region did not change upon binding. Additionally, UV-CD spectroscopy revealed that **74** had minimal impact on the α-helix structure of HSA.[272]

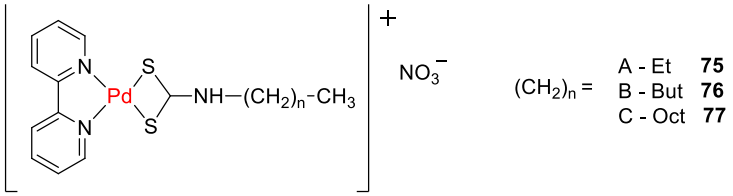
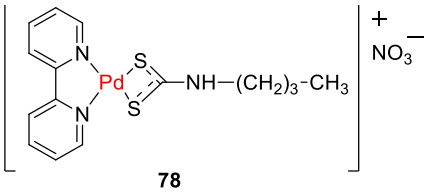


Fig. 49 Structures of dithiocarbamato palladium(II) nitrate complexes.[273]

Divisalar et al.[273] investigated a series of 2,2′-bipyridine dithiocarbamato Pd(II) nitrate complexes, where n represented either ethyl, butyl, or octyl (Fig. 49). The study found that the length of the aliphatic tail plays a significant role in the binding of these palladium complexes to HSA. The aliphatic tails were designed to resemble the structure of a fatty acid. All three molecules had moderate binding affinities, with K_d values in the medium micromolar range. **75** and **76**, which had shorter aliphatic tails, were able to bind to HSA in a 2:1 ratio, while **77** bound in a 1:1 ratio. Additionally, the binding mechanisms of the molecules were different; compound **75**'s binding to HSA was exothermic, indicating that its interaction with HSA was primarily due to H-bonding. The binding of **76** and **77** to HSA was found to be endothermic, suggesting that hydrophobic interactions were the primary means of binding. Notably, the medium-length aliphatic tail of **76** exhibited the weakest binding to HSA, with a K_d of 423 µM.

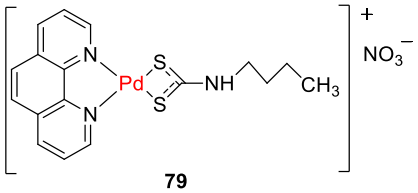
Conversely, **77**, which has a longer aliphatic tail, exhibited the strongest affinity for HSA, with a K_d of 210 µM. The binding of **75**, which has the shortest aliphatic tail, to HSA was stronger than that of ButPd (**76**), with a K_d of 278 µM. This may be due to the interaction being mediated by hydrogen bonds and electrostatic forces, rather than hydrophobic interactions.



78

Fig. 50 Structure of the dithiocarbamato palladium(II) nitrate complex **78** (ButPd).

Behbehhani *et al*.[274] used ITC to investigate the thermodynamics of complex **78** (Fig. 50) binding to HSA and determined a K_d that was significantly lower than the value reported by Divsalar *et al*. [273] The ITC analysis revealed the presence of three binding sites, whereas Trp-214 fluorescence data suggested the presence of only two binding sites. This discrepancy is not uncommon, as weak interactions may be undetectable using Trp-214 fluorescence quenching but can be detected by ITC.[246] To confirm the accuracy of the binding sites, obtaining an X-ray crystal structure or using mass spectrometry data or a fluorescent displacement assay could be useful.



79

Fig. 51 Structure of the 1,10-phenanthroline derivative Pd(But-dtc)(phen)]NO_3 (**79**).[275]

Most complexes bind to HSA with K_d ranging from 100 to 1 µM.[276,277] However, complex **79** (Fig. 51) was found to have a K_d of 0.555 µM,[275] which is significantly lower than the K_d of 2,2′-bipyridin butyl dithiocarbamato palladium(II)nitrate complexes.[273] The only structural difference between these two complexes is the replacement of bipyridine with phenanthroline. This difference could be a result of hydrophobic interactions between **79** and HSA, or it could allow **79** to bind to an alternate site. It is difficult to believe that an additional ring increases the binding by 760-fold.

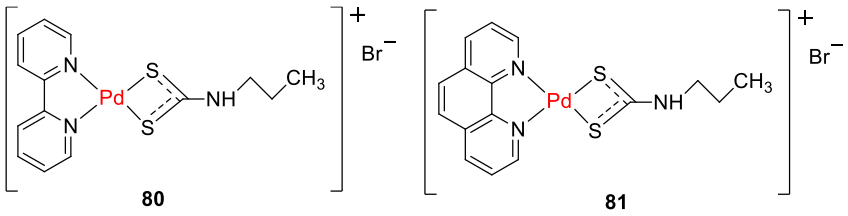


Fig. 52 Structures of [Pd(bpy)(n-pr-dtc)]Br (**80**) and [Pd(phen)(n-pr-dtc)]Br (**81**).

In a study by Saedifiar *et al*.,[278] the binding of two palladium dithiocarbamate heterocyclic aromatic derivatives to HSA was analysed: **80** and **81** (Fig. 52). The study investigated the influence of aromaticity on the binding potential of a complex to HSA. The complexes only varied in their heterocyclic motifs. **80** had a K_d of 21.37 µM, almost twice that of **81**, which had a K_d of 11.87 µM. Unlike **77**,[278] the binding of **80** and **81** to HSA had negative ΔH and ΔS values, indicating that electrostatic forces and van der Waals forces were mainly responsible for the binding. The bromide counter ions present in the complexes may have influenced the binding of the cations by binding to HSA, distorting its conformation, and allowing for a different binding mechanism to occur as compared to other studies. The influence of metal ions and counter ions on binding has been reported previously.[213]

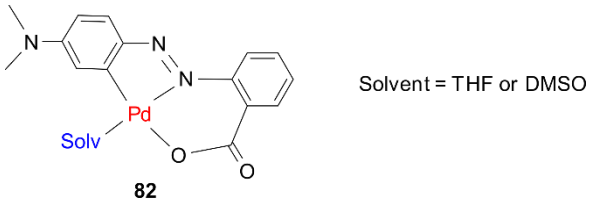
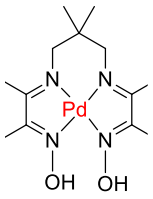


Fig. 53 Structure of 2-{[4-(dimethylamino)phenyl]diazenyl}benzoic acid)palladium(II) (MR-Pd(II), **82**).[279]

The binding of Pd(II)-MR, a square planar CNO pincer ligand (Fig. 53), to HSA was found to be hydrophobic, with a K_d of 10.59 µM, as reported by Hosseini-Kharat *et al*.[279] However, further analysis through docking studies revealed that Pd(II)-MR was docked into Sudlow's site I of HSA. The MR ligand was found in a pocket surrounded by the amino acids Lys-195, Lys-199, Trp-214, Arg-218, Arg2-22, Leu-238, Leu-260, Ala-291, and Glu-292, which suggests that hydrophobic interactions play a significant role in the methyl red···HSA interactions. Additionally, no bonds were found between the palladium(II)metal and HSA.



83

Fig. 54 Butadione Schiff base derivative (**83**).[280]

Other palladium complexes that were found to bind to HSA were butadione Schiff base derivatives[280] and oxalic acid amide derivatives[269]. The palladium butadione Schiff base (Fig. 54) was found to hydrogen bond to HSA with a K_d of 19.08 µM. This was supported by docking studies which showed the complex bound to Sudlow's site I. Two types of oxalic acid amide derivatives were tested Pd(obap) and Pd(mda). The larger Pd(obap) molecule had a lower K_d (18 µM) compared to Pd(mda) whose K_d measured 47.40 µM. However, no further analysis was used to confirm the exact binding site or the type of interaction between the incorporated molecule and HSA.

From the article's interpreted it would seem as though the size of the ligand and its aromaticity is responsible for a complex binding to HSA and not the actual palladium metal centre. However, in a study by Kazemi *et al*.,[235] a 2-hydroxy-1-allyliminomethyl-naphthalen ligand was complexed with four metal ions namely palladium(II), copper(II), vanadium(II), and nickel(II). The binding affinities were all different following the order Pd(complex) > Cu(complex) > VO(complex) > Ni(complex) indicating that the metal centre plays a role in complex binding to HSA. Docking studies showed Cu(complex), VO(complex), and Ni(complex) bound to subdomain IIA while the Pd(complex) bound to subdomain 1B and there was a strong interaction with the oxygen from Arg-186 to palladium.

1.6.7. Summary of palladium complexes

The studies discussed in this analysis have primarily used the Stern-Volmer plot and docking studies to conclude the binding affinities of palladium complexes with human serum albumin (HSA). However, a limitation of these studies is the lack of mass spectrometry data or an HSA-palladium X-ray crystal structure to confirm the binding stoichiometry of the complexes to HSA. The binding affinities of Pd complexes with HSA were found to be in the range expected for molecules interacting with HSA, except for [Pd(But-dtc)(phen)][NO_3], which had a K_d of 0.555 µM. This strong interaction may prevent the complex from dissociating from HSA and reaching its biological target. Additionally, the length of the aliphatic tail and the number of aromatic rings on a Pd(II) complex were found to influence the binding affinity to HSA, with longer

aliphatic tails and greater numbers of aromatic rings resulting in a greater binding affinity. Palladium(II) complexes are becoming increasingly popular as alternatives to Pt(II) complexes, with some complexes showing better activity against cancer cell lines than platinum drugs. However, further research is needed to confirm the binding stoichiometry and mechanism of these complexes with HSA. A summary of all the binding data of the palladium complexes is reported in Table 7.

Table 7. A summary of the biophysical characteristics of palladium(II) complexes binding to HSA.

Name of the complex	K_d (μM)	Temperature	Method used to determine K_d	Number of binding sites	The binding site	Electrostatic forces characterizing the type of binding
74[272]	1.66	36	Trp-214 fluorescence	1	ND	ΔH and ΔS > 0 Suggesting hydrophobic and ionic interactions
78[274]	3.21 2.69 1.63	N/A N/A N/A	ITC	3	ND	ΔH and ΔS > 0 Suggesting hydrophobic and ionic interactions
75[273]	278	37	Trp-214 fluorescence	2	ND	ΔH<0 and ΔS > 0 Hydrogen bonding
76[273]	423	37	Trp-214 fluorescence	2	ND	ΔH and ΔS > 0 Suggesting hydrophobic and ionic interactions
77[273]	210	37	Trp-214 fluorescence	1	ND	ΔH and ΔS > 0 Suggesting hydrophobic and ionic interactions
79[275]	0.555	27	Trp-214 fluorescence	1	ND	ΔH and ΔS > 0 Suggesting hydrophobic and ionic interactions
80[278]	21.37	38	Trp-214 fluorescence	1	ND	ΔH and ΔS < 0 Suggesting electrostatic interactions, H-bonding, and Van Der Waals interactions
81[278]	11.87	38	Trp-214 fluorescence	1	ND	ΔH and ΔS < 0 Suggesting electrostatic interactions, H-bonding, and Van Der Waals interactions
82[279]	10.59	30	Trp-214 fluorescence	1	Sudlow's site 1	ΔH and ΔS > 0 Suggesting hydrophobic and ionic interactions
83[280]	19.08	37	Trp-214 fluorescence	1	Sudlow's site 1	ΔH and ΔS < 0

						Suggesting electrostatic interactions, H-bonding, and Van Der Waals interactions
Pd(II) 2-((((2-aminoethyl)(oxo)(ethyl) amino benzoic acid) Pd(opap) [269]	18	25	Trp-214 fluorescence	1	ND	ND
Pd(II) mda[269]	47	25	Trp-214 fluorescence	1	ND	ND
Pd(II) 2-hydroxy-1-allyliminomethyl-naphthale[235]	10.64	25	Trp-214 fluorescence	1	Site 1B	ND

1.7. Aims and objectives

The aims of this work are partitioned into three individual projects, as described below.

(i) The aim of Chapters 2 and 3 is to synthesise five bis(pyrrolide-imine) Au(III) chelates, that have been shown to possess anti-cancer activity and to understand how they exert their cytotoxicity through intercalation with ctDNA and inhibition of topoisomerases or alternative methods. Within the specific scope of this study, our key aim was to show that the Au(III) chelates are able to interact with HSA using ITC (isothermal titration calorimetry) and spectroscopic methods (fluorescence and UV-CD spectroscopy) under physiological conditions. This work seeks to gauge how the metal ion and ligand architecture influence the uptake of the complexes by HSA and to delineate their preferred binding site(s). Such binding studies for metal chelate uptake by HSA determine if the Au(III) chelates are suitable candidates to be transported by the protein.

(ii) The aims of Chapters 4 and 5 were to synthesise and characterise five bis(pyrrolide-imine) platinum(II) chelates, to test their theranostic capabilities against MCF-7 cells, and to show how these charge-neutral metal chelates can bind to and potentially be transported by HSA.

(iii) In Chapters 6, we synthesised *N*,*N*'-bis[(1*E*)-1H-pyrrol-2-ylmethylene]propane-1,3-diamine (H_2PrPyrr) and metalated it with Ni(II), Pd(II) and Pt(II), to generate the corresponding isoelectronic (nd^8) square-planar M(PrPyrr) chelates. Spectroscopic methods (fluorescence and UV-CD spectroscopy) were used to probe the binding of H_2PrPyrr and the three metal chelates by HSA under physiological conditions to gauge how the metal ion influences the uptake of the isoelectronic and isomorphic complexes by HSA and to delineate their preferred binding site(s). Finally, molecular docking simulations were used to corroborate the spectroscopically elucidated binding site location(s).

1.7.1. List of specific objectives

Chapters 2 and 3

- To synthesise bis(pyrrolide-imine) Schiff base chelates and fully characterise these compounds by ^{1}H and ^{13}C NMR, UV-vis spectroscopy, and FT-IR.
- To metalate, the ligands with Au(III), resulting in Au(III) bis(pyrrolide-imine) Schiff base chelates. These complexes will be characterised by ^{1}H and ^{13}C

NMR, UV-vis spectroscopy and FT-IR, mass spectrometry, and X-ray crystallography to determine the exact geometry of the complexes as well as the counterions and interactions of these Au(III) chelates in the solid state.

- To measure the binding of the Au(III) chelates to HSA by isothermal titration calorimetry (ITC) and spectroscopic techniques, namely fluorescence and UV-CD spectroscopy.
- To measure the binding of the Au(III) chelates to ctDNA using UV-vis spectroscopy, CD, and LD spectroscopy.

Chapters 4 and 5

- To synthesise bis(pyrrolide-imine) Schiff base chelates and fully characterise these compounds by ^{1}H and ^{13}C NMR, UV-vis spectroscopy, and FT-IR.
- To metalate, these ligands with Pt(II), resulting in Pt(II) bis(pyrrolide-imine) Schiff base chelates. These complexes will be characterised by ^{1}H and ^{13}C NMR, UV-vis spectroscopy and FT-IR, mass spectrometry, and X-ray crystallography to determine the exact geometry of the complexes.
- To measure the binding of the Pt(II) chelates to HSA by isothermal titration calorimetry (ITC) and spectroscopic techniques, particularly fluorescence and UV-CD spectroscopy.
- Study the photophysics of the Pt(II) chelates by measuring their quantum yields and measuring their fluorescence in different solvents while being bound to HSA.
- Study the Pt(II) chelates by computational methods such as density functional theory (DFT) and their docking to HSA using Glide within Schrodinger 2022-1.
- Measure the cytotoxicity of the Pt(II) chelates against MCF-7 cells and obtain bioimaging data for the Pt(II) chelates after cell uptake using fluorescence microscopy.

Chapter 6

- To synthesise bis(pyrrolide-imine) Schiff base chelates and fully characterise these compounds by ^{1}H and ^{13}C NMR, UV-vis spectroscopy, and FT-IR.
- Metalate the bis(pyrrolide-imine) chelates with Ni(II), Pd(II), and Pt(II).

- To measure the binding of the Pt(II) chelates to HSA by isothermal titration calorimetry (ITC) and spectroscopic techniques, particularly fluorescence and UV-CD spectroscopy.

- Study the d^8 metal chelates by computational methods such as density functional theory (DFT) and delineate their binding to HSA *in silico* using the Glide docking module of Schrodinger 2022-1.

1.8. References

1 R. L. Siegel, K. D. Miller, H. E. Fuchs and A. Jemal, *CA. Cancer J. Clin.*, 2022, **72**, 7–33.
2 J. Ferlay, M. Colombet, I. Soerjomataram, D. M. Parkin, M. Piñeros, A. Znaor and F. Bray, *Int. J. Cancer*, 2021, **149**, 778–789.
3 B. Rosenberg, L. Van Camp, J. E. Trosko and V. H. Mansour, *Nature*, 1969, **222**, 385–386.
4 L. Zhong, Y. Li, L. Xiong, W. Wang, M. Wu, T. Yuan, W. Yang, C. Tian, Z. Miao, T. Wang and S. Yang, *Signal Transduct. Target. Ther.*, 2021, **6**, 1–48.
5 K. O. Alfarouk, C.-M. Stock, S. Taylor, M. Walsh, A. K. Muddathir, D. Verduzco, A. H. H. Bashir, O. Y. Mohammed, G. O. Elhassan, S. Harguindey, S. J. Reshkin, M. E. Ibrahim and C. Rauch, *Cancer Cell Int.*, 2015, **15**, 71.
6 S.-H. Chen and J.-Y. Chang, *Int. J. Mol. Sci.*, 2019, **20**, 4136.
7 R. Oun, Y. E. Moussa and N. J. Wheate, *Dalton Trans.*, 2018, **47**, 6645–6653.
8 I. Kostova, *Anticancer Agents Med. Chem.*, 2006, **6**, 19–32.
9 H. Zhao and Y. Ning, *Gold Bull.*, 2001, **34**, 24–29.
10 P. J. Sadler, *Gold Bull.*, 1976, **9**, 110–118.
11 P. Pedrosa, A. Carvalho, P. V. Baptista and A. R. Fernandes, *Basic Concepts Viewed Front. Inorg. Coord. Chem.*
12 D. van der Westhuizen, D. I. Bezuidenhout and O. Q. Munro, *Dalton Trans.*, 2021, **50**, 17413–17437.
13 R. W.-Y. Sun and C.-M. Che, *Coord. Chem. Rev.*, 2009, **253**, 1682–1691.
14 E. Wong and C. M. Giandomenico, *Chem. Rev.*, 1999, **99**, 2451–2466.
15 X. M. He and D. C. Carter, *Nature*, 1992, **358**, 209–215.
16 S. Curry, *Drug Metab. Pharmacokinet.*, 2009, **24**, 342–357.
17 G. Rabbani and S. N. Ahn, *Int. J. Biol. Macromol.*, 2019, **123**, 979–990.
18 M. Fasano, S. Curry, E. Terreno, M. Galliano, G. Fanali, P. Narciso, S. Notari and P. Ascenzi, *IUBMB Life*, 2005, **57**, 787–796.
19 United States, US9346832B2, 2016.
20 H. K. Matthews, C. Bertoli and R. A. de Bruin, *Nat. Rev. Mol. Cell Biol.*, 2022, **23**, 74–88.
21 J. M. Espinosa, *Transcription*, 2019, **10**, 45–46.
22 L. A. S. Kovacs, D. A. Orlando and S. B. Haase, *Cell Cycle*, 2008, **7**, 2626–2629.
23 D. Hanahan and R. A. Weinberg, *Cell*, 2011, **144**, 646–674.
24 D. Hanahan and R. A. Weinberg, *Cell*, 2000, **100**, 57–70.
25 C. Braicu, M. Buse, C. Busuioc, R. Drula, D. Gulei, L. Raduly, A. Rusu, A. Irimie, A. G. Atanasov, O. Slaby, C. Ionescu and I. Berindan-Neagoe, *Cancers*, 2019, **11**, 1–25.
26 Pavan. Bachireddy, P. K. Bendapudi and D. W. Felsher, *Clin. Cancer Res.*, 2005, **11**, 4278–4281.
27 Z. Jin and W. S. El-Deiry, *Cancer Biol. Ther.*, 2005, **4**, 147–171.

28 K. Murphy, *Janeway's Immunobiology*, Garland Science, 8th edn., 2011.
29 S. W. G. Tait and D. R. Green, *Nat. Rev. Mol. Cell Biol.*, 2010, **11**, 621–632.
30 S. H. Suhaili, H. Karimian, M. Stellato, T.-H. Lee and M.-I. Aguilar, *Biophys. Rev.*, 2017, **9**, 443–457.
31 B. Wacquier, L. Combettes and G. Dupont, *Sci. Rep.*, 2020, **10**, 3924.
32 A. Sesso, J. E. Belizário, M. M. Marques, M. L. Higuchi, R. I. Schumacher, A. Colquhoun, E. Ito and J. Kawakami, *Anat. Rec.*, 2012, **295**, 1647–1659.
33 S. J. Korsmeyer, M. C. Wei, M. Saito, S. Weiler, K. J. Oh and P. H. Schlesinger, *Cell Death Differ.*, 2000, **7**, 1166–1173.
34 T. C. Cheng, C. Hong, I. V. Akey, S. Yuan and C. W. Akey, *eLife*, 2016, **5**, e17755.
35 S. Elmore, *Toxicol. Pathol.*, 2007, **35**, 495–516.
36 H.-L. Ou and B. Schumacher, *Blood*, 2018, **131**, 488–495.
37 S. Marchi, S. Patergnani, S. Missiroli, G. Morciano, A. Rimessi, M. R. Wieckowski, C. Giorgi and P. Pinton, *Cell Calcium*, 2018, **69**, 62–72.
38 D. D. Bufalo, A. Biroccio, C. Leonetti and G. Zupi, *FASEB J.*, 1997, **11**, 947–953.
39 T. Knight, D. Luedtke, H. Edwards, J. W. Taub and Y. Ge, *Biochem. Pharmacol.*, 2019, **162**, 250–261.
40 I. Kapoor, J. Bodo, B. T. Hill, E. D. Hsi and A. Almasan, *Cell Death Dis.*, 2020, **11**, 1–11.
41 E. N. Kontomanolis, A. Koutras, A. Syllaios, D. Schizas, A. Mastoraki, N. Garmpis, M. Diakosavvas, K. Angelou, G. Tsatsaris and A. Pagkalos, *Anticancer Res.*, 2020, **40**, 6009–6015.
42 M. A. Pierotti, F. Berrino, M. Gariboldi, C. Melani, A. Mogavero, T. Negri, P. Pasanisi and S. Pilotti, *Oncogene*, 2013, **32**, 1475–1487.
43 M. Olivo, R. Bhuvaneswari, S. S. Lucky, N. Dendukuri and P. Soo-Ping Thong, *Pharmaceuticals*, 2010, **3**, 1507–1529.
44 K. W. Kohn, *Cancer Res.*, 1996, **56**, 5533–5546.
45 A. Gilman and F. S. Philips, *Science*, 1946, **103**, 409–436.
46 L. S. Goodman, M. M. Wintrobe, W. Dameshek, M. J. Goodman, A. Gilman and M. T. McLennan, *J. Am. Med. Assoc.*, 1946, **132**, 126–132.
47 R. R. Sinden, *DNA structure and function*, Gulf Professional Publishing, 1994.
48 J. D. Watson and F. H. C. Crick, *Cold Spring Harb. Symp. Quant. Biol.*, 1953, **18**, 123–131.
49 A. Oleksi, A. G. Blanco, R. Boer, I. Usón, J. Aymamí, A. Rodger, M. J. Hannon and M. Coll, *Angew. Chem. Int. Ed.*, 2006, **45**, 1167–1167.
50 B. M. Zeglis, J. A. Boland and J. K. Barton, *J. Am. Chem. Soc.*, 2008, **130**, 7530–7531.
51 R. Martinez and L. Chacon-Garcia, *Curr. Med. Chem.*, 2005, **12**, 127–151.
52 W. D. Wilson, L. Strekowski, F. A. Tanious, R. A. Watson, J. L. Mokrosz, A. Strekowska, G. D. Webster and S. Neidle, *J. Am. Chem. Soc.*, 1988, **110**, 8292–8299.
53 E. Westhof, *J. Biomol. Struct. Dyn.*, 1987, **5**, 581–600.
54 V. C. Pierre, J. T. Kaiser and J. K. Barton, *Proc. Natl. Acad. Sci.*, 2007, **104**, 429–434.
55 F. Mohamadi, N. G. J. Richards, W. C. Guida, R. Liskamp, M. Lipton, C. Caufield, G. Chang, T. Hendrickson and W. C. Still, *J. Comput. Chem.*, 1990, **11**, 440–467.
56 W. L. Jorgensen and J. Tirado-Rives, *J. Am. Chem. Soc.*, 1988, **110**, 1657–1666.
57 G. A. Kaminski, R. A. Friesner, J. Tirado-Rives and W. L. Jorgensen, *J. Phys. Chem. B*, 2001, **105**, 6474–6487.
58 M. R. Redinbo, J. J. Champoux and W. G. J. Hol, *Biochemistry*, 2000, **39**, 6832–6840.
59 J. J. Champoux, *Annu. Rev. Biochem.*, 2001, **70**, 369–413.

60 M. R. Redinbo, L. Stewart, P. Kuhn, J. J. Champoux and W. G. Hol, *Science*, 1998, **279**, 1504–1513.
61 L. Stewart, G. C. Ireton and J. J. Champoux, *J. Mol. Biol.*, 1997, **269**, 355–372.
62 J. Alsner, J. Q. Svejstrup, E. Kjeldsen, B. S. Sørensen and O. Westergaard, *J. Biol. Chem.*, 1992, **267**, 12408–12411.
63 Y.-Y. Mo, C. Wang and W. T. Beck, *J. Biol. Chem.*, 2000, **275**, 41107–41113.
64 B. L. Staker, K. Hjerrild, M. D. Feese, C. A. Behnke, A. B. Burgin Jr and L. Stewart, *Proc. Natl. Acad. Sci.*, 2002, **99**, 15387–15392.
65 M. D. Been, R. R. Burgess and J. J. Champoux, *Nucleic Acids Res.*, 1984, **12**, 3097–3114.
66 B. J. Bonven, E. Gocke and O. Westergaard, *Cell*, 1985, **41**, 541–551.
67 D. A. Koster, V. Croquette, C. Dekker, S. Shuman and N. H. Dekker, *Nature*, 2005, **434**, 671–674.
68 J. T. Stivers, T. K. Harris and A. S. Mildvan, *Biochemistry*, 1997, **36**, 5212–5222.
69 Y. Pommier, E. Leo, H. Zhang and C. Marchand, *Chem. Biol.*, 2010, **17**, 421–433.
70 D. A. Koster, K. Palle, E. S. Bot, M.-A. Bjornsti and N. H. Dekker, *Nature*, 2007, **448**, 213–217.
71 B. H. Schmidt, N. Osheroff and J. M. Berger, *Nat. Struct. Mol. Biol.*, 2012, **19**, 1147–1154.
72 A. J. Schoeffler and J. M. Berger, *Q. Rev. Biophys.*, 2008, **41**, 41–101.
73 J. L. Nitiss, *Nat. Rev. Cancer*, 2009, **9**, 338–350.
74 S. E. Mirski, J. H. Gerlach, H. J. Cummings, R. Zirngibl, P. A. Greer and S. P. Cole, *Exp. Cell Res.*, 1997, **237**, 452–455.
75 A. K. McClendon, A. C. Rodriguez and N. Osheroff, *J. Biol. Chem.*, 2005, **280**, 39337–39345.
76 A. K. McClendon, A. C. Gentry, J. S. Dickey, M. Brinch, S. Bendsen, A. H. Andersen and N. Osheroff, *Biochemistry*, 2008, **47**, 13169–13178.
77 K. R. Vann, A. A. Oviatt and N. Osheroff, *Biochemistry*, 2021, **60**, 1630–1641.
78 E. L. Zechiedrich and N. Osheroff, *EMBO J.*, 1990, **9**, 4555–4562.
79 J. Roca and J. C. Wang, *Cell*, 1992, **71**, 833–840.
80 B. H. Schmidt, A. B. Burgin, J. E. Deweese, N. Osheroff and J. M. Berger, *Nature*, 2010, **465**, 641–644.
81 B. D. Bax, G. Murshudov, A. Maxwell and T. Germe, *J. Mol. Biol.*, 2019, **431**, 3427–3449.
82 K. C. Dong and J. M. Berger, *Nature*, 2007, **450**, 1201–1205.
83 J. E. Deweese and N. Osheroff, *Biochemistry*, 2009, **48**, 1439–1441.
84 J. E. Deweese and N. Osheroff, *Nucleic Acids Res.*, 2009, **37**, 738–748.
85 T. T. Harkins, T. J. Lewis and J. E. Lindsley, *Biochemistry*, 1998, **37**, 7299–7312.
86 T. Andoh and R. Ishida, *Biochim. Biophys. Acta BBA-Gene Struct. Expr.*, 1998, **1400**, 155–171.
87 A. K. Larsen, A. E. Escargueil and A. Skladanowski, *Pharmacol. Ther.*, 2003, **99**, 167–181.
88 J. M. Fortune and N. Osheroff, *J. Biol. Chem.*, 1998, **273**, 17643–17650.
89 J. M. Fortune and N. Osheroff, .
90 N. Osheroff, *Biochemistry*, 1989, **28**, 6157–6160.
91 Y. Pommier, *ACS Chem. Biol.*, 2013, **8**, 82–95.
92 C.-C. Wu, Y.-C. Li, Y.-R. Wang, T.-K. Li and N.-L. Chan, *Nucleic Acids Res.*, 2013, **41**, 10630–10640.
93 B. K. Sinha, P. M. Politi, H. M. Eliot, D. Kerrigan and Y. Pommier, *Eur. J. Cancer Clin. Oncol.*, 1990, **26**, 590–593.
94 C. Bailly, *Chem. Rev.*, 2012, **112**, 3611–3640.
95 T. C. Johnstone, G. Y. Park and S. J. Lippard, *Anticancer Res.*, 2014, **34**, 471–476.
96 Z. H. Siddik, *Oncogene*, 2003, **22**, 7265–7279.

97 N. J. Wheate, S. Walker, G. E. Craig and R. Oun, *Dalton Trans.*, 2010, **39**, 8113–8127.
98 T. Makovec, *Radiol. Oncol.*, 2019, **53**, 148–158.
99 H. Yin, L. Liao and J. Fang, *JSM Clin Oncol Res*, 2014, **2**, 1010.
100 E. Alessio and L. Messori, *Molecules*, 2019, **24**, 1–20.
101 M. Redrado, V. Fernández-Moreira and M. C. Gimeno, *ChemMedChem*, 2021, **16**, 932–941.
102 G. Sava, S. Pacor, G. Mestroni and E. Alessio, *Clin. Exp. Metastasis*, 1992, **10**, 273–280.
103 J. Kim, S. Pramanick, D. Lee, H. Park and W. J. Kim, *Biomater. Sci.*, 2015, **3**, 1002–1017.
104 M. G. Apps, E. H. Choi and N. J. Wheate, *Endocr.-Relat. Res.*
105 I. Mármol, J. Quero, M. J. Rodríguez-Yoldi and E. Cerrada, *Cancers*, 2019, **11**, 780.
106 J. P. Coverdale, T. Laroiya-McCarron and I. Romero-Canelón, *Inorganics*, 2019, **7**, 31.
107 W. Peti, T. Pieper, M. Sommer, B. K. Keppler and G. Giester, *Eur. J. Inorg. Chem.*, 1999, 1551–1555.
108 G. Chu, *J. Biol. Chem.*, 1994, **269**, 787–790.
109 A. Basu and S. Krishnamurthy, *J. Nucleic Acids*, 2010, **2010**, e201367.
110 P. M. Takahara, A. C. Rosenzweig, C. A. Frederick and S. J. Lippard, *Nature*, 1995, **377**, 649–652.
111 N. J. Wheate and J. G. Collins, *Coord. Chem. Rev.*, 2003, **241**, 133–145.
112 H. Baruah, C. G. Barry and U. Bierbach, *Curr. Top. Med. Chem.*, 2004, **4**, 1537–1549.
113 M. Coluccia and G. Natile, *Anti-Cancer Agents Med. Chem. Former. Curr. Med. Chem.-Anti-Cancer Agents*, 2007, **7**, 111–123.
114 P. J. Bednarski, F. S. Mackay and P. J. Sadler, *Anti-Cancer Agents Med. Chem. Former. Curr. Med. Chem.-Anti-Cancer Agents*, 2007, **7**, 75–93.
115 M. D. Hall and T. W. Hambley, *Coord. Chem. Rev.*, 2002, **232**, 49–67.
116 T. M. Stonelake, K. A. Phillips, H. Y. Otaif, Z. C. Edwardson, P. N. Horton, S. J. Coles, J. M. Beames and S. J. Pope, *Inorg. Chem.*, 2020, **59**, 2266–2277.
117 J. P. Cerón-Carrasco, J. Zúñiga and A. Requena, *J. Phys. Chem. A*, , DOI:10.1021/acs.jpca.9b06216.
118 Y. Sun, F. Ding, Z. Zhou, C. Li, M. Pu, Y. Xu, Y. Zhan, X. Lu, H. Li and G. Yang, *Proc. Natl. Acad. Sci.*, 2019, **116**, 1968–1973.
119 Y. Sun, F. Ding, Z. Chen, R. Zhang, C. Li, Y. Xu, Y. Zhang, R. Ni, X. Li and G. Yang, *Proc. Natl. Acad. Sci.*, 2019, **116**, 16729–16735.
120 F. Ding, Z. Chen, W. Y. Kim, A. Sharma, C. Li, Q. Ouyang, H. Zhu, G. Yang, Y. Sun and J. S. Kim, *Chem. Sci.*, 2019, **10**, 7023–7028.
121 J. Tang, H.-Y. Yin and J.-L. Zhang, in *Inorganic and Organometallic Transition Metal Complexes with Biological Molecules and Living Cells*, ed. K. K.-W. Lo, Academic Press, 2017, pp. 1–53.
122 A. de Almeida and R. Bonsignore, *Bioorg. Med. Chem. Lett.*, 2020, **30**, 127219.
123 Y. Zhu, M. Zhang, L. Luo, M. R. Gill, C. De Pace, G. Battaglia, Q. Zhang, H. Zhou, J. Wu and Y. Tian, *Theranostics*, 2019, **9**, 2158.
124 V. H. Houlding and V. M. Miskowski, *Coord. Chem. Rev.*, 1991, **111**, 145–152.
125 K. Li, G. S. M. Tong, Q. Wan, G. Cheng, W.-Y. Tong, W.-H. Ang, W.-L. Kwong and C.-M. Che, *Chem. Sci.*, 2016, **7**, 1653–1673.
126 F. A. Cotton, G. Wilkinson, C. A. Murillo and M. Bochmann, *Advanced inorganic chemistry*, John Wiley and Sons, Inc., 1999.
127 Y. Dai, Z. Yang, S. Cheng, Z. Wang, R. Zhang, G. Zhu, Z. Wang, B. C. Yung, R. Tian, O. Jacobson, C. Xu, Q. Ni, J. Song, X. Sun, G. Niu and X. Chen, *Adv. Mater. Deerfield Beach Fla*, , DOI:10.1002/adma.201704877.
128 G. J. Higby, *Gold Bull.*, 1982, **15**, 130–140.

129 J. Doherty and E. H. Baehrecke, *Nat. Cell Biol.*, 2018, **20**, 1110–1117.
130 G. Kroemer, L. Galluzzi, P. Vandenabeele, J. Abrams, E. S. Alnemri, E. H. Baehrecke, M. V. Blagosklonny, W. S. El-Deiry, P. Golstein, D. R. Green, M. Hengartner, R. A. Knight, S. Kumar, S. A. Lipton, W. Malorni, G. Nuñez, M. E. Peter, J. Tschopp, J. Yuan, M. Piacentini, B. Zhivotovsky and G. Melino, *Cell Death Differ.*, 2009, **16**, 3–11.
131 H. J. Williams, R. F. Willkens, C. O. Samuelson Jr, G. S. Alarcón, M. Guttadauria, C. Yarboro, R. P. Polisson, S. R. Weiner, M. E. Luggen and L. M. Billingsley, *Arthritis Rheum. Off. J. Am. Coll. Rheumatol.*, 1985, **28**, 721–730.
132 P. J. Sadler and R. E. Sue, *Met.-Based Drugs*, 1994, **1**, 107–144.
133 I. Ott, *Coord. Chem. Rev.*, 2009, **253**, 1670–1681.
134 S. J. Berners-Price and A. Filipovska, *Metallomics*, 2011, **3**, 863–873.
135 J. F. Fries, D. Bloch, P. Spitz and D. M. Mitchell, *Am. J. Med.*, 1985, **78**, 56–59.
136 T. M. Simon, D. H. Kunishima, G. J. Vibert and A. Lorber, *Cancer Res.*, 1981, **41**, 94–97.
137 D. T. Felson, J. J. Anderson and R. F. Meenan, *Arthritis Rheum.*, 1990, **33**, 1449–1461.
138 S. Goenka and S. R. Simon, *Arch. Dermatol. Res.*, 2020, **312**, 213–221.
139 C. K.-L. Li, R. W.-Y. Sun, S. C.-F. Kui, N. Zhu and C.-M. Che, *Chem. - Eur. J.*, 2006, **12**, 5253–5266.
140 G. Fanali, A. Di Masi, V. Trezza, M. Marino, M. Fasano and P. Ascenzi, *Mol. Aspects Med.*, 2012, **33**, 209–290.
141 M. T. Larsen, M. Kuhlmann, M. L. Hvam and K. A. Howard, *Mol. Cell. Ther.*, 2016, **4**, 3.
142 C. K. Mirabelli, R. K. Johnson, C. M. Sung, L. Faucette, K. Muirhead and S. T. Crooke, *Cancer Res.*, 1985, **45**, 32–39.
143 M. P. Doyle, E. W. Abel and F. G. A. Stone, *Pergamon Press Oxf.*
144 S. Gromer, L. D. Arscott, C. H. Williams, R. H. Schirmeri and K. Becker, *J. Biol. Chem.*, 1998, **273**, 20096–20101.
145 J. Zhang, X. Li, X. Han, R. Liu and J. Fang, *Trends Pharmacol. Sci.*, 2017, **38**, 794–808.
146 C. F. Shaw, *Chem. Rev.*, 1999, **99**, 2589–2600.
147 E. R. T. Tiekink, *Crit. Rev. Oncol. Hematol.*, 2002, **42**, 225–248.
148 C. F. Shaw III, *Chem Rev*, 1999, **99**, 2589–600.
149 T. Zou, C. Tung Lum, C.-N. Lok, J.-J. Zhang and C.-M. Che, *Chem. Soc. Rev.*, 2015, **44**, 8786–8801.
150 R. W.-Y. Sun, C. K.-L. Li, D.-L. Ma, J. J. Yan, C.-N. Lok, C.-H. Leung, N. Zhu and C.-M. Che, *Chem. – Eur. J.*, 2010, **16**, 3097–3113.
151 C. T. Lum, X. Liu, R. W.-Y. Sun, X.-P. Li, Y. Peng, M.-L. He, H. F. Kung, C.-M. Che and M. C. Lin, *Cancer Lett.*, 2010, **294**, 159–166.
152 W. Li, Y. Xie, R. W. Sun, Q. Liu, J. Young, W. Y. Yu, C. M. Che, P. K. Tam and Y. Ren, *Br. J. Cancer*, 2009, **101**, 342–349.
153 S. Wang, W. Shao, H. Li, C. Liu, K. Wang and J. Zhang, *Eur. J. Med. Chem.*, 2011, **46**, 1914–1918.
154 S. Tu, R. Wai-Yin Sun, M. C. Lin, J. Tao Cui, B. Zou, Q. Gu, H.-F. Kung, C.-M. Che and B. C. Wong, *Cancer Interdiscip. Int. J. Am. Cancer Soc.*, 2009, **115**, 4459–4469.
155 C. T. Lum, Z. F. Yang, H. Y. Li, R. Wai-Yin Sun, S. T. Fan, R. T. P. Poon, M. C. Lin, C.-M. Che and H. F. Kung, *Int. J. Cancer*, 2006, **118**, 1527–1538.
156 C. T. Lum, A. S.-T. Wong, M. C. Lin, C.-M. Che and R. W.-Y. Sun, *Chem. Commun.*, 2013, **49**, 4364–4366.
157 C. T. Lum, R. W.-Y. Sun, T. Zou and C.-M. Che, *Chem. Sci.*, 2014, **5**, 1579–1584.
158 K. H.-M. Chow, R. W.-Y. Sun, J. B. B. Lam, C. K.-L. Li, A. Xu, D.-L. Ma, R. Abagyan, Y. Wang and C.-M. Che, *Cancer Res.*, 2010, **70**, 329–337.

159 C. K. Li, R. W. Sun, S. C. Kui, N. Zhu and C. Che, *Chem. Eur. J.*, 2006, **12**, 5253–5266.
160 R. W.-Y. Sun, C.-N. Lok, T. T.-H. Fong, C. K.-L. Li, Z. F. Yang, T. Zou, A. F.-M. Siu and C.-M. Che, *Chem. Sci.*, 2013, **4**, 1979–1988.
161 L. Messori, F. Abbate, G. Marcon, P. Orioli, M. Fontani, E. Mini, T. Mazzei, S. Carotti, T. O'Connell and P. Zanello, *J. Med. Chem.*, 2000, **43**, 3541–3548.
162 A. Casini, M. A. Cinellu, G. Minghetti, C. Gabbiani, M. Coronnello, E. Mini and L. Messori, *J. Med. Chem.*, 2006, **49**, 5524–5531.
163 F. Magherini, A. Modesti, L. Bini, M. Puglia, I. Landini, S. Nobili, E. Mini, M. A. Cinellu, C. Gabbiani and L. Messori, *JBIC J. Biol. Inorg. Chem.*, 2010, **15**, 573–582.
164 V. Milacic, D. Chen, L. Ronconi, K. R. Landis-Piwowar, D. Fregona and Q. P. Dou, *Cancer Res.*, 2006, **66**, 10478–10486.
165 L. Ronconi, L. Giovagnini, C. Marzano, F. Bettìo, R. Graziani, G. Pilloni and D. Fregona, *Inorg. Chem.*, 2005, **44**, 1867–1881.
166 M. Altaf, M. Monim-ul-Mehboob, A.-N. Kawde, G. Corona, R. Larcher, M. Ogasawara, N. Casagrande, M. Celegato, C. Borghese and Z. H. Siddik, *Oncotarget*, 2017, **8**, 490.
167 J.-J. Zhang, K.-M. Ng, C.-N. Lok, R. W.-Y. Sun and C.-M. Che, *Chem. Commun.*, 2013, **49**, 5153–5155.
168 S. P. Fricker, R. M. Mosi, B. R. Cameron, I. Baird, Y. Zhu, V. Anastassov, J. Cox, P. S. Doyle, E. Hansell and G. Lau, *J. Inorg. Biochem.*, 2008, **102**, 1839–1845.
169 Y. Zhu, B. R. Cameron, R. Mosi, V. Anastassov, J. Cox, L. Qin, Z. Santucci, M. Metz, R. T. Skerlj and S. P. Fricker, *J. Inorg. Biochem.*, 2011, **105**, 754–762.
170 K. J. Akerman, A. M. Fagenson, V. Cyril, M. Taylor, M. T. Muller, M. P. Akerman and O. Q. Munro, *J. Am. Chem. Soc.*, 2014, **136**, 5670–5682.
171 C. R. Wilson, A. M. Fagenson, W. Ruangpradit, M. T. Muller and O. Q. Munro, *Inorg. Chem.*, 2013, **52**, 7889–7906.
172 P. Calamai, S. Carotti, A. Guerri, L. Messori, E. Mini, P. Orioli and G. Paolo Speroni, *J. Inorg. Biochem.*, 1997, **66**, 103–109.
173 M. Coronnello, E. Mini, B. Caciagli, M. A. Cinellu, A. Bindoli, C. Gabbiani and L. Messori, *J. Med. Chem.*, 2005, **48**, 6761–6765.
174 C. Gabbiani, A. Casini and L. Messori, *Gold Bull.*, 2007, **40**, 73–81.
175 C.-M. Che, R. W.-Y. Sun, W.-Y. Yu, C.-B. Ko, N. Zhu and H. Sun, *Chem. Commun.*, 2003, 1718–1719.
176 C. K. Li, R. W. Sun, S. C. Kui, N. Zhu and C. Che, *Chem. Eur. J.*, 2006, **12**, 5253–5266.
177 R. W.-Y. Sun, C.-N. Lok, T. T.-H. Fong, C. K.-L. Li, Z. F. Yang, T. Zou, A. F.-M. Siu and C.-M. Che, *Chem. Sci.*, 2013, **4**, 1979–1988.
178 J. J. Yan, A. L.-F. Chow, C.-H. Leung, R. W.-Y. Sun, D.-L. Ma and C.-M. Che, *Chem. Commun.*, 2010, **46**, 3893–3895.
179 B. Bertrand, M. Bochmann, J. Fernandez-Cestau and L. Rocchigiani, *Pincer Compd.*, 2018, 673–699.
180 K. J. Akerman, A. M. Fagenson, V. Cyril, M. Taylor, M. T. Muller, M. P. Akerman and O. Q. Munro, *J. Am. Chem. Soc.*, 2014, **136**, 5670–5682.
181 B. Bertrand, J. Fernandez-Cestau, J. Angulo, M. M. D. Cominetti, Z. A. E. Waller, M. Searcey, M. A. O'Connell and M. Bochmann, *Inorg. Chem.*, 2017, **56**, 5728–5740.
182 D. C. Carter, B. Chang, J. X. Ho, K. Keeling and Z. Krishnasami, *Eur. J. Biochem.*, 1994, **226**, 1049–1052.
183 S. Sugio, A. Kashima, S. Mochizuki, M. Noda and K. Kobayashi, *Protein Eng.*, 1999, **12**, 439–446.
184 I. Petitpas, A. A. Bhattacharya, S. Twine, M. East and S. Curry, *J. Biol. Chem.*, 2001, **276**, 22804–22809.
185 A. A. Spector, *J. Lipid Res.*, 1975, **16**, 165–179.

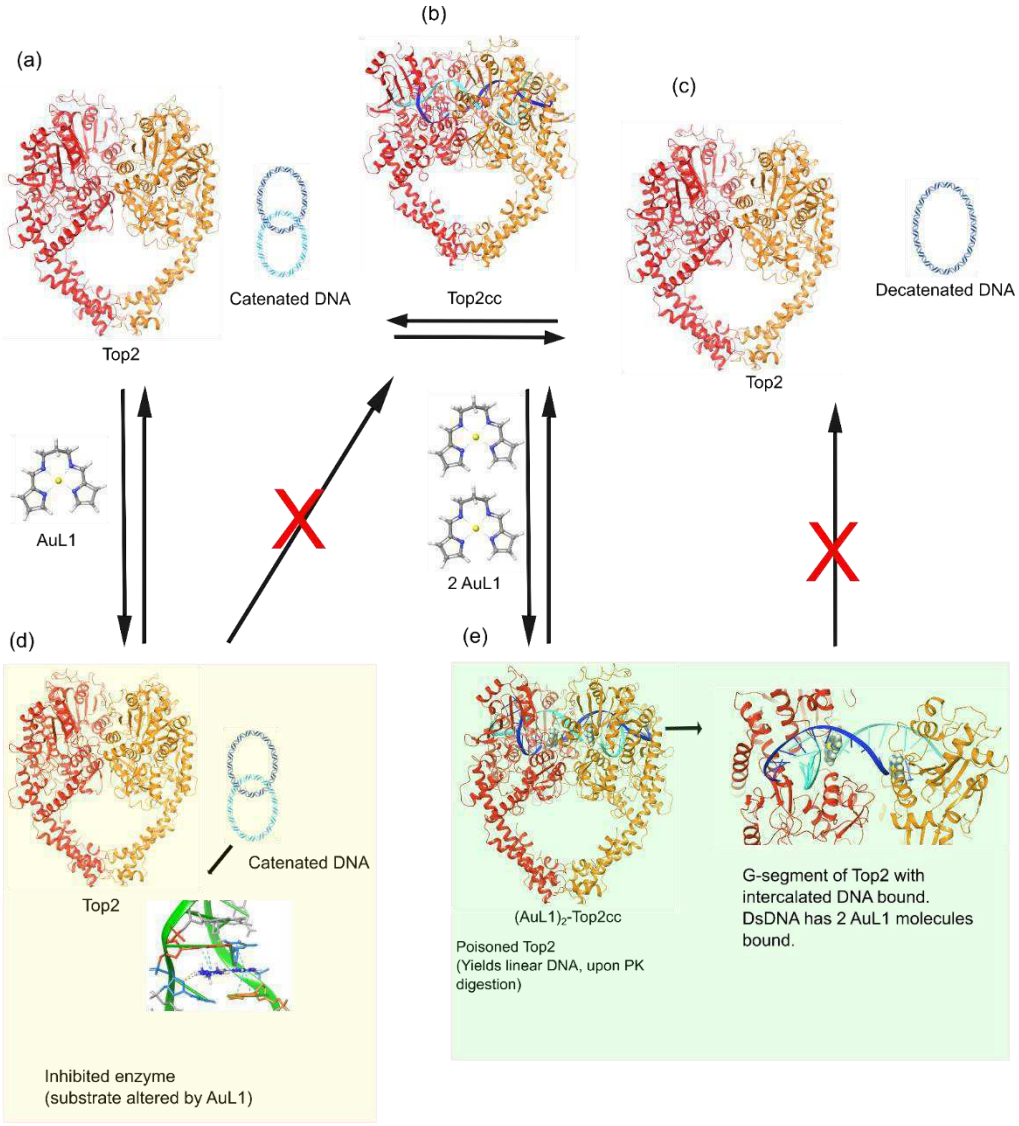
186 S. Curry, H. Mandelkow, P. Brick and N. Franks, *Nat. Struct. Biol.*, 1998, **5**, 827–835.
187 A. A. Bhattacharya, T. Grüne and S. Curry, *J. Mol. Biol.*, 2000, **303**, 721–732.
188 I. Petitpas, A. A. Bhattacharya, S. Twine, M. East and S. Curry, *J. Biol. Chem.*, 2001, **276**, 22804–22809.
189 J. Ghuman, P. A. Zunszain, I. Petitpas, A. A. Bhattacharya, M. Otagiri and S. Curry, *J. Mol. Biol.*, 2005, **353**, 38–52.
190 I. Petitpas, C. E. Petersen, C.-E. Ha, A. A. Bhattacharya, P. A. Zunszain, J. Ghuman, N. V. Bhagavan and S. Curry, *Proc. Natl. Acad. Sci.*, 2003, **100**, 6440–6445.
191 D. C. Carter and J. X. Ho, *Adv. Protein Chem.*, 1994, **45**, 153–203.
192 B. Loun and D. S. Hage, *Anal. Chem.*, 1994, **66**, 3814–3822.
193 G. Sudlow, D. J. Birkett and D. N. Wade, *Mol. Pharmacol.*, 1975, **11**, 824–832.
194 I. Fitos, J. Visy, M. Simonyi and J. Hermansson, *Chirality Pharmacol. Biol. Chem. Consequences Mol. Asymmetry*, 1999, **11**, 115–120.
195 J. Ghuman, P. A. Zunszain, I. Petitpas, A. A. Bhattacharya, M. Otagiri and S. Curry, *J. Mol. Biol.*, 2005, **353**, 38–52.
196 A. A. Bhattacharya, S. Curry and N. P. Franks, *J. Biol. Chem.*, 2000, **275**, 38731–38738.
197 P. Ascenzi, G. Fanali, M. Fasano, V. Pallottini and V. Trezza, *J. Mol. Struct.*, 2014, **1077**, 4–13.
198 A. J. Ryan, J. Ghuman, P. A. Zunszain, C. Chung and S. Curry, *J. Struct. Biol.*, 2011, **174**, 84–91.
199 S. Dasari and P. Bernard Tchounwou, *Eur. J. Pharmacol.*, 2014, **740**, 364–378.
200 J. C. Dabrowiak, *Metals in medicine*, John Wiley & Sons, 2017.
201 A. R. Timerbaev, S. S. Aleksenko, K. Polec-Pawlak, R. Ruzik, O. Semenova, C. G. Hartinger, S. Oszwaldowski, M. Galanski, M. Jarosz and B. K. Keppler, *Electrophoresis*, 2004, **25**, 1988–1995.
202 J. D. Holding, W. E. Lindup, D. A. Bowdler, M. Z. Siodlak and P. M. Stell, *Br. J. Clin. Pharmacol.*, 1991, **32**, 173–179.
203 C. Møller, H. S. Tastesen, B. Gammelgaard, I. H. Lambert and S. Stürup, *Metallomics*, 2010, **2**, 811–818.
204 J. E. Melvik, J. M. Dornish and E. O. Pettersen, *Br. J. Cancer*, 1992, **66**, 260–265.
205 S. V. Pizzo, M. W. Swaim, P. A. Roche and S. L. Gonias, *J. Inorg. Biochem.*, 1988, **33**, 67–76.
206 R. Momburg, M. Bourdeaux, M. Sarrazin, M. Chauvet and C. Briand, *J. Pharm. Pharmacol.*, 1987, **39**, 691–697.
207 G. Ferraro, L. Massai, L. Messori and A. Merlino, *Chem. Commun.*, 2015, **51**, 9436–9439.
208 W. Hu, Q. Luo, K. Wu, X. Li, F. Wang, Y. Chen, X. Ma, J. Wang, J. Liu and S. Xiong, *Chem. Commun.*, 2011, **47**, 6006–6008.
209 I. Moraleja, E. Moreno-Gordaliza, D. Esteban-Fernández, M. L. Mena, M. W. Linscheid and M. M. Gómez-Gómez, *Anal. Bioanal. Chem.*, 2015, **407**, 2393–2403.
210 B. P. Espósito and R. Najjar, *Coord. Chem. Rev.*, 2002, **232**, 137–149.
211 K. Wiglusz and L. Trynda-Lemiesz, *J. Photochem. Photobiol. Chem.*, 2014, **289**, 1–6.
212 D. Machover, E. Diaz-Rubio, A. de Gramont, A. Schilf, J.-J. Gastiaburu, S. Brienza, M. Itzhaki, G. Metzger, D. N'Daw, J. Vignoud, A. Abad, E. François, E. Gamelin, M. Marty, J. Sastre, J.-F. Seitz and M. Ychou, *Ann. Oncol.*, 1996, **7**, 95–98.
213 Y. Yue, X. Chen, J. Qin and X. Yao, *Colloids Surf. B Biointerfaces*, 2009, **69**, 51–57.

214 S. Shahraki, M. Saeidifar, F. Shiri and A. Heidari, *J. Biomol. Struct. Dyn.*, 2017, **35**, 3098–3106.
215 J. Ma, Q. Wang, Z. Huang, X. Yang, Q. Nie, W. Hao, P. G. Wang and X. Wang, *J. Med. Chem.*, 2017, **60**, 5736–5748.
216 Y.-R. Zheng, K. Suntharalingam, T. C. Johnstone, H. Yoo, W. Lin, J. G. Brooks and S. J. Lippard, *J. Am. Chem. Soc.*, 2014, **136**, 8790–8798.
217 N. Shahabadi, S. Amiri and A. (Arman) Taherpour, *J. Coord. Chem.*, 2019, **72**, 600–618.
218 A. Abedi, N. Safari, V. Amani, S. Tavajohi and S. N. Ostad, *Inorganica Chim. Acta*, 2011, **376**, 679–686.
219 D. Hha, *Trace Elem. Med*, 2001, **2**, 80–87.
220 A. L. Casey, D. Adams, T. J. Karpanen, P. A. Lambert, B. D. Cookson, P. Nightingale, L. Miruszenko, R. Shillam, P. Christian and T. S. J. Elliott, *J. Hosp. Infect.*, 2010, **74**, 72–77.
221 S. Mathews, M. Hans, F. Mücklich and M. Solioz, *Appl. Environ. Microbiol.*, 2013, **79**, 2605–2611.
222 D. Denoyer, S. Masaldan, S. La Fontaine and M. A. Cater, *Met. Integr. Biometal Sci.*, 2015, **7**, 1459–1476.
223 C. Marzano, M. Pellei, F. Tisato and C. Santini, *Anti-Cancer Agents Med. Chem.-Anti-Cancer Agents*, 2009, **9**, 185–211.
224 M. S. Fleisher and L. Loeb, *J. Exp. Med.*, 1914, **20**, 503–521.
225 Y. Yamane, K. Sakai, T. Umeda, N. Murata, S. Ishizeki, I. Ogihara, A. Takahashi, I. Iwasaki and G. Ide, *Gan*, 1984, **75**, 1062–1069.
226 J. Y. Uriu-Adams and C. L. Keen, *Mol. Aspects Med.*, 2005, **26**, 268–298.
227 K. G. Daniel, D. Chen, S. Orlu, Q. C. Cui, F. R. Miller and Q. P. Dou, *Breast Cancer Res.*, 2005, **7**, R897.
228 M. Fatfat, R. A. Merhi, O. Rahal, D. A. Stoyanovsky, A. Zaki, H. Haidar, V. E. Kagan, H. Gali-Muhtasib and K. Machaca, *BMC Cancer*, 2014, **14**, 527.
229 M. C. Linder, *Mutat. Res. Mol. Mech. Mutagen.*, 2012, **733**, 83–91.
230 Y. Gou, J. Qi, J.-P. Ajayi, Y. Zhang, Z. Zhou, X. Wu, F. Yang and H. Liang, *Mol. Pharm.*, 2015, **12**, 3597–3609.
231 A. Hussain, M. F. AlAjmi, M. T. Rehman, S. Amir, F. M. Husain, A. Alsalme, M. A. Siddiqui, A. A. AlKhedhairy and R. A. Khan, *Sci. Rep.*, 2019, **9**, 5237.
232 Z. Benkhellat, M. Allali, M. Beley, E. Wenger, M. Bernard, N. Parizel, K. Selmeczi and J.-P. Joly, *New J. Chem.*, 2014, **38**, 419–429.
233 Q. A. de Paula, J.-P. Joly, K. Selmeczi, D. E. P. Fonseca, G. F. Caramori, N. P. Farrell and A. M. Da Costa Ferreira, *J. Coord. Chem.*, 2018, **71**, 1894–1909.
234 S. Tabassum, W. M. Al-Asbahy, Mohd. Afzal and F. Arjmand, *J. Photochem. Photobiol. B*, 2012, **114**, 132–139.
235 Z. Kazemi, H. A. Rudbari, M. Sahihi, V. Mirkhani, M. Moghadam, S. Tangestaninejad, I. Mohammadpoor-Baltork and S. Gharaghani, *J. Photochem. Photobiol. B*, 2016, **162**, 448–462.
236 B. Peng, Z. Gao, X. Li, T. Li, G. Chen, M. Zhou and J. Zhang, *JBIC J. Biol. Inorg. Chem.*, 2016, **21**, 903–916.
237 G. Sava, S. Pacor, G. Mestroni and E. Alessio, *Clin. Exp. Metastasis*, 1992, **10**, 273–280.
238 E. Alessio, *Eur. J. Inorg. Chem.*, 2017, **2017**, 1549–1560.
239 P. Heffeter, K. Böck, B. Atil, M. A. Reza Hoda, W. Körner, C. Bartel, U. Jungwirth, B. K. Keppler, M. Micksche, W. Berger and G. Koellensperger, *JBIC J. Biol. Inorg. Chem.*, 2010, **15**, 737–748.
240 F. Beckford, D. Dourth, M. Shaloski, J. Didion, J. Thessing, J. Woods, V. Crowell, N. Gerasimchuk, A. Gonzalez-Sarrías and N. P. Seeram, *J. Inorg. Biochem.*, 2011, **105**, 1019–1029.
241 F. A. Beckford, *Int. J. Inorg. Chem.*, 2010, **2010**, 1–7.

242 S. Huang, S. Peng, W. Su, Z. Tang, J. Cui, C. Huang and Q. Xiao, *RSC Adv.*, 2016, **6**, 47043–47054.
243 A. G. Quiroga, J. M. Pérez, I. López-Solera, J. R. Masaguer, A. Luque, P. Román, A. Edwards, C. Alonso and C. Navarro-Ranninger, *J. Med. Chem.*, 1998, **41**, 1399–1408.
244 O. E. Offiong and S. Martelli, *Farm. Soc. Chim. Ital. 1989*, 1994, **49**, 513–518.
245 S. Huang, F. Zhu, Q. Qian, Q. Xiao and W. Su, *Biol. Trace Elem. Res.*, 2015, **164**, 150–161.
246 A. Martínez, J. Suárez, T. Shand, R. S. Magliozzo and R. A. Sánchez-Delgado, *J. Inorg. Biochem.*, 2011, **105**, 39–45.
247 A. Martínez, C. S. Rajapakse, D. Jalloh, C. Dautriche and R. A. Sánchez-Delgado, *JBIC J. Biol. Inorg. Chem.*, 2009, **14**, 863–871.
248 C. S. Rajapakse, A. Martinez, B. Naoulou, A. A. Jarzecki, L. Suarez, C. Deregnaucourt, V. Sinou, J. Schrevel, E. Musi and G. Ambrosini, *Inorg. Chem.*, 2009, **48**, 1122–1131.
249 A. I. Tomaz, T. Jakusch, T. S. Morais, F. Marques, R. F. M. de Almeida, F. Mendes, É. A. Enyedy, I. Santos, J. C. Pessoa, T. Kiss and M. H. Garcia, *J. Inorg. Biochem.*, 2012, **117**, 261–269.
250 T. S. Morais, F. Santos, L. Côrte-Real, F. Marques, M. P. Robalo, P. J. A. Madeira and M. H. Garcia, *J. Inorg. Biochem.*, 2013, **122**, 8–17.
251 T. S. Morais, F. C. Santos, L. Corte-Real and M. H. Garcia, *J. Inorg. Biochem.*, 2013, **129**, 94–101.
252 W. H. Ang, E. Daldini, L. Juillerat-Jeanneret and P. J. Dyson, *Inorg. Chem.*, 2007, **22**, 9048–9050.
253 V. Novohradský, A. Bergamo, M. Cocchietto, J. Zajac, V. Brabec, G. Mestroni and G. Sava, *Dalton Trans.*, 2015, **44**, 1905–1913.
254 A. Bergamo, R. Gagliardi, V. Scarcia, A. Furlani, E. Alessio, G. Mestroni and G. Sava, *J. Pharmacol. Exp. Ther.*, 1999, **289**, 559–564.
255 M. Brindell, I. Stawoska, J. Supel, A. Skoczowski, G. Stochel and R. van Eldik, *JBIC J. Biol. Inorg. Chem.*, 2008, **13**, 909–918.
256 M. I. Webb and C. J. Walsby, *Dalton Trans.*, 2011, **40**, 1322–1331.
257 F. Lentz, A. Drescher, A. Lindauer, M. Henke, R. A. Hilger, C. G. Hartinger, M. E. Scheulen, C. Dittrich, B. K. Keppler, U. Jaehde and in collaboration with C. E. S. for A. D. Research-EWIV, *Anticancer. Drugs*, 2009, **20**, 97.
258 M. Pongratz, P. Schluga, M. A. Jakupec, V. B. Arion, C. G. Hartinger, G. Allmaier and B. K. Keppler, *J. Anal. At. Spectrom.*, 2004, **19**, 46–51.
259 A. Bijelic, S. Theiner, B. K. Keppler and A. Rompel, *J. Med. Chem.*, 2016, **59**, 5894–5903.
260 A. S. Meigooni, S. Sabnis and R. Nath, *Endocuriether Hypertherm Oncol*, 1990, **6**, 107–17.
261 A. T. Porter and J. D. Forman, *Cancer*, 1993, **71**, 953–958.
262 J. Ruiz, N. Cutillas, C. Vicente, M. D. Villa, G. López, J. Lorenzo, F. X. Avilés, V. Moreno and D. Bautista, *Inorg. Chem.*, 2005, **44**, 7365–7376.
263 H.-Q. Li, P.-C. Lv, T. Yan and H.-L. Zhu, *Anti-Cancer Agents Med. Chem.- Anti-Cancer Agents*, 2009, **9**, 471–480.
264 R. Safirstein, J. Winston, D. Moel, S. Dikman and J. Guttenplan, *Int. J. Androl.*, 1987, **10**, 325–346.
265 R. S. Goldstein and G. H. Mayor, *Life Sci.*, 1983, **32**, 685–690.
266 H. B. Gray, *J. Am. Chem. Soc.*, 1962, **84**, 1548–1552.
267 F. Basolo, H. B. Gray and R. G. Pearson, *J. Am. Chem. Soc.*, 1960, **82**, 4200–4203.
268 A. C. Cope and E. C. Friedrich, *J. Am. Chem. Soc.*, 1968, **90**, 909–913.
269 E. M. Mrkalić, R. M. Jelić, O. R. Klisurić and Z. D. Matović, *Dalton Trans.*, 2014, **43**, 15126–15137.

270 K. Yamasaki, V. T. G. Chuang, T. Maruyama and M. Otagiri, *Biochim. Biophys. Acta BBA-Gen. Subj.*, 2013, **1830**, 5435–5443.
271 F. Zsila, Z. Bikadi, D. Malik, P. Hari, I. Pechan, A. Berces and E. Hazai, *Bioinformatics*, 2011, **27**, 1806–1813.
272 L. Yan, X. Wang, Y. Wang, Y. Zhang, Y. Li and Z. Guo, *J. Inorg. Biochem.*, 2012, **106**, 46–51.
273 A. Divsalar, M. J. Bagheri, A. A. Saboury, H. Mansoori-Torshizi and M. Amani, *J. Phys. Chem. B*, 2009, **113**, 14035–14042.
274 G. R. Behbehani, A. Divsalar, A. A. Saboury and M. J. Bagheri, *J. Solut. Chem.*, 2008, **37**, 1785–1794.
275 M. Saeidifar and H. Mansouri-Torshizi, *Nucleosides Nucleotides Nucleic Acids*, 2015, **34**, 16–32.
276 C. Dong, S. Ma and Y. Liu, *Spectrochim. Acta. A. Mol. Biomol. Spectrosc.*, 2013, **103**, 179–186.
277 Y. Wang, L. Peng, M. Bellamri, S. Langouët and R. J. Turesky, *Chem. Res. Toxicol.*, 2015, **28**, 1045–1059.
278 M. Saeidifar, H. Mansouri-Torshizi and A. Akbar Saboury, *J. Lumin.*, 2015, **167**, 391–398.
279 M. Hosseini-Kharat, K. Karami, M. Saeidifar, C. Rizzoli, R. Zahedi-Nasab, Z. Sohrabijam and T. Sharifi, *New J. Chem.*, 2017, **41**, 9897–9907.
280 S. Shahraki and A. Heydari, *J. Biomol. Struct. Dyn.*, 2018, **36**, 2807–2821.

Chapter 2 Gold(III) chelates: Dual mode inhibitors of human Topoisomerase II and their complexities of binding to human serum albumin



Gold(III) chelates: Dual mode inhibitors of human Topoisomerase II and their complexities of binding to human serum albumin.

Sheldon Sookai[a], Matthew Akerman[b], Olga Færch[c], Yasien Sayed,[c] and Orde Q. Munro*[,a,d]

[a]Molecular Sciences Institute, School of Chemistry, University of the Witwatersrand, PO WITS 2050, Johannesburg, South Africa

[b]School of Chemistry, University of KwaZulu-Natal, Pietermaritzburg, 3201, South Africa.

[c]Protein Structure-Function Research Unit, School of Molecular and Cell Biology, University of the Witwatersrand, Johannesburg, 2050, South Africa

[d]School of Chemistry University of Leeds, Woodhouse Lane, LS2 9JT, UK

[e]*Electronic Supplementary Information (ESI) available: Complete experimental details and supplementary tables and figures in PDF format, X-ray crystal structures in CIF format (CCDC 2207667 and 2207668), Cartesian coordinates for all calculated structures, and a Maestro project file containing Glide XP docking data. See DOI: 10.1039/x0xx00000x*

Topoisomerase IIα (Top2) is a key eukaryotic nuclear enzyme that catalyzes topological changes of double-stranded DNA during gene transcription and DNA replication. Anticancer drugs that inhibit Top2 are characterized as either interfacial poisons (IFPs) or catalytic inhibitors compounds (CICs). Here we describe a class of cytotoxic redox-stable cationic Au(III) Schiff base chelates (**AuL1**, **AuL2,** and **AuL3**) that are able to bind to and intercalate DNA. All three compounds were tested in the National Cancer Institute (NCI)-60 cytotoxic screen of which **AuL1** and **AuL3** had undergone the full-five dose testing. Notably, mean cytotoxic data over the 60 human cell lines revealed GI_{50} values of 7.3 μM, 11.5 μM, and IC_{50} values of 15.7 and 30.9 μM for **AuL1** and **AuL3**, respectively while **AuL2** had no significant cytotoxicity. Using hierarchical cluster analysis employing the NCI data for 21 known anticancer therapeutics, we found both **AuL1** and **AuL3** matched the mechanism of Daunorubicin a potent Top2 inhibitor. The Top2–catalyzed decatenation reaction of supercoiled DNA was studied as a function of the concentration of **AuL1**. Interestingly, **AuL1** acts as an IFP of Top2 at concentrations less than 5 μM and CICs at concentrations above 5 μM. Thereafter, we investigated the binding of the Au(III) chelates with human serum albumin (HSA) since it is responsible for transporting many exogenous compounds, including investigational and clinically deployed drugs. Steady-state fluorescence quenching data acquired on the native protein, supplemented with data from site-specific probes, indicated that the Au(III) chelates bound close to the Trp-214 (Sudlow's site I) of HSA to quench the fluorophore. The bimolecular quenching rate constants, k_q, were of the order of 10^2 times higher than the maximum diffusion-controlled collision constant of a biomolecule in water (10^{10} M^{-1} s^{-1}). The Stern-Volmer constants, K_{SV}, spanned the range 10^4 M^{-1} to 10^6 M^{-1}, while the affinity constants, K_a, measured with isothermal titration calorimetry (ITC) ranged from ~6×10^4 M^{-1} (**AuL3**) to ~1×10^5 M^{-1} (**AuL2**) at 298 K. The thermodynamics reflect entropically driven ligand uptake, while near- and far-UV CD spectroscopy indicated minimal perturbations to the structure of HSA upon ligand uptake. This study highlights the mechanisms by which the Au(III) chelates exhibit their cytotoxic activity (blocking Top2) and further highlights favorable pharmacodynamic data upon binding to HSA.

Introduction

After the discovery that the anticancer drugs etoposide and doxorubicin specifically target eukaryotic topoisomerase II (Top2), this protein has emerged as a prominent focus for anticancer therapy.[1,2] Top2 is a nuclear enzyme that relies on ATP and divalent cations, specifically Mg^{2+}, for its ability to introduce topological modifications to double-stranded DNA.[3–5] In essence, Top2 facilitates topological changes, including the disentanglement of knotted DNA during replication and the relaxation of supercoiled negative and positive DNA structures.[3–5] This process involves the transient generation of double-stranded breaks in the DNA backbone, which allows for the passage of a second individual double helix through the nucleic acid gate before resealing the break. The breakage of DNA occurs within the active site of Top2, where each promoter subunit contains an active site

tyrosine residue that initiates a nucleophilic attack on the sugar-phosphate backbone of DNA, resulting in DNA cleavage.[3,4,6] During the DNA cleavage process, Top2 effectively preserves genome integrity and conserves bond energy by covalently attaching to the newly generated 5′-terminal phosphates, which are created by the scission of the double helix and are positioned four base pairs apart on opposite strands.[6–9] These DNA intermediates cleaved by Top2 are commonly referred to as cleavage complexes (Top2cc). Under physiological conditions, Top2cc exists at low equilibrium concentrations and can be easily tolerated by the cell. However, a significant increase in the concentration of Top2cc, resulting from the impaired catalytic ability of Top2, markedly disrupts essential topological functions such as DNA replication and gene transcription, ultimately leading to apoptotic cell death.[6–9]

Drugs that inhibit Top2 can be divided into two categories: poisons, which irreversibly trap the DNA-enzyme covalent complex, and catalytic inhibitor compounds (CICs).[6] Poisons can further be classified based on their mechanism of action as either interfacial or covalent. Interfacial poisons (IFPs) exert their antineoplastic effects through a distinctive mechanism in which they non-covalently bind to the interface between Top2 and DNA, specifically targeting the tyrosyl residues within the active site.[6,10,11] IFPs are bifunctional agents as they interact with both the protein and DNA. Upon drug binding, the frequency of DNA scissions increases. During DNA cleavage, IFPs bind between the ends of the double helix at the cut scissile bonds on the G-segment of DNA. The binding of IFPs to Top2 distorts the active site of the cleavage complex and leads to the detachment of an Mg^{2+} ion from the phosphotyrosyl moiety.[12] As a result, Top2cc becomes irreversibly trapped within the active site, inhibiting ligation.[6,7,13] Stabilizing double-stranded breaks requires the presence of two drug molecules in the active site of Top2. On the other hand, covalent Top2 poisons function by enhancing Top2-mediated cleavage through the closure of the N-terminal gate.[14,15] This characteristic is evident from the inhibition of Top2 when a covalent Top2 poison is added before DNA (*in vitro*).[14,15] The precise mechanism by which covalent poisons increase the levels of Top2cc remains unknown. Both interfacial and covalent Top2 poisons exert their cytotoxic effects by inhibiting Top2, leading to the accumulation of Top2cc within the cell, ultimately inducing cell apoptosis.

CICs exert their inhibitory effects on Top2 by suppressing its catalytic activity, without causing an increase in the concentration of Top2cc. These compounds have the potential to inhibit multiple steps within the Top2 catalytic cycle, including DNA cleavage, DNA binding, ATP binding, and ATP hydrolysis.[1,4,16] The inhibitory action of CICs on these various steps has been documented in previous studies.[17–19]

Furthermore, it is crucial to investigate the binding mechanism of potential chemotherapeutic agents to human serum albumin (HSA), as it represents a vital step in understanding the plasma distribution of these drug candidates.[17] HSA is the most abundant plasma protein, with a concentration of 600 μM.[18] It plays two primary roles: regulating the osmotic pressure and facilitating the transport of exogenous and endogenous molecules.[19] Structurally, HSA is a heart-shaped, single polypeptide macromolecule composed of 585 amino acids, with a monomeric molar mass of 66.5 kDa.[20] As depicted in Scheme 2, HSA consists of three domains: I (residues 1-195), II (196-383), and III (384-585) and each domain contains two subdomains, A and B.[20,21] Notably, HSA has several binding sites, with fatty acids being the main ligands occupying seven of these sites.[22] Additionally, there are two major small molecule binding sites known as Sudlow's sites I and II, located in subdomains IIA and IIIA, respectively.[23–25] Understanding these binding sites is crucial for comprehending the pharmacodynamic and pharmacokinetic data of HSA *in vivo*, given its abundance and role as a transporter in blood plasma.[23]

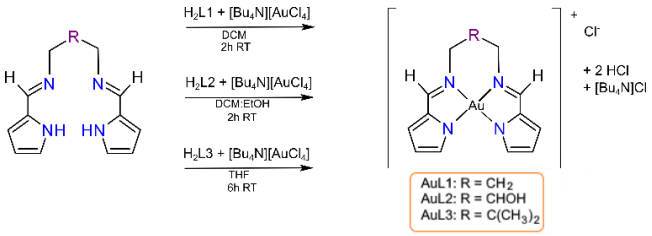
In this study, we synthesized three bis(pyrrole-imine) Schiff base Au(III) chelates, denoted as **AuL1**, **AuL2**, and **AuL3**, respectively (Scheme 1). Spectroscopic methods were employed to investigate the binding of **AuL1**, **AuL2**, and **AuL3** to HSA in KH_2PO_4 (50 mM, pH 7.5). The aim was to explore how the moieties of the carbon chain linking the imine groups in the respective metal complexes influence their uptake by HSA and to identify the preferred binding site(s). Additionally, we conducted an NCI-60 screen to assess the cytotoxicity of the three Au(III) chelates against 60 human cancer cell lines. Interestingly, both **AuL1** and **AuL3** demonstrated significant activity, while **AuL2** did not, thereby justifying a full 5-dose screening. Furthermore, our findings indicate that the mechanism of action for AuL1 involves binding to and intercalating DNA, as well as blocking Top2 activity by functioning as both IFPs and catalytic inhibitor compounds CICs.

Results and Discussion

Ligands **H_2L1**, **H_2L2** and, **H_2L3** (Scheme S1) were metalated with Au(III) by reacting the respective ligand with $[Bu_4N][AuCl_4]$ (Scheme 1) to form the Au(III) chelates **AuL1**, **AuL2** and **AuL3**. The three Au(III) chelates reflect the design of our patented class of cytotoxic molecules.[26] Specifically, we employed pyrrole-imine Schiff base chelates, due to their ability to stabilize the high oxidation state on the Au(III) ion. In this reaction, the nitrogen atoms on the pyrrole rings are concomitantly deprotonated upon metalation,[27] affording the desired cationic Au(III) chelates. None of the Au(III) chelates have been reported prior and precipitated out of the solution without any impurities.

X-ray structures

The structures of the three Au(III) chelates were elucidated by single-crystal X-ray diffraction crystallography (Fig. 1). **AuL1** crystallized in the triclinic space group P_1, while **AuL2** and **AuL3** crystallized in monoclinic space groups $P2_{1/n}$ and $P2_{1/c}$, respectively.



Scheme 1 Synthetic procedure for AuL1, AuL2, and AuL3 by reacting the appropriate bis (pyrrolide–imine) chelates with [Bu$_4$N][AuCl$_4$].

The Au(III) ions exhibit the expected four-coordinate, square planar geometry within their respective tetradentate bis(pyrrolide-imine) chelates, which is an appreciable geometry for DNA binding and cytotoxicity (Fig. 1). The Au(III) ions in salts **AuL1**, **AuL2** and **AuL3** are nominally square planar with Au–N bond distances ranging from 1.975–2.017 Å. The average Au–N$_{imine}$ distances were 2.009 (12) Å and Au–N$_{pyrrole}$ distances were 0.55% shorter at an average length of 1.998 (12) Å. This reflects that the pyrrole moieties are anionic σ-donors with more acute C–N–C angles than the corresponding C=N–C angles of the imine donors.

Overall, the observed Au–N bond distances for the Au(III) chelates are comparable to reported Au–N bond distances ranging from 1.928–2.216 Å reported for the structurally-related Au(III) complex analogues.[28,29] However, the average N$_{pyrrole}$–Au–N$_{pyrrole}$ and N$_{imine}$–Au–N$_{imine}$ bond angles for the Au(III) chelates are 102.5(8)° and 95.6(8)°, respectively, which marginally deviates from the structurally-related Au(III) complex analogues N$_{pyrrole}$–Au–N$_{pyrrole}$ and N$_{imine}$–Au–N$_{imine}$ bond angles, that were 98.83(4)° and 97.6(4)°, respectively.[29] The cation conformations of the Au(III) chelates deviate slightly from planarity, which is mainly attributed to non-bonded crystal packing and the formation of discrete π-stacked dimers. In the case of all three complexes, there were no aurophilic Au···Au contacts between cations (Au···Au distances > 4 Å). However, **AuL1**–**AuL3** do indicate the potential for π-stacking, highlighting their potential to intercalate with DNA.

DNA binding and intercalation

The Au(III) chelates in this study were designed as chemotherapeutic agents, primarily functioning as IFPs through the inhibition of topoisomerases. If the Au(III) chelates act as IFPs, they will bind to both DNA and topoisomerase.[30] Considering the planar structure of the Au(III) complexes, we anticipate their ability to bind and intercalate DNA. To test this hypothesis, we measured the binding constants, (K_a), for the non-covalent binding of **AuL1**-**AuL3** to calf thymus DNA (ctDNA) by UV-visible spectroscopic titrations. The metal-to-ligand charge transfer (MLCT) absorption band of the Au(III) chelates was monitored at 382 nm, and changes in the electronic spectrum at 382 nm indicate the interaction of the **AuL1** with ctDNA (Fig. 2a and **AuL2** and **AuL3** is represented in Fig. S37). The highest obtained ratios of [ctDNA]:[**AuL1**], [ctDNA]:[**AuL2**], and [ctDNA]:[**AuL3**] obtained, before the spectrophotometer could no longer detect accurate absorbance readings, were 11.6:1, 11.6:1 and 17.5:1, respectively.

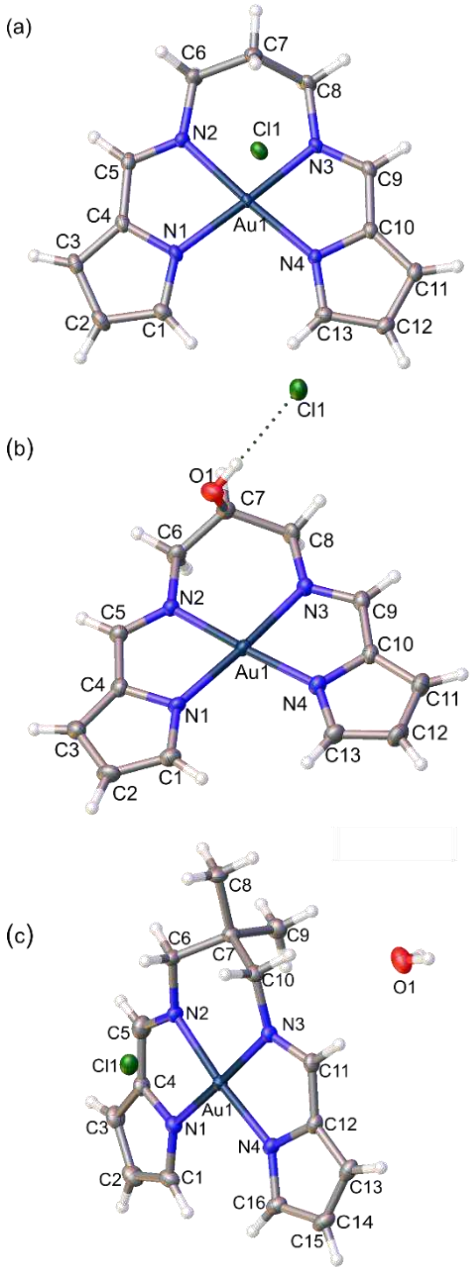


Figure. 1 View of the X-ray structures of three Au(III)-chelates are shown with their respective counterions (50% thermal ellipsoids for non-H atoms; H atoms are shown as capped cylinders). Atom color code white H, grey C, blue N, dark blue Au, red O, dark green Cl, light green F, and purple P. Crystallographic details are presented in the supporting information. Thermal ellipsoid plots show a single molecule of the asymmetric unit of (a) **AuL1**, (b) **AuL2**, and (c) **AuL3**.

Table 1 Selected bond angles and bond lengths of AuL1, AuL2, and AuL3.

Bond distances	AuL1	AuL2	AuL3
Au–$N_{pyrrole}$	1.997 (18)	1.999 (2)	1.998 (16)
Au–N_{imine}	2.017 (18)	2.001 (2)	2.009 (16)
C-C=N	1.300 (3)	1.305 (0.3)	1.304 (4)
Bond angles (°)			
$N_{pyrrole}$–Au–$N_{pyrrole}$	102.4 (8)	102.4(9)	102.7(7)
Cis–$N_{pyrrole}$–Au–N_{imine}	80.79(7)	80.99(9)	81.00(7)
Trans–$N_{pyrrole}$–Au–N_{imine}	175.92 (7)	176.5(9)	175.4(7)
N_{imine}–Au–N_{imine}	95.97(7)	95.61(9)	95.35(7)
$C_{pyrrole}$–C–N_{imine}	115.3(18)	115.3(2)	117.5(18)

An error in the parenthesis indicates the error on the last digit.

From Fig. 2a (and Fig. S37), a decrease in absorbance intensity across the characteristic MLCT peak at 382 nm and π-π* at 289 nm ranging from 55.6% ± 0.30 (**AuL1**) 51.4 ± 0.38 % (**AuL3**), accompanied with a red shift from 382 nm to 394 nm. The red shift indicates that the Au(III) chelates are positioned in a more polar environment (i.e., indicating binding to DNA). The decrease in absorbance at 382 nm during the titration with ctDNA was fitted to the Hill model[31] with an R^2 value of 0.99 (Fig. 2a insert and Figs. S37b and 37d). Using the Hill model, the affinity of the three Au(III) chelates binding to ctDNA was quantified by calculating the mean binding constant (K_a) from three independent experiments: 1.95 (± 0.095) × 10^4, 1.45 (± 0.13) × 10^4 and 2.66 ± (0.1) × 10^4 M^{-1} for **AuL1**, **AuL2** and **AuL3**, respectively at 310 K (Table 2).

Typically, the K_a values of groove, binders are marginally higher than those of intercalators, with K_a values ranging from 10^5 to 10^8 M^{-1}.[32,33] We compared the binding constants to those of other Au(III) complexes that have been shown to interact with ctDNA (Fig. S38). Au(III) macrocyclic complexes (4a) were found to bind to DNA with an apparent K_a ranging from 1.20 x 10^6 M^{-1} to 4.91 x 10^6 M^{-1}. While pseudo macrocyclic complexes had an even higher K_a ranging from 2.85 x 10^6 M^{-1} to 6.61 x 10^6 M^{-1}.[29] Both the macrocyclic complexes and pseudo macrocyclic complexes had an order of magnitude higher K_a than **AuL1**-**AuL3** analyzed in this study. Two CNC–Au(III) complexes, 4b and 4c were found to bind to DNA with a K_a of 4.5 x 10^5 M^{-1} and 5.4 x 10^5 M^{-1}, respectively.[34,35] In comparison, the Au(III) chelates in this study had a K_a of an order of magnitude higher than the carbazolide Au(III) complex (4d) binding to DNA (K_a 3.7 x 10^4 M^{-1}).[36] Overall, the K_a of the **AuL1**-**AuL3** in this study fall in the lower end range of binding for known intercalators.

Table 2 Dissociation constants (K_a) and binding stoichiometry (n) for the interaction of AuL1, AuL2, and AuL3 with ctDNA, at 310 K in 50 mM KH_2PO_4 buffer at pH 7.50.

Compound	Temp. T (K)	10^5 K_a $(M^{-1})^{a,b}$	n[c]
ctDNA–AuL1	310	0.195 (0.1)	2.05 (0.1)
ctDNA–AuL2	310	0.147(0.1)	1.86 (0.2)
ctDNA–AuL3	310	0.266 (0.1)	3.13 (0.3)

[a]K_d values (Dissociation constant) were determined by fitting the data to Hill fit curve. [b]The estimated standard deviation of the least significant digits is given in parentheses. [c]Ligand: DNA binding stoichiometry from the Hill fit of the data.

Linear and circular dichroism of DNA

Linear dichroism (LD) and circular dichroism (CD) spectroscopy were performed on a solution of sheared and helical ctDNA, respectively with increasing concentrations of **AuL1**-**AuL3** (Fig. 2b, c, and Figs. S41 and S42). Since **AuL1**-**AuL3** are achiral, they do not generate an LD or CD signal. However, once the achiral Au(III) chelates bind to and form stable complexes with dsDNA (in this case, ctDNA).

A dichroic signal (induced spectrum) is observed. If the drug interacting with dsDNA functions as a minor groove binder, it produces a positive dichroic signal. Conversely, an intercalator generates a negative dichroic signal in the chromophoric region of the complexes (MLCT band for the Au(III) chelates) or near-UV π – π* (Fig. S40).[37] All LD experiments were performed in KH_2PO_4 buffer (50 mM, pH 7.5), with ctDNA and varying [Au(III) chelate]/[DNA] ratios.

The LD spectrum of the ctDNA displays a strong negative signal at 260 nm due to the contribution of the ctDNA nucleotides (purine and pyrimidine base pairs).[38] Upon the addition of each Au(III) chelate a concentration-dependent increase in the amplitude of the 260 nm minima was observed (Figs. 2a and S41), which is associated with increasing DNA rigidity (i.e., DNA stiffening), signifying either lengthening and/or an increase in the rigidity of double-helical DNA. The result signifies that DNA is being intercalated and, therefore, being unwound (Fig 2a).[39–41] Furthermore, an induced dichroic signal that appears between 350–430 nm and peaks at 394 nm, which is a spectral region where no contribution from DNA base pairs can be detected and only the chromophoric Au(III) chelates can absorb. The Au(III) chelates are isotropic and cannot be orientated in the flow field. Therefore, the signal peaking at 394 nm is indicative of an induced LD signal and its occurrence suggests that all three Au(III) chelates form a molecular complex with ctDNA, become orientated, and are intercalators of DNA. UV CD spectroscopy was employed to visualize the conformational changes of ctDNA in the presence of the Au(III) chelates, as shown in Figs. 2c and S42.

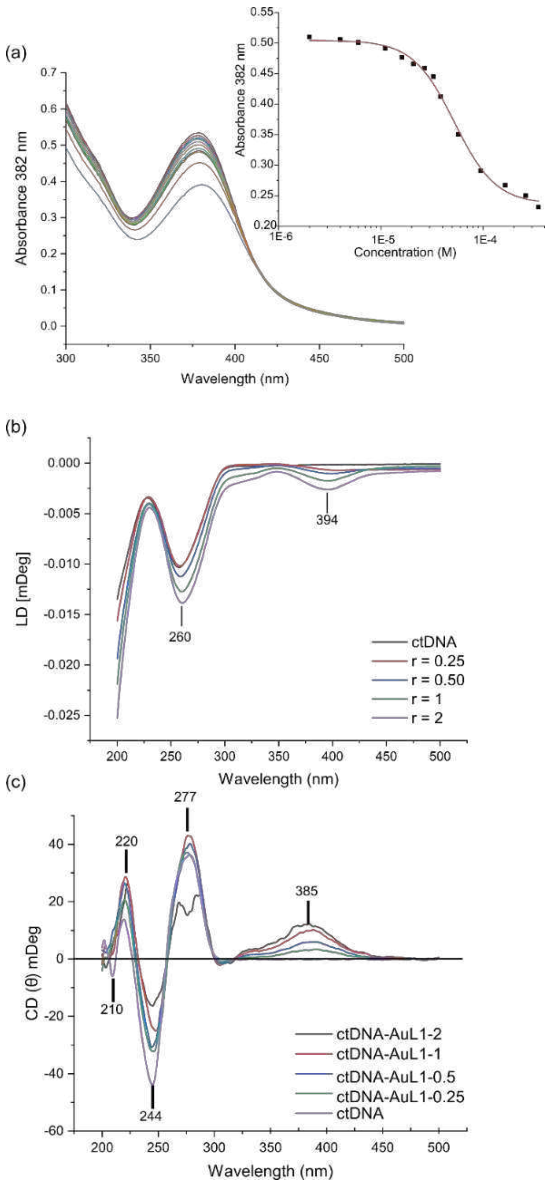


Figure. 2 (a) The UV-vis absorption spectra of **AuL1** and the insert represent the change in the absorbance at 382 nm of **AuL1** as a function of [ctDNA] fitted to the Hill model. The UV-visible absorption spectra of **AuL2** and **AuL3** are provided in the ESI the change in the absorbance at 382 nm of **AuL2** as a function of [ctDNA] fitted to the Hill model. All reactions were carried out in KH_2PO_4 and after sequential additions of ctDNA (final [ctDNA] = 342 μM bp, for **AuL1** and **AuL2** and 542 μM for **AuL3**). The Hill fits were used to calculate the dissociation constants and stoichiometric ratios of the Au(III) chelates binding to ctDNA. (b) The LD spectrum of **AuL1** with 100 μM of ctDNA at increasing Au(III) chelate]:[ctDNA] ratios (*r*) of 0.25–2 in KH_2PO_4 (50 mM, pH 7.5) at 37 °C. The intense minimum at 260 nm represents ctDNA and the 394 nm band represents an induced Au(III) chelates LD spectrum. (c) The CD spectrum of **AuL1** with 100 μM of ctDNA at increasing [Au(III) chelate]:[ctDNA] ratios (*r*) of 0.25–2 in KH_2PO_4 (50 mM, pH 7.5) at 37 °C. The intense maxima and minima from 210–277 nm represent ctDNA and the 385 nm band represents an induced Au(III) chelates CD spectrum.

Native B-form DNA exhibits four major transition bands at 210 nm, 220 nm, 244 nm, and 277 nm, which serve as markers for the double-helical B-conformation of DNA.[42,43] The maximum band at 277 nm is attributed to base stacking, while the minima bands at 210 nm, 220 nm, and 244 nm are associated with the helicity of DNA.[42,44] Upon the addition of the Au(III) chelates to the B-form DNA, the intensities of the 210 nm and 244 nm peaks decreased, while the intensity of the 277 nm peak increased. When r = 2, the 277 nm band for **AuL1** and **AuL2** (Figs. 2c and S42a) distorted, indicating DNA condensation in the presence of **AuL1** and **AuL2**. Additionally, the observed changes in the peak intensities were not indicative of a conversion from B-form DNA to A-form DNA, but rather attributed to the aggregation effect of the Au(III) chelates on ctDNA.[45] It is noteworthy that the A-form of DNA exhibits a maximum peak at 263 nm, and the presence of an ICD signal at 385 nm indicates the binding of the Au(III) chelates to ctDNA.

NCI-60 cytotoxicity screens

Compounds **AuL1**, **AuL2**, and **AuL3** underwent pre-screening by the National Cancer Institute (NCI, Bethesda, MD) against a panel of 60 human cancer cell lines, as depicted in Figs. S43-45. Among them, **AuL1** and **AuL3** exhibited sufficient cytotoxicity to warrant full five-dose screens. The mean IC_{50} values across all 60 cell lines for **AuL1** and **AuL3** were determined to be 15.7 and 30.9 μM, respectively. The significant variance observed can be attributed to variations in the cytotoxicity of the Au(III) chelates among the different groups of cancer cell lines. Notably, **AuL1** displayed the highest activity against leukemia, non-small lung cell carcinoma, as well as several colon and renal cancers (Fig. S43). In Fig. 3, a comparison is made between the best GI_{50} values for **AuL1** and **AuL3** and the analogous data for clinically deployed anticancer drugs with well-defined mechanisms of action (MOAs). Mean cytotoxicity parameters for **AuL1**–**AuL3**, obtained for each of the nine classes of human cancer in the NCI-60 screen, are listed in Figs. S43–S45, respectively. It is interesting to note, as depicted in Fig. 3, that although the GI_{50} values of **AuL1** and **AuL3** were not as low as those of commercially available anticancer drugs, the LC_{50} and IC_{50} values were lower than those of carboplatin, cisplatin, and [Au(III)(terpy)Cl]Cl_2, and similar to that of mitomycin. This seemingly anomalous data can be attributed to the different shapes of the dose-response curves for each compound. The compounds synthesized in this study exhibited much steeper (harder) dose-response curves compared to other commercial drugs. The steepness of the curve indicates that a relatively high initial concentration of the compounds is required to induce cell death; however, once this concentration is achieved, even small increases in the concentration result in high levels of cell mortality.

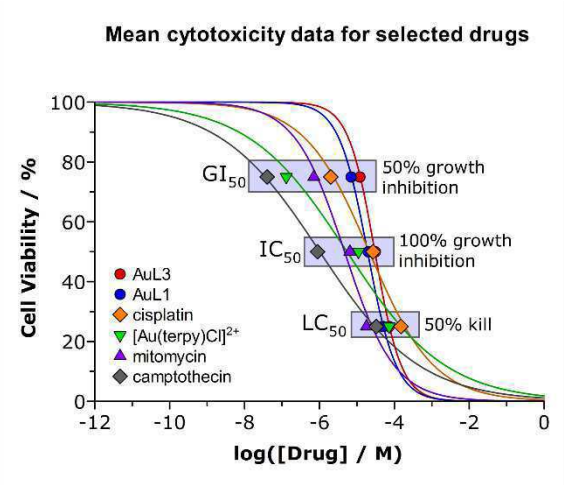


Figure. 3 Dose-response curves for three commercial anti-cancer agents (camptothecin, cisplatin, and mitomycin), one known Au(III) cytotoxic chelate ($[Au(terpy)Cl]^{2+}$ and the two Au(III) chelates that had undergone the NCI-60 five-dose screening in this work (**AuL1** and **AuL3**).

To elucidate the MOA and cellular target(s) of **AuL1** and **AuL3**, the GI_{50} data for these complexes were subjected to hierarchical cluster analysis with equivalent data for 21 compounds of known MOA from the NCI's database, and the results are presented in Fig. 4. It was found that **AuL1** is closely associated with the Top2 poison etoposide, indicating a similar MOA. Furthermore, **AuL1** exhibits a more distant relationship with the drugs daunorubicin and cisplatin. Daunorubicin is a potent Top2 poison,[46] while cisplatin has been demonstrated to function as an effective Top2 inhibitor in addition to its role as a DNA cross-linker.[47] Based on this analysis, it is hypothesized that **AuL3** shares a similar mode of binding to DNA as **AuL1**, as it also possesses the ability to bind to and intercalate with DNA.

AuL2 was comparatively inactive as compared to **AuL1** and **AuL3**. This difference in activity can likely be attributed to the presence of an OH moiety on the second position of the propyl bis(imine) linkage, which acts as an electron-withdrawing group and may impact its activity. Conversely, **AuL3** contains two electron-donating dimethyl moieties, which contribute to its activity. We propose two potential reasons for the inactivity of **AuL2**: (i) **AuL2** may be eliminated through mechanisms such as the efflux pump, a well-known mechanism responsible for the elimination of toxic compounds.[48] (ii) The presence of the OH group in **AuL2** may enhance its binding affinity to transport serum proteins, specifically HSA, thereby facilitating their elimination from cells (*vide supra*).

To confirm the MOA for both **AuL1** and **AuL3**, it is necessary to perform *in vitro* enzyme inhibition assays with topoisomerases I and II. Topoisomerase inhibitors can be categorized into two groups: irreversible DNA-enzyme covalent complex trappers (IFPs) and noncovalent protein or target DNA sequence binders (CICs). Conducting these assays will provide valuable insights into the interaction of **AuL1** and **AuL3** with the respective topoisomerases and help elucidate their specific MOAs.

Table 3 Summary of the average cytotoxicity data over 60 human cancer cell lines for compounds AuL1 and AuL2 as well as selected commercial cytotoxic agents for comparison.

Drug	GI_{50} (μM)	IC_{50} (μM)	LC_{50} (μM)
AuL1	7.3	15.7	48.9
AuL2	11.5	30.9	72.0
Cisplatin	2.0	27	>100
Carboplatin	99.6	>100	>100
$[Au^{3+}(terpy)Cl]Cl_2$	0.13	11	73
Mitomycin	0.71	6.5	18
Camptothecin	0.040	0.89	33

Topoisomerase IIα inhibition assay

AuL1 was subjected to catalytic inhibition evaluation against top2 relaxation, encompassing a wide concentration range from 0.005 to 500 μM, as depicted in Fig. 5. The agarose gel image presented in Fig. 5a illustrates that **AuL1** concentrations below 500 nM yielded undetectable levels of linear DNA cleavage product, indicating a lack of inhibition of Top2 and an absence of supercoiled DNA decatenation. However, within the range of 0.50–50 μM for **AuL1** (lanes 5–7), there is no apparent correlation between the concentration of linear DNA and the concentration of **AuL1**. The dose-response function reaches its maximum at [**AuL1**] = 5 μM before exhibiting a nonlinear decrease as the concentration of **AuL1** increases within the 50–500 μM range (lanes 7 and 8). Etoposide (VP-16), a potent Top2 inhibitor, was employed as a control to compare the activity of **AuL1**. The data suggest that the inhibition of Top2 by **AuL1** follows a biphasic dose-response function, with a transition in the reaction mechanism of **AuL1** from initially acting as an irreversible DNA-enzyme covalent complex trapper (IFP) at concentrations ranging from 0–0.5 μM, to subsequently functioning as a noncovalent protein or target DNA sequence binder (CIC) at concentrations between 50–500 μM.

Mechanistically, the first phase can be attributed to the non-covalent binding of two molecules of **AuL1** to the Top2-DNA intermediate covalent cleavage complex (Top2cc) at its two nick sites. This binding mechanism closely resembles that observed in the X-ray structure of the quaternary-$(drug)_2$-DNA enzyme covalent cleavage complex of VP-16 (etoposide; PDB 5GWK).[13] As depicted in Fig. 5, an increase in the fraction of **AuL1** from 0.5–5 μM leads to an increase in the trapped (i.e., poisoned) fraction of the DNA-enzyme intermediate covalent Top2cc during the catalytic cycle of the enzyme.

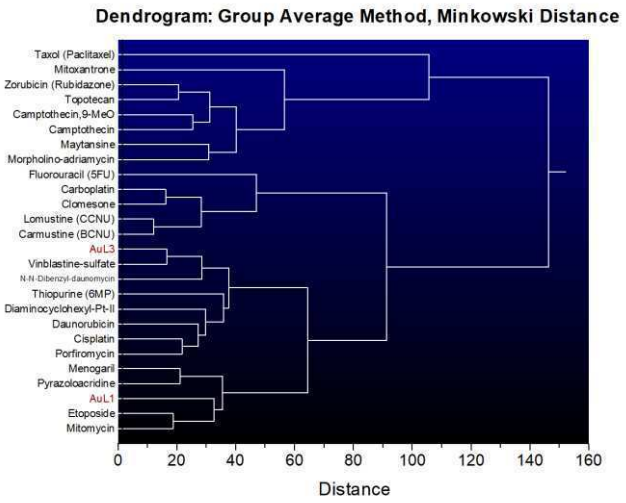


Figure. 4 Comparison of the activity profile of confocal drugs with a known mode of action and the Au(III) chelates **AuL1** and **AuL3** synthesized in this work.

At higher concentrations of **AuL1** (50–500 μM), a mechanistic switch in action occurs, wherein **AuL1** exhibits an additional target with a lower binding affinity compared to its insertion at the Top2cc nick sites. This phenomenon is evident in Fig. 5, where the formation of supercoiled DNA (SC) in lanes 7 and 8 indicates the inability of the binary DNA-enzyme complex to form due to the binding of the drug to the protein. Consequently, the compound inhibits the enzyme at these higher concentrations. As discussed earlier (Fig. 2), **AuL1** binds to and intercalates with DNA (with a K_a of 1.95 x 10^4 M^{-1}), predominantly at the AT sites of the DNA sequence.[29] It is conceivable that the binding of **AuL1** to the DNA sequence is also targeted by Top2. Therefore, as the concentration of [**AuL1**] increases, it competes with the nick site-binding and ultimately outcompetes Top2 in binding to DNA. At high concentrations of **AuL1**, the dominant mechanism of Top2 inhibition becomes catalytic inhibition rather than enzyme poisoning. This is evidenced by the inverse relationship between the intensity of the linear DNA band and [**AuL1**] when [**AuL1**] exceeds 5 μM (lanes 7 and 8, Fig. 5a).

Based on previous studies on the catalytic mechanism of Top2[49] and the enzyme poisoned by etoposide[13], we have developed a simplified mechanistic scheme (Fig. 6) that effectively summarizes the current data. The catalytic inhibition of Top2 by our **AuL1** chelates exhibits similarities to a dual-mode irreversible DNA-enzyme covalent complex trapper (IFP) catalytic inhibitor, as reported in previous studies for anti-cancer agents such as 9-hydroxyellipticine [54], adriamycin (doxorubicin)[50,51], and cis-dichloro{(isoquinolin-3-ylcarbonyl)[2-[(isoquinolin-3- ylcarbonyl) amino]phenyl] azanido} Au(III) [52]. In summary, our findings indicate that the dual-mode reaction of **AuL1** with Top2 is consistent with earlier observations on similar biphasic inhibition of the enzyme observed with other anti-cancer therapeutics. The enzyme inhibition data obtained in our study further support the MOA of **AuL1**, as identified from the *in vivo* cytotoxicity data (GI_{50} values) through hierarchical cluster analysis.

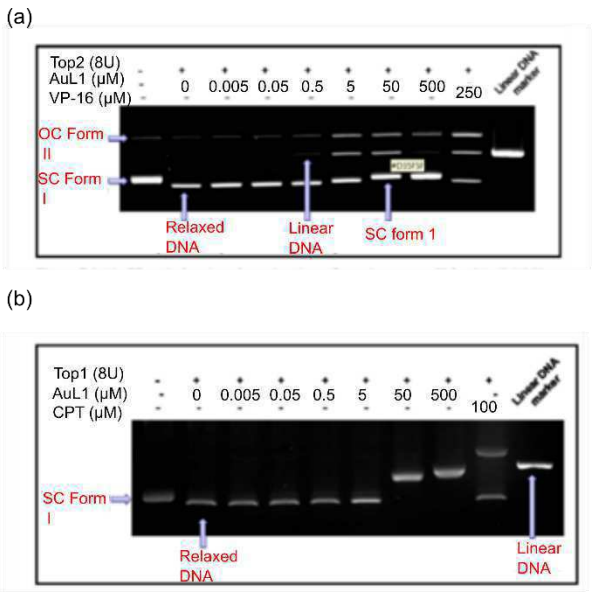


Figure. 5 (a) EB gel showing **AuL1** poisoning Top2 at low concentrations (0.5–50 μM) and catalytically inhibiting Top2 at higher concentrations (> 50 μM). (b) EB gel shows the inactivity of **AuL1** against Top1 compared to camptothecin (CPT), which is a specific inhibitor for Top1.

The Top2 inhibition assay was conducted in the presence of **AuL2**, as depicted in agarose gel Fig. S46. Interestingly, the analysis of **AuL2** demonstrates a comparable level of activity to **AuL1**. The compound is observed to poison the Top2 enzyme at low concentrations (0.5 μM) and competitively inhibit the enzyme at high concentrations (50 μM). These results closely resemble those of **AuL1**, indicating that **AuL2** is a potent poison of topoisomerase II *in vitro* and also acts as an enzyme inhibitor at higher concentrations. This finding supports the hypothesis that there may be a cellular mechanism responsible for the inactivation of the metal chelate, possibly involving an efflux pump.

To provide further evidence that the cytotoxicity of the chelates is primarily attributed to the Au(III) ion, additional experiments were conducted. These experiments involved running the same set of gel electrophoresis tests performed on **AuL1**, but this time the Top2 enzyme was incubated with supercoiled DNA and various concentrations of the palladium(II) analog of **AuL1** and H_2L1 in separate experiments. The results of these experiments are presented in Figs. S47 and S48, respectively. The palladium analog exhibited activity that was 100 times lower compared to **AuL1**, while H_2L1 showed no activity at all.

Topoisomerase I inhibition assay

To validate that **AuL1** specifically inhibits Top2 and confirm the accuracy of our hierarchical cluster analysis, a second set of experiments was conducted to assess its ability to

inhibit or poison topoisomerase I (Top1). Top1 differs from Top2 in that it induces single-strand breaks instead of double-strand breaks during the relaxation process. Top1 is also crucial for DNA transcription and synthesis. The results of the Top1 activity assay are presented in the agarose gel (Fig. 5b). Camptothecin (CPT), a potent Top1 poison, was used as a standard reference for comparison. The data indicated that concentrations of [**AuL1**] ranging from 0.005–500 μM were ineffective in poisoning or inhibiting Top1. This conclusion was drawn based on the migration of DNA with varying [**AuL1**], which did not correspond to the reference lanes (i.e., supercoiled DNA (lane 1), CPT (lane 8), and linear DNA (lane 10)). The Au(III) chelates synthesized in this study demonstrated specific targeting of Top2, highlighting their potential for further exploration as anti-cancer therapeutics. However, it is crucial to assess the binding of the Au(III) chelates to HSA since the protein plays a critical role in drug metabolism and can influence distribution and concentration.

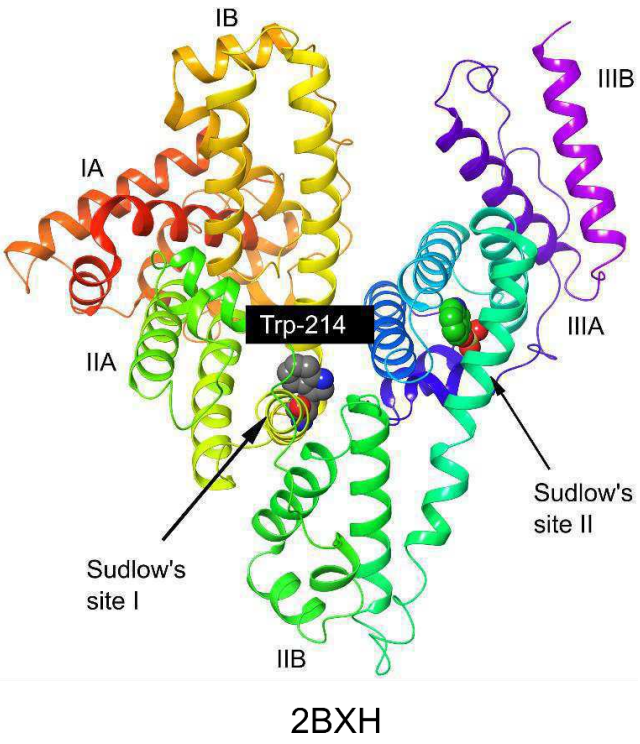
Mechanism of DNA binding

From Fig. 2, the experimental data indicates **AuL1**–**AuL3** are intercalators of DNA. Biomolecular simulations using Glide further corroborated the experimental data (Figs. 6b and S49). An example depicting the way **AuL1** might intercalate DNA was obtained with the palindromic sequence used by Barton *et al*. to study intercalation and insertion of 5'-D(CGGAAATTACCG)-3' by the cationic ruthenium complex $[Ru(bpy)_2(dppz)]^{2+}$ (PDB code: 4E1U).[53] Similar to the Ru^{2+} complex, **AuL1** was able to target the central 5'-AT-3' step in the oligonucleotide (Fig. S49, ESI), albeit with a relatively low Glide docking score (ΔG_{bind}= – 4.84 kcal/mol). **AuL1** unsurprisingly is shown to target the exact TA sites that the Au(III) macrocycles were shown to target by Akerman *et al*.[29] these sites are the lowest energy.

Fluorescence quenching measurements

When a molecule binds to a protein, it can directly influence the protein's intrinsic fluorescence, which is primarily attributed to three aromatic amino acid residues: tryptophan (Trp), tyrosine (Tyr), and phenylalanine (Phe).[54,55] Among these residues, Trp mostly contributes to the intrinsic fluorescence of a protein due to its higher quantum yield and more efficient resonance energy transfer compared to Phe and Tyr.[56] The binding of a molecule to a protein induces changes in the polarity around the fluorophore within the protein, leading to either the quenching or enhancement of its intrinsic fluorescence.[55] HSA has a single tryptophan residue (Trp-214) located in subdomain IIA and 18 tyrosine residues present in the protein.[56]

We investigated the quenching effect on the intrinsic emission spectrum of HSA (λ^{ex}, 295 nm) by progressively titrating increasing concentrations of Au(III) chelates, ranging from 0 to 97 μM, across a spectral range of 310-400 nm (Fig. 7a). The emission maximum was observed at ~342 nm in KH_2PO_4 buffer (50 mM, pH 7.5) and the intrinsic emission intensity of HSA decreased monotonically with each titration of the respective Au(III) chelates. The fluorescence emission data indicated that all three Au(III) chelates bound to HSA near the microenvironment around the Trp-214 fluorophore, resulting in its emission being quenched.



Scheme 2 X-ray structure of HSA bound to indomethacin (redrawn from PDB code 2BXH) illustrating the two main small molecule binding sites. Sudlow's site I is larger than Sudlow's site II and compounds that bind in this pocket perturb the fluorescence of Trp-214. The protein secondary structure elements are depicted schematically, colored by domain, and labeled.

The quenching of HSA's intrinsic fluorescence can arise from various mechanisms, including collisional quenching, molecular rearrangements, energy transfer, or ground state complex formation.[45,46] Upon binding of the three Au(III) chelates to HSA, the λ_{max}^{em} blue shifts were induced at ~2 nm (λ_{max}^{em} 2 nm) for **AuL1**, **AuL3**, and λ_{max}^{em} 1.48 nm for **AuL2**, respectively.

The blue shift was not as substantial as the blue shift reported for Pd(PrPyrr),[57] but the blue shift suggests that the Trp-214 residue is in a less polar environment after the uptake of the Au(III) chelates.[58,59] Two possible reasons that may explain the λ_{max}^{em} blue shifts are: (i) the oriental polarization of the tryptophan caused by ordered water molecules that lie between 15–25 Å of the amino acid and/or (ii) the electronic polarization of the indole ring on the trp residue due to the binding of the Au(III) chelates.

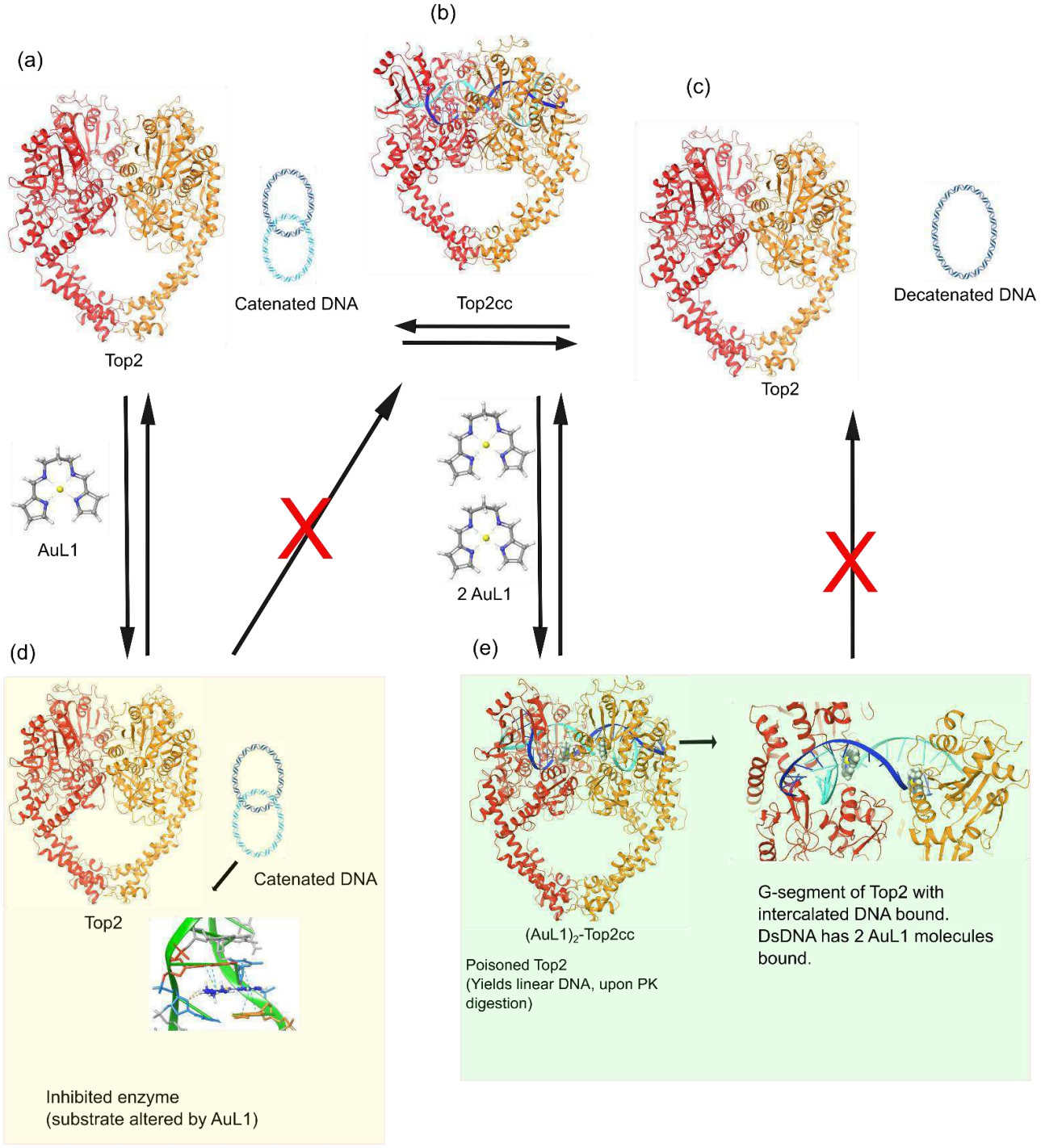


Figure.6. Illustration of key events in the catalytic cycle of human Top2. Under normal conditions (i.e., absence of chemotherapeutics) (a) catenated DNA is bound by Top2 (dsDNA; 5'-TA-3'). (b) Top2 introduces a double break, one in the G segment where it will later pass the T segment through. When a divalent cation (Mg^{2+}) is present it can activate the tyrosine residues for a nucleophilic attack on the phosphate backbone of DNA forming a phosphotyrosine linkage between every single strand and tyrosine in each subunit. The top2 clamp is closed when two ATP molecules are bound, then a T segment may pass. The clamped G-segment is the Top2-DNA cleavage complex (Top2cc). (c) Finally, hydrolysis of ATP-1 may aid in the T-segment passing, while hydrolysis of ATP-2 allows the clamp to open. Top2 2 returns to its native state with decatenated DNA. (d) If a CIC is present, it may alter the state of the DNA or have an inhibitory effect on Top2, therefore, a Top2cc is not formed. (e) If an IFP is present the Top2 cannot decatenate the DNA and a Top2cc is formed with linear DNA. The enzyme is poisoned and remains a covalent cleavage complex. Accumulation of Top2cc results in cell apoptosis.

Furthermore, the binding of the Au(III) chelates may induce some electronic polarization of Trp-214, which in turn affects the lowest energy $^1A_1 \rightarrow {}^1L_a$ ground state transition of Trp's indole ring,[47] Ultimately, the similarity in the magnitudes of the measured λ_{max}^{em} shifts indicate that all three Au(III) chelates electronically perturb Trp-214 to the same degree. Regarding the organic framework of the chelating ligands, there is likely a charge transfer from the pyrrole ring to the tryptophan indole.

Fluorescence quenching mechanism

The fluorescence quenching mechanism can be described as either static, dynamic, or a combination of both, and is typically analyzed by the Stern–Volmer equation (eq. 1),[60]

$$I_0/I = 1 + K_{SV}[Q] = 1 + k_q\tau_0\,[Q] \qquad (1)$$

where I_0 is the fluorescence intensity of HSA in the absence of the added quencher (Au(III) chelates in this work) and I is the fluorescence intensity of HSA in the presence of the Au(III) chelates. K_{SV} is the Stern-Volmer constant (M^{-1}), $[Q]$ is the molar concentration of the quencher (i.e., added Au(III) chelate), k_q is the bimolecular quenching rate constant ($M^{-1}\,s^{-1}$), and τ_0 is the average lifetime of HSA fluorescence in the absence of any quencher (6.72 ± 0.07 ns,[56] 5.60 ± 0.10 ns,[61] and 5.28 ± 0.03 ns;[62] average = 5.87 ± 0.76 ns). Typically, the quenching mechanism can be differentiated by the HSA-Au(III) complex's dependence on viscosity and temperature.[63]

From least-squares fits of eq. 1 to the dose-dependence of I_0/I, the bimolecular fluorescence quenching rate constant for the HSA···Au(III) interaction can be straightforwardly deduced from eq. 2, provided that τ_0 is known (*vide supra*).

$$k_q = {}^{K_{SV}}/_{\tau_0} \qquad (2)$$

Typically, linear Stern-Volmer plots are associated with a single class of quenching, either dynamic (diffusion-limited collisional) or static (binding-related).[60,64] The distinction between static or dynamic quenching can be made by examining the temperature dependence of K_{SV}. For dynamic quenching, the K_{SV} values increase with rising temperature due to an increase in the collisional frequency and diffusion rate. Conversely for static quenching, K_{SV} values decrease with increasing temperatures as the equilibrium formation constant for the complex decreases.[60]

Au(III) chelates based on their K_{SV} values was not possible for **AuL1** and **AuL2**, as the K_{SV} values remained relatively consistent across the temperature range (Table 4, comment under Fig. S50). The absence of suitable instrumentation to record nanosecond lifetimes prevented the determination of the quenching mechanism. However, for **AuL3**, the plot exhibited linearity over a narrower concentration range, indicating a dominant single class of quenching. In all three cases, the K_{SV} values increased with increasing temperatures, suggesting a dominant dynamic quenching mechanism (refer to Fig. S51 for an explanation of the limited concentration range used).

A summary of the K_{SV} and K_q values of the interaction of the three Au(III) chelates with HSA are presented in Table 4. Among the three chelates, the dominant quenching mechanism could only be distinguished for **AuL3**, which exhibited dynamic quenching.[79] The K_{SV} values increased with increasing temperatures, and this is a result of an increase in the diffusion rate and collisional frequency.[65] The K_{SV} at 298 K values follow the order **AuL3** > **AuL1** > **AuL2**, since the Au(III) metal ion was consistent throughout, the difference in K_{SV} is due to the organic ligand (Fig. 7b).

It is important to note that the metal ion plays a major role in in the quenching and binding of compounds to HSA. When comparing the K_{SV} of **AuL1** to the Ni(II), Pd(II) and Pt(II) chelates with the same organic ligand (2,2'-{propane-1,3-diylbis[nitrilo(*E*)methylylidene]}bis(pyrrol-1-ido) the values differed, highlighting the significance of the metal ion centre.[57]

The bimolecular quenching constant (K_q) values were determined for all three Au(III) chelates (Table 4). In each case the K_q exceeded diffusion control limit ($10^{10}\ M^{-1}\ s^{-1}$)[66] by at least two orders of magnitude. This is a strong indication that the binding of the Au(III) chelates was not randomized binding but is consistent with a significant HSA-ligand binding interaction.

Isothermal titration calorimetry (ITC)

Binding and thermodynamic parameters were analyzed using ITC, which provides quantitative thermodynamic data that can be used to interpret the major binding forces responsible for the interaction of small molecules with proteins.[74-76] In this study ITC was used to measure the heat exchange from the binding of the Au(III)-chelates (**AuL1**, **AuL2,** and **AuL3**) to HSA. This experiment served to complement the results obtained from steady-state fluorescence. The binding curve was fitted to a specific single-site binding model and was determined from Figs. 8 and Fig. S53.

The raw heat released from HSA upon binding of **AuL1**, **AuL2,** and **AuL3** is presented as a single replicate in Figs. 8 and S53 accompanied by integrated raw heat fitted to a one-site independent isothermal binding model. The thermograms in Figs. 8 and S53 illustrate the amount of heat released over time. Each peak reaches a maximum of heat either released or absorbed over time. After each injection, the heat signal returns to the baseline over time and is also accompanied by less heat than the previous titration. The decrease in heat released is due to the available binding sites on HSA becoming saturated with the Au(III) chelates.

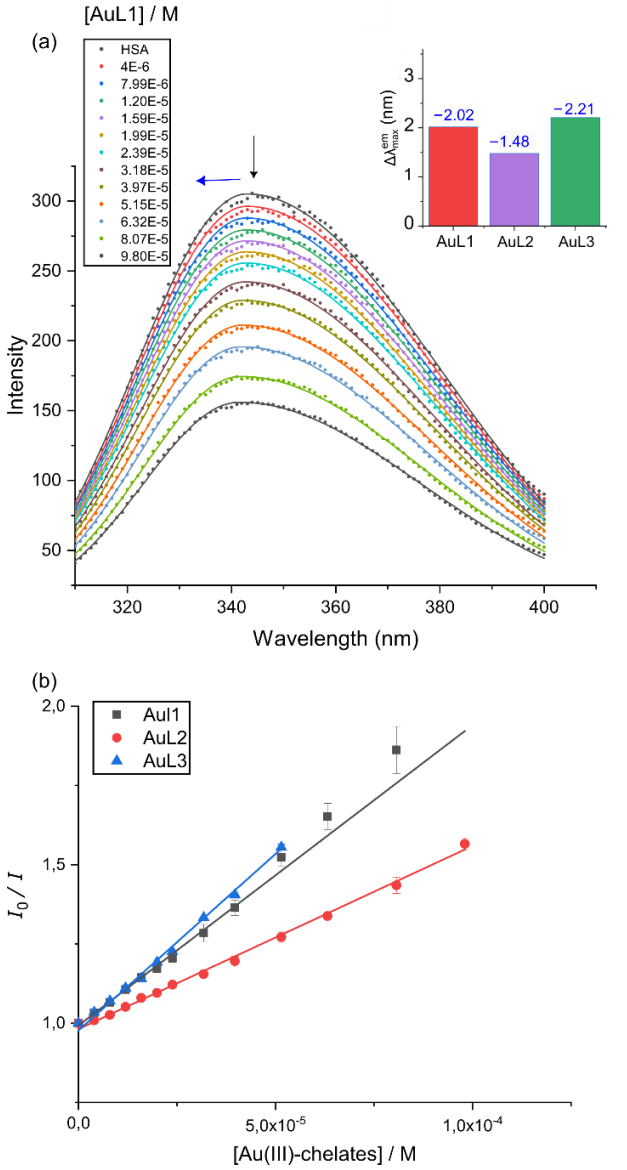


Figure. 7 (a) Emission spectra of human serum albumin (HSA, 5.0 μM) recorded as a function of the concentration of **AuL1** at 298 K in KH_2PO_4 (50 mM, pH 7.50). Analogous spectra for the reaction of HSA with **AuL2** and **AuL3** are given in Figure S50 (ESI). The wavelength shift accompanying ligand uptake ($\Delta\lambda_{max}^{em}$) is plotted as the inset to the main figure (upper right). (b) Stern-Volmer (SV) fluorescence intensity ratio plots for human serum albumin (HSA, 5.0 μM) recorded as a function of the concentration of **AuL1**, **AuL2,** and **AuL3** vs temperature (50 mM KH_2PO_4, pH 7.50). Error bars are ESDs based on the average of three independent determinations. The data are well-fitted by eq. 1 for linear Stern-Volmer emission behaviour. Analogous spectra for the reaction of HSA with all **AuL3** at 288, 298, and 310 K are given in Figure S51 (ESI).

Below each thermogram, the raw data is transformed into a binding curve.[67,68] The binding curve was fitted to a specific single-site binding model and the K_a and ΔH were determined. All other thermodynamic parameters were calculated by the following equations:

$$\Delta G = -RTlnK_a \quad (3)$$

$$\Delta G = \Delta G° + RTlnQ \quad (4)$$

Where Q is the reaction quotient. ΔG° can be calculated from eq. 4, ΔG from eq. 3 and ΔS from eq. 6. A summary of the binding and thermodynamic parameters was calculated and reported in Table 5.

The binding constant (K_a) values, 6.49 × 10^4 M^{-1} for **AuL1**, 10 × 10^4 M^{-1} for **AuL2,** and 8.77 × 10^4 M^{-1} for **AuL3**, are comparable to the (K_a) values obtained by the double-log plot (Table 2). The delineated thermodynamic parameters ΔH, $-T\Delta S$ and ΔG values from ITC reported in Table 5 are also within the same magnitude when compared with thermodynamic parameters from the temperature-dependent van't Hoff plots (Table S6) based on the fluorescence quenching analysis. In **AuL1**, **AuL2,** and **AuL3**···HSA binding system, (i) ΔH and ΔS are all positive values, suggesting that hydrophobic interaction dominates the binding between with HSA. Additionally, the value of $T\Delta S$ is larger than that of ΔH, which leads to a negative ΔG during the binding of the three Au(III) chelates with HSA. Thus, the binding is an entropy-driven process. This data satisfactorily compliments the steady-state fluorescence data.

Thermodynamics of Au(III) chelate binding to HSA

All three Au(III) chelates had a 1:1 reaction stoichiometry with native HSA; hence, a linear van't Hoff relationship was obtained from the temperature dependence on the K_a values and the plots for triplicate measurements are given in Fig. 9a. Under non-standard conditions, the enthalpy change (ΔH), entropy change (ΔS), and Gibbs free energy change (ΔG) may be gathered from the temperature dependence of the affinity constants (K_a) using eqs. 4 and 5:

$$lnK_a = -\frac{\Delta H}{RT} + \frac{\Delta S}{R} \quad (5)$$

$$\Delta G = \Delta H - T\Delta S \quad (6)$$

Table 5 presents the ITC thermodynamic data for the reaction of AuL1, AuL2, and AuL3 with HSA in KH2PO4 buffer (50 mM, pH 7.5). All three reactions are exergonic (negative ΔG),[69] with ΔG ranging from −27.5 kJ mol^{-1} for AuL1 to −28.6 kJ mol^{-1} for AuL2 at 298 K. This is visually depicted in Fig. 9b, where the ΔG values fall in a narrow range for the three Au(III) chelates. The similarity ΔG values strongly suggest a consistent binding mode of the Au(III) chelates to HSA, indicating enthalpy/entropy compensation. The energy difference is minimal and can be attributed to the binding of the three Au(III) chelates in a similar position within Sudlow's site I (Figs. 10 and S55–56, discussed later) in a 1:1 stoichiometric ratio.

Table 4. Stern-Volmer quenching constants (K_{SV}) and bimolecular quenching rate constants (k_q) for the interaction of the three Au(III) chelates with HSA at different temperatures in 50 mM KH_2PO_4 buffer at pH 7.50.

Compound	Temp. T (K)	10^{-5} K_{SV} (M^{-1})[a,c]	10^{-12} k_q (M^{-1} s^{-1})[b]	$\log(K_a$ / $M^{-1})$[c]	n[d]
AuL1	288	1.23 (0.004)	2.09	4.20 (0.07)	1.04 (0.02)
	298	1.10 (0.004)	1.82	4.46 (0.03)	1.11 (0.004)
	310	1.17 (0.010)	1.98	4.73 (0.01)	1.16 (0.01)
AuL2	288	0.61 (0.008)	1.04	4.25 (0.01)	1.13 (0.01)
	298	0.57 (0.003)	0.973	4.37 (0.07)	1.17 (0.02)
	310	0.57 (0.003)	0.979	4.49 (0.04)	1.23 (0.002)
AuL3	288	1.05 (0.004)	1.79	4.60 (0.04)	1.12 (0.01)
	298	1.08 (0.003)	1.84	4.78 (0.08)	1.17 (0.02)
	310	1.10 (0.005)	1.87	5.03 (0.03)	1.23 (0.001)

[a]K_{SV} values (Stern-Volmer constants) for the **AuL1**, **AuL2,** and **AuL3** were determined by fitting the data to eq. 1. A mean excited state lifetime, τ_0, of 5.87(76) ns for HSA was used to calculate the bimolecular quenching rate constant, k_q. [c]The estimated standard deviation of the least significant digits is given in parentheses. [d]Ligand:HSA binding stoichiometry from the fit of the data to eq. S15.

By utilizing the Gibbs-Helmholtz relationship (eq. 6) and analyzing the experimental data (Table S4), we graphically portray the influence of the bis(pyrrolide-imine) ligands on the thermodynamic parameters that govern the uptake of ligands by HSA (Fig. 9). In Fig 9c $T\Delta S/\Delta G$ is plotted against $\Delta H/\Delta G$, the data fit the linear relationship, **AuL1**, **AuL2,** and **AuL3** all lie in the bottom left quadrant where $\Delta H > 0$ and $\Delta S > 0$ which is consistent with entropic control of the reaction. For the Au(III) chelates spontaneity is assured as changes in $\Delta H/\Delta G$ are compensated for by commensurate changes in $T\Delta S/\Delta G$. The $T\Delta S/\Delta G$ and $\Delta H/\Delta G$ of the Au(III) chelate increase together in the order **AuL1** < **AuL2** < **AuL3**.

The observed trend suggests that the thermodynamic parameters of the bis(pyrrolide-imine) ligands are influenced by the motifs present on the carbon chain. Although all three Au(III) salts are cationic and share the same metal center the variation in thermodynamic parameters is primarily attributed to the organic ligand framework. At the lower end of the spectrum are **AuL1** and **AuL3**, which feature two hydrogen atoms and a dimethyl group moiety on the carbon chain linking the imine groups on the respective Au(III) chelates. The dominant interaction of **AuL1** and **AuL3** with HSA will be due to the cationic Au(III) center and π–π interactions due to the planarity of the molecules. Thereafter, **AuL2** is present, which possesses the binding capabilities of **AuL1** and **AuL3** but also possesses an OH motif, which can participate in hydrogen bonding. Interestingly the K_a values increase in the order of the Au(III) chelates on the Gibbs-Helmholtz relationship plot.

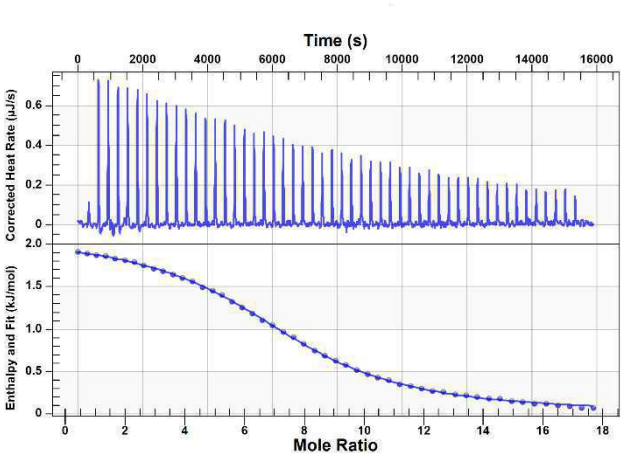


Figure. 8 Binding thermodynamic measurements of **AuL1** interacting with HSA (20 µM, in 50 mM KH_2PO_4, pH 7.5) measured by ITC. The top panel of all three plots represents the raw heat released belonging to each injection. The bottom panel indicates the integrated heat corresponding to each injection. The solid line shows the best-fitting isothermal binding model. Experiments were performed at 298 K as described in methods and materials. The data for **AuL2** and **AuL3** is presented in the ESI Fig. S53.

Table 5 Summary of the thermodynamic parameters obtained by ITC of AuL1, AuL2, and AuL3 binding to HSA.

	k_a(x 10^5 M^{-1})	ΔG (kJ·mol^{-1})	ΔH (kJ·mol^{-1})	$-T\Delta S$ (kJ·mol^{-1})
AuL1	0.649	-27.5	52.5	-79.9
AuL2	0.100	-28.6	47.3	-75.9
AuL3	0.872	-28.2	24.0	-52.2

The ΔH values for the reaction of HSA with the Au(III) chelates are significantly endothermic, measuring from 24.0 kJ mol^{-1} for **AuL3** to 52.5 kJ mol^{-1} for **AuL1**. Fig. 9b highlights the dominance of the entropy term for each of the three reactions, indicating the binding of the three Au(III) chelates to HSA is entropically driven (The result was further supported by the thermogram in Fig. 8). Interestingly, the difference in the moieties of the carbon chain linking the imine groups on the respective Au(III) chelates are highlighted in their markedly different ΔH and ΔS values. Specifically, **AuL1** is more endothermic and requires more energy than both **AuL2** and **AuL3** when binding to HSA. This is compensated for by the higher ΔS value for **AuL1** when compared to the other two Au(III) chelates.

The ΔS values for the Au(III) chelates listed in Table 5 decrease in the following order **AuL1** > **AuL2** > **AuL3** ranging from 268 J K^{-1} mol^{-1} (**AuL1**) to 175 J K^{-1} mol^{-1} (**AuL3**). The data suggest that the more hydrophilic Au(III) chelates cause substantial desolvation of ordered water molecules within Sudlow's site I on HSA upon binding.

In summation the three Au(III) chelates binding to HSA were endothermically driven, the ΔH and ΔS values were positive suggesting the main binding forces involved with HSA binding to the complexes were via hydrophobic interactions.[69,70] A positive ΔH is due to two factors, the Au(III) chelates partially destroy the hydrophobic structure within the hydrophobic cavity located in sub domain IIA, which leads to an endothermic effect. The second factor is when the Au(III) chelates enter subdomain IIA within HSA, the initial iceberg structure surrounding the Au(III)-chelates is destroyed,[71] which is a complementary experiment to the steady-state fluorescence described earlier.

Site displacement assay

To delineate the preferred binding site(s) for the Au(III) chelates, a competitive blocking assay was performed using fluorescence spectroscopy. The Au(III) chelates were titrated into solutions of native HSA and solutions of HSA that were pre-equilibrated with either (i) warfarin or (ii) dansylglycine (Fig. 10). As revealed by X-ray crystallography, warfarin binds specifically in Sudlow's site I (subdomain IIA),[72] while dansylglycine primarily binds in Sudlow's site II (subdomain IIIA).[73] By selectively and sequentially blocking the two main drug binding sites of HSA using site-specific probes, this experiment aimed to elucidate the binding site specificity of the Au(III) chelates.

It should be noted that HSA has multiple drug-binding sites,[74] and blocking a primary binding site may redirect the ligand to an alternative drug-binding site within HSA or inhibit incoming ligand binding allosterically. Nevertheless, changes in the logK_a, n, K_{SV}, and the substitution of the fluorescent probe drug itself could occur upon ligand uptake, allowing for the possible deduction of the binding site for the ligand of interest.

The three Au(III) chelates (0–9.76 x 10^{-5} M) were titrated into a solution of HSA pre-equilibrated with either HSA•{warfarin} or HSA•{dansylglycine}. The fluorescence emission spectrum of both fluorophores is shown in Fig 10a and S55-56. The HSA•{warfarin} fluorescence emission spectrum peaked at 382 nm, which was a blue shift of 8 nm from the free warfarin peak at 390 nm. Upon titration of the Au(III) chelates into the HSA•{warfarin} solution, the fluorescence intensity of HSA•{warfarin} decreased progressively with increasing concentration of the Au(III) chelates (Figs. 10a, S55, and S56). The percentage displacement of warfarin is illustrated in Fig S54. Furthermore, the redshift of the warfarin fluorescence emission intensity peak from 382 nm (HSA•{warfarin}) to 390 nm (free warfarin emission peak) provides additional evidence of warfarin displacement from HSA.

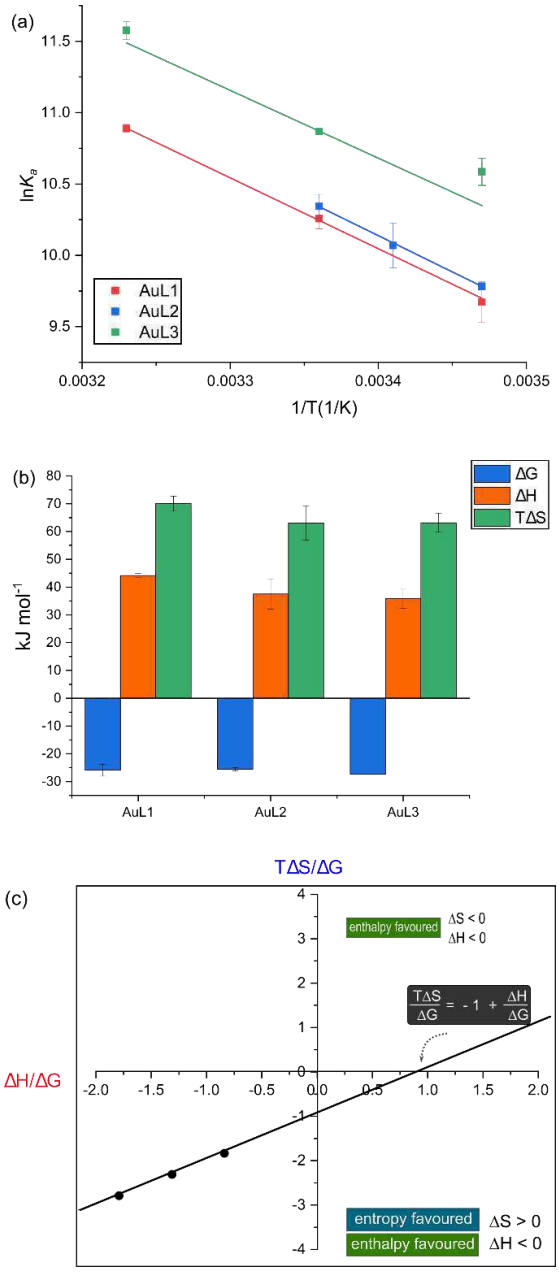


Figure. 9. (a) van't Hoff plots for the reactions of **AuL1** with HSA in 50 mM KH_2PO_4 buffer at pH 7.50. All measurements were done in triplicate; derived parameters were individually averaged, and error bars are estimated uncertainties of the mean. (b) Comparison of the thermodynamic parameters (298 K) governing the reactions of the three Au(III) chelates with HSA. (c) The plot of the Gibbs-Helmholtz relationship (eq. 5) for the reaction of the three Au(III) chelates with HSA at 298 K in 50 mM KH_2PO_4 buffer at pH 7.50. The straight line fit of the data gives R^2 = 0.9993 with a slope and intercept of 1. The plot highlights how the identity of the bis (pyrrolide-imine) Schiff base chelate influences the reaction thermodynamics. For all reactions, ΔG < 0.

The HSA•{dansylglycine} fluorescence emission spectrum peaked at 500 nm, which was a blue-shift of 58 nm from the free dansylglycine peak at 558 nm (Figs. 10b, S55

and S56). Upon titration of the Au(III) chelates into the HSA•{dansylglycine} solution, the fluorescence intensity decreased progressively with increasing concentration of the Au(III) chelates. The suspected percentage displacement of dansylglycine is presented in Fig S54. Unlike the fluorescence emission spectrum of HSA•{warfarin}, there is no peak shift suggesting dansylglycine is not being displaced from HSA. Quenching of the HSA•{dansylglycine} fluorescence by the Au(III) chelates could reflect quenching by FRET or changing the microenvironment surrounding the fluorophore. To further investigate the binding mechanism of the Au(III) chelates to HSA•{warfarin} and HSA•{dansylglycine}, we used the Stern-Volmer equation (eq. 1), the sphere of action model (eq. S8), and evaluated the binding using the double logarithmic plot (eq. S9) (Figs. 10e, S55 and S56).

The Au(III) chelates bound to HSA via a similar mechanism. **AuL1** is discussed as follows. Please refer to Figures S55 and S56, respectively, for the analysis of **AuL2** and **AuL3**. From Fig. 10c, the quenching of HSA intrinsic fluorescence and HSA•{dansylglycine} fluorescence resulted in a linear Stern-Volmer plot, indicating a single dominant quenching mechanism. The K_{SV} values of **AuL1** binding to native HSA and HSA•{dansylglycine} were 0.977 (0.032) × 10^{-5} and 1.105 (0.046) × 10^{-5} M^{-1}, respectively. Considering the similarity of the K_{SV} values, we predict dansylglycine is not displaced by **AuL1**; rather its fluorescence is quenched by **AuL1** upon its binding to HSA. Interpreting the Stern-Volmer plot of HSA•{warfarin} was more challenging, due to its upward curvature indicating the occurrence of two quenching mechanisms. At concentrations of **AuL1** ranging from 0–3.96 × 10^{-5} M, the plot was linear which we attributed to the static quenching of warfarin, the observed upward curvature is attributed to the displacement of warfarin and its quenching by the aqueous KH_2PO_4 buffer.

To gain further insight into the upward curvature observed in the HSA•{warfarin} Stern-Volmer plot, we applied the "sphere of action model" (eq. S14). A linear model suggests static quenching, whereas deviation from linearity indicates a transition from static to dynamic quenching mechanisms. From Figure 10d, only the fluorescence quenching of native HSA showed deviation from linearity. This suggests that **AuL1** acts as a dynamic quencher of HSA intrinsic fluorescence and a static quencher of both HSA•{warfarin} and HSA•{dansylglycine}. Regarding the Stern-Volmer plot for HSA•{warfarin} (Figure 10c), the initial linear portion could indicate that static quenching is the dominant mechanism. However, as the concentration of **AuL1** increases, the quenching switches from the quenching of HSA•{warfarin} to the displacement of warfarin from HSA, resulting in the quenching of warfarin fluorescence by the aqueous medium.

To gain further insights into the site preference for **AuL1**, we assessed the double log plot (Figure 10e). Initially, when **AuL1** reacts with native HSA, both Sudlow's sites I and II are available to accept the incoming chelate. Comparing the logK_a values of **AuL1** binding to native HSA and HSA•{warfarin}, we observe that the logK_a value is higher for HSA•{warfarin}, with a value of 5.71 (0.22), compared to 4.43 (0.079) for native HSA. Additionally, the logK_a for HSA•{dansylglycine} was 4.50 (0.11), which is one standard deviation away from the logK_a of **AuL1** binding to native HSA. Interpreting the logK_a values can be challenging, and we propose two possible explanations. First, the presence of warfarin in Sudlow's site I may induce conformational changes within the binding pocket, allowing **AuL1** to bind with higher affinity. Second, the value of the logK_a for **AuL1** binding to HSA•{warfarin} could be the product equilibrium constant β_2, where $log\beta_2 = logK_1 + logK_2$, where $logK_1 + logK_2$ = log 5.71.

Far-UV CD spectroscopy

The secondary structure of proteins can be easily determined using far-UV CD spectroscopy, which takes advantage of several spectral regions including peptide bonds, aromatic amino acids side chains, and disulphide bonds.[75] HSA is predominantly an α-helix protein, with α-helices constituting 67% of its structure.[76] In Fig. 11a, we employed far-UV CD spectroscopy (186–260 nm) to delineate the impact of Au(III) chelates impact the secondary structure of the protein. The far-UV CD spectrum of native HSA displayed the characteristic double minima at 208 ± 1 nm and 222 ± 1 nm, consistent with a dominantly α-helix rich protein.[77] The 208 nm electronic transitions is assigned to π–π*, the 222 nm electronic transition is assigned to the n–π* transition, and the 193 nm electronic transition translates to the π–π* transition. All three transitions involve the amide groups of the peptide backbone.[75,77] From Fig. 11a, it can be observed that upon binding of the Au(III) chelates to HSA there is minimal change in the secondary structure of the protein, despite the moderately high affinity of all three Au(III) chelates of all three Au(III) chelates for HSA (Table 4 and 5).

At each concentration of the Au(III) chelates, the spectrum of HSA undergoes changes, with both minima at 208 nm and 222 nm approaching zero, indicating alterations in the secondary structure of HSA. The maxima at 193 nm decreased with increasing concentrations of **AuL2** and **AuL3**, while with **AuL1**, there was minimal change (Figures 11a and S57). To quantify the changes in the secondary structure of HSA we further analyzed the spectra using JASCO Spectra Manager™.[78] This allowed us to calculate the percentage composition of α-helical coils, turns, and unordered coils present for each HSA···Au(III) complex (Table S6). The dominant secondary structure domains observed were α-helices (~58%), and unordered coils (~31%). The α-helicity of HSA was ~58% but it was decreased in the presence of each Au(III) chelate within a range of 3.72% (**AuL1**) to 7.83% (**AuL2**). The decrease in α-helicity was accompanied by an increase in random turns and β-sheets (Table S10).

Interestingly, the solution-state secondary structure composition of HSA differs from that of native HSA in the solid state[20] (68.5% α-helix, 0% β-sheet, 9.6% turns, and 21.9% unordered coils; PDB code 1BM0 analyzed with BeStSel[79]).

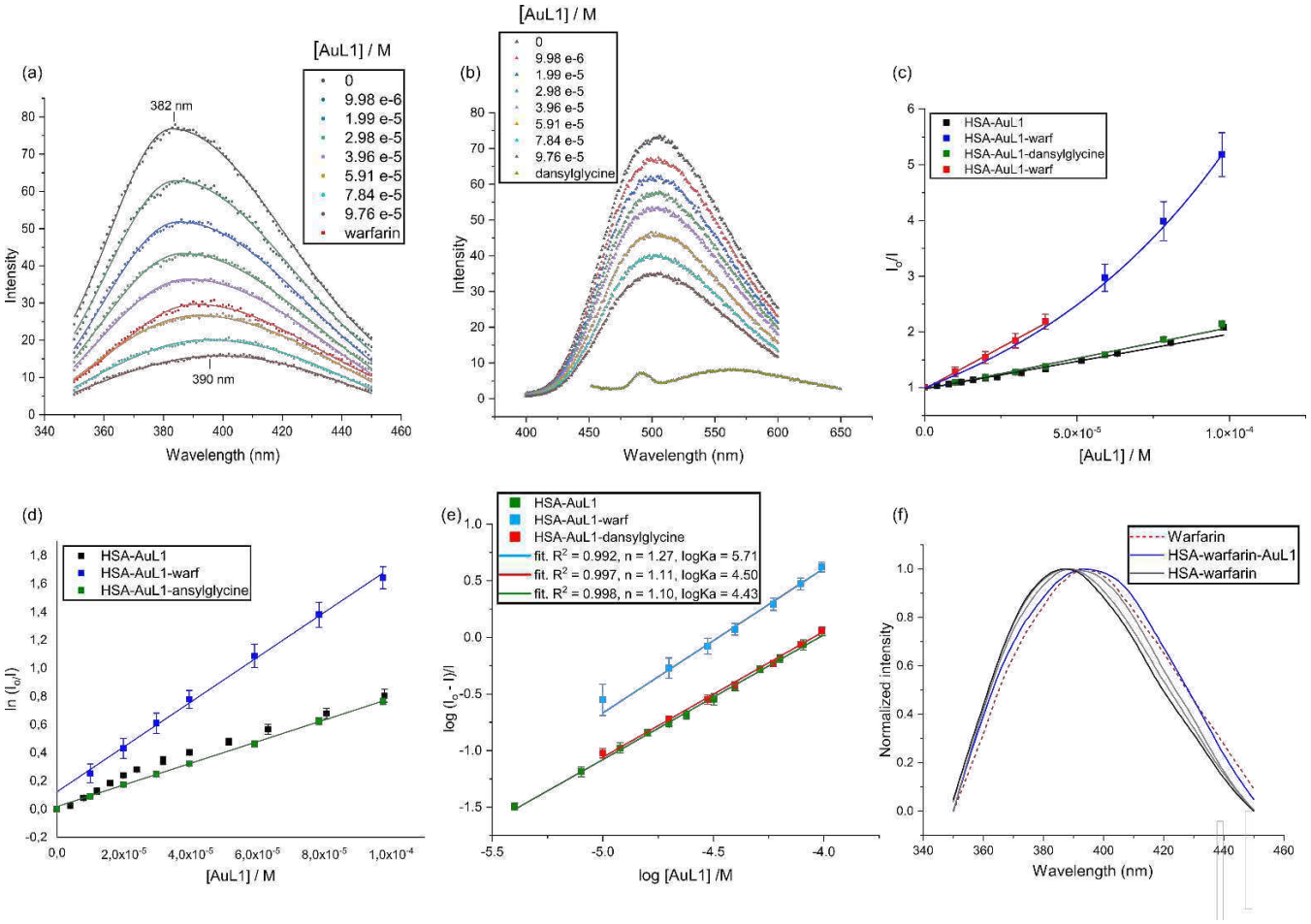


Figure. 10 Binding site determination for the reaction of AuL1 with HSA (5.0 μM protein, 50 mM KH_2PO_4, pH 7.50, 298 K). **(a)** Emission spectra of HSA···warfarin (5.0 μM warfarin λ^{ex} = 320 nm) recorded as a function of the concentration of AuL1 at 298 K. The spectra are fitted by single Gaussian functions to locate the emission maxima. Correlation coefficients, R^2, ranged from 0.990 to 0.999. **(b)** Emission spectra of HSA···dansylglycine (5.0 μM dansylglycine λ^{ex} = 340 nm) recorded as a function of the concentration of AuL1 at 298 K. The spectra are fitted by single Gaussian functions to locate the emission maxima. Correlation coefficients, R^2, ranged from 0.990 to 0.999. **(c)** Stern–Volmer (SV) plot for native HSA, HSA···Warfarin, and HSA···dansylglycine as a function of the concentration of AuL1 at 298 K. The plots are linear with an intercept of 1.0 when static quenching is operative (i.e., the quencher binds to the target protein and fluorophore(s)). The excitation and emission wavelengths for the fluorophore probes were: (i) Trp-214 (native HSA), λ^{ex} = 295 nm, λ^{em} = 340 nm; (ii) Warfarin (HSA-Warf), λ^{ex} = 320 nm, λ^{em} = 382 nm, and (iii) dansylglycine, λ^{ex} = 340 nm, λ^{em} = 500 nm. **(d)** Sphere of action model plot, $ln\left(\frac{I_0}{I}\right) = K_{SV}^{app}[Q]$, for the system. A linear plot with a zero intercept indicates static quenching by AuL1 bound in some way to the fluorophore/macromolecule. Negative deviation from linearity signals a switch from static to dynamic quenching. **(e)** Double-log plot (eq. 10) of the fluorescence quenching data, $log\left(\frac{I_0-I}{I}\right) = logK + nlog[Q]$, to enable measurement of logK_a and the reaction stoichiometry (n). **(f)** The normalized fluorescence emission spectrum of HSA···warfarin (5.0 μM warfarin λ^{ex} = 320 nm) recorded as a function of the concentration of AuL1 at 298 K to show the displacement of warfarin from HSA. Error bars indicate the standard deviation of three independent experiments.

However, our solution Far-UV CD data is consistent with solution state spectral decompositions reported previously.[80–82] Overall it is accepted that enhanced subdomain mobility and general thermal motion/disorder account for the decrease of α-helicity.[77,83]

Near-UV CD spectroscopy

To elucidate the conformational structural changes induced by the Au(III) chelates to the tertiary structure of HSA, we employed near-UV CD spectroscopy in the range of 250–310 nm (Figs. 11b and S58). A typical near-UV–CD spectrum is dominated by the fine structure of the aromatic amino acid residues symmetry, Trp (285-300 nm), Tyr (275-285 nm), and Phe (250-270 nm). Noteworthy transition peaks of HAS were observed, including two minima at 262 and 280 nm and a maxima at 290 nm which are attributed to the presence of disulfide bonds and the aromatic amino acids.[84]

The near-UV CD spectra of HSA (Figs. 11b and S58) in the absence of the Au(III) chelates exhibited a peak at 290 nm, accompanied by fine structure alterations between 290–

305 nm, attributed to the Trp-214 residue. Additionally, between 275 and 285 nm, there was a peak at 284 nm with a shoulder at 287 nm, likely originating from the 18 Tyr residues within HSA. The Phe fingerprint region, spanning 255-270 nm, displayed a peak at 257 nm. The presence of two minima at 262 and 268 nm, along with a shoulder at 279 nm, were characteristics of disulfide bonds,[75,85,86] of which HSA possesses 17.[76] Phe, Tyr, and Trp all have π–π* transitions (^1L_a and ^1L_b) and can participate in π bonding, which is crucial for DNA binding, as discussed earlier. Therefore, perturbations in the fine structure of the protein can indicate conformational changes within the protein itself or alterations in the environment surrounding the aromatic amino acids.[87]

The three Au(III) chelates induced changes to the near-UV CD spectra, indicating their binding to the protein in close enough proximity to affect the fine structure surrounding the aromatic amino acid residues. This was supported by the site displacement assay, which indicated that the Au(III) chelates bound to Sudlow's site I, as shown in Figs. 10, S55, and S56 (subdomain IIA containing Trp-214). **AuL1** and **AuL3** showed a redshift of 2 nm at 290 nm, **AuL2** caused the 290 nm band to split, and a blue shift of 1 nm was observed. There were no significant shifts in the disulfide bond fingerprint region, suggesting minimal changes to the bonds. Overall, the binding of Au(III) chelates to HSA was shown to induce slight conformational changes in both the secondary (Figs. 11a and S57) and tertiary structures (Fig. 11b and S58) of the protein. These conformational changes in the tertiary structure may account for the difference in enthalpies observed between the van't Hoff plot and the ITC data.[88]

Induced-UV CD spectroscopy

The phenomenon in which an achiral molecule binds to a chiral host and exhibits a CD signal is known as induced circular dichroism (ICD).[73,89,90] An ICD band corresponds to the absorbance wavelength of the chromophoric portion of the complex and indicates direct complexation between the two molecules, as depicted in Figure 11c.

If the symmetry of an achiral molecule is perturbed and non-zero rotational strengths are formed, it will exhibit an ICD signal.[89] In the context of this study, the Au(III) chelates were initially achiral; however, when bound to HSA, an ICD signal was observed (Figs. 11c and Fig. S59). We propose that HSA binds to and perturbs the Au(III) chelates through two mechanisms: (i) intermolecular interactions and (ii) restriction of conformational freedom.[90] In order for an ICD signal to occur, the interaction between the protein (host) and the small molecule must take place in a preferred orientation that prevents the cancellation of the ICD signal. Therefore, ICD serves as a reliable indicator of increased structural order.[91,92] In Figure 11c, we observe shifts in the ICD bands compared to the absorbance maximum that would be expected for the free Au(III) chelates.

An ideal classic supramolecular ICD system involves a non-absorbent, transparent chiral host and an absorbing achiral guest molecule. The Au(III)···HSA system exemplifies the classic example of an ideal supramolecular complex where both HSA and the Au(III) chelates fulfill the requirements of the host and guest molecules respectively.[92] The chiral environment of the HSA binding site perturbs the Au(III) chelates, resulting in the induction of rotational strength and an observable ICD signal. The ICD signal manifests as distinct bands in the UV spectrum of the Au(III) chelates, typically around 360 nm. Importantly the changes in the chiroptical region of a UV CD spectrum do not originate from ICD effects, thus near-UV and far-UV CD spectra do not contribute to the ICD signal.[93]

The thermal melt temperature of HSA

Determining the thermal melt temperature (T_m) of HSA can be an important parameter for elucidating the impact of the Au(III) chelates on the protein's binding. The T_m of a protein is defined by the midpoint at which 50% of the protein has unfolded[94] and is a representation of the proteins thermal stability. The addition of the Au(III) chelates to HSA may alter the T_m, depending on their effect on the protein. Typically, methods used to measure the T_m of a protein are differential scanning calorimetry (DSC)[95] and differential scanning fluorometry (DSF),[96] Alternatively far-UV CD spectroscopy can be employed to track the changes in proteins ellipticity in the presence of a binding ligand. We utilized this method to measure the thermal stability of HSA bound to the three Au(III) chelates.

In Fig. 11d we present the change in HSA's secondary structure as the temperature increases. It is evident that with increasing temperature, the ellipticity of HSA decreases and approaches zero, indicating the loss of its secondary structure due to thermal denaturation. To investigate whether the Au(III) chelates are capable of thermally stabilizing HSA, we incubated the chelates with HSA and measured its far-UV CD spectrum from 20°C to 90°C. By monitoring the change in ellipticity at 222 nm, we plotted the Hill fit curve to determine the T_m of native HSA and HSA in the presence of the Au(III) chelates (Fig. 11e). In Fig. 11e, the decrease in α-helices corresponds to the unfolding of HSA and the subsequent loss of secondary structure.

The addition of the Au(III) chelates to HSA did not cause a significant change in the T_m of HSA, as determined by the UV CD method (Table S7). A molecule that significantly stabilizes or destabilizes the protein will typically induce a change in T_m by more than 2°C.[96] HSA was shown to have two T_m values at 56 and 62 °C.[97]

The thermal unfolding of HSA follows the Eyring and Lumry model: native ↔ unfolded (reversible) → unfolded (irreversible).[98] T_m temperature obtained from Fig. 11e showed a single T_m that was 2 °C higher than the T_m reported by Flora *et al*.[97] This is likely due to the difference in methods utilized, Flora *et al*., (1998)[97] used DSC which is regarded as the gold standard for determining thermal properties of materials.[99] DSC is more sensitive to compared to far-UV CD to determine T_m of proteins as it measures the direct enthalpies, therefore various transitions may be observed. Far-UV CD focuses only on the α–helix content.

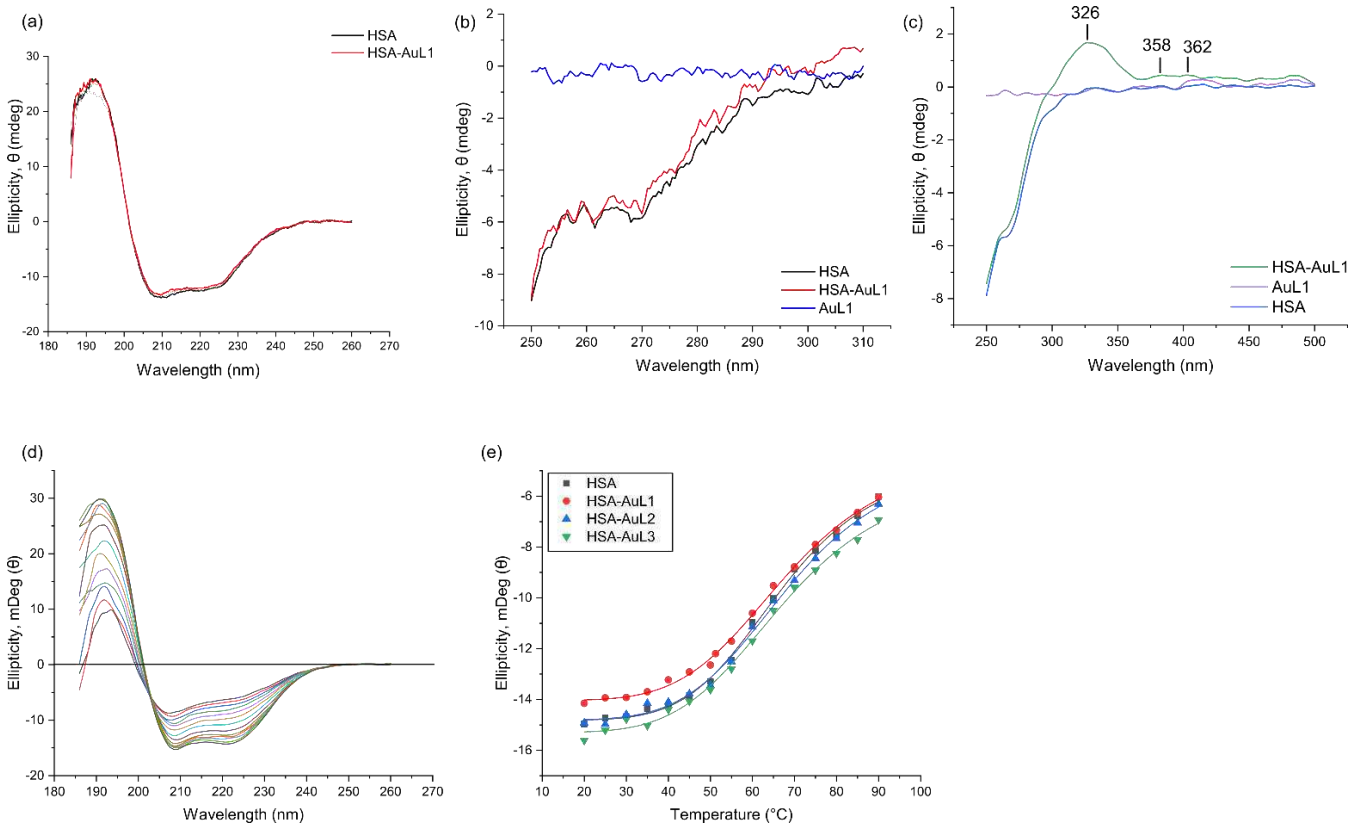


Figure. 11 (a) Plots of the far-UV CD spectra of native HSA and the protein incubated with saturating doses of (a) AuL1 recorded at 298 K in 50 mM KH_2PO_4 buffer at pH 7.5 The concentration of the Au(III) chelates ranged from 0 – 6 μM, the native protein is represented by the black line and the Au(III) chelate–HSA adduct at 6 μM is represented by the black line. The grey line represents the Au(III) chelates at 0.3, 1.5, and 3 μM. (b) Plots of the near-UV CD spectra of native HSA and the protein incubated with a 1:1 ratio AuL1 were recorded at 298 K in 50 mM KH_2PO_4 buffer at pH 7.50. The data represents unsmoothed spectra of the fine structure of the protein. Perturbations in the protein structure around Phe (250–270 nm), Tyr (~280 nm), and Trp (285–300 nm) residues may also be resolved in some different spectra. Key maxima and minima are indicated (in nm). (c) Induced circular dichroism plots of when bound to HSA in a 1:1 molar ratio (15 μM) in a 50 mM KH_2PO_4 buffer (pH 7.5) and smoothed using a relatively fine Lowess function (0.07 span). (d) Thermal unfolding of native HSA (5 μM in 50 mM KH_2PO_4, pH 7.5) as seen by far-UV CD spectroscopy. The far-UV CD was monitored from 186 – 222 nm at a temperature range of 20 – 90 °C. (e) The plot of the melting temperatures, T_m, against native HSA and HSA in the presence of the three Au(III) chelates. The midpoint for the Hill fit for each compound was determined to be the T_m and reported in Table 4.7. Each point represents the change in the ellipticity of HSA in the presence and absence of the Au(III) chelates, monitored at 222 nm.

Conclusion

In summary, three Au(III) bis (pyrrolide-imine) chelates were synthesized and their respective X-ray crystal structures were elucidated. All three Au(III) chelates were shown to bind to and intercalate DNA with a moderately low binding affinity (K_b) of 1.95 (± 0.095) × 10^4, 1.45 (± 0.13) × 10^4 and 2.66 ± (0.1) × 10^4 M^{-1} for **AuL1**, **AuL2** and **AuL3**, respectively at 310 K (Table 2). We assessed the cytotoxicity of the Au(III) complexes using the NCI-60 screen, and both **AuL1** and **AuL3** showed sufficient cytotoxicity data to warrant phase two testing, exhibiting GI_{50} values of 7.3 μM, 11.5 μM and IC_{50} values of 15.7 and 30.9 μM for **AuL1** and **AuL3**, respectively. Hierarchical cluster analysis methods revealed that **AuL1** is mechanistically equivalent to doxorubicin, a Top2 poison. **AuL2** exhibited similar Top2 inhibitory activity as **AuL1** but was likely inactive due to the cellular efflux pump. To investigate the interaction of the three Au(III) chelates with HAS, we employed complementary spectroscopic techniques to measure their uptake by the protein. All Au(III) chelates quenched the intrinsic Trp-214 fluorescence of HSA and had K_a values typical of small molecules binding to HSA (10^4 M^{-1}).[100,101] The Stern-Volmer quenching constants K_a values followed the order: **AuL2** > **AuL1** > **AuL3**, suggesting a stoichiometry leaning towards a 1:1 ligand to protein ratio. The Au(III) chelates bind to HSA with positive ΔH, ΔS, and negative ΔG values, reflecting a spontaneous entropically-driven process governed by hydrophobic and electrostatic interactions. $T\Delta S/\Delta G$ and $\Delta H/\Delta G$ increase together in the order: **AuL1**, **AuL3**, and **AuL2**. Our competitive site displacement assay point towards all three

Au(III) chelates binding to Sudlow's site I and displacement of warfarin. Finally, the induced CD spectra recorded for the metal chelates bound to HSA strikingly confirm the uptake of the intact complexes without imine group hydrolysis or demetallation.

Author Contributions

O. Q. M. and S. S. co-designed the study. S. S. synthesized and characterized the ligands, carried out the spectroscopy, X-ray crystallography collated thermodynamic data, and performed the molecular simulations. O. F under the supervision of Y. S performed the ITC experiment and analysis. NCI-60 and topoisomerase data and analysis was obtained from M. P. A. The final data analysis was performed by S. S. The manuscript, final data interpretation and figures were written and produced by S. S under the supervision of O. Q. M.

ACKNOWLEDGMENT

This work is based on research supported by the South African Research Chairs Initiative of the Department of Science and Innovation (DSI) and National Research Foundation (NRF) of South Africa (Grant No 64799, OQM). The authors thank WITS University and the NRF for funding to purchase a JASCO J-1500 MCD spectrometer (Grant No 116177, OQM) and a dual-wavelength Bruker D8 Venture X-ray diffractometer (Grant No 129920, OQM). We also thank the Centre for High Performance Computing (Project CHEM1065, CHPC, Cape Town) for both the CPU time and resources needed for the DFT simulations.

REFERENCES

(1) Nitiss, J. L. Targeting DNA Topoisomerase II in Cancer Chemotherapy. *Nat. Rev. Cancer* **2009**, *9* (5), 338–350.

(2) Walker, J. V.; Nitiss, J. L. DNA Topoisomerase II as a Target for Cancer Chemotherapy. *Cancer Invest.* **2002**, *20* (4), 570–589.

(3) Chen, S. H.; Chan, N.-L.; Hsieh, T. New Mechanistic and Functional Insights into DNA Topoisomerases. *Annu. Rev. Biochem.* **2013**, *82*, 139–170.

(4) Deweese, J. E.; Osheroff, N. Coordinating the Two Protomer Active Sites of Human Topoisomerase IIα: Nicks as Topoisomerase II Poisons. *Biochemistry* **2009**, *48* (7), 1439–1441.

(5) Stuchinskaya, T.; Mitchenall, L. A.; Schoeffler, A. J.; Corbett, K. D.; Berger, J. M.; Bates, A. D.; Maxwell, A. How Do Type II Topoisomerases Use ATP Hydrolysis to Simplify DNA Topology beyond Equilibrium? Investigating the Relaxation Reaction of Nonsupercoiling Type II Topoisomerases. *J. Mol. Biol.* **2009**, *385* (5), 1397–1408.

(6) Pommier, Y.; Leo, E.; Zhang, H.; Marchand, C. DNA Topoisomerases and Their Poisoning by Anticancer and Antibacterial Drugs. *Chem. Biol.* **2010**, *17* (5), 421–433.

(7) Deweese, J. E.; Osheroff, N. The DNA Cleavage Reaction of Topoisomerase II: Wolf in Sheep's Clothing. *Nucleic Acids Res.* **2009**, *37* (3), 738–748.

(8) Nitiss, J. L. DNA Topoisomerase II and Its Growing Repertoire of Biological Functions. *Nat. Rev. Cancer* **2009**, *9* (5), 327–337.

(9) Vos, S. M.; Tretter, E. M.; Schmidt, B. H.; Berger, J. M. All Tangled up: How Cells Direct, Manage and Exploit Topoisomerase Function. *Nat. Rev. Mol. Cell Biol.* **2011**, *12* (12), 827–841.

(10) Pommier, Y. Drugging Topoisomerases: Lessons and Challenges. *ACS Chem. Biol.* **2013**, *8* (1), 82–95.

(11) Pommier, Y.; Marchand, C. Interfacial Inhibitors: Targeting Macromolecular Complexes. *Nat. Rev. Drug Discov.* **2012**, *11* (1), 25–36.

(12) Wu, C.-C.; Li, Y.-C.; Wang, Y.-R.; Li, T.-K.; Chan, N.-L. On the Structural Basis and Design Guidelines for Type II Topoisomerase-Targeting Anticancer Drugs. *Nucleic Acids Res.* **2013**, *41* (22), 10630–10640.

(13) Wu, C.-C.; Li, T.-K.; Farh, L.; Lin, L.-Y.; Lin, T.-S.; Yu, Y.-J.; Yen, T.-J.; Chiang, C.-W.; Chan, N.-L. Structural Basis of Type II Topoisomerase Inhibition by the Anticancer Drug Etoposide. *Science* **2011**, *333* (6041), 459–462.

(14) Bender, R. P.; Ham, A.-J. L.; Osheroff, N. Quinone-Induced Enhancement of DNA Cleavage by Human Topoisomerase IIα: Adduction of Cysteine Residues 392 and 405. *Biochemistry* **2007**, *46* (10), 2856–2864.

(15) Mondrala, S.; Eastmond, D. A. Topoisomerase II Inhibition by the Bioactivated Benzene Metabolite Hydroquinone Involves Multiple Mechanisms. *Chem. Biol. Interact.* **2010**, *184* (1–2), 259–268.

(16) Andoh, T.; Ishida, R. Catalytic Inhibitors of DNA Topoisomerase II. *Biochim. Biophys. Acta BBA-Gene Struct. Expr.* **1998**, *1400* (1–3), 155–171.

(17) Akerman, M. P.; Munro, O. Q.; Mongane, M.; Staden, J. A. van; Rae, W. I. D.; Bester, C. J.; Marjanovic-Painter, B.; Szucs, Z.; Zeevaart, J. R. Biodistribution (as Determined by the Radiolabelled Equivalent) of a Gold(III) Bis(Pyrrolide-Imine) Schiff Base Complex: A Potential Chemotherapeutic. *J. Label. Compd. Radiopharm.* **2013**, *56* (9–10), 530–535.

(18) Curry, S. Lessons from the Crystallographic Analysis of Small Molecule Binding to Human Serum Albumin. *Drug Metab. Pharmacokinet.* **2009**, *24* (4), 342–357.

(19) Quinlan, G. J.; Martin, G. S.; Evans, T. W. Albumin: Biochemical Properties and Therapeutic Potential. *Hepatology* **2005**, *41* (6), 1211–1219.

(20) He, X. M.; Carter, D. C. Atomic Structure and Chemistry of Human Serum Albumin. *Nature* **1992**, *358* (6383), 209–215.

(21) Zunszain, P. A.; Ghuman, J.; Komatsu, T.; Tsuchida, E.; Curry, S. Crystal Structural Analysis of Human Serum Albumin Complexed with Hemin and Fatty Acid. *BMC Struct. Biol.* **2003**, *3* (1), 6.

(22) Fasano, M.; Curry, S.; Terreno, E.; Galliano, M.; Fanali, G.; Narciso, P.; Notari, S.; Ascenzi, P. The Extraordinary Ligand Binding Properties of Human Serum Albumin. *IUBMB Life* **2005**, *57* (12), 787–796.

(23) Rabbani, G.; Ahn, S. N. Structure, Enzymatic Activities, Glycation and Therapeutic Potential of Human Serum Albumin: A Natural Cargo. *Int. J. Biol. Macromol.* **2019**, *123*, 979–990.

(24) Sudlow, G.; Birkett, D. J.; Wade, D. N. Further Characterization of Specific Drug Binding Sites on Human Serum Albumin. *Mol. Pharmacol.* **1976**, *12* (6), 1052–1061.

(25) Sudlow, G.; Birkett, D. J.; Wade, D. N. The Characterization of Two Specific Drug Binding Sites on Human Serum Albumin. *Mol. Pharmacol.* **1975**, *11* (6), 824–832.

(26) Munro, O. Q.; Akerman, K. J.; Akerman, P. Gold Complexes for Use in the Treatment of Cancer. US9346832B2, May 24, 2016. https://patents.google.com/patent/US9346832B2/en (accessed 2021-12-04).

(27) Hüttinger, K.; Förster, C.; Bund, T.; Hinderberger, D.; Heinze, K. Stereochemical Consequences of Oxygen Atom Transfer and Electron Transfer in Imido/Oxido Molybdenum(IV, V, VI) Complexes with Two Unsymmetric Bidentate Ligands. *Inorg. Chem.* **2012**, *51* (7), 4180–4192.

(28) CT, C. CT1-3 References: 1. DF Shriver, PW Atkins, and CH Langford, Inorganic Chemistry, Oxford University Press, 1996. *BACHELOR Sci. Chem. Sess. 20172018 124 Credits 1 Univ. COURSES 20 Credits Course Code Course Name Credit 50*, 7.

(29) Akerman, K. J.; Fagenson, A. M.; Cyril, V.; Taylor, M.; Muller, M. T.; Akerman, M. P.; Munro, O. Q. Gold(III) Macrocycles: Nucleotide-Specific Unconventional Catalytic Inhibitors of Human Topoisomerase I. *J. Am. Chem. Soc.* **2014**, *136* (15), 5670–5682.

(30) Champoux, J. J. DNA Topoisomerases: Structure, Function, and Mechanism. *Annu. Rev. Biochem.* **2001**, *70* (1), 369–413.

(31) Goutelle, S.; Maurin, M.; Rougier, F.; Barbaut, X.; Bourguignon, L.; Ducher, M.; Maire, P. The Hill Equation: A Review of Its Capabilities in Pharmacological Modelling. *Fundam. Clin. Pharmacol.* **2008**, *22* (6), 633–648.

(32) Geierstanger, B. H.; Wemmer, D. E. Complexes of the Minor Groove of DNA. *Annu. Rev. Biophys. Biomol. Struct.* **1995**, *24* (1), 463–493.

(33) Pjura, P. E.; Grzeskowiak, K.; Dickerson, R. E. Binding of Hoechst 33258 to the Minor Groove of B-DNA. *J. Mol. Biol.* **1987**, *197* (2), 257–271.

(34) Li, C. K.; Sun, R. W.; Kui, S. C.; Zhu, N.; Che, C. Anticancer Cyclometalated [AuIIIm (C∧ N∧ C) ML] N+ Compounds: Synthesis and Cytotoxic Properties. *Chem. Eur. J.* **2006**, *12* (20), 5253–5266.

(35) Yan, J. J.; Chow, A. L.-F.; Leung, C.-H.; Sun, R. W.-Y.; Ma, D.-L.; Che, C.-M. Cyclometalated Gold (III) Complexes with N-Heterocyclic Carbene Ligands as Topoisomerase I Poisons. *Chem. Commun.* **2010**, *46* (22), 3893–3895.

(36) Van der Westhuizen, D.; Slabber, C. A.; Fernandes, M. A.; Joubert, D. F.; Kleinhans, G.; van der Westhuizen, C. J.; Stander, A.; Munro, O. Q.; Bezuidenhout, D. I. A Cytotoxic Bis (1, 2, 3-Triazol-5-Ylidene) Carbazolide Gold (III) Complex Targets DNA by Partial Intercalation. *Chem. Eur. J.* **2021**, *27* (32), 8295–8307.

(37) Lyng, R.; Härd, T.; Norden, B. Induced CD of DNA Intercalators: Electric Dipole Allowed Transitions. *Biopolym. Orig. Res. Biomol.* **1987**, *26* (8), 1327–1345.

(38) Nordén, B.; Kurucsev, T. Analysing DNA Complexes by Circular and Linear Dichroism. *J. Mol. Recognit.* **1994**, *7* (2), 141–155.

(39) Kubota, Y.; Hashimoto, K.; Fujita, K.; Wakita, M.; Miyanohana, E.; Fujisaki, Y. Flow Dichroism, Flow Polarized Fluorescence and Viscosity of the DNA · Acridine Complexes. *Biochim. Biophys. Acta BBA - Nucleic Acids Protein Synth.* **1977**, *478* (1), 23–32.

(40) Dedon, P. C. Determination of Binding Mode: Intercalation. *Curr. Protoc. Nucleic Acid Chem.* **2000**, *00* (1), 8.1.1-8.1.13.

(41) Galindo, M. A.; Olea, D.; Romero, M. A.; Gómez, J.; del Castillo, P.; Hannon, M. J.; Rodger, A.; Zamora, F.; Navarro, J. A. R. Design and Non-Covalent DNA Binding of Platinum(II) Metallacalix[4]Arenes. *Chem. – Eur. J.* **2007**, *13* (18), 5075–5081.

(42) Vorlícková, M. Conformational Transitions of Alternating Purine-Pyrimidine DNAs in Perchlorate Ethanol Solutions. *Biophys. J.* **1995**, *69* (5), 2033–2043.

(43) Kypr, J.; Vorlíčková, M. Circular Dichroism Spectroscopy Reveals Invariant Conformation of Guanine Runs in DNA. *Biopolym. Orig. Res. Biomol.* **2002**, *67* (4–5), 275–277.

(44) Vorlícková, M.; Kejnovská, I.; Kovanda, J.; Kypr, J. Conformational Properties of DNA Strands Containing Guanine-Adenine and Thymine-Adenine Repeats. *Nucleic Acids Res.* **1998**, *26* (6), 1509–1514.

(45) Froehlich, E.; Mandeville, J. S.; Weinert, C. M.; Kreplak, L.; Tajmir-Riahi, H. A. Bundling and Aggregation of DNA by Cationic Dendrimers. *Biomacromolecules* **2011**, *12* (2), 511–517.

(46) Cragg, G. M.; Kingston, D. G.; Newman, D. J. *Anticancer Agents from Natural Products*; CRC press, 2005.

(47) Eastman, A. The Mechanism of Action of Cisplatin: From Adducts to Apoptosis. In *Cisplatin: Chemistry and Biochemistry of a Leading Anticancer Drug*; Lippert, B., Ed.; Wiley, 1999; pp 111–134.

(48) Darvey, I. G. What Factors Are Responsible for the Greater Yield of ATP per Carbon Atom When Fatty Acids Are Completely Oxidised to CO2 and Water Compared with Glucose? *Biochem. Educ.* **1999**, *27* (4), 209–210.

(49) Dong, K. C.; Berger, J. M. Structural Basis for Gate-DNA Recognition and Bending by Type IIA Topoisomerases. *Nature* **2007**, *450* (7173), 1201–1205.

(50) Tewey, K. M.; Rowe, T. C.; Yang, L.; Halligan, B. D.; Liu, L.-F. Adriamycin-Induced DNA Damage Mediated by Mammalian DNA Topoisomerase II. *Science* **1984**, *226* (4673), 466–468.

(51) Capranico, G.; Zunino, F.; Kohn, K. W.; Pommier, Y. Sequence-Selective Topoisomerase II Inhibition by Anthracycline Derivatives in SV40 DNA: Relationship with DNA Binding Affinity and Cytotoxicity. *Biochemistry* **1990**, *29* (2), 562–569.

(52) Wilson, C. R.; Fagenson, A. M.; Ruangpradit, W.; Muller, M. T.; Munro, O. Q. Gold (III) Complexes of Pyridyl-and Isoquinolylamido Ligands: Structural, Spectroscopic, and Biological Studies of a New Class of Dual Topoisomerase I and II Inhibitors. *Inorg. Chem.* **2013**, *52* (14), 7889–7906.

(53) Song, H.; Kaiser, J. T.; Barton, J. K. Crystal Structure of Δ-[Ru (Bpy) 2 Dppz] 2+ Bound to Mismatched DNA Reveals Side-by-Side Metalloinsertion and Intercalation. *Nat. Chem.* **2012**, *4* (8), 615–620.

(54) Xie, M.-X.; Xu, X.-Y.; Wang, Y.-D. Interaction between Hesperetin and Human Serum Albumin Revealed by Spectroscopic Methods. *Biochim. Biophys. Acta BBA - Gen. Subj.* **2005**, *1724* (1), 215–224.

(55) Jr, T. P. *All About Albumin: Biochemistry, Genetics, and Medical Applications*; Academic Press, 1995.

(56) Abou-Zied, O. K.; Al-Shihi, O. I. K. Characterization of Subdomain IIA Binding Site of Human Serum Albumin in Its Native, Unfolded, and Refolded States Using Small Molecular Probes. *J. Am. Chem. Soc.* **2008**, *130* (32), 10793–10801.

(57) Sookai, S.; Munro, O. Q. Complexities of the Interaction of NiII, PdII and PtII Pyrrole-Imine Chelates with Human Serum Albumin**. *ChemistryEurope* **2023**, *1* (1), e202300012.

(58) Callis, P. R. Binding Phenomena and Fluorescence Quenching. II: Photophysics of Aromatic Residues and Dependence of Fluorescence Spectra on Protein Conformation. *J. Mol. Struct.* **2014**, *1077*, 22–29.

(59) Divsalar, A.; Bagheri, M. J.; Saboury, A. A.; Mansoori-Torshizi, H.; Amani, M. Investigation on the Interaction of Newly Designed Anticancer Pd(II) Complexes with Different Aliphatic Tails and Human Serum Albumin. *J. Phys. Chem. B* **2009**, *113* (42), 14035–14042.

(60) Gehlen, M. H. The Centenary of the Stern-Volmer Equation of Fluorescence Quenching: From the Single Line Plot to the SV Quenching Map. *J. Photochem. Photobiol. C Photochem. Rev.* **2020**, *42*, 100338.

(61) Helms, M. K.; Petersen, C. E.; Bhagavan, N. V.; Jameson, D. M. Time-Resolved Fluorescence Studies on Site-Directed Mutants of Human Serum Albumin. *FEBS Lett.* **1997**, *408* (1), 67–70.

(62) Flora, K.; Brennan, J. D.; Baker, G. A.; Doody, M. A.; Bright, F. V. Unfolding of Acrylodan-Labeled Human Serum Albumin Probed by Steady-State and Time-Resolved Fluorescence Methods. *Biophys. J.* **1998**, *75* (2), 1084–1096.

(63) Maiti, T. K.; Ghosh, K. S.; Samanta, A.; Dasgupta, S. The Interaction of Silibinin with Human Serum Albumin: A Spectroscopic Investigation. *J. Photochem. Photobiol. Chem.* **2008**, *194* (2), 297–307.

(64) Soares, S.; Mateus, N.; de Freitas, V. Interaction of Different Polyphenols with Bovine Serum Albumin (BSA) and Human Salivary α-Amylase (HSA) by Fluorescence Quenching. *J. Agric. Food Chem.* **2007**, *55* (16), 6726–6735.

(65) Ariga, G. G.; Naik, P. N.; Chimatadar, S. A.; Nandibewoor, S. T. Interactions between Epinastine and Human Serum Albumin: Investigation by Fluorescence, UV–Vis, FT–IR, CD, Lifetime Measurement and Molecular Docking. *J. Mol. Struct.* **2017**, *1137*, 485–494.

(66) Lakowicz, J. R. *Principles of Fluorescence Spectroscopy*, 3rd ed.; Springer US: Boston MA, 2006.

(67) Perozzo, R.; Folkers, G.; Scapozza, L. Thermodynamics of Protein–Ligand Interactions: History, Presence, and Future Aspects. *J. Recept. Signal Transduct.* **2004**, *24* (1–2), 1–52.

(68) Chaires, J. B. A Thermodynamic Signature for Drug–DNA Binding Mode. *Arch. Biochem. Biophys.* **2006**, *453* (1), 26–31.

(69) Ross, P. D.; Subramanian, S. Thermodynamics of Protein Association Reactions: Forces Contributing to Stability. *Biochemistry* **1981**, *20* (11), 3096–3102.

(70) Du, X.; Li, Y.; Xia, Y.-L.; Ai, S.-M.; Liang, J.; Sang, P.; Ji, X.-L.; Liu, S.-Q. Insights into Protein–Ligand Interactions: Mechanisms, Models, and Methods. *Int. J. Mol. Sci.* **2016**, *17* (2), 144.

(71) Grabowska, J.; Kuffel, A.; Zielkiewicz, J. Revealing the Frank–Evans "Iceberg" Structures within the Solvation Layer around Hydrophobic Solutes. *J. Phys. Chem. B* **2021**, *125* (6), 1611–1617.

(72) Petitpas, I.; Bhattacharya, A. A.; Twine, S.; East, M.; Curry, S. Crystal Structure Analysis of Warfarin Binding to Human Serum Albumin: ANATOMY OF DRUG SITE I *. *J. Biol. Chem.* **2001**, *276* (25), 22804–22809.

(73) Graciani, F. S.; Ximenes, V. F. Investigation of Human Albumin-Induced Circular Dichroism in Dansylglycine. *PloS One* **2013**, *8* (10), e76849.

(74) Ghuman, J.; Zunszain, P. A.; Petitpas, I.; Bhattacharya, A. A.; Otagiri, M.; Curry, S. Structural Basis of the Drug-Binding Specificity of

Human Serum Albumin. *J. Mol. Biol.* **2005**, *353* (1), 38–52.

(75) Kelly, S. M.; Jess, T. J.; Price, N. C. How to Study Proteins by Circular Dichroism. *Biochim. Biophys. Acta BBA - Proteins Proteomics* **2005**, *1751* (2), 119–139.

(76) He, X. M.; Carter, D. C. Atomic Structure and Chemistry of Human Serum Albumin. *Nature* **1992**, *358* (6383), 209–215.

(77) Sreerama, N.; Woody, R. W. Computation and Analysis of Protein Circular Dichroism Spectra. In *Methods in Enzymology*; Numerical Computer Methods, Part D; Academic Press, 2004; Vol. 383, pp 318–351.

(78) do Monte, Z. S.; Ramos, C. S. Development and Validation of a Method for the Analysis of Paroxetine HCl by Circular Dichroism. *Chirality* **2013**, *25* (4), 211–214.

(79) Micsonai, A.; Wien, F.; Bulyáki, É.; Kun, J.; Moussong, É.; Lee, Y.-H.; Goto, Y.; Réfrégiers, M.; Kardos, J. BeStSel: A Web Server for Accurate Protein Secondary Structure Prediction and Fold Recognition from the Circular Dichroism Spectra. *Nucleic Acids Res.* **2018**, *46* (W1), W315–W322.

(80) Mohammadi, F.; Bordbar, A.-K.; Divsalar, A.; Mohammadi, K.; Saboury, A. A. Analysis of Binding Interaction of Curcumin and Diacetylcurcumin with Human and Bovine Serum Albumin Using Fluorescence and Circular Dichroism Spectroscopy. *Protein J.* **2009**, *28* (3), 189–196.

(81) Tajmir-Riahi, H. A.; N'soukpoé-Kossi, C. N.; Joly, D. Structural Analysis of Protein–DNA and Protein–RNA Interactions by FTIR, UV-Visible and CD Spectroscopic Methods. *Spectroscopy* **2009**, *23* (2), 81–101.

(82) Duman, O.; Tunç, S.; Kancı Bozoğlan, B. Characterization of the Binding of Metoprolol Tartrate and Guaifenesin Drugs to Human Serum Albumin and Human Hemoglobin Proteins by Fluorescence and Circular Dichroism Spectroscopy. *J. Fluoresc.* **2013**, *23* (4), 659–669.

(83) Alam, P.; Chaturvedi, S. K.; Anwar, T.; Siddiqi, M. K.; Ajmal, M. R.; Badr, G.; Mahmoud, M. H.; Hasan Khan, R. Biophysical and Molecular Docking Insight into the Interaction of Cytosine β-D Arabinofuranoside with Human Serum Albumin. *J. Lumin.* **2015**, *164*, 123–130.

(84) Lafitte, D.; Tsvetkov, P. O.; Devred, F.; Toci, R.; Barras, F.; Briand, C.; Makarov, A. A.; Haiech, J. Cation Binding Mode of Fully Oxidised Calmodulin Explained by the Unfolding of the Apostate. *Biochim. Biophys. Acta BBA-Proteins Proteomics* **2002**, *1600* (1–2), 105–110.

(85) Ahmad, B.; Parveen, S.; Khan, R. H. Effect of Albumin Conformation on the Binding of Ciprofloxacin to Human Serum Albumin: A Novel Approach Directly Assigning Binding Site. *Biomacromolecules* **2006**, *7* (4), 1350–1356.

(86) Sun, C.; Yang, J.; Wu, X.; Huang, X.; Wang, F.; Liu, S. Unfolding and Refolding of Bovine Serum Albumin Induced by Cetylpyridinium Bromide. *Biophys. J.* **2005**, *88* (5), 3518–3524.

(87) Cheng, X.-X.; Fan, X.-Y.; Jiang, F.-L.; Liu, Y.; Lei, K.-L. Resonance Energy Transfer, PH-Induced Folded States and the Molecular Interaction of Human Serum Albumin and Icariin. *Luminescence* **2015**, *30* (7), 1026–1033.

(88) Zaidi, N.; Ajmal, M. R.; Rabbani, G.; Ahmad, E.; Khan, R. H. A Comprehensive Insight into Binding of Hippuric Acid to Human Serum Albumin: A Study to Uncover Its Impaired Elimination through Hemodialysis. *PLOS ONE* **2013**, *8* (8), e71422.

(89) Allenmark, S. Induced Circular Dichroism by Chiral Molecular Interaction. *Chirality* **2003**, *15* (5), 409–422.

(90) Tedesco, D.; Bertucci, C. Induced Circular Dichroism as a Tool to Investigate the Binding of Drugs to Carrier Proteins: Classic Approaches and New Trends. *J. Pharm. Biomed. Anal.* **2015**, *113*, 34–42.

(91) Gottarelli, G.; Lena, S.; Masiero, S.; Pieraccini, S.; Spada, G. P. The Use of Circular Dichroism Spectroscopy for Studying the Chiral Molecular Self-Assembly: An Overview. *Chirality* **2008**, *20* (3–4), 471–485.

(92) Pescitelli, G.; Bari, L. D.; Berova, N. Application of Electronic Circular Dichroism in the Study of Supramolecular Systems. *Chem. Soc. Rev.* **2014**, *43* (15), 5211–5233.

(93) Mason, S. F. Induced Circular Dichroism. *Chem. Phys. Lett.* **1975**, *32* (2), 201–203.

(94) Pantoliano, M. W.; Petrella, E. C.; Kwasnoski, J. D.; Lobanov, V. S.; Myslik, J.; Graf, E.; Carver, T.; Asel, E.; Springer, B. A.; Lane, P.; Salemme, F. R. High-Density Miniaturized Thermal Shift Assays as a General Strategy for Drug Discovery. *J. Biomol. Screen.* **2001**, *6* (6), 429–440.

(95) Bruylants, G.; Wouters, J.; Michaux, C. Differential Scanning Calorimetry in Life Science: Thermodynamics, Stability, Molecular Recognition and Application in Drug Design. *Curr. Med. Chem.* **2005**, *12* (17), 2011–2020.

(96) Niesen, F. H.; Berglund, H.; Vedadi, M. The Use of Differential Scanning Fluorimetry to Detect Ligand Interactions That Promote Protein Stability. *Nat. Protoc.* **2007**, *2* (9), 2212–2221.

(97) Flora, K.; Brennan, J. D.; Baker, G. A.; Doody, M. A.; Bright, F. V. Unfolding of Acrylodan-Labeled Human Serum Albumin Probed by Steady-State and Time-Resolved Fluorescence Methods. *Biophys. J.* **1998**, *75* (2), 1084–1096.

(98) Picó, G. A. Thermodynamic Features of the Thermal Unfolding of Human Serum Albumin. *Int. J. Biol. Macromol.* **1997**, *20* (1), 63–73.

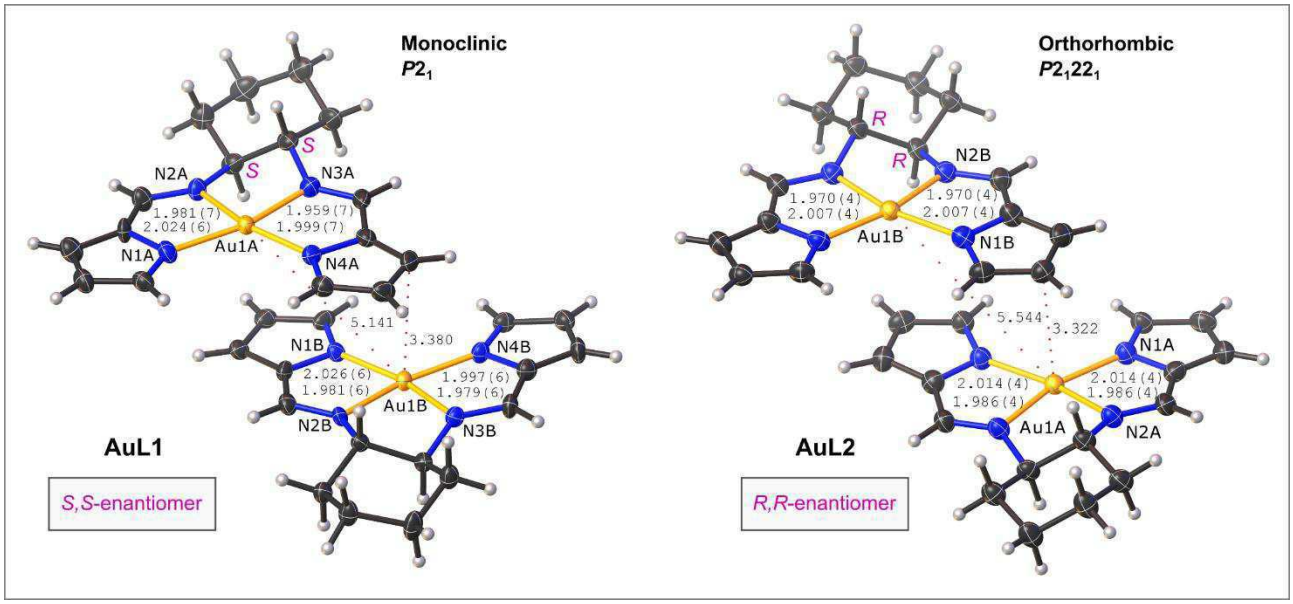
(99) Gill, P.; Moghadam, T. T.; Ranjbar, B. Differential Scanning Calorimetry Techniques: Applications in Biology and Nanoscience. *J. Biomol. Tech. JBT* **2010**, *21* (4), 167–193.

(100) Dong, C.; Ma, S.; Liu, Y. Studies of the Interaction between Demeclocycline and Human Serum Albumin by Multi-Spectroscopic and Molecular Docking Methods. *Spectrochim. Acta. A. Mol. Biomol. Spectrosc.* **2013**, *103*, 179–186.

(101) Wang, G.; Li, X.; Ding, X.; Wang, D.; Yan, C.; Lu, Y. Exploring the Mechanism of Interaction between 5-(Ethoxycarbonyl)-6-Methyl-4-(4-Methoxy-phenyl)-3,4-Dihydropyrimidin-2(1H)-One and Human Serum Albumin: Spectroscopic, Calorimetric and Molecular Modeling Studies. *J. Pharm. Biomed. Anal.* **2011**, *55* (5), 1223–1226

.

Chapter 3 Human serum albumin binds chiral cytotoxic Au(III) chelates as fully intact complexes with unique thermodynamics



ARTICLE

Human serum albumin binds chiral cytotoxic Au(III) chelates as fully intact complexes with unique thermodynamics

Received 00th January 20xx,
Accepted 00th January 20xx

DOI: 10.1039/x0xx00000x

Sheldon Sookai,[a] Matthew P. Akerman[b] and Orde Q. Munro*[,a]

Human serum albumin (HSA) is the most abundant blood protein, transporting many exogenous compounds including clinically deployed and investigational drugs that are generally organic in nature. Here, two chiral tetradentate cyclohexane-1,2-diamine-bridged bis(pyrrole-imine) ligands, **H_2L1** and **H_2L2**, were metalated with Au(III) affording the chiral cationic Au(III) complexes **AuL1** and **AuL2** (enantiomers). The pair of Au(III) complexes were used to delineate how chirality impacts the compound's affinity for HSA. Steady state fluorescence quenching data acquired on the native protein, along with data from site-specific probes, showed that the compounds bind at sites close enough to Trp-214 (subdomain IIA) of HSA to quench the fluorophore. The bimolecular quenching rate constants, K_q, were of the order of 10^2 times higher than the maximum diffusion-controlled collision constant of a biomolecule in water (10^{10} M^{-1} s^{-1}), confirming that static fluorescence quenching was the dominant mechanism. The Stern-Volmer constants, K_{SV}, were ~10^4 M^{-1} at 37 °C, while the affinity constants, K_a (37 °C), measured ~2.1×10^4 M^{-1} (**AuL1**) and ~1.2×10^4 M^{-1} (**AuL2**) for enthalpy-driven ligand uptake targeting Sudlow's site I via London dispersion forces of attraction. Although far- and near-UV CD spectroscopy indicated that both complexes minimally perturb the secondary and tertiary structure of HSA, substantial shifts in the CD spectra were recorded for both protein-bound ligands. **AuL1** and **AuL2** were analysed in the NCI-60 single-dose drug screen, giving mean growth percentages of 56.5% and 89.1%, respectively. **AuL1** was subsequently selected for a five-dose NCI-60 screen, affording GI_{50}, IC_{50} and LC_{50} values of 4.7, 9.3 and 39.8 μM, respectively. This study highlights the chemotherapeutic potential of chiral bis(pyrrolide-imine) Au(III) chelates which neither decompose nor demetallate after uptake by HSA. The data collectively suggest that transport and delivery of the compounds, subject to *in vivo* testing, might be feasible going forward.

Introduction

Cancer is the leading cause of death worldwide accounting for almost 10 million deaths in 2020 and is expected to continuously rise.[1] The fight against cancer is becoming increasingly difficult due to drug resistance, in addition to severe side effects from already existing chemotherapeutics. Since most currently available chemotherapeutic drugs are organic, metallodrugs may prove to be an attractive alternative. Metallodrugs are less investigated in pre-clinical screens and clinical trials compared to purely organic drugs, suggesting that most of their potential remains untapped.[2] The marked potential of metallodrugs was recently highlighted by an antibiotic screening centre which demonstrated that metallodrugs displayed a 10-fold higher hit rate towards ESKAPE pathogens compared with purely organic compounds.[3]

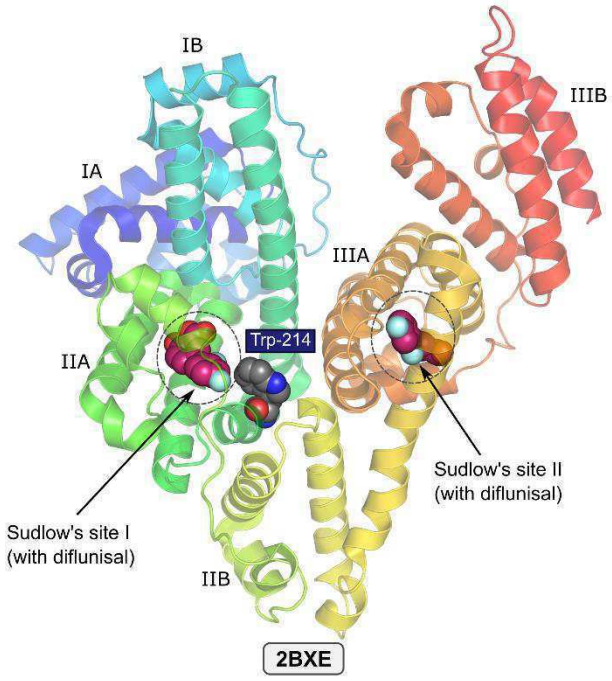
In 1965[4] it was first reported that cisplatin inhibited mitosis of bacteria; the ensuing clinical deployment of cisplatin and its analogues[5,6] as anticancer metallodrugs[7] engendered expansionary multidisciplinary studies on Pt(II) complexes[8] over several decades. Unfortunately, numerous cisplatin-resistant tumour cell lines have since emerged,[9,10] fuelling increased interest in metallodrug development especially of isoelectronic (d^8) square-planar Au(III) complexes.[11–16]

Gold(III) complexes were originally believed to be mechanistically similar to Pt(II) compounds in biological systems. However, this is not the case as the Au(III) ion is susceptible to reduction to either Au(I) and/or colloidal gold (Au(0)).[17] Therefore, it is crucial to identify appropriate multidentate ligands capable of stabilising Au(III) under physiological conditions.[18,19] Typical multidentate ligand scaffolds used to stabilise the Au(III) ion are porphyrins,[20] CNC-type pincer ligands,[13,14,21,22] and deprotonated pyrroles.[12] These ligands contain strong neutral or anionic σ-donor atoms (C, N and O) to complement the hard Au(III) ion. The strong σ-donors within the scaffold transfer electron density toward the metal centre, thereby lowering the reduction potential.[23]

Pyrrole-based ligands are imperative building blocks for various organic pharmaceuticals,[24] as epitomised by clinically approved drugs, including Tolmetin (a non-steroidal anti-inflammatory agent),[25] Glimepiride (used to manage type-2 diabetes mellitus by stimulating insulin release),[26] and Sunitinib (multi-targeted receptor tyrosine kinase inhibitor for cancer chemotherapy).[27] Of relevance here, pyrrole-imine metal chelates exhibit significant medicinal potential. The best-known example is the pentadentate macrocycle texaphyrin,[28] which complexes Lu(III)[29] and is a promising, though not FDA-approved, photodynamic therapeutic.[30] Despite being further

[a] Molecular Sciences Institute, School of Chemistry, University of the Witwatersrand, PO WITS 2050, Johannesburg, South Africa
[b] School of Chemistry and Physics, University of KwaZulu-Natal, Pietermaritzburg, 3201, South Africa
[c] † Electronic Supplementary Information (ESI) available: Complete experimental details and supplementary tables and figures in PDF format, X-ray crystal structures in CIF format (CCDC 2244592, 2244999). See DOI: 10.1039/x0xx00000x

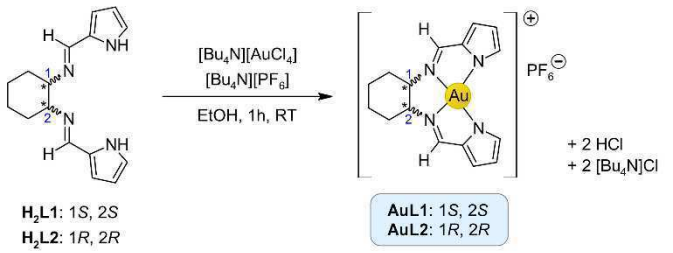
behind on the clinical development trajectory, patented tetradentate bis(pyrrolide-imine) chelates of Au(III) are promising investigational compounds for cancer[31] and mycobacterial chemotherapy.[32]



Scheme 1 X-ray structure of HSA bound to diflunisal (redrawn from PDB code 2BXE) illustrating the two main small molecule binding sites. Sudlow's site I is larger than Sudlow's site II and compounds that bind in this pocket perturb the fluorescence of Trp-214. The protein secondary structure elements are depicted schematically, coloured by domain, and labelled. A third diflunisal molecule bound centrally in domain IIB has been omitted for clarity.

Regarding anticancer Au(III) complexes, there is limited work on assessing their binding potential to serum proteins, in particular human serum albumin (HSA), which can play an essential role in determining plasma distribution, pharmacokinetic and pharmacodynamic data of metallodrugs.[33] HSA is the most abundant serum protein existing at physiological concentrations of around 600 µM.[34] The main roles of HSA are to transport both endogenous and exogenous compounds as well regulating colloidal osmotic pressure. As illustrated in Scheme 1, HSA is a single polypeptide chain consisting of three domains, namely I (residues 1–195), II (196–383), and III (384–585), that are further broken down into two subdomains A and B.[35,36] HSA has several binding sites that bind exogenous and endogenous compounds: (i) two main drug binding sites named Sudlow's site I and II, (ii) 4 thyroxine sites, (iii) 7 fatty acid sites, and (iv) several known metal ion binding sites.[37] Given the abundance and function of HSA as a blood plasma transporter, delineating the binding of a medicinal compound to HSA is central to understanding the pharmacodynamic and pharmacokinetic data of the compound *in vivo*.[38]

In this study, we synthesised 2,2'-{(1*S*,2*S*)- and 2,2'-{(1*R*,2*R*)-cyclohexane-1,2-diylbis[nitrilo(*E*)methylylidene]}bis(pyrrol-1-ido)gold(III) hexafluorophosphate(V), abbreviated [Au((1*S*,2*S*)**L1**)]PF_6 (**AuL1**) and [Au((1*R*,2*R*)**L2**)]PF_6 (**AuL2**), respectively (Scheme 2). Spectroscopic methods were used to probe the binding of **AuL1** and **AuL2** to HSA under physiological conditions to investigate how the chirality of the metal complex influences uptake by HSA and to delineate the preferred binding site(s). Finally, an NCI-60 screen was used to gauge the cytotoxicity of both Au(III) chelates against a panel of 60 human cancer cell lines. Interestingly, **AuL1** (but not its enantiomer **AuL2**) was sufficiently active to warrant full 5-dose screening.



Scheme 2 Synthetic route depicting the metalation of H_2**L1** and H_2**L2** with Au(III).

Results and discussion

Metal chelate synthesis

Gold(III) chelates **AuL1** and **AuL2** were synthesised by the method described in Scheme 1. The enantiopure bis(pyrrole-imine) Schiff base ligands (1*S*,2*S* and 1*R*,2*R* enantiomers) were specifically employed for their chirality and ability to stabilise a high oxidation state metal ion such as Au(III). In this reaction, the pyrrole nitrogen atoms are concomitantly deprotonated upon metalation, affording the desired chiral cationic Au(III) chelates. Interestingly **AuL1** and **AuL2** only precipitated when [Bu_4N][PF_6] was added to the reaction mixture. This is attributed to switching the Cl^- counterion to PF_6^-, which presumably lowers the solubility product of the salt by better ion pair formation.

X-ray crystal structures of enantiomeric AuL1 and AuL2

The structures of **AuL1** and **AuL2** were elucidated by single crystal X-ray diffraction (Fig. 1, Figs. S30–S32, and Tables S2–S7). **AuL1** and **AuL2** crystallised in the chiral space groups $P2_1$ (two independent molecules per asymmetric unit, ASU) and $P2_122_1$ (two independent half molecules per ASU), respectively. The Au(III) chelates exhibit the expected four-coordinate square planar geometry (Figs. 1 and S30) and are metrically similar enantiomers in terms of their key structural parameters such as Au–N bond lengths and bond angles subtended at the metal centre (Fig. S32, Table S8). For brevity, only the structure of **AuL1** will be discussed further given the slightly higher quality X-ray data set for this compound, its higher cytotoxicity in the NCI-60 screen, and its higher affinity for HSA (*vide infra*).

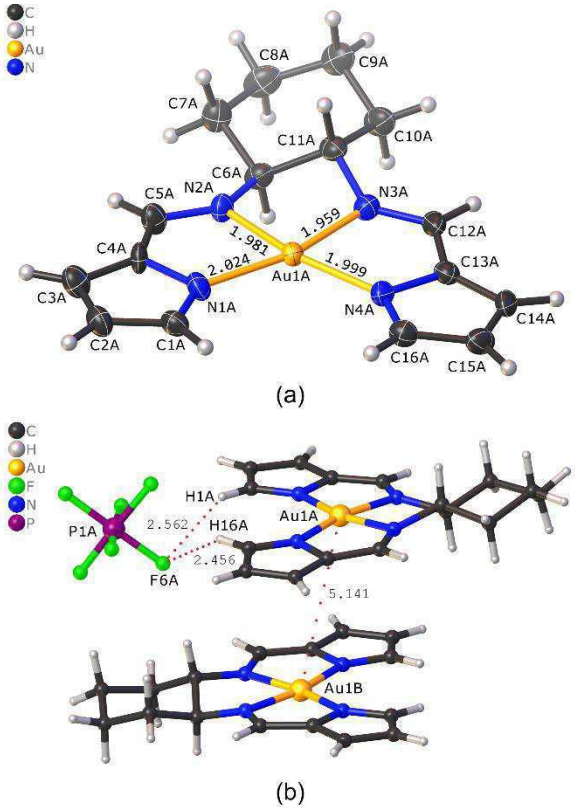


Fig. 1 (a) Labelled thermal ellipsoid view (50% probability surfaces) of the X-ray structure of [**AuL1**]$^+$ belonging to independent cation A of the asymmetric unit (ASU). The PF_6^- counterion and second independent ion pair are omitted for clarity (H atoms are shown as spheres with an arbitrary radius). Selected bond distances are in Å units. (b) Stacking relationship between independent cations A and B in the ASU; the cations have no close contacts. The long Au···Au distance of 5.1409(3) Å indicates an insignificant metal-to-metal interaction. Illustration of one of two types of noncovalent F···H–C(pyrrole) interactions found between PF_6^- and [**AuL1**]$^+$ in the crystal lattice of the salt.

The Au–N_{imine} bond distances average 1.975(11) Å, which is ~2% shorter than the Au–$N_{pyrrole}$ distances (2.012(16) Å). Regarding Au(III) complexes containing Au–$N_{pyrrole}$ and Au–N_{imine} bonds, **AuL1** is unique in the sense that its Au–N_{imine} bonds are notably shorter than the Au–$N_{pyrrole}$ bonds. This reflects the structural constraints imposed by the central 5-membered chelate ring (i.e., the chiral cyclohexyl bridge). When compared with the Au–N bond distances for the related Au(III) complexes bearing 3- or 4-carbon aliphatic chains linking the imine nitrogen atoms,[1] the Au–$N_{pyrrole}$ bond length in **AuL1** is ~1% longer and the Au–N_{imine} bond length ~1.5% shorter than those of the achiral congeners. Overall, the observed Au–N bond distances for [**AuL1**](PF_6) are comparable to previously reported Au–N bond distances, which range from 1.928 – 2.216 Å.[2] Regarding the coordination group bond angles for **AuL1**, the mean $N_{pyrrole}$–Au–$N_{pyrrole}$ bond angle (112.8 ± 0.1°) is 14.4% wider and the mean N_{imine}–Au–N_{imine} bond angle (84.4 ± 4°) 13.5% more acute compared with those reported by Akerman *et al.*[1] for the structurally-related achiral analogues. This again reflects the 2-carbon chain of the cyclohexyl ring linking the imine groups of **AuL1**, a structural scaffold which clearly sterically strains the tetradentate chelate, substantially widening and narrowing the $N_{pyrrole}$–Au–$N_{pyrrole}$ and N_{imine}–Au–N_{imine} bond angles, respectively. In short, the Au–N bond distances in **AuL1** hinge mainly on the central chelate ring's bite angle.

Considering the extended structure of **AuL1**, the only short contacts present involve the PF_6^- counterion, leading to F···H–C(pyrrole) intermolecular interactions which stabilise the crystal lattice (Fig. 1b). F···H–C nonbonded interactions are known,[40] however they seldom form strong H-bonds due to electrostatic and steric factors.[41] Even though F···H–C interactions are weaker than conventional H bonds, their role in molecular packing cannot be ignored. The **AuL1** cations and PF_6^- anions display measurable F···H–C(pyrrole) contacts, with distances ranging from 2.456 – 2.726 Å (Fig. 1b). The structural role played by fluorine is perhaps further highlighted by the fact that crystallization of **AuL1** was only possible with PF_6^- as the counterion, not Cl^-. As shown in Fig. 1, the **AuL1** cations deviate negligibly from planarity; only the atoms of the cyclohexyl groups lie out of the mean plane defined by the Au(III) ion and pyrrole-imine chelates. Any minor out of plane deviations may be attributed to the twist induced by the cyclohexyl bridging group of the ligand rather than packing interactions. Notably, there were no aurophilic Au···Au contacts between neighbouring cations since the atomic separation exceeded 5 Å for both **AuL1** and **AuL2** (Figs. 1 and S32). For both **AuL1** and **AuL2**, the cation pairs exhibit nonbonded contacts between the Au(III) ions and pyrrole β-C atoms, with those of **AuL2** (3.272 and 3.315 Å) being slightly shorter than the sum of the van der Walls radii of carbon and gold (3.36 Å).

Fluorescence quenching measurements

When a small molecule binds to a protein in close proximity to an aromatic amino acid residue (Trp, Tyr and, to a lesser extent, Phe),[42,43] the intrinsic fluorescence of that protein will be disrupted.[43] The majority of HSA's fluorescence is attributed to Trp-214 in subdomain IIA. Importantly, Trp has a higher quantum yield and a more efficient resonance energy transfer than both Tyr and Phe.[44]

Quenching of the intrinsic emission spectrum of HSA (λ^{ex}, 295 nm) was investigated by titrating the protein with **AuL1** and **AuL2** over the concentration range 0–97 μM with spectral acquisition from 310–400 nm (Fig. 2). The λ_{max}^{em} was observed at ~342 nm in phosphate buffer and the intrinsic emission intensity of HSA decreased monotonically with the addition of each aliquot of titrant (Fig. 2). The fluorescence quenching data indicate that both Au(III) chelates bind to HSA near enough to Trp-214 to alter its microenvironment, thereby quenching its fluorescence. The fluorescence quenching could be the result of different mechanisms, such as collisional quenching, molecular rearrangements, energy transfer, or ground state complex formation.[45,46]

The binding of **AuL1** and **AuL2** to HSA is accompanied by blue shifts in λ_{max}^{em} of 4.37 and 2.33 nm, respectively. The λ_{max}^{em} shift data suggest that the Trp-214 residue is in a less polar environment after the uptake of both Au(III) chelates.[47,48] Two reasons might account for the λ_{max}^{em} blue shifts: (i) disruption of

ordered water molecules that lie between 15–25 Å of the Trp-214, which may cause orientation-dependent polarisation of the fluorophore, and/or (ii) direct electronic polarization of the indole ring on the tryptophan residue by closely bound metal chelates. It is certainly feasible that binding of **AuL1** and **AuL2** by HSA both displaces ordered water molecules and induces some electronic polarization of Trp-214, which affects the lowest energy $^1A_1 \rightarrow {}^1L_a$ ground state transition of Trp's indole ring,[47] thereby causing the λ_{max}^{em} shift. Ultimately, the different magnitudes of the measured λ_{max}^{em} shifts indicate that **AuL1** electronically perturbs Trp-214 more than **AuL2**. The different chirality of each metal chelate thus impacts the electronic structure of Trp-214, possibly because of how the metal chelates are positioned within the binding site.

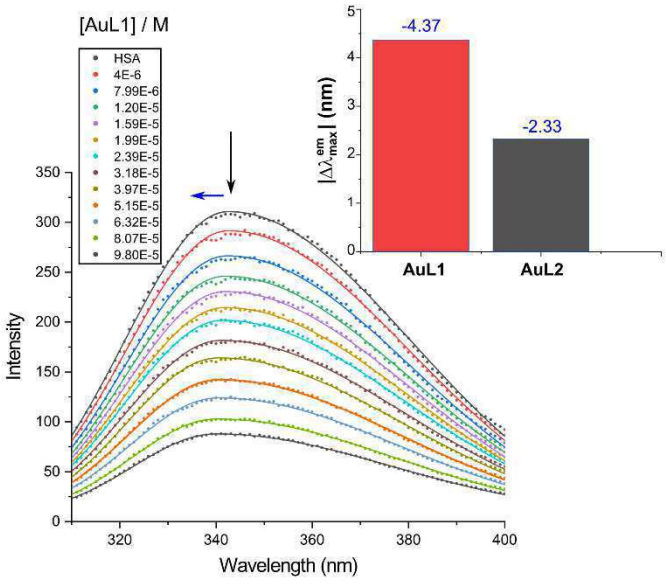


Fig. 2 Emission spectra of human serum albumin (HSA, 5.0 μM) recorded as a function of the concentration of **AuL1** at 298 K in KH_2PO_4 (50 mM, pH 7.50). Analogous spectra for the reaction of HSA with **AuL2** are given in Figure S23 (ESI). The absolute value of the wavelength shift accompanying ligand uptake ($|\Delta\lambda_{max}^{em}|$) is plotted as the inset to the main figure (upper right).

Fluorescence quenching mechanism

Protein fluorescence quenching can be described mechanistically as either static, dynamic or a combination of both, and is normally analysed using the Stern–Volmer equation (eq. 1),[49]

$$I_0/I = 1 + K_{SV}[Q] = 1 + k_q\tau_0\,[Q] \qquad (1)$$

where I_0 is the fluorescence intensity of HSA in the absence of the added quencher (Au(III) chelate herein) and I is the fluorescence intensity of HSA in the presence of the metal complex. K_{SV} is the Stern-Volmer constant (M^{-1}), while $[Q]$ is the molar concentration of the quencher (i.e., added **AuL1** or **AuL2**), k_q is the bimolecular quenching rate constant ($M^{-1}\ s^{-1}$), and τ_0 is the average lifetime of HSA fluorescence in the absence of any quencher (6.72 ± 0.07 ns,[50] 5.60 ± 0.10 ns,[51] and 5.28 ± 0.03 ns;[52] average = 5.87 ± 0.76 ns). Typically, the quenching mechanism can be differentiated by analysing the HSA···Au(III) complex's fluorescence as a function of temperature and viscosity.[53]

Table 1. Stern-Volmer quenching constants (K_{SV}) and bimolecular quenching rate constants (k_q) for the interaction of the two Au(III) cyclohexane chelates with HSA at different temperatures in 50 mM KH_2PO_4 buffer at pH 7.50.

Cpd.	Temp. T (K)	$10^{-5}\ K_{SV}$ $(M^{-1})^{a,c}$	$10^{-12}\ k_q$ $(M^{-1}\ s^{-1})^b$	$\log(K_a / M^{-1})^c$	n^d
AuL1	288	1.19 (0.09)	2.03	4.93 (0.04)	1.17 (0.01)
	298	1.96 (0.01)	3.33	4.55 (0.02)	1.05 (0.01)
	310	2.55 (0.01)	4.35	4.32 (0.04)	0.98 (0.01)
AuL2	288	1.04 (0.01)	1.77	4.80 (0.01)	1.18 (0.01)
	298	1.11 (0.01)	1.89	4.33 (0.08)	1.06 (0.02)
	310	1.16 (0.01)	1.97	4.08 (0.05)	1.01 (0.01)

[a] K_{SV} values (Stern-Volmer constants) for the five gold(III) chelates were determined from fitting the data to eq. 1. A mean excited state lifetime, τ_0, of 5.87(76) ns for HSA was used to calculate the bimolecular quenching rate constant, k_q. [c] The estimated standard deviation of the least significant digits are given in parentheses. [d] Ligand:HSA binding stoichiometry from the fit of the data to eq. 3.

From least-squares fits of eq. 1 to the dose-dependence of I_0/I, the bimolecular fluorescence quenching rate constant for the HSA···Au(III) interaction can be straightforwardly deduced from eq. 2, provided that τ_0 is known (*vide supra*).

$$k_q = {}^{K_{SV}}/_{\tau_0} \qquad (2)$$

It is widely accepted that a linear Stern-Volmer plot is associated with a single dominant quenching mechanism, either dynamic (diffusion-limited collisional) or static (binding-related).[54,55] The quenching mechanism can be differentiated by the temperature dependence of K_{SV}. When a static quenching mechanism is dominant, the K_{SV} value decreases with increasing temperature due to the decrease in the HSA-ligand formation constant. However, when a dynamic quenching mechanism is dominant, the K_{SV} values increase with increasing temperature due to an increase in the collisional frequency and diffusion rate.[56]

The Stern-Volmer plots for **AuL1** and **AuL2** (Fig. 3a) were both linear, suggesting a single class of quenching was dominant. In both cases, the K_{SV} values increased with increasing temperature, consistent with a dynamic quenching mechanism.[79] A summary of the K_{SV} and k_q values obtained for the interaction of **AuL1** and **AuL2** with HSA is given in Table 1. It is probable that the observed K_{SV} order, **AuL1** > **AuL2**, is due to the binding orientation of **AuL1** around Trp-214 (based on Fig. 2). The bimolecular quenching rate constants (k_q) determined for **AuL1** and **AuL2** exceeded the diffusion-controlled limit (10^{10} $M\ s^{-1}$)[57] by at least two orders of magnitude. These k_q values signal that the binding of both Au(III) chelates to HSA is not randomised but consistent with a significant HSA···ligand binding interaction.

Binding affinity hinges on Au(III) chelate chirality

Quenching of HSA intrinsic fluorescence as a function of ligand dose, [**AuL*n***], can be used to calculate the binding affinity (K_a)

and the stoichiometry (n). Both values can be delineated from a double log plot of the emission quenching data as a function of quencher (metal chelate) concentration, [Q] (eq. 3),[58.]

$$log\left(\frac{I_0 - I}{I}\right) = logK_a + nlog[Q] \quad (3)$$

where the intercept and slope of the curve give logK_a and n, respectively. The data for **AuL1** and **AuL2** are summarised in Table 1 and are plotted in Fig. 3b (Figs. 20 and 21). Both compounds exhibit moderate binding affinity for HSA (K_a ~10^5 M^{-1}), which is ideal for this study since we intend to show that HSA can serve as a transporter protein for this class of compounds. Importantly, it suggests that **AuL1** and **AuL2** could make use of the HSA-mediated cell entry pathway.[59] Binding constants that are too high will probably result in retention of the compounds by HSA and thus diminished delivery via the HSA-mediated pathway.

From Table 1, the logK_a values differ by up to 0.24 log units at each temperature and follow the order **AuL1** > **AuL2**; the difference in chirality clearly impacts compound uptake by the protein with the 1*S*,2*S* enantiomer being favoured. Such an outcome is not without precedent for drug enantiomers. For instance, the *S* enantiomer of warfarin has a higher binding constant than the *R* enantiomer.[60] Enantiomers can bind to the same region (binding site) or different regions depending on allosteric modulation.[61] Notably, the affinity constant data for **AuL1** and **AuL2** mirror the emission wavelength shifts induced by the binding of each Au(III) chelate to HSA (Fig. 2). The collective picture is that **AuL1** may bind closer to Trp-214 than **AuL2**, or with an orientation that induces greater electronic perturbation of the fluorophore, and fit more snugly within the binding pocket, which is presumably Sudlow's site I (Scheme 1). From Fig. 3b it can be seen that the slopes of the double log plot linear fits were ~1 at 37 °C, strongly suggesting a 1:1 binding ratio of Au(III) chelate to HSA. For both chelates, logK_a decreased with increasing temperature, consistent with an exothermic reaction (vide infra).

Thermodynamics of Au(III) chelate binding hinge on chirality

Both **AuL1** and **AuL2** follow a linear van't Hoff relationship; plots for triplicate measurements are given in Fig. 4a. Under non-standard conditions, the entropy change (ΔS), enthalpy change (ΔH), and Gibbs free energy change (ΔG), may be gathered from the temperature dependence of the affinity constants (K_a) using eqs. 4 and 5:

$$lnK_a = -\frac{\Delta H}{RT} + \frac{\Delta S}{R} \quad (4)$$

$$\Delta G = \Delta H - T\Delta S \quad (5)$$

Table 2 summarises the thermodynamic parameters for reaction of **AuL1** and **AuL2** with HSA in KH_2PO_4 buffer at neutral pH. Both reactions were exergonic,[58] with ΔG ranging from −25.5 kJ mol^{-1} for **AuL2** to −27.5 kJ mol^{-1} for **AuL1** at 298 K. As depicted graphically in Fig. 4b, the values of ΔG are remarkably similar due to enthalpy/entropy compensation. Regarding the ΔH values for the reaction of **AuL1** and **AuL2** with HSA, both are significantly exothermic, measuring –82.0 kJ mol^{-1} and –56.0 kJ mol^{-1}, respectively. Fig. 4b highlights the dominance of the enthalpy term for both reactions, indicating that uptake of the Au(III) chelates by HSA is enthalpically driven. Importantly, the difference in chirality for the two enantiomeric Au(III) chelates is strongly manifest in their markedly different ΔH and ΔS values. Specifically, the 1*S*,2*S* enantiomer has more exothermic binding to HSA compared with the 1*R*,2*R* enantiomer. However, the reverse (compensatory) scenario applies for ΔS with the 1*R*,2*R* enantiomer having a somewhat more favourable (though still negative) change in entropy for its reaction with HSA.

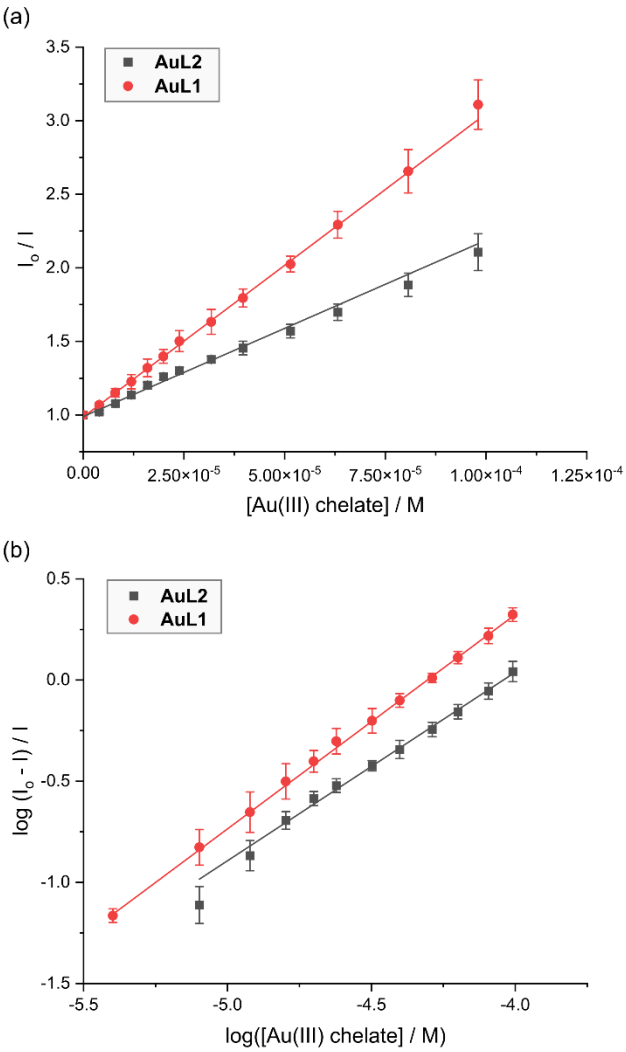


Fig. 3 (a) Stern-Volmer (SV) fluorescence intensity ratio plots for human serum albumin (HSA, 5.0 μM) recorded as a function of the concentration of **AuL1** and **AuL2** (50 mM KH_2PO_4, pH 7.50) at 37 °C. Error bars are ESD's based on the average of three independent determinations. The data are well-fitted by eq. 1 for linear SV emission behaviour. (b) Double logarithm plot of the fractional change in fluorescence intensity for human serum albumin (HSA, 5.0 μM) recorded as a function of the concentration of **AuL1** and **AuL2** (50 mM KH_2PO_4, pH 7.50) at 37 °C. Error bars are ESD's based on the average of three independent determinations. The data are described by eq. 3, which affords the affinity constant and stoichiometric coefficient for the reaction (Table 1).

The Gibbs-Helmholtz relationship (eq. 5) graphically confirms the enthalpy-driven uptake of both **AuL1** and **AuL2** by HSA (Fig. 4c, data located in the upper right quadrant) and,

furthermore, emphasises the distinctly more favourable heat of reaction for the 1*S*,2*S* enantiomer relative to the 1*R*,2*R* enantiomer. For both **AuL1** and **AuL2**, spontaneity is assured because changes in $\Delta H/\Delta G$ are compensated for by commensurate changes in $T\Delta S/\Delta G$. Because the data set is currently small (two enantiomeric compounds) we compared the $T\Delta S/\Delta G$ and $\Delta H/\Delta G$ values measured for **AuL1** and **AuL2** with three similar achiral metal Schiff base chelates (Fig. S24). From Fig. S24, it is clear that the Gibbs-Helmholtz relationship is steadfastly upheld by the current reactions of HSA with related d^8 metal chelates, irrespective of their chirality. Notably, the data yield a defined sequence along the straight-line graph with chelates of the heavier metals tending towards reactions governed by favourable entropy *and* enthalpy changes (bottom right quadrant: $\Delta H < 0$, $\Delta S > 0$).

Table 2. Thermodynamic parameters for the binding of **AuL1** and **AuL2** by HSA in 50 mM KH_2PO_4 buffer at pH 7.50.

Compound	T (K)	ΔG (kJ mol^{-1})[a]	ΔH (kJ mol^{-1})[a]	ΔS (kJ K^{-1} mol^{-1})[a]
AuL1	288	−29.36 (0.1)		
	298	−27.53 (0.1)	−82.0 (3.7)	−0.183 (0.1)
	310	−25.34 (0.2)		
AuL2	288	−26.24 (0.2)		
	298	−25.50 (0.4)	−56.0 (0.3)	−0.103 (0.1)
	310	−23.97 (0.2)		

[a]The estimated standard deviations of the least significant digits are given in parentheses.

The main binding interactions of the **AuL1** and **AuL2** with HSA are probably London dispersion forces of attraction since neither **AuL1** nor **AuL2** have typical H-bond donor or acceptor groups such as carboxylates, alcohols, or amines. The pyrrole rings could possibly engage in π-type interactions with protein residues, while the bridging cyclohexyl ring would partake in London forces of attraction (hydrophobic interactions).

Fluoroprobe site displacement assays

To determine the preferred binding site(s) for **AuL1** and **AuL2** we carried out a competitive blocking assay by fluorescence spectroscopy in which both Au(III) chelates were titrated into solutions of native HSA and solutions of HSA that were pre-equilibrated with either warfarin or dansylglycine. From X-ray crystallography, warfarin binds specifically in Sudlow's site I (subdomain IIA).[62] No X-ray structure of HSA bound to dansylglycine has been reported, but dansylglycine has been shown to primarily bind in Sudlow's site II (subdomain IIIA).[63]

Although HSA has numerous drug binding sites,[64] which can complicate interpretation of the data, the idea here is that displacement of warfarin from HSA•{warfarin} by the incoming Au(III) chelate (ligand) would signal binding in Sudlow's site I, while displacement of dansylglycine from HSA•{dansylglycine} would suggest uptake of the Au(III) chelate in Sudlow's site II. Complications are anticipated if blocking either Sudlow's site I or II site redirects binding of the incoming Au(III) chelate to an alternative drug binding site within HSA (or simply hinders its uptake by allosteric inhibition). Despite these potential limitations, changes in the logK_a, n, and K_{SV} values along with displacement of the fluoroprobe itself can help elucidate a possible binding site for the ligand of interest.

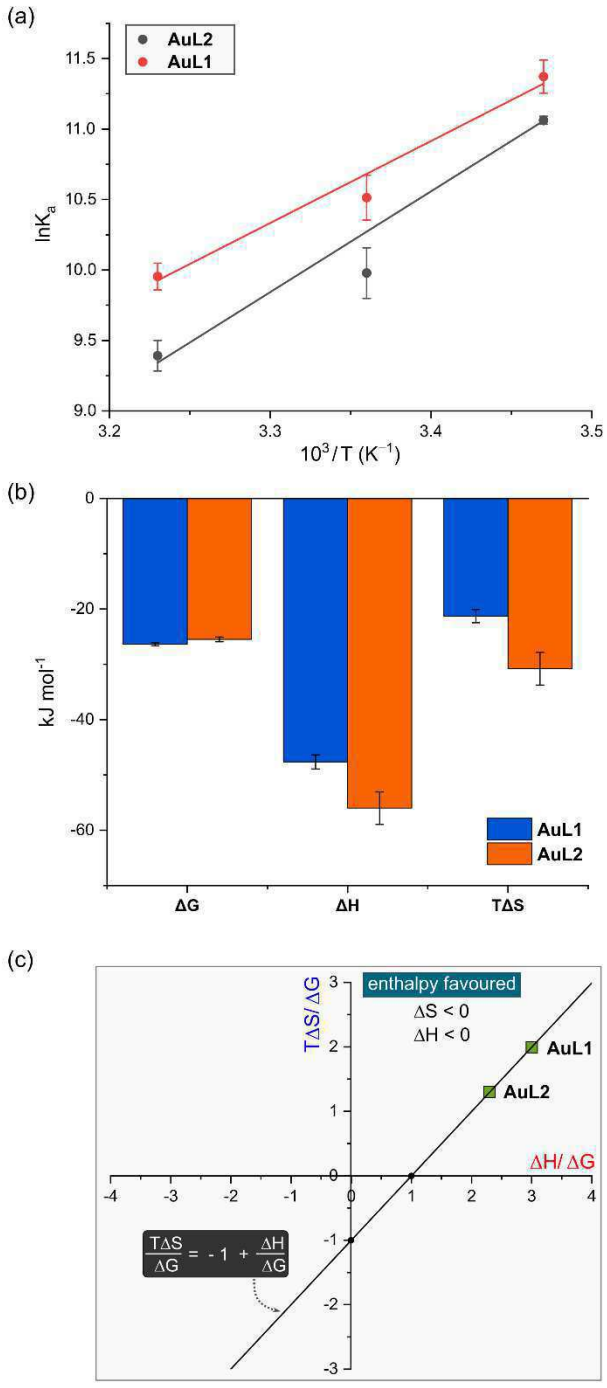


Fig. 4 (a) Linear van't Hoff plots (eq. 4) for the reactions of **AuL1** and **AuL2** with HSA in 50 mM KH_2PO_4 buffer at pH 7.50. (b) Comparison of the thermodynamic parameters governing the reactions of **AuL1** and **AuL2** with HSA (T = 298 K). (c) All measurements were done in triplicate. Derived parameters were individually averaged. Error bars are estimated uncertainties of the mean for both graphs. (c) Plot of the Gibbs-Helmholtz relationship (eq. 5) for the reaction of **AuL1** and **AuL2** with HSA at 298 K in 50 mM KH_2PO_4 buffer at pH 7.50. For all reactions, $\Delta G < 0$.

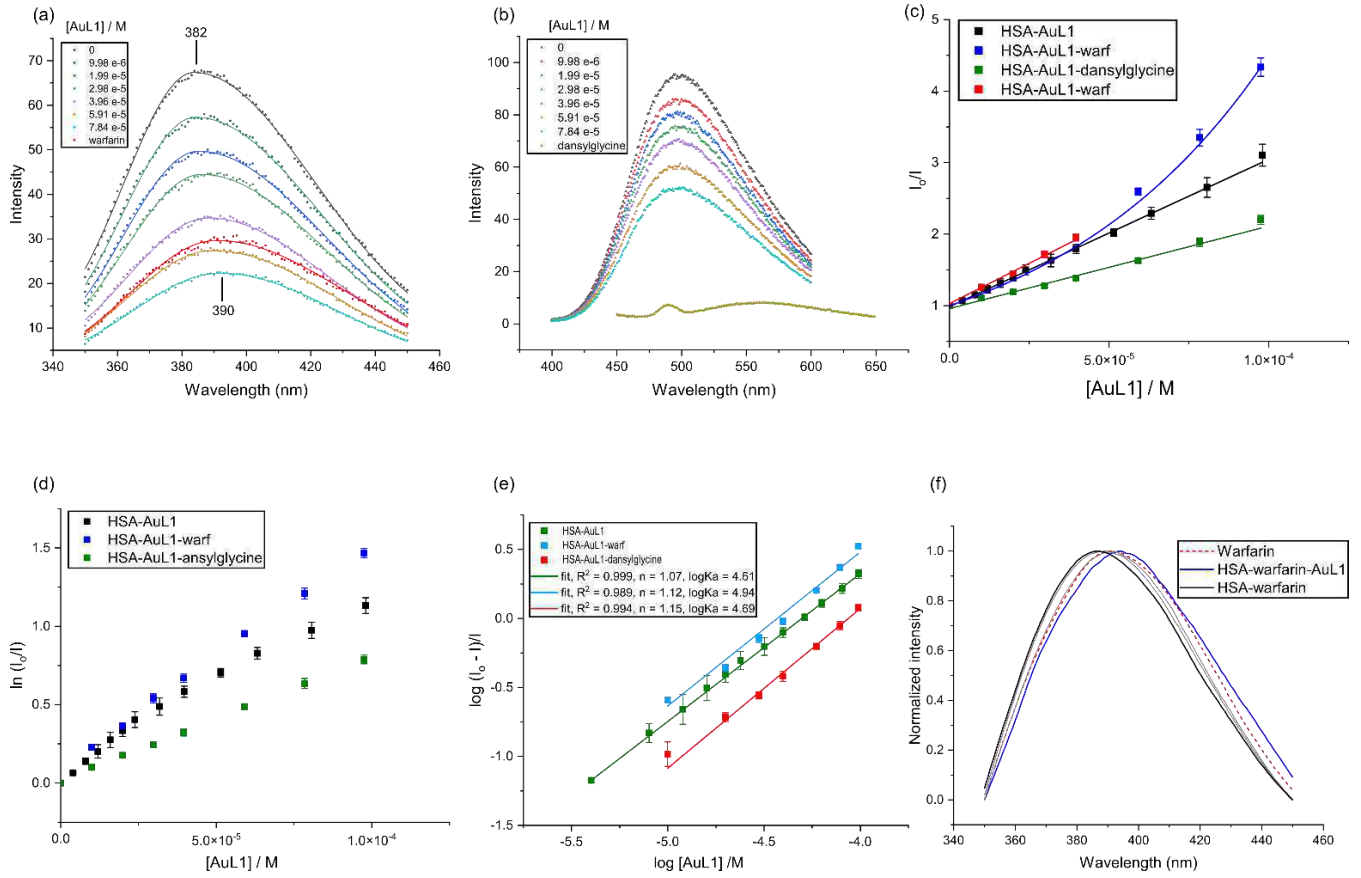


Fig. 5 Binding site determination for the reaction of **AuL1** with HSA (5.0 μM protein, 50 mM KH_2PO_4, pH 7.50, 298 K). (a) Emission spectra of HSA···warfarin (5.0 μM warfarin λ^{ex} = 320 nm) recorded as a function of the concentration of **AuL1** at 298 K. The spectra are fitted by single Gaussian functions to locate the emission maxima. Correlation coefficients, R^2, ranged from 0.990 to 0.999. (b) Emission spectra of HSA···dansylglycine (5.0 μM dansylglycine λ^{ex} = 340 nm) recorded as a function of the concentration of **AuL1** at 298 K. The spectra are fitted by single Gaussian functions to locate the emission maxima. Correlation coefficients, R^2, ranged from 0.990 to 0.999. (c) Stern–Volmer (SV) plot for native HSA, HSA···Warfarin, and HSA···dansylglycine as a function of the concentration of **AuL1** at 298 K. The plots are linear with an intercept of 1.0 when static quenching is operative (i.e., the quencher binds to the target protein and fluorophore(s)). The excitation and emission wavelengths for the fluorophore probes were: (i) Trp-214 (native HSA), λ^{ex} = 295 nm, λ^{em} = 340 nm; (ii) Warfarin (HSA-Warf), λ^{ex} = 320 nm, λ^{em} = 382 nm, and (iii) dansylglycine, λ^{ex} = 340 nm, λ^{em} = 500 nm. (d) Sphere of action model plot, $ln\left(\frac{I_0}{I}\right) = K_{SV}^{app}[Q]$, for the system. A linear plot with a zero intercept indicates static quenching by **AuL1** bound in some way to the fluorophore/macromolecule. Negative deviation from linearity signals a switch from static to dynamic quenching. (e) Double-log plot (eq. 4) of the fluorescence quenching data, $log\left(\frac{I_0-I}{I}\right) = logK + nlog[Q]$, to enable measurement of log*Ka* and the reaction stoichiometry (*n*). (f) Normalised fluorescence emission spectrum of HSA···warfarin (5.0 μM warfarin λ^{ex} = 320 nm) recorded as a function of the concentration of **AuL1** at 298 K to show the displacement of warfarin from HSA. Error bars indicate the standard deviation of three independent experiments.

AuL1 and **AuL2** (0–9.76 x 10^{-5} M) were titrated into a solution of HSA preequilibrated with either HSA•{warfarin} or HSA•{dansylglycine}. The fluorescence emission spectra of both probe fluorophores are presented in Figs. 5a and 5b (and Figs. S22a and S22b). The HSA•{warfarin} fluorescence λ_{max}^{em} peaked at 382 nm, which was blue-shifted by 8 nm from that of free warfarin (λ_{max}^{em} = 390 nm). Titration of **AuL1** and **AuL2** into the HSA•{warfarin} solution resulted in a monotonic decrease in fluorescence intensity with increasing ligand dose (Figs. 5a and S22a). The percentage displacement of warfarin is presented Fig. S23.

Further evidence of warfarin being displaced from HSA is the redshift of the warfarin fluorescence emission intensity peak from 382 nm (HSA•{warfarin}) to 390 nm (free warfarin emission peak).

The HSA•{dansylglycine} fluorescence emission spectrum peaked at 500 nm, which was a red shift of 58 nm from the free dansylglycine peak at 500 nm (Fig 5b and Fig S22b). Titration **AuL1** and **AuL2** into the HSA•{dansylglycine} solution resulted in the fluorescence λ_{max}^{em} intensity to decrease monotonically with increasing concentration of the gold(III) chelates (Fig 5b and Fig. S22b). The suspected percentage displacement of dansylglycine is presented Fig. S23. Unlike the fluorescence emission spectrum of HSA•{warfarin}, there is no peak shift of HSA•{dansylglycine} to free dansylglycine to suggest dansylglycine is being displaced from HSA. Quenching of the HSA•{dansylglycine} fluorescence by **AuL1** and **AuL2** could reflect quenching by FRET or changing the microenvironment surrounding the fluorophore. To further investigate the binding mechanism of the gold(III) cyclohexane chelates to HSA•{warfarin} and HSA•{dansylglycine}, we used the Stern-

Volmer equation (eq. 1), the sphere of action model (eq. 6) and evaluated the binding using the double logarithmic plot (eq. 3; Fig. 5c - e and Fig. S22c -e).

The Stern-Volmer plot for native HSA and HSA•{dansylglycine} was linear throughout, however, HSA•{warfarin} Stern-Volmer plot deviated from linearity, the deviation suggests two quenching mechanisms are occurring. We propose the linear portion (40 μM of **AuL1** and **AuL2**) was static quenching of warfarin, thereafter the deviation from linearity is a mechanistic switch from static to dynamic quenching and, this is a result of the displacement of warfarin, and warfarin is now quenched by the aqueous KH_2PO_4 buffer.
The Sphere of action model is a convenient interpretation of the nonlinear Stern-Volmer plot for the HSA-Au(III) cyclohexane chelate system.[57,65] It invokes the presence of a sphere of a finite volume around Trp-214 in which the probability of the quencher (Q) inducing fluorescence quenching is unity.[54] The "sphere of action model" is described by eq's. 5 and 6,

$$\frac{I_0}{I} = e^{(K_{SV}^{app}[Q])} \quad (6)$$

$$ln\left(\frac{I_0}{I}\right) = K_{SV}^{app}[Q] \quad (7)$$

where K_{SV}^{app} is the apparent static fluorescence quenching constant.

Our interpretation of the site displacement of **AuL1** and **AuL2** is that neither chelates displace dansylglycine from HSA•{dansylglycine} only warfarin is displaced; however, the presence of either fluorescent probe enhances the binding of both chelates as the logK_a values. **AuL1** logK_a values increase from 4.55 $\pm$ 0.11 (n_{total} = 1.05 $\pm$ 0.001) in the native protein to 4.94 $\pm$ 0.23 (n_{total} = 1.13 $\pm$ 0.04) and 4.74 $\pm$ 0.17 ($n$total = 1.19 $\pm$ 0.03) in HSA•{warfarin} and HSA•{dansylglycine}, respectively. Based on the logK_a and K_{SV} values each gold(III) cyclohexane chelate, both binds to HSA by the same mechanism. One interpretation is that each cyclohexane chelates bind to HSA, one in subdomain IIA and a second one binds to an alternative site in close proximity to dansylglycine to quench its fluorescence (via FRET). Therefore, both subdomain IIA and IIIA of the native protein (i.e., half- or fractionally-saturate the two sites so that n_1 + n_2 = $n$total = 1.36), but that when a drug is already located in one of these two sites, the reciprocal unbound site is fully saturated by the metal chelate. Furthermore, the presence of the drug in the alternative site may induce conformational changes to HSA, allowing HSA to have an overall higher binding affinity. This suggests a classic structural synergistic or allosteric effect (cooperative binding). A third binding site cannot be ruled out as dansylglycine is not displaced, there are several alternate binding sites known for HSA[64] and are located in subdomains IB (bilirubin[66] and hemin binding site[36]) and IIIB (propofol binding site,[98]). If both gold(III) cyclohexane molecules bind to subdomain IIIB which adjacent to IIIA in the protein, thereby facilitating efficient additive quenching of the fluorescence from bound dansylglycine.

Far-UV-CD spectroscopy

Conformational changes to the secondary structure of a protein can be simply determined by far-UV-CD spectroscopy due to the several fingerprint spectral regions (i.e., peptide bonds, aromatic amino acids side chains and disulphide bonds[67]). HSA is an α-helix rich protein, where the α-helices sum up 67% of HSA[68]. In Fig. 6a and 25a we use far-UV-CD spectroscopy (186–260 nm) to delineate how **AuL1** and **AuL2** impacts the secondary structure of the protein. The far-UV-CD spectrum of native HSA displays α-helix rich protein structure with a typical double minimum at 208 $\pm$ 1 nm and 222 $\pm$ 1 nm.[69] The 208 nm electronic transitions is assigned to π–π*, the 222 nm electronic transition is assigned to the n–π* transition, and the 193 nm electronic transition translates to the π–π* transition. All three transitions present are a result of the amide groups of peptide backbone.[67,69]

AuL1 and **AuL2** binding to HSA, results in minimal changes within the secondary structure of the protein even though both chelates bound to HSA with a moderately high (10^5 M^{-1}). Upon the titration of **AuL1** and **AuL2** into HSA the spectrum is altered in a manner indicating both minima at 208 nm and 222 nm approach 0, indicating loss of secondary structure. This was further supported by the maxima at 193 nm amplitude decreasing.

To quantify the changes in the secondary structure of HSA upon binding of **AuL1** and **AuL2** we analysed the far-UV-CD spectrum further using JASCO Spectra Manager™[70] to calculate the percentage composition of α-helical coils present in HSA···gold(III) cyclohexane chelate complex (Table S3). The dominant secondary structure domains are α-helices (~58%), and unordered coils (~31%). The α-helicity of HSA was ~58% but was reduced for the protein in the presence of both **AuL1** (4.41%) and **AuL2** (3.77%). Interestingly, the solution state secondary structure composition for HSA differs from that of native HSA in the solid state[35] (68.5% α-helix, 0% β-sheet, 9.6% turns, and 21.9% unordered coils; PDB code 1BM0 analysed with BeStSel[71]). However, our solution Far-CD data is consistent with solution state spectral decompositions reported previously.[72–74] Overall it is accepted that enhanced subdomain mobility and general thermal motion/disorder accounts for the decrease of α-helicity.[69,75]

Near UV-CD spectroscopy

To explain the conformational structural changes induced by the gold(III) cyclohexane chelates to the tertiary structure of HSA, we utilised near-UV-CD spectroscopy between 250–310 nm (Fig. 6a, Fig. S25). A standard near- UV–CD spectrum is controlled by the fine structure of Trp (285–300 nm), Tyr (275–285 nm) and Phe (250–270 nm). Important transition peaks of HSA observed were the two minima at 262 and 280 nm and a maxima at 290 nm which are a result of disulphide bonds and the aromatic amino acids.[76]

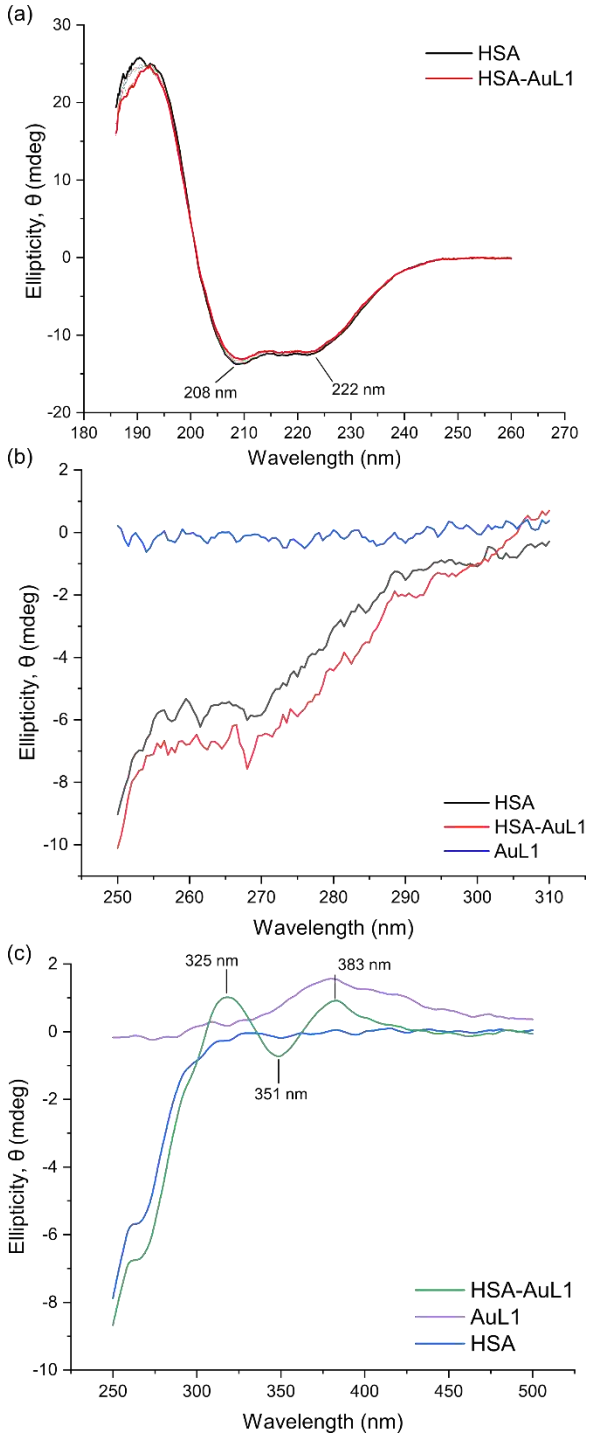


Fig.6 (a) Plot of the far-UV CD spectra of native HAS (300 nM) and the protein incubated with saturating doses of **AuL1** recorded at 298 K in 50 mM KH_2PO_4 buffer at pH 7.50. The spectra indicate native HSA (black line) and **AuL1** doses ranging from 0.3 μM to 3 μM are grey lines, saturating dose at 6 μM is the red line (Far UV-CD for **AuL2** is given in ESI Fig. S28). (b) Plot of the near UV-visible CD spectra of native HSA (300 nM) and the protein incubated with a saturating dose (6 μM) of **AuL1**. The spectra were recorded at 298 K in 50 mM KH_2PO_4 buffer at pH 7.50.). (c) Plot of spectra of the HSA-**AuL1** complex; it represents the induced CD (ICD) spectrum of HSA-**AuL1** complex, the spectra were smoothed using a Lowess function (0.07 span).

The near-UV-CD spectra of HSA (Fig. 6, S25) in the absence of the gold(III) cyclohexane chelates exhibited a peak at 290 nm with a fine structure between 290–305 nm, due to the Trp-214 residue. Between 275 and 285 nm there a single peak is present at 284 nm and a shoulder at 287 nm this is likely due to the 18 Tyr residues within HSA. The Phe fingerprint region is lies between 255 and 270 nm and displayed a peak at 257 nm. Disulfide bonds within HSA are displayed by the two minima at 262, 268 nm and a shoulder at 279 nm,[67,77,78] HSA has 17 disulfide bonds.[68] Phe, Tyr and Trp all have π-π* transitions (^1L_a and ^1L_b) and have the potential to be directly involved in π bonding. Therefore, perturbations within the proteins fine structure can be associated to conformational changes within a protein or be a result of the aromatic amino acids being placed in a different environment.[79]

Both **AuL1** and **AuL2** induced changes to the near-UV-CD spectra, indicating both chelates bound to the HSA in close enough proximity to affect the fine structure around the aromatic amino acid residues. The result was further supported by the site displacement assay (Fig. 5, S25) indicating **AuL1** and **AuL2** bound to Sudlow's site I, (subdomain IIA containing Trp-214). Furthermore, the 290 nm band had disappeared when **AuL1** bound, however there was no change in the presence of **AuL2**, further evidence indicating **AuL1** bound closer to the Trp-214 than **AuL2**. The 290 nm band was the Trp ^1L_b (0,0) band and the presence of the 279 nm band was attributed to Trp in an aqueous solution (^1L_a),[80,81] likely due to HSA conformational changes. There was no significant shift in the disulfide bond fingerprint region, suggesting negligible change to the bonds. Overall, the binding of **AuL1** and **AuL2** to HSA was shown to induce minor conformational changes in both the secondary (Fig. 6a) and tertiary structure (Fig. 6b) of the protein.

Induced-UV-CD spectroscopy

Induced circular dichroism (ICD) is a phenomenon by which an achiral molecule binds to a chiral host and acquires a CD signal.[63,82,83] An ICD band has a similar absorbance wavelength as the chromophoric portion of the complex and indicates direct complexation between two molecules as shown in Fig. 6c. An achiral molecule will exhibit an ICD signal if the symmetry is perturbed and non-zero rotational strengths are formed.[82] Within the scope of this study both **AuL1** and **AuL2** are chiral and produce CD signals (Fig 6c and S25c). However, when bound to HSA the UV-CD signal of **AuL1** has three peaks at 325 and 383 maxima and 351 nm minima. The peaks were different to the free **AuL1** which had a single maximum at 382 nm. **AuL2**···HSA had a blue shifted peak from 378 nm (free **AuL2**) to 354 nm (**AuL2**···HSA). Furthermore, a 383 nm peak was present for both **AuL1** and **AuL1**···HSA. Finally, **AuL1**-HSA produced a new peak at 351 nm (Fig. 6c).

We propose that HSA binds to and perturbs the **AuL1** and **AuL2** via two mechanisms (i) intermolecular interactions and (ii) restricting conformational freedom.[83] For an ICD signal, the protein (host) interaction with the small molecule must occur in a preferred orientation that does not allow the ICD signal to be cancelled out. Therefore, ICD is a good indicator of illustrating an increase in structure order.[84,85] In Fig 6c and S25c we observe

shifts in the ICD bands compared to where the free Au(III) cyclohexane chelates maximum absorbance would occur.

NCI-60 cytotoxicity screens

AuL1 and **AuL2** were accepted for single-dose NCI-60 cytotoxicity screens (10 µM test agent concentration) by the NCI (Bethesda, MD). Both **AuL1** and **AuL2**, were shown to possess cytotoxic activity against the 60 cancer cell lines with a mean growth percentage of 56.5% and 89.1%, respectively. Since, **AuL1** was the more active of the gold(III) cyclohexane chelates, it was selected to undergo NCI-60 five dose screen which spanned a concentration range of 10^{-8}–10^{-4} M (cytotoxicity data for **AuL1** and **AuL2** over the NCI's panel of 60 human cancer cell lines are available in the Supporting Information.).

Table 3 Summary of the average cytotoxicity data over 60 human cancer cell lines for compounds **AuL1** as well as selected commercial cytotoxic agents for comparison.

Drug	GI_{50} (µM)	IC_{50} (µM)	LC_{50} (µM)
AuL1	4.7	9.3	39.8
Cisplatin	2.0	27	>100
Carboplatin	99.6	>100	>100
$[Au^{3+}(terpy)Cl]Cl_2$	0.13	11	73
Mitomycin	0.71	6.5	18
Camptothecin	0.040	0.89	33

From the five-dose screen of **AuL1**, the lowest IC_{50} values were for the ovarian cancer cell lines non-small lung cancer NCI-522 (2 µM), colon cancer cell line SW-620 (2.57 µM)and the OVCAR-3 (2.95 µM), and the. Fig. 7 compares the best GI_{50} values for **AuL1** with analogous data for clinically deployed anticancer therapeutics that have definitive mode of action (MOAs).

Mean cytotoxicity parameters for compound **AuL1** obtained for each of the nine classes of human cancer in the NCI-60 screen are listed in Fig. S26. Collectively, the data indicate that Leukaemia and melanoma cancer cell lines are, on average, the most susceptible to the gold(III) cyclohexane complex with GI_{50} and IC_{50} values below 10 and 20 µM, respectively.

Assessment of Fig. 7 and Table 3 highlight a noteworthy point, the cytotoxicity of **AuL1**. The GI_{50} of **AuL1** is not as low as the commercial anti-cancer therapeutics. However, the IC_{50} and LC_{50} values are lower than both cisplatin, carboplatin and are within range of mitomycin. From Fig. 7, the steepness of curve indicates that the initial concentration of **AuL1** necessary to induce cell death is high in comparison to the commercially available drugs. But, once this concentration has been reached, relatively low increases in **AuL1** concentration led to high levels of cell mortality. To further highlight this fact, we compare **AuL1** to camptothecin, which is a powerful topoisomerase I inhibitor obtained as a natural product extract.

For 50% growth inhibition (a 25 % cell mortality rate), on average, a concentration of 4.7 µM of the **AuL1** is required. To induce a 75% cell death rate (LC_{50}) only an 8-fold increase in concentration is required, giving a concentration of 39.8 µM. For camptothecin to induce the same results, an increase in concentration of 825-fold is required, i.e., from 0.040 µM to 33µM. These numbers illustrate the difference in the steepness of the dose-response curves (Figure 7). It is important to note that a commercially successful anticancer compound does not need to only rely on GI_{50} values, an example is fluorouracil displays that only moderate cytotoxicity (for many cell lines the GI_{50} exceeds 10 µM), however, the drug is a widely prescribed antineoplastic antimetabolite.[86]

Despite the reduced toxicity **AuL1** compared to taxol and daunorubicin, **AuL1** is still more active than cisplatin, 5-fluorouracil and, in many cases, mitomycin. It, therefore, exhibits sufficient cytotoxicity to be used as effective chemotherapeutic agents for the treatment of several tumour cell lines, particularly leukaemia cell lines. It is also important to acknowledge that despite the increased cytotoxicity of drugs such as taxol and daunorubicin, these drugs are often not the first choice of oncologists for the treatment of various

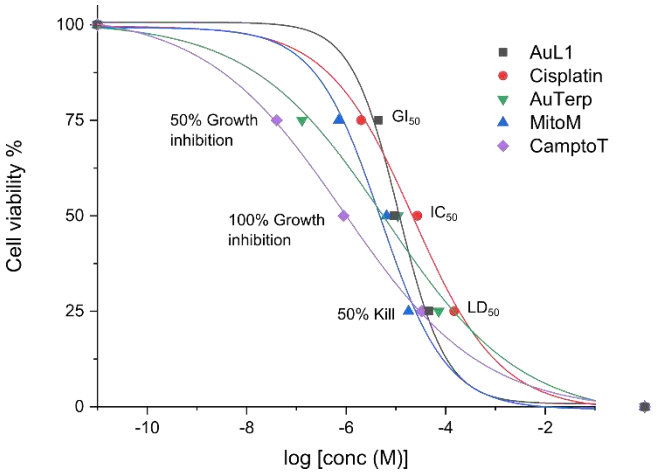


Fig. 7 Mean NCI-60 GI_{50}, IC_{50} and LC_{50} curves for three commercial anti-cancer agents (cisplatin, mitomycin and campthocein), Au(III)-Terpy and **AuL1** (synthesised in this work). Data was obtained from the DTP drug respiratory data base.[3]

tumours.[87,88] This is due to the fact that these drugs, and many others, particularly strong DNA alkylating agents, have been implicated in the onset of secondary cancers.[87,88] These secondary cancers are most commonly types of leukaemia, and are associated with the initial treatment of solid tumours during childhood.[89]

Why the 1S,2S (AuL1 enantiomer is more active than the 1R,2R (AuL2)?

Both **AuL1** and **AuL2** are chiral molecules, with **AuL1** being more active. The effect of chirality is well understood in drug design.[90] A probable reason for **AuL1** being more active than **AuL2** is that majority of proteins in the cellular environment are said to be "left-handed" since they are made up of amino acids which are mostly L-enantiomers.[91] It would appear that the (1*S*,2*S*)-enantiomer interacts more favourably with its cellular target within this lefthanded environment. It is well known that enzymes react specifically with certain substrates, and it is now believed that many drug receptors are similarly more accessible to some enantiomers.[90] Accordingly, the efficacy of one enantiomer is often heightened over the opposite enantiomer.[91,92]

In many cases one enantiomer is more active than the other. However, in some cases one enantiomer can induce undesirable side-effects. It would appear, in this case, that the (1*R*,2*R*)-enantiomer binds less strongly to the drug receptor site and as such induces a lower cytotoxicity than the (1*S*,2S)-enantiomer. This is not unexpected since it is believed that drug receptors are capable of changing their receptor site geometry to accommodate both enantiomers individually, although, inevitably, one of the enantiomers will bind more strongly to the receptor site and hence induce a greater therapeutic effect.[90] A second possibility is that the (1*S*,2S)-enantiomer is metabolised by the tumour cells more strongly to the receptor site and hence induce a greater therapeutic effect.[90] A difference in the rate of metabolism has been shown previously to affect the efficacy of one enantiomer over another.[91] In this work each enantiomer was screened separately against human cancer cell lines. In many cases drugs are administered as a racemate with equal efficacy.[90–92] It is possible that a mixture of the two enantiomers, which would be considerably more cost effective to produce, could be used with equal cytotoxic effects. This would, however, only be possible if the toxicology and metabolism of each enantiomer was fully understood.[92]

Mechanism of action

The cell screening data has shown that the **AuL1** is an effective chemotherapeutic agent. With the establishment of its cytotoxicity, the determination of the mode of action for **AuL1** is the next critical step for its development as chemotherapeutic agent. There is minimal knowledge for the mode of action of many chemotherapeutic agents, particularly metal-based compounds, therefore, determination of the specific mode of action of **AuL1** is critical to the further development of metal-based therapeutics.

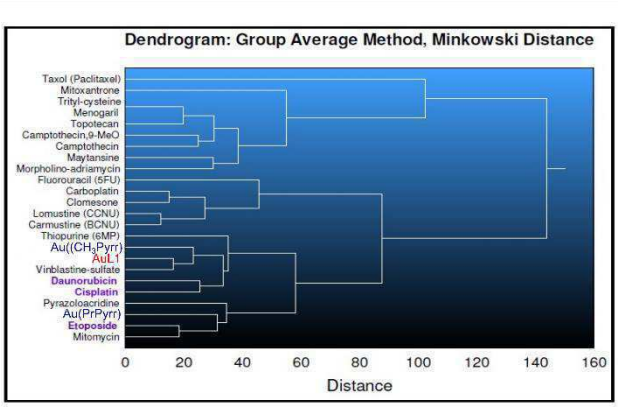


Fig. 8 Comparison of the activity profile of commercial drugs with a known mode of action, the previously patented Au(CH_3Pyrr) and Au(PrPyrr)[4] and **AuL1** synthesised in this work.

A major advantage of having **AuL1** screened for cytotoxicity by the NCI is that they are tested against a wide panel of cancer cell lines. For each cancer cell line, 180 data points are generated for **AuL1**. This large quantity of data makes it possible to accurately compare the cytotoxicity profiles of **AuL1** with those of compounds with a known mechanism of action, provided they have gone through the same screening process. This data has made it possible to perform hierarchical cluster analysis. Which is the only means for achieving a reliable statistical comparison of the cytotoxicity profiles of multiple compounds. There are several well-established methods for effecting this type of cluster analysis. Irrespective of the method chosen, the result is a grouping together of compounds with a similar cytotoxicity profile, the more similar the profile the tighter the grouping. If a compound of unknown mode of action is clustered with several compounds of known mode of action, which has been determined independently, then it is highly probable that the compound with the unknown mode of action will share the same mechanism of action as those compounds that it has been clustered with. A dendogram, using a group average method and Minkowski distance, was prepared **AuL1** along with 21 compounds of known mode of action (Fig. 8).

The dendogram in Fig. 8, obtained via hierarchical cluster analysis of the GI_{50}, IC_{50} and LC_{50} values for a range of commercial chemotherapeutic agents with known mechanisms of action, shows the probable mechanism of action for the new compounds. The cluster analysis shows that **AuL1** has been clustered with vinblastine sulphate which is an anti-microtubile drug that is similar to taxol[93], but with an opposite mode of action. Furthermore, the clustered with daunorubicin, cisplatin and more distantly to etoposide. The mechanism of cytotoxicity of **AuL1** is not clear. This is not surprising since titrations of **AuL1** with ctDNA had no detectable binding affinity, therefore its mode of action needs to be investigated further.

Conclusions

The interaction of **AuL1** and **AuL2** with HSA was investigated by complementary spectroscopic techniques to understand how the chirality of the cyclohexane bis(pyrrolide-imine) chelates affects ligand uptake by the protein. Both gold(III) chelates quenched the intrinsic Trp-214 fluorescence of HSA via a dynamic quenching mechanism and gave K_a values typical of small molecules binding to HSA (~10^4 M^{-1}).[94,95] The Stern-Volmer quenching constants (K_{SV}) and K_a values for **AuL1** were greater than **AuL2**. The present ligands bind to HSA with *negative* ΔH, ΔG and ΔS values, reflecting a spontaneous enthalpy-driven process governed by van der Waals (London dispersion) forces as well as H-bonding. $T\Delta S/\Delta G$ and $\Delta H/\Delta G$ for both gold(III) cyclohexane chelates were in the upper right corner. Both **AuL1** and **AuL2** preferred Sudlow's site I in HSA and both gold(III) cyclohexane chelates minimally perturbs the protein's secondary structure. The induced CD spectra recorded for the metal chelates bound to HSA strikingly confirm uptake of the intact complexes without imine group hydrolysis or demetallation. Finally, both **AuL1** and **AuL2** were tested against 60 cancer cell lines (NCI-60) and had a mean growth percentage of 56.5% and 89.1%, respectively. **AuL1** had undergone phase two NCI-60 testing which is a five dose response and the GI_{50}, IC_{50} and LC_{50} values were 4.7, 4.3 and 39.8 μM respectively. The dendrogram clustered **AuL1** with vinblastine sulphate which is an anti-microtubile drug that is similar to taxol, the lack of DNA binding suggests **AuL1** has a unique mode of action as compared typical gold(III) drugs and the target still needs to be identified.

Author Contributions

O. Q. M. and S. S. co-designed the study. S. S. synthesised and characterised the ligands, carried out the spectroscopy, and initial X-ray crystallography, and collated the thermodynamic data. NCI-60 data and analysis were obtained from M. P. A. The final data analysis was performed by S. S. and O. Q. M, who also completed the final X-ray crystallography section The manuscript and figures were written and produced by S. S and O. Q. M.

Conflicts of interest

The authors have no conflicts to declare.

Acknowledgements

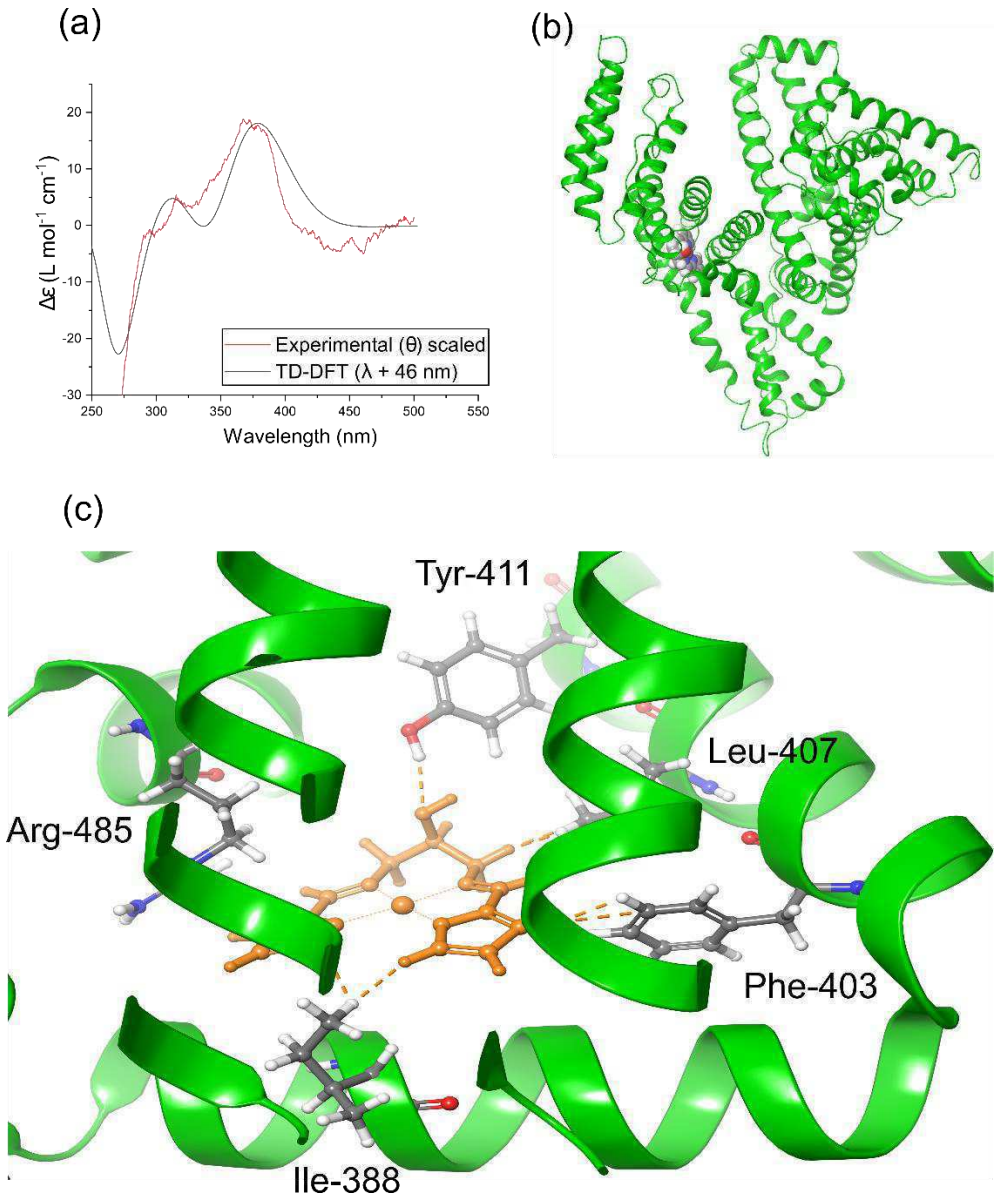
This work is based on research supported by the South African Research Chairs Initiative of the Department of Science and Innovation (DSI) and National Research Foundation (NRF) of South Africa (Grant No 64799, OQM). The authors thank WITS University and the NRF for funding to purchase a JASCO J-1500 MCD spectrometer (Grant No 116177, OQM) and a dual-wavelength Bruker D8 Venture X-ray diffractometer (Grant No 129920, OQM). We also thank the Centre for High Performance Computing (Project CHEM1065, CHPC, Cape Town) for both the CPU time and resources needed for the DFT simulations.

References

1 R. L. Siegel, K. D. Miller, H. E. Fuchs and A. Jemal, *CA. Cancer J. Clin.*, 2022, **72**, 7–33.
2 E. J. Anthony, E. M. Bolitho, H. E. Bridgewater, O. W. Carter, J. M. Donnelly, C. Imberti, E. C. Lant, F. Lermyte, R. J. Needham and M. Palau, *Chem. Sci.*, 2020, **11**, 12888–12917.
3 A. Frei, J. Zuegg, A. G. Elliott, M. Baker, S. Braese, C. Brown, F. Chen, C. G. Dowson, G. Dujardin, N. Jung, A. Paden King, A. M. Mansour, M. Massi, J. Moat, H. A. Mohamed, A. K. Renfrew, P. J. Rutledge, P. J. Sadler, M. H. Todd, C. E. Willans, J. J. Wilson, M. A. Cooper and M. A. T. Blaskovich, *Chem. Sci.*, 2020, **11**, 2627–2639.
4 B. Rosenberg, L. Van Camp and T. Krigas, *Nature*, 1965, **205**, 698–699.
5 C. J. Ziegler, A. P. Silverman and S. J. Lippard, *JBIC J. Biol. Inorg. Chem.*, 2000, **5**, 774–783.
6 L. Kelland, *Expert Opin. Investig. Drugs*, 2007, **16**, 1009–1021.
7 M. J. Hannon, *Pure Appl. Chem.*, 2007, **79**, 2243–2261.
8 T. C. Johnstone, K. Suntharalingam and S. J. Lippard, *Chem. Rev.*, 2016, **116**, 3436–3486.
9 S.-H. Chen and J.-Y. Chang, *Int. J. Mol. Sci.*, 2019, **20**, 4136.
10 L. Amable, *Pharmacol. Res.*, 2016, **106**, 27–36.
11 C. R. Wilson, A. M. Fagenson, W. Ruangpradit, M. T. Muller and O. Q. Munro, *Inorg. Chem.*, 2013, **52**, 7889–7906.
12 K. J. Akerman, A. M. Fagenson, V. Cyril, M. Taylor, M. T. Muller, M. P. Akerman and O. Q. Munro, *J. Am. Chem. Soc.*, 2014, **136**, 5670–5682.
13 D. van der Westhuizen, C. A. Slabber, M. A. Fernandes, D. F. Joubert, G. Kleinhans, C. J. van der Westhuizen, A. Stander, O. Q. Munro and D. I. Bezuidenhout, *Chem. – Eur. J.*, 2021, **27**, 8295–8307.
14 V. Milacic, D. Chen, L. Ronconi, K. R. Landis-Piwowar, D. Fregona and Q. P. Dou, *Cancer Res.*, 2006, **66**, 10478–10486.
15 G. Marcon, S. Carotti, M. Coronnello, L. Messori, E. Mini, P. Orioli, T. Mazzei, M. A. Cinellu and G. Minghetti, *J. Med. Chem.*, 2002, **45**, 1672–1677.
16 B. Bertrand, M. R. M. Williams and M. Bochmann, *Chem. – Eur. J.*, 2018, **24**, 11840–11851.
17 A. Casini, C. Hartinger, C. Gabbiani, E. Mini, P. J. Dyson, B. K. Keppler and L. Messori, *J. Inorg. Biochem.*, 2008, **102**, 564–575.
18 A. Casini and L. Messori, *Curr. Top. Med. Chem.*, 2011, **11**, 2647–2660.
19 C. Gabbiani, A. Casini, L. Messori, A. Guerri, M. A. Cinellu, G. Minghetti, M. Corsini, C. Rosani, P. Zanello and M. Arca, *Inorg. Chem.*, 2008, **47**, 2368–2379.
20 C.-M. Che, R. W.-Y. Sun, W.-Y. Yu, C.-B. Ko, N. Zhu and H. Sun, *Chem. Commun.*, 2003, 1718–1719.
21 R. D. Teo, H. B. Gray, P. Lim, J. Termini, E. Domeshek and Z. Gross, *Chem. Commun.*, 2014, **50**, 13789–13792.
22 B. Bertrand, J. Fernandez-Cestau, J. Angulo, M. M. D. Cominetti, Z. A. E. Waller, M. Searcey, M. A. O'Connell and M. Bochmann, *Inorg. Chem.*, 2017, **56**, 5728–5740.
23 L. Messori, F. Abbate, G. Marcon, P. Orioli, M. Fontani, E. Mini, T. Mazzei, S. Carotti, T. O'Connell and P. Zanello, *J. Med. Chem.*, 2000, **43**, 3541–3548.
24 V. Bhardwaj, D. Gumber, V. Abbot, S. Dhiman and P. Sharma, *RSC Adv.*, 2015, **5**, 15233–15266.
25 R. N. Brogden, R. C. Heel, T. M. Speight and G. S. Avery, *Drugs*, 1978, **15**, 429–450.
26 H. D. Langtry and J. A. Balfour, *Drugs*, 1998, **55**, 563–584.
27 M. Atkins, C. A. Jones and P. Kirkpatrick, *Nat. Rev. Drug Discov.*, 2006, **5**, 279–280.
28 S. Hannah, V. M. Lynch, N. Gerasimchuk, D. Magda and J. L. Sessler, *Org. Lett.*, 2001, **3**, 3911–3914.
29 J. L. Sessler, T. D. Mody, G. W. Hemmi and V. Lynch, *Inorg. Chem.*, 1993, **32**, 3175–3187.
30 H. Patel, R. Mick, J. Finlay, T. C. Zhu, E. Rickter, K. A. Cengel, S. B. Malkowicz, S. M. Hahn and T. M. Busch, *Clin. Cancer Res.*, 2008, **14**, 4869–4876.
31 K. J. Akerman, A. M. Fagenson, V. Cyril, M. Taylor, M. T. Muller, M. P. Akerman and O. Q. Munro, *J. Am. Chem. Soc.*, 2014, **136**, 5670–5682.
32 R. Gupta, C. Rodrigues Felix, M. P. Akerman, K. J. Akerman, C. A. Slabber, W. Wang, J. Adams, L. N. Shaw, Y.-C. Tse-Dinh, O. Q. Munro and K. H. Rohde, *Antimicrob. Agents Chemother.*, 2018, **62**, e01696-17.
33 M. P. Akerman, O. Q. Munro, M. Mongane, J. A. van Staden, W. I. D. Rae, C. J. Bester, B. Marjanovic-Painter, Z. Szucs and J. R. Zeevaart, *J. Label. Compd. Radiopharm.*, 2013, **56**, 530–535.
34 S. Curry, *Drug Metab. Pharmacokinet.*, 2009, **24**, 342–357.
35 X. M. He and D. C. Carter, *Nature*, 1992, **358**, 209–215.
36 P. A. Zunszain, J. Ghuman, T. Komatsu, E. Tsuchida and S. Curry, *BMC Struct. Biol.*, 2003, **3**, 6.
37 M. Fasano, S. Curry, E. Terreno, M. Galliano, G. Fanali, P. Narciso, S. Notari and P. Ascenzi, *IUBMB Life*, 2005, **57**, 787–796.
38 G. Rabbani and S. N. Ahn, *Int. J. Biol. Macromol.*, 2019, **123**, 979–990.
39 C. CT, *BACHELOR Sci. Chem. Sess. 20172018 124 Credits 1 Univ. COURSES 20 Credits Course Code Course Name Credit*, **50**, 7.
40 J. D. Dunitz, *ChemBioChem*, 2004, **5**, 614–621.

41 J. A. K. Howard, V. J. Hoy, D. O'Hagan and G. T. Smith, *Tetrahedron*, 1996, **52**, 12613–12622.
42 M.-X. Xie, X.-Y. Xu and Y.-D. Wang, *Biochim. Biophys. Acta BBA - Gen. Subj.*, 2005, **1724**, 215–224.
43 T. P. Jr, *All About Albumin: Biochemistry, Genetics, and Medical Applications*, Academic Press, 1995.
44 O. K. Abou-Zied and O. I. K. Al-Shihi, *J. Am. Chem. Soc.*, 2008, **130**, 10793–10801.
45 J. Ghuman, P. A. Zunszain, I. Petitpas, A. A. Bhattacharya, M. Otagiri and S. Curry, *J. Mol. Biol.*, 2005, **353**, 38–52.
46 Z.-D. Qi, B. Zhou, X. Qi, S. Chuan, Y. Liu and J. Dai, *J. Photochem. Photobiol. Chem.*, 2008, **193**, 81–88.
47 P. R. Callis, *J. Mol. Struct.*, 2014, **1077**, 22–29.
48 A. Divsalar, M. J. Bagheri, A. A. Saboury, H. Mansoori-Torshizi and M. Amani, *J. Phys. Chem. B*, 2009, **113**, 14035–14042.
49 M. H. Gehlen, *J. Photochem. Photobiol. C Photochem. Rev.*, 2020, **42**, 100338.
50 O. K. Abou-Zied and O. I. K. Al-Shihi, *J. Am. Chem. Soc.*, 2008, **130**, 10793–10801.
51 Time-resolved fluorescence studies on site-directed mutants of human serum albumin - Helms - 1997 - FEBS Letters - Wiley Online Library, https://febs.onlinelibrary.wiley.com/doi/10.1016/S0014-5793%2897%2900389-X, (accessed April 25, 2022).
52 K. Flora, J. D. Brennan, G. A. Baker, M. A. Doody and F. V. Bright, *Biophys. J.*, 1998, **75**, 1084–1096.
53 T. K. Maiti, K. S. Ghosh, A. Samanta and S. Dasgupta, *J. Photochem. Photobiol. Chem.*, 2008, **194**, 297–307.
54 S. Soares, N. Mateus and V. de Freitas, *J. Agric. Food Chem.*, 2007, **55**, 6726–6735.
55 M. H. Gehlen, *J. Photochem. Photobiol. C Photochem. Rev.*, 2020, **42**, 100338.
56 G. G. Ariga, P. N. Naik, S. A. Chimatadar and S. T. Nandibewoor, *J. Mol. Struct.*, 2017, **1137**, 485–494.
57 J. R. Lakowicz, *Principles of Fluorescence Spectroscopy*, Springer US, Boston MA, 3rd edn., 2006.
58 P. D. Ross and S. Subramanian, *Biochemistry*, 1981, **20**, 3096–3102.
59 H. Yin, L. Liao and J. Fang, *JSM Clin Oncol Res*, 2014, **2**, 1010.
60 C. Lagercrantz, T. Larsson and I. Denfors, *Comp. Biochem. Physiol. Part C Comp. Pharmacol.*, 1981, **69**, 375–378.
61 H. Rimac, C. Dufour, Ž. Debeljak, B. Zorc and M. Bojić, *Molecules*, 2017, **22**, 1153.
62 I. Petitpas, A. A. Bhattacharya, S. Twine, M. East and S. Curry, *J. Biol. Chem.*, 2001, **276**, 22804–22809.
63 F. S. Graciani and V. F. Ximenes, *PloS One*, 2013, **8**, e76849.
64 J. Ghuman, P. A. Zunszain, I. Petitpas, A. A. Bhattacharya, M. Otagiri and S. Curry, *J. Mol. Biol.*, 2005, **353**, 38–52.
65 S. A. C. Lima, A. Cordeiro-da-Silva, B. de Castro and P. Gameiro, *Biophys. Chem.*, 2007, **125**, 143–150.
66 P. A. Zunszain, J. Ghuman, A. F. McDonagh and S. Curry, *J. Mol. Biol.*, 2008, **381**, 394–406.
67 S. M. Kelly, T. J. Jess and N. C. Price, *Biochim. Biophys. Acta BBA - Proteins Proteomics*, 2005, **1751**, 119–139.
68 X. M. He and D. C. Carter, *Nature*, 1992, **358**, 209–215.
69 N. Sreerama and R. W. Woody, in *Methods in Enzymology*, Academic Press, 2004, vol. 383, pp. 318–351.
70 Z. S. do Monte and C. S. Ramos, *Chirality*, 2013, **25**, 211–214.
71 A. Micsonai, F. Wien, É. Bulyáki, J. Kun, É. Moussong, Y.-H. Lee, Y. Goto, M. Réfrégiers and J. Kardos, *Nucleic Acids Res.*, 2018, **46**, W315–W322.
72 F. Mohammadi, A.-K. Bordbar, A. Divsalar, K. Mohammadi and A. A. Saboury, *Protein J.*, 2009, **28**, 189–196.
73 H. A. Tajmir-Riahi, C. N. N'soukpoé-Kossi and D. Joly, *Spectroscopy*, 2009, **23**, 81–101.
74 O. Duman, S. Tunç and B. Kancı Bozoğlan, *J. Fluoresc.*, 2013, **23**, 659–669.
75 P. Alam, S. K. Chaturvedi, T. Anwar, M. K. Siddiqi, M. R. Ajmal, G. Badr, M. H. Mahmoud and R. Hasan Khan, *J. Lumin.*, 2015, **164**, 123–130.
76 D. Lafitte, P. O. Tsvetkov, F. Devred, R. Toci, F. Barras, C. Briand, A. A. Makarov and J. Haiech, *Biochim. Biophys. Acta BBA-Proteins Proteomics*, 2002, **1600**, 105–110.
77 B. Ahmad, S. Parveen and R. H. Khan, *Biomacromolecules*, 2006, **7**, 1350–1356.
78 C. Sun, J. Yang, X. Wu, X. Huang, F. Wang and S. Liu, *Biophys. J.*, 2005, **88**, 3518–3524.
79 X.-X. Cheng, X.-Y. Fan, F.-L. Jiang, Y. Liu and K.-L. Lei, *Luminescence*, 2015, **30**, 1026–1033.
80 A. Barth, S. R. Martin and P. M. Bayley, *Biopolym. Orig. Res. Biomol.*, 1998, **45**, 493–501.
81 B. Valeur and G. Weber, *Photochem. Photobiol.*, 1977, **25**, 441–444.
82 S. Allenmark, *Chirality*, 2003, **15**, 409–422.
83 D. Tedesco and C. Bertucci, *J. Pharm. Biomed. Anal.*, 2015, **113**, 34–42.
84 G. Gottarelli, S. Lena, S. Masiero, S. Pieraccini and G. P. Spada, *Chirality*, 2008, **20**, 471–485.
85 G. Pescitelli, L. D. Bari and N. Berova, *Chem. Soc. Rev.*, 2014, **43**, 5211–5233.
86 H. Takeda, M. Haisa, Y. Naomoto, R. Kawashima, K. Satomoto, T. Yamatuji and N. Tanaka, *Jpn. J. Cancer Res.*, 1999, **90**, 677–684.
87 A. Eastman, in *Cisplatin: Chemistry and Biochemistry of a Leading Anticancer Drug*, ed. B. Lippert, Wiley, 1999, pp. 111–134.
88 V. M. Guillem, M. Collado, M. J. Terol, M. J. Calasanz, J. Esteve, M. Gonzalez, C. Sanzo, J. Nomdedeu, P. Bolufer and A. Lluch, *Leukemia*, 2007, **21**, 1413–1422.
89 M.-C. Le Deley, T. Leblanc, A. Shamsaldin, M.-A. Raquin, B. Lacour, D. Sommelet, A. Chompret, J.-M. Cayuela, C. Bayle and A. Bernheim, *J. Clin. Oncol.*, 2003, **21**, 1074–1081.
90 T. Liljefors, P. Krogsgaard-Larsen and U. Madsen, *Textbook of drug design and discovery*, CRC Press, 2002.
91 P. Fickers, P.-H. Benetti, Y. Waché, A. Marty, S. Mauersberger, M. S. Smit and J.-M. Nicaud, *FEMS Yeast Res.*, 2005, **5**, 527–543.
92 J. McConathy and M. J. Owens, *Prim. Care Companion J. Clin. Psychiatry*, 2003, **5**, 70.
93 G. M. Cragg, D. G. Kingston and D. J. Newman, *Anticancer agents from natural products*, CRC press, 2005.
94 C. Dong, S. Ma and Y. Liu, *Spectrochim. Acta. A. Mol. Biomol. Spectrosc.*, 2013, **103**, 179–186.
95 G. Wang, X. Li, X. Ding, D. Wang, C. Yan and Y. Lu, *J. Pharm. Biomed. Anal.*, 2011, **55**, 1223–1226.

Chapter 4 Spectroscopic and computational study of the interaction of Pt(II) pyrrole-imine chelates with human serum albumin



Chapter 4

ARTICLE

Spectroscopic and computational study of the interaction of Pt(II) pyrrole-imine chelates with human serum albumin

Received 00th January 20xx,
Accepted 00th January 20xx

DOI: 10.1039/x0xx00000x

Sheldon Sookai[a] and Orde Q. Munro[a,b]*

Three bis(pyrrolide-imine) Pt(II) chelates were synthesised and characterized with different bridging alkyl groups, specifically 2-hydroxypropyl (**1**), 2,2-dimethylpropyl (**2**), and 1,2-(S,S)-(+)-cyclohexyl (**3**). Novel compounds **1** and **2** were analysed by single-crystal X-ray diffraction (space group *P*-1). The asymmetric unit of **1** comprises three independent molecules linked by hydrogen bonds involving the OH groups, forming a trimeric supramolecular structure. The Pt(II) chelates were reacted with human serum albumin (HSA) to investigate how the ligand bound to the Pt(II) ion influences the compound's affinity for HSA. Fluorescence quenching data obtained for native HSA and HSA bound to site-specific probes (warfarin, subdomain IIA; ibuprofen, subdomain IIIA) indicated that the three Pt(II) chelates bind close enough (within ~30 Å) to Trp-214 to quench its intrinsic fluorescence. The bimolecular quenching constant (k_q) was 10^3–10^4 -fold higher than the maximum diffusion-controlled collision constant in water (10^{10} M s^{-1}) at 310 K, while the affinity constants, K_a, ranged from ~5 x 10^3 to ~5 x 10^5 at 310 K, and followed the order **1** > **3** > **2**. The reactions of **1** and **3** with HSA were enthalpically driven, while that for **2** was entropically driven. Macromolecular docking simulations (Glide XP) and binding site specificity assays employing site-specific probes and UV-vis CD spectroscopy indicated that **1** and **2** target Sudlow's site II in subdomain IIIA, minimally perturbing the tertiary structure of the protein. Well-resolved induced CD signals from **1** and **2** bound to HSA in subdomain IIIA were adequately simulated by hybrid QM:MM TD-DFT methods. We conclude that the structure of the bis(pyrrolide-imine) Pt(II) chelate measurably affects its uptake by HSA without detectable decomposition or demetallation. Such compounds could thus serve as metallodrug candidates capable of utilising an HSA-mediated cellular uptake pathway.

Introduction

Schiff base metal chelates have been extensively studied for their bioactivity and potential use in pharmaceuticals, with pyrrole-imine derivatives being among the most commonly synthesised due to their ease of preparation.[1,2] These key ligands are formed by a condensation reaction between a primary aryl- or alkylamine and pyrrole-2-carboxaldehyde (or a pyrrole-2-ketone).[3] Upon reaction with suitable metal ions, deprotonation of the pyrrole nitrogen occurs. Pyrrole-imine chelating agents are therefore strong σ-donor ligands with π-bonding character that dextrously stabilize metal ions in both low and high oxidation states, including Ni(II),[4–6] Pd(II),[6–8] Pt(II),[9–11] Cu(II),[12–15] Ag(I),[16] and Au(III).[17]

Pt(II) complexes are among the most widely studied metal complexes in medicine. Since the FDA approval of cisplatin in 1978 and its significant clinical success, work on a plethora of Pt(II) metallodrug candidates has flourished[18] mainly to discover derivatives with reduced toxicity alongside responding to the emergence of cisplatin resistant tumours.[19] It is postulated that one of the main reasons for the poor therapeutic index and toxic side effects of Pt(II) compounds is their interaction with serum proteins, in particular human serum albumin (HSA).[20] For reference, after intravenous administration, between 68–98% of cisplatin is bound by serum proteins, mostly HSA, and up to five cisplatin molecules bind to a single HSA molecule.[21] To maximize the activity and improve the safety of Pt(II) metallodrugs more broadly, it is essential to understand the binding mechanism of Pt(II) complexes to HSA (and other macromolecules) and to develop novel candidates with high biological stability and good solubility.

HSA is synthesised in the liver and is the most abundant serum protein with a concentration of 35 – 50 g L^{-1}. The protein has three main functions *in vivo*: (i) aiding to maintain physiological pH, (ii) maintaining osmotic pressure, and (iii) the transport of endogenous and exogenous compounds.[22] HSA comprises a single polypeptide chain with a heart-shaped tertiary structure consisting of 585 amino acids, culminating in a molar mass of 66.5 kDa (Fig. 1).[23] The protein has three domains (I, II, and III), each made up of 10 α-helices and two subdomains (A and B).[23,24] The two main drug binding sites are located in subdomains IIA and IIIA and are commonly known as Sudlow's site I and Sudlow's site II.[25,26] Apart from Sudlow's sites I and II, HSA has several other binding sites including 4 thyroxine, 7 fatty acid, and several known metal ion binding

[a] *Molecular Sciences Institute, School of Chemistry, University of the Witwatersrand, PO WITS 2050, Johannesburg, South Africa. Email: S.Sookai92@gmail.com*
[b] *School of Chemistry University of Leeds, Woodhouse Lane, LS2 9JT, UK. Email: O.Munro@leeds.ac.uk*
[c] *† Electronic Supplementary Information (ESI) available: Complete experimental details and supplementary tables and figures in PDF format, and X-ray crystal structures in CIF format (CCDC 2271558-2271559). See DOI: 10.1039/x0xx00000x*

sites.[27] Delineating the mechanistic details of metal complex uptake by HSA is crucial to understanding *in vivo* pharmacokinetic and pharmacodynamic data of such systems, given the protein's role as the quintessential drug transporter.[28]

In this study, we synthesized three pyrrole-imine Schiff base ligands, namely 1,3-bis{[(1*E*)-1*H*-pyrrol-2-ylmethylene]amino}-propan-2-ol, 2,2-dimethyl-*N*,*N*'-bis[(1*E*)-1*H*-pyrrol-2-ylmethylene]propane-1,3-diamine and (1*S*,2*S*)-*N*,*N*'-bis[(1*E*)-1*H*-pyrrol-2-ylmethylene]cyclohexane-1,2-diamine. The ligands were then metalated with Pt(II) to obtain the respective square planar Pt(II) Schiff base chelates (Fig. 1a). Steady-state fluorescence and CD spectroscopy were used to investigate the binding of the complexes to HSA under physiological conditions, which revealed how the pyrrole-imine Schiff base ligand architecture influences the preferred binding site(s) targeted by the Pt(II) chelates. Finally, molecular docking (GLIDE XP) and TD-DFT simulations were employed to confirm the spectroscopically identified binding sites.

Results and Discussion

Metal chelate synthesis

A key objective of this work was to investigate the impact of the architecture of the current bis(pyrrolide-imine) Schiff base ligands on the chemistry of the coordinated Pt(II) ion and uptake of the complexes by HSA. To this end, we synthesised chiral **3**[10] and the two novel derivatives **1** and **2** as depicted in Scheme 1. Ligand metalation was achieved by reacting the Schiff bases with sodium acetate in a 50% (V/V) DMF-DMSO mixture, with acetate ions serving as a general base. Thereafter, $K_2[PtCl_4]$ was added and the solutions heated under reflux for 4 hours. Purification by recrystallisation followed by X-ray crystallography afforded two novel crystal structures for **1** and **2**; complex **3** had been previously reported by Shan *et al*.[10] and was not studied by X-ray diffraction methods.

X-ray structures

Both **1** and **2** crystallized in the triclinic space group *P*-1 with three and four molecules in the asymmetric unit (ASU), respectively. The Pt(II) ion adopts the expected square planar geometry within the tetradentate chelate (Fig. 2). Typically, the sum of the angles around a square planar metal centre equates to 360°. The sum of the angles around Pt in complexes **1** and **2** were 350.38 ± 0.13° and 350.63 ± 0.14°, respectively, consistent with the constraints of the three chelate rings imparted by the ligands. The slightly non-planar conformations of the ligands mainly reflect non-bonded crystal packing interactions and the formation of discrete, stacked dimers.

Complexes **1** and **2** exhibit Pt–$N_{pyrrole}$ distances of 2.011 (3) and 2.013 (3) Å, respectively, while the Pt–N_{imine} distances were marginally shorter (~0.4%), measuring 2.005 (3) and 2.002 (3) Å for complexes **1** and **2**, respectively. Shorter Pt–N_{imine} bond lengths are typical for bis(pyrrolide-imine) chelates.[10,29] The Pt–N bond distances of **1** and **2** are in agreement with the enantiomers of **3** reported by Shan *et al.,*[10] with coordination group distances ranging from 1.936 – 2.026 Å.

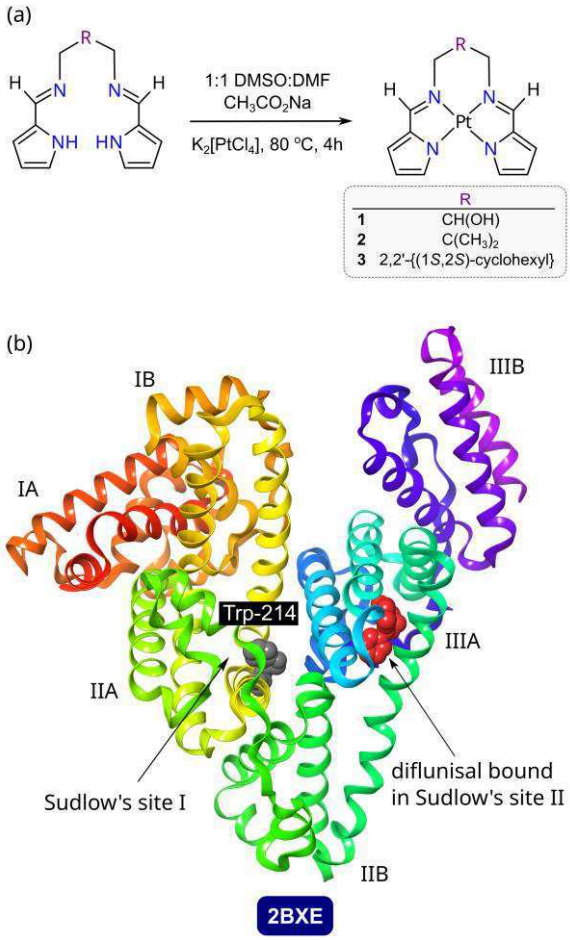


Fig. 1 (a) Schematic synthesis procedure for the metalation of the three bis(pyrrole-imine) ligands with $K_2[PtCl_4]$ relevant to this work. (b) X-ray structure of HSA bound to diflunisal (redrawn from PDB code 2BXE) illustrating the two main drug binding sites. Sudlow's site I (subdomain IIA) is larger than Sudlow's site II (Subdomain IIIA). The protein secondary structure elements are depicted schematically, coloured by domain, and labelled with Roman numerals and Arabic letters.

Regarding the coordination group bond angles for **1** and **2**, the mean $N_{pyrrole}$–Pt–$N_{pyrrole}$ bond angle (104.04 ± 0.14°) is ~8% narrower, and the mean N_{imine}–Pt–N_{imine} bond angle (95.70 ± 0.14°) ~13.9% wider compared with those reported by Shan *et al.*[10] for the structurally-related enantiomers of **3**. This reflects the 3-carbon chain linking the imine groups of **1** and **2**, which is more flexible than the sterically strained 2-carbon chain of **3**, and the resulting 6-membered chelate ring which substantially narrows and widens the $N_{pyrrole}$–Pt–$N_{pyrrole}$ and N_{imine}–Pt–N_{imine} bond angles, respectively. Furthermore, the pyrrole groups are anionic σ-donors with more acute C–$N_{pyrrole}$–C bond angles averaging 106.98 (3)° compared with the C=N_{imine}–C bonds which were more obtuse, averaging 120.87 (4)°. The C=N_{imine} bonds measured 1.299 (5) Å, reflecting the sp^2 hybridized imine carbon atom. Selected bond lengths and bond angles are summarized in Table 1.

The asymmetric unit (ASU) of complex **1** consists of three independent molecules that are linked to each other by hydrogen bonds (Fig 2b), forming a trimeric supramolecular structure. A similar trimer was observed previously for the

Please do not adjust margins

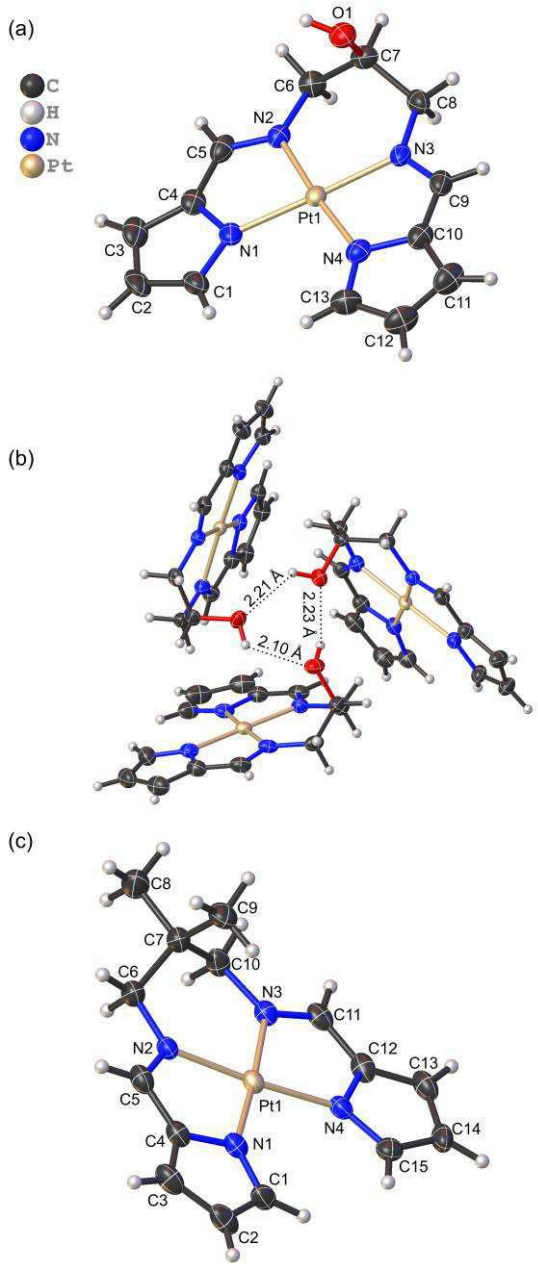


Fig. 2 (a) Labelled view of the low-temperature X-ray structure of **1**. One of the three independent molecules in the asymmetric unit is illustrated. (b) View of the asymmetric unit of the crystal structure of **1** with the three independent molecules forming an H-bonded trimer. (c) Labelled view of the low-temperature X-ray structure of **2**. One of the four independent molecules in the asymmetric unit is illustrated. Thermal ellipsoids are rendered at 35% for **1** and 50% for **2**. Hydrogen atoms are drawn as spheres with an arbitrary radius.

isoelectronic and isostructural Ni(II) derivative.[29] The OH group acts as both a hydrogen bond acceptor and donor, which results in the formation of a six-membered hydrogen-bonded ring (Fig. 2b). Typically, short bond lengths indicate a stronger bond. However, in the case of hydrogen bonding the bond length does not always correlate with the bond strength.[30] The trimeric supramolecular structure of **1** did exhibit significantly shorter (20%) hydrogen bond lengths, averaging 2.18 ± 0.01 Å, compared with the Ni(II) analogue (2.749 ± 0.002 Å). The ASU of **2** consisted of 4 independent molecules A–D (Fig. S13). Further inspection of the crystal packing of both **1** and **2** indicated molecule A of one ASU forms an inverted face-to-face stacked interaction with molecule B′ from a second ASU (Fig. S12 and S13). The symmetry-unique intermolecular Pt···Pt distances measure 3.723 and 3.771 Å and are greater than 3.5 Å, which is double the van der Waals radius of Pt,[30] and thus fall outside the range for proper dz^2(Pt)–dz^2(Pt) orbital interactions.

Table 1. Selected mean crystallographic structural parameters for compounds **1** and **2**.

	1	**2**
Bond distances (Å)		
Pt–$N_{pyrrole}$	2.011 (3)	2.013 (3)
Pt–N_{imine}	2.005 (3)	2.002 (3)
C=N	1.300 (5)	1.298 (5)
Bond angles (°)		
$N_{pyrrole}$–Pt–$N_{pyrrole}$	103.82 (14)	104.25 (14)
N_{imine}–Pt–N_{imine}	95.65 (14)	95.75 (14)
cis-$N_{pyrrole}$–Pt–N_{imine}	80.27 (14)	79.96 (13)
trans-$N_{pyrrole}$–Pt–N_{imine}	175.50 (13)	175.27 (14)
C–$N_{pyrrole}$–C	107.05 (3)	106.91 (3)
C–N_{imine}–C	120.78 (3)	120.96 (4)

HSA fluorescence quenching by 1–3

The interaction between a protein and a small molecule, located close to an aromatic amino acid residue such as Trp, Tyr, and to a lesser extent Phe,[31,32] can result in the disruption of the protein's intrinsic fluorescence.[32] Among the aromatic amino acids, Trp-214 situated in subdomain IIA is primarily responsible for the intrinsic fluorescence of HSA due to its higher quantum yield and more efficient resonance energy transfer compared to Tyr and Phe.[33] In this study, we aimed to investigate the quenching of the intrinsic emission spectrum of HSA (λ^{ex}, 295 nm) by titrating the protein with Pt(II) complexes **1**–**3** at varying concentrations with spectral acquisition from 310–400 nm (Fig. 3). The λ_{max}^{em} was observed at ~343 nm in KH_2PO_4 buffer (50 mM, pH 7.5), and the intrinsic emission intensity of HSA was quenched monotonically with the addition of each aliquot of the respective Pt(II) chelate (Figs. 3 and S14).

Since protein fluorescence quenching is dependent on the overlap between the donor fluorophore (Trp-214) and acceptor's absorbance as well as the spatial proximity of the donor and quencher, we can deduce that the current Pt(II) chelates bind to HSA within range of Trp-214 to disrupt its microenvironment and quench its fluorescence.[34,35] The mechanisms that may cause fluorescence quenching include ground state complex formation, collisional quenching, energy transfer, or molecular rearrangements.[36,37] Binding of **2** and **3** to HSA induced band broadening and redshifts in λ_{max}^{em} of +3 and +4 nm, respectively, while **1** did not induce a spectral shift, as illustrated in Fig. 3.

The λ_{max}^{em} shift data suggest that the microenvironment surrounding Trp-214 in HSA has become more hydrophilic.[38] The small redshifts in the emission maximum for **2** and **3** are comparable to that of Pt(PrPyrr) previously reported.[39] Two potential explanations accounting for the λ_{max}^{em} red shifts are: (i)

Please do not adjust margins

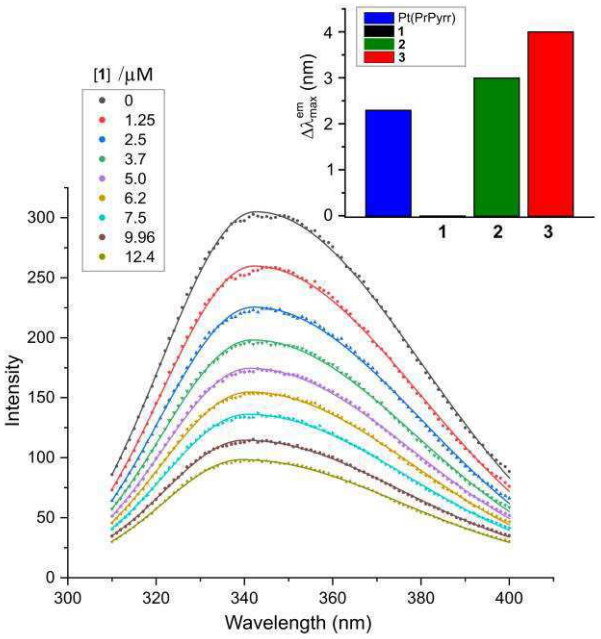


Fig. 3 Emission spectra of human serum albumin (HSA, 5.0 μM) recorded as a function of [**1**] at 298 K in KH_2PO_4 (50 mM, pH 7.50). Solid lines are least squares fits of the data to the sum of two overlapping Gaussian bands. Analogous spectra for the reaction of HSA with **2** and **3** are given in Figure S14 (ESI). The wavelength shift accompanying ligand uptake ($\Delta\lambda^{em}_{max}$) is plotted as the inset to the main figure (upper right).

the Pt(II) complexes bind to HSA sufficiently close to Trp-214 to induce direct electronic polarization of the indole ring in the residue, and/or (ii) the disruption of the ordered water molecules located within 15-25 Å of Trp-214 can lead to orientation-dependent polarization of the fluorophore. It is possible that both explanations result in the lowest energy $^1A_1 \rightarrow {}^1L_a$ ground state transition of Trp's indole ring,[34] thereby causing the λ^{em}_{max} shift. In the case of **1**, no λ^{em}_{max} shift was observed, suggesting that **1** did not induce sufficient direct electronic polarization of the indole ring in the tryptophan residue to cause a shift in the HSA emission spectrum.

Fluorescence quenching mechanism

The fluorescence quenching mechanism for a protein's intrinsic fluorescence can be described as static, dynamic, or mixed inhibition (a combination of both) and is typically analysed using the Stern–Volmer equation (eq. 1),[32]

$$I_0/I = 1 + K_{SV}[Q] = 1 + k_q\tau_0\,[Q] \qquad (1)$$

where I_0 refers to the fluorescence intensity of HSA in the absence of a quencher (Pt(II) chelate herein) and I refers to the fluorescence intensity of HSA in the presence of the quencher. K_{SV} is the Stern-Volmer constant (M^{-1}) and $[Q]$ is the molar concentration of the quencher, k_q is the bimolecular quenching rate constant (M^{-1} s^{-1}), and τ_0 is the average lifetime of HSA fluorescence in the absence of any quencher (5.60 ± 0.10 ns,[40] 6.72 ± 0.07 ns;[33] 5.28 ± 0.03 ns,[41] mean = 5.87 ± 0.76 ns). Usually, the quenching mechanism can be distinguished by analysing the HSA•{ligand} complex's fluorescence as a function of temperature and viscosity.[42]

Stern-Volmer (SV) plots for the fluorescence emission quenching of HSA as a function of temperature (298 K) and [Pt(II) chelate] are shown in Figure 4a. From the slope of the least squares fit of eq. 1 to the data, the bimolecular fluorescence quenching rate constant (k_q) for the HSA-Pt(II) chelate interaction can be calculated (eq. 2):

$$k_q = K_{SV}/\tau_0 \qquad (2)$$

The K_{SV} and k_q values describing the interaction of the Pt(II) bis(pyrrolide-imine) chelates and HSA are summarised in Table 2. Linear Stern-Volmer plots typically indicate a single dominant quenching mechanism either static (binding-related) or dynamic (diffusion-limited collisional).[31,32] The quenching mechanism may be differentiated by the K_{SV} dependence on temperature. If K_{SV} values decrease with increasing temperature, the dominant quenching mechanism is static because there is a decrease in the HSA•{ligand} complexes' formation constant (the term "ligand" is used in a biochemical context; metal complexes **1**–**3** are the ligands or quenchers herein). However, if the reverse is observed the quenching mechanism is dynamic, which is largely due to an increase in the diffusion rate and collisional frequency.[43]

The Stern Volmer plots for **1**–**3** are linear, indicating that a single quenching mechanism is dominant—either static (binding-related) or dynamic (diffusion-limited collisional).[31,32] The K_{SV} values of **1** decreased with increasing temperature, consistent with a static quenching mechanism. In contrast, the K_{SV} values of **2** and **3** increased with increasing temperature; therefore, a dynamic quenching mechanism is operative.[31,32] The k_q values for **1**–**3** all exceed the diffusion-controlled limit (1×10^{10} M^{-1} s^{-1})[44] by 2 to 3 orders of magnitude, which is consistent with significant HSA···ligand binding interactions rather than non-specific collisional interactions.[36] The K_{SV} values followed the order **1** > **2** > **3** and ranged between 10^5–10^4 M^{-1}, indicating a strong quenching phenomenon. The K_{SV} values are consistent with those of other Pt(II) complexes interacting with HSA.[39,45,46] A summary of K_{SV} and k_q values obtained for the interaction of the three Pt(II) complexes with HSA is reported in Table 2. The Stern-Volmer plots for **1**, **2** and **3** over the full range of temperatures are provided in the ESI (Fig. S15).

Ligand binding equilibrium constants

Quenching of intrinsic HSA fluorescence emission as a function of [Pt^{II}(L)], where L is the dianionic bis(pyrrolide-imine) chelating ligand, can be used to calculate the biophysical binding parameters for the interaction of **1**–**3** with HSA, i.e., the affinity constant (K_a) and the reaction stoichiometry (n). Both parameters can be obtained from a double log plot and least-squares fit of the emission quenching data as a function of increasing ligand concentration (eq. 3),[47]

$$log\left(\frac{I_0 - I}{I}\right) = logK_a + nlog[Q] \qquad (3)$$

where the intercept and the gradient of the slope equate to $\log K_a$ and n, respectively. The data for the Pt(II) chelates are

Please do not adjust margins

summarised in Table 2 and are plotted in Fig. 4b. (Similar plots for **1**–**3** at 288, 298, and 310 K are given in Fig. S16.)

The affinity constant (K_a) for **1** and **3** decreases with increasing temperature, while K_a for **2** increases with increasing temperature. The reaction stoichiometry from the slope of eq. 3 (Figs. 4b and S16) tended to deviate from unity ($0.68 < n < 1.13$). From Table 2, the K_a values follow the order **1** > **3** > **2**. The K_a for the reaction of Pt(PrPyrr) with HSA was previously reported,[39] covering a similar range to that found for **1** here. Of the three Pt(II) bis(pyrrolide-imine) chelates, **2** bound endothermically to HSA, while the binding of **1** and **3** to HSA was exothermic (see Table 3). All three Pt(II) bis(pyrrolide-imine) chelates had moderate binding affinities for HSA, suggesting non-covalent binding. Weaker ligand binding interactions are ideal since one potential application is to use HSA as a carrier protein for metal chelates. Moderate binding affinity could signify faster diffusion rates for a drug/metallodrug within the circulatory system.[37]

Table 2. Stern-Volmer quenching constants (K_{SV}) and bimolecular quenching rate constants (k_q) for the interaction of **1**–**3** with HSA at different temperatures in 50 mM KH_2PO_4 buffer at pH 7.50.

Compound	Temp. T (K)	10^{-5} K_{SV} (M^{-1})[a,c]	10^{-13} k_q (M^{-1} s^{-1})[b]	$\log(K_a$ / $M^{-1})$[c]	n[d]
1	288	1.89 (0.1)	3.22	5.84 (0.04)	1.13 (0.02)
	298	1.59 (0.2)	2.46	5.67 (0.03)	1.10 (0.01)
	310	1.16 (0.1)	2.27	5.50 (0.01)	1.06 (0.02)
2	288	0.68 (0.04)	1.16	3.25 (0.004)	0.68 (0.01)
	298	0.71 (0.04)	1.22	3.45 (0.05)	0.71 (0.01)
	310	0.95 (0.04)	1.61	3.64 (0.04)	0.73 (0.004)
3	288	0.54 (0.02)	0.93	5.17 (0.04)	1.10 (0.01)
	298	0.56 (0.01)	0.95	4.81 (0.02)	1.02 (0.01)
	310	0.65 (0.1)	1.11	4.67 (0.02)	0.98 (0.01)

[a]K_{SV} values (Stern-Volmer constants) were determined by fitting the data to linear eq. 1 to the data. A mean excited state lifetime, τ_0, of 5.87(76) ns for HSA was used to calculate the bimolecular quenching rate constant, k_q. [c]The estimated standard deviations of the least significant digits are given in parentheses. [d]Ligand:HSA binding stoichiometry from the fit of the data to eq. 3.

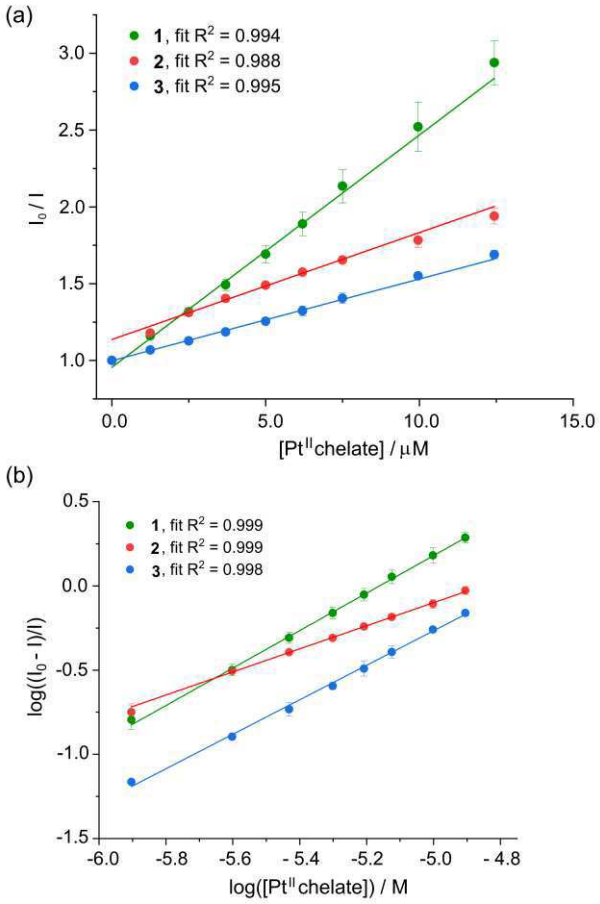


Fig. 4 (a) Stern-Volmer plot for HSA (5 μM) in KH_2PO_4 buffer (50 mM, pH 7.5) recorded as a function of [**1**–**3**] vs fluorescence intensity ratio (I_0/I) at 298 K. Each plot represents the average of three independent experiments and the error bars represent ESD's. The data are well fitted to linear eq. 1, suggesting a single quenching mechanism is dominant. (b) Double logarithm plot of the fractional change in fluorescence intensity for human serum albumin (HSA, 5.0 μM) recorded as a function of the concentration of **1**–**3** (50 mM KH_2PO_4, pH 7.50, 298 K). Error bars are ESD's based on the average of three independent determinations. The data are described by eq. 3, which affords the affinity constant and stoichiometric coefficient for the reaction (Table 2).

Thermodynamics of Pt(II) chelate binding by HSA

The reactions of the three Pt(II) chelates follow a linear van't Hoff relationship; plots for triplicate measurements are represented in Fig. 5a. Under non-standard conditions the thermodynamic parameters, i.e., enthalpy change (ΔH), entropy change (ΔS), and Gibbs free energy change (ΔG), may be deduced from eqs. 4 and 5.

$$lnK_a = -\frac{\Delta H}{RT} + \frac{\Delta S}{R} \quad (4)$$

$$\Delta G = \Delta H - T\Delta S \quad (5)$$

Table 3 summarises the thermodynamic parameters for the reaction of the current Pt(II) chelates with HSA in KH_2PO_4 buffer (50 mM, pH 7.5). All three reactions are exergonic,[47] with ΔG values of –32.3 (± 0.1), –19.5 (± 0.08) and –27.2 (± 1.4) kJ mol^{-1} for **1**, **2** and **3**, respectively at 298 K.

The enthalpy values (ΔH) for reactions of **1** and **3** with HSA are exothermic, measuring –26.2 kJ mol^{-1} and –37.4 kJ mol^{-1}, respectively. Complex **2**, in contrast, has an endothermic reaction with HSA (ΔH = +30.3 kJ mol^{-1}). Fig. 5b highlights the dominance of the enthalpy term for the reactions of **1** and **3** with HSA, while the $T\Delta S$ term is dominant for **2**. It is well established that HSA has two main small molecule binding sites that are mainly hydrophobic,[23] namely Sudlow's site I (subdomain IIA)[47] and Sudlow's site II (subdomain IIIA).[47] The favourable heats of reaction for **1** and **3** suggest that they cause minimal disruption of ordered water molecules within HSA. London dispersion forces (LDF) are likely the dominant binding forces for **1** and **3**. In the case of complex **2**, a positive enthalpy ($\Delta H > 0$) is suggestive of hydrophobic interactions.[47,48]

In Fig. 5c we used the Gibbs-Helmholtz relationship (eq. 5) and the experimental thermodynamic data (Table 3) to determine the influence that the ligand chelated to Pt(II) has on the thermodynamic parameters for complex formation with HSA. From Fig. 5c, when $T\Delta S/\Delta G$ is plotted against $\Delta H/\Delta G$, the

Please do not adjust margins

Table 3. Thermodynamic parameters for the binding of **1**, **2**, and **3** by HSA in 50 mM KH_2PO_4 buffer at pH 7.50.

Compound	T (K)	ΔG (kJ mol^{-1})[a]	ΔH (kJ mol^{-1})[a]	$T\Delta S$ (KJ mol^{-1})[a]
1	288	−32.1 (0.2)		
	298	−32.4 (0.2)	−26.2 (2.7)	6.2 (2.6)
	310	−32.5 (0.1)		
2	288	−19.3 (2.0)		
	298	−29.6(2.0)	30.3 (4.9)	47.9(4.9)
	310	−19.6 (1.6)		
3	288	−27.8 (0.3)		
	298	−25.5 (0.4)	−37.4 (2.4)	−10.2(1.5)
	310	−28.13 (0.4)		

[a]The estimated standard uncertainties of the least significant digits are given in parentheses.

resulting fit is linear with *x*- and *y*-intercepts of exactly 1. Reactions for **1** and **3** with HSA are enthalpically driven (ΔH < 0, upper and lower right quadrants) with the reaction for the hydroxy derivative **1** also being entropically favoured (ΔS > 0). Complex **2**, in contrast, exhibits a purely entropically driven reaction with HSA (ΔH > 0, ΔS > 0; lower left quadrant). In all three quadrants, spontaneity is assured (ΔG < 0) since changes in $\Delta H/\Delta G$ are compensated for by changes in $T\Delta S/\Delta G$. Exact $T\Delta S$ values for the three Pt(II) chelates are listed in Table 3. Both **1** and **2** have a positive entropy change, while **3** has a negative entropy change, with $T\Delta S$ ranging from –10.2 kJ mol^{-1} to +49 kJ mol^{-1}. Because the reaction for **2** is entropically driven, ordered water molecules are probably displaced from the ligand binding site into the buffer, suggesting hydrophobic and electrostatic interactions[47,48] could play a key role in the binding of **2** by HSA.

The HSA binding thermodynamics of **1**–**3** reported here are similar to data for other Pt(II) chelates,[45] which have moderately positive ΔH and ΔS values with both compounds binding specifically to Sudlow's site I. For further comparison, binding of the organic drugs ibuprofen[49] and several benzodiazepines[50] are characterized by moderately negative ΔH (−50 to −75 kJ mol^{-1}) and ΔS values with K_{a1} values ~10^5 M^{-1}.[51] The latter drugs bind to Sudlow's site II initially, followed by secondary site occupation at higher doses (K_{a2} values ~10^3 M^{-1}). The ΔH and ΔS values were, however, similar for both drug-binding steps.

Fluorescence-based probe displacement assays to determine the main Pt(II) chelate binding site(s)

Considering the binding constants and thermodynamic data for the uptake of **1**–**3** by HSA presented in Tables 2 and 3, it is likely that the unique steric and electronic properties of the bis(pyrrolide-imine) ligands coordinated to Pt(II) modulate the affinity and preferred binding site for each metal chelate in the protein. For **1**–**3**, these binding sites are all in close enough proximity to Trp-214 to quench its fluorescence. This hypothesis was tested by carrying out a competitive site displacement assay using fluorescence spectroscopy. For the assay, **1**–**3** were titrated into a solution of native HSA and solutions of HSA that had been pre-equilibrated with the site-specific markers warfarin and ibuprofen. Both warfarin and ibuprofen have been

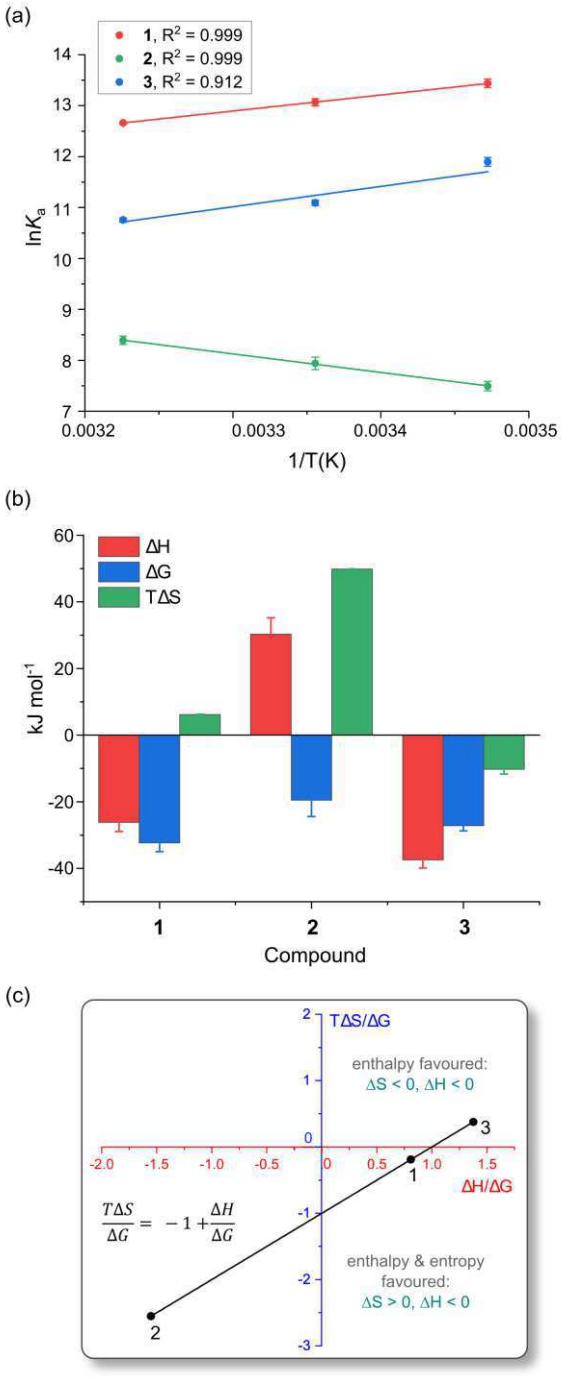


Fig. 5 (a) Linear van't Hoff plots for the reactions of **1**, **2**, and **3** with HSA in 50 mM KH_2PO_4 buffer at pH 7.50. (b) Comparison of the thermodynamic parameters (298 K) governing the reactions of **1**–**3** with HSA. All measurements were done in triplicate, derived parameters were individually averaged, and error bars are standard deviations. (c) Plot of the Gibbs-Helmholtz relationship (eq. 4) for the reaction of the three Pt(II) bis(pyrrolide-imine) chelates with HSA at 298 K in 50 mM KH_2PO_4 buffer at pH 7.50. The straight line fit of the data gives R^2 = 0.9997 with a slope and intercept of –1. For all reactions, ΔG < 0.

shown to bind to subdomain IIA[52] and IIIA,[53] respectively, using X-ray crystallography. (Ibuprofen also has a secondary binding site located between subdomains IIA and IIB.[53])

One caveat concerning the assay is that HSA has several ligand-binding sites,[53] which could make interpreting the data

Please do not adjust margins

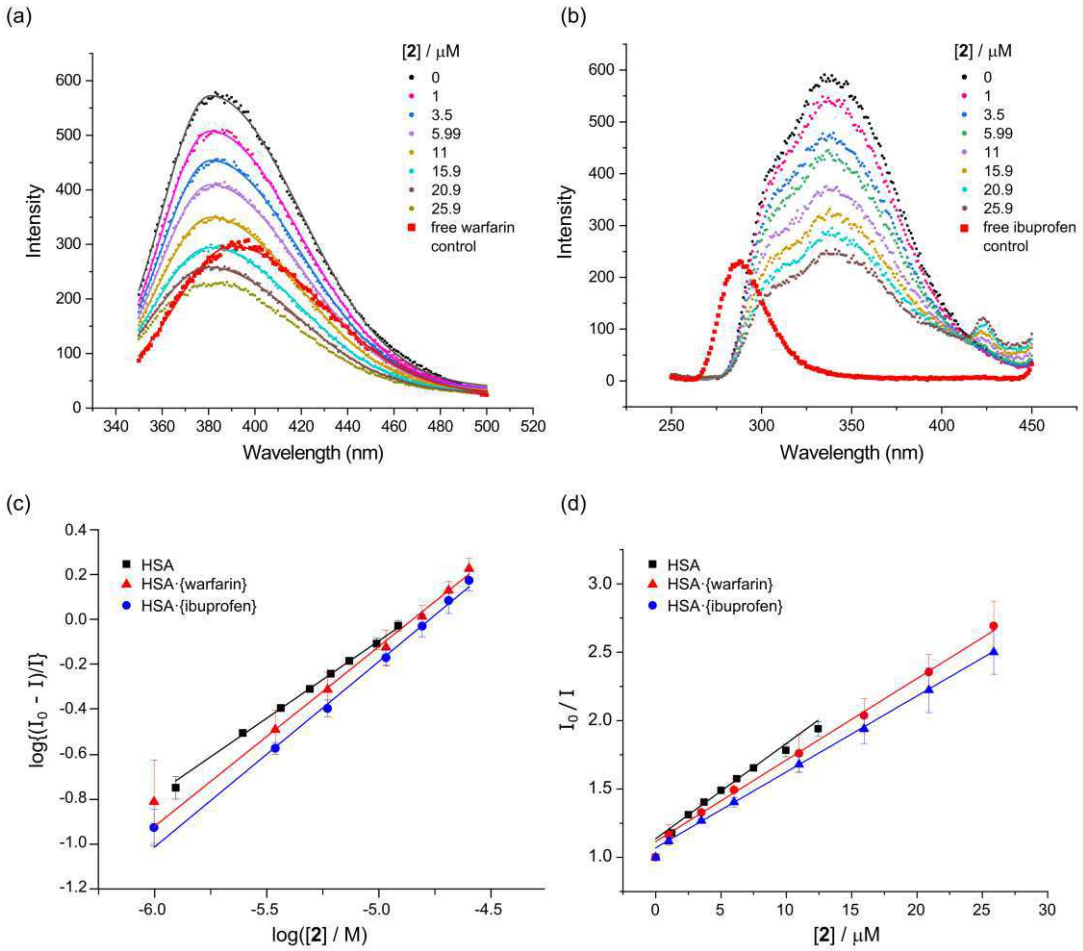


Fig. 6 Binding site determination for the reaction of **2** with HSA (5.0 μM protein, 50 mM KH_2PO_4, pH 7.50, 298 K). (a) Emission spectra of HSA•{warfarin} (5.0 μM warfarin, λ^{ex} = 320 nm) recorded as a function of the concentration of **2** at 298 K. The spectra are fitted by single Gaussian functions to locate the emission maxima. Correlation coefficients, R^2, ranged from 0.990 to 0.999. (b) Emission spectra of HSA•{ibuprofen} (5.0 μM ibuprofen, λ^{ex} = 228 nm) recorded as a function of the concentration of **2** at 298 K. (c) Stern–Volmer (SV) plot for native HSA, HSA•{warfarin}, and HSA•{ibuprofen} as a function of the concentration of **2** at 298 K. The plots are linear with an intercept of 1.0 when static quenching is operative (i.e., the quencher binds to the target protein and co-bound fluorophore(s)). The excitation and emission wavelengths for the fluorophore probes were: (i) Trp-214, λ^{ex} = 295 nm, λ^{em} = 340 nm (native HSA); (ii) warfarin, λ^{ex} = 320 nm, λ^{em} = 382 nm (HSA•{warfarin}), and (iii) ibuprofen, λ^{ex} = 228 nm, λ^{em} = 332 nm (HSA•{ibuprofen}). (d) Double-log plot (eq. 3) of the fluorescence quenching data, $log\left(\frac{I_0-I}{I}\right) = logK + nlog[Q]$, to enable measurement of logK_a and the reaction stoichiometry (n).

difficult. The idea here is that the displacement of either warfarin or ibuprofen by the incoming Pt(II) chelate would signal binding to either Sudlow's site I or II. However, if the presence of either warfarin or ibuprofen redirects the Pt(II) chelate to an alternate binding site within HSA (or prevents Pt(II) chelate uptake due to allosteric inhibition) the exact binding site may be difficult to elucidate. Although there may be certain limitations, examining changes in the logK_a, n, and K_{SV} values, as well as movements of the fluoroprobe, could reveal plausible binding locations for these metal complexes.

For **1**–**3**, the assay for their uptake by HSA in the presence of key site-specific probes has been summarised in Fig. 6 (and Figs. S17 and S18). Initially, when **1**–**3** react with native HSA, all ligand binding sites are available for complexation. The Stern-Volmer plots (Fig. 4 and Table 2) reveal **1** and **3** are dynamic quenchers, while **2** is a static quencher of HSA intrinsic fluorescence, while the double log plot (Fig. 4b) indicates a nominally 1:1 Pt(II) complex:HSA reaction stoichiometry.

Titration of **1** into HSA•{warfarin} (λ^{ex} = 320 nm, λ^{em} = 382 nm) and HSA•{ibuprofen}$_n$ (λ^{ex} = 228 nm, λ^{em} = 332 nm) resulted in a *decrease* in the measured logK_a values from 5.67 ± 0.03 (n_{total} = 1.10 ± 0.01) in the native protein to 5.28 ± 0.05 (n_{total} = 1.03 ± 0.03) and 5.38 ± 0.15 (n_{total} = 1.06 ± 0.03) for the probe-bound targets HSA•{warfarin} and HSA•{ibuprofen}$_n$, respectively. Similarly, for **3** the logK_a values *decreased* from 4.85 ± 0.20 (n_{total} = 1.02 ± 0.05) in the native protein to 3.88 ± 0.16 (n_{total} = 0.85 ± 0.04) and 4.06 ± 0.15 (n_{total} = 0.87 ± 0.03) for HSA•{warfarin} and HSA•{ibuprofen}$_n$, respectively.

In contrast, the logK_a values for the binding of **2** *increased* somewhat from 3.33 ± 0.20 (n_{total} = 1.02 ± 0.05) in the native protein to 3.88 ± 0.16 (n_{total} = 0.85 ± 0.04) and 4.06 ± 0.15 (n_{total} = 0.87 ± 0.03) for the probe-bound targets HSA•{warfarin} and HSA•{ibuprofen}$_n$, respectively. The Stern-Volmer plots for the binding of **1**–**3** by the probe-laden targets were linear throughout, consistent with a single mode of fluorescence quenching (Figs. 6d, S17 and S18).

Please do not adjust margins

The foregoing results suggest that over the concentration range examined, neither warfarin nor ibuprofen are displaced *to a substantial extent* from HSA by the incoming Pt(II) chelate. However, the fluorescence from both site-specific probes is clearly quenched by **1**–**3**, no doubt via a long-range FRET-based mechanism. Our interpretation is that all three Pt(II) complexes bind to HSA in the presence of warfarin or ibuprofen, without fully displacing either probe under the conditions employed for these experiments. Nevertheless, the probes can influence the binding affinity of **1**–**3**. The observation that the probes are not fully displaced is not unexpected, considering that the logK_a values for the binding of both warfarin (logK_a ~5.5)[52] and ibuprofen (logK_a ~6.3)[53] to native HSA are higher than those determined here for **2** and **3**, while only the logK_a value for ibuprofen uptake surpasses that of complex **1**.

One interpretation of the data is that **1**–**3** can target both Sudlow's sites I and II. However, if either of the site-specific markers is already present in one of these sites, the unbound site is vacant and becomes fully saturated by the metal chelate. Alternatively, the presence of warfarin and ibuprofen may cause subtle changes in the tertiary structure of HSA, resulting in **1**–**3** favouring alternative binding sites in the protein. Such allosteric redirection of ligand uptake could explain why the logK_a values for **1** and **3** decrease, while logK_a for **2** increases for the probe-bound targets. While the current spectroscopic data cannot pinpoint the preferred binding site with absolute certainty, our *in silico* docking and CD studies (*vide infra*) suggest that while both sites are accessible, the ibuprofen binding site (Sudlow's site II) is preferred (Fig. 9 and Table S7; *vide infra*). Because of the ambiguity of the fluorescence quenching assays in this case, we recommend that an ICD assay be conducted as a definitive cross-check for the binding site(s) favoured by a metal chelate (see Fig. 9).

Far-UV CD spectroscopy

Far-UV circular dichroism (CD) spectroscopy is a highly effective technique for analysing changes in a protein's secondary structure (i.e., α-helices, β-sheets, and random coils) upon ligand binding.[54,55] The impact of Pt(II) chelates **1** and **2** on HSA's secondary structure was measured over the 200–260 nm range (Fig. 7). The CD spectrum of native HSA displayed two minima at 208 (±1 nm) and 222 nm (±1 nm), which is typical of an α-helical rich protein (Figs. 7a and b). The electronic transitions for both minima are attributed to π–π* (208 nm) and n–π* (222 nm) excitations,[54] respectively, with the transitions originating within the amide bonds of the peptide backbone.[54,55] The far-UV CD spectrum of HSA in the presence of **1** and **2** was similar to that of native HSA, with only a minimal decrease in ellipticity (Fig. 7a and b). Both **1** and **2** exhibited moderately high binding affinities for HSA (Table 2), effecting only small CD intensity changes without a wavelength shift, even at concentrations as high as 40 μM (8-fold higher than the HSA concentration). Collectively, the data indicate that the Pt(II) chelates negligibly impact the secondary structure of HSA.

The far-UV CD data were further analysed using JASCO Spectra Manager™ to calculate the percentage composition of α-helices, turns, and other secondary structure elements present for each HSA•{Pt^{II}(L)} adduct (Table 4). The dominant secondary structure domains are α-helices (~56%), turns (~11%), and unordered coils (~32%). In solution, the secondary structure composition of HSA differs from that of native HSA in the solid state[23] (68.5 % α-helix, 0% β-sheet, 9.6% turns, and 21.9% unordered coils; PDB code 1BM0 analysed with BeStSel[56]). However, our CD data are consistent with solution state spectral decompositions reported previously by others.[57–59] It is accepted that enhanced subdomain mobility and general thermal motion/disorder account for the decrease of α helicity.[42,55]

Table 4. Summary of the far UV-CD data of HSA in the presence of **1** and **2**.

Compound	Concentration (μM)	Helix	Turn	Unordered
1	0	56.39	11.03	32.58
	5	55.15	10.43	32.42
	10	54.31	11.10	34.59
	20	54.04	10.78	35.18
	40	53.94	11.37	34.69
2	0	57.21	10.88	31.91
	5	55.72	10.67	33.61
	10	55.93	11.08	32.99
	20	55.19	11.05	33.76
	40	55.14	10.85	34.01

Near-UV and visible region CD spectroscopy

To investigate the impact of **1** and **2** on the tertiary structure of HSA, we utilised near-UV CD spectroscopy. This technique probes the electronic structure of the three aromatic amino acid residues, Trp (285–300 nm), Tyr (275–285 nm), and Phe (250–270 nm), and allows for the examination of conformational changes in the protein's tertiary structure. Moreover, induced circular dichroism (ICD) bands from the bound metal chelates were observed; these can be structurally informative when an achiral small molecule binds to a chiral host macromolecule such as a protein.[54] Here, we present the experimental near-UV CD and ICD spectra for HSA bound to the Pt(II) chelates of interest, and we complement the experimental data interpretation with results from our Glide XP[60,61] (Schrödinger Release 2022-3) molecular docking and TD-DFT simulations (ONIOM[62] CAM-B3LYP[63]/SDD[64]/GD3BJ:[65] UFF[66]) of the electronic structures of the protein-bound metal chelates (TD-DFT; time-dependent density functional theory).

Fig. 7 shows the spectra of HSA in its native form and in the presence of identical saturating doses (40 μM) of **1** and **2**. Through difference spectroscopy, we were able to resolve the ICD spectra for both Pt(II) chelates. Notably, the intensity of the ICD response for **1** was greater than that of **2**, in accord with the affinity constants (logK_a, Table 2) for uptake of the two Pt(II) chelates by HSA. A stronger ligand–HSA interaction results in a stronger ICD signal from the optically inactive ligand. This phenomenon was previously observed for related metal chelates by Sookai and Munro.[39] The presence of the ICD band

Please do not adjust margins

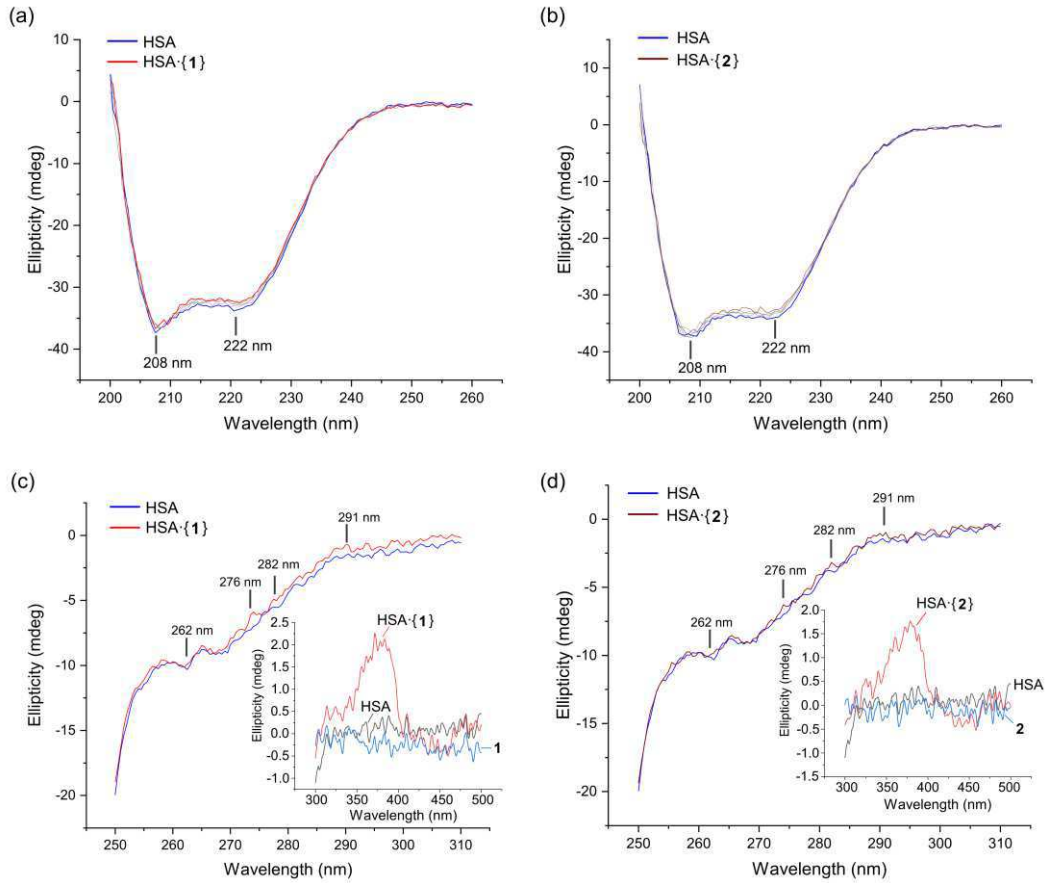


Fig. 7 Plots of the far-UV CD spectra of native HSA and the protein incubated with saturating doses of (a) **1** and (b) **2** recorded at 298 K in 50 mM KH_2PO_4 buffer at pH 7.50. The plots are unsmoothed spectra at Pt(II) bis(pyrrolide-imine) chelate doses ranging from 0 to 40 μM. Grey spectra indicate concentrations of 5, 10, and 20 μM of **1** and **2**. Band minima are indicated. Plots of the UV-visible CD spectra of native HSA (15 μM) and the protein incubated with a saturating dose (40 μM) of (c) **1** and (d) **2** were recorded at 298 K in 50 mM KH_2PO_4 buffer at pH 7.50. The graphical insets are plots of the HSA•{Pt^{II}(L)} complex; they represent the induced CD (ICD) spectrum of each achiral protein-bound ligand. Perturbations in the protein structure around Phe (250–270 nm), Tyr (~280 nm), and Trp (285–300 nm) residues may also be resolved in some difference spectra. Selected wavelengths in the UV CD spectrum are marked.

in the UV-visible region suggests that the Pt(II) chelates do not undergo decomposition, demetallation, imine hydrolysis, or ligand dissociation upon binding to HSA in solution. Unlike simple metal complexes such as cisplatin[67] and NAMI-A (*trans*-$[RuCl_4(1H\text{-indazole})_2]^-$),[68] whose ligands can dissociate from the metal, the present class of bis(pyrrolide-imine) Pt(II) chelates exhibit the potential for reversible transport *in vivo* via an HSA-mediated cellular uptake pathway.[69] This finding highlights the possibility that other polydentate chelates and macrocyclic metal complexes could be similarly transported.

The near-UV CD spectrum of native HSA typically shows two minima at 262 and 280 nm and a maximum at 290 nm due to disulphide bonds and aromatic amino acids.[70] Perturbations in this region provide insights into the conformational changes occurring in HSA. Phenylalanine and tyrosine residues have low quantum yields and extinction coefficients but high symmetry, making them less sensitive to changes in the residue's micro-environment. Tryptophan residues, in contrast, have high quantum yields and extinction coefficients but possess low symmetry. Therefore, they are most sensitive to changes in their immediate microenvironment.[71] All three amino acid residues have π-π* transitions (^1L_a and ^1L_b) and have the potential to be directly involved in π bonding. Importantly, the π-π* transitions have charge transfer character and thus respond to dielectric changes within the chromophore microenvironment such that solvent changes may affect the transition.[72] Thus, changes in the near-UV CD spectrum can be correlated to tertiary structure changes in the protein due to its interaction with other molecules or due to solvent exposure perturbing the aromatic residue's microenvironment.[73]

Near-UV CD spectra were recorded from 250-310 nm for HSA•{**1**} and HSA•{**2**} (Figs. 7c and 7d). The 291-nm Trp ^1L_b (0,0) band and Tyr and Trp overlap bands at 282 and ~276 nm (^1L_a; solvated Trp),[74,75] respectively, are all present. When **1** and **2** bind to HSA, these marker bands exhibit slight positive changes in ellipticity with a negligible wavelength shift. The change in ellipticity suggests that both Tyr and Trp are more exposed to the solvent and/or affected by the electrostatic field of the bound metal chelates. The former would occur for minor alterations in the secondary structure of HSA (Figs. 7a and 7b), i.e., the decrease in α-helicity and partial unfolding upon ligand uptake noted earlier. Partial unfolding of HSA is expected to alter both the number and arrangement of ordered water

Please do not adjust margins

molecules around Trp and Tyr, culminating in the observed, subtle perturbations for these chromophores.

Insights from DFT simulations. Based on our *in silico* docking data obtained with published protein X-ray structures and grids centred on probe ligands (warfarin, diazepam, and ibuprofen), we used hybrid QM:MM TD-DFT simulations (ONIOM method[76]) to calculate the electronic structures of HSA•{**1**} and HSA•{**2**}. The best pose taken directly from the optimized Glide XP structure (Fig. S21) was assigned to the quantum mechanics (QM) layer, and five amino acid residues (Ile-388, Leu-407, Phe-403, Tyr-411, and Arg-485) interacting with **2** in Sudlow's site II were added to the QM layer for the most accurate ICD spectrum calculation. The protein amino acid residues were simulated using molecular mechanics (UFF[66]). The TD-DFT calculated ICD spectrum of HSA•{**1**} broadly matches the key spectral features of the experimental ICD spectrum (Fig. 8a). The simulations indicate that for both ibuprofen and aromatic amino acid residues within Sudlow's sites I and II (*vide infra*, Tables S7 and S8), there are several possible binding sites within 9.6–30 Å of Trp-214 that can account for (i) FRET-based quenching of this fluorophore and (ii) location of the ligand within 5.9–12 Å of at least one Tyr residue. Interestingly, none of the binding sites are directly within Sudlow's site I; instead, the *in silico* evidence suggests that both **1** and **2** target Sudlow's site II.

Regarding the assignment of the near-UV CD and visible ICD spectra of HSA•{**1**} and HSA•{**2**}, the fine structure perturbations for the TD-DFT ICD spectra matched those observed in the experimental spectra with an amplitude of **1** > **2**, which was mainly due to the larger K_a of HSA•{**2**} compared to HSA•{**1**}. The TD-DFT data for unbound **1** (Table S5) suggest that the UV-vis absorption bands at 350–410 nm are due to ligand $^1(\pi\text{–}\pi^*)$ transitions of the bis(pyrrolide-imine) chelate, while the UV-vis absorption bands from 410–500 nm have metal-to-ligand charge transfer (MLCT) character, ^{1}[Pt(5d)→π*(Schiff base)]. The MLCT absorption bands at 380 nm exhibit a slight blue shift of ~3 nm upon uptake of the Pt(II) chelates by HSA, giving rise to the positive ICD bands at ~378 nm (Fig. 8a).

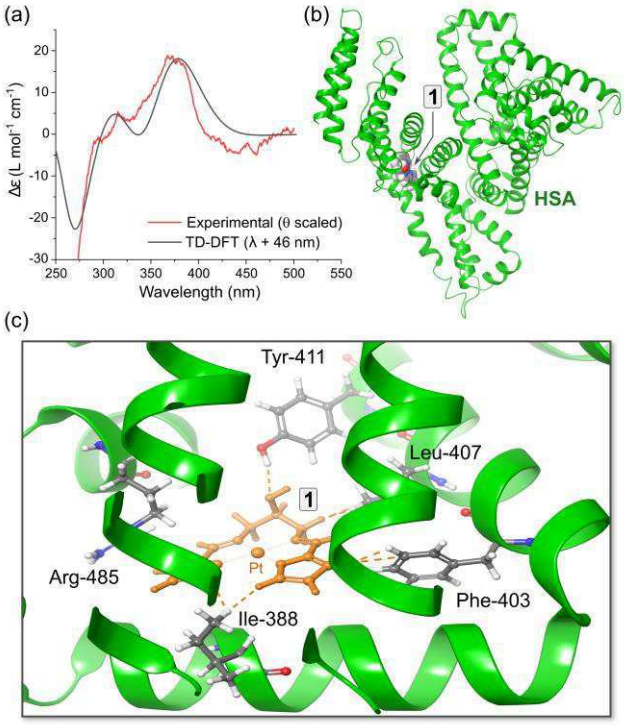


Fig. 8 (a) Comparison of the experimental ICD spectrum (Δθ) recorded for HSA•{**1**} at pH 7.5 in 50 mM (KH_2PO_4) and the CD spectrum calculated using hybrid QM:MM TD-DFT simulations (CAM-B3LYP/SDD/GD3BJ:UFF) for the top-scoring docked pose of **1** bound in subdomain IIIA (PDB code: 2BXF). The DFT-calculated spectrum of the best pose matches the experimental spectrum reasonably well; a bandwidth of 1580 cm^{-1} (hwhm) was used for the TD-DFT data. (b) Structural model used for the TD-DFT simulations showing the location of **1** within subdomain IIIA. (c) View of the metal chelate binding site containing the best pose of **1** and the closest amino acid residues.

Site displacement assay employing CD spectroscopy proves Sudlow's site II is targeted by Pt(II) chelates 1 and 2

To investigate the site-specific binding of **1** and **2** to HSA, an induced circular dichroism (ICD) site displacement assay was performed by incubating either complex in KH_2PO_4 buffer (50 mM, pH 7.5) with HSA and titrating in either warfarin (Sudlow's site I probe) or ibuprofen (Sudlow's site II probe). The Pt(II) chelates themselves are achiral and therefore do not produce a CD signal unless they are bound to a chiral host such as HSA. If the incoming site-specific probe ligand can displace the Pt(II) chelate, the ICD signal is lost due to the displaced metal chelate returning to an achiral protein-free state in solution.

As shown in Fig. 9a, for HSA•{**2**} the ICD spectrum in the near-UV region was only weakly perturbed after adding a low dose of warfarin (4.2 μM); subsequent higher doses of the probe failed to displace **2** from the protein. Importantly, the $\log K_a$ value of **2** for HSA (3.45) is significantly lower than that of warfarin for the protein (5.5),[52] which would allow complete substitution of **2** by warfarin if the Pt(II) chelate occupied Sudlow's site I. The results clearly demonstrate that Sudlow's site I is *not the main binding site* of **2** within HSA. For HSA•{**1**} (Fig. S19), there was a similarly negligible change in the ICD spectrum upon titration of warfarin into the solution of the protein complex, suggesting that warfarin did not displace **1**. This could be due to the $\log K_a$ of warfarin ($\log K_a$ = 5.5[52]) being slightly lower than that of **1** ($\log K_a$ = 5.67) or indicate that **1** (like **2**) does not bind within Sudlow's site I. At the highest concentration of warfarin (54 μM), the emergence of the warfarin-induced CD peak at 306 nm was observed.

When ibuprofen was titrated into HSA•{**2**}, there was a monotonic decrease in the ICD signal from **2** within the protein (Fig. 9b), consistent with displacement of **2** by ibuprofen into the bulk solution and confirming that **2** bound in either one or both ibuprofen binding sites (subunits IIIA or between IIA and IIIA).[27] The evidence collectively demonstrates that both Pt(II) chelates preferentially bind in Sudlow's site II (subdomain IIIA). Notably, *in silico* data (TD-DFT simulations) provided strong supporting information for the binding of **2** within Sudlow's site II of HSA by matching the key features of the experimental CD spectrum (Fig. 8a). Despite compelling spectroscopic evidence, however, only X-ray data can delineate the precise binding site(s) of **1** and **2** with absolute certainty.

Please do not adjust margins

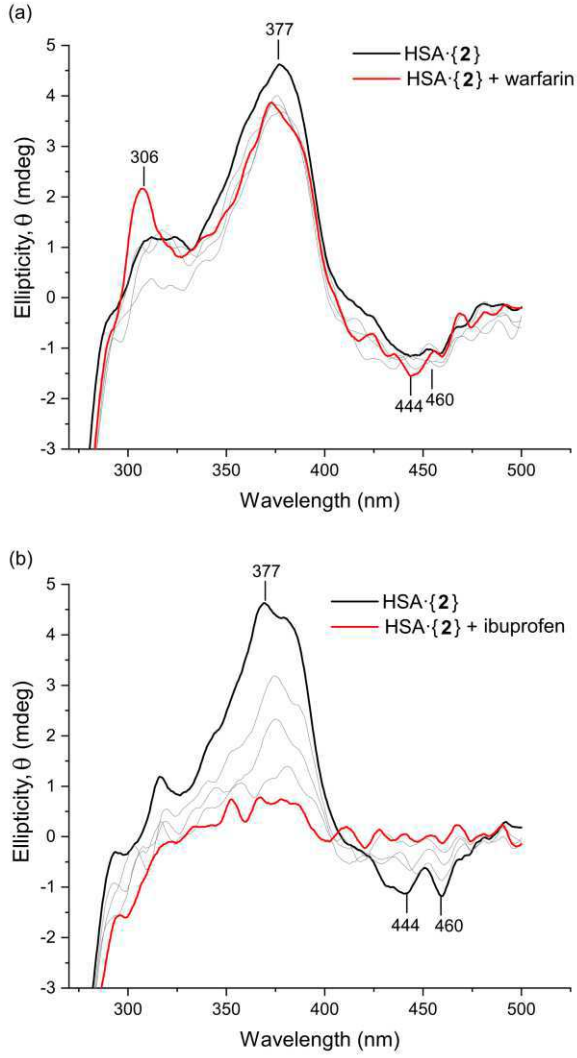


Fig. 9 Induced CD site displacement assay carried out by measuring the UV-vis CD spectrum of HSA (15 μM in 50 mM KH_2PO_4 buffer, pH 7.5) bound to **2** (15 μM). The site-specific markers warfarin (Sudlow's site I) and ibuprofen (Sudlow's site II) were titrated into the solution of HSA•{**2**} in Parts (a) and (b), respectively, at concentrations of 4.1, 8.3, 12.5, and 20.1 μM (the grey lines represent doses < 20.1 μM). The assay identifies which probe drug or marker can displace the Pt(II) chelate from its target binding site and thus delineates the true location of the metal chelate within the protein. The spectra were smoothed using a Lowess function (0.07 span) for clarity.

Macromolecular simulations – general perspectives

Docking studies were carried out using Glide XP (Schrödinger Suite 2022-3) to predict potential binding sites in HSA for **1**–**3** and were compared to previously docked control compounds (warfarin, diazepam, ibuprofen).[39] It is important to note that rigid X-ray structures of proteins are used to dock flexible ligands, and these methods provide an approximate insight into how a group of compounds may bind and interact with the target. Furthermore, docking scores usually have a poor quantitative relationship with experimental thermodynamic data (ΔG values),[77,78] because a docking experiment does not replicate a physical reaction between the macromolecule and incoming ligand in solution. Therefore, only qualitative conclusions may be drawn between the thermodynamic data (Tables 1 and 2) and docking scores (Table S7). Consequently, we have focussed on *in silico* data that confirms the experimental results (CD spectra, K_a values, and fluorescence quenching data). The key trends are discussed below.

From Table S7, HSA has several binding sites for **1** and **2**, with docking scores (ΔG_{dock}) ranging from −1.4 to − 5.2 kcal mol^{-1}. Both Pt(II) chelates repeatedly favoured similar binding locations (~3 in total including Sudlow's I and II) and a third site between subdomain IA-IIA, consistent with X-ray data for diverse drug and ligand types bound by HSA[53] and recent data reported for d^8 metal ions chelated by a related bis(pyrrolide-imine) ligand system.[39]

The binding sites targeted by the Pt(II) chelates were all located between 5–30 Å of Trp-214. Distances longer than 20 Å are less likely to cause quenching of Trp-214 fluorescence. In such instances, these may be secondary, less-favourable Pt(II) chelate binding sites. Regarding Tyr and Phe (Table S8), both amino acids were within 6–19 Å from the docked Pt(II) chelate which afforded observable perturbations in the near-UV CD spectrum between 250 and 295 nm (Figs. 7c and 7d).

The presence of warfarin and diazepam bound within HSA subdomains IIA and IIIA, respectively, minimally influenced the docking scores for the uptake of **2**, while there was a decrease in the docking score for **1** (Table S7). Thus, ΔG_{dock} for **1** is reduced from −4.62 to −1.39 kcal mol^{-1} when warfarin is present (Table S7) and from −5.15 to −2.02 kcal mol^{-1} when diazepam is present (Table S7). In both instances, **1** is redirected to less favourable binding sites. Ibuprofen bound within Sudlow's site II (subdomain IIIA, as well as at its secondary site, IIA-IIB) did not affect the docking scores of either **1** or **2**. This *in silico* result accords with the site displacement data for HSA•{ibuprofen} (Fig. 6), since neither **1** nor **2** have sufficient affinity (high enough $\log K_a$ values) to displace ibuprofen. Consequently, it seems likely that the Pt(II) chelates were redirected to alternate binding site(s) in the fluorescence quenching experiments depicted in Fig. 6.

Conclusions

The interaction of Pt(II) chelates **1**–**3** with HSA was investigated using complementary spectroscopic techniques to understand how the identity of the bis(pyrrole-imine) Schiff base ligand coordinated to the Pt(II) ion affects uptake of the complexes by the protein. All three Pt(II) chelates quenched the intrinsic Trp-214 fluorescence of HSA, with **1** exerting the effect via a static quenching mechanism, while **2** and **3** favoured a dynamic quenching mechanism. The three Pt(II) chelates had HSA affinity constants (K_a values) that were typical of many small molecule ligands for the protein (10^3 – 10^5 M^{-1}).[79,80] The Stern-Volmer quenching constants (K_{sv}) followed the order **1** > **2** > **3**, while the K_a values followed the order **1** > **3** > **2**. The reaction stoichiometry for all three Pt(II) chelates was 1:1 (Pt:HSA), with possible partial occupation of a second, lower affinity site occurring at higher concentrations.

Pt(II) chelates **1** and **3** bind to HSA with negative ΔH, ΔG, and positive ΔS values, reflecting a spontaneous enthalpy-driven process governed by van der Waals (London dispersion) forces,

Please do not adjust margins

while **2** had a positive ΔH, negative ΔG and a strongly positive ΔS, consistent with an entropically driven reaction with HSA. Glide XP docking simulations in conjunction with fluorescence and induced CD site specificity assays employing probe ligands showed that **1** and **2** bind preferentially in Sudlow's site II, with possible additional binding sites being accessible. Far- and near-UV CD spectroscopy confirmed that the binding of **1** and **2** minimally perturbs the protein's secondary structure. Finally, the induced CD spectra recorded for HSA•{**1**} and HSA•{**2**} distinctly confirm uptake of the intact complexes without imine group hydrolysis or demetallation.

Author Contributions

O. Q. M. and S. S. co-designed the study. S. S. synthesised and characterized the compounds, carried out the spectroscopy, collected and analysed the thermodynamic data, and performed the molecular simulations. O. Q. M. recorded the X-ray data. The initial manuscript was written by S. S.; the final manuscript and figures were reviewed, edited, and co-written in parts by O. Q. M.

Conflicts of interest

The authors have no conflicts to declare.

Acknowledgements

This work is based on research supported by the South African Research Chairs Initiative of the Department of Science and Innovation (DSI) and National Research Foundation (NRF) of South Africa (Grant No 64799, OQM). The authors thank WITS University and the NRF for funding to purchase a JASCO J-1500 MCD spectrometer (Grant No 116177, OQM) and a dual-wavelength Bruker D8 Venture X-ray diffractometer (Grant No 129920, OQM). We also thank the Centre for High Performance Computing (Project CHEM1065, CHPC, Cape Town) for both the CPU time and resources needed for the DFT simulations.

References

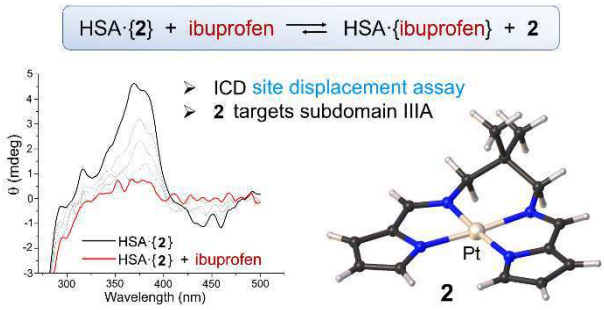
1 R. U. Braun, K. Zeitler and T. J. J. Müller, *Org. Lett.*, 2001, **3**, 3297–3300.
2 C. E. Hewton, M. C. Kimber and D. K. Taylor, *Tetrahedron Lett.*, 2002, **43**, 3199–3201.
3 M. P. Akerman and V. A. Chiazzari, *J. Mol. Struct.*, 2014, **1058**, 22–30.
4 C. H. Wei and J. R. Einstein, *Acta Crystallogr. B*, 1972, **28**, 2591–2598.
5 Y. Wang, H. Fu, F. Shen, X. Sheng, A. Peng, Z. Gu, H. Ma, J. S. Ma and J. Yao, *Inorg. Chem.*, 2007, **46**, 3548–3556.
6 S. Bhikraj, O. Q. Munro and M. P. Akerman, *Polyhedron*, 2017, **124**, 22–29.
7 J. S. Hart, G. S. Nichol and J. B. Love, *Dalton Trans.*, 2012, **41**, 5785–5788.
8 H. Liang, J. Liu, X. Li and Y. Li, *Polyhedron*, 2004, **23**, 1619–1627.
9 C. N. Iverson, C. A. G. Carter, R. T. Baker, J. D. Scollard, J. A. Labinger and J. E. Bercaw, *J. Am. Chem. Soc.*, 2003, **125**, 12674–12675.
10 X.-F. Shan, D.-H. Wang, C.-H. Tung and L.-Z. Wu, *Tetrahedron*, 2008, **64**, 5577–5582.
11 Y. Kim, J. Lee, Y.-H. Son, S.-U. Choi, M. Alam and S. Park, *J. Inorg. Biochem.*, 2020, **205**, 111015.
12 C. H. Wei, *Inorg. Chem.*, 1972, **11**, 2315–2321.
13 N. A. Bailey, A. Barrass, D. E. Fenton, M. S. L. Gonzalez, R. Moody and C. O. R. de Barbarin, *J. Chem. Soc. Dalton Trans.*, 1984, 2741–2746.
14 F. Z. C. Fellah, J.-P. Costes, F. Dahan, C. Duhayon, G. Novitchi, J.-P. Tuchagues and L. Vendier, *Inorg. Chem.*, 2008, **47**, 6444–6451.
15 Y. Hu, Q. Li, H. Li, Q. Guo, Y. Lu and Z. Li, *Dalton Trans.*, 2010, **39**, 11344–11352.
16 H. Adams, M. R. J. Elsegood, D. E. Fenton, S. L. Heath and S. J. Ryan, *J. Chem. Soc. Dalton Trans.*, 1999, 2031–2038.
17 K. J. Akerman, A. M. Fagenson, V. Cyril, M. Taylor, M. T. Muller, M. P. Akerman and O. Q. Munro, *J. Am. Chem. Soc.*, 2014, **136**, 5670–5682.
18 F. M. Muggia, A. Bonetti, J. D. Hoeschele, M. Rozencweig and S. B. Howell, *J. Clin. Oncol.*, 2015, **33**, 4219–4226.
19 C. X. Zhang and S. J. Lippard, *Curr. Opin. Chem. Biol.*, 2003, **7**, 481–489.
20 T. Boulikas, A. Pantos, E. Bellis and P. Christofis, *Cancer Ther.*, 2007, **5**, 537–583.
21 T. Makovec, *Radiol. Oncol.*, 2019, **53**, 148–158.
22 T. P. Jr, *All About Albumin: Biochemistry, Genetics, and Medical Applications*, Academic Press, 1995.
23 X. M. He and D. C. Carter, *Nature*, 1992, **358**, 209–215.
24 P. A. Zunszain, J. Ghuman, T. Komatsu, E. Tsuchida and S. Curry, *BMC Struct. Biol.*, 2003, **3**, 6.
25 G. Sudlow, D. J. Birkett and D. N. Wade, *Mol. Pharmacol.*, 1975, **11**, 824–832.
26 G. Sudlow, D. J. Birkett and D. N. Wade, *Mol. Pharmacol.*, 1976, **12**, 1052–1061.
27 M. Fasano, S. Curry, E. Terreno, M. Galliano, G. Fanali, P. Narciso, S. Notari and P. Ascenzi, *IUBMB Life*, 2005, **57**, 787–796.
28 G. Rabbani and S. N. Ahn, *Int. J. Biol. Macromol.*, 2019, **123**, 979–990.
29 M. P. Akerman, T. Chatturgoon and O. Q. Munro, *Inorg. Chim. Acta*, 2014, **421**, 292–299.
30 A. Bondi, *J. Phys. Chem.*, 1964, **68**, 441–451.
31 S. Soares, N. Mateus and V. de Freitas, *J. Agric. Food Chem.*, 2007, **55**, 6726–6735.
32 M. H. Gehlen, *J. Photochem. Photobiol. C Photochem. Rev.*, 2020, **42**, 100338.
33 O. K. Abou-Zied and O. I. K. Al-Shihi, *J. Am. Chem. Soc.*, 2008, **130**, 10793–10801.
34 P. R. Callis, *J. Mol. Struct.*, 2014, **1077**, 14–21.
35 Y. Yue, J. Liu, M. Yao, X. Yao, J. Fan and H. Ji, *Spectrochim. Acta A. Mol. Biomol. Spectrosc.*, 2012, **96**, 316–323.
36 A. Hussain, M. F. AlAjmi, M. T. Rehman, S. Amir, F. M. Husain, A. Alsalme, M. A. Siddiqui, A. A. AlKhedhairy and R. A. Khan, *Sci. Rep.*, 2019, **9**, 5237.
37 S. R. Feroz, S. B. Mohamad, N. Bujang, S. N. A. Malek and S. Tayyab, *J. Agric. Food Chem.*, 2012, **60**, 5899–5908.
38 A. Divsalar, M. J. Bagheri, A. A. Saboury, H. Mansoori-Torshizi and M. Amani, *J. Phys. Chem. B*, 2009, **113**, 14035–14042.

Please do not adjust margins

39 S. Sookai and O. Q. Munro, *ChemistryEurope*, 2023, **1**, e202300012.
40 M. K. Helms, C. E. Petersen, N. V. Bhagavan and D. M. Jameson, *FEBS Lett.*, 1997, **408**, 67–70.
41 K. Flora, J. D. Brennan, G. A. Baker, M. A. Doody and F. V. Bright, *Biophys. J.*, 1998, **75**, 1084–1096.
42 P. Alam, S. K. Chaturvedi, T. Anwar, M. K. Siddiqi, M. R. Ajmal, G. Badr, M. H. Mahmoud and R. Hasan Khan, *J. Lumin.*, 2015, **164**, 123–130.
43 G. G. Ariga, P. N. Naik, S. A. Chimatadar and S. T. Nandibewoor, *J. Mol. Struct.*, 2017, **1137**, 485–494.
44 J. R. Lakowicz, *Principles of Fluorescence Spectroscopy*, Springer US, Boston MA, 3rd edn., 2006.
45 F. Samari, B. Hemmateenejad, M. Shamsipur, M. Rashidi and H. Samouei, *Inorg. Chem.*, 2012, **51**, 3454–3464.
46 Z. Chen, S. Zhang, Z. Zhu and Y. Zhang, *New J. Chem.*, 2017, **41**, 6340–6348.
47 P. D. Ross and S. Subramanian, *Biochemistry*, 1981, **20**, 3096–3102.
48 A. Samanta, S. Jana, D. Ray and N. Guchhait, *Spectrochim. Acta. A. Mol. Biomol. Spectrosc.*, 2014, **121**, 23–34.
49 H. Aki, M. Goto and M. Yamamoto, *Thermochim. Acta*, 1995, **251**, 379–388.
50 R. E. Olson and D. D. Christ, in *Annual Reports in Medicinal Chemistry*, ed. J. A. Bristol, Academic Press, 1996, vol. 31, pp. 327–336.
51 H. Aki and M. Yamamoto, *J. Pharm. Sci.*, 1994, **83**, 1712–1716.
52 I. Petitpas, A. A. Bhattacharya, S. Twine, M. East and S. Curry, *J. Biol. Chem.*, 2001, **276**, 22804–22809.
53 J. Ghuman, P. A. Zunszain, I. Petitpas, A. A. Bhattacharya, M. Otagiri and S. Curry, *J. Mol. Biol.*, 2005, **353**, 38–52.
54 S. M. Kelly, T. J. Jess and N. C. Price, *Biochim. Biophys. Acta BBA - Proteins Proteomics*, 2005, **1751**, 119–139.
55 N. Sreerama and R. W. Woody, in *Methods in Enzymology*, Academic Press, 2004, vol. 383, pp. 318–351.
56 A. Micsonai, F. Wien, É. Bulyáki, J. Kun, É. Moussong, Y.-H. Lee, Y. Goto, M. Réfrégiers and J. Kardos, *Nucleic Acids Res.*, 2018, **46**, W315–W322.
57 F. Mohammadi, A.-K. Bordbar, A. Divsalar, K. Mohammadi and A. A. Saboury, *Protein J.*, 2009, **28**, 189–196.
58 H. A. Tajmir-Riahi, C. N. N'Soukpoe-Kossi and D. Joly, *Spectroscopy*, 2009, **23**, 81–101.
59 A. Khammari, A. A. Saboury, M. H. Karimi-Jafari, M. Khoobi, A. Ghasemi, S. Yousefinejad and O. K. Abou-Zied, *Phys. Chem. Chem. Phys.*, 2017, **19**, 10099–10115.
60 R. A. Friesner, J. L. Banks, R. B. Murphy, T. A. Halgren, J. J. Klicic, D. T. Mainz, M. P. Repasky, E. H. Knoll, M. Shelley, J. K. Perry, D. E. Shaw, P. Francis and P. S. Shenkin, *J. Med. Chem.*, 2004, **47**, 1739–1749.
61 T. A. Halgren, R. B. Murphy, R. A. Friesner, H. S. Beard, L. L. Frye, W. T. Pollard and J. L. Banks, *J. Med. Chem.*, 2004, **47**, 1750–1759.
62 F. R. Clemente, T. Vreven and M. J. Frisch, in *Quantum Biochemistry*, John Wiley & Sons, Ltd, 2010, pp. 61–83.
63 T. Yanai, D. P. Tew and N. C. Handy, *Chem. Phys. Lett.*, 2004, **393**, 51–57.
64 P. Fuentealba, H. Preuss, H. Stoll and L. Von Szentpály, *Chem. Phys. Lett.*, 1982, **89**, 418–422.
65 S. Grimme, S. Ehrlich and L. Goerigk, *J. Comput. Chem.*, 2011, **32**, 1456–1465.
66 A. K. Rappe, C. J. Casewit, K. S. Colwell, W. A. Goddard and W. M. Skiff, *J. Am. Chem. Soc.*, 1992, **114**, 10024–10035.
67 G. Ferraro, L. Massai, L. Messori and A. Merlino, *Chem. Commun.*, 2015, **51**, 9436–9439.
68 A. Bijelic, S. Theiner, B. K. Keppler and A. Rompel, *J. Med. Chem.*, 2016, **59**, 5894–5903.
69 H. Yin, L. Liao and J. Fang, *JSM Clin. Oncol. Res.*, 2014, **2**, 1010.
70 D. Lafitte, P. O. Tsvetkov, F. Devred, R. Toci, F. Barras, C. Briand, A. A. Makarov and J. Haiech, *Biochim. Biophys. Acta BBA-Proteins Proteomics*, 2002, **1600**, 105–110.
71 O. K. Abou-Zied and O. I. K. Al-Shihi, *J. Am. Chem. Soc.*, 2008, **130**, 10793–10801.
72 S. M. Kelly and N. C. Price, *Curr. Protein Pept. Sci.*, 2000, **1**, 349–384.
73 X.-X. Cheng, X.-Y. Fan, F.-L. Jiang, Y. Liu and K.-L. Lei, *Luminescence*, 2015, **30**, 1026–1033.
74 A. Barth, S. R. Martin and P. M. Bayley, *Biopolym. Orig. Res. Biomol.*, 1998, **45**, 493–501.
75 B. Valeur and G. Weber, *Photochem. Photobiol.*, 1977, **25**, 441–444.
76 T. Vreven, K. S. Byun, I. Komáromi, S. Dapprich, J. A. Montgomery, K. Morokuma and M. J. Frisch, *J. Chem. Theory Comput.*, 2006, **2**, 815–826.
77 A. R. Leach, B. K. Shoichet and C. E. Peishoff, *J. Med. Chem.*, 2006, **49**, 5851–5855.
78 G. L. Warren, C. W. Andrews, A.-M. Capelli, B. Clarke, J. LaLonde, M. H. Lambert, M. Lindvall, N. Nevins, S. F. Semus, S. Senger, G. Tedesco, I. D. Wall, J. M. Woolven, C. E. Peishoff and M. S. Head, *J. Med. Chem.*, 2006, **49**, 5912–5931.
79 C. Dong, S. Ma and Y. Liu, *Spectrochim. Acta. A. Mol. Biomol. Spectrosc.*, 2013, **103**, 179–186.
80 G. Wang, X. Li, X. Ding, D. Wang, C. Yan and Y. Lu, *J. Pharm. Biomed. Anal.*, 2011, **55**, 1223–1226.

Please do not adjust margins

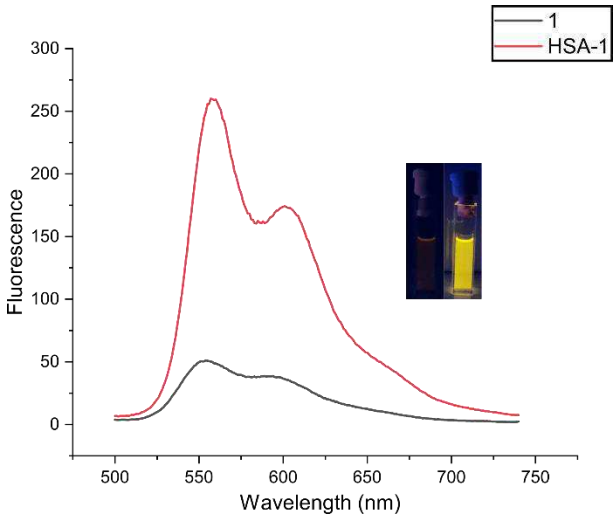
Graphical Abstract



Bis(pyrrolide-imine) chelates of Pt(II) such as **2** bind to human serum albumin (HSA) with modest affinity constants and thermodynamics controlled by the ligand architecture. Using a combination of CD and fluorescence spectroscopy with probe ligands (warfarin and ibuprofen) as well as docking and TD-DFT simulations, we found that the complexes target subdomain IIIA in HSA and bind noncovalently as intact metal chelates.

Please do not adjust margins

Chapter 5 Bioimaging Pt(II) Schiff base chelates



ARTICLE

Bioimaging Pt(II) Schiff base chelates

Sheldon Sookai,[a] Shanen Perumal [b] Mandeep Kaur [b] and Orde Munro *[a]

Received 00th January 20xx,
Accepted 00th January 20xx

DOI: 10.1039/x0xx00000x

Four Pt(II) bis(pyrrole-imine) Schiff base chelates (**1**-**4**) were synthesised through a condensation reaction, and the novel crystal structure of 2,2'-{propane-1,3-diylbis[nitrilo(E)methylylidene]}bis(pyrrol-1-ido)platinum(II) (**1**) was obtained. Pt(II) complexes **1**-**4** exhibited phosphorescence, with increased luminescence in anaerobic solvents or when bound to human serum albumin (HSA). Complex **1** had a 119-fold increase in quantum yield when bound to HSA and could detect HSA concentrations as low as 5 nM. Pt(II) complexes **1**-**3** were investigated as theranostic agents against MCF-7 breast cancer cells, but only complex **3** exhibited cytotoxicity when irradiated with UV light ($\lambda^{irridiation}$, 355 nm). Interestingly, complex **1** demonstrated equal cytotoxicity when irradiated compared to non-irradiated. Fluorescence microscopy did not reveal any target organelles, indicating that only complex **3** can be considered a potential photosensitizing agent.

Introduction

Schiff bases comprising of an imine group have for decades drawn the interest of researchers due to their relative ease of synthesis, unique roles in pharmaceuticals[1,2], and their ability to form complexes with transition metal ions. Complexes of Schiff base imines are an attractive class of complexes due to their versatility in fields such as photophysics,[3–5] catalysis,[6] investigational anticancer drug candidates,[7,8] and their uses in biological applications.[7,9]

The well-known Pt(II) complexes cisplatin, carboplatin, and oxaliplatin are widely administrated and successful anticancer clinical drugs.[10] Unfortunately, they cause severe side effects[11] and certain cancer strains have become drug resistant.[12,13] This has prompted researchers to find novel Pt-based anticancer agents with diminished toxicity and unique modes of action. These include Pt(IV) prodrugs that upon administration are reduced within a cell matrix or are reduced by irradiated light to the more active Pt(II) species, metal center.[14–16] Efforts are well documented to develop theranostic and/or photodynamic therapeutic agents (PDT's).[7,8,17,18] Metal-based theranostic compounds consists of either Ir(III),[19–22] Ru(II),[23–25] Re(I),[26–28] or Pt(II),[7,8,17,18] while less common heavy metal centers are Rh(III), Os(II)[29–31] and Pd(II).[32] The heavy metal center coupled with the organic ligand framework results in the ability of the compound to phosphoresce via metal-to-ligand charge transfer (MLCT) transitions. Theranostic agents serve as tools: diagnostic and therapeutic.[33] Key characteristics of phosphorescent heavy metal complexes employed as diagnostic tools typically in bioimaging are (i) large stokes shifts, (ii) high quantum yields, (iii) photosensitivity, (iv) two-photon absorption cross section and, (v) based on the organic ligand framework targeting of specific cellular organelles.[34,35] From a therapeutic aspect heavy metal complexes target cancer cells by one of two mechanisms: (i) generation of reactive oxygen species (ROS) such as $O_2^{\bullet-}$ and $OH^{\bullet}$[36] or (ii) direct energy transfer from the photosensitizer to $^3O_2$ reducing it to $^1O_2$.[23] Heavy metal ions that do this may also be referred to as photodynamic therapeutics (PDT). Currently there are two PDT agents undergoing clinical trials WST11 (a Pd(II) bacteriopheopharbide derivative)[32,37] and TLD-1433 (a polypyridyl Ru(II) complex).[23]

During the development of effective therapeutic agents, it is important to understand their interaction with human serum albumin (HSA). HSA is the most abundant plasma protein occurring at concentrations of 600 μM.[38] The two main functions of HSA are to maintain osmotic pressure and to transport both endogenous and exogenous compounds.[39] Furthermore, delineating the interaction of drug-like molecules with HSA is key to understanding their pharmacokinetic and pharmacodynamic data. When some phosphorescent heavy metal complexes bind to HSA there is a "switch on light effect" embarked by an increase in the quantum yield of the heavy metal complex. This is useful in bioimaging and may serve as a method to understand the mechanism by which HSA transports heavy metal complexes to tumors.[33] There have been few studies on Pt(II) Schiff base complexes being used in theranostic or PDT agents.[7]

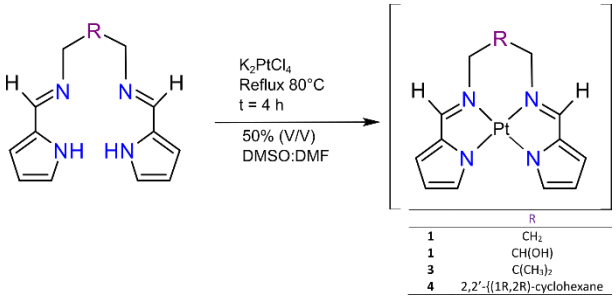
[a]*Molecular Sciences Institute, School of Chemistry, University of the Witwatersrand, PO WITS 2050, Johannesburg, South Africa*
[b]*Research Unit, School of Molecular and Cell Biology, University of the Witwatersrand, Johannesburg, 2050, South Africa*
[c]*Electronic Supplementary Information (ESI) available: Complete experimental details and supplementary tables and figures in PDF format, X-ray crystal structures in CIF format (CCDC 2207667 and 2207668), Cartesian coordinates for all calculated structures, and a Maestro project file containing Glide XP docking data. See DOI: 10.1039/x0xx00000x*

Here we report the novel crystal structure of **1** determined in a square planar geometry. The electronic absorption and emission spectra were studied under different conditions and reported as a relative quantum yield. Lastly, we examined the theranostic capabilities of Pt(II) complexes **1**–**3** against MCF-7 breast cancer cells.

Results and Discussion

X-ray crystal structure

The Pt(II) bis(pyrrole-imine) chelates were synthesised by methods previously reported.[4] Reaction scheme 1, provides a brief outline of the synthetic route used. In brief, the appropriate bis(pyrrole-imine) chelate was metalated with a Pt(II) ion from K_2PtCl_4. Complex **4** was obtained without any impurities from the method described previously,[4] while **2** and **3** were prepared by a similar method to **4**. The novel crystal structure for complex **1** was achieved by slow liquid diffusion of a DCM solution into hexane.



Scheme 1 Synthetic procedure for **1**, **2**, **3**, and **4** by reacting the appropriate bis (pyrrole – imine) chelates with H_2PtCl_4.

The single crystal of **1** obtained by slow liquid diffusion was a dark red rhombic crystal. Complex **1** (Fig. 1a) crystalised in a monoclinic $P2_1/c$ space group, the Pt(II) metal ion centre adopts a four-coordinate square planar geometry. The asymmetric unit (ASU) of **1** comprises four independent molecules (A–D; Fig. 1b), each having the square planar Pt(II) ion chelated by the tetradentate bis(pyrrole-imine) ligand. The Pt–$N_{pyrrole}$ and Pt–N_{imine} distances average 2.013(4) and 2.003(4) Å, respectively (Table S1). These bond distances are statistically equivalent to the mean Pt–$N_{pyrrole}$ and Pt–N_{imine} values of the chiral Pt(II) (*R*,*R*)-(–)- and (*S*,*S*)-(+)-1,2-bis(pyrrol-2-ylmethyleneamino)cyclohexane ligands reported by Shan *et al*.[4]

Typically, the sum of the angles around a square planar metal centre equates to 360°. The sum of the angles around **1** was 350.69° (16). The slightly non-planar conformations of the ligands mainly reflect non-bonded crystal packing interactions and the formation of discrete, stacked dimers. In Fig. 1b, the dimer formed by molecules A and B is face-to-face (in an inverted relative orientation) with a Pt1A···Pt1B separation of 3.732 (1) Å, PtN4 plane centroid-to-centroid (Ct···Ct) distance of 5.061(4) Å, mean plane separation (MPS_{AB}) of 4.020(1) Å, (Fig. 1). Both bis(pyrrolide-imine) chelates curve inwards towards the intradimer space. The monomers from the dimer formed by molecules C and D are similar to that of molecules A and B, whereby they are face-to-face (in an inverted relative orientation). Molecules C and D exhibit a Pt1C···Pt1D separation of 3.800(1) Å, a Ct···Ct distance of 5.189(4) Å, and a mean plane separation (MPS_{CD}) of 3.606(4) Å and curve inwards towards the intradimer space. The Pt···Pt bond distances are greater than 3.5 Å which is double the van der Waals radius of the Pt atom[40] and fall outside the range of dz_2(Pt)–dz_2(Pt) orbital interactions. These distances are consistent with weak (metal-metal) d^8 interactions.

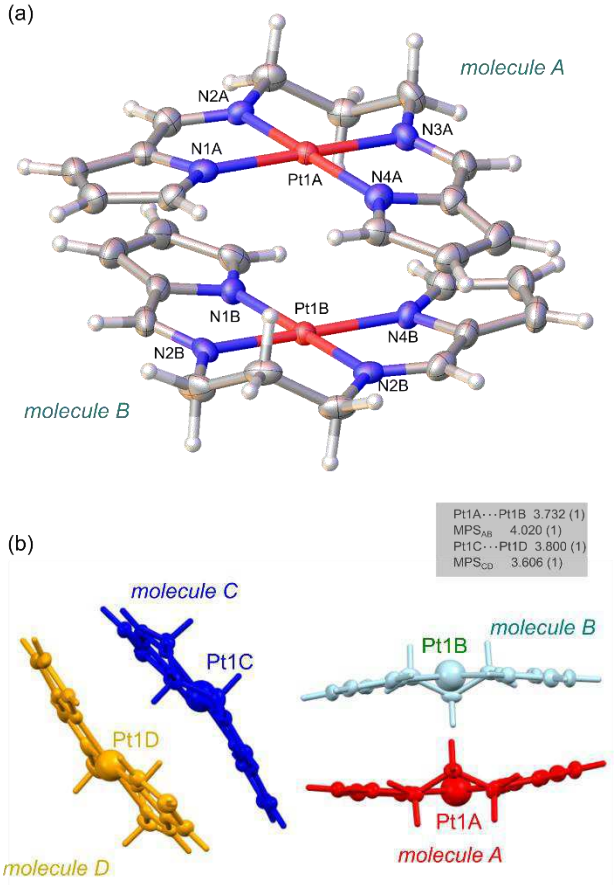


Fig. 1 (a) Partly labeled view of the X-ray structure of **1**. Two of the four independent molecules (A and B) in the asymmetric unit are illustrated. (b) View of the asymmetric unit of the crystal structure of **1** with the four independent molecules coloured according to their symmetry operators. A single type of π···π dimer formed by the metal chelates is evident from their packing. That is face-to-face (in an inverted relative orientation) for all four molecules. Thermal ellipsoids are rendered at 40% in a and 50% in b, respectively. Hydrogen atoms are drawn as spheres with an arbitrary radius and Pt(II) ions are presented as spheres in b.

UV-visible spectra and DFT simulations of the Pt(II) chelates

Complexes **1**-**4** exhibited intense absorption bands below 330 nm (ε > 25 000 M^{-1} cm^{-1} in acetonitrile and > 20 000 M^{-1} cm^{-1} in dH_2O) and moderate-to-low-intensity bands between 350 – 500 nm (ε < 25 000 M^{-1} cm^{-1} in acetonitrile and < 20 000 M^{-1} cm^{-1} in dH_2O) and are presented in Figs. 2a and S19. They exhibit ligand-centered $^1\pi$–π^* (or ^{1}LC) intra-ligand (IL) transition bands of the bis(pyrrole-imine) ligands at wavelengths below 330 nm (ε > 15 000 M^{-1} cm^{-1}). Absorption bands at longer wavelengths (350–410 nm (ε ~ 15 000 M^{-1} cm^{-1}) and 410–500

nm (ε < 15 000 M^{-1} cm^{-1}) were ascribed to the spin allowed Pt(II) perturbed, ligand ($^1\pi$–π^*) transitions and ^{1}[Pt(5d)/π*(Schiff base)] metal to ligand charge transfer (MLCT) character. The Pt(II) chelates MLCT bands are absent in the UV-vis absorption spectra of the free bis(pyrrole-imine) ligands (Fig. S13). The assignment of the UV-vis absorption bands was supplemented by a previous study of **4**[4,41]

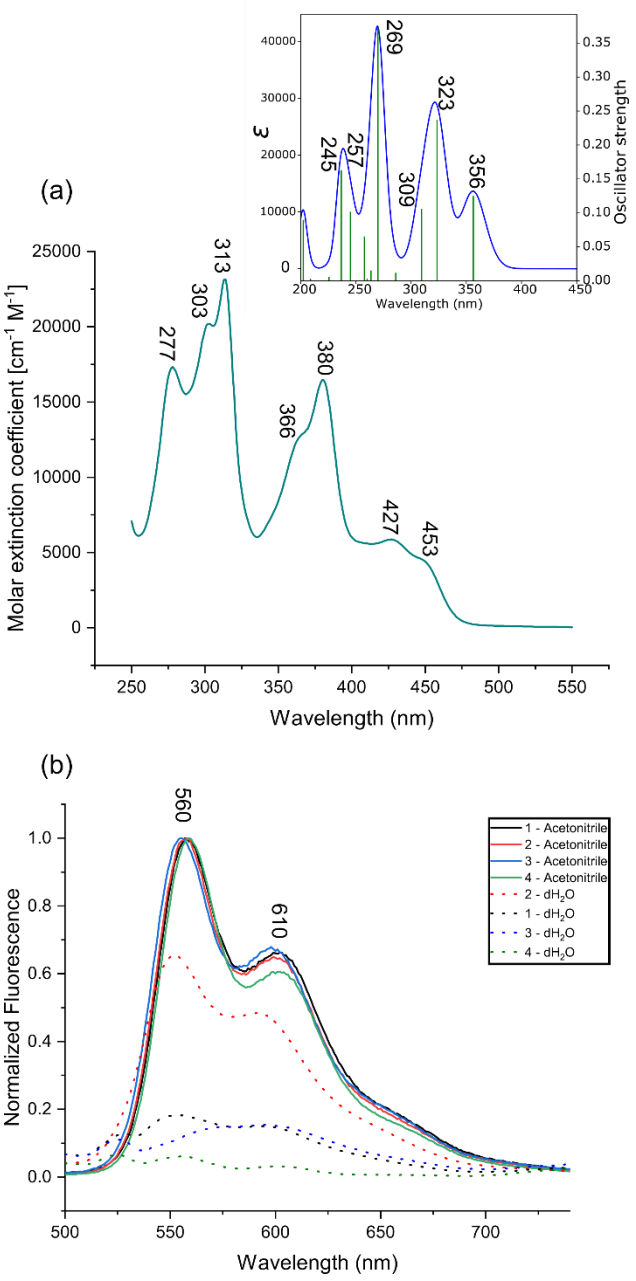


Fig.2 (a) Experimental and DFT calculated (inset) electronic absorption spectra of **3** in acetonitrile. The absorption maxima (λ_{max}) are indicated for the experimental spectrum at 427, 380, 366, 313, 303, and 277 nm. The absorption envelope for the DFT calculated envelope spectrum of **3** is plotted from 200 – 450 nm and is plotted with a bandwidth of 2000 cm^{-1} (full width at half maximum intensity, FWHM). (b) Normalized emission spectra of **1 – 4** at 298 K in acetonitrile (**1**) black, (**2**) red, (**3**) blue, and (**4**) green lines and in dH_2O (**1**) dashed black, (**2**) dashed red, (**3**) dashed blue, (**4**) dashed green lines.

TD-DFT simulations at the B3LYP/DEF2TZVP level of theory were used to assign the most intense absorbing bands of the Pt(II) chelates in acetonitrile and the spectrum for **1** is presented in the inset to Fig. 2a. The calculated maximums and major contributions of each transition are summarised in Tables. S3–S5.A comparison between the TD-DFT calculated spectrum and the experimental absorption spectrum of **1** is similar with most maxima peaks being accounted for in Fig. 2a.

Upon excitation, complexes **1–4** produced a yellow phosphorescent emission spectrum in both acetonitrile and aqueous solution that had a maximum peak at ~560 nm and a shoulder at 610 nm (Fig. 2b). Which was in agreement with prior studies of Pt(II)-bis (pyrrolide-imine) chelates.[4,42] The luminescence emission spectrum of **1**, **3,** and **4** in dH_2O had poor resolution and the peaks were not well defined. However, this was not the case for **2** (Fig. S19b), likely due to the OH motif on the bis(pyrrolide-imine) chelate which enhanced the solubility of the Pt(II) chelate in the aqueous solution.

Apparent Quantum yields of the Pt(II) Schiff base chelates

To further support the luminescence exhibited by **1–4**, we measured the luminescent emission spectra of the Pt(II) complexes in the absence of molecular oxygen ($^3O_2$) in acetonitrile and dH_2O (Fig. S15). The removal of $^3O_2$ resulted in a significant enhancement in the luminescence emission of **1–4** (Table S7). The increase in emission was due to the removal of $^3O_2$ suggesting the luminescence of **1–4** is phosphorescence. For phosphorescent molecules $^3O_2$ quenches the phosphorescence by a direct energy transfer mechanism, where energy from **1–4** reduces $^3O_2$ to $^1O_2$.[23,32] Therefore, the removal of $^3O_2$ resulted in higher luminescent emission.

To describe the luminescence of **1–3** with a higher degree of accuracy, we compared the relative quantum yields (Φ_F) of the Pt(II) complexes in DCM, bound to HSA and in both aerobic and anaerobic acetonitrile and dH_2O. The results are summarised in Tables S6 and S7. Complexes **1** and **2** had the highest (Φ_F) in dH_2O 0.0396 (± 0.0021) and 0.0654 (± 0.0042), respectively, while **3** and **4** had the highest Φ_F in DCM 0.0222 (±0.0006) and 0.0242 (±0.0013) respectively. Overall, the **1–3** had low (Φ_F) emissions in aerobic solvents (Φ_F ranging from 0.0052–0.065) and **1–2** had moderate (Φ_F) in anaerobic dH_2O (Φ_F ranging from 0.20–0.43). Furthermore, when **1–3** was bound to HSA there was a significant enhancement in (Φ_F). Based on the significant enhancement in luminescence by the removal of $^3O_2$, the structural and spectral properties of **1–3** compared to **4** may share microsecond lifetimes.[4] Therefore, the luminescence emission of **1–3** is assigned to phosphorescence from ^{3}LC excited state and ^{1,3}MLCT states.

Pt(II) chelates binding to HSA

The Pt(II) chelates in this work have been previously shown to bind to HSA with moderate affinity, ranging from 10^3–10^5 M^{-1}, and exhibit a preference for binding to subdomain IIA within HSA (as discussed in Chapter 4). It is well documented that some luminescent metal complexes exhibit enhanced luminescence upon binding to HSA.[19,43] To test the luminescent properties of the four Pt(II) chelates used in this study, we incubated 5 µM of complexes **1–3** with 5 µM of HSA. Molecules **1**, **2**, and **3** exhibited a significant enhancement in phosphoresce upon

binding to HSA as shown in Figs. 3a and S14). The phosphorescence quantum yield of HSA···**1**, HSA···**2** and HSA···**3** adducts increased by 15.6, 4.26 and 12.2-fold, respectively (as summarised in Table S6) and had a λ_{max}^{em} of ~3 nm. In contrast complex **4** exhibited very weak phosphorescence intensity in aqueous solution and negligible binding to HSA.

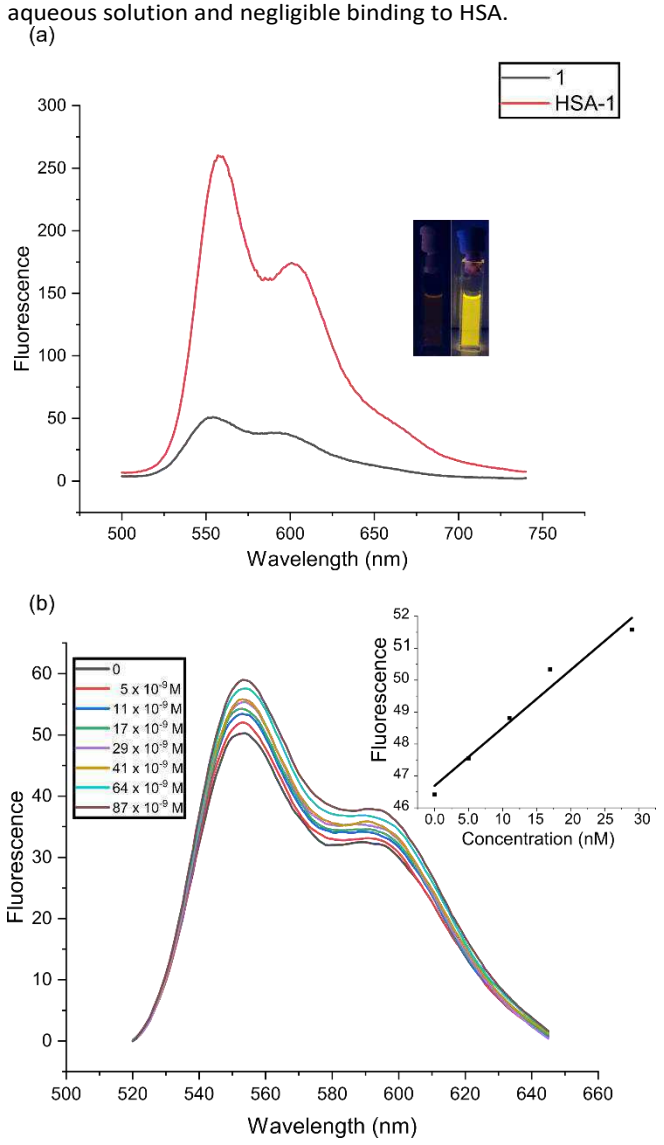
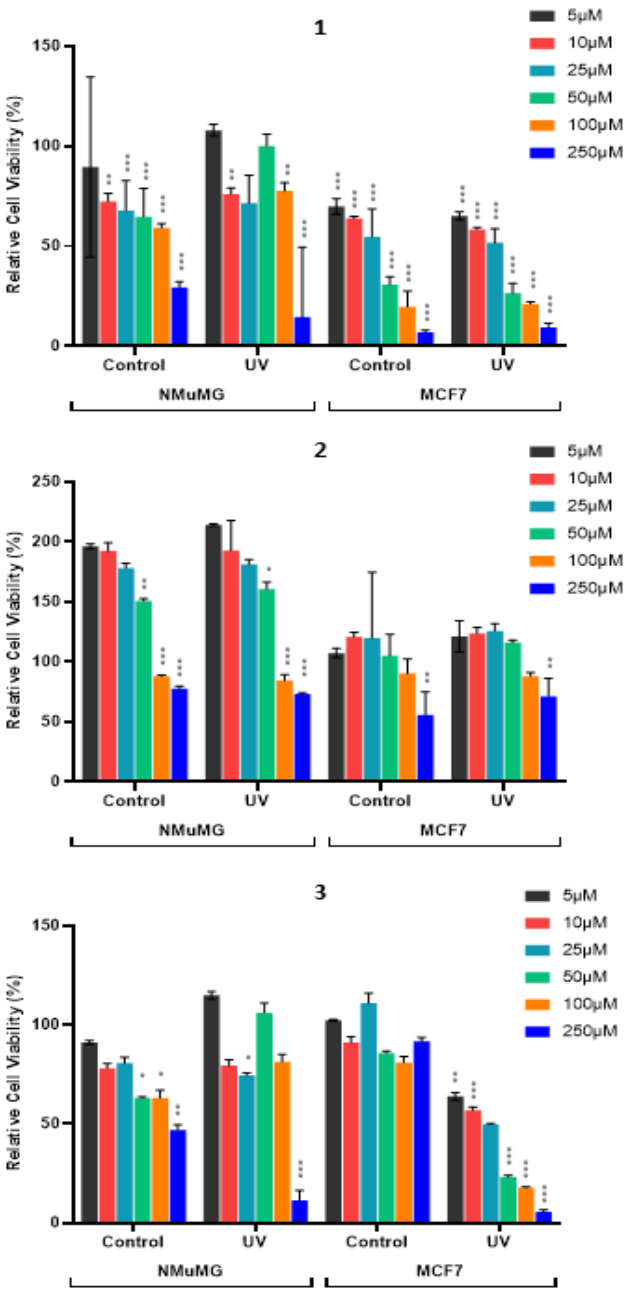


Fig. 3 (a) Fluorescence spectrum of 1 in the presence and absence of HSA in KH2PO4 (50 mM, pH 7.5). (b) Fluorescence spectrum of 1 upon increasing concentrations of HSA (0-87 μM) in KH2PO4 buffer (50 mM, pH 7.5). The insert is the linear relationship of the change in fluorescence intensity of **1** at 560 nm vs HSA concentration (0-29 nM).

Complex **1** had the highest enhancement in quantum yield when bound to HSA, as shown in Fig. S13a and Table S6, with an Φ_F of 0.0052 in acetonitrile increasing to 0.62 when bound to HSA representing a 119-fold increase in quantum yield. Since **1** was the most sensitive to luminescent enhancement in the presence of HSA, we measured the limit of detection (LOD) of HSA using **1** (Fig. 3b). HSA was detected at concentrations as low as 5 nM, with a linear relationship of 5-29 nM in KH_2PO_4 buffer. The LOD of HSA is consistent with other probes designed to detect HSA, such as Thieno[3,2-b]pyridine-5(4H)-one.[44] However, in this work, the Pt(II) chelates are not intended to be used as probes for HSA detection in biological samples. It is likely that **1** was most sensitive at detecting HSA as 2 molecules of **1** has been shown to bind to HSA by mass spectrometry.[45]

Fig. 4 Relative cell viability graphs represent the changes in cell viability percentage of



NMuMG and MCF7 cells in response to treatment with increasing concentrations of Pt(II) complexes 1(a), 2(b), and 3(c) relative to a vehicle control. Changes in viability were measured with and without exposure to UV light. Error bars represent standard deviation (n=3). Statistical significance was assessed using the Student's t-test, where * $p < 0.05$, ** $p < 0.01$, and *** $p < 0.001$.

Cytotoxicity of the Pt(II) chelates

The cytotoxic potential of Pt(II) complexes **1-3** was evaluated using the MTT assay. Complex **1** (Fig. 4a) shows a significant dose-dependent reduction of cell viability in MCF-7

cells, while only reducing the viability of NMuMG cells at higher concentrations. The cytotoxic effect of **1** did not change with UV exposure. The cytotoxicity of **1** at low concentrations in MCF-7 breast cancer cells compared to non-transformed NMuMG cells suggests a possible specificity to highly proliferative cancer cells and potential as a therapeutic compound. In contrast, complex **2** (Fig. 4b) shows no significant reduction in viability below 50% in either cell line or no response to UV exposure. The inactivity of complex **2** may be attributed to the OH functional group on the second position of the propyl bis(imine) linkage. The OH group is an electron-withdrawing group and could be favourable for uptake by cellular mechanisms such as the efflux pump which is known to detox cells of poisonous compounds.[46]

Complex **3** behaved as a photosensitizer (Fig. 4c) **3** showed little reduction in cell viability at lower concentrations in both cell lines, but after UV exposure (λ^{ex}, 355 nm), there is a significant dose-dependent reduction in the viability of MCF7 cells, but not NMuMG cells. This suggests possible specificity to highly proliferative cancer cells and potential as a PDT therapeutic compound.

Intracellular fluorescence of Pt(II) chelates

As the Pt(II) complexes emitted an enhanced quantum yield when bound to HSA, we evaluated them as photosensitisers. The intracellular fluorescence of Pt(II) complexes **1**-**3** was measured using fluorescence microscopy, shown in Fig. S20. **1** and **3** show high levels of cytoplasmic fluorescence, demonstrating cellular uptake in the absence of HSA. With the addition of HSA, intracellular fluorescence was reduced. However, it is worth noting that the fluorescence measurement was taken after 24 h, it is likely that HSA had transported the Pt(II) chelates **1** and **3** towards a certain target, and therefore quenching **1** and **3** phosphorescence. Unsurprisingly complex **2** shows a lower cellular uptake and a slight reduction with the addition of HSA. The lack of nuclear localization suggests a minimal alteration in gene expression or cell viability is caused by direct interaction with DNA, although interaction with cytoplasmic components is possible.

Conclusion

In this study, we synthesised four bis(pyrrolide-imine) chelates and obtained the novel X-ray structure of Pt(II) complex **1**. The photophysical data of the Pt(II) chelates were characterised by their apparent quantum yield (Φ_F). The bis(pyrrolide-imine) chelates heavily influenced the Φ_F in different environments and the enhancement in Φ_F in anaerobic solutions confirmed the phosphorescence of the Pt(II) chelates. Complex **1** had a 119-fold Φ_F enhancement when bound to HSA as compared to acetonitrile and was able to detect HSA at a concentration of 5 nM. Additionally, complex **1** was the only Pt(II) chelate that exhibited cytotoxicity to highly proliferative cells (MCF-7 cells), while complex **3** acted as a photosensitizer and was only cytotoxic when irradiated with UV light (355 nm). Fluorescence, microscopy was inconclusive in identifying the organelles targeted by the Pt(II) chelates.

Author Contributions

All four authors co-designed the study. S.S synthesised and characterised the ligands, carried out the spectroscopy, collated the photophysical data, and performed the initial TD-DFT simulations. SP performed the cell biology (fluorescence microscopy and cytotoxicity data). OQM did the X-ray crystallography and analysed the data for deeper correlations. The initial manuscript was co-written by SS and SP; the final manuscript and all figures were written and produced by OQM. All four authors approve the final version of the paper.

Conflicts of interest

The authors have no conflicts to declare.

Acknowledgments

This work is based on research supported by the South African Research Chairs Initiative of the Department of Science and Innovation (DSI) and the National Research Foundation (NRF) of South Africa (Grant No 64799, OQM). The authors thank WITS University and the NRF for funding to purchase a JASCO J-1500 MCD spectrometer (Grant No 116177, OQM) and a dual-wavelength Bruker D8 Venture X-ray diffractometer (Grant No 129920, OQM). We also thank the Centre for High-Performance Computing (Project CHEM1065, CHPC, Cape Town) for both the CPU time and resources needed for the DFT simulations.

References

1 R. U. Braun, K. Zeitler and T. J. J. Müller, *Org. Lett.*, 2001, **3**, 3297–3300.
2 C. E. Hewton, M. C. Kimber and D. K. Taylor, *Tetrahedron Lett.*, 2002, **43**, 3199–3201.
3 K. Li, G. S. M. Tong, Q. Wan, G. Cheng, W.-Y. Tong, W.-H. Ang, W.-L. Kwong and C.-M. Che, *Chem. Sci.*, 2016, **7**, 1653–1673.
4 X.-F. Shan, D.-H. Wang, C.-H. Tung and L.-Z. Wu, *Tetrahedron*, 2008, **64**, 5577–5582.
5 S. S. Razi, Y. H. Koo, W. Kim, W. Yang, Z. Wang, H. Gobeze, F. D'Souza, J. Zhao and D. Kim, *Inorg. Chem.*, 2018, **57**, 4877–4890.
6 W. Zhang, N. H. Lee and E. N. Jacobsen, *J. Am. Chem. Soc.*, 1994, **116**, 425–426.
7 S. Banerjee, M. S. Capper, G. J. Clarkson, H. Huang and P. J. Sadler, *Polyhedron*, 2019, **172**, 157–166.
8 J. Deng, J. Wang, M. Khan, P. Yu, F. Yang and H. Liang, *J. Inorg. Biochem.*, 2018, **185**, 10–16.
9 Q.-P. Qin, Z.-F. Wang, X.-L. Huang, M.-X. Tan, B.-Q. Zou and H. Liang, *Eur. J. Med. Chem.*, 2019, **184**, 111751.
10 E. Wong and C. M. Giandomenico, *Chem. Rev.*, 1999, **99**, 2451–2466.
11 X. Yao, K. Panichpisal, N. Kurtzman and K. Nugent, *Am. J. Med. Sci.*, 2007, **334**, 115–124.

This journal is © The Royal Society of Chemistry 20xx

12 M. P. Barr, S. G. Gray, A. C. Hoffmann, R. A. Hilger, J. Thomale, J. D. O'Flaherty, D. A. Fennell, D. Richard, J. J. O'Leary and K. J. O'Byrne, *PLOS ONE*, 2013, **8**, e54193.

13 A. K. Godwin, A. Meister, P. J. O'Dwyer, C. S. Huang, T. C. Hamilton and M. E. Anderson, *Proc. Natl. Acad. Sci.*, 1992, **89**, 3070–3074.

14 T. C. Johnstone, K. Suntharalingam and S. J. Lippard, *Chem. Rev.*, 2016, **116**, 3436–3486.

15 Y. Shi, S.-A. Liu, D. J. Kerwood, J. Goodisman and J. C. Dabrowiak, *J. Inorg. Biochem.*, 2012, **107**, 6–14.

16 Y.-R. Zheng, K. Suntharalingam, T. C. Johnstone and S. J. Lippard, *Chem. Sci.*, 2015, **6**, 1189–1193.

17 F.-U. Rahman, A. Ali, H.-Q. Duong, I. U. Khan, M. Z. Bhatti, Z.-T. Li, H. Wang and D.-W. Zhang, *Eur. J. Med. Chem.*, 2019, **164**, 546–561.

18 T. Chatzisideri, S. Thysiadis, S. Katsamakas, P. Dalezis, I. Sigala, T. Lazarides, E. Nikolakaki, D. Trafalis, O. A. Gederaas, M. Lindgren and V. Sarli, *Eur. J. Med. Chem.*, 2017, **141**, 221–231.

19 P. Zhang, H. Huang, S. Banerjee, G. J. Clarkson, C. Ge, C. Imberti and P. J. Sadler, *Angew. Chem. Int. Ed.*, 2019, **58**, 2350–2354.

20 R. Guan, Y. Chen, L. Zeng, T. W. Rees, C. Jin, J. Huang, Z.-S. Chen, L. Ji and H. Chao, *Chem. Sci.*, 2018, **9**, 5183–5190.

21 M.-H. Chen, Y. Zheng, X.-J. Cai, H. Zhang, F.-X. Wang, C.-P. Tan, W.-H. Chen, L.-N. Ji and Z.-W. Mao, *Chem. Sci.*, 2019, **10**, 3315–3323.

22 W. Lv, Z. Zhang, K. Y. Zhang, H. Yang, S. Liu, A. Xu, S. Guo, Q. Zhao and W. Huang, *Angew. Chem. Int. Ed.*, 2016, **55**, 9947–9951.

23 S. Monro, K. L. Colón, H. Yin, J. Roque, P. Konda, S. Gujar, R. P. Thummel, L. Lilge, C. G. Cameron and S. A. McFarland, *Chem. Rev.*, 2019, **119**, 797–828.

24 Z. Zhao, P. Gao, Y. You and T. Chen, *Chem. – Eur. J.*, 2018, **24**, 3289–3298.

25 H. K. Saeed, P. J. Jarman, S. Archer, S. Sreedharan, I. Q. Saeed, L. K. Mckenzie, J. A. Weinstein, N. J. Buurma, C. G. W. Smythe and J. A. Thomas, *Angew. Chem.*, 2017, **129**, 12802–12807.

26 S. Imstepf, V. Pierroz, R. Rubbiani, M. Felber, T. Fox, G. Gasser and R. Alberto, *Angew. Chem.*, 2016, **128**, 2842–2845.

27 A. P. King, S. C. Marker, R. V. Swanda, J. J. Woods, S.-B. Qian and J. J. Wilson, *Chem. – Eur. J.*, 2019, **25**, 9206–9210.

28 Z.-Y. Pan, C.-P. Tan, L.-S. Rao, H. Zhang, Y. Zheng, L. Hao, L.-N. Ji and Z.-W. Mao, *Angew. Chem.*, 2020, **132**, 18914–18921.

29 S. Lazic, P. Kaspler, G. Shi, S. Monro, T. Sainuddin, S. Forward, K. Kasimova, R. Hennigar, A. Mandel, S. McFarland and L. Lilge, *Photochem. Photobiol.*, 2017, **93**, 1248–1258.

30 P. Zhang and H. Huang, *Dalton Trans.*, 2018, **47**, 14841–14854.

31 E. C. Glazer, *Photochem. Photobiol.*, 2017, **93**, 1326–1328.

32 I. Ashur, R. Goldschmidt, I. Pinkas, Y. Salomon, G. Szewczyk, T. Sarna and A. Scherz, *J. Phys. Chem. A*, 2009, **113**, 8027–8037.

33 C.-P. Tan, Y.-M. Zhong, L.-N. Ji and Z.-W. Mao, *Chem. Sci.*, 2021, **12**, 2357–2367.

34 J. Tang, H.-Y. Yin and J.-L. Zhang, in *Inorganic and Organometallic Transition Metal Complexes with Biological Molecules and Living Cells*, ed. K. K.-W. Lo, Academic Press, 2017, pp. 1–53.

35 A. de Almeida and R. Bonsignore, *Bioorg. Med. Chem. Lett.*, 2020, **30**, 127219.

36 Y. Dai, Z. Yang, S. Cheng, Z. Wang, R. Zhang, G. Zhu, Z. Wang, B. C. Yung, R. Tian and O. Jacobson, *Adv. Mater.*, 2018, **30**, 1704877.

37 S. S. Taneja, J. Bennett, J. Coleman, R. Grubb, G. Andriole, R. E. Reiter, L. Marks, A.-R. Azzouzi and M. Emberton, *J. Urol.*, 2016, **196**, 1096–1104.

38 S. Curry, *Drug Metab. Pharmacokinet.*, 2009, **24**, 342–357.

39 G. J. Quinlan, G. S. Martin and T. W. Evans, *Hepatology*, 2005, **41**, 1211–1219.

40 A. Bondi, *J. Phys. Chem.*, 1964, **68**, 441–451.

41 T. Ogawa, W. M. C. Sameera, D. Saito, M. Yoshida, A. Kobayashi and M. Kato, *Inorg. Chem.*, 2018, **57**, 14086–14096.

42 H.-F. Xiang, S.-C. Chan, K. K.-Y. Wu, C.-M. Che and P. T. Lai, *Chem. Commun.*, 2005, 1408–1410.

43 R. Wang, X. Li and J. Yoon, *ACS Appl. Mater. Interfaces*, 2021, **13**, 19543–19571.

44 S. Lee, D.-B. Sung, S. Kang, S. Parameswaran, J.-H. Choi, J. S. Lee and M. S. Han, *Sensors*, 2019, **19**, 5298.

45 S. Sookai and O. Q. Munro, *ChemistryEurope*, 2023, **1**, e202300012.

46 I. G. Darvey, *Biochem. Educ.*, 1999, **27**, 209–210.

Chapter 6 Complexities of the interaction of Ni(II), Pd(II) and Pt(II) pyrrole-imine chelates with human serum albumin

Complexities of the interaction of Ni(II), Pd(II) and Pt(II) pyrrole-imine chelates with human serum albumin

Sheldon Sookai[a] and Orde Q. Munro*[a]

Dedicated to Prof. Helder M. Marques

[a] Mr S. Sookai, Prof. O. Q. Munro
Molecular Sciences Institute
School of Chemistry
University of the Witwatersrand, PO WITS 2050, Johannesburg (South Africa)
E-mail: orde.munro@wits.ac.za

Supporting information for this article is given via a link at the end of the document

Complexities of the interaction of Ni(II), Pd(II) and Pt(II) pyrrole-imine chelates with human serum albumin

Sheldon Sookai[a] and Orde Q. Munro*[a,b]

Dedicated to Prof. Dr. Helder M. Marques

[a] Mr S. Sookai, Prof. Dr. O. Q. Munro
Molecular Sciences Institute
School of Chemistry
University of the Witwatersrand, PO WITS 2050, Johannesburg, South Africa
[b] School of Chemistry
University of Leeds, Woodhouse Lane, LS2 9JT, UK
E-mail: o.munro@leeds.ac.uk

Supporting information for this article is given via a link at the end of the document.

Abstract: Human serum albumin (HSA) efficiently transports drugs *in vivo*: most are organic. Here, HSA binding affinity and site specificity are shown to depend on the identity of the d^8 metal ion in Ni^{II}, Pd^{II} and Pt^{II} chelates of the bis(pyrrole-imine) ligand H_2PrPyrr. Fluorescence quenching data for native and probe-bound HSA showed sites close to Trp-214 (subdomain IIA) are targeted. The Stern-Volmer constants, K_{SV}, ranged from 10^4 M^{-1} to 10^5 M^{-1} while the affinity constants, K_a, ranged from ~3.5×10^3 M^{-1} to ~1×10^6 M^{-1} at 37 °C, following the order Pd(PrPyrr) > Pt(PrPyrr) > Ni(PrPyrr) > H_2PrPyrr. Ligand uptake is enthalpically driven, hinging mainly on London dispersion forces. Induced CD spectra for the protein-bound ligands could be simulated by hybrid QM:MM TD-DFT methods, proving that the metal chelates neither decompose nor demetallate after uptake by HSA. Transport and delivery of the metal chelates by HSA *in vivo* could therefore be feasible.

Introduction

Pyrrole-based compounds have been extensively studied due to their intrinsic bioactivity and use in pharmaceuticals.[1,2] Pyrrole-imine Schiff bases are popular ligands formed by condensing pyrrole-2-carboxaldehyde with primary alkyl- or arylamines.[3] The resulting pyrrole-imine Schiff bases chelate numerous metal ions, forming stable complexes with metal–pyrrolide and metal–imine bonds after concomitant deprotonation of the pyrrole NH group. When suitable diamines are condensed with two mole equivalents of the carbonyl synthon, tetradentate bis(pyrrole-imine) Schiff base ligands are obtained (Figure 1a), and hexadentate derivatives may be similarly prepared.[4–6] Such ligands stabilize metal ions in a range of oxidation states.[7] Examples include structurally characterized $Co^{II/III}$,[8–11] $Rh^{I/III}$,[12–15] Ir^{III},[16,17] Ni^{II},[18–20] Pd^{II},[20–22] Pt^{II},[23–25] Cu^{II},[26–29] Ag^{I},[30] and Au^{III} complexes.[31]

While pyrrole compounds are key building blocks for organic pharmaceuticals,[32] e.g., Tolmetin,[33] Sunitini,[34] and Glimepiri,[35] studies over the last two decades suggest that pyrrole-imine metal chelates exhibit significant medicinal potential. The best-known example is the pentadentate macrocycle texaphyrin,[36] which complexes numerous transition and main group metal ions, including lanthanides. Texaphyrin's Lu^{III}[37] and Gd^{III}[38] complexes are promising (but not FDA-approved) compounds for photodynamic cancer chemotherapy[39] and MRI contrast[40] applications, respectively. Although further behind on the clinical development trajectory, patented tetradentate bis(pyrrolide-imine) chelates of Au^{III} are promising investigational compounds for cancer[31] and mycobacterial chemotherapy.[41] Despite these advances, limited work has been done to elucidate how these compounds bind to human serum albumin (HSA), which is critical to understanding the plasma distribution of metal chelate drug candidates.[42] In this paper, our primary aim was to use simple pyrrole-imine metal chelates to study their uptake by HSA in order to better understand whether HSA might potentially serve as a transporter/delivery vehicle for such compounds *in vivo*.

HSA is the most abundant plasma protein present at concentrations of around 600 µM.[43] Two of the main functions of HSA are regulating colloidal osmotic pressure and transportation of exogenous and endogenous compounds.[44] HSA is a heart shaped macromolecule that consists of a single polypeptide chain (585 amino acids) with a molar mass of 66.5 kDa.[45] As depicted in Figure 1b, the structure is dominated by α-helices within the three domains, namely I (residues 1–195), II (196–383), and III (384–585). Each domain is further broken down into two subdomains A and B.[45,46] The two main small molecule binding sites within HSA are in subdomains IIA and IIIA and are often referred to as Sudlow's site I and Sudlow's site II, respectively.[47–49] HSA is the quintessential drug transporter in humans and is thus widely studied as a potential vehicle for drug delivery, especially since the protein is assimilated by cancer cells *in vivo*.[50] Apart from the two main drug binding sites, other binding sites abound, including 7 fatty acid, 4 thyroxine, and several known metal ion binding sites.[51] Delineating the binding of a medicinal compound to HSA is central to understanding its pharmacodynamic and pharmacokinetic data *in vivo* given the abundance of HSA and its transporter role in blood plasma.[47] Metallodrug candidates are no exception and recent work has shown how half-sandwich Ru^{II} and Rh^{III} complexes bind to HSA as intact species through coordination to His and Glu residues with retention of the arene.[52–54] Generally, protein binding by metal complexes is accompanied by ligand dissociation[55–58]

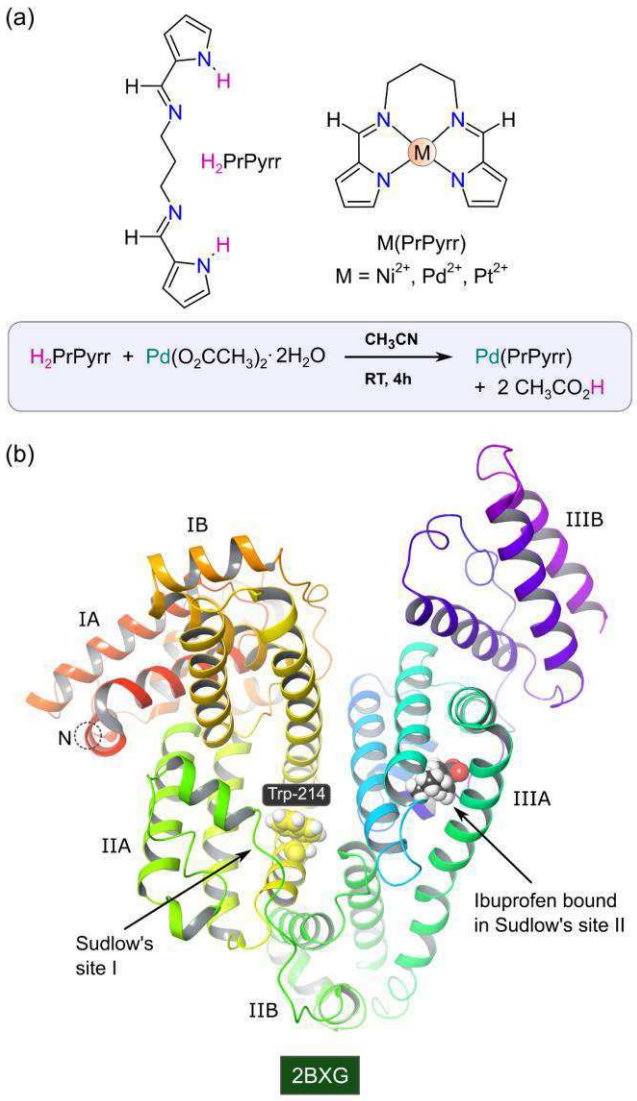
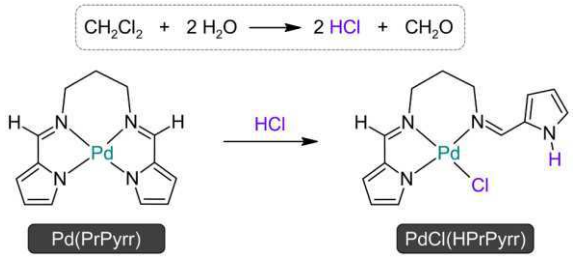


Figure 1. (a) Structures of the bis(pyrrole-imine) ligand H_2PrPyrr (*N,N′-bis*[(1*E*)-1H-pyrrol-2-ylmethylene]propane-1,3-diamine) and its neutral metal chelates with square planar d^8 metal ions relevant to this work. The method for metalation of the ligand is illustrated for the synthesis of Pd(PrPyrr); the solvate water molecules enter the bulk solvent. (b) X-ray structure of HSA bound to ibuprofen (redrawn from PDB code 2BXG) illustrating the two main small molecule binding sites. Sudlow's site I is larger than Sudlow's site II and compounds that bind in this pocket perturb the fluorescence from Trp-214. The protein secondary structure elements are depicted schematically, coloured by domain, and labelled with Roman numerals and Arabic letters. H atoms (calculated positions) were added to the bound drug and Trp-214 to enhance their visualization.

while non-dissociative binding is less common,[59–62] often though not exclusively[63] hinging on multidentate ligands that provide kinetic inertness and thermodynamic stability.[64,65] For instance, large substitution-inert mono- and multinuclear Ru^{II} complexes with bidentate ligands such as bipy (2,2′-bipyridine), phen (1,10-phenanthroline), and dppz (dipyridophenazine) are taken up by HSA ostensibly as fully intact species, often with stoichiometries ≥ 1, attesting to the promiscuity of HSA and its affinity for diverse, structurally elaborate compounds.[66–68]

Here, we synthesized a popular tetradentate *bis*(pyrrole-imine) ligand, H_2PrPyrr, and its isoelectronic (nd^8) square-planar chelates of Ni^{II}, Pd^{II}, and Pt^{II}, denoted M(PrPyrr) (Figure 1a). Spectroscopic methods were used to probe the binding of



Scheme 1. Conversion of Pd(PrPyrr) to the protonated tridentate chloro adduct, PdCl(HPrPyrr), by HCl derived from a postulated solvent decomposition reaction.

H_2PrPyrr and M(PrPyrr) by HSA under physiological conditions to gauge how the metal ion influences uptake of the complexes and to delineate their preferred binding site(s). For the first time, we show that the binding affinity, thermodynamics, and practically all aspects of the physical biochemistry of the system are surprisingly sensitive to the identity of the nd^8 metal ion. Notwithstanding the complexity of the system, we have shown that the protein binds the fully intact metal chelates. H_2PrPyrr and M(PrPyrr) are thus stable to hydrolysis and demetallation, respectively, during uptake and binding by the protein. This is particularly important because of the general apathy displayed by pharmaceutical companies towards the development of metallodrugs.

Results and Discussion

Metal chelate synthesis

Modified literature methods were used to metalate H_2PrPyrr with Ni^{II}[69] and Pt^{II}.[70] For Pt(PrPyrr), simply stirring the solution of the free ligand with $K_2[PtCl_4]$ and sodium acetate in a binary mixture of DMSO-acetonitrile (50%, V/V) for 4 days at ambient temperature (as opposed to the 4-h reaction at 80 °C in DMF employed for the cyclohexyl-bridged ligand[70]) afforded the product cleanly without formation of metal-containing by-products. The difference in reactivity of H_2PrPyrr towards Pt^{II} compared with the cyclohexyl-bridged ligands likely reflects the higher flexibility of the propyl-bridged analogue employed here. For Pd(PrPyrr), the protocol depicted in Figure 1a was followed with the use of Pd^{II} acetate affording the product cleanly; the free acetate ions serve as a suitable base for accepting the pyrrole NH protons released during metal ion chelation. We found it unnecessary to first dissolve the free ligand in ethanol, as reported elsewhere for this reaction, obviating the need for a mixed solvent system.[71]

Adventitious formation of PdCl(HPrPyrr)

For Pd(PrPyrr), protonation of the metal-bound ligand was discovered and the species found to be significant for uptake by HSA (*vide infra*). More specifically, the tridentate hemiprotonated complex PdCl(HPrPyrr) was unexpectedly obtained from a reaction in which Pd(PrPyrr) had been synthesized as depicted in Figure 1a. The crystals which grew from a mixture of CH_2Cl_2 and hexane were heterogeneous comprising Pd(PrPyrr) as the majority species and PdCl(HPrPyrr) as a minor component. The source of chloride ions for the latter reaction product may derive from the commercial solvent[72] or the hydrolysis of CH_2Cl_2 to form HCl and formaldehyde (Scheme 1),[73] possibly catalysed by

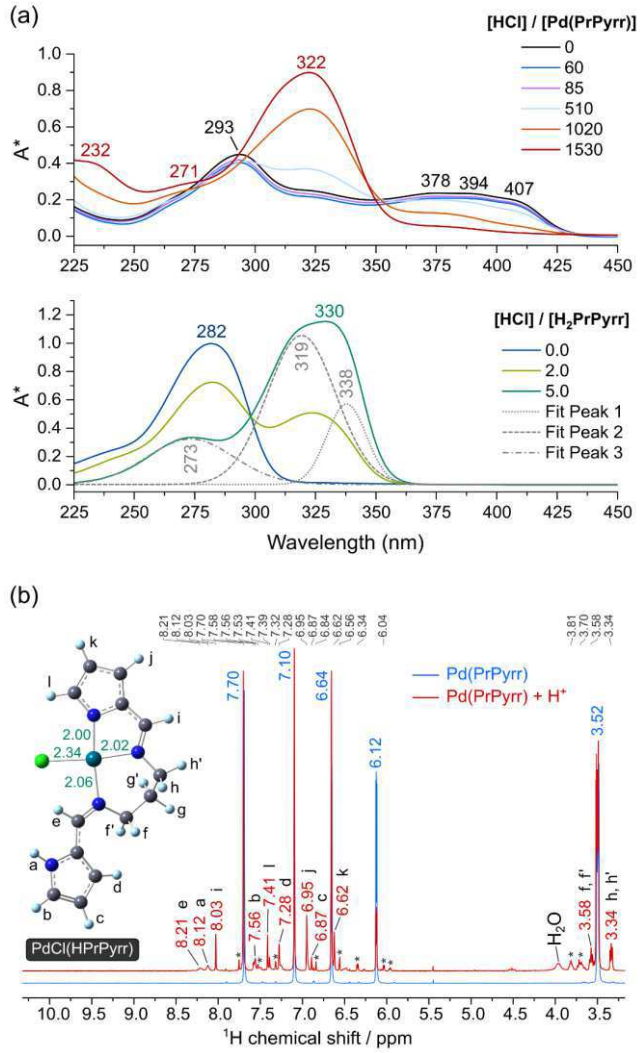


Figure 2. (a) Protonation of Pd(PrPyrr) and H_2PrPyrr studied by UV-visible spectroscopy in acetonitrile solution at 37 °C. The spectra were smoothed with an FFT filter algorithm (5-point window, OriginPro 2021). The electronic spectrum of the protonated free base ligand, $[H_4PrPyrr]^{2+}$, was deconvoluted into three Gaussian bands (fit R^2 = 0.998, $\chi^2 = 1.6 \times 10^{-4}$). There are no bands below 250 nm or above 350 nm. (b) ^{1}H NMR spectra of Pd(PrPyrr) recorded in CD_3CN in the absence (blue) and presence (red) of 2 eq of HCl in D_2O recorded at 37 °C. The DFT-calculated structure of PdCl(HPrPyrr) is shown along with signal assignments in the experimental NMR spectrum that are based on the isotropic shielding tensors calculated for the protons in the complex. DFT-calculated bond distances are in Å. The signal from the central methylene group of the propyl bridge (not shown) is overlapped with the solvent peaks at 1.97 ppm (see Fig. S2). The minor signals marked with an asterisk possibly belong to the solvated complex (Cl^- exchange).

residual acetic acid present as a by-product of the metalation of H_2PrPyrr with $Pd(O_2CCH_3)_2$. Protonation of coordinated N-donor ligands in Pd^{II} pincer complexes is known and can be achieved by simply using HCl•OEt_2 to effect the reaction.[74]

Here, experimental evidence in support of the mechanism depicted in Scheme 1 was acquired by investigating the reactions of Pd(PrPyrr) and H_2PrPyrr with HCl using UV-visible and ^{1}H NMR spectroscopy. As shown in Figure 2a, progressively increasing the concentration of HCl in an acetonitrile solution containing 20 μM Pd(PrPyrr) converts the complex into the protonated adduct PdCl(HPrPyrr). A significant excess of HCl was required to bring about complete reaction. Notably, from the spectra of the free ligand (H_2PrPyrr) recorded as a function of [HCl] (Figure 2b), addition of HCl to Pd(PrPyrr) does not lead to demetallation of the chelate and hence formation of the protonated fee base, either $[H_3PrPyrr]^+$ or $[H_4PrPyrr]^{2+}$. The species assignments above were confirmed by the TD-DFT spectra of Pd(PrPyrr) and PdCl(HPrPyrr) calculated in acetonitrile (Figure S13), which show remarkably good agreement with the experimental spectra.

Since the structural hallmark of PdCl(HPrPyrr) is its lack of symmetry and a single protonated pyrrole group, the ^{1}H NMR spectrum of Pd(PrPyrr) before and after addition of 2 eq HCl in CD_3CN confirmed the appearance of two new, moderately sharp signals at 8.12 and 8.21 ppm, which may be assigned to the pyrrole NH proton and imine CH proton of the chelate closest to the protonated pyrrole ring. Both exhibit exchange broadening. In contrast, the imine CH proton signal of the coordinated pyrrolide-imine moiety is sharp and resonates downfield (8.03 ppm) relative to the parent complex (7.70 ppm). The spectrum of Pd(PrPyrr) recorded in acidified acetonitrile is thus consistent with the structure of PdCl(HPrPyrr). The remaining signals for the protonated complex were in excellent agreement with those calculated by DFT methods (Figure S14). From Figure 2, an additional minor species of a similar structure to PdCl(HPrPyrr) is present (signals marked with an asterisk), possibly the solvent-substituted salt $[Pd(HPrPyrr)(NCCH_3)]Cl$. Since two CH_2-group resonances occur at 3.70 and 3.81 ppm for this minor species, we can rule out double-protonation of Pd(PrPyrr) as this would lead to either dissociation of the ligand from the Pd^{II} ion or formation of a symmetric structure with metal-coordination by the central chelate ring alone (i.e., there would be two dissociated pyrrole rings). Both options would give a single methylene resonance in this region of the spectrum, inconsistent with the experimental data. Collectively, the UV-visible and NMR spectroscopic data strongly support the mechanism proposed in Scheme 1.

X-ray structures of Pd(PrPyrr) and PdCl(HPrPyrr)

The ambient temperature X-ray structure of Ni(PrPyrr) has been previously described.[69] The novel low temperature X-ray structures of Pd(PrPyrr) and PdCl(HPrPyrr) delineated here are shown in Figure 3. Pd(PrPyrr) crystallized in the space group $P2_1/c$ (Table S1, Figure S15) and is structurally similar to the room temperature X-ray structure of the compound (Figure S16).[71] The asymmetric unit (ASU) for Pd(PrPyrr) comprises four independent molecules (A–D), each having the square planar Pd^{II} ion chelated by the tetradentate bis(pyrrolide-imine) ligand. The Pd–$N_{pyrrole}$ and Pd–N_{imine} distances average 2.017(6) and 2.010(11) Å, respectively (Table S2). These bond distances are statistically equivalent to the mean Pd–$N_{pyrrole}$ and Pd–N_{imine} values of 2.02(3) Å and 2.02(4) Å, respectively, calculated from 27 similar structures in the Cambridge Crystallographic Database (CSD).[75] The literature data are collated in Table S3 and plotted in Figure S17. Interestingly, despite the higher temperature data for the literature structure of PdPrPyrr,[71] which has mean Pd–$N_{pyrrole}$ and Pd–N_{imine} distances of 2.011(4) and 2.006(10) Å, respectively, the coordination group bonds are equivalent (within 1σ) to those determined here at 173 K. The nonplanar conformations of the ligands mainly reflect nonbonded crystal packing interactions and the formation of discrete π-stacked dimers (see Figure S18). Notably, DFT simulations (Figure S19) suggest the observed stacking involves significant London dispersion forces.

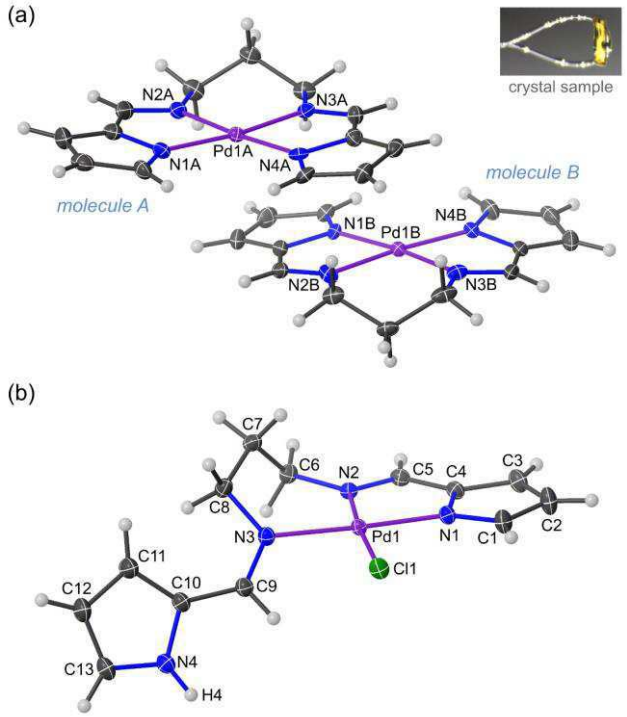


Figure 3. (a) Partly labelled view of the low-temperature X-ray structure of Pd(PrPyrr). Two of the four independent molecules (A and B) in the asymmetric unit are illustrated. (b) View of the low temperature X-ray structure of PdCl(HPrPyrr). Thermal ellipsoids are rendered at the 35% and 50% probability levels for Pd(PrPyrr) and PdCl(HPrPyrr), respectively. Hydrogen atoms are drawn as spheres with an arbitrary radius.

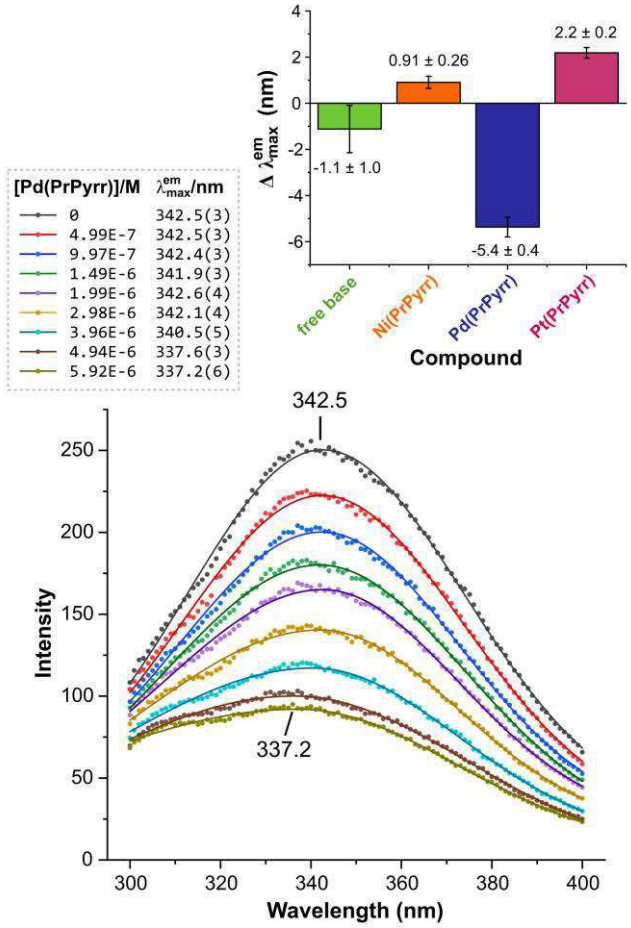


Figure 4. Emission spectra of human serum albumin (HSA, 5.0 μM) recorded as a function of the concentration of Pd(PrPyrr) at 298 K (pH 7.50). The spectra are fitted by paired asymmetric Gaussian functions to locate the emission maxima. Correlation coefficients, R^2, were all 0.997. Analogous spectra for the reaction of HSA with H_2PrPyrr, Ni(PrPyrr), and Pt(PrPyrr) are given in Figure S23 (Supporting Information). The wavelength shift accompanying ligand uptake ($\Delta\lambda^{em}_{max}$) is plotted as the inset to the main figure (upper right).

The X-ray structure of PdCl(HPrPyrr) is shown in Figure 3b. The square planar Pd^{II} ion is chelated by three of the four nitrogen donors of the monoanionic tetradentate chelate, with the protonated pyrrole ring unbound and oriented away from the chloride ligand occupying the fourth coordination site at the metal ion. The unbound pyrrole N–H group participates in intermolecular N–H···Cl hydrogen bonding (2.40 ± 0.02 Å), which leads to the formation of a one-dimensional H-bonded chain in the solid state. The polymer chain axis is colinear with the lattice 2-fold screw axis, giving the extended chain 2_1 symmetry overall (Figure S20). The Pd–$N_{pyrrole}$ and mean Pd–N_{imine} distances measure 1.993(1) and 2.015(18) Å, respectively. The individual Pd–N_{imine} bond distances, measuring 1.997(1) and 2.032(1) Å, vary significantly depending on whether the flanking pyrrole ring is metal-bound or not. The shorter distance (Pd1–N2) occurs when the pyrrole ring is metal-bound, and the imine nitrogen resides within the 5-membered chelate ring incorporating the metal ion. This reflects the binding constraints imposed by the 5-membered chelate ring on N2, which are relaxed for N3 within the larger 6-membered chelate ring (propyl bridge). The Pd–Cl distance measures 2.3204(4) Å and is typical for coordination of Pd^{II} by chloride in pyrrole-based pincers.[74] Interestingly, there are no X-ray structures for comparison with PdCl(HPrPyrr) in the literature, commensurate with the unusual nature of this species.

Ligand-dependent HSA fluorescence quenching

To delineate the mechanism and relative ability of H_2PrPyrr and its M(PrPyrr) chelates to interact with HSA, fluorescence spectroscopy was used as an informative probe. Specifically, fluorescence quenching for a protein can be described as either static, dynamic, or a combination of both. For HSA, the intrinsic fluorescence emission is largely the result of a single tryptophan residue (Trp-214, λ^{ex}= 280 nm) located in subdomain IIA, and to a lesser extent the 18 tyrosine residues present in the protein.[76] Emission quenching of HSA induced by varying concentrations of the free ligand, H_2PrPyrr, and its Group 10 d^8 M(PrPyrr) chelates (Figures 4 and S23) was characterized by a monotonic intensity decrease at the emission maximum (~343 nm) with increasing [L]. (Here, ligand L is used in a biomolecular sense.) The spectroscopic data suggest that all four ligands bind reasonably close to Trp-214 (subdomain IIA), changing the microenvironment around the fluorophore and inducing a marked dose-dependent (i.e., "static" or binding-related) quenching of the intrinsic fluorescence of HSA (*vide infra*).[77,78]

For HSA, the wavelength of the fluorescence emission maximum (λ^{em}_{max}) was dependent on the identity of the bound ligand. At the maximum doses investigated before quenching and band broadening limited fluorescence detection, H_2PrPyrr and Pd(PrPyrr) induced blue shifts relative to the native protein of −1.1 ± 1.0 and −5.4 ± 0.4 nm, respectively (identical buffer and temperature). In contrast, the Ni^{II} and Pt^{II} chelates red-shifted

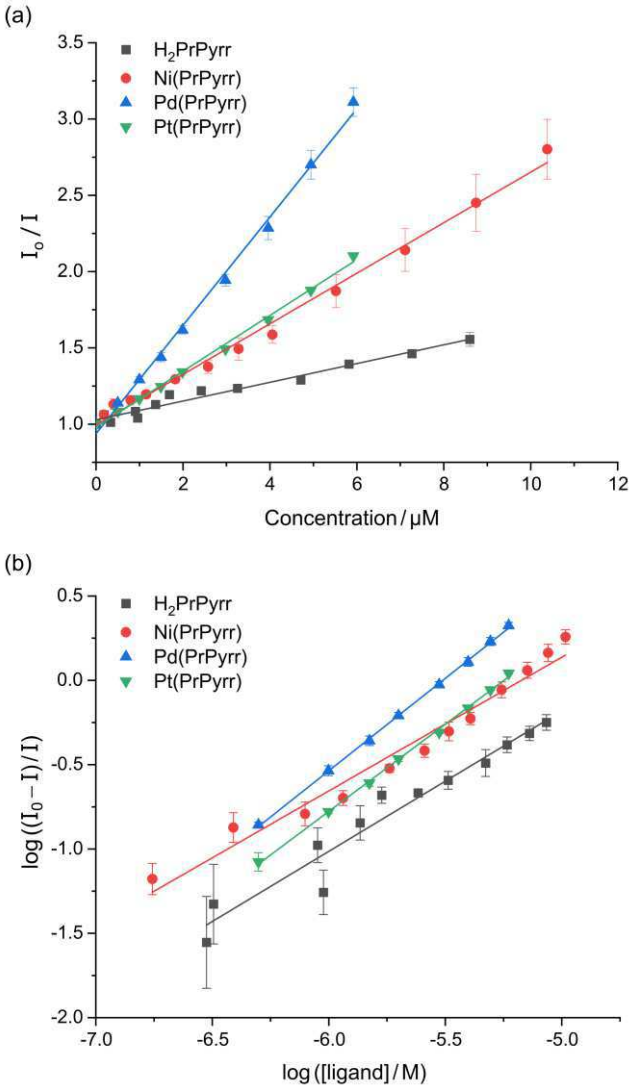


Figure 5. (a) Stern-Volmer (SV) fluorescence intensity ratio plots for human serum albumin (HSA, 5.0 μM) recorded as a function of the concentration of H_2PrPyrr, Ni(PrPyrr), Pd(PrPyrr), and Pt(PrPyrr) in 50 mM KH_2PO_4, pH 7.50, at 298 K. All data are well-fitted by eq. S3 for linear SV emission behaviour with appreciable static quenching. (b) Double logarithm plot of the fractional change in fluorescence intensity for human serum albumin (HSA, 5.0 μM) recorded as a function of the concentration of H_2PrPyrr, Ni(PrPyrr), Pd(PrPyrr), and Pt(PrPyrr) in 50 mM KH_2PO_4, pH 7.50, at 298 K. The data are described by eq. 1, which affords the affinity constant and stoichiometric coefficient for the reaction (Table 1). For both plots, error bars are estimated standard deviations based on the average of three independent determinations.

λ_{max}^{em} by up to +2.2 ± 0.2 nm in the case of the Pt^{II} derivative. While shifts of ~1 nm in λ_{max}^{em} are close to the wavelength resolution of the instrument (i.e., statistically insignificant), the notable blue shift in the emission maximum for Pd(PrPyrr) ostensibly reflects the development of a significantly less polar environment around Trp-214 after ligand uptake.[79,80] From the Hill-type function[81] used to fit the variation in HSA emission wavelength with [Pd(PrPyrr)] (Figure S24), the wavelength shift is ~99% complete when [Pd(PrPyrr)] = 6 μM.

The magnitude of the blue shift in λ_{max}^{em} for Trp observed here for the HSA•{Pd^{II}} system (relative to native HSA) is akin to that found for many other proteins (where λ_{max}^{em} ranges from 308 nm to 365 nm, but is most commonly 330–340 nm).[82] A blue shift in λ_{max}^{em} for Trp is usually caused by changes in (i) the orientational polarization of the Trp fluorophore induced by ordered water molecules within 15–25 Å of the residue and (ii) electronic polarization of the Trp indole ring. For HSA•{ligand} complexes, electronic polarization of Trp-214 induced by the bound ligand and perturbation of the ordered water structure around the fluorophore both likely underpin the observed shifts in λ_{max}^{em}. Whether a blue or red shift in λ_{max}^{em} occurs depends on the orientation and centre-to-centre distance of the ligand's dipole moment relative to the transition dipole moment for the lowest energy $^1A_1 \rightarrow {}^1L_a$ ground state transition of Trp's indole ring.[79] (This transition involves pyrrole → benzene transient charge migration.) Hence, the precise way in which the ligand is bound relative to Trp-214 will govern the sign and magnitude of $\Delta\lambda_{max}^{em}$.

The red shift in $\Delta\lambda_{max}^{em}$ of +2.2 ± 0.2 nm for HSA•{Pt(PrPyrr)} suggests that the environment around Trp-214 becomes somewhat more hydrophilic (polar) upon ligand uptake,[80] possibly reflecting rearrangement of the positions or orientations of H-bonded water molecules within a 15–25 Å radius of Trp-214. (Even though Trp and Tyr are readily excited at 280 nm, most of the intrinsic fluorescence of HSA is due to Trp-214 since it has a higher quantum yield and more efficient resonance energy transfer than Tyr;[76] see Table S6.) The key conclusion from the wavelength shift data is that the Pd^{II} system probably binds to HSA in a different manner to the Ni^{II} and Pt^{II} analogues.

Fluorescence quenching mechanism

Stern-Volmer (SV) plots of the mean fluorescence ratio recorded as a function of ligand dose are presented in Figures 5 and S25. (SV quenching theory is provided in eqs. S3 and S4 of the ESI.) The calculated SV constants, K_{SV}, and bimolecular quenching rate constants, k_q, for the interaction of the four ligands with HSA are given in Table 1. The K_{SV} values all decrease with increasing temperature and the k_q values exceed the diffusion-controlled limit (1×10^{10} M^{-1} s^{-1})[83] by 2 to 3 orders of magnitude, consistent with stable complex formation and a static fluorescence quenching mechanism (binding related). The values of K_{SV} and k_q determined here for the interaction of native HSA with H_2PrPyrr and its metal chelates are from ~2 to ~10 times larger than, for instance, those reported for HSA interacting with berberine,[84] epinastine hydrochloride,[85] primethamine and trimethoprim,[86] as well as malvidin-3-glucoside.[87]

Ligand binding equilibrium constants

To investigate metal complex integrity and affinity for HSA, we employed the changes in HSA fluorescence intensity as a function of ligand dose to calculate thermodynamic data for the binding equilibrium between the protein and titrant ligand. The biophysical parameters (Table 1) that describe the ligand's affinity for the protein (K_a) and the reaction stoichiometry (n) are delineated from a double-log plot (Figures 5b and S26) of the emission data as a function of increasing ligand concentration (eq. 1),[88]

$$log\left(\frac{I_0-I}{I}\right) = logK_a + nlog[Q] \quad (1)$$

where the intercept and slope of the curve give the affinity constant and stoichiometry, respectively. For each compound, K_a decreases with increasing temperature, consistent with a static quenching mechanism.[89,90] The stoichiometric coefficients n obtained for Pd(PrPyrr) were > 1 (e.g., 1.19 ± 0.01 at 288 K), suggesting that the reaction stoichiometry might entail the uptake

Table 1. Stern-Volmer quenching constants (K_{SV}), bimolecular quenching rate constants (k_q), association constants (K_a) and stoichiometric coefficients (n) for the interaction of H_2PrPyrr, Ni(PrPyrr), Pd(PrPyrr) and Pt(PrPyrr) with HSA at different temperatures in 50 mM KH_2PO_4 buffer at pH 7.50.

Compound	Temp. T (K)	10^{-5} K_{SV} $(M^{-1})^{a,c}$	10^{-13} k_q $(M^{-1}\ s^{-1})^{b}$	$\log(K_a$ / $M^{-1})^{c}$	n^{d}
H_2PrPyrr	288	2.12 (3)	3.61	4.04 (14)	0.76 (2)
	298	0.61 (4)	1.04	3.55 (9)	0.76 (2)
	310	0.47 (5)	0.78	2.56 (5)	0.55 (4)
Ni(PrPyrr)	288	1.69 (20)	2.88	5.15 (21)	0.97 (2)
	298	1.55 (10)	2.64	4.63 (14)	0.89 (2)
	310	1.21 (4)	2.10	4.39 (13)	0.88 (2)
	315	1.18 (4)	2.01	3.22 (14)	0.64 (2)
Pd(PrPyrr)	288	4.60 (30)	7.81	6.68 (6)	1.19 (1)
	298	3.60 (20)	6.04	6.00 (7)	1.08 (1)
	310	2.52 (10)	4.30	5.52 (17)	1.01 (2)
	315	2.10 (10)	3.52	5.28 (3)	0.99 (0)
Pt(PrPyrr)	288	2.12 (10)	3.61	5.69 (6)	1.05 (4)
	298	1.83 (1)	3.11	5.34 (18)	1.02 (3)
	310	1.34 (5)	2.28	5.23 (13)	1.02 (2)
	315	1.12 (5)	1.91	4.95 (6)	0.98 (1)

[a]K_{SV} values (Stern-Volmer constants) were determined from fitting the data to eq. S3. Using eq. S4, a mean excited state lifetime, τ_0, of 5.87(76) ns for HSA was used to calculate the bimolecular quenching rate constants, k_q. [c]The estimated standard deviations of the least significant digits are given in parentheses. [d]Ligand:HSA binding stoichiometry.

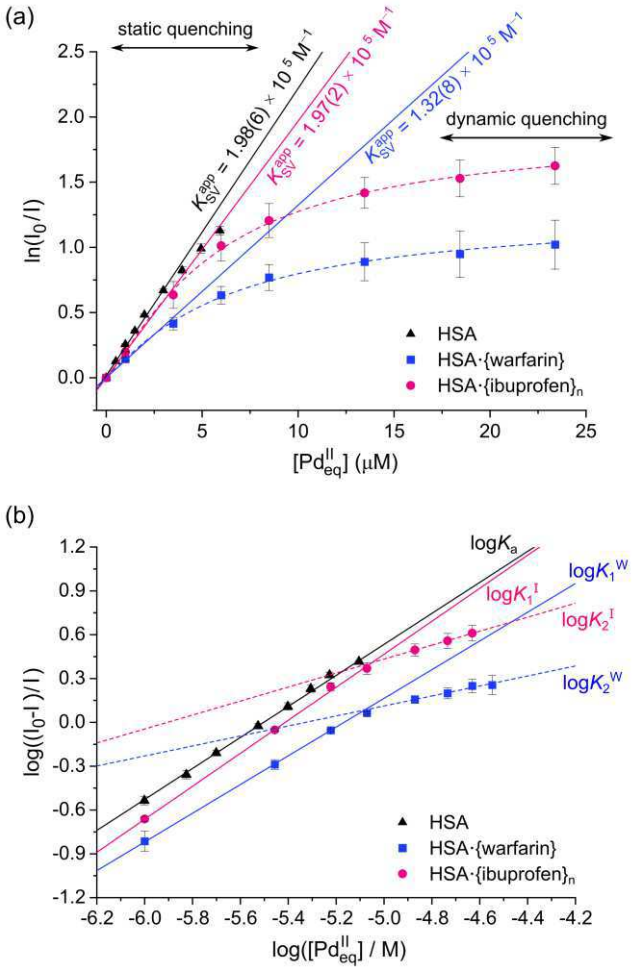


Figure 6. (a) Binding site determination for the reaction of Pd(PrPyrr) with HSA (5.0 μM protein, 50 mM KH_2PO_4, pH 7.50, 298 K) using a modified Stern-Volmer model (eq. S6), where Pd^{II}_{eq} = [Pd(PrPyrr)] + $[Pd(HPrPyrr)(OH_2)]^+$. For native HSA, Trp-214 is the fluorophore (λ^{ex} = 280 nm, λ^{em} = 340 nm). For drug-bound targets, 5.0-μM warfarin (λ^{ex} = 320 nm, λ^{em} = 382 nm) and 5.0-μM ibuprofen (λ^{ex} = 228 nm, λ^{em} = 332 nm) are the fluorophore probes. Warfarin binds specifically in Sudlow's site I (subdomain IIA), while ibuprofen is mainly bound in Sudlow's site II (subdomain IIIA). Native HSA exhibits static fluorescence (FL) quenching over the full concentration range (K_{SV} = 3.60 ± 0.2 × 10^5 M^{-1}). HSA•{warfarin} and HSA•{ibuprofen}$_n$ initially show static FL quenching, which switches to dynamic FL quenching when [Pd^{II}_{eq}] > 5 μM and the drug is displaced from the protein. The limiting values of $\ln(I_0/I)$ for HSA•{warfarin} and HSA•{ibuprofen}$_n$ were 1.27 ± 0.08 and 1.90 ± 0.06, respectively. (b) Determination of the affinity constants of Pd^{II}_{eq} for native HSA, HSA•{warfarin}, and HSA•{ibuprofen}$_n$ using eq. 1. The plot is linear for native HSA over the full concentration range ($\log K_1$ = 6.0 ± 0.07, n = 1.1 ± 0.01). There are two steps for the reaction of Pd^{II}_{eq} with HSA•{warfarin} ($\log K_1^W$ = 5.08 ± 0.05, n_1 = 0.98 ± 0.01; $\log K_2^W$ = 1.82 ± 0.17, n_2 = 0.34 ± 0.04) and HSA•{ibuprofen}$_n$ ($\log K_1^I$ = 6.11 ± 0.13, n_1 = 1.13 ± 0.02; $\log K_2^I$ = 2.82 ± 0.06, n_2 = 0.48 ± 0.01).

of two metal chelates (2:1 ligand:HSA) with fractional occupancy of the target binding sites. The behaviour of Pd(PrPyrr) with HSA contrasts that for H_2PrPyrr (n = 0.76 ± 0.02 at 288 K) and Ni(PrPyrr) (n = 0.97 ± 0.02 at 288 K), since these compounds had sharply varying reaction stoichiometries (and consequently binding site occupancies) over the temperature range investigated.

From Table 1, the $logK_a$ values follow the order Pd(PrPyrr) ≫ Pt(PrPyrr) > Ni(PrPyrr) > H_2PrPyrr. Notably, the value of $logK_a$ for the Pd^{II} chelate ranges from 6.68–5.28 (288–315 K) and is akin to the product equilibrium constant β_2, where $log\beta_2 = logK_1 + logK_2$, accounting for why the affinity constant is an order of magnitude larger than the K_a values measured for the Pt^{II} or Ni^{II} congeners. Significantly, K_1 and K_2 for the reaction of HSA with the Pd^{II} system are *unresolvable*, reflecting concurrent ligand binding. Since the isostructural neutral metal chelates Ni(PrPyrr) and Pt(PrPyrr) are similar, and neither readily undergo ligand exchange, it is expected that they will bind noncovalently to the same site in HSA with the affinity of Pt(PrPyrr) exceeding that of Ni(PrPyrr) due to enhanced London dispersion forces of attraction engendered by the electron-rich Pt^{II} ion. The $\log K_a$ values fall in the range 5.69–3.22 (288–315 K) for these chelates.

Reaction mechanism and binding site specificity

Pd^{II} chelate hydrolysis underpins its reaction with HSA. A feasible reaction for Pd(PrPyrr), given its lability and solution chemistry (Scheme 1, Figure 2), is hydrolysis of the complex to form the aqua species, eq. 2:

$$Pd(PrPyrr) + H_3O^+ \rightleftharpoons [Pd(HPrPyrr)(OH_2)]^+ \quad (2)$$

This reaction occurs spontaneously in solution and only for the Pd^{II} chelate. Therefore, *two* Pd^{II} species are present to react with HSA and, because they are structurally distinct, will likely bind in two independent sites within range of Trp-214 to collectively quench its fluorescence. Experimental evidence for the spontaneous formation of $[Pd(HPrPyrr)(OH_2)]^+$ was obtained by measuring the time-dependent electronic absorption and circular dichroism (CD) spectra of Pd(PrPyrr) in aqueous solution. The amplitude of the absorption spectrum of Pd(PrPyrr) decreases with increasing time, reflecting first-order kinetics and formation of

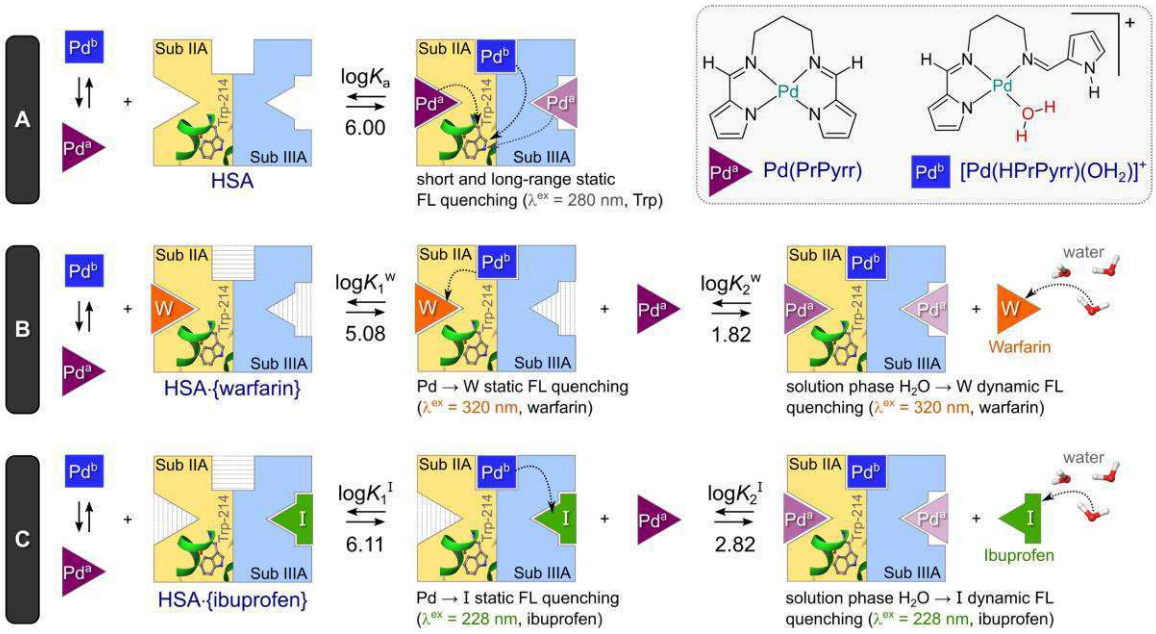


Figure 7. Proposed mechanism of interaction of a pH 7.5 equilibrium mixture of Pd(PrPyrr), comprising the tetradentate Pd^{II} chelate "Pd^a" and its tridentate aqua complex "Pd^b", with human serum albumin (HSA). The experimental affinity constants (298 K) and fluorophore excitation wavelengths are indicated; the diagram summarizes our best interpretation of the experimental data (Tables 1 and S8; Figures 5, 6 and S26) and *in silico* binding site specificity data. In **Part A**, the reaction of native HSA with the two Pd^{II} chelate species is shown. In addition to the main drug binding sites in subdomains IIA and IIIA of HSA (Sudlow's I and II, respectively), the existence of a third binding site unique to the Pd^{II} aqua complex is required to account for the spectroscopic and thermodynamic data. This binding site accommodates $[Pd(HPrPyrr)(OH_2)]^+$ and was found to be at the interfacial region between subunits IA-IIA/IIIA-IIA of the protein (GLIDE XP, Table S9). Pd(PrPyrr) preferentially binds in subdomain IIA, but also has some affinity for subdomain IIIA (indicated by different intensity purple triangles). All bound Pd^{II} chelates will contribute to efficient quenching of the emission from Trp-214 (dashed arrows). In **Part B**, HSA•{warfarin} is the reaction target. The binding pockets have diminished affinity due to allosteric effects (partial inhibition; dotted grey lines) from bound warfarin. This leads to step-wise binding of the Pd^{II} chelates with the affinity order $[Pd(HPrPyrr)(OH_2)]^+ > Pd(PrPyrr)$. Because the fluorescence titration monitors the emission from the drug probe directly (warfarin), its displacement and subsequent dynamic quenching by the solvent is readily detected. Pd(PrPyrr) fractionally occupies Sudlow's sites I and II in the product. **Part C** depicts the analogous reaction when the macromolecular target is HSA•{ibuprofen}$_n$. Notably, displacement of both warfarin and ibuprofen is mediated by Pd(PrPyrr) since $[Pd(HPrPyrr)(OH_2)]^+$ has a low affinity for these drug binding sites (Table S9) and Ni(PrPyrr) gives similar results (Figure S30; Tables S8 and S9). X-ray data will ultimately be required to confirm the proposed binding sites going forward.

$[Pd(HPrPyrr)(OH_2)]^+$ (within ~40 min, Figures S21 and S22). The time-dependent CD spectra are shown in Figure S28a along with the DFT-calculated spectrum of this species. Because Pd(PrPyrr) has exact *Cs* symmetry it has no CD spectrum. The structure of $[Pd(HPrPyrr)(OH_2)]^+$, in contrast, has C_1 symmetry with enantiomers that differ in energy by ~50 kcal mol^{-1}, thwarting racemization. The chiral hydrolysis product thus has a distinct CD spectrum that is easily measured upon its formation. Regarding the species distribution as a function of pH, the aqua complex $[Pd(HPrPyrr)(OH_2)]^+$ is prevalent over the pH range 5.5–7.5 (pK_2 = 8.37 ± 0.04) while the transition to the chloro derivative at low pH, PdCl(HPrPyrr), occurs with pK_1 = 4.62 ± 0.06 (Figure S28b). Notably, the equilibrium mixture at any pH always contains from 47 to 62% Pd(PrPyrr), as evidenced by the complexity of the UV-visible spectra (Figure S28c).

Probe displacement assays delineate the main Pd^{II} binding sites. To understand how the species distribution in eq. 2 affects the reaction of the Pd^{II} system with HSA, we carried out a competitive blocking assay in which the ligand was titrated into solutions of both native HSA and solutions that were pre-equilibrated with (i) warfarin and (ii) ibuprofen (Figure 6). As revealed by X-ray crystallography, warfarin binds specifically in Sudlow's site I (subdomain IIA),[91] while ibuprofen primarily binds in Sudlow's site II (subdomain IIIA), with a secondary site in the region between subdomains IIA and IIB (IIA-IIB).[92] By selectively and sequentially blocking the two main drug binding sites of HSA, the experiment can potentially delineate a ligand's binding site specificity. One caveat is that HSA has multiple drug binding sites.[92] Blocking a primary binding site may redirect ligand uptake to a secondary binding site within the protein (or thwart incoming ligand binding by allosteric inhibition). However, changes in the affinity constant, stoichiometry, K_{SV}, and substitution of the blocking drug itself might occur, thereby revealing a possible binding site for the ligand. The system is intricate, but we have summarized the experimental strategy used and the results obtained pictorially in Figure 7 (which also incorporates our *in silico* binding site affinity data, *vide infra*).

For brevity, uptake of the Pd^{II} species by HSA is discussed here; the remaining ligands are simpler to understand and are analysed in the ESI (Figures S30–S32). When the equilibrium mixture of Pd(PrPyrr) and $[Pd(HPrPyrr)(OH_2)]^+$ (hereafter Pd^{II}_{eq}) reacts with *native* HSA, all possible binding sites are available for ligand uptake. The Trp-214 fluorescence quenching (static over the full range), reaction stoichiometry, and $\log K_a$ data (Figs. 6a and 6b) indicate that a nominally 2:1 metal:protein complex, abbreviated HSA•$\{Pd^{II}(X)\}_2$, where X represents the ligand combinations in eq. 2, is formed by simultaneous ligand uptake in a single step ($\log K_1$ = 6.00 ± 0.07, n = 1.1 ± 0.01, 298 K). Titration of HSA•{warfarin} with Pd^{II}_{eq} while monitoring the fluorescence emission from warfarin (λ^{ex} = 320 nm, λ^{em} = 382 nm) reveals, firstly, that stepwise binding of the Pd^{II} chelate(s) occurs and, secondly, that warfarin is displaced from the protein when $[Pd^{II}_{eq}]$

> 5 μM. The latter event is highlighted by the switch from static quenching of the emission from protein-bound warfarin to dynamic quenching of *free warfarin* in the solvent when [Pd^{II}_{eq}] > 25 μM (Figure 6a). The switch in the slope of the double-log plot of Figure 6b confirms stepwise uptake of the Pd^{II} chelate(s) by HSA•{warfarin}, which is characterized by independent affinity constants for each step (logK_1^W = 5.08 ± 0.05, n_1 = 0.98 ± 0.01; logK_2^W = 1.82 ± 0.17, n_2 = 0.34 ± 0.04) and an overall binding constant logβ_2^W = 6.90, which is 0.9 log units higher than logβ_2 measured for native HSA at 298 K.

The data from these experiments indicate simultaneous uptake of two Pd^{II} complexes at distinct sites located near Trp-214 in native HSA. When warfarin is bound to HSA in Sudlow's site I (subdomain IIA), only one Pd^{II} complex is initially bound—presumably at a site somewhat removed from the warfarin-binding pocket, but close enough to quench its fluorescence by a FRET-based mechanism. Since Sudlow's site II in subdomain IIIA is vacant at lower [Pd^{II}_{eq}], ligand uptake could target this binding site, or a region close to it. However, we cannot rule out the binding of a Pd^{II} species at a unique location close to the warfarin binding site, e.g., between subdomains IB and IIA (indomethacin secondary binding site), IA-IIA (fatty acid binding site, FA2), or even the secondary ibuprofen binding site (IIA-IIB).[92] Importantly, at a sufficiently high concentration of Pd^{II}_{eq}, warfarin is displaced from the protein by the uptake of a second partial equivalent (n_2 < 1) of the metal chelate. Evidently, at least one of the Pd^{II}_{eq} species, either [Pd(HPrPyrr)(OH_2)]$^+$ or Pd(PrPyrr), binds in Sudlow's site I (subdomain IIA), thereby directly competing with warfarin. From *in silico* docking data (*vide infra*), it seems likely that Pd(PrPyrr) targets Sudlow's site I and displaces warfarin.

What happens when we block binding of Pd^{II}_{eq} at Sudlow's site II in subdomain IIIA (and/or the protein's IIA-IIB binding site) using HSA•{ibuprofen}$_n$ as the target whilst monitoring the fluorescence from ibuprofen (λ^{ex} = 228 nm, λ^{em} = 332 nm)? From Figures 6a and 6b, the data mirror the observations for the warfarin adduct of the protein. Specifically, two-step binding of the Pd^{II} chelate(s) is evident due to well-separated logK_1 and logK_2 values (logK_1^I = 6.11 ± 0.13, n_1 = 1.13 ± 0.02; logK_2^I = 2.82 ± 0.06, n_2 = 0.48 ± 0.01). Overall, logβ_2^I = 8.93 and the Pd^{II} chelates have a higher affinity for the ibuprofen adduct of the protein compared with the warfarin adduct. Interestingly, logK_1^I is almost identical to the binding of the Pd^{II} ligand to HSA, which could indicate Pd^{II} initially binds to HSA at an unpopulated site (likely Sudlow's site I), and as the ligand concentration increases, binding to a second site with lower affinity occurs. The first binding site will be within ~20 Å of the *bound ibuprofen fluorophores* to quench their emission by FRET. Crucially, displacement of ibuprofen from the protein occurs at high [Pd^{II}_{eq}]. The signature switch from static to dynamic quenching of the fluorophore when it is released into the bulk solvent is shown in Figure 6a. Interestingly, since logK_2^I > logK_2^W, ibuprofen is more readily displaced than warfarin from HSA.

One caveat is that M(PrPyrr) binding by HSA may induce conformational changes that trigger release of the blocking drug (fluorophore), even if the metal chelate does not target the drug's binding site directly (i.e., probe dissociation induced by allosteric effects). Although some uncertainty exists regarding the binding sites of the Pd^{II} chelates, the evidence points to Sudlow's sites I and II as being probable locations for ligand uptake. Such multi-site ligand binding is not uncommon—the organic drug diflunisal is known (X-ray data) to bind at multiple sites in HSA (specifically Sudlow's I and II, and between subdomains IIA and IIB).[92] Notably, ligands with multi-site binding to a promiscuous protein like HSA may fractionally populate two or more binding sites in a concerted uptake equilibrium (single step) to give an apparent reaction stoichiometry of $n \cong 1$ with a single log$K$ value.

Our analysis of the dual-ligand binding mechanism for the reaction of native HSA with the Pd^{II} system above hinges on two species in solution (eq. 2). Dual-species uptake with subsequent Trp-214 fluorescence quenching is known for 3-hydroxyflavone (3-HF) with HSA.[93] Specifically, the two tautomers of 3-HF have similar, resolvable overlapping binding constants with HSA (K_1 = 7.2 × 10^5 M^{-1} and K_2 = 2.5 × 10^5 M^{-1}) and bind in different binding sites (subdomains IIIA and IIA), affording unique Trp-214 quenching rate constants.[93] This is similar to what we observe for the two Pd^{II} species, Pd(PrPyrr) and [Pd(HPrPyrr)(OH_2)]$^+$, although we cannot resolve K_1 and K_2 for the binding of the two metal chelates due to their simultaneous uptake by the protein. Interestingly, the docking scores of the two Pd^{II} species are virtually the same (Table S9), mirroring the experimental data.

Mass spectroscopy confirms intact metal chelate uptake by HSA. We chose to analyse the complexes of HSA formed with the present metal chelates by ESI-MS to prove (i) that uptake of fully intact metal chelates occurs, (ii) multi-site binding is possible (consistent with 1 ≤ n_{total} ≤ 2), and (iii) that the Pd^{II}(X) system behaves uniquely due to dual species uptake by the protein. From Figure S33 it is clear that the species HSA•{Ni(PrPyrr)}$_2$ was formed and dominant in the sample. In the case of Pt(PrPyrr), an entirely reasonable species distribution was evident: HSA (47%), HSA•{Pt(Pr(Pyrr)} (43%), and HSA•{Pt(Pr(Pyrr)}$_2$ (10%). For the HSA-Pd^{II} system, the resolution of the data was not sufficient to distinguish between the chemical species bound, i.e., Pd(PrPyrr) and/or [Pd(HPrPyrr)(OH_2)]$^+$. However, a similar component distribution pattern to that seen for the Pt^{II} system was obtained, albeit with a lower fraction of the unbound protein: HSA (26%), HSA•{Pd(X)} (38%), and HSA•{Pd(X)}$_2$ (35%). Notably, the mass spectrum of the Pd^{II} system was unique in that satellite peaks appeared on the main bands at low m/z. Although minor in abundance, these peaks are likely due to covalent adducts formed when surface residues such as His[64] and Glu substitute Pd-bound water in [Pd(HPrPyrr)(OH_2)]$^+$. The kinetic inertness of Pt(PrPyrr) and Ni(PrPyrr) precludes the formation of such peaks.

Thermodynamics of metal chelate binding by HSA

The reactions of H_2PrPyrr and M(PrPyrr) with HSA follow a linear van't Hoff relationship; plots for triplicate measurements are given in Figure 8. Under non-standard conditions, the enthalpy change (ΔH), entropy change (ΔS), and Gibbs free energy change (ΔG), may be deduced from the temperature dependence of the affinity constants (K_a) using the van't Hoff and Gibbs-Helmholtz equations (eqs. S8–S10). Table 2 summarises the thermodynamic data for reaction of the compounds of interest with HSA in phosphate buffer at neutral pH. The reactions are all exergonic,[88] with ΔG ranging from –20.3 kJ mol^{-1} for H_2PrPyrr to –33.1 kJ mol^{-1} for Pd^{II}(X) at 298 K. As graphically portrayed in Figure 8a, the values of ΔH and $T\Delta S$ become increasingly *less negative* moving from the free ligand down the divalent Group 10 metal ions, increasing with the order 3d < 4d < 5d, while the values of ΔG display the reverse trend and become more negative going down the group. The switch in the order of ΔG evident for the Pt^{II} and Pd^{II} derivatives reflects the species distribution for the Pd^{II} system in eq. 2.

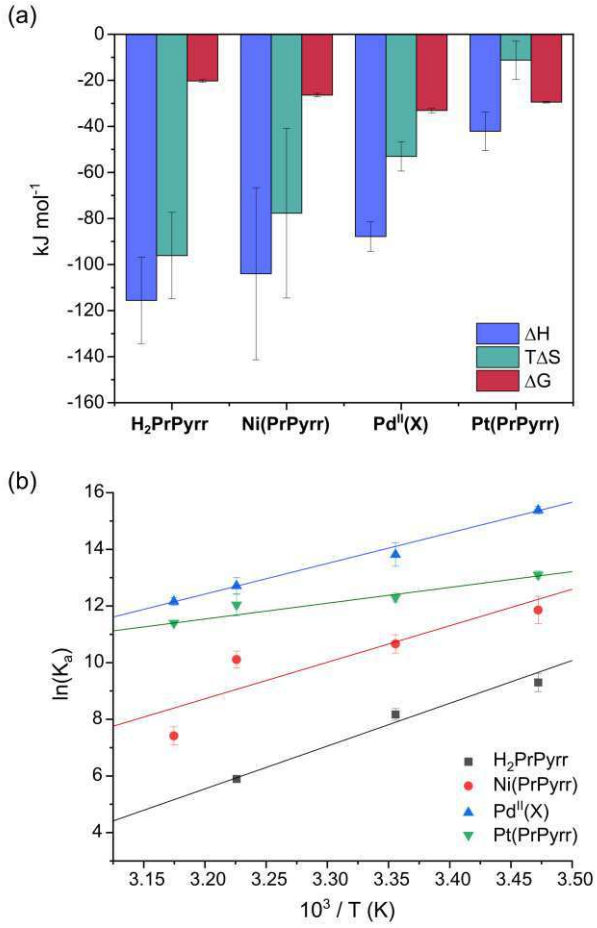


Figure 8. (a) Thermodynamic parameters governing the reactions of H_2PrPyrr and its d^8 Group 10 metal chelates with HSA (T = 298 K). Error bars are based on estimated uncertainties from the slope and intercepts of the least-squares fits of eq. S8 to the data. (b) Linear van't Hoff plots (eq. S8) for the reactions of the compounds with HSA in 50 mM KH_2PO_4 buffer at pH 7.50. Error bars are estimated uncertainties derived from averaging triplicate measurements. Pearson's *r*-values for the fits were 0.99, 0.85, 1.00, and 0.99 for H_2PrPyrr, Ni(PrPyrr), Pd^{II}(K), and Pt(PrPyrr), respectively.

The spontaneity of metal chelate binding by HSA thus increases with increasing electron density within the complexes, which occurs naturally as the size of the metal ion and its polarizability (i.e., softness) increases.[94,95] The trend is driven by the reactions becoming less exothermic and more entropically favoured with the ΔH and $T\Delta S$ terms being of similar magnitude. Since London dispersion forces (LDF) of attraction in biomolecules significantly control the tertiary structure of the macromolecule,[96] and will increase in the order 3d < 4d < 5d[95] for this class of pyrrolide-imine metal chelates, Figure 8 suggests the reaction thermodynamics hinge on a significant LDF effect.

Regarding the ΔH values for the reactions, which are exothermic and range from –42 kJ mol^{-1} for Pt(PrPyrr) to –116 kJ mol^{-1} for H_2PrPyrr, Figure 8a highlights the significance of the enthalpy term and suggests that hydrogen bonding in the case of H_2PrPyrr accounts for its large negative values of ΔH and $T\Delta S$. Since the drug binding sites known as Sudlow's I and II (subdomains IIA and IIIA) in the protein are mostly hydrophobic,[45] the large negative $T\Delta S$ values for ligand binding recorded here imply enhanced conformational rigidity and minimal disruption of the protein's ordered water or backbone structure, commensurate with ligand uptake in one or more hydrophobic pockets, a deduction confirmed by our molecular docking simulations (*vide infra*).

Table 2. Thermodynamic parameters for the binding of H_2PrPyrr, Ni(PrPyrr), Pd^{II}(X) and Pt(PrPyrr) by HSA in 50 mM KH_2PO_4 buffer at pH 7.50.

Compound	T (K)	ΔG (kJ mol^{-1})[a]	ΔH (kJ mol^{-1})[a]	ΔS (J K^{-1} mol^{-1})[a]
H_2PrPyrr	288	–22.3 (8)		
	298	–20.3 (5)	–116 (19)	–323 (96)
	310	–15.2 (3)		
Ni(PrPyrr)	288	–28.4 (1.2)		
	298	–26.4 (8)	–104 (37)	–261 (78)
	310	–26.1 (8)		
	315	–19.4 (8)		
Pd^{II}(X)[b]	288	–36.8 (3)		
	298	–33.1 (1.0)	–88 (6)	–178 (53)
	310	–30.4 (7)		
	315	–29.1 (3)		
Pt(PrPyrr)	288	–31.4 (3)		
	298	–29.5 (4)	–42 (8)	–38 (11)
	310	–28.8 (9)		
	315	–27.3 (2)		

[a]The estimated standard uncertainties of the least significant digits are given in parentheses. [b]X represents the ligand combinations shown in eq. 2.

The Gibbs-Helmholtz equation reveals the fundamentals of M(PrPyrr) binding by HSA. By using the Gibbs-Helmholtz equation (eq. S10) with the experimental data (Table 2), the role played by the d^8 metal ion in determining the thermodynamics governing ligand uptake by HSA may be delineated (Figure 9). We have coined the term "*beads on a wire plot*" for this format of the Gibbs-Helmholtz equation as the points are free to move along the straight line and will cluster informatively within three of the four quadrants depending on the specific ligands and macromolecule being investigated for a spontaneous reaction. The plot is universal. For the present system, when $T\Delta S/\Delta G$ is plotted against $\Delta H/\Delta G$, the data fit the linear relationship in the upper right quadrant of the graph where ΔH < 0, consistent with enthalpic control of the reaction. In this quadrant, spontaneity is assured as changes in $\Delta H/\Delta G$ are compensated for by commensurate changes in $T\Delta S/\Delta G$. Importantly, $T\Delta S/\Delta G$ and $\Delta H/\Delta G$ decrease together giving the order Pt(PrPyrr) < Pd^{II}(X) < Ni(PrPyrr), which follows the principal quantum number for the metal ion (5d < 4d < 3d). The trend indicates that the thermodynamics of metal chelate binding by HSA depends directly on increasing the electron density present in the complexes (i.e., LDF). The free ligand (H_2PrPyrr) has no metal centre so its binding to HSA hinges on both the π-electron density of the pyrrole-imine groups as well as the pyrrole N–H groups, which are excellent H-bond donors.[97,98]

The ligand binding thermodynamics here mirror data reported from microcalorimetry studies on the binding of drugs such as ibuprofen,[99] benzodiazepines,[100] and phenothiazines by HSA,[101] which have moderately negative ΔH (–50 to –75 kJ mol^{-1}) and ΔS values as well as sizeable K_{a1} values ~10^5 M^{-1}.[102] In the first association equilibrium, these drugs all bind in hydrophobic Sudlow's site II (subdomain IIIA) of HSA. Interestingly, a second ligand association may occur (dual-site

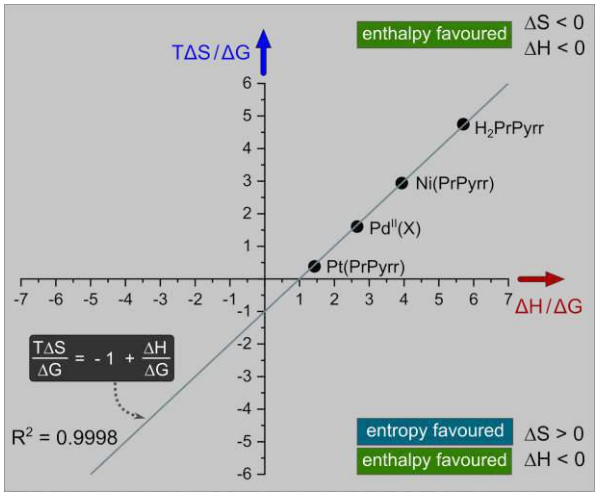


Figure 9. Plot of the Gibbs-Helmholtz relationship for the reaction of H_2PrPyrr, Ni(PrPyrr), Pd^{II}(X), and Pt(PrPyrr) with HSA at 298 K in 50 mM KH_2PO_4 buffer at pH 7.50. The straight line fit of the data gives R^2 = 0.997 with a slope of 1.001 ± 0.006 and intercept of –1 (fixed). For all reactions, ΔG < 0. The plot highlights how the identity of the d^8 metal ion influences the reaction thermodynamics. (X represents the ligand combinations shown in eq. 2.)

binding, also in subdomain IIIA) with K_{a2} values ~10^3 M^{-1} and similarly negative ΔH and ΔS values.[102] Warfarin, which binds in Sudlows's site I (subdomain IIA),[91] has broadly comparable thermodynamics[102] ($logK_{a1}$= 5.15, ΔH = –49 kJ mol^{-1}, ΔS = –12 J K^{-1} mol^{-1}) to ibuprofen (Sudlow's site II, $logK_{a1}$= 5.04, ΔH = –67 kJ mol^{-1}, ΔS = –34 J K^{-1} mol^{-1}) and Ni(PrPyrr) ($logK_a$= 4.92, ΔH = –45 kJ mol^{-1}, ΔS = –57 J K^{-1} mol^{-1}), suggesting that assigning the specific binding site of the ligand ultimately requires additional structural or spectroscopic data.

Ligand-induced HSA secondary structure changes

Ligand binding minimally perturbs HSA. Since the far UV-region CD spectra of HSA (and other proteins) are sensitive to changes in the secondary (and tertiary) structure of the protein caused by ligand binding (i.e., perturbations of α-helices, β-sheets, hairpin turns and unordered coils),[103,104] CD spectroscopy (185–260 nm) was used to delineate how H_2PrPyrr and M(PrPyrr) impact the secondary structure of the protein (Figure 10). The CD spectrum of native HSA exhibits a double minimum (208 ± 1 nm and 222 ± 1 nm), reflecting a mainly α-helical structure.[105] The electronic transitions in this region are assigned to π–π* (208 nm minimum), n–π* (222 nm minimum), and π–π* (196 nm maximum) transitions of the amide groups of the peptide backbone.[105,106] From Figures 10a–10d, HSA binds the current ligands not only with high affinity (Table 1), but also with only minor changes in its secondary structure elements (the spectrum of native HSA is similar to the spectra in the presence of saturating ligand doses). Thus, the wavelengths of the band maxima and minima are largely unshifted, with only slight changes in intensity evident (most noticeably for the 196-nm band). The isodichroic points are quite difficult to locate, but those that are discernible appear to be somewhat sensitive to the identity of the bound ligand. In particular, there is some agreement between the wavelengths of the isodichroic points for HSA•{H_2PrPyrr} and HSA•{Pd^{II}(X)} as well as those for HSA•{Ni(PrPyrr)} and HSA•{Pt(PrPyrr)}.

The CD data were analysed further (JASCO Spectra Manager™) to calculate the percentage composition of α-helical coils, β-sheets, turns, and unordered coils present for each HSA-ligand complex (Table S7). The dominant secondary structure domains are α-helices (~50%), and unordered coils (~31%), while β-sheet domains (8–19%) show the largest variation with the identity of the bound ligand. Interestingly, the secondary structure of HSA in solution differs from that of native HSA in the solid state[45] (68.5 % α-helix, 0% β-sheet, 9.6% turns, and 21.9% unordered coils; PDB code 1BM0 analysed with BeStSel[107]). Our CD data are, however, consistent with solution state spectral decompositions reported by others,[108–110] and it is understood that enhanced subdomain mobility and general thermal motion/disorder accounts for the decrease of α-helicity.[104,105]

HSA structural perturbations correlate with ligand binding thermodynamics. In Figure 10e, we have plotted the change in the secondary structure components of HSA as the percentage difference between the domain content for the native protein and that determined for the ligand-bound complex at saturation (Table S7). For the α-helix, turn, and coil regions of the structure, the ligand-induced perturbation falls within the range ± 1.3%, which is comparable to the X-ray data for HSA bound to warfarin.[91] However, for the β-sheet domains, the ligand-induced perturbation is significantly greater with a range of ± 3.1%. The complexes HSA•{H_2PrPyrr} and HSA•{Pd(PrPyrr)} exhibit the largest increase and decrease in β-sheet content, respectively.

Importantly, the ligand-induced changes in the protein secondary structure correlate with the thermodynamics of ligand binding measured independently by fluorescence spectroscopy. Thus, as shown in Figure 10f, the percentage change in the β-sheet composition, %Δ(β-sheet), is linearly co-dependent on the enthalpy and entropy changes for the reaction. Specifically, as ΔH and ΔS become more negative and positive, respectively, the β-sheet content *decreases* while the α-helix content *increases* (Figure S35). From the Gibbs-Helmholtz equation ($\Delta G = \Delta H - T\Delta S$), a more exergonic reaction (negative ΔG) reflects a decrease in β-sheet content. Ligand binding, which induces a modest increase in α-helicity, thus stabilizes the protein secondary structure,[111] in accord with the fact that α-helices are usually more stable thermodynamically than β-sheets.[112,113]

Intact metal chelates are bound by HSA

CD spectroscopy illuminates key ligand binding sites. Near-UV CD spectra provide a valuable fingerprint of protein tertiary structure perturbations, specifically those involving Trp (285–300 nm), Tyr (280 nm), and Phe (250–270 nm). Additionally, induced circular dichroism (ICD) spectra are informative when an optically inactive guest interacts with a protein and gains chirality from its chiral host.[106] Here, experimental CD spectra of the HSA-ligand complexes are included with an integrated interpretation of the data based on our Glide XP[114,115] molecular docking and TD-DFT simulations of the electronic structures of the protein-bound metal chelates. Figure 11 shows the near-UV and visible CD spectra of HSA recorded in native form and in the presence of identical saturating doses (12 μM) of H_2PrPyrr, Ni(PrPyrr), Pt(PrPyrr), and Pd^{II}(X), where X represents the ligands of eq. 2. Using difference spectroscopy, the ICD spectra were resolved for all ligands. The intensity of the ICD response followed the order Pd^{II}(X) > Pt(PrPyrr) > Ni(PrPyrr) > H_2PrPyrr, which is identical to the order of the affinity constants ($logK_a$, Table 1) for the compounds.

Evidently, the stronger the HSA-ligand interaction, the greater the induced chirality in the formally achiral ligand. Importantly, the

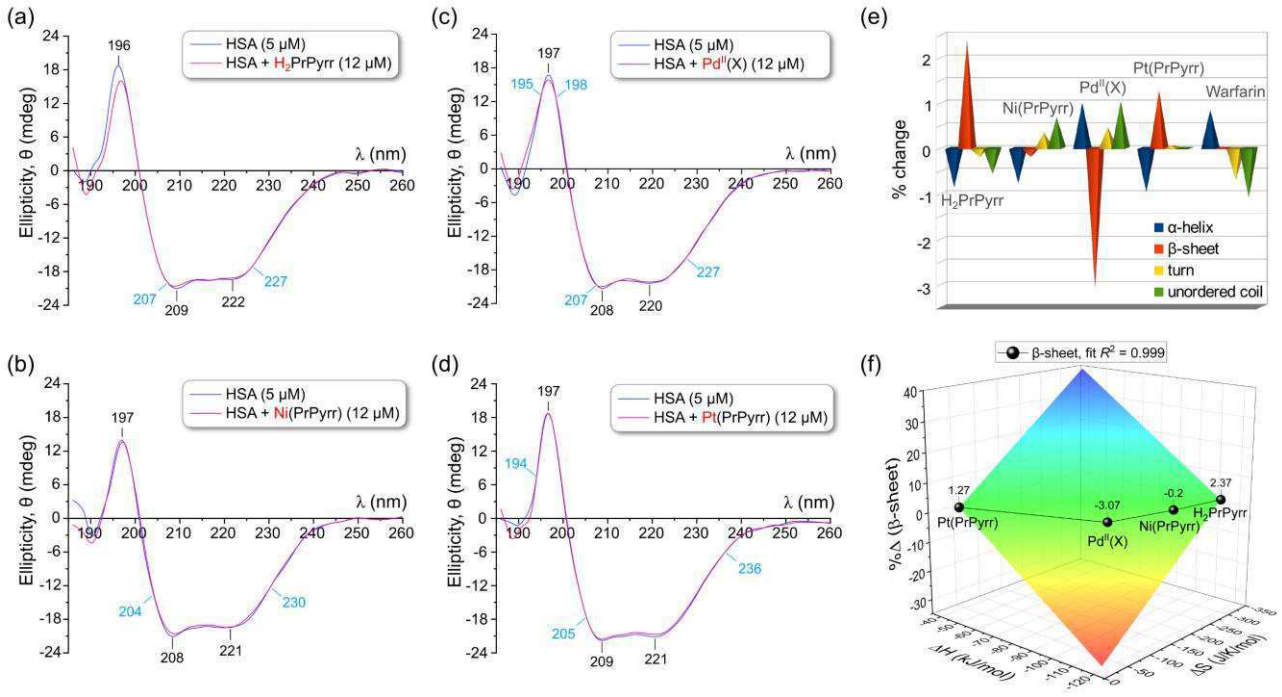


Figure 10. Plots of the far-UV CD spectra of native HSA and the protein incubated with saturating doses of (a) H_2PrPyrr, (b) Ni(PrPyrr), (c) Pd^{II}(X), and (d) Pt(PrPyrr) recorded at 298 K in 50 mM KH_2PO_4 buffer at pH 7.50. (For the Pd^{II} complex, X represents the ligand combinations of the equilibrium species depicted in eq. 2.) The spectra were smoothed using a Lowess function (0.07 span); unsmoothed spectra at ligand doses ranging from 4 μM to 12 μM are given in ESI Figure S34. Band maxima and minima (black numerals) as well as isodichroic points (blue numerals) are indicated (in nm). (e) Graph of the percentage change in the protein secondary structure delineated by fitting the CD spectra in Parts (a)–(d). Data for warfarin were determined from the X-ray structures of the native (PDB code: 1BM0) and ligand-bound (PDB code: 2BXD) proteins using the program BeStSel. Although the protein is minimally perturbed by ligand uptake, the β-sheet content decreases by as much as 3% in the case of the complex formed with the Pd^{II} chelate. (f) Three-dimensional graph showing how the percentage change in the β-sheet content of the protein correlates with the experimentally determined values of ΔH and ΔS for the reaction of each compound with HSA (T = 298 K). The relationship, $\%\Delta(\beta\text{-sheet}) = 17.8(3) + 0.514(9) \times \Delta H - 0.136(2) \times \Delta S$, reflects the fact that ΔG for the reaction becomes more favourable (negative) as the β-sheet content of the protein decreases, which is dependent on the identity of the bound ligand and is matched by a commensurate *increase* in the α-helix content of the protein (see ESI Figure S35). The correlation coefficient for the least-squares fit is exceptional considering the small sample size.

ICD spectra indicate that the complexes neither demetallate nor suffer imine hydrolysis or ligand dissociation when binding to HSA. Since ligand dissociation often accompanies HSA binding by simple metal complexes such *trans*-$[RuCl_4(1H\text{-indazole})_2]^-$ (KP1019)[55] and cisplatin,[116] the present findings highlight the potential for fully reversible transport of the present and related compounds by HSA.

For HSA•{H_2PrPyrr} and HSA•{Ni(PrPyrr)}, the weaker ICD spectra of the ligands permit delineation of subtle changes in the fine structure CD bands of the protein host (Figure S36). Clear perturbation of the signal from Tyr (~277 nm) is evident in the difference spectrum for HSA•{H_2PrPyrr} (Figure 11a), consistent with this ligand and/or its protonated forms binding adjacent to one or more tyrosine residues, perhaps aided by H-bonding.[97] From our *in silico* docking data obtained with different grids (*vide infra*, Figure S37, Tables S10 and S11) there are several possible binding sites found within 10–27 Å of Trp-214 that can account for (i) FRET-based quenching of this fluorophore and (ii) location of the ligand within 4–10 Å of at least one Tyr residue. Interestingly, none of the binding sites are directly in the main drug-binding pockets of the protein (i.e., Sudlow's sites I and II). This evidently explains why blocking these sites with warfarin and ibuprofen neither inhibited the uptake of H_2PrPyrr (and/or its protonated forms) nor resulted in displacement of the probe drugs at higher ligand doses (Table S8, Figure S30).

For HSA•{Ni(PrPyrr)}, the near-UV CD signals from Phe (~269 nm), Tyr (~279 nm), and Trp-214 (~290 nm) showed significant perturbations (Figure 11b), commensurate with binding of the Ni^{II} chelate in one or more sites containing Phe and Tyr residues and within range of Trp-214 for FRET-based quenching (~1–3 nm in an isolated biomolecule).[117] From our Glide XP data, Ni(PrPyrr) favours binding in Sudlow's site I (Tables S9, S11) and possibly also Sudlow's site II. Medium-range dipole–dipole interactions between Ni(PrPyrr) and the closest Phe and Tyr residues within the binding pocket of Sudlow's site I (Table S10, Figure S36) are thus feasible given the spatial proximity of the chromophores (e.g., Tyr-150···Ni, 7.0 Å; Phe-149···Ni, 8.5 Å), accounting for the experimental near-UV CD data.

Regarding assignment of the near-UV and visible ICD spectrum of HSA•{Ni(PrPyrr)}, peaks with positive (300–340 nm; 375–430 nm) and negative ellipticity (457 and 477 nm) are observed (Figure 11b). Since unbound Ni(PrPyrr) is achiral (exact *Cs* symmetry), it has no CD spectrum. The electronic absorption spectrum of the protein-free Ni^{II} chelate is characterized by absorption maxima with $\varepsilon > 4 \times 10^3$ M^{-1} cm^{-1} at 313, 369, 388, 409, and 433 nm in pure acetonitrile (Figure S39). Considering the TD-DFT data for Ni(PrPyrr) (Table S12), these bands may be assigned to MLCT (metal-to-ligand charge transfer) transitions from filled MOs with mainly metal 3*d*-orbital character (and some ligand π character) to vacant MOs with mainly ligand π* character. (A broad, weaker band with ε ~200 M^{-1} cm^{-1} at ~523 nm

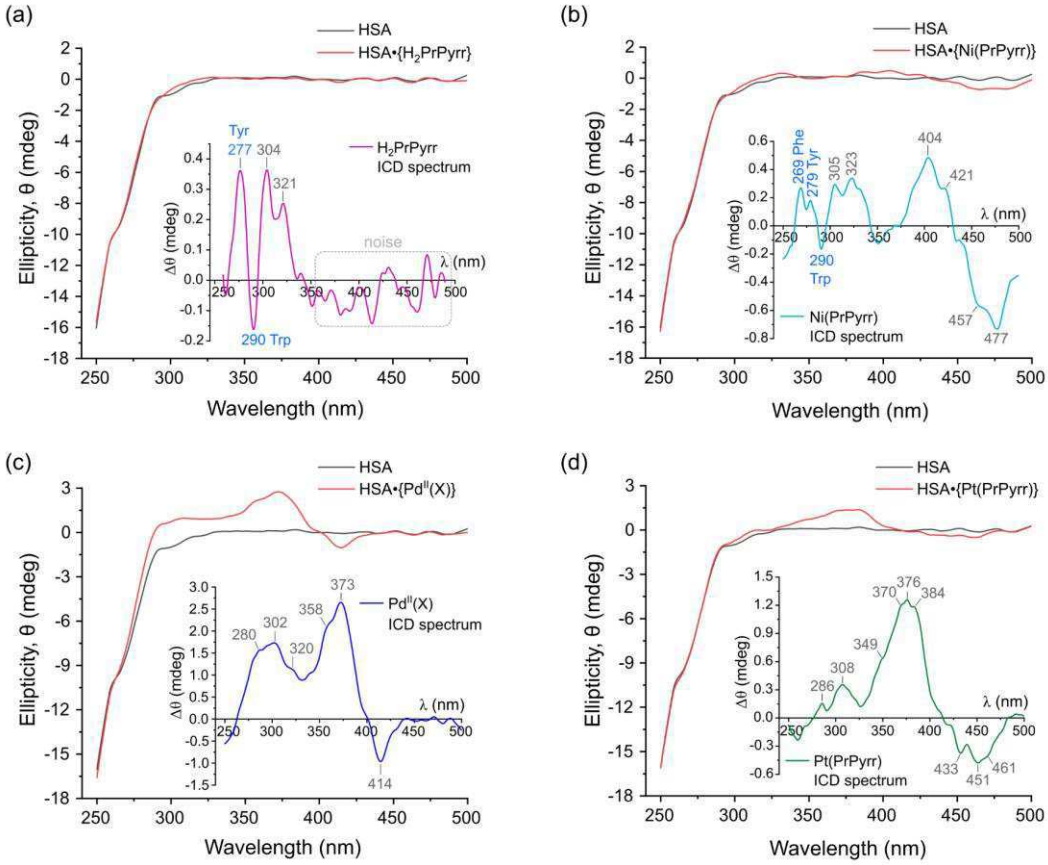


Figure 11. Plots of the near UV-visible CD spectra of native HSA (5 μM) and the protein incubated with a saturating dose (12 μM) of (a) H_2PrPyrr, (b) Ni(PrPyrr), (c) Pd^{II}(X), and (d) Pt(PrPyrr). The spectra were recorded at 298 K in 50 mM KH_2PO_4 buffer at pH 7.50 and smoothed using a relatively fine Lowess function (0.07 span). The graphical insets are plots of the difference spectra generated by subtraction of the spectrum of native HSA from that of the HSA-ligand complex; they represent the induced CD (ICD) spectrum of each achiral protein-bound ligand. (For the Pd^{II} complex, X represents the ligand combinations of the equilibrium species depicted in eq. 2) Perturbations in the protein structure around Phe (250–270 nm), Tyr (~280 nm), and Trp (285–300 nm) residues may also be resolved in some difference spectra. Key maxima and minima are indicated (in nm). H_2PrPyrr has no visible absorption spectrum; undulations > 350 nm are noise. Selected unsmoothed spectra are available in the ESI (Fig. S36). The CD spectra for all HSA•{ligand} complexes closely match the shoulder at ~262 nm of the native protein, suggesting the 17 disulphide bonds of the protein remain unchanged upon ligand uptake.

encompassing one or more *d–d* transitions of the complex is also evident.) The MLCT absorption bands at 369 and 388 nm redshift by ~20–30 nm upon uptake of the Ni^{II} chelate by HSA, giving rise to the positive ICD bands at 404 and 421 nm. Similarly, those at 409 and 433 nm equate with the negative ICD bands at 457 and 477 nm (Figure S39). The fact that signals from Ni(PrPyrr) are discernible in the experimental CD spectrum of the protein complex, HSA•{Ni(PrPyrr)}, strikingly confirms that the intact Ni^{II} chelate is noncovalently bound within the protein. Significantly, TD-DFT simulations with the best-scoring pose for Ni(PrPyrr) docked within subdomain IIA of the protein (Table S9, Figure S40) support this conclusion by reproducing the main features of the experimental ICD spectrum.

The ICD spectrum recorded for HSA•{Pt(PrPyrr)} is akin to that of HSA•{Ni(PrPyrr)} and may be similarly assigned after taking into account the blue shift in the transition energies associated with the heavier metal ion. Indeed, the ICD spectra suggest that Pt(PrPyrr) targets the same binding site(s) as Ni(PrPyrr), consistent with our *in silico* docking data (Table S10).

The ICD spectrum of HSA•{Pd^{II}(X)} is the most intense of the series and shows features reminiscent of the above M(PrPyrr) chelates, specifically the peaks with positive ellipticity at 358 and 373 nm and the peak with negative ellipticity at 414 nm. One clear difference is the stronger set of positive ellipticity bands from 280–305 nm ($\Delta\theta$ ~1.7 mdeg). These bands overlap the CD signals expected from perturbed Tyr and Trp residues; in the present system, they also reflect the interaction of HSA with the C_1-symmetry aqua complex, $[Pd(HPrPyrr)(OH_2)]^+$. We used Glide XP to dock both species depicted in eq. 2, i.e., Pd(PrPyrr) and $[Pd(HPrPyrr)(OH_2)]^+$, into HSA (PDB code: 1HA2) using a large 40^3 Å^3 grid centred on Trp-214 or the warfarin binding site as well as a similarly-constructed grid for the diazepam adduct of HSA (PDB code: 2BXF). The two best-scoring poses for the Pd^{II} chelates are located at sites in subdomain IIA of HSA (Tables S9–S11, Figure S41). Specifically, Pd(PrPyrr) favours the larger Sudlow's I site (ΔG_{dock} = –5.56 kcal mol^{-1}) in a region directly adjacent to the warfarin binding site (Figure S42), while $[Pd(HPrPyrr)(OH_2)]^+$ binds towards the protein surface between two α-helical coils belonging to subunits IA and IIA (ΔG_{dock} = –5.53 kcal mol^{-1}; Figure S41).

TD-DFT simulations confirm intact metal chelate binding. Given the stoichiometry and fluorescence quenching data for the HSA-Pd^{II} system (Table 1), attempts to calculate the ICD spectrum of the system must include both Pd^{II} chelates. A hybrid

QM:MM TD-DFT simulation (ONIOM[118] method, CAM-B3LYP[119]/SDD[120]/GD3BJ:[121] UFF[122]) was thus employed in which the two Pd^{II} chelates were assigned to the quantum mechanics (QM) layer of a model taken directly from the optimized Glide XP structure (Figure S41). Three side-chains belonging to residues closely interacting with Pd(PrPyrr) in Sudlow's site I (Arg-257, His-288, and Tyr-150) were added to the QM layer to calculate the most accurate CD spectrum (Figure S43). The remining atoms of the protein were simulated using molecular mechanics (UFF[122]). From Figure 12, the calculated CD spectrum of the system broadly matches the key features of the experimental ICD spectrum. Significantly, the analogous TD-DFT CD spectra for each Pd^{II} chelate independently bound to HSA poorly matched the experimental ICD spectrum (Figure S43), supporting our understanding of the HSA•{Pd^{II}(X)} system (i.e., dual chelate binding). One caveat is the remaining uncertainty concerning whether $[Pd(PrPyrr)(OH_2)]^+$ binds HSA non-covalently (as modelled) or covalently (e.g., via a surface residue such as His, Glu, or Cys substituting Pd-bound water). Although including noncovalently bound $[Pd(PrPyrr)(OH_2)]^+$ in the TD-DFT simulation was obligatory to match the positive ellipticity bands from 275 to 325 nm in the CD spectrum, only X-ray data will be definitive.

Macromolecular simulations reflect multi-site ligand binding

Docking studies (Glide XP) were used to predict possible HSA binding sites for the present ligands along with control compounds (warfarin, diazepam, ibuprofen). Since rigid X-ray structures of proteins are used as the hosts for flexible ligand docking, the method offers approximate insights on target binding. Notably, docking scores do not correlate quantitatively with experimental thermodynamic data (ΔG values)[123,124] because the *in silico* experiment does not try to emulate a physical reaction between the macromolecule and incoming ligand in solution. Thus, only qualitative parallels are drawn between the thermodynamic data (Tables 1, 2, and S8) and docking scores of Tables S9 and S11, with a focus on simulations enhancing our understanding of the experimental facts. The key trends are enumerated below:

1. The existence of multiple binding sites within HSA for the current ligand set is predicted from the narrow range of docking scores (ΔG_{dock} ~ –3 to –7 kcal mol^{-1}) and repeatedly favoured binding locations (~7 in total including Sudlow's I and II), consistent with X-ray data for diverse drug and ligand types bound by HSA.[92]
2. The binding site locations were all within 5–20 Å of Trp-214, accounting for facile quenching of its emission by the ligands (Table 1). Furthermore, all were within 3.5–15 Å of tyrosine and/or phenylalanine residues (Table S10), affording observable CD signal perturbations between 250 and 295 nm for at least two HSA-ligand complexes (H_2PrPyrr and Ni(PrPyrr), Figure 11).
3. Warfarin bound within HSA (subdomain IIA), generally *enhances* the docking scores for ligand uptake when forming a multi-ligand complex (Table S9). Thus, ΔG_{dock} improves from –5.17 to –6.00 kcal mol^{-1} when Ni(PrPyrr) co-binds with warfarin (Figure S38) due to enhanced lipophilic van der Waals and electrostatic energy terms. In contrast, the docking score worsens from –5.56 to –4.01 kcal mol^{-1} for Pd(PrPyrr) when warfarin is co-bound in Sudlow's site I due to van der Waals repulsion between the metal chelate and the probe (Figure S42). These trends qualitatively mirror the experimental $\log K_a$ data for several ligands (Table S8).
4. Ibuprofen bound within Sudlow's site II (subdomains IIIA and IIA-IIB) decreases the docking scores for the ligands with HSA, a trend mirrored by the reaction thermodynamics (e.g., Ni(PrPyrr) and Pd^{II}(X) binding to HSA, Table S8). Although these ligands do not compete with ibuprofen for the same binding sites in the docking experiment (Table S9), ibuprofen seemingly redirects their uptake to less-favourable binding sites relative to those in native HSA. In reality, Pd^{II}(X) and Ni(PrPyrr) easily displace ibuprofen from HSA (Figures 6 and S30), suggesting that these ligands can bind in subdomain IIIA (Table S11) or that the release of ibuprofen is triggered by allosteric effects when the ligands bind at the alternative locations.

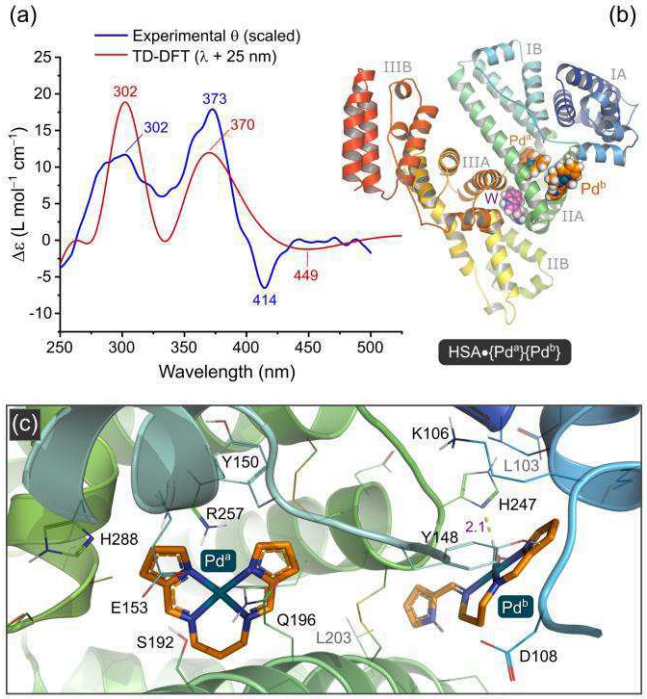


Figure 12. (a) Comparison of the experimental ICD spectrum ($\Delta\theta \times 9$ mdeg) recorded for HSA•{Pd^{II}(X)} at pH 7.5 (Figure 11c) and the CD spectrum calculated using hybrid QM:MM TD-DFT simulations (CAM-B3LYP/SDD/GD3BJ:UFF) for the top-scoring docked poses of Pd(PrPyrr), Pd^a, and $[Pd(HPrPyrr)(OH_2)]^+$, Pd^b, co-bound to HSA (PDB code: 1HA2). Both poses were required to get a reasonable match with the experimental data (Figure S43); a band width of 2500 cm^{-1} (hwhm) was used for the TD-DFT data. (b) Structural model used for the TD-DFT simulations showing the location of the two Pd^{II} chelates (orange C atoms, van der Waals radii) and Trp-214 (purple C atoms) in different regions of subdomain IIA (see also Figure S41). (c) View of the metal chelate binding sites containing the best poses of the two Pd^{II} complexes and their closest residues (1-letter codes). His-247 hydrogen bonds to the coordinated water molecule of $[Pd(HPrPyrr)(OH_2)]^+$ (O–H···N, 2.08 Å, dashed yellow cylinder). Only polar hydrogen atoms are shown.

Finally, the grid chosen for the docking simulation affects the docking-score order and *in silico* site specificity of the ligands for HSA (Tables S9 and S11). This limitation is well known with the use of a rigid receptor grid, as done here, considered best for some metalloproteins.[125] For this reason, and because there is no other way to guide the grid choice for novel ligands when X-ray data are absent, we have mainly used the data generated with a rigid receptor grid (Table S9) as opposed to that obtained with

a soft receptor and ligand potential (Table S11). The results obtained with the softer potential may, however, be equally valid.

Conclusion

The interaction of H_2PrPyrr and its Ni^{II}, Pd^{II}, and Pt^{II} chelates with human serum albumin (HSA) was investigated by complementary spectroscopic techniques to understand how the identity of the d^8 metal ion affects ligand uptake by the protein. All ligands quenched the intrinsic Trp-214 fluorescence of HSA via a static quenching mechanism. The Stern-Volmer quenching constants (K_{SV}) and affinity constants (K_a) followed the order: Pd(PrPyrr) >> Pt(PrPyrr) > Ni(PrPyrr) > H_2PrPyrr. The notably higher affinity of Pd(PrPyrr) for HSA coupled with a reaction stoichiometry, *n*, *significantly exceeding* 1:1 (ligand:HSA) reflects simultaneous uptake of two Pd^{II} species from an equilibrium mixture comprising Pd(PrPyrr) and $[Pd(HPrPyrr)(OH_2)]^+$, the latter structure being related to the crystallographically-characterized chlorido complex, PdCl(HPrPyrr). Significantly, ESI-MS data directly confirmed formation of HSA•{ligand}$_n$ species with $n \geq 1$ for the M(PrPyrr) chelates. The present ligands bind to HSA with *negative* ΔH, ΔG and ΔS values, reflecting a spontaneous enthalpy-driven process governed by van der Waals (London dispersion) forces as well as H-bonding (for H_2PrPyrr). $T\Delta S/\Delta G$ and $\Delta H/\Delta G$ together become increasingly positive, following the order Pt(PrPyrr) < Pd^{II}(X) < Ni(PrPyrr) < H_2PrPyrr, thereby inversely tracking the Group 10 metal ionic radii and polarizability order (5d > 4d > 3d). *In silico* data support the notion (gleaned from spectroscopy) that each ligand has more than one binding site in HSA and that ligand uptake minimally perturbs the protein's secondary structure. Finally, the induced CD spectra recorded for the metal chelates bound to HSA strikingly confirm uptake of the intact complexes without imine group hydrolysis or demetallation.

Experimental Section

Crystallographic data: Deposition numbers 2207667 and 2207668 contain the supplementary crystallographic data for this paper. These data are provided free of charge by the joint Cambridge Crystallographic Data Centre and Fachinformations-zentrum Karlsruhe Access Structures service. Full experimental details, computational methods, and characterization data are given in the supporting information.

Acknowledgements

This work is based on research supported by the South African Research Chairs Initiative of the Department of Science and Innovation (DSI) and National Research Foundation (NRF) of South Africa (Grant No 64799, OQM). The authors thank WITS University and the NRF for funding to purchase a JASCO J-1500 MCD spectrometer (Grant No 116177, OQM) and a dual-wavelength Bruker D8 Venture X-ray diffractometer (Grant No 129920, OQM). We also thank the Centre for High Performance Computing (Project CHEM1065, CHPC, Cape Town) for both the CPU time and resources needed for the DFT simulations.

Conflict of Interest

The authors declare no conflict of interest.

Keywords: Schiff base • metal chelate • albumin • ligand binding • DFT simulations

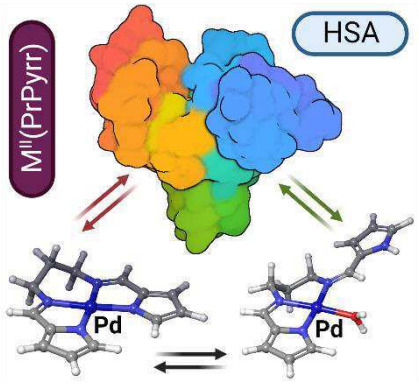
[1] R. U. Braun, K. Zeitler, T. J. J. Müller, *Org. Lett.* **2001**, *3*, 3297–3300.
[2] C. E. Hewton, M. C. Kimber, D. K. Taylor, *Tetrahedron Lett.* **2002**, *43*, 3199–3201.
[3] M. P. Akerman, V. A. Chiazzari, *J. Mol. Struct.* **2014**, *1058*, 22–30.
[4] X. Ren, B. D. Alleyne, P. I. Djurovich, C. Adachi, I. Tsyba, R. Bau, M. E. Thompson, *Inorg. Chem.* **2004**, *43*, 1697–1707.
[5] Y. Wang, T. Liang, J. Yao, T. Zhai, H. Fu, *Acta Crystallogr. Sect. E Struct. Rep. Online* **2008**, *64*, o629–o629.
[6] P. G. Sim, E. Sinn, *Inorg. Chem.* **1978**, *17*, 1288–1290.
[7] K. Hüttinger, C. Förster, T. Bund, D. Hinderberger, K. Heinze, *Inorg. Chem.* **2012**, *51*, 4180–4192.
[8] M. A. Rhine, A. V. Rodrigues, R. J. B. Urbauer, J. L. Urbauer, T. L. Stemmler, T. C. Harrop, *J. Am. Chem. Soc.* **2014**, *136*, 12560–12563.
[9] M. R. Walter, S. P. Dzul, A. V. Rodrigues, T. L. Stemmler, J. Telser, J. Conradie, A. Ghosh, T. C. Harrop, *J. Am. Chem. Soc.* **2016**, *138*, 12459–12471.
[10] D. Bandyopadhyay, M. Layek, M. Fleck, R. Saha, C. Rizzoli, *Inorganica Chim. Acta* **2017**, *461*, 174–182.
[11] S. A. Carabineiro, L. C. Silva, P. T. Gomes, L. C. J. Pereira, L. F. Veiros, S. I. Pascu, M. T. Duarte, S. Namorado, R. T. Henriques, *Inorg. Chem.* **2007**, *46*, 6880–6890.
[12] H. Brunner, B. Nuber, T. Tracht, *Tetrahedron Asymmetry* **1998**, *9*, 3763–3771.
[13] H. Brunner, A. Köllnberger, M. Zabel, *Polyhedron* **2003**, *22*, 2639–2646.
[14] S. Basu, I. Pal, R. J. Butcher, G. Rosair, S. Bhattacharya, *J. Chem. Sci.* **2005**, *117*, 167–173.
[15] Y. Haketa, M. Miyasue, Y. Kobayashi, R. Sato, Y. Shigeta, N. Yasuda, N. Tamai, H. Maeda, *J. Am. Chem. Soc.* **2020**, *142*, 16420–16428.
[16] P. Paul, M. G. Richmond, S. Bhattacharya, *J. Organomet. Chem.* **2014**, *751*, 760–768.
[17] H. Brunner, A. Köllnberger, M. Zabel, *Polyhedron* **2003**, *22*, 2639–2646.
[18] C. H. Wei, J. R. Einstein, *Acta Crystallogr. B* **1972**, *28*, 2591–2598.
[19] Y. Wang, H. Fu, F. Shen, X. Sheng, A. Peng, Z. Gu, H. Ma, J. S. Ma, J. Yao, *Inorg. Chem.* **2007**, *46*, 3548–3556.
[20] S. Bhikraj, O. Q. Munro, M. P. Akerman, *Polyhedron* **2017**, *124*, 22–29.
[21] J. S. Hart, G. S. Nichol, J. B. Love, *Dalton Trans.* **2012**, *41*, 5785–5788.
[22] H. Liang, J. Liu, X. Li, Y. Li, *Polyhedron* **2004**, *23*, 1619–1627.
[23] C. N. Iverson, C. A. G. Carter, R. T. Baker, J. D. Scollard, J. A. Labinger, J. E. Bercaw, *J. Am. Chem. Soc.* **2003**, *125*, 12674–12675.
[24] X.-F. Shan, D.-H. Wang, C.-H. Tung, L.-Z. Wu, *Tetrahedron* **2008**, *64*, 5577–5582.
[25] Y. Kim, J. Lee, Y.-H. Son, S.-U. Choi, M. Alam, S. Park, *J. Inorg. Biochem.* **2020**, *205*, 111015.
[26] C. H. Wei, *Inorg. Chem.* **1972**, *11*, 2315–2321.
[27] N. A. Bailey, A. Barrass, D. E. Fenton, M. S. L. Gonzalez, R. Moody, C. O. R. de Barbarin, *J. Chem. Soc. Dalton Trans.* **1984**, 2741–2746.
[28] F. Z. C. Fellah, J.-P. Costes, F. Dahan, C. Duhayon, G. Novitchi, J.-P. Tuchagues, L. Vendier, *Inorg. Chem.* **2008**, *47*, 6444–6451.
[29] Y. Hu, Q. Li, H. Li, Q. Guo, Y. Lu, Z. Li, *Dalton Trans.* **2010**, *39*, 11344–11352.
[30] H. Adams, M. R. J. Elsegood, D. E. Fenton, S. L. Heath, S. J. Ryan, *J. Chem. Soc. Dalton Trans.* **1999**, 2031–2038.
[31] K. J. Akerman, A. M. Fagenson, V. Cyril, M. Taylor, M. T. Muller, M. P. Akerman, O. Q. Munro, *J. Am. Chem. Soc.* **2014**, *136*, 5670–5682.
[32] V. Bhardwaj, D. Gumber, V. Abbot, S. Dhiman, P. Sharma, *RSC Adv.* **2015**, *5*, 15233–15266.
[33] R. N. Brogden, R. C. Heel, T. M. Speight, G. S. Avery, *Drugs* **1978**, *15*, 429–450.
[34] M. Atkins, C. A. Jones, P. Kirkpatrick, *Nat. Rev. Drug Discov.* **2006**, *5*, 279–280.
[35] H. D. Langtry, J. A. Balfour, *Drugs* **1998**, *55*, 563–584.

[36] S. Hannah, V. M. Lynch, N. Gerasimchuk, D. Magda, J. L. Sessler, *Org. Lett.* **2001**, *3*, 3911–3914.
[37] J. L. Sessler, T. D. Mody, G. W. Hemmi, V. Lynch, *Inorg. Chem.* **1993**, *32*, 3175–3187.
[38] W.-H. Wei, Z. Wang, T. Mizuno, C. Cortez, L. Fu, M. Sirisawad, L. Naumovski, D. Magda, J. L. Sessler, *Dalton Trans.* **2006**, 1934–1942.
[39] H. Patel, R. Mick, J. Finlay, T. C. Zhu, E. Rickter, K. A. Cengel, S. B. Malkowicz, S. M. Hahn, T. M. Busch, *Clin. Cancer Res.* **2008**, *14*, 4869–4876.
[40] C. Preihs, J. F. Arambula, D. Magda, H. Jeong, D. Yoo, J. Cheon, Z. H. Siddik, J. L. Sessler, *Inorg. Chem.* **2013**, *52*, 12184–12192.
[41] R. Gupta, C. Rodrigues Felix, M. P. Akerman, K. J. Akerman, C. A. Slabber, W. Wang, J. Adams, L. N. Shaw, Y.-C. Tse-Dinh, O. Q. Munro, K. H. Rohde, *Antimicrob. Agents Chemother.* **2018**, *62*, e01696-17.
[42] M. P. Akerman, O. Q. Munro, M. Mongane, J. A. van Staden, W. I. D. Rae, C. J. Bester, B. Marjanovic-Painter, Z. Szucs, J. R. Zeevaart, *J. Label. Compd. Radiopharm.* **2013**, *56*, 530–535.
[43] S. Curry, *Drug Metab. Pharmacokinet.* **2009**, *24*, 342–357.
[44] G. J. Quinlan, G. S. Martin, T. W. Evans, *Hepatology* **2005**, *41*, 1211–1219.
[45] X. M. He, D. C. Carter, *Nature* **1992**, *358*, 209–215.
[46] P. A. Zunszain, J. Ghuman, T. Komatsu, E. Tsuchida, S. Curry, *BMC Struct. Biol.* **2003**, *3*, 6.
[47] G. Rabbani, S. N. Ahn, *Int. J. Biol. Macromol.* **2019**, *123*, 979–990.
[48] G. Sudlow, D. J. Birkett, D. N. Wade, *Mol. Pharmacol.* **1976**, *12*, 1052–1061.
[49] G. Sudlow, D. J. Birkett, D. N. Wade, *Mol. Pharmacol.* **1975**, *11*, 824–832.
[50] V. Tuan Giam Chuang, U. Kragh-Hansen, M. Otagiri, *Pharm. Res.* **2002**, *19*, 569–577.
[51] M. Fasano, S. Curry, E. Terreno, M. Galliano, G. Fanali, P. Narciso, S. Notari, P. Ascenzi, *IUBMB Life* **2005**, *57*, 787–796.
[52] O. Dömötör, T. Pivarcsik, J. P. Mészáros, I. Szatmári, F. Fülöp, É. A. Enyedy, *Dalton Trans.* **2021**, *50*, 11918–11930.
[53] É. A. Enyedy, J. P. Mészáros, O. Dömötör, C. M. Hackl, A. Roller, B. K. Keppler, W. Kandioller, *J. Inorg. Biochem.* **2015**, *152*, 93–103.
[54] O. Dömötör, É. A. Enyedy, *JBIC J. Biol. Inorg. Chem.* **2019**, *24*, 703–719.
[55] A. Bijelic, S. Theiner, B. K. Keppler, A. Rompel, *J. Med. Chem.* **2016**, *59*, 5894–5903.
[56] L. Messori, A. Merlino, *Dalton Trans.* **2014**, *43*, 6128–6131.
[57] A. Casini, C. Temperini, C. Gabbiani, C. T. Supuran, L. Messori, *ChemMedChem* **2010**, *5*, 1989–1994.
[58] G. Ferraro, M. Paolillo, G. Sciortino, E. Garribba, A. Merlino, *Inorg. Chem.* **2022**, *61*, 16458–16467.
[59] F. Wang, J. Bella, J. A. Parkinson, P. J. Sadler, *JBIC J. Biol. Inorg. Chem.* **2005**, *10*, 147–155.
[60] D. Stanic-Vucinic, S. Nikolic, K. Vlajic, M. Radomirovic, J. Mihailovic, T. Cirkovic Velickovic, S. Grguric-Sipka, *JBIC J. Biol. Inorg. Chem.* **2020**, *25*, 253–265.
[61] L. Messori, F. G. Vilchez, R. Vilaplana, F. Piccioli, E. Alessio, B. Keppler, *Met.-Based Drugs* **2000**, *7*, 335–342.
[62] A. Casini, C. Gabbiani, E. Michelucci, G. Pieraccini, G. Moneti, P. J. Dyson, L. Messori, *JBIC J. Biol. Inorg. Chem.* **2009**, *14*, 761–770.
[63] A. Casini, G. Mastrobuoni, C. Temperini, C. Gabbiani, S. Francese, G. Moneti, C. T. Supuran, A. Scozzafava, L. Messori, *Chem. Commun.* **2006**, 156–158.
[64] G. Marcon, L. Messori, P. Orioli, M. A. Cinellu, G. Minghetti, *Eur. J. Biochem.* **2003**, *270*, 4655–4661.
[65] Y.-C. Lo, T.-P. Ko, W.-C. Su, T.-L. Su, A. H.-J. Wang, *J. Inorg. Biochem.* **2009**, *103*, 1082–1092.
[66] O. Mazuryk, K. Magiera, B. Rys, F. Suzenet, C. Kieda, M. Brindell, *JBIC J. Biol. Inorg. Chem.* **2014**, *19*, 1305–1316.
[67] A. Wragg, M. R. Gill, L. McKenzie, C. Glover, R. Mowll, J. A. Weinstein, X. Su, C. Smythe, J. A. Thomas, *Chem. – Eur. J.* **2015**, *21*, 11865–11871.
[68] B. Sun, M. K. Sundaraneedi, H. M. Southam, R. K. Poole, I. F. Musgrave, F. Richard Keene, J. Grant Collins, *Dalton Trans.* **2019**, *48*, 14505–14515.
[69] N. Biswas, S. Khanra, A. Sarkar, S. Bhattacharjee, D. P. Mandal, A. Chaudhuri, S. Chakraborty, C. R. Choudhury, *J. Coord. Chem.* **2018**, *71*, 2740–2766.
[70] X.-F. Shan, D.-H. Wang, C.-H. Tung, L.-Z. Wu, *Tetrahedron* **2008**, *64*, 5577–5582.
[71] A. Bacchi, M. Carcelli, L. Gabba, S. Ianelli, P. Pelagatti, G. Pelizzi, D. Rogolino, *Inorganica Chim. Acta* **2003**, *342*, 229–235.
[72] T. Imamura, T. Tanaka, M. Fujimoto, *Inorg. Chem.* **1985**, *24*, 1038–1041.
[73] L. Pinard, J. Mijoin, P. Ayrault, C. Canaff, P. Magnoux, *Appl. Catal. B Environ.* **2004**, *51*, 1–8.
[74] A. J. McNeece, M.-C. Chang, A. S. Filatov, J. S. Anderson, *Inorg. Chem.* **2018**, *57*, 7044–7050.
[75] C. R. Groom, I. J. Bruno, M. P. Lightfoot, S. C. Ward, *Acta Crystallogr. Sect. B Struct. Sci. Cryst. Eng. Mater.* **2016**, *72*, 171–179.
[76] O. K. Abou-Zied, O. I. K. Al-Shihi, *J. Am. Chem. Soc.* **2008**, *130*, 10793–10801.
[77] P. R. Callis, *J. Mol. Struct.* **2014**, *1077*, 14–21.
[78] Y. Yue, J. Liu, M. Yao, X. Yao, J. Fan, H. Ji, *Spectrochim. Acta. A. Mol. Biomol. Spectrosc.* **2012**, *96*, 316–323.
[79] P. R. Callis, *J. Mol. Struct.* **2014**, *1077*, 22–29.
[80] A. Divsalar, M. J. Bagheri, A. A. Saboury, H. Mansoori-Torshizi, M. Amani, *J. Phys. Chem. B* **2009**, *113*, 14035–14042.
[81] S. Goutelle, M. Maurin, F. Rougier, X. Barbaut, L. Bourguignon, M. Ducher, P. Maire, *Fundam. Clin. Pharmacol.* **2008**, *22*, 633–648.
[82] J. T. Vivian, P. R. Callis, *Biophys. J.* **2001**, *80*, 2093–2109.
[83] J. R. Lakowicz, *Principles of Fluorescence Spectroscopy*, Springer US, Boston MA, **2006**.
[84] Y.-J. Hu, Y. Liu, X.-H. Xiao, *Biomacromolecules* **2009**, *10*, 517–521.
[85] G. G. Ariga, P. N. Naik, S. A. Chimatadar, S. T. Nandibewoor, *J. Mol. Struct.* **2017**, *1137*, 485–494.
[86] X. Sun, S. Bi, J. Wu, R. Zhao, D. Shao, Z. Song, *J. Biomol. Struct. Dyn.* **2020**, *38*, 934–942.
[87] S. Soares, N. Mateus, V. de Freitas, *J. Agric. Food Chem.* **2007**, *55*, 6726–6735.
[88] P. D. Ross, S. Subramanian, *Biochemistry* **1981**, *20*, 3096–3102.
[89] X. Li, S. Wang, *New J. Chem.* **2015**, *39*, 386–395.
[90] P. D. Ross, S. Subramanian, *Biochemistry* **1981**, *20*, 3096–3102.
[91] I. Petitpas, A. A. Bhattacharya, S. Twine, M. East, S. Curry, *J. Biol. Chem.* **2001**, *276*, 22804–22809.
[92] J. Ghuman, P. A. Zunszain, I. Petitpas, A. A. Bhattacharya, M. Otagiri, S. Curry, *J. Mol. Biol.* **2005**, *353*, 38–52.
[93] A. Sytnik, I. Litvinyuk, *Proc. Natl. Acad. Sci.* **1996**, *93*, 12959–12963.
[94] P. W. Ayers, *Faraday Discuss.* **2006**, *135*, 161–190.
[95] R. G. Pearson, *J. Chem. Educ.* **1968**, *45*, 643.
[96] M. Kolář, T. Kubař, P. Hobza, *J. Phys. Chem. B* **2011**, *115*, 8038–8046.
[97] O. Q. Munro, G. L. Camp, *Acta Crystallogr. C* **2003**, *59*, o672–o675.
[98] O. Q. Munro, S. D. Joubert, C. D. Grimmer, *Chem. – Eur. J.* **2006**, *12*, 7987–7999.
[99] H. Aki, M. Goto, M. Yamamoto, *Thermochim. Acta* **1995**, *251*, 379–388.
[100] R. E. Olson, D. D. Christ, in *Annu. Rep. Med. Chem.* (Ed.: J.A. Bristol), Academic Press, **1996**, pp. 327–336.
[101] H. Aki, M. Yamamoto, *J. Pharm. Pharmacol.* **1989**, *41*, 674–679.
[102] H. Aki, M. Yamamoto, *J. Pharm. Sci.* **1994**, *83*, 1712–1716.
[103] N. J. Greenfield, *Nat. Protoc.* **2006**, *1*, 2876–2890.
[104] P. Alam, S. K. Chaturvedi, T. Anwar, M. K. Siddiqi, M. R. Ajmal, G. Badr, M. H. Mahmoud, R. Hasan Khan, *J. Lumin.* **2015**, *164*, 123–130.
[105] N. Sreerama, R. W. Woody, in *Methods Enzymol.*, Academic Press, **2004**, pp. 318–351.
[106] S. M. Kelly, T. J. Jess, N. C. Price, *Biochim. Biophys. Acta BBA - Proteins Proteomics* **2005**, *1751*, 119–139.
[107] A. Micsonai, F. Wien, É. Bulyáki, J. Kun, É. Moussong, Y.-H. Lee, Y. Goto, M. Réfrégiers, J. Kardos, *Nucleic Acids Res.* **2018**, *46*, W315–W322.
[108] F. Mohammadi, A.-K. Bordbar, A. Divsalar, K. Mohammadi, A. A. Saboury, *Protein J.* **2009**, *28*, 189–196.
[109] H. A. Tajmir-Riahi, C. N. N'soukpoé-Kossi, D. Joly, *Spectroscopy* **2009**, *23*, 81–101.
[110] O. Duman, S. Tunç, B. Kancı Bozoğlan, *J. Fluoresc.* **2013**, *23*, 659–669.
[111] G. Abrusán, J. A. Marsh, *PLOS Comput. Biol.* **2016**, *12*, e1005242.

[112] A.-S. Yang, B. Honig, *J. Mol. Biol.* **1995**, *252*, 366–376.
[113] A.-S. Yang, B. Honig, *J. Mol. Biol.* **1995**, *252*, 351–365.
[114] R. A. Friesner, J. L. Banks, R. B. Murphy, T. A. Halgren, J. J. Klicic, D. T. Mainz, M. P. Repasky, E. H. Knoll, M. Shelley, J. K. Perry, D. E. Shaw, P. Francis, P. S. Shenkin, *J. Med. Chem.* **2004**, *47*, 1739–1749.
[115] T. A. Halgren, R. B. Murphy, R. A. Friesner, H. S. Beard, L. L. Frye, W. T. Pollard, J. L. Banks, *J. Med. Chem.* **2004**, *47*, 1750–1759.
[116] G. Ferraro, L. Massai, L. Messori, A. Merlino, *Chem. Commun.* **2015**, *51*, 9436–9439.
[117] W. R. Algar, N. Hildebrandt, S. S. Vogel, I. L. Medintz, *Nat. Methods* **2019**, *16*, 815–829.
[118] F. R. Clemente, T. Vreven, M. J. Frisch, in *Quantum Biochem.*, John Wiley & Sons, Ltd, **2010**, pp. 61–83.
[119] T. Yanai, D. P. Tew, N. C. Handy, *Chem. Phys. Lett.* **2004**, *393*, 51–57.
[120] P. Fuentealba, H. Preuss, H. Stoll, L. Von Szentpály, *Chem. Phys. Lett.* **1982**, *89*, 418–422.
[121] S. Grimme, S. Ehrlich, L. Goerigk, *J. Comput. Chem.* **2011**, *32*, 1456–1465.
[122] A. K. Rappe, C. J. Casewit, K. S. Colwell, W. A. Goddard, W. M. Skiff, *J. Am. Chem. Soc.* **1992**, *114*, 10024–10035.
[123] A. R. Leach, B. K. Shoichet, C. E. Peishoff, *J. Med. Chem.* **2006**, *49*, 5851–5855.
[124] G. L. Warren, C. W. Andrews, A.-M. Capelli, B. Clarke, J. LaLonde, M. H. Lambert, M. Lindvall, N. Nevins, S. F. Semus, S. Senger, G. Tedesco, I. D. Wall, J. M. Woolven, C. E. Peishoff, M. S. Head, *J. Med. Chem.* **2006**, *49*, 5912–5931.
[125] K. M. Elokely, R. J. Doerksen, *J. Chem. Inf. Model.* **2013**, *53*, 1934–1945.

WILEY-VCH

Entry for the Table of Contents



Square planar pyrrole-imine chelates of Ni^{II}, Pd^{II}, and Pt^{II} bind avidly to human serum albumin (HSA), targeting multiple binding sites as fully intact complexes. Fluorescence from Trp-214 and bound probes (warfarin and ibuprofen) is adeptly quenched, yielding affinity and fluorescence quenching constants. *In silico* docking together with TD-DFT simulations confirm the experimental induced CD spectra of the HSA-metal chelate complexes.

WILEY-VCH

Chapter 7 Conclusion

In this work five bis(pyrrolide-imine) Schiff base chelates have been synthesised. All five ligands have been metalated with Au(III) and Pt(II), while the *N*,*N*'-bis[(1*E*)-1*H*-pyrrol-2-ylmethylene]propane-1,3-diamine ligand was also used to chelate Pd(II) and Ni(II). A summary of the structures of all twelve metal chelates is presented in Fig. 7.1.

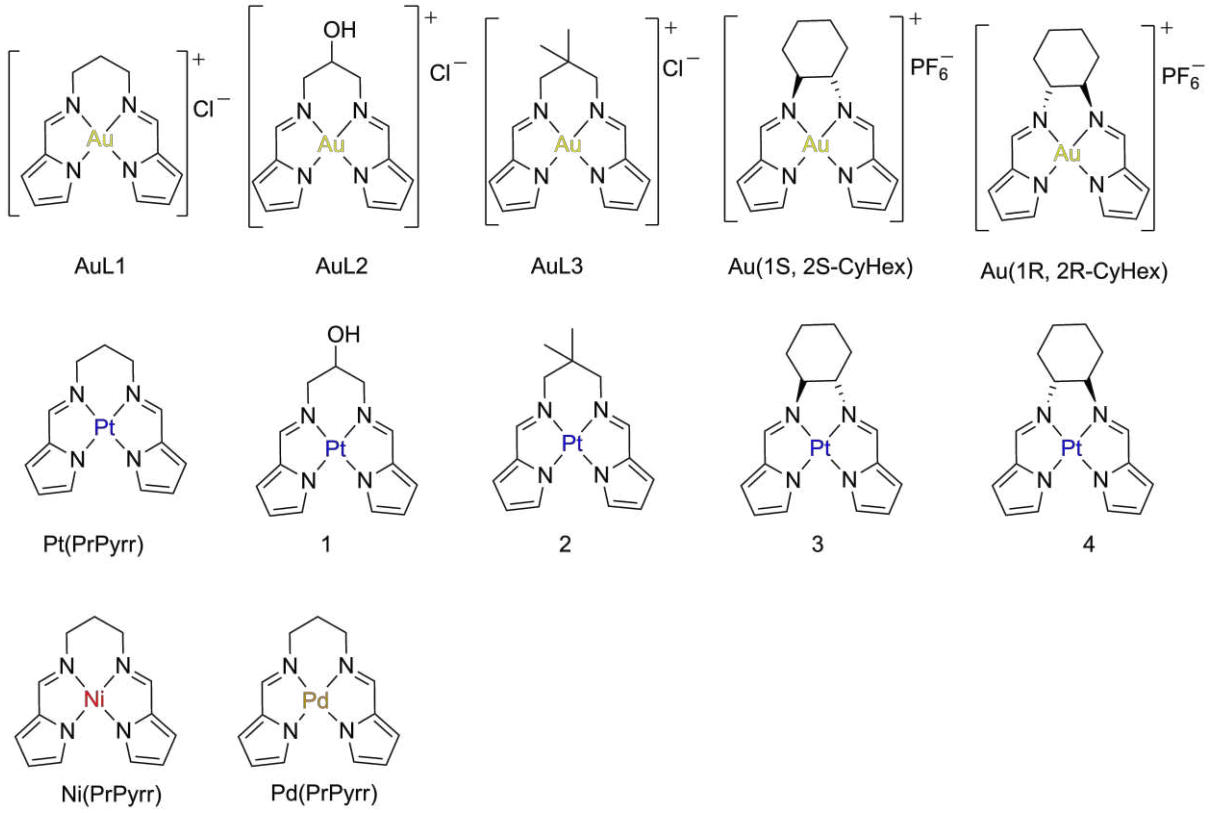


Fig. 7.1 Summary of the 12 metal chelates synthesised in this study.

7.1. Conclusion of the Au(III) work

The five Au(III) chelates cytotoxicity was tested by the NCI-60 screen, of which **AuL1**, **AuL3**, and **Au(1*S*,2*S*-CyHex)**, were sufficiently cytotoxic to warrant phase two of the NCI-60 screen. **AuL1** exhibited cytotoxicity by a dual mechanism, specifically (i) binding to and intercalating with DNA and (ii) inhibiting Top2. **AuL1** was found to inhibit topoisomerase II (Top2) by a dual mechanism: at concentrations below 5 μM, **AuL1** acts as an interfacial poison (IFP), while at concentrations above 50 μM, **AuL1** is a catalytic inhibitor compound (CIC) for the enzyme. The Inhibition of Top2 results in the inhibition of DNA transcription and replication, which results in apoptosis. It is postulated **AuL3** works via a similar mechanism. The mechanism by which **Au(1*S*,2*S*-CyHex)** works was not identified in this study but is known to be different from **AuL1** since it does not bind to DNA. A hierarchical cluster analysis suggests its MOA is similar to that of daunorubicin. The study performed an in-depth analysis of the interaction of the

Au(II) chelates to HSA, which is critical to understanding the plasma distribution of metal chelate drug candidates.

The interaction of the five Au(III) chelates with human serum albumin (HSA) was investigated by complementary spectroscopic techniques to understand how the identity of the Schiff base chelate affects ligand uptake by the protein and if the binding affinity of the Au(III) chelate will be a point of interest in its biodistribution. Therefore, we studied the biophysical binding parameters of the five Au(III) chelates to HSA by fluorescence quenching spectroscopy and ITC and found that the Au(III) chelates bind with a moderate binding affinity to HSA (10^4 – 10^5 M^{-1}). This is promising as the data suggest the Au(III) chelates can be transported by HSA, likely via the HSA-mediated pathway. All Au(III) chelates quenched the intrinsic Trp-214 fluorescence of HSA and had K_a values typical of small molecules binding to HSA. The Stern-Volmer quenching constants K_a values followed the order: **AuL2** > **AuL1** > **AuL3**, with a stoichiometry leaning towards a 1:1. The present ligands bind to HSA with *positive* ΔH, and *positive* ΔS, however, the $-T\Delta S$ term is significantly larger than the ΔH value, hence resulting in *negative* ΔG values, reflecting spontaneous entropically-driven process governed by hydrophobic and electrostatic interactions. $T\Delta S/\Delta G$ and $\Delta H/\Delta G$ increase together in the order: **AuL1**, **AuL3**, and **AuL2**. The Stern-Volmer quenching constants (K_{SV}) and K_a values for **Au(1*S*,2*S*-CyHex)** were greater than **Au(1*R*,2*R*-CyHex)**. Both Au(III) chelates of the cyclohexyl-bridged Schiff base ligands bind to HSA with *negative* ΔH, ΔG, and ΔS values, reflecting a spontaneous enthalpy-driven process governed by van der Waals (London dispersion) forces as well as H-bonding. $T\Delta S/\Delta G$ and $\Delta H/\Delta G$ for both cyclohexyl-bridged Au(III) chelates were in the upper right corner of this plot of the Gibbs-Helmholtz equation (Fig. 7.2). All five Au(III) chelates were found to target Sudlow's site I with minimal disturbance of the secondary and tertiary structure. Furthermore, the fully intact metal chelate binds to HSA as was shown using induced-UV-CD spectroscopy.

7.2. Conclusion of the platinum(II) work

Five Pt(II) chelates were synthesised of which two were novel and three novel crystal structures were obtained. Of the five Pt(II) chelates, four bound to HSA with a moderate binding affinity. The Stern-Volmer quenching constants (K_{sv}) followed the order **1** > **2** > **3**, while the K_a values followed the order **1** > **3** > **2**. The stoichiometry for all three chelates suggest a 1:1 reaction stoichiometry (Pt(II) chelate:HSA), with potential uptake at a second lower-affinity binding site. Pt(II) chelates **1** and **3** bind to HSA with negative ΔH, ΔG, and positive ΔS values, reflecting a spontaneous enthalpy-driven process governed by van der Waals (London dispersion) forces, while **2** has a positive ΔH, negative ΔG and a strongly positive ΔS indicating its reaction with HSA is endothermically driven and its main interacting forces are hydrophobic interactions and H-bonding. The platinum chelates were further tested to assess their ability as theranostic agents: (i) the cytotoxicity of the platinum chelates was poor as the IC_{50} values were greater than 100 µM.

However, the platinum chelates did exhibit phosphorescence emission with Pt(PrPyr), **1** and **2** being the most emissive.

7.3. Conclusion of the d^8 metal chelate study

The interaction of H_2PrPyrr and its Ni^{II}, Pd^{II}, and Pt^{II} chelates with human serum albumin (HSA) was investigated by complementary spectroscopic techniques to understand how the identity of the d^8 metal ion affects ligand uptake by the protein. All ligands quenched the intrinsic Trp-214 fluorescence of HSA via a static quenching mechanism. The Stern-Volmer quenching constants (K_{SV}) and affinity constants (K_a) followed the order: Pd(PrPyrr) >> Pt(PrPyrr) > Ni(PrPyrr) > H2PrPyrr. The notably higher affinity of Pd(PrPyrr) for HSA coupled with a reaction stoichiometry, *n*, *significantly exceeding* 1:1 (ligand:HSA) reflects simultaneous uptake of two Pd(II) species from an equilibrium mixture comprising Pd(PrPyrr) and $[Pd(HPrPyrr)(OH_2)]^+$. The latter structure is related to the crystallographically characterised chlorido complex, PdCl(HPrPyrr). Significantly, ESI-MS data directly confirmed the formation of HSA•{ligand}*n* species with $n \geq 1$ for the M(PrPyrr) chelates. The present ligands bind to HSA with *negative* ΔG, ΔH, and ΔS values, reflecting a spontaneous enthalpy-driven process governed by van der Waals (London dispersion) forces as well as H-bonding (for H_2PrPyrr). $T\Delta S/\Delta G$ and $\Delta H/\Delta G$ increase together in the order: Ni(PrPyrr) < Pd^{II}(X) < Pt(PrPyrr), tracking the Group 10 metal ionic radii and polarizability order (3d < 4d < 5d). *In silico* data support the notion (gleaned from spectroscopy) that each ligand has more than one binding site in HSA and that ligand uptake minimally perturbs the protein's secondary structure. Finally, the induced CD spectra recorded for the metal chelates bound to HSA strikingly confirm the uptake of the intact complexes without imine group hydrolysis or demetallation.

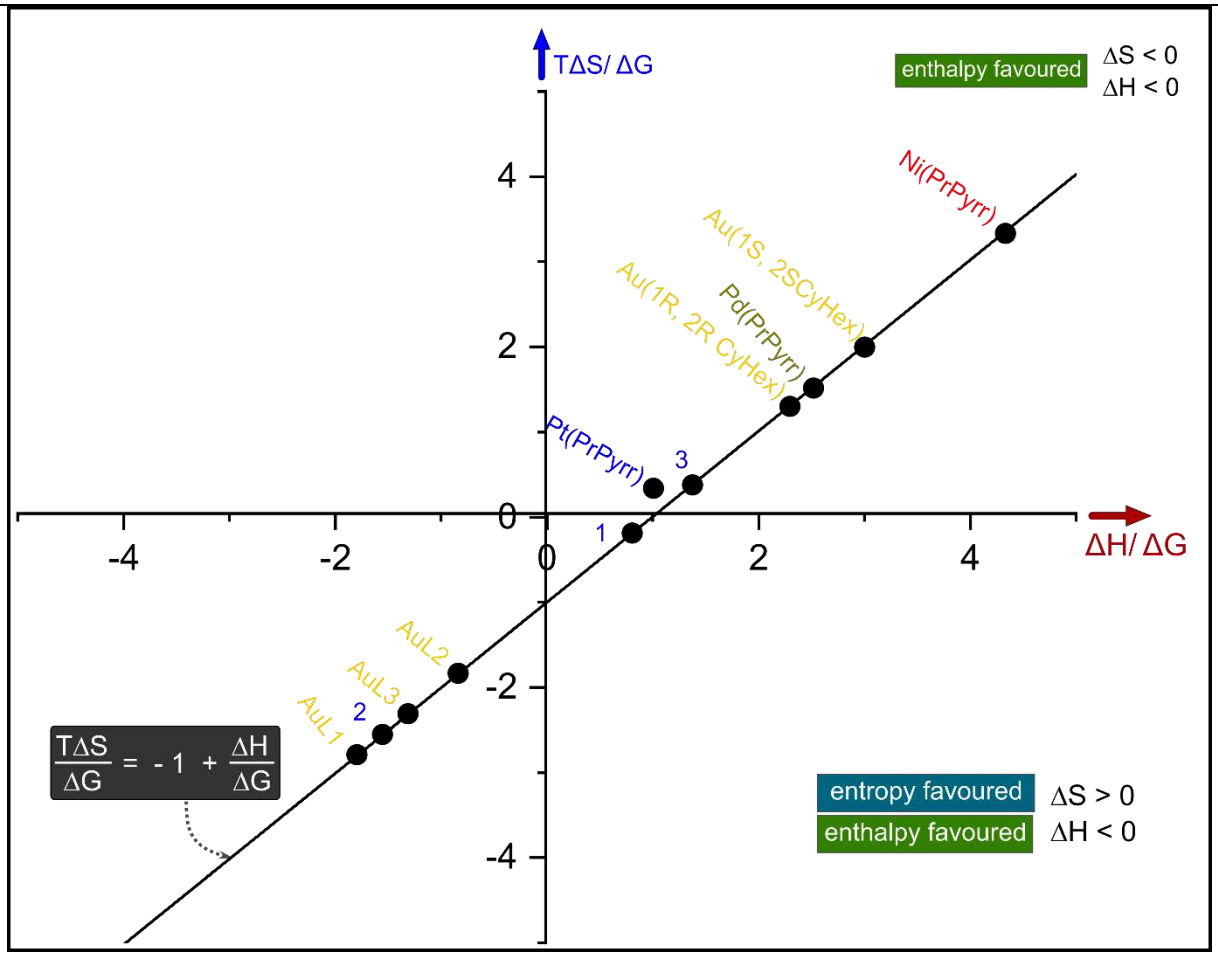


Fig. 7.2 Plot of the Gibbs-Helmholtz relationship for the reaction of the 11 metal chelates synthesised in this work with HSA at 298 K in 50 mM KH_2PO_4 buffer at pH 7.50. The straight line fit of the data gives R^2 = 0.997 with a slope of 1.005 ± 0.006 and intercept of −1 (fixed). For all reactions, $\Delta G < 0$. The plot highlights how the identity of the metal ion influences the reaction thermodynamics, and the linear relationship of the Gibbs-Helmholtz is maintained.

7.4. Future work

X-ray crystallography

One of the primary aims of this research was to identify a mode of action for the metal complexes binding to HSA. While we were able to achieve some success with identifying the binding sites and the stoichiometry of the metal complexes binding to HSA, we were unable to elucidate a crystal structure of HSA with a metal complex bound. Although we have grown crystals of native HSA which diffract to 2.3 Å resolution, our efforts to grow high-resolution X-ray quality crystals of the protein bound to the present ligands have been unfruitful. Fig. 7.3 is an image of an HSA crystal obtained from the work. A potential method to obtain the desired HSA crystals will be to grow the crystals in a capillary, therefore the crystal will not need to be removed from the mother liquor to collect an X-ray data set.

Cytotoxicity

The promising cytotoxicity data of the Au(III) chelates needs to be further investigated in the murine model against both cancer and *Mycobacterium tuberculosis*. This will allow us to delineate the efficacy of the Au(III) chelates in a live model. Furthermore, if the results are promising the Au(III) chelates can be taken further to clinical trials phase 1. **Au(1*S*,2*S*-CyHex)** from Chapter 3 needs further investigation on its mode of action as its MOA was not identified.



Fig. 7.3 HSA crystals viewed under a microscope. Unfortunately, X-ray data of the crystals revealed the absence of the Au(III) chelates, despite a relatively high-resolution structure.

Diffusion cell experiments

A diffusion cell is a specialised cell that contains two solutions (Fig. 7.4) that are separated by an Amicon size-exclusion membrane filter. One end will contain HSA loaded with the Au(III) chelate, and the other end will contain DNA. The solution of HSA-Au(III) chelate will be circulated through a peristaltic pump and into a cuvette that is housed within a spectrophotometer. In this way, we will be able to measure real-time absorbance data of the HSA-Au(III) chelates that can be correlated to real-time kinetic data. This will then allow us to follow and elucidate the transport of the Au(III) chelates from HSA to the DNA target in the receiving cell. Such an experiment would physically demonstrate metal chelate transport and delivery by HSA to a macromolecule target such as DNA, with the membrane mimicking the nuclear envelope in cells.

Cell imaging experiments

The strong emission of the Pt(II) complexes within the cell medium was a strong indication that the Pt(II) chelates have the potential to be used as a bioimaging agent. Unfortunately, the images were too low resolution and confocal microscopy images are required to identify the organelles that the Pt(II) chelates

target. Furthermore, the switch-off effect observed when Pt(PrPyrr) and **2** bound to HSA require further investigation. Using time-resolved confocal microscopy we can observe if HSA transports the platinum chelate to a specific site, with fluorescence emission quenching providing a diagnostic signal.

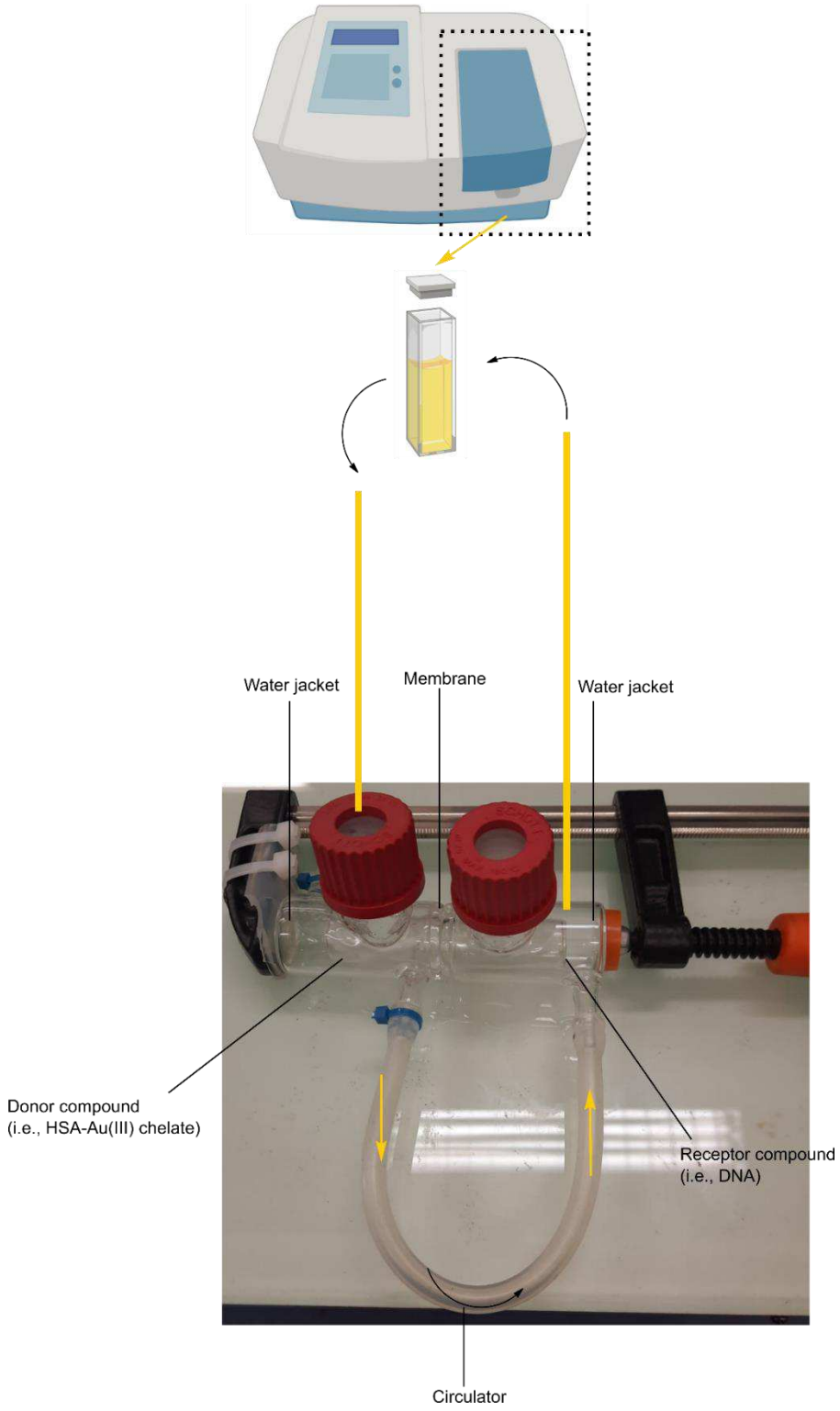


Fig. 7.4 An illustration of how the diffusion cell will function to measure the transport of the Au(III)-chelates to DNA.

Biophysical studies of metal chelate binding by HSA: Towards an understanding of metallodrug transport (V2)



By Sheldon Sookai

MSc (*cum laude)* University of KwaZulu-Natal

A thesis submitted to the Faculty of Science, University of the Witwatersrand, Johannesburg, in fulfilment of the requirements for the degree of Doctor of Philosophy

July 2023

Table of contents

Supplementary information

Gold(III) chelates: Dual mode inhibitors of human Topoisomerase II and their complexities of binding to human serum albumin..... 3

Human serum albumin binds chiral cytotoxic Au(III) chelates as fully intact complexes with unique thermodynamics 78

Spectroscopic and computational study of the interaction of Pt(II) pyrrole-imine chelates with human serum albumin. 118

Bioimaging Pt(II) Schiff base chelates 165

Complexities of the interaction of Ni(II), Pd(II) and Pt(II) pyrrole-imine chelates with human serum albumin 196

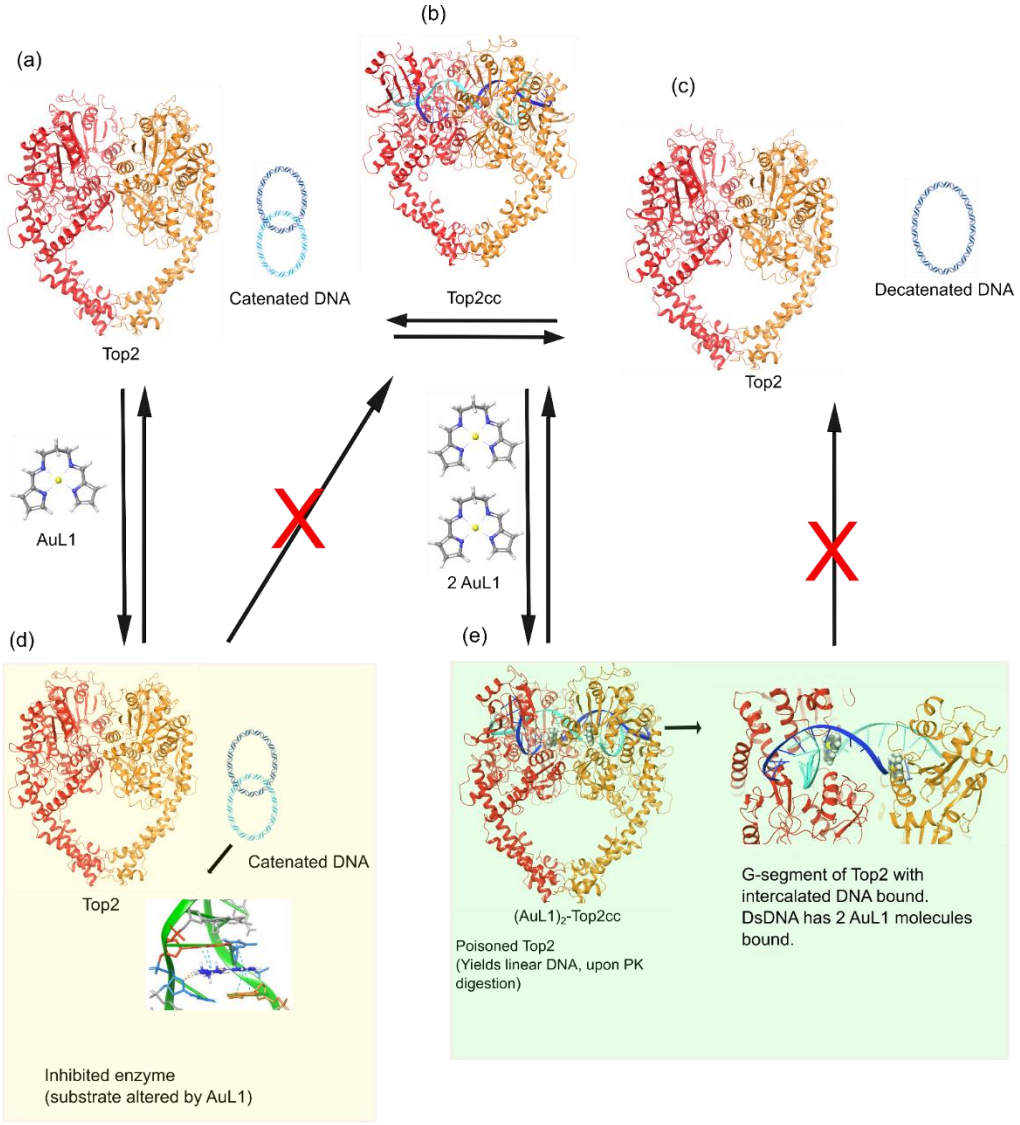
X-Ray Crystallography CIF Files..... 277

Declaration

I declare that the work presented in this thesis was carried out exclusively by me, unless stated otherwise, under the supervision of Professor Orde Q. Munro. It is being submitted for the Degree of Doctor of Philosophy in the University of the Witwatersrand, Johannesburg. It has not been submitted before for any degree or examination in any other University.



July 2023


(a)
(b)
(c)
Top2
Catenated DNA
Top2cc
Top2
Decatenated DNA
AuL1
2 AuL1
(d)
(e)
Catenated DNA
Top2
Inhibited enzyme
(substrate altered by AuL1)
(AuL1)2-Top2cc
Poisoned Top2
(Yields linear DNA, upon PK digestion)
G-segment of Top2 with intercalated DNA bound.
DsDNA has 2 AuL1 molecules bound.

Supporting Information:

Gold(III) chelates: Dual mode inhibitors of human Topoisomerase II and their complexities of binding to human serum albumin

Sheldon Sookai[a], Matthew Akerman[b], Olga Færc[c], Yasien Sayed[d] and Orde Q. Munro*[,a]

[a] *Molecular Sciences Institute, School of Chemistry, University of the Witwatersrand, PO WITS 2050, Johannesburg, South Africa*

Table of contents chapter 1

1. Experimental methods 11

1.1. Instruments and basic methods 11

1.1.1. X-ray crystallography 11

1.1.2. General spectroscopy 11

1.2. Compound synthesis 12

1.2.1. Ligand synthesis 12

Scheme 1 Representation of the condensation reaction of pyrrole-2 carboxaldehyde with respective diamino propane by (a) refluxing and (b) grinding. 12

Synthesis procedure of ligands 13

1.2.2. Synthesis of *tert*-Butylamonium Tetrachloroaurate(III) 13

1.2.3. Metallation of the bis(pyrrolide-imine) chelates 13

Scheme 2. Representation of the Au(III) metalation of the bis (pyrollide-imine) chelates..... 13

1.2.4. Characterisation of the bis(pyrrolide-imine) chelates 15

Fig. S1 N,*N*'-bis[(1*E*)-1*H*-pyrrol-2-ylmethylene]propane-1,3-diamine (H_2L1). was synthesised as described by Munro and Camp, (2003)[5] and was analysed by ^{1}H NMR, ^{13}C NMR, FT-IR and UV-Visible spectroscopy. ^{1}H NMR (400 MHz, Chloroform-*d*, 300 K) [δ, ppm]: 1.98 (t, *J* = 6.8 Hz, 2H, H-7), 3.61 (td, *J* = 6.8, 1.2 Hz, 4H, H-6), 6.23 (dd, *J* = 3.6, 2.6 Hz, 2H, H-2), 6.48 (dd, *J* = 3.6, 1.4 Hz, 2H, H-3), 6.88 (t, *J* = 1.9 Hz, 2H, H-1), 8.03 (s, 2H, H-5). ^{13}C NMR (101 MHz, Chloroform-*d*, 300 K) [δ, ppm]: 32.29 (C-7), 57.80 (C-6), 109.59 (C-2), 114.13 (C-3), 122.04 (C-1), 129.86 (C-4), 151.85 (C-5). IR (KBr pellet, cm^{-1}): 3112w δ(NH, pyrrole), 3053m br *ν*(CH, imine), 2941m *ν*(CH, $CH_2CH_2CH_2$), 2847 *ν*(CH, CH_2-N=CH), 1634s br *ν*(C=N). UV/vis (ethanol) [λ, max, nm; ε, mol^{-1} dm^3 cm^{-1}]: 289; 3.20 × 10^4**.** 15

Fig. S2 1,3-bis{[(1*E*)-1*H*-pyrrol-2-ylmethylene]amino}propan-2-ol (H_2L2). The ligand was analysed by ^{1}H NMR, ^{13}C NMR, FT-IR and UV-Visible spectroscopy. ^{1}H NMR (400 MHz, DMSO-d_6-300 K) [δ, ppm]: 3.43 (dd, *J* = 11.7, 6.5 Hz, 2H, CH_2-N=CH), 3.77 – 3.54 (m, 2H, CH_2-N=CH, H-6), 4.00 – 3.82 (m, 1H, H-7), 6.11 (t, *J* = 3.0 Hz, 2H, H-2), 6.44 (dd, *J* = 3.5, 1.5 Hz, 2H, H-3), 6.87 (t, *J* = 1.9 Hz, 2H, H-1), 8.07 (s, 2H, H-5), 11.34 (s br, 2H, DMSO-d_6 exchangeable, H-9). ^{13}C NMR (101 MHz, DMSO-d_6, 300 K) [δ, ppm]: 65.14 (C-6), 70.69 (C-7), 108.98 (C-2), 113.35 (C-3), 122.03 (C-1), 130.41 (C-4), 152.92 (C-5). IR (KBr pellet, cm-1): 3254w (NH, pyrrole), 3088m (CH, imine), 2882

(CH, H-COH), 2859 (CH, C*H*2-N=CH), 1633s (C=N), 1127 (C-O stretch). UV/vis (ethanol) [λ, max, nm; ε, mol^{-1} dm^3 cm^{-1}]: 289; 3.23 × 10^4.....15

Fig. S3 2,2-dimethyl-*N*,*N*'-bis[(1*E*)-1*H*-pyrrol-2-ylmethylene]propane-1,3-diamine (H_2L3). The ligand was analysed by ^{1}H NMR, ^{13}C NMR, FT-IR and UV-Visible spectroscopy. ^{1}H NMR (400 MHz, Chloroform-*d*, 300 K) [δ, ppm]: 0.97 (t, *J* = 4.3 Hz, 6H, H-8), 3.46 (t, *J* = 4.2 Hz, 4H, H-6), 6.26 (p, *J* = 3.2 Hz, 2H, H-2), 6.48 (dt, *J* = 6.6, 3.4 Hz, 2H, H-3), 6.90 (d, *J* = 6.1 Hz, 2H, H-1), 7.99 (t, *J* = 4.2 Hz, 2H, H-5), 9.50 (s br, 2H, H-9). ^{13}C NMR (101 MHz, Chloroform-*d* 300 K) [δ, ppm]: 24.28 (C-8), 36.96 (C-7), 69.32 (C-6), 109.44 (C-2), 114.28 (C-3), 122.20 (C-1), 130.06 (C-4), 152.17 (C-5). FT-IR (KBr pellet, cm^{-1}): 3130m br *v*(CH, imine), 2966m *v*(CH, terminal CH3), 2852m *v*(CH2, alkyl), 1635s br *v*(C=N). UV/vis (ethanol) [λ, max, nm; ε, mol^{-1} dm^3 cm^{-1}]: 289; 3.23 × 10^4.....16

1.2.5. **Characterisation of the bis(pyrrolide-imine) gold(III) chelates** 16

Fig. S4 2,2'-{propane-1,3-diylbis[nitrilo(*E*)methylylidene]}bis(pyrrol-1-ido)gold(III) chloride, [Au(L1)]Cl. The complex was analysed by ^{1}H NMR, ^{13}C NMR, UV-Visible spectroscopy, mass spectroscopy and FT-IR. IR (KBr pellet, cm^{-1}): ^{1}H NMR (400 MHz, Methanol-d_4) [δ, ppm]: 2.31 (p, *J* = 5.3 Hz, 2H, H-7), 3.88 – 3.75 (m, 4H, H-6), 6.52 (dd, *J* = 4.2, 2.3 Hz, 2H, H-2), 7.09 (d, *J* = 4.2 Hz, 2H, H-3), 7.65 (d, *J* = 2.2 Hz, 2H, H-1), 8.27 (s, 2H, H-5). ^{13}C NMR (101 MHz, Methanol-d_4 300 K) [δ, ppm]: 32.96 (C-7), 53.40 (C-6), 114.34 (C-2), 124.75 (C-3), 138.79 (C-4), 139.69 (C-1), 164.99 (C-5). FT-IR 3092m br *v*(CH, imine), 3074m *v*(CH, $CH_2CH_2CH_2$), 2936m *v*(CH, CH_2-N=CH), 1579s br *v*(C=N). UV/vis (methanol) [λ, max, nm; ε, mol^{-1} dm^3 cm^{-1}]: 288; 1.67 x 10^4; 382; 1.23 x 10^4. M/Z+ = 423.0976 M+ (calc. = 423.0884).....16

Fig. S5 2,2'-{(2-hydroxypropane-1,3-diyl)bis[nitrilo(*E*)methylylidene]} bis(pyrrol-1-ido)gold(III) chloride, [Au(L2)]Cl. The complex was further analysed by ^{1}H NMR, ^{13}C NMR, UV-Visible spectroscopy, mass spectroscopy and FT-IR. ^{1}H NMR (400 MHz, Deuterium Oxide) δ 8.09 (s, 2H, H-5), 7.40 – 7.29 (m, 2H, H-1), 6.97 (d, *J* = 4.2 Hz, 2H, H-3), 6.43 (dd, *J* = 4.2, 2.2 Hz, 2H, H-2), 4.68 (t, *J* = 3.3 Hz, 1H, H-6), 3.87 – 3.77 (m, 4H, H-7). ^{13}C NMR (101 MHz, Deuterium Oxide) δ 176.07 (C-5), 149.03 (C-1), 135.29 (C-4), 124.42 (C-3), 111.50 (C-2), 80.40 (C-7), 66.48 (C-6). FT–IR (KBr pellet, cm^{-1}): 3100m br *v*(CH, imine), 2989 (CH, H-COH), 2939 (CH, C*H*2-N=CH), 1570s br δ(C=N), 1123(C-O stretch). UV/vis (methanol) [λ, max, nm; ε, mol^{-1} dm^3 cm^{-1}]: 288; 1.4 x 10^4; 382; 1.07 x 10^4. M/Z+ = 439.0926 M+ (calc. = 439.0833).....16

Fig. S6 2,2'-{(2,2-dimethylpropane-1,3-diyl)bis[nitrilo(*E*)methylylidene]}bis (pyrrol-1-ido)gold(III) chloride, ([Au(L3)]Cl). The complex was further analysed by ^{1}H NMR, ^{13}C NMR, UV-Visible spectroscopy, mass spectroscopy and FT-IR. ^{1}H NMR (400 MHz, Chloroform-*d*) δ 8.03 (s, 1H, H-5), 6.88 (t, *J* = 1.9 Hz, 1H, H-1), 6.48 (dd, *J* = 3.6, 1.4 Hz, 1H, H-3), 6.23 (dd, *J* = 3.6, 2.6 Hz, 1H, H-2), 3.61 (td, *J* = 6.8, 1.2 Hz, 2H, H-6), 1.98 (t, *J* = 6.8 Hz, 1H, H-8). ^{13}C NMR (101 MHz, Chloroform-*d*) δ 179.80 (C-5), 152.48 (C-1), 130.49 (C-6), 122.68 (C-2), 114.95 (C-3), 110.23 (C-4), 58.44 (C-1), 32.93 (C-5). FT–IR (KBr pellet, cm-1): 3093 (CH, imine), 2970m(CH, terminal CH_3), 2926 (CH_2, alkyl), 1661 (C=N). UV/vis (ethanol) [λ, max, nm; ε, mol^{-1} dm^3 cm^{-1}]: 288; 1.4 x 10^4 , 382; 1.1x10^4. M/Z+ = 451.1276 M+ (calc. = 451.1197).....17

1.3. Single X-ray preparation 18

1.4. Fluorescence spectroscopy 18

1.5. Circular dichroism 19

1.5.1. Far-UV-CD.....19

1.5.2. Near-UV-CD and induced CD.....19

1.5.3. Circular dichroism to detect thermal melt temperature (T_m).....19

1.6. Isothermal titration calorimetry (ITC) 19
1.7. DNA binding studies 20
1.7.1. Linear dichroism 20
1.7.2. DNA Circular dichroism 20
1.7.3. DNA UV-vis titration experiments 20
1.8. NCI-60 cytotoxicity screens 21
1.9. Molecular Docking 22
2. Figures and Tables 23
2.1. General characterisation 23
Fig. S7 ^{1}H NMR of **H_2L1** in $CDCl_3$ 23
Fig. S8 ^{13}C NMR of H_2L1 in $CDCl_3$ 24
Fig. S9 ^{1}H NMR of **H_2L2** in CD_3OD 25
Fig. S10 ^{13}C NMR of **H_2L2** in CD_3OD 26
Fig. S11 ^{1}H NMR of **H_2L3** in $CDCl_3$ 27
Fig. S12 ^{13}C NMR of **H_2L3** in $CDCl_3$ 28
Fig. S13 ^{1}H NMR of **AuL1** in CD_3OD 29
Fig. S14 ^{13}C NMR of **AuL1** in CD_3OD 30
Fig. S15 ^{1}H NMR of **AuL2** in D_2O 31
Fig. S16 ^{13} NMR of **AuL2** in D_2O 32
Fig. S17 ^{1}H NMR of AuL3in DMSO–*d*6 33
Fig. S18 ^{13}C NMR of AuL3in DMSO–*d*6 34
Fig A. S19 FTIR spectrum of **H_2L1** recorded as a crushed powder sample at 298 K. 35
Fig. S20 FT-IR spectrum of **H_2L2** recorded as a crushed powder sample at 298 K. 35
Fig. S21 FT-IR spectrum of **H_2L3** recorded as a crushed powder sample at 298 K. 36
Fig. S22 FT-IR spectrum of **AuL1** recorded as a crushed powder sample at 298 K. 37
Fig. S24 FT-IR spectrum of **AuL3** recorded as a crushed powder sample at 298 K. 38
Fig. S25 UV-visible spectrum of **H_2L1** recorded in ethanol at 298 K as a function of concentration. (b) the slopes of Beer- Lambert law plots at the relevant band maxima. 39
Fig. S27 UV-visible spectrum of **H_2L3** recorded in ethanol at 298 K as a function of concentration. (b) the slopes of Beer- Lambert law plots at the relevant band maxima. 40
Fig. S28 UV-visible spectrum of **AuL1** recorded in methanol at 298 K as a function of concentration. (b) the slopes of Beer- Lambert law plots at the relevant band maxima. 40
Fig. S29 UV-visible spectrum of **AuL2** recorded in methanol at 298 K as a function of concentration. (b) the slopes of Beer- Lambert law plots at the relevant band maxima. 41
Fig. S30 UV-visible spectrum of **AuL3** recorded in ethanol at 298 K as a function of concentration. (b) the slopes of Beer- Lambert law plots at the relevant band maxima. 41

Fig. S31 ESI-MS spectrum of **AuL1**. The solid sample was dissolved in methanol with 0.1% formic acid (V/V) and the spectrum was recorded in positive ESI mode. 42

Fig. S32 ESI-MS spectrum of **AuL2**. The solid sample was dissolved in methanol with 0.1% formic acid (V/V) and the spectrum was recorded in positive ESI mode. 42

Fig. S33 ESI-MS spectrum of **AuL3**. The solid sample was dissolved in methanol with 0.1% formic acid (V/V) and the spectrum was recorded in positive ESI mode. 42

2.2. X-ray crystallography 43

Fig. S34 View of the π-π dimers formed by the cation of compound **AuL1** in the crystalline solid state. Bond distances MPS, Au···Au separation and Au···Cl^- is measured. The chelates are represented as 50% thermal ellipsoids for non-H atoms; H atoms are shown as capped cylinders. Atom colour code white H, grey C, blue N, dark blue Au, and dark green Cl. 43

Fig. S35 View of the π-π dimers formed by the cation of compound **AuL2** in the crystalline solid state. Bond distances MPS, Au···Au separation and H···Cl is measured. The chelates are represented as 50% thermal ellipsoids for non-H atoms; H atoms are shown as capped cylinders. Atom colour code white H, grey C, blue N, dark blue Au, red O and dark green Cl. 44

Fig. S36 View of the π-π dimers formed by the cation of compound **AuL3** in the crystalline solid state. Bond distances MPS, Au···Au separation is measured. The chelates are represented as 50% thermal ellipsoids for non-H atoms; H atoms are shown as capped cylinders. Atom colour code white H, grey C, blue N, dark blue Au, red O and dark green Cl. 45

2.3. Au(III) chelates interaction with DNA**.** 46

Fig. S37 The UV-vis absorption spectra of (a) **AuL2** in the presence of ctDNA (b) the change in the absorbance at 382 nm of **AuL2** as a function of [ctDNA] fitted to the Hill model. The UV-vis absorption spectra of (c) **AuL3** in the presence of ctDNA (d) the change in the absorbance at 382 nm of **AuL3** as a function of [ctDNA] fitted to the Hill model. All reactions were carried out in KH_2PO_4 and after sequential additions of ctDNA (final [ctDNA] = 342 μM bp, for **AuL2** and 542 μM for **AuL3**. The Hill fits were used to calculate the dissociation constants and stoichiometric ratios of the Au(III) chelates binding to ctDNA. 46

2.4. LD spectroscopy 48

Fig. S39 A schematic illustration of a Couette cell, used to align DNA molecules in a way in which the orientation axis is equivalent to the helical axis of DNA. The double stranded DNA highlights the manner in which an intercalating (gold) and a minor groove (blue) binding molecules bind to double stranded DNA. 48

Fig. S40 (a) The LD spectrum of EB with ctDNA, with an induced LD at 515 nm indicating binding of EB to ctDNA. (b) The best docking pose generated of EB intercalated with double stranded DNA (PDB: 2O1I).[12] (c) The LD spectrum of HS with ctDNA, with an induced LD at 347 nm indicating binding of HS to ctDNA. (d) An XRD crystal structure of HS in the minor groove of DNA (PDB: 8BNA).[13] 49

Fig. S41 The LD spectrum of (a) **AuL2** and (b) **AuL3** with 100 μM of ctDNA at increasing [Au(III) chelate]:[ctDNA] ratios (*r*) of 0.25 – 2 in KH_2PO_4 (50 mM, pH 7.5) at 37 °C. The intense minimum at 260 nm represents ctDNA and the 394 nm band represents an induced Au(III) chelates LD spectrum. 50

Fig. S42 The CD spectrum of (a) **AuL2** and (b) **AuL3** with 100 μM of ctDNA at increasing [Au(III) chelate]:[ctDNA] ratios (*r*) of 0.25 – 2 in KH_2PO_4 (50 mM, pH 7.5) at 37 °C. The intense maximums

and minimums from 210 – 277 nm represent ctDNA and the 385 nm band represents an induced Au(III) chelates CD spectrum**.** 50

2.5. NCI-60 cytotoxicity 51

Fig. S43 NCI-60 single-dose cytotoxicity screen for **AuL1**. 51

Fig. S44 NCI-60 single-dose cytotoxicity screen for **AuL2**. 52

Fig. S45 NCI-60 single-dose cytotoxicity screen for **AuL3**. 53

Fig. S46 EB agarose gel showing the *in vitro* activity of **AuL2**. This *in vitro* activity indicates that there is a cellular mechanism responsible for **AuL2** inactivity *in vivo*, likely ab efflux pump..... 54

Fig. S47 EB agarose gel showing the diminished cleavage or poisoning activity of Pd(PrPyrr) against Top2 in comparison to etoposide..... 54

Fig. S48 EB agarose gel showing the lack of activity if the metal-free ligand **H_2L1** compared to the commercially available chemotherapeutic agent VP-16 (etoposide). 55

2.6. Docking of AuL1 into DNA..... 56

Fig. S49 The lowest-energy docking pose of **AuL1** within the central 5′-AT-3′ step of the 5′-D(CGGAAAATTACCG)-3′ DNA sequence. The position of **AuL1** at the intercalation site is shown head on as well as the chemical detail of the nucleic acid residues, A and T. The DNA strand as viewed. 56

2.7. **Fluorescence spectroscopy** 57

Fig. S50 Emission spectra of human serum albumin (HSA, 5.0 μM) recorded as a function of the concentration of (a) **AuL2** and (b) **AuL3** at 298 K in KH_2PO_4 buffer (50 mM, pH 7.50). The spectra are fitted by single Bigaussian functions to locate the emission maxima. Correlation coefficients, R^2, ranged from 0.996 to 0.999. 57

2.8. Binding parameters..... 60

Fig. S52. Plots of log((I_0-I)/I) versus log([Q]) for the interaction of HSA with the three Au(III) chelates (i.e., quenchers, Q): (a) **AuL1**···HSA complex, (b) **AuL2**···HSA complex, (c) **AuL3**···HSA complex. The affinity constants are determined from the intercepts of the graphs and the stoichiometry from the slopes. Data for the Au(III) chelates···HSA systems were recorded at three different temperatures (● 288 K, ● 298 K, and ● 310 K) The relevant concentrations for the titrations were: [HSA] = 5.0 μM, and the Au(III) chelates ranged from 0 – 9.8 × 10^{-5} M at pH 7.50 in 50 mM KH_2PO_4 buffer. 60

2.9. Thermodynamic parameters by ITC..... 62

Fig. S53 Binding thermodynamic measurements of (a) **AuL1** (b) **AuL2** and (c) **AuL3** interacting with HSA (20 μM, in 50 mM KH_2PO_4, pH 7.5) measured by ITC. The top panel of all three plots represent the raw heat released belonging to each injection. The bottom panel indicates the integrated heat corresponding to each injection. The solid line shows the best fitting isothermal binding model. Experiments were performed at 398 K as described in methods and materials. 62

2.10. Site displacement assay 63

Fig. S54 Au(III) chelates displace either dansylglycine or warfarin bound to HSA. Various Au(III)-chelates (0–9.7 × 10^{-5} M) were titrated into a solution containing 5 μM HSA bound to 5 μM of either dansylglycine or warfarin. Displacement of dansylglycine or warfarin resulted in the fluorophores fluorescence being quenched. Error bars indicate the standard deviation of three independent experiments..... 63

Fig. S55 Binding site determination for the reaction of **AuL2** with HSA (5.0 μM protein, 50 mM KH_2PO_4, pH 7.50, 298 K). **(a)** Emission spectra of HSA···warfarin (5.0 μM warfarin λ^{ex} = 320 nm) recorded as a function of the concentration of **AuL2** at 298 K. The spectra are fitted by single Gaussian functions to locate the emission maxima. Correlation coefficients, R^2, ranged from 0.990 to 0.999. **(b)** Emission spectra of HSA···dansylglycine (5.0 μM dansylglycine λ^{ex} = 420 nm) recorded as a function of the concentration of **AuL2** at 298 K. **(c)** Stern–Volmer (SV) plot for native HSA, HSA···Warfarin, and HSA···dansylglycine as a function of the concentration of **AuL2** at 298 K. The plots are linear with an intercept of 1.0 when static quenching is operative (i.e., the quencher binds to the target protein and fluorophore(s)). The excitation and emission wavelengths for the fluorophore probes were: (i) Trp-214 (native HSA), λ^{ex} = 295 nm, λ^{em} = 340 nm; (ii) Warfarin (HSA-Warf), λ^{ex} = 320 nm, λ^{em} = 382 nm, and (iii) dansylglycine, λ^{ex} = 340 nm, λ^{em} = 500 nm. **(d)** Sphere of action model plot, $\mathrm{lnI0I} = \mathrm{KSVappQ}$, for the system. A linear plot with a zero intercept indicates static quenching by **AuL2** bound in some way to the fluorophore/macromolecule. Negative deviation from linearity signals a switch from static to dynamic quenching. **(e)** Double-log plot (eq. S9) of the fluorescence quenching data, $\mathrm{logI0\text{-}II} = \mathrm{logK} + \mathrm{nlogQ}$, to enable measurement of log*Ka* and the reaction stoichiometry (*n*). **(f)** Normalised fluorescence emission spectrum of HSA···warfarin (5.0 μM warfarin λ^{ex} = 320 nm) recorded as a function of the concentration of **AuL2** at 298 K to show the displacement of warfarin from HSA. Error bars indicate the standard deviation of three independent experiments. 65

Fig. S56 Binding site determination for the reaction of **AuL3** with HSA (5.0 μM protein, 50 mM KH_2PO_4, pH 7.50, 298 K). **(a)** Emission spectra of HSA···warfarin (5.0 μM warfarin λ^{ex} = 320 nm) recorded as a function of the concentration of AuL1 at 298 K. The spectra are fitted by single Gaussian functions to locate the emission maxima. Correlation coefficients, R^2, ranged from 0.990 to 0.999. **(b)** Emission spectra of HSA···dansylglycine (5.0 μM dansylglycine λ^{ex} = 420 nm) recorded as a function of the concentration of AuL3 at 298 K. **(c)** Stern–Volmer (SV) plot for native HSA, HSA···Warfarin, and HSA···dansylglycine as a function of the concentration of **AuL3** at 298 K. The plots are linear with an intercept of 1.0 when static quenching is operative (i.e., the quencher binds to the target protein and fluorophore(s)). The excitation and emission wavelengths for the fluorophore probes were: (i) Trp-214 (native HSA), λ^{ex} = 295 nm, λ^{em} = 340 nm; (ii) Warfarin (HSA-Warf), λ^{ex} = 320 nm, λ^{em} = 382 nm, and (iii) dansylglycine, λ^{ex} = 340 nm, λ^{em} = 500 nm. **(d)** Sphere of action model plot, $\mathrm{lnI0I} = \mathrm{KSVappQ}$, for the system. A linear plot with a zero intercept indicates static quenching by **AuL3** bound in some way to the fluorophore/macromolecule. Negative deviation from linearity signals a switch from static to dynamic quenching. **(e)** Double-log plot (eq. S9) of the fluorescence quenching data, $\mathrm{logI0\text{-}II} = \mathrm{logK} + \mathrm{nlogQ}$, to enable measurement of log*Ka* and the reaction stoichiometry (*n*). **(f)** Normalised fluorescence emission spectrum of HSA···warfarin (5.0 μM warfarin λ^{ex} = 320 nm) recorded as a function of the concentration of **AuL3** at 298 K to show the displacement of warfarin from HSA. Error bars indicate the standard deviation of three independent experiments. 67

2.11. CD spectroscopy..... 68

Fig. S58 Plots of the near UV CD spectra of native HSA and the protein incubated with a 1:1 (15 μM) ratio (a) **AuL2** and (b) **AuL3** recorded at 298 K in 50 mM KH_2PO_4 buffer at pH 7.50. The data represents unsmoothed spectra of the fine structure of the protein. Perturbations in the protein structure around Phe (250–270 nm), Tyr (~280 nm), and Trp (285–300 nm) residues may also be resolved in some difference spectra. Key maxima and minima are indicated (in nm). 68

Fig. S59 Induced circular dichroism plots of (a) **AuL2** and (b) **AuL3** when bound to HSA in a 1:1 molar ratio (15 μM) in a 50 mM KH_2PO_4 buffer (pH 7.5) and smoothed using a relatively fine Lowess function (0.07 span). 69

2.12. Tables 70

Table S1. Crystallization data for the bis(pyrrolide-imine) Au(III) Schiff base chelate complexes 70

Table S2. Average bond lengths and bond angles for the Au(III) Schiff base chelate complexes. 70

Table S3. Crystal system data, X-ray data collection, and structure refinement details for compounds **AuL1**, **AuL2** and **AuL3**. 71

Table S4. Selected geometrical parameters (Å, °) for the X-ray structure of **AuL1**. A labelled thermal ellipsoid plot (50% probability surfaces, H atoms drawn with arbitrary radii) is included to aid reading the tabulated data. 72

Table S5. Selected geometrical parameters (Å, °) for the X-ray structure of **AuL1**. A labelled thermal ellipsoid plot (50% probability surfaces, H atoms drawn with arbitrary radii) is included to aid reading the tabulated data. 72

Table S6. Selected geometrical parameters (Å, °) for the X-ray structure of **AuL1**. A labelled thermal ellipsoid plot (50% probability surfaces, H atoms drawn with arbitrary radii) is included to aid reading the tabulated data. 74

Table S7. Thermodynamic parameters for the binding of the Au(III) chelates by HSA in 50 mM KH_2PO_4 buffer at pH 7.50. 75

Table S8. Stern-Volmer quenching constants (K_{SV}) and binding constant (logKa) for the interaction of **AuL1**, **AuL2** and **AuL3** with HSA, HSA···warfarin and HSA···dansylglycine at 298 K in 50 mM KH_2PO_4 buffer at pH 7.50. 75

Table S9. Summary of the change in α-helicity of native and HSA in the presence of **AuL1**, **AuL2** and **AuL3** 76

Table S10. Summary of T_m of HSA in the absence and presence of Au(III)-chelates determined by using UV-CD spectroscopy. 76

3. References 77

1. Experimental methods

All solvents (HPLC grade) and chemical synthons were used as received from Merck Sigma-Aldrich® without further purification. Deuterated dimethyl sulfoxide was stored over activated 4 Å molecular sieves. Human serum albumin (HSA) was purchased from Merck Sigma-Aldrich® and used as received without further purification except for the isothermal titration calorimetry experiment (ITC). For ITC HSA was purified to its monomeric form using gel exclusion chromatography (Sepharose S-200 column). All buffer salts and fluorescent probes were purchased without any further purification from Merck Sigma-Aldrich®. Ultrapure water (Type I) was produced using a Merk-Millipore Direct-Q® 3 UV Water Purification System.

1.1. Instruments and basic methods

1.1.1. X-ray crystallography

The single crystal X-ray structure determination for **AuL1** was carried out with a three-circle Bruker Apex-II X-ray diffractometer equipped with a CCD area detector and a fine-focus sealed X-ray tube source (Mo anode). The crystal was mounted under Paratone® oil on a nylon loop (Hampton Research) and the crystal was kept at 173(1) K during data collection (Oxford CryoStream 700). Using Olex2,[1] the structure was solved with the ShelXT[2] structure solution program (intrinsic phasing) and refined with ShelXL[3] using least squares minimization.

1.1.2. General spectroscopy

Nuclear magnetic resonance (NMR) spectra were recorded on either a Bruker Avance III 400 400.21 MHz for 1H, 100.64 MHz for 13C, 162.01 MHz for 31P and 376.57 MHz for 19F or a, Bruker Avance-III-300, operating at 300.13 MHz for 1H, 75.47 MHz for 13C, 121.49 MHz for 31P and 282.40 MHz for 19F. All spectra were recorded at 298 K with 5 mm BBOZ or TBIZ probes. Deuterated solvent signals were used to correct for the reported chemical shifts in δ (in ppm). For $(CD_3)_2SO$, $CDCl_3$, D_2O and CD_3OD the δ H was referenced as 2.50, 7.26, 4.79 and 3.31 ppm respectively and the δ 13C {1H} was referenced at 39.52, 77.16, D_2O had no peak and 49 ppm, respectively. MestReNova (version 14.2.1-27684) was used to analyse NMR spectra. The coupling patterns are abbreviated as follows: s - singlet; d - double; t - triplet; q - quartet; sept – septet; m – multiplet; br s – broad signal. Proton coupling constants (J) are given in hertz (Hz). Impurities are stated on the NMR figures [4] FT-IR spectra of powder samples were recorded using a Bruker Alpha FTIR spectrometer incorporating a Bruker Platinum® diamond ATR sampling accessory. Spectra were analysed using the OPUS software package on the spectrometer (version 7.5). Mass spectra were recorded with Bruker Compact Q-TOF high-resolution mass spectrometer using Bruker Daltronics HyStar 3.2 SR4 software. Bruker Compass DataAnalysis software (Version 4.3) was used to analyse chromatograms. Samples of pure compounds (typically ca. 10 µg/mL) were prepared in HPLC grade acetonitrile or methanol for metal chelates and HPLC grade

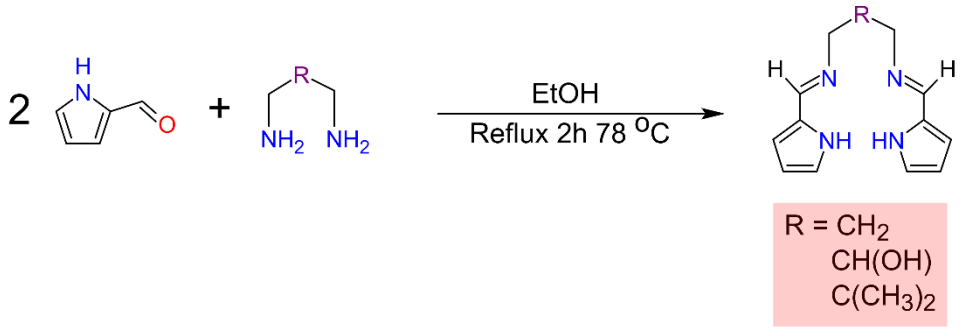
methanol for ligands. Solutions were acidified using 0.1% (V/V) formic acid. UV-visible electronic spectra were recorded using either a PerkinElmer Lambda 365 double beam spectrometer connected to a Peltier controller and multicell thermostatic cell block or an Analytik Jena Specord210 Plus double-beam instrument fitted with an external water circulating thermostatic bath and thermostatted cell holders.

The spectral data were analysed with the spectrometer software or Origin Pro 2020. Spectra were recorded (10-mm pathlength quartz cuvettes) as a function of concentration for both characterization and the determination of molar absorptivity constants.

Electronic spectra were recorded using either a PerkinElmer Lambda 365 double beam spectrometer connected to a Peltier controller and multicell thermostatic cell block or an Analytik Jena Specord210 Plus double-beam instrument fitted with an external water circulating thermostatic bath and thermostatted cell holders. The spectral data were analysed with the spectrometer software or Origin Pro 2020. Spectra were recorded (10-mm pathlength quartz cuvettes) as a function of concentration for both characterization and the determination of molar absorptivity constants.

1.2. Compound synthesis

1.2.1. Ligand Synthesis



Scheme 1 Representation of the condensation reaction of pyrrole-2 carboxaldehyde with respective diamino propane by (a) refluxing and (b) grinding.

Caveats. For **H_2L1**, **H_2L2** and **H_2L3**, upon refluxing the reaction mixture changed from a faint yellow to a bright orange colour. The colour change was an indication of the formation of the respective bis(pyrollide-imine) chelate from the condensation reaction and is potentially due to an increase in the aromaticity. The ethanol from the reactants in scheme 1a was removed using reduced pressure rotary evaporation and the resultant oil was dissolved in DCM and layered with hexane to obtain the desired ligand. All three bis(pyrrolide-imine) chelates purity and characteristics were determined using ^{1}H NMR, ^{13}C NMR, FT-IR, and UV-vis spectroscopy.

Synthesis procedure of ligands

N,*N*'-bis[(1*E*)-1*H*-pyrrol-2-ylmethylene]propane-1,3-diamine (H_2L1). The synthetic method was an adaption from the method described by Munro *et al*. Briefly, pyrrole-2-carboxaldehyde (1.4265 g, 15 mmol) and 1,3-diaminopropane (0.556 g, 7.5 mmol) were refluxed in ethanol (30 mL) for at least two hours. Within refluxing the reaction mixture changed from colourless to a clear straw yellow. Ethanol was then removed by rotary evaporation and a viscous orange coloured oil remained. The viscous orange oil was dissolved in 8 ml of DCM and layered with hexane. The solution was left overnight, affording a faint yellow polycrystalline product. A yield of 85% was obtained.

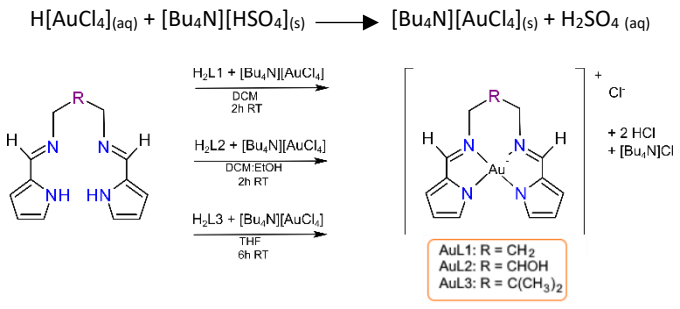
1,3-bis{[(1*E*)-1*H*-pyrrol-2-ylmethylene]amino}propan-2-ol (H_2L2). In brief the synthesis of H_2(OH)Pyrr involved refluxing pyrrole-2-carboxaldehyde (0.5706 g; 6 mmol) with 1,3-diaminopropanol (0.2704 g; 3 mmol) for 2 hours in ethanol in which time the solution changed from colourless to bright orange. The ligand was precipitated out by overnight evaporation of ethanol. A yield of 74% was obtained.

2,2-dimethyl-*N*,*N*'-bis[(1*E*)-1*H*-pyrrol-2-ylmethylene]propane-1,3-diamine (H_2L3). In brief was synthesised by refluxing pyrrole-2-carboxaldehyde (0.5706 g, 6 mmol) and 1,3-diamino-2,2-dimethyl propane (0.3066 g, 3 mmol) was refluxed in ethanol (30 mL) for one hour. The solution changed from colourless to orange. The ligand was precipitated out by overnight evaporation of the ethanol. A yield of 66% was obtained.

1.2.2. Synthesis of *tert*-Butylamonium Tetrachloroaurate(III)

Hydrogen tetrachloroaurate(III) (1.218 g) was dissolved in 50 ml of deionised water. The solution was then added to a solution of *tert*-butylamonium hydrogen sulphate (1.020 g) resulting in the formation of a bright yellow precipitate which was $[Bu_4N][AuCl_4]$ (lipophillic gold(III) salt). $[Bu_4N][AuCl_4]$ was extracted into chloroform, dried over $MgSO_4$ before been filtered and the chloroform was removed by rotary evaporation. The resulting material was a crystalline bright yellow powder (1.55 g, 88%).

1.2.3. Metallation of the bis(pyrrolide-imine) chelates



Scheme 2. Representation of the Au(III) metalation of the bis (pyrollide-imine) chelates.

Caveats. From the reaction scheme 2a, **AuL1**–**AuL3** were synthesised by stirring the respective bis(pyrrolide-imine) ligand with $[Bu_4N][AuCl_4]$ and the desired Au(III) chelate precipitated out as a homogenous yellow powder. To confirm the purity and to characterise the metal chelates ^1H NMR, ^{13}C NMR, FT-IR, UV-spectroscopy, HRMS, elemental analysis and single crystal crystallography was carried out.

2,2'-{propane-1,3-diylbis[nitrilo(*E*)methylylidene]}bis(pyrrol-1-ido)gold(III) chloride, [Au(L1)]Cl. To a 50 ml round bottom flask A 10 ml dry dichloromethane solution of $[Bu_4N][AuCl_4]$ (100 mg, 0.172 mmol) was added dropwise to a 10 ml dry dichloromethane solution of H_2L1 (52.9 mg, 0.232 mmol) and stirred at room temperature for 2 hours. A yellow-orange precipitate had formed over time which was filtered and washed with dry dichloromethane, yielding a yellow powder (71% yield). Single red crystals suitable for single crystal XRD were grown by vapour diffusion of diethyl ether into a methanol solution of the product.

2,2'-{(2-hydroxypropane-1,3-diyl)bis[nitrilo(*E*)methylylidene]} bis(pyrrol-1-ido)gold(III) chloride, [Au(L2)]Cl. To a 50 ml round bottom flask A 10 ml dry dichloromethane solution of $[Bu_4N][AuCl_4]$ (100 mg, 0.172 mmol) was added dropwise to a 20 ml dry ethanol solution of H_2L2 (105 mg, 0.430 mmol) and stirred at room temperature for 2 hours. A pale-yellow precipitate had formed over time which was filtered and washed with dry dichloromethane, yielding a yellow powder (71% yield). Single red crystals suitable for single crystal XRD were grown by vapour diffusion of diethylether into a methanol solution of the product.

2,2'-{(2,2-dimethylpropane-1,3-diyl)bis[nitrilo(*E*)methylylidene]}bis (pyrrol-1-ido)gold(III) chloride, ([Au(L3)]Cl). To a 50 ml round bottom flask $[Bu_4N][AuCl_4]$ (100 mg, 0.172 mmol) and H_2L3 (52.9 mg, 0.206 mmol) was stirred in dry tetrahydrofuran at room temperature for 2 hours. A pale-yellow precipitate had formed over time, which was filtered and washed with dry tetrahydrofuran, yielding a yellow powder (50 mg; 64% yield). Single red crystals suitable for single crystal XRD were grown by vapour diffusion of diethyl ether into an acetonitrile solution of the product. The crystalline molecule was shown to be $[Au(L3)Cl^-]$ by X-ray crystallography. Structures of 2,2'-{(2,2-dimethylpropane-1,3-diyl)bis[nitrilo(*E*)methylylidene]}bis (pyrrol-1-ido)gold(III) chloride, ([Au(L3)]Cl) showing the atom naming scheme.

2,2'-{propane-1,3-diylbis[azanylylidene(*E*)methanylylidene]}di(pyrrol-1-ide)palladium(II), Pd(PrPyrr). The complex was synthesised by adding Pd(II)acetate dihydrate (1 mmol) to a minimal volume of acetonitrile containing $H_2PrPyrr$ (1 mmol). The mixture was stirred at 293 K for 4 h. The colour changed to bright yellow. Acetonitrile was removed by rotary evaporation and the yellow precipitate was dissolved in dichloromethane.

1.2.4. Characterisation of the bis(pyrrolide-imine) chelates

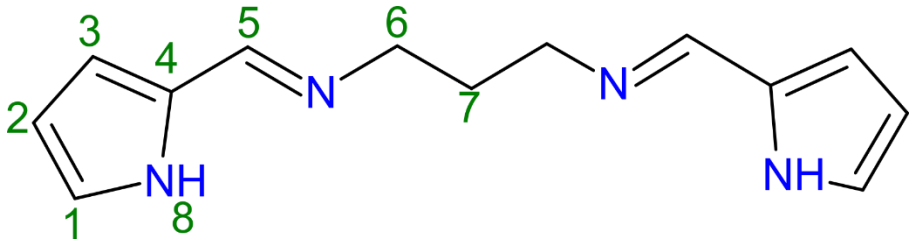


Fig. S1 N,*N*'-bis[(1*E*)-1*H*-pyrrol-2-ylmethylene]propane-1,3-diamine (H_2L1). was synthesised as described by Munro and Camp, (2003)[5] and was analysed by ^{1}H NMR, ^{13}C NMR, FT-IR and UV-Visible spectroscopy. ^{1}H NMR (400 MHz, Chloroform-*d*, 300 K) [δ, ppm]: 1.98 (t, *J* = 6.8 Hz, 2H, H-7), 3.61 (td, *J* = 6.8, 1.2 Hz, 4H, H-6), 6.23 (dd, *J* = 3.6, 2.6 Hz, 2H, H-2), 6.48 (dd, *J* = 3.6, 1.4 Hz, 2H, H-3), 6.88 (t, *J* = 1.9 Hz, 2H, H-1), 8.03 (s, 2H, H-5). ^{13}C NMR (101 MHz, Chloroform-*d*, 300 K) [δ, ppm]: 32.29 (C-7), 57.80 (C-6), 109.59 (C-2), 114.13 (C-3), 122.04 (C-1), 129.86 (C-4), 151.85 (C-5). IR (KBr pellet, cm^{-1}): 3112w δ(NH, pyrrole), 3053m br *v*(CH, imine), 2941m *v*(CH, $CH_2CH_2CH_2$), 2847 *v*(CH, CH_2-N=CH), 1634s br *v*(C=N). UV/vis (ethanol) [λ, max, nm; ε, mol^{-1} dm^3 cm^{-1}]: 289; 3.20 × 10^4.

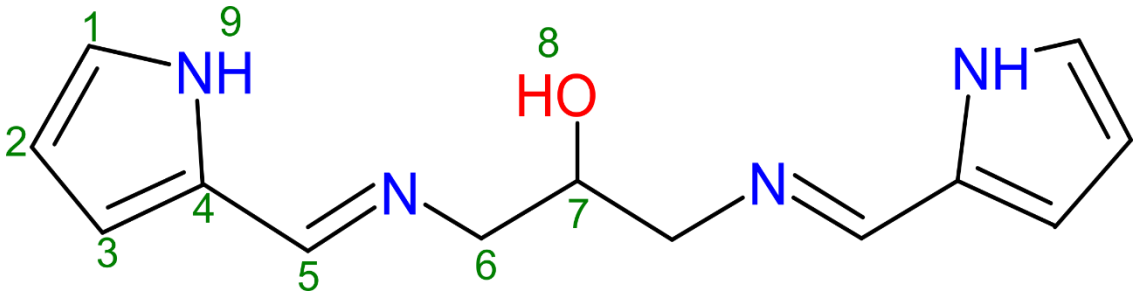


Fig. S2 1,3-bis{[(1*E*)-1*H*-pyrrol-2-ylmethylene]amino}propan-2-ol (H_2L2). The ligand was analysed by ^{1}H NMR, ^{13}C NMR, FT-IR and UV-Visible spectroscopy. ^{1}H NMR (400 MHz, DMSO-d_6-300 K) [δ, ppm]: 3.43 (dd, *J* = 11.7, 6.5 Hz, 2H, CH_2-N=CH), 3.77 – 3.54 (m, 2H, CH_2-N=CH, H-6), 4.00 – 3.82 (m, 1H, H-7), 6.11 (t, *J* = 3.0 Hz, 2H, H-2), 6.44 (dd, *J* = 3.5, 1.5 Hz, 2H, H-3), 6.87 (t, *J* = 1.9 Hz, 2H, H-1), 8.07 (s, 2H, H-5), 11.34 (s br, 2H, DMSO-d_6 exchangeable, H-9). ^{13}C NMR (101 MHz, DMSO-d_6, 300 K) [δ, ppm]: 65.14 (C-6), 70.69 (C-7), 108.98 (C-2), 113.35 (C-3), 122.03 (C-1), 130.41 (C-4), 152.92 (C-5). IR (KBr pellet, cm-1): 3254w (NH, pyrrole), 3088m (CH, imine), 2882 (CH, H-COH), 2859 (CH, C*H*2-N=CH), 1633s (C=N), 1127 (C-O stretch). UV/vis (ethanol) [λ, max, nm; ε, mol^{-1} dm^3 cm^{-1}]: 289; 3.23 × 10^4.

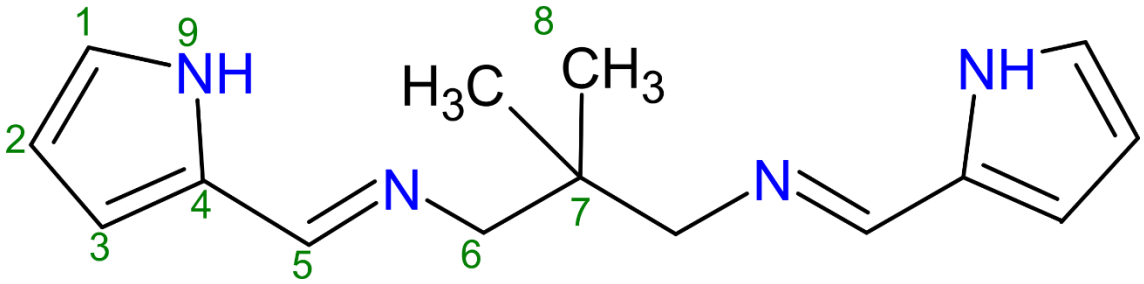


Fig. S3 2,2-dimethyl-*N*,*N*'-bis[(1*E*)-1*H*-pyrrol-2-ylmethylene]propane-1,3-diamine (H_2L3). The ligand was analysed by ^{1}H NMR, ^{13}C NMR, FT-IR and UV-Visible spectroscopy. ^{1}H NMR (400 MHz, Chloroform-*d*, 300 K) [δ, ppm]: 0.97 (t, *J* = 4.3 Hz, 6H, H-8), 3.46 (t, *J* = 4.2 Hz, 4H, H-6), 6.26 (p, *J* = 3.2 Hz, 2H, H-2), 6.48 (dt, *J* = 6.6, 3.4 Hz, 2H, H-3), 6.90 (d, *J* = 6.1 Hz, 2H, H-1), 7.99 (t, *J* = 4.2 Hz, 2H, H-5), 9.50 (s br, 2H, H-9). ^{13}C NMR (101 MHz, Chloroform-*d* 300 K) [δ, ppm]: 24.28 (C-8), 36.96 (C-7), 69.32 (C-6), 109.44 (C-2), 114.28 (C-3), 122.20 (C-1), 130.06 (C-4), 152.17 (C-5). FT-IR (KBr pellet, cm^{-1}): 3130m br *v*(CH, imine), 2966m *v*(CH, terminal CH3), 2852m *v*(CH2, alkyl), 1635s br *v*(C=N). UV/vis (ethanol) [λ, max, nm; ε, mol^{-1} dm^3 cm^{-1}]: 289; 3.23 × 10^4.

1.2.5. Characterisation of the bis(pyrrolide-imine) gold(III) chelates

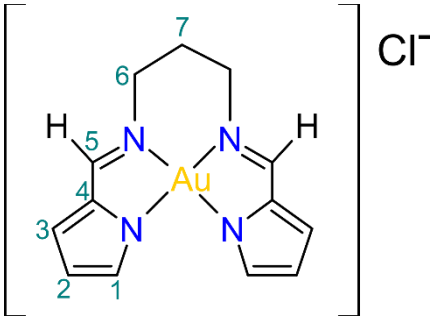


Fig. S4 2,2'-{propane-1,3-diylbis[nitrilo(*E*)methylylidene]}bis(pyrrol-1-ido)gold(III) chloride, [Au(L1)]Cl. The complex was analysed by ^{1}H NMR, ^{13}C NMR, UV-Visible spectroscopy, mass spectroscopy and FT-IR. IR (KBr pellet, cm^{-1}): ^{1}H NMR (400 MHz, Methanol-d_4) [δ, ppm]: 2.31 (p, *J* = 5.3 Hz, 2H, H-7), 3.88 – 3.75 (m, 4H, H-6), 6.52 (dd, *J* = 4.2, 2.3 Hz, 2H, H-2), 7.09 (d, *J* = 4.2 Hz, 2H, H-3), 7.65 (d, *J* = 2.2 Hz, 2H, H-1), 8.27 (s, 2H, H-5). ^{13}C NMR (101 MHz, Methanol-d_4 300 K) [δ, ppm]: 32.96 (C-7), 53.40 (C-6), 114.34 (C-2), 124.75 (C-3), 138.79 (C-4), 139.69 (C-1), 164.99 (C-5). FT-IR 3092m br *v*(CH, imine), 3074m *v*(CH, $CH_2CH_2CH_2$), 2936m *v*(CH, CH_2-N=CH), 1579s br *v*(C=N). UV/vis (methanol) [λ, max, nm; ε, mol^{-1} dm^3 cm^{-1}]: 288; 1.67 x 10^4; 382; 1.23 x 10^4. M/Z+ = 423.0976 M+ (calc. = 423.0884).

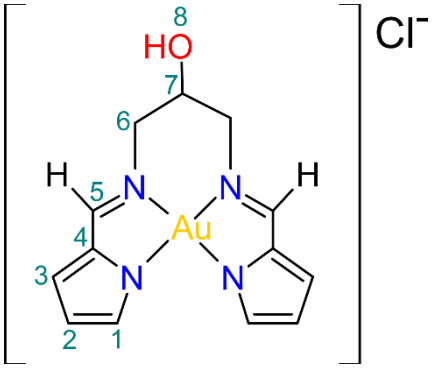


Fig. S5 2,2'-{(2-hydroxypropane-1,3-diyl)bis[nitrilo(*E*)methylylidene]} bis(pyrrol-1-ido)gold(III) chloride, [Au(L2)]Cl. The complex was further analysed by ^{1}H NMR, ^{13}C NMR, UV-Visible spectroscopy, mass spectroscopy and FT-IR. ^{1}H NMR (400 MHz, Deuterium Oxide) δ 8.09 (s, 2H, H-5), 7.40 – 7.29 (m, 2H, H-1), 6.97 (d, *J* = 4.2 Hz, 2H, H-3), 6.43 (dd, *J* = 4.2, 2.2 Hz, 2H, H-2), 4.68 (t, *J* = 3.3 Hz, 1H, H-6), 3.87 – 3.77 (m, 4H, H-7). ^{13}C NMR (101 MHz, Deuterium Oxide) δ 176.07 (C-5), 149.03 (C-1), 135.29 (C-4), 124.42 (C-3), 111.50 (C-2), 80.40 (C-7), 66.48 (C-6). FT–IR (KBr pellet, cm^{-1}): 3100m br *v*(CH, imine), 2989 (CH, H-COH), 2939 (CH, *CH*2-N=CH), 1570s br δ(C=N), 1123(C-O stretch). UV/vis (methanol) [λ, max, nm; ε, mol^{-1} dm^3 cm^{-1}]: 288; 1.4 x 10^4; 382; 1.07 x 10^4. M/Z+ = 439.0926 M+ (calc. = 439.0833).

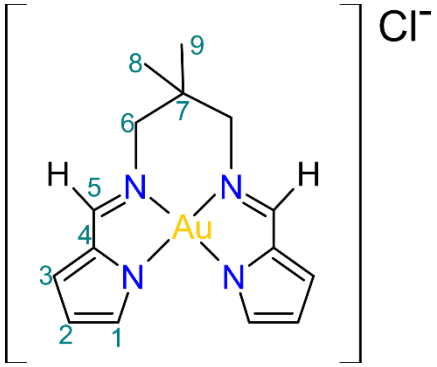


Fig. S6 2,2'-{(2,2-dimethylpropane-1,3-diyl)bis[nitrilo(*E*)methylylidene]}bis (pyrrol-1-ido)gold(III) chloride, ([Au(L3)]Cl). The complex was further analysed by ^{1}H NMR, ^{13}C NMR, UV-Visible spectroscopy, mass spectroscopy and FT-IR. ^{1}H NMR (400 MHz, Chloroform-*d*) δ 8.03 (s, 1H, H-5), 6.88 (t, *J* = 1.9 Hz, 1H, H-1), 6.48 (dd, *J* = 3.6, 1.4 Hz, 1H, H-3), 6.23 (dd, *J* = 3.6, 2.6 Hz, 1H, H-2), 3.61 (td, *J* = 6.8, 1.2 Hz, 2H, H-6), 1.98 (t, *J* = 6.8 Hz, 1H, H-8). ^{13}C NMR (101 MHz, Chloroform-*d*) δ 179.80 (C-5), 152.48 (C-1), 130.49 (C-6), 122.68 (C-2), 114.95 (C-3), 110.23 (C-4), 58.44 (C-1), 32.93 (C-5). FT–IR (KBr pellet, cm-1): 3093 (CH, imine), 2970m(CH, terminal CH_3), 2926 (CH_2, alkyl), 1661 (C=N). UV/vis (ethanol) [λ, max, nm; ε, mol^{-1} dm^3 cm^{-1}]: 288; 1.4 x 10^4 , 382; 1.1x10^4. M/Z+ = 451.1276 M+ (calc. = 451.1197).

2,2'-{propane-1,3-diylbis[azanylylidene(*E*)methanylylidene]}di(pyrrol-1-ide)palladium(II), Pd(PrPyrr). Was analysed with ^{1}H NMR (400 MHz, chloroform-*d*, 300 K) [δ, ppm]: δ 7.52 (s, 2H), 7.16 (s, 2H), 6.70 (d, *J* = 3.7 Hz, 2H), 6.22 (dt, *J* = 3.5, 1.4 Hz, 2H), 3.52 – 3.39 (m, 4H), 1.98 (p, *J* = 4.7 Hz, 2H). ^{13}C NMR (101 MHz, chloroform-*d*, 300 K) [δ, ppm]: δ 159.06, 139.16, 135.51, 116.63, 110.50, 53.44, 31.30. UV-vis (acetonitrile) [λ_{max}/nm, ε/mol^{-1} dm^3 cm^{-1}]: 294, 2.25(11) × 10^4; 322, 1.25(9) × 10^4; 374, 1.16(6) × 10^4; 390, 1.15(6) × 10^4; 404, 9.92(51) × 10^3. IR (powder, cm^{-1}): 3082m br *ν*(CH, imine), 2919m *ν*(CH, C*H*$_2$-N=CH), 1583s br *ν*(C=N). HRMS (m/z): [M+H]$^+$ calcd. for $C_{13}H_{14}N_4Pd$, 333.0333; found, 333.0375.

1.3. Single X-ray preparation

Single red crystals suitable for single crystal XRD were grown by vapour diffusion for **AuL1**, **AuL2**, and **AuL3**. About 20 mg of **AuL1** and **AuL2** was dissolved into methanol and layered diethyl ether. The crystalline molecules were shown to be [Au(L1)Cl^{-}] and [Au(L2)Cl^{-}] by X-ray crystallography. **AuL3** crystals were prepared by vapour diffusion of diethyl ether into an acetonitrile solution of the product (20 mg). The crystalline molecules were shown to be [Au(L3)Cl^{-}] by X-ray crystallography.

1.4. Fluorescence spectroscopy

Fluorescence measurements were performed on a Cary Eclipse fluorescence spectrophotometer (Varian, Australia) equipped with a 1.0 cm quartz cell and a circulating thermostat bath. The HSA concentration was kept at 5.0×10^{-6} mol dm^{-3} and the excitation and emission slit widths were fixed at 5 and 10 nm, respectively. The concentrations of the three Au(III) chelates ranged from 0–9.8 x 10^{-5} mol dm^{-3}. **AuL1**, **AuL2** and **AuL3** were dissolved in KH_2PO_4 buffer (50 mM, pH 7.5). HSA was excited at 295 nm (excitation of Trp-214 residue), and the emission spectra were recorded from 310 to 400 nm. Spectral titrations were carried out at four temperatures (288, 298 and 310 K) in triplicate.

Correction of fluorescence data**.** Inner filter correction was applied to all fluorescence data using eq. S1.[6]

$$F_{corrected} = F_{observed} * 10^{Aex*dex+Aem*dem} \quad \text{S1}$$

Where $A_{excited}$ and $A_{emission}$ are the absorbance reading at the excitation and emission wavelengths. While d is the path length of the cuvette.

Further corrections to the concentration of **AuL1**, **AuL2** and **AuL2** were not required as the concentration of both Au(III) cyclohexane chelates >> than [HSA].[7]

$$[Ligand]_{free} = [Ligand]_{added} \quad \text{S2}$$

Fluorescent probe displacement assay**.** Warfarin, dansylglycine and ibuprofen were used as specific site marker fluorescent probes for Sudlow's sites I and II, respectively. Steady-state fluorescence spectra were recorded as described above at 298 K using 5 nm excitation and emission bandwidths for warfarin and dansylglycine, while 5 nm excitation and 10 nm emission band widths were employed for ibuprofen. The fluorophores warfarin, dansylglycine and ibuprofen were equilibrated (bound) to HSA (50 mM KH_2PO_4 buffer, pH 7.50) and were excited at 320 nm, 420 nm and 228 nm, respectively. The emission spectrum was measured in the range 350 – 500 nm for warfarin, 450 – 650 nm for dansylglycine and 228 – 450 nm for ibuprofen. The HSA and fluorescence probe concentrations were both used at 5.0 μM. Titrations were performed by increasing the concentrations of the Au(III) chelates in the protein-probe solution from 0 to 97 μM.

1.5. Circular dichroism

1.5.1. Far-UV-CD

Far-UV-CD spectra of solutions of HSA (300×10^{-9} mol dm^{-3}) in the absence and presence of increasing concentrations (0–6 μM) of the three Au(III) chelates were recorded with a JASCO J-1500 CD spectrometer equipped with a Peltier temperature controller (25 °C). A scan speed of 100 nm min^{-1} was employed for spectral acquisition with a 0.5 nm data pitch and a response time of 2 s. Each spectrum was the average of three scans. Spectra were recorded over a wavelength range of 190–260 nm (0.4 cm pathlength quartz cuvette). All spectra were processed with JASCO Spectral Manager™. Each sample was corrected for the background by blanking each sample with the respective buffer. The obtained results for CD-measurements were reported as molar ellipticity (deg cm^2 mol^{-1}/ ɵ mdeg). The tertiary structure of HSA was analysed using the spectral analysis software with 66.5 kDa being the mean molecular weight of HSA.

1.5.2. Near-UV-CD and induced CD

Near UV-vis CD spectra (250–310 nm, 1.0-cm pathlength quartz cuvette, 25 °C) and CD spectroscopy (300–500 nm, 1.0-cm pathlength quartz cuvette, 25 °C) were recorded similarly to detect induced CD (ICD) signals of the achiral ligands and AuIII) chelates upon their uptake by HSA. Typically, HSA (15×10^{-6} M) was incubated with one molar equivalent of the Au(III) chelates for at least 60 min. A scan speed of 50 nm min^{-1} was used with a 0.5-nm data pitch (response time, 2 s) for the near-UV-CD and 100 nm min^{-1} for the UV-vis CD; each spectrum was the average of three scans.

1.5.3. Circular dichroism to detect thermal melt temperature (T_m)

The melting temperatures (T_m) of HSA in the presence and absence of the Au(III)-chelates were determined by measuring HSA molar ellipticity at 222 nm. HSA in the absence of the Au(III)-chelates (300 nM) was dissolved in potassium phosphate buffer (50 mM, pH 7.5) while HSA in the presence of drug had the Au(III)-chelates added at 6 μM. The samples molar ellipticity at 222 nm were measured at a temperature range of 20- 90 °C with a ramp temperature of 5 °C and holding the temperature for 2 minutes. The samples T_m was determined by finding the midpoint of the sigmoidal fit curve to the molar ellipticity at 222 nm at the various temperatures using Origin(Pro), Version 2021b. OriginLab Corporation, Northampton, MA, USA.

1.6. Isothermal titration calorimetry (ITC)

The calorimetry measurement was carried out by isothermal titration calorimetry (ITC) (nano TA Instruments, USA) at 298 K. HSA in different reaction buffers (50 mM KH_2PO_4, pH 7.5) were extensively dialyzed before titration. All solutions were degassed afterward, and the sample cell was filled with 0.02 mM of 300 μL HSA solution. Au(III) chelates (**AuL1**, **AuL2** and **AuL3**; 1.2 mM in 50 mM KH_2PO_4 buffer, pH 7.5) were dropwise injected into the cell with a volume of 5 μL (The first injection was 2 μM). The titration was afterward started with continuously stirring at 250 rpm. The raw heat rate data were integrated under injection peaks to obtain the reaction heat of each injection. The calculated heat changes were analysed using the NANOanalyze software (TA Instruments, USA) and/or NitPick for noisy baselines.

1.7. DNA binding studies

Stock solution of calf thymus DNA (ctDNA) was prepared by dissolving the sodium salt (Sigma-Aldrich) in KH_2PO_4 buffer (pH 7.5, 50 mM) and slowly agitating it overnight at 70 rpm. The concentration of the solution was determined spectrophotometrically (ε=13 200 M^{-1} cm^{-1} at 260 nm).[8] In brief Au(III) chelates (AuL1, AuL2 and AuL3) were prepared in KH_2PO_4 buffer and diluted to a concentration of ± 30 µM. Increasing concentrations of ctDNA was added to the Au(III) chelates that were incubated at 37 °C and the absorbance spectra was recorded from 200 – 500 nm using a Analytik Jena Specord210 Plus double-beam instrument fitted with an external water circulating thermostatic bath and thermostatted cell holders. Measurements were carried out in triplicates using 1.0 cm quartz cuvettes.

1.7.1. Linear dichroism

Linear dichroism (LD) measurements were performed on a Jasco-1500 magnetic circular dichroism spectropolarimeter, converted for LD, and equipped with an IBM PC and a Jasco J interface. Linear dichroism was defined as:

$$LD(\lambda) = A_{//}(\lambda) - A_{\perp}(\lambda) \qquad (S3)$$

$A_{//}$ and $A_{\perp}$ are defined as the absorbances of the sample when polarised light was oriented either parallel or perpendicular to the flow direction. The orientation was produced by a couette cell that rotated at a shear gradient of ± 1000 rpm. Each spectrum was accumulated in triplicates from 200 – 500 nm and recorded at 37 °C at [Au(III) chelate]/[ctDNA] = r = 0.25, 0.5, 1 and 2. ctDNA concentration used was at 100 µM.

1.7.2. DNA Circular dichroism

Circular dichroism (CD) measurements were performed on a Jasco-1500 magnetic circular dichroism spectropolarimeter. Measurements were carried out in triplicates using 1.0 cm quartz cuvettes. ctDNA concentration was used at 100 µM and each spectrum was accumulated in triplicates from 200 – 500 nm and recorded at 37 °C at [Au(III) chelate]/[ctDNA] = r = 0.25, 0.5, 1 and 2.

1.7.3. DNA UV-vis titration experiments

UV-vis absorption titration studies with AuL1, AuL2 and AuL3 and calf thymus DNA (ctDNA) were carried out to investigate the binding mechanism between the Au(III) chelates and DNA in KH_2PO_4 buffer (50 mM, pH 7.5). The titration involved the addition of incremental amounts of a ctDNA solution (4.20 mM, in 50 mM KH_2PO_4, pH 7.5 buffer) to a fixed concentration of the Au(III) chelate (30 µM) in a quartz cuvette with a pathlength of 1 cm. The gold absorption band was monitored at 382 nm, spectral changes at 382 nm would indicate the interaction of the Au(III) chelates with ctDNA. Figs. 2 and S37 shows the change in the absorption spectrum of the three Au(III) chelates of a representative experiment of three replicates.

The highest ratio of [ctDNA]:[AuL1], [ctDNA]:[AuL2] and [ctDNA]:[AuL3] obtained, before the spectrophotometer could no longer detect accurate absorbance readings were 11.6:1, 11.6:1 and 17.5:1, respectively. The spectrum illuminated with black represents the absorbance spectrum of the Au(III) chelates prior to the addition of ctDNA. And the various spectrum below represents the absorbance spectrum of Au(III)

chelates in the presence of increasing concentrations of ctDNA. The concentration of ctDNA used for **AuL1** and **AuL2** ranged from 0 – 348 x 10^{-6} M (Fig.2 and S37) and for **AuL3** ranged from 0 – 542 x 10^{-6} M (Fig. S32).

1.8. NCI-60 cytotoxicity screens

The human tumour cell lines of the cancer screening panel are grown in RPMI 1640 medium containing 5% foetal bovine serum and 2 mM of the amino acid L-glutamine. For most screening experiments, cells are inoculated into 96-well microtiter plates in 100 µL of solution with plating densities between 5 × 10^3 and 4 × 10^4 cells per well, depending on the doubling time of a particular cell line. After cell inoculation, the 96- well plates are incubated at 37 °C, with an atmospheric composition of 5% CO2 and 95% air at 100% relative humidity for 24 hours prior to addition of experimental drugs. After 24 hours, two plates of each cell line are fixed *in situ* with tricarboxylic acid (TCA), to represent a measurement of the cell population for each cell line at the time of drug addition (Tz). Experimental drugs are dissolved in DMSO at a concentration 400× that of the maximum desired test concentration and stored frozen prior to use. As required, an aliquot of frozen drug concentrate is thawed and diluted to twice the desired maximum test concentration with appropriate medium, containing 50 µg ml^{-1} of gentamicin (an aminoglycoside antibiotic). Four, 10-fold serial dilutions are carried out to provide a total of five drug concentrations as well as a control. Aliquots of 100 µl of these different drug dilutions are added to the appropriate wells already containing 100 µl of medium, resulting in the required final drug concentrations.

Following drug addition, the plates are incubated for an additional 48 hours at 37 °C, with an atmosphere consisting of: 5% CO2, 95% air, and 100% relative humidity. For adherent cells, the assay is terminated by the addition of cold TCA. Cells are fixed *in situ* by the gentle addition of 50 µl of cold 50% (w/v) TCA (final concentration, of 10% TCA) and incubated for 1 hour at 4 °C. The supernatant liquid is discarded, and the plates are washed repeatedly with water and air dried. Sulforhodamine B (SRB) solution (100 µl) with a concentration of 0.4% (w/v) in 1% acetic acid is added to each well, and plates are incubated for 10 minutes at room temperature. After staining, unbound dye is removed by washing repeatedly with 1% acetic acid solution and the plates are again air dried. Bound stain is subsequently solubilised with 10 mM tris(hydroxymethyl)aminomethane base, and the absorbance is read on an automated plate reader at a wavelength of 515 nm, which corresponds to _max of the dye used. This is a method of transcriptional and translational (MTT) assay. For suspension cells, the methodology is the same as above with the exception that the assay is terminated by fixing settled cells at the bottom of the wells by adding 50 µl of 80% TCA (final concentration, 16% TCA).

Using the seven absorbance measurements: time zero, (Tz), control growth, (C), and test growth in the presence of the Au(III) chelate at the five concentration levels (Ti), the percentage growth is calculated at each of the drug concentrations. Percentage growth inhibition is calculated as:

$$\left(\frac{T_i - T_z}{C - T_2}\right) x\ 100\% \quad \text{(S4)}$$

$$\left(\frac{T_i - T_z}{T_2}\right) x\ 100\% \quad \text{(S5)}$$

Eq. S4 is applicable for concentration for which Ti ≥ Tz, while eq. S4 is applicable for drug concentrations at which Ti < Tz.

Three dose response parameters are then calculated for each experimental compound from the data collected. Firstly, GI50 is calculated from:

$$\left(\frac{T_i - T_z}{C - T_z}\right) x\ 100\% = 50 \quad \text{(S6)}$$

1.9. Molecular Docking

Molecular docking was performed by methods previously reported.[9,10]

2. Figures and Tables

2.1. General characterisation

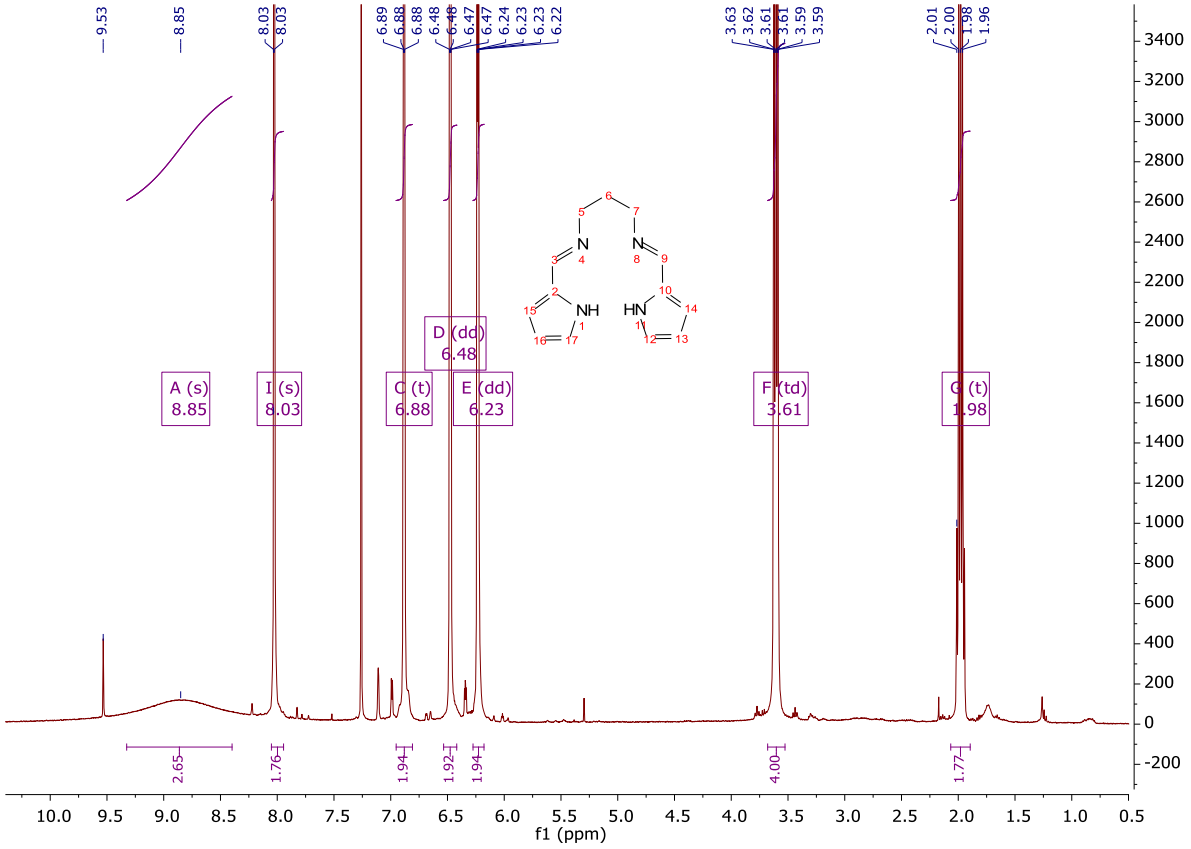


Fig. S7 ^{1}H NMR of **H_2L1** in $CDCl_3$

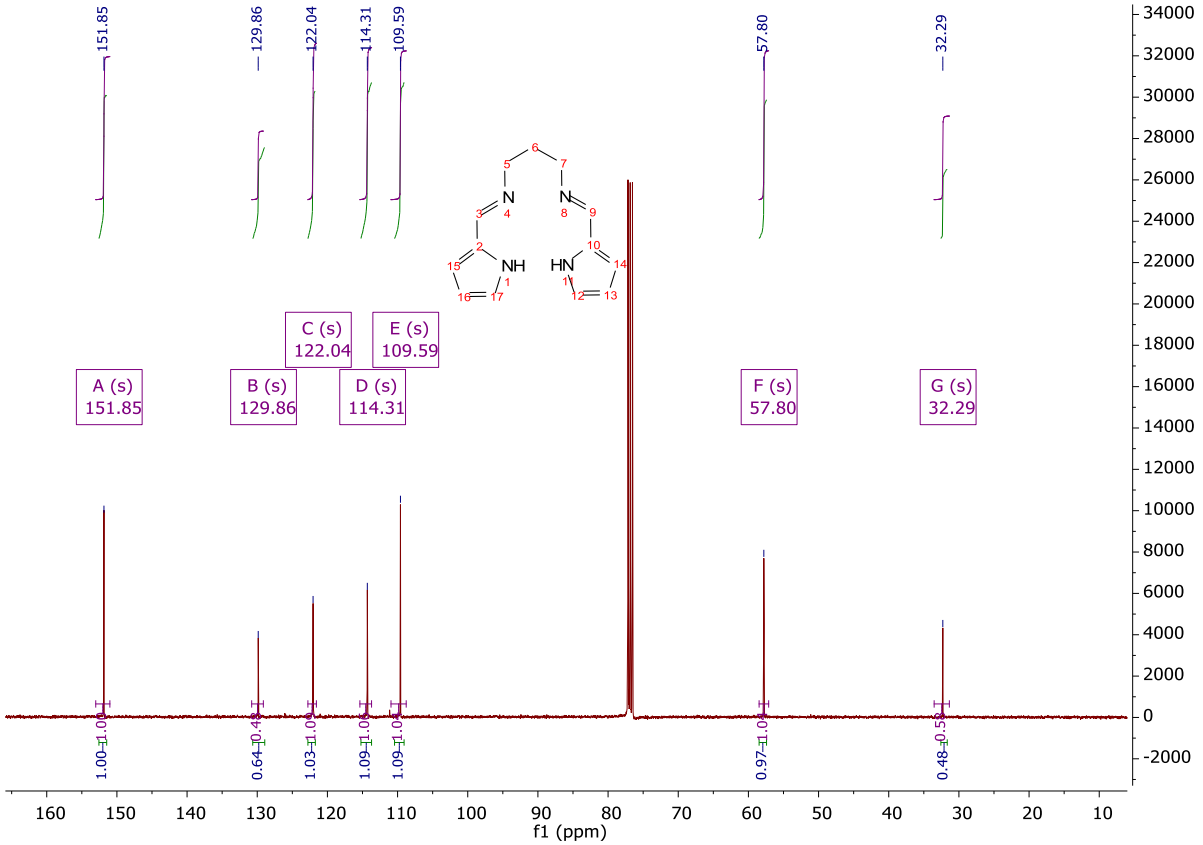


Fig. S8 ^{13}C NMR of H_2L1 in $CDCl_3$

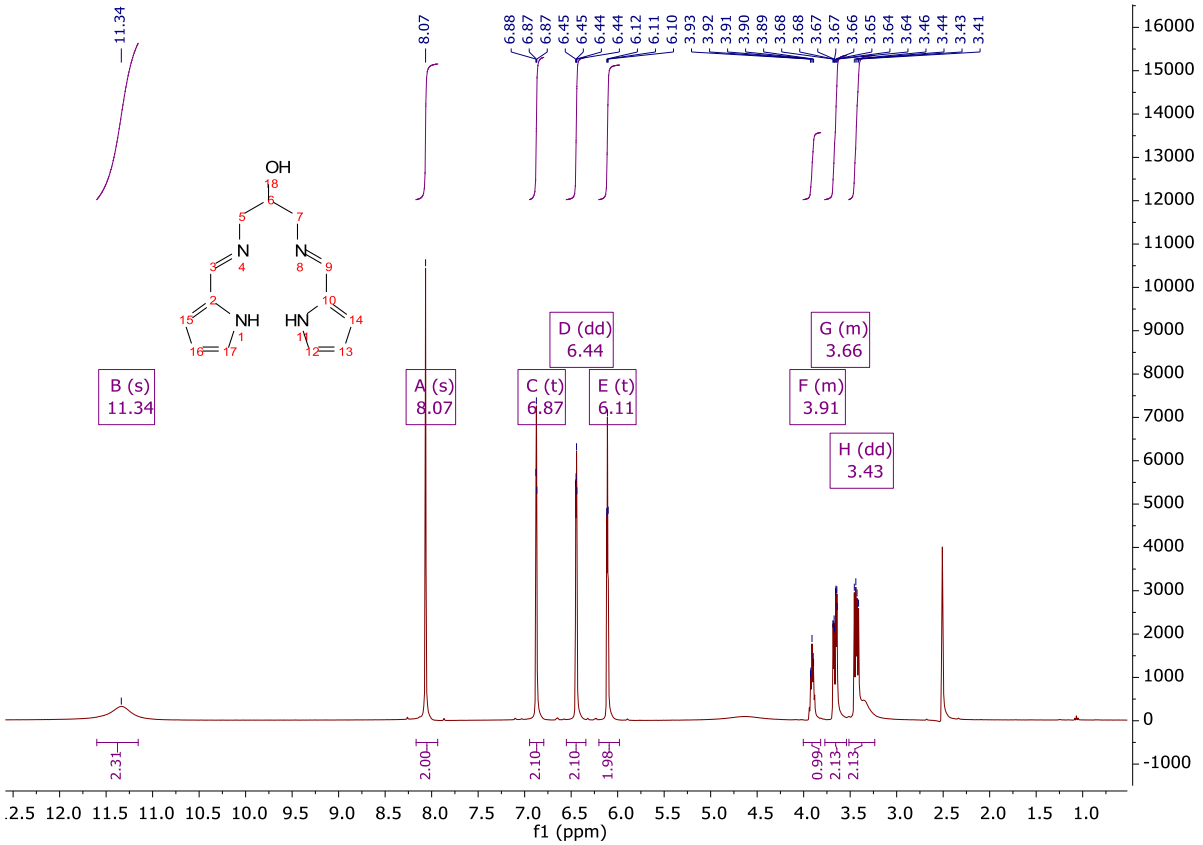


Fig. S9 ^{1}H NMR of H_2L2 in CD_3OD

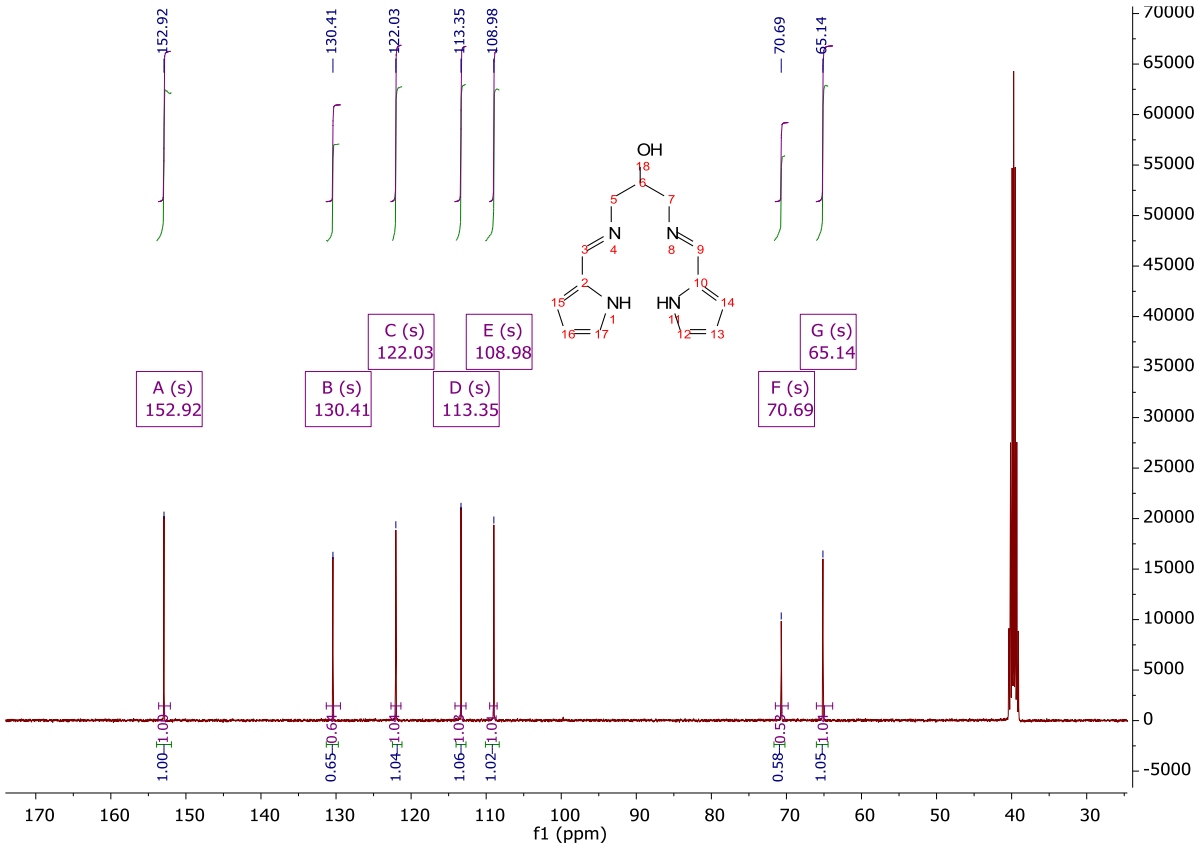


Fig. S10 ^{13}C NMR of H_2L2 in CD_3OD

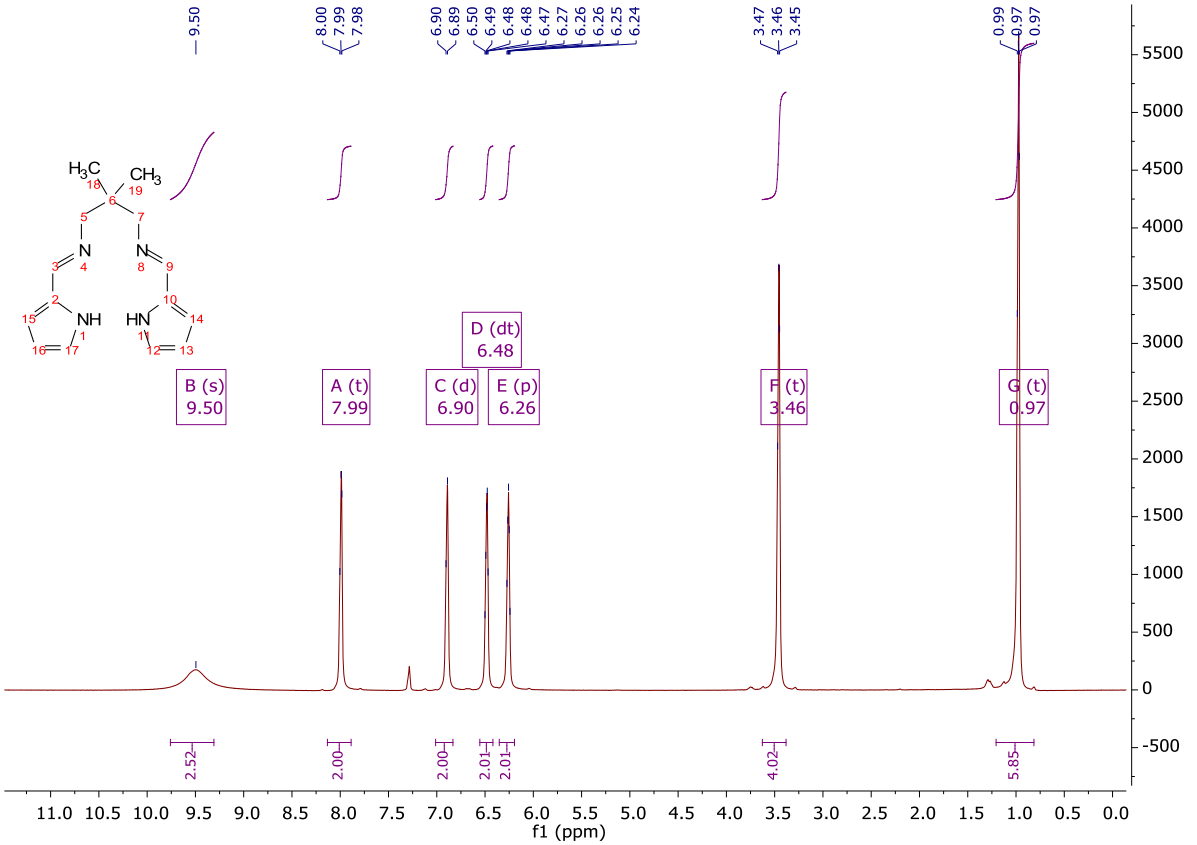


Fig. S11 ^{1}H NMR of **H_2L3** in $CDCl_3$

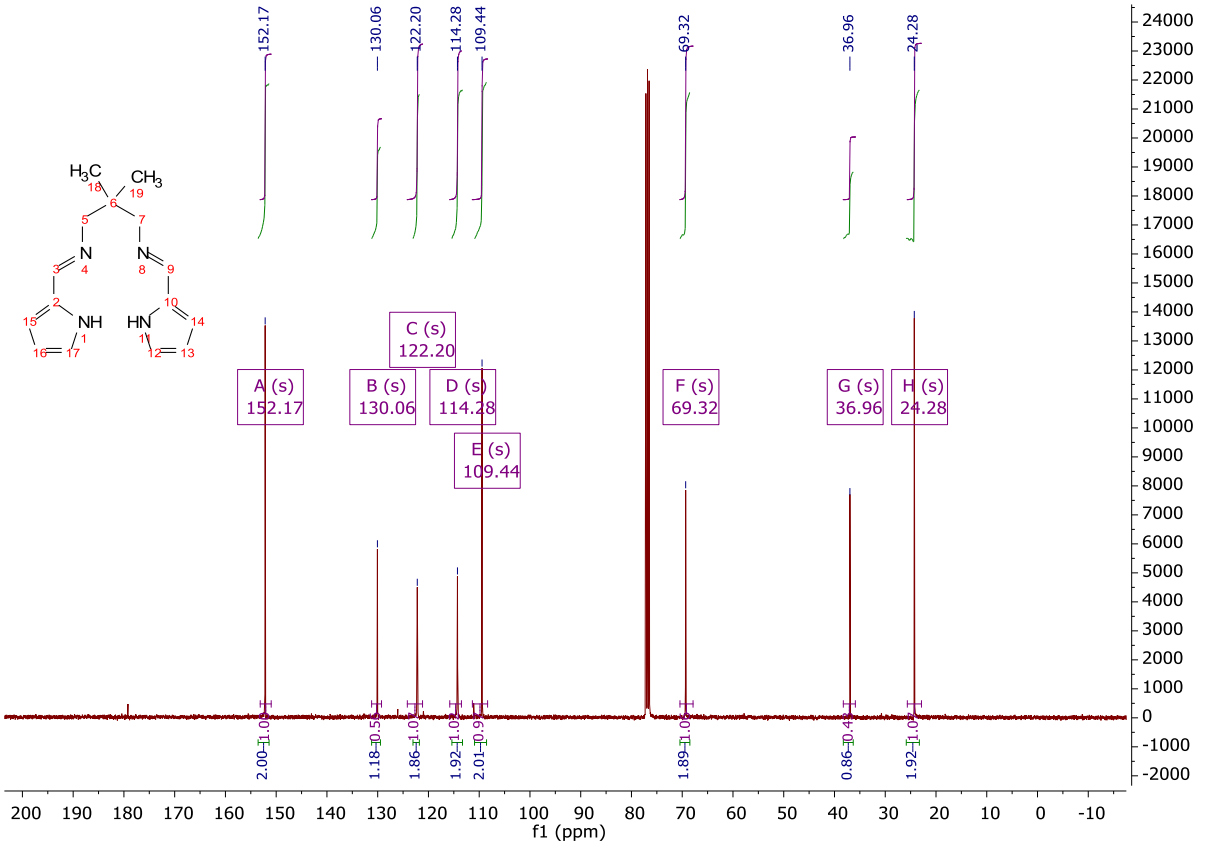


Fig. S12 ^{13}C NMR of H_2L3 in $CDCl_3$

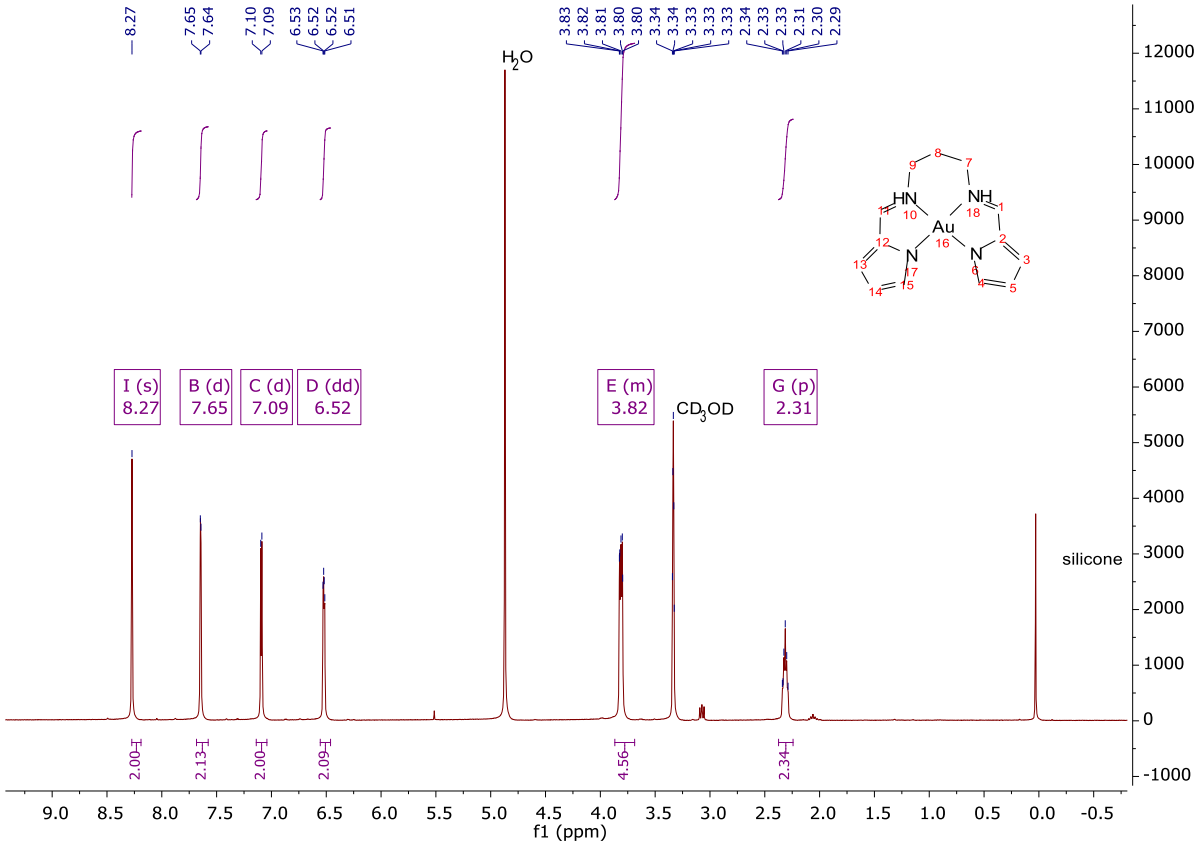


Fig. S13 ^{1}H NMR of **AuL1** in CD_3OD

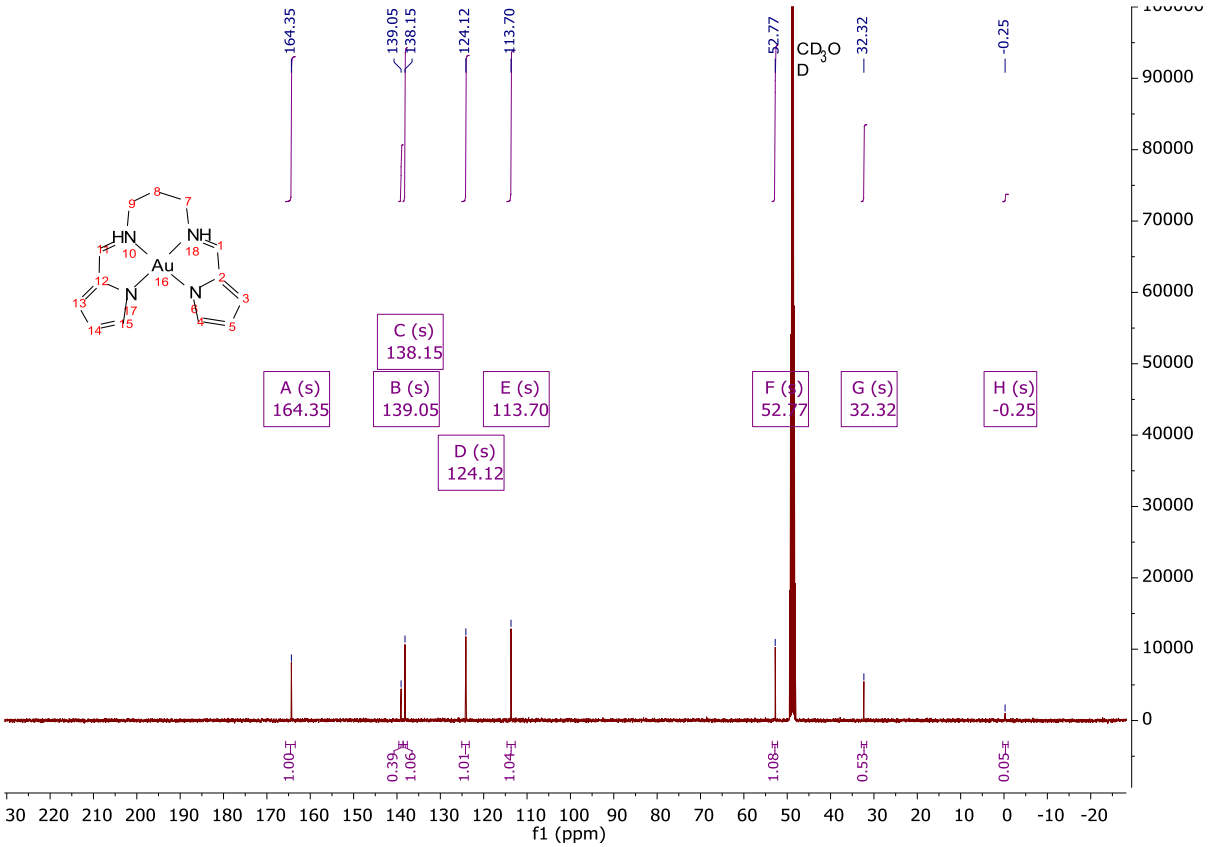


Fig. S14 ^{13}C NMR of **AuL1** in CD_3OD

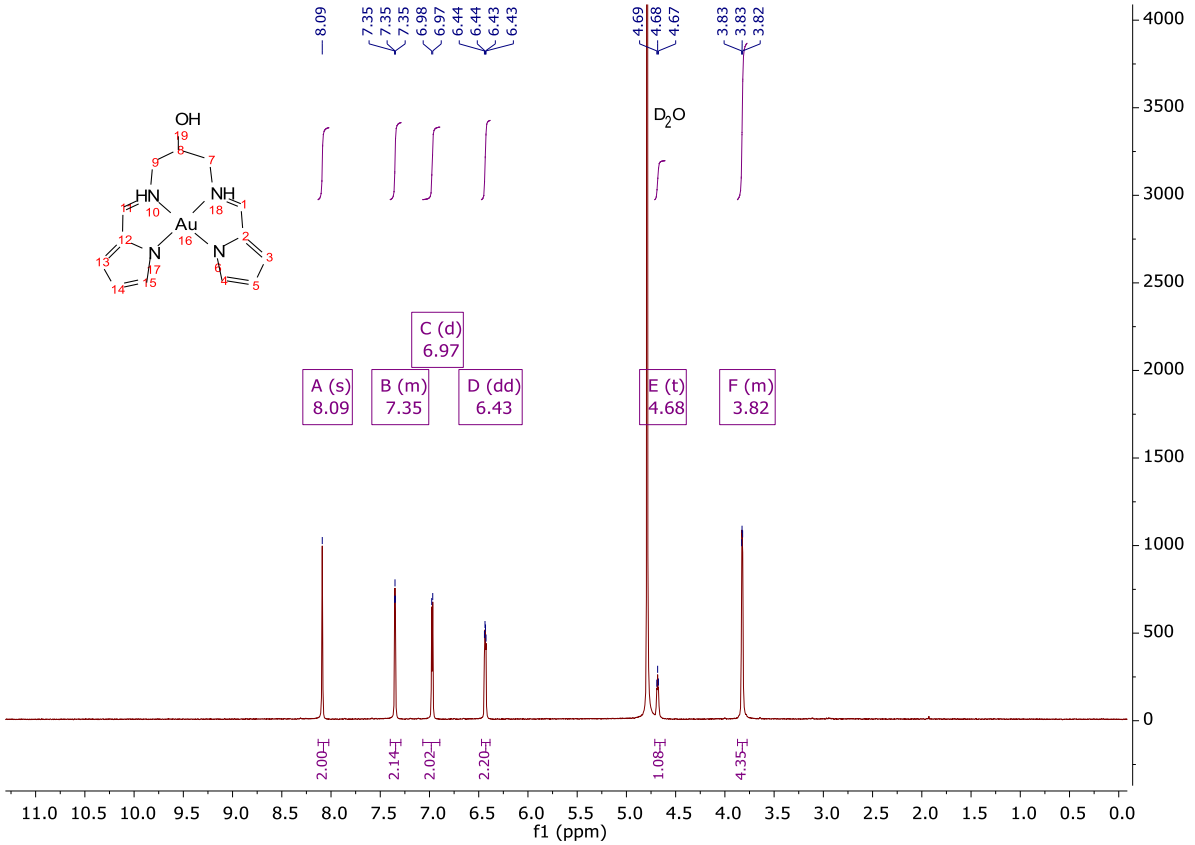


Fig. S15 ^{1}H NMR of **AuL2** in D_2O

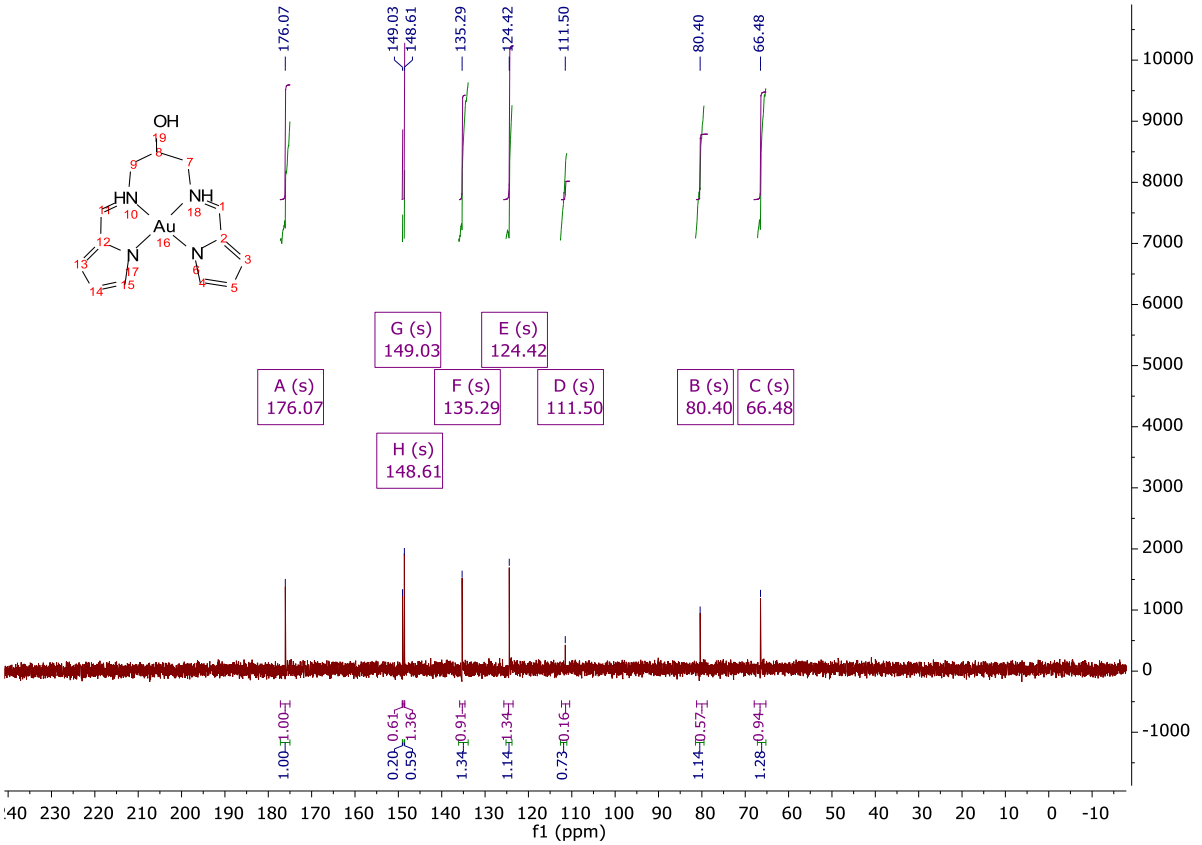


Fig. S16 ^{13} NMR of **AuL2** in D_2O

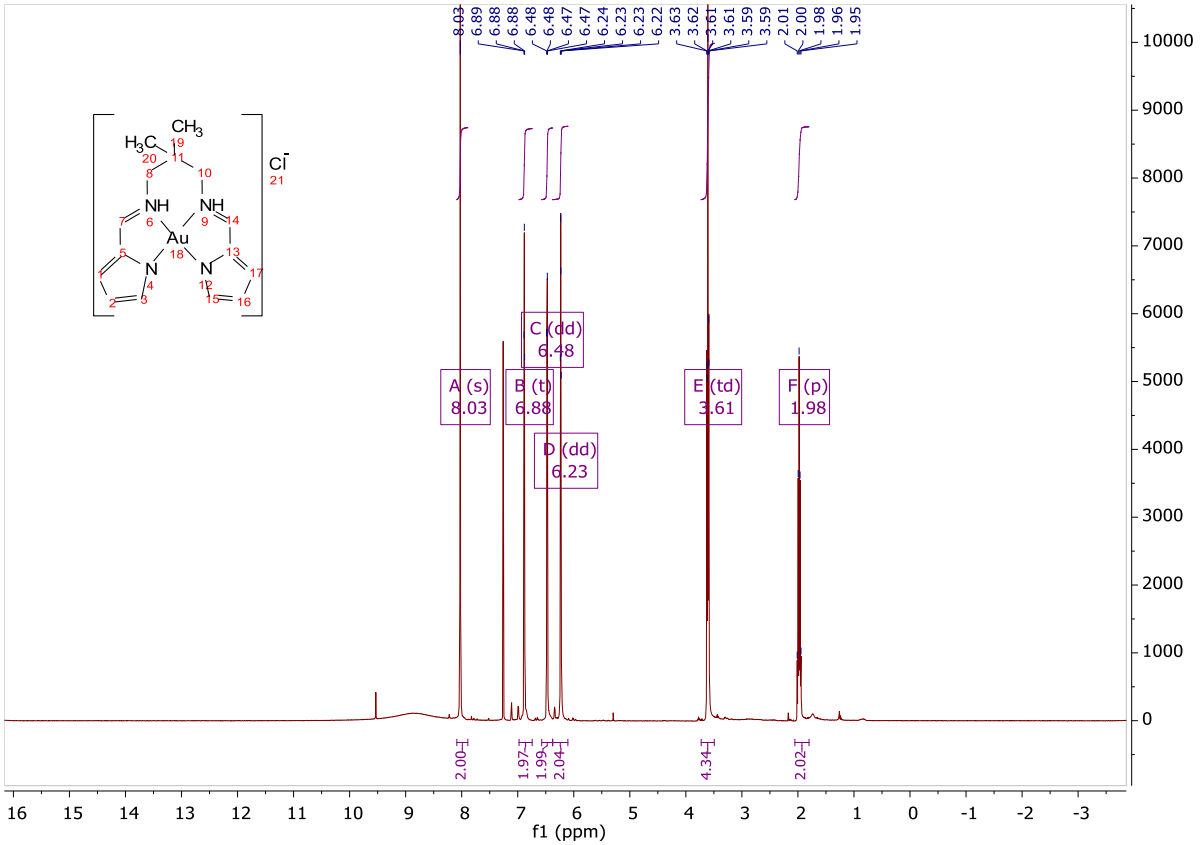


Fig. S17 ^{1}H NMR of AuL3in DMSO–*d*6

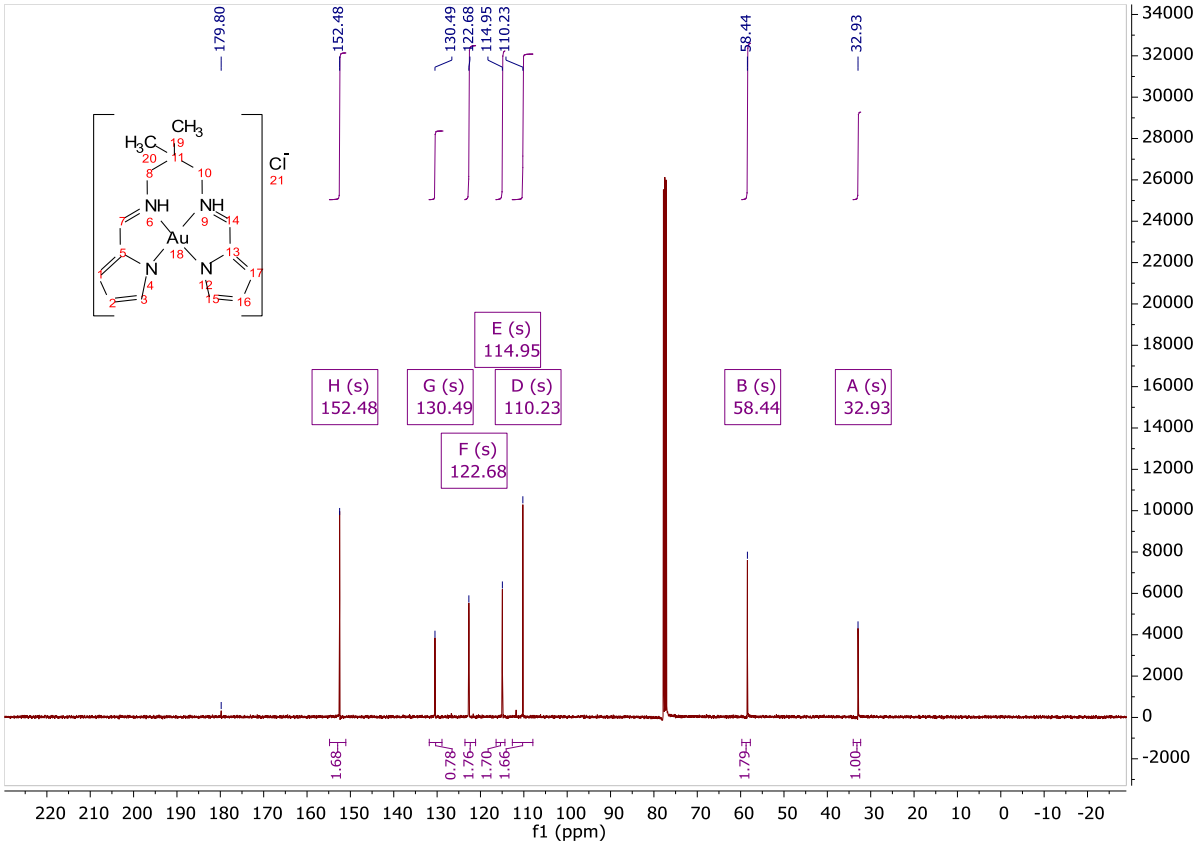


Fig. S18 ^{13}C NMR of AuL3in DMSO–*d*6

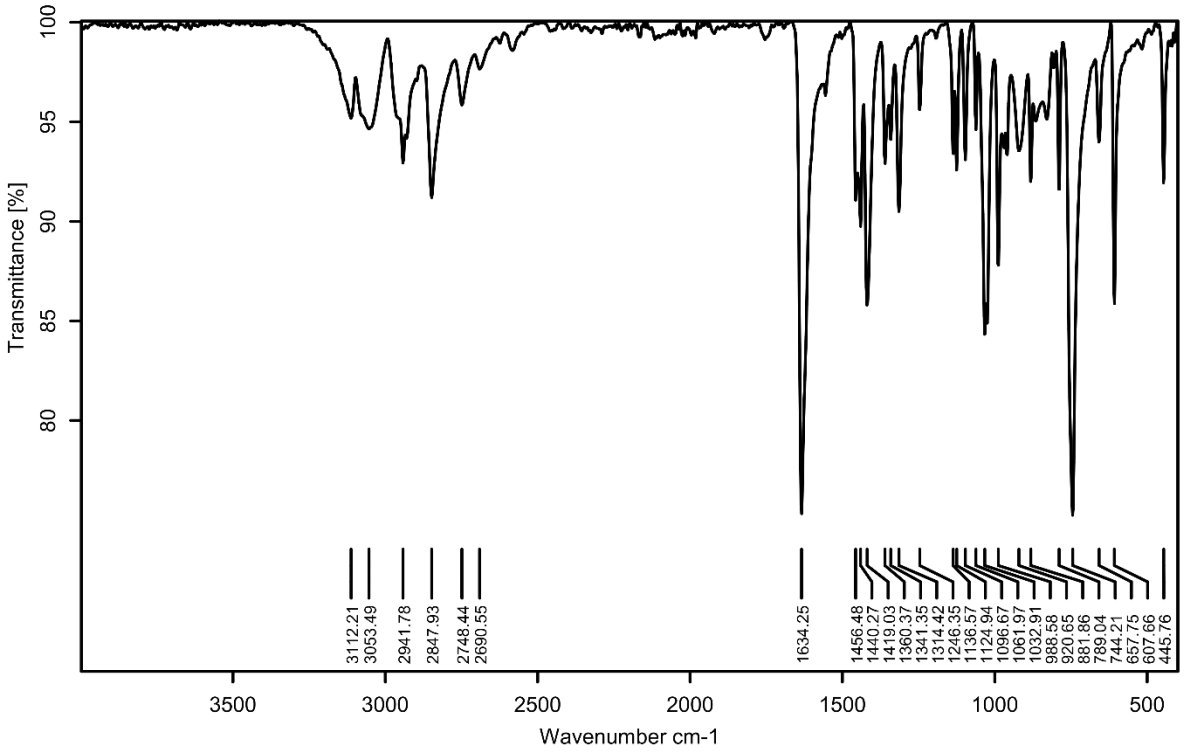


Fig A. S19 FTIR spectrum of H_2L1 recorded as a crushed powder sample at 298 K.

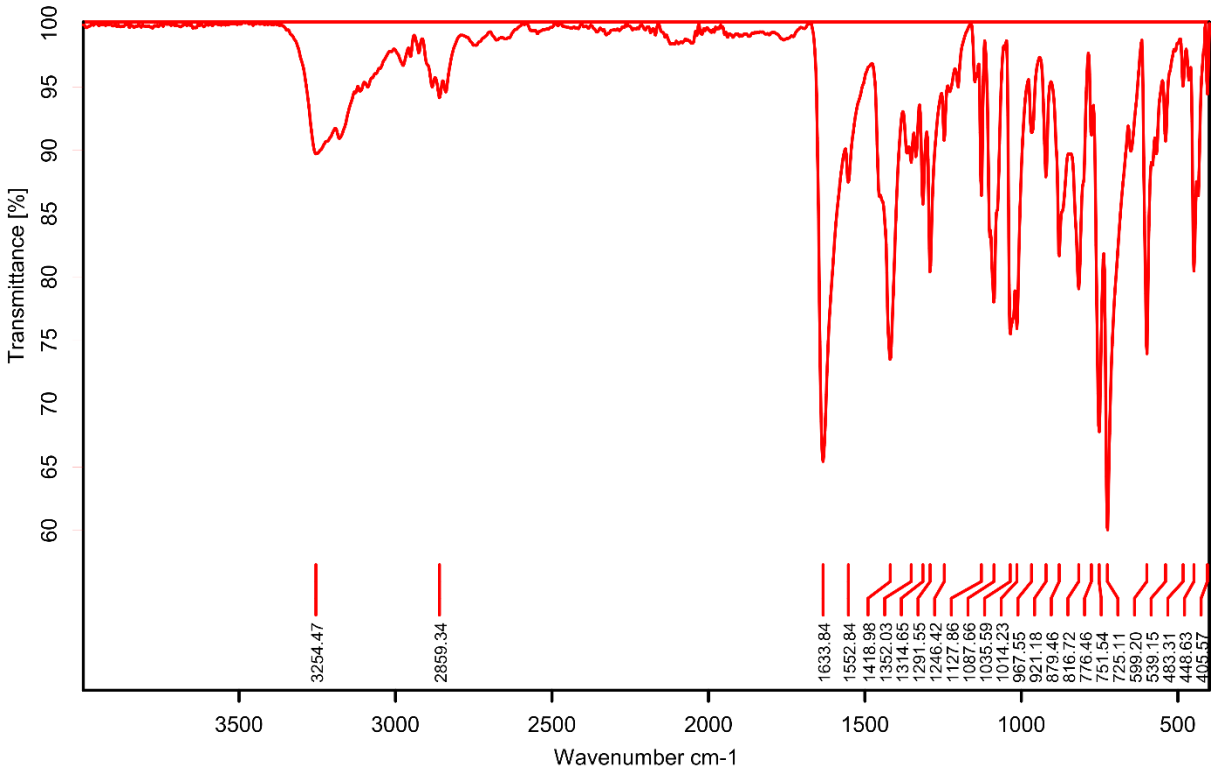


Fig. S20 FT-IR spectrum of H_2L2 recorded as a crushed powder sample at 298 K.

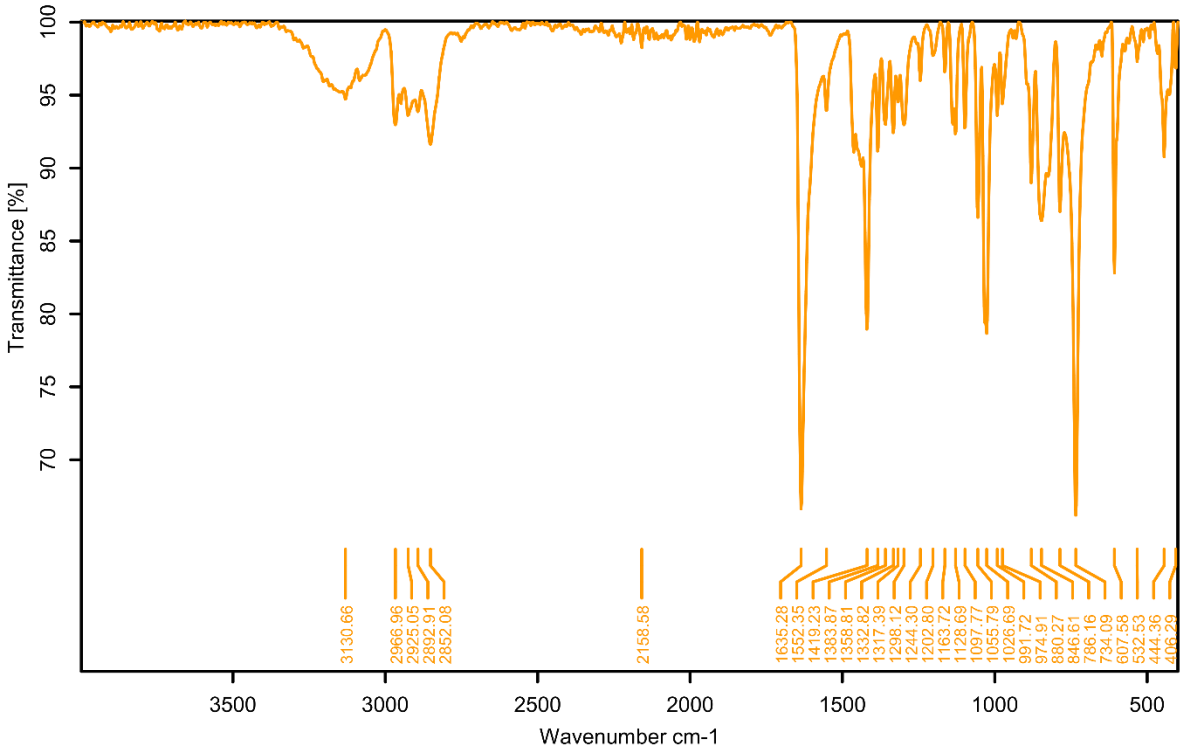


Fig. S21 FT-IR spectrum of H_2L3 recorded as a crushed powder sample at 298 K.

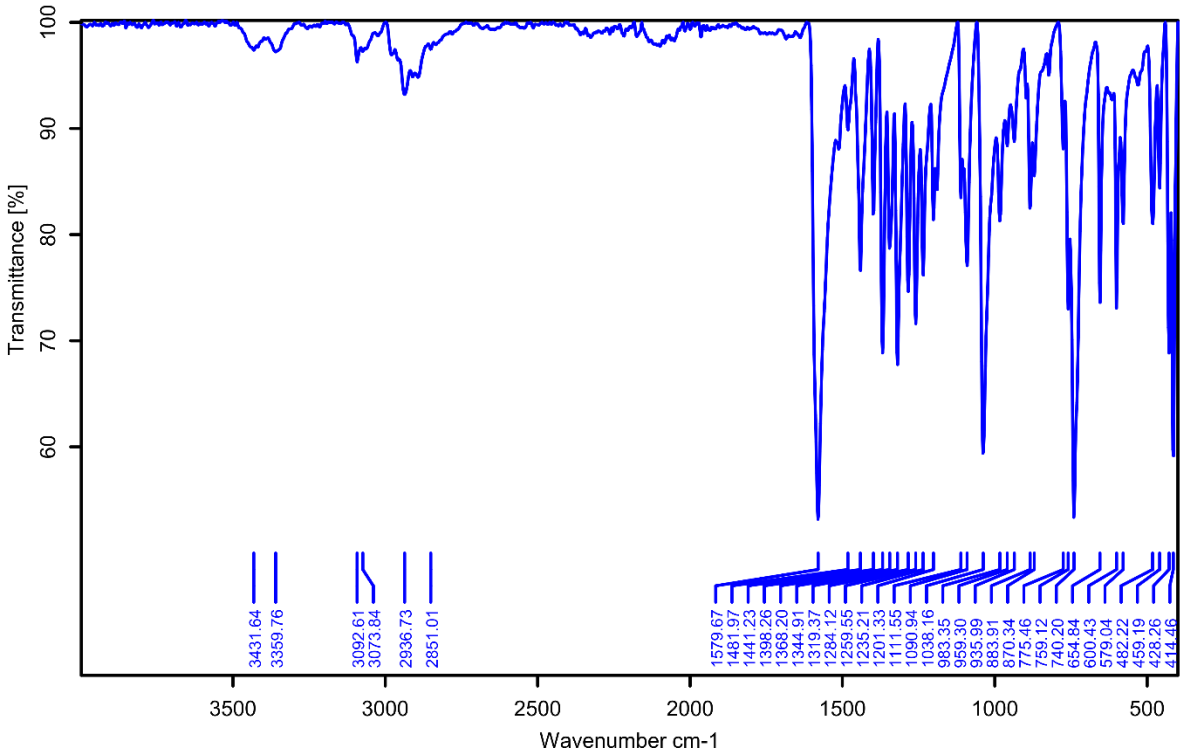


Fig. S22 FT-IR spectrum of AuL1 recorded as a crushed powder sample at 298 K.

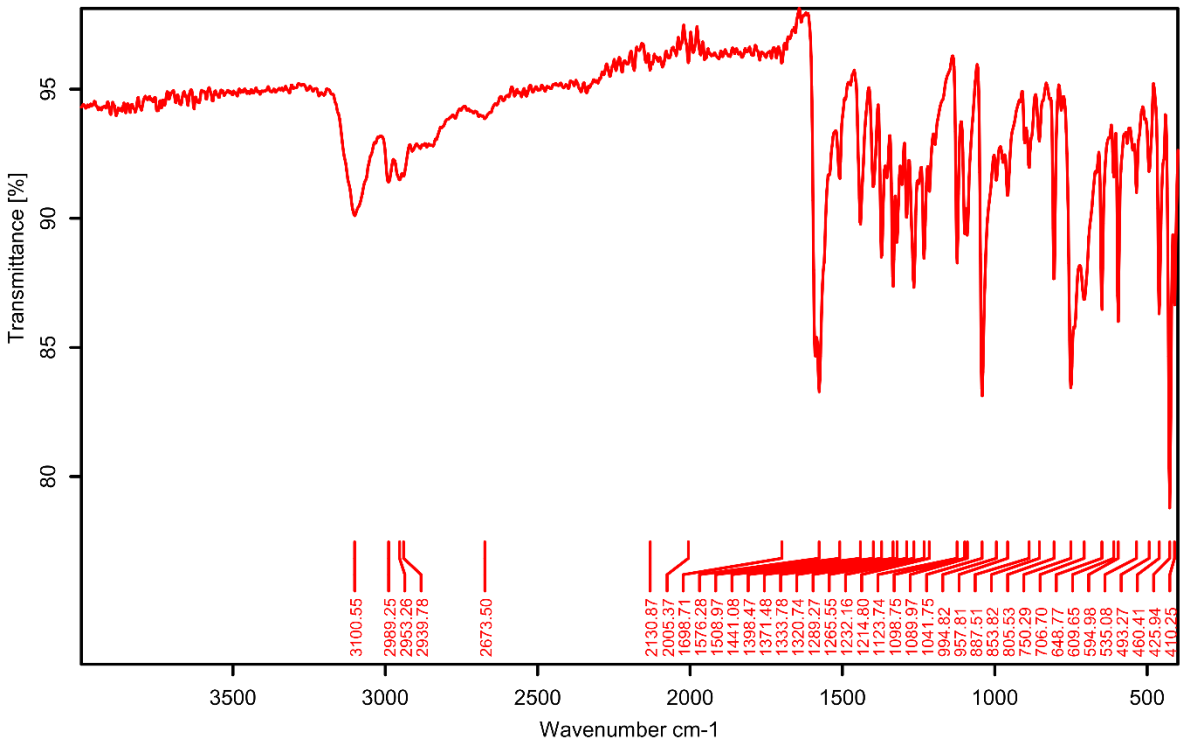


Fig. S23 FT-IR spectrum of **AuL2** recorded as a crushed powder sample at 298 K.

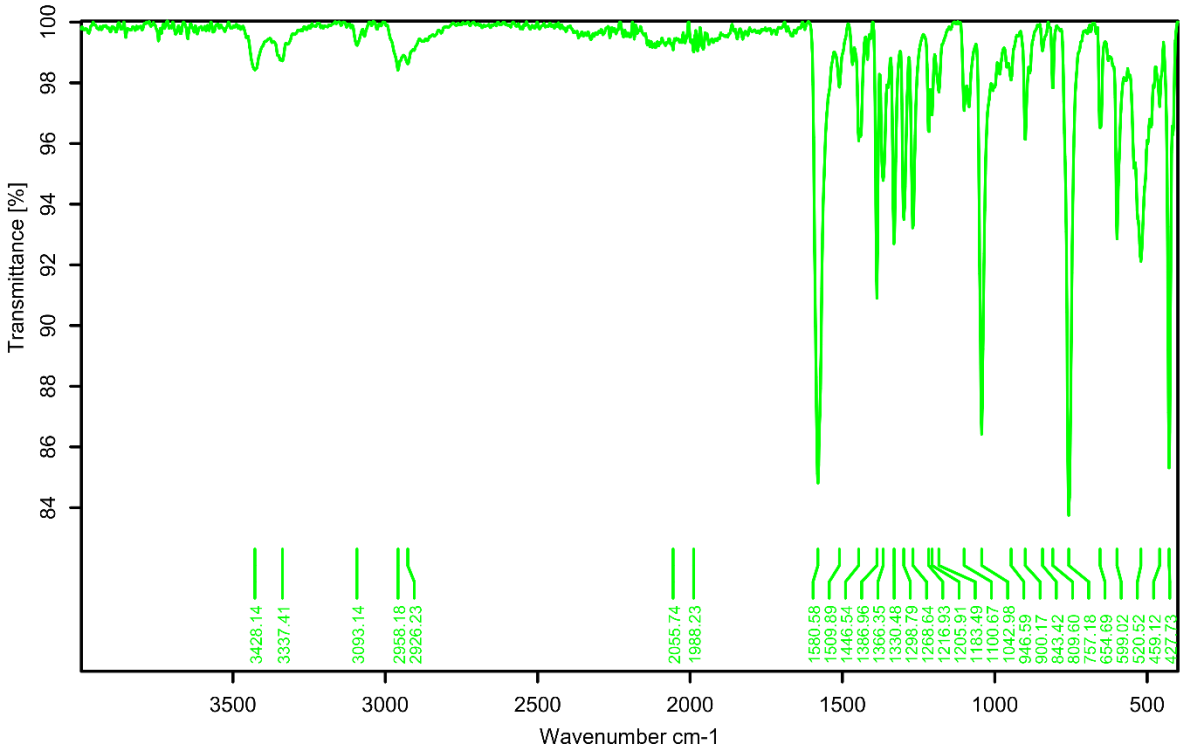


Fig. S24 FT-IR spectrum of **AuL3** recorded as a crushed powder sample at 298 K.

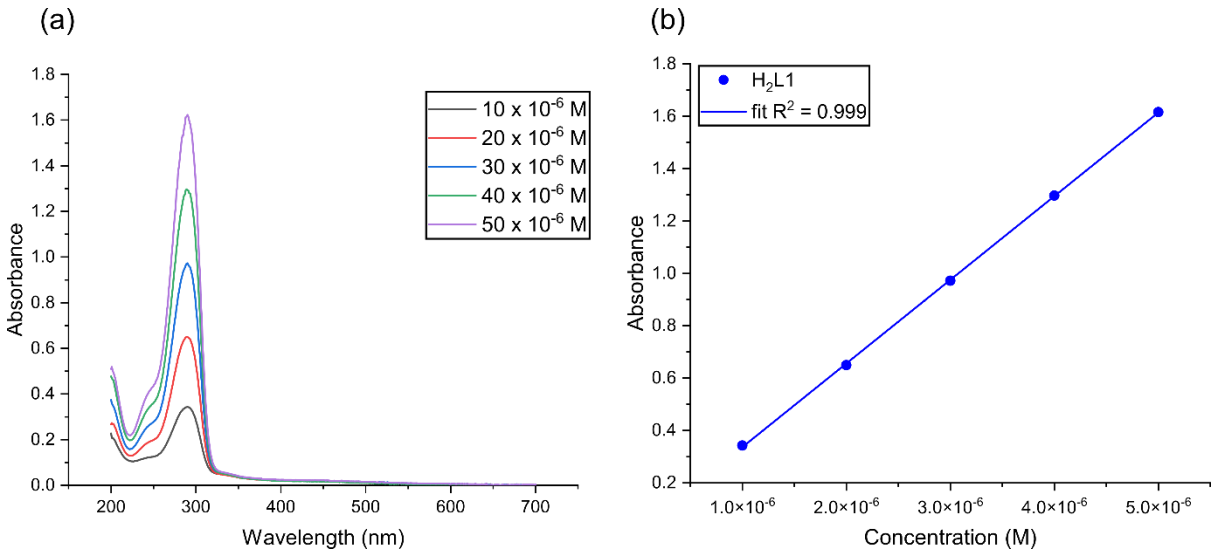


Fig. S25 UV-visible spectrum of **H_2L1** recorded in ethanol at 298 K as a function of concentration. (b) the slopes of Beer- Lambert law plots at the relevant band maxima.

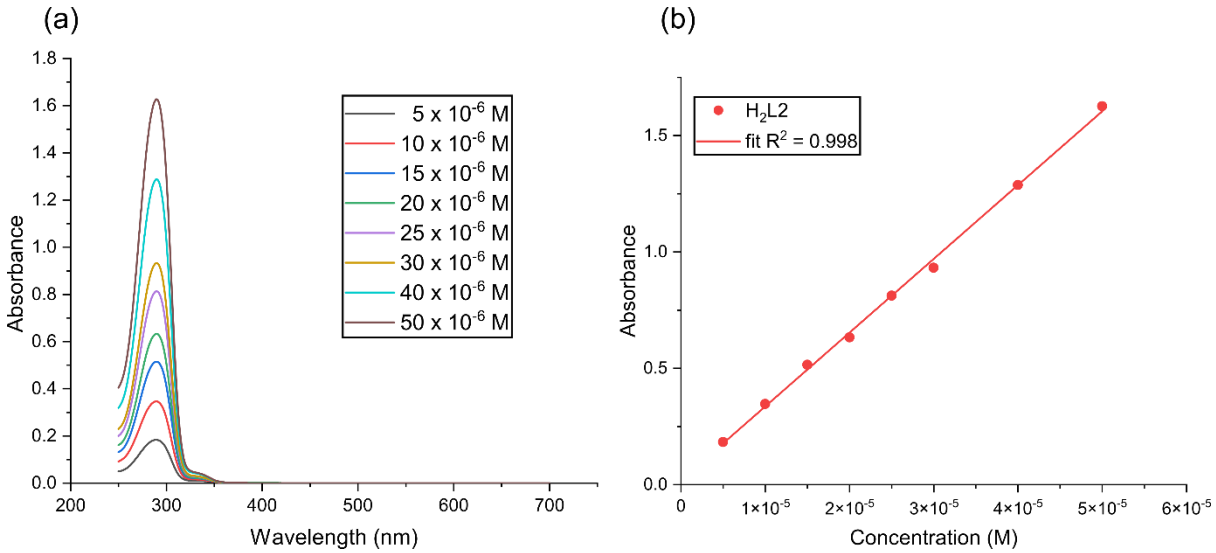


Fig. S26 UV-visible spectrum of **H_2L2** recorded in ethanol at 298 K as a function of concentration. (b) the slopes of Beer- Lambert law plots at the relevant band maxima.

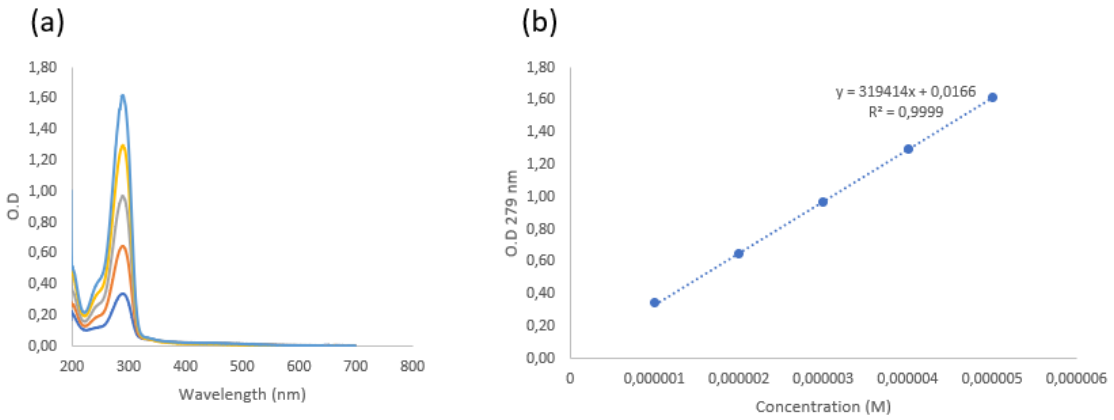


Fig. S27 UV-visible spectrum of **H_2L3** recorded in ethanol at 298 K as a function of concentration. (b) the slopes of Beer- Lambert law plots at the relevant band maxima.

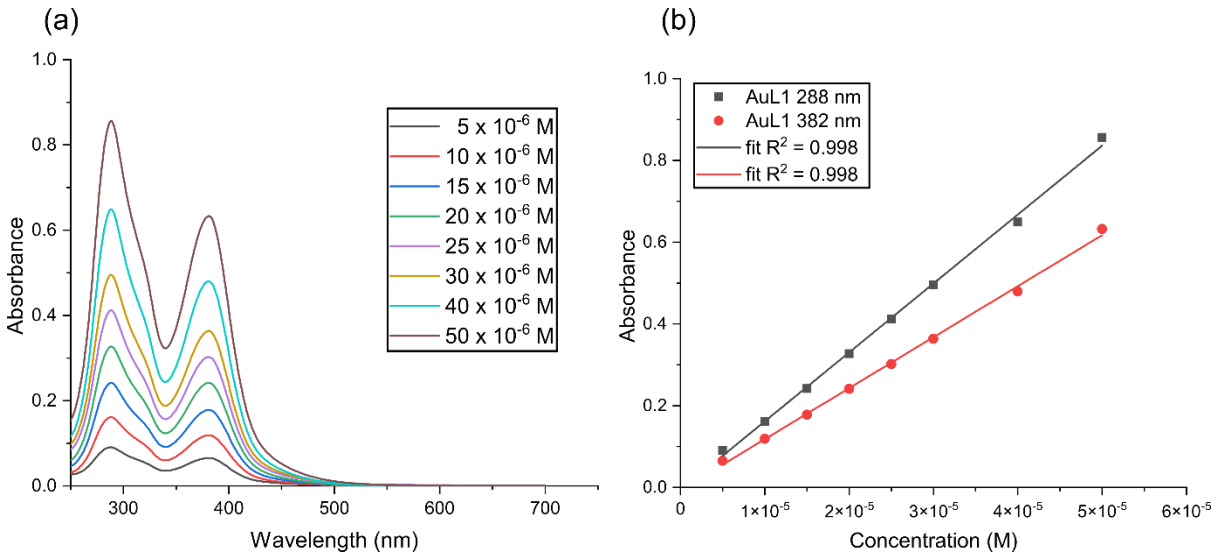


Fig. S28 UV-visible spectrum of **AuL1** recorded in methanol at 298 K as a function of concentration. (b) the slopes of Beer- Lambert law plots at the relevant band maxima.

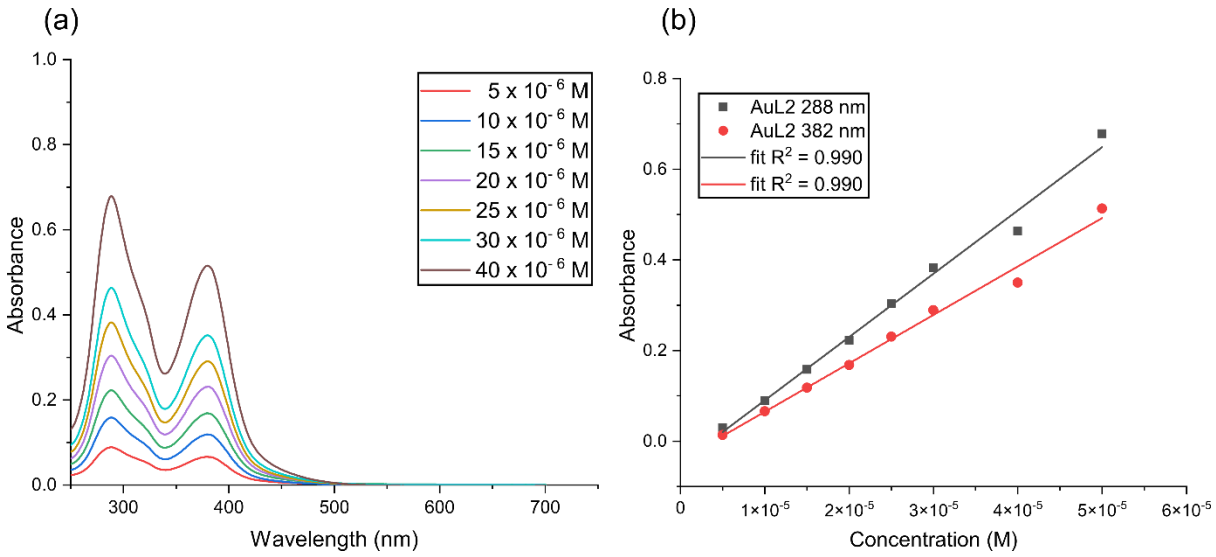


Fig. S29 UV-visible spectrum of **AuL2** recorded in methanol at 298 K as a function of concentration. (b) the slopes of Beer- Lambert law plots at the relevant band maxima.

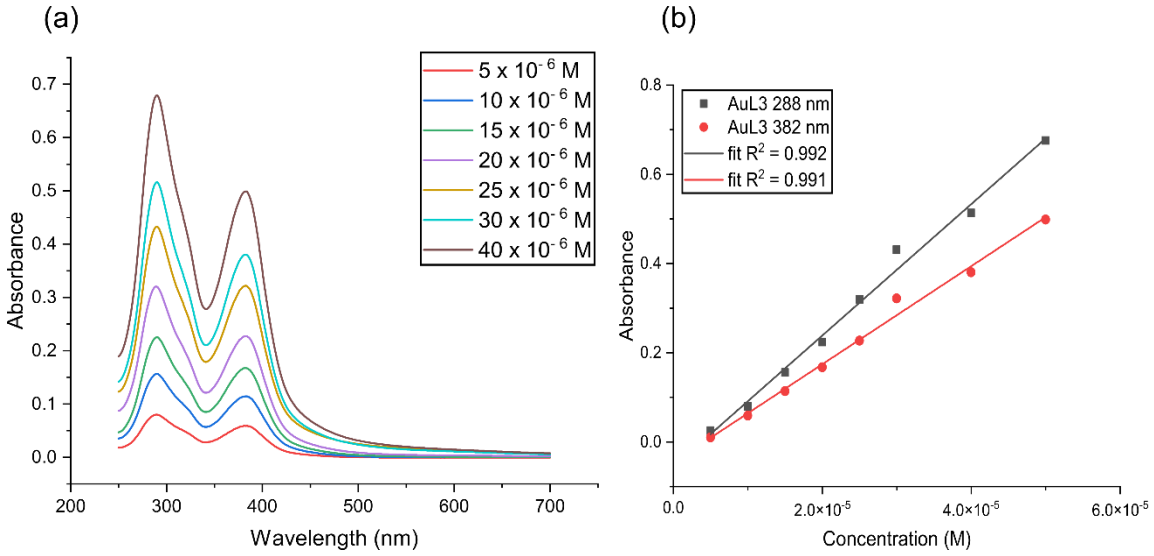


Fig. S30 UV-visible spectrum of **AuL3** recorded in ethanol at 298 K as a function of concentration. (b) the slopes of Beer- Lambert law plots at the relevant band maxima.

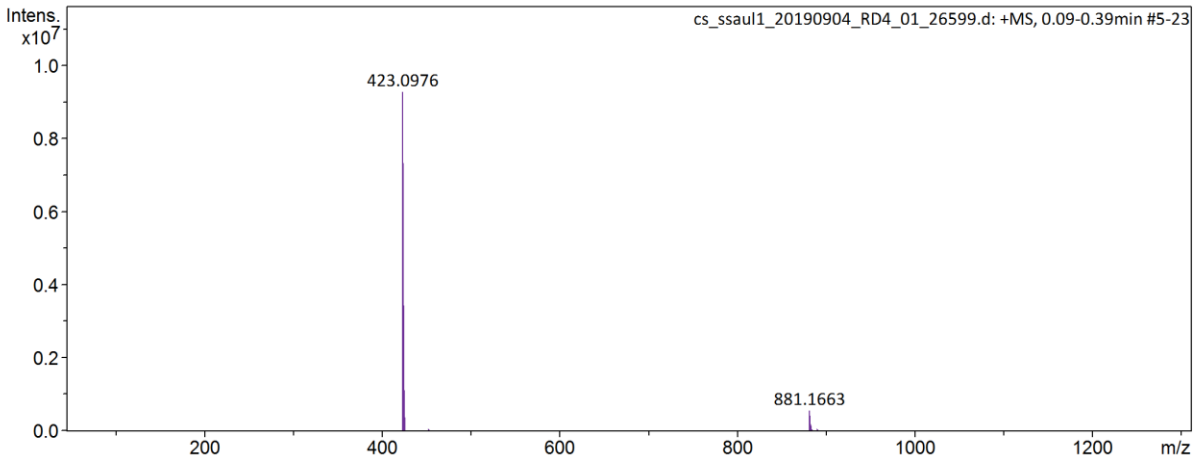


Fig. S31 ESI-MS spectrum of **AuL1**. The solid sample was dissolved in methanol with 0.1% formic acid (V/V) and the spectrum was recorded in positive ESI mode.

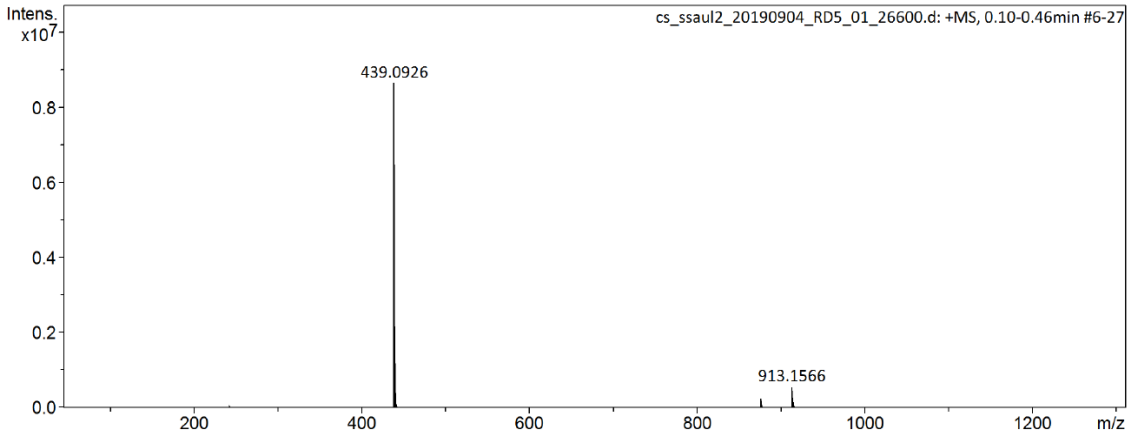


Fig. S32 ESI-MS spectrum of **AuL2**. The solid sample was dissolved in methanol with 0.1% formic acid (V/V) and the spectrum was recorded in positive ESI mode.

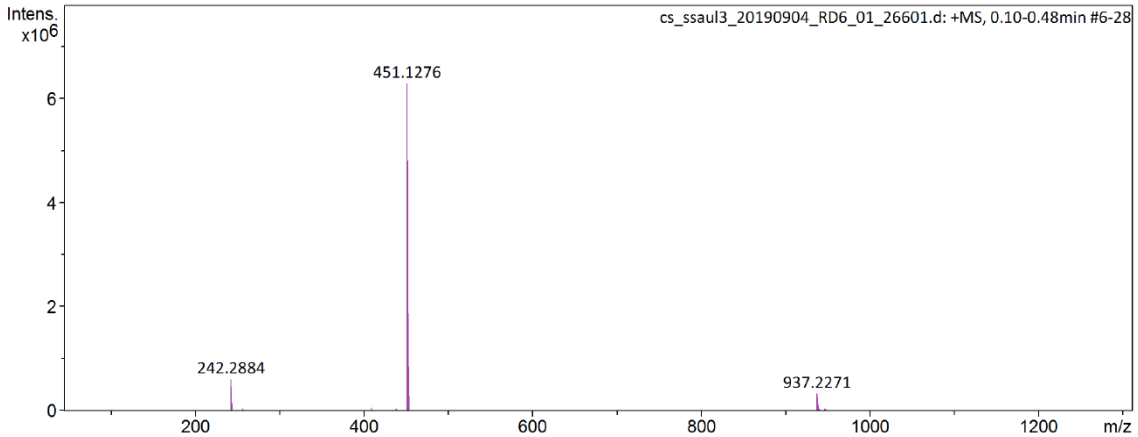


Fig. S33 ESI-MS spectrum of **AuL3**. The solid sample was dissolved in methanol with 0.1% formic acid (V/V) and the spectrum was recorded in positive ESI mode.

2.2. X-ray crystallography

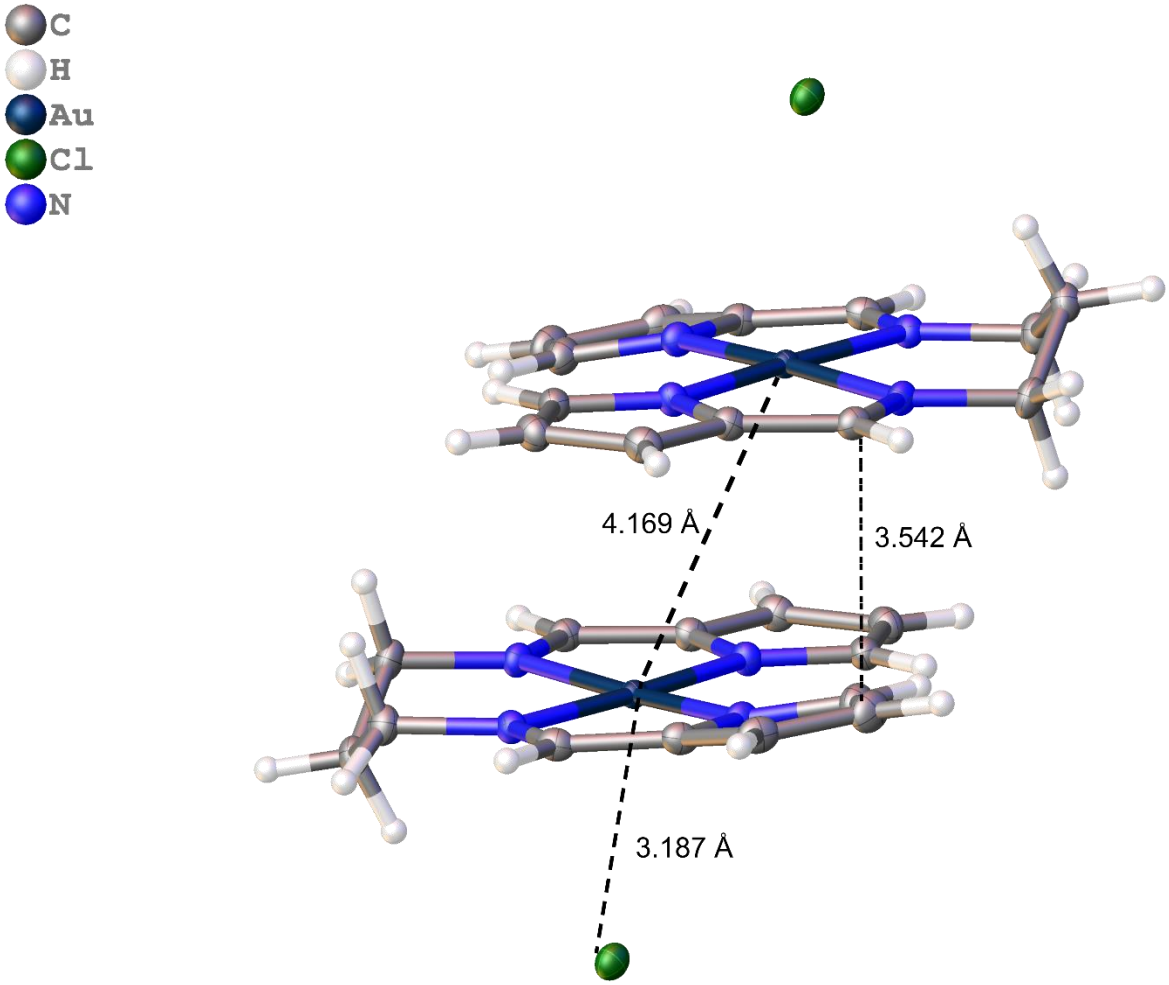


Fig. S34 View of the π-π dimers formed by the cation of compound **AuL1** in the crystalline solid state. Bond distances MPS, Au···Au separation and Au···Cl^- is measured. The chelates are represented as 50% thermal ellipsoids for non-H atoms; H atoms are shown as capped cylinders. Atom colour code white H, grey C, blue N, dark blue Au, and dark green Cl.

Comment. The ASU for **AuL1** consists of a single Au(III) chelate and its counter Cl^- anion. Within the packing, there are two adjacent **AuL1** molecules arranged in an inverted head-to-tail π stacked dimers. The have a mean plane symmetry (MPS) of 3.542 Å and Au···Au separation of 4.169 Å. There are cation–π interactions with a distance of 3.442 Å between the C=C of the pyrrole moieties and Au(III) ions of the inverted adjacent molecules. This suggest that the **AuL1** chelate has the potential for cationic–π stacking with DNA base pairs (**Fig.**). The **AuL1** dimers are potentially further stabilised by electrostatic interactions between the Au(III) metal ion and the Cl^- anion (3.187 Å).

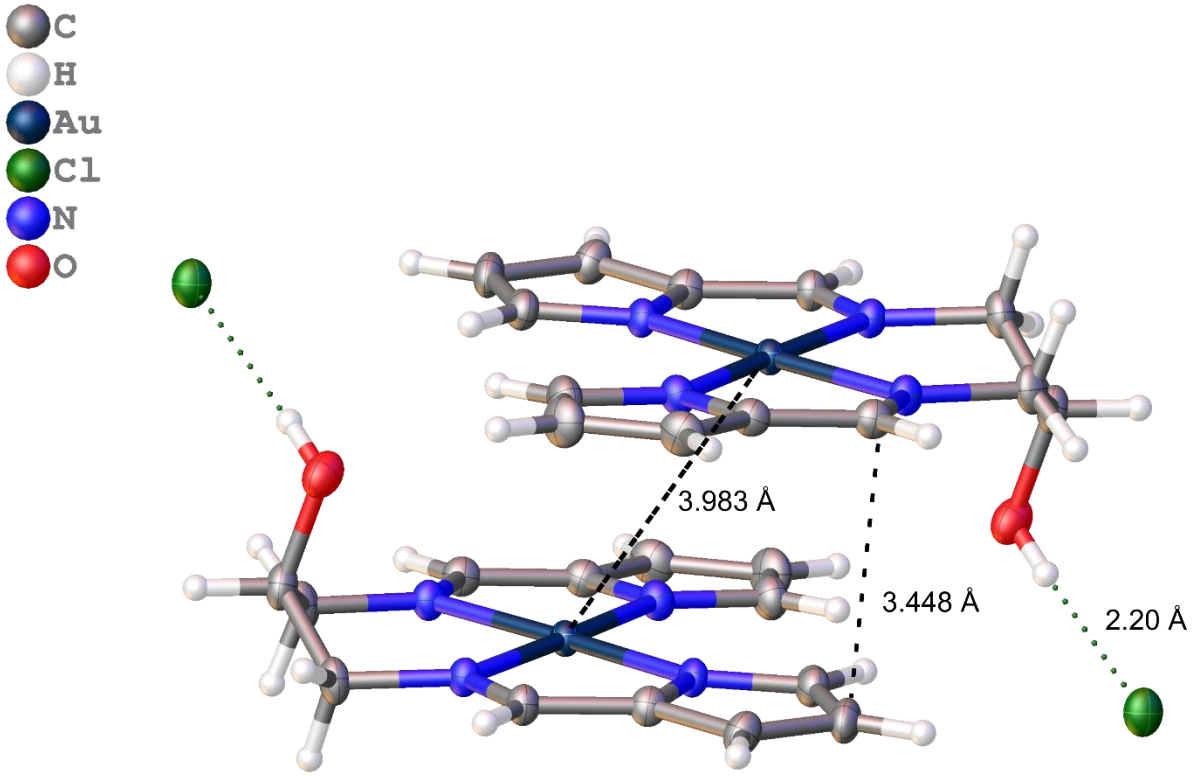


Fig. S35 View of the π-π dimers formed by the cation of compound **AuL2** in the crystalline solid state. Bond distances MPS, Au···Au separation and H···Cl is measured. The chelates are represented as 50% thermal ellipsoids for non-H atoms; H atoms are shown as capped cylinders. Atom colour code white H, grey C, blue N, dark blue Au, red O and dark green Cl.

Comment. The ASU of **AuL2** consists of a single **AuL2** cationic chelate and its corresponding Cl^- counter anion. The packing indicates two **AuL2** chelates arranged in a head-to-tail manner (Fig. S35). The Au···Au separation was 3.983 Å, which is slightly shorter than the Au···Au distance for **AuL1** (Fig. S34). The MPS was 3.635 Å. The cation to π interactions has a distance of 3.769 Å, between the double bond of the pyrrole and the Au(III) cation on the adjacent **AuL2** molecule. Similar to **AuL1**, **AuL2** has the potential for cationic π stacking with DNA base pairs. The Cl^- counter anion is 2.200 Å away from the hydrogen on the hydroxy motif, indicating a hydrogen bond. Of the three Au(III) chelates only **AuL2** showed a hydrogen bond, where the OH motif hydrogen bonds to the Cl^- counter anion. The other Au(III) chelates have no suitable hydrogen bond donors or acceptor moieties on the molecules. However, the Au(III) chelates exhibit weak electrostatic interactions. Furthermore, the planar nature of Au(III) chelates suggest the possibility of π and Au(III)···π interactions.

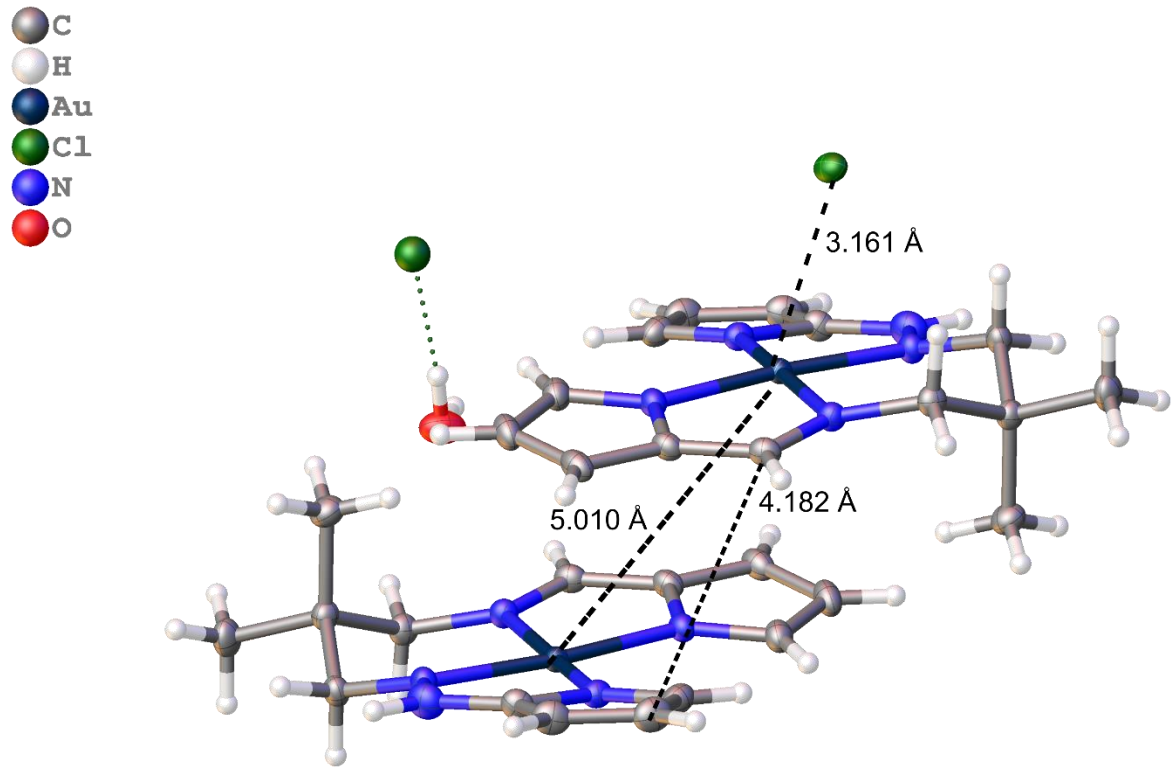


Fig. S36 View of the π-π dimers formed by the cation of compound **AuL3** in the crystalline solid state. Bond distances MPS, Au···Au separation is measured. The chelates are represented as 50% thermal ellipsoids for non-H atoms; H atoms are shown as capped cylinders. Atom colour code white H, grey C, blue N, dark blue Au, red O and dark green Cl.

Comment. The ASU of **AuL3** consist of two **AuL3** cations, two Cl^- counter anions, one of which is the corresponding counter anion of one of the **AuL3** chelates and the other is a Cl^- anion from a different AuL3 chelate found in the packing. Finally, a H_2O molecule is also present in the ASU (Fig. S36). Further, analysis of the packing indicates that there are pairs of **AuL3** chelates that are arranged in an inverted head-to-tail π stacked dimers. The **AuL3** chelates have a MPS distance of 4.182 Å and Au···Au distance of 5.010 Å. The cation to π interactions has a short distance of 5.394 Å between the C=C pyrrole moieties and Au(III) ions of the inverted adjacent molecules. As was the case for **AuL1**, **AuL2**, and **AuL3** has the potential to π stack with DNA base pairs (Fig. S36). The dimers in the stacking could be potentially stabilised by electrostatic interactions between the Au(III) metal ion centre and Cl^- counter anion (3.161 Å).

2.3. Au(III) chelates interaction with DNA.

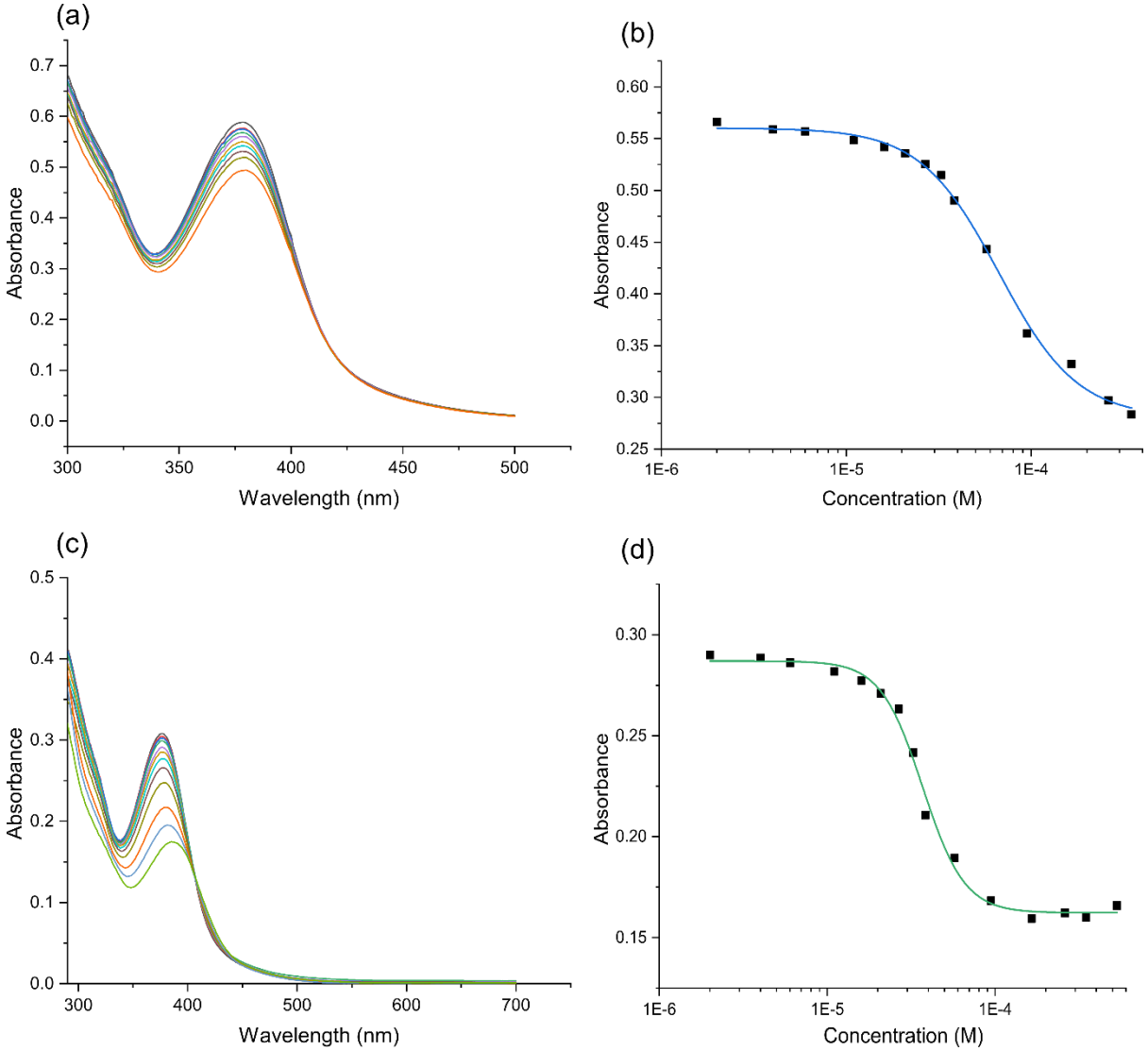
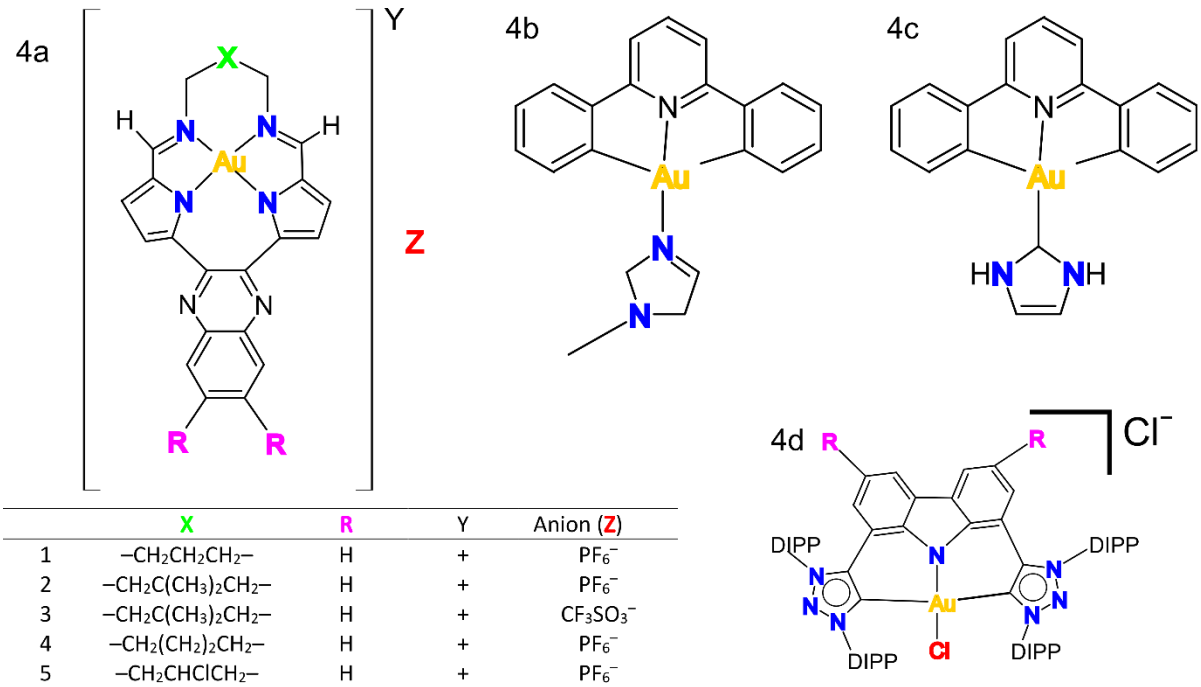


Fig. S37 The UV-vis absorption spectra of (a) **AuL2** in the presence of ctDNA (b) the change in the absorbance at 382 nm of **AuL2** as a function of [ctDNA] fitted to the Hill model. The UV-vis absorption spectra of (c) **AuL3** in the presence of ctDNA (d) the change in the absorbance at 382 nm of **AuL3** as a function of [ctDNA] fitted to the Hill model. All reactions were carried out in KH_2PO_4 and after sequential additions of ctDNA (final [ctDNA] = 342 μM bp, for **AuL2** and 542 μM for **AuL3**. The Hill fits were used to calculate the dissociation constants and stoichiometric ratios of the Au(III) chelates binding to ctDNA.



	X	R	Y	Anion (Z)
1	$-CH_2CH_2CH_2-$	H	+	PF_6^-
2	$-CH_2C(CH_3)_2CH_2-$	H	+	PF_6^-
3	$-CH_2C(CH_3)_2CH_2-$	H	+	$CF_3SO_3^-$
4	$-CH_2(CH_2)_2CH_2-$	H	+	PF_6^-
5	$-CH_2CHClCH_2-$	H	+	PF_6^-
6	$-CH_2CH_2CH_2-$	CH_3	+	PF_6^-

Fig. S38 Selected examples of Au(III) complexes with known DNA binding motifs proposed by extensive DNA-binding studies.

2.4. LD spectroscopy

LD spectroscopy is a type of absorbance spectroscopy that consists of two polarizations of light. LD can be defined by eq. 1, which states LD is the difference in absorbance of linearly polarized parallel light and the absorbance of light perpendicular to the orientation axis.[9,10]

$$LD(\lambda) = A_{//}(\lambda) - A_{\perp}(\lambda) \qquad (S7)$$

A requirement of eq. 1 is that the molecules at which light passes through is orientated. A molecule's orientation can be summarised by the orientation parameter S. If S = 1, molecules are perfectly orientated and aligned. If S = 0 the sample is isotropic (molecules are randomly orientated).

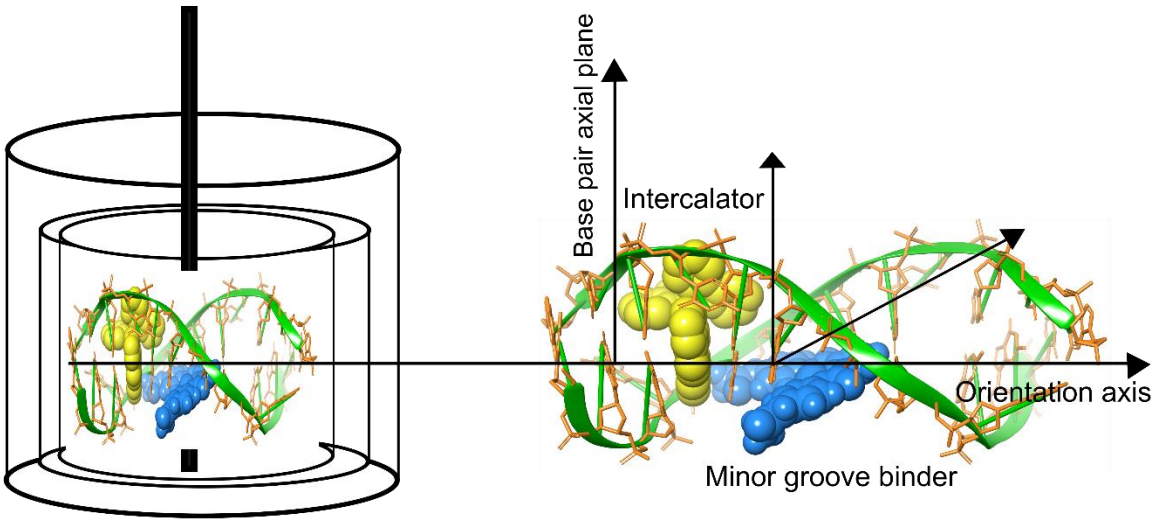


Fig. S39 A schematic illustration of a Couette cell, used to align DNA molecules in a way in which the orientation axis is equivalent to the helical axis of DNA. The double stranded DNA highlights the manner in which an intercalating (gold) and a minor groove (blue) binding molecules bind to double stranded DNA.

Both the sign and amplitude of a LD transition depends on the incident light passing through a sample. Typically, the absorbance spectrum for perfectly orientated molecules can have one of three outcomes.[10,11] (i) If the electric transition dipole moments of orientation is parallel to the orientation direction is parallel to the polarized photons of light absorbed (ie. $LD(\lambda) = A_{//}(\lambda) - A_{\perp}(\lambda)$ ($A_{//}(\lambda) > 0$). (ii) When the electric transition dipole moment is orientated perpendicular to the orientation direction, then only perpendicular-polarized light is absorbed. (iii) Lastly, when the two absorption intensities vary, this can be described by eq. S8.

$$LD^r = \frac{LD(\lambda)}{A_{iso}} = S \times \frac{3}{2} \times (3cos^2\alpha - 1) \qquad (S8)$$

Where α is the angle between the transition moment of the chromophore and the orientation axis. Based on the theory highlighted above we used LD spectroscopy to analyse the binding of **AuL1**, **AuL2** and **AuL3** to ctDNA.

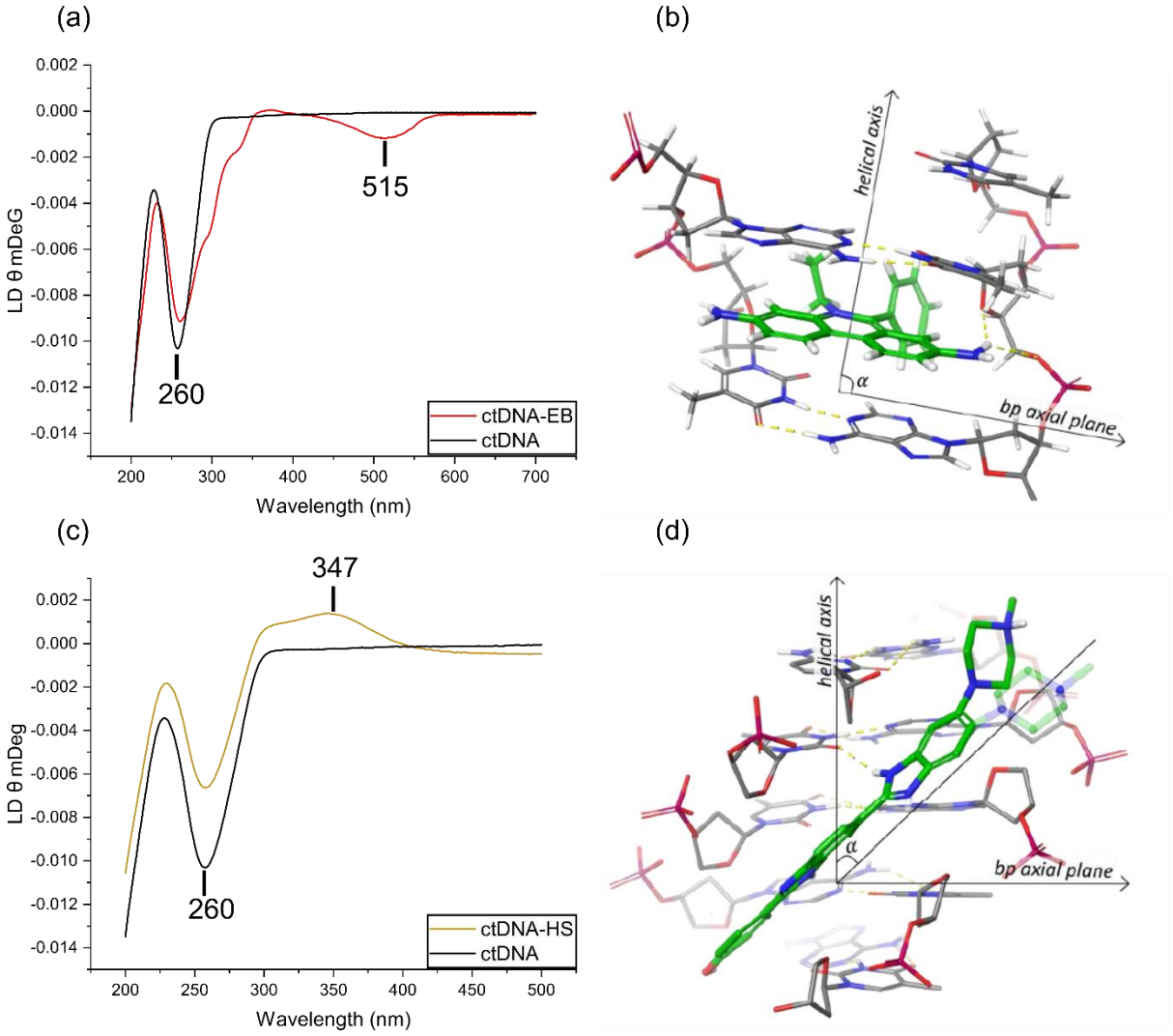


Fig. S40 (a) The LD spectrum of EB with ctDNA, with an induced LD at 515 nm indicating binding of EB to ctDNA. (b) The best docking pose generated of EB intercalated with double stranded DNA (PDB: 2O1I).[12] (c) The LD spectrum of HS with ctDNA, with an induced LD at 347 nm indicating binding of HS to ctDNA. (d) An XRD crystal structure of HS in the minor groove of DNA (PDB: 8BNA).[13]

Comment. Experimentally for macromolecular systems S can be determined in one of two ways (i) by using the known maximum LD^r or (ii) by calibration using a probe dye that has a predetermined binding geometry to DNA.[11] Ideally the selected probe should have a spectroscopy transition bands that do not align with the experimental molecules of interest (in this case the Au(III) chelates) or the native DNA. Therefore, in this work we selected ethidium bromide (EB)[14] as the intercalator probe and Hoechst 33258 (HS)[13] as the minor grove binder probe. We report the LD spectrum of ctDNA in the presence of EB and HS in Fig. S40. EB and HS are both achiral molecules isotropic molecules that do not produce a LD or CD signal (data not shown). However, when bound to ctDNA both EB (Fig. S40a) and HS (Fig. 40c) produce an induced LD signal. For EB the induced LD signal was negative with a minima at 515 nm. This is consistent with previously reported induced LD spectra of EB.[11] Furthermore, the negative induced LD spectra of EB was expected as EB is an intercalator and α is close to 90° (Fig. S40b). In the case of HS, a strong positive induced LD signal was observed with a maximum at 347 nm. This is consistent with previously reported induced LD spectra of HS.[11] From Fig. S40d we see HS is orientated close

to 45° to the base pair plane and helical axis, indicating it is a grove binder.[13] In both Fig 40a and c we see the presence of a strong minimum band at 260 nm, due to the purines and pyridines in the nucleotides of ctDNA and the induced LD signals of bot EB and HS were absent in the native DNA.

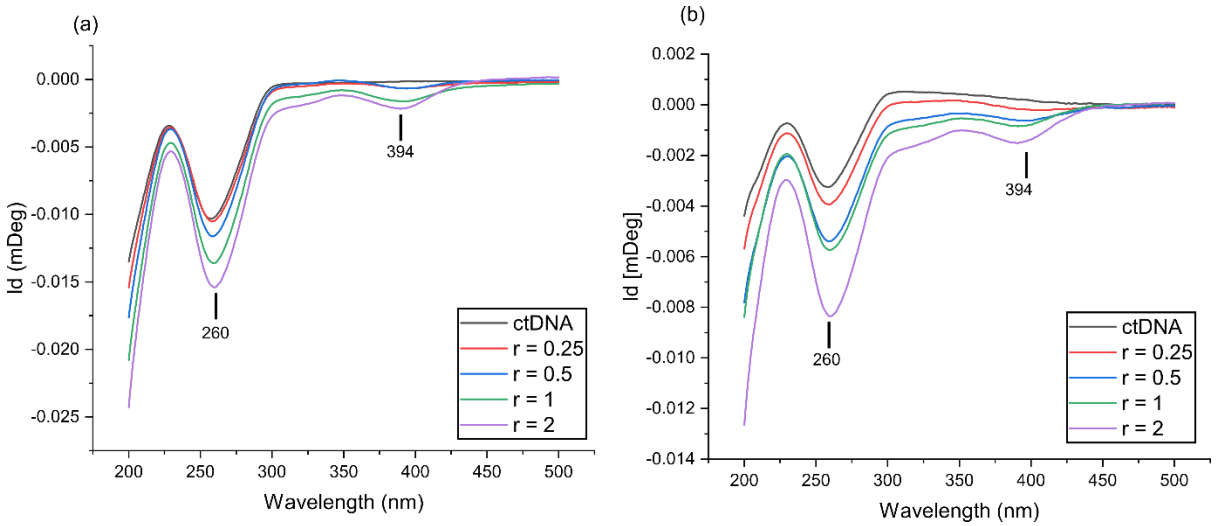


Fig. S41 The LD spectrum of (a) **AuL2** and (b) **AuL3** with 100 µM of ctDNA at increasing [Au(III) chelate]:[ctDNA] ratios (*r*) of 0.25 – 2 in KH_2PO_4 (50 mM, pH 7.5) at 37 °C. The intense minimum at 260 nm represents ctDNA and the 394 nm band represents an induced Au(III) chelates LD spectrum.

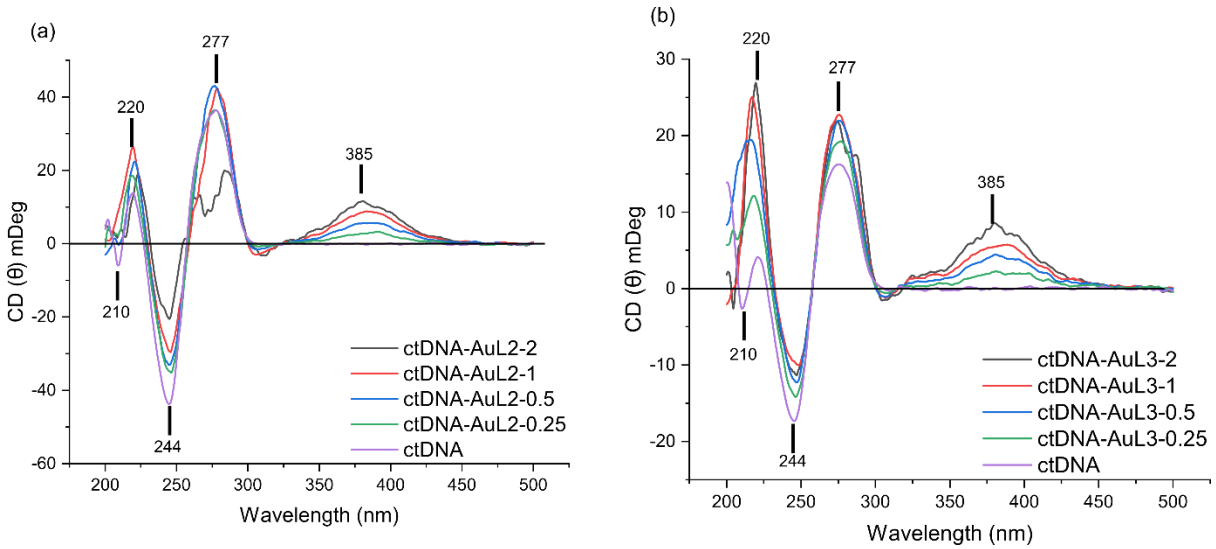


Fig. S42 The CD spectrum of (a) **AuL2** and (b) **AuL3** with 100 µM of ctDNA at increasing [Au(III) chelate]:[ctDNA] ratios (*r*) of 0.25 – 2 in KH_2PO_4 (50 mM, pH 7.5) at 37 °C. The intense maximums and minimums from 210 – 277 nm represent ctDNA and the 385 nm band represents an induced Au(III) chelates CD spectrum.

2.5. NCI-60 cytotoxicity

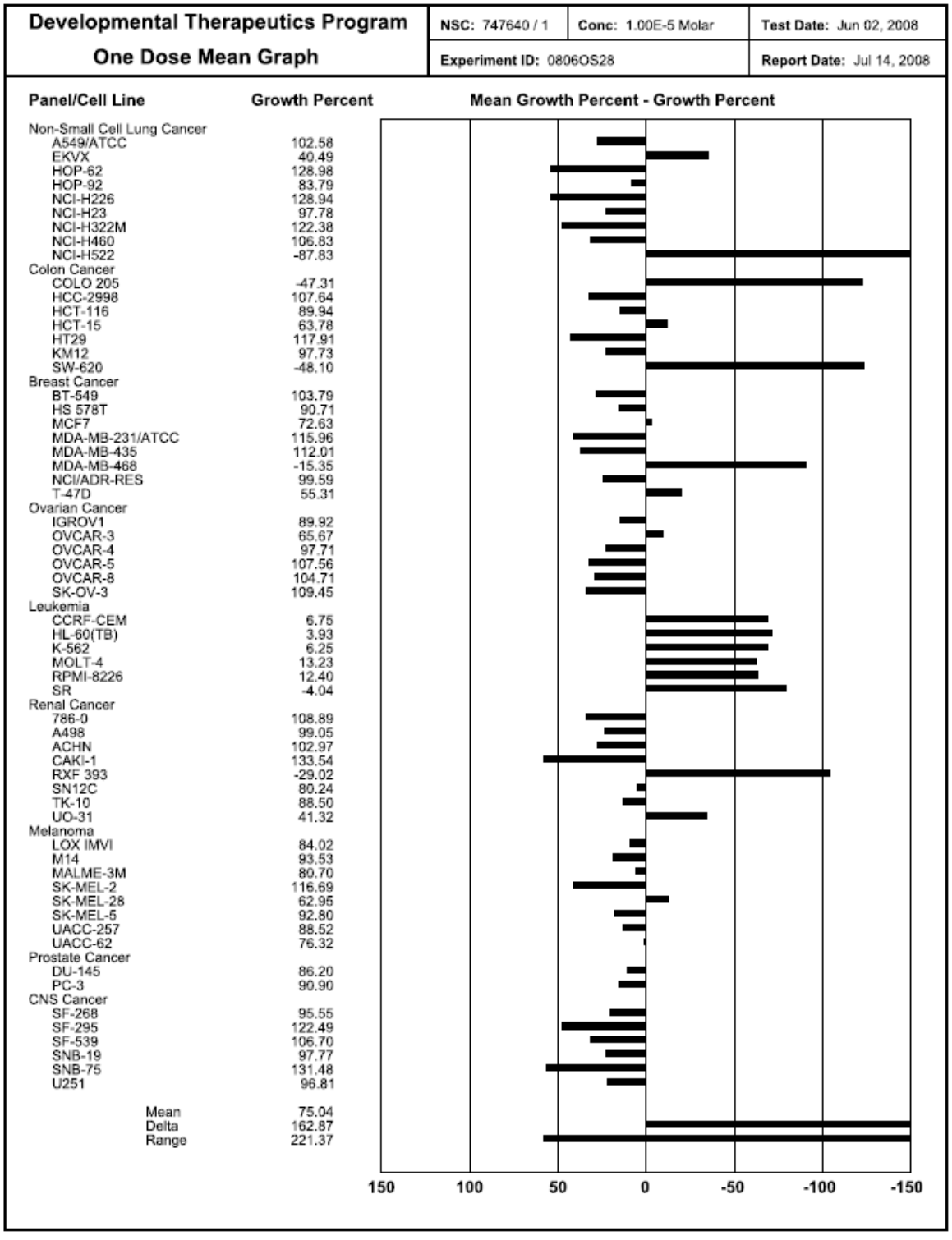


Fig. S43 NCI-60 single-dose cytotoxicity screen for **AuL1**.

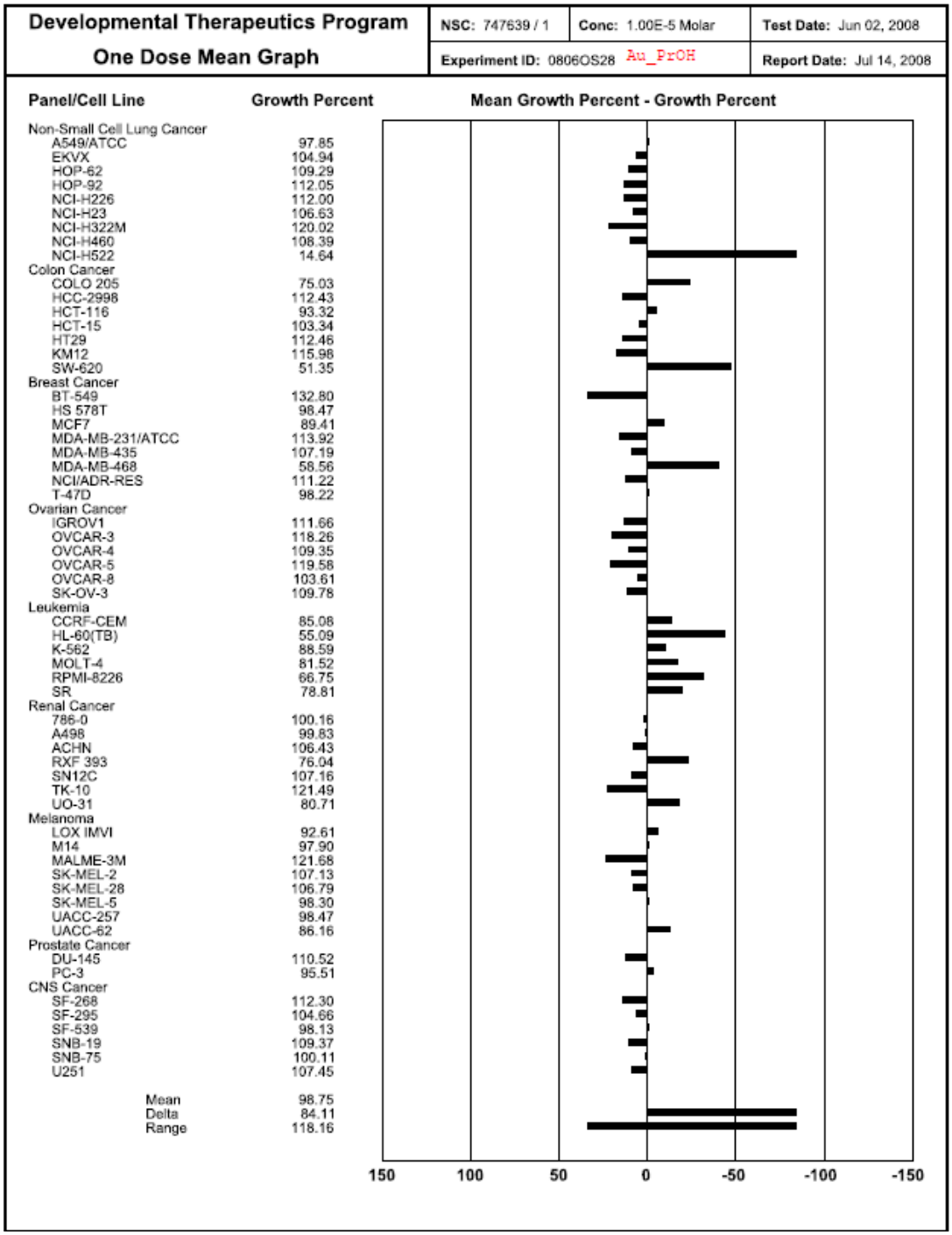


Fig. S44 NCI-60 single-dose cytotoxicity screen for **AuL2**.

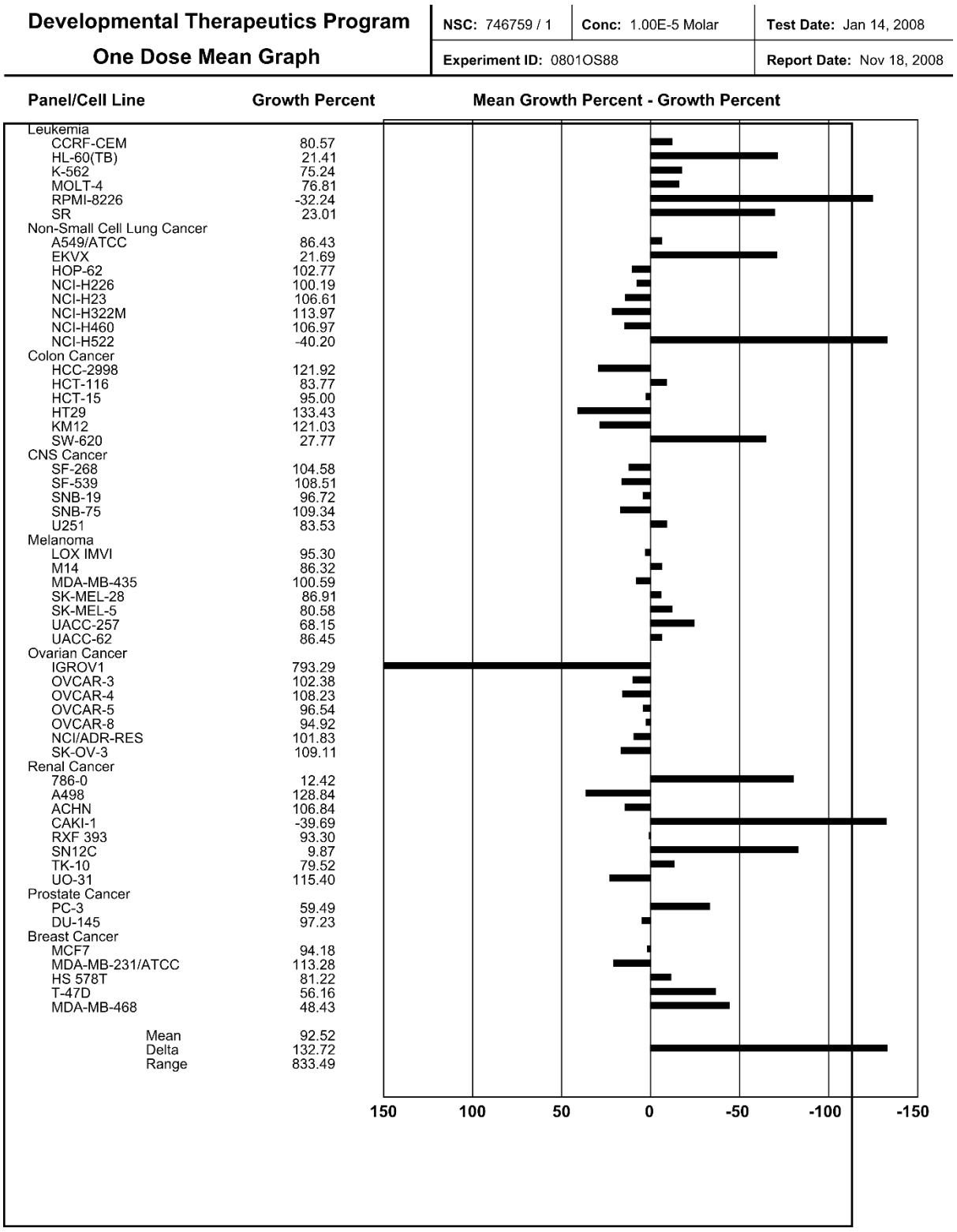


Fig. S45 NCI-60 single-dose cytotoxicity screen for AuL3.

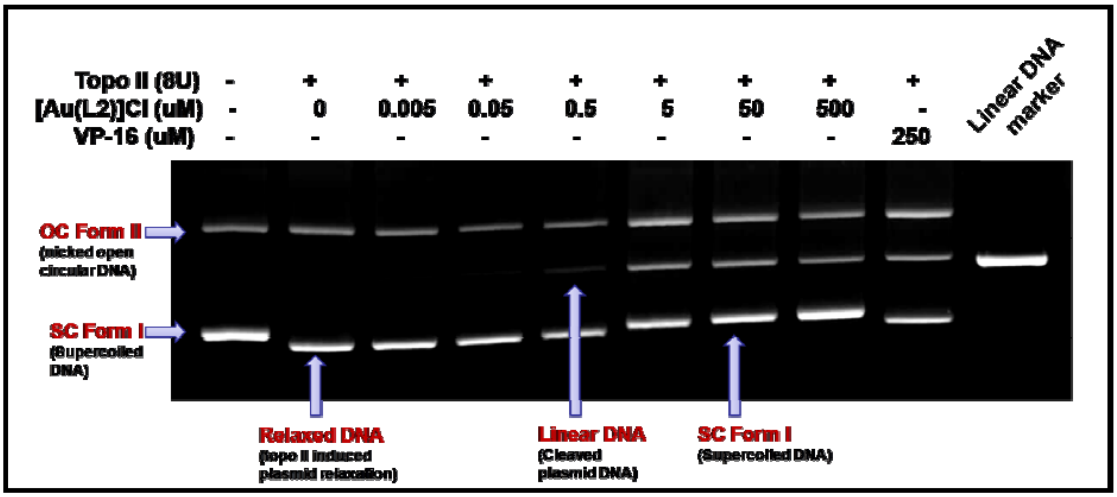


Fig. S46 EB agarose gel showing the *in vitro* activity of AuL2. This *in vitro* activity indicates that there is a cellular mechanism responsible for AuL2 inactivity *in vivo*, likely ab efflux pump.

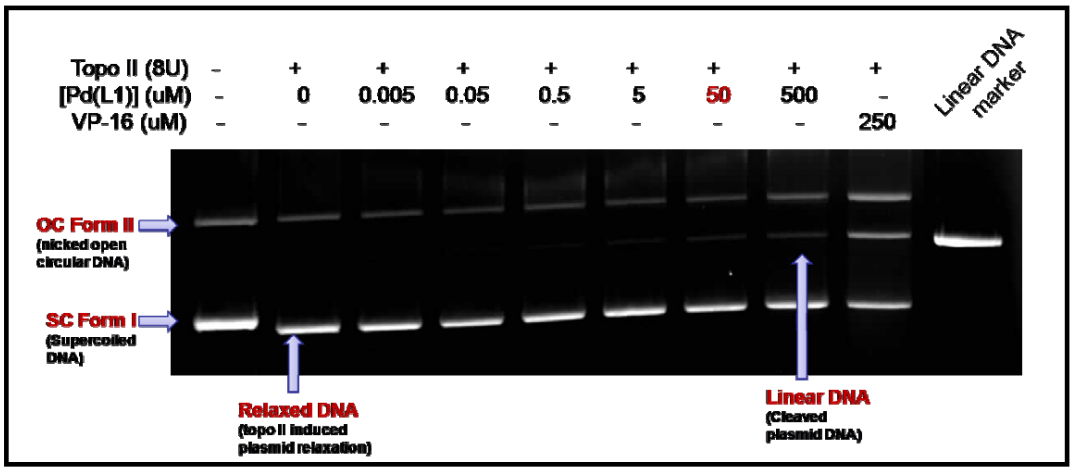


Fig. S47 EB agarose gel showing the diminished cleavage or poisoning activity of Pd(PrPyrr) against Top2 in comparison to etoposide.

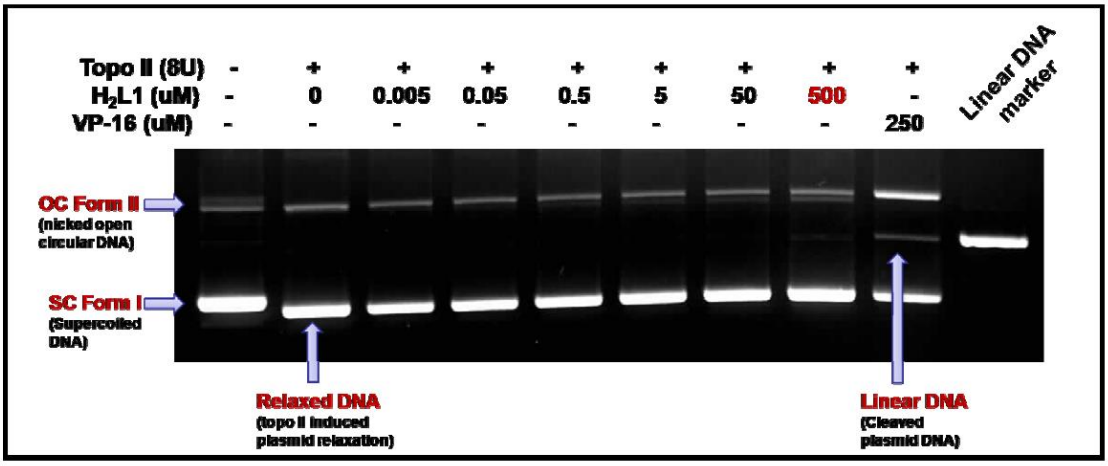


Fig. S48 EB agarose gel showing the lack of activity if the metal-free ligand H_2L1 compared to the commercially available chemotherapeutic agent VP-16 (etoposide).

Comment on Fig. S47 and 48. This reduced binding affinity manifests itself as a reduction in the formation of cleaved plasmid (linear DNA) in the gel electrophoresis experiments (Figs. S47 and S48). The EB gel in Fig. 47 shows that [Pd(PrPyrr)] is approximately 100-fold less active compared to **AuL1**. Cleaved plasmid DNA could only be detected at a concentration of 500 µM of [Pd(PrPyrr)]. This is an excellent result, as it shows that the Au^{3+} ion and the unique properties it possesses are critical to the efficacy of the Au(III) chelates synthesised in this work. The results of the EB gel (Fig. S48) indicates that the free ligand (H_2L1) alone does not induce any inhibitory or poisoning activity, even at ultra-high concentrations of the ligand. The collective results of this combination of tests are extremely encouraging as it shows that the Au(III) chelates are reaching their cellular target before they are reduced by GSH. They also show that the Au(III) ion is critical to the efficacy of the Au(III) chelates as chemotherapeutic agents both *in vivo* and *in vitro*. The rigid square planar Pd(PrPyrr) is the ideal structure for a DNA intercalator compound. However, without the electrophilicity of the Au^{3+} ion, the activity is greatly reduced.

2.6. Docking of AuL1 into DNA

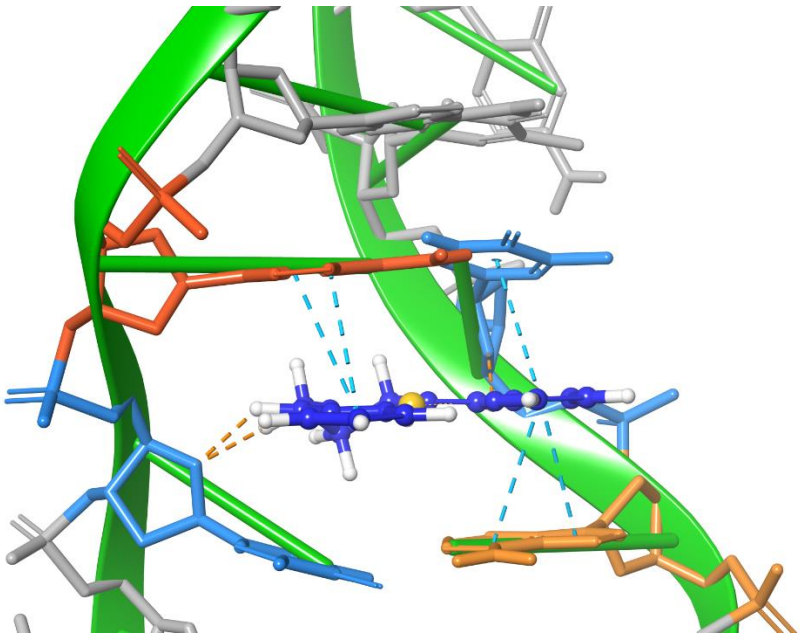


Fig. S49 The lowest-energy docking pose of **AuL1** within the central 5′-AT-3′ step of the 5′-D(CGGAAAATTACCG)-3′ DNA sequence. The position of **AuL1** at the intercalation site is shown head on as well as the chemical detail of the nucleic acid residues, A and T. The DNA strand as viewed.

2.7. Fluorescence spectroscopy

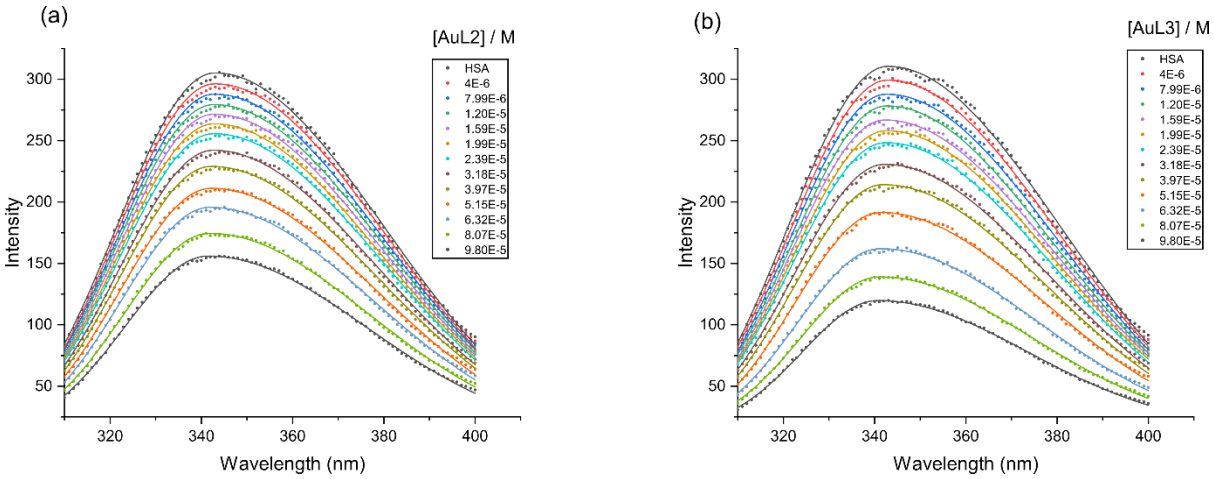


Fig. S50 Emission spectra of human serum albumin (HSA, 5.0 μM) recorded as a function of the concentration of (a) **AuL2** and (b) **AuL3** at 298 K in KH_2PO_4 buffer (50 mM, pH 7.50). The spectra are fitted by single Bigaussian functions to locate the emission maxima. Correlation coefficients, R^2, ranged from 0.996 to 0.999.

The Stern-Volmer plot recorded for HSA fluorescence quenching by **AuL3** as a function of temperature is reported in Fig. S51a. The plot clearly indicates there is a deviation from linearity and has an upward curvature at higher **AuL3** concentrations (exceeding 5.15×10^{-5} M). The upward curvature continues with increasing concentration of **AuL3**. An upward curvature in the Stern-Volmer plot has quadratic dependence and is an indicator that both static and dynamic quenching is present. The quadratic of a combined static and dynamic quencher can be given by eq. S9:

$$\frac{I}{Io} = f\frac{\boldsymbol{\gamma}}{\boldsymbol{\gamma}+\boldsymbol{Kq}[\boldsymbol{Q}]} \qquad \text{(S9)}$$

Where f is the fraction of the product that is not complexed, and rearrangement of equation can be written as eq. S10

$$\frac{Io}{I} = (1 + K_D\,[Q])\,(1 + K_S\,[Q]) \qquad \text{(S10)}$$

Where K_D and K_S are the portions of observed fluorescence that need to be delineated using lifetime measurements. Unfortunately, we do not have the appropriate equipment for fluorescence emission nano second lifetime measurements. Hence, we used a modified version of eq. 4 to calculate both the K_D and K_S graphically, using eqs. S11 and S12, respectively.

$$\frac{Io}{I} = 1 + (K_D + K_S)[Q] + K_D K_S\,[Q]^2 = 1 + K_{app}\,[Q] \qquad \text{(S11)}$$

$$K_{app} = (\frac{Io}{I} - 1)\frac{1}{[Q]} = (K_D + K_S) + K_D K_S\,[Q] \qquad \text{(S12)}$$

Treating the quenched HSA fluorescence emission data with eq. S11 yielded Fig. S51b which was a modified Stern-Volmer plot based on a quadratic to determine a dual quenching mechanism. The y – intercept of the modified Stern-Volmer plot from eq. 12 yields the (K_D + K_S) and the gradient yields $K_D K_S$.

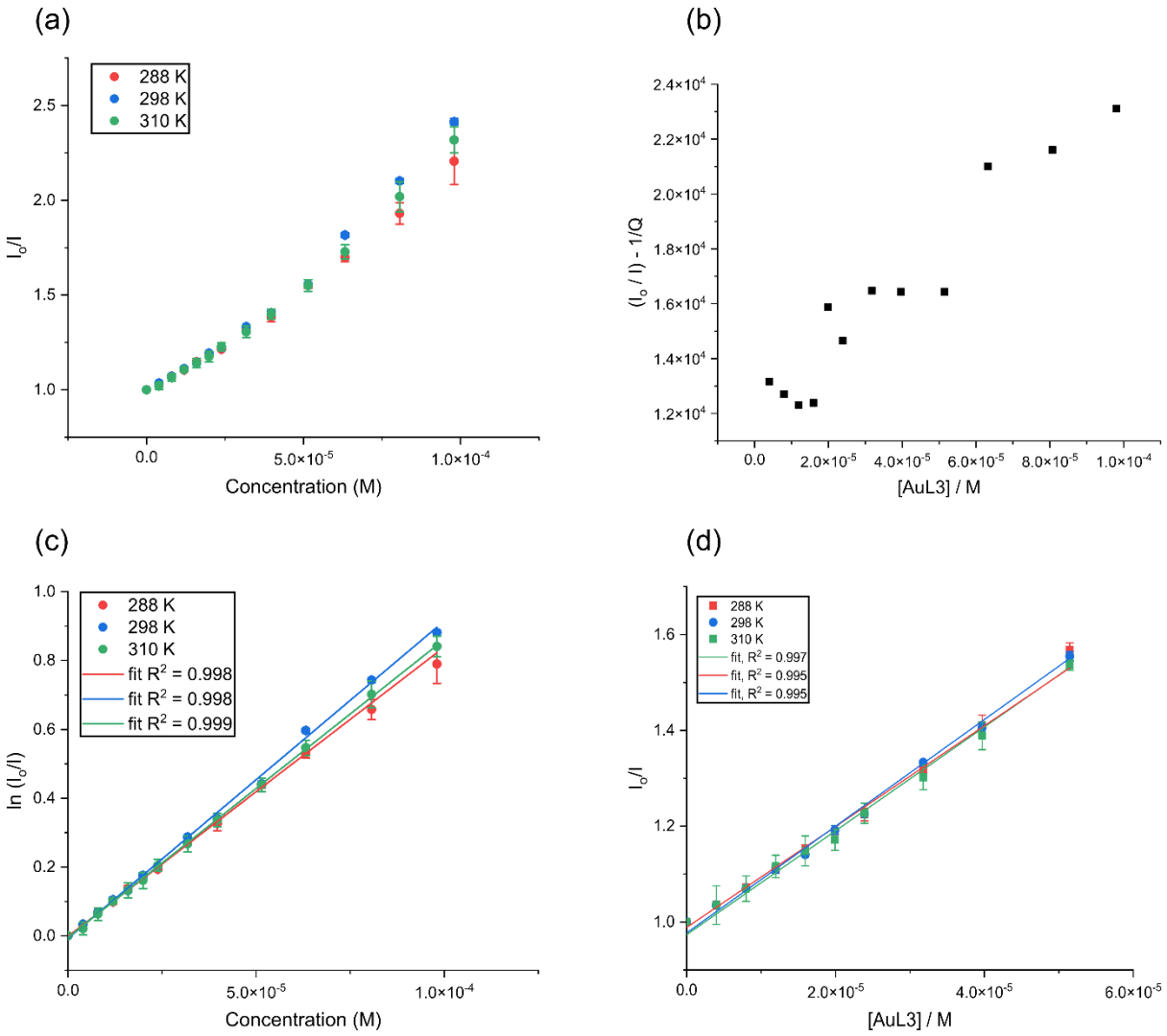


Fig. S51 Stern-Volmer plot of fluorescence quenching: (a) Classical Stern-Volmer plot of the AuL3···HSA system from 0 – 9.8 × 10–5 M. Data for the AuL3···HSA system were recorded at three different temperatures (● 288 K, ● 298 K, and ● 310 K). The plot deviates from linearity at AuL3 concentrations above 5.15 × 10–5 M. (b) Modified Stern-Volmer plot used to determine if both static and dynamic quenching mechanism were dominant, no correlation was obtained from the plot. (c) Linearization of the Stern-Volmer data AuL3···HSA system using the "sphere of action model", the slopes of the lines are the K_{SV}^{app} values, which were 0.856 (0.04) x 104, 1.96 (0.01) x 104 and 1.87 (0.05) x 104 at three different temperatures (● 288 K, ● 298 K, and ● 310 K). (d) Classical Stern-Volmer plot of the AuL3···HSA system from 0 – 5.15 × 10–5 M. Data for the AuL3···HSA system were recorded at three different temperatures (■ 288 K, ● 298 K, and ▲ 310 K). The plot used the linear portion of the classical Stern-Volmer fit to obtain usable K_{SV} data).

The modified Stern-Volmer plot showed no relationship between the treated fluorescence quenching data and the **AuL3** concentration, therefore we concluded that both static and dynamic quenching were not dominant.

An alternative interpretation to the non-linear Stern–Volmer plot of the HSA···**AuL3** system is the "sphere of action model" which suggest that the upward curvature represents a single class of quenching.[15–18] This has led to the development of second order processes the sphere of action and diffusion limited treatment.[16] The sphere of action indicates there is an finite sphere volume around the fluorophore (Trp-214) caused by **AuL3**. In this instance **AuL3** lies adjacent to the Trp-214 residue upon excitation and prevents a ground state being formed.[15] If the sphere of action was the main mechanism involved in quenching HSA intrinsic fluorescence emission it would be described by the following eqs. S13 and S14,

$$\frac{I_0}{I} = e^{(K_{SV}^{app}[Q])} \qquad \text{(S13)}$$

$$ln\left(\frac{I_0}{I}\right) = K_{SV}^{app}[Q] \qquad \text{(S14)}$$

where K_{SV}^{app} is the apparent quenching constant. By taking the natural logarithm of eq. S13, linear plots with a zero intercept (eq. S14) are expected for increasing [Q] in systems that exhibit *static quenching* by this model (Fig. S51b). Based on the plot in Fig 44b K_{SV}^{app} the calculated values for the HSA···**AuL3** system increased with increasing temperatures. This is a characteristic of dynamic quenching,[15] Whereas the "Sphere of action model" is a second order process depicting the static quenching mechanism and therefore, does not fit the data of HSA···AuL3 system.

Finally, to obtain a usable K_{SV} values, we used the linear Stern-Volmer equation (eq. 1) with a concentration range of 0–5.15 × 10^{-5} M, excluding **AuL3** concentrations above 5.15 × 10^{-5} M allowed for a linear Stern-Volmer plot (Fig. S51d) and the quenching mechanism was determined to be dynamic.

Comment. The quenching mechanism for **AuL1** and **AuL2** could not be determined because of the K_{SV} values which remained consistent over the three different temperatures tested. The absence of a relationship between the K_{SV} values and temperature and the absence of equipment able to record ns lifetimes made finding the quenching mechanism of **AuL1** and **AuL2** impossible to determine with any certainty. Other approaches made was: (i) using half the concentration of Au(III)-chelates, however, there was still no relationship between the K_{SV} values and temperature.

2.8. Binding parameters

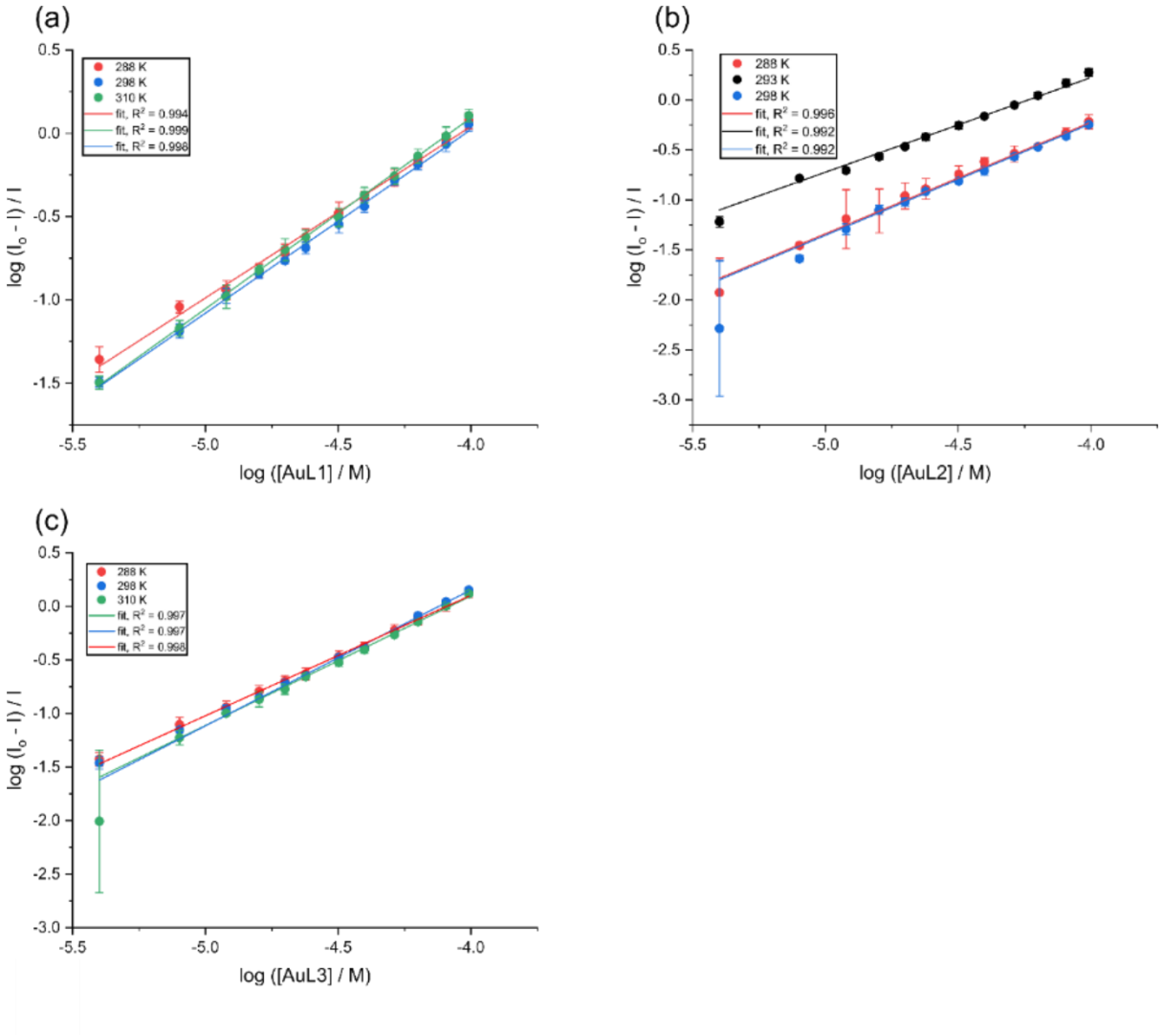


Fig. S52. Plots of log((I$_0$-I)/I) versus log([Q]) for the interaction of HSA with the three Au(III) chelates (i.e., quenchers, Q): (a) **AuL1**···HSA complex, (b) **AuL2**···HSA complex, (c) **AuL3**···HSA complex. The affinity constants are determined from the intercepts of the graphs and the stoichiometry from the slopes. Data for the Au(III) chelates···HSA systems were recorded at three different temperatures (● 288 K, ● 298 K, and ● 310 K) The relevant concentrations for the titrations were: [HSA] = 5.0 µM, and the Au(III) chelates ranged from 0 – 9.8 × 10^{-5} M at pH 7.50 in 50 mM KH_2PO_4 buffer.

Comment on Fig. S52. The quenching in HSA intrinsic fluorescence as a function of ligand (Au(III) chelate) concentration can be used to calculate the thermodynamic parameters for the binding equilibrium between the protein and Au(III) chelate. The Au(III) chelates binding affinity towards the protein (K_a) and the stoichiometry (n) are delineated from the double log plot of the quenching of the emission data as a function of the Au(III) chelate concentration (eq. S15) ,[19]

$$log\left(\frac{I_0-I}{I}\right) = logK_a + nlog[Q] \qquad \text{(S15)}$$

where the intercept and slope of the curve give the affinity constant and stoichiometry, respectively. The data are summarised in Table 3 and has been plotted for all three Au(III) chelates in Fig. S52. For **AuL1**, **AuL2** and **AuL3**, the affinity constant increased with increasing temperatures, which is suggestive that the dynamic quenching mechanism was dominant.[20,21] The stoichiometric coefficients n from the is suggestive of static quenching mechanism,[20,21] however, based on the K_{SV} values, they suggested dynamic quenching was dominant.

From Table 3, the logK_a values follow the order **AuL3** > **AuL1** > **AuL2**. All three Au(III)-chelates bound to HSA with a moderate binding affinity ranging from 10^4 – 10^5 M^{-1}. A moderate binding affinity of the Au(III)-chelates is ideal for this study, as we intend to show HSA acts as a transporter for these Au(III)-chelates. Binding affinity constants that are too high will results in the molecules being retained by HSA and will not be able to dissociate off HSA.

2.9. Thermodynamic parameters by ITC

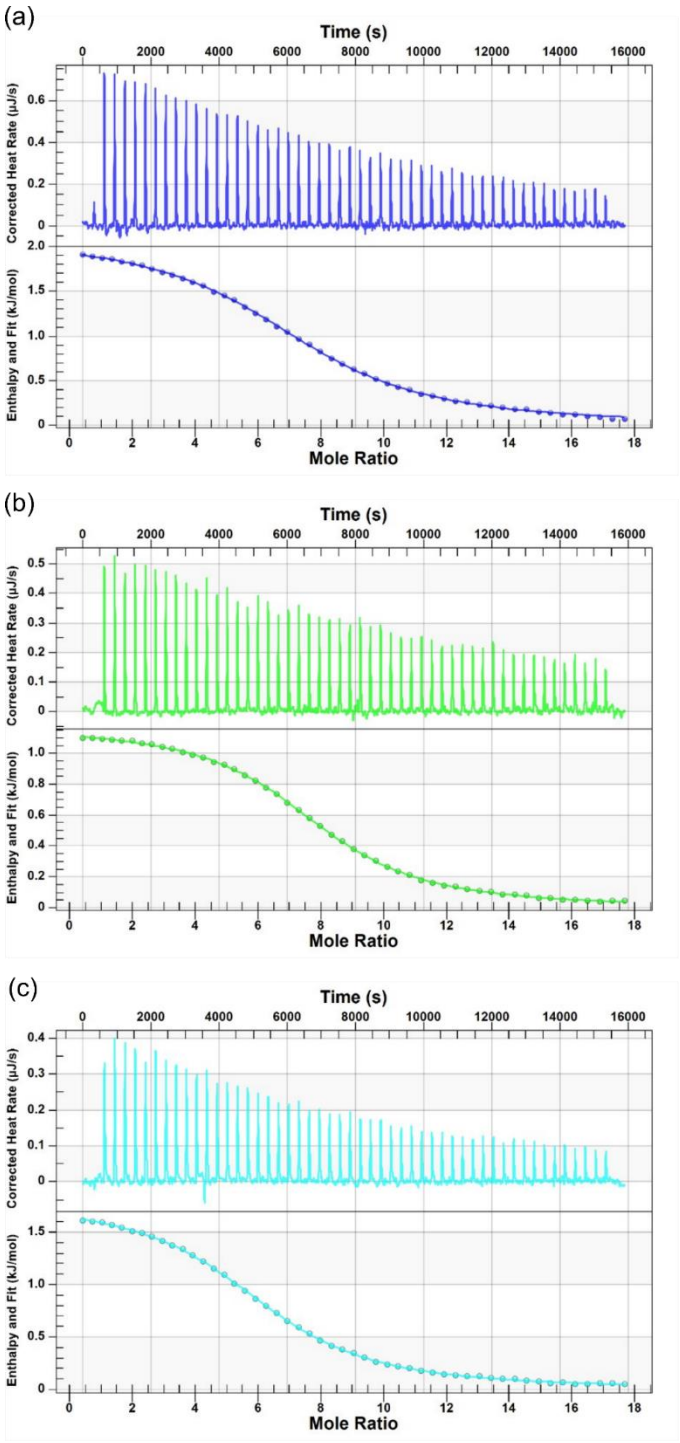


Fig. S53 Binding thermodynamic measurements of (a) **AuL1** (b) **AuL2** and (c) **AuL3** interacting with HSA (20 µM, in 50 mM KH_2PO_4, pH 7.5) measured by ITC. The top panel of all three plots represent the raw heat released belonging to each injection. The bottom panel indicates the integrated heat corresponding to each injection. The solid line shows the best fitting isothermal binding model. Experiments were performed at 398 K as described in methods and materials.

2.10. Site displacement assay

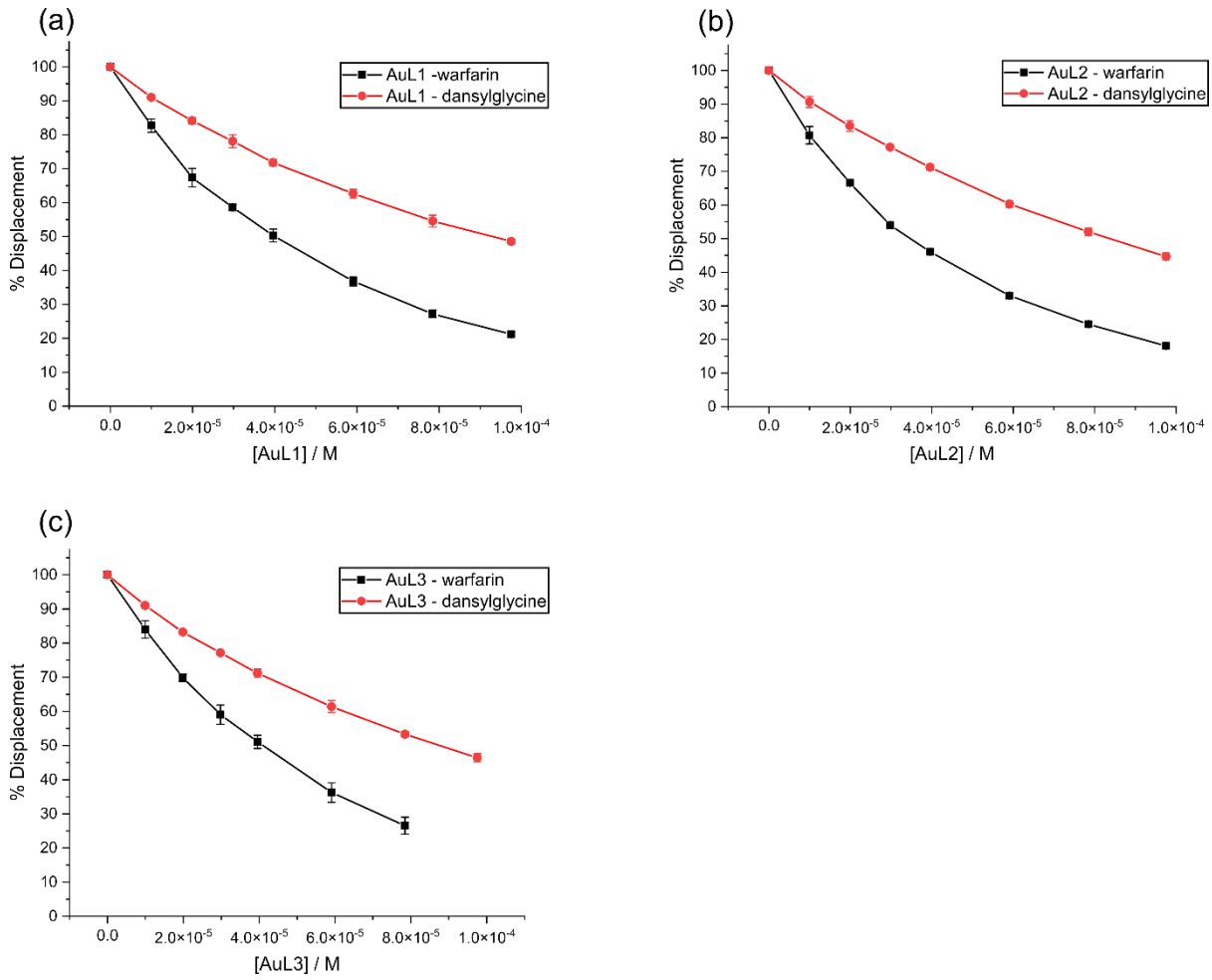


Fig. S54 Au(III) chelates displace either dansylglycine or warfarin bound to HSA. Various Au(III)-chelates (0–9.7 × 10^{-5} M) were titrated into a solution containing 5 µM HSA bound to 5 µM of either dansylglycine or warfarin. Displacement of dansylglycine or warfarin resulted in the fluorophores fluorescence being quenched. Error bars indicate the standard deviation of three independent experiments.

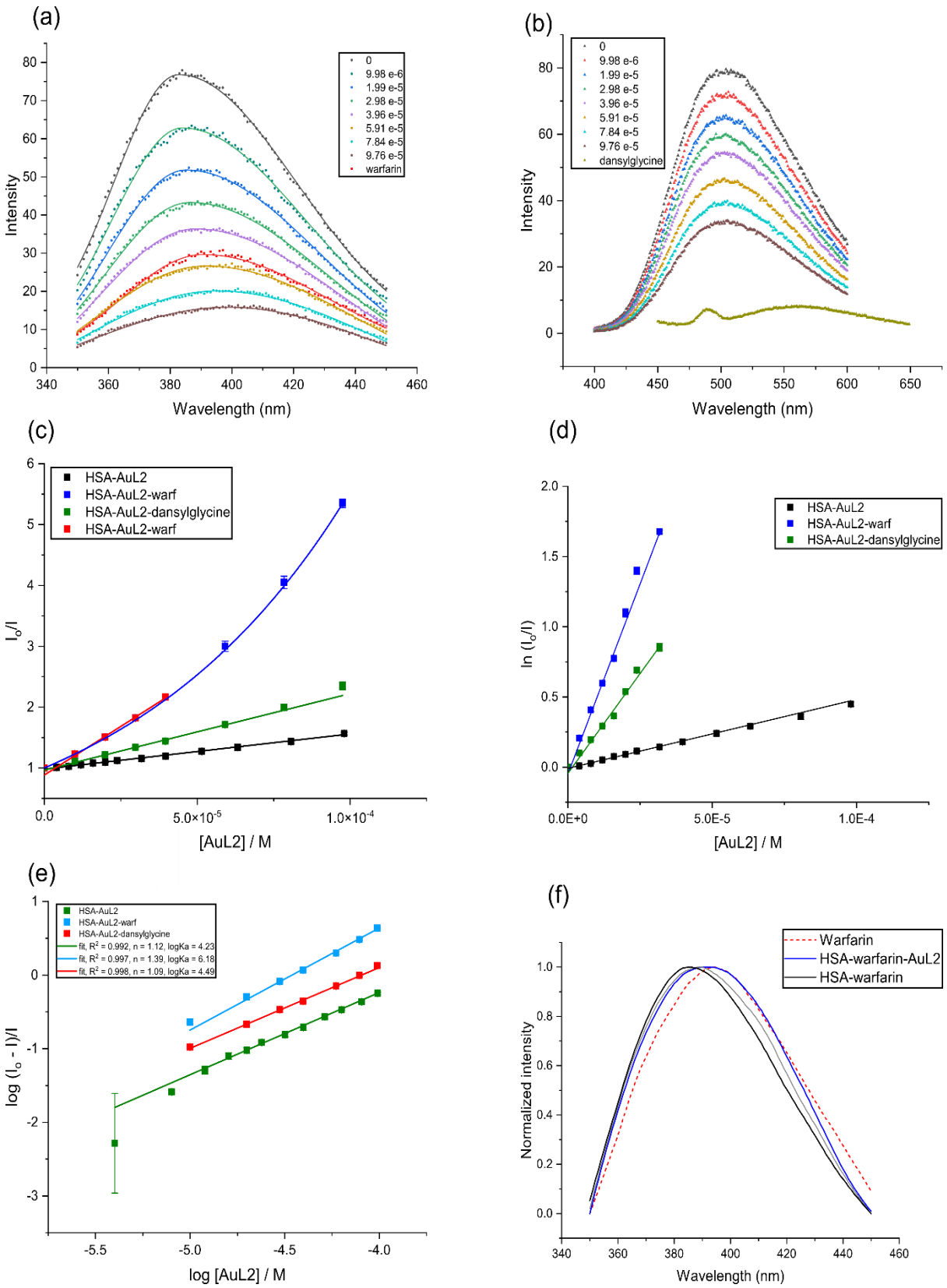

(a)
Intensity
Wavelength (nm)
0
9.98 e-6
1.99 e-5
2.98 e-5
3.96 e-5
5.91 e-5
7.84 e-5
9.76 e-5
warfarin
(b)
Intensity
Wavelength (nm)
0
9.98 e-6
1.99 e-5
2.98 e-5
3.96 e-5
5.91 e-5
7.84 e-5
9.76 e-5
dansylglycine
(c)
I0/I
[AuL2] / M
HSA-AuL2
HSA-AuL2-warf
HSA-AuL2-dansylglycine
HSA-AuL2-warf
(d)
ln (I0/I)
[AuL2] / M
HSA-AuL2
HSA-AuL2-warf
HSA-AuL2-dansylglycine
(e)
log (I0 - I)/I
log [AuL2] / M
HSA-AuL2
HSA-AuL2-warf
HSA-AuL2-dansylglycine
fit, R2 = 0.992, n = 1.12, logKa = 4.23
fit, R2 = 0.997, n = 1.39, logKa = 6.18
fit, R2 = 0.998, n = 1.09, logKa = 4.49
(f)
Normalized intensity
Wavelength (nm)
Warfarin
HSA-warfarin-AuL2
HSA-warfarin

Fig. S55 Binding site determination for the reaction of **AuL2** with HSA (5.0 μM protein, 50 mM KH_2PO_4, pH 7.50, 298 K). **(a)** Emission spectra of HSA···warfarin (5.0 μM warfarin λ^{ex} = 320 nm) recorded as a function of the concentration of **AuL2** at 298 K. The spectra are fitted by single Gaussian functions to locate the emission maxima. Correlation coefficients, R^2, ranged from 0.990 to 0.999. **(b)** Emission spectra of HSA···dansylglycine (5.0 μM dansylglycine λ^{ex} = 420 nm) recorded as a function of the concentration of **AuL2** at 298 K. **(c)** Stern–Volmer (SV) plot for native HSA, HSA···Warfarin, and HSA···dansylglycine as a function of the concentration of **AuL2** at 298 K. The plots are linear with an intercept of 1.0 when static quenching is operative (i.e., the quencher binds to the target protein and fluorophore(s)). The excitation and emission wavelengths for the fluorophore probes were: (i) Trp-214 (native HSA), λ^{ex} = 295 nm, λ^{em} = 340 nm; (ii) Warfarin (HSA-Warf), λ^{ex} = 320 nm, λ^{em} = 382 nm, and (iii) dansylglycine, λ^{ex} = 340 nm, λ^{em} = 500 nm. **(d)** Sphere of action model plot, $ln\left(\frac{I_0}{I}\right) = K_{SV}^{app}[Q]$, for the system. A linear plot with a zero intercept indicates static quenching by **AuL2** bound in some way to the fluorophore/macromolecule. Negative deviation from linearity signals a switch from static to dynamic quenching. **(e)** Double-log plot (eq. S9) of the fluorescence quenching data, $log\left(\frac{I_0-I}{I}\right) = logK + nlog[Q]$, to enable measurement of log*Ka* and the reaction stoichiometry (*n*). **(f)** Normalised fluorescence emission spectrum of HSA···warfarin (5.0 μM warfarin λ^{ex} = 320 nm) recorded as a function of the concentration of **AuL2** at 298 K to show the displacement of warfarin from HSA. Error bars indicate the standard deviation of three independent experiments.

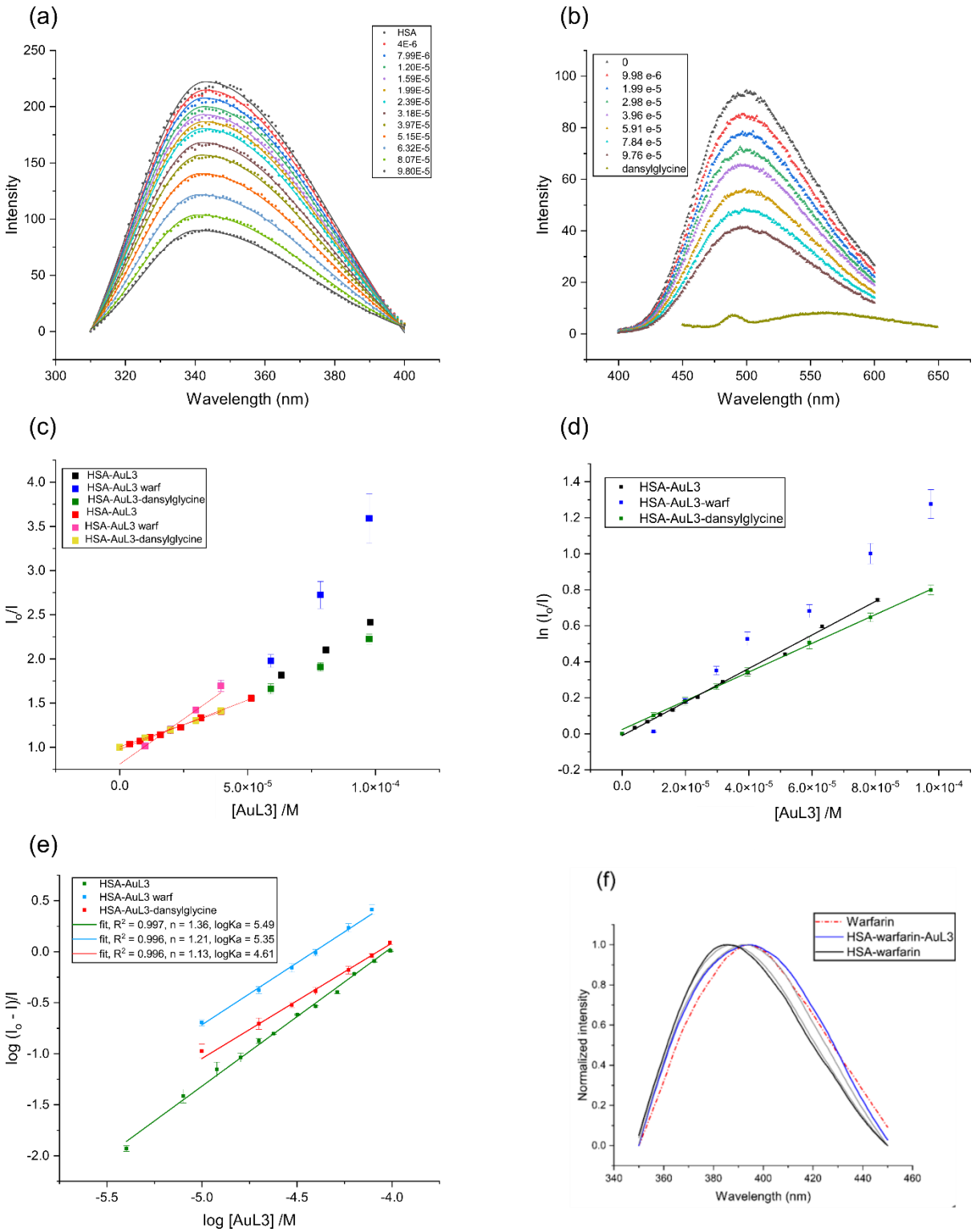

(a)
HSA
4E-6
7.99E-6
1.20E-5
1.59E-5
1.99E-5
2.39E-5
3.18E-5
3.97E-5
5.15E-5
6.32E-5
8.07E-5
9.80E-5
Intensity
Wavelength (nm)
(b)
0
9.98 e-6
1.99 e-5
2.98 e-5
3.96 e-5
5.91 e-5
7.84 e-5
9.76 e-5
dansylglycine
Intensity
Wavelength (nm)
(c)
HSA-AuL3
HSA-AuL3 warf
HSA-AuL3-dansylglycine
HSA-AuL3
HSA-AuL3 warf
HSA-AuL3-dansylglycine
I0/I
[AuL3] /M
(d)
HSA-AuL3
HSA-AuL3-warf
HSA-AuL3-dansylglycine
ln (I0/I)
[AuL3] /M
(e)
HSA-AuL3
HSA-AuL3 warf
HSA-AuL3-dansylglycine
fit, R2 = 0.997, n = 1.36, logKa = 5.49
fit, R2 = 0.996, n = 1.21, logKa = 5.35
fit, R2 = 0.996, n = 1.13, logKa = 4.61
log (I0 - I)/I
log [AuL3] /M
(f)
Warfarin
HSA-warfarin-AuL3
HSA-warfarin
Normalized intensity
Wavelength (nm)

Fig. S56 Binding site determination for the reaction of **AuL3** with HSA (5.0 μM protein, 50 mM KH_2PO_4, pH 7.50, 298 K). **(a)** Emission spectra of HSA···warfarin (5.0 μM warfarin λ^{ex} = 320 nm) recorded as a function of the concentration of AuL1 at 298 K. The spectra are fitted by single Gaussian functions to locate the emission maxima. Correlation coefficients, R^2, ranged from 0.990 to 0.999. **(b)** Emission spectra of HSA···dansylglycine (5.0 μM dansylglycine λ^{ex} = 420 nm) recorded as a function of the concentration of AuL3 at 298 K. **(c)** Stern–Volmer (SV) plot for native HSA, HSA···Warfarin, and HSA···dansylglycine as a function of the concentration of **AuL3** at 298 K. The plots are linear with an intercept of 1.0 when static quenching is operative (i.e., the quencher binds to the target protein and fluorophore(s)). The excitation and emission wavelengths for the fluorophore probes were: (i) Trp-214 (native HSA), λ^{ex} = 295 nm, λ^{em} = 340 nm; (ii) Warfarin (HSA-Warf), λ^{ex} = 320 nm, λ^{em} = 382 nm, and (iii) dansylglycine, λ^{ex} = 340 nm, λ^{em} = 500 nm. **(d)** Sphere of action model plot, $ln\left(\frac{I_0}{I}\right) = K_{SV}^{app}[Q]$, for the system. A linear plot with a zero intercept indicates static quenching by **AuL3** bound in some way to the fluorophore/macromolecule. Negative deviation from linearity signals a switch from static to dynamic quenching. **(e)** Double-log plot (eq. S9) of the fluorescence quenching data, $log\left(\frac{I_0-I}{I}\right) = logK + nlog[Q]$, to enable measurement of log*Ka* and the reaction stoichiometry (*n*). **(f)** Normalised fluorescence emission spectrum of HSA···warfarin (5.0 μM warfarin λ^{ex} = 320 nm) recorded as a function of the concentration of **AuL3** at 298 K to show the displacement of warfarin from HSA. Error bars indicate the standard deviation of three independent experiments.

Comment on Fig. S54 and S55. Both **AuL2** and **AuL3** quenched HSA•{warfarin} and HSA•{dansylglycine} monotonically, spectra are provided in Fig. S54 – S55a and b. To further investigate the quenching mechanism, we utilised the Stern-Vomer plot (eq. 1). For **AuL2** binding to HSA and HSA•{dansylglycine} produced linear plots while HSA•{warfarin} deviated from linearity, suggestive of a dual quenching mechanism. In the case of **AuL3** all three plots deviated from linearity, however, the explanation is highlighted in Fig. S51. We further investigated the deviation from linearity HSA•{warfarin} using the sphere of action model (eq. S8), once again only HSA•{warfarin} deviated from linearity. This provided sufficient evidence to conclude that at low concentrations of the Au(III) chelates (< 3.9 x 10^{-5} M^{-1}) the quenching observed was due to FRET and due to the Au(III) chelates binding in close proximity of warfarin, thereafter concentrations of Au(III) chelates above 3.96 x 10^{-5} M^{-1} were due to the displacement of warfarin from HSA and warfarin is now being quenched by the KH_2PO_4 buffer. HSA•{dansylglycine} was quenched by FRET and at no point was dansylglycine displaced. An assessment of the double log plot (Fig S54 and 55e) is used to provide further clarity on the site preference for **AuL2** and **AuL3**. Initially, when the Au(III) chelates is reacted with native HSA, Both Sudlow's sites I and II are ready to accept the incoming chelate. Assessing the $\log K_a$ of both Au(III) chelates binding to native HSA as compared to HSA•{warfarin} we observe the logKa to be higher in HSA•{warfarin}, logKa 6.18 and 5.35 for **AuL2** and **AuL3**, respectively as compared to the of native HSA logKa 4.57 (**AuL2**) and 4.78 (**AuL3**). Whereas for HSA•{dansylglycine} the $\log K_a$ was 4.49 and 4.78 for **AuL2** and **AuL3**, respectively which is one standard deviation off the $\log K_a$ of the Au(III) chelates binding to native HSA. Interpretation of the logKa maybe tricky and we offer two possible explanations. The presence of warfarin in the Sudlow's site I allows for conformational change within the binding pocket where **AuL2** and **AuL3** can bind to with a higher affinity. The value of $logK_a$ for **AuL2** and **AuL3** binding to HSA•{warfarin} could be the product equilibrium constant β_2, where $log\beta_2 = logK_1 + logK_2$, where $logK_1 + logK_2$. The binding mechanism of **AuL1**, **AuL2** and **AuL3** were all similar.

2.11. CD spectroscopy

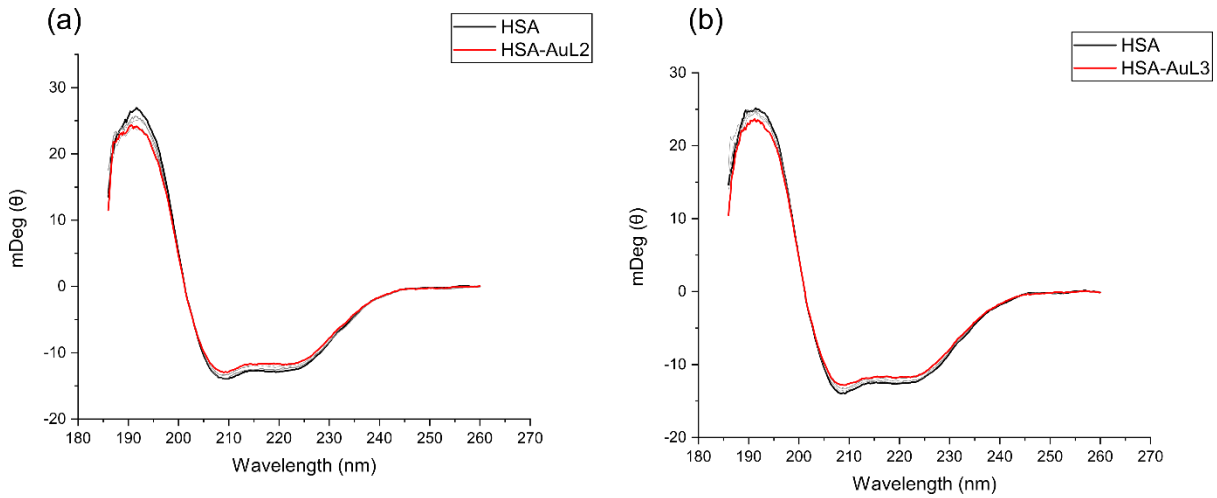


Fig. S57 Plots of the far-UV CD spectra of native HSA and the protein incubated with saturating doses of (a) **AuL2** and (b) **AuL3** recorded at 298 K in 50 mM KH2PO4 buffer at pH 7.50. The concentration of the Au(III) chelates ranged from 0 – 6 μM, the native protein is represented by the black line and the Au(III) chelate–HSA adduct at 6 μM is represented by the black line. The grey line represents the Au(III) chelates at 0.3, 1.5 and 3 μM.

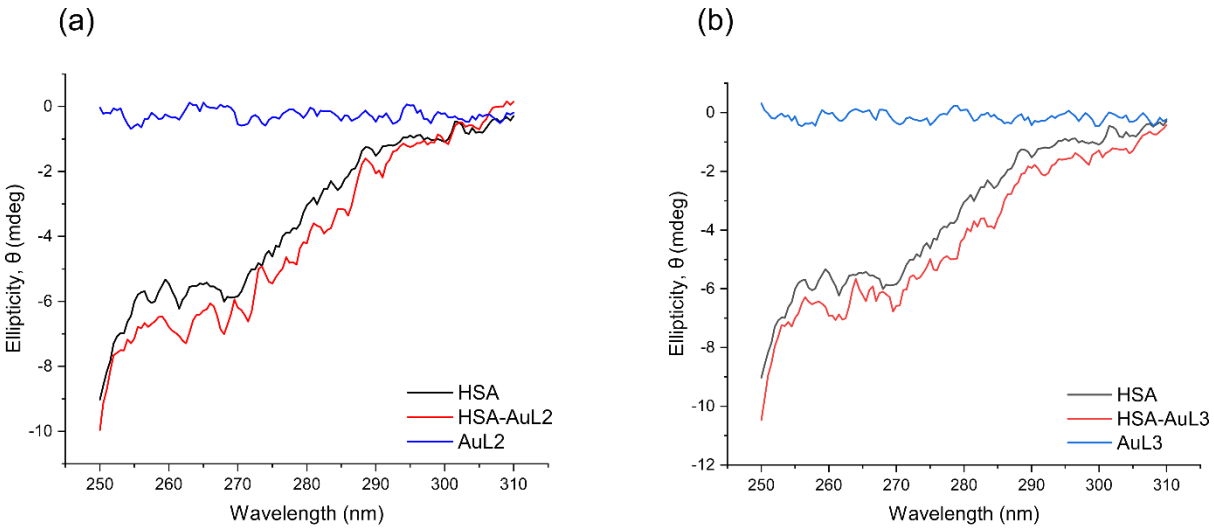


Fig. S58 Plots of the near UV CD spectra of native HSA and the protein incubated with a 1:1 (15 μM) ratio (a) **AuL2** and (b) **AuL3** recorded at 298 K in 50 mM KH_2PO_4 buffer at pH 7.50. The data represents unsmoothed spectra of the fine structure of the protein. Perturbations in the protein structure around Phe (250–270 nm), Tyr (~280 nm), and Trp (285–300 nm) residues may also be resolved in some difference spectra. Key maxima and minima are indicated (in nm).

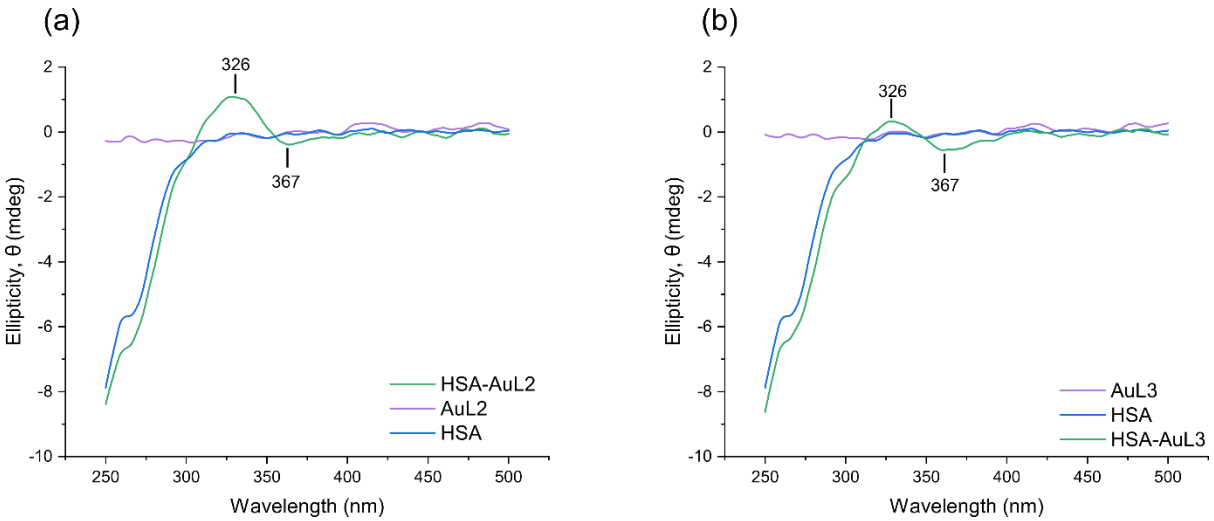


Fig. S59 Induced circular dichroism plots of (a) **AuL2** and (b) **AuL3** when bound to HSA in a 1:1 molar ratio (15 μM) in a 50 mM KH_2PO_4 buffer (pH 7.5) and smoothed using a relatively fine Lowess function (0.07 span).

2.12. Tables

Table S1. Crystallization data for the bis(pyrrolide-imine) Au(III) Schiff base chelate complexes.

	Crystal system	Space group	T/(K)	Number of crystals in the ASU	Z
AuL1	triclinic	P-1	173,15	1	2
AuL2	monoclinic	$P2_1/n$	173.15	1	4
AuL3	monoclinic	$P2_1/c$	173.15	2	8

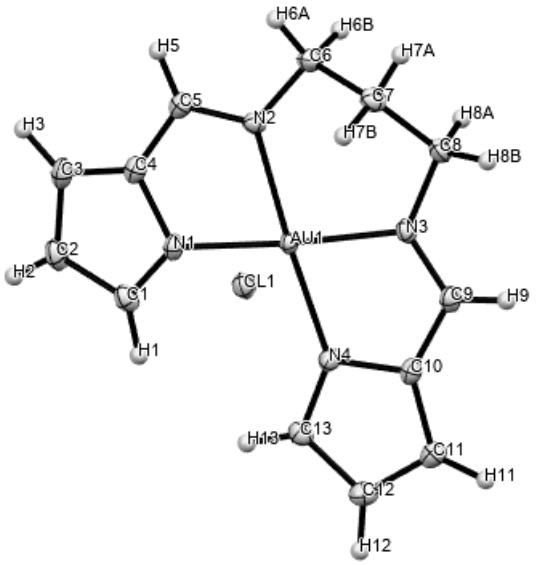
Table S2. Average bond lengths and bond angles for the Au(III) Schiff base chelate complexes.

Bond distances Å	**AuL1**	**AuL2**	**AuL3**
$Au–N_{pyrrole}$	1.997(18)	1.999(2)	1.998(16)
$Au–N_{imine}$	2.017 (18)	2.001(2)	2.009(16)
C–C=N	1.300(3)	1.305(3)	1.304(4)
Bond angles (°)			
$N_{pyrrole}–Au–N_{pyrrole}$	102.4 (8)	102.4(9)	102.7(7)
$Cis–N_{pyrrole}–Au–N_{imine}$	80.79(7)	80.99(9)	81.00(7)
$Trans–N_{pyrrole}–Au–N_{imine}$	175.92 (7)	176.5(9)	175.4(7)
$N_{imine}–Au–N_{imine}$	95.97(7)	95.61(9)	95.35(7)
$C_{pyrrole}–C–N_{imine}$	115.3(18)	115.3(2)	117.5(18)

Table S3. Crystal system data, X-ray data collection, and structure refinement details for compounds AuL1, AuL2 and AuL3.

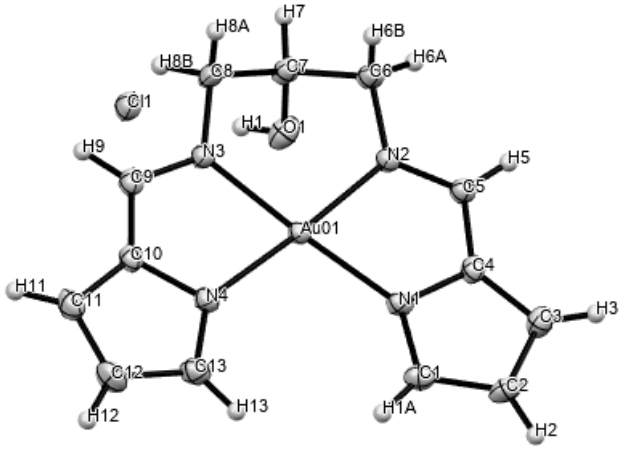
Identification code	**AuL1**	**AuL2**	**AuL3**
Empirical formula	C13H14AuClN4	C13H14AuClN4O	C15H19AuClN4O0.5
Formula weight	458.70	474.70	495.76
Temperature/K	153.15	293(2)	293(2)
Crystal system	triclinic	monoclinic	monoclinic
Space group	P-1	P21/n	P21/c
a/Å	7.5983(4)	6.9510(2)	13.6006(6)
b/Å	9.4222(5)	18.3730(6)	11.9212(5)
c/Å	10.5265(6)	10.9051(4)	19.7141(8)
α/°	68.634(2)	90	90
β/°	72.750(2)	97.7240(10)	97.219(2)
γ/°	72.193(2)	90	90
Volume/Å3	653.48(6)	1380.06(8)	3171.0(2)
Z	2	4	8
ρcalcg/cm3	2.331	2.285	2.077
μ/mm-1	11.451	10.854	9.450
F(000)	432.0	896.0	1896.0
Crystal size/mm3	0.278 × 0.201 × 0.194	0.257 × 0.162 × 0.082	0.2 × 0.18 × 0.15
Radiation	MoKα (λ = 0.71073)	MoKα (λ = 0.71073)	MoKα (λ = 0.71073)
2Θ range for data collection/°	6.404 to 61.992	6.318 to 66.572	5.916 to 66.554
Index ranges	-11 ≤ h ≤ 11, -13 ≤ k ≤ 13, -15 ≤ l ≤ 15	-10 ≤ h ≤ 10, -27 ≤ k ≤ 28, -16 ≤ l ≤ 16	-20 ≤ h ≤ 20, -18 ≤ k ≤ 18, -30 ≤ l ≤ 30
Reflections collected	66727	20943	201843
Independent reflections	4144 [Rint = 0.0295, Rsigma = 0.0099]	5300 [Rint = 0.0270, Rsigma = 0.0236]	12168 [Rint = 0.0367, Rsigma = 0.0129]
Data/restraints/parameters	4144/0/172	5300/0/182	12168/0/390
Goodness-of-fit on F2	1.265	1.166	1.053
Final R indexes [I>=2σ (I)]	R1 = 0.0138, wR2 = 0.0366	R1 = 0.0245, wR2 = 0.0461	R1 = 0.0169, wR2 = 0.0351
Final R indexes [all data]	R1 = 0.0138, wR2 = 0.0366	R1 = 0.0309, wR2 = 0.0475	R1 = 0.0213, wR2 = 0.0363
Largest diff. peak/hole / e Å-3	0.61/-1.78	1.39/-1.62	1.84/-1.36
Flack parameter			

Table S4. Selected geometrical parameters (Å, °) for the X-ray structure of AuL1. A labelled thermal ellipsoid plot (50% probability surfaces, H atoms drawn with arbitrary radii) is included to aid reading the tabulated data.



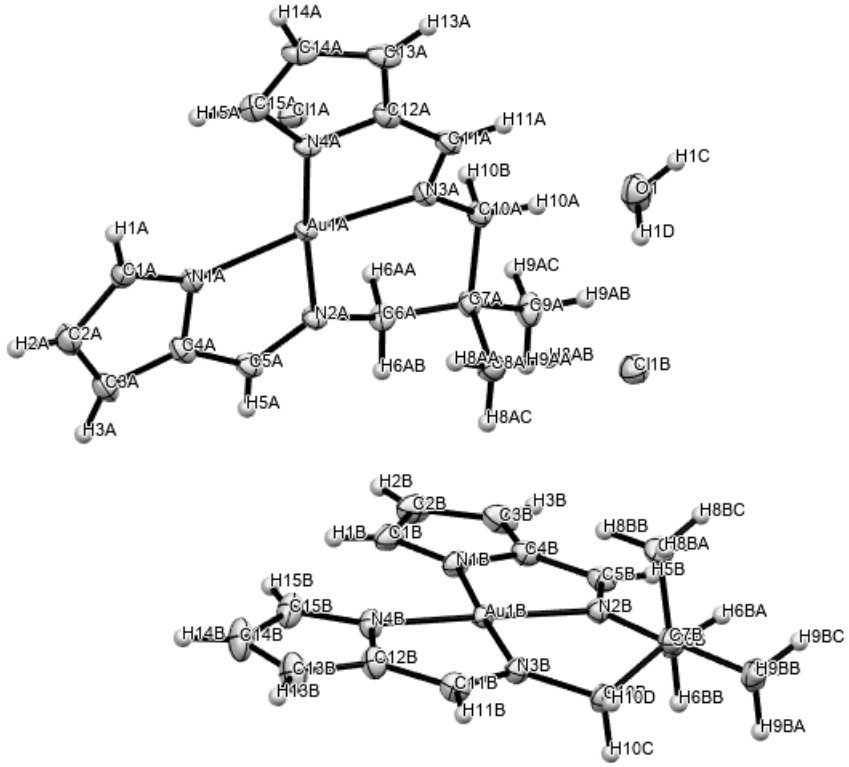
Parameter	Metric	Parameter	Metric
Au1–N3	2.012(2)	N2–C5	1.296(3)
Au1–N4	1.994(2)	N2–C6	1.466(3)
Au1–N1	2.004(2)	C8–C7	1.521(4)
Au1–N2	2.027(2)	C3–C2	1.397(4)
N3–C9	1.300(3)	C3–C4	1.395(3)
N3–C8	1.469(3)	C5–C4	1.410(4)
C9–C10	1.415(4)	C1–C2	1.399(4)
N4–C13	1.352(3)	C12–C11	1.400(4)
N4–C10	1.388(3)	C12–C13	1.395(4)
N1–C1	1.348(3)	C7–C6	1.525(4)
N1–C4	1.383(3)	C11–C10	1.393(4)

Table S5. Selected geometrical parameters (Å, °) for the X-ray structure of AuL1. A labelled thermal ellipsoid plot (50% probability surfaces, H atoms drawn with arbitrary radii) is included to aid reading the tabulated data.



Parameter	Metric	Parameter	Metric
Au01–N1	1.997(2)	N3–C8	1.470(4)
Au01–N2	2.009(2)	C4–C3	1.390(4)
Au01–N4	2.000(2)	C4–C5	1.421(4)
Au01–N3	2.014(2)	C1–C2	1.392(4)
N1–C4	1.389(3)	C9–C10	1.407(4)
N1–C1	1.354(3)	C10–C11	1.392(4)
N2–C5	1.299(3)	C3–C2	1.399(4)
N2–C6	1.467(3)	C13–C12	1.396(4)
O1–C7	1.416(4)	C7–C6	1.518(4)
N4–C10	1.382(4)	C7–C8	1.529(4)
N4–C13	1.353(4)	C11–C12	1.398(5)
N3–C9	1.311(3)		

Table S6. Selected geometrical parameters (Å, °) for the X-ray structure of **AuL1**. A labelled thermal ellipsoid plot (50% probability surfaces, H atoms drawn with arbitrary radii) is included to aid reading the tabulated data.



Parameter	Metric	Parameter	Metric
Au1A–N1A	1.9993(15)	Au1B–N1B	1.9909(15)
Au1A–N2A	2.0073(15)	Au1B–N2B	2.0094(15)
Au1A–N3A	2.0079(15)	Au1B–N3B	2.0120(15)
Au1A–N4A	2.0030(15)	Au1B–N4B	1.9976(16)
C1A–C2A	1.401(3)	C1B–C2B	1.387(3)
C1A–N1A	1.344(2)	C1B–N1B	1.354(2)
C2A–C3A	1.387(3)	C2B–C3B	1.395(3)
C3A–C4A	1.395(3)	C3B–C4B	1.390(3)
C4A–C5A	1.402(3)	C4B–C5B	1.411(3)
C4A–N1A	1.385(2)	C4B–N1B	1.387(2)
C5A–N2A	1.304(2)	C5B–N2B	1.305(2)
C6A–C7A	1.533(3)	C6B–C7B	1.526(3)
C6A–N2A	1.456(2)	C6B–N2B	1.467(2)
C7A–C8A	1.525(3)	C7B–C8B	1.526(3)
C7A–C9A	1.536(3)	C7B–C9B	1.537(3)
C7A–C10A	1.538(2)	C7B–C10B	1.532(3)
C10A–N3A	1.468(2)	C10B–N3B	1.465(2)
C11A–C12A	1.405(3)	C11B–C12B	1.413(3)
C11A–N3A	1.302(2)	C11B–N3B	1.300(2)

C12A–C13A	1.394(3)	C12B–C13B	1.388(3)
C12A–N4A	1.387(2)	C12B–N4B	1.385(2)
C13A–C14A	1.391(3)	C13B–C14B	1.393(3)
C14A–C15A	1.395(3)	C14B–C15B	1.388(3)
C15A–N4A	1.346(2)	C15B–N4B	1.350(2)

Table S7. Thermodynamic parameters for the binding of the Au(III) chelates by HSA in 50 mM KH_2PO_4 buffer at pH 7.50.

Compound	T (K)	ΔG (kJ mol^{-1})^a	ΔH (kJ mol^{-1})^a	ΔS (J K^{-1} mol^{-1})^a
AuL1	288	– 23.53 (2)		
	298	–25.88 (2)	44.15 (0.8)	–70.03 (3)
	310	–28.70 (2)		
AuL2	288	–23.42 (0.4)		
	293	–24.48 (0.5)	37.50 (5)	–63.02 (6)
	298	–25.53 (0.6)		
AuL3	288	–25.25 (0.1)		
	298	–27.37 (0.1)	35.8 (3)	–63.2 (3)
	310	–29.91 (0.2)		

^{a}The estimated standard deviations of the least significant digits are given in parentheses.

Table S8. Stern-Volmer quenching constants (K_{SV}) and binding constant (logKa) for the interaction of **AuL1**, **AuL2** and **AuL3** with HSA, HSA···warfarin and HSA···dansylglycine at 298 K in 50 mM KH_2PO_4 buffer at pH 7.50.

Compound	Temp. T (K)	$10^5\ K_{SV}$ (M^{-1})^{a,c}	log(K_a / M^{-1})^{c,d}
HSA–**AuL1**	298	1.10 (0.004)	4.46 (0.14)
HSA–**AuL1**-warfrain	298	2.97 (0.05)	5.72 (0.22)
HSA–**AuL1**-dansylglycine	298	1.10 (0.1)	4.50 (0.11)
HSA–**AuL2**	298	0.578 (0.003)	4.37 (0.14)
HSA–**AuL2**-warfrain	298	3.20 (0.1)	6.19 (0.15)
HSA–**AuL2**-dansylglycine	298	1.26 (0.03)	4.49 (0.10)
HSA–**AuL3**	298	1.08 (0.004)	4.78 (0.11)
HSA–**AuL3**-warfarin	298	2.05 (0.09)	5.35 (0.17)
HSA–**AuL3**-dansylglycine	298	1.00 (0.03)	4.61 (0.13)

$^a K_{SV}$ values (Stern-Volmer constants) were determined from fitting the data to eq. 1.. ^{c}The estimated standard deviation of the least significant digits are given in parentheses. ^{d}Ligand:HSA binding stoichiometry from the fit of the data to eq. 10.

Table S9. Summary of the change in α-helicity of native and HSA in the presence of **AuL1**, **AuL2** and **AuL3**

Au(III)-chelate	Concentration (μM)	% α–helicity
AuL1	0	58.82
	0.3	57.33
	1.5	58.53
	3	56.33
	6	55.10
AuL2	0	58.63
	0.3	58.46
	1.5	56.12
	3	56.04
	6	54.04
AuL3	0	58.02
	0.3	57.96
	1.5	56.68
	3	55.69
	6	53.75

Table S10. Summary of T_m of HSA in the absence and presence of Au(III)-chelates determined by using UV-CD spectroscopy.

	N1	N2	Average	S.D
HSA	64,21	64,86	64,535	0,459619
HSA-AuL1	64,62	64,28	64,45	0,240416
HSA-AuL2	63,96	64,89	64,425	0,657609
HSA-AuL3	63,96	68,42	66,19	3,153696

3. References

1 O. V. Dolomanov, L. J. Bourhis, R. J. Gildea, J. a. K. Howard and H. Puschmann, *J. Appl. Crystallogr.*, 2009, **42**, 339–341.

2 G. M. Sheldrick, *Acta Crystallogr. Sect. Found. Adv.*, 2015, **71**, 3–8.

3 G. M. Sheldrick, *Acta Crystallogr. Sect. C Struct. Chem.*, 2015, **71**, 3–8.

4 H. E. Gottlieb, V. Kotlyar and A. Nudelman, *J. Org. Chem.*, 1997, **62**, 7512–7515.

5 O. Q. Munro and G. L. Camp, *Acta Crystallogr. C*, 2003, **59**, o672–o675.

6 M. Van de Weert and L. Stella, *J. Mol. Struct.*, 2011, **998**, 144–150.

7 M. van de Weert, *J. Fluoresc.*, 2010, **20**, 625–629.

8 N. Busto, J. Valladolid, C. Aliende, F. A. Jalón, B. R. Manzano, A. M. Rodríguez, J. F. Gaspar, C. Martins, T. Biver, G. Espino, J. M. Leal and B. García, *Chem. – Asian J.*, 2012, **7**, 788–801.

9 J. Michl and E. W. Thulstrup, *Inc N. Y.*

10 B. Nordén and T. Kurucsev, *J. Mol. Recognit.*, 1994, **7**, 141–155.

11 M. R. Hicks, J. Kowa\lski and A. Rodger, *Chem. Soc. Rev.*, 2010, **39**, 3380–3393.

12 B. M. Zeglis, V. C. Pierre, J. T. Kaiser and J. K. Barton, *Biochemistry*, 2009, **48**, 4247–4253.

13 P. E. Pjura, K. Grzeskowiak and R. E. Dickerson, *J. Mol. Biol.*, 1987, **197**, 257–271.

14 D. Dalglkish, A. Peacocke, G. Fey and C. Harvey, *Biopolym. Orig. Res. Biomol.*, 1971, **10**, 1853–1863.

15 J. R. Lakowicz, *Principles of Fluorescence Spectroscopy*, Springer Science & Business Media, 2013.

16 D. Peak, T. C. Werner, R. M. Dennin and J. K. Baird, *J. Chem. Phys.*, 1983, **79**, 3328–3335.

17 D. K. Singh, P. K. Iyer and P. K. Giri, *Carbon*, 2012, **50**, 4495–4505.

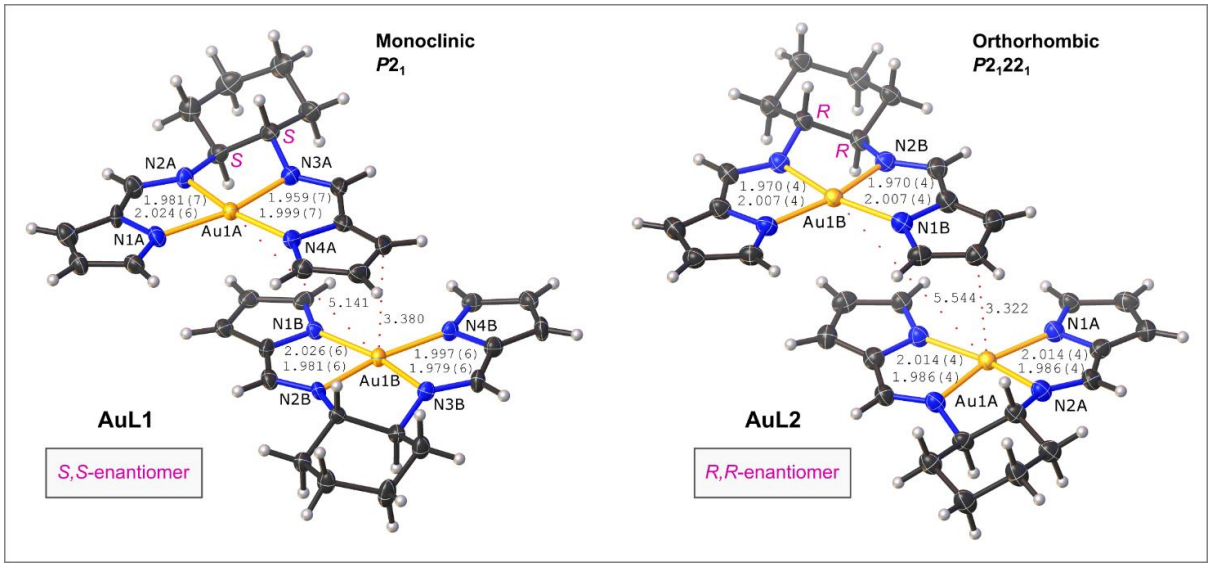
18 J. Wang, D. Wang, E. K. Miller, D. Moses, G. C. Bazan and A. J. Heeger, *Macromolecules*, 2000, **33**, 5153–5158.

19 P. D. Ross and S. Subramanian, *Biochemistry*, 1981, **20**, 3096–3102.

20 X. Li and S. Wang, *New J. Chem.*, 2015, **39**, 386–395.

21 P. D. Ross and S. Subramanian, *Biochemistry*, 1981, **20**, 3096–3102.

Supporting Information:



Human serum albumin binds chiral cytotoxic Au(III) chelates as fully intact complexes with unique thermodynamics

Sheldon Sookai,[a] Matthew P. Akerman[b] and Orde Q. Munro*[,a]

[a]*Molecular Sciences Institute, School of Chemistry, University of the Witwatersrand, PO WITS 2050, Johannesburg, South Africa*

[b]*School of Chemistry and Physics, University of KwaZulu-Natal, Pietermaritzburg, 3201, South Africa*

E-mail: orde.munro@wits.ac.za

a

Table of Contents

1. Experimental Methods 79
1.1 Instruments 79
1.1.1. Crystallography 79
1.1.2. General spectroscopy 80
1.2 Compound Synthesis 80
1.2.1. Synthesis of enantiomerically pure ligands 80
1.2.2. Synthesis of *tert*-butylammonium tetrachloroaurate(III) 80
1.2.3. Metalation of the enantiomerically pure ligands 81
1.2.4. Characterisation of the enantiomerically pure ligands 81
Scheme 1. Structures of (a) H2L1 and (b) H2L2 showing the atom numbering sequence 81
1.2.5. Characterisation of AuL1 and AuL2 82
1.3 Fluorescence Spectroscopy 82
1.4 Circular dichroism (CD) spectroscopy 83
1.5 *In vitro* cell screening 83
2. Figures and Tables 85
2.1 General Characterisation Data 85
2.2 Fluorescence spectroscopy 97
2.3 CD spectroscopy data 102
2.4 NCI-60 cytotoxicity data 104
2.5 X-ray crystal structures 108
3. References 117

1. Experimental Methods

All solvents (HPLC grade) and chemical synthons were used as received from Merck Sigma-Aldrich® without further purification. Deuterated dimethyl sulfoxide was stored over activated 4 Å molecular sieves. Human serum albumin (HSA) was purchased from Sigma and used as received without further purification. Ultrapure water (Type I) was produced using a Merk-Millipore Direct-Q® 3 UV Water Purification System.

1.1 Instruments

1.1.1. Crystallography

The single crystal X-ray structure determination for **AuL1** was carried out with a three-circle Bruker Apex-II X-ray diffractometer equipped with a CCD area detector and a fine-focus sealed X-ray tube source (Mo anode). The crystal was mounted under Paratone® oil on a nylon loop (Hampton Research) and the crystal was kept at 173(1) K during data collection (Oxford CryoStream 700). Using Olex2,[1] the structure was solved with the ShelXT[2] structure solution program (intrinsic phasing) and refined with ShelXL[3] using least squares minimization.

The single crystal X-ray structure determination for **AuL2** was carried out with a four-circle Oxford Xcalibur2 X-ray diffractometer equipped with a CCD area detector and a fine-focus sealed X-ray tube source (Mo anode). The crystal was affixed upon a glass microfibre with epoxy cement for data collection and the crystal was kept at 100(2) K during data collection (Oxford CryoStream 700). The structure was solved and refined as above using least squares minimization. Thereafter, the structure was further refined using Olex2 by implementing aspherical atomic form factors in the module NoSpherA2[4] interfaced with Orca 5.0.3.[5,6] The wavefunction for the system was determined at the PBE[7]/Jorge-DZP-DKH level of theory (relativistic Hamiltonian and basis set).[8]

1.1.2. General spectroscopy

Nuclear magnetic resonance (NMR) spectra were recorded on either a Bruker Avance III 400 (400.21 MHz for ^{1}H, 100.64 MHz for ^{13}C, 162.01 MHz for ^{31}P and 376.57 MHz for ^{19}F) or a Bruker Avance-III-300 spectrometer operating at 300.13 MHz for ^{1}H, 75.47 MHz for ^{13}C, 121.49 MHz for ^{31}P and 282.40 MHz for ^{19}F. All spectra were recorded at 298 K with 5 mm BBOZ or TBIZ probes. Deuterated solvent signals were used to correct for the reported chemical shifts in δ (in ppm). For $(CD_3)_2SO$, $CDCl_3$, D_2O and CD_3OD the δ H was referenced as 2.50, 7.26, 4.79 and 3.31 ppm, respectively, and the δ ^{13}C {^{1}H} was referenced at 39.52, 77.16, D_2O had no peak, and 49 ppm, respectively. MestReNova (version 14.2.1-27684) was used to analyse NMR spectra. The coupling patterns are abbreviated as follows: s - singlet; d - double; t - triplet; q - quartet; sept – septet; m – multiplet; br s – broad signal. Proton coupling constants (J) are given in hertz (Hz). Impurities are stated on the NMR figures.[9] FT-IR spectra of powder samples were recorded using a Bruker Alpha FTIR spectrometer incorporating a Bruker Platinum® diamond ATR sampling accessory. Spectra were analysed using the OPUS software package on the spectrometer (version 7.5). Mass spectra were recorded with a Bruker Compact Q-TOF high-resolution mass spectrometer using Bruker Daltronics HyStar 3.2 SR4 software. Bruker Compass DataAnalysis software (Version 4.3) was used to analyse chromatograms. Samples of pure compounds (typically ca. 10 µg/mL) were prepared in HPLC grade acetonitrile or methanol for metal chelates and HPLC grade methanol for ligands. Solutions were acidified using 0.1% (V/V) formic acid. UV-Vis electronic spectra were recorded using either a PerkinElmer Lambda 365 double beam spectrometer connected to a Peltier controller and multicell thermostatic cell block or an Analytik Jena Specord210 Plus double-beam instrument fitted with an external water circulating thermostatic bath and thermostatted cell holders. The spectral data were analysed with the spectrometer software or Origin Pro 2020. Spectra were recorded (10-mm pathlength quartz cuvettes) as a function of concentration for both characterisation and the determination of molar absorptivity constants.

1.2 Compound Synthesis

1.2.1. Synthesis of enantiomerically pure ligands

(1*S*,2*S*) and (1*R*,2*R*)-*N*,*N*'-bis[(1*E*)-1*H*-pyrrol-2-ylmethylene] cyclohexane -1,2-diamine (**H_2L1** and **H_2L2**). Both enantiomerically pure ligands were synthesised by grinding the enantiomerically pure (1*S*, 2*S*)- or (1*R*, 2*R*)-cyclohexane diamine (0.303 g, 2.65 mmol) with an agate pestle and mortar with pyrrole-2-carboxaldehyde (0.500 g, 5.30 mmol) for between 10 to 15 minutes, until a brown oil was formed. The brown oil was dissolved in dichloromethane and dried with $MgSO_4$ to remove the water from the condensation reaction. The solution was filtered through celite before been layered with hexane, which yielded thin white rod-shaped crystals. A yield of 65% was obtained.

1.2.2. Synthesis of *tert*-butylammonium tetrachloroaurate(III)

Hydrogen tetrachloroaurate(III) (1.218 g) was dissolved in 50 ml of deionized water. The solution was then added to a solution of *tert*-butylammonium hydrogen sulphate (1.020 g) resulting in the formation of a bright yellow precipitate which was $[Bu_4N][AuCl_4]$ (lipophilic gold(III) salt). $[Bu_4N][AuCl_4]$

was extracted into chloroform, dried over $MgSO_4$ before been filtered and the chloroform was removed by rotary evaporation. The resulting material was a crystalline bright yellow powder (1.55 g, 88%).

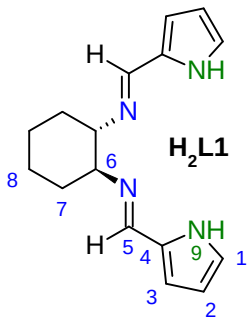
$$H[AuCl_4]_{(aq)} + [Bu_4N][HSO_4]_{(s)} \qquad [Bu_4N][AuCl_4]_{(s)} + \longrightarrow \quad H_2SO_{4\ (aq)}$$

1.2.3. Metalation of the enantiomerically pure ligands

The synthesis of 2,2'-{(1*S*,2*S*) or 2,2'-{(1*R*,2*R*)-cyclohexane-1,2-diylbis[nitrilo(*E*)methylylidene]}bis (pyrrol-1-ido)gold(III) hexafluorophosphate(V) [Au((1*S*,2*S*)**L1**)PF_6 (**AuL1**) and [Au((1*R*,2*R*)**L2**)]PF_6 (**AuL2**) occurs via the same procedure from the enantiopure ligands. To a 50 ml round bottom flask containing the pure solid ligand (201 mg, 0.750 mmol) was added 10 ml of ethanol, which was heated to dissolve the ligand. The solution was then allowed to cool to room temperature. Thereafter, a 10 ml solution of dry dichloromethane containing $[Bu_4N][PF_6]$ (133 mg, 0.344 mmol) and $[Bu_4N][AuCl_4]$ (100 mg, 0.172 mmol) was added. The solution was stirred for around 3 hours at ambient temperature until an orangish-yellow precipitate had formed. The precipitate was filtered and washed with dry dichloromethane. Red-orange crystals suitable for single crystal XRD were grown by vapour diffusion of diethyl ether into an acetonitrile solution of the product. The crystalline salts were shown to be **AuL1** and **AuL2** by X-ray crystallography.

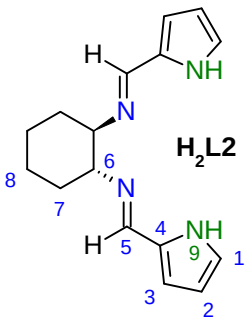
1.2.4. Characterisation of the enantiomerically pure ligands

(a)



(*E*,*E*)-*N*,*N*'-[(1*S*,2*S*)-cyclohexane-1,2-diyl]bis-[1-(1*H*-pyrrol-2-yl)methanimine]

(b)

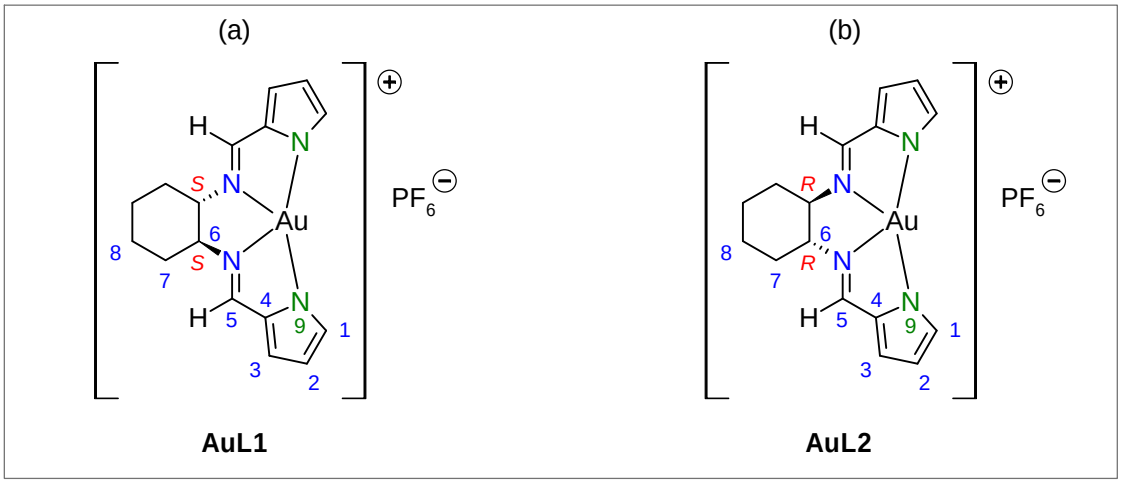


(*E*,*E*)-*N*,*N*'-[(1*R*,2*R*)-cyclohexane-1,2-diyl]bis-[1-(1*H*-pyrrol-2-yl)methanimine]

Scheme 1. Structures of (a) H2L1 and (b) H2L2 showing the atom numbering sequence.

IR (cm^{-1}): 3218w δ(NH, pyrrole), 3110m br δ(CH, imine), 2944 – 2853s ν(CH_2), 1627s ν(C=N). ^{1}H NMR (400 MHz, DMSO-d_6, 300 K) [δ, ppm]: 1.34 – 1.80 (m, 8H, H-7 and H-8), 3.23 (m, 2H, H-6), 6.01 (t, J = 3.0 Hz, 2H, H-2), 6.31(dd, $^3J_1$ = 3.5 Hz, $^3J_2$ 1.4 Hz, 2H, H-3), 6.76 (t, J = 1.9 Hz, 2H, H-1), 7.94 (s, 2H, H-5), 11.16 (s, 2H, H-9). ^{13}C NMR (101 MHz, DMSO-d_6, 298 K) [δ, ppm]: 24.70 (C-8), 33.85 (C-7), 74.09 (C-6), 109.07 (C-2), 113.61 (C-3), 122.08 (C-1), 130.33 (C-4), 151.26 (C-5). UV-vis (acetonitrile) [λ, max, nm; ε, mol^{-1} dm^3 cm^{-1}]: 289; 2.95 × 10^4 (**H_2L1**) and 2.37 x 10^4 (**H_2L2**).

1.2.5. Characterisation of AuL1 and AuL2



Scheme 2. Structures of (a) [Au((1S,2S)**L1**)PF_6 (**AuL1**) and (b) [Au((1R,2R)**L2**)]PF_6 (**AuL2**). The atom numbering scheme is indicated. The enantiomeric complexes were analysed by ^{1}H NMR, ^{13}C NMR, ^{19}F NMR and ^{32}P NMR, UV-visible spectroscopy, mass spectroscopy, and FT-IR spectroscopy as well as single crystal X-ray diffraction.

^{1}H NMR (400 MHz, DMSO-d_6) δ 8.38 (s, 1H, H-5), 7.80 (d, J = 2.0 Hz, 1H, H-1), 7.07 (d, J = 4.2 Hz, 1H, H-3), 6.47 (dd, J = 4.2, 2.1 Hz, 1H, H-2), 4.30 (d, J = 9.0 Hz, 1H, H-6), 2.61 (d, J = 12.2 Hz, 1H, H-7), 1.77 (d, J = 9.1 Hz, 1H, H-7), 1.62 (d, J = 10.2 Hz, 1H, H-8), 1.34 (q, J = 11.4, 10.4 Hz, 1H, H-8). ^{13}C NMR (101 MHz, DMSO-d6) δ 157.70 (C-5), 142.16 (C-1), 138.80 (C-4), 123.98 (C-3), 111.72 (C-2), 75.68 (C-6), 27.95 (C-7), 22.94 (C-8). ^{31}P NMR (162 MHz, DMSO-d_6) δ −127.11 – −158.79 (m). ^{19}F NMR (376 MHz, DMSO-d_6) δ −70.16 (d, J = 711.2 Hz). **AuL1** IR (cm^{-1}): 2948m br ν(CH, imine), 1563s br ν(C=N), 822s ν(PF_6). **AuL2** IR (cm^{-1}): 2945m br ν(CH, imine), 1564s br ν(C=N), 826s ν(PF_6). ESI-MS: m/z+ = 463.1276 (**AuL1**) and 463.1284 (**AuL2**); M+ (463.1197). UV-vis (MeCN) [λ_{max}, nm (ε, mol^{-1} dm^3 cm^{-1})]: 288 (1.15 × 10^4); 382 (0.47 × 10^4).

1.3 Fluorescence Spectroscopy

Fluorescence measurements were performed on a Cary Eclipse fluorescence spectrophotometer (Varian, Australia) equipped with a 1.0 cm quartz cell and a circulating thermostat bath. The HSA concentration was kept at 5.0 × 10^{-6} mol dm^{-3} and the excitation and emission slit widths were fixed at 5 nm. The concentrations of **AuL1** and **AuL2** ranged from 0 to 98 × 10^{-6} mol dm^{-3}. Both gold(III) chelates were made up in MeCN and the final MeCN concentration was under 0.1% (V/V) to prevent denaturation of HSA. HSA was excited at 295 nm (excitation of Trp-214), and the emission spectra were recorded from 310 to 400 nm. Spectral titrations were carried out at three temperatures (288, 298 and 310K) in triplicate.

Correction of fluorescence data. An inner filter effect (IFE) correction was applied to all fluorescence data using eq. S1.[10]

$$F_{corrected} = F_{observed} * 10^{Aex*dex+Aem*dem} \quad \text{S1}$$

Where A_{ex} and A_{em} are the absorbance readings at the excitation and emission wavelengths and *d* is the path length of the cuvette. The correction is required when the added ligand (metal chelate) absorbs significantly at the excitation and emission wavelengths of the fluorophore being analysed.

Further corrections to the concentration of **AuL1** and **AuL2** were not required as the concentration of both Au(III) chelates >> than [HSA].[11]

$$[Ligand]_{free} = [Ligand]_{added} \quad \text{S2}$$

Fluorescent probe displacement assay. Warfarin and ibuprofen were used as specific site marker fluorescent probes for Sudlow's sites I and II, respectively. Steady-state fluorescence spectra were recorded as described above at 298 K using 10 nm excitation and emission bandwidths for warfarin, while 5 nm excitation and 10 nm emission band widths were employed for ibuprofen. The fluorophores warfarin and dansylglycine were equilibrated (bound) to HSA (50 mM KH_2PO_4 buffer, pH 7.50) and were excited at 320 nm and 340 nm, respectively. The emission spectrum was measured in the range 350 – 500 nm for warfarin and 400 – 650 nm for dansylglycine. The HSA and fluorescence probe concentrations were both used at 5.0 μM. Titrations were performed by increasing the concentrations of **AuL1** and **AuL2** in the protein-probe solution from 0 to 98 μM for warfarin and 0 to 78 μM for dansylglycine.

1.4 Circular dichroism (CD) spectroscopy

Far UV CD spectra of solutions of HSA (5.0×10^{-9} mol dm^{-3}) in the absence and presence of increasing concentrations (0 – 6 μM) of **AuL1** and **AuL2** were recorded with a JASCO J-1500 CD spectrometer equipped with a Peltier temperature controller (25 °C). A scan speed of 100 nm min^{-1} was employed for spectral acquisition with a 0.5 nm data pitch and a response time of 2 s. Each spectrum was the average of three scans. Spectra were recorded over a wavelength range of 190–260 nm (0.4 cm pathlength quartz cuvette). All spectra were processed with JASCO Spectral Manager™.

Near UV-vis CD spectra (250–500 nm, 1.0-cm pathlength quartz cuvette, 25 °C) were recorded similarly to detect induced CD (ICD) signals of the achiral ligands and metal chelates upon their uptake by HSA. Typically, HSA (15.0×10^{-6} M) was incubated with a saturating dose (15×10^{-6} M) of either **AuL1** or **AuL2** for at least 60 min. A scan speed of 200 nm min^{-1} was used with a 0.5-nm data pitch (response time, 2 s); each spectrum was the average of three scans.

1.5 *In vitro* cell screening

The method given here is a restatement (for completeness) of that published and used by the DTP,[12] to which **AuL1** and **AuL2** were submitted for in vitro cytotoxicity screening. The human tumour cell lines of the NCI-60 cancer screening panel are grown in RPMI 1640 medium containing 5% foetal bovine serum and 2 mM of the amino acid L-glutamine. For most screening experiments, cells are inoculated into 96-well microtiter plates in 100 μL of solution with plating densities between 5×10^3 and 4×10^4 cells per well, depending on the doubling time of a particular cell line. After cell inoculation, the 96- well plates are incubated at 37 °C, with an atmospheric composition of 5% CO_2 and 95% air at 100% relative humidity for 24 hours prior to addition of experimental drugs. After 24 hours, two plates of each cell line are fixed *in situ* with tricarboxylic acid (TCA), to represent a measurement of the cell population for each cell line at the time of drug addition (Tz). Experimental drugs are dissolved in DMSO at a concentration 400× that of the maximum desired test concentration and stored frozen prior to use. As required, an aliquot of frozen drug concentrate is thawed and diluted to twice the desired maximum test concentration with appropriate medium, containing 50 μg ml^{-1} of gentamicin (an aminoglycoside antibiotic). Four, 10-fold serial dilutions are carried out to provide a total of five drug concentrations as well as a control. Aliquots of 100 μl of these different drug dilutions are added to the appropriate wells already containing 100 μl of medium, resulting in the required final drug concentrations.

Following drug addition, the plates are incubated for an additional 48 hours at 37 °C, with an atmosphere consisting of: 5% CO_2, 95% air, and 100% relative humidity. For adherent cells, the assay is terminated by the addition of cold TCA. Cells are fixed *in situ* by the gentle addition of 50 µl of cold 50% (w/v) TCA (final concentration, of 10% TCA) and incubated for 1 hour at 4 °C. The supernatant liquid is discarded, and the plates are washed repeatedly with water and air dried. Sulforhodamine B (SRB) solution (100 µl) with a concentration of 0.4% (w/v) in 1% acetic acid is added to each well, and plates are incubated for 10 minutes at room temperature. After staining, unbound dye is removed by washing repeatedly with 1% acetic acid solution and the plates are again air dried. Bound stain is subsequently solubilised with 10 mM tris(hydroxymethyl)aminomethane base, and the absorbance is read on an automated plate reader at a wavelength of 515 nm, which corresponds to λ_{max} of the dye used. This is a method of transcriptional and translational (MTT) assay. For suspension cells, the methodology is the same as above with the exception that the assay is terminated by fixing settled cells at the bottom of the wells by adding 50 µl of 80% TCA (final concentration, 16% TCA).

Using the seven absorbance measurements: time zero, (Tz), control growth, (C), and test growth in the presence of the gold(III) chelate at the five concentration levels (Ti), the percentage growth is calculated at each of the drug concentrations. Percentage growth inhibition is calculated as:

$$\left(\frac{T_i - T_z}{C - T_2}\right) x\ 100\% \qquad \text{S3}$$

$$\left(\frac{T_i - T_z}{T_2}\right) x\ 100\% \qquad \text{S4}$$

Eq. S3 is applicable for concentrations for which Ti ≥ Tz, while eq. S4 is applicable for drug concentrations at which Ti < Tz. Three dose response parameters are then calculated for each experimental compound from the data collected. Firstly, GI_{50} is calculated from:

$$\left(\frac{T_i - T_z}{C - T_2}\right) x\ 100\% = 50 \qquad \text{S5}$$

Secondly, (TGI or IC_{50}) is calculated from:

$$Ti = Tz \qquad \text{S6}$$

Thirdly LC_{50} is calculated from:

$$\left(\frac{T_i - T_z}{T_2}\right) x\ 100\% = -50 \qquad \text{S7}$$

2. Figures and Tables

2.1 General Characterisation Data

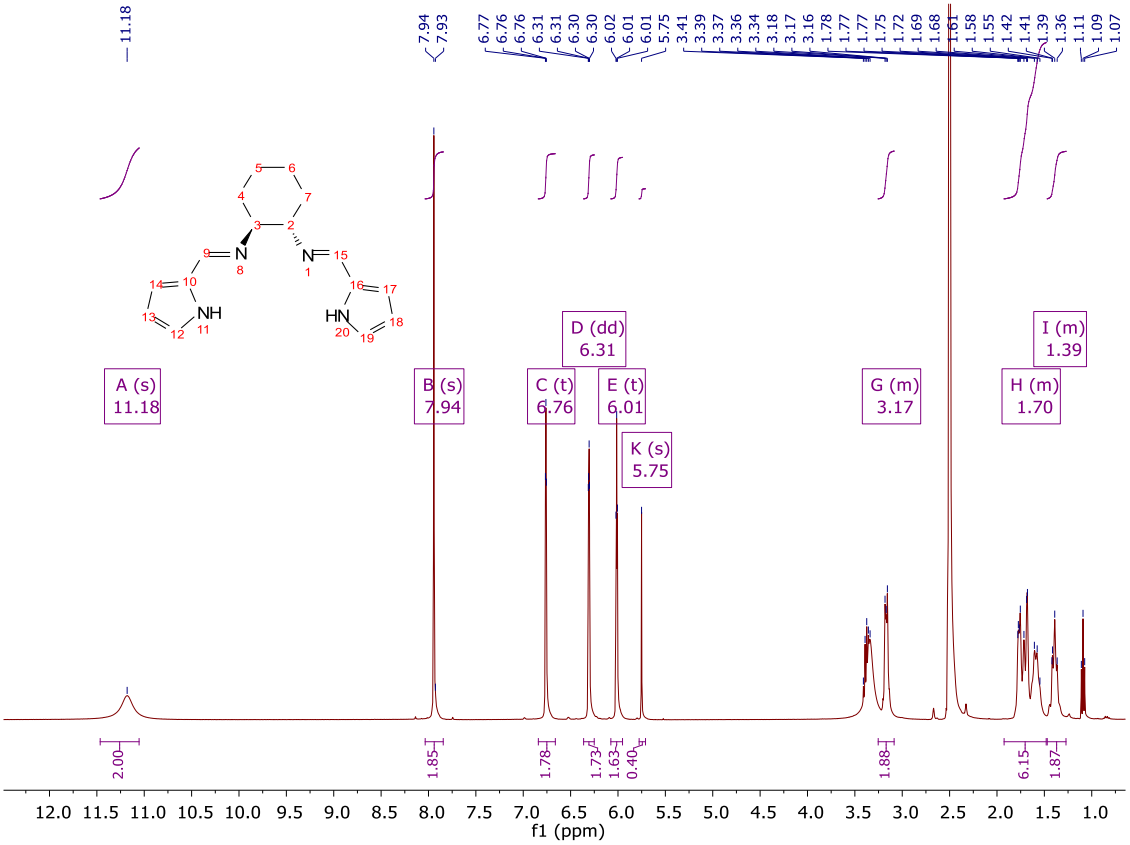


Fig. S1 ^{1}H NMR of **H_2L1** in DMSO–d6.

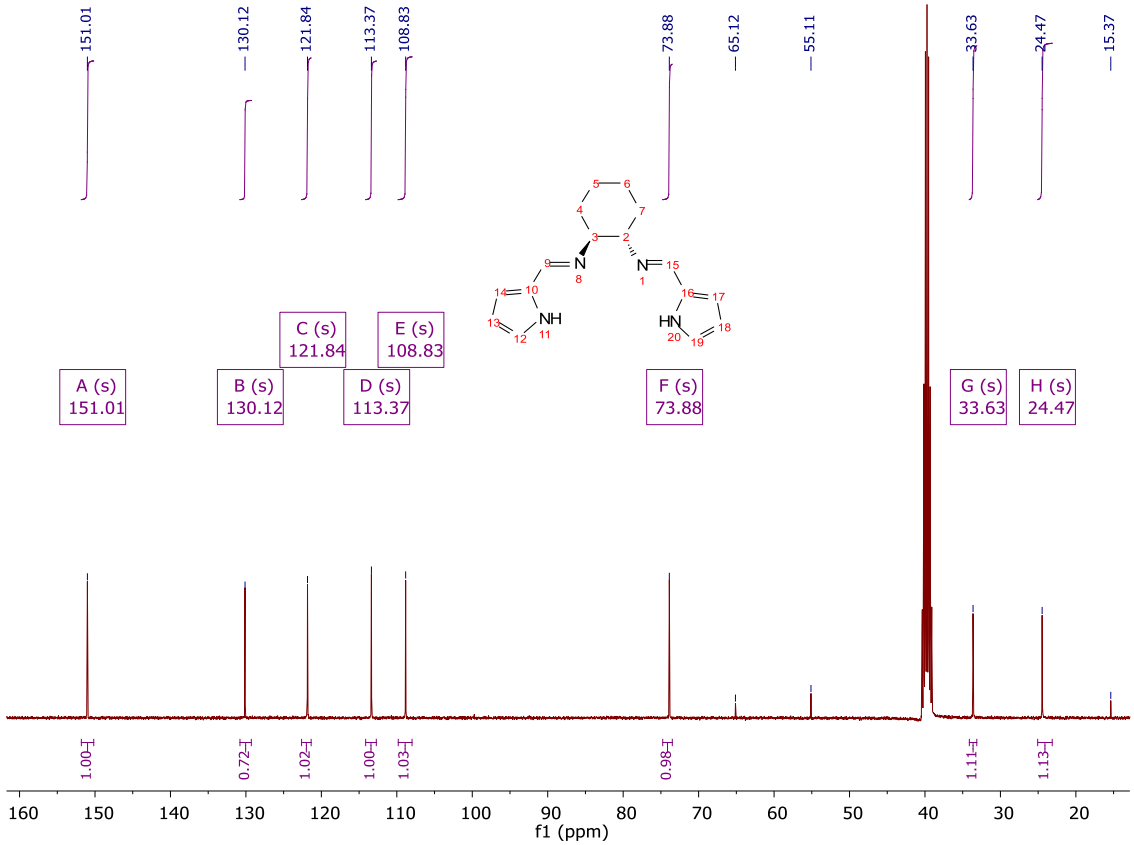


Fig. S2 ^{13}C NMR of **H_2L1** in DMSO–d6.

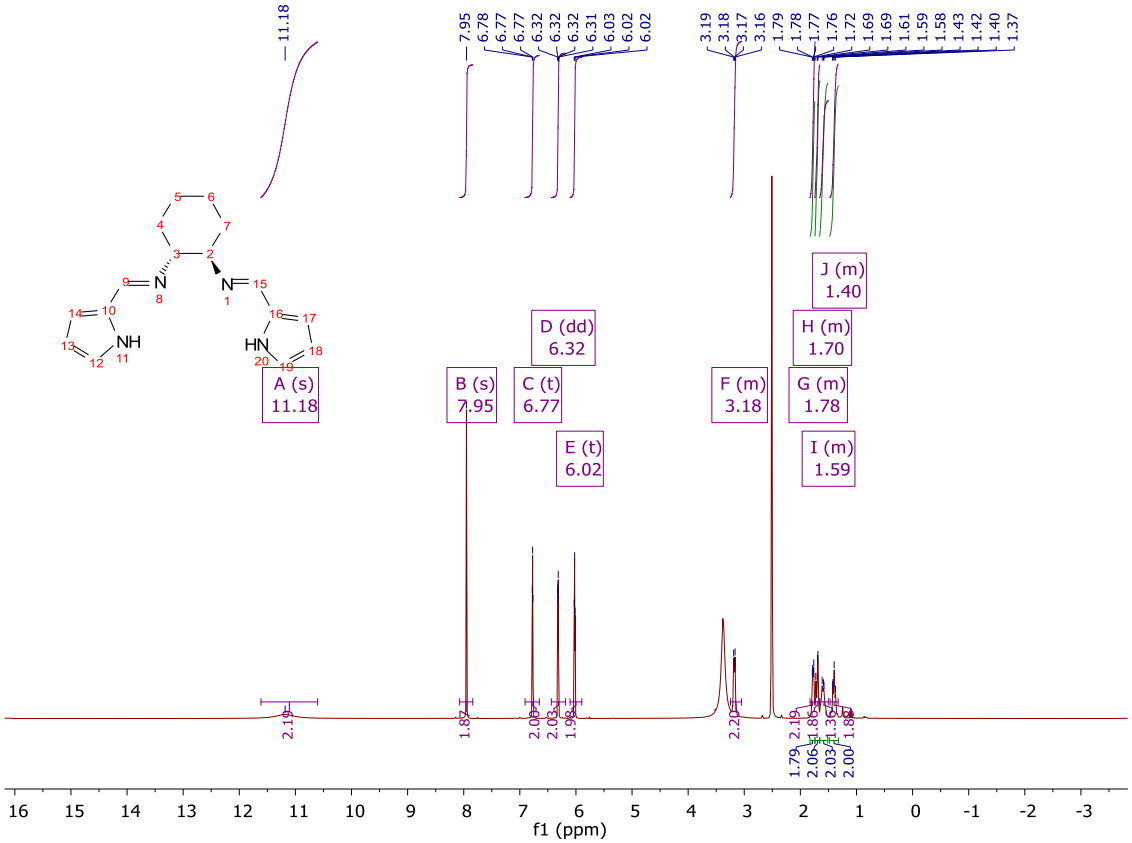


Fig. S3 ^{1}H NMR of **H_2L2** in DMSO–d6.

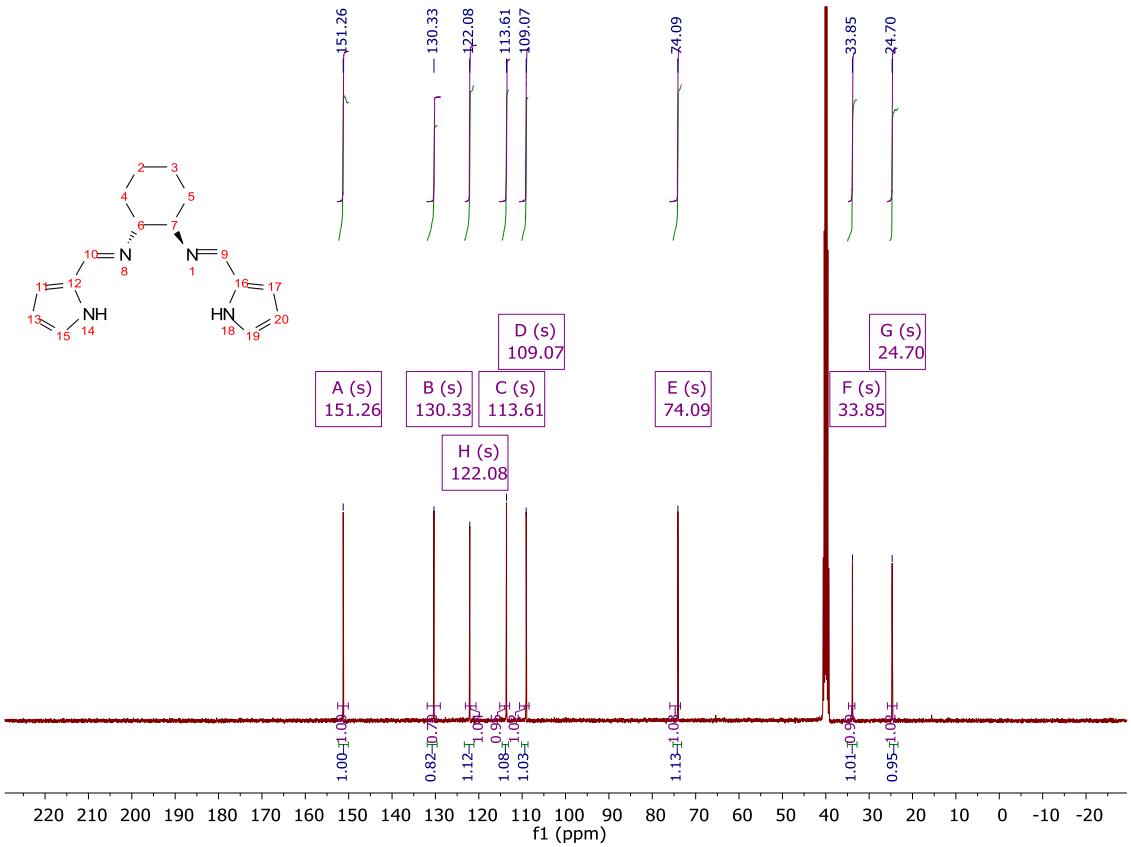


Fig. S4 ^{13}C NMR of **H_2L2** in DMSO–d6.

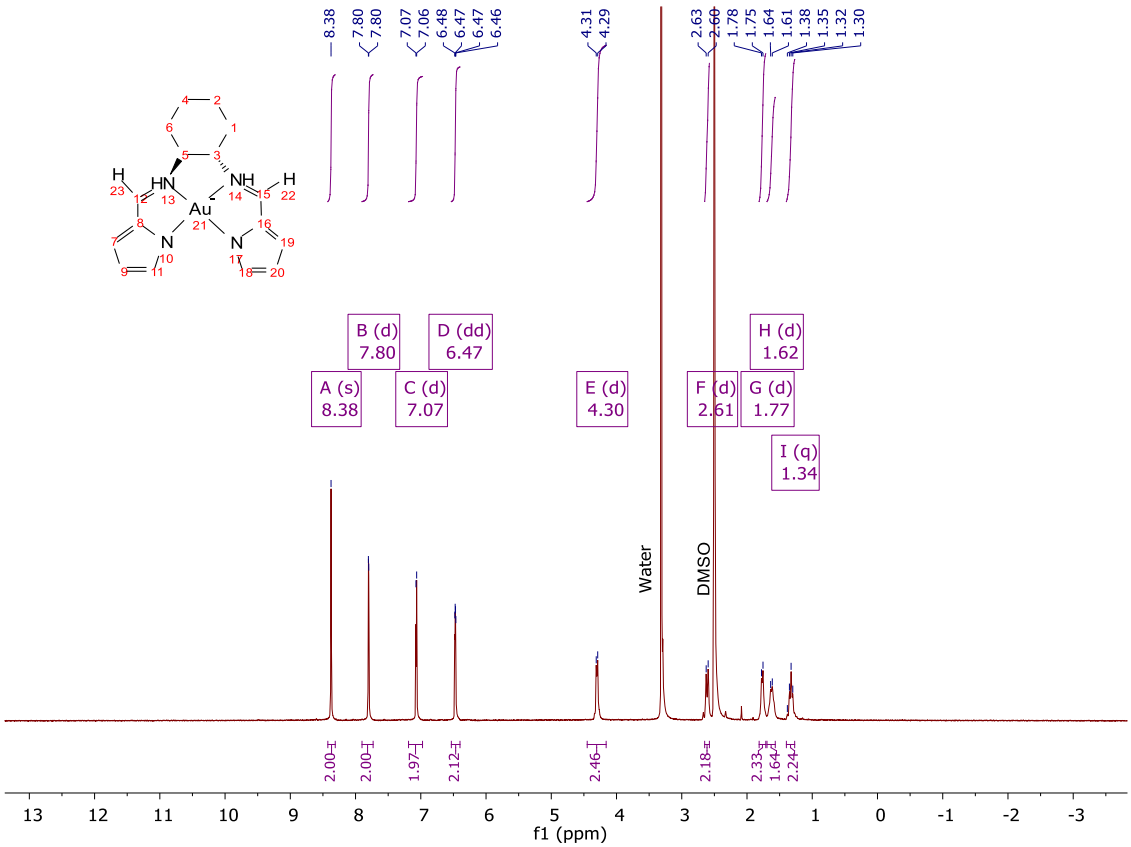


Fig. S5 ^{1}H NMR of **AuL1** in DMSO–d6.

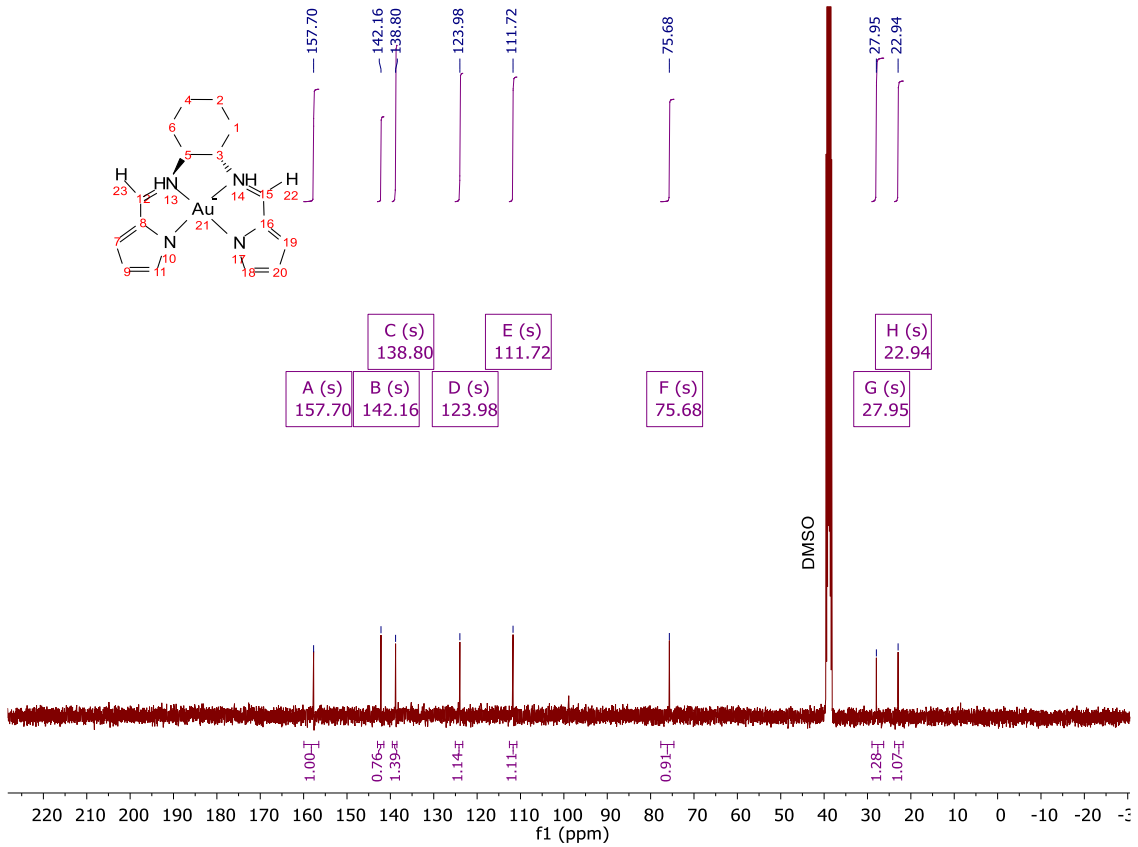


Fig. S6 ^{13}C NMR of **AuL1** in DMSO–d6.

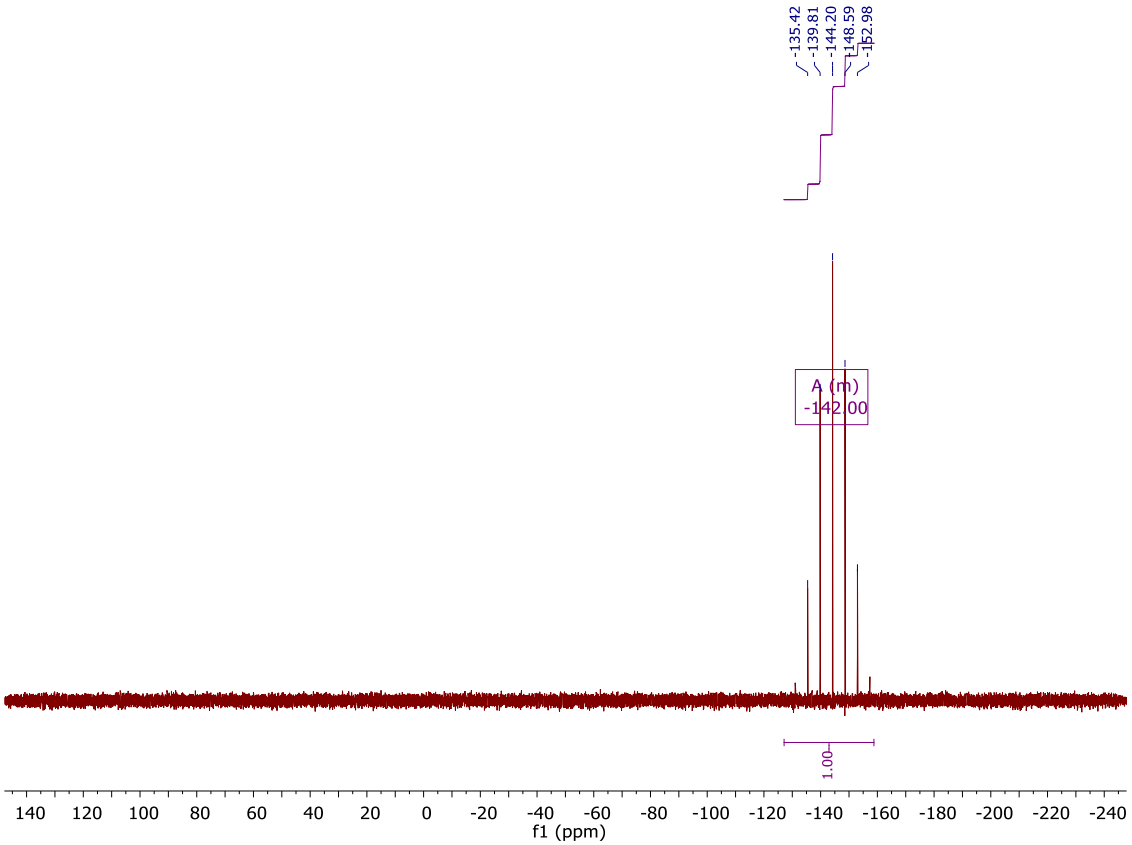


Fig. S7 ^{31}P NMR of **AuL1** in DMSO–d6

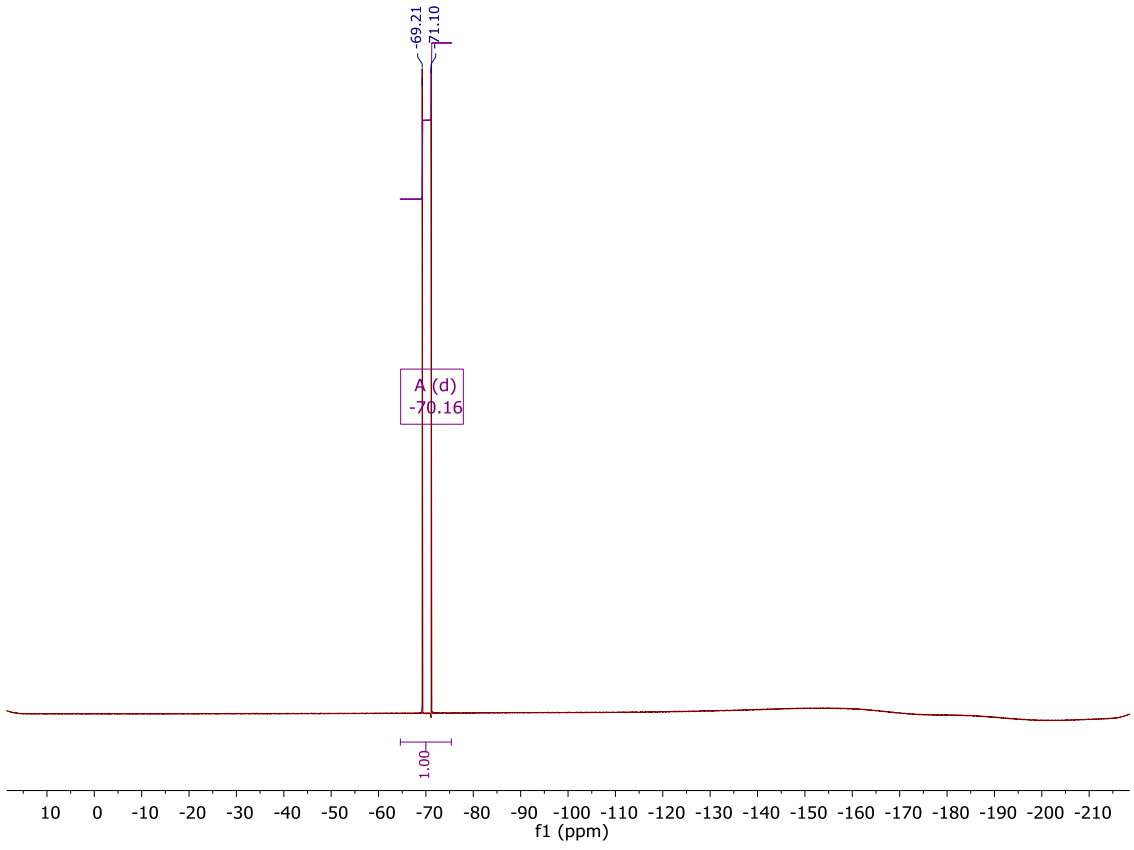


Fig. S8 ^{19}F NMR of **AuL1** in DMSO–d6

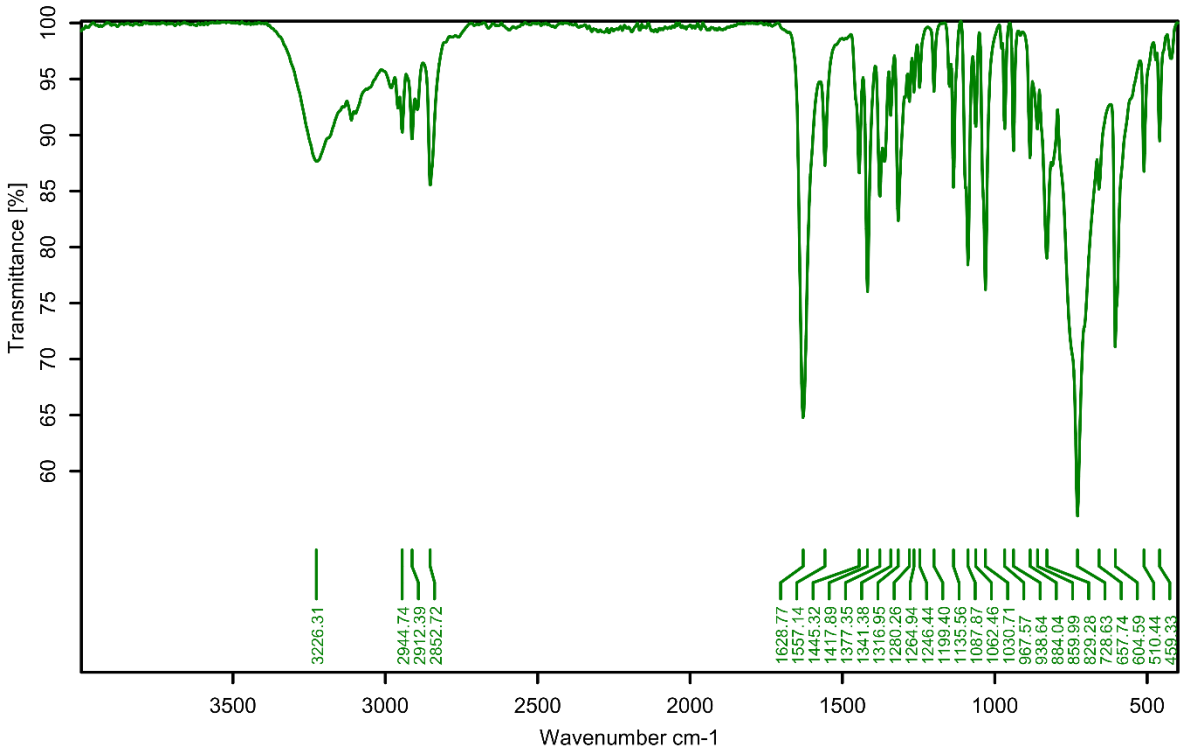


Fig. S9 FT-IR spectrum of **H_2L1** recorded as a crushed powder sample at 298 K.

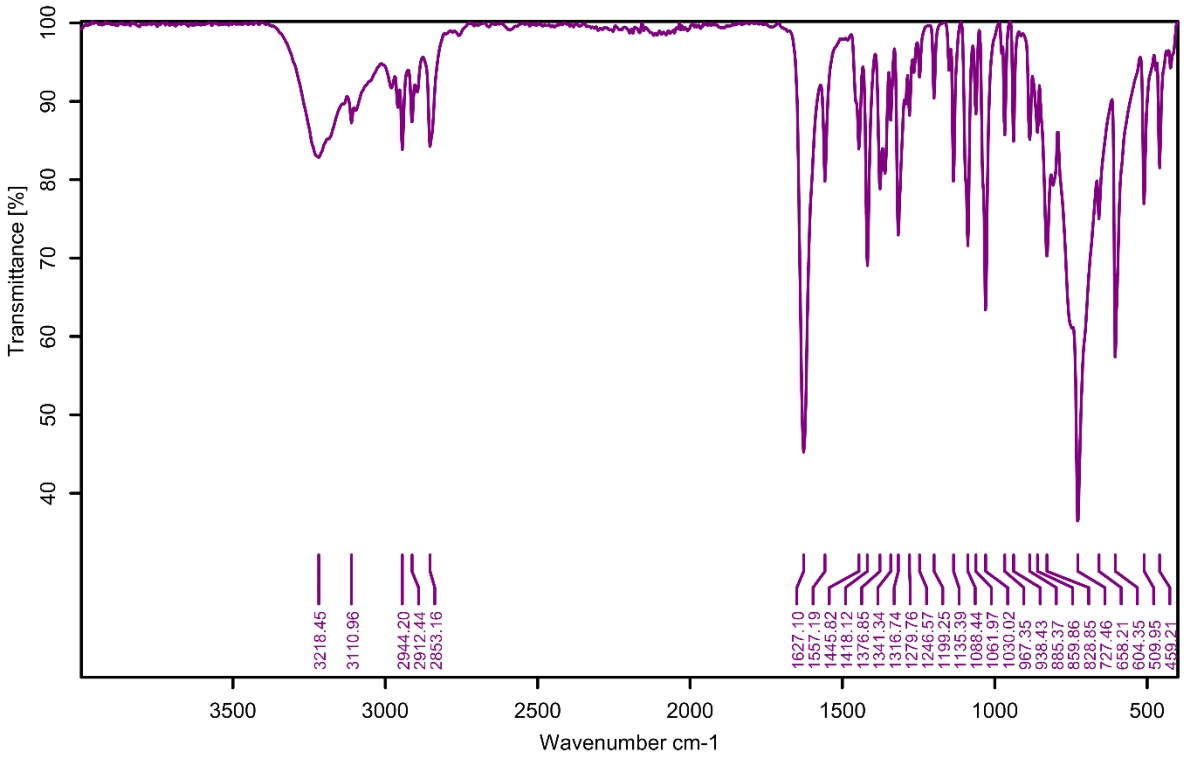


Fig. S10 FT-IR spectrum of **H_2L2** recorded as a crushed powder sample at 298 K.

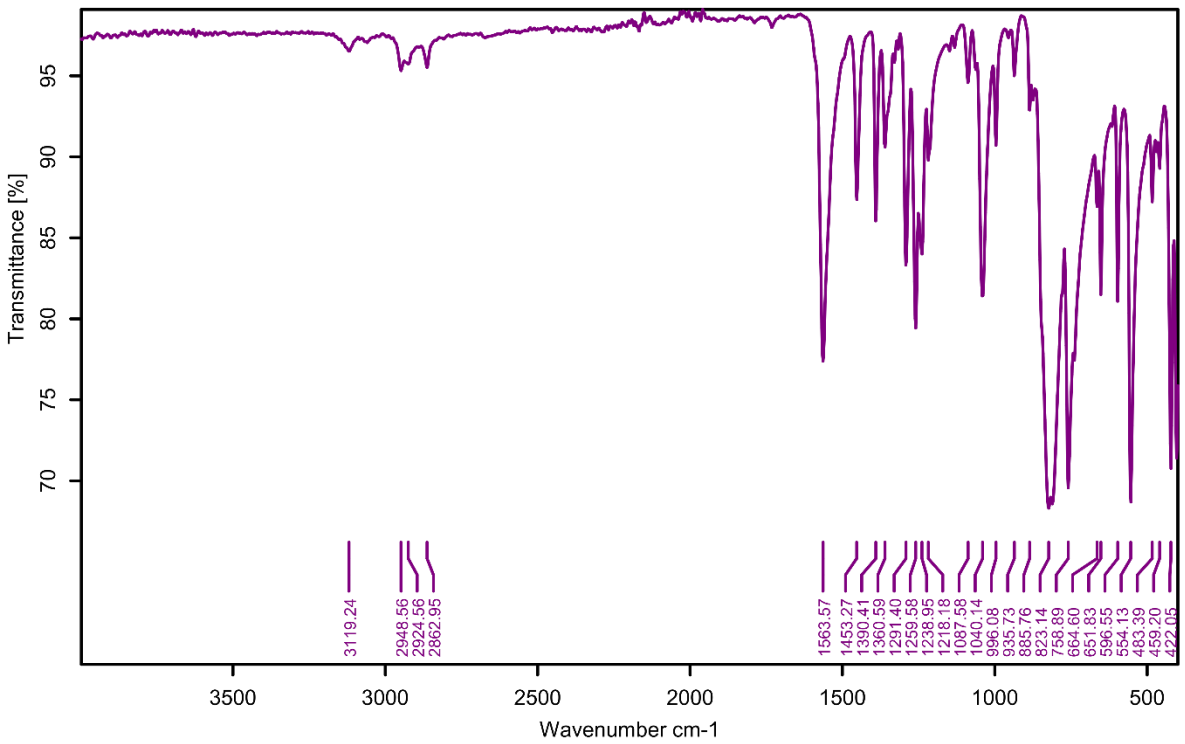


Fig. S11 FT-IR spectrum of **AuL1** recorded as a crushed powder sample at 298 K.

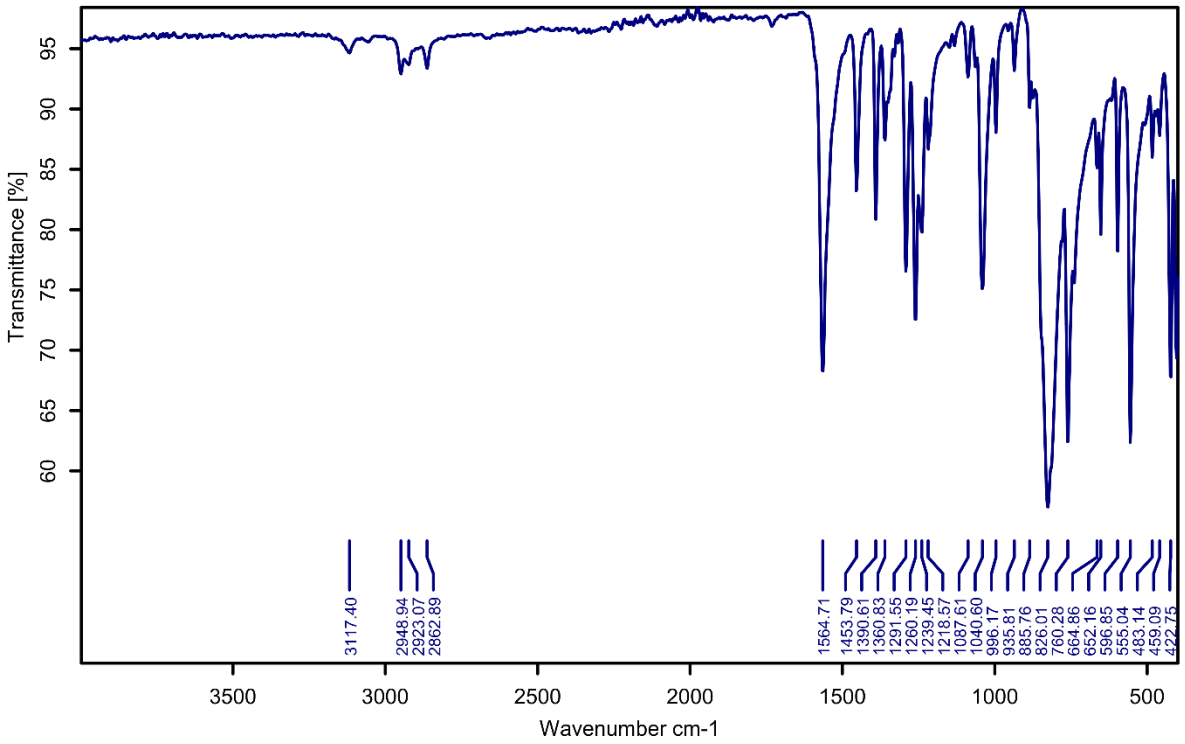


Fig. S12 FT-IR spectrum of **AuL2** recorded as a crushed powder sample at 298 K.

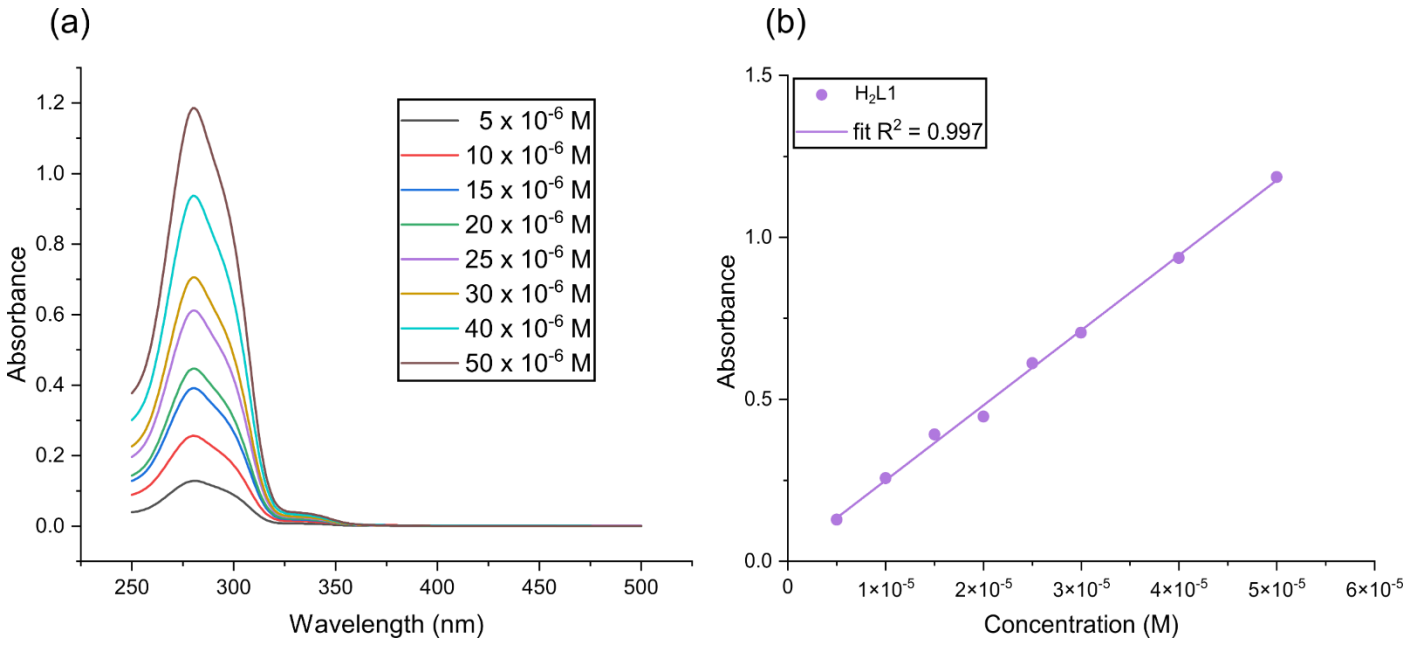


Fig. S13 UV-visible spectrum of **H_2L1** recorded in acetonitrile at 298 K as a function of concentration. The molar absorptivity of the band maximum is reported in the characterisation data and was determined from (b) the slope of a Beer-Lambert law plot at the relevant band maximum.

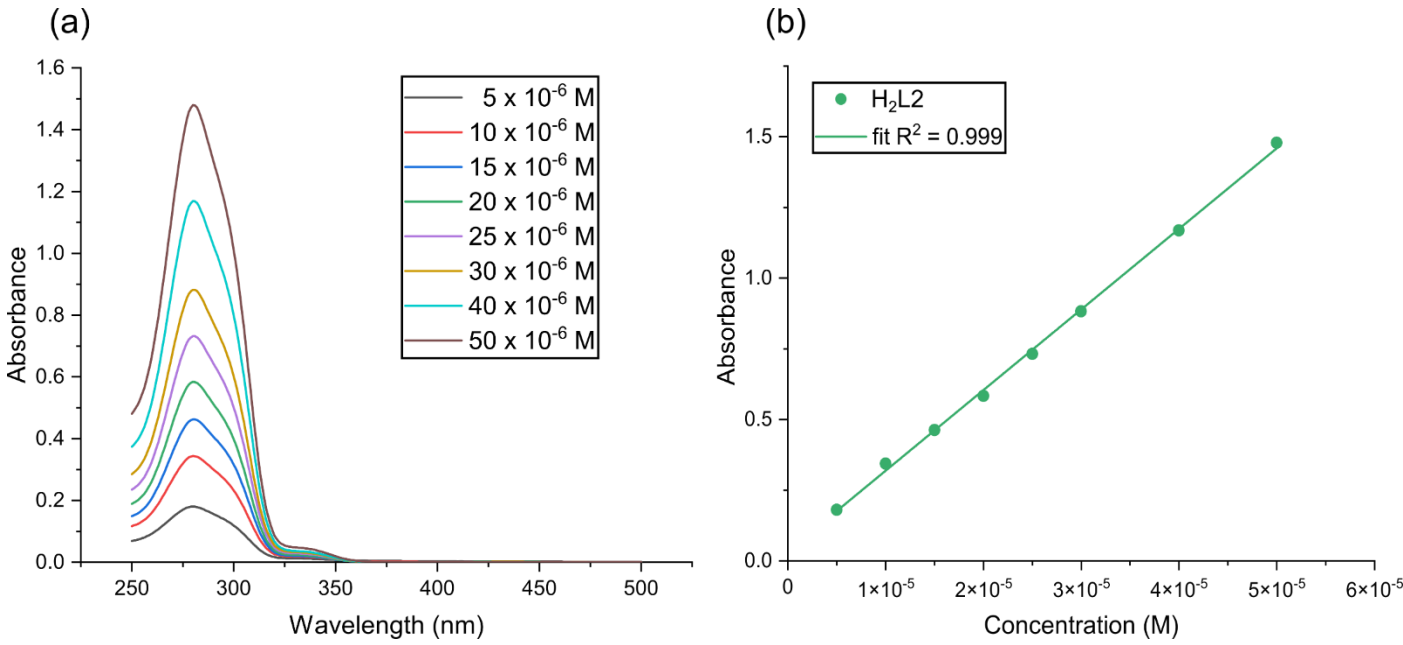


Fig. S14 UV-visible spectrum of **H_2L2** recorded in acetonitrile at 298 K as a function of concentration. The molar absorptivity of the band maximum is reported in the characterisation data and was determined from (b) the slope of a Beer-Lambert law plot at the relevant band maximum.

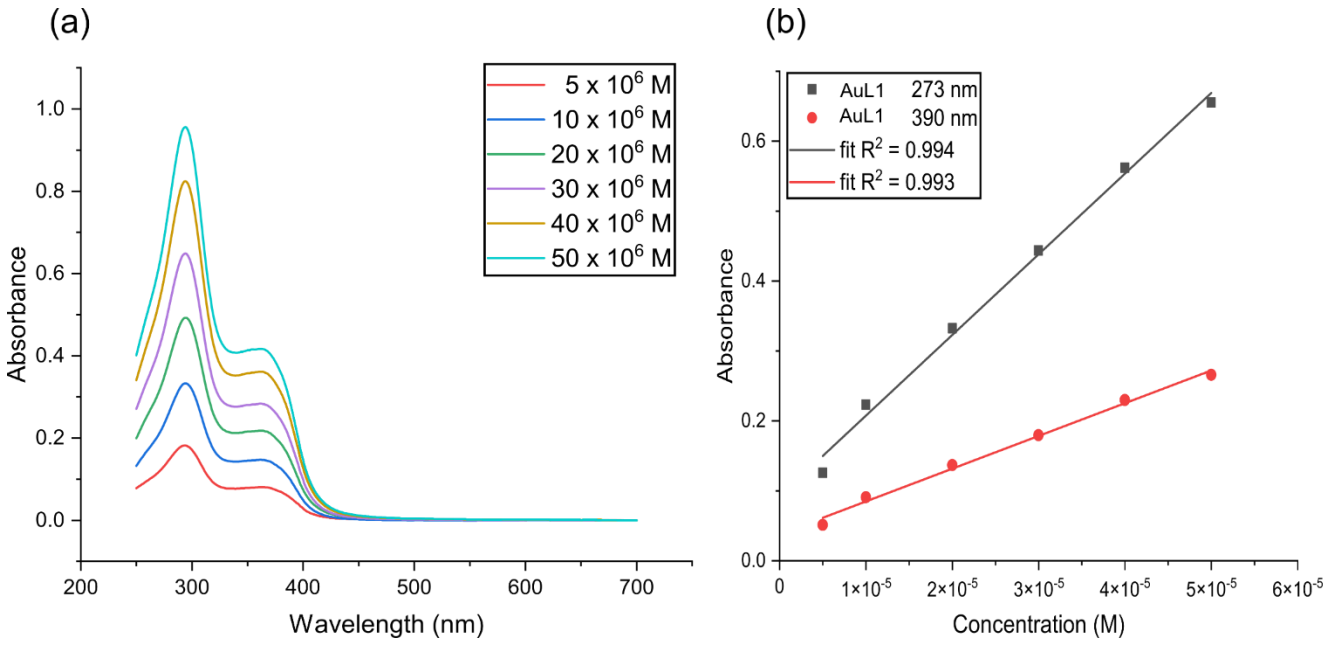


Fig. S15 UV-visible spectrum of **AuL1** recorded in acetonitrile at 298 K as a function of concentration. The molar absorptivities of key band maximum are reported in the characterisation and were determined from (b) the slopes of Beer-Lambert law plots at the relevant band maxima.

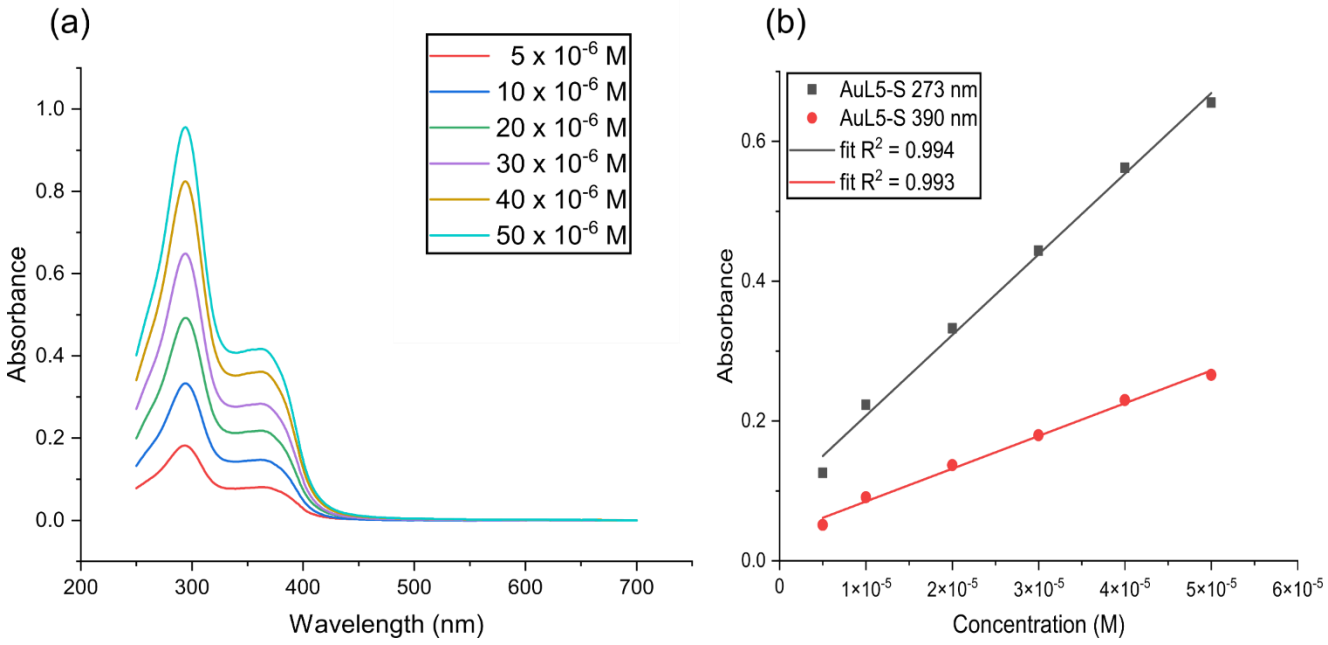


Fig. S16 UV-visible spectrum of **AuL2** recorded in acetonitrile at 298 K as a function of concentration. The molar absorptivities of key band maxima are reported in the characterisation data and were determined from (b) the slopes of Beer-Lambert law plots at the relevant band maxima.

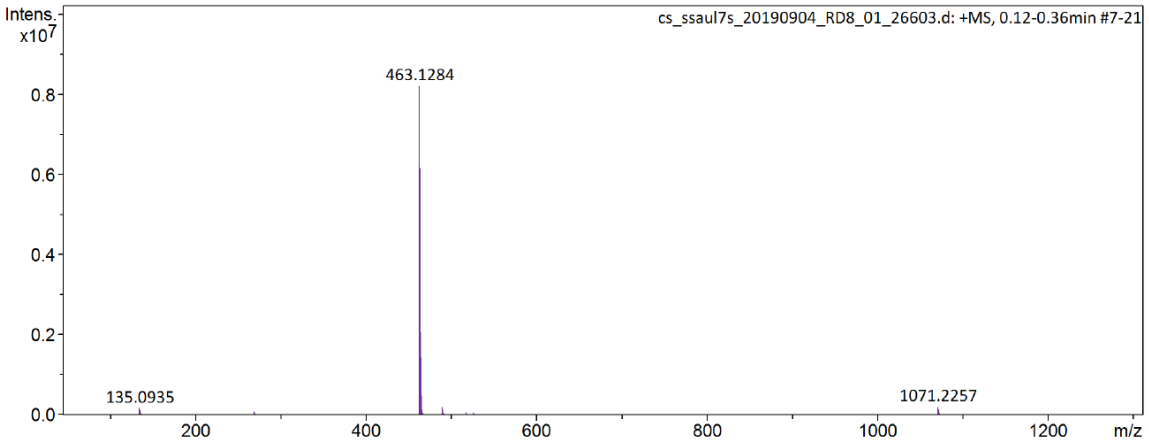


Fig. S17 ESI-MS spectrum of **AuL1**. The solid sample was dissolved in methanol with 0.1% formic acid (V/V) and the spectrum was recorded in positive ESI mode.

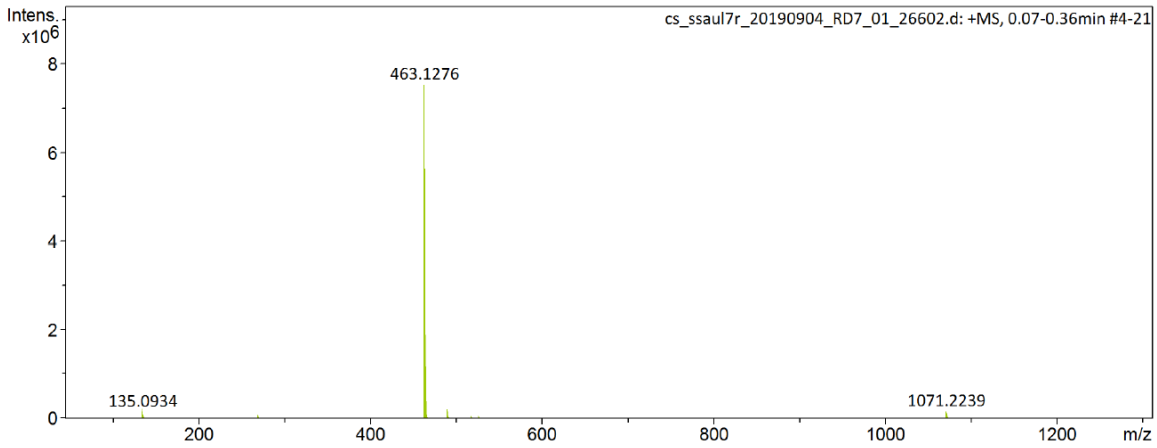


Fig. S18 ESI-MS spectrum of **AuL2**. The solid sample was dissolved in methanol with 0.1% formic acid (V/V) and the spectrum was recorded in positive ESI mode.

2.2 Fluorescence spectroscopy

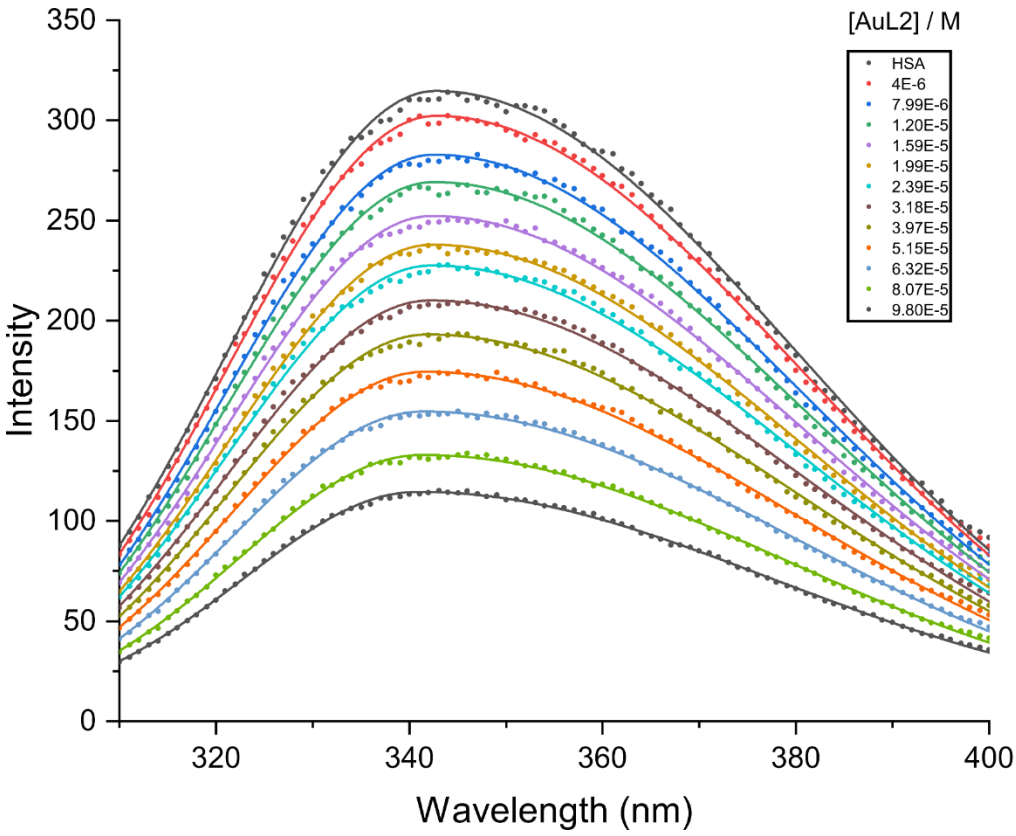


Fig. S19 Fluorescence emission spectra of HSA (5.0 µM) recorded as a function of increasing concentration of **AuL2** at 298 K. The emission spectra confirm that **AuL2** quenches the intrinsic HSA (i.e., Trp-214) fluorescence upon binding.

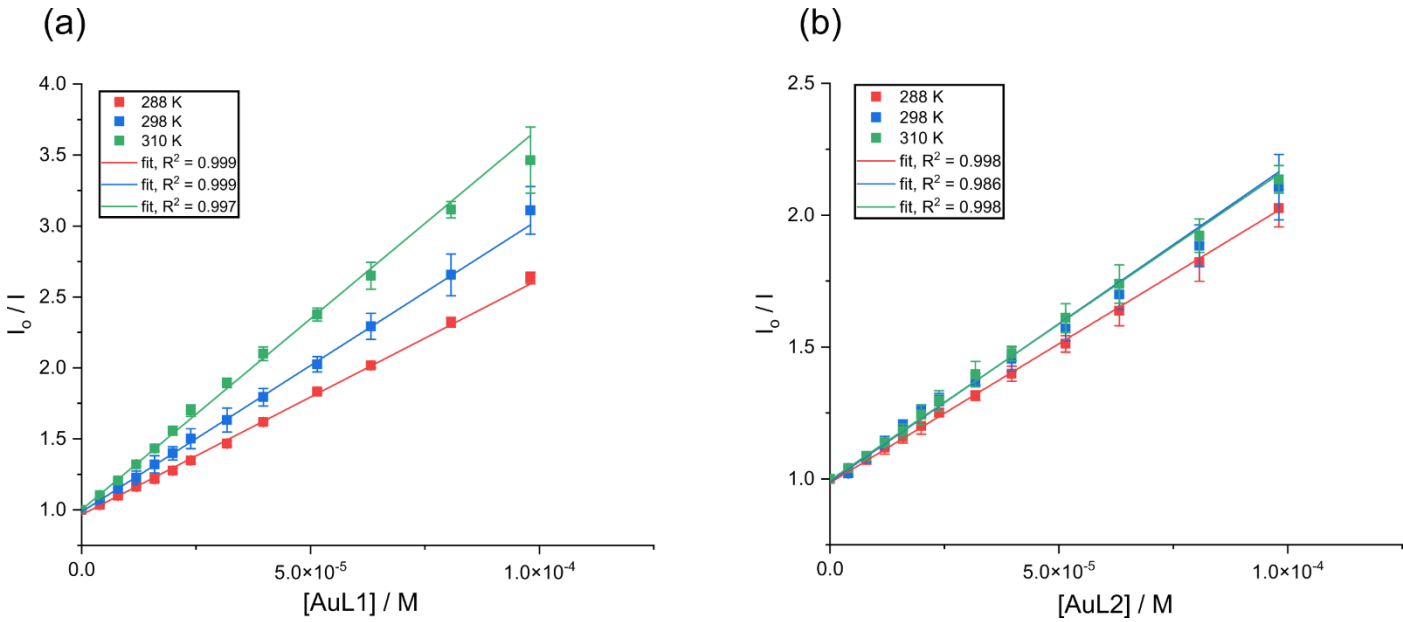


Fig. S20 Stern–Volmer plots of fluorescence quenching: **(a) AuL1**···HSA complex and **(b) AuL2**···HSA complex. Data for both gold(III) chelates were recorded at three different temperatures (■ 288 K, ■ 298 K, and ■ 310 K). The relevant concentrations for the titrations were: [HSA] = 5.0 μM, and the gold(III) chelates were 0 – 98 μM in KH_2PO_4 buffer (pH 7.50 in 50 mM). Error bars indicate the standard deviation of three independent experiments.

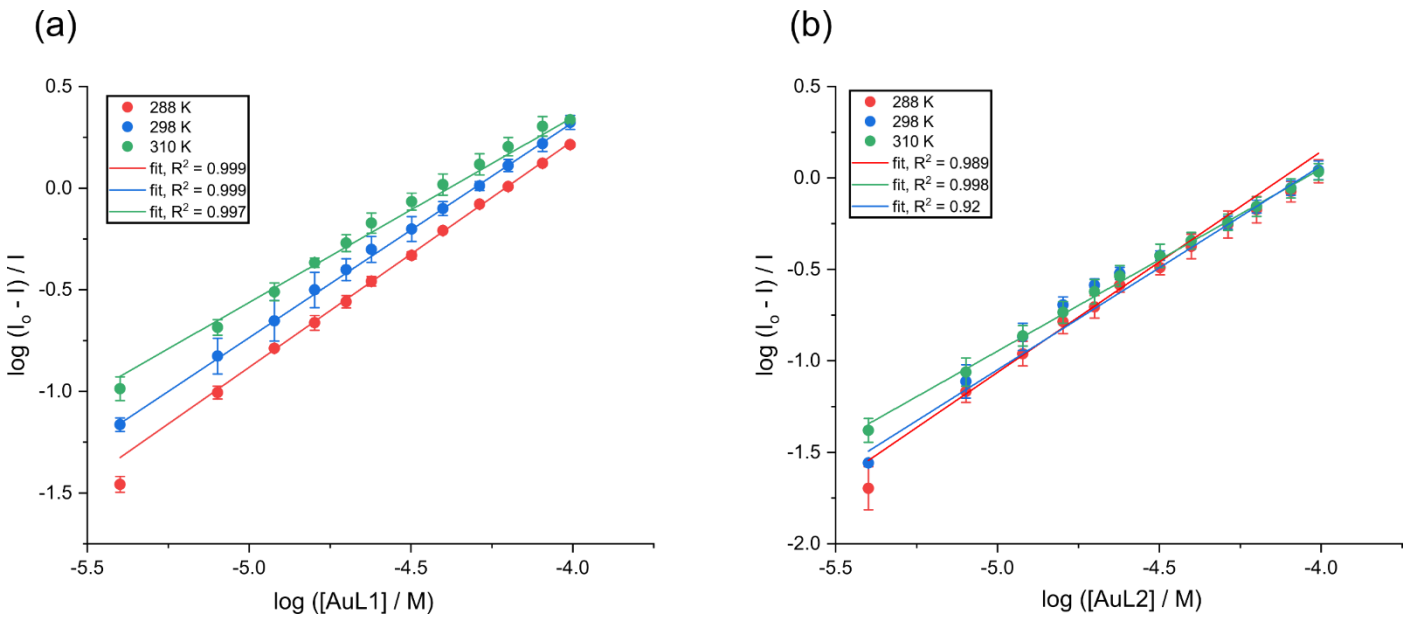


Fig. S21 Plots of log((I₀-I)/I) versus log([Q]) for the interaction of HSA with the two enantiomeric gold(III) chelates (i.e., quenchers, Q): (a) **AuL1**···HSA complex, (b) **AuL2**···HSA complex. The affinity constants are determined from the intercepts of the graphs and the stoichiometry from the slopes. Data for the gold(III) chelate···HSA systems were recorded at three different temperatures (, ● 288 K, , ● 298 K, and, ● 310 K) The relevant concentrations for the titrations were: [HSA] = 5.0 μM, and the gold(III) chelates ranged from 0 – 9.8 × 10^{-5} M at pH 7.50 in 50 mM KH_2PO_4 buffer.

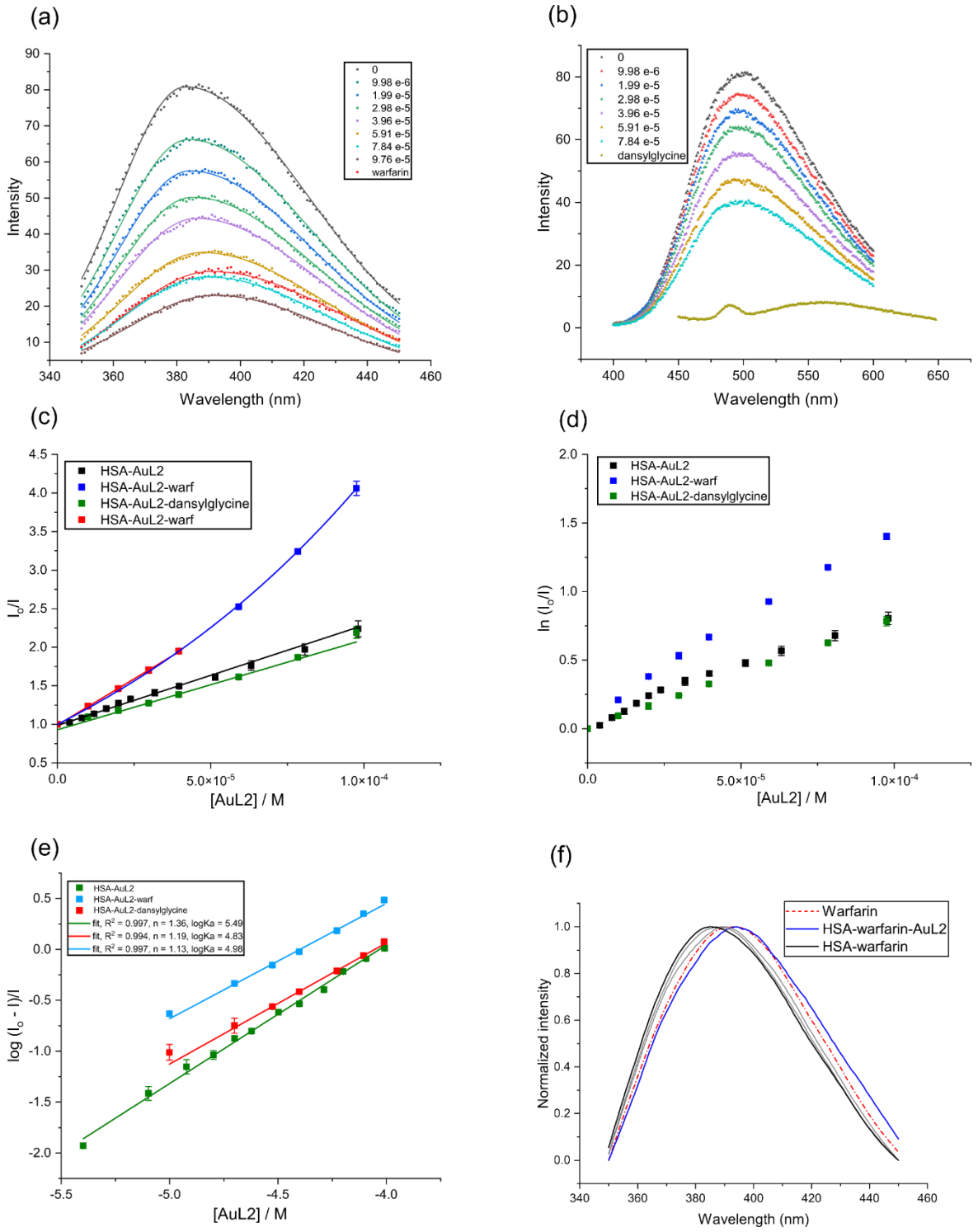


Fig. S22 Binding site determination for the reaction of **AuL2** with HSA (5.0 μM protein, 50 mM KH_2PO_4, pH 7.50, 298 K). **(a)** Emission spectra of HSA···warfarin (5.0 μM warfarin λ^{ex} = 320 nm) recorded as a function of the concentration of AuL4-R at 298 K. The spectra are fitted by single Gaussian functions to locate the emission maxima. Correlation coefficients, R^2, ranged from 0.990 to 0.999. **(b)** Emission spectra of HSA···dansylglycine (5.0 μM dansylglycine λ^{ex} = 340 nm) recorded as a function of the concentration of AuL4-R at 298 K. The spectra are fitted by single Gaussian functions to locate the emission maxima. Correlation coefficients, R^2, ranged from 0.990 to 0.999. **(c)** Stern–Volmer (SV) plot for native HSA, HSA···Warfarin, and HSA···dansylglycine as a function of the concentration of **AuL2** at 298 K. The plots are linear with an intercept of 1.0 when static quenching is operative (i.e., the quencher binds to the target protein and fluorophore(s)). The excitation and emission wavelengths for the

fluorophore probes were: (i) Trp-214 (native HSA), λ^{ex} = 295 nm, λ^{em} = 340 nm; (ii) Warfarin (HSA-Warf), λ^{ex} = 320 nm, λ^{em} = 382 nm, and (iii) dansylglycine, λ^{ex} = 340 nm, λ^{em} = 500 nm. **(d)** Sphere of action model plot, $ln\left(\frac{I_0}{I}\right) = K_{SV}^{app}[Q]$, for the system. A linear plot with a zero intercept indicates static quenching by AuL4-R bound in some way to the fluorophore/macromolecule. Negative deviation from linearity signals a switch from static to dynamic quenching. **(e)** Double-log plot (eq. 10) of the fluorescence quenching data, $log\left(\frac{I_0-I}{I}\right) = logK + nlog[Q]$, to enable measurement of logKa and the reaction stoichiometry (n). **(f)** Normalized fluorescence emission spectrum of HSA···warfarin (5.0 μM warfarin λ^{ex} = 320 nm) recorded as a function of the concentration of **AuL2** at 298 K to show the displacement of warfarin from HSA. Error bars indicate the standard deviation of three independent experiments.

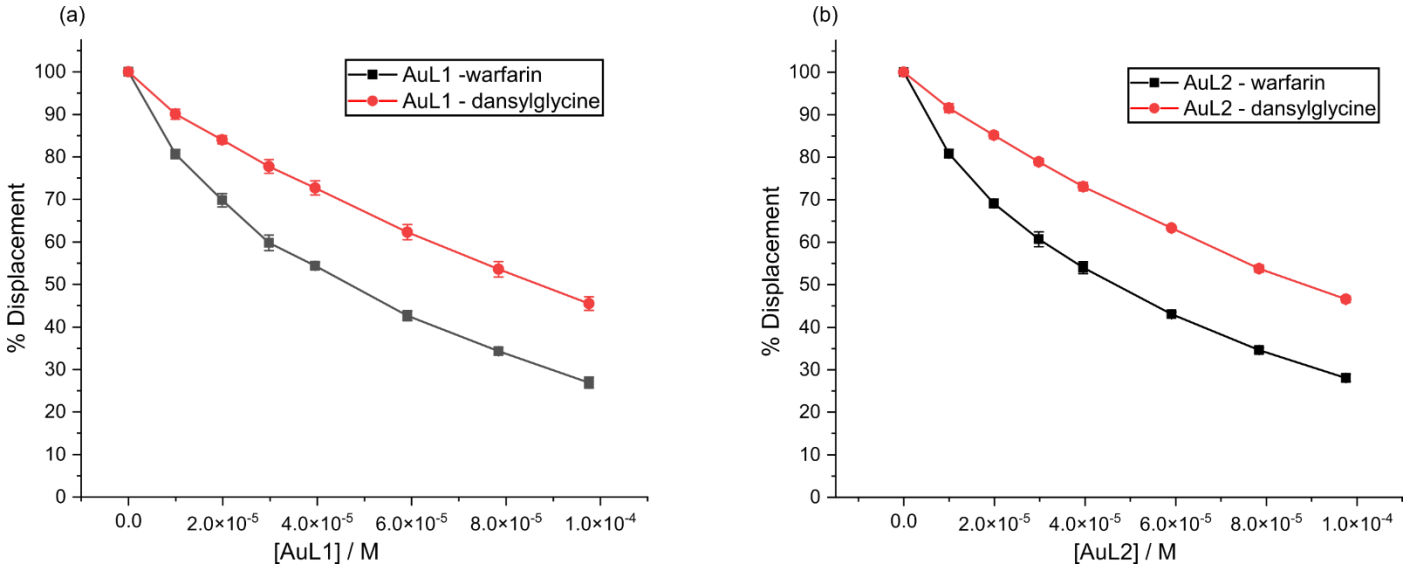


Fig. S23 AuL1 and **AuL2** displace either dansylglycine or warfarin bound to HSA. Various Au(III)-chelates (0 – 9.7 × 10^{-5} M) were titrated into a solution containing 5 μM HSA bound to 5 μM of either dansylglycine or warfarin. Displacement of dansylglycine or warfarin resulted in the fluorophores fluorescence being quenched. Error bars indicate the standard deviation of three independent experiments.

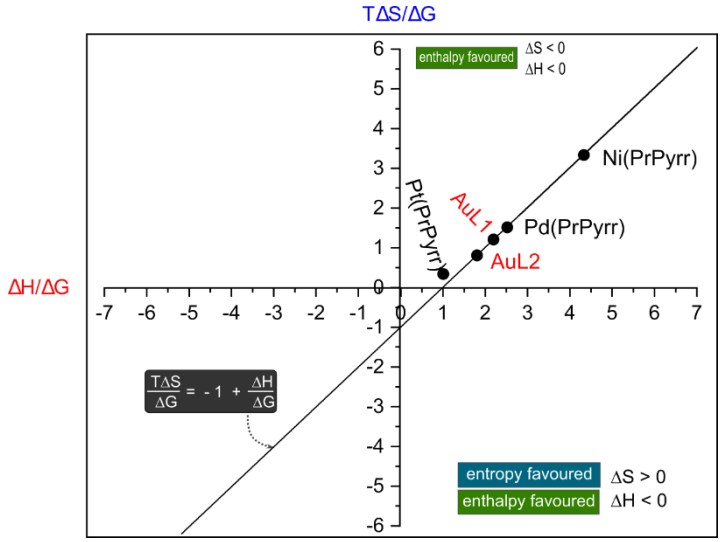


Fig. S24 Plot of the Gibbs-Helmholtz relationship (eq. 5) for the reaction of **AuL1** and **AuL2** with HSA at 298 K in 50 mM KH_2PO_4 buffer at pH 7.50 and three metal Schiff base chelates previously reported.[13] For all reactions, $\Delta G < 0$.

2.3 CD spectroscopy data

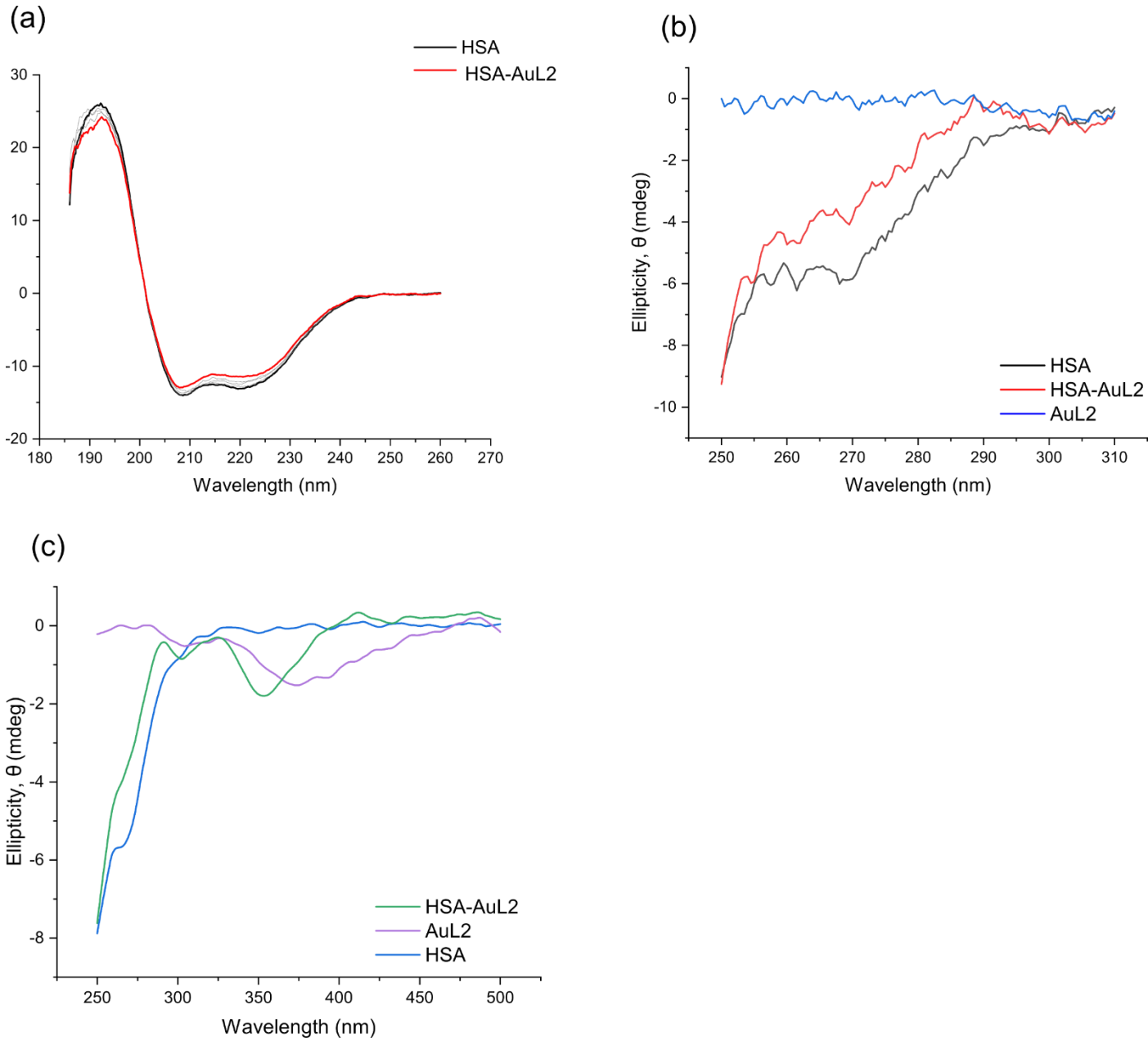


Fig. S25 (a) Far-UV CD spectra of native HAS (300 nM) and the protein incubated with saturating doses of **AuL2.** (b) near UV-visible CD spectra of native HSA (300 nM) and the protein incubated with a saturating dose (6 μM) of **AuL2**. (c) Represents the ICD spectrum of HSA in the presence of **AuL2**. The spectra were recorded at 298 K in 50 mM KH_2PO_4 buffer at pH 7.50 and ICD data was smoothed using a relatively fine Lowess function (0.07 span).

Table S1. Summary of the change in α-helicity of native and HSA in the presence of **AuL1** and **AuL2**.

Au(III) chelate	Concentration (μM)	% α–helicity
AuL1	0	58.96
	0.3	57.63
	1.5	56.90
	3	56.56
	6	56.36
AuL2	0	58.42
	0.3	58.75
	1.5	56.50
	3	56.22
	6	53.88

2.4 NCI-60 cytotoxicity data

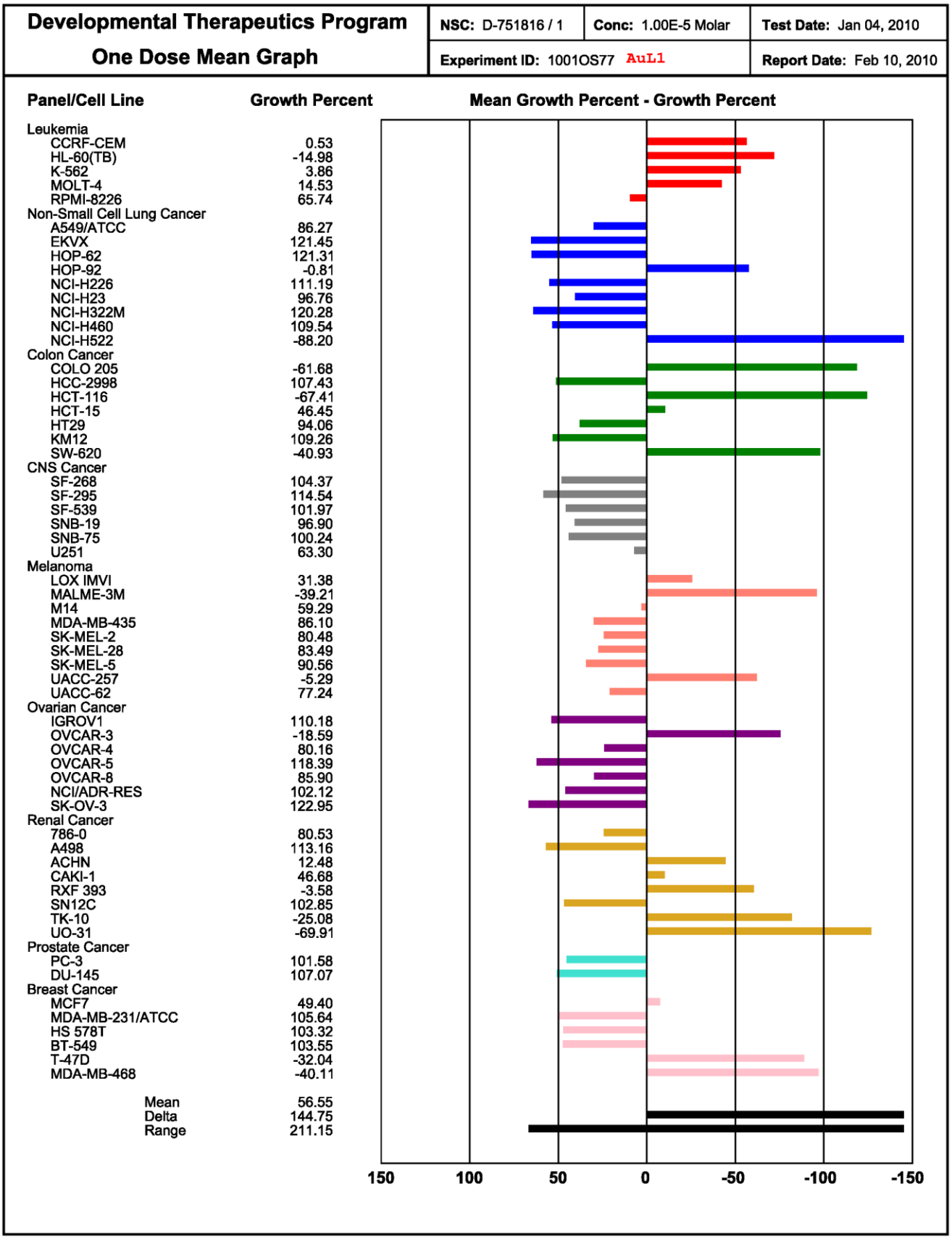


Fig. S26 NCI-60 single-dose cytotoxicity screen for **AuL1**.

Developmental Therapeutics Program

One Dose Mean Graph

NSC: D-751815 / 1	Conc: 1.00E-5 Molar	Test Date: Jan 04, 2010
Experiment ID: 1001OS77 AuL2 (1R,2R)		Report Date: Feb 10, 2010

Panel/Cell Line	Growth Percent
Leukemia	
CCRF-CEM	32.23
HL-60(TB)	76.01
K-562	28.06
MOLT-4	67.74
RPMI-8226	75.93
Non-Small Cell Lung Cancer	
A549/ATCC	99.77
EKVX	118.48
HOP-62	109.60
HOP-92	124.29
NCI-H226	118.87
NCI-H23	104.66
NCI-H322M	116.67
NCI-H460	107.79
NCI-H522	-90.27
Colon Cancer	
COLO 205	-13.93
HCC-2998	101.46
HCT-116	80.41
HCT-15	103.05
HT29	102.48
KM12	109.74
SW-620	40.87
CNS Cancer	
SF-268	96.65
SF-295	122.51
SF-539	103.84
SNB-19	99.81
SNB-75	108.18
U251	85.58
Melanoma	
LOX IMVI	48.88
MALME-3M	43.77
M14	79.24
MDA-MB-435	98.55
SK-MEL-2	95.09
SK-MEL-28	101.72
SK-MEL-5	99.05
UACC-257	81.97
UACC-62	86.74
Ovarian Cancer	
IGROV1	122.95
OVCAR-3	98.11
OVCAR-4	99.27
OVCAR-5	120.10
OVCAR-8	99.97
NCI/ADR-RES	102.65
SK-OV-3	122.08
Renal Cancer	
786-0	108.12
A498	114.06
ACHN	99.83
CAKI-1	105.68
RXF 393	66.12
SN12C	100.68
TK-10	85.44
UO-31	94.98
Prostate Cancer	
PC-3	98.42
DU-145	109.98
Breast Cancer	
MCF7	89.59
MDA-MB-231/ATCC	114.76
HS 578T	117.07
BT-549	111.61
T-47D	52.14
MDA-MB-468	58.50
Mean	89.11
Delta	179.38
Range	214.56

Mean Growth Percent - Growth Percent

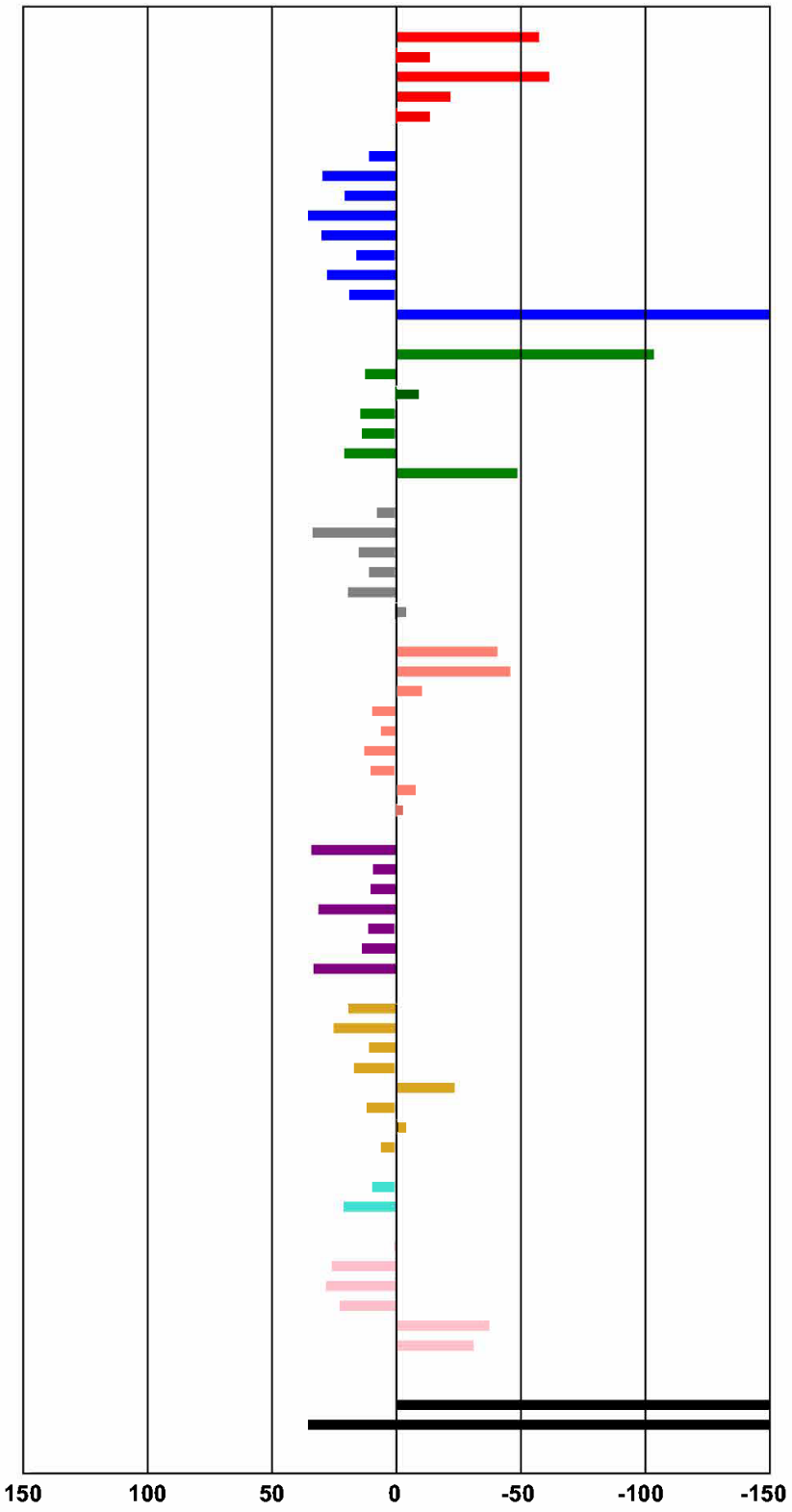


Fig. S27 NCI-60 single-dose cytotoxicity screen for **AuL2**.

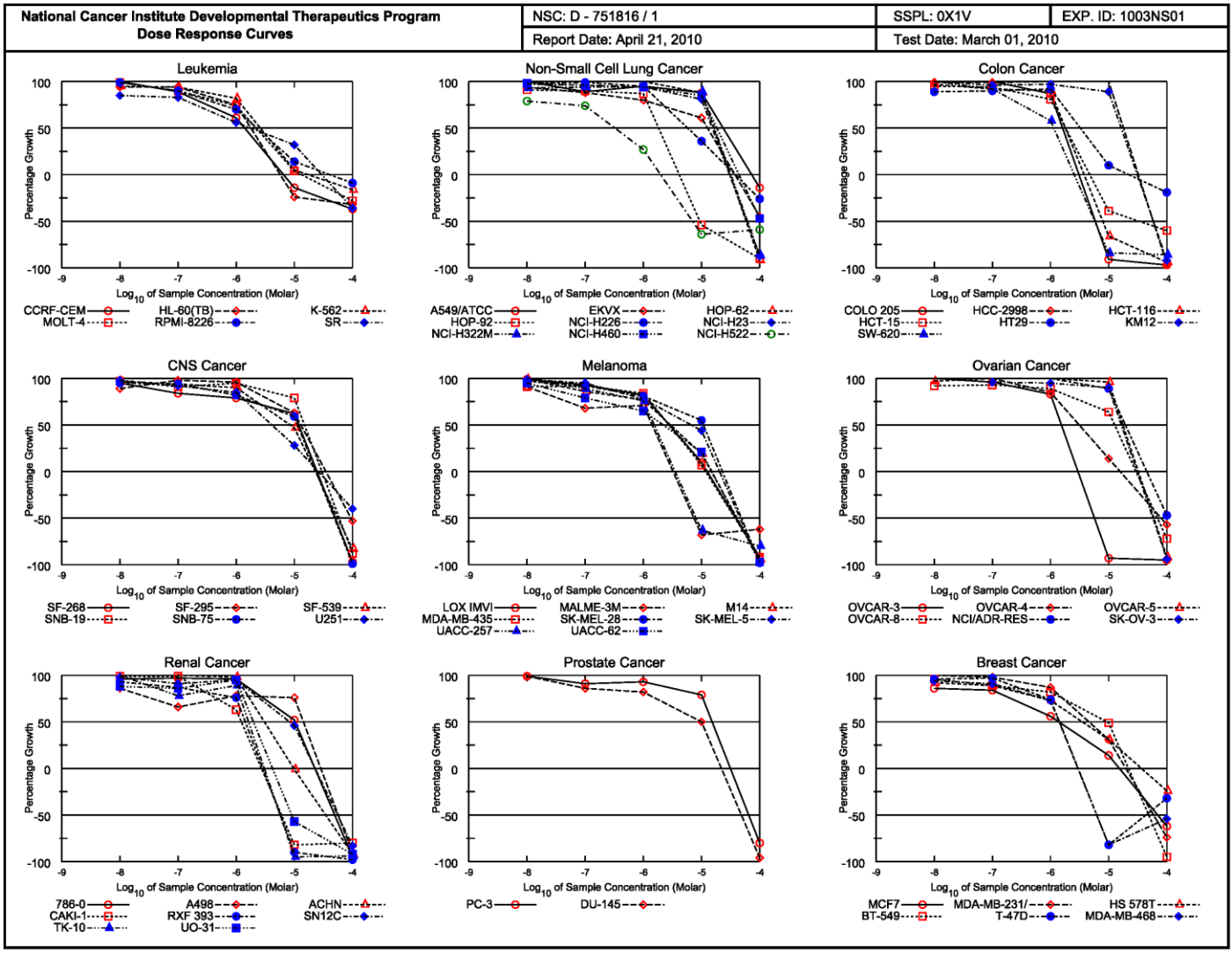


Fig. S28 NCI-60 five-dose cytotoxicity screen MTT assay graphs for **AuL1** with the panel of nine human cancer cell lines.

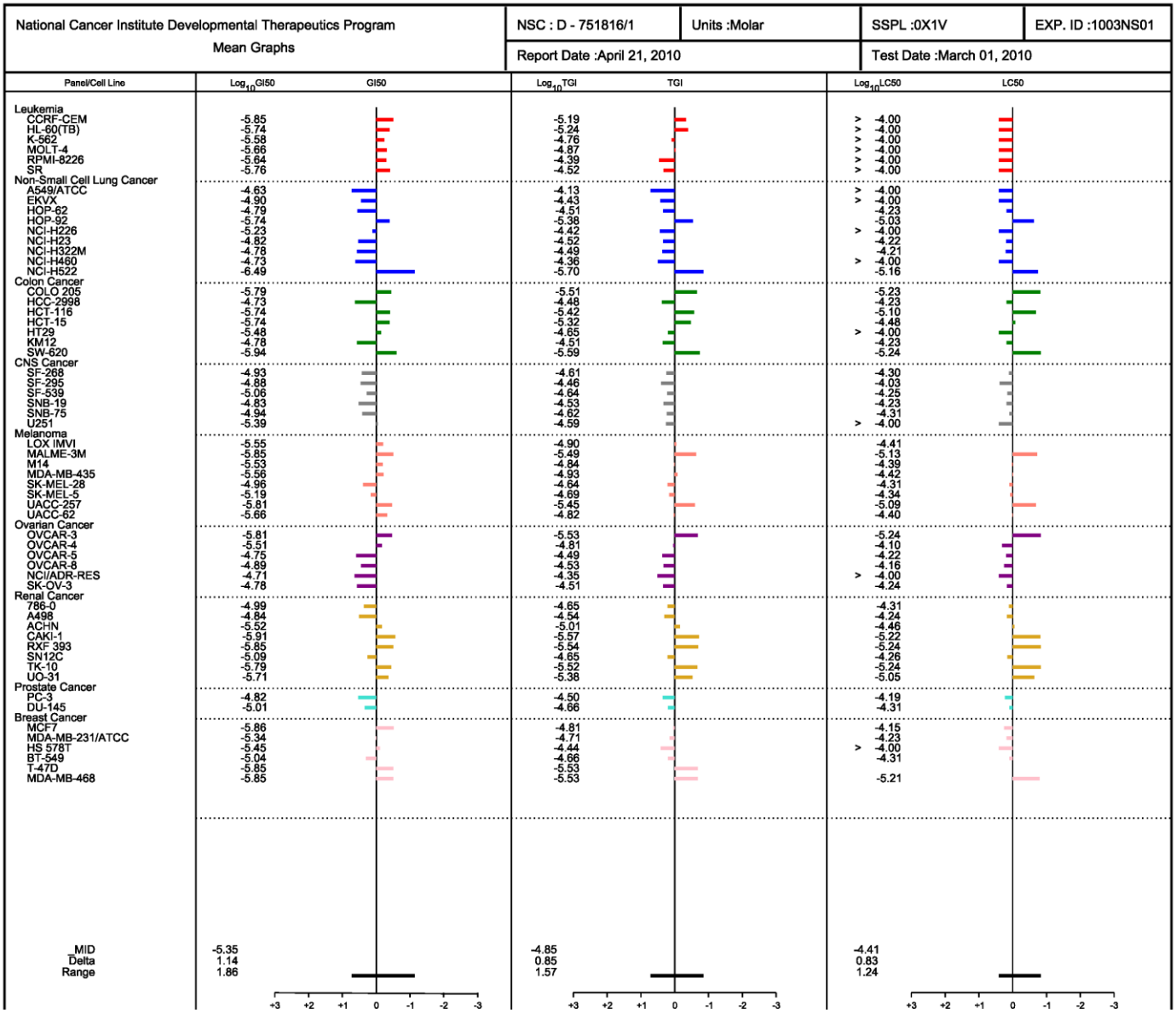


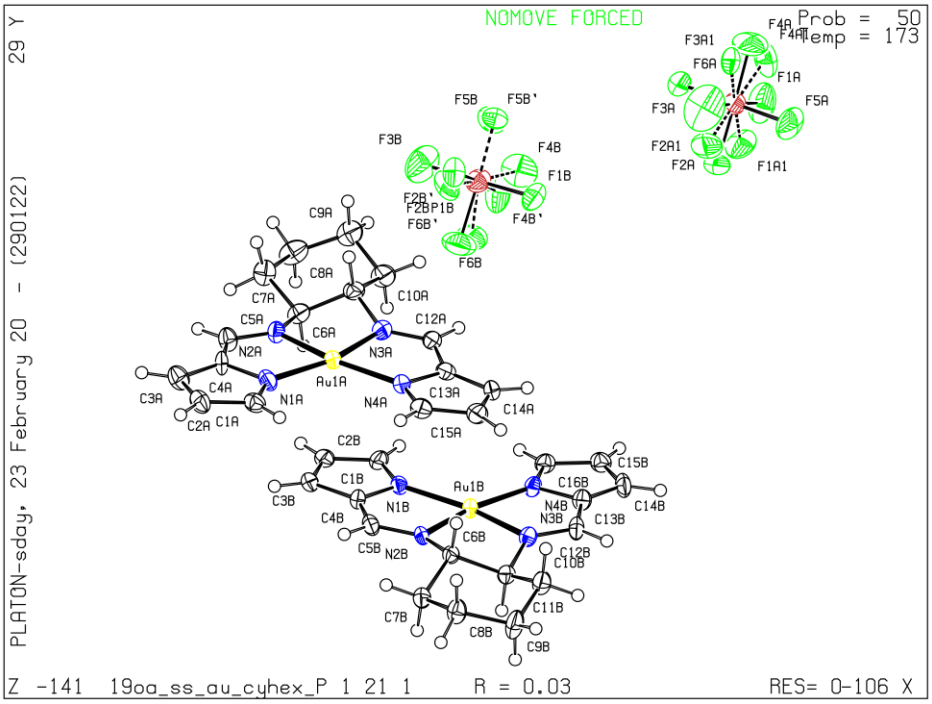
Fig. S29 NCI-60 five-dose cytotoxicity screen mean efficacy graphs for **AuL1**.

2.5 X-ray crystal structures

Table S2. Crystal system data, X-ray data collection, and structure refinement details for **AuL1**.

Identification code	19OA_SS_Au_CyHex_1S2S_0m
Empirical formula	$C_{16}H_{18}AuF_6N_4P$
Formula weight	608.28
Temperature/K	173.15
Crystal system	monoclinic
Space group	$P2_1$
a/Å	10.1292(3)
b/Å	9.7663(3)
c/Å	18.4954(6)
α/°	90
β/°	94.364(2)
γ/°	90
Volume/Å^3	1824.35(10)
Z	4
ρ_{calc} g/cm^3	2.215
μ/mm^{-1}	8.220
F(000)	1160.0
Crystal size/mm^3	0.282 × 0.125 × 0.093
Radiation	MoKα (λ = 0.71073)
2Θ range for data collection/°	2.208 to 59.342
Index ranges	-14 ≤ h ≤ 13, -13 ≤ k ≤ 13, -25 ≤ l ≤ 25
Reflections collected	28490
Independent reflections	10265 [R_{int} = 0.0277, R_{sigma} = 0.0449]
Data/restraints/parameters	10265/97/580
Goodness-of-fit on F^2	0.968
Final R indexes [I>=2σ (I)]	R_1 = 0.0256, wR_2 = 0.0418
Final R indexes [all data]	R_1 = 0.0361, wR_2 = 0.0440
Largest diff. peak/hole / e Å^{-3}	1.48/-1.34
Flack parameter	0.00011(5)
CCDC Deposit Number	2244592

Table S3. Bond lengths for **AuL1**.



Atom	Atom	Length/Å		Atom	Atom	Length/Å
Au1B	N1B	2.026(6)		N4A	C13A	1.412(9)
Au1B	N2B	1.981(6)		N4A	C16A	1.340(11)
Au1B	N3B	1.979(6)		C1A	C2A	1.376(11)
Au1B	N4B	1.997(6)		C2A	C3A	1.395(13)
N1B	C1B	1.341(11)		C3A	C4A	1.410(11)
N1B	C4B	1.374(9)		C4A	C5A	1.377(11)
N2B	C5B	1.313(10)		C6A	C7A	1.518(10)
N2B	C6B	1.474(9)		C6A	C11A	1.520(9)
N3B	C11B	1.493(8)		C7A	C8A	1.531(11)
N3B	C12B	1.301(9)		C8A	C9A	1.510(11)
N4B	C13B	1.405(11)		C9A	C10A	1.517(11)
N4B	C16B	1.343(10)		C10A	C11A	1.515(10)
C1B	C2B	1.361(10)		C12A	C13A	1.425(13)
C2B	C3B	1.387(11)		C13A	C14A	1.381(13)
C3B	C4B	1.408(12)		C14A	C15A	1.383(12)
C4B	C5B	1.394(13)		C15A	C16A	1.407(11)
C6B	C7B	1.522(9)		P1A	F6A	1.604(6)
C6B	C11B	1.533(8)		P1A	F3A	1.557(8)
C7B	C8B	1.565(10)		P1A	F5A	1.593(7)
C8B	C9B	1.526(9)		P1A	F1A	1.602(8)
C9B	C10B	1.521(11)		P1A	F4A	1.551(6)
C10B	C11B	1.518(10)		P1A	F2A	1.621(6)
C12B	C13B	1.422(11)		P1A	F2A1	1.63(3)
C13B	C14B	1.376(11)		P1A	F4A1	1.55(3)
C14B	C15B	1.381(12)		P1A	F1A1	1.46(2)
C15B	C16B	1.398(11)		P1A	F3A1	1.64(2)
Au1A	N1A	2.024(6)		P1B	F1B	1.601(6)

Atom	Atom	Length/Å		Atom	Atom	Length/Å
Au1A	N2A	1.981(7)		P1B	F2B	1.45(3)
Au1A	N3A	1.959(6)		P1B	F3B	1.598(8)
Au1A	N4A	1.999(7)		P1B	F4B	1.73(2)
N1A	C1A	1.331(11)		P1B	F5B	1.65(3)
N1A	C4A	1.393(12)		P1B	F6B	1.519(17)
N2A	C5A	1.294(9)		P1B	F4B'	1.499(12)
N2A	C6A	1.471(9)		P1B	F2B'	1.666(16)
N3A	C11A	1.489(9)		P1B	F5B'	1.56(2)
N3A	C12A	1.288(10)		P1B	F6B'	1.650(14)

Table S4. Bond angles for **AuL1**.

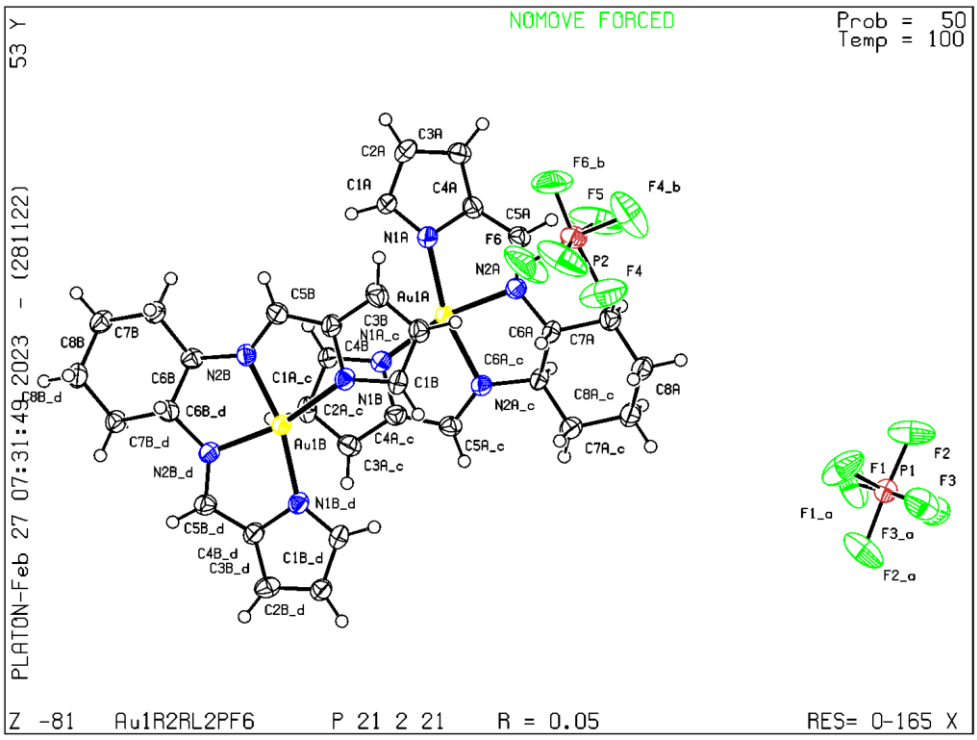
Atom	Atom	Atom	Angle/˚		Atom	Atom	Atom	Angle/˚
N2B	Au1B	N1B	81.2(3)		C9A	C8A	C7A	112.2(7)
N2B	Au1B	N4B	166.0(3)		C8A	C9A	C10A	112.4(6)
N3B	Au1B	N1B	165.8(2)		C11A	C10A	C9A	106.6(6)
N3B	Au1B	N2B	84.7(3)		N3A	C11A	C6A	106.8(5)
N3B	Au1B	N4B	81.4(3)		N3A	C11A	C10A	115.4(6)
N4B	Au1B	N1B	112.8(3)		C10A	C11A	C6A	111.6(6)
C1B	N1B	Au1B	141.2(6)		N3A	C12A	C13A	116.8(7)
C1B	N1B	C4B	108.5(7)		N4A	C13A	C12A	113.8(7)
C4B	N1B	Au1B	110.3(6)		C14A	C13A	N4A	108.4(8)
C5B	N2B	Au1B	114.8(6)		C14A	C13A	C12A	137.6(7)
C5B	N2B	C6B	131.4(7)		C13A	C14A	C15A	107.8(7)
C6B	N2B	Au1B	112.6(4)		C14A	C15A	C16A	106.9(8)
C11B	N3B	Au1B	111.3(4)		N4A	C16A	C15A	110.0(7)
C12B	N3B	Au1B	115.1(6)		F6A	P1A	F2A	88.4(3)
C12B	N3B	C11B	131.8(6)		F6A	P1A	F2A1	95.1(10)
C13B	N4B	Au1B	112.2(6)		F6A	P1A	F3A1	93.4(9)
C16B	N4B	Au1B	141.5(6)		F3A	P1A	F6A	87.9(4)
C16B	N4B	C13B	106.3(6)		F3A	P1A	F5A	92.9(5)
N1B	C1B	C2B	109.5(8)		F3A	P1A	F1A	174.5(6)
C1B	C2B	C3B	108.3(8)		F3A	P1A	F2A	88.4(5)
C2B	C3B	C4B	106.0(7)		F5A	P1A	F6A	179.1(3)
N1B	C4B	C3B	107.7(8)		F5A	P1A	F1A	89.7(4)
N1B	C4B	C5B	117.5(7)		F5A	P1A	F2A	91.1(3)
C5B	C4B	C3B	134.8(7)		F5A	P1A	F2A1	85.2(10)
N2B	C5B	C4B	116.2(7)		F5A	P1A	F3A1	87.5(9)
N2B	C6B	C7B	114.4(6)		F1A	P1A	F6A	89.5(4)
N2B	C6B	C11B	109.1(5)		F1A	P1A	F2A	86.7(4)
C7B	C6B	C11B	110.0(5)		F4A	P1A	F6A	89.4(4)
C6B	C7B	C8B	107.9(6)		F4A	P1A	F3A	92.7(6)
C9B	C8B	C7B	111.9(6)		F4A	P1A	F5A	91.1(5)

Atom	Atom	Atom	Angle/˚		Atom	Atom	Atom	Angle/˚
C10B	C9B	C8B	114.5(6)		F4A	P1A	F1A	92.1(6)
C11B	C10B	C9B	107.4(7)		F4A	P1A	F2A	177.6(6)
N3B	C11B	C6B	108.1(5)		F2A1	P1A	F3A1	84.9(14)
N3B	C11B	C10B	115.3(6)		F4A1	P1A	F6A	90.4(11)
C10B	C11B	C6B	110.1(6)		F4A1	P1A	F5A	89.4(11)
N3B	C12B	C13B	117.4(7)		F4A1	P1A	F2A1	170.0(18)
N4B	C13B	C12B	113.9(7)		F4A1	P1A	F3A1	86.5(16)
C14B	C13B	N4B	109.1(8)		F1A1	P1A	F6A	90.8(11)
C14B	C13B	C12B	136.7(8)		F1A1	P1A	F5A	88.3(11)
C13B	C14B	C15B	107.5(8)		F1A1	P1A	F2A1	92.3(17)
C14B	C15B	C16B	106.8(8)		F1A1	P1A	F4A1	96.0(19)
N4B	C16B	C15B	110.3(8)		F1A1	P1A	F3A1	175.1(15)
N2A	Au1A	N1A	81.7(3)		F1B	P1B	F4B	82.4(9)
N2A	Au1A	N4A	165.1(3)		F1B	P1B	F5B	85.7(10)
N3A	Au1A	N1A	165.6(3)		F1B	P1B	F2B'	86.9(6)
N3A	Au1A	N2A	84.1(3)		F1B	P1B	F6B'	88.4(6)
N3A	Au1A	N4A	81.4(3)		F2B	P1B	F1B	94.9(11)
N4A	Au1A	N1A	112.9(3)		F2B	P1B	F3B	83.5(11)
C1A	N1A	Au1A	141.2(7)		F2B	P1B	F4B	174.6(9)
C1A	N1A	C4A	109.8(6)		F2B	P1B	F5B	92.2(13)
C4A	N1A	Au1A	109.0(6)		F2B	P1B	F6B	98.8(12)
C5A	N2A	Au1A	114.2(6)		F3B	P1B	F1B	178.2(4)
C5A	N2A	C6A	133.4(7)		F3B	P1B	F4B	99.2(10)
C6A	N2A	Au1A	111.9(4)		F3B	P1B	F5B	93.6(10)
C11A	N3A	Au1A	110.7(4)		F3B	P1B	F2B'	91.4(6)
C12A	N3A	Au1A	116.3(6)		F3B	P1B	F6B'	91.9(6)
C12A	N3A	C11A	131.8(7)		F5B	P1B	F4B	82.9(11)
C13A	N4A	Au1A	111.5(6)		F6B	P1B	F1B	90.7(8)
C16A	N4A	Au1A	141.6(6)		F6B	P1B	F3B	90.3(8)
C16A	N4A	C13A	106.9(7)		F6B	P1B	F4B	86.0(11)
N1A	C1A	C2A	109.6(8)		F6B	P1B	F5B	168.6(16)
C1A	C2A	C3A	107.1(8)		F4B'	P1B	F1B	93.9(5)
C2A	C3A	C4A	107.7(8)		F4B'	P1B	F3B	87.9(6)
N1A	C4A	C3A	105.8(8)		F4B'	P1B	F2B'	175.7(9)
C5A	C4A	N1A	117.5(7)		F4B'	P1B	F5B'	94.2(9)
C5A	C4A	C3A	136.7(8)		F4B'	P1B	F6B'	90.2(7)
N2A	C5A	C4A	117.5(8)		F5B'	P1B	F1B	94.5(9)
N2A	C6A	C7A	114.7(5)		F5B'	P1B	F3B	85.1(9)
N2A	C6A	C11A	107.3(6)		F5B'	P1B	F2B'	89.9(9)
C7A	C6A	C11A	110.4(6)		F5B'	P1B	F6B'	174.6(10)
C6A	C7A	C8A	110.5(6)		F6B'	P1B	F2B'	85.7(8)

Table S5. Crystal system data, X-ray data collection, and structure refinement details for **AuL2**.

Identification code	Au1R2RL2PF6
Empirical formula	$C_{16}H_{18}AuF_6N_4P$
Formula weight	608.279
Temperature/K	100.15
Crystal system	orthorhombic
Space group	$P2_122_1$
a/Å	10.3951(2)
b/Å	18.2575(3)
c/Å	10.0206(2)
α/°	90
β/°	90
γ/°	90
Volume/Å^3	1901.80(6)
Z	4
ρ_{calc}g/cm^3	2.124
μ/mm^{-1}	7.886
F(000)	1155.5
Crystal size/mm^3	0.6 × 0.2 × 0.1
Radiation	Mo Kα (λ = 0.71073)
2Θ range for data collection/°	5.94 to 68.52
Index ranges	-15 ≤ h ≤ 15, -28 ≤ k ≤ 28, -15 ≤ l ≤ 13
Reflections collected	30977
Independent reflections	7216 [R_{int} = 0.0730, R_{sigma} = 0.0401]
Data/restraints/parameters	7216/0/255
Goodness-of-fit on F^2	1.046
Final R indexes [I>=2σ (I)]	R_1 = 0.0456, wR_2 = 0.1300
Final R indexes [all data]	R_1 = 0.0548, wR_2 = 0.1433
Largest diff. peak/hole / e Å^{-3}	3.78/-3.90
Flack parameter	-0.006(10)
CCDC Deposit Number	2244999

Table S6. Bond lengths for **AuL2**.



Atom	Atom	Length/Å		Atom	Atom	Length/Å
Au_{1A}	N_{1A}	2.014(4)		Au_{1B}	N_{2B}	1.970(4)
Au_{1A}	N_{1A}^{1}	2.014(4)		C_{1B}	C_{2B}	1.408(8)
Au_{1A}	N_{2A}^{1}	1.982(4)		C_{1B}	N_{1B}	1.346(5)
Au_{1A}	N_{2A}	1.982(4)		C_{2B}	C_{3B}	1.389(8)
C_{1A}	C_{2A}	1.412(8)		C_{3B}	C_{4B}	1.398(8)
C_{1A}	N_{1A}	1.349(5)		C_{4B}	C_{5B}	1.423(7)
C_{2A}	C_{3A}	1.391(7)		C_{4B}	N_{1B}	1.388(7)
C_{3A}	C_{4A}	1.403(8)		C_{5B}	N_{2B}	1.322(6)
C_{4A}	C_{5A}	1.415(7)		C_{6B}	C_{6B}^{2}	1.516(9)
C_{4A}	N_{1A}	1.393(7)		C_{6B}	C_{7B}	1.523(6)
C_{5A}	N_{2A}	1.304(6)		C_{6B}	N_{2B}	1.477(6)
C_{6A}	C_{6A}^{1}	1.552(9)		C_{7B}	C_{8B}	1.533(7)
C_{6A}	C_{7A}	1.511(6)		C_{8B}	C_{8B}^{2}	1.529(11)
C_{6A}	N_{2A}	1.463(6)		F_1	P_1	1.562(4)
C_{7A}	C_{8A}	1.530(7)		F_2	P_1^{1}	1.600(4)
C_{8A}	C_{8A}^{1}	1.528(11)		F_3	P_1	1.609(4)
Au_{1B}	N_{1B}^{2}	2.007(4)		F_4	P_2	1.614(5)
Au_{1B}	N_{1B}	2.007(4)		F_5	P_2^{3}	1.580(5)
Au_{1B}	N_{2B}^{2}	1.970(4)		F_6	P_2	1.518(5)

[1]1-X,+Y,1-Z; [2]1-X,+Y,-Z; [3]2-X,+Y,1-Z

Table S7. Bond lengths for **AuL2**.

Atom	Atom	Atom	Angle/˚		Atom	Atom	Atom	Angle/˚
N_{1A}	Au_{1A}	N_{1A}^{1}	113.2(2)		C_{8B}^{2}	C_{8B}	C_{7B}	111.7(4)
N_{2A}^{1}	Au_{1A}	N_{1A}	164.75(17)		C_{1B}	N_{1B}	Au_{1B}	141.3(4)
N_{2A}^{1}	Au_{1A}	N_{1A}^{1}	81.65(15)		C_{4B}	N_{1B}	Au_{1B}	111.3(3)
N_{2A}	Au_{1A}	N_{1A}	81.65(15)		C_{4B}	N_{1B}	C_{1B}	107.3(4)
N_{2A}	Au_{1A}	N_{1A}^{1}	164.75(17)		C_{5B}	N_{2B}	Au_{1B}	115.6(3)
N_{2A}	Au_{1A}	N_{2A}^{1}	83.7(2)		C_{6B}	N_{2B}	Au_{1B}	112.2(3)
N_{1A}	C_{1A}	C_{2A}	108.3(4)		C_{6B}	N_{2B}	C_{5B}	131.0(4)
C_{3A}	C_{2A}	C_{1A}	107.9(5)		F_1^{1}	P_1	F_1	96.2(5)
C_{4A}	C_{3A}	C_{2A}	106.8(5)		F_2^{1}	P_1	F_1	93.6(3)
C_{5A}	C_{4A}	C_{3A}	135.9(5)		F_2^{1}	P_1	F_1^{1}	88.5(3)
N_{1A}	C_{4A}	C_{3A}	108.1(5)		F_2	P_1	F_1	88.5(3)
N_{1A}	C_{4A}	C_{5A}	116.0(5)		F_2	P_1	F_1^{1}	93.6(3)
N_{2A}	C_{5A}	C_{4A}	116.6(5)		F_2	P_1	F_2^{1}	176.8(5)
N_{2A}	C_{6A}	C_{7A}	116.0(4)		F_3^{1}	P_1	F_1	174.7(3)
C_{8A}	C_{7A}	C_{6A}	110.0(4)		F_3^{1}	P_1	F_1^{1}	87.5(3)
C_{8A}^{1}	C_{8A}	C_{7A}	111.4(4)		F_3	P_1	F_1^{1}	174.7(3)
C_{1A}	N_{1A}	Au_{1A}^{1}	140.2(4)		F_3	P_1	F_1	87.5(3)
C_{4A}	N_{1A}	Au_{1A}^{1}	110.7(3)		F_3	P_1	F_2^{1}	87.5(2)
C_{4A}	N_{1A}	C_{1A}	108.9(4)		F_3^{1}	P_1	F_2^{1}	90.2(2)
C_{5A}	N_{2A}	Au_{1A}^{1}	114.9(3)		F_3	P_1	F_2	90.2(2)
C_{6A}	N_{2A}	Au_{1A}^{1}	111.5(3)		F_3^{1}	P_1	F_2	87.5(2)
C_{6A}	N_{2A}	C_{5A}	132.7(4)		F_3^{1}	P_1	F_3	89.1(4)
N_{1B}^{2}	Au_{1B}	N_{1B}	113.0(2)		F_4^{3}	P_2	F_4	87.2(5)
N_{2B}	Au_{1B}	N_{1B}	81.63(15)		F_5^{3}	P_2	F_4^{3}	86.5(3)
N_{2B}^{2}	Au_{1B}	N_{1B}	165.36(17)		F_5^{3}	P_2	F_4	84.8(3)
N_{2B}^{2}	Au_{1B}	N_{1B}^{2}	81.63(15)		F_5	P_2	F_4	86.5(3)
N_{2B}	Au_{1B}	N_{1B}^{2}	165.36(17)		F_5	P_2	F_4^{3}	84.8(3)
N_{2B}^{2}	Au_{1B}	N_{2B}	83.8(2)		F_5	P_2	F_5^{3}	167.8(6)
N_{1B}	C_{1B}	C_{2B}	109.7(4)		F_6^{3}	P_2	F_4^{3}	85.0(4)
C_{3B}	C_{2B}	C_{1B}	107.2(5)		F_6	P_2	F_4	85.0(4)
C_{4B}	C_{3B}	C_{2B}	106.5(6)		F_6	P_2	F_4^{3}	171.9(4)
C_{5B}	C_{4B}	C_{3B}	134.5(6)		F_6^{3}	P_2	F_4	171.9(4)
N_{1B}	C_{4B}	C_{3B}	109.3(5)		F_6^{3}	P_2	F_5	95.2(4)
N_{1B}	C_{4B}	C_{5B}	116.1(5)		F_6	P_2	F_5	92.4(4)
N_{2B}	C_{5B}	C_{4B}	115.3(5)		F_6^{3}	P_2	F_5^{3}	92.4(4)
N_{2B}	C_{6B}	C_{7B}	115.8(4)		F_6	P_2	F_5^{3}	95.2(4)
C_{8B}	C_{7B}	C_{6B}	108.9(4)		F_6^{3}	P_2	F_6	102.8(6)

[1]1-X,+Y,1-Z; [2]1-X,+Y,-Z; [3]2-X,+Y,1-Z

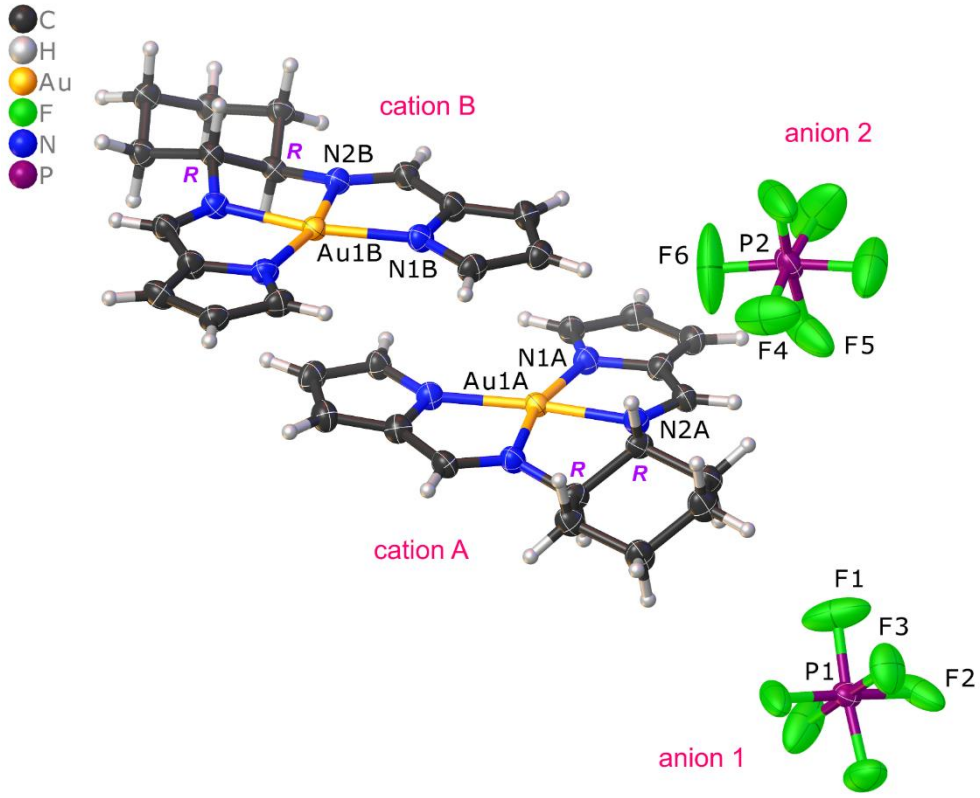


Fig. S30 Partly labelled low-temperature X-ray structure of **AuL2** (*R,R*-enantiomer, 50% thermal ellipsoids) depicting the complete ion pairs A and B. Each cation and anion for **AuL2** is located on a 2-fold axis passing through the Au(III) ion or the P atom of the anion. The cation pair geometry suggests π-π stacking interactions are operative.

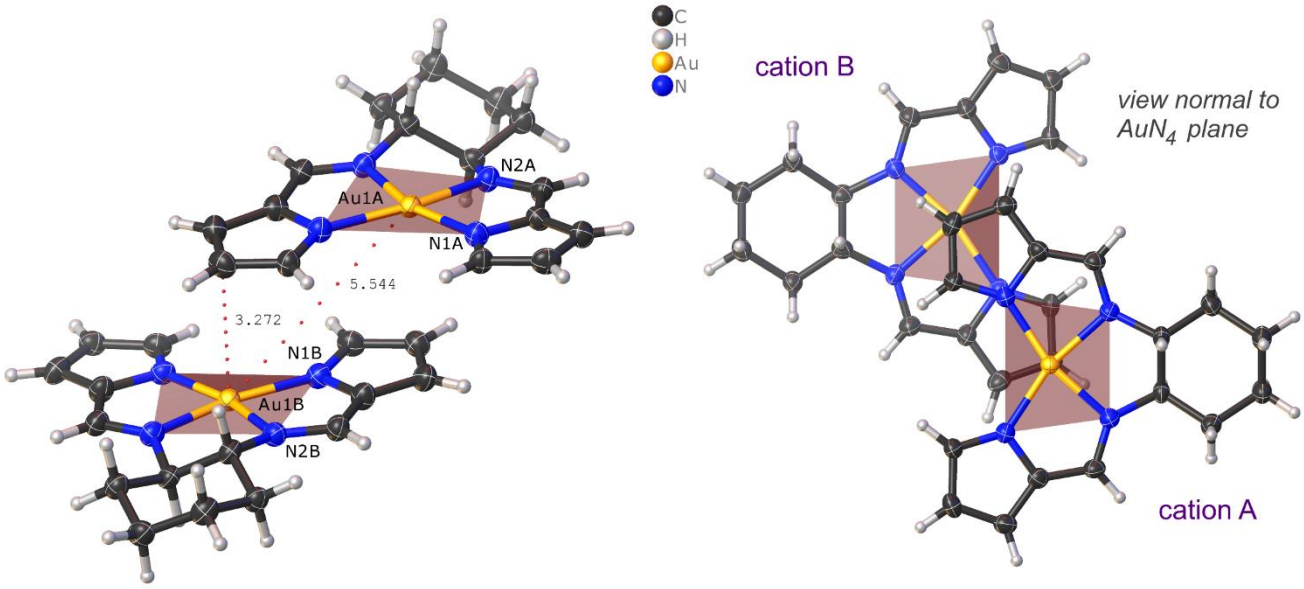


Fig. S31 Illustration of the π-π stacking geometry between independent cation pairs within the lattice of **AuL2**. The interaction distances are in Å. Note how the Au(III) ions interact axially with a pyrrole β-C atom.

Table S8. Selected bond lengths (Å) and bond angles (°) for **AuL1** and **AuL2**. Within error, chemically unique bond distances and bond angles are equivalent for the two enantiomers.

AuL1 (1S,2S)*

Au-N_{imine}	Au-$N_{pyrrole}$	C=N imine	N_{im}-Au-N_{im}	N_p-Au-N_p	cis-N_p-Au-N_{im}	trans-N_p-Au-N_{im}	C_p-C_{im}-N_{im}
1.981	2.024	1.301	84.67	112.74	81.37	165.86	117.37
1.959	1.999	1.313	84.15	112.92	81.20	166.00	116.26
1.979	2.026	1.287			81.35	165.13	116.83
1.981	1.997	1.294			81.69	165.62	117.52
AVE: 1.975	2.012	1.299	84.4	112.8	81.4	165.7	117.0
ESD: 0.011	0.016	0.011	0.4	0.1	0.2	0.4	0.6

AuL2 (1R,2R)**

Au-N_{imine}	Au-$N_{pyrrole}$	C=N imine	N_{im}-Au-N_{im}	N_p-Au-N_p	cis-N_p-Au-N_{im}	trans-N_p-Au-N_{im}	C_p-C_{im}-N_{im}
1.970	2.007	1.322	83.79	112.97	81.63	165.39	116.67
1.970	2.007	1.322	83.72	113.22	81.63	165.39	116.67
1.986	2.014	1.304			81.66	164.76	115.23
1.986	2.014	1.304			81.66	164.76	115.23
AVE: 1.978	2.011	1.313	83.8	113.1	81.6	165.1	116.0
ESD: 0.009	0.004	0.010	0.0	0.2	0.0	0.4	0.8

*There are two independent full molecules in the ASU. **There are two independent half-molecules in the ASU.

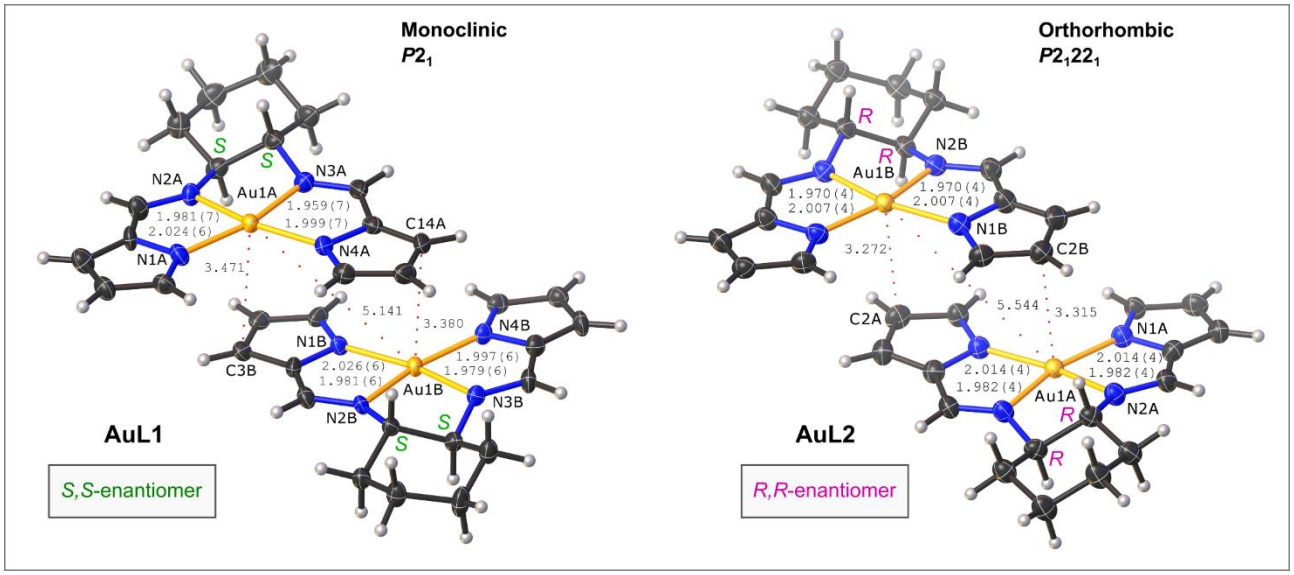


Fig. S32 Comparison of the low-temperature X-ray structures of the cation pairs formed by **AuL1** (*S,S*-enantiomer) and **AuL2** (*R,R*-enantiomer). Each cation for **AuL2** is located on a 2-fold axis passing through the Au(III) ion. Similar π-stacking is evident for both cation pairs, however, the cation pair for **AuL1** is somewhat more closely interacting, as evidenced by the shorter Au···Au and Au···C(pyrrole) nonbonded distances. All bond and interaction distances are in Å. Thermal ellipsoids are rendered at the 50% probability level.

3. References

1 O. V. Dolomanov, L. J. Bourhis, R. J. Gildea, J. a. K. Howard and H. Puschmann, *J. Appl. Crystallogr.*, 2009, **42**, 339–341.

2 G. M. Sheldrick, *Acta Crystallogr. Sect. Found. Adv.*, 2015, **71**, 3–8.

3 G. M. Sheldrick, *Acta Crystallogr. Sect. C Struct. Chem.*, 2015, **71**, 3–8.

4 F. Kleemiss, O. V. Dolomanov, M. Bodensteiner, N. Peyerimhoff, L. Midgley, L. J. Bourhis, A. Genoni, L. A. Malaspina, D. Jayatilaka, J. L. Spencer, F. White, B. Grundkötter-Stock, S. Steinhauer, D. Lentz, H. Puschmann and S. Grabowsky, *Chem. Sci.*, 2021, **12**, 1675–1692.

5 F. Neese, *WIREs Comput. Mol. Sci.*, 2012, **2**, 73–78.

6 F. Neese, *WIREs Comput. Mol. Sci.*, 2022, **12**, e1606.

7 J. P. Perdew, K. Burke and M. Ernzerhof, *Phys. Rev. Lett.*, 1996, **77**, 3865–3868.

8 C. A. de Almeida, L. P. N. M. Pinto, H. F. Dos Santos and D. F. S. Paschoal, *J. Mol. Model.*, 2021, **27**, 322.

9 H. E. Gottlieb, V. Kotlyar and A. Nudelman, *J. Org. Chem.*, 1997, **62**, 7512–7515.

10 M. Van de Weert and L. Stella, *J. Mol. Struct.*, 2011, **998**, 144–150.

11 M. van de Weert, *J. Fluoresc.*, 2010, **20**, 625–629.

12 Methodology | Databases & Tools | Developmental Therapeutics Program (DTP), https://dtp.cancer.gov/databases_tools/docs/compare/compare_methodology.htm, (accessed February 27, 2023).

13 S. Sookai and O. Munro, , DOI:10.26434/chemrxiv-2022-8v4x2.

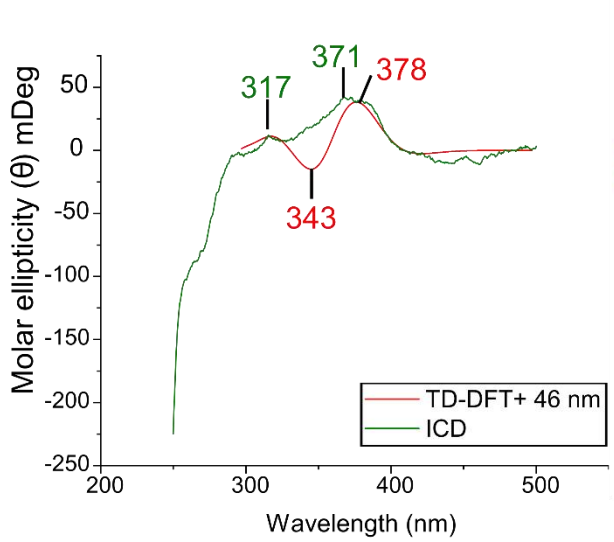
Supporting Information:

Spectroscopic and computational study of the interaction of Pt(II) pyrrole-imine chelates with human serum albumin.

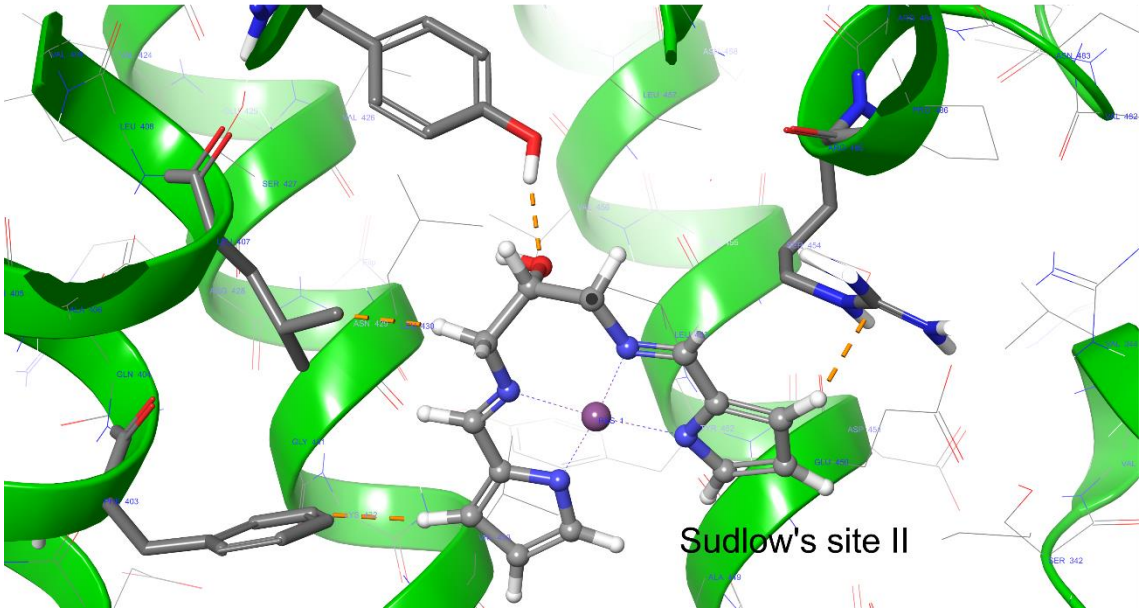
Sheldon Sookai, and Orde Q. Munro*

[a] *Molecular Sciences Institute, School of Chemistry, University of the Witwatersrand, PO WITS 2050, Johannesburg, South Africa*

E-mail: orde.munro@wits.ac.za.







Supporting Information:

Spectroscopic and computational study of the interaction of Pt(II) pyrrole-imine chelates with human serum albumin

Sheldon Sookai[a] and Orde Q. Munro[a,b]*

[a] *Molecular Sciences Institute, School of Chemistry, University of the Witwatersrand, PO WITS 2050, Johannesburg, South Africa*

E-mail: s.sookai92@gmail.com

[b] *School of Chemistry, University of Leeds, Woodhouse Lane, LS2 9JT, UK*

E-mail: o.munro@leeds.ac.uk

1. Contents

2. General experimental methods 123

3. Instruments 123

3.1.1. Crystallography 123

3.1.2. General spectroscopy 123

4. Compound synthesis 124

4.1.1. Ligand synthesis 124

4.1.2. Synthesis of Pt(II) bis(pyrrolide-imine) chelates 125

4.1.3. Characterization of bis(pyrrolide-imine) ligands 125

4.1.4. Characterization of Pt(II) bis(pyrrolide-imine) chelates 126

5. Fluorescence and CD spectroscopy 126

5.1.1. Steady state fluorescence 127

5.1.2. UV and UV-vis circular dichroism (CD) 128

6. Molecular simulations 129

6.1.1. DFT Calculations 129

6.1.2. Molecular Docking Simulations 129

7. Figures 131

7.1.1. Ligand structures 131

Fig. S1. Structures of the bis(pyrrole-imine) ligands synthesized and used in this study to chelate Pt(II): 1,3-bis(*E*){[(1*H*-pyrrol-2-yl)methylidene]amino}propan-2-ol, **1**, (*E*,*E*)-*N*,*N*'-(2,2-dimethylpropane-1,3-diyl)bis[1-(1*H*-pyrrol-2-yl)methanimine], **2**, and (*E*,*E*)-*N*,*N*'-[(1*S*)-cyclohexane-1,2-diyl]bis[1-(1*H*-pyrrol-2-yl)methanimine], **3**. 132

7.1.2. NMR, IR, and UV-vis spectra 132

Fig. S2 400 MHz ^{1}H NMR spectrum of **1** recorded in DMSO-d_6 at 300 K. 132

Fig. S3 101 MHz ^{13}C NMR spectrum of **1** recorded in DMSO-d_6 at 300 K. 133

Fig S4. FTIR spectrum of **1** recorded as a crushed powder sample at 295 K. 133

Fig. S5 UV-visible spectrum of **1** recorded in acetonitrile at 295 K as a function of concentration. The molar absorptivities of key band maximum are reported in Section 4 and were determined from the slopes of Beer-Lambert law plots at the relevant band maxima. 134

Fig. S6 400 MHz ^{1}H NMR spectrum of **2** recorded in DMSO-d_6 at 300 K. 134

Fig. S7 101 MHz ^{13}C NMR spectrum of **2** recorded in DMSO-*d*6 at 300 K. 135

Fig. S8 FTIR spectrum of **2** recorded as a crushed powder sample at 295 K. 135

Fig. S9 UV-visible spectrum of **2** recorded in acetonitrile at 295 K as a function of concentration. The molar absorptivities of key band maximum are reported in Section 4 and were determined from the slopes of Beer-Lambert law plots at the relevant band maxima. 136

Fig. S10 400 MHz ^{1}H NMR spectrum of **3** recorded in DMSO-d_6 at 300 K. This compound is known;[4] the spectral data here briefly confirm the structure of the compound and its purity. 137

Fig. S11 101 MHz ^{13}C NMR spectrum of **3** recorded in DMSO-d_6 at 300 K. 138

7.1.3. X-ray crystallography 139

Fig. S12 (a) View of the ASU of complex **1**, which comprises three independent molecules supported by hydrogen bonding interactions between the hydroxyl groups of neighbouring molecules in the solid state. The hydroxyl groups act as both hydrogen bond donors and acceptors. (b) Intermolecular π-stacking arrangements of neighbouring molecules of **1** in adjacent ASUs. The Pt···Pt distances were measured between the pair of Pt(II) ions of a centrosymmetric inversion pair. 140

Fig. S13 (a) ASU of **2** comprising four independent molecules of **2** (b) Intermolecular π-stacking arrangements of neighbouring molecules of **2** in different ASUs. The Pt···Pt distances were measured between the pair of Pt(II) ions of a centrosymmetric inversion pair. 141

7.1.4. Fluorescence spectroscopy 142

Fig. S14 Fluorescence emission spectra of HSA (5.0 μM) recorded as a function of increasing concentration of (a) **2** and (b) **3** at 298 K. Both Pt(II) bis(pyrrolide-imine) chelates had a concentration range of 0 – 12.4 μM. The emission spectra confirm that the Pt(II) complexes quench the intrinsic (i.e., Trp-214) fluorescence of HSA upon binding. 142

Fig. S15. Stern–Volmer plots of fluorescence quenching: (a) **1**···HSA, (b) **2**···HSA and (c) **3**···HSA. All three Pt(II) bis (pyrrolide-imine) chelates were recorded at three different temperatures (■ 288 K, ● 298 K, and ▲ 310 K). The relevant concentrations for the titrations were: [HSA] = 5.0 μM with **1**–**3** ranging from 0 – 12.4 μM at pH 7.50 in 50 mM KH_2PO_4 buffer. 143

Fig. S16. Plots of log((I_0-I)/I) versus log([Q]) for the interaction of HSA with several Pt(II) bis (pyrrolide-imine) chelates (i.e., quenchers, Q): (a) **1**···HSA complex, (b) **2**···HSA complex, and (c) **3**···HSA complex. The affinity constants are determined from the intercepts of the graphs and the stoichiometry from the slopes. Data for the three Pt(II) bis (pyrrolide-imine) chelates were recorded at three different temperatures (■ 288 K, ● 298 K, and ▲ 310 K). The relevant

concentrations for the titrations were: [HSA] = 5.0 μM with **1**–**3** ranging from 0 – 12.4 μM at pH 7.50 in 50 mM KH_2PO_4 buffer. 143

Fig. S17 (a) Double-log plot of the fluorescence quenching data, $logI0 - II = logK + nlogQ$, for native HSA, HSA•{warfarin}, and HSA•{Ibuprofen} as a function of the concentration of **1** at 298 K in KH_2PO_4 (50 mM, pH 7.50). This is to enable the measurement of logKa (the association constant for the Pt(II) chelate with the macromolecule target, Ka) and the reaction stoichiometry (*n*). The excitation and emission wavelengths for the fluorophore probes were: (i) Trp-214 (native HSA), λ^{ex} = 295 nm, λ^{em} = 343 nm; (ii) Warfarin (HSA-Warf), λ^{ex} = 320 nm, λ^{em} = 382 nm, and (iii) Ibuprofen (HSA-Ibu), λ^{ex} = 228 nm, λ^{em} = 332 nm. (b) Stern–Volmer (SV) plot for native HSA, HSA•{warfarin}, and HSA•{Ibuprofen} as a function of the concentration of **1** at 298 K in KH_2PO_4 (50 mM, pH 7.50). The plots are linear with an intercept of 1.0 when static quenching is dominant. Overall, the plots show that **1** binds with an approximately 1:1 mole ratio to native HSA. The presence of either drug marginally decreases the binding of **1** as the affinity constants marginally decrease. A possible interpretation is that **1** can bind (half-saturate) to both subdomain IIA and IIIA (Sudlow's site I and II) of the native protein, but that when either warfarin or ibuprofen is located in one of these two sites, the reciprocal site is fully saturated. Alternatively, warfarin or ibuprofen may alter the protein conformation to enable the uptake of an additional half-equivalent of **1** at a third site. Such additional drug binding sites are known for HSA and exist in subdomains IIIB (propofol binding site, close to site II in subdomain IIIA) and IB (hemin binding site). 143

Fig. S18 (a) Double-log plot of the fluorescence quenching data, $logI0 - II = logK + nlogQ$, for native HSA, HSA•{warfarin}, and HSA•{Ibuprofen} as a function of the concentration of **3** at 298 K in KH_2PO_4 (50 mM, pH 7.50). This is to enable the measurement of logKa (the association constant for the Pt(II) chelate with the macromolecule target, Ka) and the reaction stoichiometry (*n*). The excitation and emission wavelengths for the fluorophore probes were: (i) Trp-214 (native HSA), λ^{ex} = 295 nm, λ^{em} = 343 nm; (ii) Warfarin (HSA-Warf), λ^{ex} = 320 nm, λ^{em} = 382 nm, and (iii) Ibuprofen (HSA-Ibu), λ^{ex} = 228 nm, λ^{em} = 332 nm. (b) Stern–Volmer (SV) plot for native HSA, HSA•{warfarin}, and HSA•{Ibuprofen} as a function of the concentration of **3** at 298 K in KH_2PO_4 (50 mM, pH 7.50). The plots are linear with an intercept of 1.0 when static quenching is dominant. Overall, the plots show that **3** binds with an approximately 1:1 n value to native HSA. At no point does **3** displace either warfarin or ibuprofen from HSA•{warfarin}, and HSA•{Ibuprofen}; however, the presence of either drug marginally decreases the binding of **3** as the affinity constants marginally decrease. A possible interpretation is that **3** can bind (half-saturate) to both subdomain IIA and IIIA (Sudlow's site I and II) of the native protein, but that when either warfarin or ibuprofen is located in one of these two sites, the reciprocal site is fully saturated. Alternatively, warfarin or ibuprofen may alter the protein conformation to enable the uptake of an additional half-equivalent of **3** at a third site. Such additional drug binding sites are known for HSA and exist in subdomains IIIB (propofol binding site, close to site II in subdomain IIIA) and IB (hemin binding site). 144

7.1.5. CD- spectroscopy 145

Fig. S19 Induced CD site displacement assay carried out by measuring the UV CD of HSA (15 μM in 50 mM KH_2PO_4 buffer, pH 7.5) bound to **1** (15 μM) from 280–500 nm. Site-specific markers (a) warfarin and (b) ibuprofen were titrated into the HSA•{**1**} solution to determine the Pt(II) chelate's preferred binding site. Both site-specific markers were titrated in to give concentrations of 4.1, 8.3, 12.5, and 20.1 μM (the grey lines represent 4.1, 8.3, and 12.5 μM). The spectra were smoothed using a Lowess function (0.07 span). From Fig. S19b, it is clear that

only partial displacement of **1** is induced by the incoming probe ligand ibuprofen, while Fig. S19a indicates that incoming warfarin minimally perturbs the spectrum of HSA•{**1**} and evidently cannot displace **1** from the protein. 145

7.1.6. Molecular docking 146

Fig. S20 GLIDE XP docking analysis of the binding of **1** to HSA using the X-ray structure of HSA as the *in silico* target (PDB code 1HA2). A large target grid was generated for macromolecular ligand docking at the warfarin site (with warfarin removed), spanning 40 x 40 x 40 $Å^3$, to search for secondary binding sites radiating out (to ~20 Å) from warfarin's location in subdomain IIA. The image panels show selected phenylaniline and tyrosine residues, respectively, that are closest to the best poses for **1** (a summary of the aromatic residues for **2** is given in Table S8). Distances are in Å units. The near-UV CD spectra for HSA•{**1**} and HSA•{**2**} are shown in Figs. 7a and b of in the main text suggest that these ligands perturb Tyr and Phe chromophores in addition to Trp-214 in HSA. The above docking results support the experimental data: **2** binds in tyrosine- and phenylalanine-rich pockets within HSA with roughly the same docking score. ... 146

Fig. S21 Illustration of the binding of Pt(II) chelates **1** and **2** in subdomain IIIA (Sudlow's drug site II) of HSA as determined by GLIDE XP docking using PDB code 2BXF as the target and a large 40 × 40 × 40-$Å^3$ grid centred on the coordinates of diazepam. The *in silico* model supports the observed data suggesting both Pt(II) chelates **1** and **2** bind to Sudlow's site II (See Figs. 6 and 8 of the main paper.) 147

8. Tables 148

Table S1. Crystal data and X-ray structure refinement details for Pt(II) bis(pyrrolide-imine) chelate **1** and **2**. 148

Table S2. Selected geometrical parameters (Å, °) for the X-ray structure of **1** and **2**. A labelled thermal ellipsoid plot (50% probability surfaces) is included above to aid in reading the tabulated data. 149

Table S3. Selected geometrical parameters (Å, °) for the X-ray structure of **1** and **2**. A labelled thermal ellipsoid plot (50% probability surfaces, H atoms omitted for clarity) is included above to aid in reading the tabulated data. 152

Table S4. Selected mean crystallographic and calculated structural and conformational parameters for compounds **1** and **2**. 156

Table S5. Selected excited singlet states of TD-DFT calculations for complex **1.** 157

Table S6. Selected excited singlet states of TD-DFT calculations for complex **2.** 158

Table S7. Summary of GLIDE XP docking scores and selected interaction energy parameters for HSA targets prepared from ligand-free and ligand-bound grids based on geometry-optimized (prepared) structures derived from PDB codes 1HA2 (HSA•{warfarin} complex), 2BXF (HSA•{diazepam} complex), and 2BXG (HSA•$\{ibuprofen\}_2$ complex). The docking runs were truncated to report only the top-scoring ligand pose for each ligand. All energies are in units of kcal mol^{-1}. 159

Table S8. Summary of Glide XP docking scores (as in Table S7) and selected interaction distances for HSA targets prepared from ligand-free grids based on geometry-optimized (prepared) structures derived from PDB codes 1HA2 (HSA•{warfarin} complex) and 2BXF (HSA•{diazepam} complex). The docking runs were truncated to report only the top-scoring ligand pose for each ligand. All energies are in units of kcal mol^{-1}. 161

9. References 163

General experimental methods

Pyrrole-2-carboxaldehyde, 1,3-diaminopropane, 1,3-diaminopropan-2-ol, 1,3-diamino-2,2-dimethyl propane, (R)-(+)-1,2-diaminopropane·2HCl and (S)-(-)-1,2-diaminopropane·2HCl were all purchased from Sigma-Aldrich. All organic solvents were of HPLC grade and were used without any further purification (DMSO, DMF, THF, ethyl acetate, methanol, DCM, and hexane). Buffer reagents included potassium hydroxide (≥ 90%) flakes and potassium monobasic phosphate buffer (KH_2PO_4 ≥ 99 ACS); these were purchased from Sigma Aldrich along with lyophilized fatty acid-free HSA (≥ 97%).

Instruments

Crystallography

Single crystal X-ray data sets were recorded with a four-circle Bruker D8 Venture X-ray diffractometer equipped with a Photon II CPAD area detector and a three-circle Bruker Apex II X-ray diffractometer employing a CCD area detector; both instruments were fitted with a fine-focus sealed X-ray tube source (Mo anode). Crystals were mounted under Paratone® oil on nylon loops (Hampton Research) and the crystals were kept at 173(1) K during data collection (Oxford CryoStream 700). Using Olex2,[1] the structures were solved with the ShelXT[2] structure solution program (intrinsic phasing) and refined with ShelXL[3] using least squares minimization.

General spectroscopy

Proton (^{1}H) and carbon (^{13}C) NMR spectra were recorded on Bruker Avance III 400 and 300 NMR spectrometers at ^{1}H frequencies of 400 MHz and 300 MHz, respectively, and ^{13}C frequencies of 100 MHz and 75 MHz, respectively. Spectra were recorded at 300 K with 5 mm BBOZ or TBIZ probes. Chemical shifts for both proton and carbon were referenced using the solvent signal. MestReNova (version 14.2.1-27684) was used to analyse all NMR spectra.

FTIR spectra of powder samples were recorded using a Bruker Alpha FTIR spectrometer incorporating a Bruker Platinum diamond ATR sampling accessory. Spectra were analysed using the OPUS software package on the spectrometer (version 7.5).

Electronic spectra were recorded using either a PerkinElmer Lambda 365 double-beam spectrometer connected to a Peltier controller and a Peltier Temp multicell thermostatic cell block or an Analytik Jena Specord210 Plus double-beam instrument fitted with external water circulating thermostatic bath and thermostatic cell holders. The spectral data were analysed with the spectrometer software or Origin Pro 2020. Spectra were

recorded as a function of concentration for both characterization and the determination of molar absorptivity constants. Quartz cuvettes with a path length of 10 mm were used.

Compound synthesis

Ligand synthesis

1,3-bis{[(1*E*)-1*H*-pyrrol-2-ylmethylene]amino}propan-2-ol (H_2(OH)Pyrr). In brief, the synthesis of H_2(OH)Pyrr involved refluxing pyrrole-2-carboxaldehyde (0.5706 g; 6 mmol) with 1,3-diamino propanol (0.2704 g; 3 mmol) for 2 hours in ethanol (30 mL) in which time the solution changed from colourless to bright orange. The ligand was precipitated out by overnight evaporation of ethanol.

2,2-dimethyl-*N*,*N*'-bis[(1*E*)-1*H*-pyrrol-2-ylmethylene]propane-1,3-diamine ($H_2(CH_3)_2$Pyrr). In brief was synthesized by refluxing pyrrole-2-carboxaldehyde (0.5705 g, 6 mmol), and 1,3-diamino-2,2-dimethyl propane (0.3066 g, 3 mmol) was refluxed in ethanol (30 mL) for one hour. The solution changed from colourless to orange. The ligand was precipitated out by overnight evaporation of the ethanol.

(1*S*,2*S*)-*N*,*N*'-bis[(1*E*)-1*H*-pyrrol-2-ylmethylene] cyclohexane -1,2-diamine (H_2(-S-cyclohexane)Pyrr). The enantiomerically pure ligand was synthesized by a solid-state reaction using the enantiomerically pure (1S, 2S) cyclohexane diamine (0.303 g, 2.65 mmol) with an agate pestle and mortar with pyrrole-2-carboxaldehyde (0.500 g, 5.30 mmol) for between 10 to 15 minutes until a brown oil was formed. The brown oil was dissolved in dichloromethane and dried with $MgSO_4$ to remove the water from the condensation reaction. The solution was filtered through celite before being layered with hexane, which yielded thin white rod-shaped crystals.

Synthesis of Pt(II) bis(pyrrolide-imine) chelates

2,2'-{(2-hydroxypropane-1,3-diyl)bis[nitrilo(*E*) methylylidene]} bis(pyrrol-1-ido) platinum(II) (**1**) and 2,2'-{(2,2-dimethylpropane-1,3-diyl)bis[nitrilo(*E*)methylylidene]} bis(pyrrol-1-ido) platinum(II) (**2**), were prepared in a similar manner.[4] To a round bottom flask either H_2(OH)Pyrr (100 mg, 0.410 mmol) or $H_2(CH_3)_2$Pyrr (100 mg, 0.393 mmol) were added to 15 mL of DMF containing 2-mole equivalents of sodium acetate and the solution was heated to 80 °C. Thereafter, K_2PtCl_4 was dissolved in 15 mL of DMSO, and K_2PtCl_4 (0.410 mmol, 0.170 g) was added to the H_2(OH)Pyrr solution, while K_2PtCl_4 (0.393 mmol, 0.163 g) was similarly added to the $H_2(CH_3)_2$Pyrr solution. The solutions were then stirred at 80 °C for a further 4 h. A colour change from yellow to dark orange over time indicated spectral changes consistent with metalation and thus the formation of the target Pt(II) bis(pyrrolide-imine) chelates.

1 was water soluble. Therefore, 100 mL of cold distilled H_2O was added to the 50% (V/V) DMSO:DMF solution, which was then placed in a separating funnel. **1** was then extracted from the aqueous (DMSO:DMF) layer with ethyl acetate (5 x 250 mL). The solution was then concentrated by rotary evaporation. Red crystals suitable for X-ray diffraction were obtained by slow liquid diffusion of ether into the ethyl acetate solution of **1**.

2 was precipitated by adding 100 mL of cold distilled H_2O, and the solution was filtered by gravity filtration leaving a yellow precipitate behind. The yellow precipitate was dried overnight and then dissolved in DCM (~30 mL). DCM was removed by rotary evaporation at 40 °C, upon removal of DCM single red crystals suitable for X-ray diffraction of **2** formed.

Characterization of bis(pyrrolide-imine) ligands

1,3-bis{[(1*E*)-1*H*-pyrrol-2-ylmethylene]amino}propan-2-ol (H_2(OH)Pyrr). The ligand was analysed by ^{1}H NMR, ^{13}C NMR, FT-IR, and UV-visible spectroscopy. ^{1}H NMR (400 MHz, DMSO-d_6-300 K) [δ, ppm]: 3.43 (dd, *J* = 11.7, 6.5 Hz, 2H, CH_2-N=CH), 3.77 – 3.54 (m, 2H, CH_2-N=CH), 4.00 – 3.82 (m, 1H, H-7), 6.11 (t, *J* = 3.0 Hz, 2H, H-2), 6.44 (dd, *J* = 3.5, 1.5 Hz, 2H, H-3), 6.87 (t, *J* = 1.9 Hz, 2H, H-1), 8.07 (s, 2H, H-5), 11.34 (s br, 2H, DMSO-d_6 exchangeable, H-9). ^{13}C NMR (101 MHz, DMSO-d_6, 300 K) [δ, ppm]: 65.14 (C-6), 70.69 (C-7), 108.98 (C-2), 113.35 (C-3), 122.03 (C-1), 130.41 (C-4), 152.92 (C-5). IR (KBr pellet, cm^{-1}): 3254w (NH, pyrrole), 3088m (CH, imine), 2882 (CH, H-COH), 2859 (CH, CH_2-N=CH), 1633s (C=N), 1127 (C-O stretch). UV/vis (ethanol) [λ, max, nm; ε, mol^{-1} dm^3 cm^{-1}]: 289; 3.23 × 10^4.

2,2-dimethyl-*N*,*N*'-bis[(1*E*)-1*H*-pyrrol-2-ylmethylene]propane-1,3-diamine ($H_2(CH_3)_2$Pyrr). The ligand was analysed by ^{1}H NMR, ^{13}C NMR, FT-IR, and UV-Visible spectroscopy. ^{1}H NMR (400 MHz, Chloroform-*d*, 300 K) [δ, ppm]: 0.97 (t, *J* = 4.3 Hz, 6H, H-8), 3.46 (t, *J* = 4.2 Hz, 4H, H-6), 6.26 (p, *J* = 3.2 Hz, 2H, H-2), 6.48 (dt, *J* = 6.6, 3.4 Hz, 2H, H-3), 6.90 (d, *J* = 6.1 Hz, 2H, H-1), 7.99 (t, *J* = 4.2 Hz, 2H, H-5), 9.50 (s br, 2H, H-9). ^{13}C NMR (101 MHz, Chloroform-*d* 300 K) [δ, ppm]: 24.28 (C-8), 36.96 (C-7), 69.32 (C-6), 109.44 (C-2), 114.28 (C-3), 122.20 (C-1), 130.06 (C-4), 152.17 (C-5). FT-IR (KBr pellet, cm^{-1}): 3130m br *ν*(CH, imine), 2966m *ν*(CH, terminal CH_3), 2852m *ν*(CH_2, alkyl), 1635s br *ν*(C=N). UV-vis (ethanol) [λ, max, nm; ε, mol^{-1} dm^3 cm^{-1}]: 289; 3.23 × 10^4.

(1*S*,2*S*)-*N*,*N*'-bis[(1*E*)-1*H*-pyrrol-2-ylmethylene] cyclohexane -1,2-diamine (H_2(-S-cyclohexane)Pyrr). The ligand was analysed by ^{1}H NMR (400 MHz, DMSO-d_6, 300 K) [δ, ppm]: 1.34 – 1.80 (m, 8H, H-7, and H-8), 3.23 (m, 2H, H-6), 6.01 (t, *J* = 3.0 Hz, 2H, H-2), 6.31(dd, $^3J_1$ = 3.5 Hz, $^3J_2$ 1.4 Hz, 2H, H-3), 6.76 (t, *J* = 1.9 Hz, 2H, H-1), 7.94 (s, 2H, H-5), 11.16 (s, 2H, H-9). ^{13}C NMR (101 MHz, DMSO-d_6, 298 K) [δ, ppm]: 24.70 (C-8), 33.85 (C-7), 74.09 (C-6), 109.07 (C-2), 113.61 (C-3), 122.08 (C-1), 130.33 (C-4), 151.26 (C-5). UV-vis (acetonitrile) [λ, max, nm; ε, mol^{-1} dm^3 cm^{-1}]: 289; 2.37 x 10^4.

Characterization of Pt(II) bis(pyrrolide-imine) chelates

2,2'-{(2-hydroxypropane-1,3-diyl)bis[nitrilo(*E*) methylylidene]} bis(pyrrol-1-ido) platinum(II) (1). ^{1}H NMR (400 MHz, DMSO-d_6) δ 8.19 (s, 1H; H-15), 7.20 (s, 2H; H-9), 6.65 (d, *J* = 3.8 Hz, 2H; H-11), 6.17 (dd, *J* = 3.8, 1.9 Hz, 2H; H-10), 5.30 (d, *J* = 4.5 Hz, 1H; H-1)), 4.03 – 3.95 (m, 2H; H-14), 3.82 (d, *J* = 14.0 Hz, 2H; H-14), 3.66 (dd, *J* = 14.1, 7.6 Hz, 2H; H-19). ^{13}C NMR (101 MHz, DMSO-d_6) δ 161.75 (C-15), 140.88 (C-9), 135.52 (C-12), 117.25 (C-11), 110.84 (C-10), 70.47 (C-19), 59.76 (C-14). IR (KBr pellet, cm^{-1}): 3083 (CH, imine), 2990 (CH, H-COH), 2904 (CH, CH_2-N=CH), 1575 (C=N), 1126 (C-O stretch). [λ_{max}/nm, ε/mol^{-1} dm^3 cm^{-1}]: 277, 1.64 × 10^4; 303, 1.91 × 10^4; 313, 2.11 × 10^4; 382, 1.55 × 10^4.

2,2'-{(2,2-dimethylpropane-1,3-diyl)bis[nitrilo(*E*)methylylidene]} bis(pyrrol-1-ido) platinum(II) (2). ^{1}H NMR (400 MHz, DMSO-d_6) δ 8.16 (s, 2H; H-14), 7.21 (s, 2H; H-10), 6.66 (d, *J* = 3.8 Hz, 2H; H-12), 6.18 (dd, *J* = 3.9, 1.9 Hz, 2H; H-11), 3.48 (s, 4H; H-16), 1.05 (s, 6H; H-19). ^{13}C NMR (101 MHz, DMSO-d_6) δ 161.23 (C-14), 140.78 (C-16), 135.44 (C-13), 117.21 (C-12), 110.88 (C-11), 64.52 (C-16), 38.78 (C-17), 23.90 (C-19). IR (KBr pellet, cm^{-1}): 3085 (CH, imine), 3015m (CH, terminal CH_3), 2933 (CH_2, alkyl), 1652 (C=N). IR (cm^{-1}): 2919m br *ν*(CH, imine), 1566s br *ν*(C=N). [λ_{max}/nm, ε/mol^{-1} dm^3 cm^{-1}]: 277, 1.64 × 10^4; 303, 1.85 × 10^4; 313, 2.06 × 10^4; 382, 1.51 × 10^4.

2,2'-{(1*S*,2*S*)-cyclohexane-1,2-diylbis[nitrilo(*E*)methylylidene]}bis(pyrrol-1-ido)platinum(II) (3). ^{1}H NMR (400 MHz, DMSO-d_6) δ 8.15 (s, 2H; H-8)), 7.10 (s, 3H; H-12), 6.64 (d, *J* = 3.8 Hz, 3H; H-10), 6.14 (dd, *J* = 3.9, 1.8 Hz, 3H; H-11), 3.92 (d, *J* = 8.8 Hz, 4H; H-6), 2.56 (s, 1H; H-2), 1.75 (d, *J* = 8.8 Hz, 3H; H-1), 1.49 (d, *J* = 10.6 Hz, 2H; H-1), 1.39 – 1.13 (m, 3H; H-1). ^{13}C NMR (101 MHz, DMSO-d_6) δ 152.99 (C-8), 144.32 (C-12), 135.92 (C-9), 117.61 (C-10), 109.38 (C-11), 73.06 (C-6), 26.99 (C-1), 23.24 (C-2). IR (cm^{-1}): 2945m br *ν*(CH, imine), 1564s br *ν*(C=N).[λ_{max}/nm, ε/mol^{-1} dm^3 cm^{-1}]: 277, 1.89 × 10^4; 303, 1.73 × 10^4; 316, 1.89 × 10^4; 382, 2.04 × 10^4.

Fluorescence and CD spectroscopy

Steady state fluorescence

Pt(II) bis(pyrrolide-imine) chelates binding to and quenching HSA fluorescence. Pt(II) bis(pyrrolide-imine) chelates (0 – 1.24 x 10^{-5} M in DMSO) were titrated into a solution of HSA (5 x 10^{-6} M) in KH_2PO_4 buffer (50 x 10^{-6} M, pH7.5). The excitation slit width was 5 nm and the emission slit width was 10 nm. The protein was excited at 282 nm and the fluorescence emission was measured from 310 nm to 400 nm for all temperatures.

Fluorescent probe displacement assay. Warfarin and ibuprofen were used as fluorescent site-specific marker probes for Sudlow's sites I and II, respectively. Steady-state fluorescence spectra were recorded as described above at 298 K using 10 nm excitation and emission bandwidths for warfarin, while 5 nm excitation and 10 nm emission bandwidths were employed for ibuprofen. The fluorophores warfarin and ibuprofen were equilibrated (bound) to HSA (50 mM KH_2PO_4 buffer, pH 7.50) and were excited at 320 nm and 228 nm, respectively. The emission spectrum was measured in the range of 350 – 500 nm for warfarin and 228 – 450 nm for ibuprofen. The HSA and fluorescence probe concentrations were both used at 5.0 µM. Titrations were performed by increasing the concentrations of the Pt(II) bis(pyrollide-imine) chelates in the protein-probe solution from 0 to 25.9 µM.

Correction of fluorescence data. Inner filter effect (IFE) correction was applied to all fluorescence data using eq. S1.[5]

$$F_{corrected} = F_{observed} * 10^{Aex*dex+Aem*dem} \qquad \text{S1}$$

Where $A_{excited}$ and $A_{emission}$ are the absorbance reading at the excitation and emission wavelengths. While d is the path length of the cuvette.

Further corrections were applied to the concentration of the ligand. i.e., if $[Ligand]_{added}$ was not equal to $[Ligand]_{free}$, the free ligand concentration was calculated using eq. S2[6]

$$[Ligand]_{free} = [Ligand]_{added} - \frac{F_o}{F_o} - \frac{F}{F_c} * [HSA] \qquad S2$$

UV and UV-vis circular dichroism (CD)

General CD spectroscopy. Far-UV CD spectra of solutions of HSA (3.0×10^{-7} mol dm^{-3}) in the absence and presence of increasing concentrations (0–40 μM) of Pt(II) bis(pyrrolide-imine) chelates were recorded with a JASCO J-1500 CD spectrometer equipped with a Peltier temperature controller (25 °C). A scan speed of 100 nm min^{-1} was employed for spectral acquisition with a 0.5 nm data pitch and a response time of 2 s. Each spectrum was the average of three scans. Spectra were recorded over a wavelength range of 200–260 nm (0.4 cm pathlength quartz cuvette). All spectra were processed with JASCO Spectral Manager™.

Near-UV region CD spectra (250–310 nm, 1.0-cm pathlength quartz cuvette, 25 °C) and UV-vis CD spectra (300–500 nm, 1.0-cm pathlength quartz cuvette, 25 °C) were recorded similarly to detect induced CD (ICD) signals of the achiral ligands and Pt(II) metal chelates upon their uptake by HSA. Typically, HSA (15×10^{-6} M) was incubated (25 °C) with one molar equivalent of the Pt(II) bis(pyrrolide-imine) chelates for at least 60 min in 50 mM KH_2PO_4 buffer at pH 7.5. A scan speed of 50 nm min^{-1} was used with a 0.5-nm data pitch (response time, 2 s) for the near UV-vis CD spectrum and 100 nm min^{-1} for the UV-vis CD spectrum; each spectrum was the average of three scans.

Site displacement assay by UV-vis CD spectroscopy. Typically, two cuvettes were set up with HSA in buffer (15×10^{-6} M) and incubated with one molar equivalent of the candidate Pt(II) bis(pyrrolide-imine) chelate for at least 60 min in 50 mM KH_2PO_4 buffer at pH 7.5 (25 °C). A scan speed of 50 nm min^{-1} was used with a 0.5-nm data pitch (response time, 2 s) for the near-UV CD spectra and 100 nm min^{-1} for the UV-vis CD spectra; each spectrum was the average of three scans. Thereafter, two site-specific markers, namely warfarin (Sudlow's site I) or ibuprofen (Sudlow's site II), were titrated into the solution; spectra were recorded as above after each aliquot of titrant added had been equilibrated in the reaction solution for 10 minutes.

Analysis of CD spectra to determine secondary structure composition. We utilised the JWMVS-529 Protein Secondary Structure Analysis program, incorporated in JASCO's Spectra Manager™ package, to analyse the secondary structure composition of HSA based on the recorded CD spectra. This program employs a library of 26 protein CD spectra (176–260 nm) provided by JASCO to establish a calibration model.[7] By applying the partial least squares (PLS) method and principal component regression (PCR) techniques,[8] the experimental CD spectra were fitted to the calibration model, allowing for accurate estimation of the fractional composition of α-helix, β-sheet, turn, and unordered coil

structures. Notably, this approach significantly enhances the assessment of β-sheet motifs, which lack strong specific CD marker bands. We opted for these methods over an older algorithm, the JWSSE-513 Protein Secondary Structure Analysis program, offered by JASCO, which employs a classical least squares (CLS) fitting algorithm based on the reference spectra set of Yang et al.[9] Although other methods for protein secondary structure prediction can be found in the literature, we did not utilize them in this study as suitable methods were readily available in JASCO's Spectra Manager™ package on the spectrometer's controlling computer.[10,11]

Molecular simulations

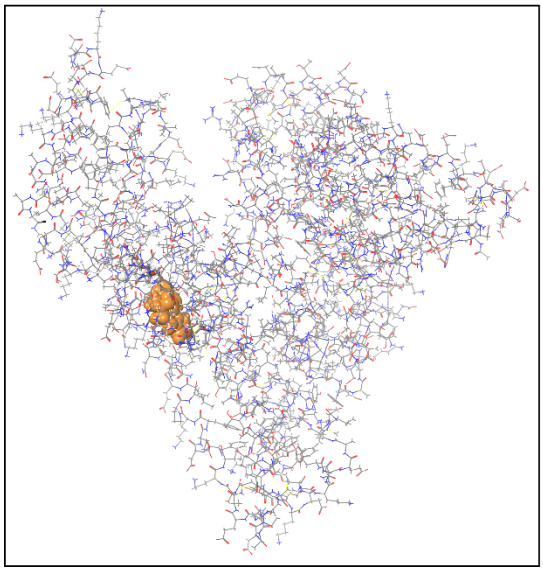
All *in silico* studies were carried out as reported by Sookai and Munro.[12] The methods are reiterated briefly below.

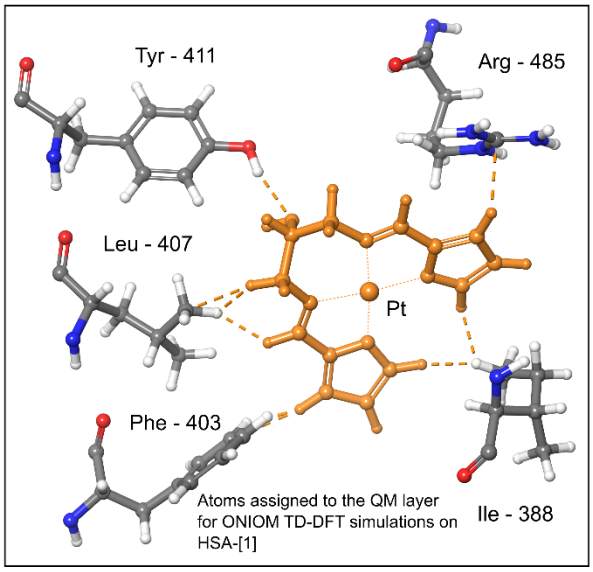
DFT Calculations

Simulations were performed to calculate optimized structures, vibrational frequencies, and electronic spectra for Pt(II) chelates **1** and **2** using Gaussian 16 Rev C.01[13] at the CAM-B3LYP[14]/DEF2-QZVP[15] level of theory using the GD3BJ empirical dispersion correction.[16] Structures were also calculated using the SDD basis set.[17] The default geometry convergence criteria in Gaussian 16 were applied. Nuclear shielding tensors were calculated by the default GIAO method[18,19] in Gaussian. Input Pt(II) chelate structures were derived from the X-ray structure atomic coordinates (C_1 symmetry). Simulations were carried out *in vacuo* and in acetonitrile solvent continua (SCRF PCM method[20]). GaussView 6.0.16[21] was used for preparing input files and data visualization. GaussSum 3.0 was used to visualize electronic spectra and tabulate transition assignments.[22] All geometry-optimized structures were characterized by positive frequency eigenvalues, indicating that true minima were located on the global potential energy surface for each system.

Time-dependent DFT (TD-DFT) simulations were carried out using the above method (CAM-B3LYP) and basis sets in Gaussian 16 for all small molecules. Typically, 60 excited singlet states were computed to cover the full spectral range (150–900 nm). TD-DFT simulations on protein complexes required the use of the ONIOM[23] method employing two layers: a high or quantum mechanical (QM) layer computed at the CAM-B3LYP/SDD/GD3BJ level of theory and a low layer (molecular mechanics) calculated using the UFF[24] force field. The input structures for the single-point calculations were derived from the best-scoring poses of the ligands of interest docked within the relevant binding site in HSA taken directly from the output of a GLIDE XP[25] docking run with the relevant X-ray structure target (e.g., PDB code: 2BXF). For the QM layer of HSA•{**1**}, all atoms of the metal chelate were included at the high level. Three amino acid side chains (Ile-388, Phe-403, Leu-407 Arg-485, and Tyr-411) were included in the QM layer around **1** located within Sudlow's site II in the simulations for HSA•{**1**} to achieve an electronic structure that best-matched

experiment, specifically the calculated CD spectrum of the macromolecular complex. This is illustrated in the two boxes below.





Molecular Docking Simulations

System preparation. The 2.5-Å and 2.95-Å X-ray crystal structures of HSA in complex with warfarin,[26] diazepam,[27] and ibuprofen[27] were retrieved from the Protein Data Bank (PDB ID codes: 1HA2, 2BXF, and 2BXG). The structure of HSA was pre-processed, minimized, and refined using the Protein Preparation Wizard[28] employed in Schrödinger Suite 2022-3. This step included eliminating crystallographic waters within 5 Å of the ligand binding site, adding missing hydrogen atoms and side chain atoms, as well as assigning the appropriate charge and protonation state of the receptor structure (pH = 7.4) using Prime. Finally, the protein structure was subjected to energy minimization using Macromodel[29] and the S-OPLS force-field[30,31] with a RMSD cut-off value of 0.30 Å to resolve steric clashes among closely spaced residues arising from the addition of hydrogen atoms.

The structures of Pt(II) complexes **1** and **2** for docking inputs were obtained by DFT simulations at the CAM-B3LYP/DEF2-QZVP level of theory in a water solvent continuum (SCRF PCM model) and implementing the GD3BJ empirical dispersion energy correction. Minor adjustments were required to prepare the metal chelate structures for docking with GLIDE. First, the metal was given a +2 charge and the pyrrole nitrogen atoms were each given a −1 charge. Second, the bonds from the four N-donor atoms to the metal ion were assigned bond orders of zero. This step is mandatory as it obviates the need for specific force field parameters involving the metal ion; the coordination geometry is then restrained to remain similar to the input DFT-calculated geometry by GLIDE during optimization and fitting. Lastly, partial charges were assigned to the structures using the S-OPLS force-field.

Molecular docking. Docking was performed with GLIDE[25,32,33] to identify the best-fit orientation of the compounds (ligands) into both Sudlow's site I (exemplified by PDB code 1HA2) or Sudlow's site II (PDB code 2BXF) and any sites within ~20 Å of each site.[34] The appropriate hard receptor grid was generated based upon a set of centre coordinates using a cube with dimensions 40 × 40 × 40 $Å^3$ in each case. The grid box employed was a factor of 4 times larger than the default box size (10 × 10 × 10 $Å^3$) and centred on the centroid of the relevant HSA-bound drug (warfarin or diazepam) or protein residue (typically Trp-214). The drug was then automatically removed prior to grid generation. This strategy was adopted because the metal chelates are slightly larger than the typical small molecule drugs bound in Sudlow's sites I and II and we wanted to ensure appropriate sampling of any atypical binding sites close to the main drug-binding pockets.

The metal chelates and free ligand species were then flexibly docked into the relevant binding site grids using the extra precision (XP) docking protocols of GLIDE; aromatic hydrogens were included as H-bond donors. The best-scoring pose for each compound with each PDB structure of native HSA was saved and selected for further analysis.

Docking simulations on HSA targets containing pre-bound drugs (warfarin, diazepam, and ibuprofen) were also performed to evaluate the ability of the protein to take up the metal chelates at binding site locations close to the bound drugs as well as secondary sites located further away. These experiments were performed as described above with grids centred on Trp-214 at the core of the protein. The ligand/drug present in the X-ray structure was retained when setting up the receptor grid. These unconventional experiments were specifically aimed at understanding our fluorescence titration data for HSA pre-equilibrated with warfarin and ibuprofen.

Figures

Ligand structures

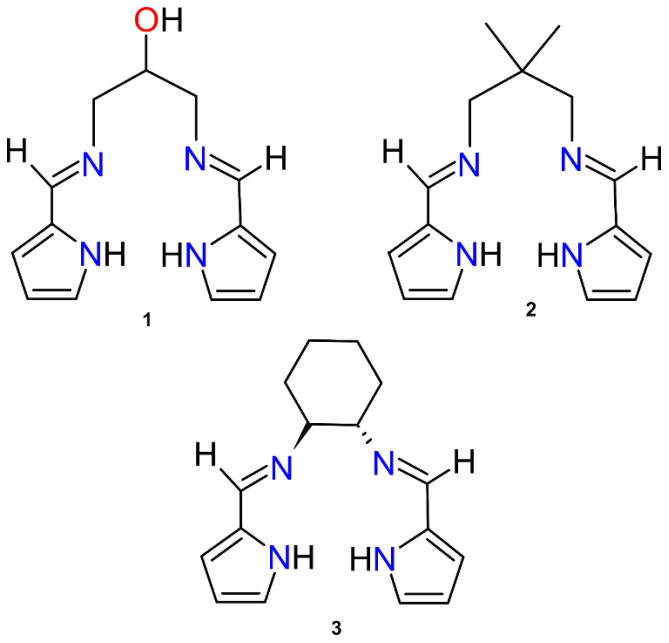


Fig. S1. Structures of the bis(pyrrole-imine) ligands synthesized and used in this study to chelate Pt(II): 1,3-bis(*E*){[(1*H*-pyrrol-2-yl)methylidene]amino}propan-2-ol, **1**, (*E*,*E*)-*N*,*N*'-(2,2-dimethylpropane-1,3-diyl)bis[1-(1*H*-pyrrol-2-yl)methanimine], **2**, and (*E*,*E*)-*N*,*N*'-[(1*S*)-cyclohexane-1,2-diyl]bis[1-(1*H*-pyrrol-2-yl)methanimine], **3**.

NMR, IR, and UV-vis spectra

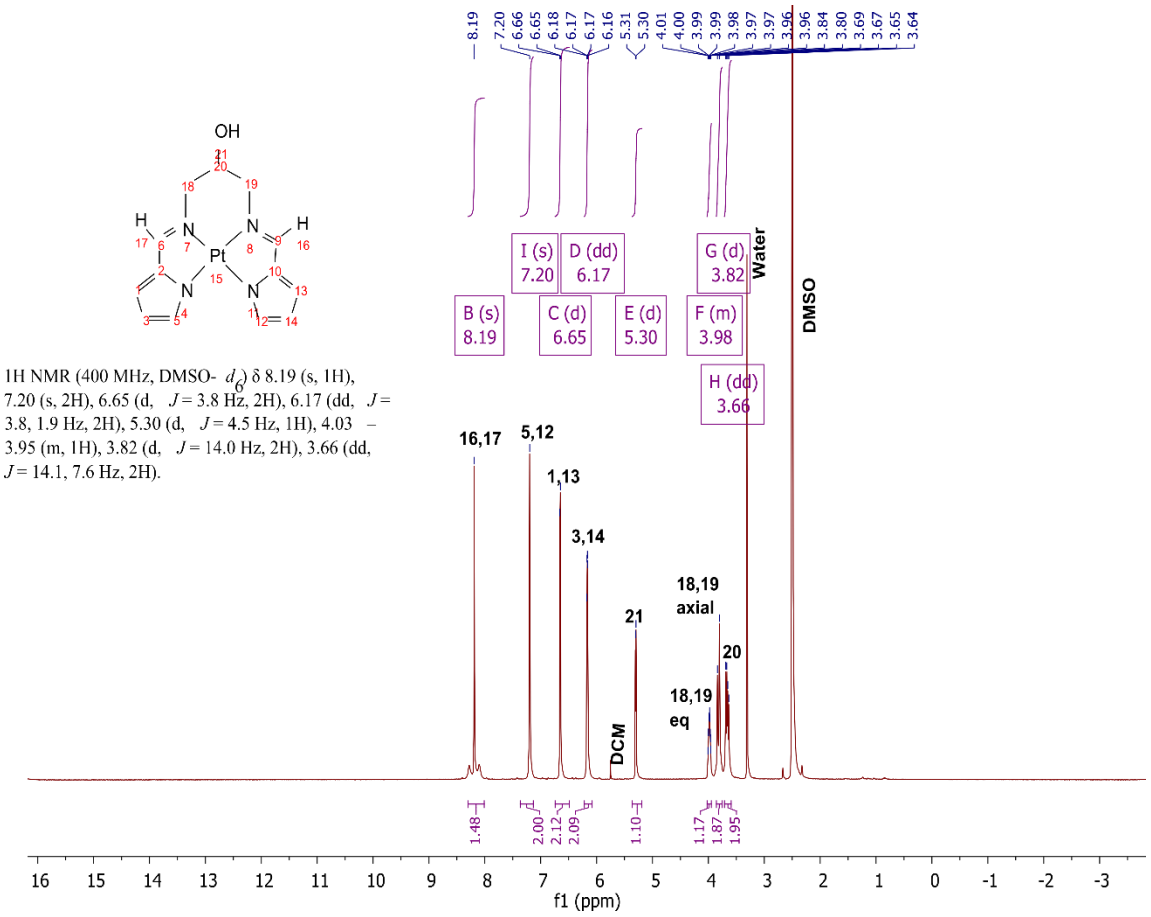


Fig. S2 400 MHz ^{1}H NMR spectrum of **1** recorded in DMSO-d_6 at 300 K.

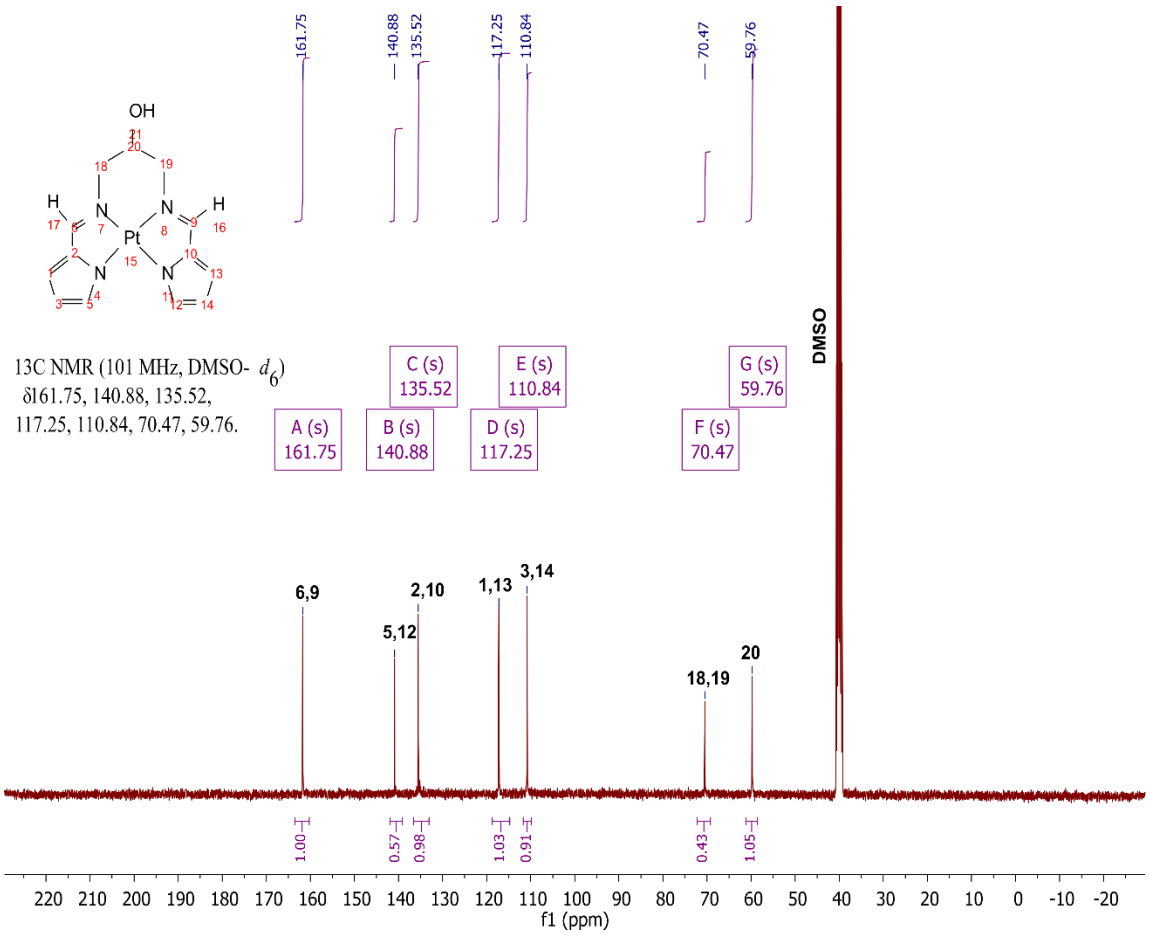


Fig. S3 101 MHz ^{13}C NMR spectrum of **1** recorded in DMSO-d_6 at 300 K.

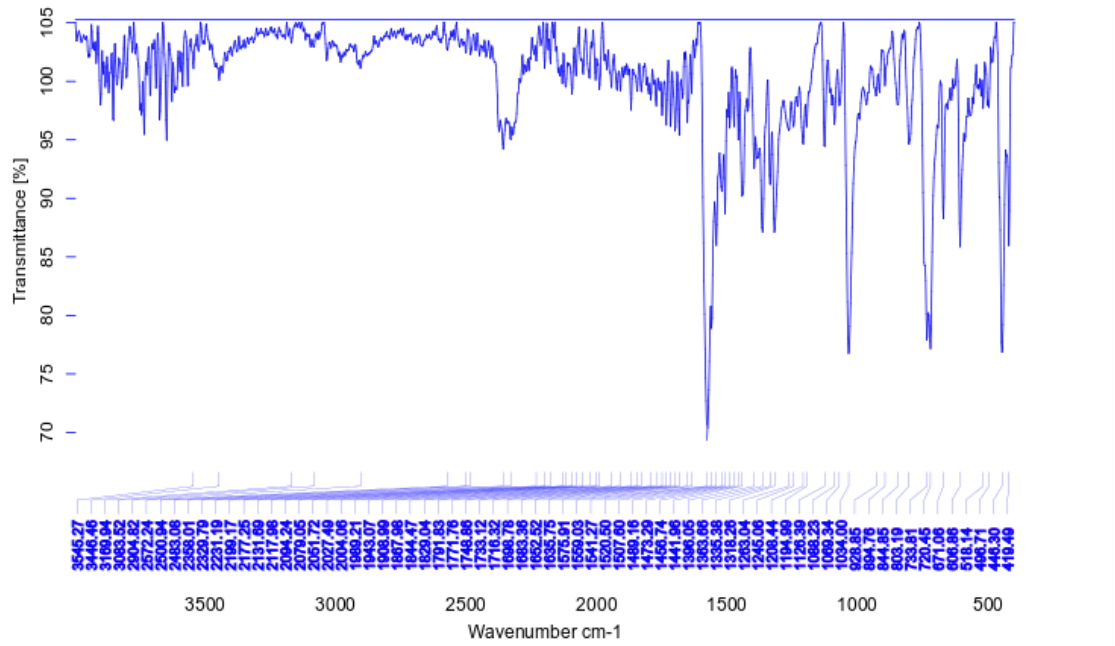


Fig S4. FTIR spectrum of **1** recorded as a crushed powder sample at 295 K.

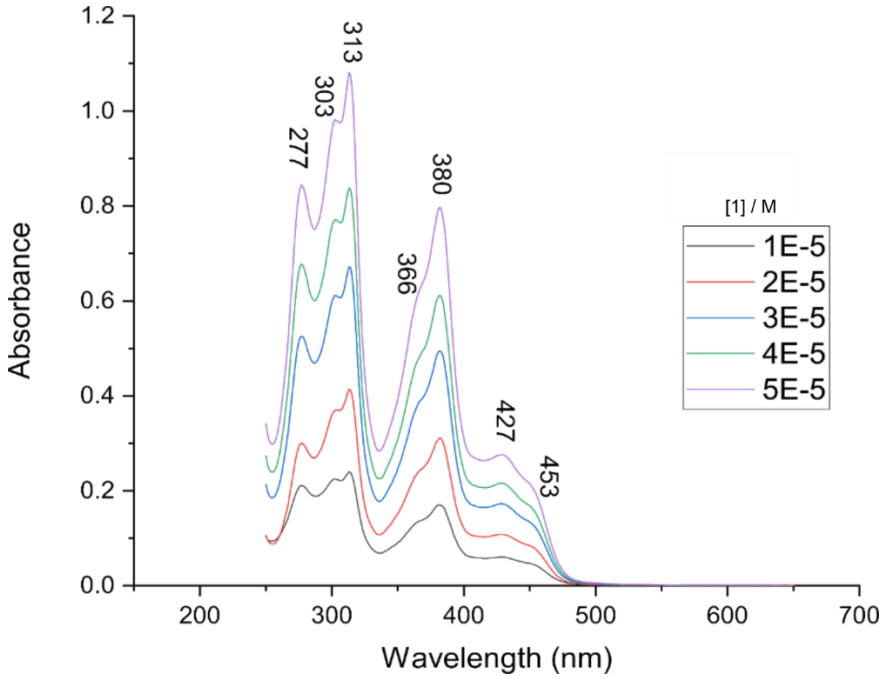


Fig. S5 UV-visible spectrum of **1** recorded in acetonitrile at 295 K as a function of concentration. The molar absorptivities of key band maximum are reported in Section 4 and were determined from the slopes of Beer-Lambert law plots at the relevant band maxima.

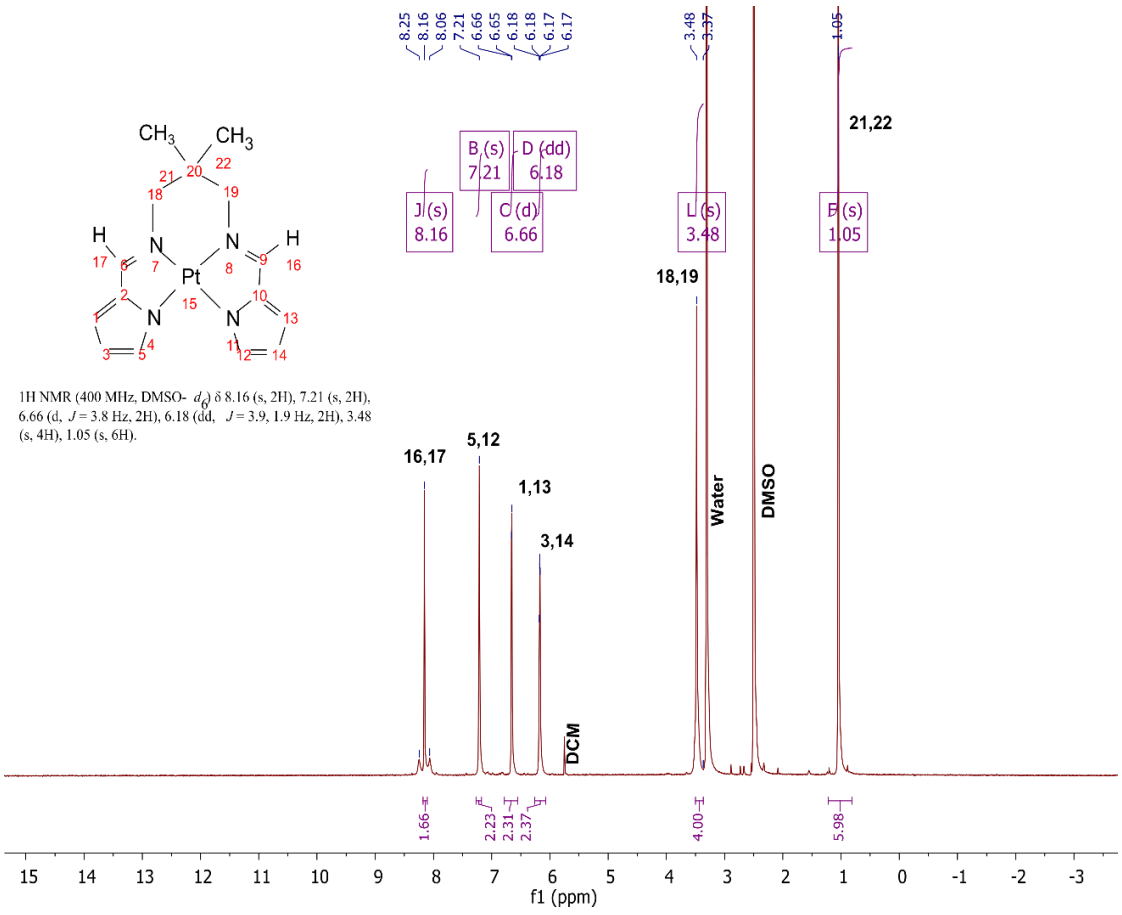


Fig. S6 400 MHz ^{1}H NMR spectrum of **2** recorded in DMSO-d_6 at 300 K.

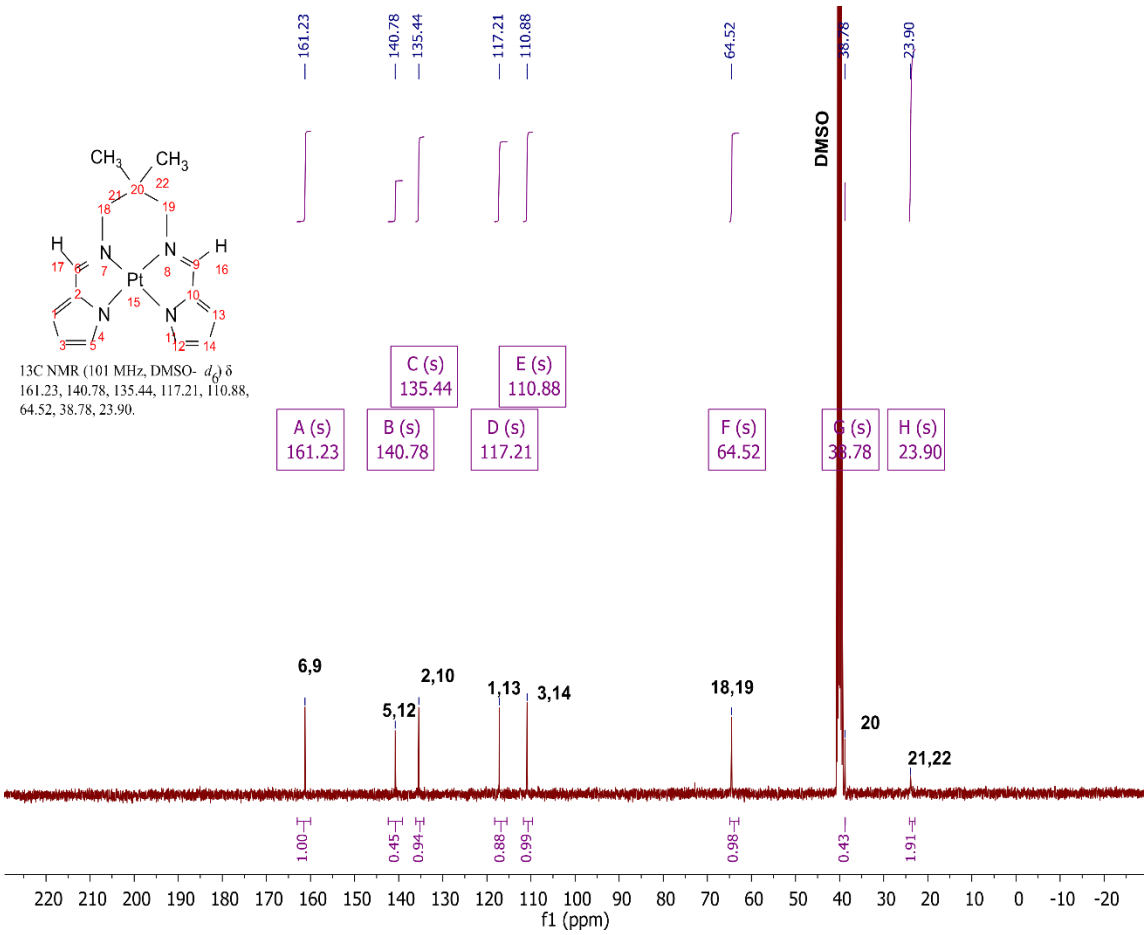


Fig. S7 101 MHz ^{13}C NMR spectrum of **2** recorded in DMSO-*d*6 at 300 K.

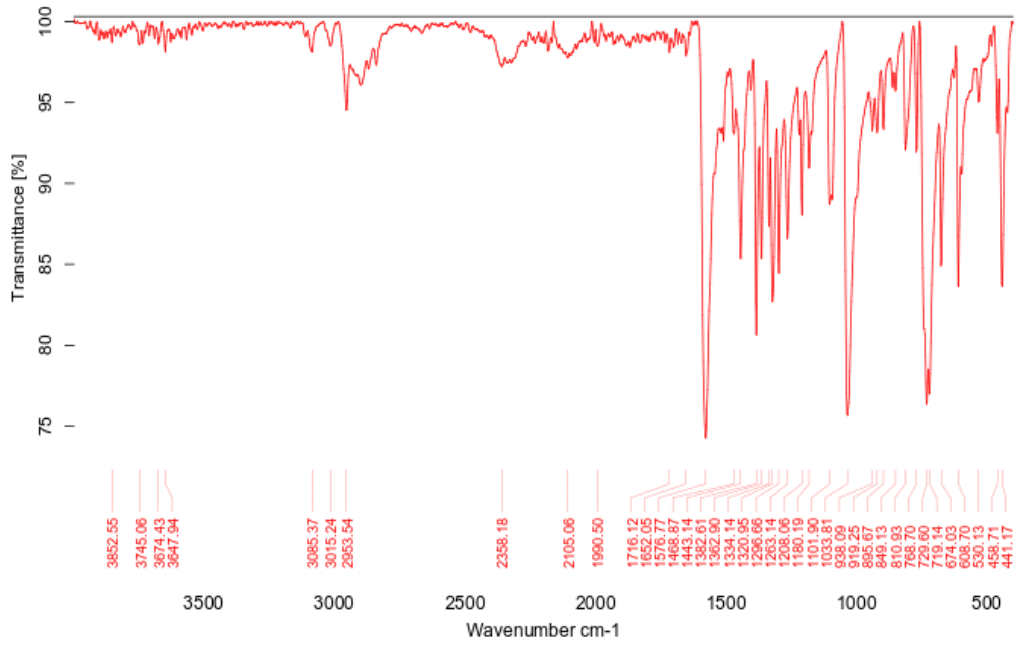


Fig. S8 FTIR spectrum of **2** recorded as a crushed powder sample at 295 K.

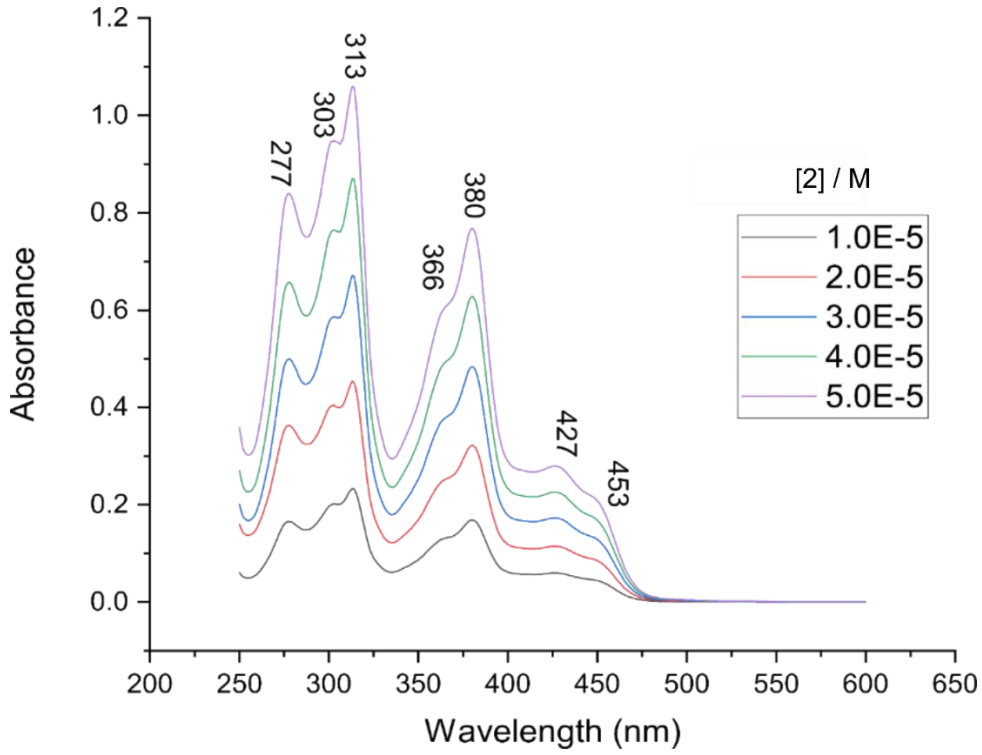


Fig. S9 UV-visible spectrum of **2** recorded in acetonitrile at 295 K as a function of concentration. The molar absorptivities of key band maximum are reported in Section 4 and were determined from the slopes of Beer-Lambert law plots at the relevant band maxima.

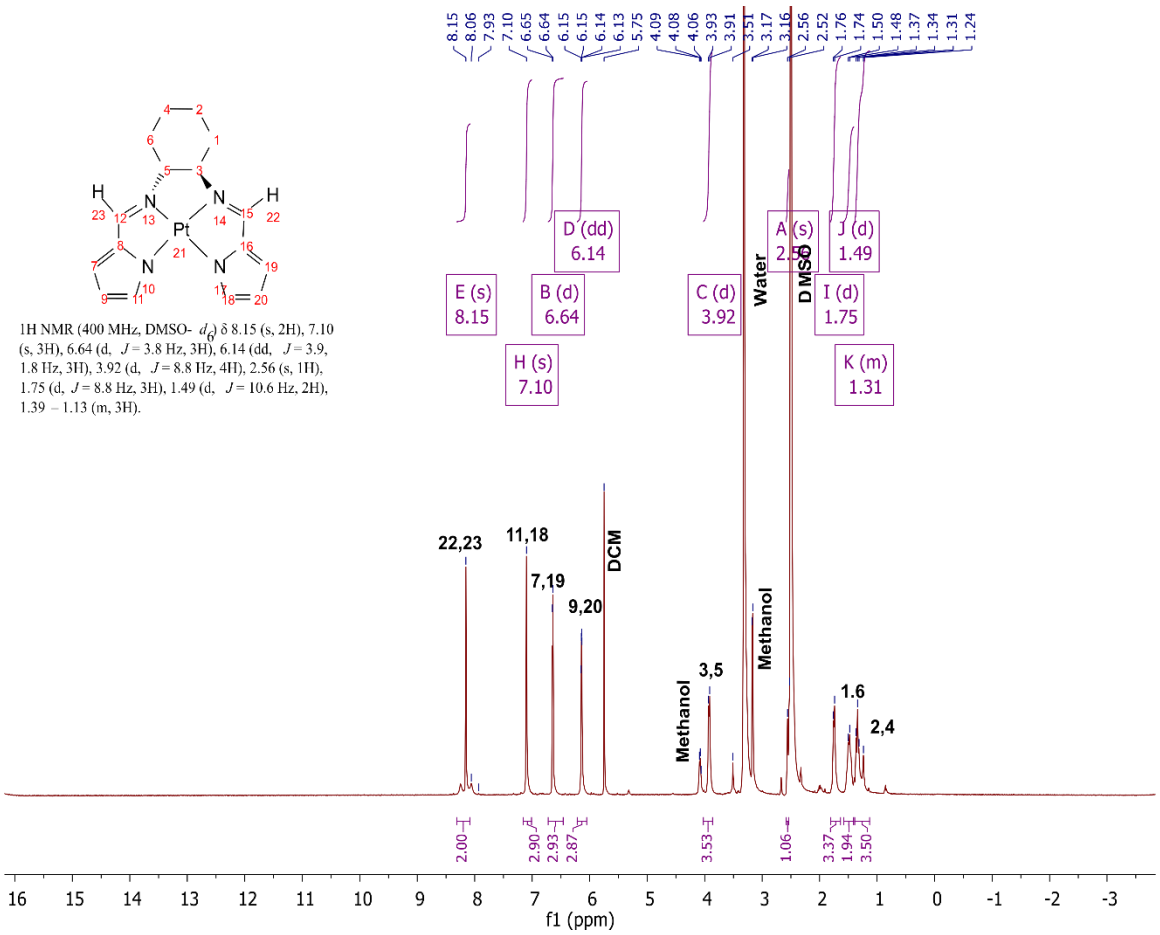


Fig. S10 400 MHz ^{1}H NMR spectrum of **3** recorded in DMSO-d_6 at 300 K. This compound is known;[4] the spectral data here briefly confirm the structure of the compound and its purity.

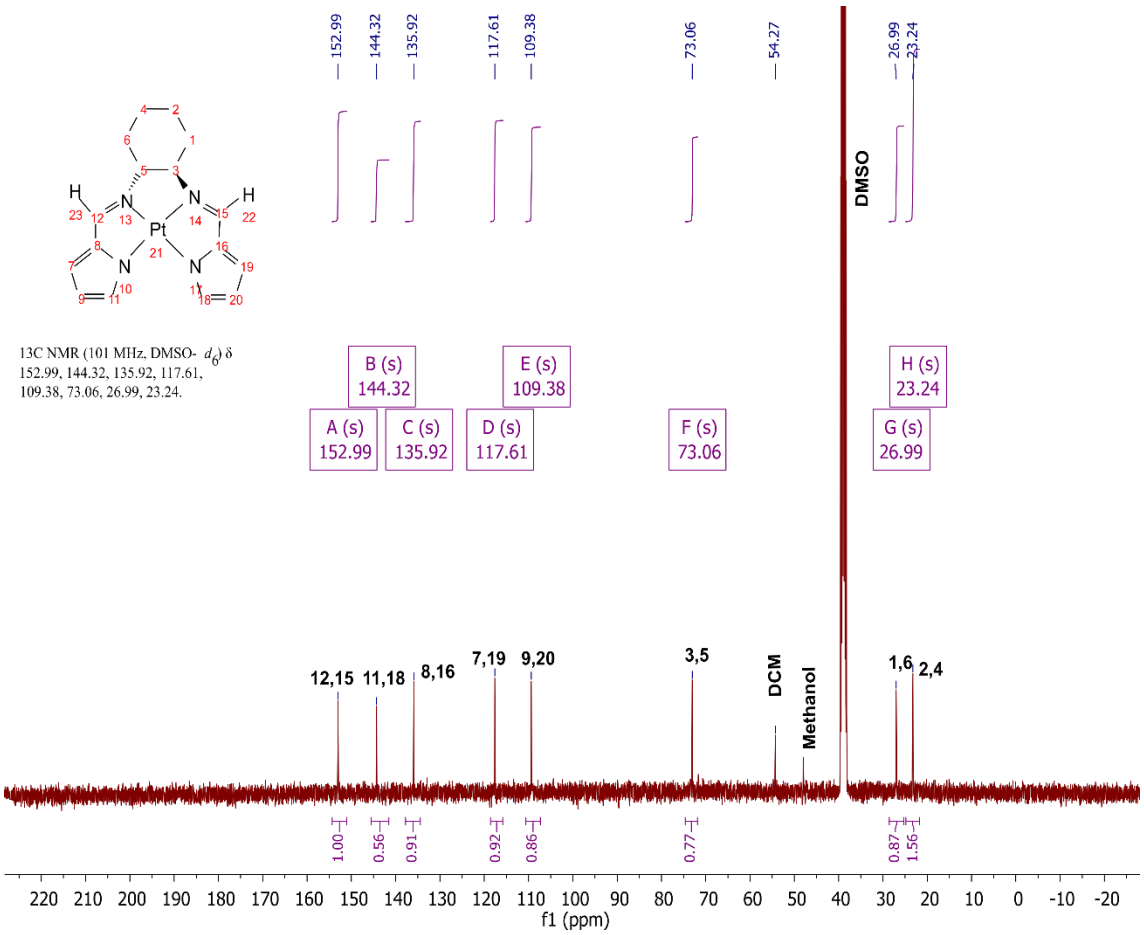


Fig. S11 101 MHz ^{13}C NMR spectrum of **3** recorded in DMSO-d_6 at 300 K.

X-ray crystallography

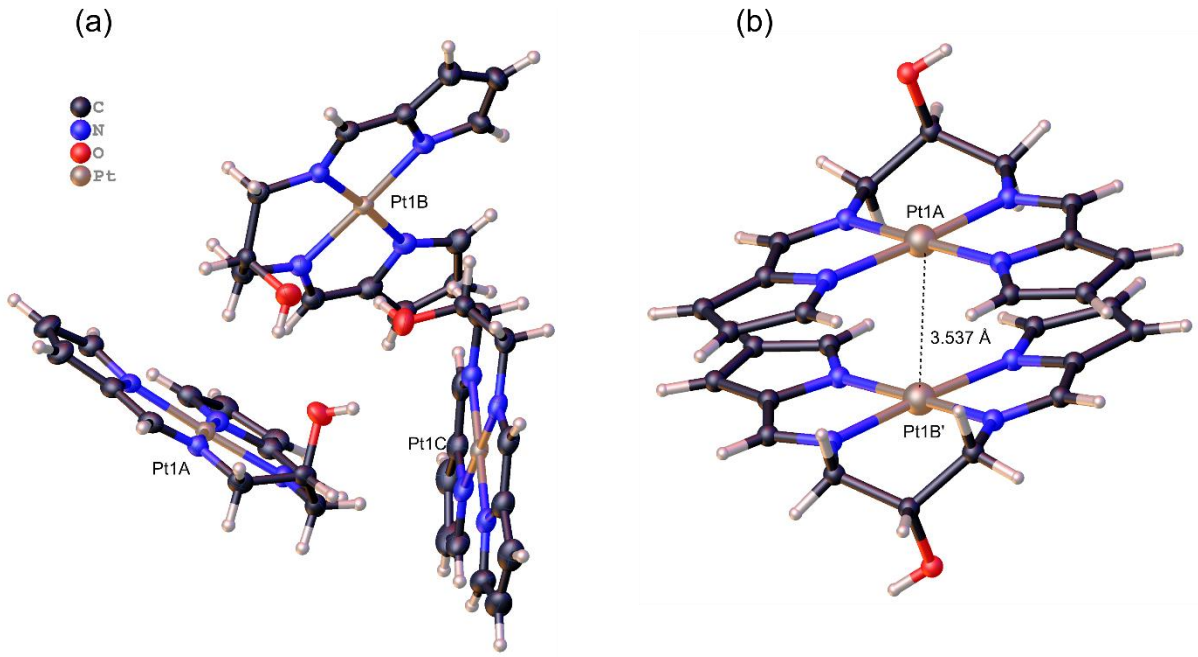


Fig. S12 (a) View of the ASU of complex **1**, which comprises three independent molecules supported by hydrogen bonding interactions between the hydroxyl groups of neighbouring molecules in the solid state. The hydroxyl groups act as both hydrogen bond donors and acceptors. (b) Intermolecular π-stacking arrangements of neighbouring molecules of **1** in adjacent ASUs. The Pt···Pt distances were measured between the pair of Pt(II) ions of a centrosymmetric inversion pair.

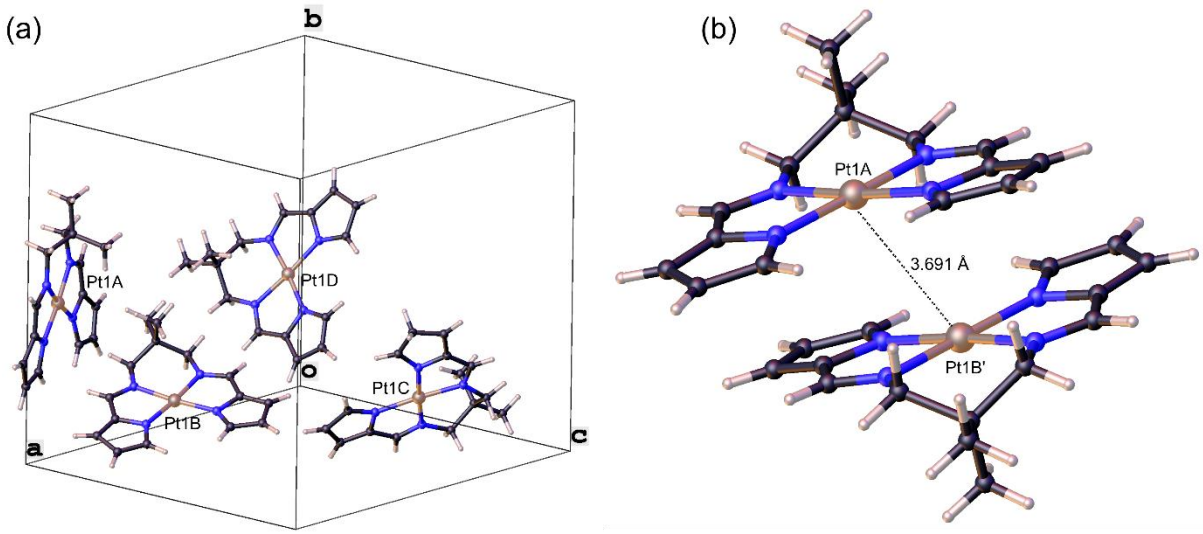


Fig. S13 (a) ASU of **2** comprising four independent molecules of **2** (b) Intermolecular π-stacking arrangements of neighbouring molecules of **2** in different ASUs. The Pt···Pt distances were measured between the pair of Pt(II) ions of a centrosymmetric inversion pair.

Fluorescence spectroscopy

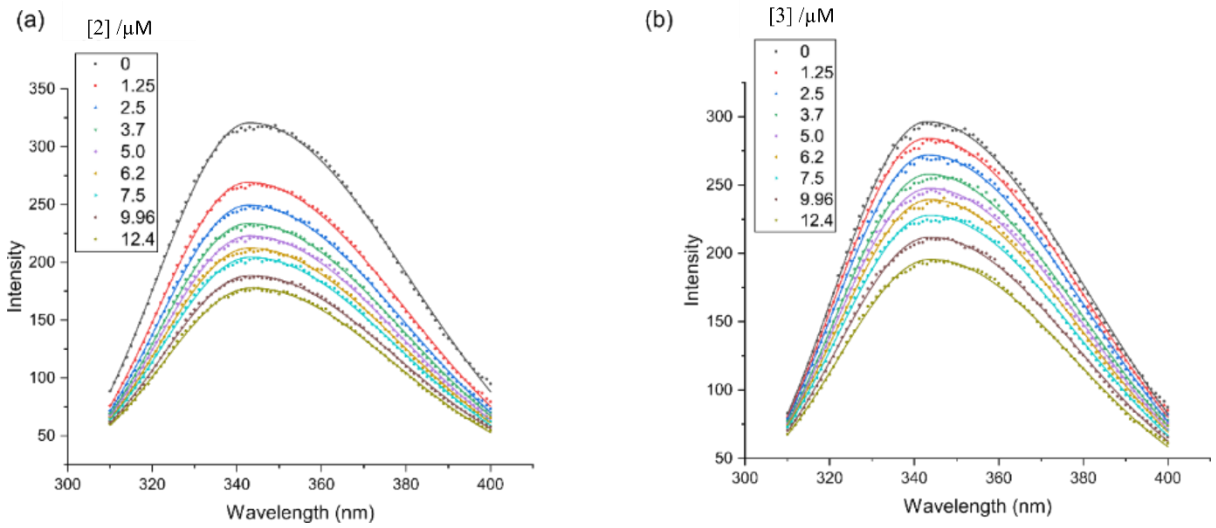


Fig. S14 Fluorescence emission spectra of HSA (5.0 μM) recorded as a function of increasing concentration of (a) **2** and (b) **3** at 298 K. Both Pt(II) bis(pyrrolide-imine) chelates had a concentration range of 0 – 12.4 μM. The emission spectra confirm that the Pt(II) complexes quench the intrinsic (i.e., Trp-214) fluorescence of HSA upon binding.

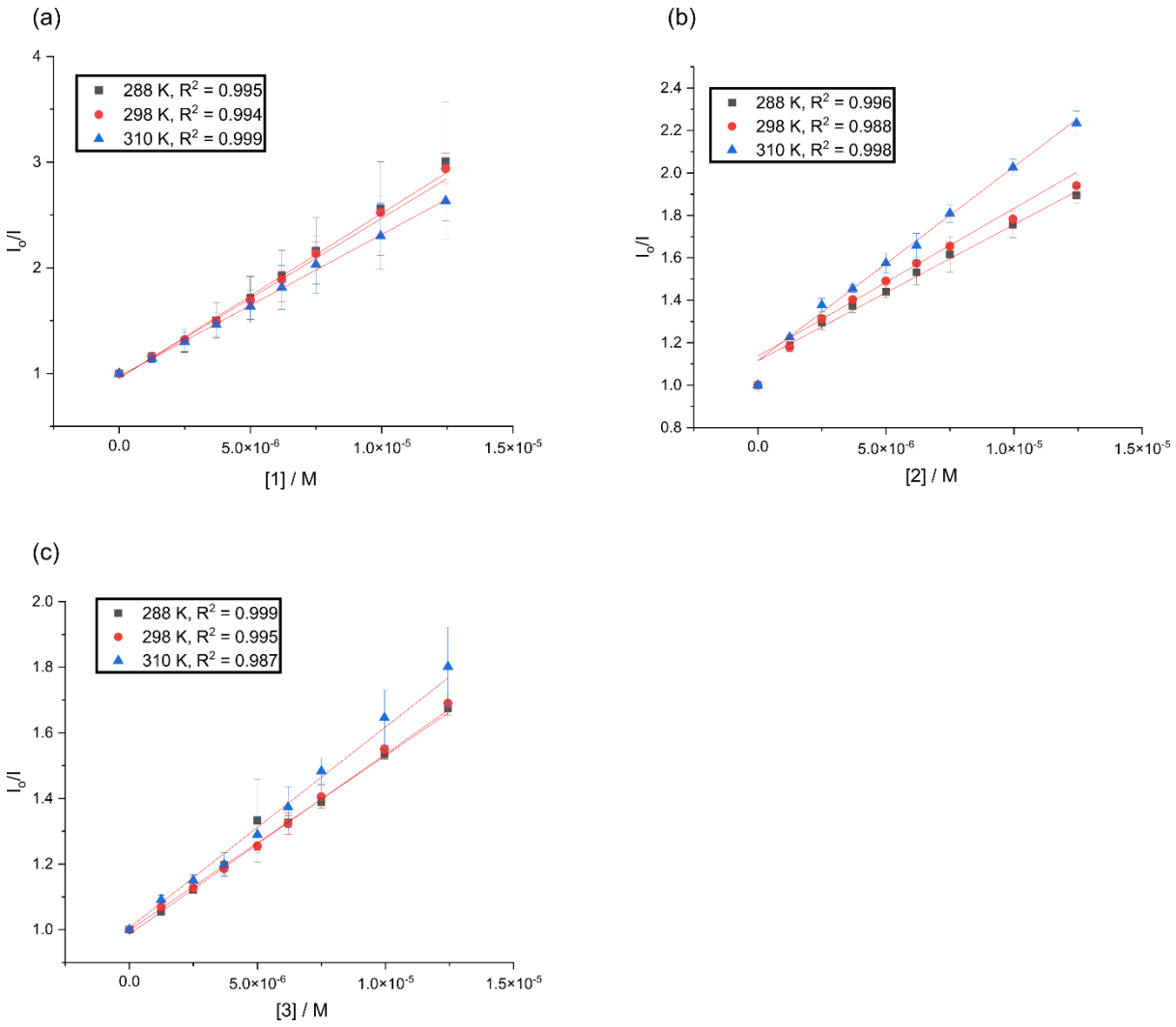


Fig. S15. Stern–Volmer plots of fluorescence quenching: (a) **1**···HSA, (b) **2**···HSA and (c) **3**···HSA. All three Pt(II) bis (pyrrolide-imine) chelates were recorded at three different temperatures (■ 288 K, ● 298 K, and ▲ 310 K). The relevant concentrations for the titrations were: [HSA] = 5.0 μM with **1**–**3** ranging from 0 – 12.4 μM at pH 7.50 in 50 mM KH_2PO_4 buffer.

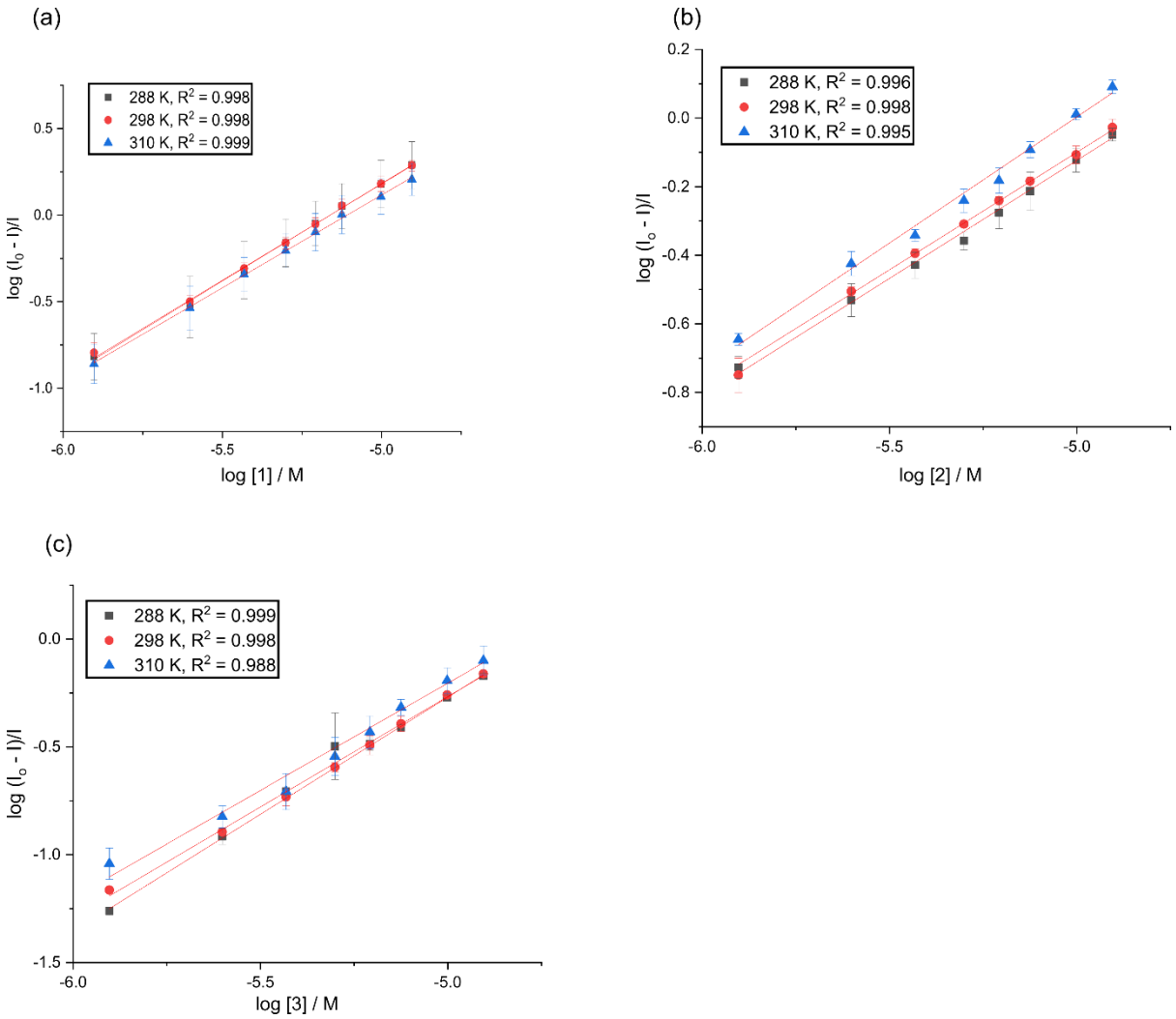


Fig. S16. Plots of log((I$_0$-I)/I) versus log([Q]) for the interaction of HSA with several Pt(II) bis (pyrrolide-imine) chelates (i.e., quenchers, Q): (a) **1**···HSA complex, (b) **2**···HSA complex, and (c) **3**···HSA complex. The affinity constants are determined from the intercepts of the graphs and the stoichiometry from the slopes. Data for the three Pt(II) bis (pyrrolide-imine) chelates were recorded at three different temperatures (■ 288 K, ● 298 K, and ▲ 310 K). The relevant concentrations for the titrations were: [HSA] = 5.0 μM with **1**–**3** ranging from 0 – 12.4 μM at pH 7.50 in 50 mM KH_2PO_4 buffer.

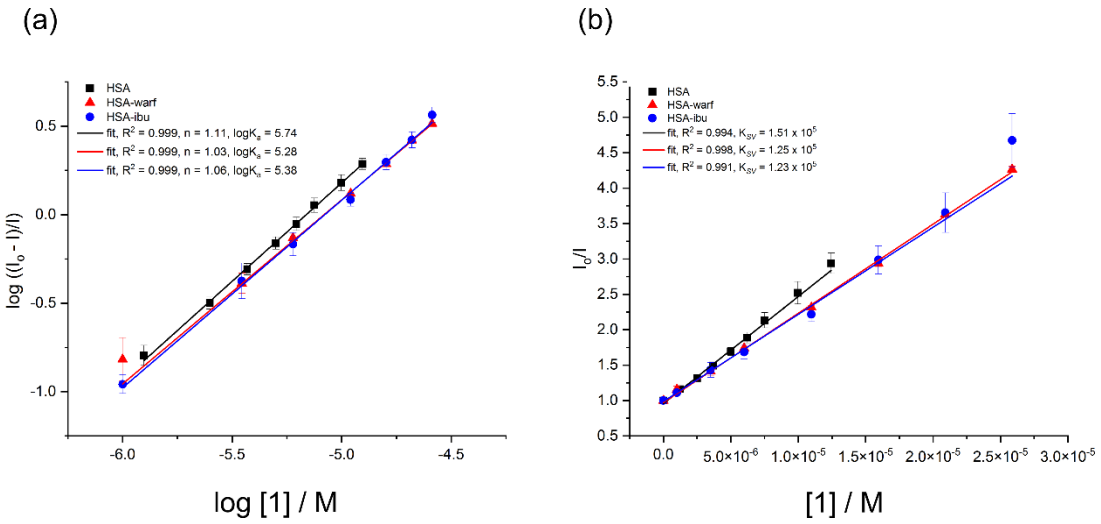


Fig. S17 (a) Double-log plot of the fluorescence quenching data, $log\left(\frac{I_0-I}{I}\right) = logK + nlog[Q]$, for native HSA, HSA•{warfarin}, and HSA•{Ibuprofen} as a function of the concentration of **1** at 298 K in KH_2PO_4 (50 mM, pH 7.50). This is to enable the measurement of logK_a (the association constant for the Pt(II) chelate with the macromolecule target, K_a) and the reaction stoichiometry (*n*). The excitation and emission wavelengths for the fluorophore probes were: (i) Trp-214 (native HSA), λ^{ex} = 295 nm, λ^{em} = 343 nm; (ii) Warfarin (HSA-Warf), λ^{ex} = 320 nm, λ^{em} = 382 nm, and (iii) Ibuprofen (HSA-Ibu), λ^{ex} = 228 nm, λ^{em} = 332 nm. (b) Stern–Volmer (SV) plot for native HSA, HSA•{warfarin}, and HSA•{Ibuprofen} as a function of the concentration of **1** at 298 K in KH_2PO_4 (50 mM, pH 7.50). The plots are linear with an intercept of 1.0 when static quenching is dominant. Overall, the plots show that **1** binds with an approximately 1:1 mole ratio to native HSA. The presence of either drug marginally decreases the binding of **1** as the affinity constants marginally decrease. A possible interpretation is that **1** can bind (half-saturate) to both subdomain IIA and IIIA (Sudlow's site I and II) of the native protein, but that when either warfarin or ibuprofen is located in one of these two sites, the reciprocal site is fully saturated. Alternatively, warfarin or ibuprofen may alter the protein conformation to enable the uptake of an additional half-equivalent of **1** at a third site. Such additional drug binding sites are known for HSA and exist in subdomains IIIB (propofol binding site, close to site II in subdomain IIIA) and IB (hemin binding site).

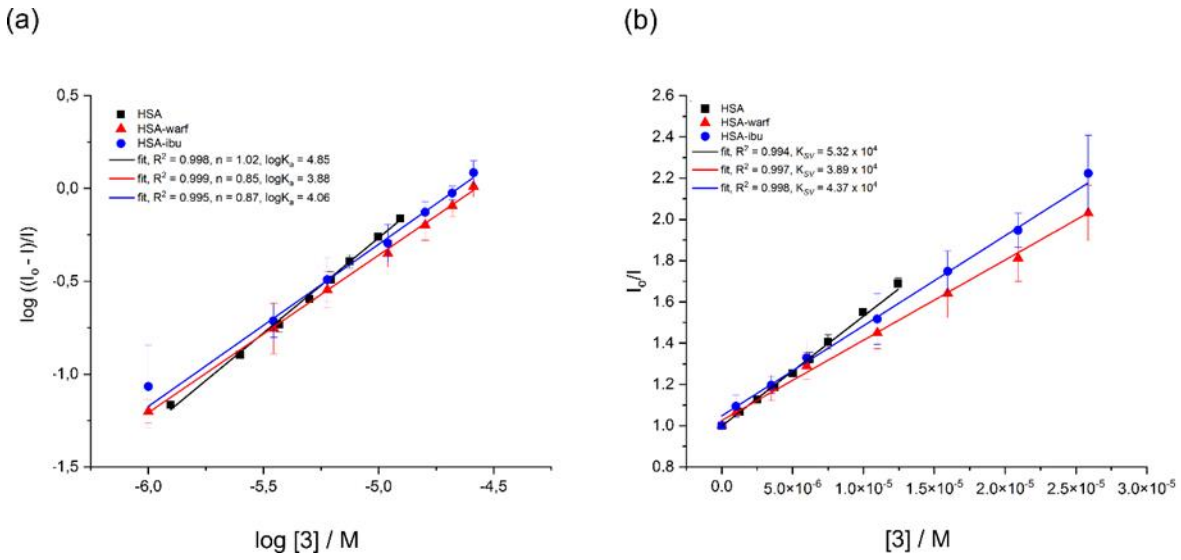


Fig. S18 (a) Double-log plot of the fluorescence quenching data, $log\left(\frac{I_0-I}{I}\right) = logK + nlog[Q]$, for native HSA, HSA•{warfarin}, and HSA•{Ibuprofen} as a function of the concentration of **3** at 298 K in KH_2PO_4 (50 mM, pH 7.50). This is to enable the measurement of logK_a (the association constant for the Pt(II) chelate with the macromolecule target, K_a) and the reaction stoichiometry (*n*). The excitation and emission wavelengths for the fluorophore probes were: (i) Trp-214 (native HSA), λ^{ex} = 295 nm, λ^{em} = 343 nm; (ii) Warfarin (HSA-Warf), λ^{ex} = 320 nm, λ^{em} = 382 nm, and (iii) Ibuprofen (HSA-Ibu), λ^{ex} = 228 nm, λ^{em} = 332 nm. (b) Stern–Volmer (SV) plot for native HSA, HSA•{warfarin}, and HSA•{Ibuprofen} as a function of the concentration of **3** at 298 K in KH_2PO_4 (50 mM, pH 7.50). The plots are linear with an intercept of 1.0 when static quenching is dominant. Overall, the plots show that **3** binds with an approximately 1:1 n value to native HSA. At no point does **3** displace either warfarin or ibuprofen from HSA•{warfarin}, and HSA•{Ibuprofen}; however, the presence of either drug marginally decreases the binding of **3** as the affinity constants marginally decrease. A possible interpretation is that **3** can bind (half-saturate) to both subdomain IIA and IIIA (Sudlow's site I and II) of the native protein, but that when either warfarin or ibuprofen is located in one of these two sites, the reciprocal site is fully saturated. Alternatively, warfarin or ibuprofen may alter the protein conformation to enable the uptake of an additional half-equivalent of **3** at a third site. Such additional drug binding sites are known for HSA and exist in subdomains IIIB (propofol binding site, close to site II in subdomain IIIA) and IB (hemin binding site).

CD- spectroscopy

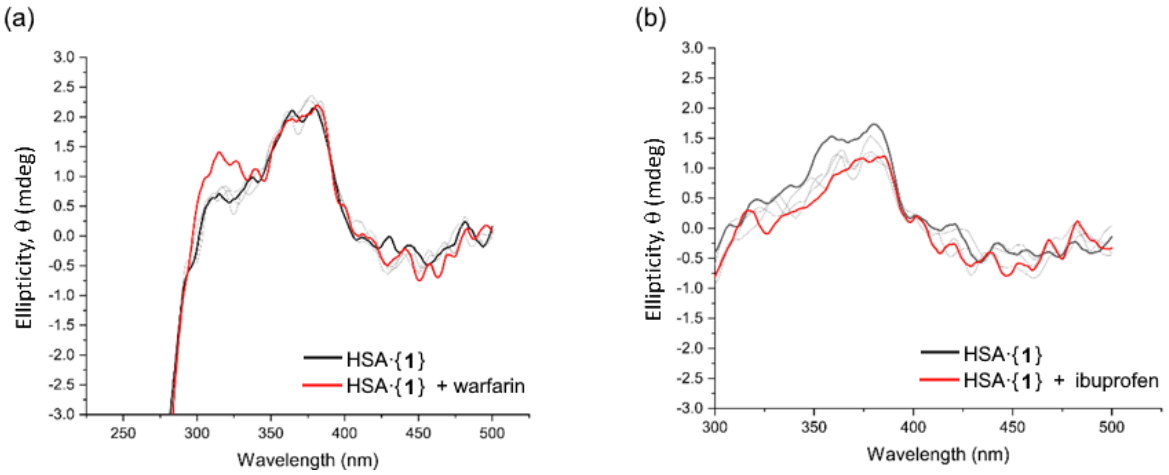


Fig. S19 Induced CD site displacement assay carried out by measuring the UV CD of HSA (15 µM in 50 mM KH_2PO_4 buffer, pH 7.5) bound to **1** (15 µM) from 280–500 nm. Site-specific markers (a) warfarin and (b) ibuprofen were titrated into the HSA•{**1**} solution to determine the Pt(II) chelate's preferred binding site. Both site-specific markers were titrated in to give concentrations of 4.1, 8.3, 12.5, and 20.1 µM (the grey lines represent 4.1, 8.3, and 12.5 µM). The spectra were smoothed using a Lowess function (0.07 span). From Fig. S19b, it is clear that only partial displacement of **1** is induced by the incoming probe ligand ibuprofen, while Fig. S19a indicates that incoming warfarin minimally perturbs the spectrum of HSA•{**1**} and evidently cannot displace **1** from the protein.

Molecular docking

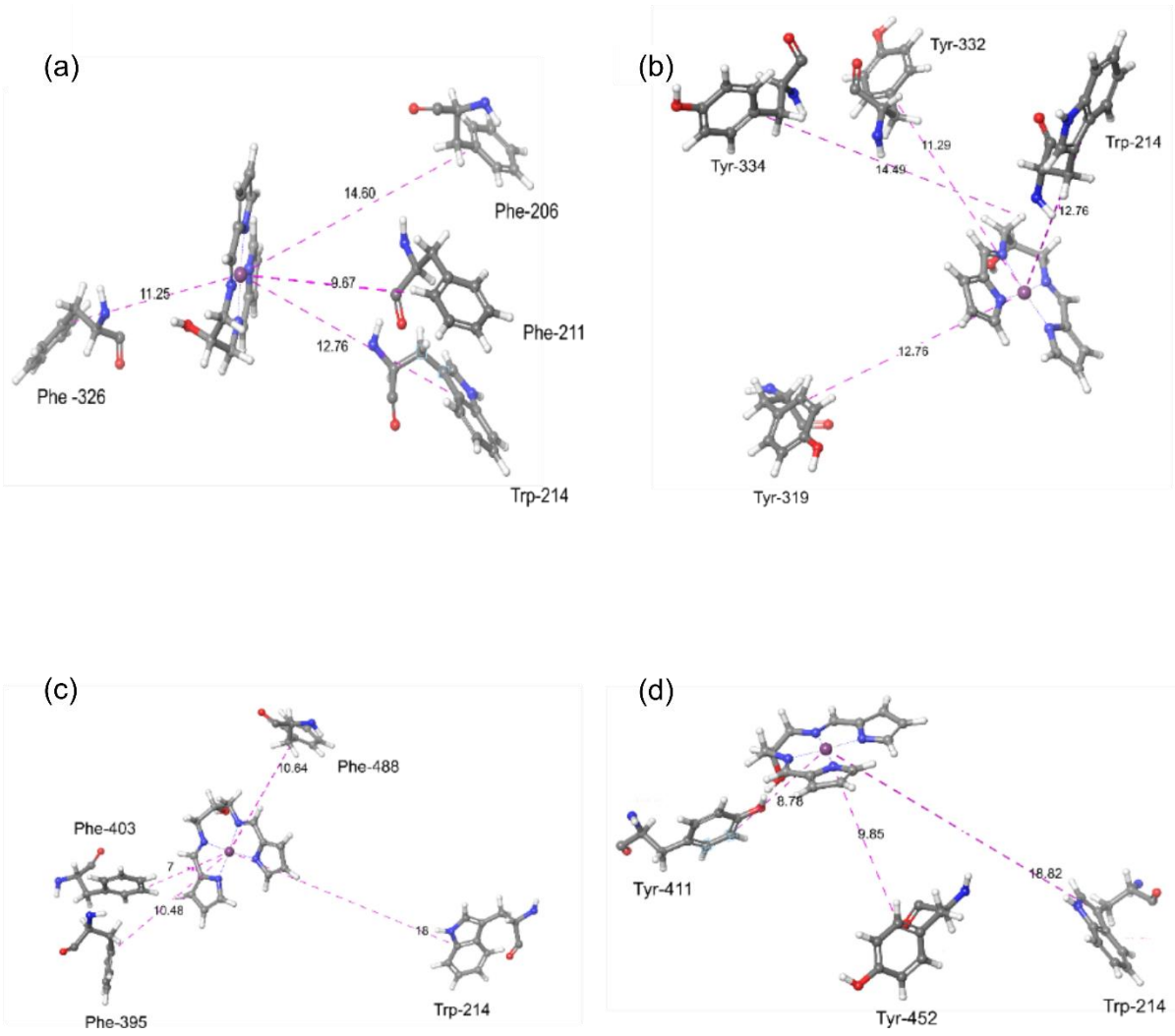
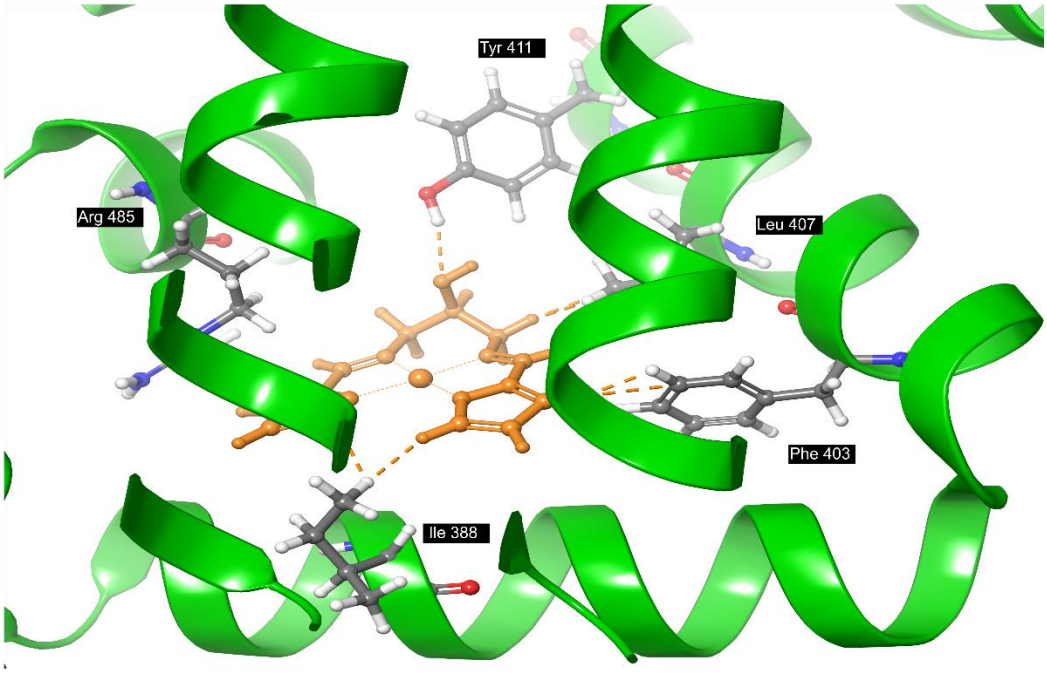


Fig. S20 GLIDE XP docking analysis of the binding of **1** to HSA using the X-ray structure of HSA as the *in silico* target (PDB code 1HA2). A large target grid was generated for macromolecular ligand docking at the warfarin site (with warfarin removed), spanning 40 x 40 x 40 $Å^3$, to search for secondary binding sites radiating out (to ~20 Å) from warfarin's location in subdomain IIA. The image panels show selected phenylaniline and tyrosine residues, respectively, that are closest to the best poses for **1** (a summary of the aromatic residues for **2** is given in Table S8). Distances are in Å units. The near-UV CD spectra for HSA•{**1**} and HSA•{**2**} are shown in Figs. 7a and b of in the main text suggest that these ligands perturb Tyr and Phe chromophores in addition to Trp-214 in HSA. The above docking results support the experimental data: **2** binds in tyrosine- and phenylalanine-rich pockets within HSA with roughly the same docking score.

(a)



(b)

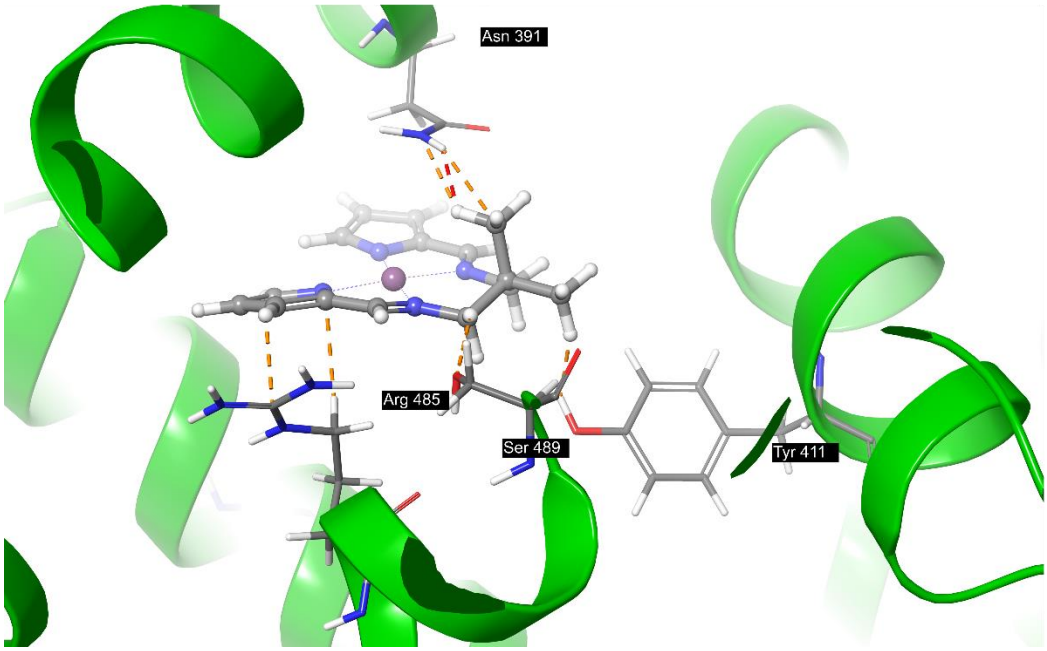


Fig. S21 Illustration of the binding of Pt(II) chelates **1** and **2** in subdomain IIIA (Sudlow's drug site II) of HSA as determined by GLIDE XP docking using PDB code 2BXF as the target and a large 40 × 40 × 40-Å^3 grid centred on the coordinates of diazepam. The *in silico* model supports the observed data suggesting both Pt(II) chelates **1** and **2** bind to Sudlow's site II (See Figs. 6 and 8 of the main paper.)

Tables

Table S1. Crystal data and X-ray structure refinement details for Pt(II) bis(pyrrolide-imine) chelates **1** and **2**.

Empirical formula	$C_{13}H_{14}N_4OPt$ (**1**)	$C_{15}H_{18}N_4Pt$ (**2**)
CCDC deposit number	**2271559**	**2271558**
Formula weight	437.37	449.42
Temperature/K	173(2)	173(2)
Crystal system	triclinic	triclinic
Space group	*P*-1	*P*-1
a/Å	9.0752(19)	13.7803(5)
b/Å	12.639(3)	15.2877(5)
c/Å	18.870(3)	16.8165(6)
α/°	108.653(7)	103.788(2)
β/°	90.856(8)	104.926(2)
γ/°	96.322(9)	107.795(2)
Volume/Å^3	2035.3(7)	3059.76(19)
Z	6	8
Pcalc g/cm^3	2.141	1.951
μ/mm^{-1}	10.338	9.167
F(000)	1236.0	1712.0
Crystal size/mm^3	0.180 × 0.050 × 0.050	0.227 × 0.161 × 0.076
Radiation	MoKα (λ = 0.71073 Å)	MoKα (λ = 0.71073 Å)
Index ranges	-13 ≤ h ≤ 13, -19 ≤ k ≤ 19, -29 ≤ l ≤ 29	-19 ≤ h ≤ 19, -21 ≤ k ≤ 21, -24 ≤ l ≤ 24
Reflections collected	139345	113600
Independent reflections	15567 [R_{int} = 0.0636, R_{sigma} = 0.0358]	18723 [R_{int} = 0.0665, R_{sigma} = 0.0536]
Data/restraints/parameters	15567/0/514	18723/0/729
Goodness-of-fit on F^2	1.050	1.004
Final R indexes [I>=2σ (I)]	R_1 = 0.0308, wR_2 = 0.0643	R_1 = 0.0327, wR_2 = 0.0527
Final R indexes [all data]	R_1 = 0.0444, wR_2 = 0.0689	R_1 = 0.0586, wR_2 = 0.0590
Largest diff. peak/hole / e Å^{-3}	1.90/-1.46	0.96/-1.10

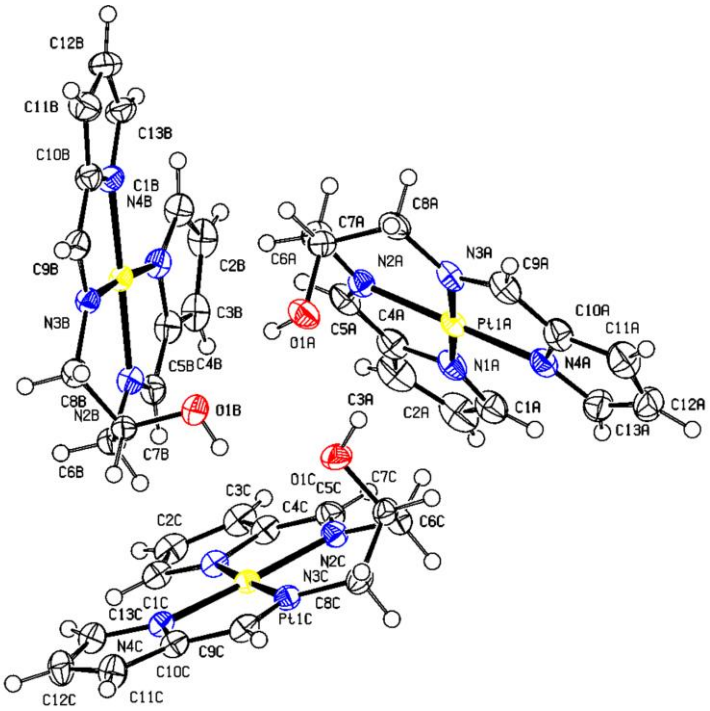


Table S2. Selected geometrical parameters (Å, °) for the X-ray structure of **1** and **2**. A labelled thermal ellipsoid plot (50% probability surfaces) is included above to aid in reading the tabulated data.

	Atom	Length/Å		Atom	Length/Å
Pt1C	N3C	2.009(3)	N2A	C5A	1.290(5)
Pt1C	N2C	2.009(3)	N2A	C6A	1.452(6)
Pt1C	N4C	2.012(3)	N1B	C1B	1.354(5)
Pt1C	N1C	2.017(3)	N1B	C4B	1.386(5)
Pt1B	N2B	2.003(3)	C5A	C4A	1.420(7)
Pt1B	N3B	2.004(3)	C9C	C10C	1.423(6)
Pt1B	N4B	2.011(3)	C3A	C2A	1.384(8)
Pt1B	N1B	2.017(3)	C3A	C4A	1.409(6)
Pt1A	N2A	2.000(3)	C4C	C3C	1.389(6)
Pt1A	N1A	2.008(4)	C4C	C5C	1.420(6)
Pt1A	N3A	2.009(3)	C2B	C3B	1.399(7)
Pt1A	N4A	2.014(4)	C2B	C1B	1.407(6)
O1B	C7B	1.413(5)	C9A	C10A	1.425(7)
O1C	C7C	1.410(5)	C10C	C11C	1.395(6)
N3A	C9A	1.292(6)	C9B	C10B	1.419(6)
N3A	C8A	1.464(6)	C8B	C7B	1.518(6)
O1A	C7A	1.428(5)	C4B	C3B	1.397(6)
N1C	C1C	1.356(5)	C4B	C5B	1.423(6)
N1C	C4C	1.388(5)	C7B	C6B	1.523(6)
N2C	C5C	1.304(5)	C3C	C2C	1.405(7)
N2C	C6C	1.465(5)	C2C	C1C	1.392(6)
N4C	C13C	1.345(5)	C2A	C1A	1.386(7)
N4C	C10C	1.386(5)	C10A	C11A	1.398(7)

N3C	C9C	1.294(5)	C8A	C7A	1.525(6)
N3C	C8C	1.456(5)	C8C	C7C	1.523(6)
N4A	C13A	1.345(6)	C12B	C11B	1.385(6)
N4A	C10A	1.373(6)	C12B	C13B	1.404(7)
N4B	C13B	1.352(5)	C10B	C11B	1.397(6)
N4B	C10B	1.382(5)	C11A	C12A	1.387(8)
N3B	C9B	1.306(5)	C11C	C12C	1.393(6)
N3B	C8B	1.467(5)	C7C	C6C	1.521(6)
N2B	C5B	1.304(5)	C12C	C13C	1.392(6)
N2B	C6B	1.460(5)	C12A	C13A	1.404(7)
N1A	C1A	1.358(6)	C6A	C7A	1.517(6)
N1A	C4A	1.393(6)			

Atom			Angle/°	Atom			Angle/°
N3C	Pt1C	N2C	95.58(14)	C2A	C3A	C4A	105.9(4)
N3C	Pt1C	N4C	80.47(13)	N1C	C4C	C3C	109.9(4)
N2C	Pt1C	N4C	174.81(13)	N1C	C4C	C5C	114.7(3)
N3C	Pt1C	N1C	175.57(13)	C3C	C4C	C5C	135.5(4)
N2C	Pt1C	N1C	80.13(14)	C3B	C2B	C1B	107.0(4)
N4C	Pt1C	N1C	103.88(13)	N2C	C5C	C4C	116.9(4)
N2B	Pt1B	N3B	95.66(13)	N3A	C9A	C10A	117.6(4)
N2B	Pt1B	N4B	175.79(13)	N4C	C10C	C11C	109.6(4)
N3B	Pt1B	N4B	80.19(13)	N4C	C10C	C9C	114.8(3)
N2B	Pt1B	N1B	80.38(14)	C11C	C10C	C9C	135.5(4)
N3B	Pt1B	N1B	175.65(13)	N3B	C9B	C10B	116.5(4)
N4B	Pt1B	N1B	103.74(14)	N3B	C8B	C7B	113.3(3)
N2A	Pt1A	N1A	80.27(15)	N1B	C4B	C3B	109.1(4)
N2A	Pt1A	N3A	95.70(15)	N1B	C4B	C5B	114.8(4)
N1A	Pt1A	N3A	175.50(15)	C3B	C4B	C5B	136.0(4)
N2A	Pt1A	N4A	175.66(14)	O1B	C7B	C8B	108.6(3)
N1A	Pt1A	N4A	103.89(16)	O1B	C7B	C6B	113.2(3)
N3A	Pt1A	N4A	80.19(15)	C8B	C7B	C6B	114.5(3)
C9A	N3A	C8A	121.3(4)	N2B	C5B	C4B	116.8(4)
C9A	N3A	Pt1A	114.7(3)	C4C	C3C	C2C	105.7(4)
C8A	N3A	Pt1A	123.8(3)	C1C	C2C	C3C	107.9(4)
C1C	N1C	C4C	107.2(3)	C3A	C2A	C1A	108.0(4)
C1C	N1C	Pt1C	139.8(3)	C4B	C3B	C2B	106.7(4)
C4C	N1C	Pt1C	113.0(3)	N4A	C10A	C11A	110.7(4)

C5C	N2C	C6C	120.8(3)	N4A	C10A	C9A	114.3(4)
C5C	N2C	Pt1C	115.4(3)	C11A	C10A	C9A	135.0(5)
C6C	N2C	Pt1C	123.8(3)	N1A	C4A	C3A	109.5(4)
C13C	N4C	C10C	106.9(3)	N1A	C4A	C5A	114.4(4)
C13C	N4C	Pt1C	140.5(3)	C3A	C4A	C5A	136.2(5)
C10C	N4C	Pt1C	112.5(3)	N3A	C8A	C7A	113.1(3)
C9C	N3C	C8C	121.2(3)	N1C	C1C	C2C	109.3(4)
C9C	N3C	Pt1C	115.0(3)	N3C	C8C	C7C	112.1(3)
C8C	N3C	Pt1C	123.9(3)	C11B	C12B	C13B	107.3(4)
C13A	N4A	C10A	107.4(4)	N4B	C10B	C11B	109.4(4)
C13A	N4A	Pt1A	139.4(3)	N4B	C10B	C9B	114.9(4)
C10A	N4A	Pt1A	113.0(3)	C11B	C10B	C9B	135.7(4)
C13B	N4B	C10B	107.3(3)	C12B	C11B	C10B	106.6(4)
C13B	N4B	Pt1B	139.7(3)	N1A	C1A	C2A	110.3(5)
C10B	N4B	Pt1B	113.0(3)	C12A	C11A	C10A	104.5(5)
C9B	N3B	C8B	120.9(3)	C12C	C11C	C10C	106.0(4)
C9B	N3B	Pt1B	115.4(3)	O1C	C7C	C6C	112.7(3)
C8B	N3B	Pt1B	123.8(3)	O1C	C7C	C8C	107.9(3)
C5B	N2B	C6B	120.4(4)	C6C	C7C	C8C	114.0(3)
C5B	N2B	Pt1B	115.3(3)	N2B	C6B	C7B	113.0(3)
C6B	N2B	Pt1B	124.3(3)	N2C	C6C	C7C	113.6(3)
C1A	N1A	C4A	106.2(4)	C13C	C12C	C11C	107.5(4)
C1A	N1A	Pt1A	141.0(3)	C11A	C12A	C13A	108.8(5)
C4A	N1A	Pt1A	112.7(3)	N1B	C1B	C2B	109.4(4)
C5A	N2A	C6A	120.1(4)	N4C	C13C	C12C	110.1(4)
C5A	N2A	Pt1A	115.6(3)	N4B	C13B	C12B	109.5(4)
C6A	N2A	Pt1A	124.1(3)	N2A	C6A	C7A	115.2(4)
C1B	N1B	C4B	107.7(3)	N4A	C13A	C12A	108.6(5)
C1B	N1B	Pt1B	139.5(3)	O1A	C7A	C6A	112.9(4)
C4B	N1B	Pt1B	112.7(3)	O1A	C7A	C8A	107.2(4)
N2A	C5A	C4A	117.0(4)	C6A	C7A	C8A	114.5(4)
N3C	C9C	C10C	117.2(3)				

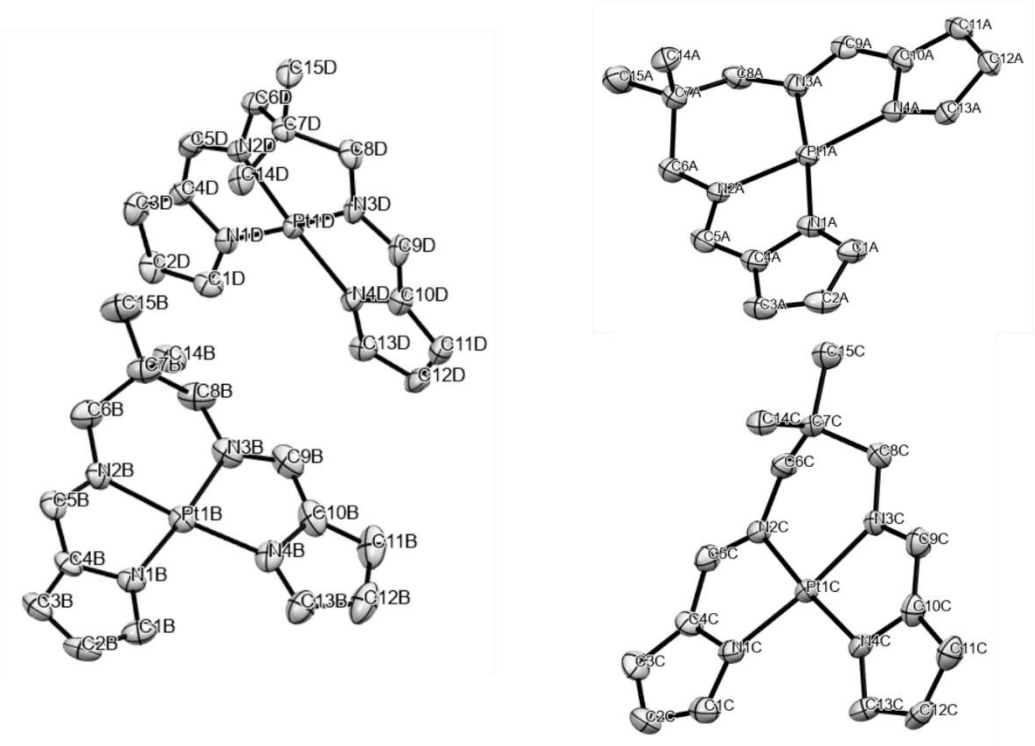


Table S3. Selected geometrical parameters (Å, °) for the X-ray structure of **1** and **2**. A labelled thermal ellipsoid plot (50% probability surfaces, H atoms omitted for clarity) is included above to aid in reading the tabulated data.

Atom	Length/Å	Atom	Length/Å
Pt1A N1A	2.016(3)	Pt1C N1C	2.013(3)
Pt1A N2A	2.005(3)	Pt1C N2C	2.003(3)
Pt1A N3A	2.003(3)	Pt1C N3C	2.001(3)
Pt1A N4A	2.010(3)	Pt1C N4C	2.015(3)
N1A C1A	1.344(5)	N1C C1C	1.344(5)
N1A C4A	1.377(5)	N1C C4C	1.375(5)
N2A C5A	1.304(5)	N2C C5C	1.293(5)
N2A C6A	1.467(5)	N2C C6C	1.460(5)
N3A C8A	1.466(5)	N3C C8C	1.470(5)
N3A C9A	1.298(5)	N3C C9C	1.300(5)
N4A C10A	1.383(5)	N4C C10C	1.387(5)
N4A C13A	1.343(5)	N4C C13C	1.352(5)
C1A C2A	1.390(6)	C1C C2C	1.390(6)
C2A C3A	1.388(6)	C2C C3C	1.391(6)
C3A C4A	1.396(5)	C3C C4C	1.380(6)
C4A C5A	1.435(6)	C4C C5C	1.421(6)
C6A C7A	1.536(5)	C6C C7C	1.539(5)
C7A C8A	1.531(6)	C7C C8C	1.535(5)

Atom		Length/Å	Atom		Length/Å
C7A	C14A	1.528(6)	C7C	C14C	1.516(6)
C7A	C15A	1.534(6)	C7C	C15C	1.535(5)
C9A	C10A	1.416(6)	C9C	C10C	1.417(6)
C10A	C11A	1.384(6)	C10C	C11C	1.398(6)
C11A	C12A	1.398(6)	C11C	C12C	1.381(6)
C12A	C13A	1.389(6)	C12C	C13C	1.387(6)
Pt1B	N1B	2.013(3)	Pt1D	N1D	2.010(3)
Pt1B	N2B	2.000(3)	Pt1D	N2D	2.000(3)
Pt1B	N3B	1.996(4)	Pt1D	N3D	2.009(3)
Pt1B	N4B	2.012(4)	Pt1D	N4D	2.012(3)
N1B	C1B	1.340(5)	N1D	C1D	1.336(5)
N1B	C4B	1.383(5)	N1D	C4D	1.375(5)
N2B	C5B	1.295(5)	N2D	C5D	1.304(5)
N2B	C6B	1.470(5)	N2D	C6D	1.460(5)
N3B	C8B	1.467(6)	N3D	C8D	1.467(5)
N3B	C9B	1.296(6)	N3D	C9D	1.291(5)
N4B	C10B	1.388(6)	N4D	C10D	1.385(5)
N4B	C13B	1.351(6)	N4D	C13D	1.354(5)
C1B	C2B	1.388(6)	C1D	C2D	1.391(6)
C2B	C3B	1.369(6)	C2D	C3D	1.391(6)
C3B	C4B	1.398(6)	C3D	C4D	1.389(6)
C4B	C5B	1.421(6)	C4D	C5D	1.414(6)
C6B	C7B	1.545(6)	C6D	C7D	1.544(5)
C7B	C8B	1.539(6)	C7D	C8D	1.534(5)
C7B	C14B	1.522(6)	C7D	C14D	1.523(5)
C7B	C15B	1.526(6)	C7D	C15D	1.528(5)
C9B	C10B	1.411(7)	C9D	C10D	1.421(6)
C10B	C11B	1.402(7)	C10D	C11D	1.382(6)
C11B	C12B	1.378(7)	C11D	C12D	1.385(6)
C12B	C13B	1.394(6)	C12D	C13D	1.392(6)

Atom	Atom	Atom	Angle/˚	Atom	Atom	Atom	Angle/˚
N2A	Pt1A	N1A	80.20(13)	N1C	Pt1C	N4C	104.34(13)
N2A	Pt1A	N4A	175.22(13)	N2C	Pt1C	N1C	79.76(13)
N3A	Pt1A	N1A	175.41(14)	N2C	Pt1C	N4C	175.67(13)
N3A	Pt1A	N2A	95.63(13)	N3C	Pt1C	N1C	174.26(13)
N3A	Pt1A	N4A	79.95(13)	N3C	Pt1C	N2C	95.77(13)
N4A	Pt1A	N1A	104.15(13)	N3C	Pt1C	N4C	80.22(13)
C1A	N1A	Pt1A	140.1(3)	C1C	N1C	Pt1C	138.8(3)
C1A	N1A	C4A	107.0(3)	C1C	N1C	C4C	107.1(4)
C4A	N1A	Pt1A	112.9(3)	C4C	N1C	Pt1C	113.5(3)

Atom	Atom	Atom	Angle/˚	Atom	Atom	Atom	Angle/˚
C5A	N2A	Pt1A	115.9(3)	C5C	N2C	Pt1C	115.4(3)
C5A	N2A	C6A	120.6(3)	C5C	N2C	C6C	122.3(3)
C6A	N2A	Pt1A	123.5(2)	C6C	N2C	Pt1C	122.1(2)
C8A	N3A	Pt1A	123.8(2)	C8C	N3C	Pt1C	124.1(2)
C9A	N3A	Pt1A	115.4(3)	C9C	N3C	Pt1C	115.5(3)
C9A	N3A	C8A	120.9(3)	C9C	N3C	C8C	120.3(3)
C10A	N4A	Pt1A	113.3(3)	C10C	N4C	Pt1C	112.6(3)
C13A	N4A	Pt1A	140.3(3)	C13C	N4C	Pt1C	140.1(3)
C13A	N4A	C10A	106.2(3)	C13C	N4C	C10C	107.1(3)
N1A	C1A	C2A	110.0(4)	N1C	C1C	C2C	109.8(4)
C3A	C2A	C1A	107.4(4)	C1C	C2C	C3C	107.0(4)
C2A	C3A	C4A	105.9(4)	C4C	C3C	C2C	106.5(4)
N1A	C4A	C3A	109.6(4)	N1C	C4C	C3C	109.7(4)
N1A	C4A	C5A	115.2(3)	N1C	C4C	C5C	114.0(4)
C3A	C4A	C5A	135.1(4)	C3C	C4C	C5C	136.1(4)
N2A	C5A	C4A	115.8(4)	N2C	C5C	C4C	117.2(4)
N2A	C6A	C7A	113.6(3)	N2C	C6C	C7C	113.7(3)
C8A	C7A	C6A	111.6(3)	C8C	C7C	C6C	110.2(3)
C8A	C7A	C15A	106.3(4)	C14C	C7C	C6C	111.1(3)
C14A	C7A	C6A	110.6(4)	C14C	C7C	C8C	112.2(3)
C14A	C7A	C8A	110.9(3)	C14C	C7C	C15C	109.8(3)
C14A	C7A	C15A	109.8(4)	C15C	C7C	C6C	106.9(3)
C15A	C7A	C6A	107.3(3)	C15C	C7C	C8C	106.4(3)
N3A	C8A	C7A	114.5(3)	N3C	C8C	C7C	114.5(3)
N3A	C9A	C10A	117.2(4)	N3C	C9C	C10C	116.8(4)
N4A	C10A	C9A	114.2(4)	N4C	C10C	C9C	114.8(4)
N4A	C10A	C11A	110.3(4)	N4C	C10C	C11C	108.6(4)
C11A	C10A	C9A	135.3(4)	C11C	C10C	C9C	136.5(4)
C10A	C11A	C12A	106.0(4)	C12C	C11C	C10C	107.0(4)
C13A	C12A	C11A	106.8(4)	C11C	C12C	C13C	107.3(4)
N4A	C13A	C12A	110.8(4)	N4C	C13C	C12C	110.0(4)
N2B	Pt1B	N1B	79.94(14)	N1D	Pt1D	N4D	104.20(13)
N2B	Pt1B	N4B	175.53(15)	N2D	Pt1D	N1D	79.77(13)
N3B	Pt1B	N1B	175.29(15)	N2D	Pt1D	N3D	96.06(13)
N3B	Pt1B	N2B	95.89(15)	N2D	Pt1D	N4D	175.94(13)
N3B	Pt1B	N4B	79.84(16)	N3D	Pt1D	N1D	174.79(12)
N4B	Pt1B	N1B	104.27(15)	N3D	Pt1D	N4D	80.03(13)
C1B	N1B	Pt1B	140.4(3)	C1D	N1D	Pt1D	139.2(3)
C1B	N1B	C4B	106.5(4)	C1D	N1D	C4D	107.2(3)
C4B	N1B	Pt1B	113.0(3)	C4D	N1D	Pt1D	113.3(3)
C5B	N2B	Pt1B	115.8(3)	C5D	N2D	Pt1D	115.7(3)
C5B	N2B	C6B	120.4(4)	C5D	N2D	C6D	121.8(3)
C6B	N2B	Pt1B	123.8(3)	C6D	N2D	Pt1D	122.3(2)
C8B	N3B	Pt1B	123.3(3)	C8D	N3D	Pt1D	123.7(2)
C9B	N3B	Pt1B	116.2(3)	C9D	N3D	Pt1D	115.4(3)

Atom	Atom	Atom	Angle/˚	Atom	Atom	Atom	Angle/˚
C9B	N3B	C8B	120.5(4)	C9D	N3D	C8D	120.9(3)
C10B	N4B	Pt1B	112.7(3)	C10D	N4D	Pt1D	113.0(3)
C13B	N4B	Pt1B	139.9(3)	C13D	N4D	Pt1D	140.1(3)
C13B	N4B	C10B	107.4(4)	C13D	N4D	C10D	106.8(3)
N1B	C1B	C2B	110.3(4)	N1D	C1D	C2D	110.9(4)
C3B	C2B	C1B	107.6(4)	C3D	C2D	C1D	105.8(4)
C2B	C3B	C4B	106.3(4)	C4D	C3D	C2D	107.3(4)
N1B	C4B	C3B	109.2(4)	N1D	C4D	C3D	108.8(4)
N1B	C4B	C5B	114.5(4)	N1D	C4D	C5D	114.8(4)
C3B	C4B	C5B	135.8(4)	C3D	C4D	C5D	136.2(4)
N2B	C5B	C4B	116.6(4)	N2D	C5D	C4D	116.3(4)
N2B	C6B	C7B	114.5(4)	N2D	C6D	C7D	114.4(3)
C8B	C7B	C6B	110.5(4)	C8D	C7D	C6D	110.6(3)
C14B	C7B	C6B	111.3(4)	C14D	C7D	C6D	110.6(3)
C14B	C7B	C8B	110.6(4)	C14D	C7D	C8D	111.3(3)
C14B	C7B	C15B	110.1(4)	C14D	C7D	C15D	110.9(3)
C15B	C7B	C6B	106.6(4)	C15D	C7D	C6D	106.0(3)
C15B	C7B	C8B	107.6(4)	C15D	C7D	C8D	107.2(3)
N3B	C8B	C7B	114.0(4)	N3D	C8D	C7D	114.9(3)
N3B	C9B	C10B	116.3(4)	N3D	C9D	C10D	117.1(4)
N4B	C10B	C9B	114.9(4)	N4D	C10D	C9D	114.5(4)
N4B	C10B	C11B	108.5(5)	C11D	C10D	N4D	109.1(4)
C11B	C10B	C9B	136.5(5)	C11D	C10D	C9D	136.4(4)
C12B	C11B	C10B	106.9(5)	C10D	C11D	C12D	107.5(4)
C11B	C12B	C13B	107.6(5)	C11D	C12D	C13D	106.6(4)
N4B	C13B	C12B	109.6(5)	N4D	C13D	C12D	110.1(4)

Table S4. Selected mean crystallographic and calculated structural and conformational parameters for compounds **1** and **2**.

	1		**2**	
	XRD	**DFT**	**XRD**	**DFT**
Bond distances (Å)				
$Pt\text{-}N_{pyrrole}$	2.011 (3)	2.026	2.013 (3)	2.026
$Pt\text{-}N_{imine}$	2.005 (3)	2.02	2.002 (3)	2.019
C=N	1.30 (5)	1.29	1.298 (5)	1.29
Bond angles (°)				
$N_{pyrrole}\text{-}Pt\text{-}N_{pyrrole}$	103.82 (14)	104.9	104.25 (14)	105.12
$N_{imine}\text{-}Pt\text{-}N_{imine}$	95.65 (14)	95.87	95.75 (14)	95.45
$cis\text{-}N_{pyrrole}\text{-}Pt\text{-}N_{imine}$	80.27 (14)	79.58	79.96 (13)	79.,66
$trans\text{-}N_{pyrrole}\text{-}Pt\text{-}N_{immine}$	175.50 (13)	175.04	175.27 (14)	174.54
$C\text{-}N_{pyrrole}\text{-}C$	107.05 (3)	107.48	106.91 (3)	107.5
$C\text{-}N_{immine}\text{-}C$	120.78 (3)	121.31	120.96 (4)	121.59

Table S5. Selected excited singlet states of TD-DFT calculations for complex **1.**

Excited states	Energy/ eV (λ nm)	Wavelength (nm)	Oscillator strength		Major contributions (%)
1	3.4631	358	0.1163	Singlet-A	HOMO->LUMO (86%) H-3->LUMO (4%), H-2->L+1 (4%)
2	3.8112	324	0.2345	Singlet-A	H-1->LUMO (75%), HOMO->L+1 (19%)
3	3.9897	310	0.1042	Singlet-A	H-2->LUMO (53%), H-1->LUMO (12%), HOMO->L+1 (28%) H-3->L+1 (4%)
4	4.3064	287	0.0113	Singlet-A	H-4->LUMO (97%) H-3->LUMO (2%)
5	4.527	273	0.0005	Singlet-A	H-5->L+2 (12%), H-3->L+2 (13%), HOMO->L+2 (61%)
6	4.5794	270	0.3445	Singlet-A	H-3->LUMO (31%), H-1->L+1 (56%) H-2->L+1 (8%)
7	4.6797	264	0.0122	Singlet-A	H-4->L+2 (60%), H-2->LUMO (16%) H-3->L+1 (2%), H-1->LUMO (4%), HOMO->L+1 (7%)

Table S6. Selected excited singlet states of TD-DFT calculations for complex **2.**

Excited states	Energy/ eV (λ nm)	Wavelength (nm)	Oscillator strength		Major contributions (%)
1	3.48	356	0.1249	Singlet-A	HOMO->LUMO (86%) H-3->LUMO (4%), H-2->L+1 (4%), H-1->L+1 (2%)
2	3.8327	323	0.2375	Singlet-A	H-1->LUMO (74%), HOMO->L+1 (20%)
3	4.0071	309	0.1061	Singlet-A	H-2->LUMO (54%), H-1->LUMO (13%), HOMO->L+1 (26%) H-3->L+1 (4%)
4	4.3339	286	0.0118	Singlet-A	H-4->LUMO (94%) H-3->LUMO (5%)
5	4.5513	272	0.0001	Singlet-A	H-5->L+2 (13%), H-3->L+2 (14%), HOMO->L+2 (64%)
6	4.5935	269	0.3738	Singlet-A	H-3->LUMO (31%), H-1->L+1 (56%) H-4->LUMO (2%), H-2->L+1 (8%)

Table S7. Summary of GLIDE XP docking scores and selected interaction energy parameters for HSA targets prepared from ligand-free and ligand-bound grids based on geometry-optimized (prepared) structures derived from PDB codes 1HA2 (HSA•{warfarin} complex), 2BXF (HSA•{diazepam} complex), and 2BXG (HSA•{ibuprofen}$_2$ complex). The docking runs were truncated to report only the top-scoring ligand pose for each ligand. All energies are in units of kcal mol^{-1}.

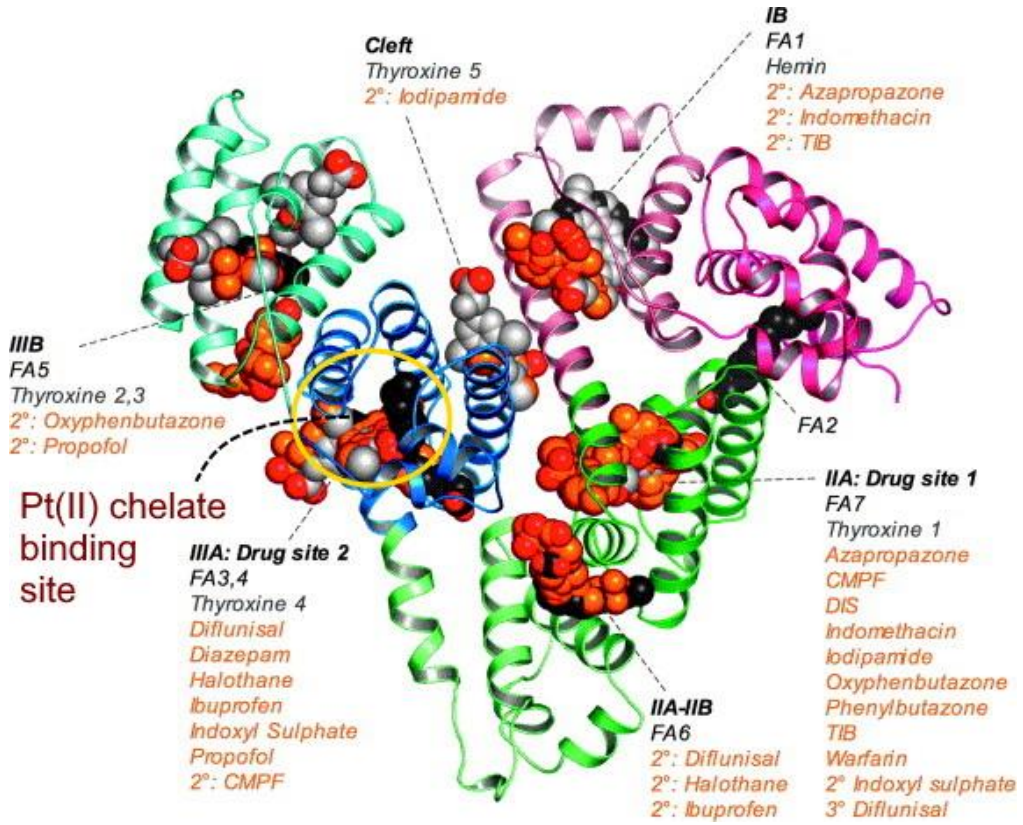
Ligand or drug	Binding site location	ligand effic.	ligand effic. sa	glide ligand effic. ln	XP GScore	glide Evdw	glide ECoul	glide energy	glide Einternal	glide Emodel	XP H Bond	XP Lipo. EvdW	XP EElectro
1HA2 - No warfarin bound in subdomain IIA of protein docking grid (Sudlow's Site I)													
ibuprofen	IA	-0.533	-1.315	-2.158	-8.001	-22.998	-1.285	-24.283	3.939	-31.178	0	-4.64	-0.096
Warfarin	IIA	-0.327	-0.929	-1.817	-7.513	-42.858	-2.647	-45.506	3.007	-63.649	-0.353	-5.865	-0.199
Diazepam	IIA-IIB	-0.251	-0.681	-1.256	-5.019	-25.042	-0.568	-25.610	1.048	-33.330	0	-3.979	-0.043
2	IA-IIA	-0.242	-0.657	-1.212	-4.843	-23.547	-0.339	-23.887	0.000	-30.228	0.000	-2.533	-0.025
1	IA-IIA	-0.243	-0.648	-1.171	-4.617	-23.762	-0.579	-24.341	0.325	-31.517	0.000	-2.614	-0.043
1HA2 - Warfarin bound in subdomain IIA of protein (Sudlow's Site I)													
Ibuprofen	IIIA	-0.590	-1.455	-2.387	-8.850	-26.042	-10.132	-36.174	8.038	-47.749	-0.667	-4.515	-0.760
Warfarin	IIIA	-0.365	-1.039	-2.032	-8.404	-35.237	-1.045	-36.282	5.918	-51.380	-0.541	-5.201	-0.078
Diazepam	IIIA	-0.295	-0.800	-1.476	-5.896	-32.921	0.055	-32.866	0.050	-43.701	-0.175	-4.435	0.004
2	IIA	-0.244	-0.662	-1.221	-4.880	-21.885	-3.481	-25.366	0.000	-28.067	-0.073	-2.544	-0.261
1	IIIA	-0.073	-0.195	-0.352	-1.390	-21.763	-2.510	-24.273	0.000	-34.975	-0.326	-2.596	-0.188
2BXF - No diazepam bound in subdomain IIIA of protein docking grid (Sudlow's Site II)													
Diazepam	IIIA	-0.452	-1.226	-2.260	-9.032	-44.241	-2.966	-47.207	1.236	-67.088	-0.688	-6.504	-0.222
Warfarin	IIIA	-0.318	-0.905	-1.770	-7.320	-33.986	-1.476	-35.462	4.800	-45.147	0	-6.367	-0.111
1	IIA-IIIA	-0.271	-0.723	-1.304	-5.145	-25.912	0.049	-25.863	0.325	-29.973	-0.697	-3.854	0.004
2	IIA-IIIA	-0.233	-0.633	-1.168	-4.666	-27.806	-0.203	-28.010	0.000	-35.104	0.000	-4.079	-0.015
Ibuprofen	IIIA	-0.287	-0.707	-1.159	-4.298	-20.072	-5.986	-26.058	1.780	-33.284	-1.111	-2.381	-0.449
2BXF - Diazepam bound in subdomain IIIA (Sudlow's Site II)													
Ibuprofen	IIA	-0.528	-1.302	-2.136	-7.922	-23.084	-5.223	-28.307	4.642	-39.436	-0.695	-2.911	-0.392
2	IIIA	-0.248	-0.674	-1.243	-4.967	-25.346	-0.204	-25.551	0.000	-33.215	0.000	-2.550	-0.015
1	IIIA	-0.106	-0.284	-0.513	-2.023	-22.867	-1.419	-24.286	0.324	-31.138	0.000	-1.879	-0.106
Warfarin	IB-IIIA cleft	-0.185	-0.526	-1.029	-4.257	-34.837	-2.655	-37.492	4.110	-49.074	-0.819	-3.158	-0.199
Diazepam	IIA-IIB	-0.190	-0.515	-0.949	-3.793	-34.404	-1.145	-35.549	0.175	-43.894	-0.123	-3.024	-0.086

2BXG - 2x ibuprofen bound, one in subdomain IIIA (Sudlow's Site II) and the second between subdomains IIA and IIB													
Ibuprofen	IIA-Trp214	-0.529	-1.304	-2.139	-7.932	-19.805	-3.976	-23.781	0	-27.136	0	-3.243	-0.298
2	IA-IIA	-0.240	-0.651	-1.200	-4.795	-22.218	0.478	-21.739	0.000	-30.041	0.000	-2.549	0.036
1	IA-IIA	-0.242	-0.645	-1.164	-4.593	-22.051	-0.508	-22.559	0.324	-29.124	0.000	-2.392	-0.038
Warfarin	IB-IIIA cleft	-0.197	-0.560	-1.094	-4.525	-31.451	-8.021	-39.472	4.671	-53.459	-1.341	-2.360	-0.602
Diazepam	IB-IIIA cleft	-0.180	-0.490	-0.903	-3.610	-28.813	-0.407	-29.220	0.369	-40.636	0	-3.212	-0.031

Table S8. Summary of Glide XP docking scores (as in Table S7) and selected interaction distances for HSA targets prepared from ligand-free grids based on geometry-optimized (prepared) structures derived from PDB codes 1HA2 (HSA•{warfarin} complex) and 2BXF (HSA•{diazepam} complex). The docking runs were truncated to report only the top-scoring ligand pose for each ligand. All energies are in units of kcal mol^{-1}.

Ligand or drug	Binding site location [a]	XP GScore	Distance to Trp-214 (Å) [b]	Closest tyrosine residues (Å) [b]	Closest phenylalanine residues (Å) [b]
1HA2 - No warfarin bound in subdomain IIA of protein docking grid (Sudlow's Site I)					
Ibuprofen	IA	-8.001	30.4	Tyr-30 (10.8), Tyr-150 (13.6), Tyr-148 (18.0)	Phe-19 (5.6), Phe-27 (7.5), Phe-49 (9.1)
Warfarin	IIA	-7.513	5.3	Tyr-150 (9.5), Tyr-263 (11.3), Tyr-452 (17.0)	Phe-211 (5.9), Phe-223 (8.3)
Diazepam	IIA-IIB	-5.019	11.3	Tyr-353 (11.9), Tyr-319 (12.2), Tyr334 (13.9)	Phe-206 (5.2), Phe-211 (11.3), Phe-330 (11.1)
1	IA-IIA	-4.843	11,6	Tyr-319 (12,4), Tyr-334 (16,7), Tyr-263 (16)	Phe-228 (7,7), Phe-326 (9), Phe-263 (10.1)
2	IA-IIA	-4.617	9,6	Tyr-319 (11.8), Tyr-332 (10,2), Tyr-334 (15)	Phe-228 (8,6), Phe-326 (9), Phe-211 (10,1)
2BXF - No diazepam bound in subdomain IIIA of protein docking grid (Sudlow's Site II)					
Diazepam	IIIA	-9.032	17.0	Tyr-411 (9.5), Tyr-452 (9.6), Tyr-341 (13.4)	Phe-403 (6.0), Phe-395 (9.0), Phe-488 (12.5)
Warfarin	IIIA	-7.320	17.0	Tyr-452 (9.5), Tyr-411 (10.4), Tyr-341 (13.3)	Phe-403 (5.3), Phe-395 (7.8), Phe-488 (12.2)
2	IIIA	-5.145	29.0	Tyr-370 (7.1), Tyr-353 (9,5), Tyr-319 (12.0)	Phe-403 (5.3), Phe-395 (7.8), Phe-488 (12.2)
1	IIIA	-4.666	30.0	Tyr-370 (5.9), Tyr-353 (9.6), Tyr-319 (11.3)	Phe-374 (13.7), Phe-309 (14.1), Phe-377 (14.4)
Ibuprofen	IIIA	-4.298	20.9	Tyr-411 (6.0), Tyr-452 (12.1), Tyr-341(19.3)	Phe-309 (12.1), Phe-374 (14.3), Phe-353 (14.0)

[a] Binding site regions (see **Footnote Figure** overleaf) are defined according to Figure 7 in the paper by Ghuman *et al*.[35] [b] Distance measured between the closest ring centroid pair of the ligand and residue. For metal chelates, the distance to the metal ion from the closest ring centroid is given.



Footnote Figure: Modified from Figure 7 of Ghuman et al.[35]; "Summary of the ligand binding capacity of HSA as defined by crystallographic studies to date. Ligands are depicted in space-filling representation; oxygen atoms are coloured red; all other atoms in fatty acids (myristic acid), other endogenous ligands (hemin, thyroxin), and drugs are coloured dark grey, light grey, and orange, respectively." The yellow ellipse indicates where the most probable binding site is located for the Pt(II) chelates in the present docking and spectroscopic studies.

References

1 O. V. Dolomanov, L. J. Bourhis, R. J. Gildea, J. A. K. Howard and H. Puschmann, *J. Appl. Crystallogr.*, 2009, **42**, 339–341.
2 G. M. Sheldrick, *Acta Crystallogr. Sect. Found. Adv.*, 2015, **71**, 3–8.
3 G. M. Sheldrick, Acta Crystallogr. Sect. C Struct. Chem., 2015, **71**, 3–8.
4 X.-F. Shan, D.-H. Wang, C.-H. Tung and L.-Z. Wu, *Tetrahedron*, 2008, **64**, 5577–5582.
5 M. Van de Weert and L. Stella, *J. Mol. Struct.*, 2011, **998**, 144–150.
6 M. van de Weert, *J. Fluoresc.*, 2010, **20**, 625–629.
7 P. Geladi and B. R. Kowalski, *Anal. Chim. Acta*, 1986, **185**, 1–17.
8 J. G. Lees, A. J. Miles, R. W. Janes and B. A. Wallace, *BMC Bioinformatics*, 2006, **7**, 507.
9 J. T. Yang, C.-S. C. Wu and H. M. Martinez, in *Methods in Enzymology*, Academic Press, 1986, vol. 130, pp. 208–269.
10 T. Shiratori, S. Goto, T. Sakaguchi, T. Kasai, Y. Otsuka, K. Higashi, K. Makino, H. Takahashi and K. Komatsu, *Biochem. Biophys. Rep.*, 2021, **28**, 101153.
11 A. Micsonai, F. Wien, É. Bulyáki, J. Kun, É. Moussong, Y.-H. Lee, Y. Goto, M. Réfrégiers and J. Kardos, *Nucleic Acids Res.*, 2018, **46**, W315–W322.
12 S. Sookai and O. Q. Munro, *ChemistryEurope*, 2023, e202300012.
13 M. J. Frisch, G. W. Trucks, H. B. Schlegel, G. E. Scuseria, M. A. Robb, J. R. Cheeseman, G. Scalmani, V. Barone, G. A. Petersson, H. Nakatsuji, X. Li, M. Caricato, A. V. Marenich, J. Bloino, B. G. Janesko, R. Gomperts, B. Mennucci, H. P. Hratchian, J. V. Ortiz, A. F. Izmaylov, J. L. Sonnenberg, D. Williams-Young, F. Ding, F. Lipparini, F. Egidi, J. Goings, B. Peng, A. Petrone, T. Henderson, D. Ranasinghe, V. G. Zakrzewski, J. Gao, N. Rega, G. Zheng, W. Liang, M. Hada, M. Ehara, K. Toyota, R. Fukuda, J. Hasegawa, M. Ishida, T. Nakajima, Y. Honda, O. Kitao, H. Nakai, T. Vreven, K. Throssell, J. A. Montgomery Jr., J. E. Peralta, F. Ogliaro, M. J. Bearpark, J. J. Heyd, E. N. Brothers, K. N. Kudin, V. N. Staroverov, T. A. Keith, R. Kobayashi, J. Normand, K. Raghavachari, A. P. Rendell, J. C. Burant, S. S. Iyengar, J. Tomasi, M. Cossi, J. M. Millam, M. Klene, C. Adamo, R. Cammi, J. W. Ochterski, R. L. Martin, K. Morokuma, O. Farkas, J. B. Foresman and D. J. Fox, *Gaussian 16 Revision C.01*, 2016.
14 T. Yanai, D. P. Tew and N. C. Handy, *Chem. Phys. Lett.*, 2004, **393**, 51–57.
15 F. Weigend and R. Ahlrichs, *Phys. Chem. Chem. Phys.*, 2005, **7**, 3297–3305.
16 S. Grimme, S. Ehrlich and L. Goerigk, *J. Comput. Chem.*, 2011, **32**, 1456–1465.
17 P. Fuentealba, H. Preuss, H. Stoll and L. Von Szentpály, *Chem. Phys. Lett.*, 1982, **89**, 418–422.
18 J. R. Cheeseman, G. W. Trucks, T. A. Keith and M. J. Frisch, *J. Chem. Phys.*, 1996, **104**, 5497–5509.
19 R. Ditchfield, *Mol. Phys.*, 1974, **27**, 789–807.
20 F. Lipparini, G. Scalmani, B. Mennucci, E. Cancès, M. Caricato and M. J. Frisch, *J. Chem. Phys.*, 2010, **133**, 014106.
21 R. Dennington, T. A. Keith and J. M. Millam, *GaussView Version 6*, 2019.
22 N. M. O'boyle, A. L. Tenderholt and K. M. Langner, *J. Comput. Chem.*, 2008, **29**, 839–845.
23 F. R. Clemente, T. Vreven and M. J. Frisch, in *Quantum Biochemistry*, John Wiley & Sons, Ltd, 2010, pp. 61–83.
24 A. K. Rappe, C. J. Casewit, K. S. Colwell, W. A. Goddard and W. M. Skiff, *J. Am. Chem. Soc.*, 1992, **114**, 10024–10035.

25 T. A. Halgren, R. B. Murphy, R. A. Friesner, H. S. Beard, L. L. Frye, W. T. Pollard and J. L. Banks, *J. Med. Chem.*, 2004, **47**, 1750–1759.
26 I. Petitpas, A. A. Bhattacharya, S. Twine, M. East and S. Curry, *J. Biol. Chem.*, 2001, **276**, 22804–22809.
27 J. Ghuman, P. A. Zunszain, I. Petitpas, A. A. Bhattacharya, M. Otagiri and S. Curry, *J. Mol. Biol.*, 2005, **353**, 38–52.
28 G. Madhavi Sastry, M. Adzhigirey, T. Day, R. Annabhimoju and W. Sherman, *J. Comput. Aided Mol. Des.*, 2013, **27**, 221–234.
29 F. Mohamadi, N. G. J. Richards, W. C. Guida, R. Liskamp, M. Lipton, C. Caufield, G. Chang, T. Hendrickson and W. C. Still, *J. Comput. Chem.*, 1990, **11**, 440–467.
30 W. L. Jorgensen and J. Tirado-Rives, *J. Am. Chem. Soc.*, 1988, **110**, 1657–1666.
31 G. A. Kaminski, R. A. Friesner, J. Tirado-Rives and W. L. Jorgensen, *J. Phys. Chem. B*, 2001, **105**, 6474–6487.
32 R. A. Friesner, J. L. Banks, R. B. Murphy, T. A. Halgren, J. J. Klicic, D. T. Mainz, M. P. Repasky, E. H. Knoll, M. Shelley, J. K. Perry, D. E. Shaw, P. Francis and P. S. Shenkin, *J. Med. Chem.*, 2004, **47**, 1739–1749.
33 J. R. Greenwood, D. Calkins, A. P. Sullivan and J. C. Shelley, *J. Comput. Aided Mol. Des.*, 2010, **24**, 591–604.
34 Z. Fakhar, B. Faramarzi, S. Pacifico and S. Faramarzi, *J. Biomol. Struct. Dyn.*, 2021, **39**, 6171–6183.
35 J. Ghuman, P. A. Zunszain, I. Petitpas, A. A. Bhattacharya, M. Otagiri and S. Curry, *J. Mol. Biol.*, 2005, **353**, 38–52.

Supporting Information:

Bioimaging Pt(II) Schiff base chelates

Sheldon Sookai,[a] Shanen Perumal,[b] Mandeep Kaur[b] and Orde Q. Munro*[a]

[a]*Molecular Sciences Institute, School of Chemistry, University of the Witwatersrand, PO WITS 2050, Johannesburg, South Africa*

[b]*Research Unit, School of Molecular and Cell Biology, University of the Witwatersrand, Johannesburg, 2050, South Africa*

Table of contents

1. Experimental methods 168
1.1. Instrumentation 168
1.1.1. Crystallography 168
1.1.2. General spectroscopy 168
1.2. Compound synthesis 168
1.2.1. Ligand synthesis 168
1.2.2. Complex synthesis 169
1.2.3. Ligand characterisation 169
1.2.4. Pt(II) chelate characterisation 170
1.3. Fluorescence emission spectroscopy 171
1.4. TD-DFT simulations 171
1.5. Cytotoxicity assays 171
1.6. Fluorescent microscopy 172
2. Figures and Tables 172
2.1. General characterization data 172
Scheme S1 . Structures of the bis(pyrrolide-imine) chelates synthesised. (a) 2,2'-{propane-1,3-diylbis[nitrilo(E)methylylidene]}bis(pyrrol-1-ido) (**1**), (b) 2,2'-{(2-hydroxypropane-1,3-diyl)bis[nitrilo(E) methylylidene]} bis(pyrrol-1-ido) (**2**), (c) 2,2'-{(2,2-dimethylpropane-1,3-diyl)bis[nitrilo(E)methylylidene]} bis(pyrrol-1-ido) (**3**) , (d) 2,2'-{(1R,2R)-cyclohexane-1,2-diylbis[nitrilo(E)methylylidene]}bis(pyrrol-1-ido) (**4**) 172
Fig. S1. 400 MHz 1H NMR spectrum of **1** recorded in DMSO-d6 at 300 K. This compound is known3 the spectral data here briefly confirm the structure of the compound and its purity. 173
Fig. S2 101 MHz ^{13}C NMR spectrum of **2** recorded in DMSO-*d*6 at 300 K. 174
Fig. S3. UV-visible spectrum of **1** recorded in CH_3CN at 295 K as a function of concentration. . 174
Fig. S4 400 MHz ^{1}H NMR spectrum of **2** recorded in DMSO-*d*6 at 300 K. 175

Fig. S5 101 MHz ^{13}C NMR spectrum of **2** recorded in DMSO-*d*6 at 300 K. 176

Fig. S6 UV-visible spectrum of **2** recorded in acetonitrile at 295 K as a function of concentration. The molar absorptivities of key band maximum are reported in the main paper and were determined from the slopes of Beer- Lambert law plots at the relevant band maxima. 177

Fig. S7 400 MHz ^{1}H NMR spectrum of **3** recorded in DMSO-*d*6 at 300 K. 178

Fig. S8 101 MHz ^{13}C NMR spectrum of **3** recorded in DMSO-*d*6 at 300 K. 179

Fig. S9 UV-visible spectrum of **3** recorded in acetonitrile at 295 K as a function of concentration. The molar absorptivities of key band maximum are reported in the main paper and were determined from the slopes of Beer- Lambert law plots at the relevant band maxima. 180

Fig. S10 400 MHz ^{1}H NMR spectrum of **4** recorded in DMSO-*d*6 at 300 K. This compound is known[2] the spectral data here briefly confirm the structure of the compound and its purity. 181

Fig. S11 101 MHz ^{13}C NMR spectrum of **4** recorded in DMSO-*d*6 at 300 K. 182

2.2. X-ray crystallography 183

Fig. S12 (a) Unit cell contents for the X-ray structures of **1** (space group $P2_1/c$) determined at 173.15 K. (b) ASU of **1** consisting of four identical molecules with two pairs of intermolecular π – stacking arrangements. The Pt-Pt distances was measured between the two pairs of the Pt(II) bis(Pyrollide-imine) metal chelate. 183

2.3. Steady state absorbance and fluorescence spectroscopy Pt(II) chelates binding to HSA. 184

Fig. S13 Overlayed UV-vis absorption spectra of Pt(II) bis (pyrrolide-imine) chelates 1–4 and their corresponding free ligands. The free ligands are represented by the solid black line and has a single absorbance peak in the UV region. The corresponding Pt(II) bis (pyrrolide-imine) chelates are represented by the solid red line and have several absorption peaks in the UV and visible region 184

Fig. S14 Fluorescence emission spectrum of four Pt(II) bis(pyrrolide-imine) chelates (a) **2**, (b) **3**, and **4** represented by solid black line. The Pt(II) bis(pyrollide-imine) chelates were then incubated with HSA and the enhanced fluorescence emission spectrum was measured of (a) **2**···HSA, (b) **3**···HSA, (c) and **4**···HSA represented by solid red line. The relevant concentrations of the Pt(II) bis(pyrrolide-imine) chelates and HSA were 5 μM and were measured in KH_2PO_4 (50 mM, pH 7.5). The excitation and emission wavelengths for the Pt(II) bis(pyrollide-imine) chelates were λ^{ex} = 382 nm and $\lambda^{emission}$ was measured from 500 – 740 nm. 185

Fig. S15 (a) Fluorescence emission spectra of the five Pt(II) bis(pyrrolide-imine) chelates (10 μM) in KH_2PO_4 buffer (50 mM, pH 7.5) ($\lambda_{ex}^{382\ nm}$). (b) Fluorescence emission spectra of **1**,**3**,**4** and Pt(cyclohexane)Pyrr (10 μM) in deoxygenated KH_2PO_4 buffer (50 mM, pH 7.5) ($\lambda_{ex}^{382\,nm}$) molecular $^3O_2$ was removed by bubbling the solution with $Ar_{(g)}$ for 3 min. (c) The fluorescence emission spectrum of **2** went beyond the scale of the fluorescence-spectrophotometer. Therefore, the slit width had to be changed to show the increase in fluoresce intensity of Pt(OH)Pyrr when O_2 was removed with $Ar_{(g)}$. This perfectly highlights the significant enhancement in luminescence of **2** in an aqueous medium. 186

2.4. Quantum yields. 187

Fig. S16 Calibration curves based on the absorbance of the Pt(II) bis(pyrolide-imine) chelates plotted against the area under the fluorescence emission spectra of the respective Pt(II) bis(pyrolide-imine) chelates. The calibration curves of **1**, **2** and **3** were plotted to obtain the gradient to input into eq. 1. Using the eq. 1 the Φ_F was calculated in (a) acetonitrile, (b) DCM, (c) dH_2O and (d) HSA. **4** was used as the standard reference as its Φ_F had been reported previously[2]. Figures are representative of a single sample calculation; all data was performed in triplicates and the respective Φ_F are reported in Table S6 and S7. 187

2.5. TD-DFT simulations 188

Fig. S17 (a) Experimental and (b) DFT calculated (inset) electronic absorption spectra of **2** in acetonitrile. The absorption maxima (λ_{max}) are indicated for the experimental spectrum at 430, 383, 366, 314, 305 and 278 nm. The absorption envelope for the DFT calculated envelope spectrum of **2** is plotted from 200 – 450 nm and is plotted with a band width of 2000 cm^{-1} (full width at half maximum intensity, FWHM). 188

Fig. S18 (a) Experimental and (b) DFT calculated (inset) electronic absorption spectra of **3** in acetonitrile. The absorption maxima (λ_{max}) are indicated for the experimental spectrum at 430, 383, 366, 314, 305 and 278 nm. The absorption envelope for the DFT calculated envelope spectrum of **3** is plotted from 200 – 450 nm and is plotted with a band width of 2000 cm^{-1} (full width at half maximum intensity, FWHM). 188

Fig. 19 UV-vis spectrum of (a) (**1**) green, (**2**) blue, (**3**) red and (**4**) black in acetonitrile (50 x 10^{-6} M) and (b) **(1)** green, (**2**) blue, (**3**) red and (**4**) black in dH_2O (50 x 10^{-6} M). 189

2.6. Fluorescence microscopy 189

Fig. S20 Representative images of intracellular fluorescence of Pt(II) complexes **1-3** in NMuMG cells with (HSA+) and without (HSA-) the addition of 10 µM HSA, visualised using the Floid™ Cell Imaging System (Thermo Fisher Scientific, USA). Nuclei were stained red using NucRed™ Dead (Thermo Fisher Scientific, USA) and the blue light emission of the complexed in the cell was captured. 189

2.7. Tables. 190

Table S1. Crystal data and X-ray structure refinement details for Pt(II) bis(pyrrolide-imine) chelate **1**. 190

Table S2. Selected mean crystallographic and calculated structural and conformational parameters for compounds **1**. 190

Table S3. Selected excited singlet states of TD-DFT calculations for complex **1**. 191

Table S4. Selected excited singlet states of TD-DFT calculations for complex **2**. 192

Table S5. Selected excited singlet states of TD-DFT calculations for complex **3.** 193

Table S6. Calculated quantum yields for the Pt(II) bis(pyrrolide-imine) chelates in different solvents. 194

Table S7. Calculated quantum yields for the Pt(II) bis(pyrrolide-imine) chelates in different anaerobic acetonitrile and dH_2O. 194

3. References. 195

1. Experimental methods

All solvents (HPLC grade) and chemical synthons (pyrrole-2 carboxaldehyde and diamines) were used as received from Merck Sigma-Aldrich® without further purification. Deuterated dimethyl sulfoxide was stored over activated 4 Å molecular sieves. Human serum albumin (HSA) 99% purity was purchased from Sigma and used as received without further purification. Ultrapure water (Type I) was produced using a Merk-Millipore Direct-Q® 3 UV Water Purification System.

1.1. Instrumentation

1.1.1. Crystallography

Single crystal X-ray structure determinations were carried out with a four-circle Bruker D8 Venture X-ray diffractometer equipped with a Photon II CPAD area detector and a fine-focus sealed X-ray tube source (Mo anode). Crystals were mounted under Paratone® oil on nylon loops (Hampton Research) and the crystals were kept at 173(1) K during data collection (Oxford CryoStream 700). Using Olex2,1 the structures were solved with the ShelXT2 structure solution program (intrinsic phasing) and refined with ShelXL3 using least squares minimization.

1.1.2. General spectroscopy

Proton and carbon NMR spectra were recorded on Bruker Avance III 400 and 300 NMR spectrometers at 1H frequencies of 400 MHz and 300 MHz, respectively, and 13C frequencies of 100 MHz and 75 MHz, respectively. Spectra were recorded at 298 K with 5 mm BBOZ or TBIZ probes. Chemical shifts for both proton and carbon were referenced using the solvent signal. MestReNova (version 14.2.1-27684) was used to analyse NMR spectra. FTIR spectra of powder samples were recorded using a Bruker Alpha FTIR spectrometer incorporating a Bruker Platinum® diamond ATR sampling accessory. Spectra were analysed using the OPUS software package on the spectrometer (version 7.5). Mass spectra were recorded with Bruker Compact Q-TOF high-resolution mass spectrometer using Bruker Daltronics HyStar 3.2 SR4 software. Bruker Compass DataAnalysis software (Version 4.3) was used to analyse chromatograms. Samples of pure compounds (typically ca. 10 µg/mL) were prepared in HPLC-grade acetonitrile or ethanol for metal chelates and HPLC-grade methanol for ligands. Solutions were acidified using 0.1% (V/V) formic acid to obtain spectra in ESI+ mode. Electronic spectra were recorded using either a PerkinElmer Lambda 365 double-beam spectrometer connected to a Peltier controller and multicell thermostatic cell block or an Analytik Jena Specord210 Plus double-beam instrument fitted with an external water circulating thermostatic bath and thermostatted cell holders. The spectral data were analysed with the spectrometer software or Origin Pro 2020. Spectra were recorded (10-mm pathlength quartz cuvettes) as a function of concentration for both characterization and the determination of molar absorptivity constants.

1.2. Compound synthesis

1.2.1. Ligand synthesis

***N*,*N*'-bis[(1*E*)-1H-pyrrol-2-ylmethylene]propane-1,3-diamine (H_2PrPyrr).** The synthetic method was an adaption from the method described by Munro *et al*.[1] Briefly, pyrrole-2-carboxaldehyde (1.4265 g, 15 mmol) and 1,3-diaminopropane (0.556 g, 7.5 mmol) were refluxed in ethanol (30 mL) for two hours. During refluxing, the reaction mixture changed from colourless to a clear straw yellow. Ethanol was then removed by rotary evaporation, leaving a viscous orange coloured oil. Finally, the viscous orange oil was dissolved in a minimal volume of dichloromethane and layered with hexane. The solution was left overnight, affording a faint yellow polycrystalline product.

1,3-bis{[(1*E*)-1*H*-pyrrol-2-ylmethylene]amino}propan-2-ol (H_2(OH)Pyrr). In brief the synthesis of H_2(OH)Pyrr involved refluxing pyrrole-2-carboxaldehyde (0.5706 g; 6 mmol) with 1,3-diaminopropanol (0.2704 g; 3 mmol) for 2 hours in ethanol in which time the solution changed from colourless to bright orange. The ligand was

precipitated out by overnight evaporation of ethanol. The ligand was analysed by ^{1}H NMR, ^{13}C NMR, FT-IR and UV-Visible spectroscopy.

2,2-dimethyl-*N*,*N*'-bis[(1*E*)-1*H*-pyrrol-2-ylmethylene]propane-1,3-diamine ($H_2(CH_3)_2$Pyrr). In brief was synthesised by refluxing pyrrole-2-carboxaldehyde (0.5706 g, 6 mmol) and 1,3-diamino-2,2-dimethyl propane (0.3066 g, 3 mmol) was refluxed in ethanol (30 mL) for one hour. The solution changed from colourless to orange. The ligand was precipitated out by overnight evaporation of the ethanol. The ligand was analysed by ^{1}H NMR, ^{13}C NMR, FT-IR and UV-Visible spectroscopy.

(1*R*,2*R*)-*N*,*N*'-bis[(1*E*)-1*H*-pyrrol-2-ylmethylene] cyclohexane -1,2-diamine (H_2(-R-cyclohexane)Pyrr). The enantiomerically pure ligand was synthesised by a solid state reaction using the enantiomerically pure (1R, 2R) cyclohexane diamine (0.303 g, 2.65 mmol) with an agate pestle and mortar with pyrrole-2-carboxaldehyde (0.500 g, 5.30 mmol) for between 10 to 15 minutes, until a brown oil was formed. The brown oil was dissolved in dichloromethane and dried with $MgSO_4$ to remove the water from the condensation reaction. The solution was filtered through celite before been layered with hexane, which yielded thin white rod-shaped crystals.

1.2.2. Complex synthesis

All bis(pyrrolide-imine) chelates and Pt(II) bis(pyrrolide-imine) chelates were synthesised by methods previously reported.[2,3]

1.2.3. Ligand characterisation

***N*,*N*'-bis[(1*E*)-1H-pyrrol-2-ylmethylene]propane-1,3-diamine (H_2PrPyrr).** ^{1}H NMR (400 MHz, chloroform-*d*, 300 K) [δ, ppm]: 1.98 (t, *J* = 6.8 Hz, 2H, H-7), 3.61 (td, *J* = 6.8, 1.2 Hz, 4H, H-6), 6.23 (dd, *J* = 3.6, 2.6 Hz, 2H, H-2), 6.48 (dd, *J* = 3.6, 1.4 Hz, 2H, H-3), 6.88 (t, *J* = 1.9 Hz, 2H, H-1), 8.03 (s, 2H, H-5). ^{13}C NMR (101 MHz, chloroform-*d*, 300 K) [δ, ppm]: 32.29 (C-7), 57.80 (C-6), 109.59 (C-2), 114.13 (C-3), 122.04 (C-1), 129.86 (C-4), 151.85 (C-5). IR (KBr pellet, cm^{-1}): 3112w δ(NH, pyrrole), 3053m br *v*(CH, imine), 2941m *v*(CH, $CH_2CH_2CH_2$), 2847 *v*(CH, CH_2-N=CH), 1634s br *v*(C=N). UV-vis (ethanol) [λ_{max}/nm, ε/mol^{-1} dm^3 cm^{-1}]: 289, 3.20 × 10^4.

1,3-bis{[(1*E*)-1*H*-pyrrol-2-ylmethylene]amino}propan-2-ol (H_2(OH)Pyrr). ^{1}H NMR (400 MHz, DMSO-d_6- 300 K) [δ, ppm]: 3.43 (dd, *J* = 11.7, 6.5 Hz, 2H, CH_2-N=CH), 3.77 – 3.54 (m, 2H, CH_2-N=CH), 4.00 – 3.82 (m, 1H, H-7), 6.11 (t, *J* = 3.0 Hz, 2H, H-2), 6.44 (dd, *J* = 3.5, 1.5 Hz, 2H, H-3), 6.87 (t, *J* = 1.9 Hz, 2H, H-1), 8.07 (s, 2H, H-5), 11.34 (s br, 2H, DMSO-d_6 exchangeable, H-9). ^{13}C NMR (101 MHz, DMSO-d_6, 300 K) [δ, ppm]: 65.14 (C-6), 70.69 (C-7), 108.98 (C-2), 113.35 (C-3), 122.03 (C-1), 130.41 (C-4), 152.92 (C-5). IR (KBr pellet, cm-1): 3254w (NH, pyrrole), 3088m (CH, imine), 2882 (CH, H-COH), 2859 (CH, C*H*2-N=CH), 1633s (C=N), 1127 (C-O stretch). UV/vis (ethanol) [λ, max, nm; ε, mol^{-1} dm^3 cm^{-1}]: 289; 3.23 × 10^4.

2,2-dimethyl-*N*,*N*'-bis[(1*E*)-1*H*-pyrrol-2-ylmethylene]propane-1,3-diamine ($H_2(CH_3)_2$Pyrr). ^{1}H NMR (400 MHz, Chloroform-*d*, 300 K) [δ, ppm]: 0.97 (t, *J* = 4.3 Hz, 6H, H-8), 3.46 (t, *J* = 4.2 Hz, 4H, H-6), 6.26 (p, *J* = 3.2 Hz, 2H, H-2), 6.48 (dt, *J* = 6.6, 3.4 Hz, 2H, H-3), 6.90 (d, *J* = 6.1 Hz, 2H, H-1), 7.99 (t, *J* = 4.2 Hz, 2H, H-5), 9.50 (s br, 2H, H-9). ^{13}C NMR (101 MHz, Chloroform-*d* 300 K) [δ, ppm]: 24.28 (C-8), 36.96 (C-7), 69.32 (C-6), 109.44 (C-2), 114.28 (C-3), 122.20 (C-1), 130.06 (C-4), 152.17 (C-5). FT-IR (KBr pellet, cm^{-1}): 3130m br *v*(CH, imine), 2966m *v*(CH, terminal CH3), 2852m *v*(CH2, alkyl), 1635s br *v*(C=N). UV/vis (ethanol) [λ, max, nm; ε, mol^{-1} dm^3 cm^{-1}]: 289; 3.23 × 10^4.

(1*R*,2*R*)-*N*,*N*'-bis[(1*E*)-1*H*-pyrrol-2-ylmethylene] cyclohexane -1,2-diamine (H_2(-R cyclohexane)Pyrr. . ^{1}H NMR (400 MHz, DMSO-d_6, 300 K) [δ, ppm]: 1.34 – 1.80 (m, 8H, H-7 and H-8), 3.23 (m, 2H, H-6), 6.01 (t, *J* = 3.0 Hz, 2H, H-2), 6.31(dd, $^{3}J_1$ = 3.5 Hz, $^{3}J_2$ 1.4 Hz, 2H, H-3), 6.76 (t, *J* = 1.9 Hz, 2H, H-1), 7.94 (s, 2H, H-5), 11.16 (s, 2H, H-9). ^{13}C NMR (101 MHz, DMSO-d_6, 298 K) [δ, ppm]: 24.70 (C-8), 33.85 (C-7), 74.09 (C-6), 109.07 (C-2), 113.61 (C-3), 122.08 (C-1), 130.33 (C-4), 151.26 (C-5). UV/vis (acetonitrile) [λ, max, nm; ε, mol^{-1} dm^3 cm^{-1}]: 289; 2.95 × 10^4 (H_2L4R)

1.2.4. Pt(II) chelate characterisation

Pt(II)-chelate characterization. 2,2'-{propane-1,3-diylbis[nitrilo(*E*)methylylidene]}bis(pyrrol-1-ido)platinium(II) (1). ^{1}H NMR (400 MHz, DMSO-d_6, 300 K) δ 8.15 (s, 2H; H-2), 7.19 (s, 2H; H-16), 6.64 (d, *J* = 3.7 Hz, 2H; H-18), 6.16 (dd, *J* = 3.7, 1.8 Hz, 2H; H-17), 3.84 – 3.63 (m, 4H; H-4), 1.94 (p, *J* = 4.5 Hz, 2H; H-5). ^{13}C NMR (101 MHz, DMSO-d_6, 300 K) δ 160.72 (C-2), 140.83 (C-16), 135.41 (C-14), 117.31 (C-18), 110.92 (C-17), 54.29 (C-4), 32.02 (C-5). UV-vis (acetonitrile) [λ_{max}/nm, ε/mol^{-1} dm^3 cm^{-1}]: 279, 1.67 × 10^4; 304, 1.40 × 10^4; 334, 1.31 × 10^4; 385, 8.56 × 10^3. IR (KBr pellet, cm^{-1}): HRMS data: 422.097.

2,2'-{(2-hydroxypropane-1,3-diyl)bis[nitrilo(*E*) methylylidene]} bis(pyrrol-1-ido) platinum(II) (2). ^{1}H NMR (400 MHz, DMSO-d_6) δ 8.19 (s, 1H; H-15), 7.20 (s, 2H; H-9), 6.65 (d, *J* = 3.8 Hz, 2H; H-11), 6.17 (dd, *J* = 3.8, 1.9 Hz, 2H; H-10), 5.30 (d, *J* = 4.5 Hz, 1H; H-1)), 4.03 – 3.95 (m, 2H; H-14), 3.82 (d, *J* = 14.0 Hz, 2H; H-14), 3.66 (dd, *J* = 14.1, 7.6 Hz, 2H; H-19). ^{13}C NMR (101 MHz, DMSO-d_6) δ 161.75 (C-15), 140.88 (C-9), 135.52 (C-12), 117.25 (C-11), 110.84 (C-10), 70.47 (C-19), 59.76 (C-14). IR (KBr pellet, cm^{-1}): 3083 (CH, imine), 2990 (CH, H-COH), 2904 (CH, C*H*2-N=CH), 1575 (C=N), 1126(C-O stretch). [λ_{max}/nm, ε/mol^{-1} dm^3 cm^{-1}]: 277, 1.64 × 10^4; 303, 1.91 × 10^4; 313, 2.11 × 10^4; 382, 1.55 × 10^4.

2,2'-{(2,2-dimethylpropane-1,3-diyl)bis[nitrilo(*E*)methylylidene]} bis(pyrrol-1-ido) platinum(II) (3). ^{1}H NMR (400 MHz, DMSO-d_6) δ 8.16 (s, 2H; H-14), 7.21 (s, 2H; H-10), 6.66 (d, *J* = 3.8 Hz, 2H; H-12), 6.18 (dd, *J* = 3.9, 1.9 Hz, 2H; H-11), 3.48 (s, 4H; H-16), 1.05 (s, 6H; H-19). ^{13}C NMR (101 MHz, DMSO-d_6) δ 161.23 (C-14), 140.78 (C-16), 135.44 (C-13), 117.21 (C-12), 110.88 (C-11), 64.52 (C-16), 38.78 (C-17), 23.90 (C-19). IR (KBr pellet, cm^{-1}): 3085 (CH, imine), 3015m(CH, terminal CH3), 2933 (CH2, alkyl), 1652 (C=N). IR (cm^{-1}): 2919m br *v*(CH, imine),1566s br *v*(C=N). [λ_{max}/nm, ε/mol^{-1} dm^3 cm^{-1}]: 277, 1.64 × 10^4; 303, 1.85 × 10^4; 313, 2.06 × 10^4; 382, 1.51 × 10^4.

2,2'-{(1*R*,2*R*)-cyclohexane-1,2-diylbis[nitrilo(*E*)methylylidene]}bis(pyrrol-1-ido)platinum(II) (4). ^{1}H NMR (400 MHz, DMSO-d_6) δ 8.15 (s, 2H; H-8), 7.10 (s, 3H; H-12), 6.64 (d, *J* = 3.8 Hz, 3H; H-10), 6.14 (dd, *J* = 3.9, 1.8 Hz, 3H; H-11), 4.03 – 3.80 (m, 3H; H-6), 2.56 (s, 1H; H-2), 1.75 (d, *J* = 8.7 Hz, 3H; H-1), 1.57 – 1.42 (m, 3H; H-1), 1.34 (t, *J* = 10.3 Hz, 3H). ^{13}C NMR (101 MHz, DMSO-d_6) δ 153.82 (C-8), 145.15 (C-12), 136.74 (C-9), 118.43 (C-10), 110.20 (C-11), 73.88 (C-6), 27.82 (C-1), 24.06 (C-2). IR (cm^{-1}): 2919m br *v*(CH, imine),1566s br *v*(C=N). [λ_{max}/nm, ε/mol^{-1} dm^3 cm^{-1}]: 277, 1.89 × 10^4; 303, 1.73 × 10^4; 316, 1.89 × 10^4; 382, 2.04 × 10^4.

1.3. Fluorescence emission spectroscopy

Appropriate amounts of each of the 5 Pt(II) bis(pyrrolide-immine) chelates were weighed and dissolved into either acetonitrile or DMSO to obtain a 5 x 10^{-3} M stock solution. The fluorescence emission spectrum was achieved by diluting the stock solutions of Pt(II) bis(pyrrolide-immine) chelates to 10 x 10^{-6} M in either acetonitrile or KH_2PO_4 (50 mM, pH 7.5) and were measured on a Cary Eclipse fluorescence spectrophotometer (Varian, Australia) equipped with a 1.0 cm quartz cell and a circulating thermostat bath. Excitation and emission slit widths were fixed at 10 nm. The Pt(II) bis(pyrrolide-immine) chelates were excited at 382 nm and the fluorescence emission was measured from 500 nm to 750 nm.

Fluorescence emission spectroscopy of deoxygenated Pt(II) bis(pyrrolide-immine) chelates.
Pt(II) bis(pyrrolide-immine) chelates (10 x 10^{-6} M) in either acetonitrile or KH_2PO_4 (50 mM, pH 7.5) were bubbled with argon gas for 3 minutes before the fluorescence emission spectrum was measured as described above.

Quantum yields. $\boldsymbol{\Phi F = (As)/Ax)(Fx/Fs)(nx/ns)^2}$ **(1)**

The relative quantum yield (ΦF) of the Pt(II) bis(pyrrolide-imine) chelates were determined by previously reported methods.[4,5] 4 was used as the standard reference as its quantum yield had been previously determined.[2] Using eq. 1 the relative quantum yields for **1**, **2** and **3** were determined in acetonitrile, DCM, dH_2O, when bound to HSA and in the absence of O_2. The Pt(II) chelates were dissolved in the respective solvents and were diluted until their $\lambda^{excitation}$ was between 0.01 and 0.1.
The same samples $\lambda^{emission}$ was then measured between 500 – 750 nm. Each of the samples were measured in triplicates. The area under the fluorescence emission spectrum for the Pt(II)-chelates was measured using Origin Pro 2020 as well was the respective solvents alone. Area of the solvent was subtracted from the area of the Pt(II)-chelate in the solvent as a blank. Finally, we plotted the area of the Pt(II)-chelates against the absorbance of the Pt(II)-chelates to be used in eq. 1 to calculate the relative quantum yield. Fpr eq. 1 Φ_F is the quantum yield, A_s and A_x are the absorbances of the unknown sample and the reference. F_x and F_s are the areas under the fluorescence emission spectrum curves for the unknown samples and the reference sample respectively. Finally, n represent the refractive index of the respective solvents. The refractive indexes for dH_2O, acetonitrile and DCM were 1.333, 1.3441 and 1.4241 respectively.

1.4. TD-DFT simulations

Simulations were performed to calculate optimised structures, vibrational frequencies, and electronic spectra for **1**, **2** and **3** using Gaussian 16 Rev C.01[6] at the CAM-B3LYP[7]/DEF2-QZVP[8] level of theory using the GD3BJ empirical dispersion correction.[9] Structures were also calculated using the SDD basis set.[10] The default geometry convergence criteria in Gaussian 16 were applied. Nuclear shielding tensors were calculated by the default GIAO method[11,12] in Gaussian. Simulations were carried out *in vacuo* and in acetonitrile solvent continua (SCRF PCM method[13]). GaussView 6.0.16[14] was used for preparing input files and data visualization. GaussSum 3.0 was used to visualise electronic spectra and tabulate transition assignments.[15] All geometry-optimised structures were characterised by positive frequency eigenvalues, indicating that true minima were located on the global potential energy surface for each system. Time-dependent DFT (TD-DFT) simulations were carried out using the above method (CAM-B3LYP) and basis sets in Gaussian 16 for all small molecules. Typically, 60 excited singlet states were computed to cover the full spectral range (150–900 nm).

1.5. Cytotoxicity assays

Cytotoxicity assays were performed to assess the changes in cell viability following treatment of NMuMG (nontransformed mouse mammary gland epithelial cells) and MCF7 (human epithelial breast cancer cells) with the Pt(II) complexes. The MTT assay is a colorimetric assay used to assess cell viability based on the reduction of the yellow 3-(4,5-Dimethylthiazol-z-yl)-2,5 diphenyltetrazolium bromide

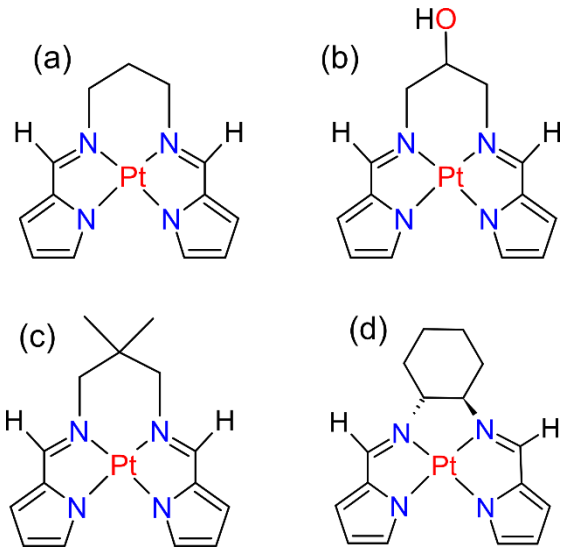
(MTT) to its purple insoluble formazan crystals in the mitochondria of viable cells. Cells were seeded in a 96-well plate at a density of 5 000 cells per well. After incubation at 37°C for 24 hours, cells were treated with chelates at varying concentrations for 24 hours at 37°C. Following incubation, the cells were exposed to UV light for 20 minutes and control cells were exposed to visible light. 5 µL of MTT (Sigma-Aldrich, UK) at a concentration of 5 mg/mL was added to each well, followed by a 3-hour incubation at 37°C. Formazan crystals were dissolved in solubilizing solution overnight at 37°C and optical density was measured at a wavelength of 570 nm using a Multiskan GO Microplate Reader (Thermo Fisher Scientific. USA). Percentage cell viability was calculated relative to the untreated control.

1.6. Fluorescent microscopy

Intracellular localization and fluorescence were determined using fluorescent microscopy. NMuMG cells were seeded at a density of 20 000 cells per well onto 12 mm glass coverslips in a 24-well plate. After incubation at 37°C for 24 hours, cells were treated with Pt(II) complexes with the addition of 10 µM HSA, or dH_2O, for the control for 2 hours at 37°C, followed by fixation with 4% formaldehyde for 10 minutes. Nuclei were stained with NucRed™ Dead (Thermo Fisher Scientific, USA). Cells were visualised using the Floid™ Cell Imaging System (Thermo Fisher Scientific, USA).

2. Figures and Tables

2.1. General characterization data



Scheme S1 . Structures of the bis(pyrrolide-imine) chelates synthesised. (a) 2,2'-{propane-1,3-diylbis[nitrilo(E)methylylidene]}bis(pyrrol-1-ido) (**1**), (b) 2,2'-{(2-hydroxypropane-1,3-diyl)bis[nitrilo(E) methylylidene]} bis(pyrrol-1-ido) (**2**), (c) 2,2'-{(2,2-dimethylpropane-1,3-diyl)bis[nitrilo(E)methylylidene]} bis(pyrrol-1-ido) (**3**) , (d) 2,2'-{(1R,2R)-cyclohexane-1,2-diylbis[nitrilo(E)methylylidene]}bis(pyrrol-1-ido) (**4**).

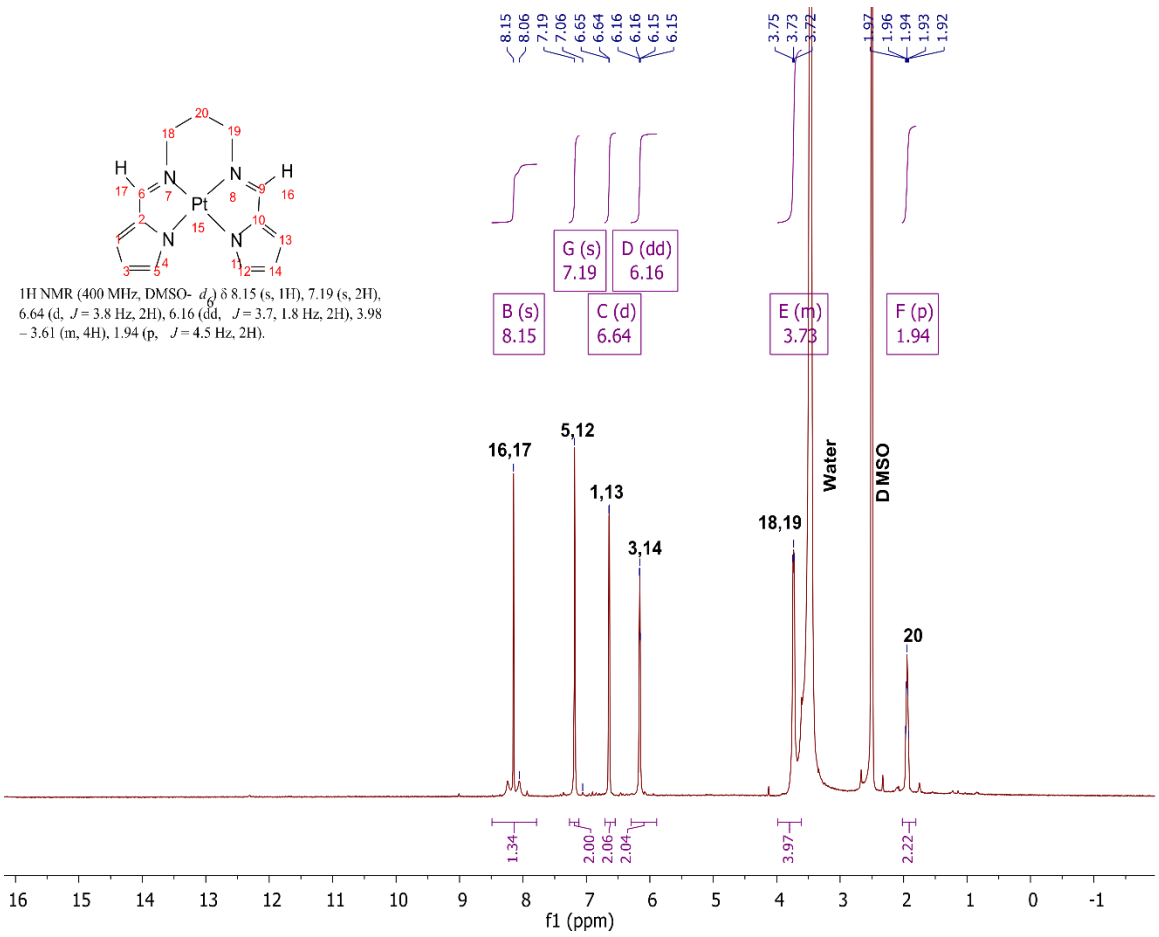


Fig. S1. 400 MHz 1H NMR spectrum of **1** recorded in DMSO-d6 at 300 K. This compound is known3 the spectral data here briefly confirm the structure of the compound and its purity.

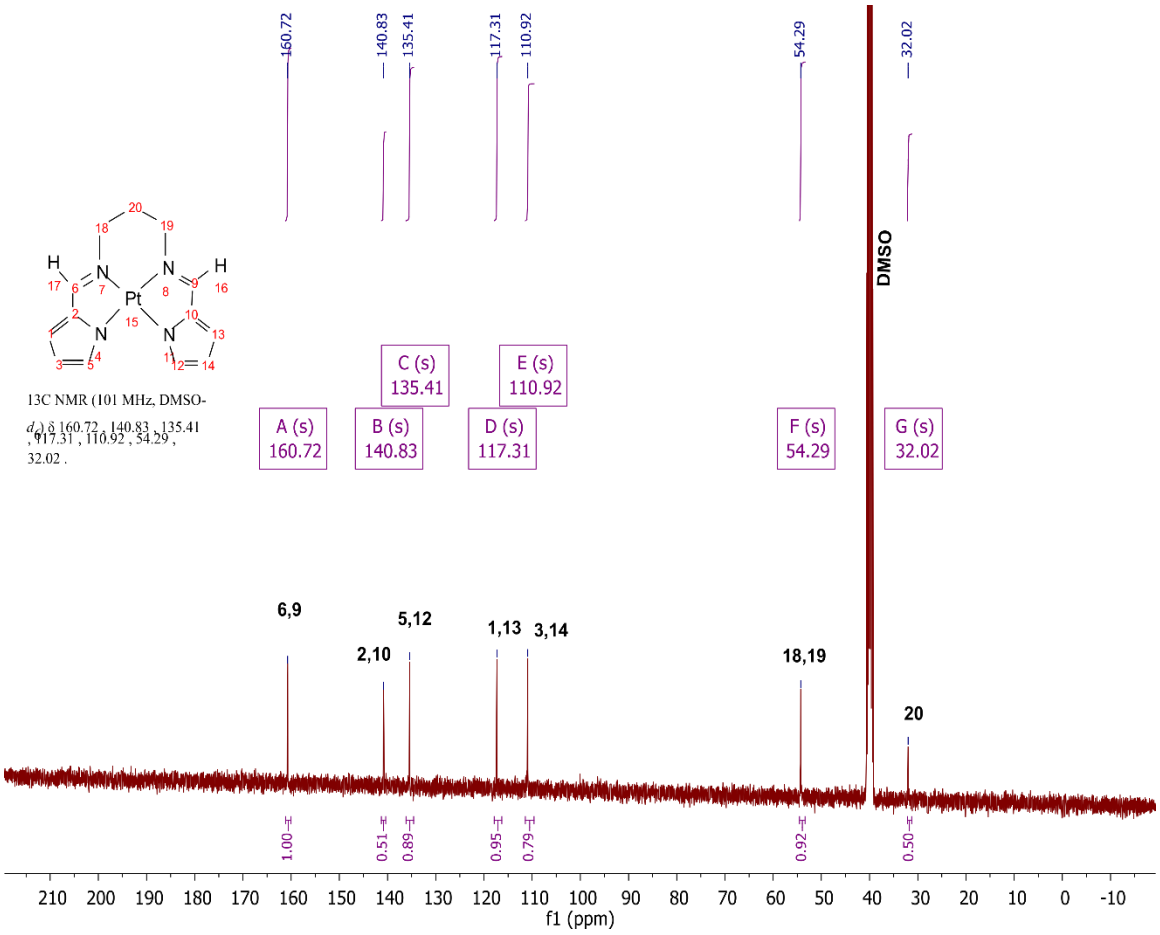


Fig. S2 101 MHz ^{13}C NMR spectrum of **2** recorded in DMSO-*d*6 at 300 K.

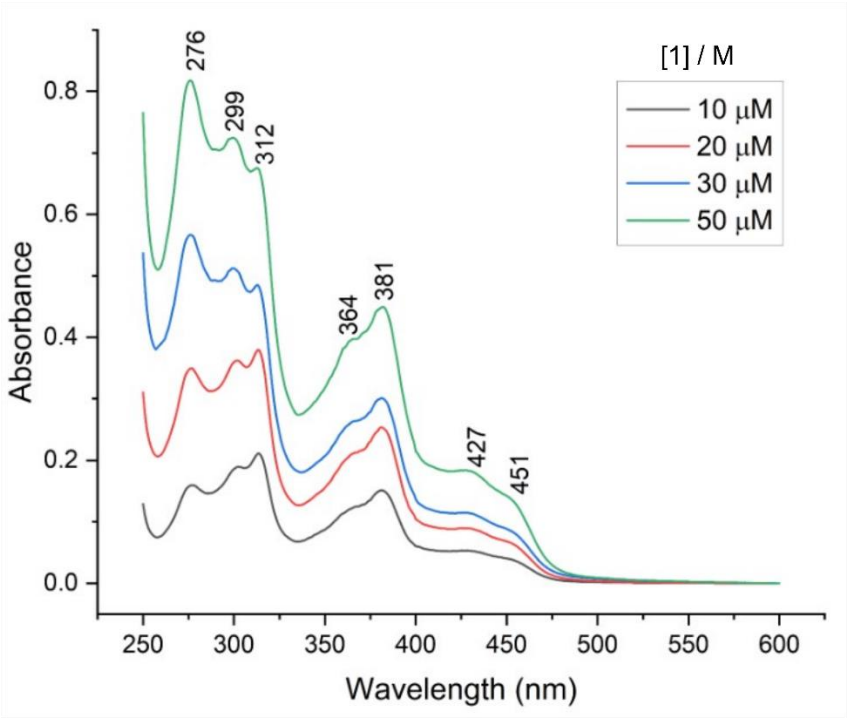


Fig. S3. UV-visible spectrum of **1** recorded in CH_3CN at 295 K as a function of concentration.

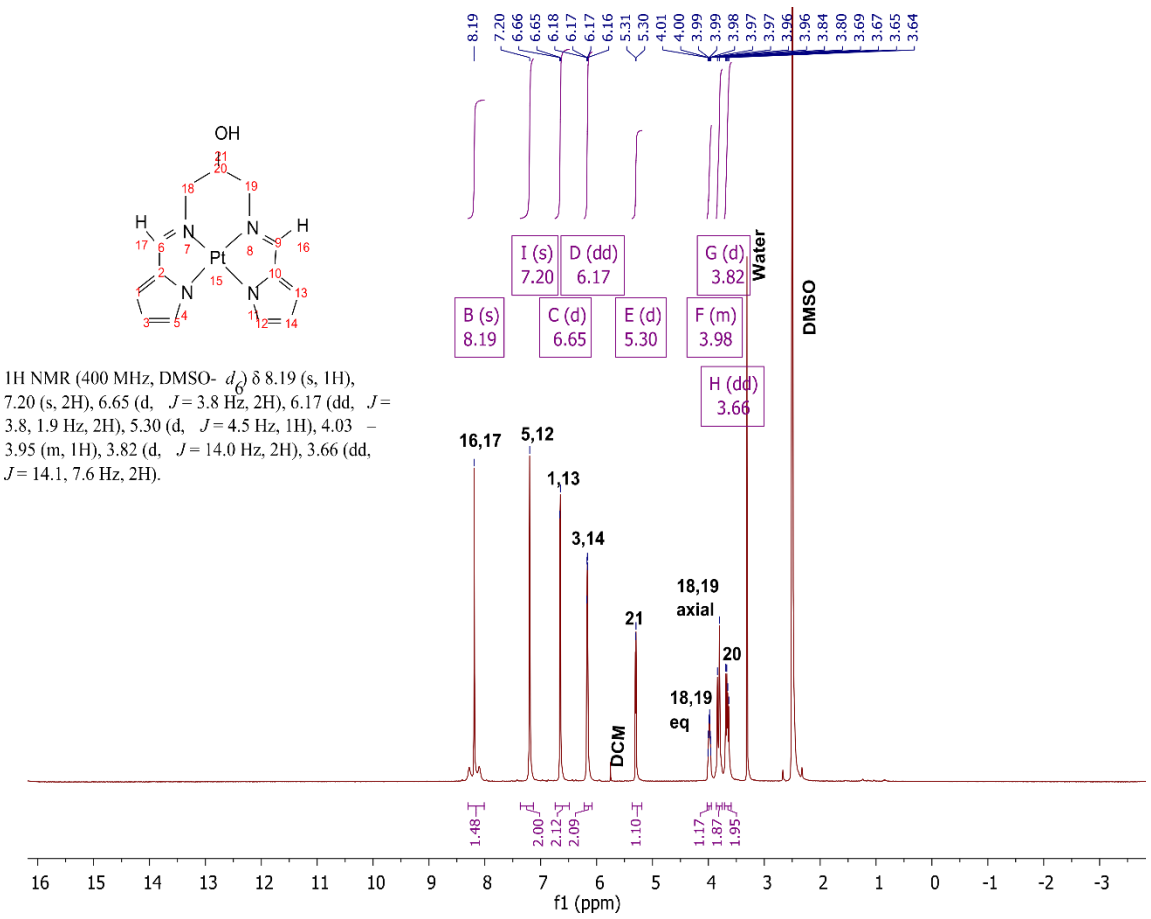


Fig. S4 400 MHz ^{1}H NMR spectrum of **2** recorded in DMSO-*d*6 at 300 K.

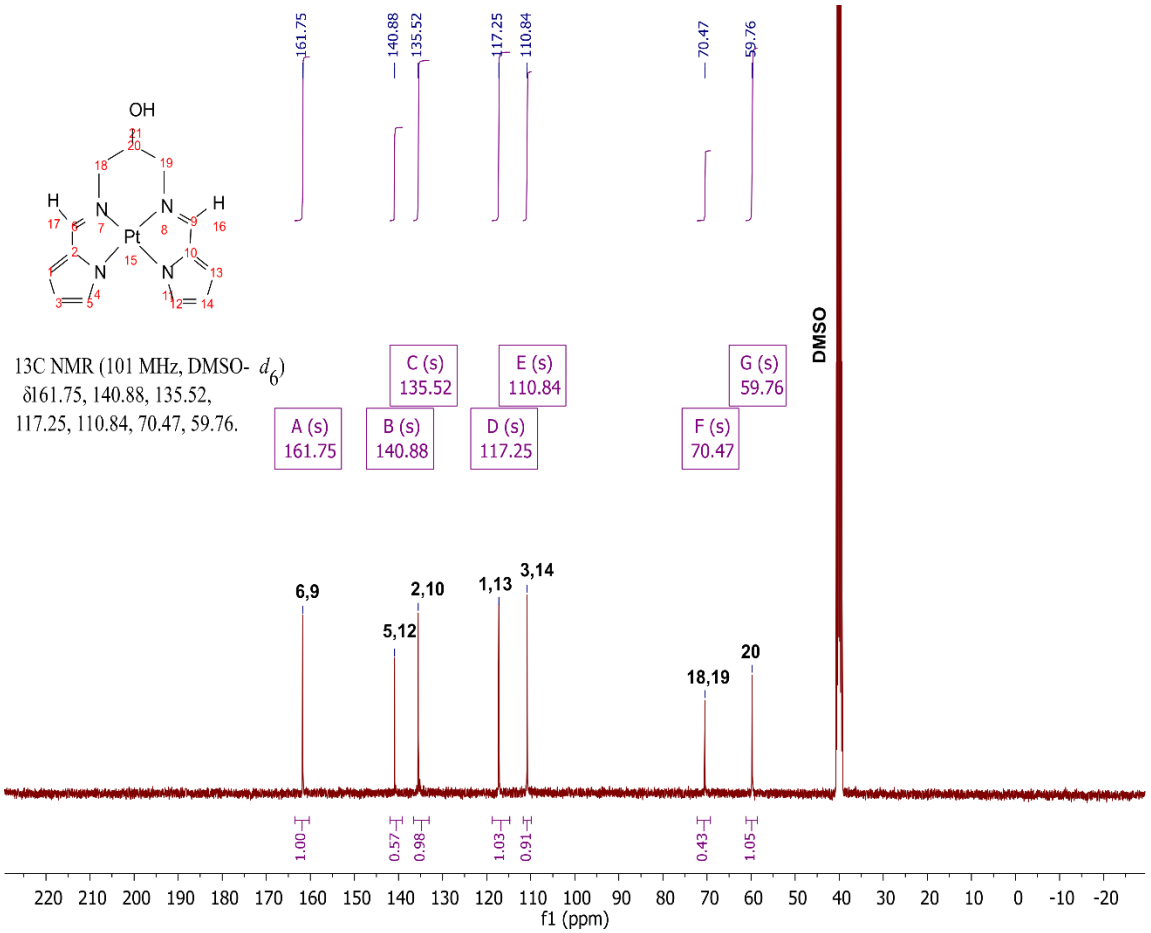


Fig. S5 101 MHz ^{13}C NMR spectrum of **2** recorded in DMSO-*d*6 at 300 K.

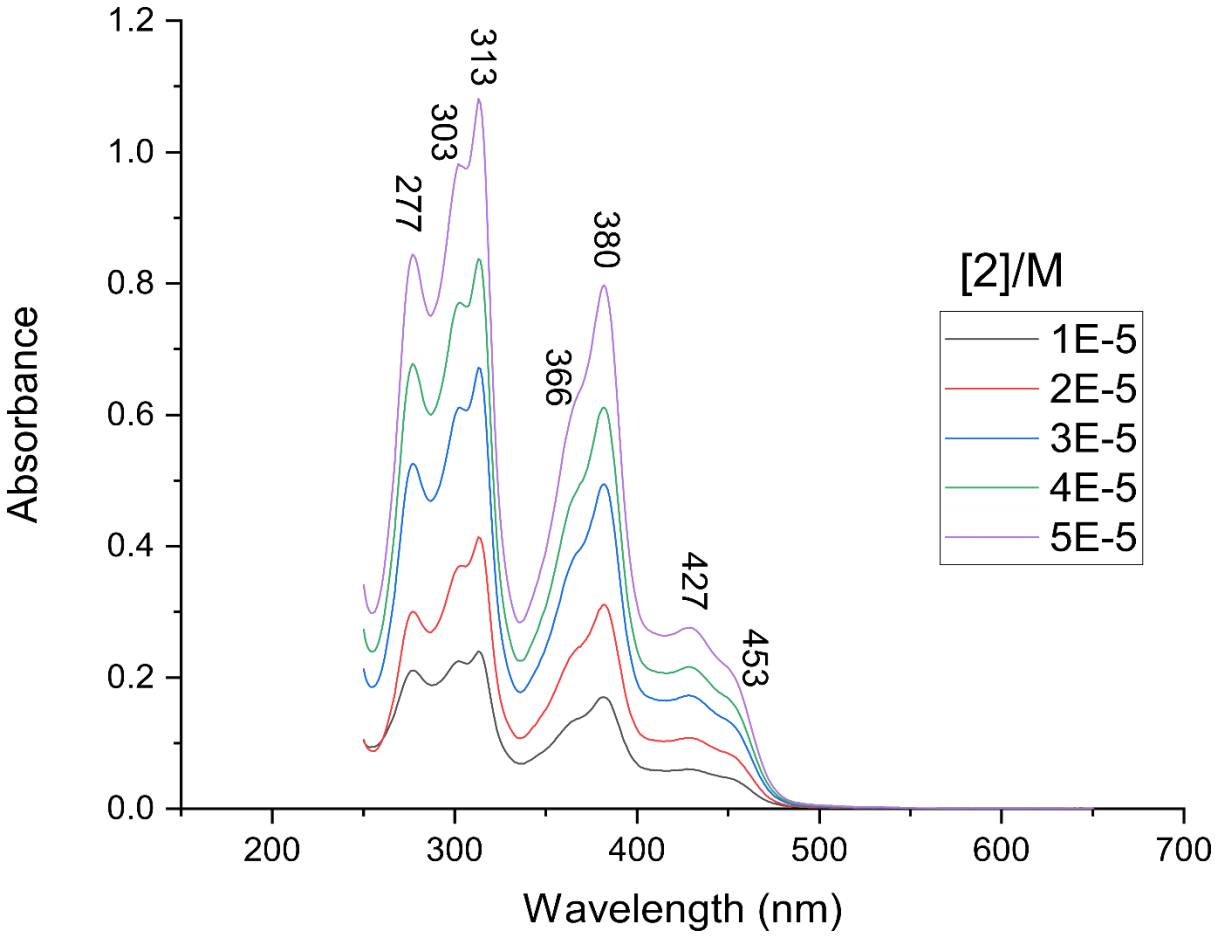


Fig. S6 UV-visible spectrum of **2** recorded in acetonitrile at 295 K as a function of concentration. The molar absorptivities of key band maximum are reported in the main paper and were determined from the slopes of Beer- Lambert law plots at the relevant band maxima.

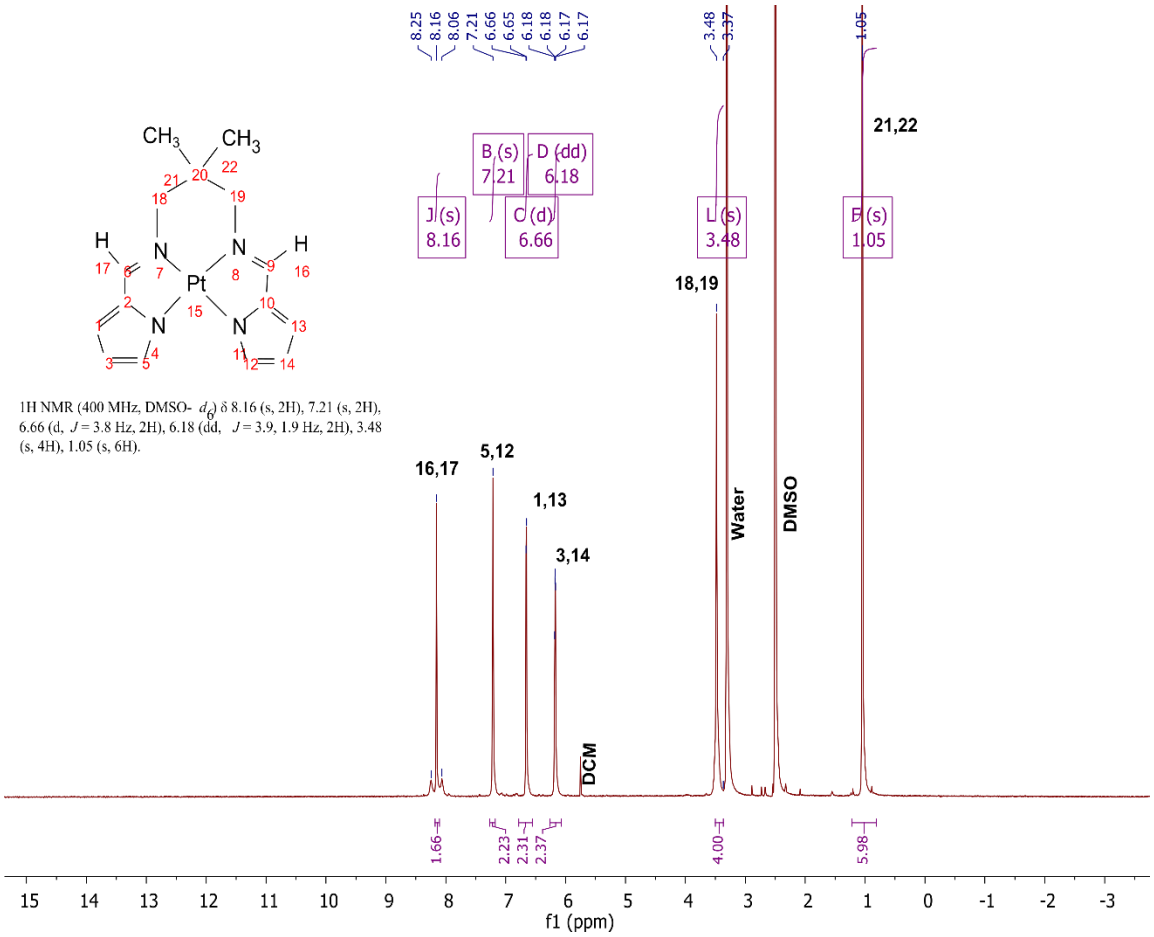


Fig. S7 400 MHz ^{1}H NMR spectrum of **3** recorded in DMSO-*d*6 at 300 K.

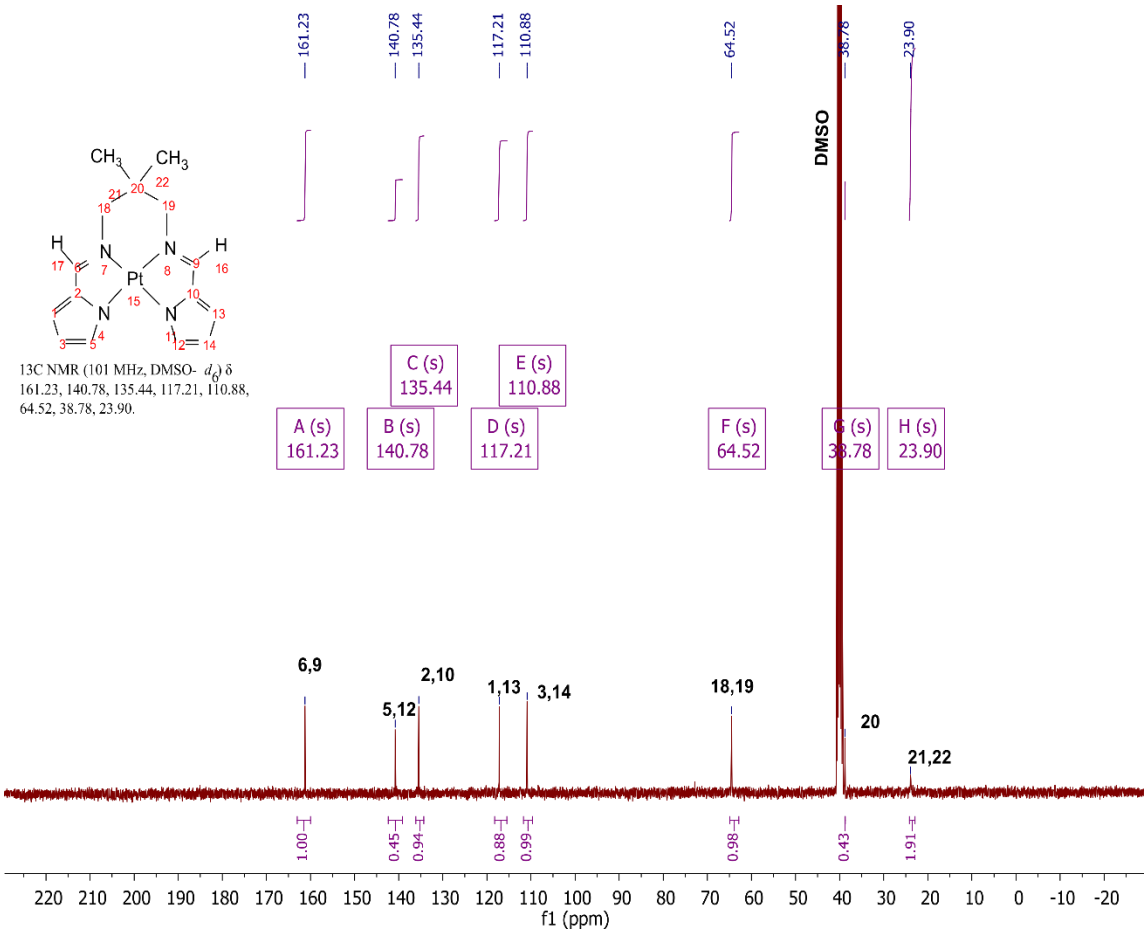


Fig. S8 101 MHz ^{13}C NMR spectrum of **3** recorded in DMSO-*d*6 at 300 K.

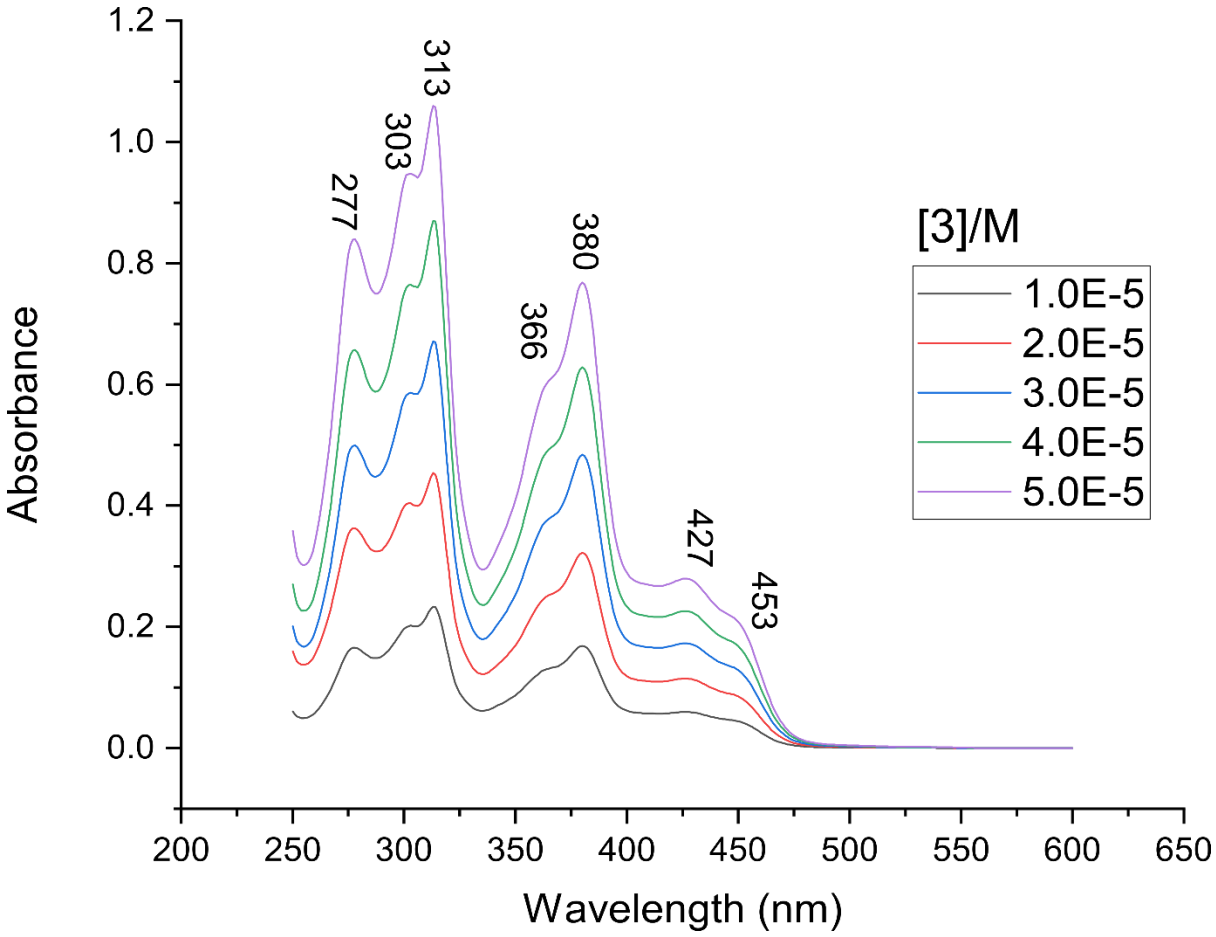


Fig. S9 UV-visible spectrum of **3** recorded in acetonitrile at 295 K as a function of concentration. The molar absorptivities of key band maximum are reported in the main paper and were determined from the slopes of Beer- Lambert law plots at the relevant band maxima.

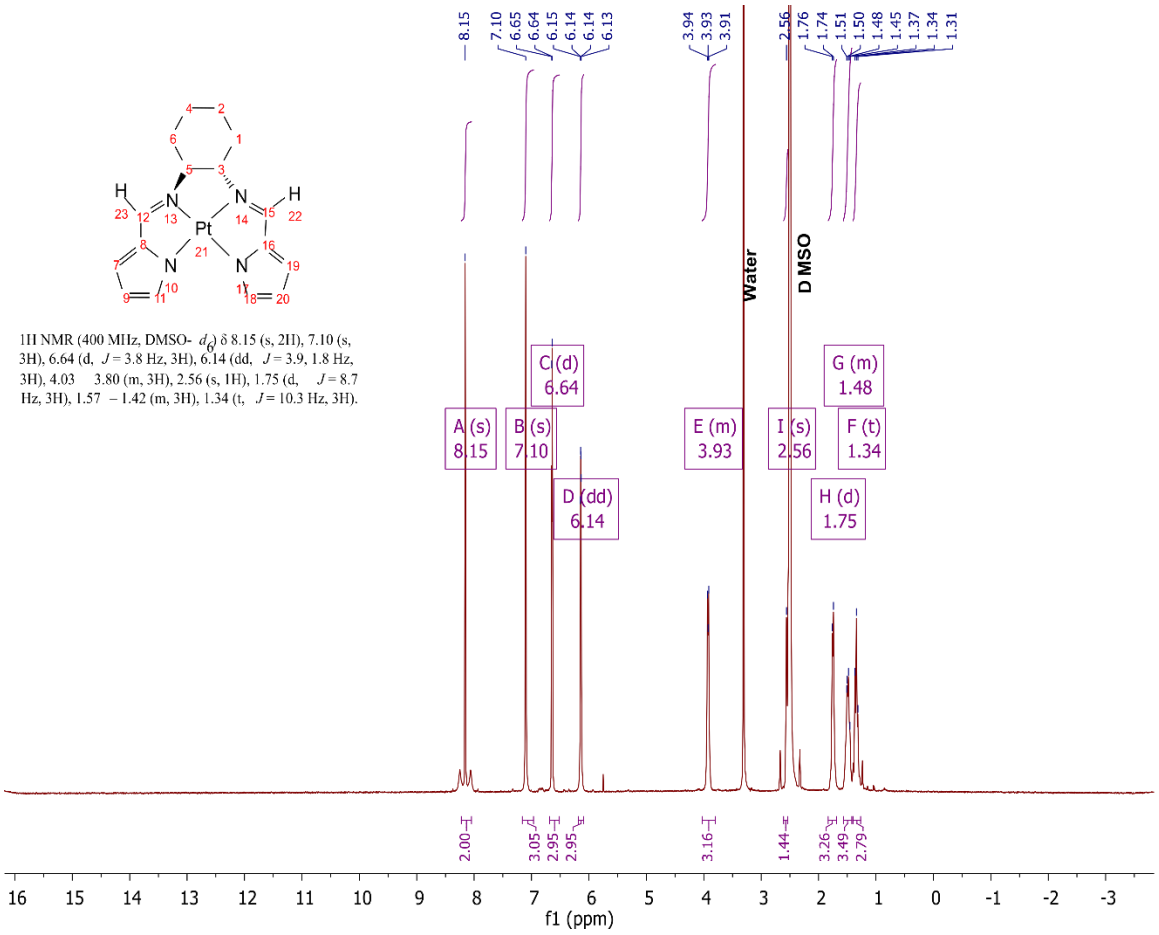


Fig. S10 400 MHz ^{1}H NMR spectrum of **4** recorded in DMSO-*d*6 at 300 K. This compound is known[2] the spectral data here briefly confirm the structure of the compound and its purity.

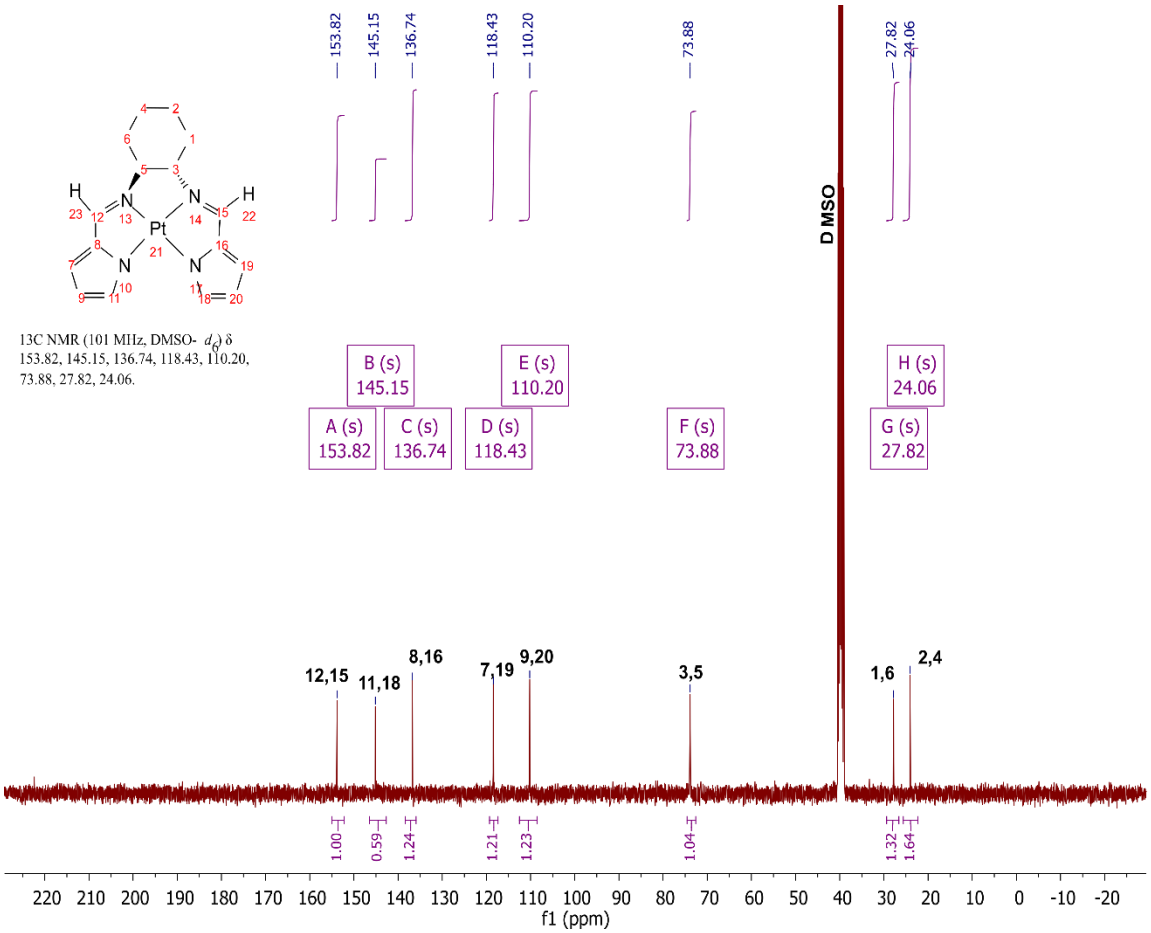
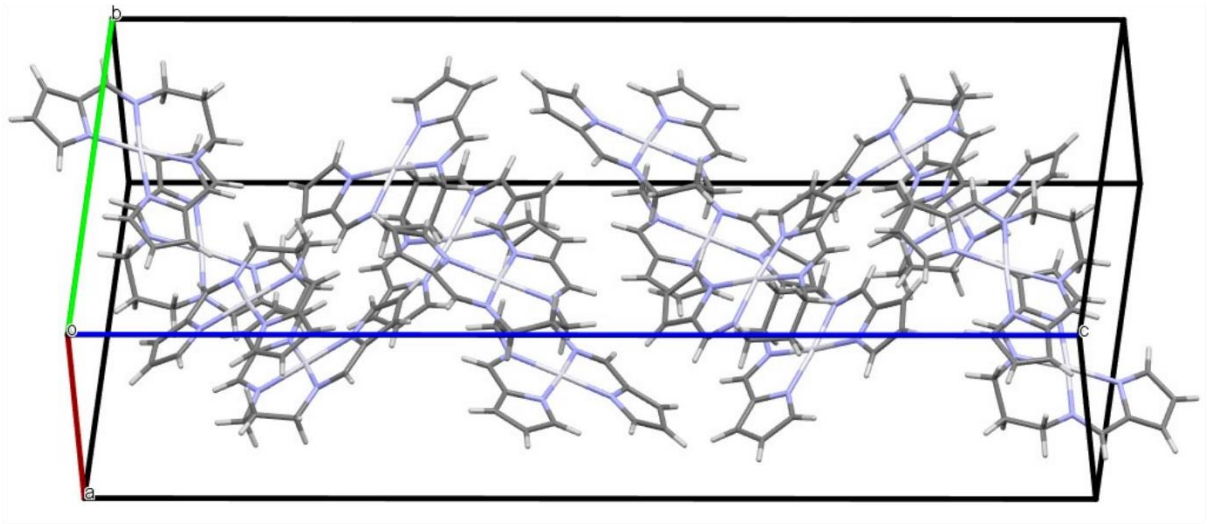


Fig. S11 101 MHz ^{13}C NMR spectrum of **4** recorded in DMSO-*d*6 at 300 K.

2.2. X-ray crystallography

(a)



(b)

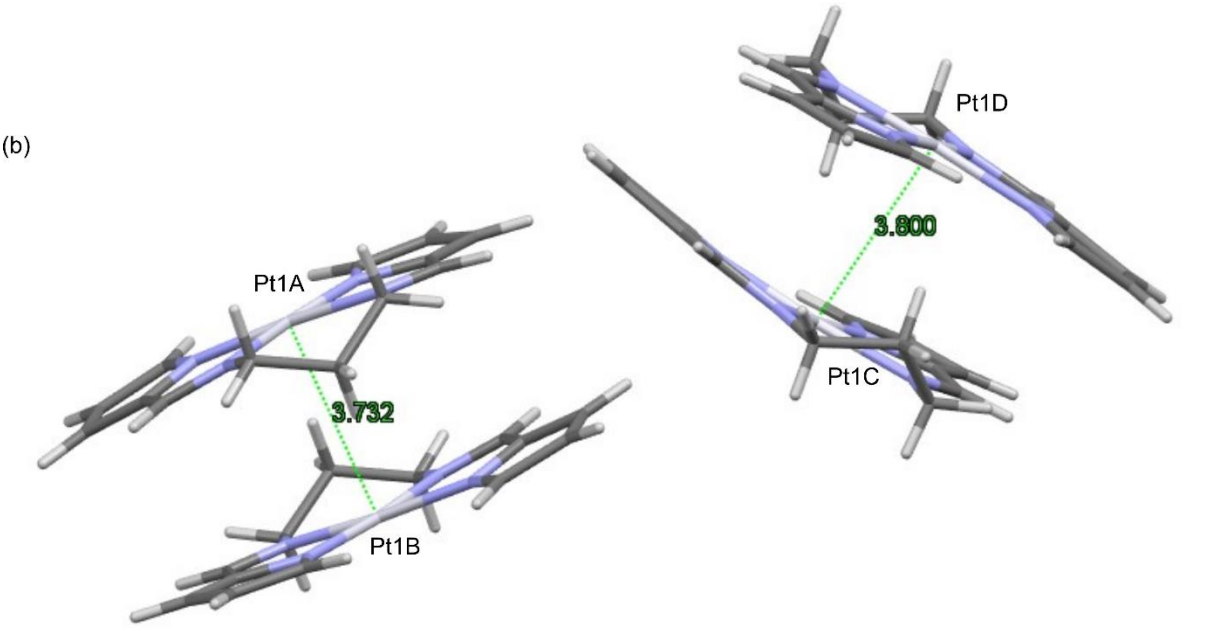


Fig. S12 (a) Unit cell contents for the X-ray structures of **1** (space group $P2_1/c$) determined at 173.15 K. (b) ASU of **1** consisting of four identical molecules with two pairs of intermolecular π – stacking arrangements. The Pt-Pt distances was measured between the two pairs of the Pt(II) bis(Pyrollide-imine) metal chelate.

2.3. Steady state absorbance and fluorescence spectroscopy Pt(II) chelates binding to HSA.

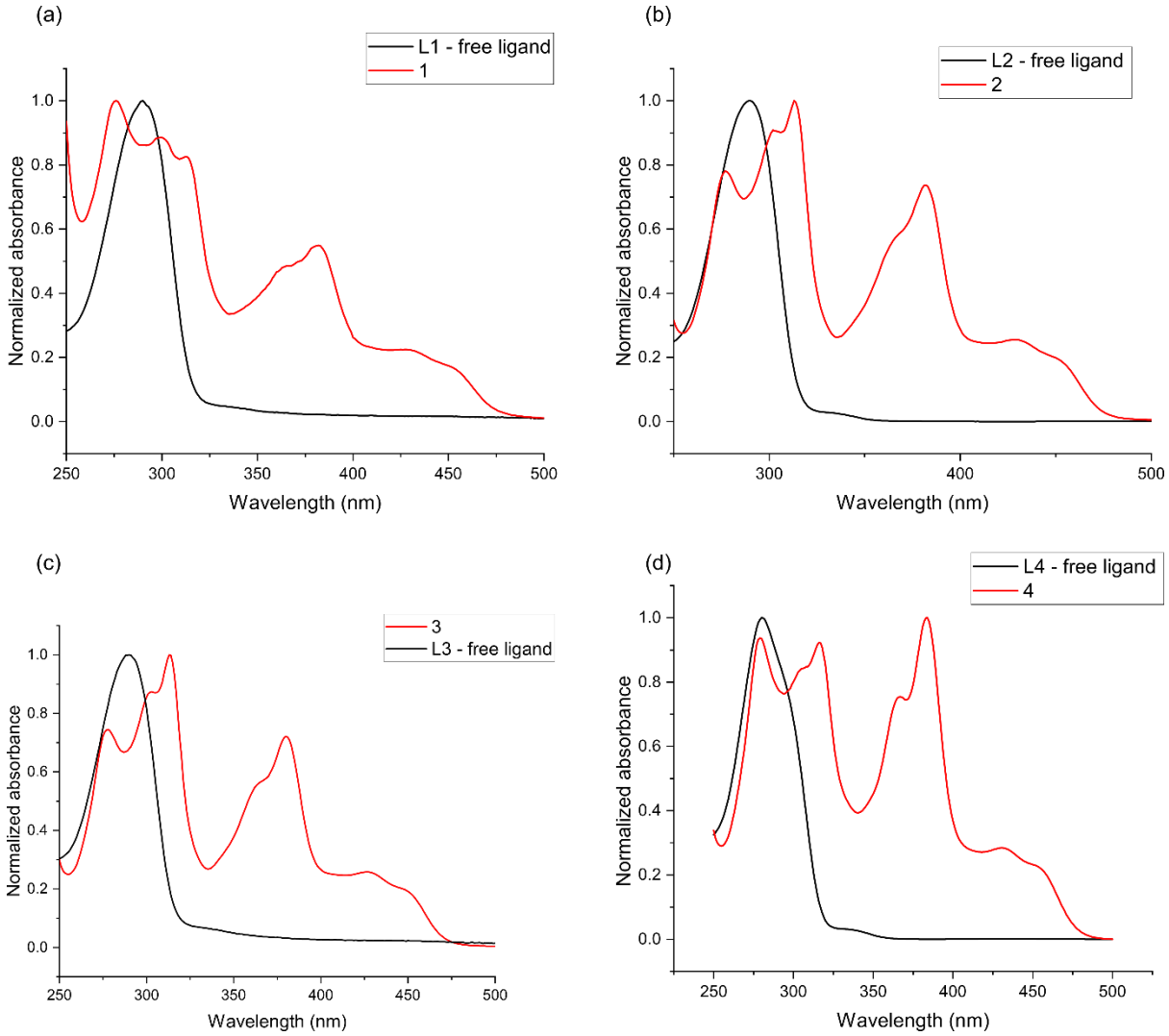


Fig. S13 Overlayed UV-vis absorption spectra of Pt(II) bis (pyrrolide-imine) chelates 1–4 and their corresponding free ligands. The free ligands are represented by the solid black line and has a single absorbance peak in the UV region. The corresponding Pt(II) bis (pyrrolide-imine) chelates are represented by the solid red line and have several absorption peaks in the UV and visible region.

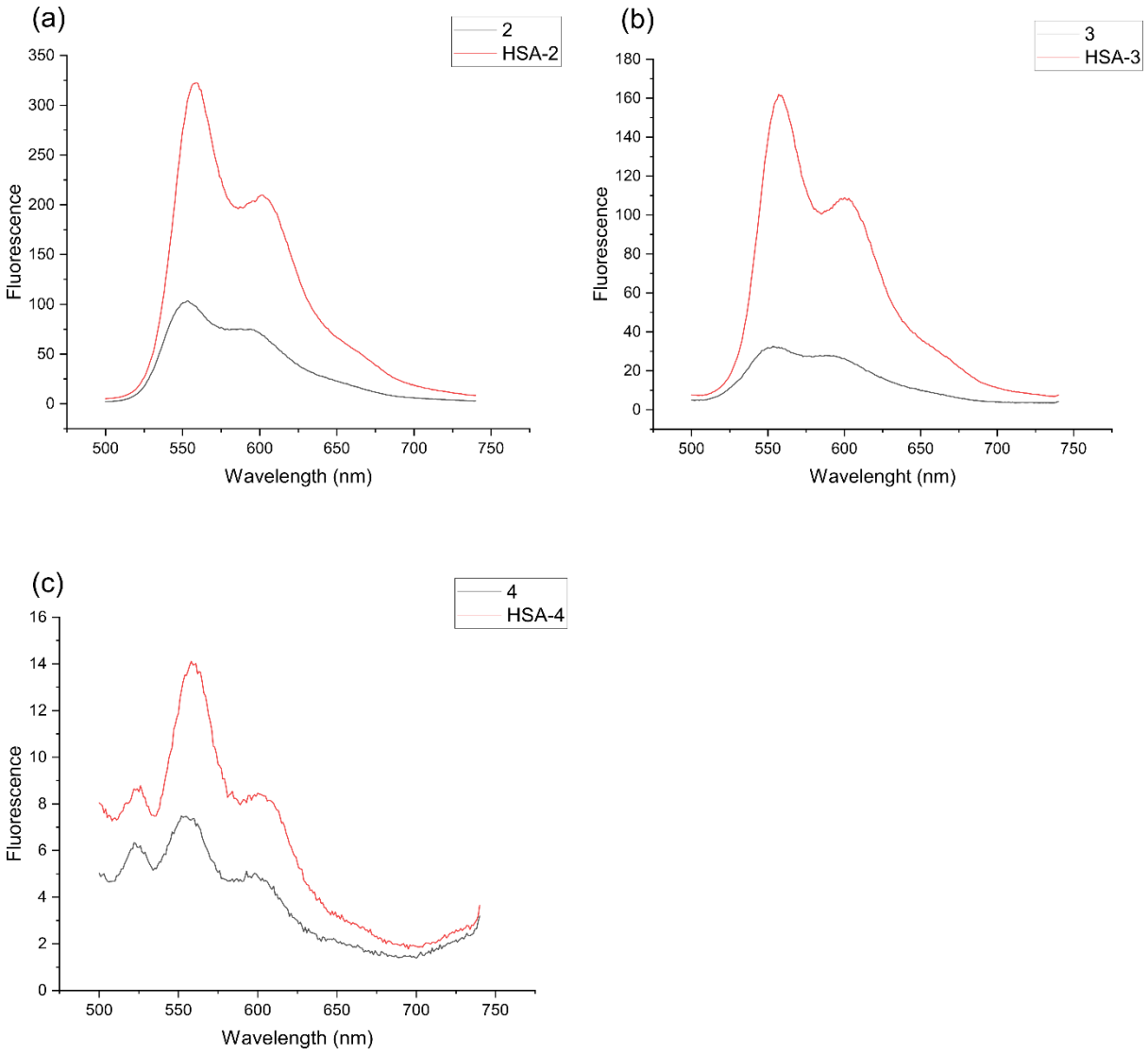


Fig. S14 Fluorescence emission spectrum of four Pt(II) bis(pyrrolide-imine) chelates (a) **2**, (b) **3**, and **4** represented by solid black line. The Pt(II) bis(pyrollide-imine) chelates were then incubated with HSA and the enhanced fluorescence emission spectrum was measured of (a) **2**···HSA, (b) **3**···HSA, (c) and **4**···HSA represented by solid red line. The relevant concentrations of the Pt(II) bis(pyrrolide-imine) chelates and HSA were 5 μM and were measured in KH_2PO_4 (50 mM, pH 7.5). The excitation and emission wavelengths for the Pt(II) bis(pyrollide-imine) chelates were λ^{ex} = 382 nm and $\lambda^{emission}$ was measured from 500 – 740 nm.

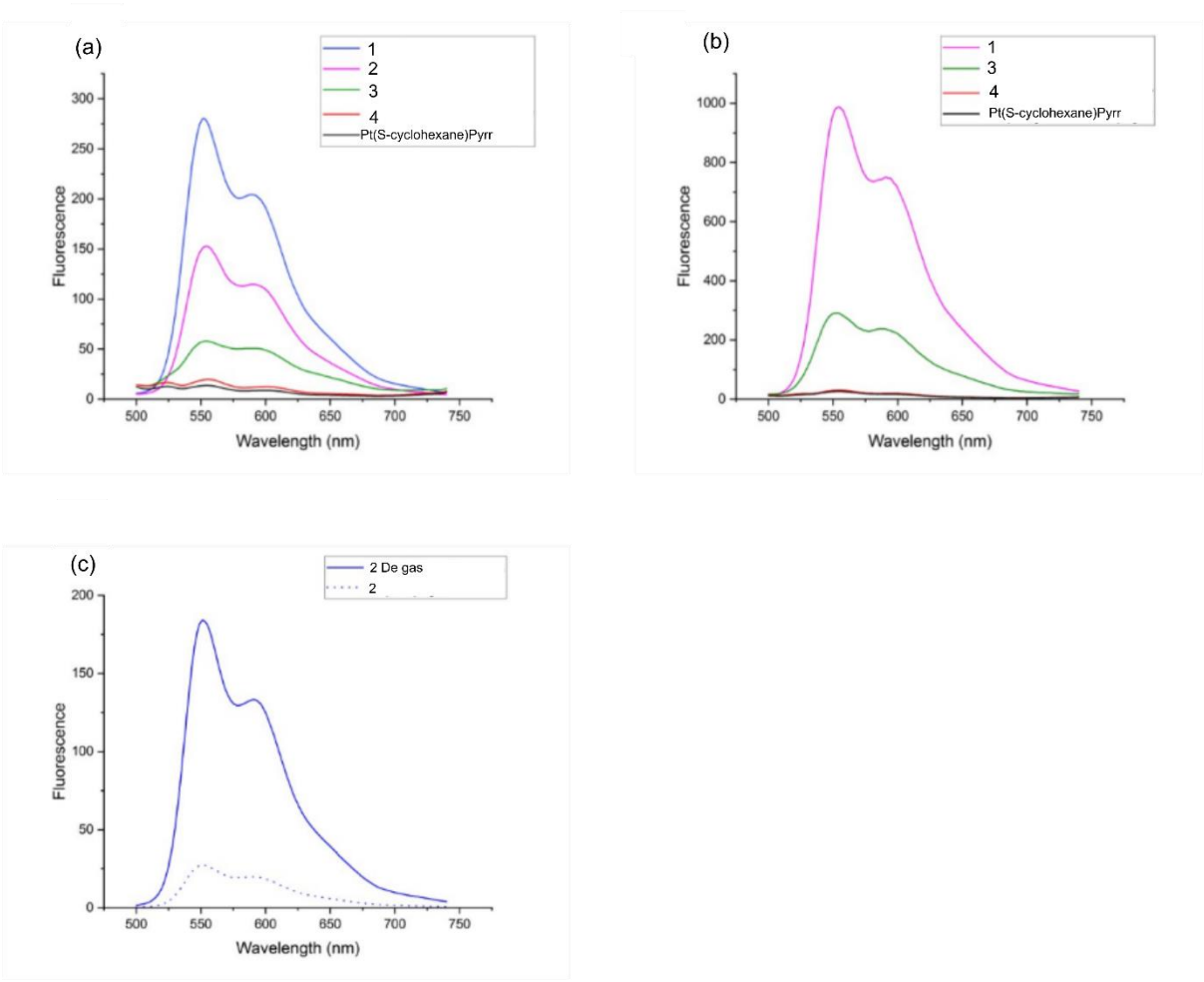


Fig. S15 (a) Fluorescence emission spectra of the five Pt(II) bis(pyrrolide-imine) chelates (10 µM) in KH_2PO_4 buffer (50 mM, pH 7.5) ($\lambda_{ex}^{382\ nm}$). (b) Fluorescence emission spectra of **1**,**3**,**4** and Pt(cyclohexane)Pyrr (10 µM) in deoxygenated KH_2PO_4 buffer (50 mM, pH 7.5) ($\lambda_{ex}^{382\ nm}$) molecular $^3O_2$ was removed by bubbling the solution with $Ar_{(g)}$ for 3 min. (c) The fluorescence emission spectrum of **2** went beyond the scale of the fluorescence-spectrophotometer. Therefore, the slit width had to be changed to show the increase in fluoresce intensity of Pt(OH)Pyrr when O_2 was removed with $Ar_{(g)}$. This perfectly highlights the significant enhancement in luminescence of **2** in an aqueous medium.

2.4. Quantum yields

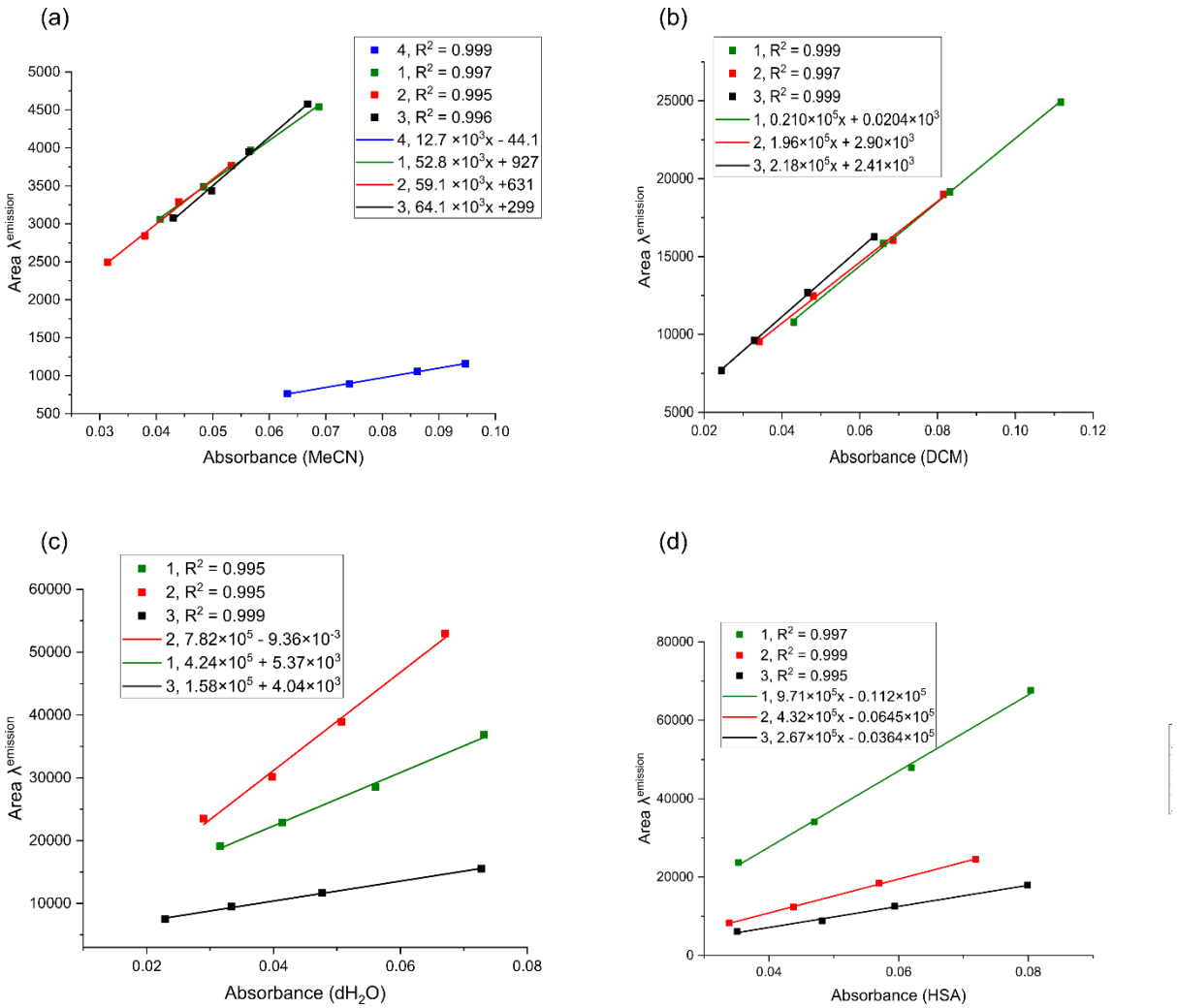


Fig. S16 Calibration curves based on the absorbance of the Pt(II) bis(pyrolide-imine) chelates plotted against the area under the fluorescence emission spectra of the respective Pt(II) bis(pyrolide-imine) chelates. The calibration curves of **1**, **2** and **3** were plotted to obtain the gradient to input into eq. 1. Using the eq. 1 the Φ_F was calculated in (a) acetonitrile, (b) DCM, (c) dH_2O and (d) HSA. **4** was used as the standard reference as its Φ_F had been reported previously[2]. Figures are representative of a single sample calculation; all data was performed in triplicates and the respective Φ_F are reported in Table S6 and S7.

2.5. TD-DFT simulations

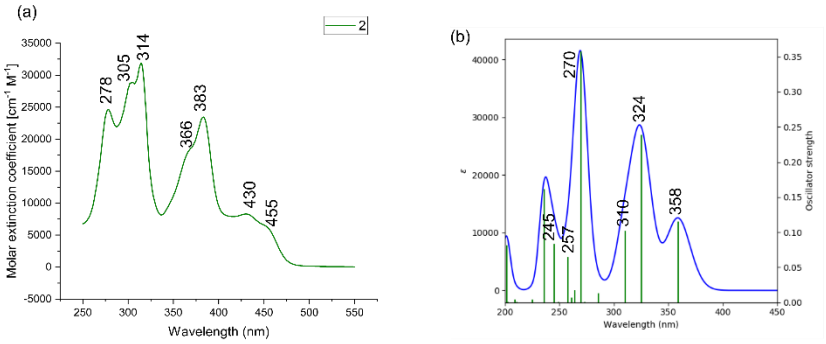


Fig. S17 (a) Experimental and (b) DFT calculated (inset) electronic absorption spectra of **2** in acetonitrile. The absorption maxima (λ_{max}) are indicated for the experimental spectrum at 430, 383, 366, 314, 305 and 278 nm. The absorption envelope for the DFT calculated envelope spectrum of **2** is plotted from 200 – 450 nm and is plotted with a band width of 2000 cm^{-1} (full width at half maximum intensity, FWHM).

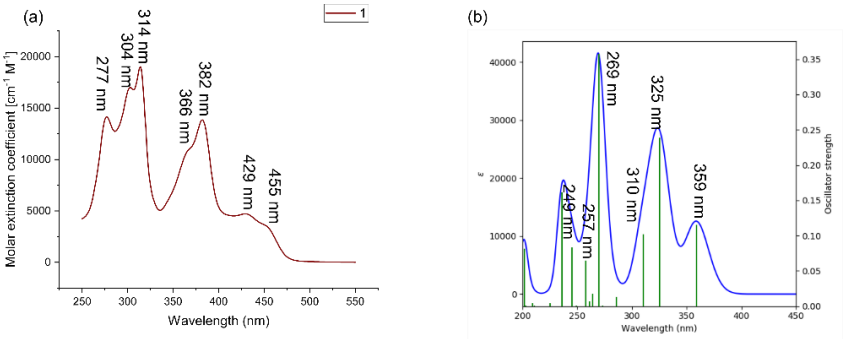


Fig. S18 (a) Experimental and (b) DFT calculated (inset) electronic absorption spectra of **3** in acetonitrile. The absorption maxima (λ_{max}) are indicated for the experimental spectrum at 430, 383, 366, 314, 305 and 278 nm. The absorption envelope for the DFT calculated envelope spectrum of **3** is plotted from 200 – 450 nm and is plotted with a band width of 2000 cm^{-1} (full width at half maximum intensity, FWHM).

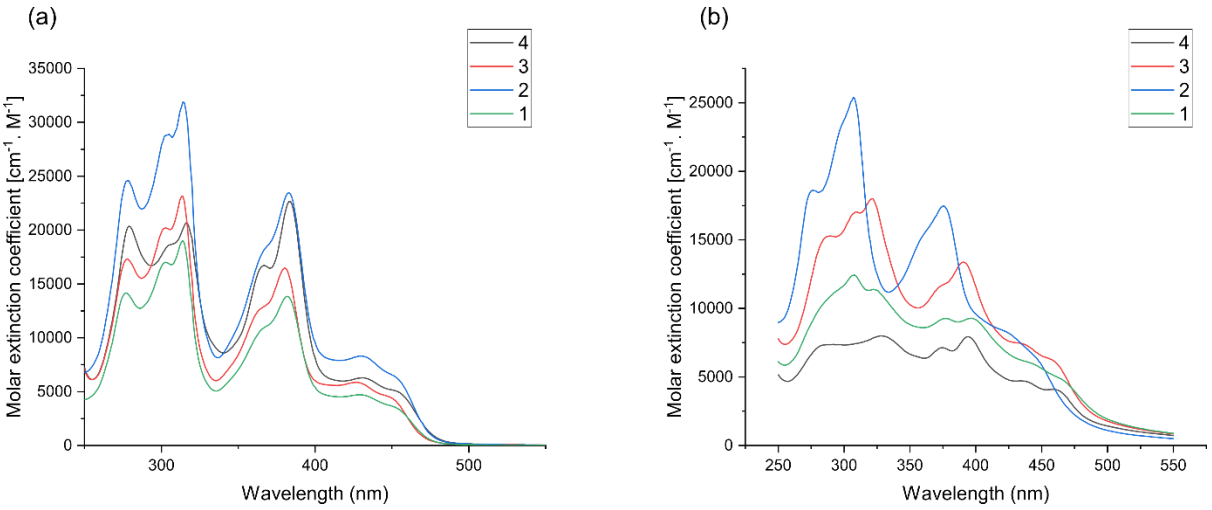


Fig. 19 UV-vis spectrum of (a) (**1**) green, (**2**) blue, (**3**) red and (**4**) black in acetonitrile (50 x 10^{-6} M) and (b) (**1**) green, (**2**) blue, (**3**) red and (**4**) black in dH_2O (50 x 10^{-6} M).

2.6. Fluorescence microscopy

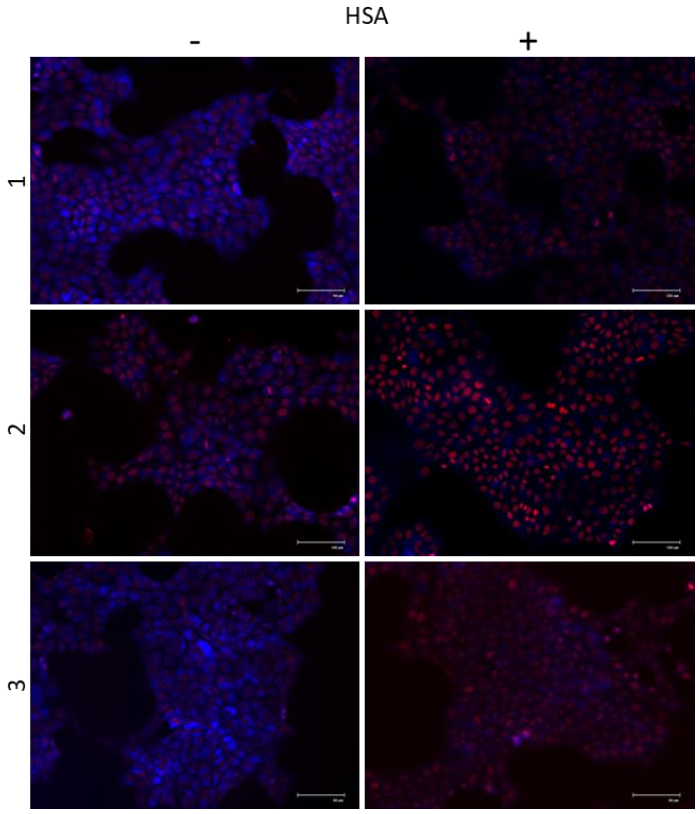


Fig. S20 Representative images of intracellular fluorescence of Pt(II) complexes **1-3** in NMuMG cells with (HSA+) and without (HSA-) the addition of 10 µM HSA, visualised using the Floid™ Cell Imaging System (Thermo Fisher Scientific, USA). Nuclei were stained red using NucRed™ Dead (Thermo Fisher Scientific, USA) and the blue light emission of the complexed in the cell was captured.

2.7. Tables

Table S1. Crystal data and X-ray structure refinement details for Pt(II) bis(pyrrolide-imine) chelate **1**.

Identification code	mo_21ov_ss_PtPrPyrr_2_0m
Empirical formula	$C_{13}H_{14}N_4Pt$
Formula weight	421.37
Temperature/K	173.0
Crystal system	monoclinic
Space group	$P2_1/c$
a/Å	8.0540(3)
b/Å	16.8279(5)
c/Å	36.8486(12)
α/°	90
β/°	90.7200(10)
γ/°	90
Volume/Å^3	4993.8(3)
Z	16
ρ_{calc}g/cm^3	2.242
μ/mm^{-1}	11.226
F(000)	3168.0
Crystal size/mm^3	0.237 × 0.146 × 0.136
Radiation	MoKα (λ = 0.71073)
2Θ range for data collection/°	5.058 to 61.438
Index ranges	$-11 \leq h \leq 11$, $-22 \leq k \leq 24$, $-52 \leq l \leq 52$
Reflections collected	163404
Independent reflections	15408 [R_{int} = 0.0359, R_{sigma} = 0.0208]
Data/restraints/parameters	15408/0/650
Goodness-of-fit on F^2	1.307
Final R indexes [I>=2σ (I)]	R_1 = 0.0333, wR_2 = 0.0577
Final R indexes [all data]	R_1 = 0.0381, wR_2 = 0.0587
Largest diff. peak/hole / e Å^{-3}	1.94/-2.43

Table S2. Selected mean crystallographic and calculated structural and conformational parameters for compounds **1**.

	1	
	XRD	**DFT**
Bond distances (Å)		
Pt-$N_{pyrrole}$	2.013 (4)	2,027
Pt-N_{imine}	2.003 (4)	2,022
C=N	1.294 (4)	1,29
Bond angles (°)		
$N_{pyrrole}$-Pt-$N_{pyrrole}$	103.92 (16)	104,82
N_{imine}-Pt-N_{imine}	96.29 (17)	96,11
cis-$N_{pyrrole}$-Pt-N_{imine}	79.83 (16)	79,51
trans-$N_{pyrrole}$-Pt-N_{immine}	175.3 (16)	175,4
C-$N_{pyrrole}$-C	106.81 (4)	107,47
C-N_{immine}-C	121.06 (4)	121,69

Table S3. Selected excited singlet states of TD-DFT calculations for complex **1**.

Excited states	Energy/ eV (λ nm)	Wavelength (nm)	Oscillator strength		Major contributions (%)
1	3,4549	358	0.115	Singlet-A	HOMO->LUMO (87%) H-3->LUMO (4%), H-2->L+1 (4%)
2	3,8122	325	0.238	Singlet-A	H-1->LUMO (78%), HOMO->L+1 (17%)
3	3,9981	309	0.1061	Singlet-A	H-2->LUMO (56%), H-1->LUMO (10%), HOMO->L+1 (27%) H-3->L+1 (4%)
4	4,3347	310	0.1025	Singlet-A	H-4->LUMO (94%) H-3->LUMO (5%)
5	4,534	286	0.013	Singlet-A	H-5->L+2 (14%), H-3->L+2 (14%), HOMO->L+2 (64%)
6	4,599	273	0.0002	Singlet-A	H-3->LUMO (33%), H-1->L+1 (53%) H-4->LUMO (2%), H-2->L+1 (8%)
7	37093.4381897	269	0.3576	Singlet-A	H-4->L+2 (56%), H-2->LUMO (18%), HOMO->L+1 (10%) H-3->L+1 (3%), H-3->L+2 (2%), H-1->LUMO (4%)
8	37876.6025403	264	0.0172	Singlet-A	H-7->L+2 (14%), H-2->L+2 (26%), H-1->L+2 (53%)
9	38312.9484864	261	0.0069	Singlet-A	H-4->L+2 (31%), H-2->LUMO (20%), HOMO->L+1 (34%) H-5->L+1 (3%), H-3->L+1 (3%), H-1->LUMO (2%)

Table S4. Selected excited singlet states of TD-DFT calculations for complex 2.

Excited states	Energy/ eV (λ nm)	Wavelength (nm)	Oscillator strength		Major contributions (%)
1	3,4631	358	0.1163	Singlet-A	HOMO->LUMO (86%) H-3->LUMO (4%), H-2->L+1 (4%)
2	3,8112	324	0.2345	Singlet-A	H-1->LUMO (75%), HOMO->L+1 (19%)
3	3,9897	310	0.1042	Singlet-A	H-2->LUMO (53%), H-1->LUMO (12%), HOMO->L+1 (28%) H-3->L+1 (4%)
4	4,3064	287	0.0113	Singlet-A	H-4->LUMO (97%) H-3->LUMO (2%)
5	4,527	273	0.0005	Singlet-A	H-5->L+2 (12%), H-3->L+2 (13%), HOMO->L+2 (61%)
6	4,5794	270	0.3445	Singlet-A	H-3->LUMO (31%), H-1->L+1 (56%) H-2->L+1 (8%)
7	4,6797	264	0.0122	Singlet-A	H-4->L+2 (60%), H-2->LUMO (16%) H-3->L+1 (2%), H-1->LUMO (4%), HOMO->L+1 (7%)

Table S5. Selected excited singlet states of TD-DFT calculations for complex 3.

Excited states	Energy/ eV (λ nm)	Wavelength (nm)	Oscillator strength		Major contributions (%)
1	3,48	356	0.1249	Singlet-A	HOMO->LUMO (86%)
					H-3->LUMO (4%),
					H-2->L+1 (4%),
					H-1->L+1 (2%)
2	3,8327	323	0.2375	Singlet-A	H-1->LUMO (74%),
					HOMO->L+1 (20%)
3	4,0071	309	0.1061	Singlet-A	H-2->LUMO (54%),
					H-1->LUMO (13%),
					HOMO->L+1 (26%)
					H-3->L+1 (4%)
4	4,3339	286	0.0118	Singlet-A	H-4->LUMO (94%)
					H-3->LUMO (5%)
5	4,5513	272	0.0001	Singlet-A	H-5->L+2 (13%),
					H-3->L+2 (14%),
					HOMO->L+2 (64%)
6	4,5935	269	0.3738	Singlet-A	H-3->LUMO (31%),
					H-1->L+1 (56%)
					H-4->LUMO (2%),
					H-2->L+1 (8%)

Quantum yield

$$\boldsymbol{\Phi F = (As)/Ax)(Fx/Fs)(nx/ns)^2} \quad \textbf{(1)}$$

Where Φ_F is the quantum yield, A_s and A_x are the absorbances of the unknown sample and the reference. F_x and F_s are the areas under the fluorescence emission spectrum curves for the unknown samples and the reference sample respectively. Finally, n represent the refractive index of the respective solvents. The refractive indexes for dH_2O, acetonitrile and DCM were 1.333, 1.3441 and 1.4241 respectively.

Table S6. Calculated quantum yields for the Pt(II) bis(pyrrolide-imine) chelates in different solvents.

Chelate	Solvent							
	Acetonitrile Φ_F		DCM Φ_F		dH2O Φ_F		HSA Φ_F	
1	0,0052	0,0005	0,0204	0,0007	0,0396	0,0021	0,6181	0,0128
2	0,0057	0,0005	0,0205	0,0008	0,0654	0,0042	0,2786	0,0103
3	0,0057	0,0003	0,0222	0,0006	0,0132	0,0009	0,1609	0,0117
4	0,0080	N.D	0,0242	0,0013	N.D	N.D	N.D	N.D

Table S7. Calculated quantum yields for the Pt(II) bis(pyrrolide-imine) chelates in different anaerobic acetonitrile and dH_2O.

Sample	Solvent	Φ_F
1	MeCN-saturated with $Ar_{(g)}$	0.1055
2	MeCN-saturated with $Ar_{(g)}$	0.187
3	MeCN-saturated with $Ar_{(g)}$	0.2067
4	MeCN-saturated with $Ar_{(g)}$	0.012
1	dH_2O saturated with $Ar_{(g)}$	0.3177
2	dH_2O saturated with $Ar_{(g)}$	0.4252
3	dH_2O saturated with $Ar_{(g)}$	0.0507

3. References.

1 O. Q. Munro and G. L. Camp, *Acta Crystallogr. C*, 2003, **59**, o672–o675.
2 X.-F. Shan, D.-H. Wang, C.-H. Tung and L.-Z. Wu, *Tetrahedron*, 2008, **64**, 5577–5582.
3 S. Sookai and O. Munro, , DOI:10.26434/chemrxiv-2022-8v4x2.
4 C. Würth, M. Grabolle, J. Pauli, M. Spieles and U. Resch-Genger, *Nat. Protoc.*, 2013, **8**, 1535–1550.
5 S. Fery-Forgues and D. Lavabre, *J. Chem. Educ.*, 1999, **76**, 1260.
6 M. J. Frisch, G. W. Trucks, H. B. Schlegel, G. E. Scuseria, M. A. Robb, J. R. Cheeseman, G. Scalmani, V. Barone, G. A. Petersson, H. Nakatsuji, X. Li, M. Caricato, A. V. Marenich, J. Bloino, B. G. Janesko, R. Gomperts, B. Mennucci, H. P. Hratchian, J. V. Ortiz, A. F. Izmaylov, J. L. Sonnenberg, D. Williams-Young, F. Ding, F. Lipparini, F. Egidi, J. Goings, B. Peng, A. Petrone, T. Henderson, D. Ranasinghe, V. G. Zakrzewski, J. Gao, N. Rega, G. Zheng, W. Liang, M. Hada, M. Ehara, K. Toyota, R. Fukuda, J. Hasegawa, M. Ishida, T. Nakajima, Y. Honda, O. Kitao, H. Nakai, T. Vreven, K. Throssell, J. A. Montgomery Jr., J. E. Peralta, F. Ogliaro, M. J. Bearpark, J. J. Heyd, E. N. Brothers, K. N. Kudin, V. N. Staroverov, T. A. Keith, R. Kobayashi, J. Normand, K. Raghavachari, A. P. Rendell, J. C. Burant, S. S. Iyengar, J. Tomasi, M. Cossi, J. M. Millam, M. Klene, C. Adamo, R. Cammi, J. W. Ochterski, R. L. Martin, K. Morokuma, O. Farkas, J. B. Foresman and D. J. Fox, *Gaussian 16 Revision C.01*, 2016.
7 T. Yanai, D. P. Tew and N. C. Handy, *Chem. Phys. Lett.*, 2004, **393**, 51–57.
8 F. Weigend and R. Ahlrichs, *Phys. Chem. Chem. Phys.*, 2005, **7**, 3297–3305.
9 S. Grimme, S. Ehrlich and L. Goerigk, *J. Comput. Chem.*, 2011, **32**, 1456–1465.
10 P. Fuentealba, H. Preuss, H. Stoll and L. Von Szentpály, *Chem. Phys. Lett.*, 1982, **89**, 418–422.
11 J. R. Cheeseman, G. W. Trucks, T. A. Keith and M. J. Frisch, *J. Chem. Phys.*, 1996, **104**, 5497–5509.
12 R. Ditchfield, *Mol. Phys.*, 1974, **27**, 789–807.
13 F. Lipparini, G. Scalmani, B. Mennucci, E. Cancès, M. Caricato and M. J. Frisch, *J. Chem. Phys.*, 2010, **133**, 014106.
14 R. Dennington, T. A. Keith and J. M. Millam, *GaussView Version 6*, 2019.
15 N. M. O'boyle, A. L. Tenderholt and K. M. Langner, *J. Comput. Chem.*, 2008, **29**, 839–845.

Supporting Information:

Complexities of the interaction of Ni(II), Pd(II) and Pt(II) pyrrole-imine chelates with human serum albumin

Sheldon Sookai[a] and Orde Q. Munro*[a,b]

[a] *Molecular Sciences Institute, School of Chemistry, University of the Witwatersrand, PO WITS 2050, Johannesburg, South Africa*

[b] *School of Chemistry, University of Leeds, Woodhouse Lane, Leeds, LS2 9JT, UK*

E-mail: o.munro@leeds.ac.uk

Table of Contents

1. Experimental Methods 201

1.1 Instruments and Basic Methods 201

1.2 Compound Synthesis and Characterization 202

1.3 Fluorescence Spectroscopy 205

Box 1. *Left:* Stern-Volmer plots (298 K) for Pd(PrPyrr) before and after applying the IFE correction of equation S1. The uncorrected fluorescence quenching data follow a cubic function and are markedly nonlinear. 207

Box 2. *Left:* Three independent titrations for the uptake of Ni(PrPyrr) by HSA (298 K).. 208

1.4 Circular dichroism (CD) spectroscopy 209

1.5 DFT Calculations 210

1.6 Molecular Docking Simulations 211

2. Figures 214

2.1 General Characterization Data 214

Figure S1. 400 MHz ^{1}H NMR spectrum of Ni(PrPyrr) recorded in DMSO-d_6 at 300 K. This compound is known;[5] the spectral data here briefly confirm the structure of the compound and its purity. 214

Figure S2. 101 MHz ^{13}C NMR spectrum of Ni(PrPyrr) recorded in DMSO-d_6 at 300 K. 214

Figure S3. 400 MHz ^{1}H NMR spectrum of Pd(PrPyrr) recorded in $CDCl_3$ at 300 K. This compound is known;[55] the ^{1}H NMR spectral data here briefly confirm the structure of the compound. Solvent impurity peaks are labelled. 215

Figure S4. 101 MHz ^{13}C NMR spectrum of Pd(PrPyrr) recorded in $CDCl_3$ at 300 K. Although the compound is known,[55] ^{13}C NMR data have not been reported for it in the literature. 215

Figure S5. 400 MHz 1H NMR spectrum of Pd(PrPyrr) recorded in CD_3CN at 300 K. This spectrum was recorded on a sample from the same bulk solid as in Figure S3 to confirm that the solvent contaminants were not part of the solid reaction product. 216

Figure S6. ESI-MS spectrum of Pd(PrPyrr). The solid sample was dissolved in methanol with 0.1% formic acid (V/V) and the spectrum was recorded in positive ESI mode. mMass 5.5.0 was used to simulate the isotope pattern.[56] No ESI-MS data are available in the literature[55] for this compound. 216

Figure S7. UV-visible spectrum of Pd(PrPyrr) recorded in CH_3CN at 295 K as a function of concentration. The molar absorptivities for selected band maxima are reported in the Experimental Section and were determined from the slopes of the inset Beer-Lambert law plots. Electronic spectra for the compound were not reported in the original literature.[55] 217

Figure S8. 400 MHz ^{1}H NMR spectrum of Pt(PrPyrr) recorded in DMSO-d_6 at 300 K. Spin–spin coupling (^3J, ^{195}Pt–^{1}H) between Pt and the imine CH protons in the chelate is evident, measuring 36.1 Hz, and is in accord with the literature range of 15–50 Hz.[57] 217

Figure S9. 101 MHz ^{13}C NMR spectrum of Pt(PrPyrr) recorded in DMSO-d_6 at 300 K. 218

Figure S10. FTIR spectrum of Pt(PrPyrr) recorded as a crushed powder sample at 295 K. 218

Figure S11. ESI-MS spectrum of Pt(PrPyrr). The solid sample was dissolved in methanol with 0.1% formic acid (V/V) and the spectrum was recorded in positive ESI mode. Parent ion adducts are assigned. mMass 5.5.0 was used to simulate the isotope pattern.[56] 219

Figure S12. UV-visible spectrum of Pt(PrPyrr) recorded in CH_3CN at 295 K as a function of concentration... 219

2.2 Advanced Spectroscopy and Reactions 220

Figure S13. *Top*: experimental UV-visible spectra for Pd(PrPyrr) and H_2PrPyrr recorded with different HCl mole ratios in acetonitrile at 37 °C. *Bottom*: Electronic spectra for Pd(PrPyrr) and PdCl(HPrPyrr) calculated using TD-DFT at the CAM-B3LYP/DEF2-QZVP/GD3BJ level of theory in an acetonitrile solvent continuum. 220

Figure S14. *Top*: DFT-calculated ^{1}H NMR spectrum of PdCl(HPrPyrr) at the CAM-B3LYP/def2qzvp level of theory (CH_3CN solvent continuum). 221

2.3 X-Ray Crystallography and DFT Simulations 222

Figure S15. Side-on and top views of the two types of stacked dimer formed by Pd(PrPyrr). 222

Figure S16. Comparison of the unit cell contents for the room temperature X-ray structure of PdPrPyrr (purple, space group $P2_1/a$, CSD code: XUVQIO[55]) and the low temperature structure determined in this work (cyan, space group $P2_1/c$). 223

Figure S17. Histograms of the Pd–N_{imine} and Pd–$N_{pyrrole}$ bond distances for a selection of 27 out of 55 Pd(II) complexes with Pd–$N_{pyrrole}$ coordination involving a mono-substituted pyrrole ring in the Cambridge Structural Database (CSD).. 224

Figure S18 (a). View of the two types of intermolecular π-stacking arrangements for molecules in the crystal lattice of PdPrPyrr. 225

Figure S18 (b). Top: View approximately down the unit cell c-axis of the 1D chain of noncovalently interacting near-centrosymmetric dimers formed in the crystal lattice of Pd(PrPyrr) (173 K data set). 225

Figure S19. Left: DFT-calculated structures of the AB' noncovalent dimer (C_i symmetry) formed between two molecules of Pd(PrPyrr) in the gas phase. 227

Figure S20. Views highlighting the 1D H-bonded chain formed in the crystal lattice of PdCl(HPrPyrr), which is stabilized by (alkyl)C–H···Cl and (pyrrole)N–H···Cl hydrogen bonds (dashed light blue cylinders). 228

2.4. Speciation 229

Figure S21. (A) Absorbance spectra of 45 μM Pd(PrPyrr) measured over 170 min (in 5 min intervals) from 260 – 700 nm in KH_2PO_4 buffer (50 mM pH 7.5). 229

Figure S22. Comparison of the calculated electronic absorption spectrum of $[Pd(HPrPyrr)(OH_2)]^+$ (TD-DFT, cam-b3lyp/sdd/gd3bj in water) with the experimental spectrum recorded in KH_2PO_4 buffer (50 mM pH 7.5) at 60 min after the start of the hydrolysis reaction (Figure S21A). 230

2.5 Fluorescence Spectroscopy 231

Figure S23. Fluorescence emission spectra of HSA (5.0 μM) recorded as a function of increasing concentration of (A) H_2PrPyrr, (B) Ni(PrPyrr), and (C) Pt(PrPyrr) at 298 K. The emission spectra confirm that the free base and metal chelates quench the intrinsic HSA (i.e., Trp-214) fluorescence upon binding. 231

Figure S24. Fluorescence emission maximum of HSA (5.0 μM) recorded as a function of increasing concentration of $Pd^{II}(X)$ at 298 K (pH 7.5), where X represents the ligand sets coordinated to Pd(II) as a result of the equilibrium mixture: $Pd(PrPyrr) + H_3O^+ \rightleftarrows [Pd(HPrPyrr)(OH_2)]^+$. 232

Figure S25. Stern–Volmer plots of fluorescence quenching: **(A)** H_2PrPyrr···HSA complex, **(B)** Ni(PrPyrr)···HSA complex, **(C)** Pd(PrPyrr)···HSA complex, and **(D)** Pt(PrPyrr)···HSA complex. 233

Figure S26. Plots of $\log((I_0\text{-}I)/I)$ versus log([Q]) for the interaction of HSA with several ligands (i.e., quenchers, Q) at specific temperatures: **(A)** H_2PrPyrr···HSA complex, **(B)** Ni(PrPyrr)···HSA complex, **(C)** Pd(PrPyrr)···HSA complex, and **(D)** Pt(PrPyrr)···HSA complex. 234

Figure S27. Stern–Volmer (SV) plot for native HSA as a function of the concentration of Pd(PrPyrr) at 298 K (pH 7.50, λ^{ex} = 280 nm, λ^{em} = 340 nm). 235

Figure S28a. UV-visible CD spectra recorded for Pd(PrPyrr) initially and after 90 minutes in a solvent comprising acetonitrile (80%, V/V) and distilled H_2O (20%, V/V) at 310 K.. 236

Figure S28b. (A) UV-visible spectra of Pd(PrPyrr) recorded as a function of pH at 37 °C. The inset highlights the spectral changes at lower pH. 237

Figure S28c. (A) Uncorrected normalized TD-DFT calculated electronic absorption spectra (CAM-B3LYP/SDD, SCRF = water) for the four Pd(II) complexes present in the equilibrium scheme of Figure S28b. 238

Figure S29. (A) Emission spectra of HSA•$\{warfarin\}_n$ (5.0 μM warfarin λ^{ex} = 320 nm) recorded as a function of increasing concentration of Pd(PrPyrr) at 298 K from 0 – 30 μM.. 239

Figure S30. (**A**) Stern–Volmer (SV) plot for native HSA, HSA···Warfarin, and HSA···Ibuprofen as a function of the concentration of Ni(PrPyrr) at 298 K (pH 7.50, *T* = 298 K)..... 240

Figure S31. (**A**) Sphere of action model plot, $lnI0I = KSVappQ$, for native HSA, HSA···Warfarin, and HSA···Ibuprofen as a function of the concentration of Pt(PrPyrr) at 298 K (pH 7.50). 241

Figure S32. (**A**) Stern–Volmer (SV) plot for native HSA, HSA···Warfarin, and HSA···Ibuprofen as a function of the concentration of H_2PrPyrr at 298 K (pH 7.50, *T* = 298 K)..... 242

2.5.1. Comments on Figures S30–S32 243

2.6 Protein Mass Spectrometry..... 245

Figure S33 (a). ESI-MS data for complexes of HSA formed with Ni(PrPyrr), Pd^{II}(X), and Pt(PrPyrr). 245

Figure S33 (b). ESI-mass spectrum recorded for an aqueous solution of HSA (5 μM) containing 25 μM Pd^{II} (eq) with injection via the instrument sample loop containing acetonitrile as the carrier solvent. 247

2.7 Circular Dichroism Spectroscopy..... 248

Figure S34. Plots of the far-UV CD spectra of native HSA and the protein incubated with saturating doses of (a) H_2PrPyrr, (b) Ni(PrPyrr), (c) Pd(PrPyrr), and (d) Pt(PrPyrr) recorded at 298 K in 50 mM KH_2PO_4 buffer at pH 7.50. The data are unsmoothed, and each spectrum is the average of three individual spectral scans..... 248

Figure S35. Three-dimensional graph showing how the change in the α-helix content of the protein correlates with the experimentally determined values of ΔH and ΔS for the reaction of each compound with HSA (*T* = 298 K). 248

Figure S36. Plots of the near UV CD spectra of native HSA (5 μM) and the protein incubated with a saturating dose (12 μM) of H_2PrPyrr. 249

2.8 Macromolecular Simulations..... 250

Figure S37. GLIDE XP docking analysis of the binding of H_2PrPyrr, $[H_3PrPyrr]^+$, and Ni(PrPyrr) to HSA using the X-ray structure of HSA with warfarin bound in subdomain IIA as the *in silico* target (PDB code 1HA2)..... 250

Figure S38. *Top:* Close-up view of the best pose of Ni(PrPyrr) docked within Sudlow's site I (subdomain IIA) of HSA (PDB code 1HA2) with warfarin removed from the grid. 251

Figure S39. (a) Induced CD spectrum recorded for the complex formed between HSA and Ni(PrPyrr) at 298 K in 50 mM KH_2PO_4 buffer at pH 7.50. 252

Figure S40. *Left*: comparison of the experimental induced CD spectrum (ICD) recorded for HSA•{Ni(PrPyrr)} at 298 K in 50 mM KH_2PO_4 buffer at pH 7.50 and the TD-DFT calculated electronic CD spectrum for the best pose of Ni(PrPyrr) docked into Sudlow's site I (subdomain IIA) of HSA (PDB code: 1HA2)..... 253

Figure S41. (a) GLIDE XP docking analysis of the binding of Pd(PrPyrr) and $[Pd(HPrPyrr)(OH_2)]^+$ to HSA using the X-ray structure of HSA with warfarin bound in subdomain IIA as the *in silico* target (PDB code 1HA2). 254

Figure S42. Illustration of the adjacent, yet somewhat overlapping, binding sites for warfarin and Pd(PrPyrr) in subdomain IIA (Sudlow's drug site I) of HSA as determined by GLIDE XP docking using PDB code 1HA2 as the target and a large 40 × 40 × 40-$Å^3$ grid centred on the coordinates of warfarin..... 255

Figure S43. Plot of the experimental and calculated electronic circular dichroism spectra (CAM-B3LYP/SDD/GD3BJ:UFF level of theory) for Glide XP docking models (Table S9) of HSA bound to a selection of Pd(II) chelate poses..... 256

3. Tables..... 257

Table S1. Crystal data and X-ray structure refinement details for Pd(PrPyrr). 257

Table S2. Selected geometrical parameters (Å, °) for the X-ray structure of Pd(PrPyrr). A labelled thermal ellipsoid plot (40% probability surfaces, H atoms omitted for clarity) is included to aid reading the tabulated data. 258

Table S3. Metal-to-nitrogen bond distances for 27 pyrrolide and pyrrolide-imine complexes of Pd(II) in the CSD. 259

Table S4. Crystal data and X-ray structure refinement details for PdCl(HPrPyrr). 261

Table S5. Selected geometrical parameters (Å, °) for the X-ray structure of PdCl(HPrPyrr). A labelled thermal ellipsoid plot (50% probability surfaces, H atoms drawn with arbitrary radii) is included to aid reading the tabulated data. 262

Table S6. A comparison of HSA Trp-214 quenching by Ni(PrPyrr), Pd(PrPyrr)[a] and Pt(PrPyrr) measured at the peak emission wavelength after excitation at 280 nm and 295 nm. 264

Table S7. Secondary structure composition of HSA in the presence of H_2PrPyr, Ni(PrPyrr), Pd(PrPyrr) and Pt(PrPyrr) at different concentrations. CD spectral data were recorded at 298 K in 50 mM KH_2PO_4 buffer at pH 7.50. 264

Table S8. Comparison of the binding of H_2PrPyrr, Ni(PrPyrr), Pd(PrPyrr), and Pt(PrPyrr), as well as fluorophore quenching, to HSA and its noncovalent complexes with warfarin (Warf) and ibuprofen (Ibu).[a,b] 265

Table S9. Summary of GLIDE XP docking scores and selected interaction energy parameters for HSA targets prepared from ligand-free and ligand-bound grids based on geometry-optimized (prepared) structures derived from PDB codes 1HA2 (HSA···warfarin complex), 2BXF (HSA···diazepam complex), and 2BXG (HSA···bis(ibuprofen) complex). 266

Table S10. Summary of Glide XP docking scores (as in Table S9) and selected interaction distances for HSA targets prepared from ligand-free grids based on geometry-optimized (prepared) structures derived from PDB codes 1HA2 (HSA···warfarin complex) and 2BXF (HSA···diazepam complex). 269

Table S11. Summary of Glide XP docking scores and selected interaction energy parameters for HSA targets prepared from ligand-free grids based on geometry-optimized (prepared) structures derived from PDB codes 1HA2 (HSA···warfarin complex) and 2BXF (HSA···diazepam complex). 270

Table S12. Electronic excited states for Cs symmetry Ni(PrPyrr) calculated by TD-DFT at the CAM-B3LYP/def2qzvp/GD3BJ level of theory in an acetonitrile solvent continuum. 271

4. References 274

1. Experimental Methods

All solvents (HPLC grade) and chemical synthons were used as received from Merck Sigma-Aldrich® without further purification. Deuterated dimethyl sulfoxide was stored over activated 4 Å molecular sieves. Human serum albumin (HSA) was purchased from Sigma and used as received without further purification. Ultrapure water (Type I) was produced using a Merk-Millipore Direct-Q® 3 UV Water Purification System.

1.1 Instruments and Basic Methods

Crystallography. Single crystal X-ray structure determinations were carried out with a four-circle Bruker D8 Venture X-ray diffractometer equipped with a Photon II CPAD area detector and a fine-focus sealed X-ray tube source (Mo anode). Crystals were mounted under Paratone® oil on nylon loops (Hampton Research) and the crystals were kept at 173(1) K during data collection (Oxford CryoStream 700). Using Olex2,[1] the structures were solved with the ShelXT[2] structure solution program (intrinsic phasing) and refined with ShelXL[3] using least squares minimization.

General spectroscopy. Proton and carbon NMR spectra were recorded on Bruker Avance III 400 and 300 NMR spectrometers at ^{1}H frequencies of 400 MHz and 300 MHz, respectively, and ^{13}C frequencies of 100 MHz and 75 MHz, respectively. Spectra were recorded at 298 K with 5 mm BBOZ or TBIZ probes. Chemical shifts for both proton and carbon were reference using the solvent signal. MestReNova (version 14.2.1-27684) was used to analyse NMR spectra. FTIR spectra of powder samples were recorded using a Bruker Alpha FTIR spectrometer incorporating a Bruker Platinum® diamond ATR sampling accessory. Spectra were analysed using the OPUS software package on the spectrometer (version 7.5). Mass spectra were recorded with Bruker Compact Q-TOF high-resolution mass spectrometer using Bruker Daltronics HyStar 3.2 SR4 software. Bruker Compass DataAnalysis software (Version 4.3) was used to analyse chromatograms. Samples of pure compounds (typically ca. 10 µg/mL) were prepared in HPLC grade acetonitrile or ethanol for metal chelates and HPLC grade methanol for ligands. Solutions were acidified using 0.1% (V/V) formic acid to obtain spectra in ESI+ mode. Electronic spectra were recorded using either a PerkinElmer Lambda 365 double beam spectrometer connected to a Peltier controller and multicell thermostatic cell block or an Analytik Jena Specord210 Plus double-beam instrument fitted with an external water circulating thermostatic bath and thermostatted cell holders. The spectral data were analysed with the spectrometer software or Origin Pro 2020. Spectra were recorded (10-mm pathlength quartz cuvettes) as a function of concentration for both characterization and the determination of molar absorptivity constants.

Protein mass spectrometry. A freshly prepared solution of HSA (5 µM) was made up in distilled water, containing 25 µM of either Ni(PrPyrr), Pd(PrPyrr) or Pt(PrPyrr). The sample was incubated at 4 °C for 16 h to allow the metal chelates to bind to HSA. Native HSA was used at 5 µM and dissolved into distilled water prior to the mass spectroscopy experiment being run. Mass spectra were measured by either direct injection of the aqueous sample or using the instrument's injection loop and acetonitrile (with 0.1% V/V formic acid) as the carrier solvent.

1.2 Compound Synthesis and Characterization

***N,N'*-bis[(1*E*)-1H-pyrrol-2-ylmethylene]propane-1,3-diamine (H_2PrPyrr).** The synthetic method was an adaption from the method described by Munro *et al*.[4] Briefly, pyrrole-2-carboxaldehyde (1.4265 g, 15 mmol) and 1,3-diaminopropane (0.556 g, 7.5 mmol) were refluxed in ethanol (30 mL) for two hours. During refluxing, the reaction mixture changed from colourless to a clear straw yellow. Ethanol was then removed by rotary evaporation, leaving a viscous orange coloured oil. Finally, the viscous orange oil was dissolved in a minimal volume of dichloromethane and layered with hexane. The solution was left overnight, affording a faint yellow polycrystalline product. H_2PrPyrr (2.4376 g, 80% yield) was analysed by ^{1}H NMR, ^{13}C NMR, FT-IR and UV-visible spectroscopy, giving data in agreement with the earlier literature.[4] ^{1}H NMR (400 MHz, chloroform-*d*, 300 K) [δ, ppm]: 1.98 (t, *J* = 6.8 Hz, 2H, H-7), 3.61 (td, *J* = 6.8, 1.2 Hz, 4H, H-6), 6.23 (dd, *J* = 3.6, 2.6 Hz, 2H, H-2), 6.48 (dd, *J* = 3.6, 1.4 Hz, 2H, H-3), 6.88 (t, *J* = 1.9 Hz, 2H, H-1), 8.03 (s, 2H, H-5). ^{13}C NMR (101 MHz, chloroform-*d*, 300 K) [δ, ppm]: 32.29 (C-7), 57.80 (C-6), 109.59 (C-2), 114.13 (C-3), 122.04 (C-1), 129.86 (C-4), 151.85 (C-5). IR (KBr pellet, cm^{-1}): 3112w δ(NH, pyrrole), 3053m br *ν*(CH, imine), 2941m *ν*(CH, $CH_2CH_2CH_2$), 2847 *ν*(CH, CH_2-N=CH), 1634s br *ν*(C=N). UV-vis (ethanol) [λ_{max}/nm, ε/mol^{-1} dm^3 cm^{-1}]: 289, 3.20 × 10^4.

2,2'-{propane-1,3-diylbis[azanylylidene(*E*)methanylylidene]}di(pyrrol-1-ide)nickel(II), Ni(PrPyrr). The complex was synthesized by modification of the literature method.[5] Briefly, Ni(II)acetate tetrahydrate (1 mmol in 7.5 ml methanol) was added to a methanolic solution of H_2PrPyrr (1 mmol) at 295 K. The colour changed almost instantly from clear to a light red. After ~1 h a dark brick-red precipitate had formed which was isolated by gravity filtration of the methanolic solution. Red crystals suitable for X-ray diffraction were obtained by slow liquid diffusion of hexane into an acetonitrile solution of Ni(PrPyrr). ^{1}H NMR (400 MHz, DMSO-d_6, 300 K) [δ, ppm]: δ 7.57 (s, 2H), 6.80 (s, 2H), 6.50 (d, *J* = 3.5 Hz, 2H), 5.97 (dd, *J* = 3.6, 1.9 Hz, 2H), 3.23 – 3.08 (m, 4H), 1.70 (p, *J* = 4.3, 3.9 Hz, 2H). ^{13}C NMR (101 MHz, DMSO-d_6, 300 K) [δ, ppm]: δ 162.47, 140.20, 136.17, 116.37, 112.00, 52.41, 28.99. FT-IR (powder, cm^{-1}): 3092m br *ν*(CH, imine), 3074m *ν*(CH, $CH_2C\mathit{H}_2CH_2$), 2936m *ν*(CH, $C\mathit{H}_2$-N=CH), 1579s br *ν*(C=N). UV-vis (acetonitrile) [λ_{max}/nm, ε/mol^{-1} dm^3 cm^{-1}]: 313, 2.68 × 10^4; 374, 8.56 × 10^3; 385, 9.16 × 10^3; 432, 4.92 × 10^3. HRMS (m/z): $[M+H]^+$ calcd. for $C_{13}H_{14}N_4Ni$, 285.0645; found, 285.0688.

2,2'-{propane-1,3-diylbis[azanylylidene(*E*)methanylylidene]}di(pyrrol-1-ide)palladium(II), Pd(PrPyrr). The complex was synthesized by adding Pd(II)acetate dihydrate (1 mmol) to a minimal volume of acetonitrile containing H_2PrPyrr (1 mmol). The mixture was stirred at 293 K for 4 h. The colour changed to bright yellow. Acetonitrile was removed by rotary evaporation and the yellow precipitate was dissolved in dichloromethane. Yellow rod-shaped crystals suitable for X-ray diffraction were obtained by slow liquid diffusion of hexane into the dichloromethane solution of Pd(PrPyrr). ^{1}H NMR (400 MHz, chloroform-*d*, 300 K) [δ, ppm]: δ 7.52 (s, 2H), 7.16 (s, 2H), 6.70 (d, *J* = 3.7 Hz, 2H), 6.22 (dt, *J* = 3.5, 1.4 Hz, 2H), 3.52 – 3.39 (m, 4H), 1.98 (p, *J* = 4.7 Hz, 2H). ^{13}C NMR (101 MHz, chloroform-*d*, 300 K) [δ, ppm]: δ 159.06, 139.16, 135.51, 116.63, 110.50, 53.44, 31.30. UV-vis (acetonitrile) [λ_{max}/nm, ε/mol^{-1} dm^3 cm^{-1}]: 294, 2.25(11) × 10^4; 322, 1.25(9) × 10^4; 374, 1.16(6) × 10^4; 390, 1.15(6) × 10^4; 404, 9.92(51) × 10^3. IR (powder, cm^{-1}): 3082m br *ν*(CH, imine), 2919m *ν*(CH, $C\mathit{H}_2$-N=CH), 1583s br *ν*(C=N). HRMS (m/z): $[M+H]^+$ calcd. for $C_{13}H_{14}N_4Pd$, 333.0333; found, 333.0375.

Crystal Data for Pd(PrPyrr). $C_{13}H_{14}N_4Pd$ (*M* = 332.68 g/mol): monoclinic, space group $P2_1/c$ (no. 14), *a* = 8.0357(7) Å, *b* = 16.8130(13) Å, *c* = 37.009(3) Å, *β* = 90.722(2)°, *V* = 4999.7(7) $Å^3$, *Z* = 16, *T* = 173.00 K, μ(MoKα) = 1.471

mm^{-1}, D_{calc} = 1.768 g/cm^3, 241730 reflections measured (5.07° ≤ 2Θ ≤ 61.434°), 15378 unique (R_{int} = 0.0352, R_σ = 0.0148) which were used in all calculations. The final R_1 was 0.0783 (I > 2σ(I)) and wR_2 was 0.1833 (all data).

Chloro(2-{(*E*)-[(3-{(*Z*)-[(1*H*-pyrrol-2-yl)methylidene]amino}propyl)imino]methyl}pyrrol-1-ide)palladium(II), PdCl(HPrPyrr). A crude yellow powder sample of Pd(PrPyrr) was dissolved in dichloromethane and recrystallized by slow liquid diffusion utilizing hexane layered over the dichloromethane solution of the complex in a capped crystallizing tube. This resulted in the formation of two morphologically distinct types of crystals. Specifically, the bulk of the crystals formed were light yellow rod-shaped crystals of Pd(PrPyrr). The minor crystalline product comprised orange block-shaped crystals, later found to be PdCl(HPrPyrr) by X-ray diffraction. Because of the intrinsically low yield of this crystalline product and the difficulties we encountered trying to reproduce and scale the conditions leading to its formation, analytical data for the compound are currently limited to its X-ray structure and both ^{1}H NMR and UV-vis spectra for its formation in solution.

Crystal Data for PdCl(HPrPyrr). $C_{13}H_{15}ClN_4Pd$ (*M* =369.14 g/mol): monoclinic, space group $P2_1/n$ (no. 14), *a* = 12.4781(5) Å, *b* = 7.9715(4) Å, *c* = 14.0369(6) Å, *β* = 102.440(2)°, *V* = 1363.46(11) $Å^3$, *Z* = 4, *T* = 153.00 K, μ(MoKα) = 1.548 mm^{-1}, D_{calc} = 1.798 g/cm^3, 45957 reflections measured (5.912° ≤ 2Θ ≤ 66.33°), 5199 unique (R_{int} = 0.0335, R_σ = 0.0189) which were used in all calculations. The final R_1 was 0.0210 (I > 2σ(I)) and wR_2 was 0.0487 (all data).

2,2'-{propane-1,3-diylbis[azanylylidene(*E*)methanylylidene]}di(pyrrol-1-ide)platinum(II), Pt(PrPyrr). The complex was synthesized by adding K[$PtCl_4$] (1 mmol) dissolved in DMSO (7.5 ml) to a solution of sodium acetate (2 mmol) and H_2PrPyrr (1 mmol, dissolved in 7.5 ml acetonitrile). The mixture was stirred at ambient temperature for 4 days until the colour had changed to a bright orange. Acetonitrile was removed by rotary evaporation, leaving only the DMSO phase. Deionized water was then added to the DMSO solution of the complex to precipitate Pt(PrPyrr) as a bright yellow solid, which was isolated by gravity filtration and dried. Single crystals of Pt(PrPyrr), however, were unsuitable for X-ray diffraction were obtained by slow liquid diffusion of hexane into a THF solution of the complex. ^{1}H NMR (400 MHz, DMSO-d_6, 300 K) [δ, ppm]: δ 8.15 (s, 1H), 7.19 (s, 2H), 6.64 (d, *J* = 3.7 Hz, 2H), 6.16 (dd, *J* = 3.7, 1.8 Hz, 2H), 3.84 – 3.63 (m, 4H), 1.94 (p, *J* = 4.5 Hz, 2H). ^{13}C NMR (101 MHz, DMSO-d_6, 300 K) [δ, ppm]: δ 160.72, 140.83, 135.41, 117.31, 110.92, 54.29, 32.02. UV-vis (acetonitrile) [λ_{max}/nm, ε/mol^{-1} dm^3 cm^{-1}]: 279, 1.67 × 10^4; 304, 1.40 × 10^4; 313, 1.31 × 10^4; 385, 8.56 × 10^3. IR (powder, cm^{-1}): 3083m br *ν*(CH, imine), 2914m *ν*(CH, CH_2-N=CH), 1582s br *ν*(C=N). HRMS (m/z): $[M+H]^+$ calcd. for $C_{13}H_{14}N_4Pt$, 422.0942; found, 422.0970.

Spectroscopic study of the protonation of Pd(PrPyrr). Pd(PrPyrr) (15 mM) was analysed by ^{1}H NMR spectroscopy (400 MHz, acetonitrile-d_3) in the absence and presence of HCl at different mole ratios (1:1) and (1:2) to detect protonation and conversion to PdCl(HPrPyrr). The HCl titrant was prepared by diluting a concentrated stock solution of 10.2 M HCl into D_2O prior to adding appropriate aliquots to the solution of Pd(PrPyrr) in acetonitrile-d_3 to achieve the required mole ratios. The solutions were incubated for 30 minutes prior to spectral acquisition at 37 °C. UV-vis spectra of Pd(PrPyrr) dissolved in acetonitrile were recorded between 250–700 nm in the absence and presence of HCl. Individual solutions containing Pd(PrPyrr) (20 μM) were prepared with HCl concentrations ranging from 10 μM–30.6 mM and incubated for 30 minutes prior to recording spectra at 37 °C.

Spectroscopic pKa determinations and solution species characterization. A 10× multicomponent buffer was made up of 10 mM each of potassium dihydrogen phosphate, MES, MOPS, TRIS and CHES buffers, as well as 1.0 M KCl at 25 °C. The buffer stock solution was prepared and titrated to either pH 3.0 or 10.0 with either HCl or KOH before being made up to final volume. The starting titration solution contained 85 μM of Pd(PrPyrr), 5% (V/V) acetonitrile, and 1.0 mM of the multicomponent buffer and the total volume was made up to 50.0 mL with deionized water. The titration was carried out in a thermostatted titration vessel from Metrohm (37 °C). Specifically, the starting solution was added at either pH 3.00 or 12.00 and a calibrated pH electrode (37 °C) was inserted into the solution. The solution was magnetically stirred and circulated real-time through a 1.0 cm pathlength quartz UV-visible flow cuvette housed within the spectrometer cell holder at 37 °C using a peristaltic pump (Watson-Marlow 120S). The initial spectrum at pH = 3.00 or 12.00 was recorded from 210 nm to 700 nm. Negligible volumes (< 0.5 μL) of either concentrated KOH or HCl were then carefully diffused via glass capillary into the starting solution to shift the pH in discrete steps (~0.2 to 0.5 pH units) through the full titration range. After each titrant addition, the pH was recorded when the pH value had completely stabilized. This was followed by acquisition of the UV-visible spectrum of the solution circulating through the flow-cuvette. The instrument set-up is indicated in the photograph below.



The titrations (pH 10 → pH 3 and pH 3 → pH 12) were not fully reversible due to the existence of multiple species derived from Pd(PrPyrr) and its coexistence throughout the pH range, particularly ~pH 7. The data sets were thus converted to the change in absorbance with pH (i.e., ΔA vs. pH), truncated at neutral pH where ΔA was essentially invariant with pH, and then merged to give the complete titration curve.

Attempted crystallization of $[Pd(HPrPyrr)(OH)_2]^+$. The following experiments were carried out in an attempt to crystallize $[Pd(HPrPyrr)(OH_2)]^+$ due to its significance in binding equilibria with HSA.

(1) Pd(PrPyrr) was dissolved in a mixture of deionized water and acetonitrile (5%). The solution was then equilibrated in a closed vessel with pure acetonitrile by slow vapour diffusion.

(2) Pd(PrPyrr) was dissolved in a mixture of deionized water and acetonitrile (5%) and the solution layered with pure acetonitrile in an effort to grow crystals by slow liquid diffusion.

(3) The experiments above were repeated with solutions of Pd(PrPyrr) that had first been acidified by 1 drop of concentrated perchloric acid in each crystallization vessel.

(4) Attempts were made to grow the crystals in water alone. Unfortunately, Pd(PrPyrr) was insoluble at the required high concentrations, leading to precipitation of the compound. The precipitate was thus removed by filtration and the pale-yellow filtrate allowed to slowly evaporate. However, no crystals were obtained by this method.

In methods (1) to (3) above, crystals formed within a couple of hours (much faster than when a dichloromethane solution of Pd(PrPyrr) is layered with hexane) in each of the above experiments. More than 10 crystals (several from each experiment) were examined on the X-ray diffractometer. However, in all cases the unit cell constants obtained matched those of Pd(PrPyrr). The evidence suggests that the tetradentate chelate Pd(PrPyrr) forms a significant fraction of the total species present in solutions that contain acetonitrile, consistent with the chelate effect shifting the Pd(PrPyrr) + H_3O^+ ⇌ $[Pd(HPrPyrr)(OH_2)]^+$ equilibrium to the left. Based on the quantifiable role of dispersion in the crystal packing of Pd(PrPyrr) (Figure S19), it is possible that these interactions underpin a more favourable lattice energy for Pd(PrPyrr) and thus its crystallization under a range of conditions.

1.3 Fluorescence Spectroscopy

Fluorescence measurements were performed on a Cary Eclipse fluorescence spectrophotometer (Varian, Australia) equipped with a 1.0 cm quartz cell and a circulating thermostat bath. The HSA concentration was kept at 5.0×10^{-6} mol dm^{-3} and the excitation and emission slit widths were fixed at 5 nm. The concentrations of H_2PrPyrr and Ni(PrPyrr) ranged from 5×10^{-7} to 2.1×10^{-5} mol dm^{-3} while those of Pd(PrPyrr) and Pt(PrPyrr) ranged from 5.0×10^{-7} mol dm^{-3} to 5.92×10^{-6} mol dm^{-3}. Each complex was made up in DMSO and the final DMSO concentration was under 0.1% (V/V) to prevent denaturation of HSA. HSA was excited at 280 nm (excitation of Trp and Tyr residues), and the emission spectra were recorded from 300 to 400 nm. Spectral titrations were carried out at four temperatures (288, 298, 310, and 315 K) in triplicate.

Fluorescent probe displacement assay. Warfarin and ibuprofen were used as specific site marker fluorescent probes for Sudlow's sites I and II, respectively. Steady-state fluorescence spectra were recorded as described above at 298 K using 10 nm excitation and emission bandwidths for warfarin, while 5 nm excitation and 10 nm emission band widths were employed for ibuprofen. The fluorophores warfarin and ibuprofen were equilibrated (bound) to HSA (50 mM KH_2PO_4 buffer, pH 7.50) and were excited at 320 nm and 228 nm, respectively. The emission spectrum was measured in the range 350 – 500 nm for warfarin and 228 – 450 nm for ibuprofen. The HSA and fluorescence probe concentrations were both used at 5.0 µM. Titrations were performed by increasing the concentrations of H_2PrPyrr, Ni(PrPyrr), Pd(PrPyrr), and Pt(PrPyrr) in the protein-probe solution from 0 to 23.4 µM. Fluorescence emission measurements on DMSO were carried out, and showed there was no emission from DMSO affecting the emission spectra.

Correction of fluorescence data. The inner filter effect (IFE) correction was applied to all fluorescence data using eq. S1:[6]

$$F_{corrected} = F_{observed} * 10^{A_{ex} \times d_{ex} + A_{em} \times d_{em}} \quad \text{S1}$$

Where A_{ex} and A_{em} are the absorbance readings at the excitation and emission wavelengths, respectively, while d is the path length of the cuvette. The IFE correction was mandatory due to the strong absorbance of the ligands of interest near the excitation and emission wavelengths of Trp-214 and Tyr in the protein.

Further corrections were applied to the concentration of the ligand, i.e., if $[Ligand]_{added}$ was not equal to $[Ligand]_{free}$, the free ligand concentration was calculated using eq. S2, where I_0, I, and I_∞ are the initial, measured, and end-point fluorescence intensities:[7]

$$[Ligand]_{free} = [Ligand]_{added} - \frac{I_o - I}{I_o - I_\infty} \times [HSA] \quad \text{S2}$$

Equation S2 was applied to the data for H_2PrPyrr and Ni(PrPyrr); the correction was not required for the other ligands and could technically be ignored for all ligands here because the affinity constants ($logK$) are not very large (< 6).

Stern-Volmer model. Fluorescence quenching is normally described by the Stern-Volmer (SV) equation (eq. S3),[8]

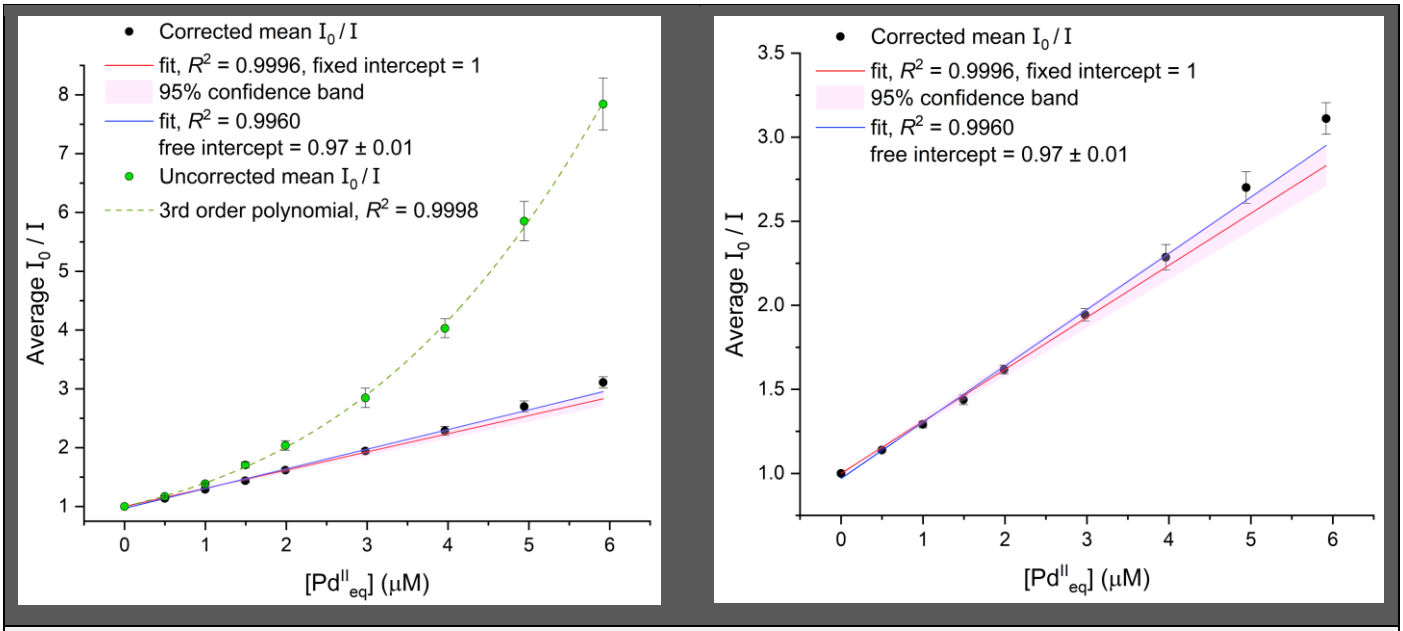
$$I_0/I = 1 + K_{SV}[Q] = 1 + k_q\tau_0\,[Q] \quad \text{S3}$$

where I_0 is the fluorescence intensity of HSA in the absence of the added quencher (metal chelate or free base ligand in this work) and I is the fluorescence intensity of HSA in the presence of the ligand. K_{SV} is the Stern-Volmer constant (M^{-1}), $[Q]$ is the molar concentration of the quencher, k_q is the bimolecular quenching rate constant ($M^{-1}\,s^{-1}$), and τ_0 is the average lifetime of HSA fluorescence in the absence of any quencher (5.28 ± 0.03 ns,[9] 5.60 ± 0.10 ns,[10] 6.72 ± 0.07 ns;[11] mean = 5.87 ± 0.76 ns). The bimolecular quenching rate constant is given by eq. S4:

$$k_q = {K_{SV}}/{\tau_0} \quad \text{S4}$$

Typically, linear SV plots (eq. S3) are associated with a single class of quenching, either dynamic (diffusion-limited collisional) or static (binding-related).[12] The specific class of quenching can be distinguished by the temperature dependence of K_{SV}. For dynamic quenching, the K_{SV} values increase with increasing temperature mainly due to an increase in the collisional frequency and diffusion rate, while for static quenching, K_{SV} values decrease with increasing temperatures because the equilibrium formation constant for the complex decreases with increasing temperature.[13]

Linearity of Stern-Volmer plots. When a ligand binds to a protein such as HSA and the reaction is detected by analysing the induced fluorescence changes in the emission signal of Trp-214 as a function of ligand dose at a fixed temperature, it is mandatory to process the data using eq. S1 prior to analysis with the Stern-Volmer equation (S3) to deduce the fluorescence quenching constant.[6] The literature unfortunately contains studies that have failed to consider many of the factors (other than genuine association of the ligand with the protein target) that can cause real or apparent quenching of the fluorophore. The issues have been pointed out and discussed in detail and with clarity by van de Weert and colleagues.[6,7] To illustrate the effect that eq. S1 has on the data recorded in the present study, the graphs in Box 1 below indicate the magnitude of the correction for fluorescence quenching titrations involving uptake of the Pd(II) chelate by HSA at 298 K.



Box 1. *Left:* Stern-Volmer plots (298 K) for Pd(PrPyrr) before and after applying the IFE correction of equation S1. The uncorrected fluorescence quenching data follow a cubic function and are markedly nonlinear. The data are, however, linearised by applying the appropriate correction. The plotted data represent the average of three independent measurements. The linear fit for the corrected data is better when the intercept is allowed to freely refine during least squares fitting, despite equation S3 requiring it to be exactly 1.00 (*Right*). All Stern-Volmer plots in the paper were fitted without constraints as one way to gage the quality of the data. The last data point on the curve at a concentration ~6 μM is a statistical outlier. However, the upward "drift" of the points > 4.5 μM likely reflects imperfect correction of the data, especially considering the substantial magnitude of the correction applied in this region of the plot.

In the case of the Ni(II) chelate, Ni(PrPyrr), individual titrations with HSA were less concordant than was the case for Pd(PrPyrr), as shown in Box 2 below. This means that the mean data set (plotted in Figure 5a of the main text as the unconstrained linear fit) shows an apparent nonlinearity, which increases as the quencher concentration increases. Deviations from linearity, though slight, were also seen to increase with decreasing temperature, commensurate with the higher affinity constant and stoichiometry in each case (see Table 1 of the main text). This may be taken as evidence for multi-site binding of a given ligand with HSA.[14] That said, when one considers the constrained linear fit in Box 2, the minor deviation from linearity is negligible. Notably, the SV constants of Table 1 (main text) were thus obtained under conditions for which the SV plot is valid.

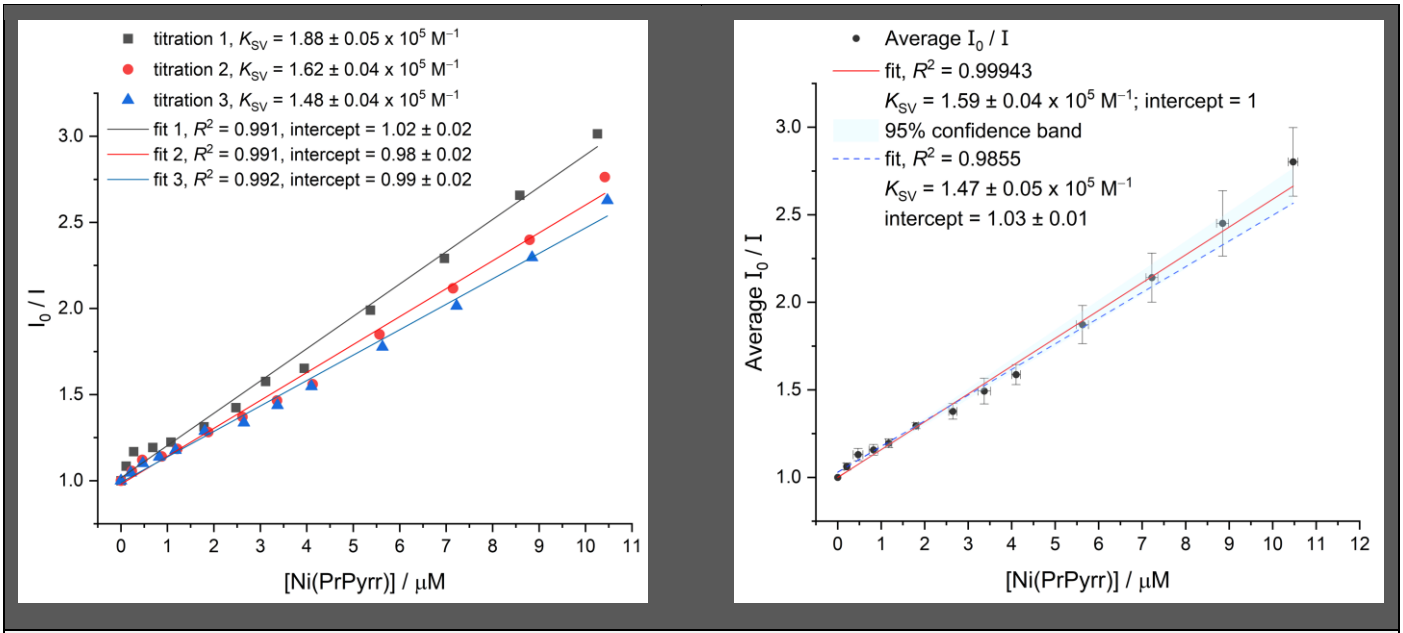
Sphere of action model. This modified SV-type fluorescence quenching model[15,16] invokes the presence of a sphere of a finite volume around Trp-214 in which the probability of the quencher (Q) inducing fluorescence quenching is unity.[12] The "sphere of action model" is described by eqs. S5 and S6,

$$\frac{I_0}{I} = e^{(K_{SV}^{app}[Q])} \quad \text{S5}$$

$$ln\left(\frac{I_0}{I}\right) = K_{SV}^{app}[Q] \quad \text{S6}$$

where K_{SV}^{app} is the apparent static fluorescence quenching constant. By taking the natural logarithm of eq. S5, linear plots with a zero intercept (eq. S6) are expected for increasing [Q] in systems that exhibit *static quenching*

(binding-related). Importantly, if the slope changes at high concentrations of the quencher, then the system has switched from a static quenching mechanism to one that is *dynamic*, which involves collisional quenching.



Box 2. *Left:* Three independent titrations for the uptake of Ni(PrPyrr) by HSA (298 K). Although the second and third titrations are more concordant, the procedure used for all Stern-Volmer (SV) plots in this work, including that for Ni(PrPyrr), was to average three independent data sets to give the constants listed in Table 1 of the main text. *Right:* The mean SV data for Ni(PrPyrr) has large error bars at higher concentrations due to divergence (slope differences) of the underlying/individual SV plots. The data point at the highest concentration (~10 μM) is a clear outlier in all plots. Individual plots are all linear with negligible upward curvature at concentrations < 8 μM. Any nonlinearity in the mean SV plot can be ascribed to divergence in the individual curves, averaging of the data, and correction with eq. S1 and/or S2. Note that the data in Table 1 of the main text were obtained by averaging the individual slopes of each SV plot (left) rather than using the slope fitting the mean data set (right).

Thermodynamic data for ligand binding. Affinity constants, K_a, determined from the fluorescence data for the binding of the present compounds by HSA (eq. S7)[17] were used in the van't Hoff equation (eq. S8) to determine ΔH and ΔS for the reaction from linear least-squares fits of the data. The Gibbs energy ΔG for each ligand binding reaction at 298 K was calculated from K_a directly using eq. S9, while the Gibbs-Helmholtz equation (eq. S10) was used to plot thermodynamic relationships.

$$log\left(\frac{I_0 - I}{I}\right) = logK_a + nlog[Q] \quad \text{S7}$$

$$lnK_a = -\frac{\Delta H}{RT} + \frac{\Delta S}{R} \quad \text{S8}$$

$$\Delta G = -RTlnK_a \quad \text{S9}$$

$$\Delta G = \Delta H - T\Delta S \quad \text{S10}$$

Linearity of double-log (D-L) plots. The affinity constant of a ligand for a protein such as HSA is often determined by a double-log (D-L) plot of the data (eq. S7). As pointed out by Grossweiner,[18] the standard D-L plot can be modified to take into account the bound fraction of the added ligand such that one can use the total quencher concentration directly if preferred,

$$\log\left\{\frac{F_0 - F}{F - F_\infty}\right\} = \log K + c \log [Q]_{total} \qquad \text{S11}$$

where F_0, F, and F_∞ are the initial, measured, and final fluorescence intensities at the analysis wavelength of the titration and K and c are the affinity constant and reaction stoichiometry, respectively. Whether one uses eq. S7 or eq. S11, Grossweiner has shown that double-log plots of this type are typically only reliable for deducing K when the reaction stoichiometry is close to 1. Keeping this in mind, and the fact that other linear methods of analysis such as Scatchard plots suffer from similar pitfalls and non-linear behaviour,[19–21] Figure S26 indicates that for all ligand binding reactions at all temperatures, acceptable linearity was observed upon application of eq. S7 to the data. It should be noted that applying eqs. S1 and S2 to the data followed by averaging triplicate titrations at a given temperature does introduce more scatter into the mean data set, as shown in Figure 5b of the main text. This is also evident in Figure S26.

Non-linear Stern-Volmer model. The Stern-Volmer model is linear, but deviations from linearity may occur. An upward curvature in a plot of I_0/I vs. [Q] may be analysed using the extended nonlinear SV equation reported by Campbell *et al.*[22] and, in rearranged format, by Ciotta *et al.*,[23] eq. S11,

$$\frac{I_0}{I} = \frac{1}{1 - \frac{1}{2[F_0]}\left[Z - \sqrt{Z^2 - 4[F_0][Q_0]}\right]} \qquad \text{S12}$$

where $[F_0]$ and $[Q_0]$ are the experimental concentrations of the fluorophore (HSA) and quencher (ligand), respectively, and Z incorporates the Stern-Volmer constant, eq. S12:

$$Z = \frac{1}{K_{SV}} + [F_0] + [Q_0] \qquad \text{S13}$$

The application of eq. S12 was not required here since data correction by eq. S1 (the inner filter effect correction, IFE) afforded linear Stern-Volmer plots. One would only need to consider this model if, after applying the IFE correction, SV plots were still significantly nonlinear.

1.4 Circular dichroism (CD) spectroscopy

Far UV CD spectra of solutions of HSA (300×10^{-9} mol dm^{-3}) in the absence and presence of increasing concentrations (0 – 12 μM) of H_2PrPyrr, Ni(PrPyrr), Pd(PrPyrr) and Pt(PrPyrr) were recorded with a JASCO J-1500 CD spectrometer equipped with a Peltier temperature controller (25 °C, 50 mM KH_2PO_4 buffer, pH 7.50). A scan speed of 100 nm min^{-1} was employed for spectral acquisition with a 0.5 nm data pitch and a response time of 2 s. Each spectrum was the average of three scans. Spectra were recorded over a wavelength range of 190–260 nm (0.4 cm pathlength quartz cuvette). All spectra were processed with JASCO Spectral Manager™.

Near UV-vis CD spectra (250–500 nm, 1.0-cm pathlength quartz cuvette, 25 °C, 50 mM KH_2PO_4 buffer, pH 7.50) were recorded similarly to detect induced CD (ICD) signals of the achiral ligands and metal chelates upon their uptake by HSA. Typically, HSA (5.0×10^{-6} M) was incubated with a saturating dose (12×10^{-6} M) of either H_2PrPyrr, Ni(PrPyrr), Pd(PrPyrr) or Pt(PrPyrr) for at least 60 min. A scan speed of 200 nm min^{-1} was used with a 0.5-nm data pitch (response time, 2 s); each spectrum was the average of three scans.

Analysis of CD spectra to determine secondary structure composition. We employed the JWMVS-529 Protein Secondary Structure Analysis program within JASCO's Spectra Manager™ package (supplied with the spectrometer) to analyse the fractional composition of secondary structure domains within HSA as a function of ligand dose. The algorithm employed uses a library of 26 protein CD spectra (176–260 nm) to generate a calibration model based on these spectra (created by JASCO). Experimental CD spectra were then fitted to the model via a partial least squares (PLS) method[24] and principal component regression (PCR) techniques[25] to accurately estimate the percentage of α-helix, β-sheet, turn, and unordered coil structure present. The approach markedly improves assessment of the β-sheet motifs, which is important as this structural element has no strong specific CD marker band. Use of the above methods was favoured over an older algorithm available from JASCO (the JWSSE-513 Protein Secondary Structure Analysis program), which uses a classical least squares (CLS) fitting algorithm based upon the reference spectra set of Yang *et al*.[26] Other methods are available in the literature for protein secondary structure prediction.[27,28] These were not used here for direct fitting of the experimental spectra due to the availability of suitable methods within JASCO's Spectra Manager™ package on the computer controlling the spectrometer.

CD study of the aquation of Pd(PrPyrr). The UV-visible CD spectra of Pd(PrPyrr) (50 μM), dissolved in a solution containing acetonitrile and distilled water (20% V/V) were measured from 200 – 500 nm at time 0 and after 90 minutes. A scan speed of 100 nm min^{-1} was employed for spectral acquisition with a 0.5 nm data pitch and a response time of 2 s. Each spectrum was the average of three scans. Spectra were recorded in a 1.0 cm pathlength quartz cuvette at a temperature of 310 K.

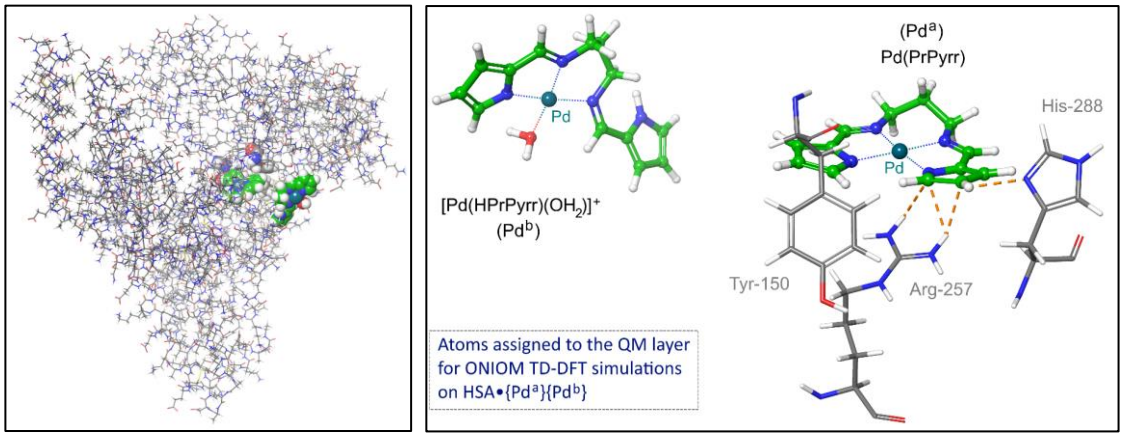
The hydrolysis of Pd(PrPyrr) was also measured by UV spectroscopy; 30 μM of Pd(PrPyrr) was incubated in KH_2PO_4 in either the absence or presence of HSA. The absorbance spectra were measured from 250 – 300 nm every 5-min until no changes in the spectra were visible. Spectra were recorded in a 1.0 cm pathlength quartz cuvette at a temperature of 310 K.

1.5 DFT Calculations

Simulations were performed to calculate optimized structures, vibrational frequencies, and electronic spectra for Ni(PrPyrr), Pd(PrPyrr), PdCl(HPrPyrr), Pt(PrPyrr), and free ligand species using Gaussian 16 Rev C.01[29] at the CAM-B3LYP[30]/DEF2-QZVP[31] level of theory using the GD3BJ empirical dispersion correction.[32] Structures were also calculated using the SDD basis set.[33] The default geometry convergence criteria in Gaussian 16 were applied. Nuclear shielding tensors were calculated by the default GIAO method[34,35] in Gaussian. Metal chelates of the tetradentate anion $PrPyrr^{2-}$ were constrained to *Cs* symmetry. Simulations were carried out *in vacuo* and in water/acetonitrile solvent continua (SCRF PCM method[36]). GaussView 6.0.16[37] was used for preparing input files and data visualization. GaussSum 3.0 was used to visualize electronic spectra and tabulate transition assignments.[38] All geometry-optimized structures were characterized by positive frequency eigenvalues, indicating that true minima were located on the global potential energy surface for each system.

Time-dependent DFT (TD-DFT) simulations were carried out using the above method (CAM-B3LYP) and basis sets in Gaussian 16 for all small molecules. Typically, 60 excited singlet states were computed to cover the full spectral range (150–900 nm). TD-DFT simulations on protein complexes required the use of the ONIOM[39] method employing two layers: a high or quantum mechanical (QM) layer computed at the CAM-B3LYP/SDD/GD3BJ level

of theory and a low layer (molecular mechanics) calculated using the UFF[40] force field. The input structures for the single-point calculations were derived from the best-scoring poses of the ligands of interest docked within the relevant binding site in HSA taken directly from the output of a GLIDE XP[41] docking run with the relevant X-ray structure target (e.g., PDB code: 1HA2). For the QM layer of HSA•{Ni(PrPyrr)}, all atoms of the metal chelate were included at the high level. For the protein complexed with the Pd(II) species Pd(PrPyrr), Pd^a, and $[Pd(HPrPyrr)(OH_2)]^+$, Pd^b, the QM layer comprised either the single metal chelate being investigated, e.g., HSA•{Pd^a}, or the co-bound pair of metal chelates located within their respective binding sites, i.e., HSA•{Pd^a}{Pd^b}. Three amino acid side chains (Arg-257, His-288, and Tyr-150) were included in the QM layer around Pd^a located within Sudlow's site I in the simulations of HSA•{Pd^a}{Pd_b} to achieve an electronic structure that best-matched experiment, specifically the calculated CD spectrum of the macromolecular complex. This is illustrated in the two boxes below. For HSA•{Pd^a}{Pd^b}, 120 excited singlet states were calculated owing to the presence of two absorbing chromophores in the protein and the fact that ~50–60 states are required per ligand to calculate a reliable absorbance or CD spectrum.



1.6 Molecular Docking Simulations

System preparation. The 2.5-Å and 2.95-Å X-ray crystal structures of HSA in complex with warfarin,[42] diazepam,[43] and ibuprofen[43] were retrieved from the Protein Data Bank (PDB ID codes: 1HA2, 2BXF, and 2BXG). The structure of HSA was pre-processed, minimized, and refined using the Protein Preparation Wizard[44] employed in Schrödinger Suite 2022-3. This step included eliminating crystallographic waters within 5 Å of the ligand binding site, adding missing hydrogen atoms and side chain atoms, as well as assigning the appropriate charge and protonation state of the receptor structure (pH = 7.4) using Prime. Finally, the protein structure was subjected to energy minimization using Macromodel[45] and the S-OPLS force-field[46,47] with a RMSD cut-off value of 0.30 Å to resolve steric clashes among closely spaced residues arising from the addition of hydrogen atoms.

The LigPrep module of Schrödinger was used to prepare ionization states and geometry-optimized input structures for H_2PrPyrr using a pH range of 7.4 ± 2.0. The structures of Ni(PrPyrr), Pd(PrPyrr), Pt(PrPyrr), and $[Pd(HPrPyrr)(OH_2)]^+$ used for docking inputs were obtained by DFT simulations at the CAM-B3LYP/DEF2-QZVP level of theory in a water solvent continuum (SCRF PCM model) and implementing the GD3BJ empirical dispersion energy correction. Minor adjustments were required to prepare the metal chelate structures for docking with GLIDE. First, the metal was given a +2 charge and the pyrrole nitrogen atoms were each given a −1 charge. Second, the bonds from the four N-donor atoms to the metal ion were assigned bond orders of zero. This step is

mandatory as it obviates the need for specific force field parameters involving the metal ion; the coordination geometry is then restrained to remain similar to the input DFT-calculated geometry by GLIDE during optimization and fitting. Lastly, partial charges were assigned to the structures using the S-OPLS force-field.

Molecular docking. Docking was performed with GLIDE[41,48,49] to identify the best-fit orientation of the compounds (ligands) into both Sudlow's site I (exemplified by PDB code 1HA2) or Sudlow's site II (PDB code 2BXF) and any sites within ~20 Å of each site.[50] The appropriate receptor grid was generated based upon a set of centre coordinates using a cube with dimensions $40 \times 40 \times 40$ Å^3 in each case. The grid box employed was a factor of 4 times larger than the default box size ($10 \times 10 \times 10$ Å^3) and centred on the centroid of the relevant HSA-bound drug (warfarin or diazepam) or protein residue (typically Trp-214). The drug was then automatically removed prior to grid generation. This strategy was adopted because the metal chelates are slightly larger than the typical small molecule drugs bound in Sudlow's sites I and II and we wanted to ensure appropriate sampling of any atypical binding sites close to the main drug-binding pockets. Two types of grid were tested: (i) a hard, rigid receptor grid that is offered as the default in GLIDE and (ii) a softer grid created by scaling the van der Waals radii of the nonpolar atoms of the receptor by a factor of 0.70. Docking simulations employing the soft receptor grid also employed soft ligands with nonpolar atoms similarly scaled (van der Waals radii $\times$ 0.70).

The metal chelates and free ligand species were then flexibly docked into the relevant binding site grids using the standard precision (SP) and extra precision (XP) docking protocols of GLIDE; aromatic hydrogens were included as H-bond donors. Up to four best-scoring poses for each compound with each PDB structure of native HSA were saved and selected for further analysis.

Docking simulations on HSA targets containing pre-bound drugs (warfarin, diazepam, and ibuprofen) were also performed to evaluate the ability of the protein to take up the metal chelates (as well as H_2PrPyrr and its protonated derivatives) at binding site locations close to the bound drugs as well as secondary sites located further away. These experiments were performed as described above with grids centred on Trp-214 at the core of the protein. The ligand/drug present in the X-ray structure was retained when setting up the receptor grid. These unconventional experiments were specifically aimed at understanding our fluorescence titration data for HSA pre-equilibrated with warfarin and ibuprofen.

Caveats. Docking scores are very approximate estimates of the binding affinity of the ligand for the protein. It has been shown that they do *not* correlate with experimentally measured binding constants.[51,52] Currently, the major limitation is that protein conformational flexibility in the form of dynamic motion of side-chain residues, coils and helices (which may open channels or pockets within the macromolecule transiently), as well as solvation/desolvation of both the ligand and the receptor, and the electronic/electrostatic contribution from metal ions to ligand uptake, to name a few factors, are not considered by even the best docking algorithms (GLIDE). Ligand flexibility is accounted for by GLIDE, but this is mainly useful for predicting chemically meaningful ligand conformations (poses),[52] and not for accurately calculating the free energy of binding which requires precisely determining many contributions to the binding free energy. Bearing the above limits in mind, docking ligands flexibly into a static macromolecular target (receptor) can be useful for suggesting: [1] possible ligand binding sites, [2] conformations likely to be adopted by a ligand within a binding site, and [3], for very similar ligands, providing an idea of their possible binding site preferences. Because the protein itself is kept static during

a docking simulation, current docking protocols are intrinsically poor at predicting the relative binding affinity of a given ligand for multiple binding sites within the protein target. In short, the results of docking simulations must be treated with great CAUTION and the limitations in the method considered when attempting to draw parallels with experimental data. We have therefore interpreted our docking simulation data rather guardedly and have mainly considered the trends that provide further insight in support of the experimental data, i.e., rigorous, reproducible experimental measurements.

2. Figures

2.1 General Characterization Data

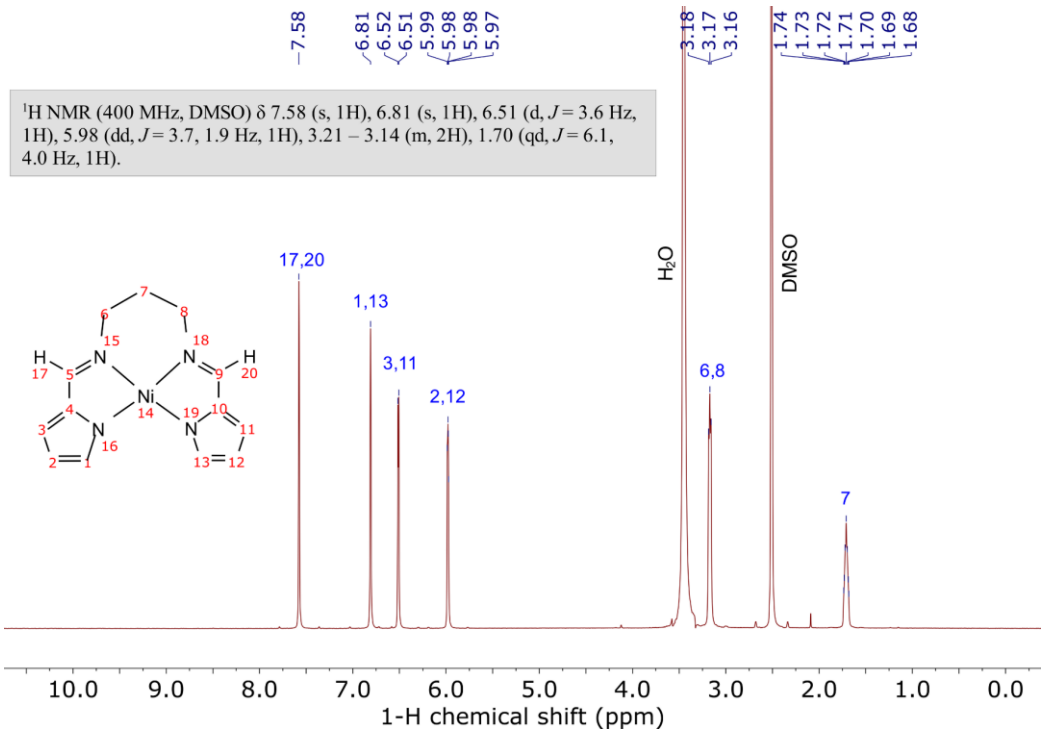


Figure S1. 400 MHz ^{1}H NMR spectrum of Ni(PrPyrr) recorded in DMSO-d_6 at 300 K. This compound is known;[5] the spectral data here briefly confirm the structure of the compound and its purity.

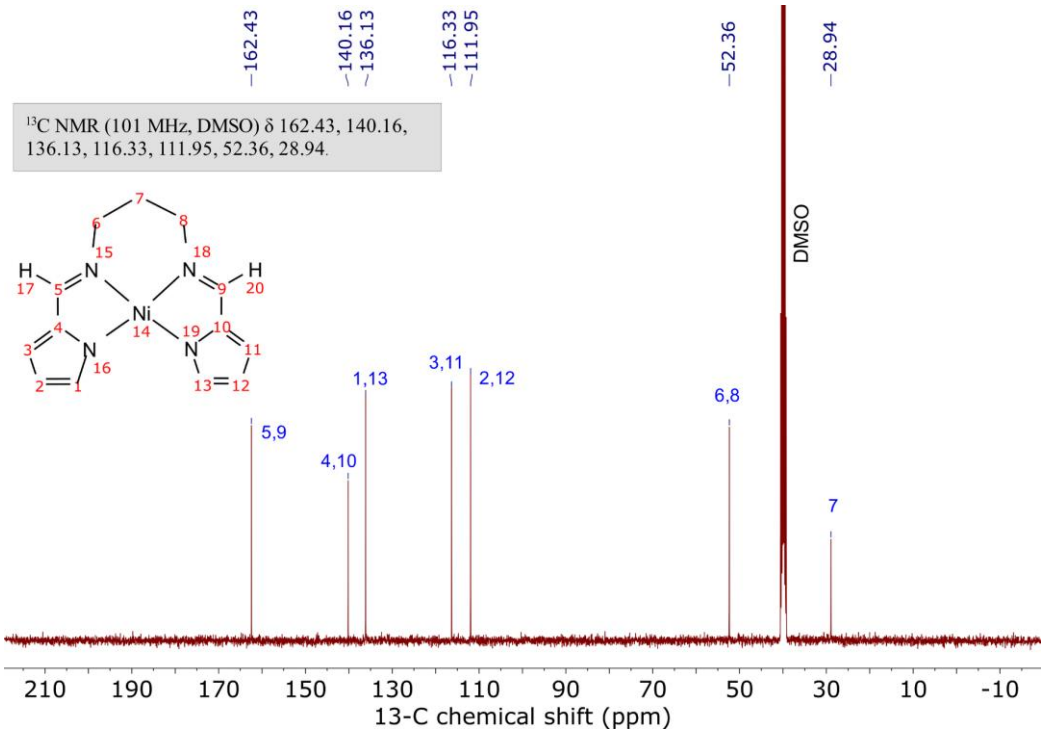


Figure S2. 101 MHz ^{13}C NMR spectrum of Ni(PrPyrr) recorded in DMSO-d_6 at 300 K.

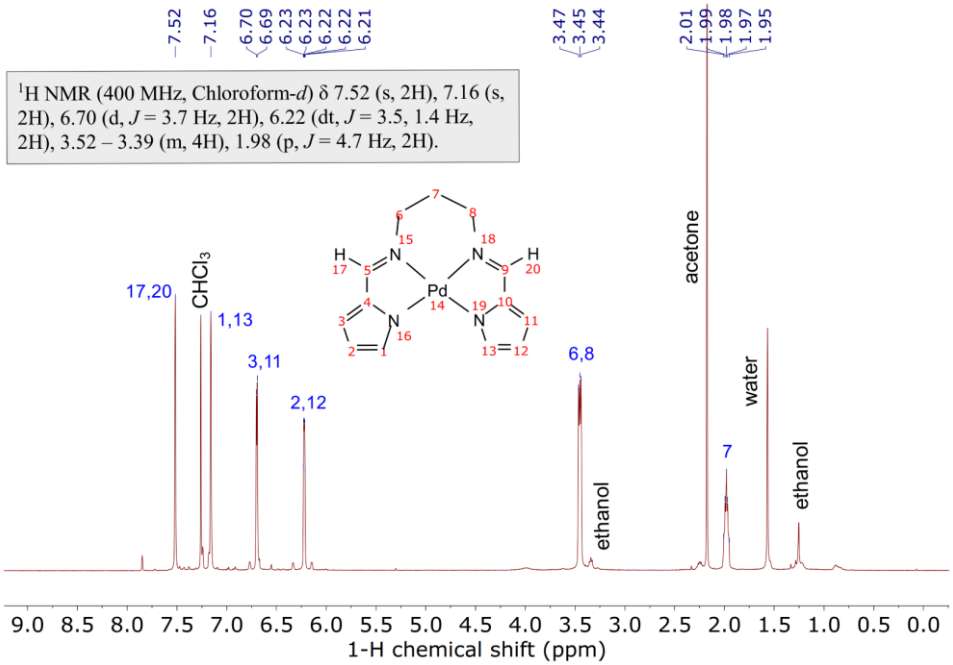


Figure S3. 400 MHz ^{1}H NMR spectrum of Pd(PrPyrr) recorded in $CDCl_3$ at 300 K. This compound is known;[53] the ^{1}H NMR spectral data here briefly confirm the structure of the compound. Solvent impurity peaks are labelled.

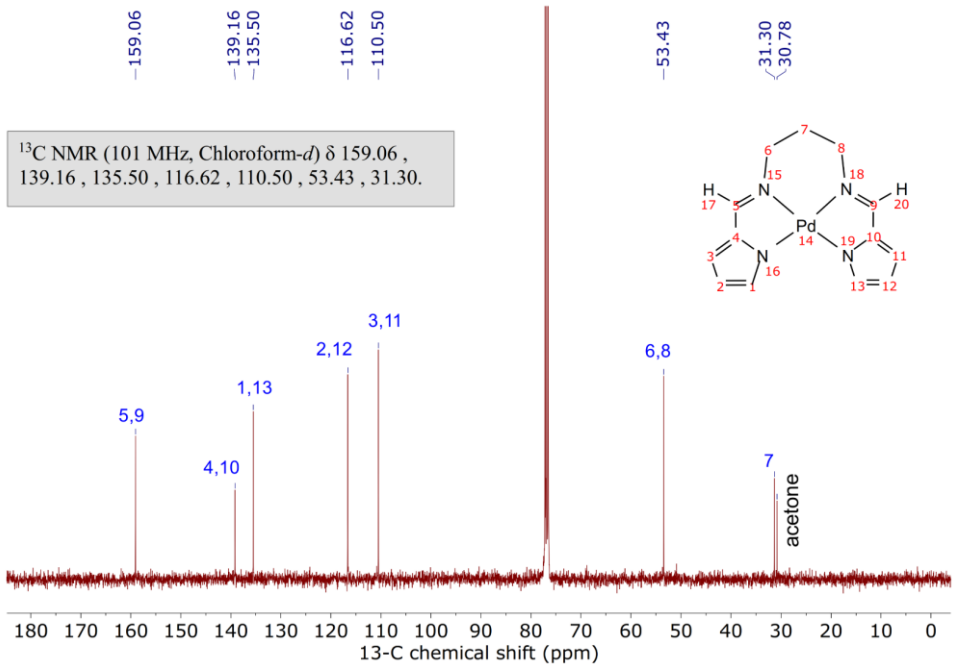


Figure S4. 101 MHz ^{13}C NMR spectrum of Pd(PrPyrr) recorded in $CDCl_3$ at 300 K. Although the compound is known,[53] ^{13}C NMR data have not been reported for it in the literature.

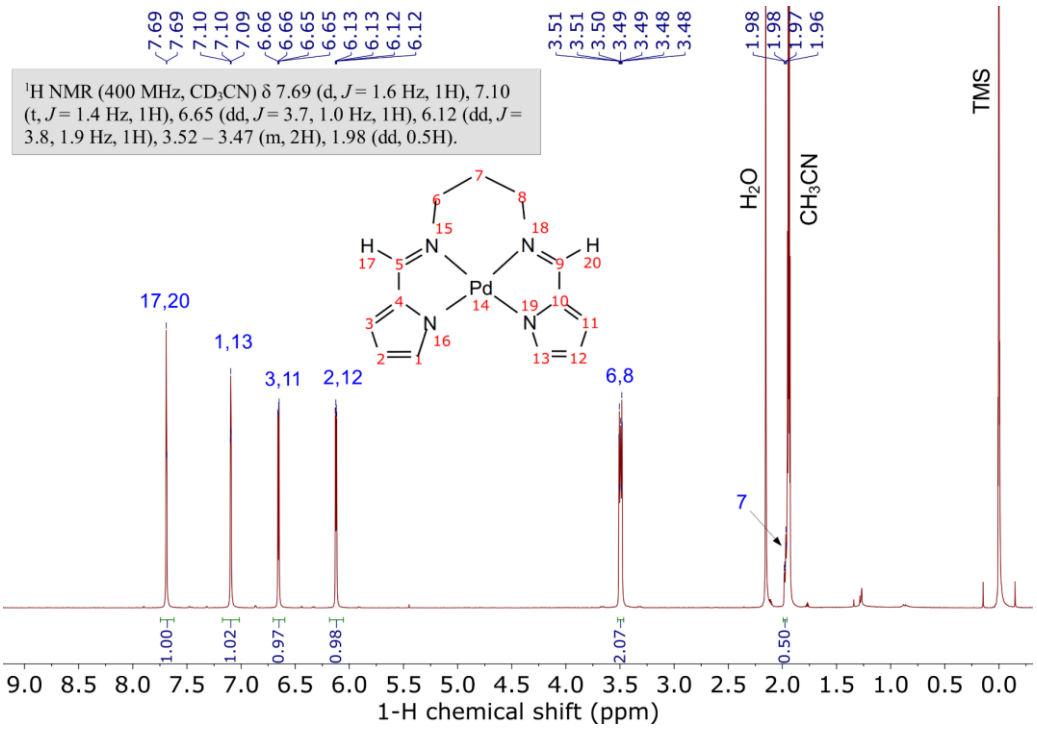


Figure S5. 400 MHz 1H NMR spectrum of Pd(PrPyrr) recorded in CD_3CN at 300 K. This spectrum was recorded on a sample from the same bulk solid as in Figure S3 to confirm that the solvent contaminants were not part of the solid reaction product.

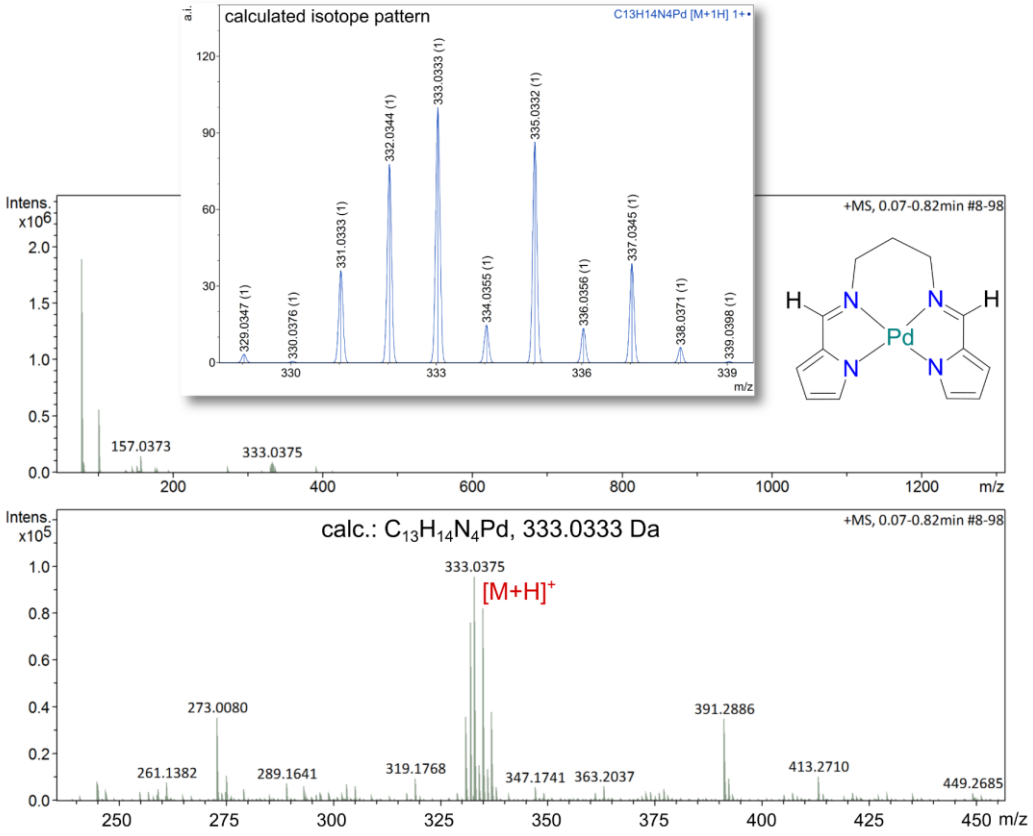


Figure S6. ESI-MS spectrum of Pd(PrPyrr). The solid sample was dissolved in methanol with 0.1% formic acid (V/V) and the spectrum was recorded in positive ESI mode. mMass 5.5.0 was used to simulate the isotope pattern.[54] No ESI-MS data are available in the literature[53] for this compound.

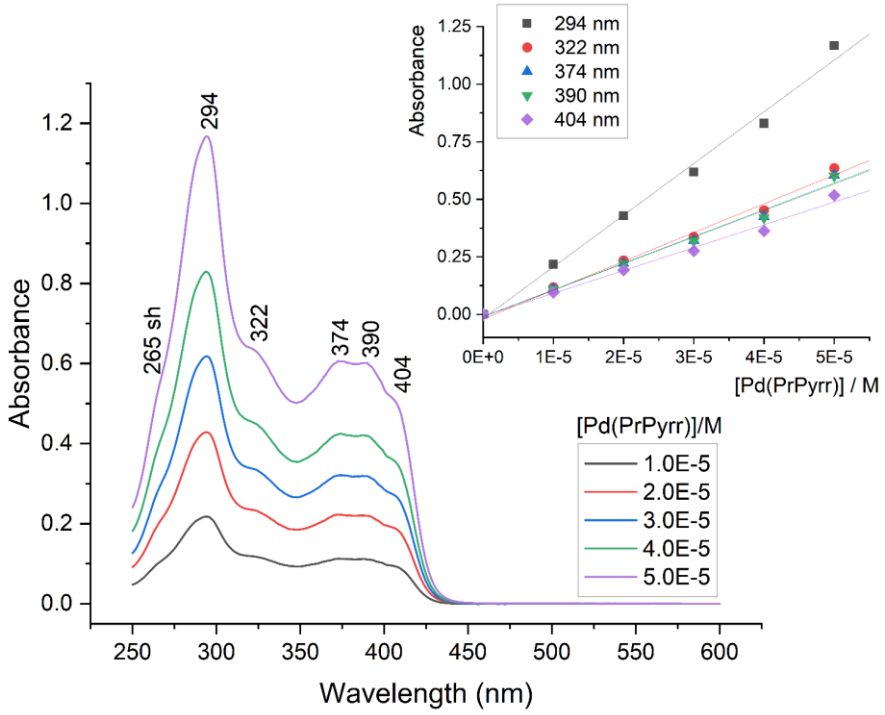


Figure S7. UV-visible spectrum of Pd(PrPyrr) recorded in CH_3CN at 295 K as a function of concentration. The molar absorptivities for selected band maxima are reported in the Experimental Section and were determined from the slopes of the inset Beer-Lambert law plots. Electronic spectra for the compound were not reported in the original literature.[53]

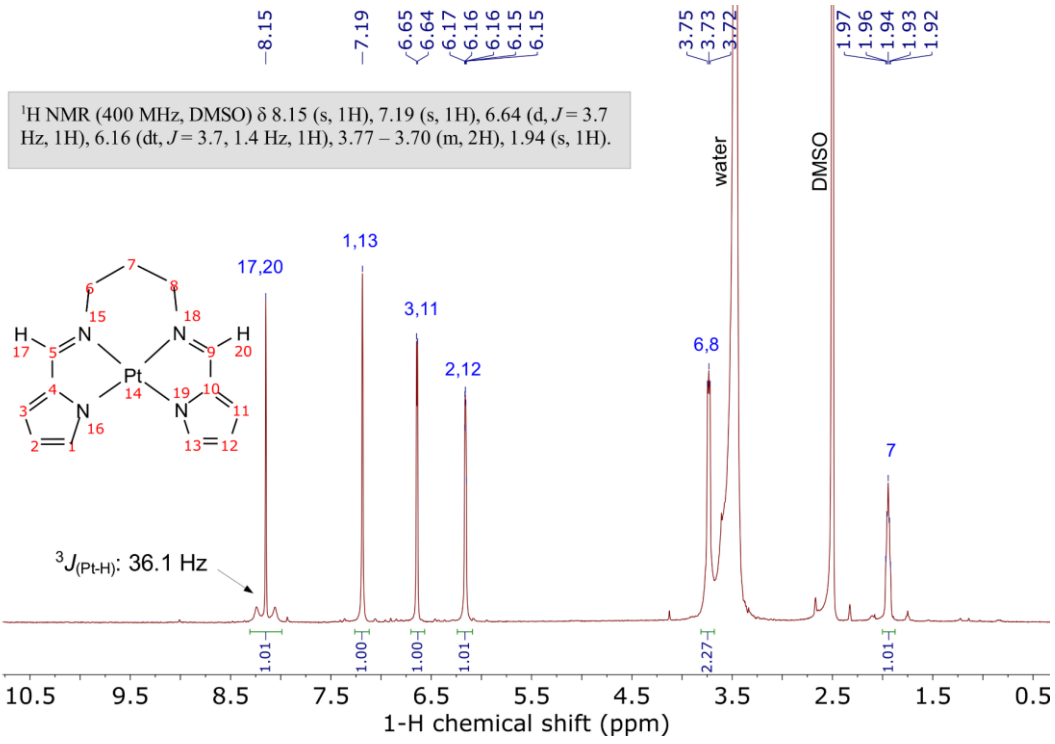


Figure S8. 400 MHz ^{1}H NMR spectrum of Pt(PrPyrr) recorded in DMSO-d_6 at 300 K. Spin–spin coupling (^3J, ^{195}Pt–^{1}H) between Pt and the imine CH protons in the chelate is evident, measuring 36.1 Hz, and is in accord with the literature range of 15–50 Hz.[55]

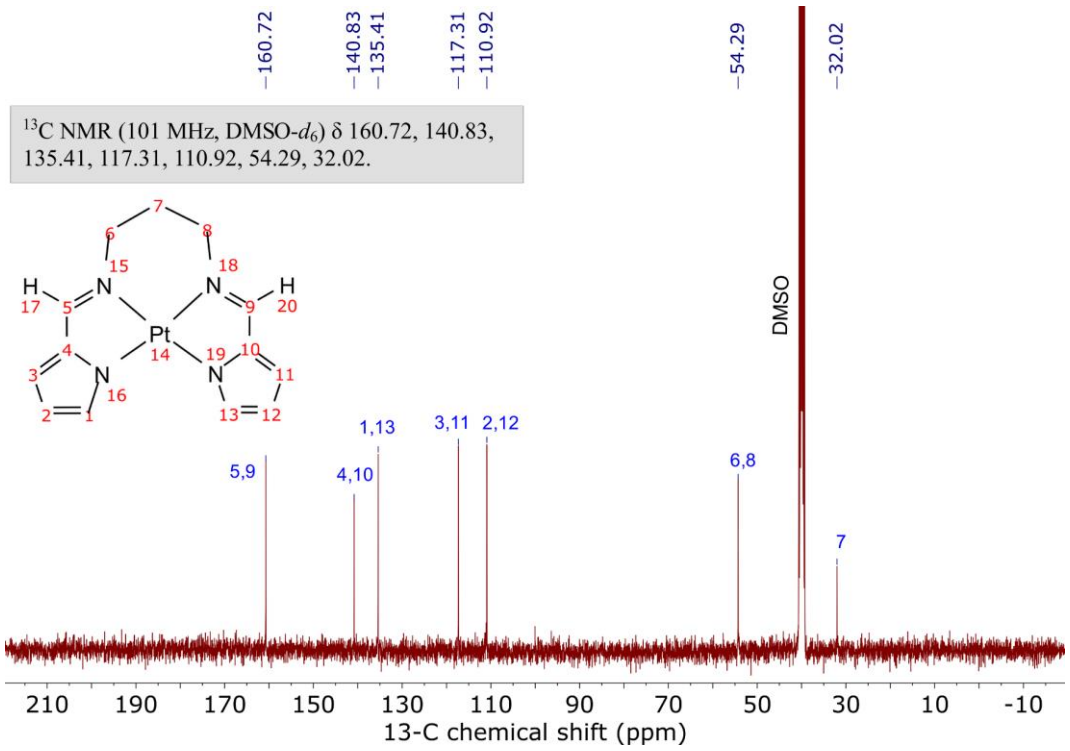


Figure S9. 101 MHz ^{13}C NMR spectrum of Pt(PrPyrr) recorded in DMSO-d_6 at 300 K.

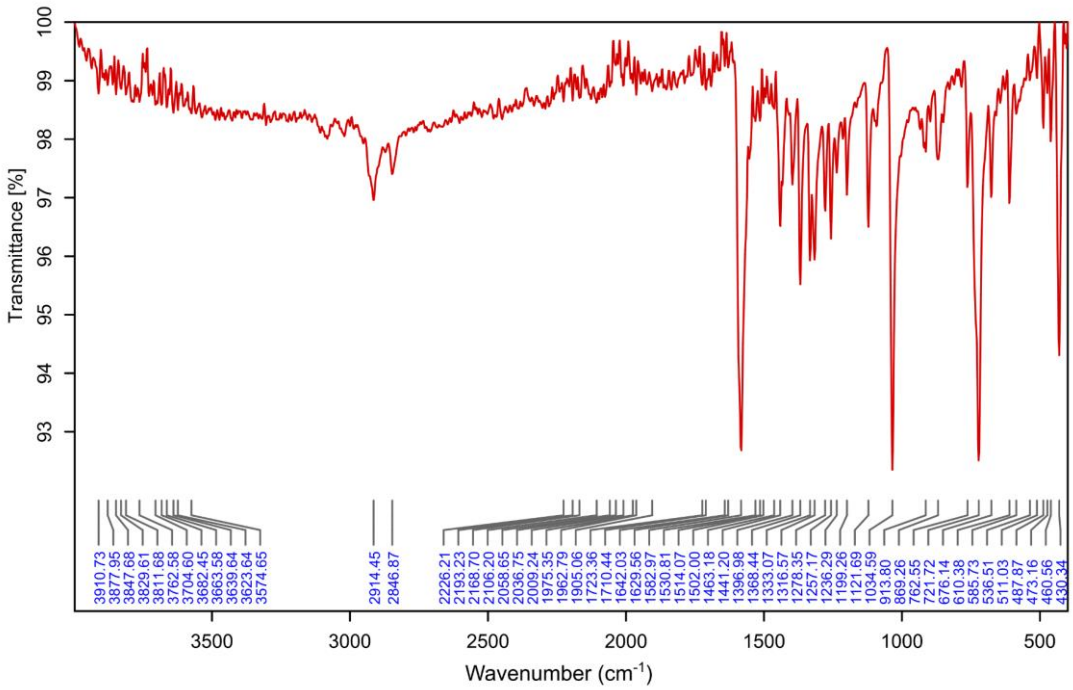


Figure S10. FTIR spectrum of Pt(PrPyrr) recorded as a crushed powder sample at 295 K.

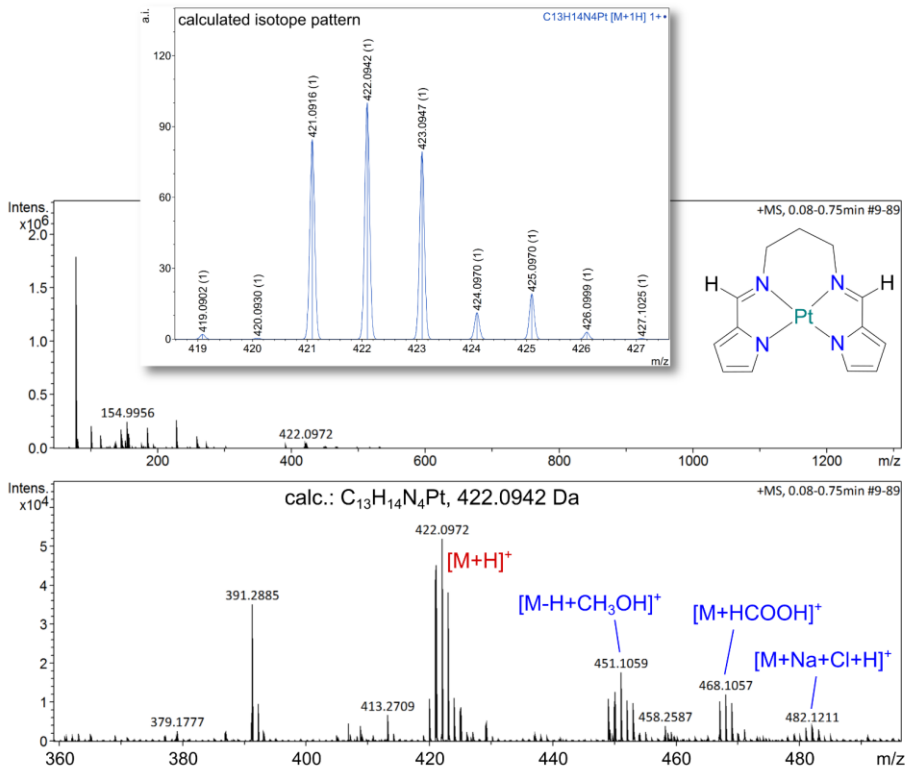


Figure S11. ESI-MS spectrum of Pt(PrPyrr). The solid sample was dissolved in methanol with 0.1% formic acid (V/V) and the spectrum was recorded in positive ESI mode. Parent ion adducts are assigned. mMass 5.5.0 was used to simulate the isotope pattern.[54]

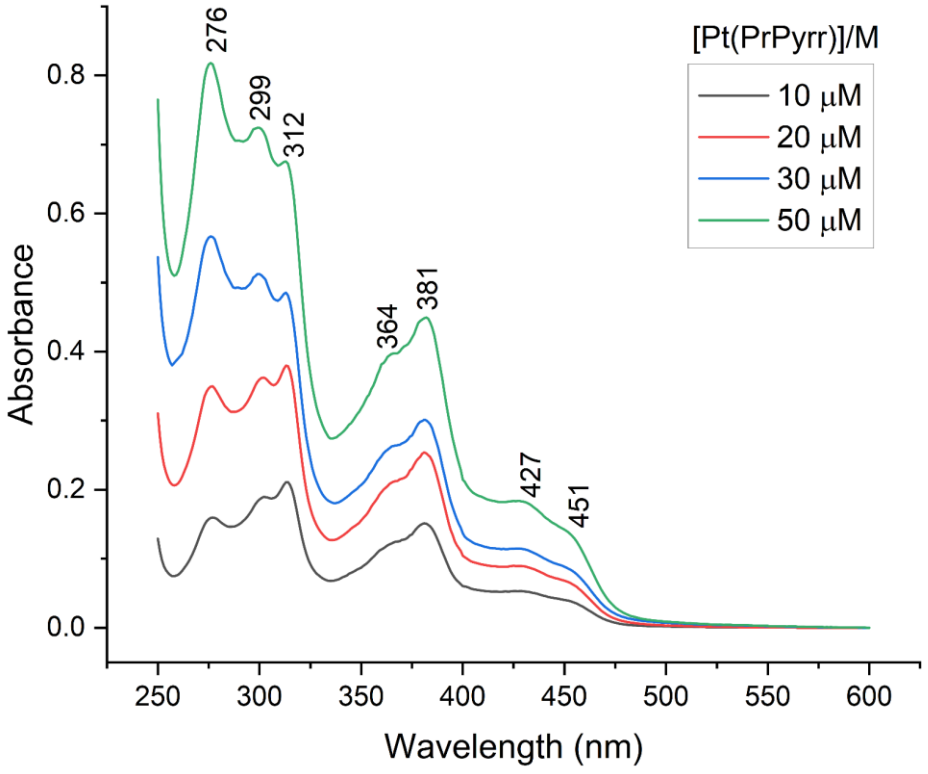


Figure S12. UV-visible spectrum of Pt(PrPyrr) recorded in CH_3CN at 295 K as a function of concentration.

2.2 Advanced Spectroscopy and Reactions

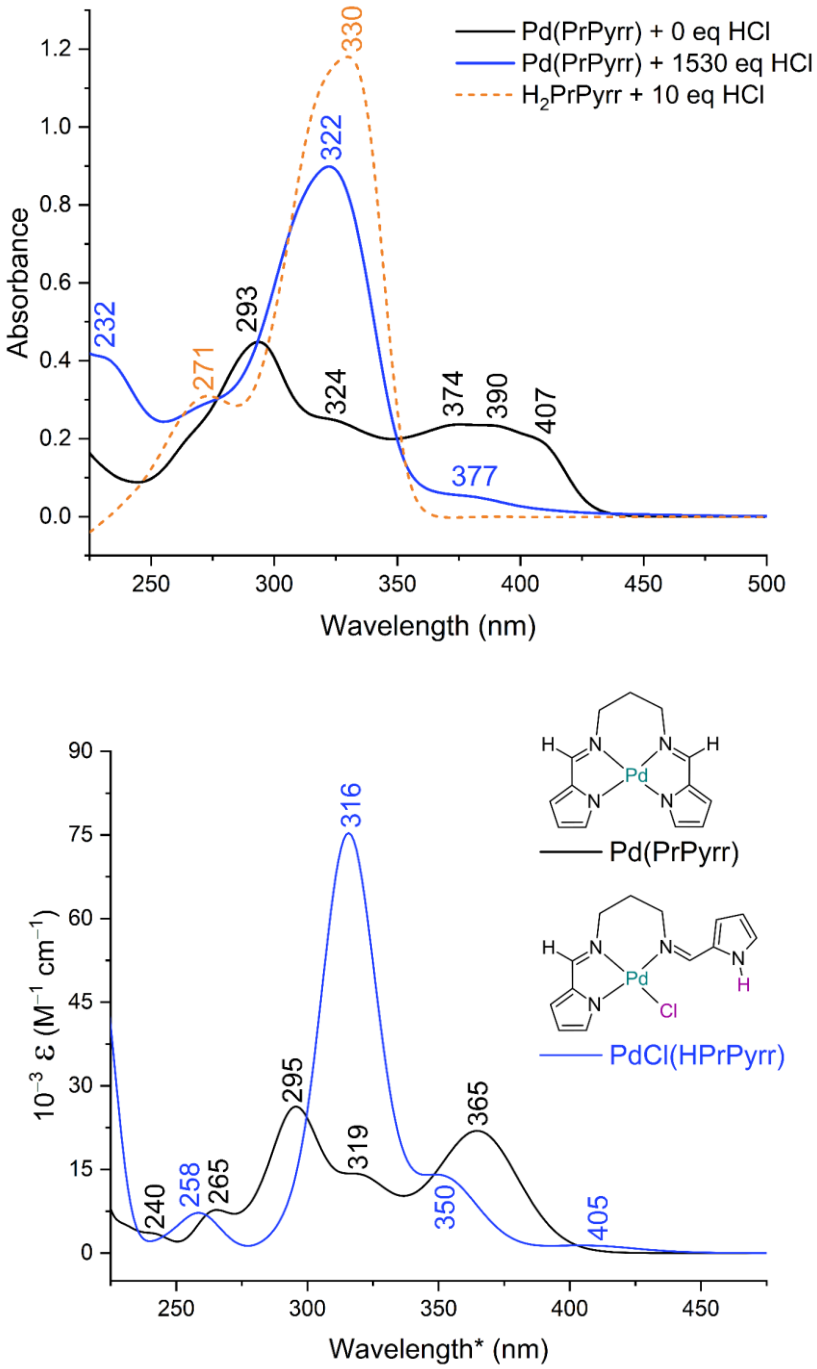


Figure S13. *Top*: experimental UV-visible spectra for Pd(PrPyrr) and H_2PrPyrr recorded with different HCl mole ratios in acetonitrile at 37 °C. *Bottom*: Electronic spectra for Pd(PrPyrr) and PdCl(HPrPyrr) calculated using TD-DFT at the CAM-B3LYP/DEF2-QZVP/GD3BJ level of theory in an acetonitrile solvent continuum. The wavelength data have been scaled by +35 nm because the method overestimates the transition energies relative to the experimental band maxima. The theoretical spectra match the experimental spectra for the given structures. The experimental spectrum of the protonated free base ligand, $[H_4PrPyrr]^{2+}$, is inconsistent with the spectrum recorded for the Pd(II) chelate in the presence of a large excess of HCl, confirming that demetallation did not occur.

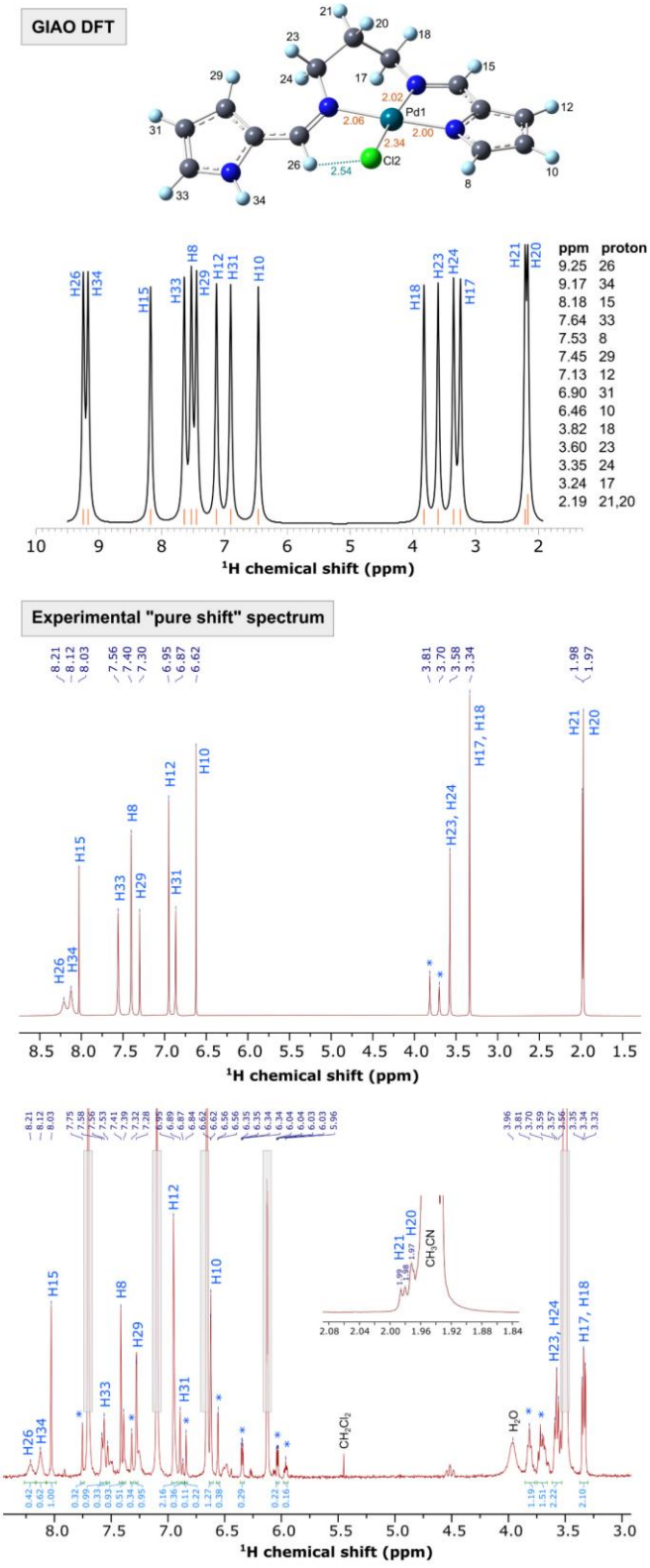


Figure S14. *Top*: DFT-calculated ^{1}H NMR spectrum of PdCl(HPrPyrr) at the CAM-B3LYP/def2qzvp level of theory (CH_3CN solvent continuum). *Bottom*: experimental 1H NMR spectrum of a CD3CN solution of Pd(PrPyrr) with 2.0 eq of HCl. Signals due to Pd(PrPyrr) are masked with transparent grey rectangles. *Centre*: Pure shift ^{1}H NMR spectrum determined from the major peak multiplets of the experimental NMR spectrum (bottom). The pure shift spectrum removes spin-coupling and permits assignment of the major species in solution by matching peaks to the DFT-calculated NMR spectrum.

2.3 X-Ray Crystallography and DFT Simulations

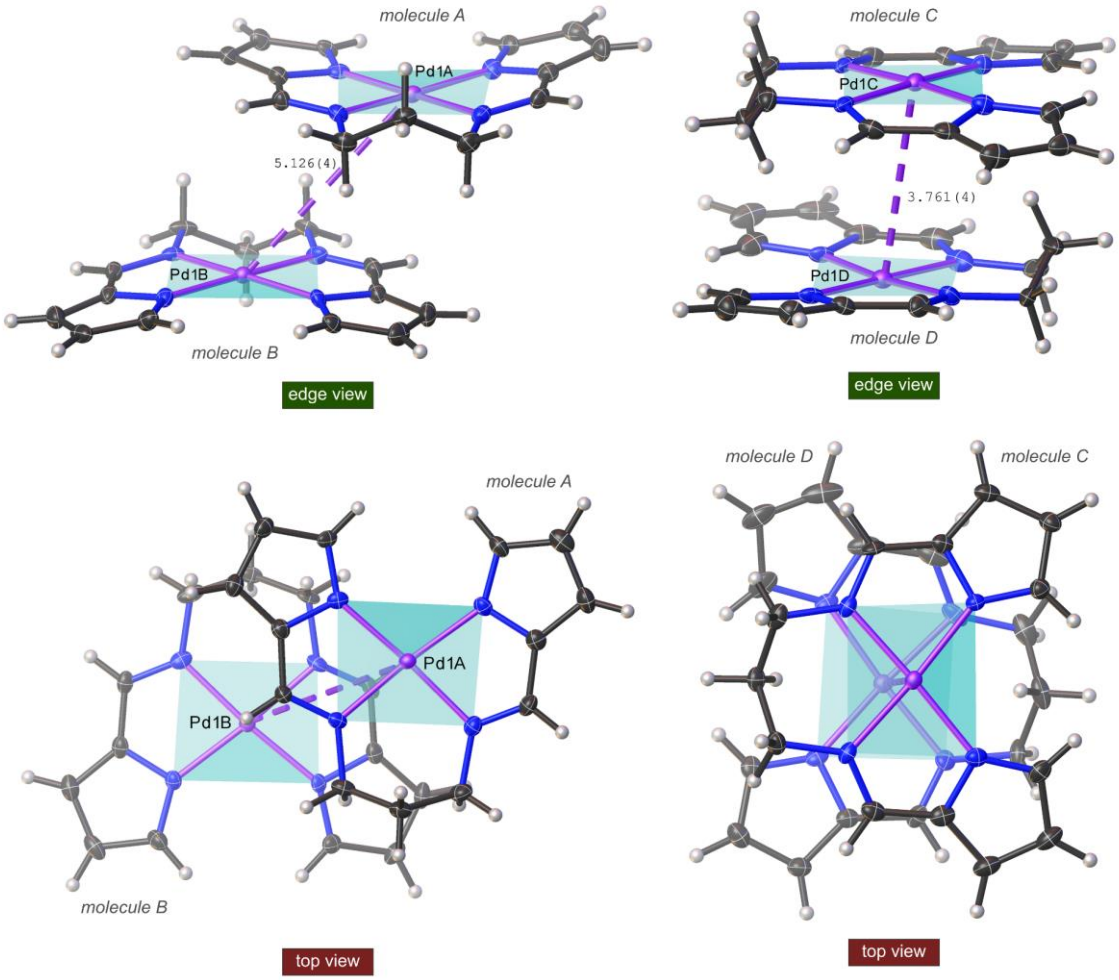


Figure S15. Side-on and top views of the two types of stacked dimer formed by Pd(PrPyrr). Left: molecules A and B in the asymmetric unit form a laterally offset dimer with a Pd1A···Pd1B distance of 5.126(4) Å. Right: Molecules C and D form a more nearly eclipsed dimer with a shorter metal···metal interaction distance. Pd1C···Pd1D = 3.761(4) Å. In both cases, the top views are normal to the 5-atom mean plane passing through the metal ion and nitrogen donor atoms (PdN4).

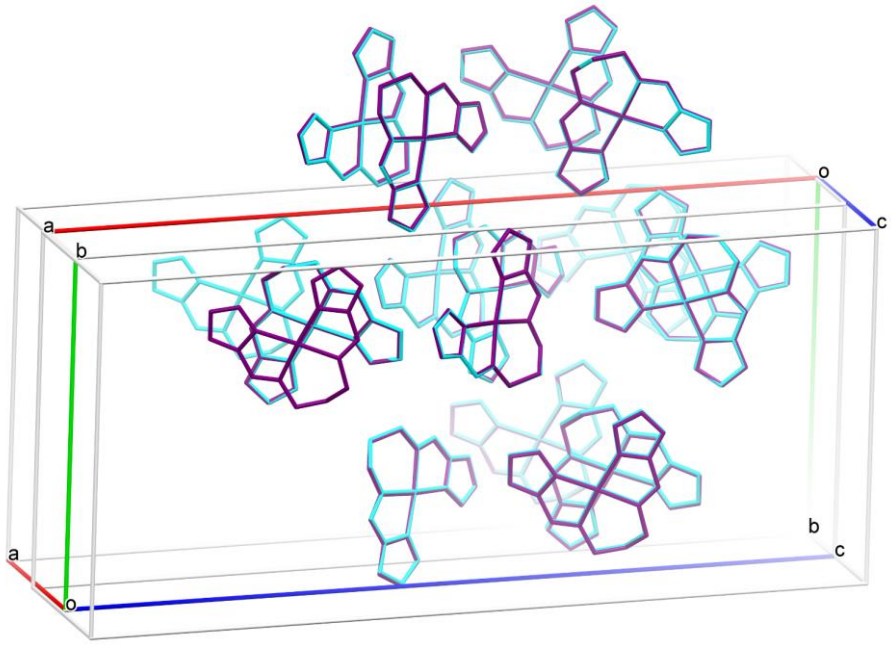


Figure S16. Comparison of the unit cell contents for the room temperature X-ray structure of PdPrPyrr (purple, space group $P2_1/a$, CSD code: XUVQIO[53]) and the low temperature structure determined in this work (cyan, space group $P2_1/c$). The root mean square deviation (RMSD) is 0.0825 Å and the calculated powder X-ray diffraction patterns (not shown) have a similarity index of 0.9963. The structures are therefore crystallographically equivalent; the measurable differences are attributed mainly to the temperature differences for the two data sets.

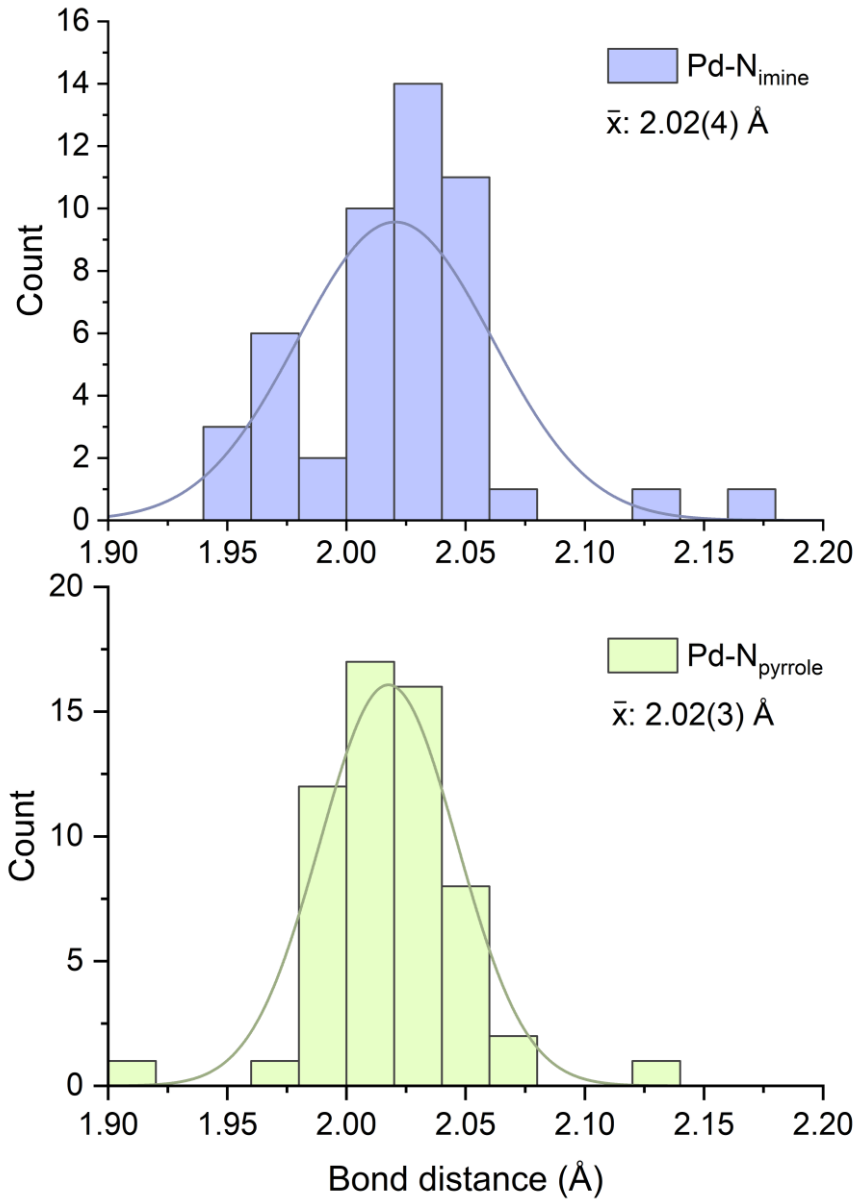


Figure S17. Histograms of the Pd–N_{imine} and Pd–$N_{pyrrole}$ bond distances for a selection of 27 out of 55 Pd(II) complexes with Pd–$N_{pyrrole}$ coordination involving a mono-substituted pyrrole ring in the Cambridge Structural Database (CSD).[56] The search fragment was: Pd–NCCH$(CH)_2$. The mean bond distance and estimated standard deviation are indicated in each case.

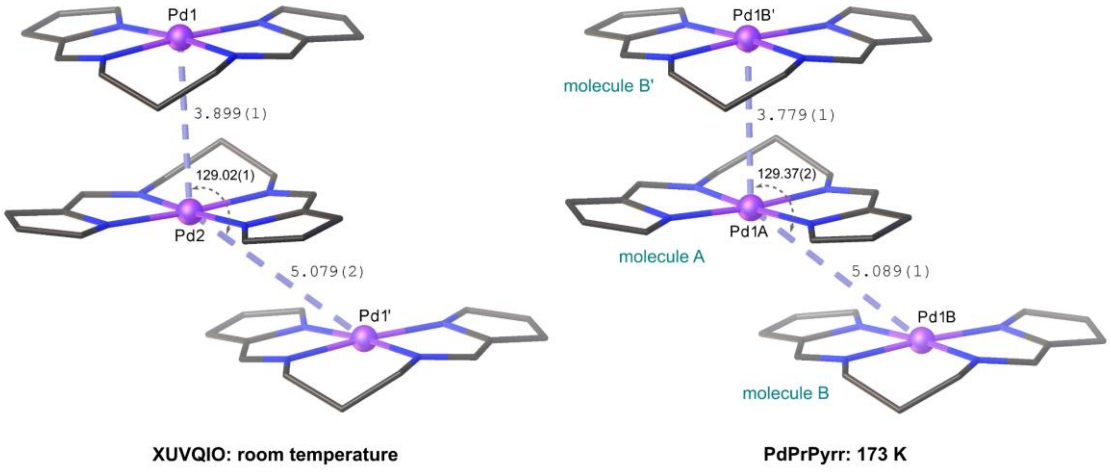


Figure S18 (a). View of the two types of intermolecular π-stacking arrangements for molecules in the crystal lattice of PdPrPyrr. The structure at the left reflects the room temperature data reported by Bacchi *et al.*;[53] the equivalent interactions at 173 K determined in this study for the compound are indicated at the right. Metal atoms are labelled; bond distances and bond angles are in units of Å and degrees. respectively. Symmetry operator codes: Pd1′ (*x*. *y*. 1 + *z*); Pd1B′ (1 + *x*. *y*. *z*). Lowering the temperature shortens the closest Pd···Pd interaction whilst lengthening the second, laterally offset interaction.

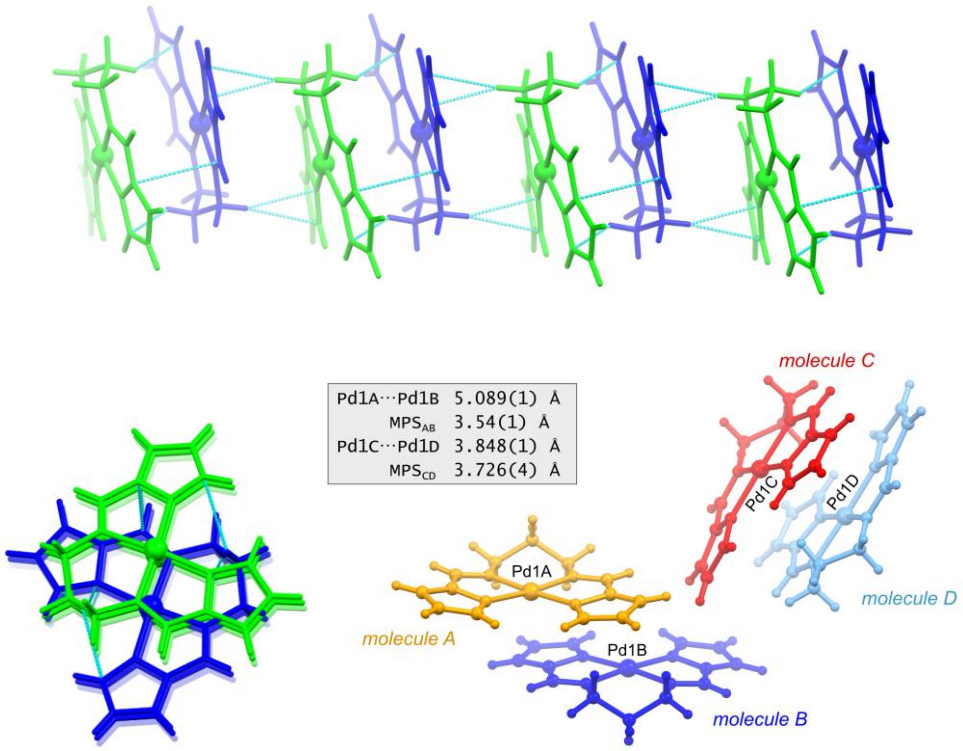


Figure S18 (b). Top: View approximately down the unit cell c-axis of the 1D chain of noncovalently interacting near-centrosymmetric dimers formed in the crystal lattice of Pd(PrPyrr) (173 K data set). Only independent molecules A (green) and B (blue) are shown for clarity. A similar 1D chain is formed by stacked independent molecules C and D. Each structure is rendered as a stick model with the metal ion shown as a ball with an arbitrarily chosen radius. Noncovalent contacts between atoms are shown as dashed light blue cylinders (distance < ∑{van der Waals radii} – 0.10 Å). The interactions belong to two main types, namely (alkyl)C–H···C(π) and C(π)···C(π), with the latter occurring between stacked pyrrolide-imine groups. Bottom left: view approximately down the unit cell a-axis of the noncovalent 1D chain formed by independent molecules A (green) and B (blue) in the crystal lattice of Pd(PrPyrr). Bottom right: asymmetric unit showing all four independent molecules.

Comment on Figure S18:

The dimer formed by molecules A and B encompasses laterally displaced face-to-face stacked monomers with a Pd1A···Pd1B separation of 5.089(1) Å, PdN4 plane centroid-to-centroid (Ct···Ct) distance of 5.126(4) Å, mean plane separation (MPS_{AB}) of 3.54(1) Å, and lateral shift (LS) of 3.77(1) Å. Each bis(pyrrolide-imine) chelate curves outward from the intradimer space by virtue of the pyrrole rings being canted slightly below the PdN4 mean plane. The mean perpendicular out-of-plane atomic displacement for the pyrrole β-carbons is 0.28(8) Å. In contrast, the monomers in the dimer formed by molecules C and D are nearly eclipsed (though in an inverted relative orientation) and exhibit a minimal PdN4 mean plane lateral offset (LS) of 0.55(1) Å, a Pd1C···Pd1D separation of 3.848(1) Å, a Ct···Ct distance of 3.761(4) Å, and a mean plane separation (MPS_{CD}) of 3.726(4) Å. In contrast to dimer AB, the ligands of dimer CD curve inward towards the intradimer space. The nature of the distortion evidently pushes the monomer units slightly apart to limit van der Waals repulsion, accounting for the larger MPS value compared with dimer AB. The ligand curvature relative to the 5-atom PdN4 mean plane for each monomer within dimer CD results in a mean perpendicular out-of-plane atomic displacement for the pyrrole β-carbons of 0.28(11) Å, which is akin to that observed for dimer AB.

Further inspection of the crystal packing for Pd(PrPyrr) indicates that molecule A of the ASU forms a near-eclipsed inverted dimer with molecule B′ [symmetry code: 1 + *x*, *y*, *z*] within the unit cell which is similar in structure to dimer CD (Figure S18b). The geometry of dimer AB′ is characterized by a $MPS_{AB'}$ ~3.659(4) Å, a LS of 0.422(11) Å, and a Pd1A···Pd1B′ distance of 3.779(1) Å. Since the van der Waals radius of Pd(II) is estimated to be ~1.70 Å[57] to 1.86 Å,[58] the intradimer Pd···Pd nonbonded distance for this chelate pair in the low-temperature X-ray structure falls short of the sum of the van der Waals radii of the interacting atoms and is consistent with a *weak* metal–metal (d^8–d^8) interaction. The fundamental nature of this type of interaction has been nicely delineated by Bercaw *et al*. for tight acetate-bridged Pd(II) dimers[59] and Marino *et al*. for weaker pyrophosphate-bridged Pd(II) dimers.[60] Notably, this interaction is absent in the room temperature X-ray structure of Pd(PrPyrr) (Pd1···Pd2, 3.899(1) Å;[53] Figure S16), confirming the role played by temperature-induced lattice compression in driving formation of the metal···metal interaction the current system. DFT simulations (Figure S19, *in vacuo*) suggest the observed stacking probably encompasses several intermolecular forces of attraction, especially London dispersion forces, which collectively contribute to stabilization of the solid-state dimers.

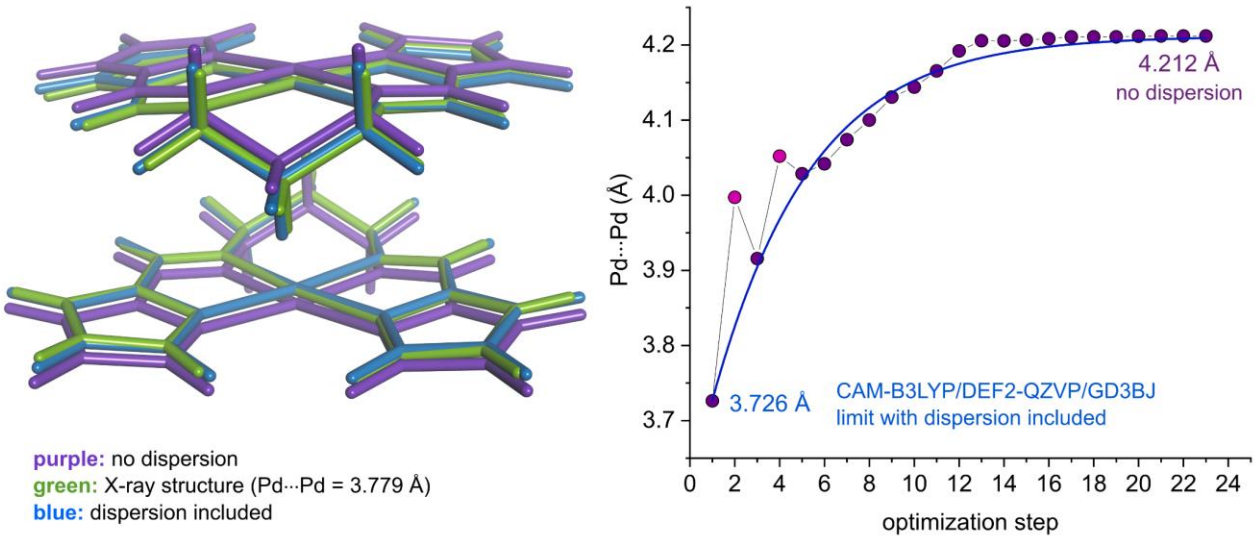


Figure S19. Left: DFT-calculated structures of the AB' noncovalent dimer (C_i symmetry) formed between two molecules of Pd(PrPyrr) in the gas phase. The simulations were carried out at the CAM-B3LYP/DEF2-QZVP level of theory both with (blue) and without (purple) application of the GD3BJ empirical dispersion correction and have been fitted to the X-ray structure (green) determined at 173 K by nonlinear least-squares minimization. The similarity indices between the blue/green and purple/green structures are 0.999 and 0.990, respectively. Right: graph of the Pd···Pd internuclear distance plotted as a function of the optimization step during geometry optimization of the dimer with empirical dispersion excluded. The data show that the low temperature X-ray structure of the AB' noncovalent dimer is only accurately modelled when dispersion is taken into account in the simulation, confirming the notion that the Pd(II) chelates dimerise mainly as a result of noncovalent London dispersion forces of attraction. The solid blue curve has no physical significance and merely gives an idea of the idealized refinement trajectory during geometry optimization. The data points coloured in pink were not included in the curve fitting purely for cosmetic reasons but are significant steps for the geometry optimization.

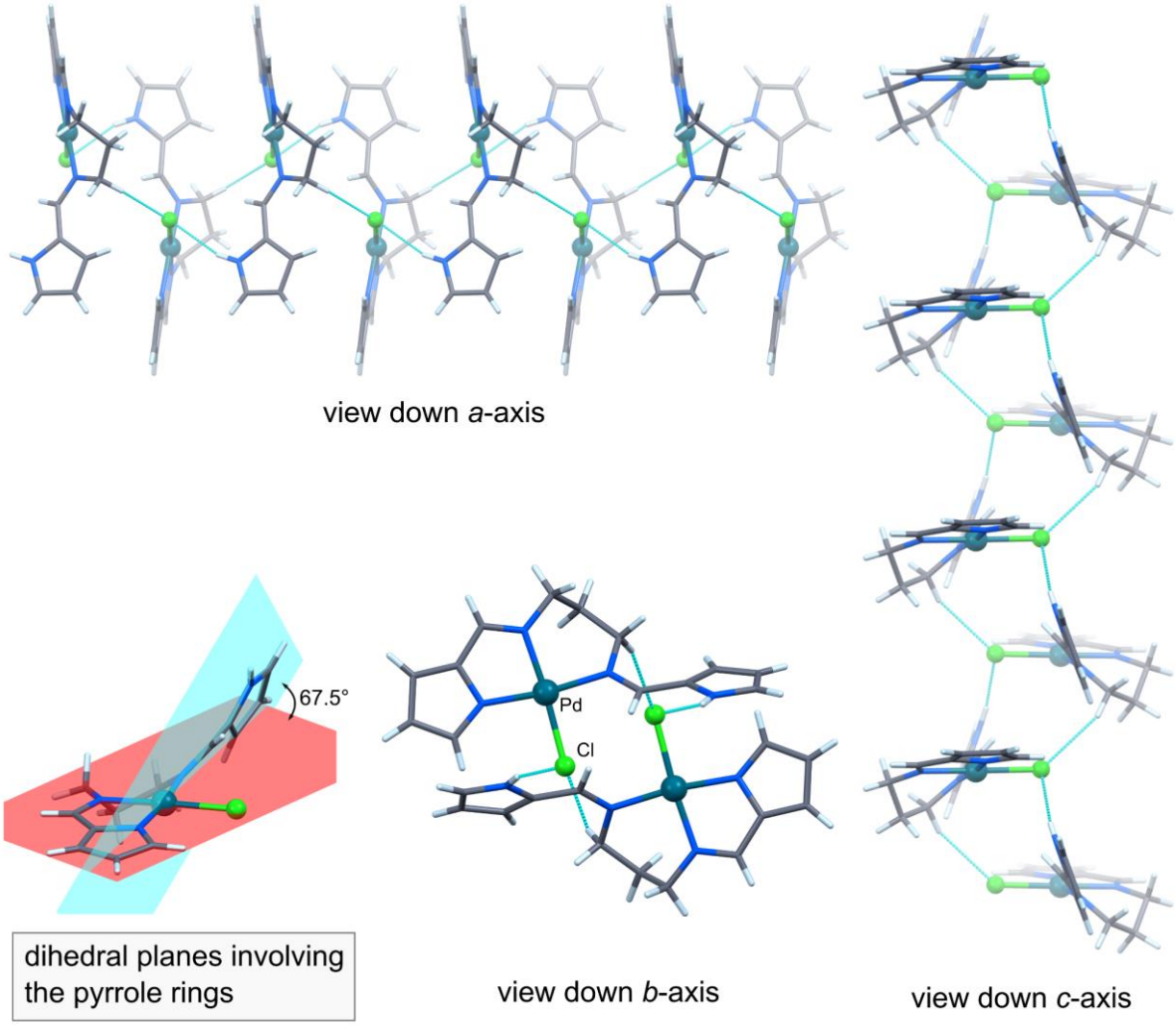


Figure S20. Views highlighting the 1D H-bonded chain formed in the crystal lattice of PdCl(HPrPyrr), which is stabilized by (alkyl)C–H···Cl and (pyrrole)N–H···Cl hydrogen bonds (dashed light blue cylinders). The 1D chain extended structure (H-bonded polymer) is viewed down the crystallographic *a*-, *b*-, and *c*-axes as indicated. The H-bonds to the non-coordinated pyrrole N–H group account for its orientation, which is canted by 67.5° relative to the chelated pyrrolide-imine group in the molecular structure.

2.4. Speciation

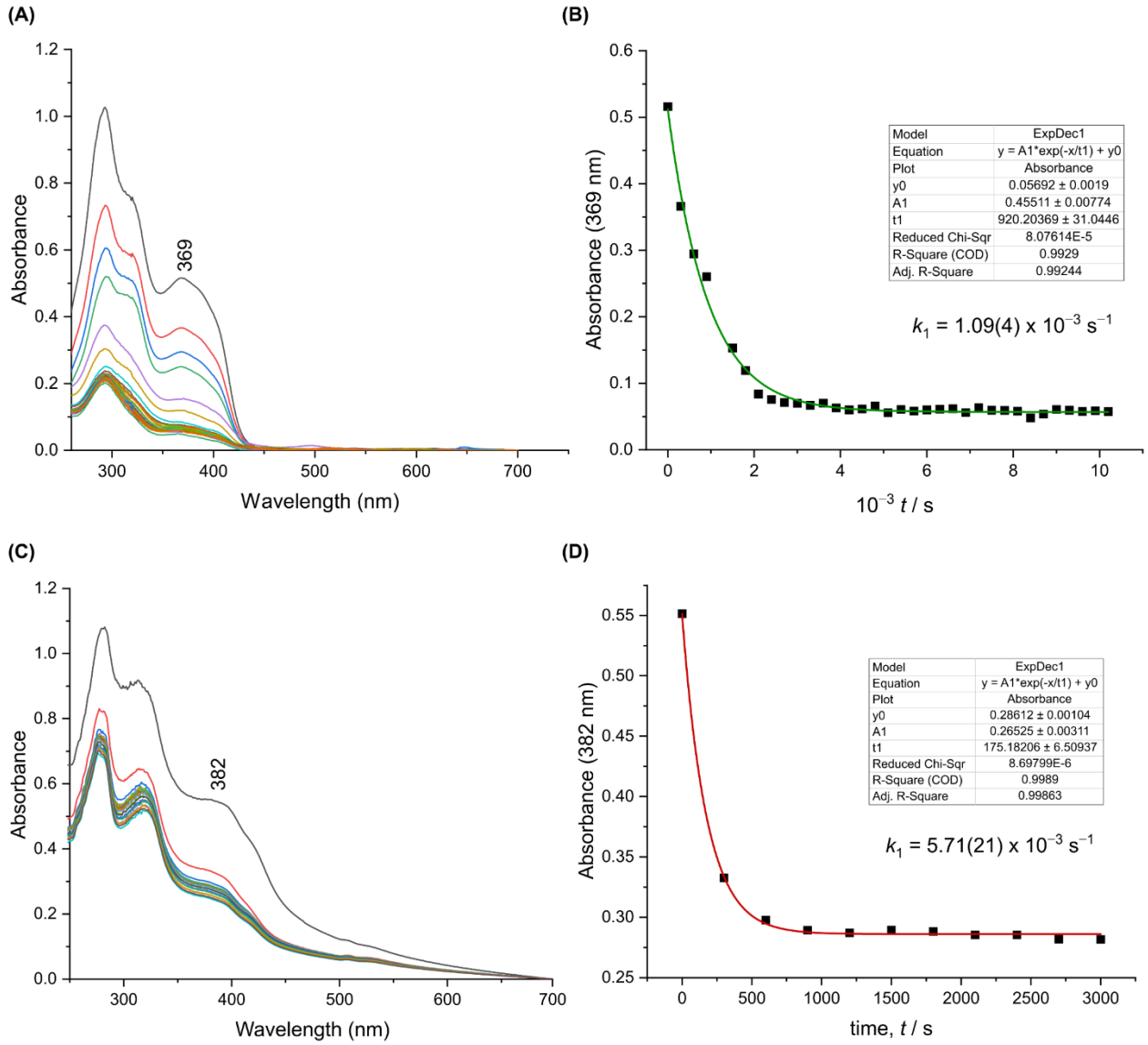


Figure S21. (A) Absorbance spectra of 45 µM Pd(PrPyrr) measured over 170 min (in 5 min intervals) from 260 – 700 nm in KH_2PO_4 buffer (50 mM pH 7.5). (B) Absorbance measurements for the Pd(PrPyrr) MLCT band at 369 nm over a time period of 170 min (in 5 min intervals). (C) Absorbance spectra of 45 µM Pd(PrPyrr) bound to HSA (25 µM) measured over 170 min (in 5 min intervals) from 250 – 700 nm in KH_2PO_4 buffer (50 mM pH 7.5). (D) Absorbance measurements of the Pd(PrPyrr) bound to HSA, MLCT band at 382 nm, over a time period spanning the first 50 min of the 170-min acquisition (in 5 min intervals). The curves in (B) and (D) are fitted to a first order exponential decay function.

Comment on Figure S21: Based on Figure S21(A-B), Pd(PrPyrr) is spontaneously hydrolysed in aqueous buffer. The complex does not decompose or demetallate; this is supported by the presence of the MLCT band present at 369 nm even after 170 min. We propose that the decrease in amplitude of the spectra is a result of Pd(PrPyrr) being hydrolysed to $[Pd(HPrPyrr)(OH_2)]^+$. The reaction takes ~40 min for the complete hydrolysis of Pd(PrPyrr). Secondly, we incubated Pd(PrPyrr) with HSA and the absorbance spectra were measured (Figures S21 C and D). It appears as though after initial hydrolysis of Pd(PrPyrr), the complex is stabilized by HSA. This suggests that two species may bind to HSA i.e., Pd(PrPyrr) and $[Pd(HPrPyrr)(OH_2)]^+$ or that the extent of the equilibrium is altered

for the protein-bound metal chelate relative to the free metal chelate. Notably, the hydrolysis reaction for Pd(PrPyrr) is about five times faster in the presence of HSA, suggesting the potential involvement of protonated amino acid side chains in catalysis of the reaction.

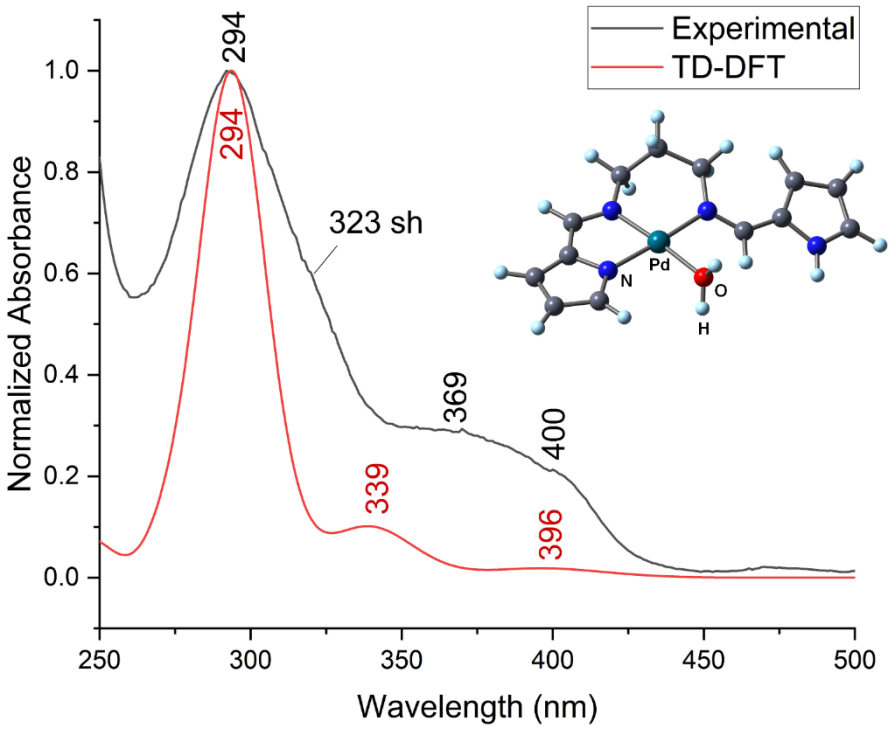


Figure S22. Comparison of the calculated electronic absorption spectrum of $[Pd(HPrPyrr)(OH_2)]^+$ (TD-DFT, cam-b3lyp/sdd/gd3bj in water) with the experimental spectrum recorded in KH_2PO_4 buffer (50 mM pH 7.5) at 60 min after the start of the hydrolysis reaction (Figure S21A). The DFT-calculated spectrum is wavelength-corrected (+10 nm) to align the most intense band at 294 nm with that of the experimental spectrum. The shoulder at 323 nm in the experimental spectrum is likely due to one or more vibronic transitions which are not taken into account in the DFT simulation. The broad bands at 369 and 400 nm in the experimental spectrum similarly reflect several longer-wavelength vibronic transitions in addition to the fundamental transitions between the zeroth vibrational levels of the ground and excited states occurring in this wavelength range (339 and 396 nm). Overall, there is good agreement between the calculated and observed absorption spectrum of $[Pd(HPrPyrr)(OH_2)]^+$.

2.5 Fluorescence Spectroscopy

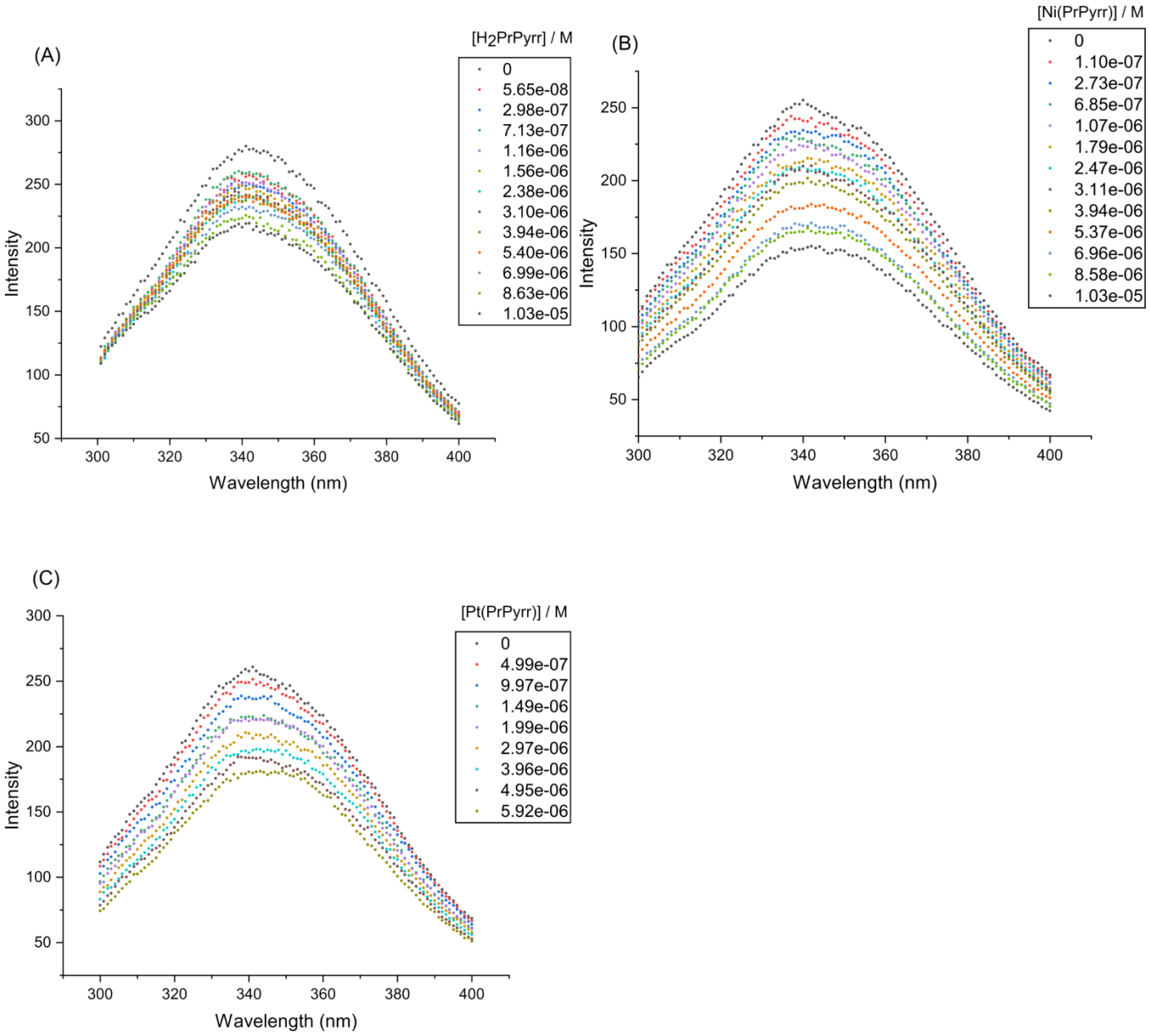


Figure S23. Fluorescence emission spectra of HSA (5.0 µM) recorded as a function of increasing concentration of (A) H_2PrPyrr, (B) Ni(PrPyrr), and (C) Pt(PrPyrr) at 298 K. The emission spectra confirm that the free base and metal chelates quench the intrinsic HSA (i.e., Trp-214) fluorescence upon binding.

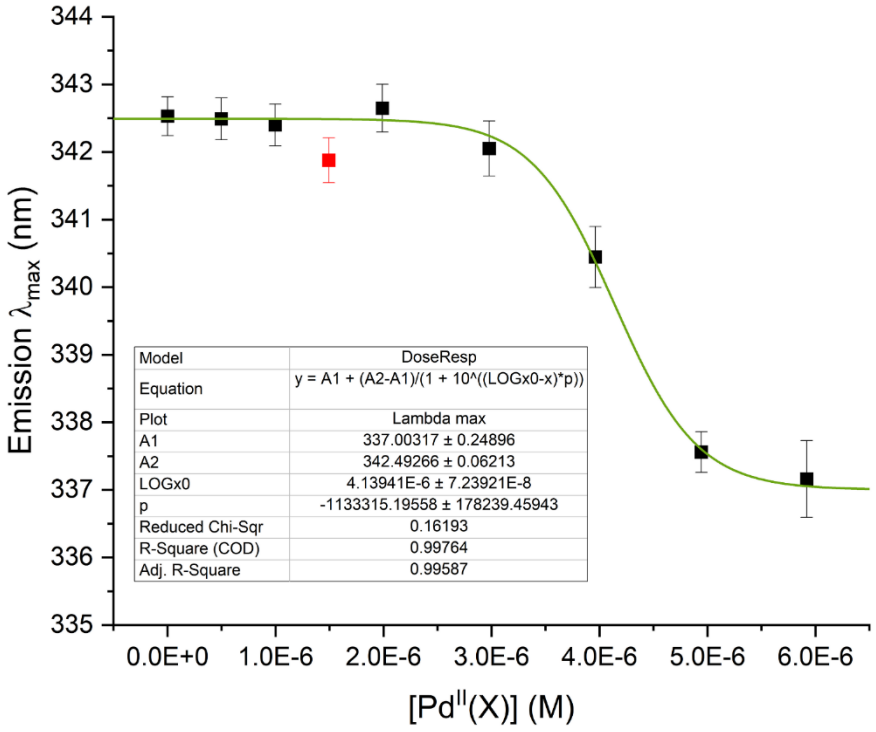


Figure S24. Fluorescence emission maximum of HSA (5.0 μM) recorded as a function of increasing concentration of $Pd^{II}(X)$ at 298 K (pH 7.5), where X represents the ligand sets coordinated to Pd(II) as a result of the equilibrium mixture: $Pd(PrPyrr) + H_3O^+ \rightleftarrows [Pd(HPrPyrr)(OH_2)]^+$. The abscissa may also be regarded as $[Pd^{II}]_{total}$. The data are fitted to a simple dose-response sigmoidal binding function (with the red point omitted from the fit). Complete quenching of the signal is observed for $[Pd^{II}(X)] > 10$ μM. From the data available, the fitted function indicates that the observed *blue wavelength shift* of the emission maximum, $\Delta\lambda_{max}^{em}$, is 5.5 nm. The graph confirms that binding of $Pd^{II}(X)$ by the protein has a particularly marked effect on the emission from the single Trp-214 residue. The effect is substantially larger than that recorded for the free base ligand ($H_2PrPyrr$), Ni(PrPyrr), and Pt(PrPyrr), pointing to the possibility that the two species within the $Pd^{II}(X)$ system yield a different mechanism of interaction with HSA (i.e., distinct binding modes).

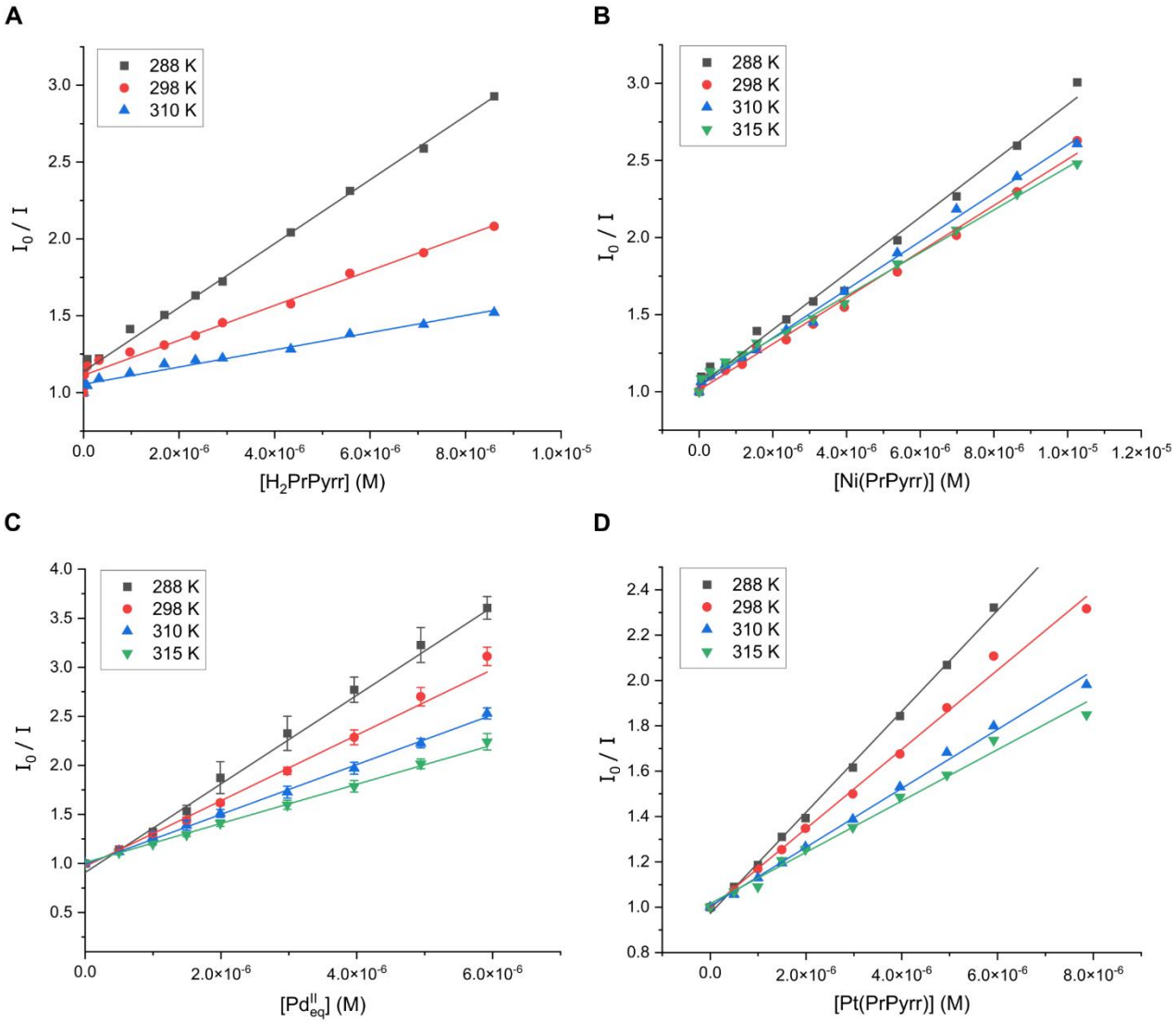


Figure S25. Stern–Volmer plots of fluorescence quenching: **(A)** H_2PrPyrr···HSA complex, **(B)** Ni(PrPyrr)···HSA complex, **(C)** Pd(PrPyrr)···HSA complex, and **(D)** Pt(PrPyrr)···HSA complex. Data for the Pd(PrPyrr)···HSA complex are also given in the main paper, but are repeated here to enable comparison across each system. Data for the H_2PrPyrr···HSA system were recorded at three different temperatures (■ 288 K, ● 298 K, and ▲ 310 K) due to the relatively invariant nature of the curves at 310 and 315 K, whereas the Ni(PrPyrr)···HSA, Pd(PrPyrr)···HSA and Pt(PrPyrr)···HSA systems were analysed at four temperatures (■ 288 K, ● 298 K, ▲ 310 K, and ▼ 315 K). The relevant concentrations for the titrations were: [HSA] = 5.0 μM, [H_2PrPyrr] and [metal chelates] = 0 – 13.6 μM, at pH 7.50 in 50 mM KH_2PO_4 buffer. Note that three titrations were performed at each temperature for each ligand and that the data reported in Table 1 of the main text were derived by averaging the three individual K_{SV} values (i.e., slopes) from individual linear least-squares fits of the Stern-Volmer plots. For the purpose of this figure, selected individual titrations are shown for each ligand other than the Pd(II) chelate for which triplicate titrations were averaged to highlight the standard deviations of each data point. In all cases, the raw fluorescence data were corrected using eqs. S1 and S2; the concentrations shown on the abscissa in each plot are thus free ligand (quencher) concentrations.

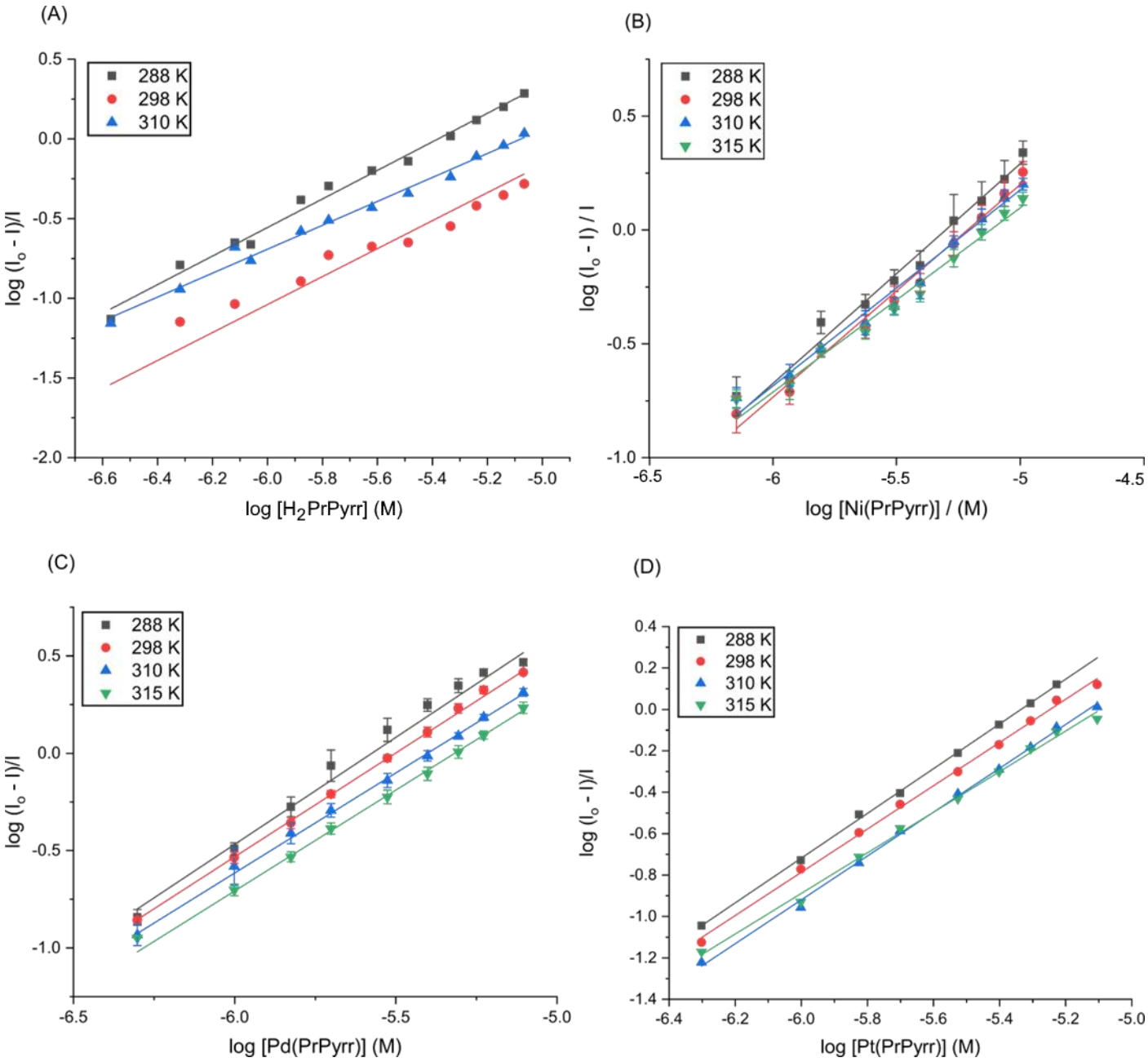


Figure S26. Plots of log((I$_0$-I)/I) versus log([Q]) for the interaction of HSA with several ligands (i.e., quenchers, Q) at specific temperatures: **(A)** H_2PrPyrr···HSA complex, **(B)** Ni(PrPyrr)···HSA complex, **(C)** Pd(PrPyrr)···HSA complex, and **(D)** Pt(PrPyrr)···HSA complex. Data for the Pd(PrPyrr)···HSA complex are also given in the main paper and are included here to allow readers to easily compare the data; the affinity constants are determined from the intercepts of the graphs and the stoichiometry from the slopes. Data for the H_2PrPyrr···HSA system were recorded at three different temperatures (■ 288 K, ● 298 K, and ▲ 310 K) due to the relatively invariant nature of the curves at 310 and 315 K, whereas the Ni(PrPyrr)···HSA, Pt(PrPyrr)···HSA, and Pt(PrPyrr)···HSA systems were analysed at four temperatures (■ 288 K, ● 298 K, ▲ 310 K, and ▼ 315 K). The relevant concentrations for the titrations were: [HSA] = 5.0 μM, [H_2PrPyrr] and [metal chelates] = 0 – 13.6 μM, at pH 7.50 in 50 mM KH_2PO_4 buffer.

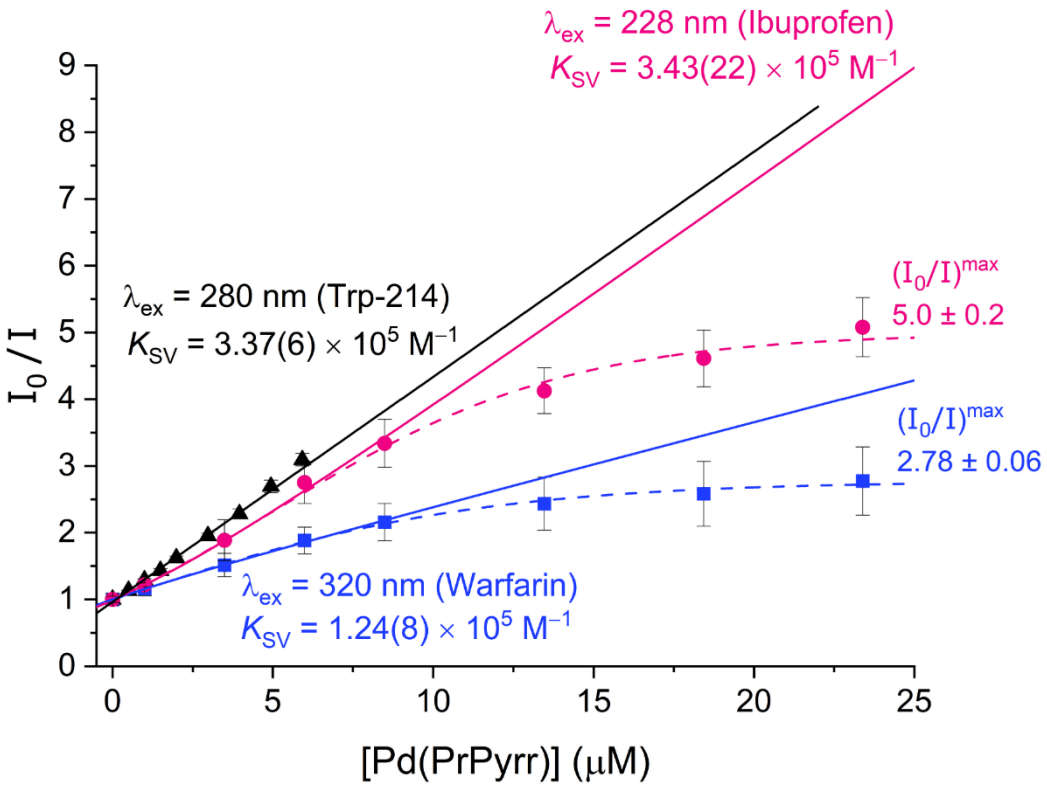


Figure S27. Stern–Volmer (SV) plot for native HSA as a function of the concentration of Pd(PrPyrr) at 298 K (pH 7.50, λ^{ex} = 280 nm, λ^{em} = 340 nm). SV plots for the competition equilibrium study in which Pd(PrPyrr) reacts with the pre-equilibrated HSA···Warfarin and HSA···Ibuprofen protein-drug complexes are shown. These plots are only linear when [Pd(PrPyrr)] < 10 μM; thereafter, they deviate negatively from linearity with increasing dose. This behaviour contrasts that of native HSA; the binding of > 1 equivalents (2 > n >1) of Pd(PrPyrr) to the protein and the maintenance of a static Trp-214 quenching mechanism throughout accounts for the native HSA data. In the case of HSA···Warfarin and HSA···Ibuprofen, the quenching mechanism is initially static due to Pd(PrPyrr) binding to the drug-protein adduct and quenching the emission from bound warfarin (λ^{ex} = 320 nm, λ^{em} = 382 nm) and ibuprofen (λ^{ex} = 228 nm, λ^{em} = 332 nm). At higher doses, Pd(PrPyrr) displaces warfarin and ibuprofen from the protein; their fluorescence emission is then quenched by water via a dynamic quenching mechanism. The dynamic quenching has diffusion-controlled kinetics and is independent of the concentration of Pd(PrPyrr). The ratio I_0/I reaches a fixed value, and the slope of the curve is zero in the limit of dynamic quenching.

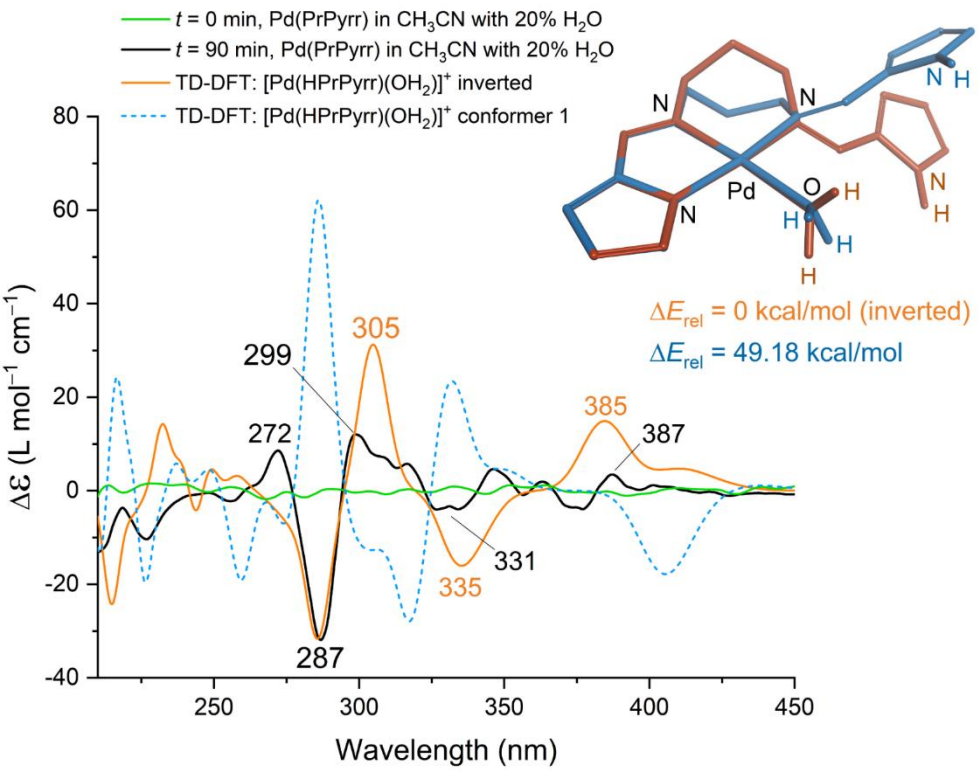
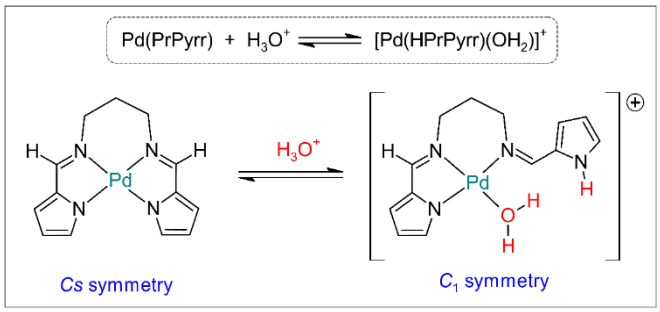


Figure S28a. UV-visible CD spectra recorded for Pd(PrPyrr) initially and after 90 minutes in a solvent comprising acetonitrile (80%, V/V) and distilled H_2O (20%, V/V) at 310 K. The CD spectrum of the aqua complex $[Pd(HPrPyrr)(OH_2)]^+$ calculated by TD-DFT (CAM-B3LYP/SDD/GD3BJ) in a water solvent continuum is shown for two conformers (enantiomers) of the complex related by inversion. The calculated spectra were scaled by λ + 20 nm to match the experimental peak with negative ellipticity at 287 nm. A band width of 700 cm^{-1} (half width at half maximum) was used to produce the spectral envelopes. The DFT-calculated spectra have intensity units of L mol^{-1} cm^{-1}. The experimental spectra were scaled in amplitude by a factor of 4 to be approximately on the same scale as the TD-DFT spectra. The units of the experimental spectra are ellipticity in millidegrees. The experimental spectra were smoothed (to a minor degree) using a Lowess function (span = 0.03). Note that the starting complex, Pd(PrPyrr), has exact *Cs* symmetry and thus exhibits no CD spectrum; it will not be detectable whether it is present or entirely absent at equilibrium.

Comment on Figure S28a:



The experimental spectrum best matches the DFT-calculated spectrum for the orange conformer (enantiomer), which has the lowest relative energy of the two conformers. The hydrolysis product is thus the *thermodynamic product* of the reaction and racemization is not energetically favoured, accounting for the fact that a CD spectrum is obtained for the experimental system. The energy difference between the C_1-symmetry enantiomers after applying the thermal free energy correction (T = 298.15 K) to the electronic energies from the frequency calculations on the DFT-optimized structures is: ΔG_{corr} = 49.53 kcal mol^{-1}. Thus, we conclude that the enantiomers differ in energy by ~50 kcal mol^{-1}. We obtained further experimental evidence for the existence of the aqua complex at physiological pH by measuring the pKa of the aqua ⇌ hydroxo equilibrium (Figure S29a); the spectroscopic titration also confirmed formation of the chloro complex at low pH and the persistence of Pd(PrPyrr) throughout the pH range in the equilibrium mixture.

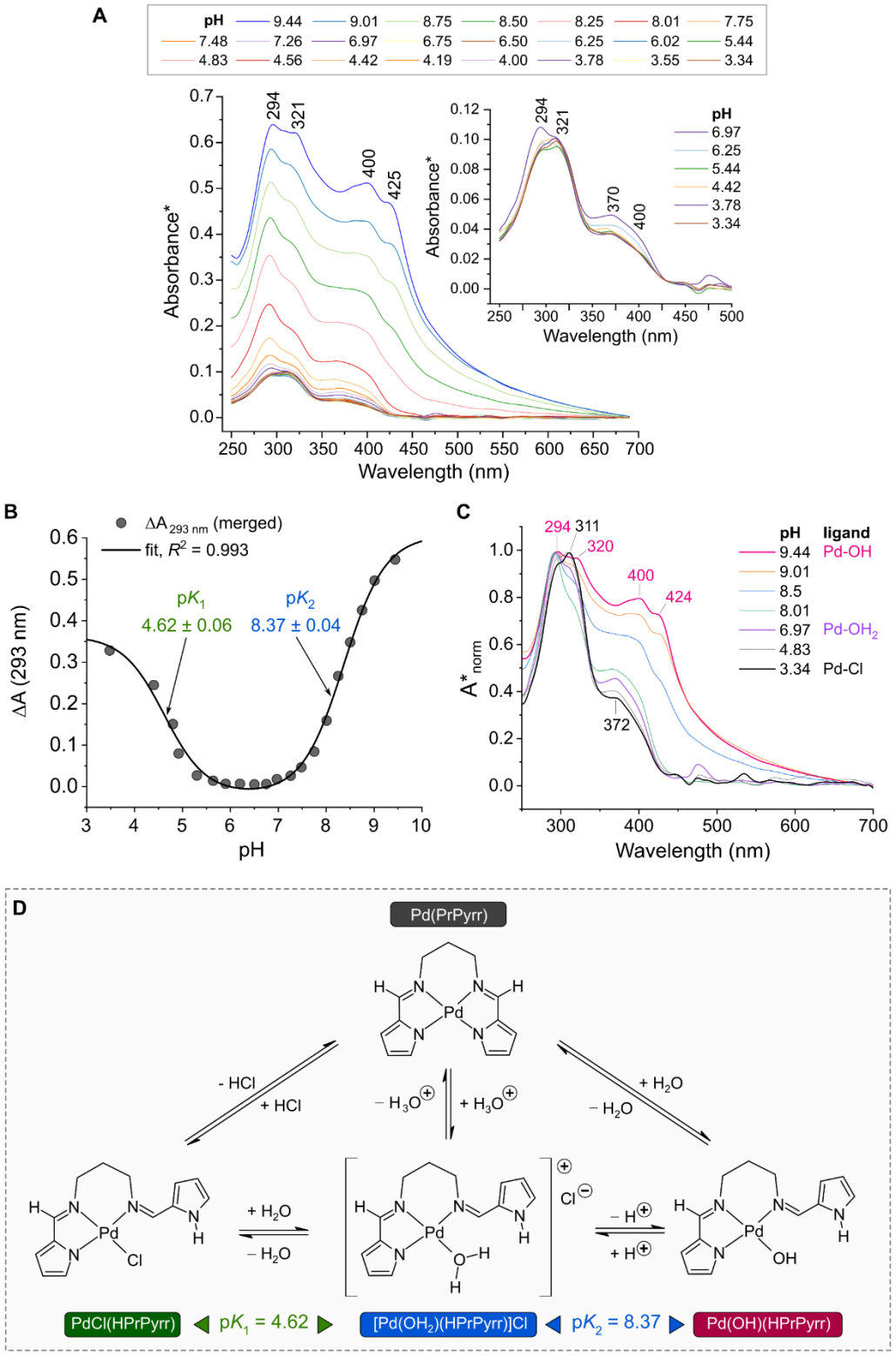


Figure S28b. (A) UV-visible spectra of Pd(PrPyrr) recorded as a function of pH at 37 °C. The inset highlights the spectral changes at lower pH. (B) Plot of the change in absorbance at 293 nm as a function of pH. The curve is a nonlinear fit of the data to a standard two-step pK_a equilibrium function ($AH_2 \rightleftharpoons AH + H^+$, K_1; $AH \rightleftharpoons A + H^+$, K_2). (C) Normalized absorption spectra at selected pH values throughout the titration's full pH range. The plot places spectra on the same scale to enable better discernment of the spectral features at key pH values in the titration. (d) Scheme summarizing the species distribution gleaned from consideration of the spectra and pKa values delineated from the titration curve. The dominant species at pH 7 involve the equilibrium Pd(PrPyrr) + H_3O^+ ⇌ $[Pd(HPrPyrr)(OH_2)]^+$.

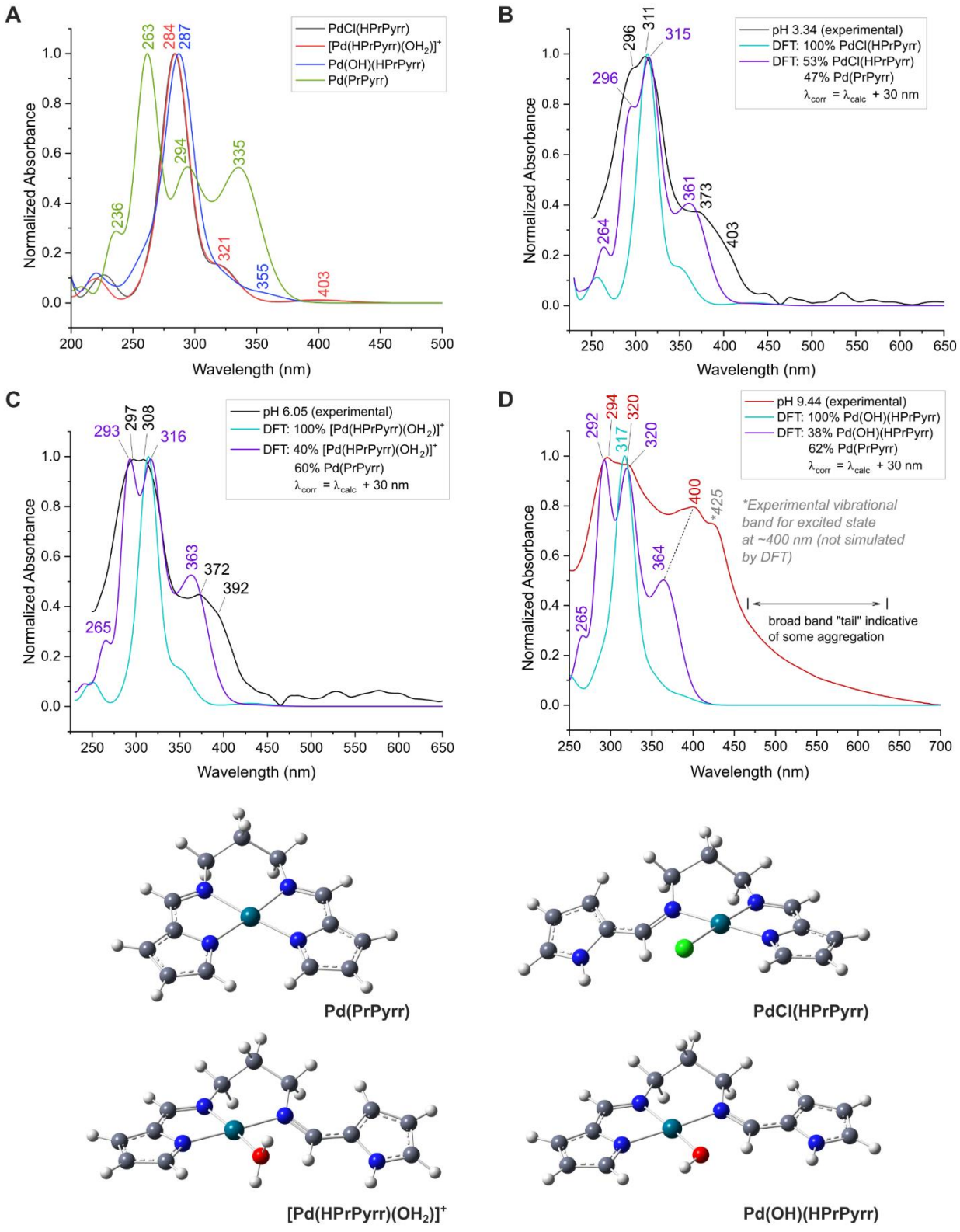


Figure S28c. (A) Uncorrected normalized TD-DFT calculated electronic absorption spectra (CAM-B3LYP/SDD, SCRF = water) for the four Pd(II) complexes present in the equilibrium scheme of Figure S28b. Parts (B)–(D) show the best-matching DFT-calculated spectral pair summations for the experimental spectra recorded at pH 3.34, pH 6.05, and pH 9.44. The high pH experimental spectrum reflects aggregation-induced broadening, which is not simulated by the TD-DFT spectra. The DFT-calculated lowest-energy structures of the four compounds involved in the pH-dependent equilibrium are shown as ball and stick models. (Key: H = white, C = grey, N = blue, O = red, Pd = blue green.)

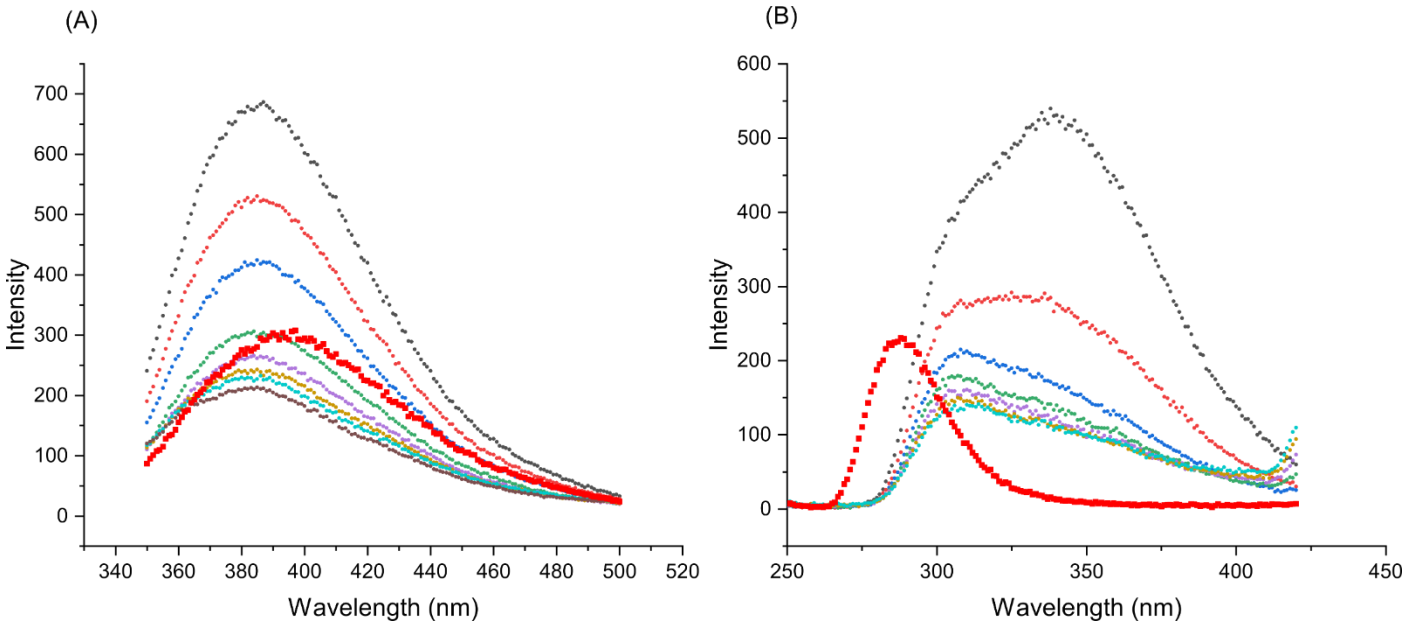


Figure S29. (A) Emission spectra of HSA•{warfarin}$_n$ (5.0 μM warfarin λ^{ex} = 320 nm) recorded as a function of increasing concentration of Pd(PrPyrr) at 298 K from 0 – 30 μM. **(B)** Emission spectra of HSA•{ibuprofen}$_n$ (5.0 μM ibuprofen λ^{ex} = 228 nm) recorded as a function of increasing concentration of Pd(PrPyrr) at 298 K from 0 – 30 μM. In both cases the emission spectrum of the fluoroprobe in the absence of HSA is indicated by red squares.

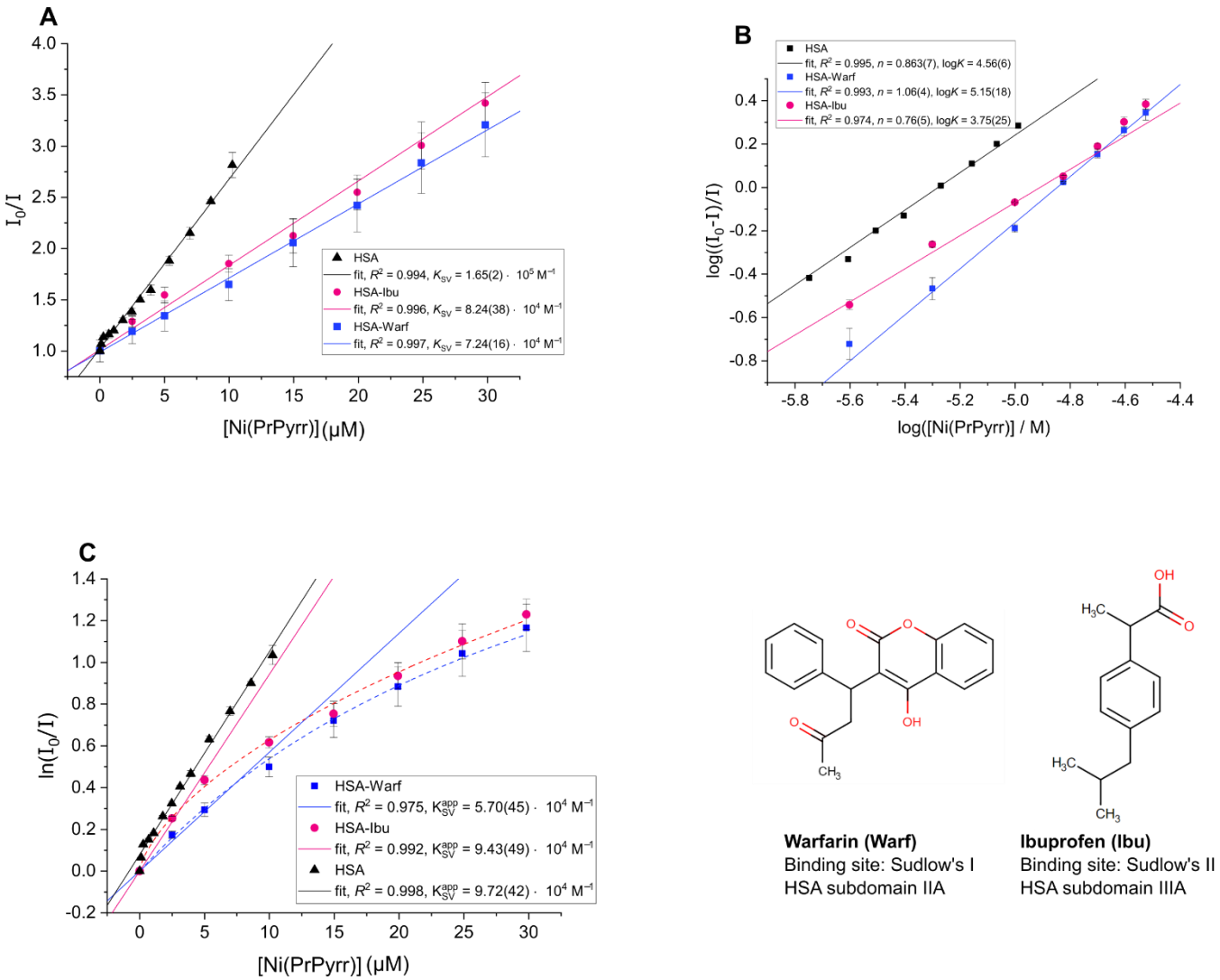


Figure S30. (**A**) Stern–Volmer (SV) plot for native HSA, HSA···Warfarin, and HSA···Ibuprofen as a function of the concentration of Ni(PrPyrr) at 298 K (pH 7.50, T = 298 K). The plots are linear with an intercept of 1.0 when static quenching is operative (i.e., the quencher binds to the target protein and fluorophore(s)). The excitation and emission wavelengths for the fluorophore probes were: (i) Trp-214 (native HSA), λ^{ex} = 280 nm, λ^{em} = 340 nm; (ii) Warfarin (HSA-Warf), λ^{ex} = 320 nm, λ^{em} = 382 nm, and (iii) Ibuprofen (HSA-Ibu), λ^{ex} = 228 nm, λ^{em} = 332 nm.

(**B**) Double-log plot of the fluorescence quenching data, $log\left(\frac{I_0-I}{I}\right) = logK + nlog[Q]$, to enable measurement of log$K$ (the association constant for the Ni^{2+} chelate with the macromolecule target, K_a) and the reaction stoichiometry (n). (**C**) Sphere of action model plot, $ln\left(\frac{I_0}{I}\right) = K_{SV}^{app}[Q]$, for the system. A linear plot with a zero intercept indicates static quenching by the quenching ligand bound in some way to the fluorophore/macromolecule. Negative deviation from linearity signals a switch from static to dynamic quenching and release of the fluorophore from the protein host, whereafter diffusion-controlled dynamic quenching of the fluorophore by the solvent ensues. The structures of the probe fluorophores and their binding site preferences (known from X-ray crystallography) are shown. Because the binding constant for Ni(PrPyrr) to native HSA and HSA-Warf are *equivalent* within 1 standard deviation and changing the target to HSA-Ibu reduces the logK value by more than an order of magnitude, Ni(PrPyrr) preferentially targets Sudlow's site II in subdomain IIIA of HSA. Because Ni(PrPyrr) partially displaces warfarin and ibuprofen (Plot C), it is not impossible that both sites are targeted to some degree. One can view this as one equivalent of Ni(PrPyrr) binding to Sudlow's site I and II simultaneously to fractionally saturate each site and give an overall stoichiometry of 1:1 for the reaction.

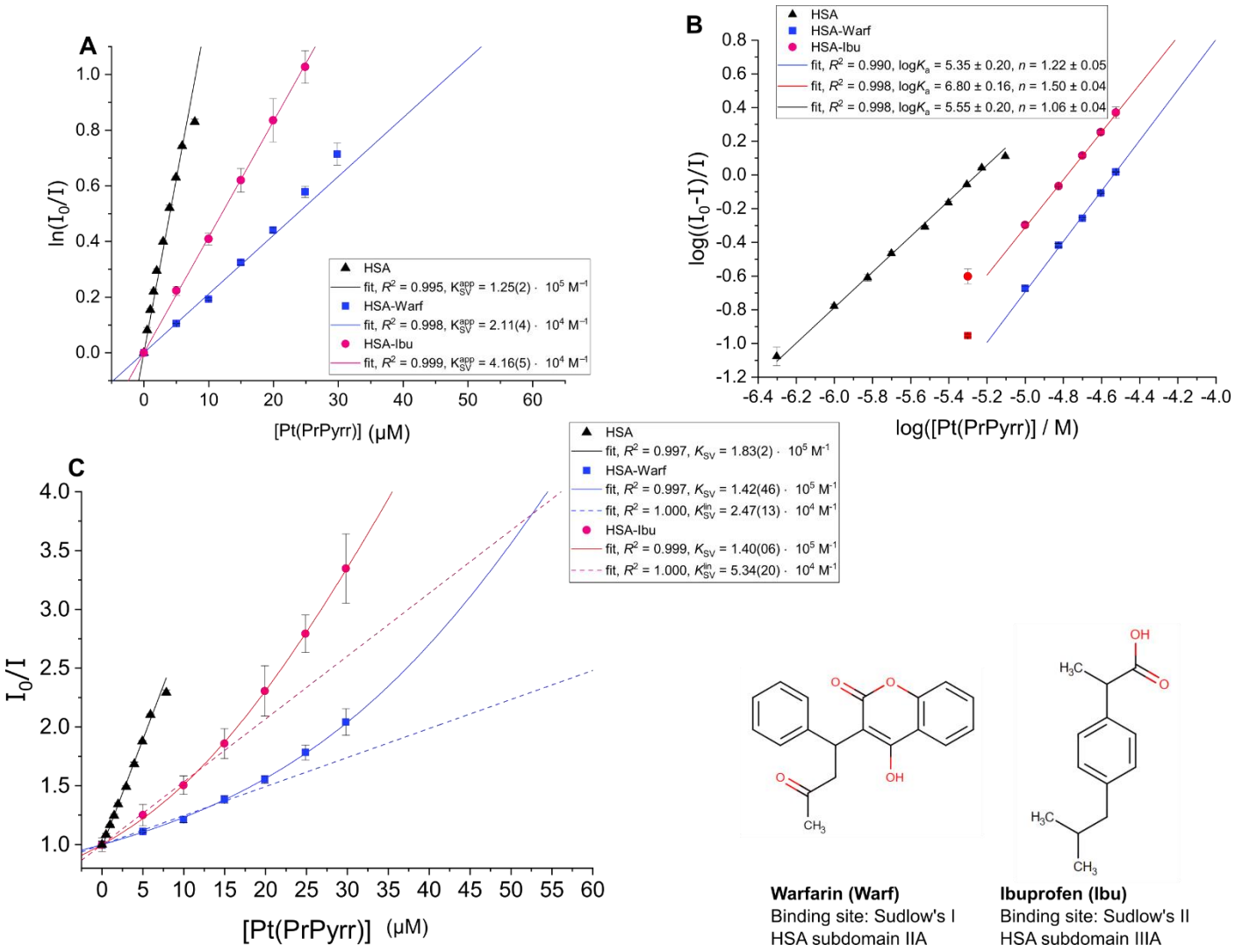


Figure S31. (**A**) Sphere of action model plot, $ln\left(\frac{I_0}{I}\right) = K_{SV}^{app}[Q]$, for native HSA, HSA···Warfarin, and HSA···Ibuprofen as a function of the concentration of Pt(PrPyrr) at 298 K (pH 7.50). The plots are linear with a zero intercept when static quenching is operative (i.e., the quencher binds to the target protein and fluorophore(s)). The excitation and emission wavelengths for the fluorophore probes were: (i) Trp-214 (native HSA), λ^{ex} = 280 nm, λ^{em} = 340 nm; (ii) Warfarin (HSA-Warf), λ^{ex} = 320 nm, λ^{em} = 382 nm, and (iii) Ibuprofen (HSA-Ibu), λ^{ex} = 228 nm, λ^{em} = 332 nm.

(**B**) Double-log plot of the fluorescence quenching data, $log\left(\frac{I_0-I}{I}\right) = logK + nlog[Q]$, to enable measurement of log*K* (the association constant for the Pt^{2+} chelate with the macromolecule target, K_a) and the reaction stoichiometry (*n*). (**C**) Stern–Volmer (SV) plot for native HSA, HSA···Warfarin, and HSA···Ibuprofen as a function of the concentration of Pt(PrPyrr) at 298 K (pH 7.50, *T* = 298 K). The plots are linear with an intercept of 1.0 when static quenching is operative (i.e., the quencher binds to the target protein and fluorophore(s)). Positive deviation from linearity with an upward curvature signals a ligand binding stoichiometry > 1.0; the data have been fitted to the nonlinear SV model (see eq. S12). The structures of the probe fluorophores and their binding site preferences (known from X-ray crystallography) are shown. Overall, the plots show that Pt(PrPyrr) binds with an approximately 1:1 stoichiometry to native HSA. At no point does Pt(PrPyrr) displace warfarin or ibuprofen from HSA···Warfarin and HSA···Ibuprofen; however, the presence of either drug *enhances* the binding of Pt(PrPyrr) as the log*K* values increase by more than 1 log unit. One possible interpretation is that the Pt(II) chelate can bind (half-saturate) both Sudlow's site I and II of the native protein, but that when a drug is located in one of these two sites, the reciprocal site is fully saturated. Furthermore, the bound drug may alter the protein conformation to enable the uptake of an additional half-equivalent of Pt(PrPyrr) at a third site. Such additional drug binding sites are known for HSA and exist in subdomains IIIB (propofol binding site, close to site II in subdomain IIIA) and IB (hemin binding site). From the response functions in Plot C, Pt(PrPyrr) is likely partly taken up in subdomain IIIB.

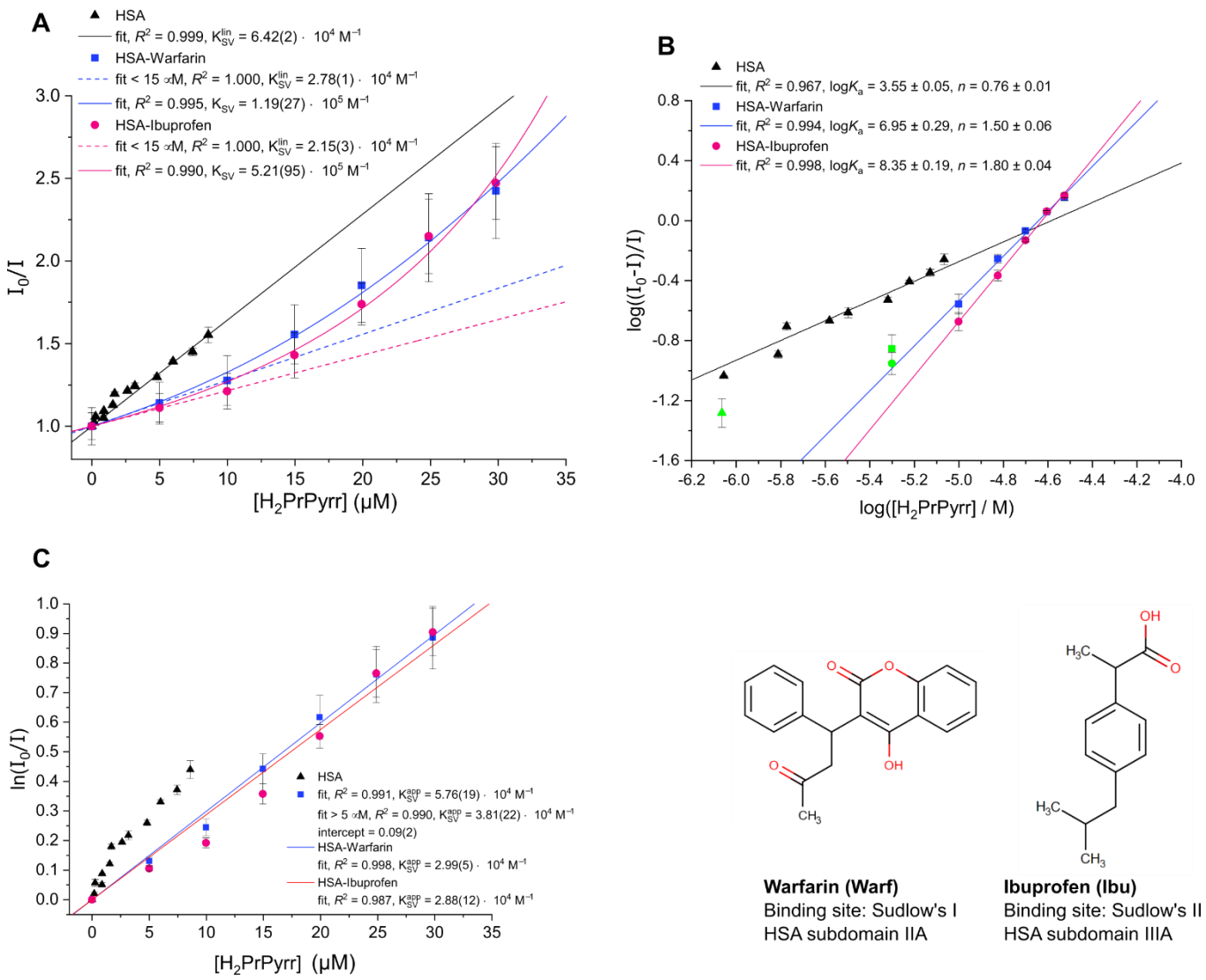


Figure S32. (**A**) Stern–Volmer (SV) plot for native HSA, HSA···Warfarin, and HSA···Ibuprofen as a function of the concentration of H_2PrPyrr at 298 K (pH 7.50, T = 298 K). The plots are linear with an intercept of 1.0 when static quenching is operative (i.e., the quencher binds to the target protein and fluorophore(s)). Positive deviation from linearity with an upward curvature signals a ligand binding stoichiometry > 1.0; the data have been fitted to the nonlinear SV model (see eq. S12). The excitation and emission wavelengths for the fluorophore probes were: (i) Trp-214 (native HSA), λ^{ex} = 280 nm, λ^{em} = 340 nm; (ii) Warfarin (HSA-Warf), λ^{ex} = 320 nm, λ^{em} = 382 nm, and (iii) Ibuprofen (HSA-Ibu), λ^{ex} = 228 nm, λ^{em} = 332 nm.

(**B**) Double-log plot of the fluorescence quenching data, $log\left(\frac{I_0-I}{I}\right) = logK + nlog[Q]$, to enable measurement of log$K$ (the association constant for H_2PrPyrr with the macromolecule target, K_a) and the reaction stoichiometry (n). Points in green were omitted from curve fitting. (**C**) Sphere of action model plot, $ln\left(\frac{I_0}{I}\right) = K_{SV}^{app}[Q]$, for the system. A linear plot with a zero intercept indicates static quenching by the quenching ligand bound in some way to the fluorophore/macromolecule. For native HSA, the slope changes when [H_2PrPyrr] > 5 μM. Because Trp-214 cannot dissociate from the protein and full dynamic quenching cannot be achieved, the ligand may directly perturb the fluorophore by, for example, H-bonding to it. The fluxional nature of such bonding may partly mimic aspects of collisional quenching leading to the non-zero intercept. The structures of the probe fluorophores and their binding site preferences (known from X-ray crystallography) are shown. Overall, the plots show that H_2PrPyrr binds with an approximately 1:1 stoichiometry to native HSA. At no point does H_2PrPyrr displace warfarin or ibuprofen. However, the presence of either drug *enhances* the binding of H_2PrPyrr (synergistic effect) as the log$K$ values increase by *more than 2.5 log units*. One possible interpretation is that H_2PrPyrr can bind (half-saturate) both Sudlow's site I and II of the native protein, but that when a drug is already located in one of these two sites, the reciprocal site is fully saturated. Furthermore, the bound drug may alter the protein conformation to enable the uptake of an additional *full* equivalent of H_2PrPyrr at a third site (n is 1.80 when HSA···Ibuprofen is the target). Such additional drug binding sites are known for HSA and exist in subdomains IIIB (propofol binding site, close to site II in subdomain IIIA) and IB (hemin binding site).

2.5.1. Comments on Figures S30–S32

Binding of Ni(PrPyrr) by HSA. The analogous titration data for Ni(PrPyrr) (Table S8 in the main paper, Figure S30) reflect an apparent single binding equilibrium in which uptake of the metal chelate is diminished in the ibuprofen-bound target, HSA•{ibuprofen}$_n$, but seemingly unaffected in the warfarin-bound target relative to native HSA. This suggests Ni(PrPyrr) either uniquely targets Sudlow's site II (binding in or close to the ibuprofen primary binding site in subdomain IIIA), or that the Ni(II) chelate targets both sites with the location of the Ni(II) chelate in the larger warfarin binding pocket (subdomain IIA) being displaced from the position occupied by warfarin itself. Thus, Ni(PrPyrr) and warfarin may co-locate in subdomain IIA of HSA, which would afford a similar affinity constant for uptake of the Ni(II) chelate by the two targets—native HSA and HSA•{warfarin}. Interestingly, and as discussed in the main paper, our *in silico* docking data confirm the feasibility of Ni(PrPyrr) co-binding adjacent to warfarin in subdomain IIA. From the "sphere of action" plot of Figure S30, Ni(PrPyrr) begins to displaces both ibuprofen and warfarin from HSA at higher doses since these probes exhibit enhanced dynamic quenching by the solvent when [Ni(PrPyrr)] > 30 μM. The spectroscopic data collectively suggest that Ni(PrPyrr) exhibits single-step multi-site binding to HSA, simultaneously targeting both subdomain IIA and IIIA, with a cumulative binding stoichiometry of $n \sim 1$.

Binding of Pt(PrPyrr) by HSA. The picture is slightly more complicated (yet still conceptually accounted for by Figure 7 in the main paper) for the binding of Pt(PrPyrr) and H_2PrPyrr to HSA pre-equilibrated with the fluorescent drug probes (Figs. S31 and S32). These plots show that Pt(PrPyrr) binds with an approximately 1:1 stoichiometry to *native* HSA. At no point does Pt(PrPyrr) displace warfarin or ibuprofen from HSA•{warfarin} and HSA•{ibuprofen}$_n$; however, the presence of either drug *enhances* the binding of Pt(PrPyrr) as the $\log K_a$ values increase from 5.34 ± 0.20 ($n_{total} = 1.02 \pm 0.05$) in the native protein to 6.80 ± 0.16 ($n_{total} = 1.50 \pm 0.04$) and 6.76 ± 0.15 ($n_{total} = 1.41 \pm 0.03$) in HSA•{warfarin} and HSA•{ibuprofen}$_n$, respectively. One interpretation is that the Pt(II) chelate can bind in *both* Sudlow's site I and II of the native protein (i.e., half- or fractionally-saturate the two sites so that $n_1 + n_2 = n_{total} = 1.22$), but that when a drug is already located in one of these two sites, the reciprocal unbound site is fully saturated by the metal chelate. Furthermore, the bound drug (warfarin or ibuprofen) subtly alters the protein conformation to enable the uptake of an additional half equivalent of Pt(PrPyrr) at a third site, as evidenced by $n_{total} \sim 1.5$ for either protein target. This points to a classic structural synergistic or allosteric effect (cooperative binding). It is also possible that Pt(PrPyrr) may bind alongside warfarin in the larger Sudlow's I pocket (subdomain IIA), like Ni(PrPyrr), and that warfarin···Pt(PrPyrr) London forces of attraction enhance the microscopic binding constant at this site. This notion is well-supported by our *in silico* docking experiments (*vide infra*) and could at least partly explain why Pt(PrPyrr) does not induce the dissociation of warfarin at higher doses. Regarding the existence of additional drug binding sites, many are known for HSA[43] and are located in subdomains IIIB (propofol binding site, close to Sudlow's site II in subdomain IIIA) and IB (bilirubin[61] and hemin

binding site[62]). From the steep initially linear and thence upwardly-curved Stern-Volmer response function for Pt(PrPyrr) binding to HSA•{ibuprofen}$_n$, Pt(PrPyrr) is possibly partially taken up in subdomain IIIB, which is adjacent to subdomain IIIA in the protein, thereby facilitating efficient additive quenching of the fluorescence from bound ibuprofen (the first equivalent of the quencher being bound in the adjacent pocket, Sudlow's site I).

Binding of H_2PrPyrr by HSA. In the case of H_2PrPyrr, similar but somewhat lower affinity binding to that seen for Pt(PrPyrr) with *native* HSA is observed ($\log K_a$ = 3.55 $\pm$ 0.09, n_{total} = 0.76 $\pm$ 0.01). Likewise, H_2PrPyrr cannot displace warfarin or ibuprofen (Figure S32). As before, the presence of either drug *enhances* the binding of the ligand H_2PrPyrr (via a structural synergistic effect) as the $\log K_a$ values increase by *more than 2.5 log units* for the warfarin-loaded target ($\log K_a$ = 6.95 $\pm$ 0.29, n_{total} = 1.50 $\pm$ 0.06, HSA•{warfarin}) and ibuprofen-bound target ($\log K_a$ = 8.35 $\pm$ 0.19, n_{total} = 1.80 $\pm$ 0.04, HSA•{ibuprofen}$_n$). As with Pt(PrPyrr), half-saturation of Sudlow's site I and II of the *native* protein can account for n_{total} = 1, and when a drug is already located in one of these two sites, the reciprocal site is fully saturated as the ligand dose increases (keeping n_{total} = 1). The presence of a pre-bound drug (warfarin or ibuprofen) clearly facilitates the uptake of an additional *near-full* equivalent of H_2PrPyrr at a third site (n_{total} is ~2 when HSA•{ibuprofen}$_n$ is the target). The third site is presently difficult to pinpoint from the available spectroscopic data; our *in silico* docking study (Table S9, *vide infra*) suggests the neutral free ligand targets subdomain IA in the absence of ibuprofen, which is adjacent to the hemin and bilirubin binding site (subdomain IB).[61] When ibuprofen is present, however, H_2PrPyrr targets subdomain IIA while the protonated species $[H_3PrPyrr]^+$ and $[H_4PrPyrr]^{2+}$ are surface-bound in the IB-IIIA cleft (Table S9). Although a pH of 7.5 is maintained experimentally in the titrations, protonation of the Schiff base free ligand is possible upon ligand uptake by HSA, depending on the specific binding site and which polar residues interact with the ligand. Interestingly, $[H_3PrPyrr]^+$ binds adjacent to warfarin in subdomain IIA of HSA•{warfarin} *in silico* (Table S9), suggesting that if this cationic species is formed under the present experimental conditions, then dissociation of warfarin from HSA would be thwarted at higher doses.

2.6 Protein Mass Spectrometry

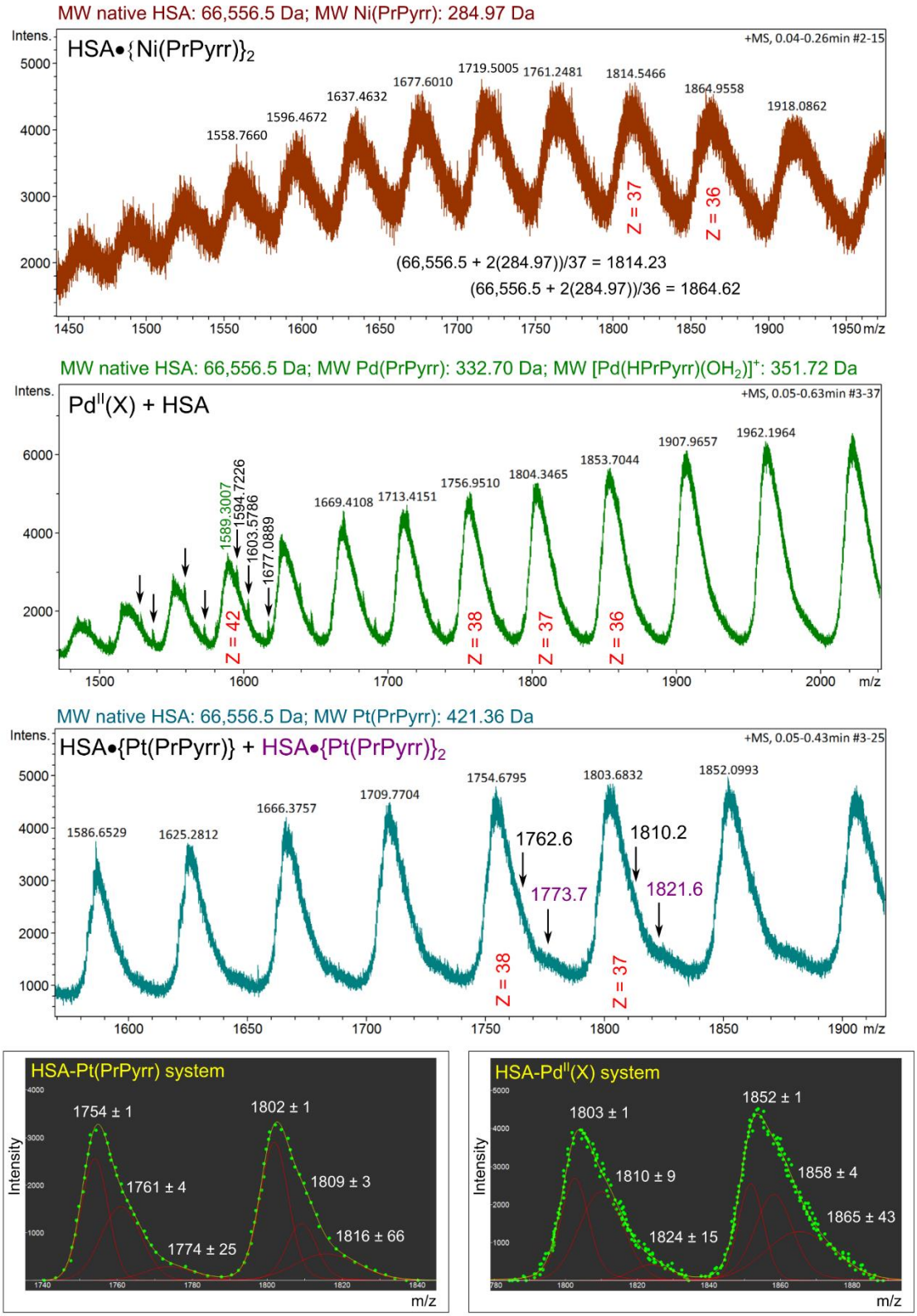


Figure S33 (a). ESI-MS data for complexes of HSA formed with Ni(PrPyrr), $Pd^{II}(X)$, and Pt(PrPyrr). The bottom panels show peak deconvolution plots (6 Voigt functions, R^2 = 0.995 for the Pt^{2+} system, R^2 = 0.990 for the Pd^{2+} system) for two of the peaks in the spectrum of the Pt(II) adduct (left) and Pd(II) adduct (right). The information of relevance in the spectra is discussed briefly overleaf.

Comments on Figure S33 (a):

For the adduct formed between HSA and Ni(PrPyrr), only the 2:1 metal:protein complex exists as shown by the numerical analysis of the peaks in the top mass spectrum. For the adduct formed between HSA and Pt(PrPyrr) shown in the lowest of the three mass spectra, the asymmetric shape of the peaks indicates a mixture of species is present, specifically native HSA, HSA•{Pt(Pr(Pyrr)} (calculated masses marked in black where shoulders on the main bands appear), and possibly some 2:1 metal:protein adduct, HSA•{Pt(Pr(Pyrr)}$_2$ (calculated masses marked in purple). The bottom left plot shows a peak deconvolution fit of the spectral envelope (using 6 Voigt functions) for two of the peaks in spectrum. Using the component peak areas for the Z = 38 adducts, the percentage composition of the sample was determined: 47% HSA, 43% HSA•{Pt(Pr(Pyrr)}, and 10% HSA•{Pt(Pr(Pyrr)}$_2$. This data serves as experimental proof for the multi-site binding of Pt(PrPyrr) to HSA. From Table 1 in the main paper, the reaction stoichiometry ranges from 0.98 to 1.05 as the temperature is lowered from 315 to 288 K. A stoichiometry with n > 1 can only be obtained if multiple binding sites exist, which is consistent with our GLIDE XP data in Tables S9 and S11. This means that the *in silico* docking data, fluorescence titration data, and mass spectrometry are all fully consistent and support the multi-site binding of *structurally intact* Pt(PrPyrr) chelates by the protein.

Regarding the mass spectrum of the HSA-Pd(II) system, it is clearly more complicated than that seen for the reaction of Pt(PrPyrr) with HSA. However, like the HSA-Pt(II) system, the broad asymmetric signals are a reflection of several species: native HSA and HSA•{Pd(X)}$_{1–2}$. This is illustrated if we consider the peak deconvolution at Z = 36 from the plot at the bottom right of Figure S33 (a):

```
(66556.5+1(332.7)+0(351.72))/36 = 1858.03 m/z          (eq. S13)

(66556.5+0(332.7)+1(351.72))/36 = 1858.56 m/z          (eq. S14)

(66556.5+1(332.7)+1(351.72))/36 = 1867.80 m/z          (eq. S15)

(66556.5+2(332.7)+0(351.72))/36 = 1867.28 m/z          (eq. S16)

(66556.5+0(332.7)+2(351.72))/36 = 1868.33 m/z          (eq. S17)
```

Equations S11–S15 show that the signals can be interpreted as reflecting native HSA (m/z ~1852, ca. 26%), HSA•{Pd(X)} ca. 38%, and HSA•{Pd(X)}$_2$ ca. 35%, with the resolution of the data being insufficient to distinguish between the exact Pd(II) species bound. In other words, we do not know if the 2:1 metal:protein complex is a single ligand species, HSA•{Pd(PrPyrr)}$_2$, or a mixed ligand species HSA•{Pd(PrPyrr)}{Pd(HPrPyrr)(OH$_2$)$^+$}. Despite this shortfall, the mass spectral data support the key findings in the main paper regarding multiple ligand uptake by the protein for the Pd(II) system.

One last point is that there are arrays of sharper peaks that become resolved on the weaker signals at low *m/z* for the HSA-Pd(II) system; they are marked with black arrows in Figure S33 (a). These signals could reflect covalent adducts formed when surface residues such as His and Glu substitute the aqua ligand of [Pd(HPrPyrr)(OH$_2$)]$^+$ to form [Pd(HPrPyrr)(His-HSA)]$^+$ or Pd(HPrPyrr)(Glu-HSA). We regard this as evidence for the existence of the aqua complex as discussed in the main paper (i.e., as written in eq. 2). This reaction is not feasible for Pt(PrPyrr) or Ni(PrPyrr), due to their kinetic inertness, which is why these satellite peaks are absent from their mass spectra. Moreover, the satellite signals are only seen when the sample of HSA is directly injected into the instrument from

an aqueous aliquot comprising 5 μM HSA and 25 μM Pd^{II} (eq), where Pd^{II} (eq) is the equilibrium mixture comprising $[Pd(HPrPyrr)(OH_2)]^+$ and Pd(PrPyrr). If the sample is injected into the mass spectrometer using acetonitrile as the carrier and the injection loop on the instrument, then these satellite peaks are not observed. This presumably occurs because acetonitrile promotes dissociation of any surface-bound Pd(II) chelates. The relevant ESI-MS spectrum recorded for HSA with the Pd(II) system in the presence of acetonitrile is shown in Figure S33 (b) below; satellite peaks are clearly absent.

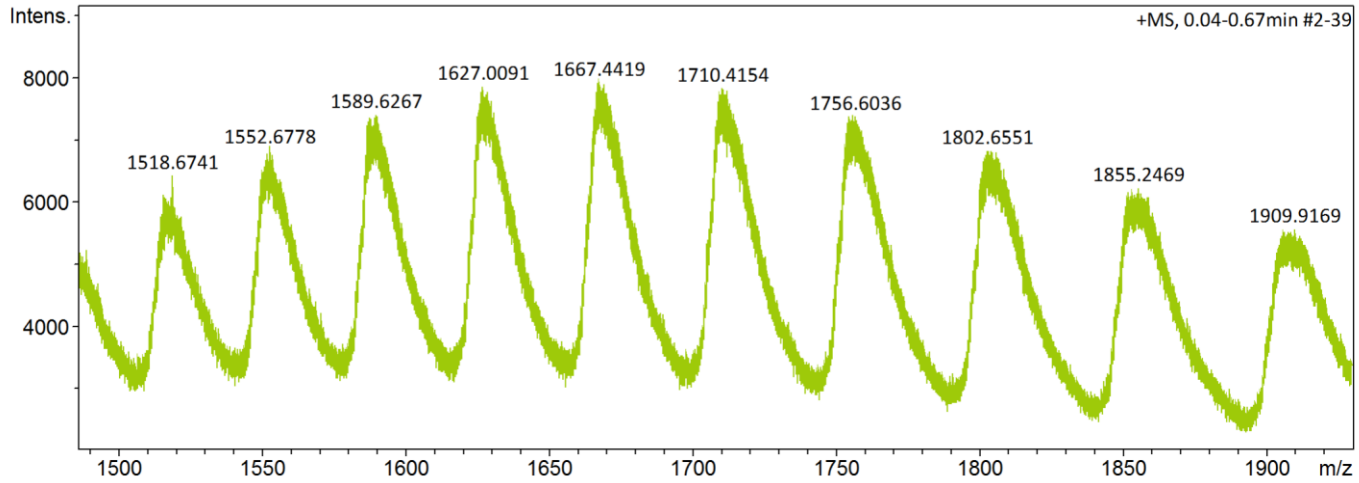


Figure S33 (b). ESI-mass spectrum recorded for an aqueous solution of HSA (5 μM) containing 25 μM Pd^{II} (eq) with injection via the instrument sample loop containing acetonitrile as the carrier solvent.

2.7 Circular Dichroism Spectroscopy

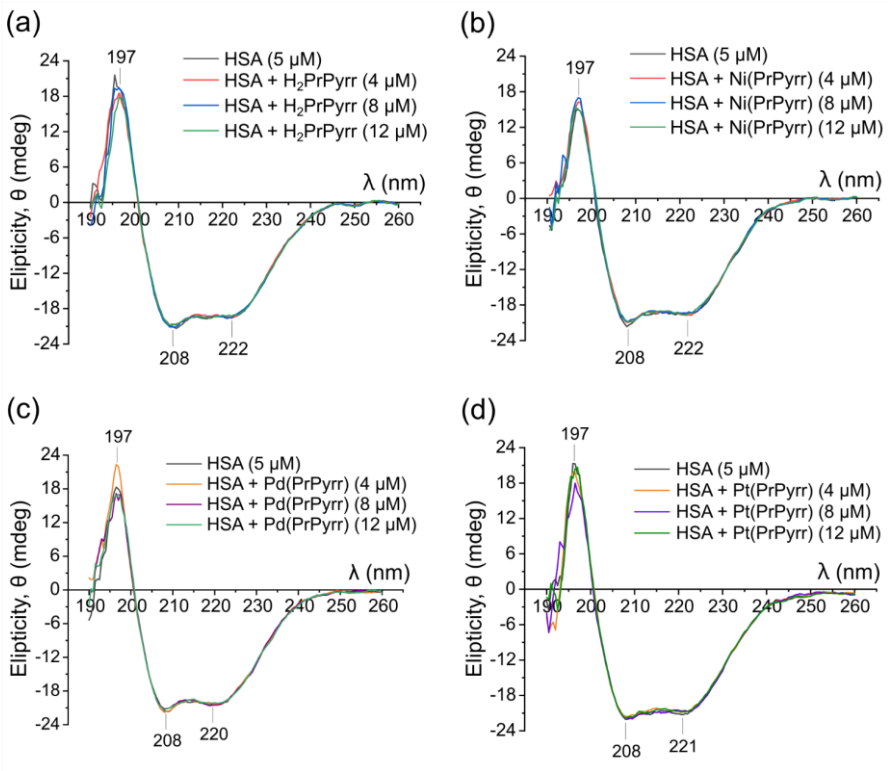


Figure S34. Plots of the far-UV CD spectra of native HSA and the protein incubated with saturating doses of (a) H_2PrPyrr, (b) Ni(PrPyrr), (c) Pd(PrPyrr), and (d) Pt(PrPyrr) recorded at 298 K in 50 mM KH_2PO_4 buffer at pH 7.50. The data are unsmoothed, and each spectrum is the average of three individual spectral scans.

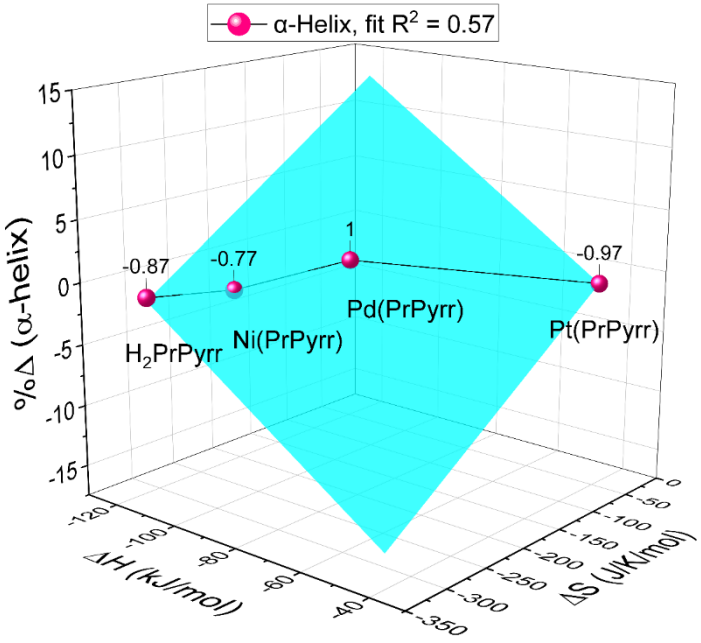


Figure S35. Three-dimensional graph showing how the change in the α-helix content of the protein correlates with the experimentally determined values of ΔH and ΔS for the reaction of each compound with HSA (T = 298 K). The relationship, $\%\Delta(\alpha\text{-helix}) = -7.1(2.9) - 0.192(78) \times \Delta H + 0.050(21) \times \Delta S$, reflects the fact that ΔG for the reaction becomes *more* favourable (more negative) as the β-sheet content of the protein decreases (see main paper) and the α-helix content of the protein *increases*, which is dependent on the identity of the bound ligand.

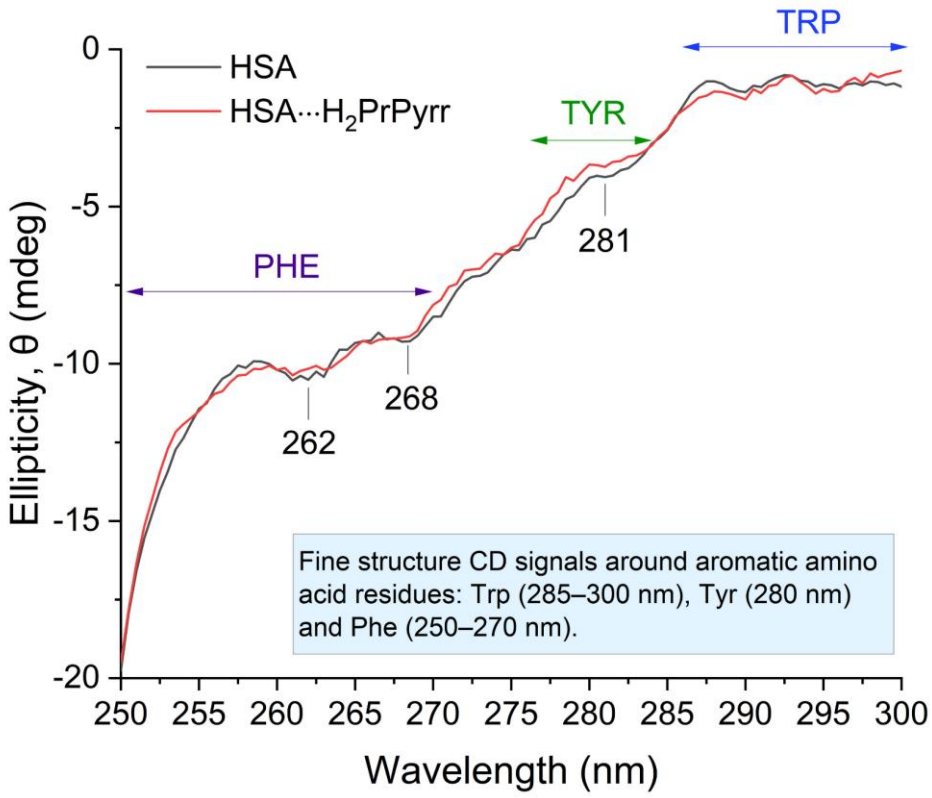


Figure S36. Plots of the near UV CD spectra of native HSA (5 μM) and the protein incubated with a saturating dose (12 μM) of H_2PrPyrr. The spectra were recorded at 298 K in 50 mM KH_2PO_4 buffer at pH 7.50 and represent the average of three spectral scans in each case. No other smoothing functions were applied to the data. The figure highlights the perturbations induced upon binding of the achiral ligand H_2PrPyrr to HSA. Spectral regions in which the CD signals of HSA (and other proteins) may be assigned to the amino acid residues Phe, Tyr, and Trp are indicated.

2.8 Macromolecular Simulations

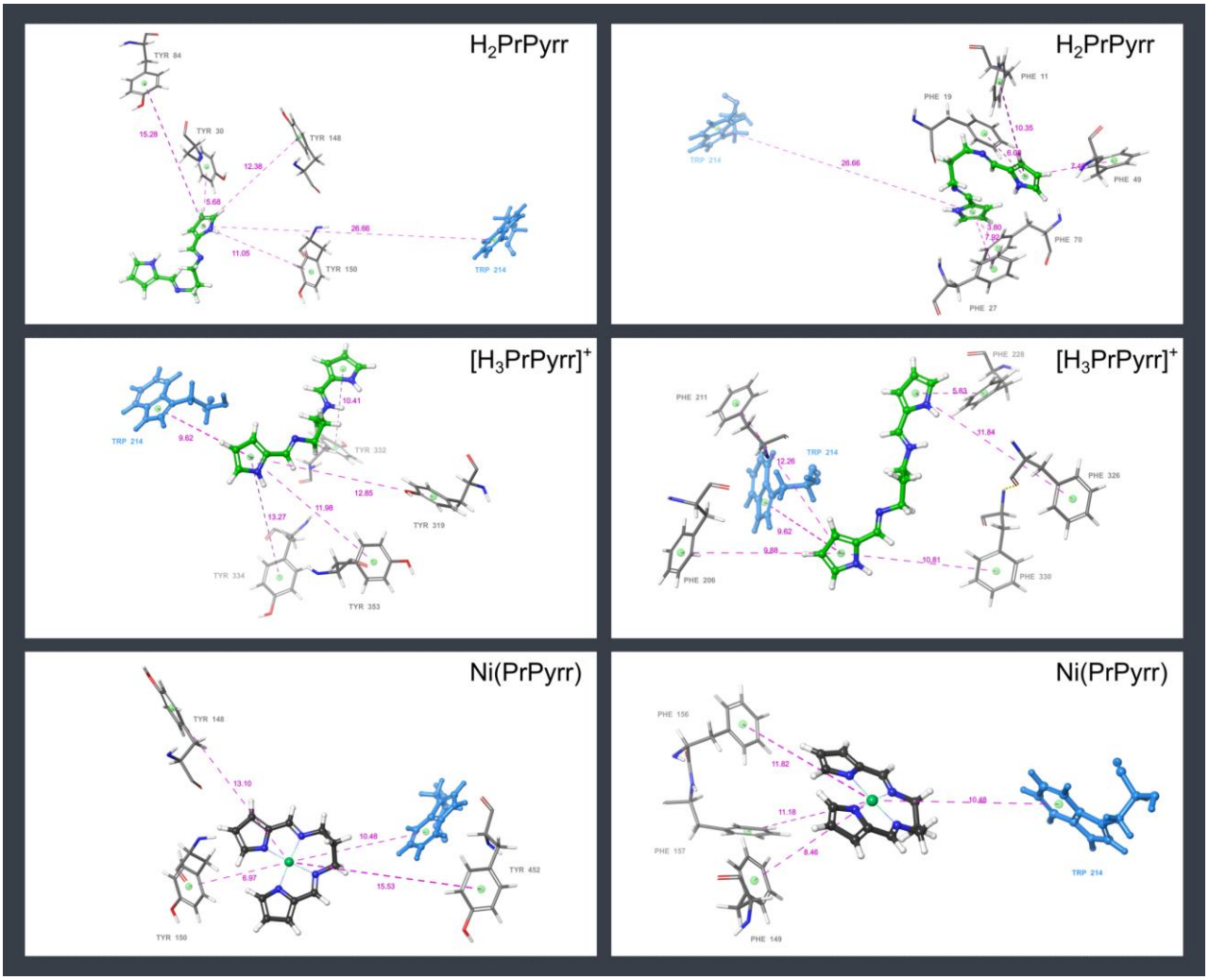


Figure S37. GLIDE XP docking analysis of the binding of H_2PrPyrr, $[H_3PrPyrr]^+$, and Ni(PrPyrr) to HSA using the X-ray structure of HSA with warfarin bound in subdomain IIA as the *in silico* target (PDB code 1HA2). A large target grid was generated for ligand docking at the warfarin site (with warfarin removed), spanning 40 x 40 x 40 $Å^3$, thereby facilitating a search of secondary binding sites radiating out (to ~20 Å) from warfarin's location. The image panels on the left and right show selected tyrosine and phenylaniline residues, respectively, that are closest to the best poses for the ligands. Trp-214 is rendered in blue. Distances are in Å units. Table S10 summarizes the docking scores and distances for all ligands with 1HA2 as the docking target, including the present ligands. The near-UV CD spectra for HSA•{H_2PrPyrr} and HSA•{Ni(PrPyrr)} shown in Figs. 11a and 11b of the in the main text suggest that these ligands perturb Tyr and Phe chromophores in addition to Trp-214 in HSA. The above docking results clearly support the experimental data: both H_2PrPyrr and the protonated species, $[H_3PrPyrr]^+$, bind in tyrosine- and phenylalanine-rich pockets within HSA with roughly the same docking score. The Ni(II) chelate binds firmly in subdomain IIA (Sudlow's site I) within 11 Å from Tyr-214 and is also located within range of several Tyr and Phe residues to impact their absorption of circularly polarized near-UV electromagnetic radiation, as seen in Figure 11b of the main text.

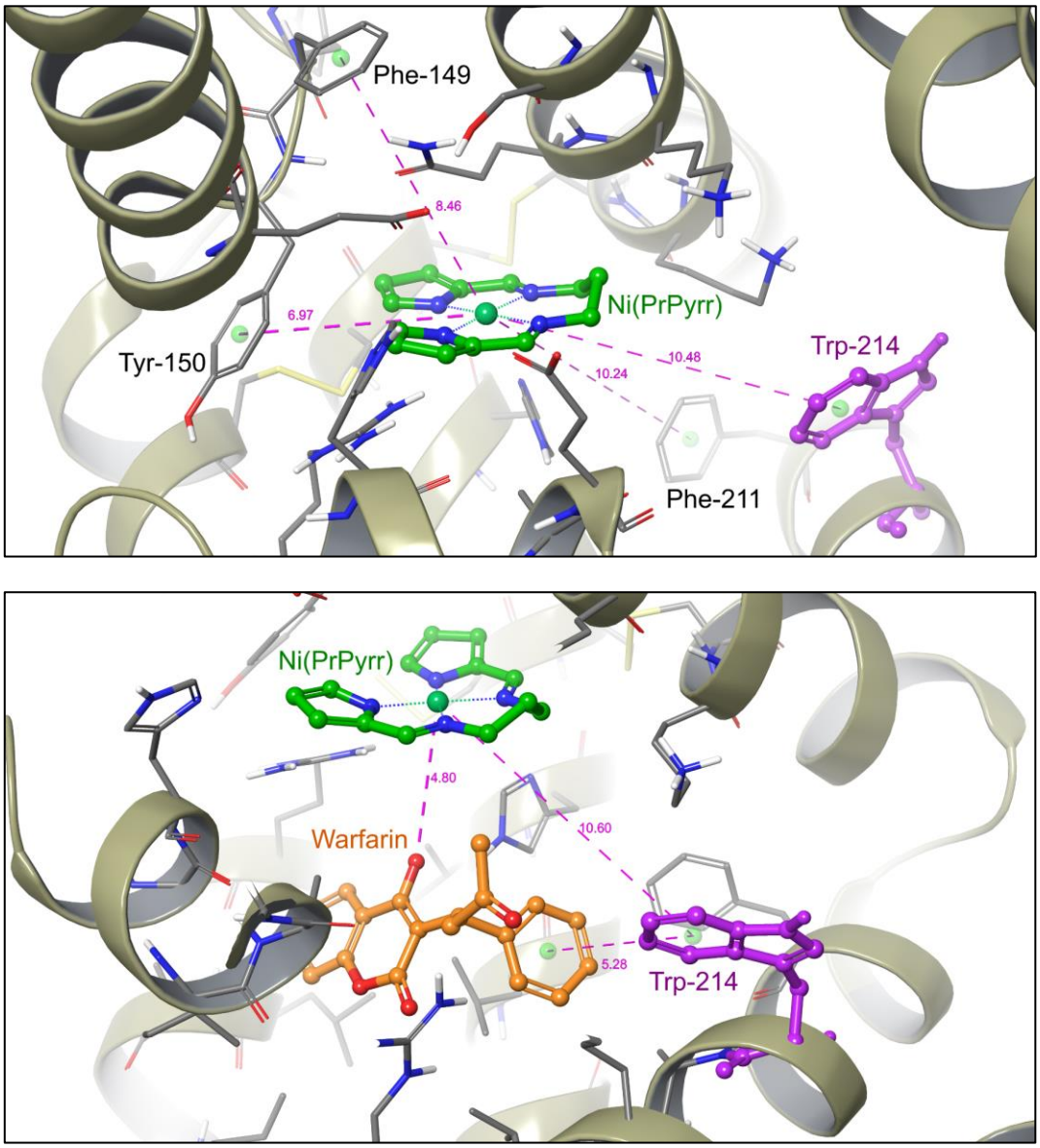


Figure S38. *Top:* Close-up view of the best pose of Ni(PrPyrr) docked within Sudlow's site I (subdomain IIA) of HSA (PDB code 1HA2) with warfarin removed from the grid. *Bottom:* Close-up view of the best pose of Ni(PrPyrr) docked within Sudlow's site I with warfarin present in the grid at its normal binding site determined by X-ray crystallography. Trp-214 is rendered in purple. Distances to key aromatic residues are shown as dashed pink lines (Å units); only polar H atoms are included. The *in silico* data support the following experimental data, as presented in the main text: (i) Ni(PrPyrr) quenches the fluorescence of Trp-214 probably by a FRET-based mechanism (the separation distance is < 11 Å and there is overlap of the UV spectra for each chromophore), (ii) Ni(PrPyrr) binding perturbs the CD signals from Phe and Tyr residues in the protein at 269 and 279 nm, respectively (the residues in question are located within 11 Å of the metal ion), and (iii) Ni(PrPyrr) displaces warfarin upon metal chelate uptake by the warfarin-bound target, HSA•{warfarin} (Figure S30). For the latter phenomenon, it is worth noting that Ni(PrPyrr) binds in Sudlow's site I at a location displaced by about 4–6 Å away from the warfarin binding site in the same pocket. However, as shown by the significantly distorted (nonplanar) pose of Ni(PrPyrr) in the lower panel, steric constraints clearly exist when Ni(PrPyrr) and warfarin co-bind in Sudlow's site I, suggesting that the metal chelate may displace warfarin from its binding site in an actual experimental ligand binding assay carried out in solution (Figure S30).

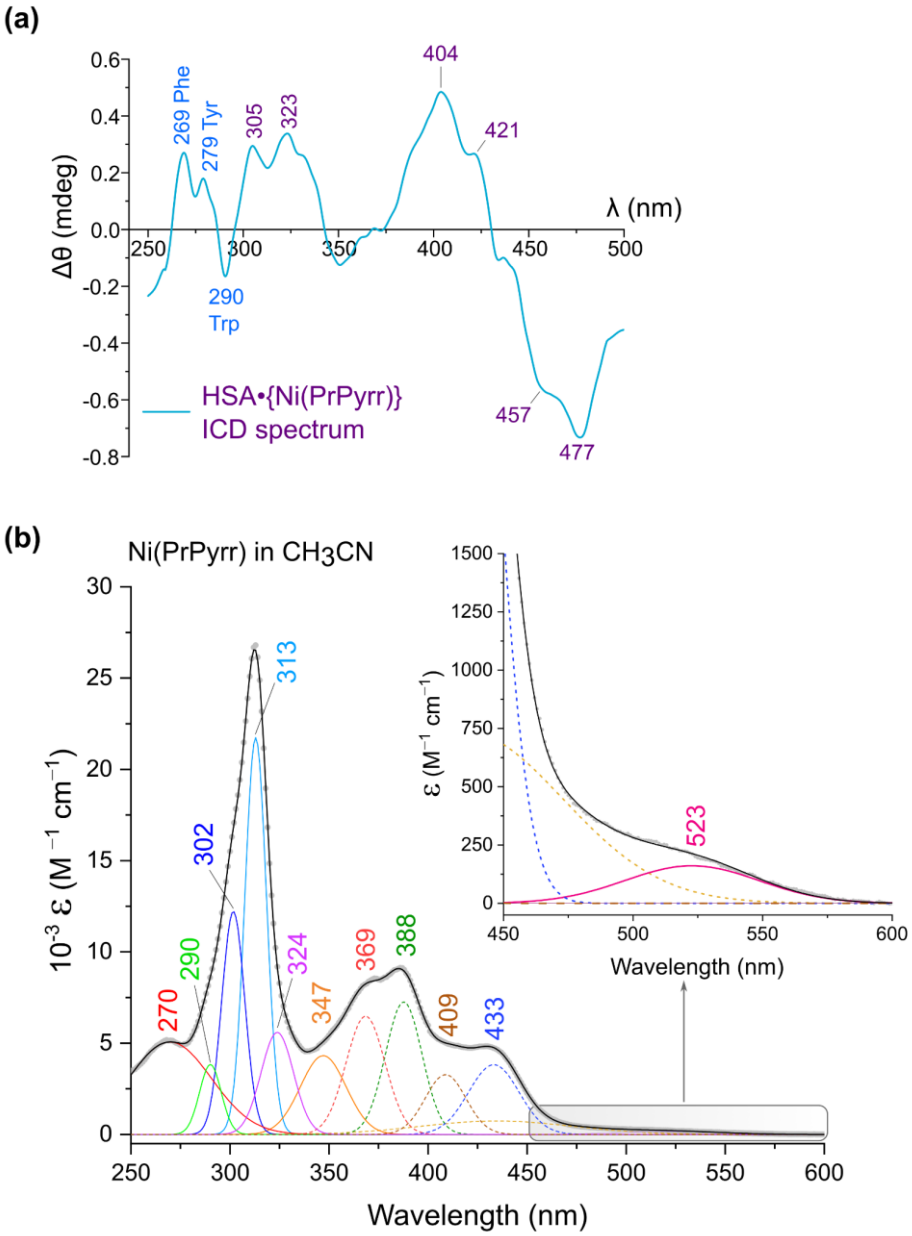


Figure S39. (a) Induced CD spectrum recorded for the complex formed between HSA and Ni(PrPyrr) at 298 K in 50 mM KH_2PO_4 buffer at pH 7.50. The spectrum was produced by subtracting the CD spectrum of native HSA from that of the complex, HSA•{Ni(PrPyrr)}. Peaks marked in purple font are from transitions involving the Ni(II) chelate. (b) Electronic absorption spectrum of Ni(PrPyrr) recorded in acetonitrile solution at 298 K (grey points). The spectral data were fitted to the sum of 12 peaks (Voigt functions) shown as constituent bands in a range of colours (solid and dashed curves). The heavy black line represents the fit of the spectral data (R^2 = 0.99992). The peaks at 457 and 477 nm in the ICD spectrum likely correspond to the bands at 409 and 433 nm in the absorption spectrum. Notwithstanding the expected solvent-induced frequency shift for the spectral bands, the plots suggest that the lowest-energy LMCT excited states of Ni(PrPyrr) exhibit a red shift upon binding to the protein.

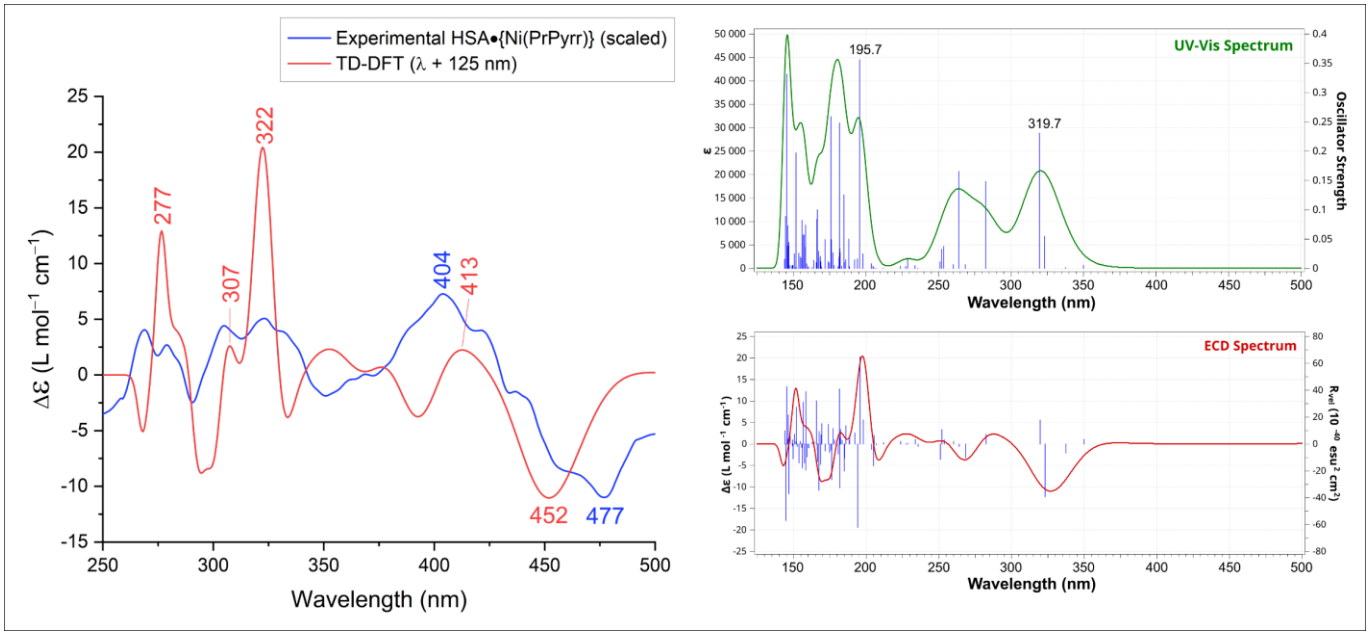


Figure S40. *Left*: comparison of the experimental induced CD spectrum (ICD) recorded for HSA•{Ni(PrPyrr)} at 298 K in 50 mM KH_2PO_4 buffer at pH 7.50 and the TD-DFT calculated electronic CD spectrum for the best pose of Ni(PrPyrr) docked into Sudlow's site I (subdomain IIA) of HSA (PDB code: 1HA2). The experimental spectrum has an arbitrarily scaled amplitude and was produced by subtraction of the CD spectrum of native HSA from that of HSA•{Ni(PrPyrr)}. The DFT-calculated spectrum (band width = 1500 cm^{-1}, hwhm) has been wavelength-corrected to properly match the experimental band energies. GLIDE XP (Schrödinger Release 2022-3) was used for the docking simulation. The electronic spectrum of the protein-ligand complex was calculated using the ONIOM method in Gaussian 16 at the CAM-B3LYP/SDD/GD3BJ level of theory and 85 excited singlet states. Only the Ni(II) chelate was incorporated in the high-level (QM) layer for the DFT simulation; the entire protein was modelled in a low layer using the UFF force field with atomic partial charges electronically embedded in the QM layer. *Right:* uncorrected electronic absorption and CD spectra for the system showing the spectral envelopes and individual transition intensities.

Note that unbound Ni(PrPyrr) has Cs symmetry and has no electronic CD spectrum. The simulations confirm the validity of the docking model by reasonably accounting for the primary features in the experimental ICD spectrum of the HSA•{Ni(PrPyrr)} complex. There are obvious discrepancies (such as the peaks at 277 and 322 nm) which likely reflect a relatively simple simulation conducted with a minimalistic QM layer in the absence of a PCM solvent model. Since the binding site for Ni(PrPyrr) is deeply buried, lack of a solvent model is less important than exclusion of all amino acid side chains within 6–8 Å of the metal chelate. A larger QM layer might improve the model further at the cost of increased computational time.

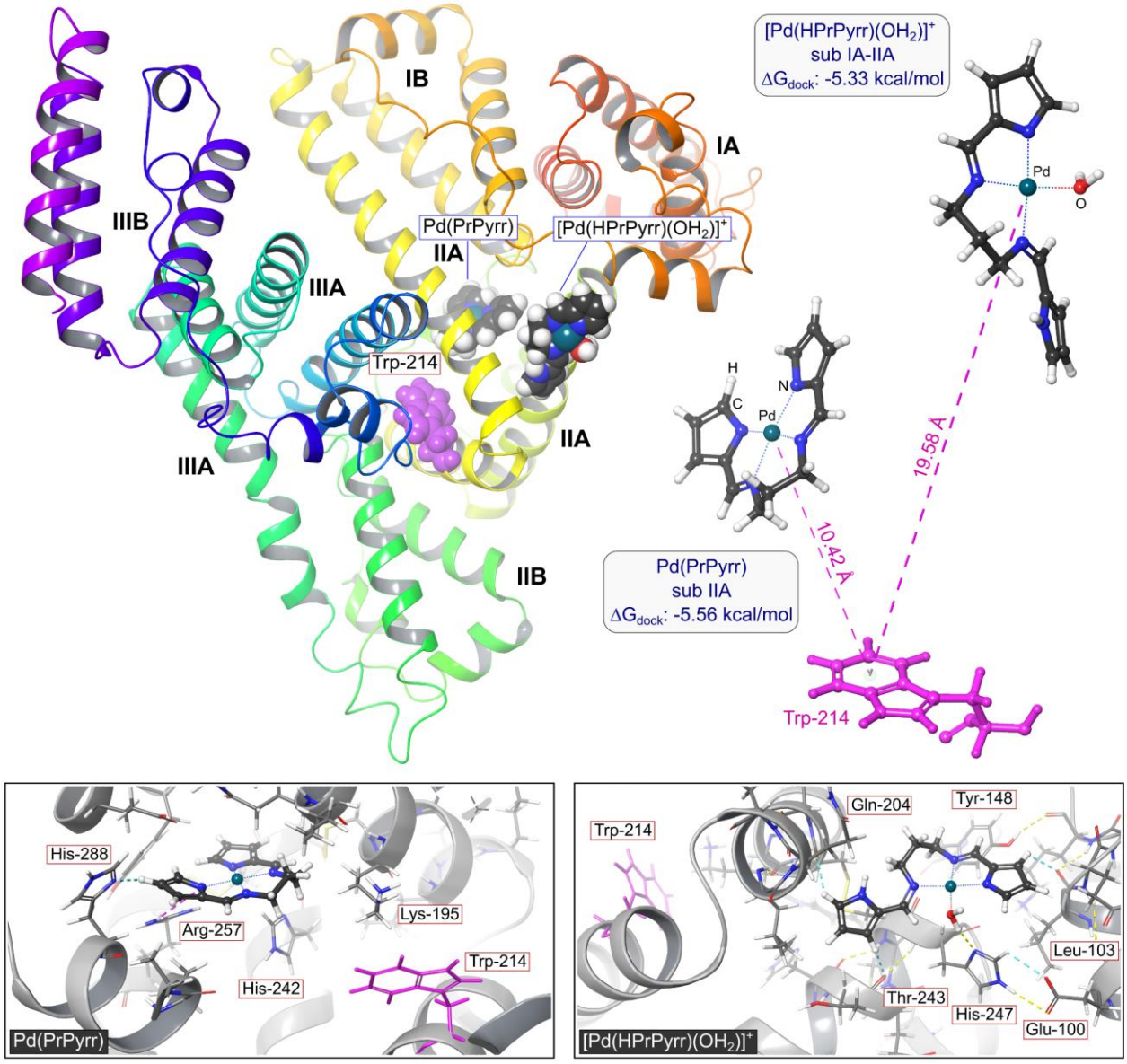


Figure S41. (a) GLIDE XP docking analysis of the binding of Pd(PrPyrr) and $[Pd(HPrPyrr)(OH_2)]^+$ to HSA using the X-ray structure of HSA with warfarin bound in subdomain IIA as the *in silico* target (PDB code 1HA2). A large target grid was generated for ligand docking at the warfarin site (with warfarin removed), spanning 40 x 40 x 40 $Å^3$, thereby facilitating a search of secondary binding sites radiating out (to ~20 Å) from warfarin's location. The structure shown displays the ligand poses (dark grey carbon atoms) with the most favourable docking scores (top right illustration) for the two metal chelates located within two unique binding sites close to Trp-214 (pink). The location of Pd(PrPyrr) relative to Trp-214 is displayed more closely in the lower left highlighted rectangle; the region is histidine-rich. The Pd(II) ion is located 10.42 Å away from the centroid of the benzene ring of Trp-214, which means that the metal chelate is displaced towards the edge of the binding pocket. Warfarin, which π-bonds with the benzene ring of Trp-214 (crystallographic centroid···centroid separation, 5.24 Å; 1HA2), would be able to co-bind with Pd(PrPyrr) by fitting into the binding site between Trp-214 and Pd(PrPyrr). The cationic complex $[Pd(HPrPyrr)(OH_2)]^+$ binds in the surface-exposed IA-IIA cleft of the protein with the Pd(II) ion located 19.58 Å from the centroid of Trp-214's benzene ring. The binding interactions include H-bonding of the coordinated water to His-247 as well as pyrrole C–H···O=C hydrogen bonds to the peptide backbone (lower right rectangle).

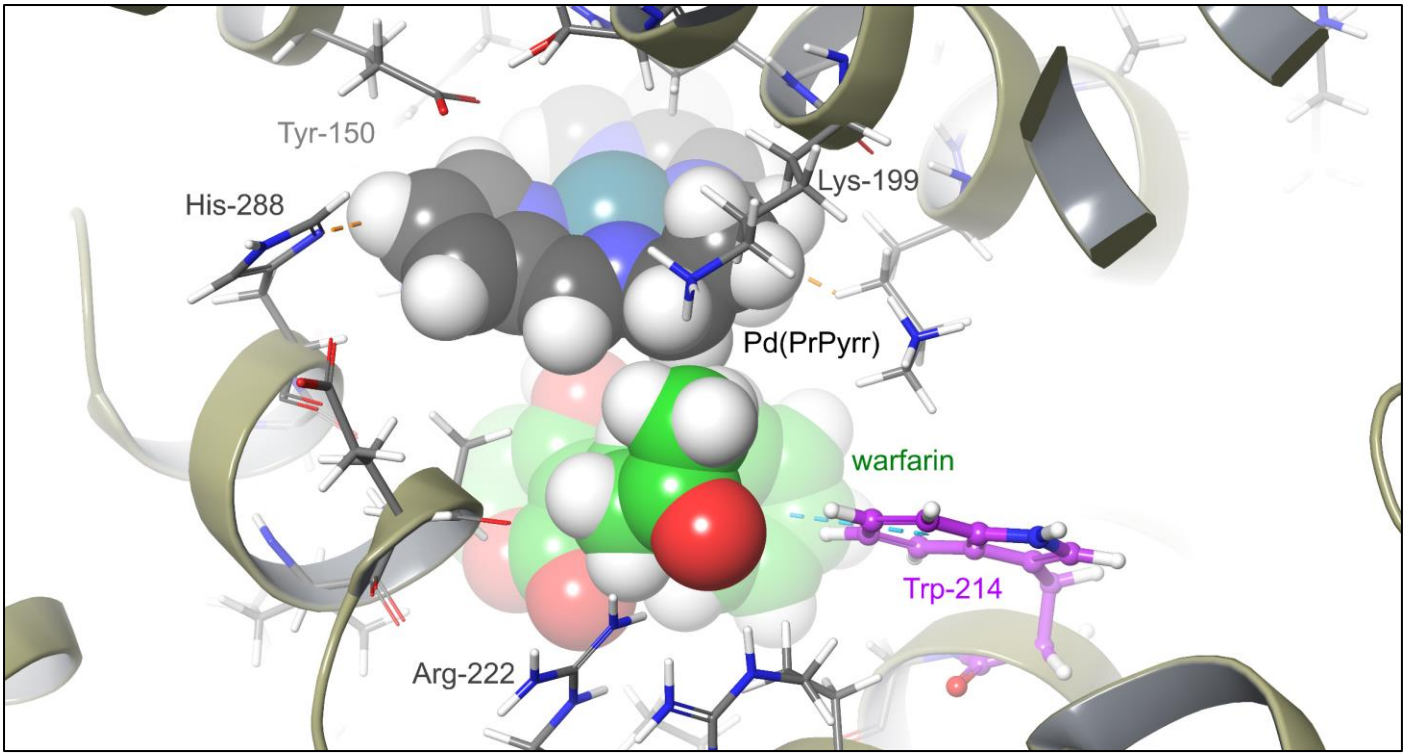


Figure S42. Illustration of the adjacent, yet somewhat overlapping, binding sites for warfarin and Pd(PrPyrr) in subdomain IIA (Sudlow's drug site I) of HSA as determined by GLIDE XP docking using PDB code 1HA2 as the target and a large 40 × 40 × 40-Å^3 grid centred on the coordinates of warfarin. Steric interactions between Pd(PrPyrr) and warfarin illustrated in this figure are expected to be significant enough in the real system for Pd(PrPyrr) to displace warfarin from the warfarin-bound protein at higher doses, thereby releasing the probe drug into the bulk solution. The *in silico* model supports the observed switch from static to dynamic fluorescence quenching observed when Pd(PrPyrr) is titrated into a solution of HSA•{warfarin} and the emission from warfarin, initially bound and then released, is monitored. (See Figs. 6 and 7 of the main paper.)

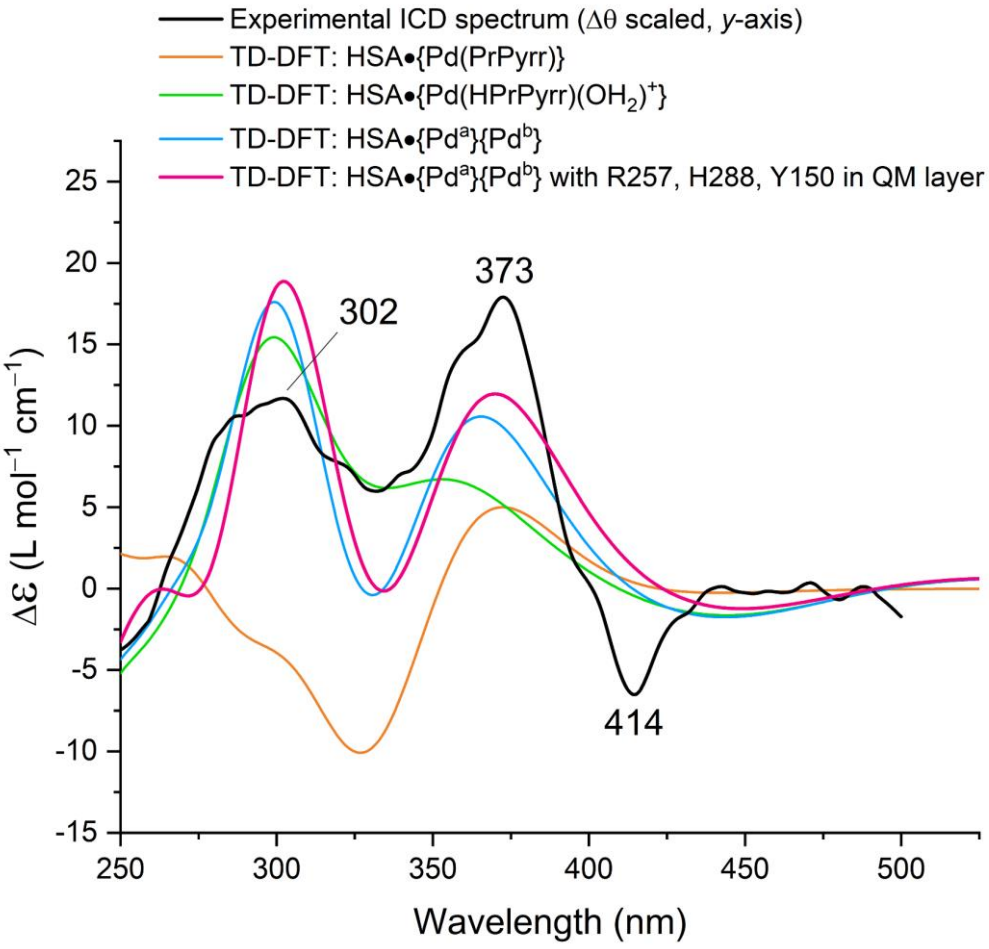


Figure S43. Plot of the experimental and calculated electronic circular dichroism spectra (CAM-B3LYP/SDD/GD3BJ:UFF level of theory) for Glide XP docking models (Table S9) of HSA bound to a selection of Pd(II) chelate poses. The ONIOM method was employed for the simulations with 2 layers: (i) a high (QM) layer at the DFT level of theory for the metal chelate(s) and (ii) a low layer comprising all protein atoms modelled by molecular mechanics with the UFF force field. The experimental spectrum (black) is the induced CD spectrum (ICD, $\Delta\theta$ in mdeg) calculated by subtraction of the CD spectrum of native HSA from that of HSA•{$Pd^{II}(X)$}; its amplitude is arbitrarily scaled to appear of a similar intensity to the DFT-calculated spectra ($\Delta\varepsilon$ in units of L mol^{-1} cm^{-1}). The y-axis units are thus not the same for the experimental and calculated spectra. All TD-DFT spectra are wavelength-scaled (λ + 25 nm) to achieve energy parity for the main bands with those of the experimental spectrum. The spectra in orange and green are the TD-DFT spectra for the best poses of Pd(PrPyrr) and $[Pd(HPrPyrr)(OH_2)]^+$ docked individually into their optimum binding sites in HSA (subdomains IIA and IIA-IIB, respectively). The blue and pink spectra are TD-DFT spectra calculated for the best poses of *both* Pd(II) chelates co-bound within HSA at their optimum binding sites. The pink spectrum was calculated using a QM layer that included Arg-258, His-288, and Tyr-150 around Pd(PrPyrr) in Sudlow's site I as well as $[Pd(HPrPyrr)(OH_2)]^+$. All simulated spectra have a band width of 2500 cm^{-1} (hwhm).

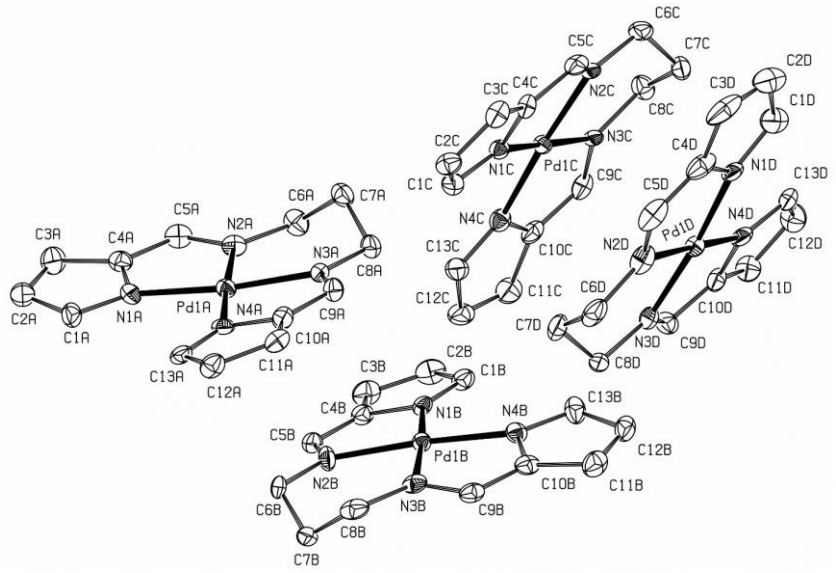
The plots show that the TD-DFT ECD spectrum of the HSA-Pd(II) system is most similar to the experimental spectrum when both metal chelates are present in the protein. Augmenting the QM layer to include three of the closest amino acid side-chains that interact with Pd(PrPyrr) in Sudlow's site I offers the best agreement between the calculated and experimental ECD spectrum.

3. Tables

Table S1. Crystal data and X-ray structure refinement details for Pd(PrPyrr).

Crystal data: CCDC 2207668	
Chemical formula	$C_{13}H_{14}N_4Pd$
M_r	332.68
Crystal system. space group	Monoclinic. $P2_1/c$
Temperature (K)	173
a. *b*. *c* (Å)	8.0357 (7). 16.8130 (13). 37.009 (3)
b (°)	90.722 (2)
V (Å^3)	4999.7 (7)
Z	16
Radiation type	Mo *K*a
μ (mm^{-1})	1.47
Crystal size (mm)	0.4 × 0.06 × 0.05
Data collection	
Diffractometer	Bruker *APEX*-II CCD
Absorption correction	Multi-scan *SADABS2016*/2 (Bruker. 2016/2) was used for absorption correction. wR_2(int) was 0.0674 before and 0.0551 after correction. The ratio of minimum to maximum transmission is 0.6805. The l/2 correction factor is not present.
T_{min}. T_{max}	0.480. 0.706
No. of measured. independent and observed [$I > 2s(I)$] reflections	241730. 15378. 15087
R_{int}	0.035
$(\sin q/l)_{max}$ (Å^{-1})	0.719
Refinement	
$R[F^2 > 2s(F^2)]$. $wR(F^2)$. S	0.078. 0.183. 1.15
No. of reflections	15378
No. of parameters	638
No. of restraints	6
H-atom treatment	H-atom parameters constrained
	$w = 1/[s^2(F_o^2) + 121.9447P]$ where $P = (F_o^2 + 2F_c^2)/3$
$D\rho_{max}$. $D\rho_{min}$ (e Å^{-3})	2.66. -3.53

Table S2. Selected geometrical parameters (Å, °) for the X-ray structure of Pd(PrPyrr). A labelled thermal ellipsoid plot (40% probability surfaces, H atoms omitted for clarity) is included to aid reading the tabulated data.



Parameter	Metric	Parameter	Metric
N1A—Pd1A	2.026 (7)	N1C—Pd1C	2.021 (7)
N2A—Pd1A	2.002 (7)	N2C—Pd1C	2.014 (7)
N3A—Pd1A	1.995 (7)	N3C—Pd1C	2.001 (8)
N4A—Pd1A	2.012 (7)	N4C—Pd1C	2.022 (7)
N1B—Pd1B	2.017 (7)	N1D—Pd1D	2.012 (7)
N2B—Pd1B	2.014 (7)	N2D—Pd1D	2.022 (8)
N3B—Pd1B	1.997 (7)	N3D—Pd1D	2.005 (8)
N4B—Pd1B	2.014 (7)	N4D—Pd1D	2.010 (8)
N2A—Pd1A—N1A	80.6 (3)	N1C—Pd1C—N4C	102.6 (3)
N2A—Pd1A—N4A	175.7 (3)	N2C—Pd1C—N1C	80.2 (3)
N3A—Pd1A—N1A	173.7 (3)	N2C—Pd1C—N4C	176.2 (3)
N3A—Pd1A—N2A	94.9 (3)	N3C—Pd1C—N1C	174.8 (3)
N3A—Pd1A—N4A	81.4 (3)	N3C—Pd1C—N2C	95.8 (3)
N4A—Pd1A—N1A	102.9 (3)	N3C—Pd1C—N4C	81.2 (3)
N2B—Pd1B—N1B	80.5 (3)	N1D—Pd1D—N2D	80.9 (4)
N2B—Pd1B—N4B	175.4 (3)	N3D—Pd1D—N1D	174.5 (3)
N3B—Pd1B—N1B	174.8 (3)	N3D—Pd1D—N2D	94.9 (4)
N3B—Pd1B—N2B	95.0 (3)	N3D—Pd1D—N4D	81.1 (3)
N3B—Pd1B—N4B	81.3 (3)	N4D—Pd1D—N1D	102.9 (3)
N4B—Pd1B—N1B	103.1 (3)	N4D—Pd1D—N2D	175.9 (3)
C2A—C1A—N1A—Pd1A	171.5 (7)	C2C—C1C—N1C—Pd1C	177.0 (7)
C3A—C4A—N1A—Pd1A	-173.9 (7)	C3C—C4C—N1C—Pd1C	-177.0 (6)
C4A—C5A—N2A—Pd1A	-5.1 (11)	C4C—C5C—N2C—Pd1C	-4.6 (10)
C5A—C4A—N1A—Pd1A	5.7 (10)	C5C—C4C—N1C—Pd1C	3.3 (9)
C7A—C6A—N2A—Pd1A	-34.9 (11)	C7C—C6C—N2C—Pd1C	-32.9 (10)

C7A—C8A—N3A—Pd1A	36.2 (10)	C7C—C8C—N3C—Pd1C	33.7 (10)
C9A—C10A—N4A—Pd1A	-4.7 (9)	C9C—C10C—N4C—Pd1C	-6.4 (9)
C10A—C9A—N3A—Pd1A	1.7 (11)	C10C—C9C—N3C—Pd1C	6.2 (10)
C11A—C10A—N4A—Pd1A	176.0 (6)	C11C—C10C—N4C—Pd1C	170.9 (6)
C12A—C13A—N4A—Pd1A	-175.5 (7)	C12C—C13C—N4C—Pd1C	-166.4 (8)
C2B—C1B—N1B—Pd1B	172.8 (8)	C2D—C1D—N1D—Pd1D	169.8 (7)
C3B—C4B—N1B—Pd1B	-175.9 (6)	C3D—C4D—N1D—Pd1D	-173.2 (6)
C4B—C5B—N2B—Pd1B	-1.3 (11)	C4D—C5D—N2D—Pd1D	-3.8 (12)
C5B—C4B—N1B—Pd1B	4.2 (9)	C5D—C4D—N1D—Pd1D	3.6 (10)
C7B—C6B—N2B—Pd1B	-33.8 (11)	C7D—C6D—N2D—Pd1D	-35.6 (11)
C7B—C8B—N3B—Pd1B	31.8 (10)	C7D—C8D—N3D—Pd1D	34.4 (11)
C9B—C10B—N4B—Pd1B	-5.3 (10)	C9D—C10D—N4D—Pd1D	-3.4 (9)
C10B—C9B—N3B—Pd1B	7.2 (10)	C10D—C9D—N3D—Pd1D	1.4 (11)
C11B—C10B—N4B—Pd1B	173.6 (6)	C11D—C10D—N4D—Pd1D	176.6 (6)
C12B—C13B—N4B—Pd1B	-171.1 (7)	C12D—C13D—N4D—Pd1D	-174.8 (8)

Table S3. Metal-to-nitrogen bond distances for 27 pyrrolide and pyrrolide-imine complexes of Pd(II) in the CSD.

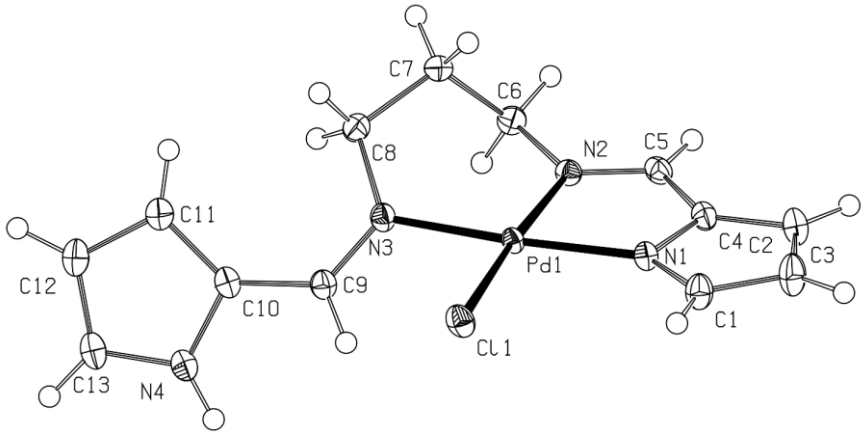
Ref Code	**Pd-$N_{pyrrole}$ (Å)**	**Pd-N_{imine} (Å)**	**Ref Code**	**Pd-$N_{pyrrole}$ (Å)**	**Pd-N_{imine} (Å)**
BAWBIM	2.008	2.037	VAPHUR	2.047	2.018
	2.011	2.035	VAPJAZ	2.063	2.02
BEZWUZ	2.124	2.121		2.044	2.021
BEZXEK	2.004	2.168	XADJES	2.027	2.053
BEZXIO	2.03	2.052		2.027	2.053
	2.027	2.052	XULXEK	2.063	2.006
DOJXAD	1.966			2.046	1.962
EDUREC	2.022	2.041		2.046	1.959
	2.022	2.041	XUVQIO	2.006	2.01
EKAPUB	1.914	1.996		2.006	2.001
FEHYOJ		2.001		2.013	2
	1.995			2.01	2.027
FEJKEN	1.992			2.016	2.001
FUNJAC	2.005			2.018	1.995
JITCEK	2	1.962		2.008	2.007
KEDMEN	1.985			2.012	2.005
KELFAJ	1.999		YIYDEQ	2.042	2.007
KIQGIA	1.983		ZENYUP	2.009	2.023
	1.987			1.993	2.036
	1.991				
	1.991				
LERRAD	2.018	2.049			
	2.018	2.043			
	2.02	2.036			
	2.02	2.036			
	2.043	2.053			

	2.049	2.053			
LUHYAR	2.038	2.06			
	2.032	2.058			
REDTOM	1.998	2.033			
REDTUS	1.99	2.027			
REDVAA	1.991	2.022			
SOGMOR	2.034	1.958			
	2.039	1.963			
	2.037	2.028			
	2.042	2.026			
	2.026	1.961			
	2.026	1.967			
	2.03	1.958			
	2.019	1.961			

Table S4. Crystal data and X-ray structure refinement details for PdCl(HPrPyrr).

Crystal data: CCDC 2207667	
Chemical formula	$C_{13}H_{15}ClN_4Pd$
M_r	369.14
Crystal system, space group	Monoclinic, $P2_1/n$
Temperature (K)	153
a, *b*, *c* (Å)	12.4781 (5), 7.9715 (4), 14.0369 (6)
b (°)	102.440 (2)
V (Å^3)	1363.46 (11)
Z	4
Radiation type	Mo *K*a
m (mm^{-1})	1.55
Crystal size (mm)	0.22 × 0.17 × 0.13
Data collection	
Diffractometer	Bruker *APEX*-II CCD
Absorption correction	Integration *SADABS2016*/2 (Bruker,2016/2) was used for absorption correction. wR_2(int) was 0.0588 before and 0.0517 after correction. The ratio of minimum to maximum transmission is 0.8413. The λ/2 correction factor is not present.
T_{min}, T_{max}	0.550, 0.654
No. of measured, independent and observed [$I > 2\sigma(I)$] reflections	45957, 5199, 4747
R_{int}	0.034
$(\sin\theta/\lambda)_{max}$ (Å^{-1})	0.770
Refinement	
$R[F^2 > 2\sigma(F^2)]$, $wR(F^2)$, *S*	0.021, 0.049, 1.08
No. of reflections	5199
No. of parameters	176
H-atom treatment	H atoms treated by a mixture of independent and constrained refinement
$D\rho_{max}$, $D\rho_{min}$ (e Å^{-3})	0.59, -0.79

Table S5. Selected geometrical parameters (Å, °) for the X-ray structure of PdCl(HPrPyrr). A labelled thermal ellipsoid plot (50% probability surfaces, H atoms drawn with arbitrary radii) is included to aid reading the tabulated data.



Parameter	Metric	Parameter	Metric
Pd1—Cl1	2.3203 (4)	C4—C5	1.4225 (19)
Pd1—N1	1.9931 (11)	C5—H5	0.9500
Pd1—N2	1.9973 (11)	C6—H6A	0.9900
Pd1—N3	2.0326 (11)	C6—H6B	0.9900
N1—C1	1.3496 (18)	C6—C7	1.529 (2)
N1—C4	1.3813 (17)	C7—H7A	0.9900
N2—C5	1.3032 (17)	C7—H7B	0.9900
N2—C6	1.4598 (17)	C7—C8	1.5250 (19)
N3—C8	1.4714 (18)	C8—H8A	0.9900
N3—C9	1.2995 (18)	C8—H8B	0.9900
N4—C10	1.3841 (18)	C9—H9	0.9500
N4—C13	1.3561 (18)	C9—C10	1.4439 (18)
N4—H4	0.89 (2)	C10—C11	1.396 (2)
C1—H1	0.9500	C11—H11	0.9500
C1—C2	1.403 (2)	C11—C12	1.404 (2)
C2—H2	0.9500	C12—H12	0.9500
C2—C3	1.403 (2)	C12—C13	1.382 (2)
C3—H3	0.9500	C13—H13	0.9500
C3—C4	1.3962 (19)		
N1—Pd1—Cl1	94.51 (4)	N2—C6—H6A	110.1
N1—Pd1—N2	80.89 (5)	N2—C6—H6B	110.1
N1—Pd1—N3	172.75 (5)	N2—C6—C7	107.87 (11)
N2—Pd1—Cl1	175.40 (3)	H6A—C6—H6B	108.4
N2—Pd1—N3	91.90 (5)	C7—C6—H6A	110.1
N3—Pd1—Cl1	92.69 (4)	C7—C6—H6B	110.1
C1—N1—Pd1	139.50 (10)	C6—C7—H7A	108.7
C1—N1—C4	107.65 (11)	C6—C7—H7B	108.7
C4—N1—Pd1	112.80 (9)	H7A—C7—H7B	107.6
C5—N2—Pd1	114.82 (9)	C8—C7—C6	114.06 (12)

C5—N2—C6	123.16 (12)	C8—C7—H7A	108.7
C6—N2—Pd1	121.59 (9)	C8—C7—H7B	108.7
C8—N3—Pd1	121.27 (9)	N3—C8—C7	113.51 (11)
C9—N3—Pd1	119.32 (10)	N3—C8—H8A	108.9
C9—N3—C8	119.30 (11)	N3—C8—H8B	108.9
C10—N4—H4	124.2 (14)	C7—C8—H8A	108.9
C13—N4—C10	109.81 (13)	C7—C8—H8B	108.9
C13—N4—H4	125.8 (14)	H8A—C8—H8B	107.7
N1—C1—H1	125.3	N3—C9—H9	115.8
N1—C1—C2	109.48 (13)	N3—C9—C10	128.31 (13)
C2—C1—H1	125.3	C10—C9—H9	115.8
C1—C2—H2	126.4	N4—C10—C9	118.08 (13)
C3—C2—C1	107.23 (13)	N4—C10—C11	106.87 (12)
C3—C2—H2	126.4	C11—C10—C9	134.63 (14)
C2—C3—H3	127.0	C10—C11—H11	126.3
C4—C3—C2	106.05 (13)	C10—C11—C12	107.39 (14)
C4—C3—H3	127.0	C12—C11—H11	126.3
N1—C4—C3	109.59 (12)	C11—C12—H12	126.1
N1—C4—C5	114.87 (11)	C13—C12—C11	107.71 (13)
C3—C4—C5	135.42 (13)	C13—C12—H12	126.1
N2—C5—C4	116.61 (12)	N4—C13—C12	108.19 (13)
N2—C5—H5	121.7	N4—C13—H13	125.9
C4—C5—H5	121.7	C12—C13—H13	125.9
Pd1—N1—C1—C2	-176.91 (13)	C2—C3—C4—N1	0.06 (18)
Pd1—N1—C4—C3	177.78 (10)	C2—C3—C4—C5	175.75 (17)
Pd1—N1—C4—C5	1.12 (15)	C3—C4—C5—N2	-176.31 (16)
Pd1—N2—C5—C4	0.06 (16)	C4—N1—C1—C2	0.00 (18)
Pd1—N2—C6—C7	41.74 (14)	C5—N2—C6—C7	-130.34 (13)
Pd1—N3—C8—C7	17.60 (16)	C6—N2—C5—C4	172.64 (12)
Pd1—N3—C9—C10	177.53 (11)	C6—C7—C8—N3	47.00 (17)
N1—C1—C2—C3	0.0 (2)	C8—N3—C9—C10	-6.3 (2)
N1—C4—C5—N2	-0.80 (19)	C9—N3—C8—C7	-158.51 (13)
N2—C6—C7—C8	-80.00 (14)	C9—C10—C11—C12	-172.56 (16)
N3—C9—C10—N4	162.00 (14)	C10—N4—C13—C12	-1.90 (17)
N3—C9—C10—C11	-26.5 (3)	C10—C11—C12—C13	-0.75 (19)
N4—C10—C11—C12	-0.39 (18)	C11—C12—C13—N4	1.62 (18)
C1—N1—C4—C3	-0.04 (17)	C13—N4—C10—C9	175.11 (12)
C1—N1—C4—C5	-176.70 (13)	C13—N4—C10—C11	1.42 (17)
C1—C2—C3—C4	-0.06 (19)		

Table S6. A comparison of HSA Trp-214 quenching by Ni(PrPyrr), Pd(PrPyrr)[a] and Pt(PrPyrr) measured at the peak emission wavelength after excitation at 280 nm and 295 nm.

		λ^{ex} = 280 nm	λ^{ex} = 295 nm
Complex	**Concentration (μM)**	**I_0/I**	**I_0/I**
Ni(PrPyrr)	0.00	1.00	1.00
	4.00	0.49	0.37
	8.00	0.20	0.20
	12.00	0.13	0.09
Pd(PrPyrr)	0.00	1.00	1.00
	4.00	0.31	0.33
	8.00	0.21	0.24
	12.00	0.19	0.21
Pt(PrPyrr)	0.00	1.00	1.00
	4.00	0.52	0.53
	8.00	0.43	0.45
	12.00	0.37	0.37

[a] This complex is most likely an equilibrium mixture of the species Pd(PrPyrr) and $[Pd(HPrPyrr)(OH_2)]^+$.

Table S7. Secondary structure composition of HSA in the presence of H_2PrPyr, Ni(PrPyrr), Pd(PrPyrr) and Pt(PrPyrr) at different concentrations. CD spectral data were recorded at 298 K in 50 mM KH_2PO_4 buffer at pH 7.50.

Ligand	**C_L (μM)[a]**	**α-Helix**	**β-sheet**	**Turn**	**Unordered coil**
H_2PrPyr	0	50.87	8.42	10.61	33.16
	4	48.31	16.66	9.69	30.48
	8	48.94	15.78	9.77	30.77
	12	50	10.79	10.41	32.59
% change		-0.87	2.37	-0.2	-0.57
Ni(PrPyrr)	0	49.83	11.38	10.14	32.29
	4	48.31	16.66	9.69	30.48
	8	49.89	10.36	10.5	32.79
	12	49.06	11.18	10.48	32.97
% change		-0.77	-0.2	0.34	0.68
Pd(PrPyrr)[b]	0	49.41	15.56	9.55	30.51
	4	48.75	18.8	9.21	29.2
	8	48.18	17.22	9.5	30.3
	12	50.41	12.49	10.01	31.54
% change		1.00	-3.07	0.46	1.03
Pt(PrPyrr)	0	52.76	10.43	9.85	31.43
	4	51.5	11.38	9.98	31.76
	8	52.93	7.94	10.28	32.94
	12	51.79	11.7	9.91	31.4
% change		-0.97	1.27	0.06	-0.03

[a] Total ligand or metal chelate concentration. [b] This complex is most likely an equilibrium mixture of the species Pd(PrPyrr) and $[Pd(HPrPyrr)(OH_2)]^+$.

Table S8. Comparison of the binding of H_2PrPyrr, Ni(PrPyrr), Pd(PrPyrr), and Pt(PrPyrr), as well as fluorophore quenching, to HSA and its noncovalent complexes with warfarin (Warf) and ibuprofen (Ibu).[a,b]

	HSA	ESD	HSA-Warf	ESD	HSA-Ibu	ESD
H_2PrPyrr						
K_{SV} / M^{-1}	6.12E+04	0.29E+04	1.19E+05	2.70E+04	5.21E+05	9.50E+04
n	0.76	0.02	1.50	0.06	1.80	0.04
logK	3.55	0.09	6.95	0.29	8.35	0.19
Ni(PrPyrr)						
K_{SV} / M^{-1}	1.55E+05	0.1E+05	7.24E+04	1.56E+03	8.24E+04	3.77E+03
n	0.89	0.02	1.06	0.04	0.76	0.05
logK	4.63	0.14	5.15	0.18	3.75	0.25
Pd(PrPyrr)[c]						
K_{SV} / M^{-1}	3.55E+06	1.20E+05	1.24E+05	8.12E+03	3.43E+05	2.17E+04
n	1.08	0.01	0.98	0.01	1.13	0.02
logK	6.00	0.07	5.08	0.05	6.11	0.13
Pt(PrPyrr)						
K_{SV} / M^{-1}	1.83E+05	9.00E+02	1.42E+05	4.60E+02	1.40E+05	6.00E+03
n	1.02	0.01	1.50	0.04	1.41	0.03
logK	5.34	0.18	6.80	0.16	6.76	0.15

[a]Reaction conditions: 5.0 μM protein, 50 mM KH_2PO_4, pH 7.50, *T* = 298 K. The Stern-Volmer (SV) fluorescence quenching constant (K_{SV}) was determined from fits of plots of I_0/I vs. [ligand]. [b]The HSA-Warf and HSA-Ibu complexes induced cooperative binding of both H_2PrPyrr and Pt(PrPyrr) to the protein target, characterized by 1.0 < n < 2.0 and an increase in logK relative to binding of these ligands to the native protein. [c]This complex is most likely an equilibrium mixture of the species Pd(PrPyrr) and $[Pd(HPrPyrr)(OH_2)]^+$.

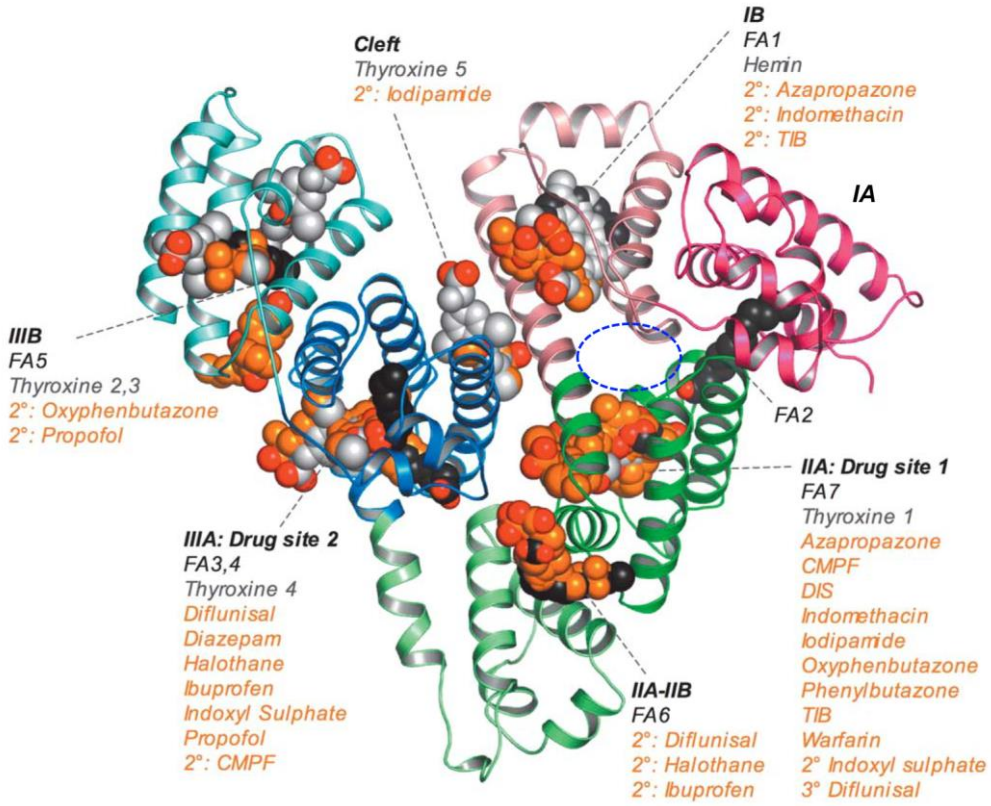
Table S9. Summary of GLIDE XP docking scores and selected interaction energy parameters for HSA targets prepared from ligand-free and ligand-bound grids based on geometry-optimized (prepared) structures derived from PDB codes 1HA2 (HSA···warfarin complex), 2BXF (HSA···diazepam complex), and 2BXG (HSA···bis(ibuprofen) complex). The docking runs were truncated to report only the top-scoring ligand pose for each ligand. All energies are in units of kcal mol^{-1}.

Ligand or drug	Binding site location[a]	ligand effic.	ligand effic. sa	glide ligand effic. ln	XP GScore	glide E_{vdw}	glide E_{Coul}	glide energy	glide $E_{internal}$	glide E_{model}	XP H Bond	XP Lipo. E_{vdW}	XP $E_{Electro}$
1HA2 - No warfarin bound in subdomain IIA of protein docking grid (Sudlow's Site I)													
Ibuprofen	IA	-0.533	-1.315	-2.158	-8.001	-22.998	-1.285	-24.283	3.939	-31.178	0	-4.64	-0.096
Warfarin	IIA	-0.327	-0.929	-1.817	-7.513	-42.858	-2.647	-45.506	3.007	-63.649	-0.353	-5.865	-0.199
$[H_4PrPyrr]^{2+}$	IA-IIA	-0.380	-0.978	-1.687	-6.466	-20.981	-21.034	-42.015	5.580	-55.787	-0.842	-1.395	-1.578
$H_2PrPyrr$	IA	-0.375	-0.964	-1.663	-6.373	-36.667	0.385	-36.282	5.550	-53.079	0	-4.865	0.029
$[H_3PrPyrr]^{+}$	IIA-IIB	-0.361	-0.929	-1.602	-6.142	-37.516	-6.096	-43.612	2.966	-58.501	-0.7	-4.358	-0.457
Pd(PrPyrr)	IIA	-0.309	-0.810	-1.430	-5.563	-21.487	-5.214	-26.701	0	-33.174	-0.924	-1.856	-0.391
$[Pd(OH_2)(HPrPyrr)]^{+}$	IA-IIA	-0.280	-0.748	-1.351	-5.329	-24.123	-6.146	-30.269	2.568	-35.366	-0.706	-2.458	-0.461
Ni(PrPyrr)	IIA	-0.287	-0.753	-1.330	-5.173	-22.526	-3.870	-26.396	0	-33.410	-0.626	-1.837	-0.290
Pt(PrPyrr)	IIA	-0.282	-0.739	-1.305	-5.078	-21.656	-4.625	-26.280	0	-33.372	-0.856	-1.857	-0.347
Diazepam	IIA-IIB	-0.251	-0.681	-1.256	-5.019	-25.042	-0.568	-25.610	1.048	-33.330	0	-3.979	-0.043
2BXF - No diazepam bound in subdomain IIIA of protein docking grid (Sudlow's Site II)													
Diazepam	IIIA	-0.452	-1.226	-2.260	-9.032	-44.241	-2.966	-47.207	1.236	-67.088	-0.688	-6.504	-0.222
Warfarin	IIIA	-0.318	-0.905	-1.770	-7.320	-33.986	-1.476	-35.462	4.800	-45.147	0	-6.367	-0.111
$H_2PrPyrr$	IIIA	-0.279	-0.718	-1.238	-4.747	-34.538	-4.385	-38.923	4.103	-53.037	-0.614	-3.365	-0.329
$[Pd(OH_2)(HPrPyrr)]^{+}$	IB-IIIA cleft	-0.228	-0.609	-1.099	-4.336	-26.422	-8.541	-34.964	2.548	-41.121	-1.165	-2.245	-0.641
Ibuprofen	IIIA	-0.287	-0.707	-1.159	-4.298	-20.072	-5.986	-26.058	1.780	-33.284	-1.111	-2.381	-0.449
$[H_4PrPyrr]^{2+}$	IB-IIIA cleft	-0.249	-0.640	-1.104	-4.233	-26.744	-16.841	-43.585	1.547	-62.410	-0.700	-2.458	-1.263
$[H_3PrPyrr]^{+}$	IB-IIIA cleft	-0.229	-0.588	-1.014	-3.888	-29.142	-13.549	-42.691	7.636	-54.977	-1.162	-2.198	-1.016
Pd(PrPyrr)	IIA-IIIA cleft	-0.155	-0.407	-0.718	-2.794	-25.018	-1.373	-26.391	0	-32.797	0	-2.331	-0.103
Ni(PrPyrr)	IB-IIIA cleft	-0.144	-0.377	-0.665	-2.588	-27.428	1.782	-25.646	0	-28.352	0	-2.660	0.134
Pt(PrPyrr)	IB-IIIA cleft	-0.132	-0.345	-0.610	-2.372	-26.079	1.734	-24.345	0	-26.776	0	-2.601	0.130
1HA2 - Warfarin bound in subdomain IIA of protein (Sudlow's Site I)													
Ibuprofen	IIIA	-0.590	-1.455	-2.387	-8.850	-26.042	-10.132	-36.174	8.038	-47.749	-0.667	-4.515	-0.760
Warfarin	IIIA	-0.365	-1.039	-2.032	-8.404	-35.237	-1.045	-36.282	5.918	-51.380	-0.541	-5.201	-0.078
$[H_4PrPyrr]^{2+}$	IA-IIA	-0.380	-0.976	-1.683	-6.453	-21.484	-19.469	-40.953	2.178	-56.175	-0.525	-1.519	-1.460
$[H_3PrPyrr]^{+}$	IIA-warfarin	-0.376	-0.966	-1.665	-6.384	-26.394	-13.367	-39.761	1.092	-59.130	-1.630	-2.176	-1.002

Ligand or drug	Binding site location[a]	ligand effic.	ligand effic. sa	glide ligand effic. ln	XP GScore	glide E_{vdw}	glide E_{Coul}	glide energy	glide $E_{internal}$	glide E_{model}	XP H Bond	XP Lipo. E_{vdW}	XP $E_{Electro}$
Ni(PrPyrr)	IIA-warfarin	-0.333	-0.874	-1.542	-6.001	-21.214	-4.031	-25.244	0	-29.44	-0.739	-2.460	-0.302
Diazepam	IIIA	-0.295	-0.800	-1.476	-5.896	-32.921	0.055	-32.866	0.050	-43.701	-0.175	-4.435	0.004
H_2PrPyrr	IIA-IIB	-0.345	-0.886	-1.529	-5.861	-41.518	-1.976	-43.494	2.868	-59.352	0	-5.033	-0.148
Pt(PrPyrr)	IIA-warfarin	-0.316	-0.829	-1.464	-5.695	-22.338	-3.867	-26.205	0	-27.071	-0.769	-2.540	-0.290
$[Pd(OH_2)(HPrPyrr)]^+$	IIA surface	-0.284	-0.758	-1.368	-5.397	-23.815	-6.617	-30.432	0.062	-34.440	-0.737	-2.463	-0.496
Pd(PrPyrr)	IB-IIA-warfarin	-0.223	-0.584	-1.031	-4.010	-20.641	-5.636	-26.277	0	-33.096	-0.326	-0.965	-0.423
2BXG - 2x ibuprofen bound, one in subdomain IIIA (Sudlow's Site II) and the second between subdomains IIA and IIB													
$[H_4PrPyrr]^{2+}$	IB-IIIA cleft	-0.475	-1.221	-2.106	-8.074	-22.872	-24.86	-47.732	6.574	-59.917	-1.250	-2.011	-1.865
Ibuprofen	IIA-Trp214	-0.529	-1.304	-2.139	-7.932	-19.805	-3.976	-23.781	0	-27.136	0	-3.243	-0.298
$[H_3PrPyrr]^+$	IB-IIIA cleft	-0.324	-0.833	-1.436	-5.506	-26.39	-14.687	-41.077	5.893	-55.776	-1.590	-1.559	-1.102
Warfarin	IB-IIIA cleft	-0.197	-0.560	-1.094	-4.525	-31.451	-8.021	-39.472	4.671	-53.459	-1.341	-2.360	-0.602
$[Pd(OH_2)(HPrPyrr)]^+$	IB-IIIA cleft	-0.234	-0.625	-1.128	-4.448	-26.136	-6.036	-32.173	0.828	-39.517	-0.480	-1.688	-0.453
H_2PrPyrr	IIA	-0.256	-0.657	-1.133	-4.344	-36.901	-2.717	-39.618	3.064	-55.115	-0.116	-3.083	-0.204
Ni(PrPyrr)	IIA-IIB	-0.226	-0.593	-1.048	-4.076	-22.966	-4.375	-27.341	0	-33.466	-0.829	-2.181	-0.328
Pt(PrPyrr)	IIA-IIB	-0.202	-0.530	-0.935	-3.639	-21.424	-4.979	-26.404	0	-32.970	-0.900	-2.085	-0.373
Diazepam	IB-IIIA cleft	-0.180	-0.490	-0.903	-3.610	-28.813	-0.407	-29.220	0.369	-40.636	0	-3.212	-0.031
Pd(PrPyrr)	IB-IIIA cleft	-0.182	-0.477	-0.842	-3.277	-26.268	-2.133	-28.400	0	-34.539	0	-2.480	-0.160
2BXF - Diazepam bound in subdomain IIIA (Sudlow's Site II)													
Ibuprofen	IIA	-0.528	-1.302	-2.136	-7.922	-23.084	-5.223	-28.307	4.642	-39.436	-0.695	-2.911	-0.392
$[H_4PrPyrr]^{2+}$	IB-IIIA cleft	-0.453	-1.164	-2.007	-7.694	-23.582	-22.821	-46.403	4.971	-60.306	-1.655	-1.379	-1.712
$[Pd(OH_2)(HPrPyrr)]^+$	IB-IIIA cleft	-0.305	-0.813	-1.468	-5.790	-25.840	-9.425	-35.266	0.435	-47.873	-1.330	-1.905	-0.707
$[H_3PrPyrr]^+$	IB-IIIA cleft	-0.333	-0.856	-1.476	-5.659	-22.183	-21.892	-44.074	1.772	-53.721	-1.919	-1.276	-1.642
Ni(PrPyrr)	IIA-IIB	-0.280	-0.735	-1.298	-5.048	-26.382	-1.171	-27.553	0	-36.157	0	-2.136	-0.088
Pd(PrPyrr)	IIA-IIB	-0.278	-0.728	-1.285	-4.999	-26.235	-1.351	-27.586	0	-35.945	-0.018	-2.154	-0.101
Pt(PrPyrr)	IIA-IIB	-0.261	-0.684	-1.208	-4.698	-25.831	-1.110	-26.940	0	-35.832	-0.007	-2.162	-0.083
H_2PrPyrr	IIA surface	-0.265	-0.682	-1.176	-4.508	-28.634	-5.370	-34.004	2.587	-45.367	-1.250	-2.925	-0.403
Warfarin	IB-IIIA cleft	-0.185	-0.526	-1.029	-4.257	-34.837	-2.655	-37.492	4.110	-49.074	-0.819	-3.158	-0.199
Diazepam	IIA-IIB	-0.190	-0.515	-0.949	-3.793	-34.404	-1.145	-35.549	0.175	-43.894	-0.123	-3.024	-0.086

[a]**IIA**: Binding occurs in subdomain IIA (i.e., within the same pocket as favoured by warfarin, Sudlow's site I). **IIIA**: The binding site occurs within the pocket of subdomain IIIA (i.e., within the same pocket as favoured by diazepam and ibuprofen, Sudlow's site II). Other regions are defined according to Figure 7 in the paper by Ghuman *et al*.[43] This figure is reproduced below to aid the reader in interpreting the binding site

locations for the present compounds within HSA. [b]Docking scores are very approximate estimates of the binding affinity of the ligand for the protein. It has been shown that they do *not* correlate at all well with experimentally measured binding constants. Part of the reason for this is that protein conformational flexibility, dynamic motion, solvation/desolvation, and the contribution from metal ions to name a few factors, are not considered in the docking algorithm's scoring function. Ligand flexibility is accounted for by Glide, but this is good for predicting chemically meaningful ligand conformations (poses) only, and not for accurately calculating the free energy of binding which requires precisely determining many contributions to the binding free energy. Docking therefore is suitable for suggesting: [1] possible ligand binding sites, [2] conformations likely to be adopted by a ligand within a binding site, and [3] for very similar ligands, providing an idea of their possible affinity order for a given binding site. Because the protein itself is kept static during a docking simulation, docking is much poorer at predicting the relative binding affinity of a given ligand for multiple binding sites within the protein.



Footnote Figure: Modified from Figure 7 of Reference 16; "Summary of the ligand binding capacity of HSA as defined by crystallographic studies to date. Ligands are depicted in space-filling representation; oxygen atoms are coloured red; all other atoms in fatty acids (myristic acid), other endogenous ligands (hemin, thyroxin) and drugs are coloured dark-grey, light grey and orange, respectively." The dashed ellipse indicates where ligands bind adjacent to and in contact with warfarin in the present docking studies.

Table S10. Summary of Glide XP docking scores (as in Table S9) and selected interaction distances for HSA targets prepared from ligand-free grids based on geometry-optimized (prepared) structures derived from PDB codes 1HA2 (HSA···warfarin complex) and 2BXF (HSA···diazepam complex). The docking runs were truncated to report only the top-scoring ligand pose for each ligand. All energies are in units of kcal mol^{-1}.

Ligand or drug	Binding site location[a]	XP GScore	Distance to Trp-214 (Å)[b]	Closest tyrosine residues (Å)[b]	Closest phenylalanine residues (Å)[b]
1HA2 - No warfarin bound in subdomain IIA of protein docking grid (Sudlow's Site I)					
Ibuprofen	IA	-8.001	30.4	Tyr-30 (10.8), Tyr-150 (13.6), Tyr-148 (18.0)	Phe-19 (5.6), Phe-27 (7.5), Phe-49 (9.1)
Warfarin	IIA	-7.513	5.3	Tyr-150 (9.5), Tyr-263 (11.3), Tyr-452 (17.0)	Phe-211 (5.9), Phe-223 (8.3)
$[H_4PrPyrr]^{2+}$	IA-IIA	-6.466	17.2	Tyr-148 (3.8), Tyr-30 (12.5), Tyr-150 (13.0)	Phe-149 (11.8), Phe-102 (12.7)
$H_2PrPyrr$	IA	-6.373	26.7	Tyr-30 (5.7), Tyr-50 (11.1), Tyr-148 (12.4)	Phe-70 (3.8), Phe-19(6.1), Phe-49(7.4), Phe-27 (7.9)
$[H_3PrPyrr]^{+}$	IIA-IIB	-6.142	9.6	Tyr-332 (10.4), Tyr-353 (12.0), Tyr-319 (12.9)	Phe-228 (5.8), Phe-206 (9.9), Phe-330 (10.8)
Pd(PrPyrr)	IIA	-5.563	10.4	Tyr-150 (7.0), Tyr-148 (13.1), Tyr-30 (18.1)	Phe-149 (8.6), Phe-211 (10.1), Phe-157 (11.3)
$[Pd(OH_2)(HPrPyrr)]^{+}$	IA-IIA	-5.329	19.6	Tyr-148 (7.0), Tyr-30 (12.7), Tyr-150 (15.5)	Phe-211 (14.2), Phe-102 (15.4), Phe-206 (16.3)
Ni(PrPyrr)	IIA	-5.173	10.5	Tyr-150 (7.0), Tyr-148 (13.1), Tyr-452 (15.5)	Phe-149 (8.5), Phe-211 (10.2), Phe-157 (11.2)
Pt(PrPyrr)	IIA	-5.078	10.4	Tyr-148 (7.0), Tyr-150 (13.1)	Phe-149 (8.6), Phe-157 (11.3), Phe-156 (11.9)
Diazepam	IIA-IIB	-5.019	11.3	Tyr-353 (11.9), Tyr-319 (12.2), Tyr334 (13.9)	Phe-206 (5.2), Phe-211 (11.3), Phe-330 (11.1)
2BXF - No diazepam bound in subdomain IIIA of protein docking grid (Sudlow's Site II)					
Diazepam	IIIA	-9.032	17.0	Tyr-411 (9.5), Tyr-452 (9.6), Tyr-341 (13.4)	Phe-403 (6.0), Phe-395 (9.0), Phe-488 (12.5)
Warfarin	IIIA	-7.320	17.0	Tyr-452 (9.5), Tyr-411 (10.4), Tyr-341 (13.3)	Phe-403 (5.3), Phe-395 (7.8), Phe-488 (12.2)
$H_2PrPyrr$	IIIA	-4.747	17.0	Tyr-411 (6.0), Tyr-452 (11.6), Tyr-341 (13.0)	Phe-403 (10.0), Phe-488 (12.8), Phe-395 (15.2)
$[Pd(OH_2)(HPrPyrr)]^{+}$	IB-IIIA cleft	-4.336	19.2	Tyr-148 (10.0), Tyr-452 (13.5), Tyr-150 (16.4)	Phe-149 (10.3), Phe-157 (14.2), Phe-488 (17.5)
Ibuprofen	IIIA	-4.298	20.9	Tyr-411 (6.0), Tyr-452 (12.1), Tyr-341(19.3)	Phe-403 (7.6), Phe-488 (10.2), Phe-395 (12.3)
$[H_4PrPyrr]^{2+}$	IB-IIIA cleft	-4.233	16.2	Tyr-148 (6.2), Tyr-150 (12.8), Tyr-452 (13.9)	Phe-149 (8.3), Phe-211 (16.3, Phe-206 (16.7)
$[H_3PrPyrr]^{+}$	IB-IIIA cleft	-3.888	17.3	Tyr-148 (7.0), Tyr-452 (14.0), Tyr-140 (14.4)	Phe-149 (8.9), Phe-206 (17.3), Phe-211 (17.5)
Pd(PrPyrr)	IIA-IIIA cleft	-2.794	9.1	Tyr-452 (6.3), Tyr-150 (14.4), Tyr-148 (18.5)	Phe-157 (14.3), Phe-149 (15.0), Phe-223 (16.0)
Ni(PrPyrr)	IB-IIIA cleft	-2.588	19.1	Tyr-148 (10.1), Tyr-452 (13.3), Tyr-138 (15.0)	Phe-148 (9.8), Phe-157 (13.6), Phe-488 (17.9)
Pt(PrPyrr)	IB-IIIA cleft	-2.372	19.1	Tyr-148 (10.0), Tyr-452 (13.3), Tyr-138 (15.3)	Phe-148 (10.0), Phe-157 (13.8), Phe-488 (17.6)

[a] Binding site regions are defined according to Figure 7 in the paper by Ghuman *et al*.[43] [b] Distance measured between the closest ring centroid pair of the ligand and residue. For metal chelates, the distance to the metal ion from the closest ring centroid is given.[a] Binding site regions are defined according to Figure 7 in the paper by Ghuman *et al*.[43] [b] Distance measured between the closest ring centroid pair of the ligand and residue. For metal chelates, the distance to the metal ion from the closest ring centroid is given.

Table S11. Summary of Glide XP docking scores and selected interaction energy parameters for HSA targets prepared from ligand-free grids based on geometry-optimized (prepared) structures derived from PDB codes 1HA2 (HSA···warfarin complex) and 2BXF (HSA···diazepam complex). A van der Waals radius scale factor of 0.70 was used for the nonpolar atoms within both the grid *and* the incoming ligand to *soften the interaction potential*. The docking runs were truncated to report only the top-scoring ligand pose for each ligand. All energies are in units of kcal mol^{-1}. Note that this "softened potential approach" allows one to sample alternative binding sites in the protein; the XP docking scores and energy components will, however, not be directly comparable to those listed in Tables S9 and S10 because the grid is not the same.

Ligand or drug	Binding site location[a]	glide ligand efficiency	glide ligand effic. sa	glide ligand effic. ln	XP GScore	glide E_{vdw}	glide E_{Coul}	glide energy	glide $E_{internal}$	glide E_{model}	XP H Bond	XP Lipophilic E_{vdW}	XP $E_{Electro}$
1HA2 - No warfarin bound in subdomain IIA of protein docking grid (Sudlow's Site I)													
Ibuprofen	IIIA	-0.749	-1.847	-3.029	-11.232	-10.321	-8.964	-19.285	2.490	-25.011	-2.345	-2.749	-3.922
Warfarin	IA	-0.387	-1.101	-2.153	-8.904	-17.828	0.890	-16.938	3.591	-25.143	-0.983	-5.166	0.067
Diazepam	IA	-0.427	-1.159	-2.137	-8.539	-16.343	-0.526	-16.869	1.428	-24.746	-1.189	-4.011	-0.039
$[Pd(OH_2)(HPrPyrr)]^+$	IA-IIA	-0.381	-1.016	-1.834	-7.233	-15.033	-8.405	-23.439	0.117	-24.939	-1.024	-1.942	-0.630
$H_2PrPyrr$	IB-IIA	-0.322	-0.829	-1.429	-5.479	-15.245	-7.064	-22.309	3.914	-28.655	-1.325	-3.038	-0.530
$[H_3PrPyrr]^+$	IB-IIA	-0.294	-0.755	-1.302	-4.992	-15.651	-7.284	-22.935	1.724	-34.670	-1.060	-3.003	-0.546
$[H_4PrPyrr]^{2+}$	IA-IIA	-0.273	-0.703	-1.213	-4.648	-16.953	-19.081	-36.034	3.430	-51.203	-1.327	-2.942	-1.431
Ni(PrPyrr)	IA-IIA	-0.256	-0.671	-1.184	-4.608	-17.060	2.489	-14.571	0	-14.202	0	-2.702	0.187
Pd(PrPyrr)	IA-IIA	-0.245	-0.641	-1.132	-4.405	-17.629	2.456	-15.173	0	-15.277	0	-2.642	0.184
Pt(PrPyrr)	IA-IIA	-0.226	-0.591	-1.044	-4.060	-15.639	2.259	-13.380	0	-15.413	0	-2.553	0.169
2BXF - No diazepam bound in subdomain IIIA of protein docking grid (Sudlow's Site II)													
Warfarin	IIIA	-0.285	-0.811	-1.585	-6.557	-20.466	0.856	-19.610	5.154	-26.327	-0.354	-5.273	0.064
Diazepam	IIIA	-0.327	-0.888	-1.637	-6.542	-17.140	-3.262	-20.402	0.029	-28.339	-1.034	-4.460	-0.245
$H_2PrPyrr$	IIA-IIIA cleft	-0.348	-0.894	-1.541	-5.908	-14.671	-4.025	-18.696	3.648	-23.386	-1.018	-2.625	-0.302
Ibuprofen	IIA	-0.390	-0.962	-1.577	-5.848	-11.021	-4.913	-15.934	4.681	-16.154	-0.793	-2.122	-0.368
$[H_3PrPyrr]^+$	IIA-IIB	-0.316	-0.813	-1.403	-5.377	-9.458	-12.223	-21.681	2.330	-27.805	-1.775	-1.170	-0.917
$[Pd(OH_2)(HPrPyrr)]^+$	IB-IIIA cleft	-0.260	-0.695	-1.255	-4.949	-11.087	-7.246	-18.333	2.709	-19.720	-1.187	-1.587	-0.543
Ni(PrPyrr)	IIIA	-0.234	-0.613	-1.083	-4.212	-15.366	-1.526	-16.892	0	-21.832	-0.247	-2.944	-0.114
$[H_4PrPyrr]^{2+}$	IIA-IIB	-0.239	-0.613	-1.058	-4.055	-8.463	-15.028	-23.492	2.706	-29.887	-2.312	-0.668	-1.127
Pd(PrPyrr)	IIIA	-0.224	-0.587	-1.036	-4.029	-15.116	-1.680	-16.796	0	-21.331	-0.115	-2.972	-0.126
Pt(PrPyrr)	IIIA	-0.203	-0.532	-0.939	-3.653	-14.841	-1.902	-16.743	0	-21.188	0	-2.954	-0.143

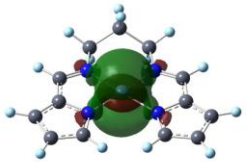
[a]**IIA**: Binding occurs in subdomain IIA (i.e., within the same pocket as favoured by warfarin, Sudlow's site I). **IIIA**: The binding site occurs within the pocket of subdomain IIIA (i.e., within the same pocket as favoured by diazepam and ibuprofen, Sudlow's site II). Other regions are defined according to Figure 7 in the paper by Ghuman *et al*.[43]

Table S12. Electronic excited states for Cs symmetry Ni(PrPyrr) calculated by TD-DFT at the CAM-B3LYP/def2qzvp/GD3BJ level of theory in an acetonitrile solvent continuum. A maximum of four contributing transitions are given (H = HOMO, L = LUMO). Selected MOs are shown at the end of the table.

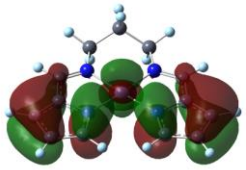
State	Energy/ cm-1	λ/nm	Oscillator strength	Symmetry	Transition 1	Contrib. (%)	Transition 2	Contrib. (%)	Transition 3	Contrib. (%)	Transition 4	Contrib. (%)
1	16944.9	590.1	0.0001	Singlet-A"	H-4→L+2	95	H-4→L+1	3				
2	17299.8	578.0	0	Singlet-A"	H-5→L+2	46	H-3→L+2	23	H-1→L+2	23	H-10→L+2	3
3	18480.6	541.1	0	Singlet-A'	H-6→L+2	49	H-2→L+2	35	H-11→L+2	3	HOMO→L+2	8
4	22722.3	440.1	0	Singlet-A"	H-7→L+2	87	H-9→L+2	3	H-7→L+1	3		
5	29840.1	335.1	0.2365	Singlet-A'	H-1→LUMO	78	H-5→LUMO	2	H-3→LUMO	5	H-2→L+1	2
6	30419.2	328.7	0.0695	Singlet-A"	H-1→L+1	21	HOMO→LUMO	74				
7	34362.4	291.0	0.0001	Singlet-A'	HOMO→L+2	84	H-2→L+2	8	HOMO→L+1	3		
8	34476.2	290.1	0.1538	Singlet-A"	H-2→LUMO	71	H-6→LUMO	3	H-3→L+1	7	H-1→L+1	9
9	35967.5	278.0	0.0002	Singlet-A"	H-3→L+2	15	H-1→L+2	70	H-5→L+2	8	H-1→L+1	3
10	36239.3	275.9	0.0075	Singlet-A'	H-4→LUMO	97						
11	37971.0	263.4	0.3795	Singlet-A'	H-3→LUMO	48	H-2→L+1	14	HOMO→L+1	30	H-5→LUMO	2
12	39582.5	252.6	0.0472	Singlet-A"	H-2→LUMO	17	H-1→L+1	55	HOMO→LUMO	14	H-5→L+1	6
13	40768.9	245.3	0.0133	Singlet-A'	H-3→LUMO	19	H-1→LUMO	16	HOMO→L+1	52	H-2→L+1	6
14	41246.4	242.4	0	Singlet-A"	H-4→L+1	93	H-4→L+2	3				
15	42238.4	236.8	0.0458	Singlet-A'	H-5→LUMO	25	H-3→LUMO	11	H-2→L+1	52	H-6→L+1	4
16	43804.0	228.3	0.0044	Singlet-A"	H-6→LUMO	38	H-3→L+1	49	H-1→L+1	5		
17	43872.5	227.9	0.001	Singlet-A'	H-6→L+2	41	H-2→L+2	51	HOMO→L+2	2		
18	45309.8	220.7	0	Singlet-A"	H-5→L+2	31	H-3→L+2	58	H-10→L+2	2		
19	45571.1	219.4	0.0032	Singlet-A'	H-1→L+3	68	HOMO→L+6	19	H-1→L+4	4	H-1→L+5	3
20	45626.8	219.2	0	Singlet-A"	H-1→L+6	20	HOMO→L+3	66	HOMO→L+4	5	HOMO→L+5	4
21	47014.1	212.7	0.0052	Singlet-A'	H-6→L+1	18	H-5→LUMO	55	H-3→LUMO	7	H-2→L+1	9
22	47283.4	211.5	0.001	Singlet-A"	H-6→LUMO	42	H-5→L+1	25	H-3→L+1	19	H-2→LUMO	3
23	48775.6	205.0	0.0238	Singlet-A'	H-1→L+4	85	H-1→L+3	6				
24	49011.9	204.0	0.0002	Singlet-A'	H-7→LUMO	96						
25	49088.5	203.7	0.0148	Singlet-A"	HOMO→L+4	84	HOMO→L+3	7				
26	50694.4	197.3	0	Singlet-A"	H-2→L+3	59	H-1→L+6	12	H-3→L+6	6	H-2→L+4	4
27	51123.5	195.6	0.0006	Singlet-A"	H-8→LUMO	74	H-14→L+1	3	H-13→LUMO	4	H-9→L+1	8

State	Energy/ cm-1	λ/nm	Oscillator strength	Symmetry	Transition 1	Contrib. (%)	Transition 2	Contrib. (%)	Transition 3	Contrib. (%)	Transition 4	Contrib. (%)
28	51397.7	194.6	0.0446	Singlet-A'	H-3→L+3	21	H-1→L+5	20	HOMO→L+6	33	H-2→L+6	8
29	51706.6	193.4	0.0037	Singlet-A"	HOMO→L+5	69	H-1→L+6	9	H-1→L+9	7	HOMO→L+7	5
30	51873.5	192.8	0.0151	Singlet-A'	H-9→LUMO	40	H-8→L+1	11	H-1→L+5	18	H-13→L+1	4
31	51988.9	192.3	0.007	Singlet-A'	H-9→LUMO	20	H-1→L+5	36	H-8→L+1	5	H-3→L+3	6
32	53172.9	188.1	0.0039	Singlet-A"	H-6→LUMO	10	H-5→L+1	38	H-3→L+1	10	H-2→L+4	14
33	53281.8	187.7	0.0144	Singlet-A'	H-6→L+1	50	H-4→L+3	12	H-8→L+2	5	H-5→LUMO	7
34	53789.9	185.9	0.0161	Singlet-A"	H-1→L+6	33	HOMO→L+3	12	HOMO→L+8	14	H-5→L+1	2
35	54023.0	185.1	0.0004	Singlet-A"	H-2→L+4	57	H-6→L+4	3	H-5→L+1	8	H-3→L+1	2
36	54269.8	184.3	0.0033	Singlet-A'	H-3→L+3	20	H-2→L+6	16	H-1→L+8	13	HOMO→L+6	17
37	54517.4	183.4	0.0002	Singlet-A"	H-7→L+1	73	H-13→LUMO	4	H-12→LUMO	8	H-9→L+1	5
38	54626.3	183.1	0.0429	Singlet-A'	H-4→L+3	47	H-4→L+4	18	H-12→L+2	4	H-9→LUMO	3
39	55033.6	181.7	0.4755	Singlet-A"	H-5→L+1	12	H-1→L+16	14	HOMO→L+10	46	H-3→L+1	2
40	55057.8	181.6	0.5581	Singlet-A'	H-8→L+2	65	H-11→L+1	3	H-8→L+1	6	H-6→L+1	3
41	55312.7	180.8	0.0106	Singlet-A'	H-4→L+4	19	H-1→L+10	33	H-8→L+2	4	H-6→L+1	5
42	55524.8	180.1	0.0333	Singlet-A'	H-4→L+3	16	H-4→L+4	26	H-1→L+10	18	H-12→L+2	2
43	55899.1	178.9	0.0122	Singlet-A"	H-12→LUMO	25	H-9→L+1	32	H-7→L+1	18	H-13→LUMO	3
44	56335.4	177.5	0.1947	Singlet-A"	H-9→L+2	17	HOMO→L+7	28	H-2→L+5	6	H-2→L+7	2
45	56391.9	177.3	0.0057	Singlet-A'	H-3→L+4	54	H-8→L+1	7	H-5→L+3	3	H-5→L+4	3
46	56478.2	177.1	0.012	Singlet-A'	H-8→L+1	35	H-4→L+4	22	H-14→LUMO	8	H-12→L+1	3
47	56609.6	176.6	0.0046	Singlet-A'	H-1→L+7	48	H-3→L+3	2	H-1→L+3	6	H-1→L+5	7
48	56670.1	176.5	0.4485	Singlet-A"	H-9→L+2	43	HOMO→L+7	13	H-10→L+2	2	H-2→L+10	4
49	57168.6	174.9	0.0528	Singlet-A"	H-3→L+6	11	H-2→L+5	11	H-2→L+7	10	HOMO→L+8	11
50	57615.4	173.6	0.0239	Singlet-A'	H-5→L+3	13	H-3→L+3	12	H-2→L+6	35	H-3→L+4	9
51	57826.7	172.9	0	Singlet-A"	H-2→L+5	10	H-1→L+9	21	HOMO→L+7	12	HOMO→L+8	20
52	58123.5	172.0	0.0037	Singlet-A'	H-1→L+8	37	HOMO→L+6	11	HOMO→L+11	22	H-3→L+3	3
53	58293.7	171.5	0.0003	Singlet-A"	H-2→L+10	21	H-1→L+17	12	HOMO→L+19	10	H-11→LUMO	8
54	58386.5	171.3	0.0274	Singlet-A'	H-1→L+12	20	HOMO→L+9	38	H-10→LUMO	2	H-3→L+5	3
55	58791.4	170.1	0.1859	Singlet-A'	H-10→LUMO	14	H-3→L+10	10	H-11→L+1	2	H-8→L+2	3
56	59136.6	169.1	0.0004	Singlet-A"	H-2→L+5	20	H-1→L+9	20	HOMO→L+12	20	H-6→L+3	4

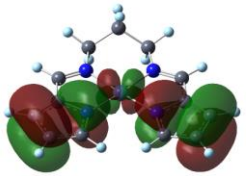
State	Energy/ cm-1	λ/nm	Oscillator strength	Symmetry	Transition 1	Contrib. (%)	Transition 2	Contrib. (%)	Transition 3	Contrib. (%)	Transition 4	Contrib. (%)
57	59326.9	168.6	0.0005	Singlet-A"	H-3→L+6	29	H-2→L+5	20	H-2→L+8	14	H-1→L+11	13
58	60285.1	165.9	0.0365	Singlet-A'	H-10→LUMO	49	H-11→L+1	6	H-9→LUMO	5	H-3→L+5	5
59	60497.2	165.3	0.0186	Singlet-A'	H-3→L+5	38	H-2→L+9	13	H-10→LUMO	4	H-3→L+7	9
60	60590.8	165.0	0.0926	Singlet-A"	H-11→LUMO	55	H-10→L+1	14	H-2→L+10	4	H-1→L+17	5



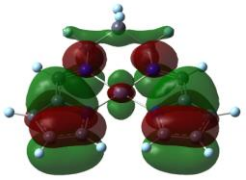
HOMO-4, -0.31100 Har



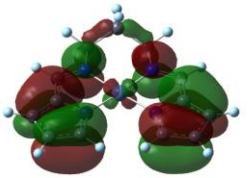
HOMO-3, -0.29943 Har



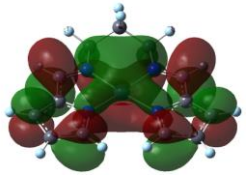
HOMO-2, -0.28655 Har



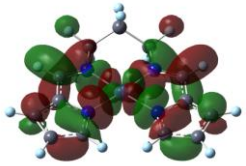
HOMO-1, -0.26103 Har



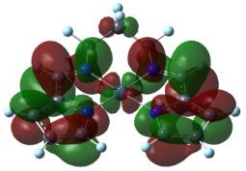
HOMO, -0.26062 Har, MO 74



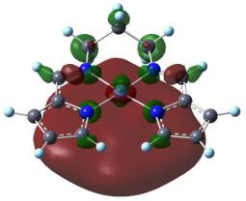
LUMO, -0.02292 Har, MO 75



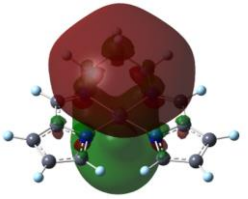
LUMO+1, 0.00163 Har



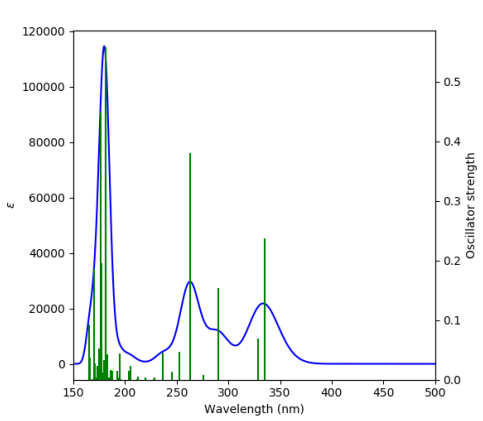
LUMO+2, 0.00620 Har

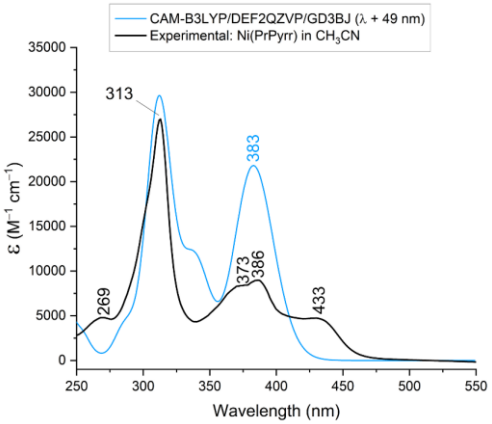


LUMO+3, 0.04130 Har



LUMO+4, 0.04601 Har





4. References

[1] O. V. Dolomanov, L. J. Bourhis, R. J. Gildea, J. A. K. Howard, H. Puschmann, *J. Appl. Crystallogr.* **2009**, *42*, 339–341.
[2] G. M. Sheldrick, *Acta Crystallogr. Sect. A Found. Adv.* **2015**, *71*, 3–8.
[3] G. M. Sheldrick, *Acta Crystallogr. Sect. C Struct. Chem.* **2015**, *71*, 3–8.
[4] O. Q. Munro, G. L. Camp, *Acta Crystallogr. C* **2003**, *59*, o672–o675.
[5] N. Biswas, S. Khanra, A. Sarkar, S. Bhattacharjee, D. P. Mandal, A. Chaudhuri, S. Chakraborty, C. R. Choudhury, *J. Coord. Chem.* **2018**, *71*, 2740–2766.
[6] M. Van de Weert, L. Stella, *J. Mol. Struct.* **2011**, *998*, 144–150.
[7] M. van de Weert, *J. Fluoresc.* **2010**, *20*, 625–629.
[8] M. H. Gehlen, *J. Photochem. Photobiol. C Photochem. Rev.* **2020**, *42*, 100338.
[9] K. Flora, J. D. Brennan, G. A. Baker, M. A. Doody, F. V. Bright, *Biophys. J.* **1998**, *75*, 1084–1096.
[10] M. K. Helms, C. E. Petersen, N. V. Bhagavan, D. M. Jameson, *FEBS Lett.* **1997**, *408*, 67–70.
[11] O. K. Abou-Zied, O. I. K. Al-Shihi, *J. Am. Chem. Soc.* **2008**, *130*, 10793–10801.
[12] S. Soares, N. Mateus, V. de Freitas, *J. Agric. Food Chem.* **2007**, *55*, 6726–6735.
[13] G. G. Ariga, P. N. Naik, S. A. Chimatadar, S. T. Nandibewoor, *J. Mol. Struct.* **2017**, *1137*, 485–494.
[14] C. Liu, Z. Liu, J. Wang, *PLOS ONE* **2017**, *12*, e0176208.
[15] J. R. Lakowicz, *Principles of Fluorescence Spectroscopy*, Springer US, Boston MA, **2006**.
[16] S. A. C. Lima, A. Cordeiro-da-Silva, B. de Castro, P. Gameiro, *Biophys. Chem.* **2007**, *125*, 143–150.
[17] P. D. Ross, S. Subramanian, *Biochemistry* **1981**, *20*, 3096–3102.
[18] L. I. Grossweiner, *J. Photochem. Photobiol. B* **2000**, *58*, 175–177.
[19] K. Zierler, *Trends Biochem. Sci.* **1989**, *14*, 314–317.
[20] C. Wofsy, B. Goldstein, *Math. Biosci.* **1992**, *112*, 115–154.
[21] G. Schwarz, *Biophys. Struct. Mech.* **1976**, *2*, 1–12.
[22] K. Campbell, A. Zappas, U. Bunz, Y. S. Thio, D. G. Bucknall, *J. Photochem. Photobiol. Chem.* **2012**, *249*, 41–46.
[23] E. Ciotta, P. Prosposito, R. Pizzoferrato, *J. Lumin.* **2019**, *206*, 518–522.
[24] P. Geladi, B. R. Kowalski, *Anal. Chim. Acta* **1986**, *185*, 1–17.
[25] J. G. Lees, A. J. Miles, R. W. Janes, B. A. Wallace, *BMC Bioinformatics* **2006**, *7*, 507.
[26] J. T. Yang, C.-S. C. Wu, H. M. Martinez, in *Methods Enzymol.*, Academic Press, **1986**, pp. 208–269.
[27] T. Shiratori, S. Goto, T. Sakaguchi, T. Kasai, Y. Otsuka, K. Higashi, K. Makino, H. Takahashi, K. Komatsu, *Biochem. Biophys. Rep.* **2021**, *28*, 101153.
[28] A. Micsonai, F. Wien, É. Bulyáki, J. Kun, É. Moussong, Y.-H. Lee, Y. Goto, M. Réfrégiers, J. Kardos, *Nucleic Acids Res.* **2018**, *46*, W315–W322.
[29] M. J. Frisch, G. W. Trucks, H. B. Schlegel, G. E. Scuseria, M. A. Robb, J. R. Cheeseman, G. Scalmani, V. Barone, G. A. Petersson, H. Nakatsuji, X. Li, M. Caricato, A. V. Marenich, J. Bloino, B. G. Janesko, R. Gomperts, B. Mennucci, H. P. Hratchian, J. V. Ortiz, A. F. Izmaylov, J. L. Sonnenberg, D. Williams-Young, F. Ding, F. Lipparini, F. Egidi, J. Goings, B. Peng, A. Petrone, T. Henderson, D. Ranasinghe, V. G. Zakrzewski, J. Gao, N. Rega, G. Zheng, W. Liang, M. Hada, M. Ehara, K. Toyota, R. Fukuda, J. Hasegawa, M. Ishida, T. Nakajima, Y. Honda, O. Kitao, H. Nakai, T. Vreven, K. Throssell, J. A. Montgomery Jr., J. E. Peralta, F. Ogliaro, M. J. Bearpark, J. J. Heyd, E. N. Brothers, K. N. Kudin, V. N. Staroverov, T. A. Keith, R. Kobayashi, J. Normand, K. Raghavachari, A. P. Rendell, J. C. Burant, S. S. Iyengar, J. Tomasi, M. Cossi, J. M. Millam, M.

Klene, C. Adamo, R. Cammi, J. W. Ochterski, R. L. Martin, K. Morokuma, O. Farkas, J. B. Foresman, D. J. Fox, *Gaussian 16 Revision C.01*, **2016**.
[30] T. Yanai, D. P. Tew, N. C. Handy, *Chem. Phys. Lett.* **2004**, *393*, 51–57.
[31] F. Weigend, R. Ahlrichs, *Phys. Chem. Chem. Phys.* **2005**, *7*, 3297–3305.
[32] S. Grimme, S. Ehrlich, L. Goerigk, *J. Comput. Chem.* **2011**, *32*, 1456–1465.
[33] P. Fuentealba, H. Preuss, H. Stoll, L. Von Szentpály, *Chem. Phys. Lett.* **1982**, *89*, 418–422.
[34] J. R. Cheeseman, G. W. Trucks, T. A. Keith, M. J. Frisch, *J. Chem. Phys.* **1996**, *104*, 5497–5509.
[35] R. Ditchfield, *Mol. Phys.* **1974**, *27*, 789–807.
[36] F. Lipparini, G. Scalmani, B. Mennucci, E. Cancès, M. Caricato, M. J. Frisch, *J. Chem. Phys.* **2010**, *133*, 014106.
[37] R. Dennington, T. A. Keith, J. M. Millam, *GaussView Version 6*, **2019**.
[38] N. M. O'boyle, A. L. Tenderholt, K. M. Langner, *J. Comput. Chem.* **2008**, *29*, 839–845.
[39] F. R. Clemente, T. Vreven, M. J. Frisch, in *Quantum Biochem.*, John Wiley & Sons, Ltd, **2010**, pp. 61–83.
[40] A. K. Rappe, C. J. Casewit, K. S. Colwell, W. A. Goddard, W. M. Skiff, *J. Am. Chem. Soc.* **1992**, *114*, 10024–10035.
[41] T. A. Halgren, R. B. Murphy, R. A. Friesner, H. S. Beard, L. L. Frye, W. T. Pollard, J. L. Banks, *J. Med. Chem.* **2004**, *47*, 1750–1759.
[42] I. Petitpas, A. A. Bhattacharya, S. Twine, M. East, S. Curry, *J. Biol. Chem.* **2001**, *276*, 22804–22809.
[43] J. Ghuman, P. A. Zunszain, I. Petitpas, A. A. Bhattacharya, M. Otagiri, S. Curry, *J. Mol. Biol.* **2005**, *353*, 38–52.
[44] G. Madhavi Sastry, M. Adzhigirey, T. Day, R. Annabhimoju, W. Sherman, *J. Comput. Aided Mol. Des.* **2013**, *27*, 221–234.
[45] F. Mohamadi, N. G. J. Richards, W. C. Guida, R. Liskamp, M. Lipton, C. Caufield, G. Chang, T. Hendrickson, W. C. Still, *J. Comput. Chem.* **1990**, *11*, 440–467.
[46] W. L. Jorgensen, J. Tirado-Rives, *J. Am. Chem. Soc.* **1988**, *110*, 1657–1666.
[47] G. A. Kaminski, R. A. Friesner, J. Tirado-Rives, W. L. Jorgensen, *J. Phys. Chem. B* **2001**, *105*, 6474–6487.
[48] R. A. Friesner, J. L. Banks, R. B. Murphy, T. A. Halgren, J. J. Klicic, D. T. Mainz, M. P. Repasky, E. H. Knoll, M. Shelley, J. K. Perry, D. E. Shaw, P. Francis, P. S. Shenkin, *J. Med. Chem.* **2004**, *47*, 1739–1749.
[49] J. R. Greenwood, D. Calkins, A. P. Sullivan, J. C. Shelley, *J. Comput. Aided Mol. Des.* **2010**, *24*, 591–604.
[50] Z. Fakhar, B. Faramarzi, S. Pacifico, S. Faramarzi, *J. Biomol. Struct. Dyn.* **2020**, *0*, 1–13.
[51] A. R. Leach, B. K. Shoichet, C. E. Peishoff, *J. Med. Chem.* **2006**, *49*, 5851–5855.
[52] G. L. Warren, C. W. Andrews, A.-M. Capelli, B. Clarke, J. LaLonde, M. H. Lambert, M. Lindvall, N. Nevins, S. F. Semus, S. Senger, G. Tedesco, I. D. Wall, J. M. Woolven, C. E. Peishoff, M. S. Head, *J. Med. Chem.* **2006**, *49*, 5912–5931.
[53] A. Bacchi, M. Carcelli, L. Gabba, S. Ianelli, P. Pelagatti, G. Pelizzi, D. Rogolino, *Inorganica Chim. Acta* **2003**, *342*, 229–235.
[54] M. Strohalm, D. Kavan, P. Novák, M. Volný, V. Havlíček, *Anal. Chem.* **2010**, *82*, 4648–4651.
[55] B. M. Still, P. G. A. Kumar, J. R. Aldrich-Wright, W. S. Price, *Chem. Soc. Rev.* **2007**, *36*, 665–686.
[56] C. R. Groom, I. J. Bruno, M. P. Lightfoot, S. C. Ward, *Acta Crystallogr. Sect. B Struct. Sci. Cryst. Eng. Mater.* **2016**, *72*, 171–179.
[57] T. W. Hambley, *Inorg. Chem.* **1998**, *37*, 3767–3774.
[58] S. S. Batsanov, *Inorg. Mater.* **2001**, *37*, 871–885.

[59] J. E. Bercaw, A. C. Durrell, H. B. Gray, J. C. Green, N. Hazari, J. A. Labinger, J. R. Winkler, *Inorg. Chem.* **2010**, *49*, 1801–1810.
[60] N. Marino, C. H. Fazen, J. D. Blakemore, C. D. Incarvito, N. Hazari, R. P. Doyle, *Inorg. Chem.* **2011**, *50*, 2507–2520.
[61] P. A. Zunszain, J. Ghuman, A. F. McDonagh, S. Curry, *J. Mol. Biol.* **2008**, *381*, 394–406.
[62] P. A. Zunszain, J. Ghuman, T. Komatsu, E. Tsuchida, S. Curry, *BMC Struct. Biol.* **2003**, *3*, 6.

CIF Files

CIF File AuL1

checkCIF/PLATON report

Structure factors have been supplied for datablock(s) 19ov_ss_aupr_0m

THIS REPORT IS FOR GUIDANCE ONLY. IF USED AS PART OF A REVIEW PROCEDURE FOR PUBLICATION, IT SHOULD NOT REPLACE THE EXPERTISE OF AN EXPERIENCED CRYSTALLOGRAPHIC REFEREE.

No syntax errors found. CIF dictionary Interpreting this report

Datablock: 19ov_ss_aupr_0m

Bond precision: C-C = 0.0040 A Wavelength=0.71073

Cell: a=7.5983(4) b=9.4222(5) c=10.5265(6)
alpha=68.634(2) beta=72.750(2) gamma=72.193(2)

Temperature: 153 K

	Calculated	Reported
Volume	653.48(6)	653.48(6)
Space group	P -1	P -1
Hall group	-P 1	-P 1
Moiety formula	C13 H14 Au N4, Cl	C13 H14 Au N4, Cl
Sum formula	C13 H14 Au Cl N4	C13 H14 Au Cl N4
Mr	458.70	458.70
Dx,g cm-3	2.331	2.331
Z	2	2
Mu (mm-1)	11.451	11.451
F000	432.0	432.0
F000'	428.63	
h,k,lmax	10,12,14	10,12,14
Nref	3321	3311
Tmin,Tmax	0.079,0.108	0.401,0.749
Tmin'	0.033	

Correction method= # Reported T Limits: Tmin=0.401 Tmax=0.749
AbsCorr = MULTI-SCAN

Data completeness= 0.997 Theta(max)= 28.495

```
                                                        wR2(reflections)=
R(reflections)= 0.0140( 3305)
                                                        0.0364( 3311)
S = 1.279                       Npar= 172
The following ALERTS were generated. Each ALERT has the
format        test-name_ALERT_alert-type_alert-level.
Click on the hyperlinks for more details of the test.
```

Alert level C

```
PLAT910_ALERT_3_C Missing # of FCF Reflection(s) Below Theta(Min).          5 Note
PLAT911_ALERT_3_C Missing FCF Refl Between Thmin & STh/L=    0.600          6
Report
PLAT934_ALERT_3_C Number of (Iobs-Icalc)/Sigma(W) > 10 Outliers ..          1 Check
PLAT972_ALERT_2_C Check Calcd Resid. Dens.  1.56Ang From C3             -1.63 eA-3
```

Alert level G

```
PLAT154_ALERT_1_G The s.u.'s on the Cell Angles are Equal ..(Note)      0.002
Degree PLAT432_ALERT_2_G Short Inter X...Y Contact  C1       ..C9       .
3.15 Ang.
                                                1-x,1-y,1-z  =      2_666 Check
PLAT794_ALERT_5_G Tentative Bond Valency for Au1       (III)     .       3.28 Info
PLAT913_ALERT_3_G Missing # of Very Strong Reflections in FCF ....          2 Note
PLAT933_ALERT_2_G Number of HKL-OMIT Records in Embedded .res File          4 Note
PLAT961_ALERT_5_G Dataset Contains no Negative Intensities .......     Please Check
PLAT967_ALERT_5_G Note: Two-Theta Cutoff Value in Embedded .res ..       57.0
Degree
PLAT978_ALERT_2_G Number C-C Bonds with Positive Residual Density.          4 Info
```

```
  0 ALERT level A = Most likely a serious problem - resolve or explain
  0 ALERT level B = A potentially serious problem, consider carefully
  4 ALERT level C = Check. Ensure it is not caused by an omission or oversight
  8 ALERT level G = General information/check it is not something unexpected

  1 ALERT type 1 CIF construction/syntax error, inconsistent or missing data
  4 ALERT type 2 Indicator that the structure model may be wrong or deficient
  4 ALERT type 3 Indicator that the structure quality may be low
  0 ALERT type 4 Improvement, methodology, query or suggestion
  3 ALERT type 5 Informative message, check
```

It is advisable to attempt to resolve as many as possible of the alerts in all categories. Often the minor alerts point to easily fixed oversights, errors and omissions in your CIF or refinement strategy, so attention to these fine details can be worthwhile. In order to resolve some of the more serious problems it may be necessary to carry out additional measurements or structure refinements. However, the purpose of your study may justify the reported deviations and the more serious of these should normally be commented upon in the discussion or experimental section of a paper or in the "special_details" fields of the CIF. checkCIF was carefully designed to identify outliers and unusual parameters, but every test has its limitations and alerts that are not important in a particular case may appear. Conversely, the absence of alerts does not guarantee there are no aspects of the results needing attention. It is up to the individual to critically assess their own results and, if necessary, seek expert advice.

Publication of your CIF in IUCr journals

A basic structural check has been run on your CIF. These basic checks will be run on all CIFs submitted for publication in IUCr journals (*Acta Crystallographica*, *Journal of Applied*

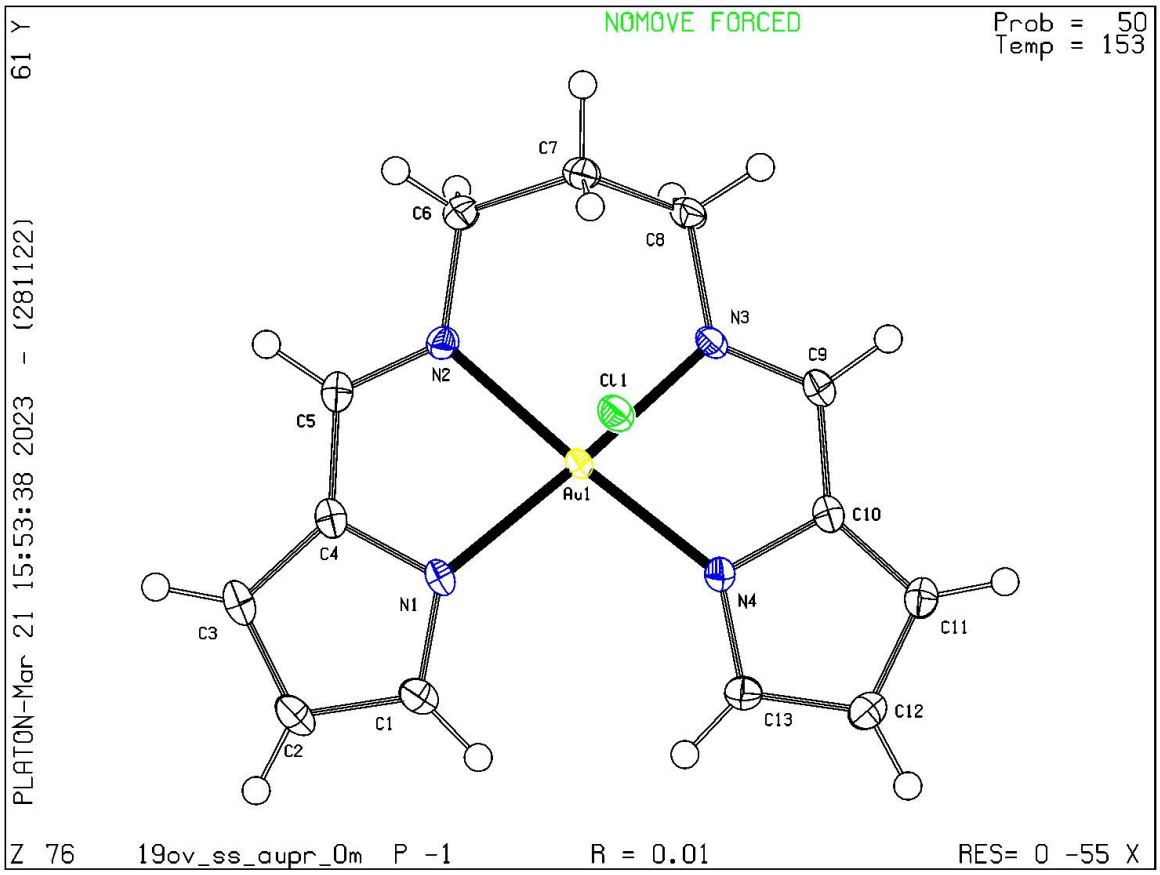
Crystallography, *Journal of Synchrotron Radiation*); however, if you intend to submit to *Acta Crystallographica Section C* or *E* or *IUCrData*, you should make sure that full publication checks are run on the final version of your CIF prior to submission.

Publication of your CIF in other journals

Please refer to the *Notes for Authors* of the relevant journal for any special instructions relating to CIF submission.

PLATON version of 28/11/2022; check.def file version of 28/11/2022

Datablock 19ov_ss_aupr_0m - ellipsoid plot



CIF File AuL2

checkCIF/PLATON report

Structure factors have been supplied for datablock(s) auproh_ms

THIS REPORT IS FOR GUIDANCE ONLY. IF USED AS PART OF A REVIEW PROCEDURE FOR PUBLICATION, IT SHOULD NOT REPLACE THE EXPERTISE OF AN EXPERIENCED CRYSTALLOGRAPHIC REFEREE.

No syntax errors found. CIF dictionary Interpreting this report

Datablock: auproh_ms

```
Bond precision: C-C = 0.0045 A            Wavelength=0.71073
Cell:    a=6.9510(2)    b=18.3730(6)    c=10.9051(4)    alpha=90
                beta=97.724(1) gamma=90
Temperature:     293 K

                Calculated                Reported
Volume          1380.06(8)                1380.06(8)
Space group     P 21/n                    P 1 21/n 1
Hall group      -P 2yn                    -P 2yn
Moiety formula C13 H14 Au N4 O, Cl        C13 H14 Au N4 O, Cl
Sum formula     C13 H14 Au Cl N4 O        C13 H14 Au Cl N4 O
Mr              474.70                    474.70
Dx,g cm-3       2.285                     2.285
Z               4                         4
Mu (mm-1)       10.854                    10.854
F000            896.0                     896.0
F000'           889.28
h,k,lmax        10,28,16                  10,28,16
Nref            5325                      5300
Tmin,Tmax       0.139,0.411               0.474,0.747
Tmin'           0.053
Correction method= # Reported T Limits: Tmin=0.474 Tmax=0.747
AbsCorr = MULTI-SCAN

Data completeness= 0.995          Theta(max)= 33.286

R(reflections)= 0.0245( 4746)     wR2(reflections)= 0.0474( 5300)

S = 1.165                 Npar= 182
```

The following ALERTS were generated. Each ALERT has the format **test-name_ALERT_alert-type_alert-level.**
Click on the hyperlinks for more details of the test.

Alert level C

```
PLAT906_ALERT_3_C Large K Value in the Analysis of Variance ......      3.147 Check
PLAT911_ALERT_3_C Missing FCF Refl Between Thmin & STh/L=    0.600          2
Report
PLAT934_ALERT_3_C Number of (Iobs-Icalc)/Sigma(W) > 10 Outliers ..          1 Check
PLAT972_ALERT_2_C Check Calcd Resid. Dens.  0.72A   From Au01          -1.66 eA-3
PLAT972_ALERT_2_C Check Calcd Resid. Dens.  0.70A   From Au01          -1.52 eA-3
PLAT977_ALERT_2_C Check Negative Difference Density on H00A            -0.48 eA-3
```

Alert level G

```
PLAT007_ALERT_5_G Number of Unrefined Donor-H Atoms ..............          1
Report
PLAT199_ALERT_1_G Reported _cell_measurement_temperature ..... (K)        293 Check
PLAT200_ALERT_1_G Reported   _diffrn_ambient_temperature ..... (K)        293 Check
PLAT720_ALERT_4_G Number of Unusual/Non-Standard Labels ..........         34 Note
PLAT793_ALERT_4_G Model has Chirality at C00G        (Centro SPGR)         S
Verify
PLAT794_ALERT_5_G Tentative Bond Valency for Au01      (III)     .       3.33 Info
PLAT910_ALERT_3_G Missing # of FCF Reflection(s) Below Theta(Min).          3 Note
PLAT912_ALERT_4_G Missing # of FCF Reflections Above STh/L=  0.600         20 Note
PLAT913_ALERT_3_G Missing # of Very Strong Reflections in FCF ....          1 Note
PLAT978_ALERT_2_G Number C-C Bonds with Positive Residual Density.          3 Info
```

```
    0 ALERT level A = Most likely a serious problem - resolve or explain
    0 ALERT level B = A potentially serious problem, consider carefully
    6 ALERT level C = Check. Ensure it is not caused by an omission or oversight
   10 ALERT level G = General information/check it is not something unexpected

    2 ALERT type 1 CIF construction/syntax error, inconsistent or missing data
4   ALERT type 2 Indicator that the structure model may be wrong or deficient
5   ALERT type 3 Indicator that the structure quality may be low
    3 ALERT type 4 Improvement, methodology, query or suggestion
    2 ALERT type 5 Informative message, check
```

It is advisable to attempt to resolve as many as possible of the alerts in all categories. Often the minor alerts point to easily fixed oversights, errors and omissions in your CIF or refinement strategy, so attention to these fine details can be worthwhile. In order to resolve some of the more serious problems it may be necessary to carry out additional measurements or structure refinements. However, the purpose of your study may justify the reported deviations and the more serious of these should normally be commented upon in the discussion or experimental section of a paper or in the "special_details" fields of the CIF. checkCIF was carefully designed to identify outliers and unusual parameters, but every test has its limitations and alerts that are not important in a particular case may appear. Conversely, the absence of alerts does not guarantee there are no aspects of the results needing attention. It is up to the individual to critically assess their own results and, if necessary, seek expert advice.

Publication of your CIF in IUCr journals

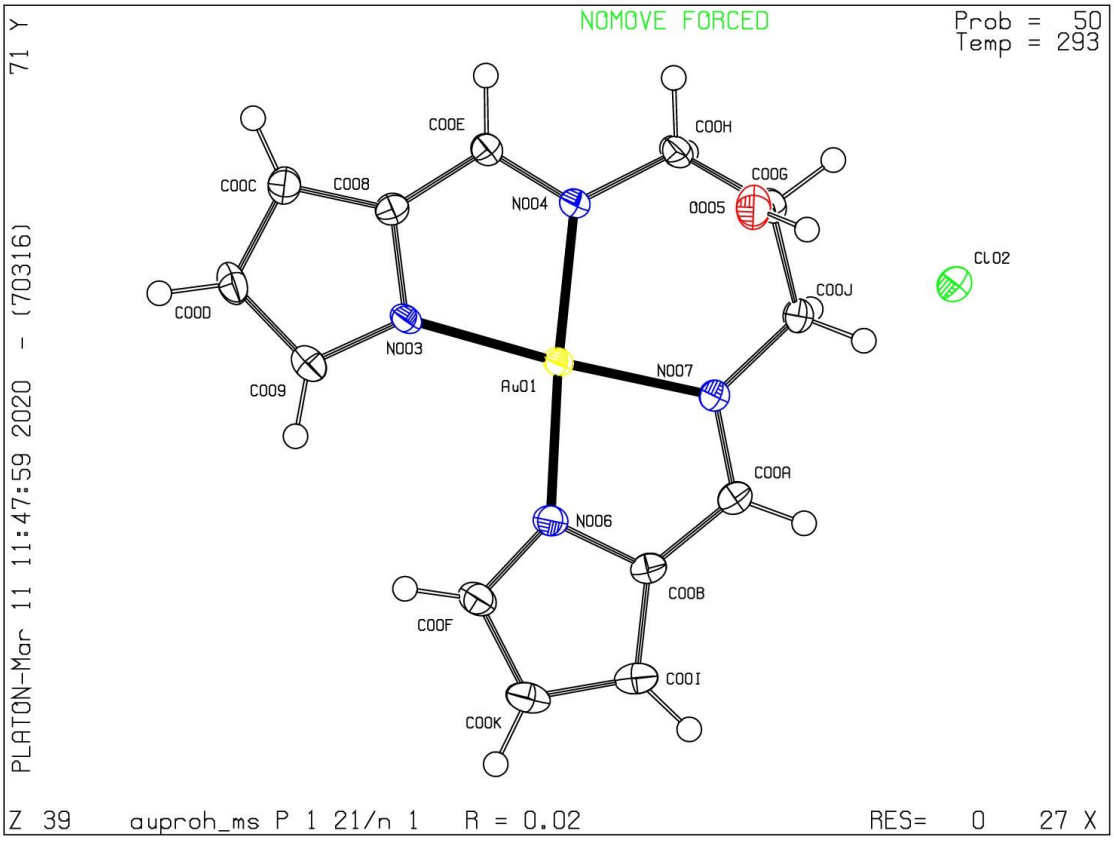
A basic structural check has been run on your CIF. These basic checks will be run on all CIFs submitted for publication in IUCr journals (*Acta Crystallographica*, *Journal of Applied Crystallography*, *Journal of Synchrotron Radiation*); however, if you intend to submit to *Acta Crystallographica Section C* or *E* or *IUCrData*, you should make sure that full publication checks are run on the final version of your CIF prior to submission.

Publication of your CIF in other journals

Please refer to the *Notes for Authors* of the relevant journal for any special instructions relating to CIF submission.

PLATON version of 22/12/2019; check.def file version of 13/12/2019

Datablock auproh_ms - ellipsoid plot



CIF File AuL3

checkCIF/PLATON report

Structure factors have been supplied for datablock(s) aume2pr_ms_sx

THIS REPORT IS FOR GUIDANCE ONLY. IF USED AS PART OF A REVIEW PROCEDURE FOR PUBLICATION, IT SHOULD NOT REPLACE THE EXPERTISE OF AN EXPERIENCED CRYSTALLOGRAPHIC REFEREE.

No syntax errors found. CIF dictionary Interpreting this report

Datablock: aume2pr_ms_sx

```
Bond precision:  C-C = 0.0030 A            Wavelength=0.71073

Cell:
                  a=13.6006(6)    b=11.9212(5)    c=19.7141(8)    alpha=90
                  beta=97.219(2) gamma=90
Temperature:      293 K

                  Calculated                  Reported
Volume            3171.0(2)                   3171.0(2)
Space group       P 21/c                      P 1 21/c 1
Hall group        -P 2ybc                     -P 2ybc
Moiety formula    2(C15 H18 Au N4), 2(Cl), H2 2(C15 H18 Au N4), 2(Cl), H2
                  O                           O
Sum formula       C30 H38 Au2 Cl2 N8 O        C30 H38 Au2 Cl2 N8 O
Mr                991.52                      991.51
Dx,g cm-3         2.077                       2.077
Z                 4                           4
Mu (mm-1)         9.450                       9.450
F000              1896.0                      1896.0
F000'             1882.48
h,k,lmax          18,16,26                    18,16,26
Nref              8446                        8420
Tmin,Tmax         0.165,0.242                 0.575,0.747
Tmin'             0.139
Correction method= # Reported T Limits: Tmin=0.575 Tmax=0.747
AbsCorr = MULTI-SCAN

Data completeness= 0.997            Theta(max)= 29.000

                                                    wR2(reflections)=
R(reflections)= 0.0125( 7844)
                                                    0.0279( 8420)

S = 1.116                   Npar= 395
The following ALERTS were generated. Each ALERT has the
format        test-name_ALERT_alert-type_alert-level.
Click on the hyperlinks for more details of the test.
```

Alert level C

```
PLAT910_ALERT_3_C Missing # of FCF Reflection(s) Below Theta(Min).          9
Note
PLAT911_ALERT_3_C Missing FCF Refl Between Thmin & STh/L=    0.600         17
Report
```

Alert level G

```
PLAT007_ALERT_5_G Number of Unrefined Donor-H Atoms ..............          2
Report
PLAT199_ALERT_1_G Reported _cell_measurement_temperature ..... (K)        293
Check
PLAT200_ALERT_1_G Reported   _diffrn_ambient_temperature ..... (K)        293
Check
PLAT720_ALERT_4_G Number of Unusual/Non-Standard Labels ..........         16
Note
PLAT790_ALERT_4_G Centre of Gravity not Within Unit Cell: Resd.  #          3
Note
              Cl
PLAT794_ALERT_5_G Tentative Bond Valency for Au1A      (III)     .       3.33
Info
PLAT794_ALERT_5_G Tentative Bond Valency for Au1B      (III)     .       3.35
Info  PLAT883_ALERT_1_G No Info/Value for _atom_sites_solution_primary .
Please Do !
PLAT913_ALERT_3_G Missing # of Very Strong Reflections in FCF ....          1
Note
PLAT933_ALERT_2_G Number of HKL-OMIT Records in Embedded .res File         20
Note
PLAT967_ALERT_5_G Note: Two-Theta Cutoff Value in Embedded .res ..       58.0
Degree
PLAT978_ALERT_2_G Number C-C Bonds with Positive Residual Density.          8
Info
```

```
    0 ALERT level A = Most likely a serious problem - resolve or explain
    0 ALERT level B = A potentially serious problem, consider carefully
    2 ALERT level C = Check. Ensure it is not caused by an omission or oversight
   12 ALERT level G = General information/check it is not something unexpected

    3 ALERT type 1 CIF construction/syntax error, inconsistent or missing data
2   ALERT type 2 Indicator that the structure model may be wrong or deficient
3   ALERT type 3 Indicator that the structure quality may be low
    2 ALERT type 4 Improvement, methodology, query or suggestion
    4 ALERT type 5 Informative message, check
```

Validation response form

Please find below a validation response form (VRF) that can be filled in and pasted into your CIF.

```
# start Validation Reply Form
_vrf_PLAT910_aume2pr_ms_sx
;
PROBLEM: Missing # of FCF Reflection(s) Below Theta(Min).          9 Note
RESPONSE: ...
;
_vrf_PLAT911_aume2pr_ms
_sx
;
```

```
PROBLEM: Missing FCF Refl Between Thmin & STh/L=    0.600         17 Report
RESPONSE: ...
;
# end Validation Reply Form
```

It is advisable to attempt to resolve as many as possible of the alerts in all categories. Often the minor alerts point to easily fixed oversights, errors and omissions in your CIF or refinement strategy, so attention to these fine details can be worthwhile. In order to resolve some of the more serious problems it may be necessary to carry out additional measurements or structure refinements. However, the purpose of your study may justify the reported deviations and the more serious of these should normally be commented upon in the discussion or experimental section of a paper or in the "special_details" fields of the CIF. checkCIF was carefully designed to identify outliers and unusual parameters, but every test has its limitations and alerts that are not important in a particular case may appear. Conversely, the absence of alerts does not guarantee there are no aspects of the results needing attention. It is up to the individual to critically assess their own results and, if necessary, seek expert advice.

Publication of your CIF in IUCr journals

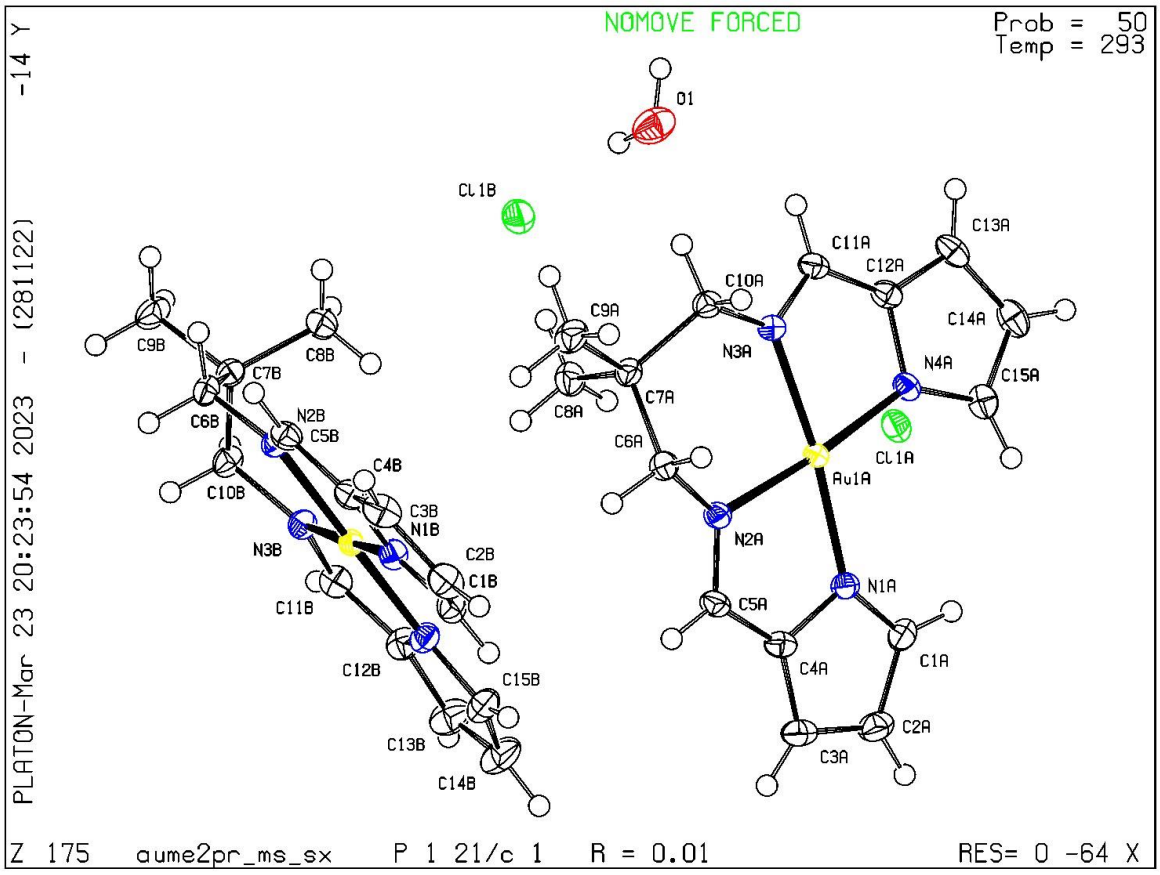
A basic structural check has been run on your CIF. These basic checks will be run on all CIFs submitted for publication in IUCr journals (*Acta Crystallographica*, *Journal of Applied Crystallography*, *Journal of Synchrotron Radiation*); however, if you intend to submit to *Acta Crystallographica Section C* or *E* or *IUCrData*, you should make sure that full publication checks are run on the final version of your CIF prior to submission.

Publication of your CIF in other journals

Please refer to the *Notes for Authors* of the relevant journal for any special instructions relating to CIF submission.

PLATON version of 28/11/2022; check.def file version of 28/11/2022

Datablock aume2pr_ms_sx - ellipsoid plot


NOMOVE FORCED
Prob = 50
Temp = 293
PLATON-Mar 23 20:23:54 2023 - (281122) -14 Y
O1
Cl1B
C9B
C8B
C7B
C6B
N2B
C5B
C4B
C10B
C3B
N1B
N3B
C2B
C1B
C11B
C12B
C15B
C13B
C14B
C13A
C11A
C12A
C10A
C14A
C9A
N3A
N4A
C15A
C8A
C7A
C6A
Cl1A
Au1A
N2A
N1A
C5A
C1A
C4A
C2A
C3A
Z 175 aume2pr_ms_sx P 1 21/c 1 R = 0.01
RES= 0 -64 X

CIF File Au(1S, 2S-CyHex)

checkCIF/PLATON report

Structure factors have been supplied for datablock(s) 19oa_ss_au_cyhex_1s2s_0m

THIS REPORT IS FOR GUIDANCE ONLY. IF USED AS PART OF A REVIEW PROCEDURE FOR PUBLICATION, IT SHOULD NOT REPLACE THE EXPERTISE OF AN EXPERIENCED CRYSTALLOGRAPHIC REFEREE.

No syntax errors found. CIF dictionary Interpreting this report

Datablock: 19oa_ss_au_cyhex_1s2s_0m

Bond precision: C-C = 0.0111 A Wavelength=0.71073

Cell:
a=10.1292(3) b=9.7663(3) c=18.4954(6) alpha=90
beta=94.364(2) gamma=90

Temperature: 173 K

	Calculated	Reported
Volume	1824.35(10)	1824.35(10)
Space group	P 21	P 1 21 1
Hall group	P 2yb	P 2yb
Moiety formula	C16 H18 Au N4, F6 P	C16 H18 Au N4, F6 P
Sum formula	C16 H18 Au F6 N4 P	C16 H18 Au F6 N4 P
Mr	608.28	608.28
Dx,g cm-3	2.215	2.215
Z	4	4
Mu (mm-1)	8.220	8.220
F000	1160.0	1160.0
F000'	1153.31	
h,k,lmax	14,13,25	14,13,25
Nref	10354[5463]	10265
Tmin,Tmax	0.303,0.466	0.508,0.793
Tmin'	0.095	

Correction method= # Reported T Limits: Tmin=0.508 Tmax=0.793
AbsCorr = NUMERICAL

Data completeness= 1.88/0.99 Theta(max)= 29.671

R(reflections)= 0.0256(8748) wR2(reflections)= 0.0440(10265)

S = 0.968 Npar= 580

The following ALERTS were generated. Each ALERT has the format **test-name_ALERT_alert-type_alert-level**. Click on the hyperlinks for more details of the test.

Alert level C

```
PLAT342_ALERT_3_C Low Bond Precision on  C-C Bonds ..............    0.01114 Ang.
```

Alert level G

```
PLAT003_ALERT_2_G Number of Uiso or Uij Restrained non-H Atoms ...         16
Report
PLAT111_ALERT_2_G ADDSYM Detects New (Pseudo) Centre of Symmetry .        100 %Fit
PLAT112_ALERT_2_G ADDSYM Detects New (Pseudo) Symm. Elem         c         83 %Fit
PLAT113_ALERT_2_G ADDSYM Suggests Possible Pseudo/New  Space Group      P21/c Check
              Check Model Parameter Symmmetry for Reflection Data Support
PLAT186_ALERT_4_G The CIF-Embedded .res File Contains ISOR Records          2
Report
PLAT244_ALERT_4_G Low    'Solvent' Ueq as Compared to Neighbors of        P1A Check
PLAT244_ALERT_4_G Low    'Solvent' Ueq as Compared to Neighbors of        P1B Check
PLAT302_ALERT_4_G Anion/Solvent/Minor-Residue Disorder (Resd  3  )        57% Note
PLAT302_ALERT_4_G Anion/Solvent/Minor-Residue Disorder (Resd  4  )         57%
Note  PLAT432_ALERT_2_G Short Inter X...Y Contact  F4A     ..C5B     .      2.75
Ang.                                                    x,y,1+z  =      1_556
Check PLAT432_ALERT_2_G Short Inter X...Y Contact  F6B'    ..C12A    .      2.75
Ang.                                                      x,y,z  =      1_555
Check PLAT432_ALERT_2_G Short Inter X...Y Contact  F6B     ..C12A    .      2.78
Ang.                                                      x,y,z  =      1_555
Check PLAT720_ALERT_4_G Number of Unusual/Non-Standard Labels .........       20
Note
PLAT791_ALERT_4_G Model has Chirality at C6A         (Sohnke SpGr)          S
Verify
PLAT791_ALERT_4_G Model has Chirality at C6B         (Sohnke SpGr)          S
Verify
PLAT791_ALERT_4_G Model has Chirality at C11A        (Sohnke SpGr)          S
Verify
PLAT791_ALERT_4_G Model has Chirality at C11B        (Sohnke SpGr)          S
Verify
PLAT794_ALERT_5_G Tentative Bond Valency for Au1A      (III)     .       3.47 Info
PLAT794_ALERT_5_G Tentative Bond Valency for Au1B      (III)     .       3.41 Info
PLAT850_ALERT_4_G Check Flack Parameter Exact Value 0.00 with s.u.       0.00 Check
PLAT860_ALERT_3_G Number of Least-Squares Restraints .............         97 Note
PLAT870_ALERT_4_G ALERTS Related to Twinning Effects Suppressed ..          ! Info
PLAT912_ALERT_4_G Missing # of FCF Reflections Above STh/L=  0.600         23 Note
PLAT933_ALERT_2_G Number of HKL-OMIT Records in Embedded .res File          3 Note
```

```
    0 ALERT level A = Most likely a serious problem - resolve or explain
0   ALERT level B = A potentially serious problem, consider carefully
1   ALERT level C = Check. Ensure it is not caused by an omission or oversight
   24 ALERT level G = General information/check it is not something unexpected

    0 ALERT type 1 CIF construction/syntax error, inconsistent or missing data
    8 ALERT type 2 Indicator that the structure model may be wrong or deficient
    2 ALERT type 3 Indicator that the structure quality may be low
   13 ALERT type 4 Improvement, methodology, query or suggestion
    2 ALERT type 5 Informative message, check
```

It is advisable to attempt to resolve as many as possible of the alerts in all categories. Often the minor alerts point to easily fixed oversights, errors and omissions in your CIF or refinement strategy, so attention to these fine details can be worthwhile. In order to resolve some of the more serious problems it may be necessary to carry out additional measurements or structure refinements. However, the purpose of your study may justify the reported deviations and the more serious of these should normally be commented upon in the discussion or experimental section of a paper or in the "special_details" fields of the CIF. checkCIF was carefully designed to identify outliers and unusual parameters, but every test has its limitations and alerts that are not important in a particular

case may appear. Conversely, the absence of alerts does not guarantee there are no aspects of the results needing attention. It is up to the individual to critically assess their own results and, if necessary, seek expert advice.

Publication of your CIF in IUCr journals

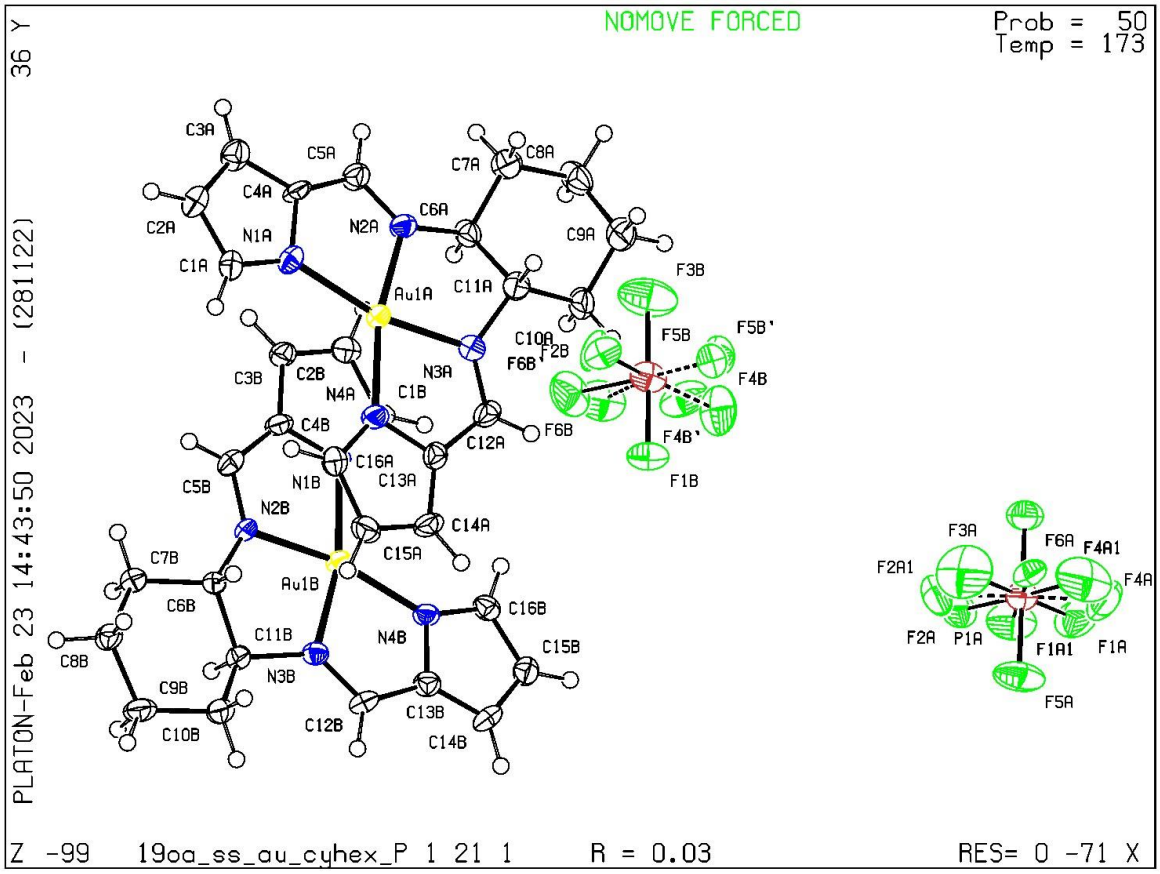
A basic structural check has been run on your CIF. These basic checks will be run on all CIFs submitted for publication in IUCr journals (*Acta Crystallographica*, *Journal of Applied Crystallography*, *Journal of Synchrotron Radiation*); however, if you intend to submit to *Acta Crystallographica Section C* or *E* or *IUCrData*, you should make sure that full publication checks are run on the final version of your CIF prior to submission.

Publication of your CIF in other journals

Please refer to the *Notes for Authors* of the relevant journal for any special instructions relating to CIF submission.

PLATON version of 28/11/2022; check.def file version of 28/11/2022

Datablock 19oa_ss_au_cyhex_1s2s_0m - ellipsoid plot



CIF File Au(1R, 2R-CyHex)

checkCIF/PLATON report

Structure factors have been supplied for datablock(s) Au1R2RL2PF6

THIS REPORT IS FOR GUIDANCE ONLY. IF USED AS PART OF A REVIEW PROCEDURE FOR PUBLICATION, IT SHOULD NOT REPLACE THE EXPERTISE OF AN EXPERIENCED CRYSTALLOGRAPHIC REFEREE.

No syntax errors found. CIF dictionary Interpreting this report

Datablock: Au1R2RL2PF6

Bond precision: C-C = 0.0076 A Wavelength=0.71073

Cell: a=10.3951(2) b=18.2575(3) c=10.0206(2)
alpha=90 beta=90 gamma=90

Temperature: 100 K

	Calculated	Reported
Volume	1901.80(6)	1901.80(6)
Space group	P 21 2 21	P 21 2 21
Hall group	P 2ac 2ac	P 2ac 2ac
Moiety formula	C16 H18 Au N4, F6 P	C16 H18 Au N4, F6 P
Sum formula	C16 H18 Au F6 N4 P	C16 H18 Au F6 N4 P
Mr	608.28	608.28
Dx,g cm-3	2.125	2.124
Z	4	4
Mu (mm-1)	7.886	7.886
F000	1160.0	1155.5
F000’	1153.31	
h,k,lmax	16,28,15	15,28,15
Nref	7916[4416]	7216
Tmin,Tmax	0.164,0.454	0.089,0.510
Tmin’	0.008	

Correction method= # Reported T Limits: Tmin=0.089 Tmax=0.510 AbsCorr = MULTI-SCAN

Data completeness= 1.63/0.91 Theta(max)= 34.260

R(reflections)= 0.0456(5766) wR2(reflections)= 0.1433(7216)

S = 1.046 Npar= 255

The following ALERTS were generated. Each ALERT has the format **test-name_ALERT_alert-type_alert-level**. Click on the hyperlinks for more details of the test.

Alert level C

PLAT068_ALERT_1_C Reported F000 Differs from Calcd (or Missing)... Please Check

PLAT910_ALERT_3_C Missing # of FCF Reflection(s) Below Theta(Min). 5 Note

PLAT911_ALERT_3_C Missing FCF Refl Between Thmin & STh/L= 0.600 5 Report

Alert level G

PLAT073_ALERT_1_G H-atoms ref, but _hydrogen_treatment Reported as constr Check

PLAT111_ALERT_2_G ADDSYM Detects New (Pseudo) Centre of Symmetry . 100 %Fit

PLAT112_ALERT_2_G ADDSYM Detects New (Pseudo) Symm. Elem n 86 %Fit

PLAT112_ALERT_2_G ADDSYM Detects New (Pseudo) Symm. Elem b 86 %Fit

PLAT112_ALERT_2_G ADDSYM Detects New (Pseudo) Symm. Elem c 86 %Fit

PLAT113_ALERT_2_G ADDSYM Suggests Possible Pseudo/New Space Group Pbcn Check

Check Model Parameter Symmmetry for Reflection Data Support

PLAT244_ALERT_4_G Low 'Solvent' Ueq as Compared to Neighbors of P1 Check

PLAT244_ALERT_4_G Low 'Solvent' Ueq as Compared to Neighbors of P2 Check

PLAT720_ALERT_4_G Number of Unusual/Non-Standard Labels ..... 8 Note

PLAT791_ALERT_4_G Model has Chirality at C6A (Sohnke SpGr) R Verify

PLAT791_ALERT_4_G Model has Chirality at C6B (Sohnke SpGr) R Verify

PLAT794_ALERT_5_G Tentative Bond Valency for Au1A (III) . 3.39 Info

PLAT794_ALERT_5_G Tentative Bond Valency for Au1B (III) . 3.49 Info

PLAT802_ALERT_4_G CIF Input Record(s) with more than 80 Characters 1 Info

PLAT912_ALERT_4_G Missing # of FCF Reflections Above STh/L= 0.600 270 Note

PLAT933_ALERT_2_G Number of HKL-OMIT Records in Embedded .res File 6 Note

PLAT960_ALERT_3_G Number of Intensities with I < - 2*sig(I) ... 8 Check

PLAT978_ALERT_2_G Number C-C Bonds with Positive Residual Density. 0 Info

PLAT979_ALERT_1_G NoSpherA2 Scattering Factors Used ..... Please Note

0 **ALERT level A** = Most likely a serious problem - resolve or explain

0 **ALERT level B** = A potentially serious problem, consider carefully

3 **ALERT level C** = Check. Ensure it is not caused by an omission or oversight

19 **ALERT level G** = General information/check it is not something unexpected

3 ALERT type 1 CIF construction/syntax error, inconsistent or missing data 7 ALERT type 2 Indicator that the structure model may be wrong or deficient

3 ALERT type 3 Indicator that the structure quality may be low 7 ALERT type 4 Improvement, methodology, query or suggestion

2 ALERT type 5 Informative message, check

It is advisable to attempt to resolve as many as possible of the alerts in all categories. Often the minor alerts point to easily fixed oversights, errors and omissions in your CIF or refinement strategy, so attention to these fine details can be worthwhile. In order to resolve some of the more serious problems it may be necessary to carry out additional measurements or structure refinements. However, the purpose of your study may justify the reported deviations and the more serious of these should normally be commented upon in the discussion or experimental section of a paper or in the "special_details" fields of the CIF. checkCIF was carefully designed to identify outliers and unusual parameters, but every test has its limitations and alerts that are not important in a particular case may appear. Conversely, the absence of alerts does not guarantee there are no aspects of the results needing attention. It is up to the individual to critically assess their own results and, if necessary, seek expert advice.

Publication of your CIF in IUCr journals

A basic structural check has been run on your CIF. These basic checks will be run on all CIFs submitted for publication in IUCr journals (*Acta Crystallographica*, *Journal of Applied*

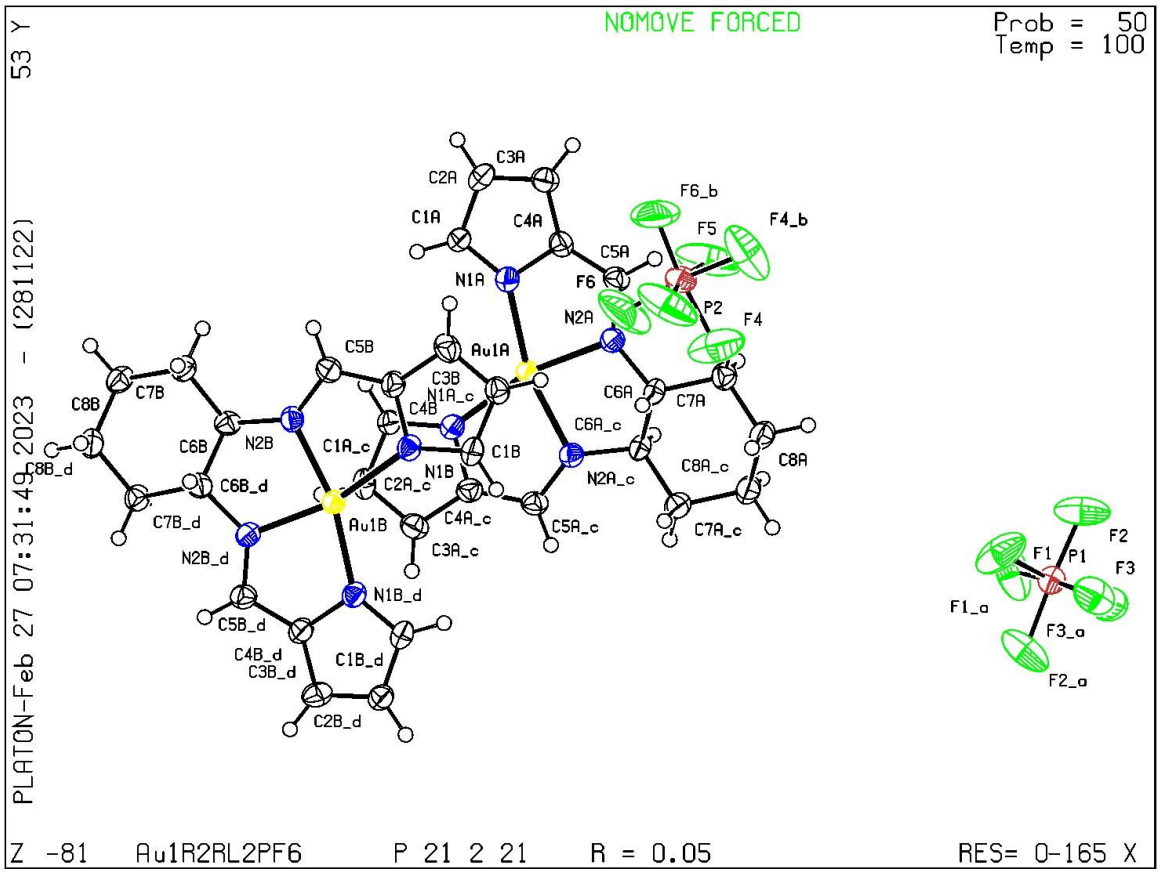
Crystallography, *Journal of Synchrotron Radiation*); however, if you intend to submit to *Acta Crystallographica Section C* or *E* or *IUCrData*, you should make sure that full publication checks are run on the final version of your CIF prior to submission.

Publication of your CIF in other journals

Please refer to the *Notes for Authors* of the relevant journal for any special instructions relating to CIF submission.

PLATON version of 28/11/2022; check.def file version of 28/11/2022

Datablock Au1R2RL2PF6 - ellipsoid plot


NOMOVE FORCED
Prob = 50
Temp = 100
53 Y
PLATON-Feb 27 07:31:49 2023 - (281122)
Z -81 Au1R2RL2PF6 P 21 2 21 R = 0.05 RES= 0-165 X
C3A
C2A
C1A
C4A
F6_b
F5
F4_b
C5A
N1A
F6
P2
F4
N2A
C5B
Au1A
C3B
N1A_c
C4B
C6A
C7A
C8B
C7B
C6A_c
C6B
N2B
C1A_c
C1B
C8A
C8B_d
N1B
N2A_c
C8A_c
C6B_d
C2A_c
C7B_d
Au1B
C4A_c
C5A_c
C7A_c
C3A_c
N2B_d
N1B_d
C5B_d
C4B_d
C3B_d
C1B_d
C2B_d
F2
F1
P1
F3
F1_a
F3_a
F2_a

CIF File Pt(II) chelate 2

checkCIF (basic structural check) running

Checking for embedded fcf data in CIF ...
Found embedded fcf data in CIF. Extracting fcf data from uploaded CIF, please wait .....

checkCIF/PLATON (basic structural check)

Structure factors have been supplied for datablock(s) 21ma_SS_PtMe2PrPyrr

THIS REPORT IS FOR GUIDANCE ONLY. IF USED AS PART OF A REVIEW PROCEDURE FOR PUBLICATION, IT SHOULD NOT REPLACE THE EXPERTISE OF AN EXPERIENCED CRYSTALLOGRAPHIC REFEREE.

No syntax errors found. CIF dictionary
Please wait while processing .... Interpreting this repor t

Structure factor report

Datablock: 21ma_SS_PtMe2PrPyrr

```
Bond precision:  C-C = 0.0071 A          Wavelength=0.71073
Cell:   a=13.7803(5)  b=15.2877(5)  c=16.8165(6)
       alpha=103.788(2)beta=104.926(2)gamma=107.795(2)
 Temperature:173 K
                Calculated                  Reported
Volume          3059.8(2)                  3059.76(19)
Space group      P -1                       P -1
Hall group       -P 1                       -P 1
Moiety formulaC15 H18 N4 Pt [+ solvent]    C15 H18 N4 Pt
Sum formula   C15 H18 N4 Pt [+ solvent]    C15 H18 N4 Pt
Mr              449.41                     449.42
Dx,g cm-3       1.951                      1.951
Z                8                          8
```

Mu (mm-1)	9.167	9.167
F000	1712.0	1712.0
F000'	1699.67	
h,k,lmax	19,21,24	19,21,24
Nref	18775	18723
Tmin,Tmax	0.185,0.498	0.222,0.568
Tmin'	0.115	

Correction method= # Reported T Limits: Tmin=0.222 Tmax=0.568 AbsCorr = NUMERICAL

Data completeness= 0.997 Theta(max)= 30.565

wR2(reflections)= 0.0590(18723)

R(reflections)= 0.0327(13600)

S = 1.004 Npar= 729

The following ALERTS were generated. Each ALERT has the format **test-name_ALERT_alert-type_alert-level**.

Click on the hyperlinks for more details of the test.

Alert level C

PLAT905_ALERT_3_C Negative K value in the Analysis of Variance ... -0.199 Report

PLAT977_ALERT_2_C Check Negative Difference Density on H12A -0.33 eA-3

Alert level G

PLAT154_ALERT_1_G The s.u.'s on the Cell Angles are Equal ..(Note) 0.002 Degree

PLAT605_ALERT_4_G Largest Solvent Accessible VOID in the Structure 100 A**3

PLAT720_ALERT_4_G Number of Unusual/Non-Standard Labels ..... 16 Note

PLAT794_ALERT_5_G Tentative Bond Valency for Pt1A (II) . 2.34 Info

And 3 other PLAT794 Alerts More ...

PLAT868_ALERT_4_G ALERTS Due to the Use of _smtbx_masks Suppressed ! Info

PLAT910_ALERT_3_G Missing # of FCF Reflection(s) Below Theta(Min). 1 Note

PLAT912_ALERT_4_G Missing # of FCF Reflections Above STh/L= 0.600 53 Note

PLAT978_ALERT_2_G Number C-C Bonds with Positive Residual Density. 0 Info

---

0 **ALERT level A** = Most likely a serious problem - resolve or explain

0 **ALERT level B** = A potentially serious problem, consider carefully

2 **ALERT level C** = Check. Ensure it is not caused by an omission or oversight

11 **ALERT level G** = General information/check it is not something unexpected

1 ALERT type 1 CIF construction/syntax error, inconsistent or missing data
2 ALERT type 2 Indicator that the structure model may be wrong or deficient
2 ALERT type 3 Indicator that the structure quality may be low
4 ALERT type 4 Improvement, methodology, query or suggestion
4 ALERT type 5 Informative message, check

It is advisable to attempt to resolve as many as possible of the alerts in all categories. Often the minor alerts point to easily fixed oversights, errors and omissions in your CIF or refinement strategy, so attention to these fine details can be worthwhile. In order to resolve some of the more serious problems it may be necessary to carry out additional measurements or structure refinements. However, the purpose of your study may justify the reported deviations and the more serious of these should normally be commented upon in the discussion or experimental section of a paper or in the "special_details" fields of the CIF. checkCIF was carefully designed to identify outliers and unusual parameters, but every test has its limitations and alerts that are not important in a particular case may appear. Conversely, the absence of alerts does not guarantee there are no aspects of the results needing attention. It is up to the individual to critically assess their own results and, if necessary, seek expert advice.

Publication of your CIF in IUCr journals

A basic structural check has been run on your CIF. These basic checks will be run on all CIFs submitted for publication in IUCr journals (*Acta Crystallographica*, *Journal of Applied Crystallography*, *Journal of*

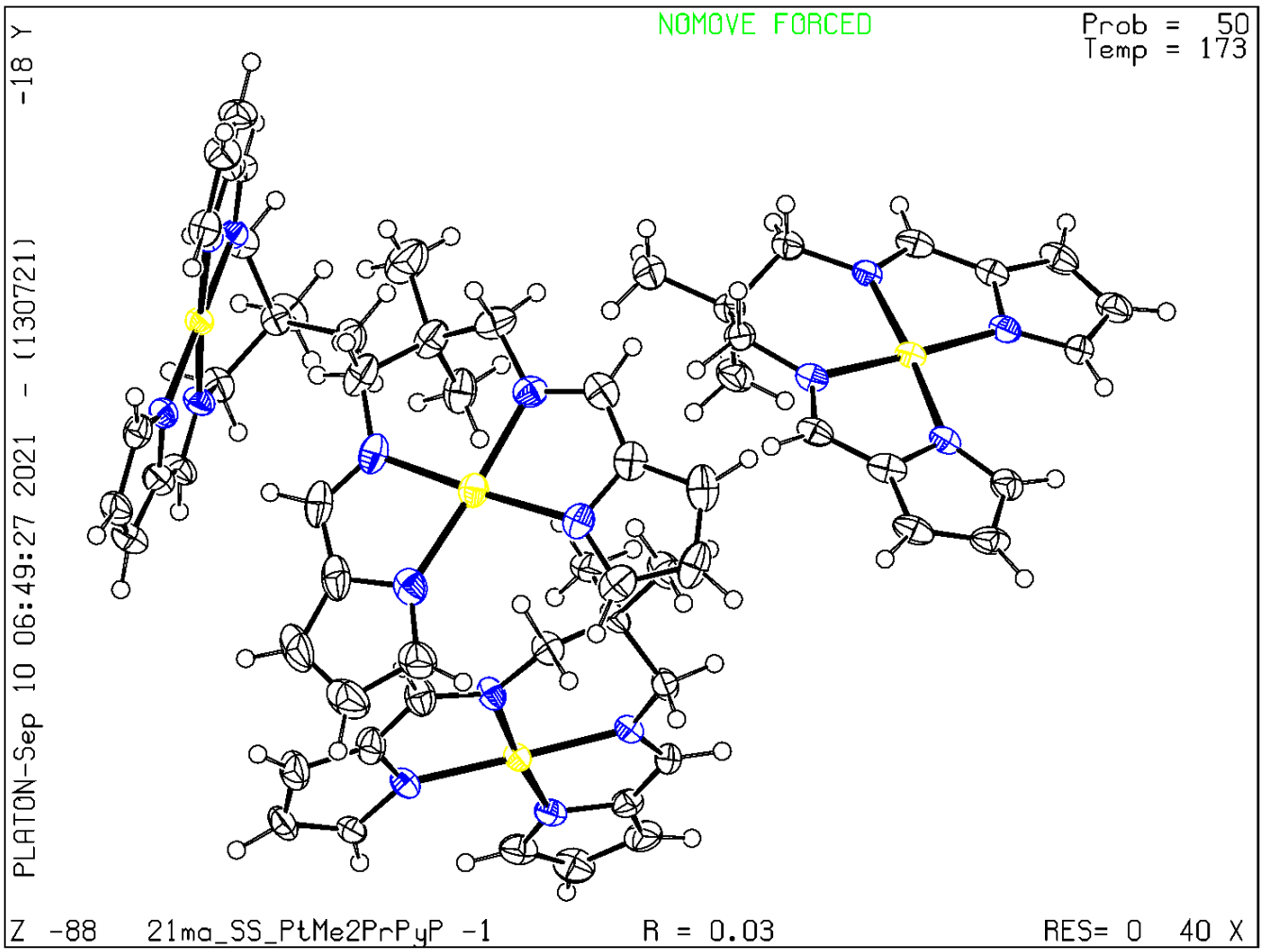
Synchrotron Radiation); however, if you intend to submit to *Acta Crystallographica Section C* or *E* or *IUCrData*, you should make sure that full publication checks are run on the final version of your CIF prior to submission.

Publication of your CIF in other journals

Please refer to the *Notes for Authors* of the relevant journal for any special instructions relating to CIF submission.

PLATON version of 13/07/2021; check.def file version of 13/07/2021

Datablock 21ma_SS_PtMe2PrPyrr - ellipsoid plot



Download CIF editor (publCIF) from the IUCr
Download CIF editor (enCIFer) from the CCDC
Test a new CIF entry

checkCIF (basic structural check) running

Checking for embedded fcf data in CIF ...

Found embedded fcf data in CIF. Extracting fcf data from uploaded CIF, please wait .....

checkCIF/PLATON (basic structural check)

Structure factors have been supplied for datablock(s) mo_21ov_ss_ptprohpyrr_2_0m

THIS REPORT IS FOR GUIDANCE ONLY. IF USED AS PART OF A REVIEW PROCEDURE FOR PUBLICATION, IT SHOULD NOT REPLACE THE EXPERTISE OF AN EXPERIENCED CRYSTALLOGRAPHIC REFEREE.

No syntax errors found. CIF dictionary

Please wait while processing .... Interpreting this repor t

Structure factor report

CIF File Pt(II) chelate 1

Datablock: mo_21ov_ss_ptprohpyrr_2_0m

```
Bond precision:  C-C = 0.0066 A           Wavelength=0.71073
Cell:   a=9.0752(19)   b=12.639(3)    c=18.870(3)
       alpha=108.653(7)beta=90.856(8)gamma=96.322(9)
 Temperature:173 K
                Calculated                  Reported
Volume          2035.4(7)                   2035.3(7)
Space group      P -1                        P -1
Hall group       -P 1                        -P 1
Moiety formulaC13 H14 N4 O Pt [+ solvent]  C13 H14 N4 O Pt
Sum formula   C13 H14 N4 O Pt [+ solvent]   C13 H14 N4 O Pt
Mr              437.36                      437.37
Dx,g cm-3       2.141                       2.141
Z                6                           6
Mu (mm-1)       10.338                      10.338
F000            1236.0                      1236.0
F000'           1226.82
h,k,lmax        14,19,29                    13,19,29
Nref            15709                       15567
Tmin,Tmax       0.543,0.596                 0.252,0.568
Tmin'           0.154
 Correction method= # Reported T Limits: Tmin=0.252 Tmax=0.568 AbsCorr =
NUMERICAL
Data completeness= 0.991  Theta(max)= 33.284
                        wR2(reflections)= 0.0689(
 R(reflections)= 0.0308( 12755)
                                  15567)
S = 1.050          Npar= 514
```

The following ALERTS were generated. Each ALERT has the format **test-name_ALERT_alert-type_alert-level**.

Click on the hyperlinks for more details of the test.

Alert level C

PLAT910_ALERT_3_C Missing # of FCF Reflection(s) Below Theta(Min). 5 Note

PLAT911_ALERT_3_C Missing FCF Refl Between Thmin & STh/L= 0.600 11 Report
PLAT934_ALERT_3_C Number of (Iobs-Icalc)/Sigma(W) > 10 Outliers .. 1 Check
PLAT977_ALERT_2_C Check Negative Difference Density on H1C -0.60 eA-3
And 2 other PLAT977 Alerts More ...

Alert level G

PLAT007_ALERT_5_G Number of Unrefined Donor-H Atoms ..... 3 Report

PLAT605_ALERT_4_G Largest Solvent Accessible VOID in the Structure 150 A**3

PLAT720_ALERT_4_G Number of Unusual/Non-Standard Labels ..... 15 Note

PLAT793_ALERT_4_G Model has Chirality at C7A (Centro SPGR) S Verify **And 2 other PLAT793 Alerts** More ...

PLAT794_ALERT_5_G Tentative Bond Valency for Pt1A (II) . 2.35 Info **And 2 other PLAT794 Alerts** More ...

PLAT868_ALERT_4_G ALERTS Due to the Use of _smtbx_masks Suppressed ! Info

PLAT912_ALERT_4_G Missing # of FCF Reflections Above STh/L= 0.600 123 Note

PLAT913_ALERT_3_G Missing # of Very Strong Reflections in FCF .... 1 Note

PLAT933_ALERT_2_G Number of OMIT Records in Embedded .res File ... 12 Note

PLAT978_ALERT_2_G Number C-C Bonds with Positive Residual Density. 0 Info

0 **ALERT level A** = Most likely a serious problem - resolve or explain

0 **ALERT level B** = A potentially serious problem, consider carefully

6 **ALERT level C** = Check. Ensure it is not caused by an omission or oversight

14 **ALERT level G** = General information/check it is not something unexpected

0 ALERT type 1 CIF construction/syntax error, inconsistent or missing data

5 ALERT type 2 Indicator that the structure model may be wrong or deficient

4 ALERT type 3 Indicator that the structure quality may be low

7 ALERT type 4 Improvement, methodology, query or suggestion

4 ALERT type 5 Informative message, check

It is advisable to attempt to resolve as many as possible of the alerts in all categories. Often the minor alerts point to easily fixed oversights, errors and omissions in your CIF or refinement strategy, so attention to these fine details can be worthwhile. In order to resolve some of the more serious problems it may be necessary to carry out additional measurements or structure refinements. However, the purpose of your study may justify the reported deviations and the more serious of these should normally be commented upon in the discussion or experimental section of a paper or in the "special_details" fields of the CIF. checkCIF was carefully designed to identify outliers and unusual parameters, but every test has its limitations and alerts that are not important in a particular case may appear. Conversely, the absence of alerts does not guarantee there are no aspects of the results needing attention. It is up to the individual to critically assess their own results and, if necessary, seek expert advice.

Publication of your CIF in IUCr journals

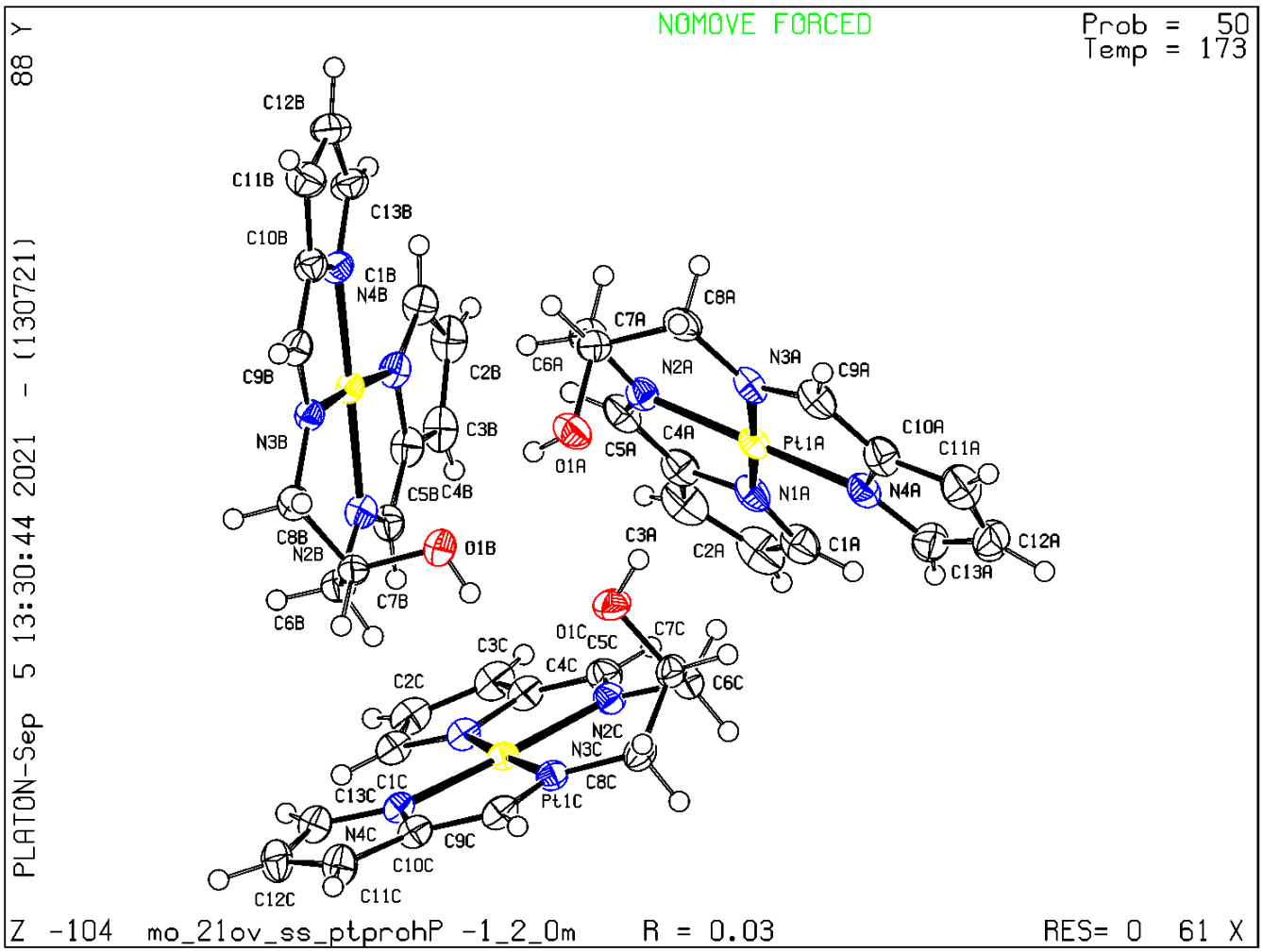
A basic structural check has been run on your CIF. These basic checks will be run on all CIFs submitted for publication in IUCr journals (*Acta Crystallographica*, *Journal of Applied Crystallography*, *Journal of Synchrotron Radiation*); however, if you intend to submit to *Acta Crystallographica Section C* or *E* or *IUCrData*, you should make sure that full publication checks are run on the final version of your CIF prior to submission.

Publication of your CIF in other journals

Please refer to the *Notes for Authors* of the relevant journal for any special instructions relating to CIF submission.

PLATON version of 13/07/2021; check.def file version of 13/07/2021

Datablock mo_21ov_ss_ptprohpyrr_2_0m - ellipsoid plot



Download CIF editor (publCIF) from the IUCr
Download CIF editor (enCIFer) from the CCDC
Test a new CIF entry

CIF File Pt(PrPyrr)

checkCIF/PLATON report

Structure factors have been supplied for datablock(s) mo_21ov_ss_ptprpyrr_2_0m

THIS REPORT IS FOR GUIDANCE ONLY. IF USED AS PART OF A REVIEW PROCEDURE FOR PUBLICATION, IT SHOULD NOT REPLACE THE EXPERTISE OF AN EXPERIENCED CRYSTALLOGRAPHIC REFEREE.

No syntax errors found. CIF dictionary Interpreting this report

Datablock: mo_21ov_ss_ptprpyrr_2_0m

Bond precision:	C-C = 0.0076 A	Wavelength=0.71073	
Cell:	a=8.0540(3)	b=16.8279(5)	c=36.8486(12)
	alpha=90	beta=90.720(1)	gamma=90
Temperature:	173 K		

	Calculated	Reported
Volume	4993.8(3)	4993.8(3)
Space group	P 21/c	P 1 21/c 1
Hall group	-P 2ybc	-P 2ybc
Moiety formula	C13 H14 N4 Pt	C13 H14 N4 Pt
Sum formula	C13 H14 N4 Pt	C13 H14 N4 Pt
Mr	421.36	421.37
Dx,g cm-3	2.242	2.242
Z	16	16
Mu (mm-1)	11.226	11.226
F000	3168.0	3168.0
F000’	3143.47	
h,k,lmax	11,24,52	11,24,52
Nref	15554	15408
Tmin,Tmax	0.152,0.217	0.605,0.746
Tmin’	0.064	

Correction method= # Reported T Limits: Tmin=0.605 Tmax=0.746

AbsCorr = MULTI-SCAN

Data completeness= 0.991 Theta(max)= 30.719

wR2(reflections)=

R(reflections)= 0.0333(14131)

0.0587(15408)

S = 1.307 Npar= 650

The following ALERTS were generated. Each ALERT has the format **test-name_ALERT_alert-type_alert-level**. Click on the hyperlinks for more details of the test.

Alert level B

PLAT972_ALERT_2_B Check Calcd Resid. Dens. 0.87Ang From N2A -2.71 eA-3

Alert level C

PLAT906_ALERT_3_C Large K Value in the Analysis of Variance ..... 4.319 Check

PLAT910_ALERT_3_C Missing # of FCF Reflection(s) Below Theta(Min). 8 Note

PLAT911_ALERT_3_C Missing FCF Refl Between Thmin & STh/L= 0.600 17 Report

PLAT913_ALERT_3_C Missing # of Very Strong Reflections in FCF .... 4 Note

PLAT971_ALERT_2_C Check Calcd Resid. Dens. 0.91Ang From Pt1A 1.69 eA-3

PLAT972_ALERT_2_C Check Calcd Resid. Dens. 1.13Ang From N4B -2.04 eA-3

PLAT972_ALERT_2_C Check Calcd Resid. Dens. 1.93Ang From Pt1C -1.76 eA-3

PLAT972_ALERT_2_C Check Calcd Resid. Dens. 0.80Ang From N1C -1.75 eA-3

PLAT972_ALERT_2_C Check Calcd Resid. Dens. 1.13Ang From N4B -1.73 eA-3

PLAT972_ALERT_2_C Check Calcd Resid. Dens. 0.64Ang From Pt1A -1.55 eA-3

Alert level G

PLAT083_ALERT_2_G SHELXL Second Parameter in WGHT Unusually Large 22.17 Why ?

PLAT720_ALERT_4_G Number of Unusual/Non-Standard Labels ..... 24 Note

PLAT794_ALERT_5_G Tentative Bond Valency for Pt1A (II) . 2.35 Info

PLAT794_ALERT_5_G Tentative Bond Valency for Pt1B (II) . 2.36 Info

PLAT794_ALERT_5_G Tentative Bond Valency for Pt1C (II) . 2.33 Info

PLAT794_ALERT_5_G Tentative Bond Valency for Pt1D (II) . 2.34 Info

PLAT912_ALERT_4_G Missing # of FCF Reflections Above STh/L= 0.600 121 Note

PLAT933_ALERT_2_G Number of HKL-OMIT Records in Embedded .res File 10 Note

PLAT978_ALERT_2_G Number C-C Bonds with Positive Residual Density. 0 Info

0 **ALERT level A** = Most likely a serious problem - resolve or explain

1 **ALERT level B** = A potentially serious problem, consider carefully

10 **ALERT level C** = Check. Ensure it is not caused by an omission or oversight

9 **ALERT level G** = General information/check it is not something unexpected

0 ALERT type 1 CIF construction/syntax error, inconsistent or missing data

10 ALERT type 2 Indicator that the structure model may be wrong or deficient

4 ALERT type 3 Indicator that the structure quality may be low

2 ALERT type 4 Improvement, methodology, query or suggestion 4
ALERT type 5 Informative message, check

Validation response form

Please find below a validation response form (VRF) that can be filled in and pasted into your CIF.

start Validation Reply Form

_vrf_PLAT972_mo_21ov_ss_ptprpyrr_2_0m

;

PROBLEM: Check Calcd Resid. Dens. 0.87Ang From N2A -2.71 eA-3 RESPONSE: ...

;

_vrf_PLAT906_mo_21ov_ss_ptprpyrr_2_0m

;

PROBLEM: Large K Value in the Analysis of Variance ..... 4.319 Check RESPONSE: ...

;

_vrf_PLAT910_mo_21ov_ss_ptprpyrr_2_0m

;

PROBLEM: Missing # of FCF Reflection(s) Below Theta(Min). 8 Note RESPONSE: ...

;

_vrf_PLAT911_mo_21ov_ss_ptprpyrr_2_0m

;

PROBLEM: Missing FCF Refl Between Thmin & STh/L= 0.600 17 Report RESPONSE: ...

;

_vrf_PLAT913_mo_21ov_ss_ptprpyrr_2_0m

;

PROBLEM: Missing # of Very Strong Reflections in FCF .... 4 Note RESPONSE: ...

;

_vrf_PLAT971_mo_21ov_ss_ptprpyrr_2_0m

;

PROBLEM: Check Calcd Resid. Dens. 0.91Ang From Pt1A 1.69 eA-3 RESPONSE: ...

;

end Validation Reply Form

It is advisable to attempt to resolve as many as possible of the alerts in all categories. Often the minor alerts point to easily fixed oversights, errors and omissions in your CIF or refinement strategy, so attention to these fine details can be worthwhile. In order to resolve some of the more serious problems it may be necessary to carry out additional measurements or structure refinements. However, the purpose of your study may justify the reported deviations and the more serious of these should normally be commented upon in the discussion or experimental section of a paper or in the "special_details" fields of the CIF. checkCIF was carefully designed to identify outliers and unusual parameters, but every test has its limitations and alerts that are not important in a particular case may appear. Conversely, the absence of alerts does not guarantee there are no aspects of the results needing attention. It is up to the individual to critically assess their own results and, if necessary, seek expert advice.

Publication of your CIF in IUCr journals

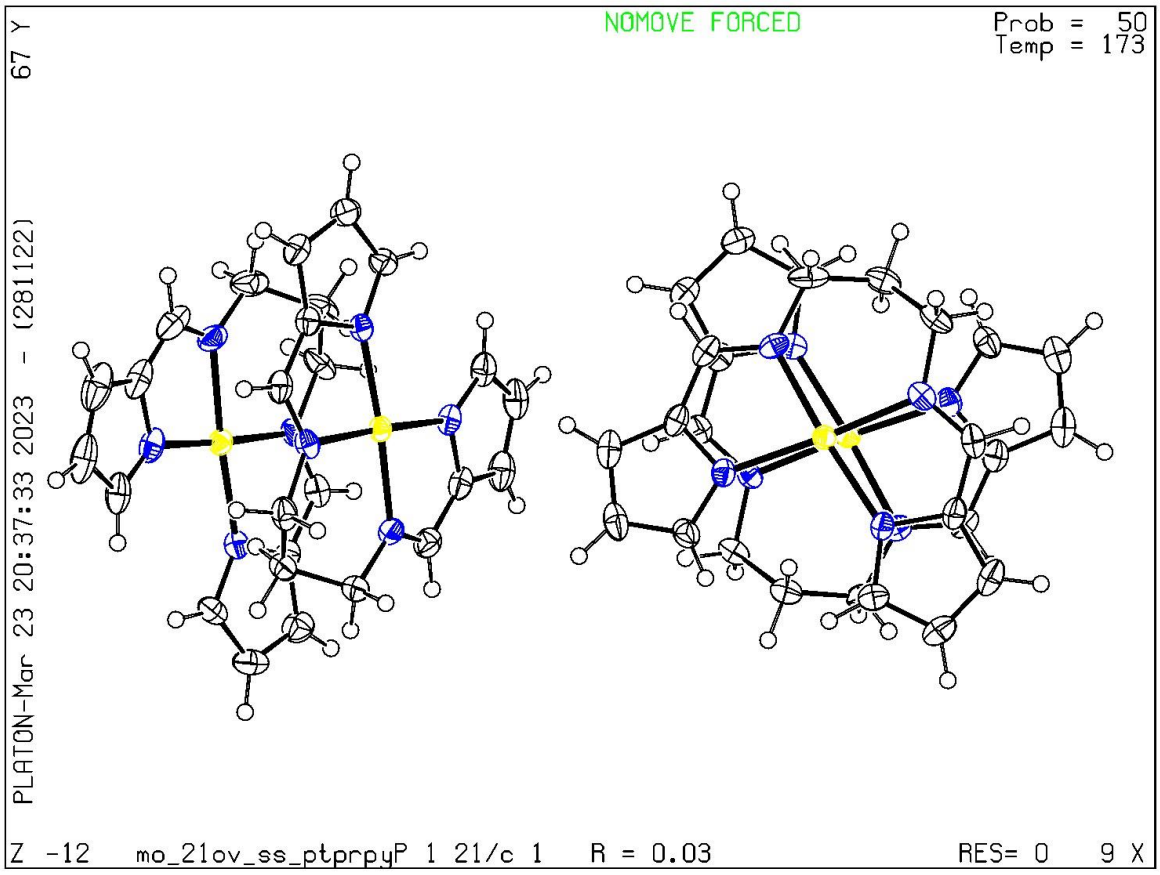
A basic structural check has been run on your CIF. These basic checks will be run on all CIFs submitted for publication in IUCr journals (*Acta Crystallographica*, *Journal of Applied Crystallography*, *Journal of Synchrotron Radiation*); however, if you intend to submit to *Acta Crystallographica Section C* or *E* or *IUCrData*, you should make sure that full publication checks are run on the final version of your CIF prior to submission.

Publication of your CIF in other journals

Please refer to the *Notes for Authors* of the relevant journal for any special instructions relating to CIF submission.

PLATON version of 28/11/2022; check.def file version of 28/11/2022

Datablock mo_21ov_ss_ptprpyrr_2_0m - ellipsoid plot


NOMOVE FORCED
Prob = 50
Temp = 173
67 Y
PLATON-Mar 23 20:37:33 2023 - (281122)
Z -12 mo_21ov_ss_ptprpyP 1 21/c 1 R = 0.03
RES= 0 9 X